



UNIVERSITY OF IOANNINA
SCHOOL OF SCIENCES
PHYSICS DEPARTMENT

Cosmological Observational Constraints on Modified Gravity Theories

Foteini Skara

PH.D. THESIS

IOANNINA 2022



ΠΑΝΕΠΙΣΤΗΜΙΟ ΙΩΑΝΝΙΝΩΝ
ΣΧΟΛΗ ΘΕΤΙΚΩΝ ΕΠΙΣΤΗΜΩΝ
ΤΜΗΜΑ ΦΥΣΙΚΗΣ

Κοσμολογικοί Παρατηρησιακοί
Περιορισμοί σε Τροποποιημένες
Θεωρίες Βαρύτητας

Φωτεινή Σκάρα

ΔΙΔΑΚΤΟΡΙΚΗ ΔΙΑΤΡΙΒΗ

ΙΩΑΝΝΙΝΑ 2022

"Look deep into nature, and then you will understand everything better."
Albert Einstein

*"This dissertation is dedicated to my daughters, Myrsini and Filareti, and my husband, George.
I am truly thankful for having them in my life".*

Three-member advisory committee:

1. Leandros Perivolaropoulos (Supervisor), Professor, Physics Department, University of Ioannina, Greece
2. George Leontaris, Emeritus Professor, Physics Department, University of Ioannina, Greece
3. Panagiota Kanti, Professor, Physics Department, University of Ioannina, Greece

Seven-member PhD thesis examination committee:

1. Leandros Perivolaropoulos (Supervisor), Professor, Physics Department, University of Ioannina
2. Athanasios Dedes, Professor, Physics Department, University of Ioannina, Greece (substituting Emeritus Professor Georgios Leontaris due to legal constraints)
3. Panagiota Kanti, Professor, Physics Department, University of Ioannina, Greece
4. Christos Tsagas, Professor, Department of Physics, Aristotle University of Thessaloniki, Greece
5. Nikolaos Stergioulas, Professor, Department of Physics, Aristotle University of Thessaloniki, Greece
6. Savvas Nesseris, Associate Professor, Instituto de Fisica Teorica (IFT UAM-CSIC), Spain
7. Emmanuel Saridakis, Senior Researcher (Researcher Grade B), Institute for Astronomy, Astrophysics, Space Applications and Remote Sensing (IAASARS), National Observatory of Athens, Greece

Contents

Acknowledgments	ix
List of Publications	x
Abstract	xii
List of Figures	xxii
List of Tables	xxxii
1 Introduction	1
1.1 Elements of General Relativity	1
1.1.1 Geometry and gravity-The metric	1
1.1.2 Geodesics	1
1.1.3 Einstein’s field equations	2
1.2 Elements of Cosmology	3
1.2.1 Cosmic Expansion-Hubble’s law	3
1.2.2 Redshift	4
1.2.3 Comoving Coordinates-Scale Factor	4
1.2.4 The Friedmann – Lemaître – Robertson – Walker geometry	5
1.2.5 Friedmann equations	6
1.2.6 Equation of state	7
1.2.7 Cosmological parameters	8
1.2.8 Cosmological Distances	10
1.3 The Λ CDM cosmological model	10
2 Challenges for ΛCDM: Hubble Tension	15
2.1 Introduction	15
2.2 Methods for measuring H_0 and data	15
2.2.1 Standard candles as probes of luminosity distance	15
2.2.2 Sound horizon as standard ruler: early time calibrators	23
2.2.3 Time delays: gravitational lensing	26
2.2.4 Standard sirens: gravitational waves	28
2.2.5 Megamaser technique	31
2.2.6 Tully-Fisher relation (TFR) as distance indicator	32
2.2.7 Extragalactic background light γ -ray attenuation	33
2.2.8 Cosmic chronometers	34
2.2.9 HII galaxy measurements	35
2.2.10 Combinations of data	36
2.2.11 The current status - Historic evolution	42
2.3 Theoretical models	43

2.3.1	Late time deformations of the Hubble expansion rate $H(z)$	44
2.3.2	Deformations of the Hubble expansion rate $H(z)$ with additional interactions/degrees of freedom	48
2.3.3	Deformations of the Hubble expansion rate $H(z)$ with inhomogeneous/anisotropic modifications	50
2.3.4	Late time modifications - Transition/Recalibration of the SnIa absolute luminosity	51
2.3.5	Early time modifications of sound horizon	54
3	Challenges for ΛCDM: Other Tensions	62
3.1	Growth tension	62
3.1.1	Methods and data	62
3.1.2	Theoretical models	67
3.2	CMB anisotropy anomalies	70
3.2.1	Hints for a closed Universe (CMB vs BAO)	70
3.2.2	Anomalously strong ISW effect	71
3.2.3	CMB cold spot	72
3.2.4	Cosmic hemispherical power asymmetry	72
3.2.5	Quadrupole-octopole alignment	73
3.2.6	Lack of large-angle CMB temperature correlations	73
3.2.7	Anomaly on super-horizon scales	74
3.2.8	The lensing anomaly	74
3.2.9	High-low l consistency	75
3.2.10	The preference for odd parity correlations	75
3.3	Cosmic dipoles	76
3.3.1	Velocity radio dipole	76
3.3.2	Quasar dipole	78
3.3.3	Fine structure constant α dipole	78
3.4	BAO curiosities	79
3.5	Parity violating rotation of CMB linear polarization (Cosmic Birefringence)	79
3.6	Small-scale curiosities	80
3.6.1	The core-cusp curiosity	80
3.6.2	The missing satellites problem (or dwarf galaxy problem)	81
3.6.3	The Too Big To Fail (TBTf) problem	81
3.6.4	The problem of satellite planes	81
3.6.5	The angular momentum catastrophe	81
3.6.6	Baryonic Tully-Fisher Relation (BTFR)	82
3.6.7	The void phenomenon	82
3.7	Age of the Universe	82
3.8	The Lithium problem	83
3.9	Quasars Hubble diagram	83
3.10	Oscillating signals in short range gravity experiments	84
3.11	Anomalously low baryon temperature	85
3.12	Colliding clusters with high velocity	85
4	Constraining Power of Cosmological Observables on Cosmological Parameters as a Function of Redshift	86
4.1	Introduction	86
4.2	Growth of Density Perturbations: The Observables $f\sigma_8$ and $f(z)$	89
4.3	Baryon Acoustic Oscillations: the Observables $D_V(z) \times \frac{r_s^{fid}}{r_s}$, $H \times \frac{r_s}{r_s^{fid}}$ and $D_A \times \frac{r_s^{fid}}{r_s}$	93
4.3.1	BAO Observables and their Variation with Cosmological Parameters.	93
4.3.2	Contour Shapes and Redshift Ranges	96
4.4	Distance Moduli from SnIa and from Gravitational Waves	98

4.5	Conclusions	100
5	Modified Model for Gravity through Dimensional Reduction	101
5.1	Introduction	102
5.2	Spherically Symmetric Metrics in GR and Perfect Fluids	103
5.3	Modifying Spherically Symmetric GR through Dimensional Reduction	104
5.4	Special Cases - Reconstruction of Gravitational Action	107
5.4.1	Vacuum GR and Grumiller's gravity model	107
5.4.2	Reconstruction of Geometric Potential	108
5.4.3	Fitting Velocity Rotation Curves	108
5.5	Conclusions	111
6	Observational Constraints on the GUP Parameter with Maximum Length Quantum Mechanics	114
6.1	Introduction	115
6.2	Toy Model: The position variance of the Harmonic Oscillator under GUP	117
6.3	Primordial spectra of cosmological fluctuations with GUP	118
6.4	Observational Constraints	122
6.5	Conclusions	125
7	Tensions and Constraints on Modified Gravity Parameters from the E_G statistic and RSD data and Implications for Weakening Gravity	126
7.1	Introduction	127
7.2	Theoretical background	128
7.2.1	E_G statistic	128
7.2.2	The effective Newton's constant parameter μ_G and the light deflection parameter Σ_G	129
7.3	Observational Constraints	131
7.3.1	Scale Independent Analysis	131
7.3.2	Scale Dependent Data Compilations	138
7.4	Conclusions	140
8	Scalar Tachyonic Instabilities in Gravitational Backgrounds: Existence and Growth Rate	142
8.1	Introduction	142
8.2	KG equation in SdS/RN-dS spacetimes	146
8.2.1	Schwarzschild-deSitter background	146
8.2.2	Reissner-Nordström-deSitter background	148
8.3	Numerical solution: Parameter region for instability, Growth rate.	151
8.4	Limiting cases with a single horizon: pure desitter and pure Schwarzschild spacetimes	155
8.4.1	Pure deSitter background	155
8.4.2	Pure Schwarzschild background	156
8.5	Conclusions	159
9	Constraints on Horndeski Modified Gravity - Weak Gravity on a ΛCDM Background	161
9.1	Introduction	161
9.2	Stability and generic forms of μ_G and Σ_G for viable Horndeski theories	163
9.3	Reconstruction of the α_M, α_B functions from observational constraints on μ_G, Σ_G	167
9.4	Flat Λ CDM background	169
9.5	Conclusions	171

10 Transition Model in light of Cepheid SnIa Calibrator data: Alleviating the Hubble Tension	173
10.1 Introduction	174
10.2 Theoretical background - Method - Data	175
10.2.1 Standard candles	176
10.2.2 Cepheid calibration	176
10.2.3 Datasets	178
10.3 Search for transition	179
10.3.1 Case I: Fitting individual R_W and global M_H^W	181
10.3.2 Case II: Fitting individual M_H^W with fixed global R_W	184
10.3.3 Case III: Fitted individual M_H^W and a global R_W	187
10.4 Model Selection	190
10.5 Transition as a possible solution of Hubble tension	194
10.6 Conclusions	195
11 Gravitational Transitions via the Explicitly Broken Symmetron Screening Mechanism	197
11.1 Introduction	198
11.2 Review of the symmetron screening	199
11.3 Asymmetron Domain Walls	202
11.3.1 Dynamical equations and energetics of spherical asymmetron configurations	203
11.3.2 Spherical wall interaction with a matter shell: A toy model	206
11.4 Static stable spherical wall configurations in the presence of matter	206
11.4.1 Analytic considerations	206
11.4.2 Numerical energy minimization	207
11.4.3 Observational considerations	211
11.5 Conclusions	213
12 Summary-Conclusions-Outlook	215
12.1 Summary and Conclusions	215
12.2 Existing and Upcoming missions/experiments	220
Appendices	226
A List of Used Acronyms	227
B Constraining Power of Cosmological Observables on Cosmological Parameters as a Function of Redshift	231
B.1 Data Used in the Analysis	231
C Observational Constraints on the GUP Parameter with Maximum Length Quantum Mechanics	236
C.1 From generalized commutator to generalized uncertainty	236
D Tensions and Constraints on Modified Gravity Parameters from the E_G statistic and RSD data and Implications for Weakening Gravity	237
D.1 Analysis of subsets of datapoints with less correlation	237
D.2 Data used in the analysis	238
E Scalar Tachyonic Instabilities in Gravitational Backgrounds	243
E.1 Analytical form of SSC curves	243

F	Constraints on Horndeski Modified Gravity - Weak Gravity on a ΛCDM Background	244
F.1	Definitions	244
F.2	Data used in the analysis	244
G	Transition Model in light of Cepheid SnIa Calibrator data: Alleviating the Hubble Tension	246
G.1	Matrices of system of equations	246
G.2	Data used in the analysis	249
H	Gravitational Transitions via the Explicitly Broken Symmetron Screening Mechanism	255
H.1	Cluster collection	255
I	Numerical Algorithms	257
	Bibliography	258

Acknowledgments

First and foremost, I would like to extend my sincere thanks to my Supervisor Professor Leandros Perivolaropoulos for the interest, support and guidance he has provided me all these years. The excellent cooperation and his valuable advice helped me achieve my dream of being introduced to the fascinating and impressive world of modern Cosmology.

Moreover, I would like to thank the other members of the three-member advisory committee, Emeritus Professor George Leontaris and Professor Panagiota Kanti for the supervision and monitoring of my work. Furthermore, I warmly thank the members of the seven-member committee for their time in reading this dissertation.

Finally, a special thanks to my family for their encouragement and support all through my studies.

List of Publications

Within the context of my PhD dissertation, nine peer-reviewed articles have been produced. They are listed here for reference in descending chronological order.

- [1]. **Constraining power of cosmological observables: blind redshift spots and optimal ranges,**
L. Kazantzidis, L. Perivolaropoulos, F. Skara,
Published in **Phys.Rev. D99 (2019) no.6, 063537**,
DOI: [10.1103/PhysRevD.99.063537](https://doi.org/10.1103/PhysRevD.99.063537).

- [2]. **Reconstructing a Model for Gravity at Large Distances from Dark Matter Density Profiles,**
L. Perivolaropoulos, F. Skara,
Published in **Phys.Rev. D99 (2019) no.12, 124006**,
DOI: [10.1103/PhysRevD.99.124006](https://doi.org/10.1103/PhysRevD.99.124006).
The numerical files for the reproduction of the figures can be found in the "Reconstructing a Model for Gravity at Large Distances from Dark Matter Density Profiles" [GitHub](#) repository."

- [3]. **Primordial Power Spectra of Cosmological Fluctuations with Generalized Uncertainty Principle and Maximum Length Quantum Mechanics,**
F. Skara, L. Perivolaropoulos,
Published in **Phys.Rev. D100 (2019) no.12, 123527**,
DOI: [10.1103/PhysRevD.100.123527](https://doi.org/10.1103/PhysRevD.100.123527).
The numerical files for the reproduction of the figures can be found in the "Primordial Power Spectra of Cosmological Fluctuations with GUP" [GitHub](#) repository."


- [4]. **Tension of the E_G statistic and redshift space distortion data with the Planck - Λ CDM model and implications for weakening gravity,**
F. Skara, L. Perivolaropoulos,
Published in **Phys.Rev. D101 (2020) 063521**,
DOI: [10.1103/PhysRevD.101.063521](https://doi.org/10.1103/PhysRevD.101.063521).
The numerical files for the reproduction of the figures can be found in the "Tension of the E_G statistic and RSD data with the Λ CDM" [GitHub](#) repository."


- [5]. **Scalar tachyonic instabilities in gravitational backgrounds: Existence and growth rate,**
L. Perivolaropoulos, F. Skara,
Published in **Phys.Rev.D 102 (2020) 10, 104034**,
DOI: [10.1103/PhysRevD.102.104034](https://doi.org/10.1103/PhysRevD.102.104034).
The numerical files for the reproduction of the figures can be found in the "Scalar tachyonic instabilities in gravitational background" [GitHub](#) repository."

- [6]. **Weak gravity on a Λ CDM background,**
Radouane Gannouji, Leandros Perivolaropoulos, David Polarski, Foteini Skara,

Published in **Phys.Rev.D** 103 (2021) 6, 063509,
DOI: [10.1103/PhysRevD.103.063509](https://doi.org/10.1103/PhysRevD.103.063509).

- [7]. **Challenges for Λ CDM: An update**,
Leandros Perivolaropoulos, Foteini Skara,
Under review in New Astronomy Reviews,
Arxiv: [2105.05208](https://arxiv.org/abs/2105.05208).

- [8]. **Hubble tension or a transition of the Cepheid SnIa calibrator parameters**,
Leandros Perivolaropoulos, Foteini Skara,
Published in **Phys.Rev.D** 104 (2021) 12, 123511,
DOI: [10.1103/PhysRevD.104.123511](https://doi.org/10.1103/PhysRevD.104.123511).
The numerical files for the reproduction of the figures can be found in the "Cepheid SnIa Calibrator Data Transition  repository."

- [9]. **Gravitational transitions via the explicitly broken symmetron screening mechanism**,
Leandros Perivolaropoulos, Foteini Skara,
Under review in Physical Review D,
Arxiv: [2203.10374](https://arxiv.org/abs/2203.10374).
The numerical files for the reproduction of the figures can be found in the "Gravitational transitions via the explicitly broken symmetron screening mechanism  repository."

During the final stages of my PhD studies, I also worked in parallel on the following article

- [10]. **Cosmology Intertwined: A Review of the Particle Physics, Astrophysics, and Cosmology Associated with the Cosmological Tensions and Anomalies**,
Abdalla, Elcio and others,
Snowmass Collaboration: Eleonora Di Valentino et al.,
Contribution to the 2022 Snowmass Summer Study,
Published in **JHEAp** 34 (2022) 49-211,
Arxiv: [2203.06142](https://arxiv.org/abs/2203.06142)

Abstract

My Ph.D. dissertation deals with cosmological observational constraints on modified gravity theories. The General Relativity (GR) proposed by Einstein in 1915 is the fundamental theory of gravity interpretation and has succeeded in a wide range of tests. The discovery of the accelerating expansion of the universe, however, has given a strong impetus to the formulation of new modified theories of gravity. Modified theories of gravity such as Scalar Tensor (ST), $f(R)$ theories etc. try to give answers where the GR fails. The established cosmological model based on the GR is obviously not considered complete. The studied modified theories can give a theoretical framework which will include the GR and can lead to the understanding of the structures of the universe. These theories are necessary to incorporate gravitational phenomena at all scales and at all times. The theories should be consistent with all experimental data and able to explain early time and late time acceleration. They must also describe all the cosmological eras and the transition from one epoch to another.

In Chapter 1, we present elements of GR and Cosmology and their basic concepts. At the end of the chapter we present an introduction to the standard Lambda Cold Dark Matter (Λ CDM) model. The Λ CDM model is a simple and generic model that has been shown to be consistent with a wide range of cosmological observations including geometric and dynamical probes. Despite its successes, Λ CDM is confronted with challenges at both the theoretical and the observational level. These challenges of the standard Λ CDM model have been emerging during the past few years as the accuracy of cosmological observations improves. A well known observational difficulty corresponds to the tension between the cosmic microwave background (CMB) measured value of the Hubble constant H_0 in the context of the Λ CDM model and the local measurements from supernovae and lensing time delay indicators, with local measurements suggesting a higher value. Another observational puzzle for Λ CDM involves persisting indications from observational probes measuring the growth of matter perturbations that the observed growth is weaker than the growth predicted by the standard Planck/ Λ CDM parameter values. Modified gravity (MG) models constitute a prime theoretical candidate to explain these tensions.

Thus in Chapter 2 and 3 we discuss in a unified manner many existing signals in cosmological and astrophysical data that appear to be in some tension (2σ or larger) with the standard Λ CDM model as defined by the Planck18 parameter values. In addition to the major well studied 5σ challenge of Λ CDM (the Hubble H_0 tension) and other well known tensions (the growth tension and the lensing amplitude A_L anomaly), we discuss a wide range of other less discussed less-standard signals which appear at a lower statistical significance level than the H_0 tension which may also constitute hints towards new physics. For example such signals include cosmic dipoles (fine structure constant α , velocity and quasar dipoles), CMB asymmetries, BAO Ly α tension, age of the universe issues, the Lithium problem, small scale curiosities like the core-cusp and missing satellite problems, quasars Hubble diagram, oscillating short range gravity signals etc. We collectively present the current status of these signals and their level of significance, with emphasis to the Hubble tension and refer to recent resources where more details can be found for each signal. We also discuss possible theoretical approaches and modified models that can potentially explain the non-standard nature of some of these signals.

In Chapter 4, we determine the optimum and the blind redshift ranges of basic cosmological observables with respect to three cosmological parameters: the matter density parameter Ω_m , the equation of state parameter w (assumed constant), and a modified gravity parameter g_a which parametrizes a possible evolution of the effective Newton's constant G_{eff} . In an optimum range of redshifts, the observable

can constrain the parameter in the most effective manner while in the blind redshift ranges the observable values may be degenerate with respect to the cosmological parameter values and thus inefficient in constraining the given parameter.

In Chapter 5, we study modified model for gravity through dimensional reduction. Using the Navarro-Frenk-White (NFW) dark matter density profile we reconstruct an effective field theory model for gravity at large distances from a central object by demanding that the vacuum solution has the same gravitational properties as the NFW density profile has in the context of GR. The dimensionally reduced reconstructed action for gravity leads to a vacuum metric that includes a modified Rindler acceleration term in addition to the Schwarzschild and cosmological constant terms. The new term is free from infrared curvature singularities and leads to a much better fit of observed galaxy velocity rotation curves than the corresponding simple Rindler term of the Grumiller metric, at the expense of one additional parameter. When the new parameter is set to zero the new metric term reduces to a Rindler constant acceleration term. We use galactic velocity rotation data to find the best fit values of the parameters of the reconstructed geometric potential and discuss possible cosmological implications.

In Chapter 6, we obtain observational constraints on the Generalization of the Uncertainty Principle (GUP) parameter with maximum length quantum mechanics. We derive the generalized form of the primordial power spectrum of cosmological perturbations generated during inflation due to the quantum fluctuations of scalar and tensor degrees of freedom in the context of a generalization of quantum mechanics involving a maximum measurable length scale. The existence of such a scale is motivated by the existence of the particle horizon in cosmology and would lead to a GUP to a form which implies the existence of a maximum position and a minimum momentum uncertainty. The GUP implies a generalization of the commutation relation between conjugate operators including fields and their conjugate momenta. We showed that the Generalized Field Commutation (GFC) relation between a scalar field and its conjugate momentum which is implied by the GUP leads to a modified primordial spectrum of scalar perturbation.

In Chapter 7 we obtain constraints on modified gravity parameters from the E_G statistic and real-space clustering and redshift space distortion (RSD) data. The E_G statistic is a powerful probe for detecting deviations from GR by combining weak lensing (WL), RSD measurements thus probing both the lensing and the growth effective Newton constants (G_L and G_{eff}). We present phenomenologically motivated parametrizations for the effective Newton's constant parameter μ_G and the light deflection parameter Σ_G and describe how we use them in order to probe possible deviations from GR on cosmological scales. We use compilations of $f\sigma_8$ and E_G data along with the theoretical expressions for $f\sigma_8$ and E_G which involve μ_G and Σ_G to derive constraints on these parameters and to identify the tension level between the Planck/ Λ CDM parameter values favoured by Planck 2018 and the corresponding parameter values favored by the two datasets.

Scalar fields are used to describe a wide range of degrees of freedom in various physical systems in cosmology, gravitational theories, modified gravity scalar degrees of freedom like $f(R)$ theories or ST theories etc. A stabilizing effect of multiple horizons on tachyonic instabilities may have various interesting implications. Therefore in Chapter 8, we study the tachyonic instabilities in the dynamic evolution of a free massive scalar field Φ with potential equation of the form $V(\phi) = m^2\phi^2$. We focus on the existence of instabilities and their growth rate in the following non flat (curved) gravitational backgrounds: Reissner-Nordstrom-deSitter (RN-dS) and Schwarzschild-deSitter (SdS). We use spherical tortoise coordinates r_* in the context of an instability ansatz, to transform the Klein Gordon (KG) equation $\square\Phi + m^2\Phi = 0$ to a Schrodinger-like Regge-Wheeler equation for the radial function $u_l(r_*)$ with potential that depends on the angular scale l , the dimensionless parameters $\xi \equiv 9M^2\Lambda$ and $q \equiv Q/M$ as well as the scalar field mass m^2 . The existence of unstable modes that are finite at the two horizons, is equivalent with the existence of bound states of this Regge-Wheeler equation. We solve the Regge-Wheeler equation numerically and identify the range $m^2(q, \xi)$ for which bound states (unstable modes) exist. In the parameter range that remains unstable ($m^2 < m_{cr}^2(q, \xi)$) we find the growth rate Ω of the instabilities. In the end of Chapter, we discuss the scalar tachyonic instabilities in the limiting cases of pure deSitter and pure Schwarzschild backgrounds.

In Chapter 9 we focus on the Horndeski modified gravity which provides a general framework to

construct models of dark energy inside GR. In the context of the α parametrization as $\alpha_i = \alpha_{i0} a^s$ (where $i = M, B$, a is the scale factor and α_{i0} (α_{M0}, α_{B0}), s are arbitrary parameters) and the Horndeski modified gravity models obeying stability, velocity of gravitational waves c_T equals c and quasistatic approximation (QSA) on subhorizon scales, we derive the allowed parameter regions for various values of the exponent s . We also obtain the allowed forms of the growth and lensing reduced (dimensionless) gravitational couplings $\mu_G \equiv G_{\text{growth}}/G$ and $\Sigma_G \equiv G_{\text{lensing}}/G$ comparing our results with previous studies. We use compilations of $f\sigma_8$ and E_G data along with the theoretical expressions for $f\sigma_8$ and E_G statistics data in order to derive constraints on μ_G and Σ_G and to obtain the allowed range of the functions $\alpha_M(a)$ and $\alpha_B(a)$. Finally, we consider the growth index $\gamma(z)$ and identify the $(\alpha_{M0}, \alpha_{B0}, s)$ parameter region that corresponds to specific signs of $\gamma_0 - \gamma_0^{\Lambda\text{CDM}}$, and $\gamma_1 - \gamma_1^{\Lambda\text{CDM}}$.

In Chapter 10 we study models involving a transition in Cepheid SnIa Calibrator parameters. We use Cepheid SnIa calibrator data to investigate the effects of variation of the Cepheid calibration empirical parameters R_W (Cepheid Wesenheit color-luminosity parameter) and M_H^W (Cepheid Wesenheit H-band absolute magnitude). We do not enforce a universal value of these empirical Cepheid calibration parameters, instead we allow for variation of either of these parameters for each individual galaxy. We consider various cases (models) allowing for different types of empirical parameter variation and use criteria which penalize models with large numbers of parameters for model selection and model comparison. Models involving a transition in R_W are slightly favored over models where there is a transition in M_H^W . We investigate the impact of the allowed types of parameter variation on the SnIa absolute magnitude M_B and on the corresponding derived value of Hubble constant H_0 . The models involving a transition lead to values of H_0 that are consistent with the CMB inferred values thus eliminating the Hubble tension.

In Chapter 11 we study a model which offers an interesting novel approach for the modification of GR in distinct spatial sectors. We generalize the symmetron screening mechanism by allowing for an explicit symmetry breaking of the symmetron ϕ^4 potential by the inclusion of a cubic term $\varepsilon\phi^3$. Due to the explicit symmetry breaking induced by the cubic term we call this field the 'asymmetron'. For large matter density $\rho > \rho_* \equiv \mu^2 M^2 + \frac{9}{4}\varepsilon\eta M^2$ the effective potential has a single minimum at $\phi = 0$ leading to restoration of GR as in the usual symmetron screening mechanism. For low matter density however, there is a false vacuum and a single true vacuum due to the explicit symmetry breaking. This is expected to lead to an unstable network of domain walls with slightly different value of the gravitational constant G on each side of the wall. This network would be in constant interaction with matter overdensities and would lead to interesting observational signatures which could be detected as gravitational and expansion rate transitions in redshift space. Such a gravitational transition has been recently proposed for the resolution of the Hubble tension.

In Chapter 12, we summarize and discuss the results of the present Thesis. In the Appendices we present a list of acronyms, useful proofs and types, tables with data and codes used in the individual analyses. Finally, an extensive Bibliography is presented.

Εκτεταμένη Περίληψη

Η διδακτορική μου διατριβή ασχολείται με κοσμολογικούς παρατηρησιακούς περιορισμούς σε τροποποιημένες θεωρίες βαρύτητας. Η Γενική Θεωρία της Σχετικότητας (ΓΘΣ) που προτάθηκε το 1915 από τον Einstein αποτελεί τη θεμελιώδη θεωρία ερμηνείας της βαρύτητας και έχει επιτυχία σε ένα ευρύ φάσμα δοκιμασιών. Είναι συνεπής με τη συντριπτική πλειοψηφία των πειραμάτων και των παρατηρήσεων από τις sub-mm κλίμακες έως τις κοσμολογικές κλίμακες. Η ανακάλυψη της επιταχυνόμενης διαστολής του σύμπαντος που βασίστηκε σε παρατηρήσεις των υπερκαινοφανών τύπου Ia το 1998 έδωσε ωστόσο ένα ισχυρό κίνητρο για διατύπωση νέων τροποποιημένων θεωριών βαρύτητας. Η εξήγηση που δίνεται στα πλαίσια της ΓΘΣ για αυτήν την επιταχυνόμενη διαστολή του σύμπαντος είναι η ύπαρξη της σκοτεινής ενέργειας σε ποσοστό $\sim 70\%$ της συνολικής υλοενέργειας του σύμπαντος. Η εισαγωγή της κοσμολογικής σταθεράς και η ερμηνεία της ως ενέργεια του κενού είναι προβληματική, μια που υπολογισμοί δείχνουν ότι υπάρχει μια τεράστια απόκλιση των μέτρων των πυκνοτήτων ενέργειας τους. Οι τροποποιημένες θεωρίες της βαρύτητας όπως για παράδειγμα οι βαθμοταυστικές θεωρίες, οι $f(R)$ θεωρίες κ.α. προσπαθούν να δώσουν απαντήσεις εκεί που η ΓΘΣ αδυνατεί. Το καθιερωμένο κοσμολογικό μοντέλο το οποίο στηρίζεται στη ΓΘΣ είναι φανερό ότι δεν μπορεί να θεωρείται ολοκληρωμένο. Στη παρούσα διδακτορική διατριβή γίνεται μελέτη τροποποιημένων θεωριών οι οποίες μπορούν να δώσουν ένα θεωρητικό πλαίσιο το οποίο θα συμπεριλάβει τη ΓΘΣ και μπορεί να οδηγήσει στη κατανόηση των δομών του σύμπαντος. Οι θεωρίες αυτές είναι απαραίτητο να ενσωματώνουν τα βαρυτικά φαινόμενα σε όλες τις κλίμακες και σε όλους τους χρόνους. Οι θεωρίες θα πρέπει να είναι σύμφωνες με όλα τα πειραματικά δεδομένα και να μπορούν να εξηγήσουν την early time και την late time επιτάχυνση. Επίσης πρέπει να περιγράφουν όλες τις κοσμολογικές εποχές και την μετάβαση από την μία εποχή στην άλλη.

Στο κεφάλαιο 1 της παρούσας διδακτορικής διατριβής γίνεται μια σύντομη ανασκόπηση της ΓΘΣ. Παρουσιάζονται οι βασικές έννοιες και τα μαθηματικά εργαλεία της γεωμετρίας των καμπύλων χώρων. Μελετάται η δομή του χωροχρόνου και πως αυτή συνδέεται με την κατανομή ύλης και ενέργειας και γράφεται η ταυστική μορφή των πεδιακών εξισώσεων της ΓΘΣ. Επιπλέον στο ίδιο κεφάλαιο γίνεται μία παρουσίαση των καταλυτικών εννοιών της Κοσμολογίας όπως η διαστολή του Hubble, η κοσμολογική ερυθρή μετατόπιση και η κοσμολογική μετρική του χωροχρόνου Friedmann-Lemaître-Roberson-Walker (FLRW). Η μελέτη των μοντέλων του σύμπαντος γίνεται με τις εξισώσεις Friedmann οι οποίες εξάγονται από την μετρική FLRW. Στην συνέχεια παρουσιάζονται οι κοσμολογικές παράμετροι που σχετίζονται με την σταθερά του Hubble, την ηλικία του σύμπαντος και τις συγκεντρώσεις των διάφορων συστατικών του. Στο τέλος του κεφαλαίου γίνεται μια εισαγωγή στο τυπικό κοσμολογικό μοντέλο Lambda Cold Dark Matter (Λ CDM).

Το μοντέλο Λ CDM είναι ένα απλό και γενικό μοντέλο που έχει αποδειχθεί ότι είναι συνεπές με ένα ευρύ φάσμα κοσμολογικών παρατηρήσεων, συμπεριλαμβανομένων γεωμετρικών και δυναμικών ανιχνευτών. Παρά τις επιτυχίες του, το Λ CDM έρχεται αντιμέτωπο με προκλήσεις τόσο σε θεωρητικό όσο και σε επίπεδο παρατήρησης. Η εγκυρότητα του κοσμολογικού μοντέλου Λ CDM το οποίο στηρίζεται στη ορθότητα της ΓΘΣ και στην κοσμολογική αρχή της ομοιογένειας και της ισοτροπίας σε ένα επίπεδο Σύμπαν ερευνάται. Η έρευνα χρησιμοποιεί τα σύγχρονα κοσμολογικά δεδομένα και τους κοσμολογικούς παρατηρησιακούς περιορισμούς που αυτά εισάγουν στις παραμέτρους των τροποποιημένων θεωριών βαρύτητας. Τα δεδομένα σχετίζονται με ένα ευρύ φάσμα κοσμολογικών παρατηρησιακών ανιχνευτών, συμπεριλαμβανομένων των πειραμάτων της Κοσμικής Ακτινοβολίας Υποβάθρου (CMB), των φωτομετρικών και φασματοσκοπικών ερευνών γαλαξιών, της προσπάθειας μέτρησης ακουστικών ταλαντώσεων βαρυονίων, του ασθενούς φαινομένου των βαρυτικών φακών, καθώς και των παραμορφώσεων στο χώρο της ερυθράς μετατόπισης.

Οι τρέχουσες έρευνες που κάνουν χρήση τα σύγχρονα κοσμολογικά δεδομένα οδηγούν σε μια σαφή

ύπαρξη ασυνεπειών, ασυμβατοτήτων και αποκλίσεων μεταξύ των τιμών παραμέτρων που προσδιορίστηκαν χρησιμοποιώντας διαφορετικούς παρατηρησιακούς ανιχνευτές. Η εντονότερη ασυμβατότητα εμφανίζεται στην τιμή της σταθεράς Hubble H_0 που ευνοείται από την τελευταία έκδοση των CMB δεδομένων από Planck και αυτής που ευνοείται από τα δεδομένα του διαστημικού τηλεσκοπίου Hubble. Μια άλλη λιγότερο έντονη απόκλιση εμφανίζεται στις τιμές των παραμέτρων Ω_m και σ_8 που προκύπτουν από τα δεδομένα από Planck CMB και αυτών από τις διαταραχές πυκνότητας (RSD και WL).

Τα κεφάλαια 2 και 3 είναι αφιερωμένα σε μία εκτενή παρουσίαση με ενοποιημένο τρόπο πολλών υπαρχόντων σημάτων σε κοσμολογικά και αστροφυσικά δεδομένα που φαίνεται να είναι σε κάποια ασυμβατότητα (2σ ή μεγαλύτερη) με το τυπικό κοσμολογικό μοντέλο Λ CDM όπως ορίζεται από τις τιμές των παραμέτρων από Planck18. Εκτός από τη μεγάλη καλώς μελετημένη πρόκληση 5σ του Λ CDM της κρίσης της σταθεράς του Hubble και των γνωστών ανωμαλιών ανάπτυξης και πλάτους φακού, συζητάμε ένα ευρύ φάσμα άλλων λιγότερο τυπικών σημάτων που εμφανίζονται σε χαμηλότερο επίπεδο στατιστικής σημασίας από αυτήν της σταθεράς του Hubble και που μπορούν επίσης να αποτελούν υποδείξεις προς μια νέα φυσική. Για παράδειγμα, τέτοια σήματα περιλαμβάνουν κοσμικά δίπολα (όπως της σταθεράς λεπτής υφής, τα δίπολα ταχύτητας και κβάζαρ), ασυμμετρίες CMB (όπως η έλλειψη ισχύος σε μεγάλες γωνιακές κλίμακες, η ασυμβατότητα μικρών έναντι μεγάλων κλιμάκων, η ανωμαλία ψυχρού σημείου, οι ενδείξεις για ένα κλειστό σύμπαν, η ανωμαλία σε κλίμακες υπερ-οριζόντα, η ευθυγράμμιση τετράπολων-οκταπόλων, η ανωμαλία ισχυρής επίδρασης ISW, η ασυμμετρία κοσμικής ημισφαιρικής ισχύος, η ανωμαλία φακού, η προτίμηση για συσχετισμούς περιττής ισοτιμίας, η ισοτιμία παραβίασης της περιστροφής της CMB γραμμικής πόλωσης κ.λπ.), προβλήματα των βαρυονικών ακουστικών ταλαντώσεων, προβλήματα μικρής κλίμακας, θέματα ηλικίας του Σύμπαντος, πρόβλημα του λιθίου, ανωμαλίες μικρής κλίμακας, Hubble διάγραμμα από κβάζαρ, ταλαντευόμενα σήματα βαρύτητας μικρής εμβέλειας, ανώμαλη χαμηλή βαρυονική θερμοκρασία κ.λπ. Ο στόχος αυτών των δύο κεφαλαίων είναι η παρουσίαση συλλογικά της τρέχουσας κατάστασης αυτών των σημάτων και το επίπεδο ασυμβατότητας τους, με έμφαση στην κρίση της σταθεράς του Hubble και η αναφορά σε πρόσφατες πηγές όπου μπορούν να βρεθούν περισσότερες λεπτομέρειες για κάθε σήμα. Επίσης γίνεται μια εκτενή συζήτηση και παρουσίαση πιθανών θεωρητικών προσεγγίσεων που μπορεί δυνητικά να εξηγήσουν τη μη τυπική φύση ορισμένων από αυτά τα σήματα και να δώσουν λύσεις στα υπάρχοντα προβλήματα του κοσμολογικού μοντέλου Λ CDM. Ένα ευρύ φάσμα μοντέλων έχει χρησιμοποιηθεί για την αντιμετώπιση της ασυμβατότητας H_0 εισάγοντας πρόσθετους βαθμούς ελευθερίας στο μοντέλο Λ CDM όπου επιτρέπεται να ποικίλλουν πρόσθετες παράμετροι, όπως η πεμπτουσία στην οποία ένα βαθμωτό πεδίο παίζει το ρόλο της σκοτεινής ενέργειας ή τροποποιημένη βαρύτητα στην οποία η Γενική Σχετικότητα τροποποιείται σε κοσμολογική κλίμακα.

Όπως τονίσαμε στα κεφάλαια 2 και 3, η εγκυρότητα του κοσμολογικού μοντέλου Λ CDM βρίσκεται επί του παρόντος υπό εντατική έρευνα χρησιμοποιώντας ένα ευρύ φάσμα κοσμολογικών ανιχνευτών. Αυτή η έρευνα αποκάλυψε την παρουσία ασυμβατοτήτων μέσα στο μοντέλο Λ CDM, δηλαδή ασυνεπειών μεταξύ των τιμών των παραμέτρων που προσδιορίστηκαν χρησιμοποιώντας διαφορετικούς ανιχνευτές παρατήρησης. Προκύπτει επομένως το ακόλουθο ερώτημα: Είναι αυτές οι ασυμβατότητες μια πρώιμη ένδειξη της ανάγκης για μια τροποποιημένη θεωρία βαρύτητας πέρα από το τυπικό μοντέλο ή είναι αποτέλεσμα συστηματικών/στατιστικών διακυμάνσεων στα δεδομένα; Η ανάλυση που παρουσιάζεται στο επόμενο κεφάλαιο 4 στοχεύει να αντιμετωπίσει αυτό το ερώτημα. Στο κεφάλαιο αυτό γίνεται μελέτη της περιοριστικής ισχύος (ευαισθησίας) ενός ευρέος φάσματος παρατηρήσιμων ποσοτήτων πάνω σε κοσμολογικές παραμέτρους ως συνάρτηση της ερυθρής μετατόπισης στην οποία έγινε η μέτρηση. Τα βασικά ερωτήματα με τα οποία ασχοληθήκαμε σε αυτό το κεφάλαιο είναι: α) Ποια είναι η εξαρτώμενη από την κοσμολογική ερυθρή μετατόπιση εξάρτηση της περιοριστικής δύναμης μιας συγκεκριμένης παρατηρήσιμης ποσότητας σε σχέση με μια δεδομένη κοσμολογική παράμετρο; β) Υπάρχει μια βέλτιστη κλίμακα ερυθρής μετατόπισης όπου η περιοριστική ισχύς μιας παρατηρήσιμης ποσότητας είναι μέγιστη σε σχέση με μια δεδομένη κοσμολογική παράμετρο; γ) Υπάρχουν τυφλά σημεία ερυθρής μετατόπισης όπου μια παρατηρήσιμη ποσότητα είναι εκφυλισμένη σε σχέση με συγκεκριμένες κοσμολογικές παραμέτρους;

Συγκεντρώσαμε σύγχρονες συλλογές μετρήσεων των κοσμολογικών παρατηρήσεων και προσδιορίσαμε την ευαισθησία αυτών των παρατηρήσεων ως συνάρτηση της ερυθρής μετατόπισης για τρεις κοσμολογικές παραμέτρους: τη παράμετρο πυκνότητας, τη παράμετρο καταστατικής εξίσωσης της σκοτεινής ενέργειας και μία παράμετρο που περιγράφει την εξέλιξη της σταθεράς του Νεύτωνα. Για κάθε παρατηρούμενη ποσότητα εισάγαμε μια νέα στατιστική ως μέτρηση της περιοριστικής ισχύος της σε σχέση με μια κοσμολογική

παράμετρο σε συνάρτηση της ερυθρής μετατόπισης. Διαπιστώσαμε την ύπαρξη 'τυφλών' σημείων ερυθρής μετατόπισης και βέλτιστων σημείων για τις παρατηρήσιμες ποσότητες σε σχέση με τις παραμέτρους. Σε ένα βέλτιστο εύρος ερυθρών μετατοπίσεων, η παρατηρήσιμη ποσότητα μπορεί να περιορίσει την παράμετρο με τον πιο αποτελεσματικό τρόπο, ενώ στις τυφλές περιοχές ερυθρής μετατόπισης, οι παρατηρήσιμες ποσότητες μπορεί να είναι εκφυλισμένες σε σχέση με τις τιμές των κοσμολογικών παραμέτρων και επομένως αναποτελεσματικές στον περιορισμό της δεδομένης παραμέτρου.

Στο κεφάλαιο 5 ακολούθησε η μελέτη ενός τροποποιημένου μοντέλου της βαρύτητας μέσω της μείωσης διαστάσεων. Εφαρμόσαμε μια εναλλακτική προσέγγιση με μια γεωμετρική περιγραφή της δυναμικής της ύλης σε γαλαξιακές κλίμακες χωρίς σκοτεινή ύλη. Τα βασικά ερωτήματα με τα οποία ασχοληθήκαμε είναι: α) Είναι δυνατόν να γενικευθεί η θεμελιώδης διαδιάστατη γεωμετρική δράση (και το δυναμικό του βαθμωτού πεδίου που προκύπτει από την σύμπτυξη των διαστάσεων) έτσι ώστε η αντίστοιχη σφαιρικά συμμετρική μετρική του κενού να αναπαράγει τις παρατηρούμενες καμπύλες περιστροφής ταχύτητας των γαλαξιών εξίσου καλά με τη καθιερωμένη κατανομή της πυκνότητας ύλης; β) Εάν ναι, ποια είναι η μορφή του απαιτούμενου δυναμικού γεωμετρικού βαθμωτού πεδίου και πώς σχετίζεται με το απλό δυναμικό Rindler; γ) Μπορεί να αναπαραχθεί μια τυχαία σφαιρικά συμμετρική μετρική του κενού από ένα σωστά επιλεγμένο γεωμετρικό δυναμικό βαθμωτού πεδίου;

Χρησιμοποιώντας το προφίλ πυκνότητας σκοτεινής ύλης Navarro-Frenk-White (NFW) ανακατασκευάσαμε ένα μοντέλο θεωρίας βαρύτητας αποτελεσματικού πεδίου σε μεγάλες αποστάσεις από ένα κεντρικό αντικείμενο, απαιτώντας η λύση του κενού να έχει τις ίδιες βαρυτικές ιδιότητες με το προφίλ πυκνότητας NFW στο πλαίσιο της ΓΘΣ. Η διαστατικά μειωμένη ανοικοδομημένη δράση για τη βαρύτητα οδηγεί σε μία μετρική κενού που περιλαμβάνει έναν τροποποιημένο όρο επιτάχυνσης Rindler επιπλέον των τυπικών όρων Schwarzschild και κοσμολογικής σταθεράς. Ο νέος όρος είναι απαλλαγμένος από τις ανωμαλίες καμπυλότητας της υπέρυθρης ακτινοβολίας και οδηγεί σε πολύ καλύτερη προσαρμογή των παρατηρημένων καμπυλών περιστροφής ταχύτητας γαλαξία από τον αντίστοιχο απλό όρο Rindler της μετρικής Grumiller, σε βάρος μιας επιπλέον παραμέτρου. Όταν η νέα παράμετρος έχει οριστεί στο μηδέν, ο νέος μετρικός όρος μειώνεται σε μία Rindler σταθερά επιτάχυνσης. Χρησιμοποιήσαμε δεδομένα περιστροφής γαλαξιακής ταχύτητας για να βρούμε τις καλύτερες τιμές προσαρμογής των παραμέτρων του δομημένου γεωμετρικού δυναμικού και συζητήσαμε πιθανές κοσμολογικές επιπτώσεις. Γενικά η ακολουθούμενη μείωση των διαστάσεων στο πλαίσιο της σφαιρικής συμμετρίας προσφέρει μια ενδιαφέρουσα άποψη για την τροποποίηση της ΓΘΣ και μπορεί να οδηγήσει σε ένα ευρύ φάσμα δοκίμων των τροποποιημένων μοντέλων της βαρύτητας.

Κεντρικό ζητούμενο της θεμελιώδους έρευνας είναι η ενοποίηση των δύο μεγάλων φυσικών θεωριών της Κβαντικής Θεωρίας (ΚΘ) και της Γενικής Σχετικότητας (ΓΣ) στο πλαίσιο της Κβαντικής Βαρύτητας (ΚΒ). Μια κρίσιμη κλίμακα στο πλαίσιο αυτής της ενοποίησης είναι η κλίμακα Planck η οποία έχει αποδειχθεί ότι είναι η ελάχιστη μετρήσιμη κλίμακα εάν ισχύουν τόσο η ΚΘ όσο και η ΓΣ. Η ύπαρξη ενός τέτοιου ελάχιστου μετρήσιμου μήκους μπορεί να οδηγήσει σε τροποποίηση της Αρχής της Αβεβαιότητας του Heisenberg στη καλούμενη ως Γενικευμένη Αρχή της Αβεβαιότητας (ΓΑΑ). Αντίστοιχα, υπάρχει ένα μέγιστο μετρήσιμο μήκος που σχετίζεται με τον κοσμολογικό ορίζοντα των σωματιδίων, το οποίο παρέχει λόγω αιτιότητας μια κλίμακα μέγιστου μετρήσιμου μήκους στο Σύμπαν. Αυτή η ύπαρξη ενός τέτοιου μέγιστου μετρήσιμου μήκους οδηγεί σε τροποποιημένη έκδοση της ΓΑΑ. Στο κεφάλαιο 6 ερευνηθήκαν οι επιδράσεις της τροποποιημένης ΓΑΑ στο πρωταρχικό φάσμα ισχύος των κοσμολογικών διαταραχών που γεννήθηκαν κατά τη διάρκεια του πληθωρισμού λόγω κβαντικών διακυμάνσεων. Τα βασικά ερωτήματα με τα οποία ασχοληθήκαμε είναι: α) Ποια είναι η παραμόρφωση του φάσματος ισχύος των διαταραχών που παράγεται κατά τον πληθωρισμό λόγω της παραμόρφωσης της άλγεβρας Heisenberg που αντιστοιχεί στην ύπαρξη ενός μέγιστου μετρήσιμου μήκους; β) Ποιοι περιορισμοί μπορούν να επιβληθούν στη θεμελιώδη παράμετρο που σχετίζεται με την μέγιστη αβεβαιότητα θέσης από το παρατηρούμενο φάσμα ισχύος των πρωταρχικών διακυμάνσεων;

Έτσι στο πλαίσιο μιας γενίκευσης της κβαντικής μηχανικής που περιλαμβάνει μια κλίμακα μέγιστου μετρήσιμου μήκους εξάγαμε τη γενικευμένη μορφή του αρχέγονου φάσματος ισχύος των κοσμολογικών διαταραχών που δημιουργούνται κατά τη διάρκεια του πληθωρισμού λόγω των κβαντικών διακυμάνσεων των βαθμωτών και ταυστικών βαθμών ελευθερίας. Η ύπαρξη μιας τέτοιας κλίμακας υποκινείται όπως προαναφέρθηκε από την ύπαρξη του ορίζοντα των σωματιδίων στην κοσμολογία και οδηγεί σε μια γενίκευση της αρχής της αβεβαιότητας σε μια μορφή που συνεπάγεται την ύπαρξη μιας μέγιστης θέσης και μιας

ελάχιστης αβεβαιότητας ορμής. Η ΓΑΑ συνεπάγεται μια γενίκευση της σχέσης μετάθεσης μεταξύ συζευγμένων τελεστών συμπεριλαμβανομένων των πεδίων και των συζυγών ορμών τους. Ειδικότερα δείξαμε ότι η Γενικευμένη σχέση Μετάθεσης Πεδίου (ΓΜΠ) μεταξύ ενός βαθμωτού πεδίου και της συζυγούς ορμής του που υπονοείται από τη ΓΑΑ οδηγεί σε ένα τροποποιημένο αρχέγονο φάσμα βαθμωτών διαταραχών. Με τη βοήθεια παρατηρησιακών περιορισμών του φασματικού δείκτη οδηγήθηκαμε σε περιορισμούς των παραμέτρων του μοντέλου που μας βοήθησε να εκτιμήσουμε το μέγιστο μετρήσιμο μήκος. Αυτό βρέθηκε να είναι μία τάξη μεγέθους μεγαλύτερο από το σημερινό κοσμολογικό ορίζοντα.

Παρά την συνέπεια του Planck/ Λ CDM μοντέλου με τα δεδομένα κοσμικού υποβάθρου στις μεγάλες κοσμολογικές κλίμακες έχει πρόσφατα καταστεί εμφανής η ύπαρξη μιας ήπιας ασυμβατότητας ανάμεσα στο μοντέλο Planck/ Λ CDM με μερικές παρατηρήσεις σε ενδιαμέσες κοσμολογικές κλίμακες (ερυθρές μετατοπίσεις $z \leq 0.6$). Ένα τροποποιημένο μοντέλο βαρύτητας αποτελεί έναν κύριο θεωρητικό υποψήφιο για να εξηγήσει αυτή την ασυμβατότητα. Ο συνδυασμός των κοσμολογικών ανιχνευτών είναι ένα ισχυρό εργαλείο για την αναγνώριση του κατάλληλου μοντέλου. Ωστόσο οι επιδράσεις των μοντέλων τροποποιημένης βαρύτητας δεν διακρίνονται από τη ΓΘΣ σε επίπεδο γεωμετρικού κοσμολογικού υποβάθρου. Η ύπαρξη ενός μοντέλου τροποποιημένης βαρύτητας μπορεί να ταυτοποιηθεί μόνο με τη διερεύνηση της δυναμικής των κοσμολογικών διαταραχών χρησιμοποιώντας συγκεκριμένα στατιστικά στοιχεία που λαμβάνονται μέσω των ανιχνευτών δυναμικών παρατηρήσιμων ποσοτήτων, όπως η συσχέτιση δύο σημείων και το φάσμα ισχύος της κατανομής των γαλαξιών, τα RSD και WL.

Ορμώμενοι από την παραπάνω διαπίστωση στο κεφάλαιο 7 πραγματοποιήσαμε μελέτη της ασυμβατότητας των δεδομένων στατιστικής E_G και δεδομένων που σχετίζονται με παραμορφώσεις στο χώρο ερυθράς μετατόπισης (RDS) με το Planck/ Λ CDM μοντέλο. Τα βασικά ερωτήματα που θέσαμε είναι τα ακόλουθα: α) Ποιες είναι οι αποτελεσματικές φαινομενολογικές παραμετροποιήσεις που εξαρτώνται από την ερυθρή μετατόπιση των γενικευμένων κανονικοποιημένων σταθερών Newton $\mu_G(z)$ και $\Sigma_G(z)$ οι οποίες είναι συνέπειες και με τα όρια από την πυρηνοσύνθεση και με τις παρατηρήσεις στο ηλιακό σύστημα που δείχνουν ότι η ΓΘΣ αποκαθίσταται σε υψηλό z και στη σημερινή εποχή; β) Ποιοι είναι οι περιορισμοί που επιβάλλονται από τα E_G και $f\sigma_8$ επικαιροποιημένα σετ δεδομένων για τις παραμέτρους των παραπάνω παραμετροποιήσεων; γ) Οι περιορισμοί αυτοί ενισχύουν τις ενδείξεις για την εξασθένιση της βαρύτητας σε μικρές ερυθρές μετατοπίσεις z που υποδηλώνουν μόνο τα δεδομένα του $f\sigma_8$ όπως υποδεικνύουν προηγούμενες μελέτες;

Έτσι κατασκευάζοντας σύγχρονες συλλογές δεδομένων $f\sigma_8$ και E_G βασισμένων σε παρατηρήσεις που περιγράφουν το ρυθμό αύξησης των κοσμολογικών διαταραχών (RSD) και ασθενών φακών (WL) εκτιμήσαμε τις ασυμβατότητες μεταξύ των βέλτιστων τιμών παραμέτρων από Planck/ Λ CDM και των βέλτιστων τιμών των παραμέτρων που επιτυγχάνονται στο πλαίσιο μιας τροποποιημένης θεωρίας βαρύτητας στα πλαίσια κατάλληλης παραμετροποιημένης εξέλιξης των γενικευμένων κανονικοποιημένων σταθερών ανάπτυξης και φακών μ_G και Σ_G αντίστοιχα. Βρήκαμε ότι το επίπεδο ασυμβατότητας αυξάνει από τα 3.5σ όταν η ανάλυση γίνεται μόνο με τη χρήση της συλλογής δεδομένων $f\sigma_8$ στα 6σ όταν εισάγουμε στην ανάλυση τη συλλογή δεδομένων E_G . Αυτά τα αποτελέσματα ενισχύουν περαιτέρω τις ενδείξεις για weakening modified gravity που συζητήθηκε σε άλλες πρόσφατες μελέτες.

Τα βαθμωτά πεδία χρησιμοποιούνται για να περιγράψουν ένα ευρύ φάσμα βαθμών ελευθερίας σε ένα ποικίλο σύνολο φυσικών συστημάτων στη σωματιδιακή φυσική, την κοσμολογία και την φυσική συμπεκνωμένης ύλης. Μια σταθεροποιητική επίδραση πολλαπλών οριζόντων στις ταχυονικές αστάθειες μπορεί να έχει διάφορες ενδιαφέρουσες συνέπειες. Για παράδειγμα, οι ταχυονικές αστάθειες των θεωριών $f(R)$ και των βαθμοταυστικών θεωριών μπορεί να καθυστερήσουν σημαντικά σε υπόβαθρα που περιλαμβάνουν κοσμολογικούς ορίζοντες με πιθανές συνέπειες για την ανάπτυξη προθέρμανσης μετά τον πληθωρισμό. Στο κεφάλαιο 8 γίνεται μελέτη των ταχυονικών ασταθειών στη δυναμική εξέλιξη ενός ελεύθερου μαζικού βαθμωτού πεδίου Φ με εξίσωση δυναμικού της μορφής $V(\phi) = m^2\phi^2$. Ειδικότερα είναι γνωστό ότι η αντίστοιχη εξίσωση Klein Gordon (KG) $\square\Phi + m^2\Phi = 0$ έχει ταχυονικές ασταθείς καταστάσεις σε μεγάλες κλίμακες ($k^2 < |m|^2$) για $m^2 < m_{cr}^2 = 0$ σε επίπεδο χωρόχρονο Minkowski με το μέγιστο ρυθμό ανάπτυξης $\Omega_F(m) = |m|$ να επιτυγχάνεται σε $k = 0$. Με δεδομένο αυτήν την ύπαρξη ταχυονικών ασταθειών για $m^2 < 0$ στην παρουσία ενός επίπεδου υποβάθρου (Minkowski background) θέσαμε τα παρακάτω ερωτήματα: α) Παραμένουν οι βαθμωτές ταχυονικές αστάθειες για $m^2 < 0$ παρουσία ενός μη επίπεδου (καμπύλου) υποβάθρου; β) Αν ναι, πώς αλλάζει ο χρόνος αστάθειας και ο ρυθμός ανάπτυξης σε καμπύλο υπόβαθρο; γ) Ποιες είναι οι τιμές παραμέτρων μιας μετρικής καμπύλου υποβάθρου που απαιτούνται για να αυξήσουν σημαντικά τη διάρκεια

ζωής της αστάθειας σε σύγκριση με την τιμή της σε ένα επίπεδο υπόβαθρο;

Η έρευνα επικεντρώθηκε στην ύπαρξη των ασταθειών και στο ρυθμό ανάπτυξης τους στα παρακάτω μη επίπεδα (καμπύλα) βαρυτικά υπόβαθρα: Reissner-Nordstrom-deSitter (RN-dS), Schwarzschild-deSitter (SdS), pure deSitter, pure Schwarzschild. Τα βασικά συμπεράσματα που εξάγαμε είναι: α) Η κρίσιμη τιμή της μάζας του βαθμωτού πεδίου m_{cr}^2 σε καμπύλο υπόβαθρο είναι $m_{cr}^2 = 0$ όπως στο επίπεδο υπόβαθρο (όπου για $m^2 < m_{cr}^2$ ταχυονική αστάθεια αναπτύσσεται), β) Η βαθμωτή ταχυονική αστάθεια της εξίσωσης Klein-Gordon έχει βραδύτερο ρυθμό ανάπτυξης στο καμπύλο υπόβαθρο σε σύγκριση με το επίπεδο χωρόχρονο για όλες τις μετρικές παραμέτρους όπου υπάρχει κοσμολογικός ορίζοντας.

Όπως προαναφέρθηκε, η ασυμβατότητα ανάπτυξης, αν δεν οφείλεται σε στατιστικά ή συστηματικά σφάλματα, μπορεί να υποδηλώνει την ανάγκη για πρόσθετους βαθμούς ελευθερίας που επεκτείνουν το Λ CDM μοντέλο. Μια γενική προέλευση τέτοιων βαθμών ελευθερίας με φυσικά κίνητρα είναι η επέκταση της $\Gamma\Theta\Sigma$ σε μοντέλα τροποποιημένης βαρύτητας. Μια μεγάλη ποικιλία τέτοιων μοντέλων έχουν προταθεί μέχρι στιγμής για να λυθεί η ασυμβατότητα ανάπτυξης. Μια ευρεία κατηγορία τέτοιων τροποποιημένων θεωριών παρέχεται από τη βαρύτητα Horndeski που αποτελεί ένα γενικευμένο μοντέλο βαρύτητας. Τα μοντέλα βαρύτητας Horndeski είναι η πιο γενική βαθμοταυστική θεωρία που περιλαμβάνει βαθμωτό βαθμό ελευθερίας σε τέσσερις διαστάσεις με εξισώσεις κίνησης δεύτερης τάξης, επομένως αποφεύγεται η αστάθεια Ostrogradsky. Παρέχει ένα γενικό πλαίσιο για την κατασκευή μοντέλων σκοτεινής ενέργειας εντός της $\Gamma\Theta\Sigma$ καθώς και πληθωρισμού.

Στο κεφάλαιο 9 γίνεται μελέτη του Horndeski μοντέλου βαρύτητας σε Λ CDM υπόβαθρο με χρήση τεσσάρων ελεύθερων ανεξάρτητων συναρτήσεων του χρόνου, της α βάσης, $\alpha_i(t)$ ($i = M, K, B, T$) που περιγράφει οποιαδήποτε απόκλιση από την $\Gamma\Theta\Sigma$ όπου $\alpha_i(t) = 0$. Η διερεύνηση των μοντέλων Horndeski, έγινε υποθέτοντας: α) συμπεριφορά πρώιμου χρόνου που είναι σύμφωνη με την $\Gamma\Theta\Sigma$, β) ταχύτητα βαρυτικών κυμάτων ίση με την ταχύτητα του φωτός, γ) ανεξαρτησία κλίμακας k των συναρτήσεων $\alpha_i(t)$ σε κλίμακες κάτω από τον ορίζοντα του ήχου (subhorizon) του βαθμωτού πεδίου ($k \gg aH/c_s$) στην σχεδόν στατική προσέγγιση (Quasi-Static Approximation (QSA)), δ) ρυθμό διαστολής υπόβαθρου του σύμπαντος $H(z)$ που αντιστοιχεί σε μια επίπεδη κοσμολογία Λ CDM, ε) εξάρτηση των συναρτήσεων $\alpha_i(t)$ από τον παράγοντα κλίμακας a της μορφής $\alpha_i = \alpha_{i0} a^s$ όπου οι σταθερές α_{i0} είναι σημερινές τιμές και το s είναι κάποιος θετικός εκθέτης που καθορίζει την χρονική εξέλιξη για το θεωρούμενο τροποποιημένο μοντέλο βαρύτητας.

Κάνοντας χρήση των παραπάνω υποθέσεων εξάγαμε τις επιτρεπόμενες περιοχές των παραμέτρων του μοντέλου για διάφορες τιμές του εκθέτη s . Λάβαμε επίσης τις επιτρεπόμενες μορφές των βαρυτικών παραμέτρων ανάπτυξης και φακού $\mu_G \equiv G_{\text{growth}}/G$ και $\Sigma_G \equiv G_{\text{lensing}}/G$ συγκρίνοντας τα αποτελέσματά μας με προηγούμενες μελέτες. Χρησιμοποιήσαμε συλλογές δεδομένων $f\sigma_8$ και E_G μαζί με τις θεωρητικές εκφράσεις για τα στατιστικά δεδομένα $f\sigma_8$ και E_G προκειμένου να εξάγουμε περιορισμούς στις παραμέτρους μ_G και Σ_G και να λάβουμε το επιτρεπόμενο εύρος των συναρτήσεων $\alpha_M(a)$ και $\alpha_B(a)$. Η ασθενής βαρύτητα είναι ένα δύσκολο καθεστώς που πρέπει να επιτευχθεί στο πλαίσιο βιώσιμων τροποποιημένων θεωριών βαρύτητας. Δείξαμε ότι υποθέτοντας μια τέλεια βιώσιμη λύση υποβάθρου, Λ CDM, μπορούμε να περιορίσουμε τα μοντέλα Horndeski χρησιμοποιώντας δεδομένα $f\sigma_8$ και E_G . Τέλος, εξετάσαμε τον δείκτη ανάπτυξης $\gamma(z)$ και προσδιορίσαμε την περιοχή παραμέτρων $(\alpha_{M0}, \alpha_{B0}, s)$ που αντιστοιχεί σε συγκεκριμένες περιπτώσεις $\gamma_0 - \gamma_0^{\Lambda\text{CDM}}$ και $\gamma_1 - \gamma_1^{\Lambda\text{CDM}}$ (όπου $\gamma_0 \equiv \gamma(z=0)$ και $\gamma_1 \equiv \frac{d\gamma}{dz}|_{z=0}$).

Η πιο ενδιαφέρουσα ασυμβατότητα μεγάλης κλίμακας είναι αυτή της σταθεράς του Hubble όπως συζητήσαμε στο κεφάλαιο 2. Χρησιμοποιώντας μια προσέγγιση κλίμακας απόστασης, οι τοπικές μετρήσεις της σταθεράς Hubble H_0 οδηγούν σε τιμές που είναι σημαντικά υψηλότερες από αυτές που συνάγονται χρησιμοποιώντας τη γωνιακή κλίμακα διακυμάνσεων του CMB στο πλαίσιο του μοντέλου Λ CDM. Ο τοπικός προσδιορισμός της σταθεράς Hubble H_0 χρησιμοποιώντας μια προσέγγιση κλίμακας απόστασης εξαρτάται από μια αλυσίδα μετρήσεων απόστασης. Στην προσέγγιση της κλίμακας κοσμικής απόστασης, κάθε βήμα της κλίμακας απόστασης χρησιμοποιεί μεθόδους παράλλαξης ή/και τη γνωστή εγγενή φωτεινότητα μιας τυπικής πηγής κεριού για να προσδιορίσει την απόλυτη (εγγενή) φωτεινότητα ενός πιο φωτεινού τυπικού κεριού που βρίσκεται στον ίδιο γαλαξία. Έτσι, τα τυπικά κεριά υψηλής φωτεινότητας βαθμονομούνται για το επόμενο βήμα, προκειμένου να φτάσουν σε αποστάσεις φωτεινότητας υψηλής ερυθρής μετατόπισης. Εάν μία από τις μετρήσεις απόστασης υπόκειται σε συστηματικά σφάλματα ή νέα φυσική, όλα τα επόμενα σκαλοπάτια της κοσμικής κλίμακας απόστασης είναι λάθος.

Η προσέγγιση της κλίμακας απόστασης βασίζεται σε μια μέθοδο στην οποία πρωτοστάτησε η Henrietta Swan Leavitt. Συνειδητοποίησε ότι ένας τύπος παλλόμενων αστεριών που είναι γνωστοί ως μεταβλητοί

Κηφείδες έχουν μια περίοδο παλμών που εξαρτάται από τη φωτεινότητά τους. Αυτή η σχέση Περίοδου-Φωτεινότητας (ΠΦ) ονομάζεται νόμος Leavitt. Γνωρίζοντας τη φωτεινότητα ενός Κηφείδα σημαίνει ότι η απόσταση φωτεινότητάς του μπορεί να προσδιοριστεί απλά παρατηρώντας τη φωτεινότητά του που έχει μειωθεί από αυτή την απόσταση. Επομένως, οι Κηφείδες των οποίων η φωτεινότητα συσχετίζεται με τις περιόδους μεταβλητότητάς τους μπορεί να είναι τα πρώτα τυπικά κεριά στην κοσμική κλίμακα της απόστασης. Τριγωνομετρικές μέθοδοι παράλλαξης μπορούν να χρησιμοποιηθούν για τη βαθμονόμηση των τυπικών κεριών μεταβλητών Κηφείδων στο τοπικό Σύμπαν. Στη συνέχεια, χρησιμοποιώντας τις μετρούμενες αποστάσεις φωτεινότητας των βαθμονομημένων Κηφείδων, λαμβάνεται η εγγενής φωτεινότητα των κοντινών ($D \approx 20 - 40 \text{ Mpc}$) απίστευτα φωτεινού τύπου Ia υπερκαινοφανών (SnIa) που κατοικούν στους ίδιους γαλαξίες με τους Κηφείδες. Αυτή η βαθμονόμηση του νέου τύπου τυπικού κεριού SnIa καθορίζει το απόλυτο μέγεθος του M_B και στη συνέχεια χρησιμοποιείται για SnIa σε πιο απομακρυσμένους γαλαξίες (στη ροή Hubble) για τη μέτρηση των H_0 ($z \in [0.01, 0.1]$) και $H(z)$ ($z \in [0.01, 2.3]$) μέσω της μέτρησης των αποστάσεων φωτεινότητάς τους. Είναι φανερό ότι το μοντέλο που χρησιμοποιείται για τη βαθμονόμηση των Κηφείδων μπορεί να επηρεάσει τον καθορισμό της σταθεράς του Hubble.

Ορώμενοι από τα παραπάνω στο κεφάλαιο 10 χρησιμοποιήσαμε δεδομένα από Κηφείδες και υπερκαινοφανείς τύπου Ia για να διερευνήσουμε τα αποτελέσματα της διακύμανσης των εμπειρικών παραμέτρων βαθμονόμησης των Κηφείδων. Δείξαμε ότι τα μοντέλα όπου επιτρέπεται μια τέτοια διακύμανση ευνοούνται με βάση τα κριτήρια επιλογής μοντέλων AIC και BIC. Τα μοντέλα που ευνοούνται σταθερά και από τα δύο, το AIC και το BIC, περιλαμβάνουν μια μετάβαση είτε στην παράμετρο χρώματος-φωτεινότητας R_W είτε στο απόλυτο μέγεθος M_H^W των Κηφείδων σε απόσταση μεταξύ 10 και 20 Mpc . Στο πλαίσιο ενός ομοιογενούς Σύμπαντος όπου τηρείται η κοσμολογική αρχή, αυτό θα ήταν μια χρονική μετάβαση μεταξύ περίπου 25 - 70 εκατομμυρίων ετών πριν. Τα μοντέλα που περιλαμβάνουν μετάβαση στο R_W ευνοούνται ελαφρώς έναντι των μοντέλων όπου υπάρχει μετάβαση στο M_H^W . Και οι δύο κατηγορίες μοντέλων οδηγούν σε τιμές H_0 που είναι συμβατές με τις συναγόμενες τιμές από CMB εξαλείφοντας έτσι την ασυμβατότητα της σταθεράς του Hubble. Μια τέτοια μετάβαση των παραμέτρων των Κηφείδων θα μπορούσε να προκαλείται από μια θεμελιώδη φυσική μετάβαση. Το μέγεθος της μετάβασης είναι συνεπές με το μέγεθος που απαιτείται για την επίλυση της ασυμβατότητας της σταθεράς του Hubble στο πλαίσιο μιας θεμελιώδους βαρυτικής μετάβασης που λαμβάνει χώρα από μια ξαφνική αύξηση της έντασης των βαρυτικών αλληλεπιδράσεων G_{eff} κατά περίπου 10% σε ερυθρές μετατοπίσεις $z \leq 0.01$. Μια τέτοια μετάβαση θα αύξανε απότομα το απόλυτο μέγεθος των υπερκαινοφανών τύπου Ia κατά $\Delta M_B \approx 0.2$. Το εύρος απόστασης/χρονικής κλίμακας που αντιστοιχεί σε αυτή τη μετάβαση είναι σύμφωνο με μια πρόσφατη ανάλυση που δείχνει μια παρόμοια μετάβαση στο πλαίσιο των Tully-Fisher δεδομένων και είναι επίσης συνεπές με τα δεδομένα ιστορίας του ηλιακού συστήματος. Λόγω της αποτελεσματικότητας μιας βαρυτικής μετάβασης στην επίλυση των ασυμβατοτήτων Hubble και ανάπτυξης, προκύπτει το ερώτημα: Υπάρχουν θεωρητικά μοντέλα που μπορούν γενικά να προβλέψουν μια τέτοια μετάβαση σε χωρικό ή χρονικό επίπεδο σε $z_t \lesssim 0,01$;

Με σκοπό να δώσουμε απάντηση στο παραπάνω ερώτημα στο κεφάλαιο 11 παρουσιάζουμε ένα μοντέλο που προσφέρει μια ενδιαφέρουσα νέα προσέγγιση για την τροποποίηση της ΓΘΣ σε διακριτούς χωρικούς τομείς. Γενικεύσαμε το symmetron-screening μηχανισμό επιτρέποντας μια ρητή διακοπή της συμμετρίας του symmetron ϕ^4 δυναμικού κατά τον κυβικό όρο $\varepsilon\phi^3$. Σε ένα τέτοιο screening βαθμωτό πεδίο (asymmetron) τα δύο τοπικά ελάχιστα του δυναμικού σε περιοχές χαμηλής πυκνότητας δεν είναι ούτε εκφυλισμένα ούτε συμμετρικά ($\phi_+ \neq -\phi_-$). Επομένως υπάρχει ένα ψευδές και ένα μόνο αληθινό κενό λόγω της ρητής διακοπής της συμμετρίας. Αυτό αναμένεται να οδηγήσει σε ένα ασταθές asymmetron domain wall δίκτυο που περιλαμβάνει μια μετάβαση στην τιμή της ενεργού βαρυτικής σταθεράς G_{eff} σε πλαίσιο αναφοράς Jordan καθώς διασχίζεται το asymmetron wall. Το δίκτυο θα βρισκόταν σε συνεχή αλληλεπίδραση με τις υπερπυκνότητες της ύλης και θα οδηγούσε σε ενδιαφέρουσες παρατηρησιακές υπογραφές που θα μπορούσαν να ανιχνευθούν ως μεταπτώσεις βαρυτικού ρυθμού και διαστολής στο χώρο της ερυθρής μετατόπισης. Στο πλαίσιο αυτό έχει συζητηθεί η συνάφεια αυτών των asymmetron wall διαμορφώσεων με πρόσφατα δεδομένα από cluster προφίλ που μπορεί να ερμηνευθεί ως ένδειξη για διακριτές βαρυτικές ιδιότητες ορισμένων clusters. Η βαρυτική μετάβαση που προκύπτει από αυτό το asymmetron μοντέλο μπορεί να οδηγήσει στην επίλυση της ασυμβατότητας της σταθεράς του Hubble όπως επίσης και της ασυμβατότητας της ανάπτυξης.

Στο κεφάλαιο 12, που αποτελεί και το τελευταίο κεφάλαιο της παρούσας διατριβής παρουσιάζουμε τα συνολικά συμπεράσματα της. Επιπλέον γίνεται αναφορά σε υπάρχουσες και επερχόμενες αποστολές (πειρά-

ματα) που αναμένεται να βελτιώσουν την ποιότητα και την ποσότητα των δεδομένων. Η ανάλυση αυτών των δεδομένων μπορεί να δώσει απαντήσεις στα ενδιαφέροντα ανοιχτά κοσμολογικά ερωτήματα που εξετάζονται σε αυτή τη διατριβή.

Κλείνοντας, στα Παραρτήματα παραθέτουμε μια λίστα με ακρωνύμια, χρήσιμες αποδείξεις και τύπους, πίνακες με δεδομένα και κώδικες που χρησιμοποιήθηκαν στις επιμέρους αναλύσεις. Τέλος, παρατίθεται μία σύγχρονη και εκτεταμένη Βιβλιογραφία.

List of Figures

1.1	Edwin Hubble’s original plot of the velocity-distance relation among extra-galactic nebulae (from Ref. [11]).	4
1.2	The luminosity distance is obtained from the apparent and absolute luminosities.	9
1.3	The angular diameter distance is obtained from the angular and physical scales.	9
2.1	The $1\sigma - 3\sigma$ confidence contours in the parametric space $(\Omega_{0m}, \mathcal{M})$. The blue contours correspond to the $1\sigma - 3\sigma$ full Pantheon dataset (1048 SnIa datapoints) best fit, while the red contours describe the $1\sigma - 3\sigma$ confidence contours of the four bins (from left to right). The black points represent the best fit of each bin, while the green dot represents the best fit value indicated by the full Pantheon dataset ($\Omega_{0m} = 0.285$ and $\mathcal{M} = 23.803$) (from Ref. [12]).	18
2.2	The best fit values of \mathcal{M} (left panel) and Ω_{0m} (right panel) as well as the 1σ errors for the four bins, including the systematic uncertainties. This oscillating behaviour relatively improbable in the context of constant underlying \mathcal{M} and Ω_{0m} (from Ref. [12]).	19
2.3	The snapshots show the radial mass profile of perturbation as a function of the comoving radius of an initially point-like overdensity located at the origin for redshifts $z = 6824, 1440, 848, 478, 79, 10$. The time after the Big Bang are given in each snapshots. The black, blue, red, and green lines correspond to the dark matter, baryons, photons, and neutrinos (all perturbations are fractional for that species), respectively. The top snapshots are for the early time before recombination where the overdensities in photons and baryons evolve together, the middle snapshots for soon after but close to recombination where the baryons freeze at the location reached with the photons forming a thick spherical shell, and the bottom snapshots are for long after recombination where the baryon overdensities start to gravitationally grow like dark matter overdensities (from Ref. [13]).	21
2.4	The Planck18 CMB angular power spectrum $\mathcal{D}_l^{TT} \equiv l(l+1)/(2\pi)C_l^{TT}$ (top) and residual angular power spectrum (bottom) of temperature fluctuations as a function of multipole moment l . The light blue line in the upper panel is the best-fitting to the Planck TT, TE, EE+lowE+lensing likelihoods assuming the base- Λ CDM cosmology. The red points correspond to the binned Planck data. The lowest multipole range ($l \leq 30$) is dominated by cosmic variance (approximated as Gaussian), while positions and amplitudes of the acoustic peaks are accurately constrained (from Ref. [14]).	22
2.5	The signature of baryonic acoustic oscillations in galaxy two-point correlation function $\xi(s)$ as measured by Ref. [15] using the luminous red galaxy samples of the Sloan Digital Sky Survey. The data show the existence of a baryonic acoustic peak in the galaxy correlation function $\xi(s)$ around the comoving separation scale $100 h^{-1}\text{Mpc}$. The solid green, red, and blue lines correspond to model predictions with $\Omega_{0m}h^2 = 0.12, 0.13$ and 0.14 , respectively. All models are taken to have the same $\Omega_{0b}h^2 = 0.024$ and $n = 0.98$. The magenta line corresponds to a model with no baryons and $\Omega_{0m}h^2 = 0.105$, which has no acoustic peaks (from Ref. [15]).	24
2.6	Schematic illustration of a typical gravitational lens system.	27

2.7	The probability of different values of H_0 with the maximum at $H_0 = 70.0_{-8.0}^{+12.0}$ $\text{km s}^{-1} \text{Mpc}^{-1}$ (solid blue curve) derived by BNS event GW170817. The dashed and dotted lines show minimal 68.3% (1σ) and 95.4% (2σ) credible intervals. The shaded green and orange bands show the 1σ and 2σ constraints from the analysis of the CMB data obtained by the Planck [16] and from the analysis of the SnIa data obtained by SHOES [17] respectively (from Ref. [18]).	30
2.8	The Hubble constant H_0 values with the 68% CL constraints derived by recent measurements. The value of the Hubble constant H_0 is derived by early time approaches based on sound horizon, under the assumption of a Λ CDM background.	39
2.9	The one dimensional relative probability density value of H_0 derived by recent measurements (Planck CMB [14], ACT+WMAP CMB [19], BAO+RSD [20], BAO+WMAP CMB [21], BAO+BBN [22], SnIa-Cepheid [23], SnIa-TRGB [24], SnIa-Miras [25], SBF [26], SnelI [27], TD lensing [28], GW Standard Sirens [29], Masers [30], Tully Fisher [31], γ -ray attenuation [32], cosmic chronometers [33], HII galaxy [34]). All measurements are shown as normalized Gaussian distributions. Notice that the tension is not so much between early and late time approaches but more between approaches that calibrate based on low z ($z \lesssim 0.01$) gravitational physics and those that are independent of this assumption. For example cosmic chronometers and γ -ray attenuation which are late time but independent of late gravitational physics are more consistent with the CMB-BAO than with late time calibrators.	40
2.10	The Hubble constant as a function of publication date, using a set of different tools. Symbols in orange denote values of H_0 determined in the late Universe with a calibration based on the Cepheid distance scale (Key Project (KP) [35], SHOES [17, 23, 36–40], Carnegie Hubble Program (CHP) [41]). Symbols in purple denote derived values of H_0 from analysis of the CMB data based on the sound horizon standard ruler (First Year WMAP (WMAP1) [42], Three Year WMAP (WMAP3) [43], Five Year WMAP (WMAP5) [44], Seven Year WMAP (WMAP7) [45], Nine Year WMAP (WMAP9) [46], Planck13 (P13) [47], Planck15 (P15) [16], Planck18 (P18) [14], BAO [22]). The orange and purple shaded regions demonstrate the evolution of the uncertainties in these values which have been decreasing for both methods. The most recent measurements disagree at greater than 5σ	41
2.11	Left panel: The comoving Hubble parameter as a function of redshift. The black line corresponds to the best fit obtained from the Planck18 CMB when the Λ CDM model is considered, while the grey areas are the 1σ regions. The blue point at redshift zero denotes the inferred Hubble measurement by HST survey [39]. The orange points, green point, and yellow points correspond to BAO data from BOSS DR12 survey [48], BOSS DR14 quasar sample [49], and SDSS DR12 $\text{Ly}\alpha$ sample [38] respectively. The arrows indicate approaches for the resolution of the Hubble tension: Down arrow (blue) corresponds to decrease of the Riess et. al. (2019) datapoint due to systematics or transition of the absolute magnitude M (light blue arrow). Up arrow (black) corresponds to recalibration of r_s which shifts the whole curve up or and late time deformation of $H(z)$ (adapted from Ref. [14]). Right panel: The comoving Hubble parameter as a function of redshift for a wCDM phantom modification of Λ CDM model which drives upward the low z part of the $H(z)$ curve shown in left panel. Thus it brings the $z = 0$ prediction of the CMB closer to the H_0 result of the local measurements (late time $H(z)$ deformation).	42
2.12	The predicted value of h as a function of the fixed w assuming one parameter dark energy (wCDM) model. The theoretically predicted best fit values of h for different values of w in the case of the wCDM model (orange line), whereas the linear fitting that has been made (dashed blue line). The redpoints correspond to the actual best fit values, including the errorbars, of h for specific values of w obtained by fitting these models to the CMB TT anisotropy (from Ref. [50]).	43

2.13	The predicted form of the CMB TT anisotropy spectrum with $w = -1$, $h = 0.67$, $\Omega_{0m} = 0.314$ for Λ CDM (blue line) and with $w = -1.2$, $h = 0.74$, $\Omega_{0m} = 0.263$ (green line). Red points correspond to the binned high- l and low- l Planck data (from Ref. [50]).	45
2.14	The Pantheon binned SnIa absolute magnitudes Eq. (2.76) M_i (blue points) [51] for a Planck/ Λ CDM luminosity distance. The data are inconsistent with the SnIa absolute magnitude $M^< = -19.24$ calibrated by Cepheids but the inconsistency disappears if there is a transition in the absolute magnitude with amplitude $\Delta M \simeq -0.2$ at redshift $z_t \simeq 0.01$ (from Ref. [52]).	52
2.15	The potential V/V_0 (with $V_0 = m^2 f^2$, $n = 3$ in Eq. (2.80)) as a function of ϕ/f at early times ($H \gg m$) (left panel) when the field ϕ is initially frozen in its potential due to Hubble friction and acts as a cosmological constant with equation of state $w_\phi = -1$, and at a critical redshift z_c when the Hubble parameter drops below some value ($H \sim m$) (right panel) and the field becomes dynamical and begins to oscillate around its minimum which is locally $V \sim \phi^{2n}$	55
2.16	Fractional contribution of EDE to the cosmic energy budget as a function of redshift (adapted from Ref. [53]).	55
2.17	CMB TT power spectrum. The black solid and the red dashed lines correspond to Λ CDM model with $H_0 = 68.07 \text{ km s}^{-1} \text{ Mpc}^{-1}$ and EDE model with $H_0 = 71.15 \text{ km s}^{-1} \text{ Mpc}^{-1}$ respectively (from Ref. [53]).	56
2.18	Posterior 1D and 2D distributions of the cosmological Λ CDM parameters reconstructed from a run to all data (including Planck high l polarization) in EDE (red) and the Λ CDM (blue) scenario. The gray bands correspond to the SH0ES determination of H_0 (adapted from Ref. [54]).	57
3.1	The value of S_8 with the 68% CL constraints derived by recent measurements.	68
3.2	Mollweide-projection view of preferred directions in galactic coordinates for different cosmological observations (see Table 3.2).	76
4.1	$\Delta f \sigma_8$ as a function of redshift for g_a in the range $g_a \in [-1.5, 1.5]$ superimposed with the early growth data (left panel), late data (middle panel) and full growth data (right panel).	88
4.2	The sensitivity measure S for the observable $f \sigma_8$ (i.e. $\frac{\Delta f \sigma_8}{\Delta P} V_{\text{eff}}^{1/2}$) for $P = g_\alpha$ (left panel), $P = w$ (middle panel), and $P = \Omega_m$ (right panel)	91
4.3	$\Delta f \sigma_8$ as a function of redshift for w in the range $w \in [-1.5, -0.5]$ superimposed with the early growth data (left panel), late data (middle panel) and full growth data (right panel).	92
4.4	$\Delta f \sigma_8$ as a function of redshift for Ω_m in the range $\Omega_m \in [0.25, 0.35]$ superimposed with the early growth data (left panel), late data (middle panel) and full growth data (right panel).	92
4.5	$\Delta f(z)$ as a function of redshift superimposed with the Euclid mock data for different values of Ω_m (left panel), w (middle panel), and g_α (right panel).	92
4.6	The deviation $\Delta D_V(z) \times \frac{r_s^{fid}}{r_s}$ as a function of the redshift z for different values of Ω_m (left panel) and w (right panel).	94
4.7	The deviation $\Delta H \times \frac{r_s}{r_s^{fid}}$ as a function of the redshift z for different values of Ω_m (left panel) and w (right panel)	95
4.8	The deviation $\Delta H(z)$ as a function of redshift using the full compilation of Table B.4 in the Appendix B, for various values of Ω_m (left panel) and w (right panel).	95
4.9	The deviation $\Delta D_A \times \frac{r_s^{fid}}{r_s}$ as a function of the redshift z for different values of Ω_m (left panel) and w (right panel)	96
4.10	The BAO observable distances for the Planck/ Λ CDM best-fit parameter values along with the corresponding data from Table B.2 in the Appendix B. The data appear to be in good agreement with the Planck/ Λ CDM predictions.	97

4.11	The $1\sigma - 3\sigma$ contours in the $\Omega_m - w$ parametric space. The contours describe the corresponding confidence regions using the full compilation of $D_V(z) \times \frac{r_s^{fid}}{r_s}$ data (left panel), low redshift ($z < 0.55$) data (middle panel) and high redshift ($z > 0.55$) data (right panel) from Table B.2 in the Appendix B. The red and green dots describe the Planck/ Λ CDM best fit and the best-fit values from the compilation of $D_V(z) \times \frac{r_s^{fid}}{r_s}$ data. Notice that at high z close to the blind spot for Ω_m and the optimum redshift for w , the thickness of the contours (uncertainty) increases along the Ω_m axis and decreases along the w axis (the contours are rotated clockwise) as expected from Fig. 4.6.	98
4.12	The deviation of the distance modulus observable $\Delta\mu$ as a function of redshift for Ω_m (left panel), w (middle panel) and g_α (right panel) superimposed with the JLA data of Table B.3 in the Appendix B.	99
4.13	The sensitivity measure as a function of redshift z for Ω_m (left panel), g_α (middle panel) and w (right panel).	99
4.14	The deviation of the gravitational wave distance modulus with the parameter g_a . The only existing datapoint does not lead to any useful constraints.	100
5.1	The effective potential Eq. (5.55) that determines the velocity rotation curves for parameter values $l = 10$, $M = 2$. The GR prediction (continuous blue line) is obtained for $\alpha = 0$ while the upper and lower red short-dashed lines correspond to the Rindler metric ($\beta = 0$) with $\alpha > 0$ and $\alpha < 0$ respectively. The upper and lower pink long-dashed lines correspond to the metric of the reconstructed potential ($\beta > 0$) for $\alpha > 0$ and $\alpha < 0$ respectively. In the later cases the GR prediction is obtained for large enough values of r	109
5.2	The best fit forms of the velocity profiles Eq. (5.57) (red dashed curve) and Eq. (5.58) (green continuous curve) on the observed halo profiles (thick dots) of two typical galaxies (S:610359 left panel and S:702916 right panel). The blue continuous shows the fit of GR without dark matter which is clearly poor.	110
6.1	The deformation of the HUP in accordance with Eq. (6.4) after rescaling to dimensionless form using a characteristic length scale of the quantum system (from Ref. [55]).	116
6.2	The best fit forms of the scalar spectral index Eq. (6.76) (blue curve for HUP and red curve for GFC Eq. (6.52)) on the observed data (thick dots). The green and brown continuous curves correspond to -1σ and $+1\sigma$ deviation of the parameter $\bar{\mu}$ respectively. The light green and the orange dashed curves correspond to observationally allowed range for the spectral index n_S at approximately 2σ level.	123
6.3	The $1\sigma - 3\sigma$ contours in the $(\lambda, \bar{\mu})$ parametric space. The contours describe the corresponding confidence regions obtained from the full data set (left panel), large scales ($k < 0.015 h/\text{Mpc}$) data (middle panel), and small scales ($k > 0.015 h/\text{Mpc}$) data (right panel). The red and green points correspond to the HUP and GUP best fits respectively.	124
7.1	The $f\sigma_8(z)$ data compilation from Table D.3 used in the present analysis. The subset of the data with less correlation is indicated with dark red. The red curve shows the Planck18/ Λ CDM prediction (parameter values $\Omega_{0m} = 0.315$, $g_a = 0$, $\sigma_8 = 0.811$), the blue curve shows the best fit of the $f\sigma_8(z)$ in the context of parametrizations Eq. (7.14) with a Λ CDM background (parameter values $\Omega_{0m} = 0.272$, $g_a = -1.306$, $\sigma_8 = 0.886$) and the shaded regions correspond to 1σ confidence level around the best fit (see also Table 7.2).	132

- 7.2 The $E_G(z)$ data compilation from Table D.4 (scales $3 < R < 150h^{-1}Mpc$) used in the present analysis. The subset of the data with less correlation is indicated with dark red. The red curve shows the theoretical prediction based on the Planck18/ Λ CDM parameter values ($\Omega_{0m} = 0.315$, $\sigma_8 = 0.811$, $\mu_G = 1$, $\Sigma_G = 1$), the blue curve shows the best fit theoretical prediction based on the parametrizations (7.14) and (7.15) with parameter values ($\Omega_{0m} = 0.313$, $g_a = -0.129$, $g_b = -2.308$). Notice that the best fit is significantly below the Planck/ Λ CDM theoretical prediction and implies weaker gravity ($\mu_G < 1$ and $\Sigma_G < 1$) at the 4.6σ level (see also Table 7.2). 132
- 7.3 The three $1\sigma - 7\sigma$ confidence contours in 2D projected parameter spaces of the parameter space ($\Omega_{0m}, \sigma_8, g_a$) in the context of parametrization Eq. (7.14) with $n = 2$ including the fiducial correction factor Eq. (7.17). The RSD data $f\sigma_8(z)$ from Table D.3 of the Appendix D was used. The third parameter in each contour was fixed to the best fit value. The red and green dots describe the Planck18/ Λ CDM best fit and the best-fit values from data. 133
- 7.4 The three $1\sigma - 5\sigma$ confidence contours in 2D projected parameter spaces of the parameter space (Ω_{0m}, g_a, g_b) in the context of parametrizations Eqs. (7.14) and (7.15) with $n = 2, m = 2$. The data $E_G(z)$ from Table D.4 of the Appendix D were used. The third parameter in each contour was fixed to the best fit value. The red and green dots describe the Planck18/ Λ CDM best fit and the best-fit values from data. 134
- 7.5 The six $1\sigma - 7\sigma$ confidence contours in 2D projected parameter spaces of the parameter space ($\Omega_{0m}, \sigma_8, g_a, g_b$) in the context of parametrizations Eqs. (7.14) and (7.15) with $n = 2$ and $m = 2$ including the fiducial correction factor Eq. (7.17). The data $E_G(z)$ and $f\sigma_8(z)$ from Tables D.4 and D.3 of the Appendix D was used. The third and the fourth parameter in each contour were fixed to the best fit values. The red and green dots describe the Planck18/ Λ CDM best fit and the best-fit values from data. 134
- 7.6 Left: The $1\sigma - 2\sigma$ confidence contour of the parameter space ($\Omega_{0m}, \sigma_8, g_a$) in the context of parametrization Eq.(7.14) with $n = 2$ including the fiducial correction factor Eq. (7.17). The RSD data $f\sigma_8(z)$ from Table D.3 of the Appendix D was used. The red and green dots describe the Planck18/ Λ CDM best fit and the best-fit values from data. Right: The $1\sigma - 2\sigma$ confidence contour of the parameter space (Ω_{0m}, g_a, g_b) in the context of parametrizations Eqs. (7.14) and (7.15) with $n = 2$. The data $E_G(z)$ from Table D.4 of the Appendix D was used. The red and green dots describe the Planck18/ Λ CDM best fit and the best-fit values from data. The 3D contours include only the surfaces in 3D while the intermediate space is not filled. Thus, the white gaps that appear in the right figure between the surfaces, simply correspond to the white background seen from behind. 135
- 7.7 Evolution of μ_G and Σ_G as functions of the scale factor a considering the best fit values for g_a and g_b in the context of parametrizations Eqs. (7.14) and (7.15) with $n = 2, m = 2$. The data $E_G(z)$ and $f\sigma_8(z)$ from Tables D.4 and D.3 of the Appendix D was used. The dashed curves correspond to 1σ deviations of the parameters μ_G and Σ_G . The red lines correspond to the GR- Λ CDM model. 137
- 7.8 The confidence contours of the parameter space ($\sigma_8 - \Omega_m$) in the context of GR (left panel) and in the presence of the MG parameter g_a (fixing $w = -1$) in the context of parametrization Eq. (7.14) with $n = 2$. We have considered both the case of a marginalized MG parameter value (right panel) and the case of setting g_a to its best fit value (middle panel). The red and green dots describe the Planck18/ Λ CDM best fit and the best-fit values from data. The $f\sigma_8(z)$ data compilations of datapoints with less correlation from Table D.3 of the Appendix D was used. Notice the reduction of tension between the growth data best fit and the Planck/ Λ CDM parameter values when the MG degree of freedom is introduced. 138

- 7.9 The confidence contours of the parameter space ($\sigma_8\text{-}\Omega_m$) in the context of GR (left panels) and in the presence of the w parameter (fixing $g_a = 0$ and $g_b = 0$). We have considered both the case of a marginalized w ($[-1.5, -0.5]$) parameter value (right panels) and the case of setting w to its best fit value (-0.94 and -1.29 from $f\sigma_8(z)$ and $f\sigma_8(z) + E_G(z)$ data respectively) (middle panels). The red and green dots describe the Planck18/ Λ CDM best fit and the best-fit values from data. The $E_G(z)$ and $f\sigma_8(z)$ data compilations of datapoints with less correlation from Tables D.4 and D.3 of the Appendix D was used. Notice that the reduction of tension between the best fit parameter values and Planck/ Λ CDM is less efficient when the w degree of freedom (modified background expansion rate) is introduced compared to the MG degree of freedom g_a shown in Fig. 7.8. 139
- 7.10 Measurements of E_G as a function of scale R in the range $0.15 < z < 0.43$ (left panel) and $0.43 < z < 1.2$ (right panel). The data $E_G(R)$ from Tables D.5 and D.6 of the Appendix D was used. The dashed black line shows the Planck18/ Λ CDM prediction at $z = 0.3$, the dotted black line shows the Planck18/ Λ CDM prediction at $z = 0.7$, while the dotted-dashed black line and the large dashed black line shows the best fit of the E_G in the context of parametrizations Eqs. (7.14) and (7.15) at $z = 0.3$ and at $z = 0.7$ respectively. 140
- 8.1 The critical values $\xi_{H,C}(q^2)$ (with $0 < q^2 < 9/8$) and $\xi_{-,H}(q^2)$ (with $1 < q^2 < 9/8$) as a function of q^2 at which $r_H = r_C$ and $r_- = r_H$ respectively (left panel). The colored shaded regions correspond to the physical corresponding regions of Fig. 8.6 discussed below. The metric function $f(r)$ as a function of r in the case of the RN-dS/SdS/RN spacetimes for critical value $\xi_{H,C}$ (when event and cosmological horizons coincide) and $\xi_{-,H}$ (when inner Cauchy and outer event horizons coincide) (right panel). The blue, green and red solid curves correspond to RN-dS spacetime while the purple and orange dashed curves correspond to RN and SdS spacetime respectively. 148
- 8.2 The m^2M^2 dependent Regge-Wheeler dimensionless potentials VM^2 (left panel) and V_*M^2 (middle panel) as a function of r/M and r_*/M respectively in the cases of the SdS ($Q = 0$) (red curves) and RN-dS ($Q/M = 0.9$) (blue curves) spacetimes for angular scale $l = 0$ and dimensionless parameter fixed to $\xi = 0.5$. The solid curves correspond to the critical value of the scalar field mass $m_{cr}^2M^2 = 0$. The right panel demonstrates the process for identifying the zero eigenvalue eigenstate i.e. setting $\Omega = 0$ in Eq. (8.39) and increasing the dimensionless parameter m^2M^2 until the solution $u_0(r_*/M)$ satisfies both end boundary conditions (8.56)-(8.59) for $\Omega = 0$. This value of m^2M^2 is the critical value for the considered value of ξ . The potential gets deeper and more accepting to bound states (instabilities) as the m^2M^2 gets lower. 150
- 8.3 The ξ dependent Regge-Wheeler dimensionless potentials VM^2 (left panel) and V_*M^2 (middle panel) as a function of r/M and r_*/M respectively in the case of the SdS (solid curves) and RN-dS (dashed curves) spacetimes for angular scale $l = 0$ and critical value for $m^2 = m_{cr}^2 = 0$. The radial function $u_0(r_*/M)$ (right panel) which is the radial zero mode solution of Schrodinger like equation (8.39) with $\Omega = 0$ and boundary conditions (8.56) and (8.57) at large negative r_* . For critical value of the scalar field mass $m_{cr}^2M^2 = 0$ the boundary conditions (8.58) and (8.59) at large positive r_* are satisfied. The brown and purple dotted curves correspond to the pure Schwarzschild ($Q = 0, \xi = 0$) and RN ($Q \neq 0, \xi = 0$) backgrounds respectively. The potential gets deeper as ξ decreases and Q/M increases. However, since the local maximum of the potential also increases as the potential gets deeper, the critical value $m_{cr}M$ for the existence of bound states remains the same and equal to zero in all cases. 150

- 8.4 The critical value of the scalar field mass $m_{cr}^2 M^2$ is zero and independent of the dimensionless parameter ξ (with $\xi \in [0, \xi_{H,C}(q)]$) in the case of the SdS and RN-dS spacetime (blue straight line) for $l = 0$. The solid curves show the form of $m_{cr}(q, \xi)^2 M^2$ that saturates the Sufficient for Instability Criterion (SIC) Eq. (8.60) while the corresponding dashed curves shows the forms of $m_{cr}(q, \xi)^2 M^2$ that saturate the Sufficient for Stability Criterion (SSC) Eq. (8.61) for three values of Q/M . As expected, the exact value of $m_{cr} M = 0$ is between the SIC lines (lower lines) and SSC lines (upper lines) so that none of the criteria is violated (SSC or SIC). 152
- 8.5 The dimensionless growth rate of the instability ΩM as a function of the dimensionless parameters ξ and $q^2 = Q^2/M^2$ for scalar field mass $m^2 M^2 = -0.05$ (cyan surface) and $m^2 M^2 = -0.2$ (yellow surface). 152
- 8.6 The ξ dependent relative growth rate of the instability Ω/Ω_F (with Ω_F the growth rate of the instability in flat spacetime) as a function of the dimensionless parameter $q^2 = Q^2/M^2$ for the scalar field mass $m^2 M^2 = -0.05$ (left panel) and $m^2 M^2 = -0.2$ (right panel). The curves for a given parameter value ξ (with $\xi < 1$) turn out to be straight lines. The range of values of ξ and q is determined by the physically interesting parameter region between the green and blue lines of Fig. 8.1. The parameter region corresponding to linear behavior of $\Omega(q^2)$ (yellow region) is also shown in Fig. 8.1. 154
- 8.7 The ξ dependent dimensionless growth rate of the instability ΩM as a function of the scalar field mass $m^2 M^2$ (with $m(\xi)^2 < m_{cr}(\xi)^2 = 0$) for dimensionless parameters $Q^2/M^2 = 0$ (SdS spacetime) (left panel) and $Q^2/M^2 = 0.3$ (RN-dS spacetime) (right panel). The green dashed curves correspond to $\Omega M(m^2 M^2)$ in the case of the Minkowski spacetime. Clearly, for a given field mass, the growth rate is more suppressed in the absence of charge and for higher values of ξ 155
- 8.8 The m^2/Λ dependent Regge-Wheeler dimensionless potential V_*/Λ as a function of $r_*\sqrt{\Lambda}$ in the case of the deSitter spacetime ($M = 0, \xi = 0$) for angular scale $l = 0$. The green solid curve corresponds to the critical value of the scalar field mass $m_{cr}^2/\Lambda = 0$. The dotted ($m^2/\Lambda > 0$) and dashed ($m^2/\Lambda < 0$) curves correspond to non-existence of bound states (stabilities) and existence of bound states (instabilities) respectively. 157
- 8.9 The dimensionless growth rate of the instability $\Omega/\sqrt{\Lambda}$ as a function of the scalar field mass m^2/Λ (with $m < m_{cr} = 0$) in the case of deSitter spacetime. Clearly $\Omega(m^2/\Lambda) < |m|$ as in the other cases where a cosmological horizon is present. 158
- 8.10 The $m^2 M^2$ dependent Regge-Wheeler dimensionless potentials $V M^2$ (left panel) and $V_* M^2$ (right panel) as a function of r/M and r_*/M respectively in the case of the Schwarzschild spacetime ($\Lambda = 0, \xi = 0$) for angular scale $l = 0$. The blue solid curves correspond to the critical value of the scalar field mass $m_{cr}^2 M^2 = 0$. The dotted ($m^2 M^2 > 0$) and dashed ($m^2 M^2 < 0$) curves correspond to non-existence of bound states (stabilities) and existence of bound states (instabilities) respectively. 158
- 9.1 The stability (no ghost) region in the $\alpha_{M0}-\alpha_{B0}$ parameter space is shown and divided into a weak gravity regime today, $\mu_{G,0} \equiv \mu_G(z = 0) < 1$ (green area), and a strong gravity regime today, $\mu_{G,0} > 1$ (blue area). This is obtained by demanding $c_s^2(z) > 0$ at all times and assuming a flat Λ CDM background together with the parametrization Eq. (9.18) used here for the values $s = 0.5, 1, 1.5, 2, 2.5, 3$. The dark blue and dark green regions indicate $\gamma_0 > \gamma_0^{\Lambda CDM}$, while the light blue and light green regions correspond to $\gamma_0 < \gamma_0^{\Lambda CDM}$. Finally, the red curve determines the regions where either $\gamma_1 > \gamma_1^{\Lambda CDM}$ or $\gamma_1 < \gamma_1^{\Lambda CDM}$. We see in particular that for $s \leq 2$, essentially the weak gravity regime today is selected. In the light green region, μ_G crosses 1 downwards with expansion, while it crosses upwards in the dark blue region. 170

9.2	The best fit values of α_{B0} and α_{M0} are shown for $s = 0.5, 1, 1.5, 2$ using the combined constraints from the $f\sigma_8$ and E_G data, 1σ and 2σ confidence regions are drawn (red curves). As in Fig. 9.1, the green area corresponds to weak gravity today while the blue area represents strong gravity today. Observations give the constraint $\gamma_0 > \gamma_0^{\Lambda CDM}$ for $s < 2$, marginally allowing $\gamma_0 < \gamma_0^{\Lambda CDM}$ for $s = 2$. Note that for higher values of s , the best fit moves outside the colored region and is therefore ruled out.	171
10.1	Fitting individual R_W to Cepheid data as derived from our work (red points) and from Ref. [56] (blue points). For illustration purposes, the D_L axis has been shifted slightly for our values so that the error bars do not overlap. The red and blue dotted lines correspond to $R_W = 0.366$ and $R_W = 0.369$ respectively. These R_W values are taken using the derived individual parameters of anchor galaxies and M31 (due to its proximity) $R_{W,k}$	179
10.2	The best fit $R_{W,bf}$ for various Σ_1 and Σ_2 datasets as a function of the critical dividing distance $D_c \in [0.01, 37]$ Mpc as derived using the individual R_W (red points in Fig. 10.1). The dark red points correspond to the dataset with galaxies that have distance below D_c , whereas the red points regard galaxies with distances above D_c	181
10.3	The σ -distances between the various Σ_1 and Σ_2 datasets as a function of the critical dividing distance D_c as derived using the individual values of R_W . The red and blue lines correspond to the red (our results) and blue (the results in Ref. [56]) points of Fig. 10.2 respectively. A transition of the σ -distance at $D_c \simeq 22$ Mpc is apparent.	182
10.4	Fitting individual M_H^W to Cepheid data for global R_W with a fixed value 0.386. Anchor galaxies are denoted with dark red points and SnIa host galaxies with green points. The dotted line corresponds to $M_H^W = -5.98$ mag as derived using the individual values of anchor galaxies and M31 (due to its proximity) $M_{H,k}^W$	183
10.5	The best fit $M_{H,bf}^W$ for various Σ_1 and Σ_2 datasets as a function of the critical distances D_c as derived using the individual values of M_H^W (points in Fig. 10.4). The dark green points correspond to the dataset with galaxies that have distance below D_c , whereas the green points regard galaxies with distances above D_c	183
10.6	The green line represents the σ -distances between the various Σ_1 and Σ_2 datasets as a function of the critical distances D_c as derived using the individual values of M_H^W . In contrast the yellow lines correspond to 68% (one standard deviation) range of the σ -distances as a function of the critical distances D_c produced by a Monte Carlo simulation of 100 sample datasets assuming artificial homogeneity of the M_H^W data. The simulations have been performed for randomly varying M_H^W values with a Gaussian probability distribution with mean $M_H^W = -6$ mag provided by the full M_H^W datapoints and standard deviation equal to the corresponding 1σ error.	185
10.7	The σ -distances as a function of the critical distances D_c for 100 sample datasets with random distance values, normally distributed inside their individual $1-\sigma$ range as derived using the individual values of M_H^W . A transition of the σ -distance at $D_c \simeq 22$ Mpc remains present for practically all of the Monte Carlo samples.	185
10.8	The green lines represent the 68% range of the σ -distances as a function of the critical distances D_c produced by a Monte Carlo simulation of 100 sample datasets. The simulations have been performed for randomly varying galaxy distance values with a Gaussian probability distribution with mean equal to the measured distance and standard deviation equal to the corresponding 1σ error. In contrast the pink region correspond to a Monte Carlo simulation of 100 sample datasets assuming artificial homogeneity of the M_H^W data. In addition to this homogeneity the simulations have been performed for randomly varying galaxy distance values with a Gaussian probability distribution.	186
10.9	Fitting individual M_H^W to Cepheid data with a free global R_W . Anchor galaxies are denoted with cyan points and SnIa host galaxies with magenta points. The dotted line corresponds to $M_H^W = -5.90$ mag as derived using the individual values of anchor galaxies and M31 (due to its proximity) $M_{H,k}^W$	186

10.10	The one dimensional relative probability density values of the color luminosity parameter and the Cepheid absolute magnitude as derived using the DSS method for the cases I, II, and III. All measurements are shown as normalized Gaussian distributions. Notice that the best fit values one for galaxies at distances $D < D_c$ and one for galaxies at $D > D_c$ are inconsistent with each other at a level larger than 3σ	187
10.11	The best fit values of the parameter R_W for base/base-SHOES, I and IV models as derived using Cepheid data. Note that in terms of the AIC and BIC, fitting for two universal values of R_W with global M_H^W is the preferred model (case IV, green region).	188
10.12	The best fit values of the parameter M_H^W for base/base-SHOES, III and V models as derived using the Cepheid data. Note that in terms of the AIC and BIC, fitting for two universal values of M_H^W with global R_W is the preferred model among the models shown (case V, cyan region).	188
10.13	The ΔAIC and ΔBIC of models with different free parameter set compared to base (subindex 1) and base-SHOES (subindex 2) models. Clearly, the case IV (two universal R_W and a global M_H^W) is the best model and on the other hand, the case II (a global R_W and individual M_H^W) is the worst one.	189
10.14	The one dimensional relative probability density value of SnIa absolute magnitude M_B for all cases studied in this analysis compared to that obtained using CMB calibration. All measurements are shown as normalized Gaussian distributions. Clearly, for all cases where we do not consider the universality of parameters R_W and M_H^W (i.e. I, II, III, IV, V, VI) the M_B is consistent with the CMB determination value.	192
10.15	The one dimensional relative probability density value of H_0 as derived using the Eq. (10.37) (solid lines) and the Eq. (10.39) (dashed lines) for all cases studied in this analysis compared to that from the Planck CMB measurement (grey line). All measurements are shown as normalized Gaussian distributions. It is evident that for all cases where we break the assumption of universality of the parameters R_W and M_H^W (i.e. I, II, III, IV, V, VI) the derived values of H_0 are consistent with the corresponding predicted Planck CMB best fit value.	193
11.1	Schematic plots of the asymmetron effective potential Eq. (11.31) in vacuum (purple) and in high density (green) cosmological regions. Notice the asymmetric form of the effective potential in which the degeneracy of the vacua is slightly broken. However in the presence of sufficiently high density, a single minimum at $\phi = 0$ restores GR as in the symmetron case.	204
11.2	The geometry of the spherical domain wall in the presence of spherical matter shell. . . .	205
11.3	The scalar field ϕ as a function of the distance r corresponds to the solution in the case of monotonic matter density increasing towards the center (with $R_m = 1$). In this resulting minimum energy field configuration we see a collapse of the wall due to tension. The energy minimization was performed numerically using $N = 150$ lattice points.	207
11.4	The scalar field ϕ as a function of the distance r corresponds to the solution obtained from the energy minimization method in the case of increasing matter density. This field configuration appears to be stabilized by the combined effects of the wall tension and the attraction of the increased matter density as r increases.	208
11.5	Left panel: The matter density of the spherical matter shell of the form (11.49) with radius $R_m = 15$. Middle panel: The scalar field ϕ in symmetron case ($\varepsilon = 0$) as a function of the distance r corresponds to the solution obtained from the energy minimization method in the case of matter density of the spherical matter shell of the form (11.49) with radius $R_m = 15$. The final minimum energy configuration is independent of the initial guess shown here in blue. Right panel: The scalar field ϕ in asymmetron case ($\varepsilon = 0.2$) as a function of the distance r corresponds to the solution obtained from the energy minimization method in the case of matter density of the spherical matter shell of the form (11.49) with radius $R_m = 15$	209

11.6	The form of the asymmetron (with $\varepsilon = 0.2$) effective potential for the case $\rho = 0$ (vacuum) and $\rho = 3$ (high density) (see Figs. 11.1 and 11.5). The red points represent the value of the field and show how the asymmetron field changes as the wall is crossed by increasing r .	209
11.7	Simulation of time evolution of the perturbed scalar field corresponding to a perturbed spherical asymmetron domain wall. The wall gets trapped at the matter shell as expected (collapse is avoided).	210
11.8	Mollweide projection view of 12 cluster locations of Ref. [57] in galactic coordinates (see Table H.1). The colour of the points on the plot corresponds to their σ significance for a deviation from the GR, which is indicated in the horizontal colour bar. Four clusters (in shaded green regions-bubbles) have large negative value for Ξ_1 parameter, significantly ($> 3\sigma$) different from the GR ($\Xi_1 = 0$) expectation. The size of the points R_{point} was designed according to the size of the clusters R_{500} and their distance D .	212

List of Tables

1.1	Special cases of the equation of state parameter w_i and the corresponding relations $p_i = p(\rho_i)$, $\rho_i = \rho_i(a)$ and $a = a(t)$	8
2.1	The Hubble constant H_0 values at 68% CL through direct and indirect measurements by different methods.	36
3.1	The value of the structure growth parameter combination $S_8 \equiv \sigma_8(\Omega_{0m}/0.3)^{0.5}$, the matter density parameter Ω_{0m} and the the power spectrum amplitude σ_8 at 68% CL through direct and indirect measurements by different methods.	63
3.2	The amplitudes and the directions (l, b) (galactic coordinates) from different cosmological observations (Fig. 3.2) along with the corresponding references. The amplitude of CMB dipole has derived using the Eq. (3.33) (see e.g. Ref. [58]).	77
4.1	Some recent and future large-scale structure surveys. Photometric surveys focus mainly on WL, while spectroscopic surveys measure mainly RSD. The redshift range shifts to higher redshifts for stage III and stage IV surveys.	87
5.1	The best fit values of parameters and the corresponding value of the adjusted R^2 of the velocity profiles Eqs. (5.57) and (5.58) on the observed halo profiles of two typical galaxies S:610359 and S:702916 (rotation curve data obtained from Ref. [59]).	111
6.1	The best fit values of parameters λ and $\bar{\mu}$ with the corresponding 1σ standard deviations for the fitted spectral index on the observed data [60].	125
7.1	Planck18/ Λ CDM parameters values [14] based on TT,TE,EE+lowE+lensing likelihoods. .	127
7.2	Planck18/ Λ CDM based on TT,TE,EE+lowE+ lensing likelihoods best fit [14] and the best-fit values from data.	136
7.3	Sigma differences of the best fit contours from Planck18/ Λ CDM.	137
10.1	Fitting results and model comparison tests for different models. For the ΔAIC and ΔBIC the comparisons are made respect to base (base-SH0ES) models. The value of H_0 derived using the Eq. (10.37) (black font) and the Eq. (10.39) (green font). The best fit parameters of SnIa absolute magnitude M_B and the value of H_0 in the parentheses correspond to intrinsic scatter of LMC Cepheids $\sigma_{LMC} = 0$	189
10.2	The interpretation of differences ΔAIC and ΔBIC according to the calibrated Jeffreys' scale [61] (see also Refs. [62–66]). However, it should be noted that the Jeffreys' scale has to be interpreted with care [63] because has been shown to lead to different qualitative conclusions.	191
10.3	Ranking of models according to AIC and BIC criteria. We see that in terms of the AIC and BIC fitting for two universal values of R_W with global M_H^W is the preferred model (case IV).	191

12.1	Some existing and upcoming large-scale structure missions/experiments.	219
12.2	Some existing and upcoming CMB missions/experiments.	219
12.3	Some existing and upcoming GW experiments/observatories	220
A.1	List of used acronyms.	227
B.1	The compilation of RSD data used in our analysis (from Ref. [67]).	231
B.2	A compilation of BAO data that have been published from 2006 until 2018 in chronological order	232
B.3	The JLA binned data used in our analysis (from Ref. [68]).	233
B.4	The $H(z)$ data compilation used in our analysis (from Ref. [69]).	234
D.1	Planck18/ Λ CDM based on TT,TE,EE+lowE+ lensing likelihoods best fit [14] and the best-fit values from data compilation of datapoints with less correlation.	237
D.2	Sigma differences of the best fit contours from Planck18/ Λ CDM. The $E_G(z)$ and $f\sigma_8(z)$ data compilations of datapoints with less correlation from Tables D.4 and D.3 was used.	238
D.3	The $f\sigma_8$ updated data compilation of Ref. [67] used in our analysis. The subset of the datapoints with less correlation is indicated with bold font in the index.	238
D.4	The $E_G(z)$ data compilation used in our analysis. The subset of the datapoints with less correlation is indicated with bold font in the index.	239
D.5	The $E_G(R)$ data compilation in the range $0.15 < z < 0.43$ used in our analysis.	240
D.6	The $E_G(R)$ data compilation in the range $0.43 < z < 1.2$ used in our analysis.	241
F.1	The $f\sigma_8$ updated data compilation of Ref. [4] used in our analysis.	244
F.2	The $E_G(z)$ data compilation of Ref. [4] used in our analysis.	245
G.1	Photometric data for MW Cepheids from Table 1 in Ref. [40].	249
G.2	Photometric data for LMC Cepheids from Table 2 in Ref. [39].	250
G.3	WFC3-IR data for 1486 Cepheids in the anchor galaxy NGC 4258 and in the host galaxies from Table 4 in Ref. [17]. An electronic version of the complete table is available at [70].	252
G.4	Approximations for distance parameters from Table 5 in Ref. [17].	253
H.1	The collection of 12 clusters. From left to right the columns correspond to: Abell names, galactic coordinates (from NED), redshifts (from NED), luminosity distances (from NED), the halo radii for overdensity of $\Delta = 500$ with respect to the critical density of the universe at the cluster's redshift, the modified gravity parameters Ξ_1 and $\bar{\gamma}$ which track the departure of DHOST theory from GR as derived by Ref. [57] and the corresponding σ significances.	255

Chapter 1

Introduction

Modern cosmology has its foundations in Einstein's general relativity (GR). GR is the simplest successful theory for gravity. It is consistent with the vast majority of experiments and observations from sub-mm scales up to cosmological horizon scales [71, 72]. Alternative modified theories of gravity include more degrees of freedom and parameters which are strongly constrained by a wide range of experiments and astrophysical/cosmological observations to be very close to the values predicted by GR (see e.g. [73–76]).

In this introductory chapter, we present elements of GR and Cosmology and their basic concepts. At the end of the chapter we present an introduction to the standard Lambda Cold Dark Matter (Λ CDM) model.

1.1 Elements of General Relativity

1.1.1 Geometry and gravity-The metric

The geometric background on which the GR is based is the spacetime. The spacetime is the mathematical model that unites space and time in one continuum and is a four-dimensional pseudo-Riemannian manifold. In the Special Relativity (SR) we have the flat spacetime or Minkowski spacetime while in the GR we consider that the spacetime is curved by the presence of matter/energy. For each point of 4-dimensional spacetime we can define a 4-set of coordinates x^0, x^1, x^2, x^3 that can be referred as $\{x^\alpha\}$.

The geometry of spacetime is characterized by the way the distance of two points is measured. If ds the elementary spacetime distance or line element between two adjacent points then

$$ds^2 = g_{\alpha\beta} dx^\alpha dx^\beta, \quad (1.1)$$

where $g_{\alpha\beta}$ is a metric tensor that describes the geometrical properties of the spacetime. The spacetime as a manifold with the introduction of the metric acquires a certain shape. The metric tensor in GR describes the gravitational potential.

1.1.2 Geodesics

In flat space, straight lines are the most important curves. A straight line in the Euclidean space is the only curve that simultaneously conveys its own tangent vector. More specifically, the tangent to the line at one point is parallel to the tangent to the previous point. In a curved space, there are respectively the curves that meet the requirement of the parallel transport of the tangent carrier. These curves are called geodesics. If the tangent vector to the geodesic curve $x^\mu(\lambda)$ (where λ a affine parameter (e.g. the

distance) measured along the curve which monotonically increases along the particle's path) is $dx^\mu/d\lambda$ then the geodesic equation holds

$$\frac{d^2 x^\alpha}{d\lambda^2} + \Gamma_{\mu\nu}^\alpha \frac{dx^\mu}{d\lambda} \frac{dx^\nu}{d\lambda} = 0 , \quad (1.2)$$

where $\Gamma_{\mu\nu}^\alpha$ is the Christoffel symbol defined as

$$\Gamma_{\mu\nu}^\alpha = \frac{1}{2} g^{\alpha\lambda} (g_{\lambda\mu,\nu} + g_{\lambda\nu,\mu} - g_{\mu\nu,\lambda}) , \quad (1.3)$$

where $g^{\alpha\lambda}$ is the inverse of $g_{\alpha\lambda}$ and the commas denote partial differentiation i.e. $g_{\lambda\mu,\nu} \equiv \partial g_{\lambda\mu}/\partial x^\nu$.

At the flat spacetime where the Christoffel symbols are zero the solution of the geodesic equation is the straight lines. The geodesic curves based on the principles of the GR represent the 'straight lines' of the curved spacetime over which the particles move under the influence of gravity alone (absence of any other forces) performing a free fall.

1.1.3 Einstein's field equations

The study of the inherent curvature of a spacetime is done through the Riemann tensor $R_{\mu\beta\nu}^\alpha$, a four-order tensor of the curvature. This tensor describes the deviation of the curve spacetime from the flat spacetime. In the case of flat spacetime the Riemann tensor is zero. The contraction of the first and third index of the Riemann tensor gives the Ricci tensor

$$R_{\mu\nu} = R_{\mu\alpha\nu}^\alpha . \quad (1.4)$$

The Ricci tensor in terms of the Christoffel symbol expressed as

$$R_{\mu\nu} = \Gamma_{\mu\nu,\alpha}^\alpha - \Gamma_{\mu\alpha,\nu}^\alpha + \Gamma_{\mu\nu}^\alpha \Gamma_{\alpha\beta}^\beta - \Gamma_{\mu\beta}^\alpha \Gamma_{\alpha\nu}^\beta , \quad (1.5)$$

where the commas denote partial differentiation. From Eqs. (1.3) and (1.5) we see that the Ricci tensor depends on the metric and its derivatives.

The contraction of the Ricci tensor gives the scalar curvature of $g_{\mu\nu}$ or Ricci scalar defined at each point of the manifold

$$R = g^{\mu\nu} R_{\mu\nu} = R_\mu^\mu . \quad (1.6)$$

The Einstein tensor that describes the curvature of spacetime in the field equations of GR is defined as

$$G_{\mu\nu} \equiv R_{\mu\nu} - \frac{1}{2} g_{\mu\nu} R . \quad (1.7)$$

Fundamental properties of the Einstein tensor are that it is symmetric $G_{\mu\nu} = G_{\nu\mu}$ and divergenceless¹ $\nabla_\mu G^{\mu\nu} = 0$ which holds as a contraction of the Bianchi identities.

The Einstein's field equations relate the Einstein tensor describing the geometry to the energy-momentum tensor describing the energy

$$G_{\mu\nu} = \kappa T_{\mu\nu} , \quad (1.8)$$

where $\kappa = 8\pi G$ ($c = 1$), $G = 6.67 \cdot 10^{-11} \text{ m}^3 \text{ s}^{-2} \text{ Kg}^{-1}$ is the bare Newton's constant and $T_{\mu\nu}$ is the energy-momentum tensor, defined by

$$T_{\mu\nu} \equiv -\frac{2}{\sqrt{-g}} \frac{\delta(\mathcal{L}_m \sqrt{-g})}{\delta g^{\mu\nu}} , \quad (1.9)$$

with \mathcal{L}_m the matter Lagrangian and g the determinant of the metric.

¹The symbol ∇_μ denotes the covariant derivative operator. Also, for the covariant derivative we use the symbol “; μ ”.

The energy-momentum tensor $T_{\mu\nu}$ of matter components is the generalization in the four-dimensional spacetime of the following three-dimensional physical quantities: energy density, momentum density, energy flux density and momentum flux density. It is a second-order symmetric tensor.

Note that we can derive the Einstein's field equations (1.8) by varying with respect to the metric the action of the gravitational theory given by

$$S = S_{EH} + S_m = \int d^4x \sqrt{-g} \left[\frac{R}{16\pi G} + \mathcal{L}_m \right], \quad (1.10)$$

where S_{EH} is the Einstein–Hilbert action and S_m is the action for the matter fields.

Einstein's field equations are a system of ten conjugated nonlinear differential equations. The cosmological dynamics can be obtained by solving these equations.

1.2 Elements of Cosmology

1.2.1 Cosmic Expansion-Hubble's law

Both Lemaître in 1927 and Hubble in 1929 discovered that galaxies appear to be moving away from Earth. In addition, the recession velocity v_r at which galaxies appear to move away from us is proportional to the distance d of the galaxy from Earth. This behavior of velocity is known as Hubble's law. We can describe Hubble's law with the relation [11]

$$v_r = H d, \quad (1.11)$$

where H is the Hubble parameter.

The Hubble parameter is a function of time but is independent of position at any time. The value $H(t_0) = H_0$ at the present time t_0 is called Hubble constant.

Because of the uncertainty in the exact value of the Hubble constant H_0 it is common to be written as

$$H_0 = 100 h \text{ Km s}^{-1} \text{ Mpc}^{-1} = 2.1332 h \cdot 10^{-42} \text{ GeV}, \quad (1.12)$$

where h is a factor which describes the uncertainty.

The Hubble constant corresponds to the slope of the line in the Hubble diagram which plots the velocity against the distance (see Fig. 1.1).

The recession velocity is also called Hubble flow and suggests that the expanding universe is evolving evenly in all directions. Expanding universe means that the universe has a finite age, or at least that it has expanded in a finite time from a state of very high density. Thermal radiation indicates that the universe was initially much warmer than it is today and has cooled. The extremely dense and warm universe in its early stages form the basis of the Lemaître Big Bang theory² which has been advocated and developed by George Gamow.

We define the Hubble time or Hubble age t_H as the inverse of the Hubble constant

$$t_H = \frac{1}{H_0}. \quad (1.13)$$

For $H_0 = 67.8 \text{ km s}^{-1} \text{ Mpc}^{-1}$ the Hubble time is $t_H = 4.55 \cdot 10^{17} \text{ s} = 14.4 \text{ Gyr}$. This is different from the real age of the universe which is approximately $t_U = 13.8 \text{ Gyr}$.

Also, the Hubble radius or Hubble length R_H is defined as

$$R_H = \frac{c}{H_0}, \quad (1.14)$$

where c is the speed of light. The Hubble radius is the distance between the Earth and the galaxies which are currently receding from us at the speed of light and thus corresponds roughly to the size of the visible universe.

²The term Big Bang was first used by the astrophysicist Fred Hoyle, an opponent of the theory of Gamow, who did not use the term to describe the theory but to taunt it.

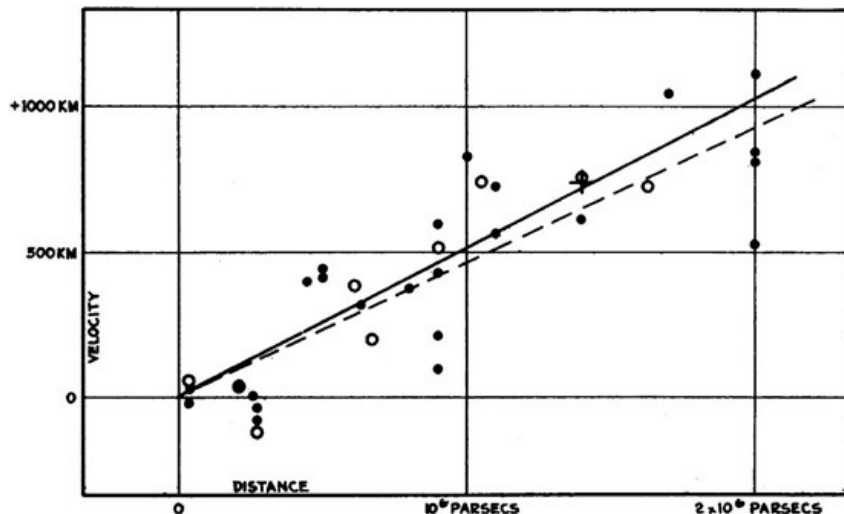


Figure 1.1: Edwin Hubble's original plot of the velocity-distance relation among extra-galactic nebulae (from Ref. [11]).

1.2.2 Redshift

Hubble made his discovery based on Slipher's earlier observations by studying the spectral lines of galaxies. He observed the shift of the spectral lines towards the red part of the spectrum and concluded that the galaxies were moving away. This phenomenon is called redshift and is reminiscent of the Doppler effect. However in reality as we will see below the coordinates of the galaxies do not change but space expands and supports the galaxies.

A galaxy is observed to have a redshift parameter (stretching factor) defined by the formula:

$$z \equiv \frac{\lambda_{ob} - \lambda_{em}}{\lambda_{em}}, \quad (1.15)$$

where λ_{ob} is the wavelength of the spectral line that we observe and λ_{em} the wavelength of the spectral line that it emits. The redshift z is zero today and increases with distance.

The velocity v at which a galaxy moves away from the observer and the redshift z are related to the Doppler relationship:

$$1 + z = \sqrt{\frac{1 + \beta}{1 - \beta}}, \quad (1.16)$$

where $\beta = v/c$. If $\beta \ll 1$ then we obtain

$$v \simeq cz, \quad (1.17)$$

which is approximately valid for small z .

1.2.3 Comoving Coordinates-Scale Factor

The comoving coordinate system is suitable for a space that isotropically expands. In this coordinate system, galaxies remain stationary. In a perfectly homogeneous and isotropic universe all observers are comoving in the sense that their coordinates \mathbf{x} remain unchanged. The relationship between the physical coordinate \mathbf{r} and the comoving coordinate or distance parameter \mathbf{x} is linear:

$$\mathbf{r} = a(t)\mathbf{x}, \quad (1.18)$$

where $a(t)$ is a ratio parameter called cosmic (or cosmological) scale factor. The scale factor depends only on time.

In the expanding universe using the scale factor it is possible to determine the length r_0 at some point in time t_0 if the length r_1 is known at some earlier point in time t_1 ($t_0 > t_1$)

$$r_0 = \frac{a(t_0)}{a(t_1)} r_1 , \quad (1.19)$$

If we denote by t_0 the present time then by condition the present scale factor is normalized to $a_0 = a(t_0) = 1$.

The relation which connect the scale factor with the redshift is given by

$$a(t) = \frac{a_0}{1+z} = \frac{1}{1+z} . \quad (1.20)$$

From Eq. (1.18) we can find the total velocity

$$\dot{\mathbf{r}} = \dot{a}\mathbf{x} + a\dot{\mathbf{x}} \Rightarrow v_{tot} = v_r + v_p , \quad (1.21)$$

where dot denotes a derivative with respect to time t , $v_r = \frac{\dot{a}}{a}\mathbf{r}$ is the recessional velocity and $v_p = a\dot{\mathbf{x}}$ is the peculiar velocity which can be considered negligible on cosmological scales. Thus the Hubble law Eq. (1.11) emerges

$$v_{tot} \simeq v_r = H\mathbf{r} , \quad (1.22)$$

where H is the Hubble parameter defined as $H \equiv \frac{\dot{a}}{a}$. Clearly, it is an observable measure of the rate at which the universe is expanding.

Using the conformal time

$$\tau = \int_0^t \frac{dt}{a(t)} , \quad (1.23)$$

we obtain the conformal Hubble parameter

$$\mathcal{H} \equiv \frac{da}{ad\tau} = aH . \quad (1.24)$$

We also introduce another convenient dimensionless deceleration parameter q that measures whether the expansion rate is increasing or decreasing

$$q \equiv -\frac{\ddot{a}}{aH^2} = -\frac{\ddot{a}a}{\dot{a}^2} . \quad (1.25)$$

In an accelerating (decelerating) universe we have $q < 0$ ($q > 0$).

The dimensionless normalized Hubble parameter is defined as:

$$E \equiv \frac{H}{H_0} . \quad (1.26)$$

1.2.4 The Friedmann – Lemaître – Robertson – Walker geometry

The assumption that the universe at large scales is isotropic and homogeneous leads to the choice of a coordinate system for 4-dimensional spacetime so that we have its separation into a temporal and three spatial dimensions. The general metric in this case takes a simple form³:

$$ds^2 = g_{\mu\nu} dx^\mu dx^\nu = g_{00}(dx^0)^2 + g_{ij} dx^i dx^j = -dt^2 + dl^2 , \quad (1.27)$$

where dl is the three-dimensional or spatially expanding metric of homogeneous and isotropic space. This form of metric was developed by Friedmann (1924) as a solution to Einstein's field equations, and

³We choose the Greek letter indices to run from 0 to 3 (the 0 reserved for the time-like coordinate) and the Latin letter indices to run from 1 to 3 (spatial coordinates).

was subsequently derived from the isotropy and homogeneity of the universe only by Robertson (1936) and Walker (1936). Almost all modern cosmologists rely on this Friedmann-Lemaître-Roberson-Walker (FLRW) metric.

The universe under the assumption of the cosmological principle is described by the FLRW metric ($c = 1$)

$$ds^2 = -dt^2 + a(t)^2 \left[\frac{dr^2}{1 - Kr^2} + r^2(d\theta^2 + \sin^2\theta d\phi^2) \right] , \quad (1.28)$$

where t is the physical cosmic time, (r, θ, ϕ) are comoving spatial coordinates, K characterizes the constant spatial curvature of the spatial slices. The values $K = -1, 0, +1$ correspond to open hyperbolic space (negative spatial curvature), flat Euclidean space (zero spatial curvature), and closed hyperspherical space (positive spatial curvature) respectively.

Setting

$$d\chi^2 = \frac{dr^2}{1 - Kr^2} , \quad (1.29)$$

in order to remove the singularity, we obtain

$$r = S_K(\chi) = \begin{cases} \sin \chi & K = +1 , \\ \chi & K = 0 , \\ \sinh \chi & K = -1 , \end{cases} \quad (1.30)$$

and the FLRW metric takes the more convenient form

$$ds^2 = -dt^2 + a(t)^2 [d\chi^2 + S_K^2(d\theta^2 + \sin^2\theta d\phi^2)] , \quad (1.31)$$

where (χ, θ, ϕ) are comoving coordinates and $\chi \in [0, \infty]$ in spaces with $K = -1, 0$ and $\chi \in [0, \pi]$ in spaces with $K = +1$.

1.2.5 Friedmann equations

From the FLRW metric Eq. (1.28) and the Eqs. (1.3), (1.5) and (1.6) we obtain the Ricci tensor and the scalar curvature

$$R_{00} = -3(H^2 + \dot{H}) = -3\frac{\ddot{a}}{a} , \quad (1.32)$$

$$R_{ij} = g_{ij}a^2(3H^2 + \dot{H} + \frac{2K}{a^2}) , \quad (1.33)$$

$$R_{i0} = R_{0i} = 0 , \quad (1.34)$$

$$R = 6(2H^2 + \dot{H} + \frac{K}{a^2}) = 6\left(\frac{\ddot{a}}{a} + \frac{\dot{a}^2}{a^2} + \frac{K}{a^2}\right) . \quad (1.35)$$

The energy content of the universe is considered to behave as a perfect fluid and the energy-momentum tensor $T_{\mu\nu}$ is given by

$$T_{\mu\nu} = (\rho + p)u_\mu u_\nu + pg_{\mu\nu} , \quad (1.36)$$

where p and ρ are the pressure and matter density of the fluid respectively which are some functions of time. Also u_μ is the four-velocity of the fluid in comoving coordinates.

Using Einstein's equations (1.8), the equations for the dynamic evolution of the FLRW universe known as the Friedmann equations can be derived. From the (00) component (temporal part) of the Einstein equations we obtain the first which gives the rate of expansion of the universe

$$H^2 = \left(\frac{\dot{a}}{a}\right)^2 = \frac{8\pi G}{3}\rho - \frac{K}{a^2} , \quad (1.37)$$

and from the (ii) components (spacial part) we obtain the second

$$3H^2 + 2\dot{H} = -8\pi Gp - \frac{K}{a^2} . \quad (1.38)$$

From the above two equations, eliminating the term K/a^2 , a third equation (acceleration equation) results:

$$\frac{\ddot{a}}{a} = -\frac{4\pi G}{3}(\rho + 3p) . \quad (1.39)$$

Also the equation of fluid resulting from the first law of thermodynamics that expresses the principle of the energy–momentum conservation ($T_{;\mu}^{\mu\nu} = 0$) applied to a homogeneous and isotropic expansion is given by

$$\dot{\rho} + 3H(\rho + p) = 0 . \quad (1.40)$$

This equation is also called continuity equation and can in fact be derived directly from Eqs. (1.37) and (1.39) by eliminating \ddot{a} (multiplying Eq. (1.37) by a^2 , differentiating and using Eq. (1.39)).

1.2.6 Equation of state

The Friedmann equations of the previous subsection will be completed if for fluid we define a equation which relates the pressure with density⁴ $p = p(\rho)$ which is valid for all times of the evolution of the universe.

We can define a general linear relationship for the individual components of the cosmological fluid using a equation-of-state parameter w_i as (with $c = 1$)

$$w_i = \frac{p_i(t)}{\rho_i(t)} , \quad (1.41)$$

where the index i expresses the individual components of the cosmic fluid. For radiation or relativistic particles, photons, neutrinos, non-relativistic matter, baryons, cold dark matter, dark energy, cosmological constant and curvature we have $i = r$, $i = \gamma$, $i = \nu$, $i = m$, $i = b$, $i = c$, $i = DE$, $i = \Lambda$ and $i = K$ respectively. Considering photons and neutrinos as radiation (relativistic matter) and baryons (such as protons and neutrons) and cold dark matter as non-relativistic matter we have

$$\rho_m = \rho_b + \rho_c , \quad (1.42)$$

$$\rho_r = \rho_\gamma + \rho_\nu . \quad (1.43)$$

For constant equation-of-state parameter w_i , the Eq. (1.40) integrates to

$$\rho_i \propto a^{-3(1+w_i)} , \quad \rho_i \propto (1+z)^{3(1+w_i)} , \quad (1.44)$$

and from Eq. (1.37) we obtain for the evolution during a component dominated era

$$a \propto t^{\frac{2}{3(1+w)}} . \quad (1.45)$$

The most common and useful special cases of the equation of state parameter w_i and the corresponding relations $p_i = p(\rho_i)$, $\rho_i = \rho_i(a)$ and $a = a(t)$ are shown in Table 1.1.

⁴In general, the pressure can depend both on density and on internal degrees of freedom of the fluid i.e. entropy s . In the case of barotropic fluid the entropy is zero $s = 0$.

Table 1.1: Special cases of the equation of state parameter w_i and the corresponding relations $p_i = p(\rho_i)$, $\rho_i = \rho_i(a)$ and $a = a(t)$.

	Cosmological Constant	Domain Walls	Curvature	Pressureless Matter	Radiation
w_i	-1	$-\frac{2}{3}$	$-\frac{1}{3}$	0	$\frac{1}{3}$
p_i	ρ_{DE}	$-\frac{2}{3}\rho_{DW}$	$-\frac{1}{3}\rho_K$	0	$\frac{1}{3}\rho_r$
ρ_i	constant	$\propto a^{-1}$	$\propto a^{-2}$	$\propto a^{-3}$	$\propto a^{-4}$
a	$\propto e^{Ht}$	$\propto t^2$	$\propto t$	$\propto t^{2/3}$	$\propto t^{1/2}$

1.2.7 Cosmological parameters

As critical density ρ_{crit} we define the density of the total amount of matter and energy contained in the universe in any form when the curvature is $K = 0$ (open spatially flat universe). Thus using Eq. (1.37) the critical density is given by

$$\rho_{\text{crit}} = \frac{3H^2}{8\pi G} . \quad (1.46)$$

Its current value depends only on the value of the Hubble constant H_0

$$\rho_{\text{crit},0} = \frac{3H_0^2}{8\pi G} = 1.88 h^2 \cdot 10^{-29} \text{ g cm}^{-3} . \quad (1.47)$$

Generally, the energy density of the individual component of a multi-component fluid can be expressed in units of the critical density by introducing the corresponding dimensionless density parameter

$$\Omega_i \equiv \frac{\rho_i}{\rho_{\text{crit}}} = \frac{8\pi G \rho_i}{3H^2} . \quad (1.48)$$

Also we have

$$\Omega_K \equiv -\frac{K}{a^2 H^2} , \quad (1.49)$$

and

$$\Omega_\Lambda \equiv \frac{\Lambda}{3H^2} . \quad (1.50)$$

The density parameters determine the evolution of the universe. For radiation, matter, curvature and cosmological constant Eq. (1.37) can be rewritten as

$$H^2 = H_0^2 [\Omega_{0r} a^{-4} + \Omega_{0m} a^{-3} + \Omega_{0K} a^{-2} + \Omega_{0\Lambda}] , \quad (1.51)$$

and using Eq. (1.26) the dimensionless normalized Hubble parameter as

$$E = [\Omega_{0r} a^{-4} + \Omega_{0m} a^{-3} + \Omega_{0K} a^{-2} + \Omega_{0\Lambda}]^{1/2} , \quad (1.52)$$

where Ω_{0i} (with $i = (r, m, K, \Lambda)$) are the density parameters today. Considering $a = 1$ in Eq. (1.51) these density parameters obey the following relation

$$\Omega_{0r} + \Omega_{0m} + \Omega_{0K} + \Omega_{0\Lambda} = 1 . \quad (1.53)$$

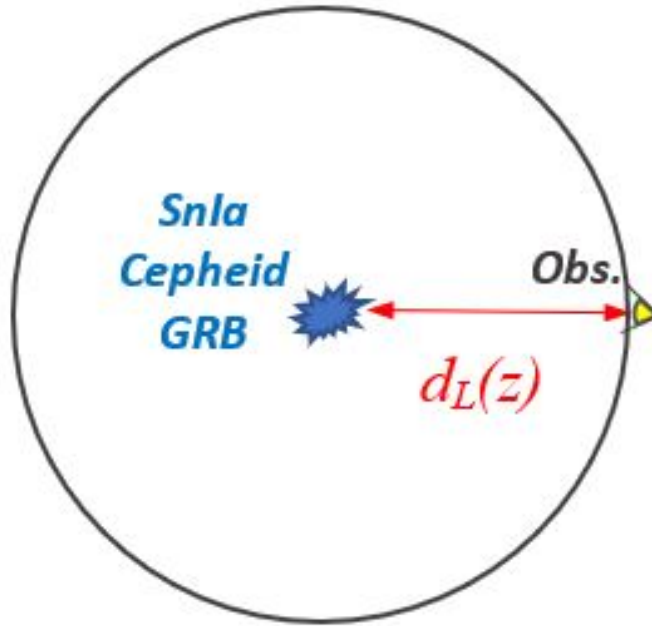


Figure 1.2: The luminosity distance is obtained from the apparent and absolute luminosities.

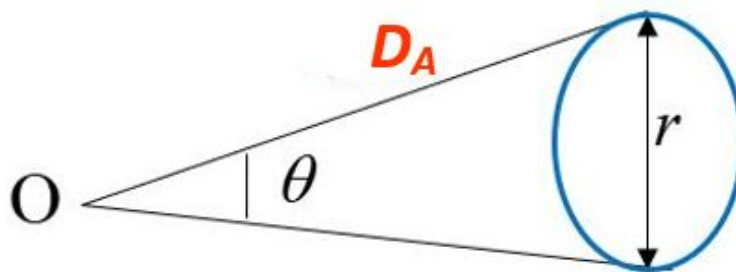


Figure 1.3: The angular diameter distance is obtained from the angular and physical scales.

1.2.8 Cosmological Distances

Distances to cosmological objects constitute the most common way to probe the cosmic metric and the expansion history of the Universe. In this subsection we present the two main cosmological distances used to probe the cosmic expansion history.

- **Luminosity distance**

Consider a luminous cosmological source of absolute luminosity L (emitted power) and an observer (Fig. 1.2) at a distance d_L from the luminous source. In a static cosmological setup, the power radiated by the luminous source is conserved and distributed in the spherical shell with area $4\pi d_L^2$ and therefore the apparent luminosity l (energy flux) detected by the observer is

$$l = \frac{L}{4\pi d_L^2} . \quad (1.54)$$

Eq. (1.54) defines the quantity d_L known as *luminosity distance*. It is straightforward to show that in an expanding flat Universe, where the energy is not conserved due to the increase of the photon wavelength and period with time, the luminosity distance can be expressed as [77, 78]

$$d_L(z)_{th} = c(1+z) \int_0^z \frac{dz'}{H(z')} . \quad (1.55)$$

The luminosity distance is an important cosmological observable that is measured using standard candles (see Subsection 2.2.1)

- **Angular diameter distance**

Consider a source (standard ruler) with a physical scale r that subtends an angle θ in the sky (Fig. 1.3). In Euclidean space, assuming that θ is small, the physical angular diameter distance D_A is defined as [77, 79]

$$D_A(z) = \frac{r}{\theta} . \quad (1.56)$$

A particularly useful standard ruler is the sound horizon at recombination calibrated by the peaks of the CMB anisotropy spectrum and observed either directly through the CMB anisotropies or through its signatures in the large scale structure (Baryon Acoustic Oscillations (BAO)) (see Subsection 2.2.2).

It is straightforward to show that in an expanding flat Universe the physical angular diameter distance can be expressed as e.g. [77]

$$D_A(z)_{th} = \frac{c}{(1+z)} \int_0^z \frac{dz'}{H(z')} . \quad (1.57)$$

The luminosity and angular diameter distances can be measured using standard candles and standard rulers thus probing the cosmic expansion rate at both the present time ($H(z=0) \equiv H_0$) and at higher redshifts ($H(z)$).

1.3 The Λ CDM cosmological model

The concordance or standard Λ Cold Dark Matter (Λ CDM) cosmological model [80–82] is a well defined, predictive and simple cosmological model (see Ref. [83], for a review). It is defined by a set of simple assumptions:

- The Universe consists of radiation (photons, neutrinos), ordinary matter (baryons and leptons), cold (non-relativistic) dark matter (CDM) [84–90] being responsible for structure formation and cosmological constant Λ [82, 91], a homogeneous form of energy which is responsible for the late time observed accelerated expansion. The cosmological constant is currently associated with a dark energy or vacuum energy whose density remains constant even in an expanding background (see Refs. [81, 92–94], for a review).
- General Relativity (GR) [95] is the correct theory that describes gravity on cosmological scales. Thus, the action currently relevant on cosmological scales reads

$$S = \int d^4x \sqrt{-g} \left[\frac{1}{16\pi G} (R - 2\Lambda) + \frac{1}{4\alpha} F_{\mu\nu} F^{\mu\nu} + \mathcal{L}_m(\psi, A) \right], \quad (1.58)$$

where α is the fine structure constant, G is Newton’s constant, $F_{\mu\nu}$ is the electromagnetic field-strength tensor and \mathcal{L}_m is the Lagrangian density for all matter fields ψ_m .

- The Cosmological Principle (CP) states that the Universe is statistically homogeneous and isotropic in space and matter at sufficiently large scales ($\gtrsim 100$ Mpc).
- There are six independent (free) parameters: the baryon $\omega_b = \Omega_{0b} h^2$ and cold dark matter $\omega_c = \Omega_{0c} h^2$ energy densities (where $h = H_0/100 \text{ km s}^{-1} \text{ Mpc}^{-1}$ is the dimensionless Hubble constant and $\Omega_X \equiv \rho_X/\rho_{\text{crit}}$ is the density of component X relative to the critical density), the angular diameter distance to the sound horizon at last scattering θ_s , the amplitude A_s and tilt n_s of primordial scalar fluctuations and the reionization optical depth τ .
- The spatial part of the cosmic metric is assumed to be flat ($K = 0$) described by the FLRW metric

$$ds^2 = -dt^2 + a(t)^2 (dr^2 + r^2 d\theta^2 + r^2 \sin^2 \theta d\phi^2), \quad (1.59)$$

which emerges from the CP.

Assuming this form of the metric and Einstein’s field equations with a Λ -term we obtain the Friedmann equations which may be written as

$$H^2 \equiv \frac{\dot{a}^2}{a^2} = \frac{8\pi G \rho + \Lambda c^2}{3}, \quad (1.60)$$

$$\frac{\ddot{a}}{a} = -\frac{4\pi G}{3} \left(\rho + \frac{3p}{c^2} \right) + \frac{\Lambda c^2}{3}. \quad (1.61)$$

The cosmological constant may also be viewed as a cosmic dark energy fluid with equation of state parameter

$$w = \frac{p_\Lambda}{\rho_\Lambda} = -1, \quad (1.62)$$

where ρ_Λ and p_Λ are the energy density and the pressure of the dark energy respectively.

- A primordial phase of cosmic inflation (a period of rapid accelerated expansion) is also assumed in order to address the horizon and flatness problems [96–99]. During this period, Gaussian scale invariant primordial fluctuations are produced from quantum fluctuations in the inflationary epoch.

Fundamental generalizations of the standard Λ CDM model may be produced by modifying the defining action (1.58) by generalizing the fundamental constants to dynamical variables in the existing action or adding new terms. Thus the following extensions of Λ CDM emerge:

- Promoting Newton’s constant to a dynamical degree of freedom by allowing it to depend on a scalar field Φ as $G \rightarrow G(\Phi(r, t))$ where the dynamics of Φ is determined by kinetic and potential terms added to the action. This class of theories is known as ‘scalar-tensor theories’ with its most general form with second order dynamical equations the Horndeski theories [100, 101] (see also Refs. [102, 103], for a comprehensive review).

- Promoting the cosmological constant to a dynamical degree of freedom by the introduction of a scalar field (quintessence) with $\Lambda \rightarrow V(\Phi(r, t))$ and the introduction of a proper kinetic term.
- Allowing for a dynamical Fine Structure Constant (Maxwell Dilaton theories) with $\alpha \rightarrow \alpha(\Phi(r, t))$ [104–108] (see also Ref. [109], for a review).
- Addition of new terms to the action which may be functions of the Ricci scalar, the torsion scalar or other invariants ($(f(R), f(T), \dots)$) [96, 110–117].

The Λ CDM model has been remarkably successful in explaining most properties of a wide range of cosmological observations including the accelerating expansion of the Universe [118, 119], the power spectrum and statistical properties of the cosmic microwave background (CMB) anisotropies [120], the spectrum and statistical properties of large scale structures of the Universe [83, 121] and the observed abundances of different types of light nuclei hydrogen, deuterium, helium, and lithium [122–125].

Despite of its remarkable successes and simplicity, the validity of the cosmological standard model Λ CDM is currently under intense investigation (see Refs. [10, 126–130], for a review). This is motivated by a range of profound theoretical and observational difficulties of the model.

The most important theoretical difficulties that plague Λ CDM are the fine tuning [94, 131, 132] and coincidence problems [133, 134]. The first fundamental problem is associated with the fact that there is a large discrepancy between observations and theoretical expectations on the value of the cosmological constant Λ (at least 60 orders of magnitude) [94, 131, 135, 136] and the second is connected to the coincidence between the observed vacuum energy density Ω_Λ and the matter density Ω_m which are approximately equal nowadays despite their dramatically different evolution properties. The anthropic principle has been considered as a possible solution to these problems. It states that these ‘coincidences’ result from a selection bias towards the existence of human life in the context of a multiverse [137, 138].

In addition to the above theoretical challenges, there are signals in cosmological and astrophysical data that appear to be in some tension (2σ or larger) with the standard Λ CDM model as specified by the Planck18 parameter values [14, 139]. The most intriguing large scale tensions are the following⁵ [10] (see also Refs. [140, 141], for a recent overview of the main tensions):

- **The Hubble tension ($> 5\sigma$):** (see Section 2.2) Using a distance ladder approach, the local (late or low redshift) measurements of the Hubble constant H_0 are measured to values that are significantly higher than those inferred using the angular scale of fluctuations of the CMB in the context of the Λ CDM model. Combined local direct measurements of H_0 are in 5σ tension (or more if combinations of local measurements are used) with CMB indirect measurements of H_0 [28, 142, 143].
- **The growth tension ($2 - 3\sigma$):** (see Section 3.1) Direct measurements of the growth rate of cosmological perturbations (Weak Lensing, Redshift Space Distortions (peculiar velocities), Cluster Counts) indicate a lower growth rate than that indicated by the Planck/ Λ CDM parameter values at a level of about $2 - 3\sigma$ [144–146]. In the context of General Relativity such lower growth rate would imply a lower matter density and/or a lower amplitude of primordial fluctuation spectrum than that indicated by Planck/ Λ CDM [4, 67, 147, 148].
- **CMB anisotropy anomalies ($2 - 3\sigma$):** (see Section 3.2) These anomalies include lack of power on large angular scales, small vs large scales tension (different best fit values of cosmological parameters), cold spot anomaly, hints for a closed Universe (CMB vs BAO), anomaly on super-horizon scales, quadrupole-octopole alignment, anomalously strong ISW effect, cosmic hemispherical power asymmetry, lensing anomaly, preference for odd parity correlations, parity violating rotation of CMB linear polarization (cosmic birefringence) etc. (see Refs. [149, 150], for a review).
- **Cosmic dipoles ($2 - 5\sigma$):** (see Section 3.3) The large scale velocity flow dipole [151, 152], the Hubble flow variance in the cosmic rest frame [153], the dipole anisotropy in radio source count

⁵We use the term ‘curiosity’ as a term describing a discrepancy between datasets in Λ CDM best fit parameter values at a level with a statistical significance $\lesssim 3\sigma$.

[154], the quasar density dipole [58] and the fine structure constant dipole (quasar spectra) [155, 156] indicate that the validity of the cosmological principle may have to be reevaluated.

- **Baryon Acoustic Oscillations (BAO) curiosities ($2.5 - 3\sigma$):** (see Section 3.4) There is a discrepancy between galaxy and Lyman- α (Ly α) BAO at an effective redshift of $z \sim 2.34$ [22, 157, 158].
- **Parity violating rotation of CMB linear polarization (Cosmic Birefringence):** (see Section 3.5) The recent evidence of the non zero value of birefringence poses a problem for standard Λ CDM cosmology and indicates a hint of a new ingredient beyond this standard model. In particular using a novel method developed in Refs. [159–161], a non-zero value of the isotropic cosmic birefringence $\beta_a = 0.35 \pm 0.14$ deg (68% C.L) was recently detected in the Planck18 polarization data at a 2.4σ statistical significance level by Ref. [162].
- **Small-scale curiosities:** (see Section 3.6) Observations on galaxy scales indicate that the Λ CDM model faces several problems (core-cusp problem, missing satellite problem, too big to fail problem, angular momentum catastrophe, satellite planes problem, baryonic Tully-Fisher relation problem, void phenomenon etc.) in describing structures at small scales (see Refs. [163, 164], for a review).
- **Age of the Universe:** (see Section 3.7) The age of the Universe as obtained from local measurements using the ages of oldest stars in the Milky Way (MW) appears to be marginally larger and in some tension with the corresponding age obtained using the CMB Planck18 data in the context of Λ CDM cosmology [165].
- **The Lithium problem ($2 - 4\sigma$):** (see Section 3.8) Measurements of old, metal-poor stars in the Milky Way’s halo find 5 times less lithium than that BBN predicts [166].
- **Quasars Hubble diagram ($\sim 4\sigma$):** (see Section 3.9) The distance modulus-redshift relation for the sample of 1598 quasars at higher redshift ($0.5 < z < 5.5$) is in some tension with the concordance Λ CDM model indicating some hints for phantom late time expansion [167–169].
- **Oscillating signals in short range gravity experiments:** (see Section 3.10) A reanalysis of short range gravity experiments has indicated the presence of an oscillating force signal with sub-millimeter wavelength [170, 171].
- **Anomalously low baryon temperature ($\sim 3.8\sigma$):** (see Section 3.11) The Experiment to Detect the Global Epoch of Reionization Signature (EDGES) collaboration [172] using global (sky-averaged) 21-cm absorption signal, reports anomalously low baryon temperature $T_b \approx 4\text{K}$ at $z \approx 17$ (half of its expected value).
- **Colliding clusters with high velocity ($\sim 6\sigma$):** (see Section 3.12) The El Gordo (ACT-CL J0102-4915) galaxy cluster at $z = 0.87$ is in its formation process which occurs by a collision of two subclusters with mass ratio 3.6 merging at a very high velocity $V_{\text{infall}} \simeq 2500$ km/s. Such cluster velocities at such a redshift are extremely rare in the context of Λ CDM as demonstrated by Ref. [173] using the estimation of Ref. [174] for the expected number of merging clusters from interrogation of the DarkSky simulations.

The well known Hubble tension and the other less discussed curiosities of Λ CDM at a lower statistical significance level may hint towards new physics (see Ref. [175], for a review).

In the context of the above observational puzzles the following strategic questions emerge

- What are the current cosmological and astrophysical datasets that include the above non-standard signals?
- What is the statistical significance of each signal?

- Is there a common theoretical framework that may explain simultaneously many non-standard signals?

These questions will be discussed in the Chapters 2 and 3. There have been previous works [176, 177] collecting and discussing signals in data that are at some statistical level in tension with the standard Λ CDM model but these are by now outdated and the more detailed and extended update provided by our work may be a useful resource. In the Chapters 2 and 3 we present the current status of the tensions, their level of significance and refer to recent resources where more details can be found for each signal. We also discuss possible theoretical approaches that can explain the non-standard nature of these signals.

In Table A.1 of the Appendix A we list the used acronyms. Also in Appendix I we provide the links of the github repositories which include the algorithms used for the numerical analysis and for construction of the figures of this dissertation.

Chapter 2

Challenges for Λ CDM: Hubble Tension

In this Chapter we focus on the Hubble tension. We provide a list of observational probes that can lead to measurements of the Hubble constant, point out the current tension level among different probes and discuss some of the possible generic extensions of Λ CDM model that can address this tension.

2.1 Introduction

The most prominent tension in the context of Λ CDM model is the H_0 tension which indicates 5σ level inconsistencies between the local direct measurements of H_0 and the CMB indirect measurements of H_0 [28, 142, 143]. The Planck/ Λ CDM best fit value is $H_0 = 67.4 \pm 0.5 \text{ km s}^{-1} \text{ Mpc}^{-1}$ [14] while the local measurements using Cepheid calibrators by the Supernovae H_0 for the Equation of State (SH0ES) of dark energy team indicate $H_0 = 73.04 \pm 1.04 \text{ km s}^{-1} \text{ Mpc}^{-1}$ ($\sim 5\sigma$) [23] (see Refs. [127, 178, 179], for a review). In the previous analysis by the SH0ES team [40] using the Gaia Early Data Release 3 (EDR3) parallaxes [180] a value of $H_0 = 73.2 \pm 1.3 \text{ km s}^{-1} \text{ Mpc}^{-1}$ is obtained, at a 4.2σ tension with the prediction from Planck18 CMB observations. A wide range of local observations appear to be consistently larger than the Planck/ Λ CDM measurement of H_0 at various levels of statistical significance [28, 142, 143]. Theoretical models addressing the Hubble tension utilize either a recalibration of the Planck/ Λ CDM standard ruler (the sound horizon) assuming new physics before the time of recombination [181–183] or a deformation of the Hubble expansion rate $H(z)$ at late times [50, 184] or a transition/recalibration of the SnIa absolute luminosity due to late time new physics [52]. For more detailed discussions of the proposed new-physics models see Refs. [127–129, 185].

2.2 Methods for measuring H_0 and data

The measurement of the Hubble constant H_0 which is the local expansion rate of the Universe, is of fundamental importance to cosmology. This measurement has improved in accuracy through a number of probes (see Ref. [186], for a review of most well established probes).

2.2.1 Standard candles as probes of luminosity distance

The luminosity distance to a source may be probed using standardizable candles like Type Ia supernovae (SnIa) ($z < 2.3$) [51, 68, 118, 119] and gamma-ray bursts (GRBs) ($0.1 < z \lesssim 9$) [187–210].

Surveys can indicate the distance-redshift relation of SnIa by measuring their peak luminosity that is tightly correlated with the shape of their characteristic light curves (luminosity as a function of time after the explosion) [211] and the redshifts of host galaxies. The latest and largest SnIa dataset available

that incorporates data from six different surveys is the Pantheon sample consisting of a total of 1048 SnIa in the redshift range $0.01 < z < 2.26$ (the number of SnIa with $z > 1.4$ is only six) [51]. More recently, the Pantheon+ sample which comprises 18 different samples has been released [212, 213] (see also Refs. [214, 215]). Refs. [212, 213] present 1701 light curves of 1550 distinct SnIa in the redshift range $0.001 < z < 2.26$ including SnIa which are in very nearby galaxies ($z \lesssim 0.01$) with measured Cepheid distances. For determination of H_0 the SH0ES team [23] uses as calibrator sample 42 SnIa in the 37 Cepheid hosts and 277 SnIa in the Hubble flow ($0.0233 < z < 0.15$) from the Pantheon+ sample.

The apparent magnitude¹ m_{th} of SnIa in the context of a specified form of $H(z)$, is related to their luminosity distance $d_L(z)$ of Eq. (1.55) in Mpc as

$$m_{th}(z) = M + 5 \log_{10} \left[\frac{d_L(z)}{Mpc} \right] + 25 . \quad (2.2)$$

Using now the dimensionless Hubble free luminosity distance

$$D_L(z) = \frac{H_0 d_L(z)}{c} , \quad (2.3)$$

the apparent magnitude can be written as

$$m_{th}(z) = M + 5 \log_{10} [D_L(z)] + 5 \log_{10} \left[\frac{c/H_0}{Mpc} \right] + 25 . \quad (2.4)$$

The use of Eq. (2.4) to measure H_0 using the measured apparent magnitudes of SnIa requires knowledge of the value of the SnIa absolute magnitude M which can be obtained using calibrators of local SnIa at $z < 0.01$ (closer than the start of the Hubble flow) in the context of a distance ladder (e.g. Ref. [216]) using calibrators like Cepheid stars.

In the cosmic distance ladder approach each step of the distance ladder uses parallax methods and/or the known intrinsic luminosity of a standard candle source to determine the absolute (intrinsic) luminosity of a more luminous standard candle residing in the same galaxy. Thus highly luminous standard candles are calibrated for the next step in order to reach out to high redshift luminosity distances.

SnIa standard candles and their calibration

- **SnIa-Cepheid:** Geometric anchors may be used to calibrate the Cepheid variable star standard candles at the local Universe (primary distance indicators) whose luminosities are correlated with their periods of variability². The MW, the Large Magellanic Cloud (LMC) and NGC 4258 are used as distance geometric anchor galaxies. For Cepheids in the anchor galaxies there are three different ways of geometric distance calibration of their luminosities: trigonometric parallaxes in the MW [38, 40, 219–224], Detached Eclipsing Binary Stars (DEBs) in the LMC [225] and water masers (see Subsection 2.2.5) in NGC 4258 [226, 227]. The DEBs technique relies on surface-brightness relations and is a one-step distance determination to nearby galaxies independent from Cepheids [228].

Using the measured distances of the calibrated Cepheid stars the intrinsic luminosity of nearby SnIa residing in the same galaxies as the Cepheids is obtained. This SnIa calibration which fixes M is then used for SnIa at distant galaxies to measure H_0 ($z \in [0.01, 0.1]$) and $H(z)$ ($z \in [0.01, 2.3]$).

¹The apparent magnitude m of an astrophysical source detected with flux l is defined as

$$m = -2.5 \log_{10} \left(\frac{l}{l_0} \right) , \quad (2.1)$$

where l_0 is a reference flux (zero point). The absolute magnitude M of an astrophysical source is the apparent magnitude the source would have if it was placed at a distance of 10 pc from the observer.

²The period–luminosity (PL) relation is also called the Leavitt law [217, 218].

- **SnIa-TRGB:** Instead of Cepheid variable stars, the Tip of the Red Giant Branch (TRGB) stars in the Hertzsprung-Russell diagram [229, 230] and Miras [25, 231] (see also [232], for a review) can be used as calibrators of SnIa. The Red Giant stars have nearly exhausted the hydrogen in their cores and have just began helium burning (helium flash phase). Their brightness can be standardized using parallax methods and they can serve as bright standard candles visible in the local Universe for the subsequent calibration of SnIa.
- **SnIa-Miras:** Miras (named for the prototype star Mira) are highly evolved low mass variable stars at the tip of Asymptotic Giant Branch (AGB) stars e.g. [233]. The water megamaser as distance indicator (see Subsection 2.2.5) can be used to calibrate the Mira PL relation [231]. Miras with short period (< 400 days) have low mass progenitors and are present in all galaxy types or in the halos of galaxies, eliminating the necessity for low inclination SnIa host galaxies.
- **SBF:** Another method to determine the Hubble constant based on calibration of the peak absolute magnitude of SnIa is the Surface Brightness Fluctuations (SBF) method [234–236]. SBF is a secondary³ luminosity distance indicator that uses stars in the old stellar populations (II) and can reach larger distances than Cepheids even inside the Hubble flow region where the recession velocity is larger than local peculiar velocities ($z > 0.01$) [237–243]. For SBF calibration Ref. [26] uses both Cepheids and TRGB demonstrating that these calibrators are consistent with each other.

Assume that a galaxy includes a number of stars covering a range of luminosity. Using SBF in the galaxy image for the determination of its distance, the ratio \bar{L} of the second and first moments of the stellar luminosity function in the galaxy is used along with the mean flux per star \bar{l} as follows [237, 239]

$$d^2 = \frac{\bar{L}}{4\pi\bar{l}}, \quad (2.5)$$

where

$$\bar{L} = \frac{\int n(L)L^2 dL}{\int n(L)L dL} = \frac{\sigma_L^2}{\langle L \rangle}, \quad (2.6)$$

with $n(L)$ the expectation number of stars with luminosity L . Thus SBF can be viewed as providing an average brightness. A galaxy with double distance appears with double smoothness due to the effect of averaging.

Alternative cosmological standard candles

- **SneII:** An independent method to determine the Hubble constant utilizes Type II supernovae (SneII) as cosmic distance indicators [244]. SneII are characterised by the presence of hydrogen lines in their spectra [245, 246]. This feature distinguishes SneII from other types of supernovae. Their light curve shapes include a plateau of varying steepness and length differ significantly from those of SnIa. The use of SneII as standard candles is motivated by the fact that they are more abundant than SnIa [247, 248] (although 1-2 mag fainter [249]) and are produced by different stellar populations than SnIa which are more difficult to standardize. The SneII progenitors (red super giant stars) however are better understood than those of SnIa.

Different SneII distance-measurement techniques have been proposed and tested. These include, the expanding photosphere method [250–252], the spectral-fitting expanding atmosphere method [253, 254], the standardized candle method [255], the photospheric magnitude method [256] and the photometric color method [257]. For example, the standardized candle method is based on the relation between the luminosity and the expansion velocity of the photosphere [255, 258–260].

- **GRBs:** In addition to SnIa and SneII, GRBs are widely proposed as standard candles to trace the Hubble diagram at high redshifts [198, 199, 261–263]. However GRBs distance calibration is

³Nearby Cepheids or stellar population models are used for the empirical or theoretical calibration of the SBF distances respectively.

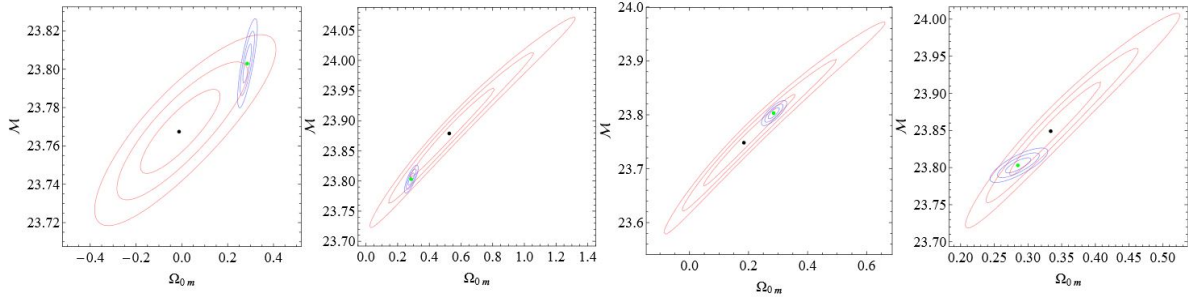


Figure 2.1: The $1\sigma - 3\sigma$ confidence contours in the parametric space $(\Omega_{0m}, \mathcal{M})$. The blue contours correspond to the $1\sigma - 3\sigma$ full Pantheon dataset (1048 SnIa datapoints) best fit, while the red contours describe the $1\sigma - 3\sigma$ confidence contours of the four bins (from left to right). The black points represent the best fit of each bin, while the green dot represents the best fit value indicated by the full Pantheon dataset ($\Omega_{0m} = 0.285$ and $\mathcal{M} = 23.803$) (from Ref. [12]).

not easy and various cosmology independent methods (see e.g. Ref. [264]) or phenomenological relations (see e.g. Ref. [265, 266]) have been proposed for their calibration.

Furthermore GRBs can be combined with other probes to study the redshift evolution of Hubble constant [267] (see Ref. [268], for a review).

Using SnIa to measure H_0 and $H(z)$: The best fit values of the parameter H_0 and the deceleration parameter q_0 may be obtained⁴ [269] using local distance ladder measurements (e.g. Cepheid calibration up to $z \simeq 0.01$) to measure directly M , low z measurements of the SnIa apparent magnitude $m(z)$ and a kinematic local expansion of $D_L(z)$ ($z < 0.1$) as e.g. [270]

$$D_L(z, q_0) = z \left[1 + \frac{1}{2}(1 - q_0)z \right]. \quad (2.7)$$

Alternatively, q_0 may be fixed to its Λ CDM value $q_0 = -0.55$ and H_0 may be fit as a single parameter [17, 37, 39].

Using higher z SnIa the best fit parameters of Λ CDM may be obtained by fitting the Λ CDM expansion rate $H(z)$

$$H^2(z) = H_0^2 [\Omega_{0m}(1+z)^3 + (1 - \Omega_{0m})], \quad (2.8)$$

where Ω_{0m} is the matter density parameter today. Using Eqs. (1.55), (2.3) and (2.8), the Hubble free luminosity distance can be written as

$$D_L(z, \Omega_{0m}) = (1+z) \int_0^z \frac{dz'}{[\Omega_{0m}(1+z')^3 + (1 - \Omega_{0m})]^{1/2}}. \quad (2.9)$$

A key assumption in the use of SnIa in the measurement of H_0 and $H(z)$ is that they are standardizable and after proper calibration they have a fixed absolute magnitude independent of redshift⁵. This assumption has been tested in Refs. [12, 277–285].

⁴ q_0 is the current deceleration parameter defined as $q_0 \equiv -\frac{1}{H_0^2} \frac{d^2 \alpha(t)}{dt^2} \Big|_{t=t_0}$.

⁵The possibility for intrinsic luminosity evolution of SnIa with redshift was first pointed out by Ref. [271]. Also, the assumption that the luminosity of SnIa is independent of host galaxy properties (e.g. host age, host morphology, host mass) and local star formation rate has been discussed in Refs. [272–276].

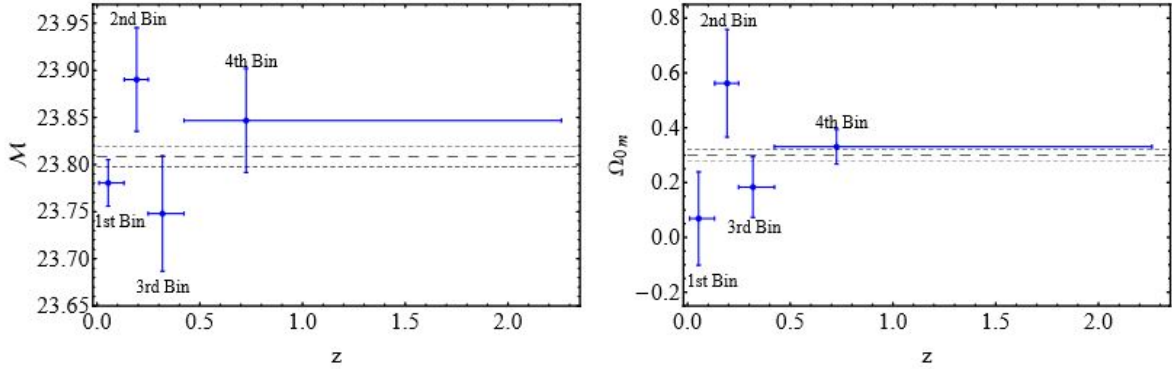


Figure 2.2: The best fit values of \mathcal{M} (left panel) and Ω_{0m} (right panel) as well as the 1σ errors for the four bins, including the systematic uncertainties. This oscillating behaviour relatively improbable in the context of constant underlying \mathcal{M} and Ω_{0m} (from Ref. [12]).

Using the degenerate combination

$$\mathcal{M} = M + 5 \log_{10} \left[\frac{c/H_0}{\text{Mpc}} \right] + 25 \quad (2.10)$$

into Eq. (2.4), we obtain

$$m(z, M, H_0, \Omega_{0m})_{th} = \mathcal{M}(M, H_0) + 5 \log_{10} [D_L(z, \Omega_{0m})] . \quad (2.11)$$

The theoretical prediction (2.11) may now be used to compare with the observed m_{obs} data and to obtain the best fits for the parameters \mathcal{M} and Ω_{0m} . Using the maximum likelihood analysis the best fit values for these parameters may be found by minimizing the quantity

$$\chi^2(\mathcal{M}, \Omega_{0m}) = \sum_i \frac{[m_{obs,i} - m_{th}(z_i; \mathcal{M}, \Omega_{0m})]^2}{\sigma_i^2} . \quad (2.12)$$

The results from the recent analysis by Ref. [12] using the SnIa Pantheon data [51] (consisting of 1048 datapoints in the redshift range $0.01 < z < 2.3$ sorting them from lowest to highest redshift and dividing them in four equal uncorrelated bins) in the context of a Λ CDM model are shown in Figs. 2.1 and 2.2⁶. An oscillating signal for \mathcal{M} and Ω_{0m} (2σ) is apparent in Fig. 2.2 and its statistical significance may be quantified using simulated data [280, 281].

The presence of large scale inhomogeneities at low z including voids or a supercluster [286] can be a plausible physical explanation for this curious behavior. In the context of a local void model the analysis by Ref. [12] indicated that the value of H_0 increases by 2 – 3% which is less than the 9% required to address the Hubble tension. The bias and systematics induced by such inhomogeneities on the Hubble diagram within a well-posed fully relativistic framework (light cone averaging formalism [287] has been discussed in Ref. [288]).

Ref. [52] has pointed out that this H_0 tension is related to the mismatch between the SnIa absolute magnitude calibrated by Cepheids at $z < 0.01$ [269, 289]

$$M^< = -19.2334 \pm 0.0404 , \quad (2.13)$$

⁶For $M = -19.24$ as indicated by Cepheid calibrators [269] of SnIa at $z < 0.01$ and the SnIa local determination $H_0 = 74 \text{ km s}^{-1} \text{ Mpc}^{-1}$ [39] Ref. [12] finds $\mathcal{M} = 23.80$ which is consistent with the full Pantheon SnIa best fit shown in Fig. 2.1.

and the SnIa absolute magnitude using the parametric free inverse distance ladder calibrating SnIa absolute magnitude using the sound horizon scale [290]

$$M^> = -19.401 \pm 0.027 . \quad (2.14)$$

Thus a transition in the absolute magnitude with amplitude $\Delta M \simeq 0.2$ may provide a solution to this tension (see Subsection 2.3.4 and in Ref. [291], for a relevant talk). Alternatively if this discrepancy is not due to systematics [185, 292], it could be an indication of incorrect estimate of the sound horizon scale due e.g. to early dark energy [293] or to late phantom dark energy [50].

Note also that Ref. [294] finds discrepancies between 'Joint Light-curve Analysis' (JLA) SnIa and Pantheon SnIa datasets which imply an uncertainty in the calibration of the absolute magnitude or equivalently of the Hubble constant which is large enough to undermine the claim for Hubble tension.

Observational data - Constraints

- **SnIa-Cepheid:** Using the analysis of the Hubble Space Telescope (HST) observations [216] the Hubble constant H_0 value has been measured from Cepheid-calibrated supernovae (using 70 long-period Cepheids in the LMC) by the SH0ES collaboration [17, 37, 39]. The analysis by the SH0ES team using this local model-independent measurement refers $H_0 = 73.04 \pm 1.04 \text{ km s}^{-1} \text{ Mpc}^{-1}$ [23], which results in 5σ tension with the value estimated by CMB Planck18 [14] assuming the Λ CDM model while in previous analysis by SH0ES team [40] using the Gaia Early Data Release 3 (EDR3) parallaxes [180] and reaching 1.8% precision by improving the calibration a value of $H_0 = 73.2 \pm 1.3 \text{ km s}^{-1} \text{ Mpc}^{-1}$ is obtained, a 4.2σ tension with the prediction from Planck18 CMB observations. Ref. [38] analysing the HST data, using Cepheids as distance calibrators reports $H_0 = 73.48 \pm 1.66 \text{ km s}^{-1} \text{ Mpc}^{-1}$. A reanalysis of the SH0ES collaboration results using a cosmographic method allowing also the deceleration parameter q_0 to be a free parameter by Ref. [289] leads to $H_0 = 74.30 \pm 1.45 \text{ km s}^{-1} \text{ Mpc}^{-1}$.

Ref. [295] considered companion and average cluster parallaxes instead of direct Cepheid parallaxes and obtained $H_0 = 72.8 \pm 1.9$ (statistical + systematics) ± 1.9 (ZP) $\text{ km s}^{-1} \text{ Mpc}^{-1}$ when all Cepheids are considered and $H_0 = 73.0 \pm 1.9$ (statistical + systematics) ± 1.9 (ZP) $\text{ km s}^{-1} \text{ Mpc}^{-1}$ for fundamental mode pulsators only (where ZP is the second Gaia data release (GDR2) [296] parallax zero point).

Various other previous estimates of H_0 have been obtained by treatments of the distance ladder [297–299]. In particular, Ref. [297] finds $H_0 = 72.8 \pm 1.6$ (statistical) ± 2.7 (systematic) $\text{ km s}^{-1} \text{ Mpc}^{-1}$ using SnIa as standard candles in the near-infrared (NIR), Ref. [298] finds $H_0 = 73.2 \pm 2.3 \text{ km s}^{-1} \text{ Mpc}^{-1}$ analysing the final data release of the Carnegie Supernova Project⁷ (CSP) I [300] and Ref. [299] finds $H_0 = 73.15 \pm 1.78 \text{ km s}^{-1} \text{ Mpc}^{-1}$ using a Bayesian hierarchical model of the local distance ladder.

- **SnIa-TRGB:** The Carnegie–Chicago Hubble Program⁸ (CCHP) [229] using calibration of SnIa with the TRGB method estimates $H_0 = 69.8 \pm 0.8$ ($\pm 1.1\%$ stat) ± 1.7 ($\pm 2.4\%$ sys) $\text{ km s}^{-1} \text{ Mpc}^{-1}$ [301] and a revision of their measurements has lead to $H_0 = 69.6 \pm 0.8$ ($\pm 1.1\%$ stat) ± 1.7 ($\pm 2.4\%$ sys) $\text{ km s}^{-1} \text{ Mpc}^{-1}$ [230]. Recently, the updated TRGB calibration applied to a distant sample of SnIa from the CCHP lead to a value of the Hubble constant of $H_0 = 69.8 \pm 0.6$ (stat) ± 1.6 (sys) $\text{ km s}^{-1} \text{ Mpc}^{-1}$ [302]. Using the LMC and the NGC 4258 as TRGB calibration of the SnIa distance ladder, the SH0ES team finds $H_0 = 72.4 \pm 2 \text{ km s}^{-1} \text{ Mpc}^{-1}$ [303] and $H_0 = 71.1 \pm 1.9 \text{ km s}^{-1} \text{ Mpc}^{-1}$ [227] respectively. Refs. [230, 302, 304] argue that the difference in the derived value of H_0 by SH0ES team compared to CCHP was due to incorrect assumptions regarding calibration of the TRGB in the LMC made by Ref. [303]. A value of $H_0 = 65.8 \pm 3.5$ (stat) ± 2.4 (sys) $\text{ km s}^{-1} \text{ Mpc}^{-1}$ is obtained by Ref. [305] using peculiar velocities and

⁷<https://csp.obs.carnegiescience.edu>

⁸<https://carnegiescience.edu/projects/carnegie-hubble-program>

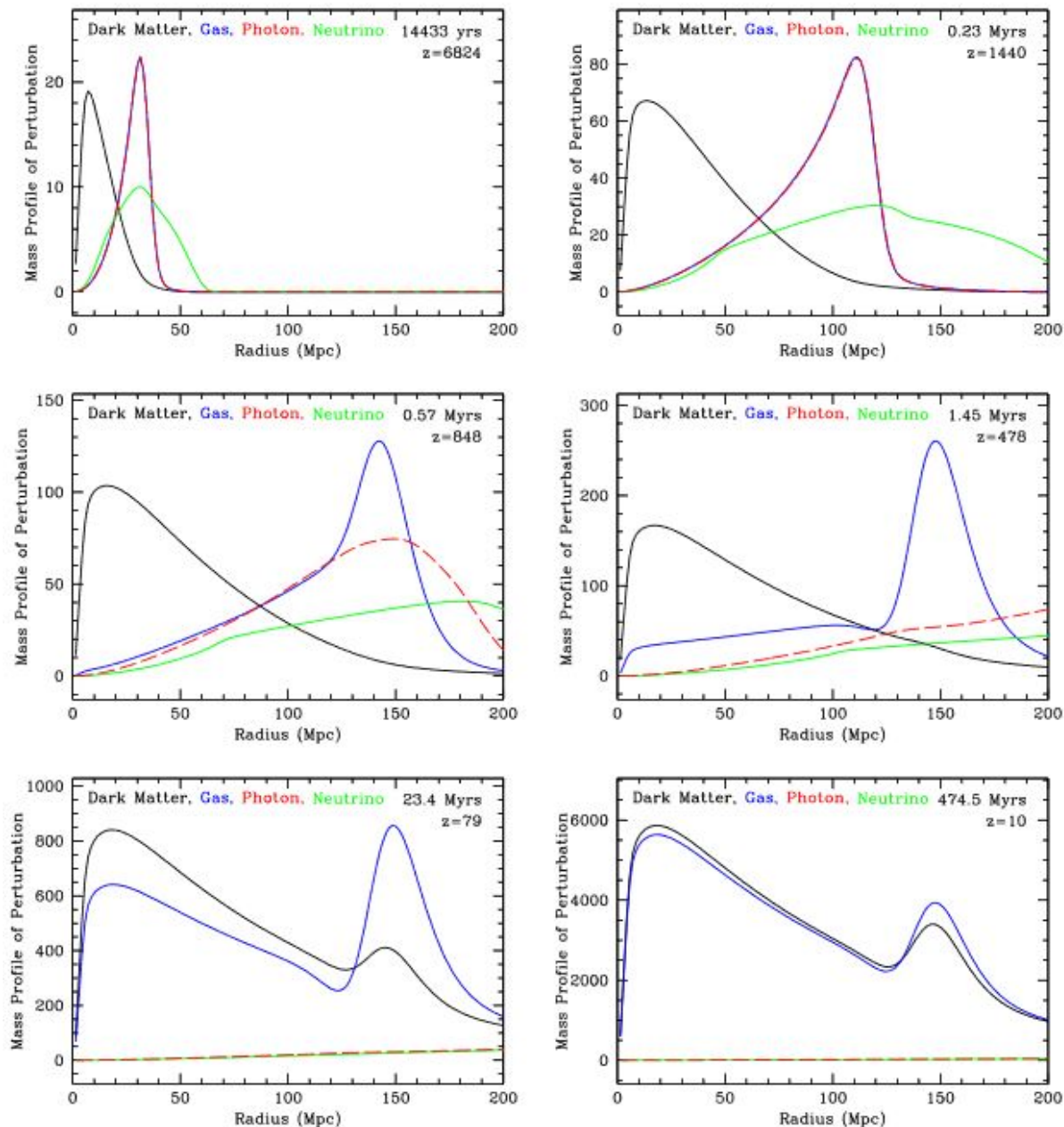


Figure 2.3: The snapshots show the radial mass profile of perturbation as a function of the comoving radius of an initially point-like overdensity located at the origin for redshifts $z = 6824, 1440, 848, 478, 79, 10$. The time after the Big Bang are given in each snapshots. The black, blue, red, and green lines correspond to the dark matter, baryons, photons, and neutrinos (all perturbations are fractional for that species), respectively. The top snapshots are for the early time before recombination where the overdensities in photons and baryons freeze together, the middle snapshots for soon after but close to recombination where the baryons freeze at the location reached with the photons forming a thick spherical shell, and the bottom snapshots are for long after recombination where the baryon overdensities start to gravitationally grow like dark matter overdensities (from Ref. [13]).

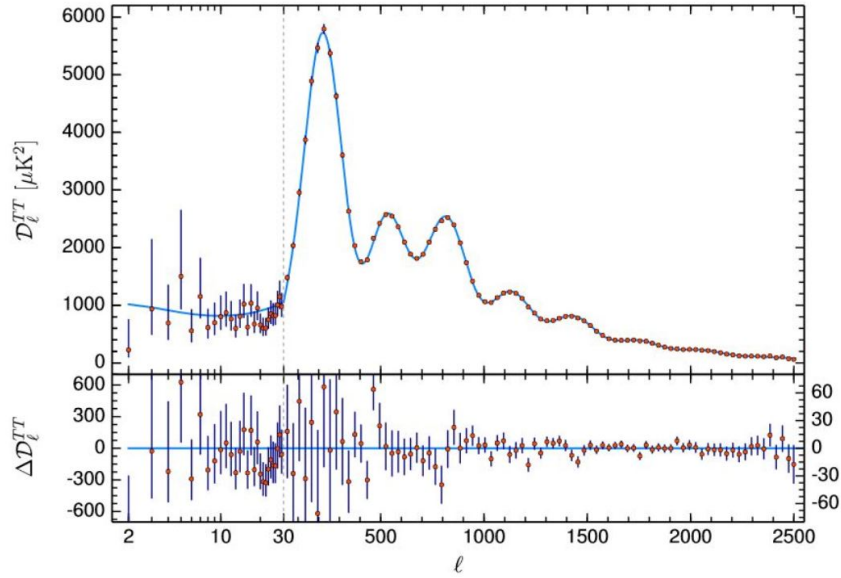


Figure 2.4: The Planck18 CMB angular power spectrum $\mathcal{D}_l^{TT} \equiv l(l+1)/(2\pi)C_l^{TT}$ (top) and residual angular power spectrum (bottom) of temperature fluctuations as a function of multipole moment l . The light blue line in the upper panel is the best-fitting to the Planck TT, TE, EE+lowE+lensing likelihoods assuming the base- Λ CDM cosmology. The red points correspond to the binned Planck data. The lowest multipole range ($l < 30$) is dominated by cosmic variance (approximated as Gaussian), while positions and amplitudes of the acoustic peaks are accurately constrained (from Ref. [14]).

TRGB distances of 33 galaxies located between the Local Group and the Virgo cluster (~ 16.5 Mpc) (mainly the sample of Virgo infall galaxies from Ref. [306]).

More recently, Ref. [307] has reported a measurement of $H_0 = 72.1 \pm 2.0 \text{ km s}^{-1} \text{ Mpc}^{-1}$ using the TRGB distance indicator calibrated from the European Space Agency (ESA) Gaia mission Early Data Release 3 (EDR3) trigonometric parallax of Omega Centauri [180]. Ref. [308] finds $H_0 = 71.5 \pm 1.8 \text{ km s}^{-1} \text{ Mpc}^{-1}$ combining TRGB measurements with either the Pantheon or CSP samples of supernova. Finally, Ref. [24] using NIR only cosmological analysis and TRGB distances to calibrate the SnIa luminosity of the CSP and RAISIN (an anagram for “SnIa in the IR”) samples [309, 310] and Ref. [311] using TRGB calibration of SnIa observed by the Zwicky Transient Facility (ZTF) [312, 313] report $H_0 = 72.4 \pm 3.3 \text{ km s}^{-1} \text{ Mpc}^{-1}$ and $H_0 = 76.94 \pm 6.4 \text{ km s}^{-1} \text{ Mpc}^{-1}$ respectively.

- **SnIa-Miras:** Calibration of SnIa in the host NGC 1559 galaxy with the Miras method using a sample of 115 oxygen-rich Miras⁹ discovered in maser host NGC 4258 galaxy, has lead to a measurement of the Hubble constant as $H_0 = 73.3 \pm 4 \text{ km s}^{-1} \text{ Mpc}^{-1}$ [25].
- **SBF:** Calibrating the SnIa luminosity with SBF method and extending it into the Hubble flow by using a sample of 96 SnIa in the redshift range $0.02 < z < 0.075$, extracted from the Combined Pantheon Sample has lead to the measurement $H_0 = 70.50 \pm 2.37 \text{ (stat)} \pm 3.38 \text{ (sys)} \text{ km s}^{-1} \text{ Mpc}^{-1}$ by Ref. [236]. Previously Ref. [235] combining distance measurement with the corrected recession velocity of NGC 4993 reported a Hubble constant $H_0 = 71.9 \pm 7.1 \text{ km s}^{-1} \text{ Mpc}^{-1}$. A new measurement of the Hubble constant $H_0 = 73.3 \pm 0.7 \pm 2.4 \text{ km s}^{-1} \text{ Mpc}^{-1}$ has recently been obtained based on a set of 63 SBF [26] distances extending out to 100 Mpc.

⁹Miras can be divided into oxygen- and carbon-rich Miras.

- **SneII:** SneII have also been used for the determination of H_0 . Using 7 SneII as cosmological standardisable candles with host-galaxy distances measured from Cepheid variables or the TRGB the Hubble constant was measured to be $H_0 = 75.8_{-4.9}^{+5.2} \text{ km s}^{-1} \text{ Mpc}^{-1}$ [244]. More recently, Ref. [27] found $H_0 = 75.4_{-3.7}^{+3.8} \text{ km s}^{-1} \text{ Mpc}^{-1}$ using 13 SneII.

2.2.2 Sound horizon as standard ruler: early time calibrators

Before recombination ($z > 1100$), the primeval plasma of coupled baryons to photons (baryon-photon fluid) oscillates as spherical sound waves emanating from baryon gas perturbations are driven by photon pressure. At recombination when the Universe has cooled enough the electrons and protons combine to form hydrogen (see e.g. Ref. [314]), photons decouple from baryons and propagate freely since the pressure becomes negligible. Thus the spherical sound wave shells of baryons become frozen. This process which was first detected in the galaxy power spectrum by Refs. [15, 315] is illustrated in Fig. 2.3. It inflicts a unique Baryon Acoustic Oscillations (BAO) scale on the CMB anisotropy spectrum peaks shown in Fig. 2.4 and on the matter large scale structure (LSS) power spectrum on large scales at the radius of the sound horizon (the distance that the sound waves have traveled before recombination). This scale emerges as a peak in the correlation function $\xi(s)$ ¹⁰ as illustrated in Fig. 2.5 or equivalently as damped oscillations in the LSS power spectrum [15, 317–319]. The characteristic BAO scale is also imprinted in the Lyman- α ($\text{Ly}\alpha$) forest absorption lines of neutral hydrogen in the intergalactic medium (IGM) detected in quasar (QSO) spectra.

The measured angular scale of the sound horizon θ_s at the drag epoch when photon pressure vanishes can be used to probe the Hubble expansion rate using the standard ruler relation e.g. [320, 321]

$$\theta_s = \frac{r_s}{d_A}, \quad (2.16)$$

where $d_A \equiv \frac{D_A}{a} \equiv (1+z)D_A = c \int_0^z \frac{dz'}{H(z')}$ is the comoving angular diameter distance to last scattering (at redshift $z \approx 1100$) and r_s is the radius of sound horizon at last scattering.

The radius r_s of the sound horizon at last scattering can be calculated by the distance that sound can travel from the Big Bang, $t = 0$, to time t_d at the drag epoch when the photon pressure can no longer prevent gravitational instability in baryons. This happens shortly after the time t_s of the last scattering when the optical depth due to Thomson scattering reaches unity [317]. Thus [322]

$$\begin{aligned} r_s &= \int_0^{t_d} \frac{c_s(a)}{a(t)} dt = \int_{z_d}^{\infty} \frac{c_s(z)}{H(z; \rho_b, \rho_\gamma, \rho_c)} dz = \\ &= \int_0^{a_d} \frac{c_s(a)}{a^2 H(a; \rho_b, \rho_\gamma, \rho_c)} da, \end{aligned} \quad (2.17)$$

where the drag redshift z_d corresponds to time t_d , ρ_b , ρ_c and ρ_γ denote the densities for baryon, cold dark matter and radiation (photons) respectively and c_s is the sound speed in the photon-baryon fluid given by [323, 324]

$$c_s = \frac{c}{\sqrt{3 \left(1 + \frac{3\rho_b}{4\rho_\gamma}\right)}} = \frac{c}{\sqrt{3 \left(1 + \frac{3\omega_b}{4\omega_\gamma} a\right)}}. \quad (2.18)$$

The expansion rate $H(z)$ depends on the ratio of the matter density to radiation density and the sound speed determined by the baryon-to-photon ratio. Both the matter-to-radiation ratio and the baryon-to-photon ratio can be estimated from the details of the acoustic peaks in CMB anisotropy power spectrum

¹⁰The correlation function is defined as the excess probability of one galaxy to be found within a given distance of another. Using the Landy-Szalay estimator [316] this function can be computed [15]

$$\xi(s) \equiv \langle \delta(x)\delta(x+s) \rangle = \frac{DD(s) - 2DR(s) + RR(s)}{RR(s)}, \quad (2.15)$$

where s is the comoving galaxy separation distance and $DD(s)$, $RR(s)$ and $DR(s)$ correspond to the number of galaxy pairs with separations s in real-real, random-random and real-random catalogs, respectively.

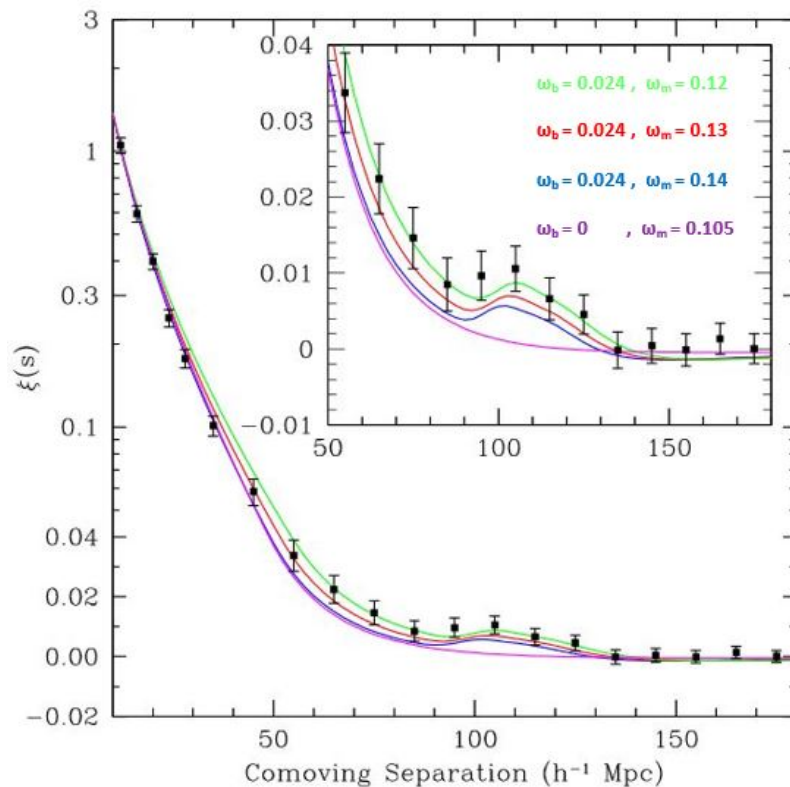


Figure 2.5: The signature of baryonic acoustic oscillations in galaxy two-point correlation function $\xi(s)$ as measured by Ref. [15] using the luminous red galaxy samples of the Sloan Digital Sky Survey. The data show the existence of a baryonic acoustic peak in the galaxy correlation function $\xi(s)$ around the comoving separation scale $100 h^{-1} \text{Mpc}$. The solid green, red, and blue lines correspond to model predictions with $\Omega_{0m} h^2 = 0.12, 0.13$ and 0.14 , respectively. All models are taken to have the same $\Omega_{0b} h^2 = 0.024$ and $n = 0.98$. The magenta line corresponds to a model with no baryons and $\Omega_{0m} h^2 = 0.105$, which has no acoustic peaks (from Ref. [15]).

(see e.g. Ref. [325]). Thus the CMB is possible to lead to an independent determination of the radius of sound horizon. Alternatively an independent determination of the radius of sound horizon can be obtained using primordial deuterium measurements [22, 326]. Now using the Eqs. (1.57) and (2.16) we can write the angular size of the sound horizon as

$$\theta_s = \frac{H_0 r_s}{c \int_0^{z_a} \frac{dz'}{E(z')}} , \quad (2.19)$$

where $E(z)$ is the dimensionless normalized Hubble parameter defined by Eq. (1.26) and for a flat Λ CDM model is given by

$$E(z) = [\Omega_{0m}(1+z)^3 + (1 - \Omega_{0m})]^{1/2} . \quad (2.20)$$

Eq. (2.19) indicates that there is a degeneracy between r_s , H_0 and $E(z)$. Thus H_0 can not be derived using the BAO data alone which constrain $E(z)$ and the degeneracy is broken when r_s is fixed using either CMB power spectra [49] or deuterium abundance [22, 326].

For example $r_s = 147.05 \pm 0.30$ Mpc is inferred from Planck18 TT,TE,EE+lowE CMB data [14]. Using the independent determination of r_s , measuring the angular acoustic scale θ_s from the location of the first acoustic peak in the CMB spectrum and fitting the integral in Eq. (2.19) using low z BAO or SnIa data, the Hubble constant H_0 can be derived. This is the 'inverse distance ladder' approach [322, 327, 328] which uses the sound horizon scale calibrated by the CMB peaks or by Big Bang Nucleosynthesis (BBN) [329] instead of the SnIa absolute magnitude M calibrated by Cepheid stars to obtain H_0 .

The deformation of the expansion rate $H(a)$ before recombination using additional components like early dark energy that increase $H(a)$ in Eq. (2.17) and thus decrease r_s and increase the predicted value of H_0 for fixed measured θ_s in Eq. (2.19), has been used as a possible approach to the solution of the Hubble tension. A challenge for this class of models is the required fine-tuning so that the evolution of $H(z)$ returns quickly to its standard form after recombination for consistency with lower z cosmological probes and growth measurements [330]. The assumed increase of $H(z)$ at early times has been claimed to lead to a worsened growth tension [331] as discussed below even though the issue is under debate [332, 333].

Observational data - Constraints

- **CMB:** The measurement of the Hubble constant H_0 using the sound horizon at recombination as standard ruler calibrated by the CMB anisotropy spectrum is model dependent and is based on assumptions about the nature of dark matter and dark energy as well as on an uncertain list of relativistic particles (see Ref. [334], for a review). The best fit value obtained by the Planck18/ Λ CDM CMB temperature, polarization, and lensing power spectra is $H_0 = 67.36 \pm 0.54$ km s⁻¹ Mpc⁻¹ [14]. The measurements of the CMB from the combination Atacama Cosmology Telescope (ACT)¹¹ and Wilkinson Microwave Anisotropy Probe (WMAP) estimated the Hubble constant to be $H_0 = 67.6 \pm 1.1$ km s⁻¹ Mpc⁻¹ and from ACT alone to be $H_0 = 67.9 \pm 1.5$ km s⁻¹ Mpc⁻¹ [19]. Note that the analysis of the nine-year data release of WMAP [335] alone prefers a value for the Hubble constant $H_0 = 70.0 \pm 2.2$ km s⁻¹ Mpc⁻¹. More recently, Ref. [336] obtains CMB-based constraints on Hubble parameter $H_0 = 67.49 \pm 0.53$ km s⁻¹ Mpc⁻¹ using combined South Pole Telescope¹² (SPT), Planck, and ACT DR4 datasets. Ref. [337] finds $H_0 = 68.8 \pm 1.5$ km s⁻¹ Mpc⁻¹ using SPT-3G data alone, while a previous analysis of SPT data by Ref. [338] results in $H_0 = 71.3 \pm 2.1$ km s⁻¹ Mpc⁻¹.
- **BAO:** The analysis of the wiggle patterns of BAO is an independent way of measuring cosmic distance using the CMB sound horizon as a standard ruler. This measurement has improved in accuracy through a number of galaxy surveys which detect this cosmic distance scale: the Sloan Digital Sky Survey (SDSS) supernova survey [339, 340] encompassing the Baryon Oscillation

¹¹<https://act.princeton.edu>

¹²<https://pole.uchicago.edu>

Spectroscopic Survey (BOSS) which has completed three different phases [341]. Its fourth phase (SDSS-IV) [342] encompasses the Extended Baryon Oscillation Spectroscopic Survey (eBOSS) [343] (see also Refs. [344–348]), the WiggleZ Dark Energy Survey [349–351], the 2-degree Field Galaxy Redshift Survey (2dFGRS) [315, 352], the 6-degree Field Galaxy Survey (6dFGS) [353–355].

More recently, BAO measurements have been extended in the context of quasar redshift surveys and Ly α absorption lines of neutral hydrogen in the IGM detected in QSO spectra using the complete eBOSS survey. The measurement of BAO scale using first the auto-correlation of Ly α function [356–358] and then the Ly α -quasar cross-correlation function [359, 360] or both the auto- and cross-correlation functions [361] pushed BAO measurements to higher redshifts ($z \sim 2.4$). Recent studies present BAO measurements from the Ly α using the eBOSS sixteenth data release (DR16) [362] of the SDSS IV e.g. [361].

As discussed in subsection 2.2.2 BAO data alone cannot constrain H_0 because BAO observations measure the combination $H_0 r_s$ rather than H_0 and r_s individually (where r_s is the radius of sound horizon). Using the CMB calibrated physical scale of the sound horizon and the combination of BAO with SnIa data (i.e inverse distance ladder) the value $H_0 = 67.3 \pm 1.1 \text{ km s}^{-1} \text{ Mpc}^{-1}$ was reported which is in agreement with the value obtained by CMB data alone [322]. The analysis by Ref. [20] using a combination of BAO measurements from 6dFGS [354], Main Galaxy Sample (MGS) [363], BOSS DR12 and eBOSS DR14 quasar sample in a flat Λ CDM cosmology reports $H_0 = 69.13 \pm 2.34 \text{ km s}^{-1} \text{ Mpc}^{-1}$. Using BAO measurements and CMB data from WMAP, Ref. [21] reported the constraints of $H_0 = 68.36_{-0.52}^{+0.53} \text{ km s}^{-1} \text{ Mpc}^{-1}$. The analysis by Ref. [22] combining galaxy and Ly α forest BAO with a precise estimate of the primordial deuterium abundance (BBN) results in $H_0 = 66.98 \pm 1.18 \text{ km s}^{-1} \text{ Mpc}^{-1}$ for the flat Λ CDM model. Ref. [364] finds $H_0 = 67.35 \pm 0.97 \text{ km s}^{-1} \text{ Mpc}^{-1}$ using BOSS galaxy and eBOSS, with the BBN prior independent from the CMB anisotropies. Ref. [365] obtains $H_0 = 68.5 \pm 2.2 \text{ km s}^{-1} \text{ Mpc}^{-1}$ performing a analysis for the cosmological parameters of the DR12 BOSS data using the Effective Field Theory of Large-Scale Structure (EFTofLSS) formalism¹³ and Ref. [371] obtains $H_0 = 68.7 \pm 1.5 \text{ km s}^{-1} \text{ Mpc}^{-1}$ assuming a BBN prior on the baryon fraction of the energy density instead of the baryon/dark-matter ratio.

Recently, Ref. [372] reported the constraints of $H_0 = 69.6 \pm 1.8 \text{ km s}^{-1} \text{ Mpc}^{-1}$ using BAO data, including the released eBOSS DR16, and CMB data from Planck. Ref. [373] infers $H_0 = 68.19 \pm 0.99 \text{ km s}^{-1} \text{ Mpc}^{-1}$ imposing BBN priors on the baryon density and combining the BOSS Full Shape with the BAO measurements from BOSS and eBOSS. Also, a new analysis of galaxy 2-point functions in the BOSS survey, including full-shape information and post-reconstruction BAO by Ref. [374] results in $H_0 = 69.23 \pm 0.77 \text{ km s}^{-1} \text{ Mpc}^{-1}$ and a full-shape analysis of BOSS DR12 by Ref. [375] results in $H_0 = 68.31_{-0.86}^{+0.83} \text{ km s}^{-1} \text{ Mpc}^{-1}$. A previous analysis of BOSS DR12 on anisotropic galaxy clustering in Fourier space by Ref. [376] gives $H_0 = 67.9 \pm 1.1 \text{ km s}^{-1} \text{ Mpc}^{-1}$. Finally, analyzing the BOSS DR12 galaxy power spectra using a new approach based on the horizon scale at matter-radiation equality Ref. [377] finds $H_0 = 69.5_{-3.5}^{+3.0} \text{ km s}^{-1} \text{ Mpc}^{-1}$ and adding Planck lensing Ref. [378] finds $H_0 = 70.6_{-5.4}^{+3.0} \text{ km s}^{-1} \text{ Mpc}^{-1}$.

2.2.3 Time delays: gravitational lensing

Gravitational lensing time-delay cosmography can be used to measure H_0 . This approach was first proposed by Ref. [379] and recently implemented by Ref. [28, 380, 381] (see also [382, 383], for clear reviews). Strong gravitational lensing [379] arises from the gravitational deflection of light rays of a background source when an intervening lensing mass distribution (e.g. a massive galaxy or cluster of galaxies) exists along the line of sight. The light rays go through different paths such that multiple images of the background source appear around the intervening lens [384].

The time delay Δt_{AB} between two images $\theta_{\mathbf{A}}$ and $\theta_{\mathbf{B}}$ by a single deflector originating from the same

¹³The EFTofLSS formalism can provide a prediction of the LSS clustering in the mildly non-linear regime [366–370].

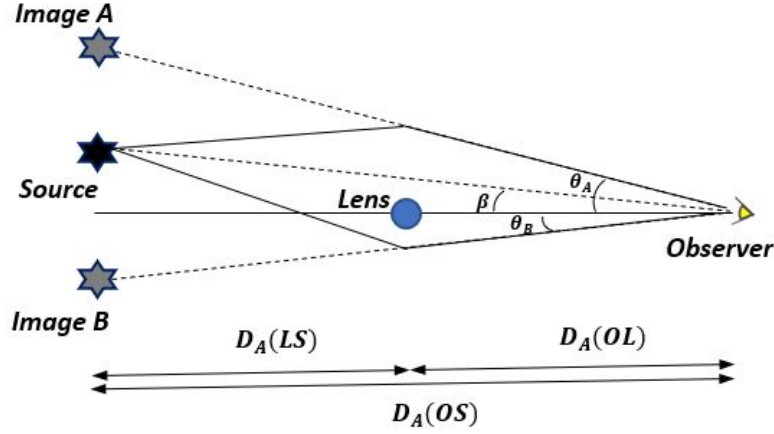


Figure 2.6: Schematic illustration of a typical gravitational lens system.

source at angle β shown in Fig. 2.6 is given as [385]

$$\Delta t_{AB} = \frac{1 + z_L}{c} \frac{D_A(OL)D_A(OS)}{D_A(LS)} [\phi(\theta_A, \beta) - \phi(\theta_B, \beta)] , \quad (2.21)$$

where z_L is the lens redshift, $D_A(OL)$ is the angular diameter distance to the lens, $D_A(OS)$ is the angular diameter distance to the source, $D_A(LS)$ is the angular diameter distance between the lens and the source and $\phi(\theta, \beta)$ is the Fermat potential e.g. [385]

$$\phi(\theta, \beta) = \frac{(\theta - \beta)^2}{2} - \psi(\theta) , \quad (2.22)$$

with $\psi(\theta)$ the lensing potential at the image direction. The time delay Δt_{AB} in Eq. (2.21) is thus connected to the time delay distance defined as e.g. [385, 386]

$$D_{\Delta t} = \frac{1 + z_L}{c} \frac{D_A(OL)D_A(OS)}{D_A(LS)} . \quad (2.23)$$

This distance is inversely proportional to H_0

$$D_{\Delta t} \propto \frac{1}{H_0} , \quad (2.24)$$

and thus its measurement constrains H_0 . Strongly lensed quasars (bright and time variable sources) lensed by a foreground lensing mass are used to measure the above observable time delay on cosmologically interesting scales [28, 387–390]. Active galactic nuclei (AGN) constitute another background source which may be used to measure the time delay [391–393]. Recently, Ref. [394] proposed the strongly lensed SnIa as a precise late-universe probe to improve the measurements on the Hubble constant and cosmic curvature. The inference of H_0 from $D_{\Delta t}$ is relatively insensitive to the assumed background cosmology.

Note that a source of systematic effects in time delay cosmography is the uncertainty of the mass along the line of sight modeling with respect to the mass sheet transformation (MST). This is a mathematical degeneracy e.g. [395–400] and can bias the strong lensing determination of Hubble constant [401].

Observational data - Constraints

Strong gravitational lensing time delay measurements of H_0 are consistent with the local measurements using late time calibrators and in mild tension with Planck e.g. [390]. The method of the measurement

of H_0 Lenses in COSMOGRAIL’s Wellspring (H0LiCOW) collaboration [28] is independent of the cosmic distance ladder and is based on time delays between multiple images of the same source, as occurs in strong gravitational lensing.

Using joint analysis of six gravitationally lensed quasars with measured time delays from the COSMOlogical MONitoring of GRAvitational Lenses (COSMOGRAIL) project, the value $H_0 = 73.3_{-1.8}^{+1.7}$ $\text{km s}^{-1} \text{Mpc}^{-1}$ was obtained which is in 3.1σ tension with Planck CMB. Assuming the Universe is flat and using lensing systems from the lensing program H0LiCOW and the Pantheon supernova compilation a value of $H_0 = 72.2 \pm 2.1$ $\text{km s}^{-1} \text{Mpc}^{-1}$ was reported by the analysis of Ref. [402]. A similar value of $H_0 = 72.8_{-1.7}^{+1.6}$ $\text{km s}^{-1} \text{Mpc}^{-1}$ was found using updated H0LiCOW dataset consisting of six lenses [403]. The reanalysis of the four publicly released lenses distance posteriors from the H0LiCOW by [404] leads to $H_0 = 73.65_{-2.26}^{+1.95}$ $\text{km s}^{-1} \text{Mpc}^{-1}$. The analysis of the strong lens system DES J0408 – 5354 by [380] for strong lensing insights into dark energy survey collaboration (STRIDES), infers $H_0 = 74.2_{-3.0}^{+2.7}$ $\text{km s}^{-1} \text{Mpc}^{-1}$ in the Λ CDM cosmology. The analysis by [381] based on the strong lensing and using Time-Delay COSMOgraphy (TDCOSMO^{14, 15}) data set alone infers $H_0 = 74.5_{-6.1}^{+5.6}$ $\text{km s}^{-1} \text{Mpc}^{-1}$ and using a joint hierarchical analysis of the TDCOSMO and Sloan Lens ACS (SLACS) [406] sample reports $H_0 = 67.4_{-3.2}^{+4.1}$ $\text{km s}^{-1} \text{Mpc}^{-1}$. Ref. [407] based on a joint analysis of 3 strong lensing system, using ground-based adaptive optics (AO) from SHARP AO effort and the HST finds $H_0 = 76.8 \pm 2.6$ $\text{km s}^{-1} \text{Mpc}^{-1}$. A reanalysis of six of the TDCOSMO lenses using a power-law mass profile model results in $H_0 = 74.2 \pm 1.6$ $\text{km s}^{-1} \text{Mpc}^{-1}$ [405]. Analysing 8 strongly, quadruply lensing systems Ref. [408] presents a determination of the Hubble constant $H_0 = 71.8_{-3.3}^{+3.9}$ $\text{km s}^{-1} \text{Mpc}^{-1}$ which is consistent with both early and late Universe observations. The value $H_0 = 73.6_{-1.6}^{+1.8}$ $\text{km s}^{-1} \text{Mpc}^{-1}$ was reported by Ref. [409] by combining the observations of ultra-compact structure in radio quasars and strong gravitational lensing with quasars acting as background source.

2.2.4 Standard sirens: gravitational waves

An independent and potentially highly effective approach for the measurement of $H(z)$ and the Hubble constant is the use of gravitational wave (GW) observations and in particular those GW bursts that have an electromagnetic (EM) counterpart (standard sirens) [410–414]. In analogy with the traditional standard candles, it is possible to use standard sirens to directly measure the luminosity distance d_L of the GW source.

Standard sirens involve the combination of a GW signal and its independently observed EM counterpart. Such counterpart may involve short gamma-ray bursts (SGRBs) signal from binary neutron star mergers [415] or associated isotropic kilonova emission [416, 417] and enables the immediate identification of the host galaxy. In contrast to traditional standard candles such as SNIa calibrated by Cepheid variables, standard sirens do not require any form of cosmological distance ladder. Instead they are calibrated in the context of general relativity through the observed GW waveform.

The simultaneous observations of the GW signal and its EM counterpart (multi-messenger observations) of nearby compact-object merger leads to a measurement of the luminosity distance which depends on the inclination angle of the binary orbit with respect to the line of sight and the redshift (measured using photons) of the host galaxy respectively. An EM counterpart detected with a GW observation can further constrain the inclination angle and may also indicate the source’s sky position and the GW merger’s time and phase e.g. [414].

In the case of GW events with small enough localization volumes without an observed EM counterpart (dark sirens) [418] a statistical analysis over a set of potential host galaxies within the event localization region may provide redshift information. A candidate for such statistical method is a merger of stellar-mass binary black holes¹⁶ (BBH) which is usually not expected to result in bright EM counterparts unless it takes place in significantly gaseous environment [424]. For example, GW190521 [425] is a

¹⁴TDCOSMO collaboration [405] was formed by members of H0LiCOW, STRIDES, COSMOGRAIL and SHARP.

¹⁵<http://www.tdcosmo.org/>

¹⁶The stability analysis of the structures around black holes have been widely employed in the literature e.g. [419–423].

possible candidate with EM counterpart corresponding to a stellar-origin BBH merger in active galactic nucleus (AGN) disks [426] detected by ZTF [312, 313].

Alternatively, in the absence of an EM counterpart the redshift can be determined by exploiting information on the properties of the source (e.g. the knowledge of neutron star equation of state) to derive frequency-dependent features in the waveform [427] or using the gravitational waveform to determine the redshift of the mass distribution of the sources [428, 429]. Also, Ref. [430] uses an alternative method, presented in Ref. [431], for redshift determination by the statistical knowledge of the redshift distribution of sources. Ref. [432] argues that any absolute determination of H_0 may be biased due to the fundamental degeneracy between redshift and H_0 and therefore can not lead to reliable determination of H_0 . According to [432] the reliable determination of H_0 with GW can only be achieved using standard sirens.

The luminosity distance-redshift relation Eq. (1.55) determines the Universe's expansion history and the associated cosmological parameters including the Hubble constant H_0 [18, 433]. In particular using the mergers of binary neutron stars (BNS), or a binary of a neutron star with a stellar-mass black hole (NS-BH), which are excellent standard sirens, both the luminosity distance (from the gravitational wave waveform) and redshift of the host galaxy (from the electromagnetic counterpart) can be measured.

Using a BNS or a NS-BH merger, the distance to the source can be estimated from the detected amplitude $\langle h \rangle$ (r.m.s. - averaged over detector and source orientations) of the GW signal by the expression [410, 434–437]

$$d = C f^{-2} \langle h \rangle^{-1} \tau^{-1} , \quad (2.25)$$

where f is the gravitational wave frequency, $\tau \equiv f/\dot{f}$ is the timescale of frequency change, C is a known numerical constant. Assuming a flat¹⁷ Universe the luminosity distance can then be obtained from the relation

$$d(z) = \frac{1}{1+z} d_L(z) . \quad (2.26)$$

For nearby sources, the recession velocity using the Hubble's law is determined by the Eq. (1.11)

$$v_r(z) = H_0 d(z) , \quad (2.27)$$

and using Eqs. (1.55), (2.3) and (2.26) is given by

$$v_r(z) = \frac{H_0 d_L(z)}{1+z} = \frac{c D_L(z)}{1+z} = c H_0 \int_0^z \frac{dz'}{H(z')} . \quad (2.28)$$

At low redshifts using the local expansion Eq. (2.7) we obtain

$$v_r(z) = \frac{cz}{1+z} \left[1 + \frac{1}{2}(1 - q_0)z \right] , \quad (2.29)$$

which is approximated for $d \leq 100 \text{ Mpc}$ (or $z \leq 0.03$) as

$$v_r(z) = cz = H_0 d . \quad (2.30)$$

Using Eqs. (2.27) and (2.29), the equation for the determination of H_0 as a function of observables, z and d is e.g. [438]

$$H_0 = \frac{cz}{d(1+z)} \left[1 + \frac{1}{2}(1 - q_0)z \right] , \quad (2.31)$$

where the deceleration parameter may be set by a fit to the GW data or may be fixed to its Planck/ Λ CDM best fit form ($q_0 = -0.55$).

¹⁷In an open (closed) Universe the distance in Hubble's law is given $d(z) = \frac{1}{1+z} \frac{\chi}{\sinh \chi} d_L(z)$ ($d(z) = \frac{1}{1+z} \frac{\chi}{\sin \chi} d_L(z)$) .

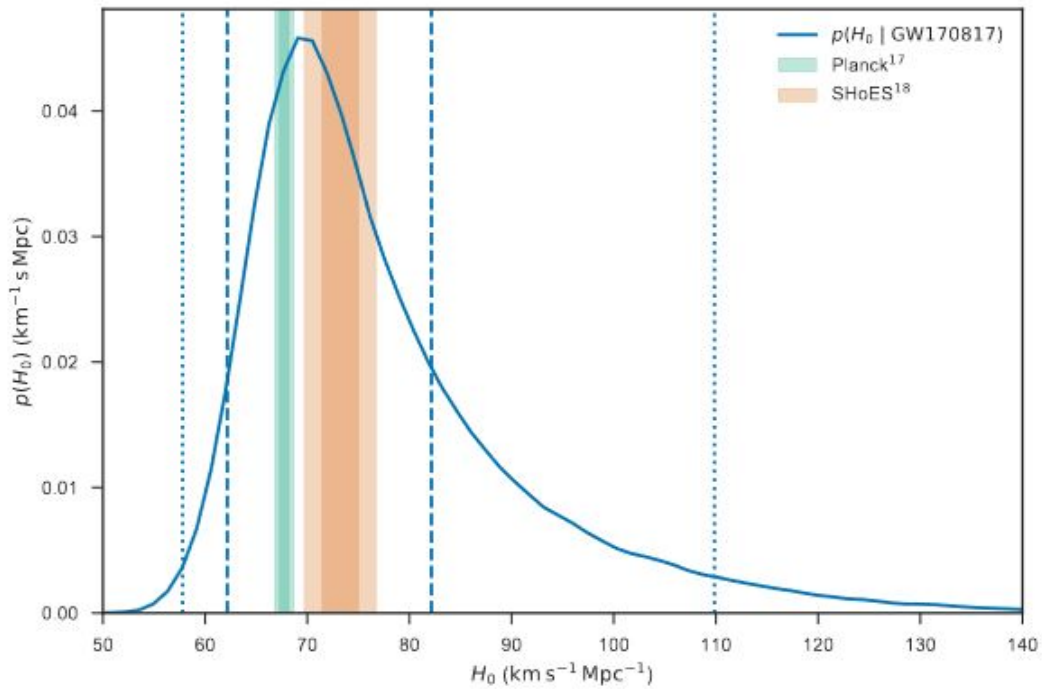


Figure 2.7: The probability of different values of H_0 with the maximum at $H_0 = 70.0^{+12.0}_{-8.0}$ km s⁻¹ Mpc⁻¹ (solid blue curve) derived by BNS event GW170817. The dashed and dotted lines show minimal 68.3% (1σ) and 95.4% (2σ) credible intervals. The shaded green and orange bands show the 1σ and 2σ constraints from the analysis of the CMB data obtained by the Planck [16] and from the analysis of the SNIa data obtained by SH0ES [17] respectively (from Ref. [18]).

Observational data - Constraints

The first multi-messenger detection of a BNS merger, GW170817, by LIGO [439] and Virgo [440] interferometers enabled the first standard siren measurement of the Hubble constant H_0 . Using the BNS merger GW170817, the distance to the source was estimated to be $d = 43.8_{-6.9}^{+2.9}$ Mpc (i.e. at redshift $z \sim 0.01$) from the detected amplitude $\langle h \rangle$ (r.m.s. - averaged over detector and source orientations) of the GW signal by the Eq. (2.25) [18]. Also using the Hubble flow velocity $v_H = 3017 \pm 166$ km s $^{-1}$ inferred from measurement of the redshift of the host galaxy, NGC 4993 (NGC 4993 was identified as the unique host galaxy), the Hubble constant was determined to be $H_0 = 70.0_{-8.0}^{+12.0}$ km s $^{-1}$ Mpc $^{-1}$ [18] (see Fig. 2.7) by using Eq. (2.30).

Using continued monitoring of the the radio counterpart of GW17081 combining with earlier GW and EM data Ref. [441] obtains a improved measurement of $H_0 = 68.9_{-4.6}^{+4.7}$ km s $^{-1}$ Mpc $^{-1}$. Note that using the BNS merger GW170817 in Ref. [433] and a statistical analysis (as first proposed in Ref. [410]) over a catalog of potential host galaxies, the Hubble constant was determined to be $H_0 = 77.0_{-18.0}^{+37.0}$ km s $^{-1}$ Mpc $^{-1}$. Using density-estimation Likelihood-Free Inference (LFI) Ref. [442] focused on the inference of the cosmological expansion H_0 from GW-selected catalogues of BNS mergers with EM counterparts.

Also using the BBH merger GW170814 as a standard (dark) siren in the absence of an electromagnetic counterpart, combined with a photometric redshift catalog from the Dark Energy Survey (DES) [443] the analysis by Ref. [444] results in $H_0 = 75_{-32}^{+40}$ km s $^{-1}$ Mpc $^{-1}$. Using multiple GW observations (the BNS event GW170817 and the BBH events observed by advanced LIGO and Virgo in their first and second observing runs) in Ref. [445] the Hubble constant was constrained as $H_0 = 69.0_{-8.0}^{+16.0}$ km s $^{-1}$ Mpc $^{-1}$. Using the event GW190814 from merger of a black hole with a lighter compact object the Hubble constant was measured to be $H_0 = 75_{-13}^{+59}$ km s $^{-1}$ Mpc $^{-1}$ [29]. In Ref. [446] the BBH merger GW190521 was analysed choosing the NRSur7dq4 waveform¹⁸ for the estimation of luminosity distance, after marginalizing over matter density Ω_{0m} when the Λ CDM model is considered and using its EM counterpart ZTF19abahr¹⁹ as identified in Ref. [424] the Hubble constant was measured to be $H_0 = 50.4_{-19.5}^{+28.1}$ km s $^{-1}$ Mpc $^{-1}$. The same study [446] choosing different types of waveform finds $H_0 = 43.1_{-11.4}^{+24.6}$ km s $^{-1}$ Mpc $^{-1}$ and $H_0 = 62.2_{-19.7}^{+29.5}$ km s $^{-1}$ Mpc $^{-1}$. Combining their results with the binary neutron star event GW170817 leads to $H_0 = 67.6_{-4.2}^{+4.3}$ km s $^{-1}$ Mpc $^{-1}$. In Ref. [448] for the same GW-EM event, assuming a flat w CDM model has obtained $H_0 = 48_{-10}^{+23}$ km s $^{-1}$ Mpc $^{-1}$.

The analysis by Ref. [449] using 47 gravitational-wave sources from the Third LIGO–Virgo–KAGRA Gravitational-Wave Transient Catalog (GWTC-3), infers $H_0 = 68_{-7}^{+12}$ km s $^{-1}$ Mpc $^{-1}$. Ref. [450] finds $H_0 = 72.77_{-7.55}^{+11.0}$ km s $^{-1}$ Mpc $^{-1}$ using the best available gravitational wave events, uniform galaxy catalog from the Dark Energy Spectroscopic Instrument (DESI) [451, 452] Legacy Survey and combining with the GW170817. The value $H_0 = 88.6_{-34.3}^{+17.1}$ km s $^{-1}$ Mpc $^{-1}$ for GW190521 event was reported, and $H_0 = 73.4_{-10.7}^{+6.9}$ km s $^{-1}$ Mpc $^{-1}$ was obtained when combing the GW190521 with the results of the neutron star merger GW170817 [453]. More recently, Ref. [454] reported $H_0 = 67_{-3.8}^{+6.3}$ km s $^{-1}$ Mpc $^{-1}$ combining the bright standard siren measurement from GW170817 with a better measurement of peculiar velocity.

2.2.5 Megamaser technique

Observations of water megamasers which are found in the accretion disks around supermassive black holes (SMBHs) in AGN have been demonstrated to be powerful one-step geometric probes for measuring extragalactic distances [455–457].

Assuming a Keplerian circular orbit around the SMBH, the centripetal acceleration and the velocity

¹⁸NRSur7dq4 is a numerical relativity surrogate 7-dimensional approximate waveform model of binary black hole merger with mass ratios $q \equiv \frac{m_1}{m_2} \leq 4$ [447]. This model is made publicly available through the gwsurrogate (see <https://pypi.org/project/gwsurrogate>) and surfinBH (see <https://pypi.org/project/surfinBH>) Python packages.

¹⁹The ZTF19abahr event was reported by ZTF [312]. This candidate EM counterpart is flare after a kicked BBH merger in the accretion disk of an AGN [426] with peak luminosity occurred 50 days after the BBH event GW19052. The ZTF19abahr was first observed after 34 days from the GW detection at the sky direction ($RA = 192.42625^0$, $Dec = 34.82472^0$) and was associated with an AGN J124942.3 + 344929 at redshift $z = 0.438$ [424].

of a masing cloud are given as [457]

$$A = \frac{V^2}{r}, \quad (2.32)$$

$$V = \sqrt{\frac{GM}{r}}, \quad (2.33)$$

where G is the Newton's constant, M is the mass of the central supermassive black hole, and r is the distance of a masing cloud from the supermassive black hole.

The angular scale θ subtended by r is given by

$$\theta = \frac{r}{d}, \quad (2.34)$$

where d is the distance to the galaxy.

Thus, from the velocity and acceleration measurements obtained from the maser spectrum, the distance to the maser may be determined

$$d = \frac{V^2}{A\theta}, \quad (2.35)$$

where A is measured from the change in Doppler velocity with time by monitoring the maser spectrum on month timescales. Using Hubble's law the Hubble constant may be approximated as [457]

$$H_0 \approx \frac{v_r}{d}, \quad (2.36)$$

where v_r is the measured recessional velocity.

In order to constrain the Hubble constant the Megamaser Cosmology Project (MCP) Ref. [458] uses angular diameter distance measurements to disk megamaser-hosting galaxies well into the Hubble flow (50 – 200 Mpc). These distances are independent of standard candle distances and their measurements do not rely on distance ladders, gravitational lenses or the CMB [30]. Early measurements of H_0 using masers tended to favor lower values of $H_0 \simeq 67 \text{ km s}^{-1} \text{ Mpc}^{-1}$ while more recent measurements favor higher values $H_0 \simeq 73 \text{ km s}^{-1} \text{ Mpc}^{-1}$ as shown in Table 2.1.

Observational data - Constraints

Recently, the Megamaser Cosmology Project (MCP) [458] using geometric distance measurements to megamaser-hosting galaxies and assuming a global velocity uncertainty of 250 km s^{-1} associated with peculiar motions of the maser galaxies constrains the Hubble constant to be $H_0 = 73.9 \pm 3 \text{ km s}^{-1} \text{ Mpc}^{-1}$ [30]. Previously the MCP reported results on galaxies, UGC 3789 with $H_0 = 68.9 \pm 7.1 \text{ km s}^{-1} \text{ Mpc}^{-1}$ [457], NGC 6264 with $H_0 = 68.0 \pm 9.0 \text{ km s}^{-1} \text{ Mpc}^{-1}$ [459], NGC 6323 with $H_0 = 73^{+26}_{-22} \text{ km s}^{-1} \text{ Mpc}^{-1}$ [460] and NGC 5765*b* with $H_0 = 66.0 \pm 6.0 \text{ km s}^{-1} \text{ Mpc}^{-1}$ [461]. Ref. [227] uses a improved distance estimation of the maser galaxy NGC 4258 (also known as Messier 106) to calibrate the Cepheid-SN Ia distance ladder combined with geometric distances from MW parallaxes and DEBs in the LMC. The measured value of the Hubble constant is $H_0 = 73.5 \pm 1.4 \text{ km s}^{-1} \text{ Mpc}^{-1}$.

2.2.6 Tully-Fisher relation (TFR) as distance indicator

The Tully-Fisher (TF) method is a historically useful distance indicator based on the empirical relation between the intrinsic total luminosity (or the stellar mass) of a spiral galaxy²⁰ and its rotation velocity (or neutral hydrogen (HI) 21 cm emission line width) [464]. This method has been used widely in measuring extragalactic distances e.g. [465].

²⁰Similarly, in the case of an elliptical galaxy the Faber–Jackson (FJ) empirical power-law relation $L \propto \sigma^{\gamma_{\text{FJ}}}$ (where L is the luminosity of galaxy, σ the velocity dispersion of its stars and γ_{FJ} is a index close to 4) [462] can be used as a distance indicator. The FJ relation is the projection of the fundamental plane (FP) of elliptical galaxies which defined as $R_{\text{eff}} \propto \sigma^{s_1} I_{\text{eff}}^{s_2}$ (where R_{eff} is the effective radius and I_{eff} is the mean surface brightness within R_{eff}) [463].

The Baryonic Tully Fisher relation (BTFR) [466–469] connects the rotation speed V_c and total baryonic mass M_b (stars plus gas) of a spiral galaxy as

$$M_b = A_c V_c^s, \quad (2.37)$$

where s (with $s \approx 3 - 4$ [466, 469, 470]) is a parameter and $\log A_c$ is the zero point in a log-log BTFR plot. This relation has been measured for hundreds of galaxies. The rotation speed V_c can be measured independently of distance while the total baryonic mass M_b may be used as distance indicator since it is connected to the intrinsic luminosity. Thus, the BTFR is a useful cosmic distance indicator approximately independent of redshift and thus can be used to obtain H_0 .

The BTFR has a smaller amount of scatter with a corresponding better accuracy as a distance indicator than the classic TF relation [470]. In addition the BTFR recovers two decades in velocity and six decades in mass [466, 469, 471–474].

A simple heuristic analytical derivation for the BTFR is obtained [475] by considering a star rotating with velocity v in a circular orbit of radius R around a central mass M . Then the star velocity is connected with the central mass as

$$v^2 = G M_b/R \implies v^4 = (G M_b/R)^2 \sim M_b S G^2, \quad (2.38)$$

where G is Newton’s constant and S the surface density $S \equiv M/R^2$ which may be shown to be approximately constant [476]. From Eqs. (2.37) and (2.38) we have

$$A_c \sim G^{-2} S^{-1}, \quad (2.39)$$

which indicates that the zero point intercept of the BTFR can probe both galaxy formation dynamics (through e.g. S) and possible fundamental constant dynamics (through G) [477].

Observational data - Constraints

The analysis by Ref. [31] using infrared data of sample galaxies and the Tully Fisher relation determined the value of Hubble constant to be $H_0 = 76.0 \pm 1.1$ (stat.) ± 2.3 (sys.) $\text{km s}^{-1} \text{Mpc}^{-1}$. In Ref. [474] a value of $H_0 = 75.1 \pm 2.3$ (stat.) ± 1.5 (sys.) $\text{km s}^{-1} \text{Mpc}^{-1}$ was found using Baryonic Tully Fisher relation for 95 independent Spitzer photometry and accurate rotation curves (SPARC) galaxies²¹ (up to distances of ~ 130 Mpc).

2.2.7 Extragalactic background light γ -ray attenuation

This method is based on the fact that the extragalactic background light (EBL) which is a diffuse radiation field that fills the Universe from ultraviolet (UV) through infrared wavelength induces opacity for very high energy (VHE) photons (≥ 30 GeV) induced by photon-photon interaction [479]. In this process a γ -ray and an EBL photon in the intergalactic medium may annihilate and produce an electron-positron pair [480]. The induced attenuation in the spectra of γ -ray sources is characterized by an optical depth $\tau_{\gamma\gamma}$ that scales as $n\sigma_T l$ (where n is the photon density of the EBL, σ_T is the Thomson cross section, and l is the distance from the γ -ray source to Earth). The cosmic evolution and the matter content of the Universe determine the γ -ray optical depth and the amount of γ -ray attenuation along the line of sight [32, 481]. Thus a derivation of H_0 can be obtained by measuring the γ -ray optical depth with the γ -ray telescopes [482]. This derivation is independent and complementary to that based on the distance ladder and CMB and seems to favor lower values of H_0 as shown in Table 2.1.

²¹The SPARC catalogue contains 175 nearby (up to distances of ~ 130 Mpc) late-type galaxies (spirals and irregulars) [470, 478]. The SPARC data are publicly available at <http://astroweb.cwru.edu/SPARC>.

Observational data - Constraints

The analysis by Ref. [481] using extragalactic background light γ -ray attenuation data from Fermi Large Area Telescope (Fermi-LAT) derives $H_0 = 67.4^{+6.0}_{-6.2} \text{ km s}^{-1} \text{ Mpc}^{-1}$ and $\Omega_{0m} = 0.14^{+0.06}_{-0.07}$. The analysis by Ref. [32] fitting the $> 10 \text{ GeV}$ extragalactic background data with modeled extragalactic background spectrum results in $H_0 = 64.9^{+4.6}_{-4.3} \text{ km s}^{-1} \text{ Mpc}^{-1}$ and $\Omega_{0m} = 0.31^{+0.13}_{-0.14}$.

2.2.8 Cosmic chronometers

Cosmic chronometers are objects whose evolution history is known. For instance such objects are some types of galaxies. The observation of these objects at different redshifts and the corresponding differences in their evolutionary state has been used to obtain the value of $H(z)$ at each redshift z .

The cosmic chronometer technique for the determination of H_0 was originally suggested in Ref. [483] and is based on the quasi-local ($0.07 \lesssim z \lesssim 2.36$) measurements along the Hubble flow of the Hubble parameter expressed as

$$H(z) = -\frac{1}{1+z} \frac{dz}{dt} . \quad (2.40)$$

Thus, the expansion rate may be obtained by measuring the age difference Δt between two old and passively evolving galaxies²² which are separated by a small redshift interval Δz , to infer the dz/dt [484, 485].

This approach determines the $H_0 = H(z=0)$ independent of the early-Universe physics and is not based on the distance ladder e.g. [33, 483, 486–488]. The estimated H_0 values are more consistent with the values estimated from recent CMB and BAO data than those values estimated from SnIa. The value of H_0 can not be derived using the cosmic chronometers observations alone because there is a background degeneracy between H_0 and Ω_{0m} and this degeneracy is broken when these observations are combined.

Observational data - Constraints

In Ref. [486] the value of Hubble constant was found to be $H_0 = 68.3^{+2.7}_{-2.6} \text{ km s}^{-1} \text{ Mpc}^{-1}$ in the flat Λ CDM model relying on 28 $H(z)$ measurements and their extrapolation to redshift zero. Analysing 31 $H(z)$ data determined by the cosmic chronometric (CCH) method, and 5 $H(z)$ data by BAO observations and using the Gaussian Process (GP) method [489–492] to determine a continuous $H(z)$ function the Hubble constant is estimated to be $H_0 \sim 67 \pm 4 \text{ km s}^{-1} \text{ Mpc}^{-1}$ by Ref. [33]. Also using the GP an extension of this analysis by Ref. [488], including the $H(z)$ measurements obtained from Pantheon compilation and HST CANDELS and CLASH Multi-Cycle Treasury (MCT) programs, finds $H_0 = 67.06 \pm 1.68 \text{ km s}^{-1} \text{ Mpc}^{-1}$ which is more consistent again with the lower range of values for H_0 . The GP method [493] is used as a 'non-parametric' technique which does not assume any parametrization or any cosmological model (see Ref. [494], for a discussion about GP as model independent method). The GP modeling approach has been performed by several authors to reconstruct cosmological parameters and thus to extract cosmological information directly from data (see e.g Refs. [495, 496, 496–533]).

Recently, a analysis by Ref. [268] reported $H_0 = 67.8^{+8.7}_{-7.2} \text{ km s}^{-1} \text{ Mpc}^{-1}$ and $H_0 = 66.5 \pm 5.4 \text{ km s}^{-1} \text{ Mpc}^{-1}$ for a generic open w CDM and for a flat Λ CDM respectively. The analysis by Ref. [268] examine the possible effects that can systematically bias the measurement and can affect the CC method. It should be pointed out however that the quality and reliability of cosmic chronometer data has been challenged by some authors. This is partly due to the fact that these datapoints are not model independent and are obtained by combining several datasets [488]. This has improved significantly in the context of the aforementioned analysis by Ref. [268] where a detailed study of the covariance matrix and the effects of systematics has been implemented.

²²These galaxies form only a few new stars and become fainter and redder with time. The time that has elapsed since they stopped star formation can be deduced.

2.2.9 HII galaxy measurements

The ionized hydrogen gas (HII) galaxies (HIIG) emit massive and compact bursts generated by the violent star formation (VSF) in dwarf irregular galaxies. The HIIG measurements can be used to probe the background evolution of the Universe. This method of H_0 determination is based on the standard candle calibration provided by a $L - \sigma$ (luminosity-velocity dispersion) relation. This relation exists in HIIGs and Giant extragalactic HII regions (GEHR) in nearby spiral and irregular galaxies. The turbulent emission line ionized gas velocity dispersion σ of the prominent Balmer lines²³ H-alpha ($H\alpha$) and H-beta ($H\beta$) relates with its integrated emission line luminosity L [534–543]. The relationship between $L(H\beta)$ and $\sigma(H\beta)$ has a small enough scatter to define a cosmic distance indicator (that can be utilized out to $z \sim 4$) independently of redshift and can be approximated as [537–545]

$$\log L(H\beta) = \nu \log \sigma(H\beta) + \kappa , \quad (2.41)$$

where ν and κ are constants representing the slope and the logarithmic luminosity at $\log \sigma(H\beta) = 0$.

From Eq. (1.54) the luminosity $L(H\beta)$ is given by

$$L(H\beta) = 4\pi d_L^2 l(H\beta) . \quad (2.42)$$

Thus using Eq. (2.41), the distance modulus $\mu \equiv m - M$ of an HIIG can be obtained [540–545]

$$\mu_{obs} = 2.5 [\nu \log \sigma(H\beta) + \kappa - \log l(H\beta)] - 100.2 . \quad (2.43)$$

This observational distance modulus can be compared with the theoretical distance modulus. From the Eq. (2.2) this is given

$$\mu_{th}(z) = 5 \log_{10} \left[\frac{d_L(z)}{Mpc} \right] + 25 . \quad (2.44)$$

Using now the dimensionless Hubble free luminosity distance Eq. (2.3) this can be written as

$$\mu_{th}(z) = 5 \log_{10} [D_L(z)] + 5 \log_{10} \left[\frac{c/H_0}{Mpc} \right] + 25 . \quad (2.45)$$

In order to obtain the best fit values for the parameters Ω_{0m} and H_0 this theoretical prediction may now be used to compared with the observed μ_{obs} data. Using the maximum likelihood analysis the best fit values for these parameters may be found in the usual manner by minimizing the quantity

$$\chi^2(H_0, \Omega_{0m}) = \sum_i \frac{[\mu_{obs,i} - \mu_{th}(z_i; H_0, \Omega_{0m})]^2}{\varepsilon_i^2} , \quad (2.46)$$

where ε_i is the uncertainty of the i th measurement.

Observational data - Constraints

Using 156 HII galaxy measurements as a new distance indicator and implementing the model-independent GP, the Hubble constant was found to be $H_0 = 76.12^{+3.47}_{-3.44} \text{ km s}^{-1} \text{ Mpc}^{-1}$ which is more consistent with the recent local measurements [546]. Using data of 130 giant HII regions in 73 galaxies with Cepheid determined distances the best estimate of the Hubble parameter is $H_0 = 71.0 \pm 2.8$ (random) ± 2.1 (systematic) $\text{ km s}^{-1} \text{ Mpc}^{-1}$ [34].

²³The Balmer series, or Balmer lines is one of a set of six named series describing the spectral line emissions of the hydrogen atom. This is characterized by the electron transitioning from $n \geq 3$ to $n = 2$ (where n is the principal quantum number of the electron). The transitions $n = 3$ to $n = 2$ and $n = 4$ to $n = 2$ are called H-alpha and H-beta respectively.

2.2.10 Combinations of data

The Hubble constant H_0 values at 68% CL through direct and indirect measurements obtained by the different methods described in this Section 2.2 are shown in Table 2.1 and described in more detail below in Fig. 2.8. Also the relative probability density value of H_0 was derived by recently published studies in the literature are shown in Fig. 2.9.

Cosmological parameter degeneracies from each individual probe can be broken using combination of probes. The multi-probe analysis are crucial for independent H_0 determination and are required in order to reduce systematic uncertainties [547, 548] (see Ref. [268], for a review).

The analysis by Ref. [28] using a combination of SH0ES and H0LiCOW results reports $H_0 = 73.8 \pm 1.1$ $\text{km s}^{-1} \text{Mpc}^{-1}$ which raises the Hubble tension to 5.3σ between late Universe determinations of H_0 and Planck. This has been discredited by Ref. [401] who points out that an artificial reduction of the allowed degrees of freedom can lead to very precise but inaccurate estimates of H_0 based on gravitational lens time delays.

The analysis by Ref. [549] using a combination of the Dark Energy Survey (DES) [145, 550, 551] clustering and weak lensing measurements with BAO and BBN experiments assuming a flat Λ CDM model with minimal neutrino mass ($\Sigma m_\nu = 0.06$ eV) finds $H_0 = 67.2_{-1.0}^{+1.2}$ $\text{km s}^{-1} \text{Mpc}^{-1}$ which is consistent with the value obtained with CMB data.

Using an extension of the standard GP formalism, and a combination of low-redshift expansion rate data (SnIa+BAO+CC) the Hubble constant was estimated to be $H_0 = 68.52_{-0.94}^{+0.94+2.51(\text{sys})}$ $\text{km s}^{-1} \text{Mpc}^{-1}$ by Ref. [526]. Using an alternative method Ref. [552] analysing the current CMB lensing data from Planck combined with Pantheon supernovae and using conservative priors, finds an r_s independent constraint of $H_0 = 73.5 \pm 5.3$ $\text{km s}^{-1} \text{Mpc}^{-1}$. Analysing low-redshift cosmological data from SnIa, BAO, strong gravitanional lensing, $H(z)$ measurements using cosmic chronometers and growth measurements from LSS observations for Λ CDM model Ref. [553] finds $H_0 = 70.30_{-1.35}^{+1.36}$ $\text{km s}^{-1} \text{Mpc}^{-1}$ which is in $\sim 2\sigma$ tension with various low and high redshift observations.

Table 2.1: The Hubble constant H_0 values at 68% CL through direct and indirect measurements by different methods.

Dataset	H_0 [$\text{km s}^{-1} \text{Mpc}^{-1}$]	Year	Refs.
Planck CMB	67.27 ± 0.60	2020	[14]
Planck CMB+lensing	67.36 ± 0.54	2020	[14]
Planck+SPT+ACT CMB	67.49 ± 0.53	2021	[336]
eBOSS+Planck CMB	69.6 ± 1.8	2020	[372]
SPT-3G CMB	68.8 ± 1.5	2021	[337]
ACT CMB	67.9 ± 1.5	2020	[554]
ACT+WMAP CMB	67.6 ± 1.1	2020	[554]
SPT CMB	71.3 ± 2.1	2018	[338]
WMAP9 CMB	70.0 ± 2.2	2013	[335]
BAO+WMAP CMB	$68.36_{-0.52}^{+0.53}$	2019	[21]
BOSS correlation function+BAO+BBN	68.19 ± 0.99	2022	[373]
P+BAO+BBN	69.23 ± 0.77	2022	[374]
P+Bispectrum+BAO+BBN	$68.31_{-0.86}^{+0.83}$	2022	[375]
BAO+BBN	66.98 ± 1.18	2018	[22]
BOSS DR12+BBN	68.5 ± 2.2	2020	[365]
BOSS DR12+BBN	68.7 ± 1.5	2020	[371]

Continued on next page

Table 2.1 – continued from previous page

Dataset	H_0 [$km\ s^{-1}Mpc^{-1}$]	Year	Refs.
BOSS DR12+BBN	67.9 ± 1.1	2020	[376]
BOSS+eBOSS+BBN	67.35 ± 0.97	2020	[364]
LSS t_{eq} standard ruler	$69.5^{+3.0}_{-3.5}$	2022	[377]
LSS t_{eq} standard ruler+lensing	$70.6^{+3.0}_{-5.4}$	2020	[378]
BAO+RSD	69.13 ± 2.34	2017	[20]
SnIa-Cepheid	73.04 ± 1.04	2022	[23]
SnIa-Cepheid	74.30 ± 1.45	2021	[289]
SnIa-Cepheid	73.20 ± 1.30	2021	[40]
SnIa-Cepheid	74.03 ± 1.42	2019	[39]
SnIa-Cepheid	73.48 ± 1.66	2018	[38]
SnIa-Cepheid	72.80 ± 2.70	2020	[295]
SnIa-Cepheid	73.00 ± 2.70	2020	[295]
SnIa-TRGB	76.94 ± 6.4	2022	[311]
SnIa-TRGB	72.4 ± 3.3	2022	[24]
SnIa-TRGB	71.5 ± 1.8	2021	[308]
SnIa-TRGB	69.8 ± 1.7	2021	[302]
SnIa-TRGB	65.8 ± 4.2	2021	[305]
SnIa-TRGB	72.10 ± 2.10	2020	[307]
SnIa-TRGB	69.60 ± 1.90	2020	[230]
SnIa-TRGB	69.80 ± 1.90	2019	[301]
SnIa-TRGB	71.1 ± 1.9	2019	[227]
SnIa-TRGB	72.40 ± 2.00	2019	[303]
SnIa-Miras	73.30 ± 4.00	2020	[25]
SBF	73.30 ± 2.50	2021	[26]
SBF	70.50 ± 4.10	2020	[236]
SBF	71.90 ± 7.10	2018	[235]
SneII	$75.4^{+3.8}_{-3.7}$	2022	[27]
SneII	$75.8^{+5.2}_{-4.9}$	2020	[244]
Time-delay (TD) lensing	$71.8^{+3.9}_{-3.3}$	2021	[408]
TD lensing	$73.3^{+1.7}_{-1.8}$	2020	[28]
TD lensing	$72.8^{+1.6}_{-1.7}$	2020	[403]
TD lensing	72.2 ± 2.1	2020	[402]
TD lensing	$73.65^{+1.95}_{-2.26}$	2020	[404]
TD lensing	74.2 ± 1.6	2020	[405]
TD lensing	$73.6^{+1.8}_{-1.6}$	2021	[409]
TD lensing	$74.2^{+2.7}_{-3.0}$	2020	[380]
TD lensing	$74.5^{+5.6}_{-6.1}$	2020	[381]
TD lensing+SLACS	$67.4^{+4.1}_{-3.2}$	2020	[381]
TD lensing+SLACS	76.8 ± 2.6	2019	[407]
GW Standard Sirens	$67^{+6.3}_{-3.8}$	2022	[454]
GW Standard Sirens	68^{+12}_{-7}	2021	[449]
GW Standard Sirens	$72.77^{+11.0}_{-7.55}$	2021	[450]
GW Standard Sirens	$73.4^{+6.9}_{-10.7}$	2021	[453]
GW Standard Sirens	75^{+59}_{-13}	2020	[29]

Continued on next page

Table 2.1 – continued from previous page

Dataset	H_0 [$km\ s^{-1}Mpc^{-1}$]	Year	Refs.
GW Standard Sirens	$50.4^{+28.1}_{-19.5}$	2020	[446]
GW Standard Sirens	$67.6^{+4.3}_{-4.2}$	2020	[446]
GW Standard Sirens	48^{+23}_{-10}	2020	[448]
GW Standard Sirens	$69.0^{+16.0}_{-8.0}$	2019	[445]
GW Standard Sirens	75^{+40}_{-32}	2019	[444]
GW Standard Sirens	$68.9^{+4.7}_{-4.6}$	2019	[441]
GW Standard Sirens	$77.00^{+37.00}_{-18.00}$	2019	[433]
GW Standard Sirens	$70.0^{+12.0}_{-8.0}$	2017	[18]
Masers	73.90 ± 3.00	2020	[30]
Masers	73.50 ± 1.40	2019	[227]
Masers	66.0 ± 6.0	2016	[461]
Masers	$73.0^{+26.0}_{-22.0}$	2015	[460]
Masers	68.0 ± 9.0	2013	[459]
Masers	68.9 ± 7.1	2013	[457]
Tully Fisher	76.00 ± 2.60	2020	[31]
Tully Fisher	75.1 ± 2.80	2020	[474]
γ -ray attenuation	$67.4^{+6.0}_{-6.2}$	2019	[481]
γ -ray attenuation	$64.9^{+4.6}_{-4.3}$	2019	[32]
HII galaxy	71.00 ± 2.8	2018	[34]
HII galaxy	$76.12^{+3.47}_{-3.44}$	2017	[546]
Cosmic chronometers, flat Λ CDM with systematics	66.5 ± 5.4	2022	[268]
Cosmic chronometers, open w CDM with systematics	$67.8^{+8.7}_{-7.2}$	2022	[268]
Cosmic chronometers, without systematics	67.06 ± 1.68	2018	[488]
Cosmic chronometers, without systematics	67.00 ± 4.00	2018	[33]
Cosmic chronometers, without systematics	$68.3^{+2.7}_{-2.6}$	2017	[486]
H(z)+BAO+SN-Pantheon+SN-DES+QSO+HIIG+ GRB	69.7 ± 1.2	2022	[555]
CMB (r_s -independent)+lensing+Pantheon	73.5 ± 5.3	2021	[552]
SnIa-Cepheid and TD lensing	73.8 ± 1.1	2020	[28]
SnIa+BAO+TD lensing+cosmic chronometers+ LSS	$70.30^{+1.36}_{-1.35}$	2019	[553]
BAO+BBN+WL-CC	$67.20^{+1.2}_{-1.0}$	2018	[549]
SnIa+BAO+CC	$68.52^{+0.94+2.51(sys)}_{-0.94}$	2018	[526]

More recently, the joint analysis of lower-redshift, non-CMB, data such as BAO, $H(z)$, SnIa, QSO, HII and GRBs by Ref. [555] has given a model-independent determinations of the Hubble constant, $H_0 = 69.7 \pm 1.2\ km\ s^{-1}\ Mpc^{-1}$ (see also Refs. [556–559], for previous joint analyses).

Many other estimates of H_0 have been obtained in the literature within the standard Λ CDM model or in alternative scenarios by using joint analysis [509, 512]. In addition, many analyses using various combinations of data assuming a Λ CDM model or a extended model beyond Λ CDM cosmology investigate whether the H_0 tension persists (or not). For example Ref. [560] uses non-CMB data and specifically adopt the data from BAO, BBN, and SnIa to study the H_0 tension. They show that this tension exists in a broad framework beyond the standard Λ CDM model.

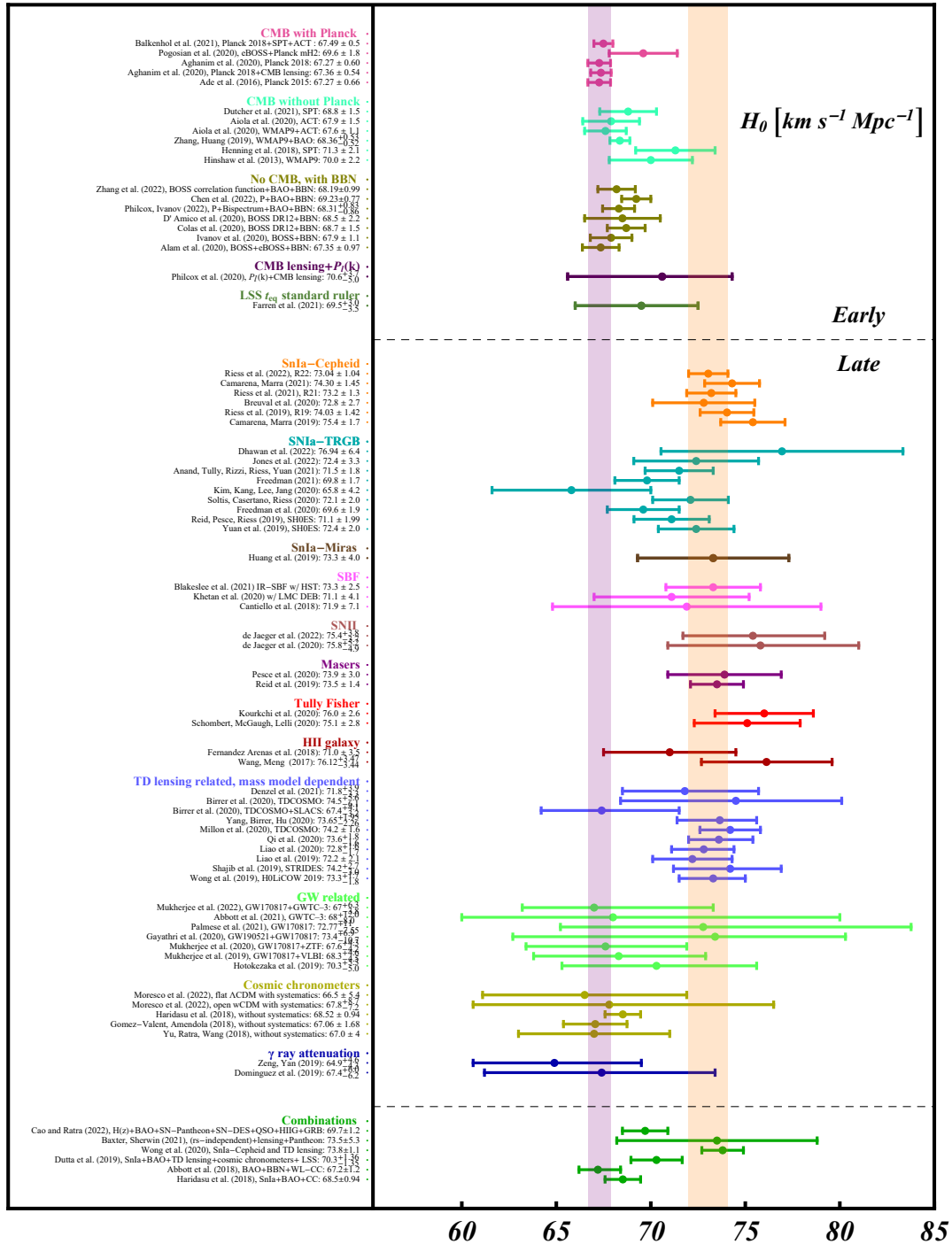


Figure 2.8: The Hubble constant H_0 values with the 68% CL constraints derived by recent measurements. The value of the Hubble constant H_0 is derived by early time approaches based on sound horizon, under the assumption of a Λ CDM background.

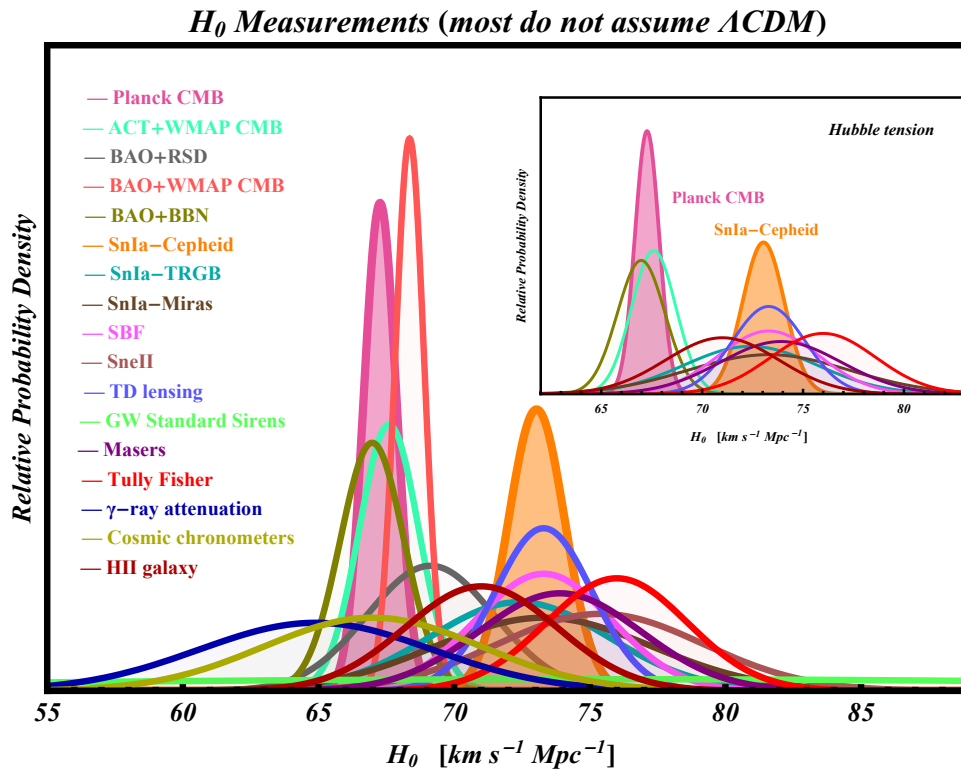


Figure 2.9: The one dimensional relative probability density value of H_0 derived by recent measurements (Planck CMB [14], ACT+WMAP CMB [19], BAO+RSD [20], BAO+WMAP CMB [21], BAO+BBN [22], SnIa-Cepheid [23], SnIa-TRGB [24], SnIa-Miras [25], SBF [26], SneII [27], TD lensing [28], GW Standard Sirens [29], Masers [30], Tully Fisher [31], γ -ray attenuation [32], cosmic chronometers [33], HII galaxy [34]). All measurements are shown as normalized Gaussian distributions. Notice that the tension is not so much between early and late time approaches but more between approaches that calibrate based on low z ($z \lesssim 0.01$) gravitational physics and those that are independent of this assumption. For example cosmic chronometers and γ -ray attenuation which are late time but independent of late gravitational physics are more consistent with the CMB-BAO than with late time calibrators.

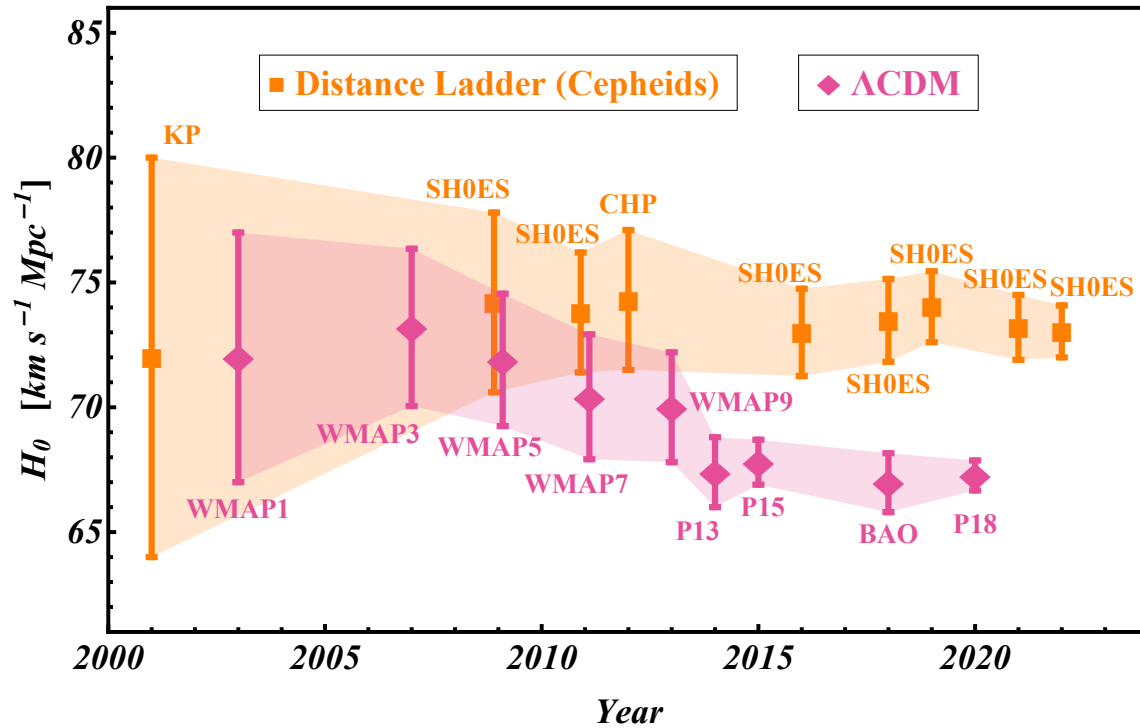


Figure 2.10: The Hubble constant as a function of publication date, using a set of different tools. Symbols in orange denote values of H_0 determined in the late Universe with a calibration based on the Cepheid distance scale (Key Project (KP) [35], SH0ES [17, 23, 36–40], Carnegie Hubble Program (CHP) [41]). Symbols in purple denote derived values of H_0 from analysis of the CMB data based on the sound horizon standard ruler (First Year WMAP (WMAP1) [42], Three Year WMAP (WMAP3) [43], Five Year WMAP (WMAP5) [44], Seven Year WMAP (WMAP7) [45], Nine Year WMAP (WMAP9) [46], Planck13 (P13) [47], Planck15 (P15) [16], Planck18 (P18) [14], BAO [22]). The orange and purple shaded regions demonstrate the evolution of the uncertainties in these values which have been decreasing for both methods. The most recent measurements disagree at greater than 5σ .

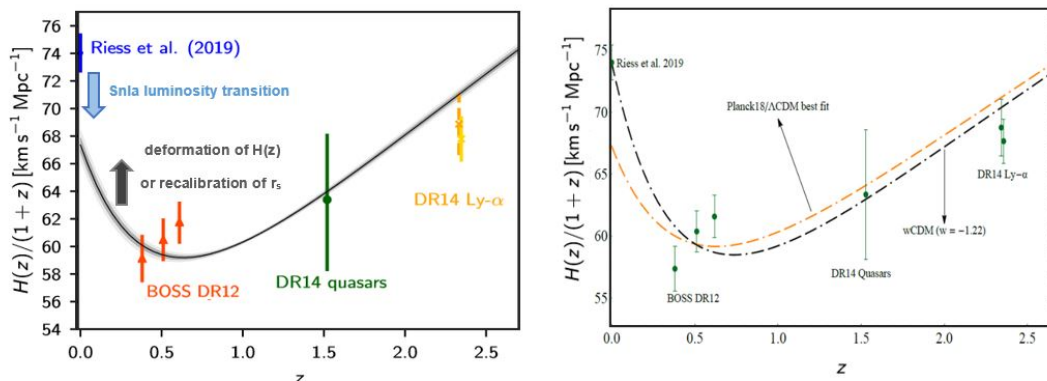


Figure 2.11: Left panel: The comoving Hubble parameter as a function of redshift. The black line corresponds to the best fit obtained from the Planck18 CMB when the Λ CDM model is considered, while the grey areas are the 1σ regions. The blue point at redshift zero denotes the inferred Hubble measurement by HST survey [39]. The orange points, green point, and yellow points correspond to BAO data from BOSS DR12 survey [48], BOSS DR14 quasar sample [49], and SDSS DR12 Ly α sample [38] respectively. The arrows indicate approaches for the resolution of the Hubble tension: Down arrow (blue) corresponds to decrease of the Riess et. al. (2019) datapoint due to systematics or transition of the absolute magnitude M (light blue arrow). Up arrow (black) corresponds to recalibration of r_s which shifts the whole curve up or and late time deformation of $H(z)$ (adapted from Ref. [14]). Right panel: The comoving Hubble parameter as a function of redshift for a wCDM phantom modification of Λ CDM model which drives upward the low z part of the $H(z)$ curve shown in left panel. Thus it brings the $z = 0$ prediction of the CMB closer to the H_0 result of the local measurements (late time $H(z)$ deformation).

2.2.11 The current status - Historic evolution

Hubble's initial value in 1929 for the expansion rate, now called the Hubble constant, was approximately $500 \text{ km s}^{-1} \text{ Mpc}^{-1}$. From the 1970s, through the 80s and into the 90s the value of H_0 was estimated to be between 50 and $100 \text{ km s}^{-1} \text{ Mpc}^{-1}$ [561]. Of interest is the historical Hubble constant debate between, for example, long series of papers by Gérard de Vaucouleurs, who claimed that the value of H_0 is $90 < H_0 < 100 \text{ km s}^{-1} \text{ Mpc}^{-1}$ e.g. [562, 563], and Allan Sandage, who claimed the value is $50 < H_0 < 55 \text{ km s}^{-1} \text{ Mpc}^{-1}$ [564, 565] (see Ref. [566], for a historical review).

During the last decades there has been remarkable progress in measuring the Hubble constant. The available technology and measurement methods determine the accuracy of this quantity. The Hubble constant as a function of publication date, using a set of different methods is shown in Fig. 2.10. The values of H_0 determined in the late Universe with a calibration based on the Cepheid distance scale and the derived values of H_0 from analysis of the CMB anisotropy spectrum data are shown. The uncertainties in these values have been decreasing for both methods and the recent measurements disagree beyond 4σ .

Furthermore the comoving Hubble expansion rate as a function of redshift obtained from the Planck18 CMB is shown in Fig. 2.11 along with a few relevant data-points demonstrating the Hubble tension.

The basic strategic questions emerge

- How can $H(z)$ derived from Cepheid late time calibrators (blue point in Fig. 2.11) become consistent with $H(z)$ derived from the sound horizon early time calibrator (black line in Fig. 2.11)?
- What type of systematics could move the blue point down or shift black line up in Fig. 2.11 in early and late time calibrators?
- To what extent can dynamical dark energy address the Hubble tension by distorting the black line in Fig. 2.11?

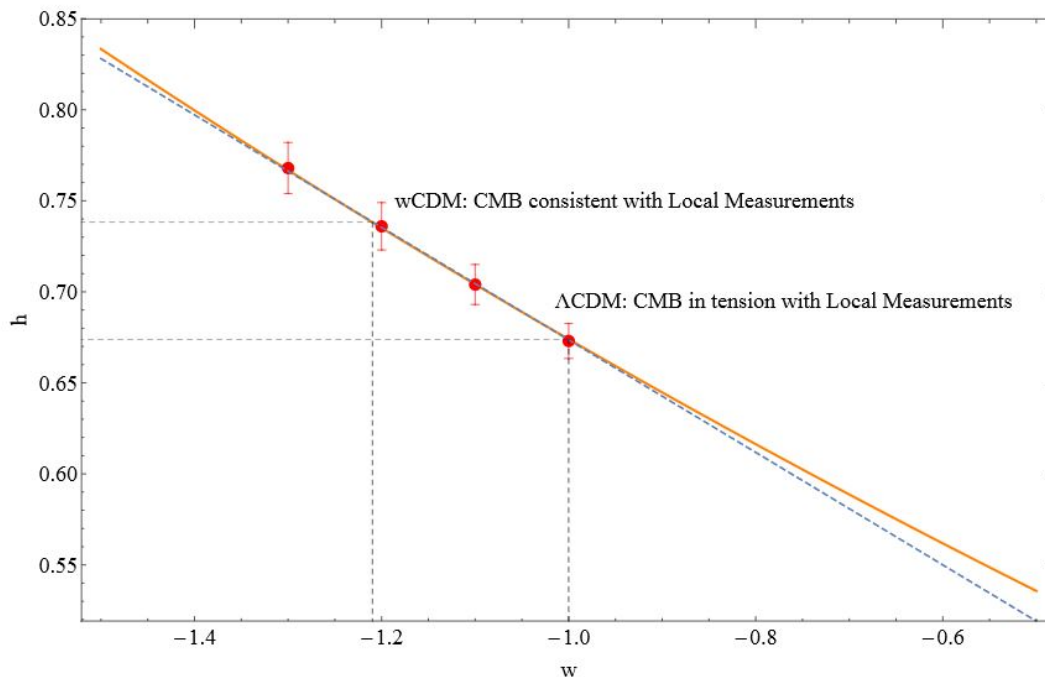


Figure 2.12: The predicted value of h as a function of the fixed w assuming one parameter dark energy (wCDM) model. The theoretically predicted best fit values of h for different values of w in the case of the wCDM model (orange line), whereas the linear fitting that has been made (dashed blue line). The red points correspond to the actual best fit values, including the errorbars, of h for specific values of w obtained by fitting these models to the CMB TT anisotropy (from Ref. [50]).

These important Hubble tension questions will be discussed in the next subsection.

2.3 Theoretical models

A wide range of models have been used to address the H_0 tension by introducing additional degrees of freedom to Λ CDM model where additional parameters are allowed to vary such as quintessence [567–581], in which a scalar field plays the role of dark energy or modified gravity [582–587], in which General Relativity is modified on cosmological scales (see Refs. [135, 588], for a review).

The extensions of Λ CDM model which can be used to resolve the Hubble constant H_0 tension fall into two categories: models with late time and models with early time modification (in the epoch before the recombination) (see Refs. [127, 128, 185], for a review).

The models with late time modification can be divided in four broad classes: deformations of the Hubble expansion rate $H(z)$ at late times e.g. late time phantom dark energy [50, 184], deformations of the Hubble expansion rate $H(z)$ with additional interactions/degrees of freedom e.g. interacting dark energy [589, 590] and decaying dark matter [591]), deformations of the Hubble expansion rate $H(z)$ due to inhomogeneous/anisotropic modifications e.g. inhomogeneous causal horizons [592] and transition/recalibration of the SnIa absolute luminosity [12] or combination of the previous classes e.g. late $w - M$ phantom transition [593].

Model selection statistical tools and approaches include the Akaike Information Criterion (AIC) [594], the Bayesian Information Criterion (BIC) [595] and the Deviance Information Criterion (DIC) [596] and Bayesian model comparison e.g. [63, 597–600]. These tools have been developed and used to test, discriminate and compare the proposed models [62, 601–603] (see also Ref. [10], for a list of statistical

tools).

2.3.1 Late time deformations of the Hubble expansion rate $H(z)$

These late time models for the solution of the Hubble tension use a late time smooth deformation of the Hubble expansion rate Planck18/ Λ CDM $H(z)$ so that it can match the locally measured value of H_0 while keeping the radius r_s of the sound horizon at the last scattering surface (see Subsection 2.2.2). Many of these models effectively fix the comoving distance to the last scattering surface and the matter energy density $\omega_m = \Omega_{0m}h^2$ to values consistent with Planck/ Λ CDM to maintain consistency with the CMB anisotropy spectrum while introducing late time phantom dark energy to deform $H(z)$ so that it matches the local measurements of $H(z)$. The required phantom behavior of such $H(z)$ deformations can not be provided by minimally coupled quintessence models and therefore such models have been shown to be unable to resolve the Hubble tension [604, 605]. These models have three problems

- They tend to worsen the fit to low z distance probes such as BAO and SnIa e.g. [50]
- They tend to worsen level of the growth tension [606].
- They tend to predict a lower value of SnIa absolute magnitude than the one determined by local Cepheid calibrators shown in Eq. (2.2) [52, 269, 289].

Thus, these models can not fully resolve the Hubble tension [328, 477, 495, 496, 607–616].

Physical models where the deformation of $H(z)$ may be achieved include the following: phantom dark energy e.g. [50], running vacuum model e.g. [617], phenomenologically emergent dark energy [618], vacuum phase transition e.g. [619], phase transition in dark energy e.g. [620]. Plethora of late dark energy models with an equation of state $w \neq -1$ ($w < -1$ or $w > -1$) both constant or dynamical with redshift e.g. [621] were proposed to address the Hubble tension. Recently, using a model-independent approach and a fully analytical analysis Refs. [622, 623] derived a set of necessary conditions that any late dark energy model must satisfy in order to potentially address both the Hubble and the growth tensions. In particular, solving the H_0 tension requires $w(z) < -1$ at some z and solving both the H_0 and σ_8 tensions demands time-varying dark energy equation of state which cross the phantom divide. However Ref. [606] has shown that $H(z)$ deformation approaches to the Hubble tension tend to worsen the σ_8 growth tension.

The following models may be classified in this class of theories: the holographic dark energy [624–631], the considering Chevallier - Polarski - Linder (CPL) [632–634] parameterization [635], the considering w dependence on non-vanishing spatial curvature [636], the phantom brane dark energy [637, 638], the negative cosmological constant [639–641], the negative dark energy [642], the graduated dark energy [643], the simple-graduated dark energy [644], the Λ_s CDM model (sign-switching) [645], the transitional dark energy [646], the frame dependent dark energy [647], the running H_0 with redshift [648, 649], the varying gravitational constant [650], the deviation from the cold dark matter [651] and the phantom crossing [652]. For example in the case of the holographic dark energy model [625] and phantom crossing [652] models the tension on H_0 appears to be significantly alleviated within 1σ even though the three problems mentioned above do remain.

Phantom dark energy

The deformation of $H(z)$ through the implementation of late time phantom dark energy [50, 184, 653–656] can address the Hubble tension as shown in Fig. 2.11.

The analysis by Ref. [50] indicates that mildly phantom models with mean equation of state parameter $w = -1.2$ have the potential to alleviate this tension. It was shown that the best fit value of H_0 in the context of the CMB power spectrum is degenerate with a constant equation of state parameter w . The CMB anisotropy spectrum was shown to be unaffected when changing $H(z)$ provided that specific parameter combinations remain unchanged. These cosmological parameters fix to high accuracy the form

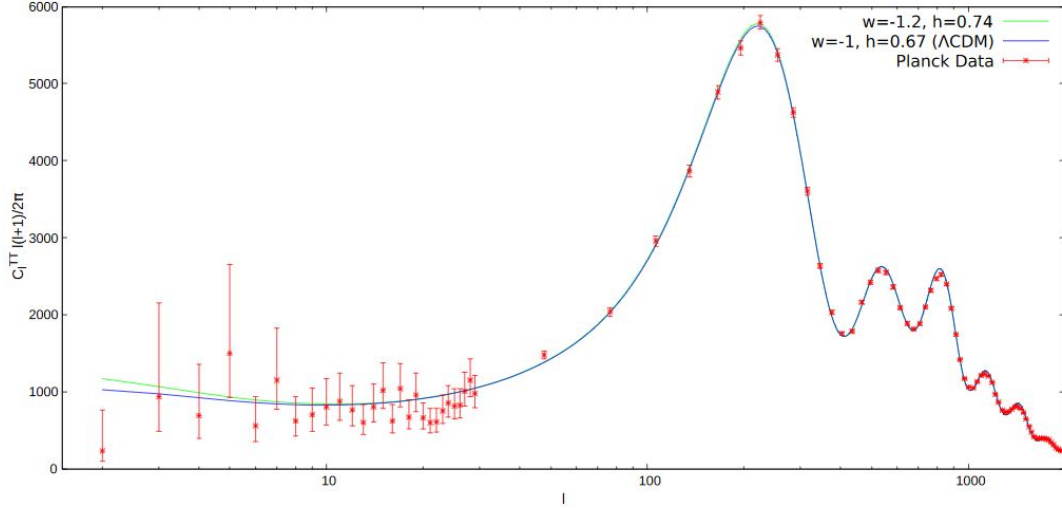


Figure 2.13: The predicted form of the CMB TT anisotropy spectrum with $w = -1$, $h = 0.67$, $\Omega_{0m} = 0.314$ for Λ CDM (blue line) and with $w = -1.2$, $h = 0.74$, $\Omega_{0m} = 0.263$ (green line). Red points correspond to the binned high- l and low- l Planck data (from Ref. [50]).

of the CMB anisotropy spectrum. The values of these parameters as determined by the Planck/ Λ CDM CMB temperature power spectrum are the following [14].

$$\omega_{m,Planck} = 0.1430 \pm 0.0011, \quad (2.47)$$

$$\omega_{b,Planck} = 0.02237 \pm 0.00015, \quad (2.48)$$

$$\omega_{r,Planck} = (4.64 \pm 0.3) 10^{-5}, \quad (2.49)$$

$$\omega_{k,Planck} = -0.0047 \pm 0.0029, \quad (2.50)$$

$$d_{A,Planck} = (4.62 \pm 0.08) (\text{km s}^{-1} \text{Mpc}^{-1})^{-1}, \quad (2.51)$$

where $\omega_{i,Planck} = \Omega_{0i,Planck} h^2$ is the energy density of component i and $d_{A,Planck}$ is the comoving angular diameter distance.

Using the Eq. (1.57) the comoving angular diameter distance d_A to the recombination surface is ($c = 1$)

$$d_A = \int_0^{z_r} \frac{dz}{H(z)} = \int_0^{z_r} \frac{dz}{h(z) 100 \text{ km s}^{-1} \text{Mpc}^{-1}}, \quad (2.52)$$

where $z_r \simeq 1100$ is the redshift of recombination and $h(z) = H(z) (100 \text{ km s}^{-1} \text{Mpc}^{-1})^{-1}$ is the dimensionless Hubble parameter which in general takes the form

$$h(z) = [\omega_r(1+z)^4 + \omega_m(1+z)^3 + (h^2 - \omega_r - \omega_m)f_{DE}(z)]^{1/2}, \quad (2.53)$$

where $h = h(z=0)$ and $f_{DE}(z)$ determines the evolution of dark energy.

In the context of a simple one parameter parametrization where the equation of state w remains constant in time and redshift (wCDM model), $f_{DE}(z)$ takes the simple form

$$f_{DE}(z) = (1+z)^{3(1+w)}. \quad (2.54)$$

If the four energy densities Eqs. (2.47), (2.48), (2.49) and (2.50) and the observed value of the comoving angular diameter Eq. (2.51) are fixed then they provide the analytically predicted best fit value of the Hubble parameter H_0 (or h) given the dark energy equation of state parameter $w(w_0, w_1, \dots, z)$ where

w_0, w_1, \dots are the parameters entering the $w(z)$ parametrization. Thus assuming a flat Universe ($\omega_k = 0$) and solving the following equation with respect to h

$$d_A(\omega_{m,Planck}, \omega_{r,Planck}, \omega_{b,Planck}, h = 0.674, w = -1) = d_A(\omega_{m,Planck}, \omega_{r,Planck}, \omega_{b,Planck}, h, w), \quad (2.55)$$

it is straightforward to derive the degeneracy function $h(z = 0, w) \equiv h$ shown in Fig. 2.12 (continuous orange line). In the range $w \in [-1.5, -1]$, $h(w)$ is approximated as a straight line (dashed blue line in Fig. 2.12)

$$h(w) \approx -0.3093w + 0.3647. \quad (2.56)$$

For $w = -1$, this linear degeneracy equation leads to the best fit dimensionless Hubble constant $h = 0.674$ as expected while for $w = -1.217$ the corresponding predicted CMB best fit is $h = 0.74$ which is consistent with the value obtained by local distance ladder measurements. The invariance of the CMB power spectrum when the cosmological parameters are varied along the above described degeneracy directions is shown in Fig. 2.13. This method of Ref. [50] can be used to find general degeneracy relations between $f_{DE}(z)$ and H_0 and fixing $h = 0.74$ gives infinite $f_{DE}(z)$, $w(z)$ forms that can potentially resolve the H_0 problem if they can also properly fit the low z data (e.g. BAO, SnIa, Cepheid value of absolute luminosity M). Low z distance data (BAO and SnIa) will determine which one of these forms is observationally favored. However, none of these forms can provide a quality of fit to low z data equally good or better than Λ CDM despite the introduced additional parameters. In addition, these models suffer from the other two problems mentioned above (worse growth tension and lower value of SnIa absolute magnitude).

Running vacuum model

The running vacuum models (RVM) [617, 657–662, 662–676] (see Refs. [136, 677–683], for a review) attempts to address both the Hubble constant H_0 tension [684] and the σ_8 growth tension using a mechanism that has common features with the IDE models e.g. [685–690] (for relaxing the growth tension, see Subsection 3.1.2).

The RVM of the cosmic evolution is well motivated by the generic idea of renormalization group formalism which is used in Quantum Field Theory (QFT) [691–693] (see also Refs. [669, 694], for a approach using adiabatic regularization and renormalization techniques). In the RVM the cosmological constant, the corresponding vacuum energy density and pressure are assumed to be functions of the Hubble rate e.g. a power series of the Hubble rate and its cosmic time derivative with even time derivatives of the scale factor [695]

$$\Lambda = a_0 + \sum_{k=1} a_k H^{2k} + \sum_{k=1} b_k \dot{H}^k, \quad (2.57)$$

$\rho_\Lambda = \rho_\Lambda(H) = \frac{\Lambda(H)}{8\pi G}$ and $p_\Lambda = p_\Lambda(H) = -\rho_\Lambda(H)$ respectively.

For the current Universe the vacuum energy density can be written in the relatively simple form e.g. [679, 684, 695, 696]

$$\rho_\Lambda(H) = \frac{\Lambda(H)}{8\pi G} = \frac{3}{8\pi G} (c_0 + \nu H^2), \quad (2.58)$$

where $c_0 = H_0^2(\Omega_{0\Lambda} - \nu) \simeq \frac{\Lambda_0}{3}$ (with Λ_0 the current value) is an integration constant which is fixed by the boundary condition $\rho_\Lambda(H_0) = \rho_{\Lambda,0}$ (with $\rho_{\Lambda,0}$ the current value) and ν is a dimensionless running parameter which characterizes the dynamics of the vacuum at low energy. For $\nu = 0$ the vacuum energy remains constant at all times and for $\nu > 0$ the vacuum energy density decreases with the time. In QFT the running parameter is $|\nu| \simeq 10^{-6} - 10^{-3}$ [691] but in RVM it has been treated as a free parameter by fitting to the observational data e.g. [695, 696].

Phenomenologically emergent dark energy

Phenomenologically emergent dark energy (PEDE) is a zero freedom dark energy scenario proposed by Ref. [618]. In this model the dark energy density has the following form

$$\tilde{\Omega}_{DE}(z) = \Omega_{0DE} [1 - \tanh(\log_{10}(1+z))] , \quad (2.59)$$

where $\Omega_{0DE} = 1 - \Omega_{0m} - \Omega_{0r}$.

The dark energy in this model has no effective presence in the past and emerges at the later times and with the same number (six) of parameters compared to the spatially flat Λ CDM scenario. It has the potential for alleviating the H_0 tension [618, 697–702]. The generalised emergent dark energy (GEDE) model has one extra dimensionless free parameter Δ including both Λ CDM model as well as the PEDE model as two of its special limits introduced by Ref. [703]. In the GEDE model the dark energy density has the following form [704]

$$\tilde{\Omega}_{DE}(z) = \Omega_{0DE} \frac{1 - \tanh\left(\Delta \log_{10}\left(\frac{1+z}{1+z_t}\right)\right)}{1 + \tanh(\Delta \log_{10}(1+z_t))} , \quad (2.60)$$

where z_t is the transition redshift where dark energy density equals to matter density. For $\Delta = 0$ and $\Delta = 1$ this model recovers Λ CDM and PEDE model respectively. Using the latest observational Hubble dataset [705] revisited and constrained the free parameters of the PEDE and GEDE models.

Other versions of the PEDE model are the Modified Emergent Dark Energy (MEDE) [706] and the Transitional Dark Energy (TDE) [707] models. The MEDE model with one extra degree of freedom reduces the Hubble tension to 2.4σ [706] even though it also suffers from the three problems of the late time $H(z)$ deformation models.

Vacuum phase transition

Vacuum phase transition [619, 702, 708, 709] based on vacuum metamorphosis (VM) or vacuum cold dark matter model (VCDM) [710–712] has the potential to address the H_0 tension. This mechanism with six free parameters as the spatially flat Λ CDM. It also assumes a phase transition in the nature of the vacuum similar to Sakharov’s induced gravity [713]. The phase transition occurs when the evolving Ricci scalar curvature R becomes equal to the value of scalar field mass squared m^2 [619]

$$R = 6(\dot{H} + H^2) = m^2 , \quad (2.61)$$

where the dot corresponds to the derivative with respect to cosmic time t . After the transition the Ricci scalar curvature remains constant with $R = m^2$ and this changes the expansion rate below ($z < z_t$) due to the phase transition

$$\frac{H^2}{H_0^2} = \Omega_{0m}(1+z)^3 + \Omega_{0m}(1+z)^3 + M \left\{ 1 - \left[3 \left(\frac{4}{3\Omega_{0m}} \right)^4 M(1-M)^3 \right]^{-1} \right\} , \quad z > z_t , \quad (2.62)$$

$$\frac{H^2}{H_0^2} = (1-M)(1+z)^4 + M , \quad z \leq z_t , \quad (2.63)$$

where $M = \frac{m^2}{12H_0^2}$ and $z_t = -1 + \frac{3\Omega_{0m}}{4(1-M)}$ is the transition redshift.

Phase transition in dark energy

- Phase transition in dark energy explored by [620, 714–716] can address the Hubble tension. Generalizing this model by assigning a more realistic time evolution of dark energy Ref. [717] proposes the critically emergent dark energy (CEDE) model.

In Ref. [718] the form of phase transition parametrized phenomenologically by a hyperbolic tangent function. This scenario for dark energy is similar used independently as PEDE and GEDE.

- Late dark energy (LDE) transition [609] at redshifts $z \ll 0.1$ can reduce the Hubble tension. This class of $H(z)$ deformation models has a more intense form of the third problem of the deformation class as they predict a significantly lower value of the SnIa absolute magnitude than the other $H(z)$ deformation models [289, 593].

In this scenario the true Hubble constant is given by [609, 719]

$$H_0^2 = \tilde{H}_0^2(1 + 2\delta) , \quad (2.64)$$

where \tilde{H}_0 is the prediction for a flat Λ CDM model in the context of a CMB sound horizon calibration.

In Refs. [609, 720] it was shown that this model can not fully resolve the Hubble problem as it would imply a transition in the SnIa apparent magnitude which is not observed. These models however become viable in the context of a SnIa absolute magnitude transition [52, 593].

2.3.2 Deformations of the Hubble expansion rate $H(z)$ with additional interactions/degrees of freedom

There exist several varieties of the models for the solution of the Hubble tension which use deformations of the Hubble expansion rate $H(z)$ with additional interactions/degrees of freedom. For example the interacting dark energy models e.g. [589, 590] with an extra non-gravitational interaction between the components of the Universe and the decaying dark matter models e.g. [591] with additional degrees of freedom are able to alleviate the Hubble constant H_0 tension.

The following models may be classified in this class of theories: multi-interacting dark energy [721], new interacting dark energy [722], interacting vacuum energy [723], metastable dark energy [724, 725], Quintom dark energy [726], cannibal dark matter [727], baryons-dark energy interacting [728] [see also 729, 730], swampland conjectures [731–733], nonlocal gravity [734, 735], late time transitions in the quintessence field [736], Galileon gravity [737–741], $f(R)$ gravity [742–745], $f(T)$ gravity [497, 532, 746–752], $f(T, B)$ gravity [753], $f(Q)$ gravity [754], Brans-Dicke gravity [755, 756], minimal theory of massive gravity [757], scale-dependent gravity [758], unimodular gravity [759, 760], the screened fifth forces [761, 762], the minimally modified gravity [763], the Lifshitz cosmology [764], the Milne cosmology [765], 4D Gauss-Bonnet gravity [766], the generalized Chaplygin gas [767], the unified cosmologies [768], the Λ -gravity [769, 770], the $\Lambda(t)$ -model [771, 772], the bulk viscous cosmology [773–776] and the surface tension hypothesis [777]. For instance in the case of the metastable dark energy [725], generalized Chaplygin gas [767] and Galileon gravity [737] models the tension on H_0 appears to be significantly alleviated to within about 1σ even though the there problems of the $H(z)$ deformation models remain to be addressed.

Interacting dark energy

In the cosmological interacting dark energy (IDE) models [589, 590, 778–819] (see Refs. [820, 821], for a review) the dark components of the Universe i.e dark matter (DM) and dark energy (DE) have an extra non-gravitational interaction. The IDE model was proposed to address the coincidence problem e.g. [822–830]. In addition the interaction between the dark fluids has been shown to be effective in substantially alleviating the Hubble constant H_0 tension [589, 590, 792, 799, 800, 814, 819, 831–836] or in addressing the structure growth σ_8 tension between the values inferred from the CMB and the WL measurements [837–840] (see Subsection 3.1.2) or in solving the two tensions simultaneously [794, 804, 809].

In IDE cosmology assuming spatially flat Friedmann-Lemaître-Robertson-Walker background and pressureless dark matter ($w_c = 0$) the equations of evolution of the dark matter and dark energy densities ρ_c and ρ_{DE} respectively are given by [841]

$$\dot{\rho}_c + 3H\rho_c = Q(t) , \quad (2.65)$$

$$\dot{\rho}_{DE} + 3H(1 + w_{DE})\rho_{DE} = -Q(t) , \quad (2.66)$$

where the dot corresponds to the derivative with respect to cosmic time t , $w_{DE} = \frac{p_{DE}}{\rho_{DE}}$ is the equation of state of dark energy and Q represents the interaction rate between the dark sectors (i.e. the rate of energy transfer between the dark fluids). For $Q < 0$ energy flows from dark matter to dark energy, whereas for $Q > 0$ the energy flow is opposite.

These models combine the deformation of $H(z)$ with an extra modification of the growth rate of perturbations due to the tuned evolution of $\Omega_m(z)$ induced by the interaction term Q . This additional tuning allows for a simultaneous improvement of the growth tension in contrast to models that involve a simple $H(z)$ deformation.

Various phenomenological IDE models were proposed in the literature where the rate of the interaction Q has a variety of possible functional forms [842]. For example in some classes of IDE models the rate of the interaction Q is proportional to the energy density of dark energy $Q = \delta H \rho_{DE}$ [590, 794, 804, 809] or cold dark matter $Q = \delta H \rho_c$ [792] (where δ is a constant and $\delta = 0$ in the Λ CDM cosmology), or some combination of the two. Note that in the case of functional form $Q = \delta H \rho_c$ instabilities develop in the dark sector perturbations at early times [843].

Decaying dark matter

Decaying dark matter into dark radiation (i.e. an unknown relativistic species that is not directly detectable), which has been first analysed by Ref. [844] and studied by Refs. [845–853], provides a promising scenario to relieve the Hubble constant H_0 tension e.g. [591]. Also, it has been shown that this scenario can resolve the σ_8 growth tension [854, 855] or the two tensions simultaneously [856] by a similar mechanism as in the IDE models. However, using the Planck data the analysis of the model by Refs. [857, 858] has shown that the cosmological tensions are only slightly alleviated (see Ref. [859], for a different result).

In these models assuming spatially flat Friedmann-Lemaître-Robertson-Walker Universe, pressureless dark matter, $w_c = 0$ and equation of state of dark radiation $w_{DR} = 1/3$, the equations of evolution of the dark matter and dark radiation densities ρ_c and ρ_{DR} respectively are given by [841]

$$\dot{\rho}_c + 3H\rho_c = -\Gamma\rho_c , \quad (2.67)$$

$$\dot{\rho}_{DR} + 4H\rho_{DR} = \Gamma\rho_c , \quad (2.68)$$

where $\Gamma = \frac{1}{\tau}$ is the decay rate of dark matter particles (with τ the particle's lifetime). In the literature a variety of possible functional forms of the decay rate has been explored [854, 857, 859, 860]. For example in some cases the decay rate is proportional to the Hubble rate, $\Gamma \propto H$ [856]. Constraints on the decay rate of dark matter have been obtained by the analysis of Refs. [854, 861].

A model with decaying dark matter into dark radiation in early/late Universe ($\tau \ll t_s$ / $\tau \gg t_s$, where t_s is the time of last scattering) increases/decreases the expansion rate $H(a; \rho_b, \rho_\gamma, \rho_c, \rho_{DR}, \rho_{DE})$ at high/low redshifts as it predicts a smaller matter content and a larger radiation content as time evolves (the early/late Universe is dominated by the radiation/matter and the dark radiation density decreases more rapidly than the matter density, $\rho_{DR} \propto a^{-4}$ and $\rho_c \propto a^{-3}$). In the case of $\tau \ll t_s$, the faster cosmological expansion $H(z)$ decreases the scale of the sound horizon r_s in Eq. (2.17) because the baryon-to-photon ratio, and thus c_s in Eq. (2.18), is tightly constrained by CMB fluctuations and BBN [862]. In the context of the degeneracy $H_0 r_s$ shown in Eq. (2.19) the lower scale of the sound horizon r_s yields a larger value of H_0 . In the case of $\tau \gg t_s$, the lower dimensionless normalized Hubble rate $E(z)$ in the late-time leads to a larger value of H_0 since θ_s and r_s must be kept fixed in Eq. (2.19). Accordingly, both early and late decaying dark matter model are able to alleviate the Hubble constant H_0 tension (see Refs. [863, 864], for a detailed discussion).

There are alternative decaying dark matter models such as the light dark matter [865], the dynamical dark matter [866], the many-body or 2-body decaying cold dark matter scenarios [867] and the decaying warm dark matter scenario [868]. In the 2-body decaying cold dark matter scenario the decaying dark matter produces two particles, one massive warm dark matter particle and one massless relativistic

particle (dark radiation). This scenario can address the Hubble constant H_0 tension [869–871] and the σ_8 growth tension [872].

A self-interacting dark matter model with a light force mediator coupled to dark radiation studied by Refs. [873, 874]. This model can simultaneously reduce the tension between CMB and low-redshift astronomical observations of H_0 and σ_8 .

Ref. [875] pointed out that a dark particle from reheating [876] can alleviate the H_0 tension through its decay to relativistic component which contributes to the dark radiation.

Recently, Ly- α constraints on possible models of dark-matter physics have been evaluated by Ref. [877]. In particular the Ly- α bounds on different classes of dark-matter velocity distributions have been obtained.

2.3.3 Deformations of the Hubble expansion rate $H(z)$ with inhomogeneous/anisotropic modifications

Models where the cosmological principle and the FLRW metric are relaxed by considering inhomogeneous/anisotropic modifications have the potential to resolve the Hubble problem [878]. Physical models where the deformation of $H(z)$ may be achieved with inhomogeneous/anisotropic modifications, include the following: Chameleon dark energy e.g. [879], cosmic voids [880] and inhomogeneous causal horizons [592], charged dark matter [881–883], Bianchi type I spacetime [884] and emerging spatial curvature [885, 886].

Chameleon dark energy

Chameleon dark energy [887, 888] (see also Refs.[889–897]) attempts to address the Hubble constant H_0 tension by introducing a cosmic inhomogeneity in the Hubble expansion rate at late-time from the chameleon field coupled to the local matter overdensities [879]. This field trapped at a higher potential energy density acts as an effective cosmological constant and results in a faster local expansion rate than that of the background with lower matter density.

Cosmic voids

In cosmic void models the local H_0 departs significantly from the cosmic mean H_0 because of the presence of an under-dense region (local void) [898]. However in Refs. [880, 899] it was shown that this alternative theory is inconsistent with current observations. The analysis was based on the assumption of the validity of standard Λ CDM and a study of the sample variance in the local measurements of the Hubble constant this alternative theory has been shown inconsistent with current observations. Ref. [880] estimated that the required radius of void to resolve the tension in H_0 is about 150 Mpc and density contrast of $\delta \equiv \frac{\rho - \bar{\rho}}{\bar{\rho}} \simeq -0.8$ which is inconsistent at $\sim 20\sigma$ with the Λ CDM cosmology [899, 900].

In the context of this inconsistency, Ref. [900] considered a cosmological Milgromian dynamics or modified Newtonian dynamics (MOND) model [901] with the presence of 11eV/ c^2 sterile neutrinos²⁴ to show that the Keenan-Barger-Cowie (KBC) void²⁵ has the potential to resolve the Hubble tension.

Inhomogeneous Causal Horizons

Ref. [592] proposed a simple solution to the H_0 tension based on causally disconnected regions of the CMB temperature anisotropy maps from Planck [908]. It was pointed out that CMB maps show ‘causal horizons’ where cosmological parameters have distinct values. This could be justified by the fact that these regions of the Universe have never been in causal contact. Thus it was shown that the Hubble constant H_0 takes values which differ up to 20% among different causally disconnected regions. These

²⁴Sterile neutrinos are a special kind of neutrino with right handed chirality that might interact only through gravity [902, 903] (see Refs. [904–906], for a review). They have been proposed to resolve some anomalies in neutrino data.

²⁵The KBC void [907] is a large local underdensity between 40 and 300 Mpc (i.e. $0.01 \lesssim z \lesssim 0.07$) around the Local Group.

cosmological parameter inhomogeneities are in agreement with the model of the Universe proposed in Ref. [909] (see also Refs. [910–912] for details) where the cosmological constant is simply formulated as a boundary term in the Einstein equations and where 'Causal Horizons' naturally arise. Thus if there are similar 'causal horizons' in the local universe (i.e, $z < 1100$), then 20% variations between the local and high- z measures of H_0 are indeed to be expected [592].

2.3.4 Late time modifications - Transition/Recalibration of the SnIa absolute luminosity

This class of models can address the problems of the $H(z)$ deformation models (especially the low M problem) by assuming a rapid variation (transition) of the SnIa intrinsic luminosity and absolute magnitude due e.g. to a gravitational physics transition at a redshift $z_t \lesssim 0.01$ [52, 477, 593].

Gravity and evolution of the SnIa intrinsic luminosity

As shown in the recent analysis by Ref. [12] there are abnormal features which may be interpreted as evolution of the measured parameter combination \mathcal{M} (see Section 2.2.1). This measured parameter combination \mathcal{M} in Eq. (2.10) depends on the absolute magnitude M and on the Hubble constant H_0 (M and H_0 are degenerate parameters). Any variation of the parameter \mathcal{M} is due to a variation of M which could be induced by a varying $\mu_G(z) \equiv \frac{G(z)}{G_0}$ (where G_0 is the local value of the Newton's constant $G(z)$). If the calibrated SnIa absolute magnitude M were truly constant then the parameter \mathcal{M} should also be constant (independent of redshift).

A possible variation of the absolute magnitude M and equivalently of the absolute luminosity

$$L \sim 10^{-2M/5} , \quad (2.69)$$

could be due to a variation of the fine structure constant α or the Newton's constant G .

If the absolute luminosity is proportional to the Chandrasekhar mass $L \sim M_{Ch}$ we have [913, 914]

$$L \sim G^{-3/2} . \quad (2.70)$$

Thus L will increase as G decreases²⁶.

Under these assumptions, we obtain

$$M(z) - M_0 = \frac{15}{4} \log \mu_G(z) , \quad (2.71)$$

where M_0 corresponds to a reference local value of the absolute magnitude and $\mu_G \equiv \frac{G}{G_0}$ is the relative effective gravitational constant (with G the strength of the gravitational interaction and G_0 the locally measured Newton's constant).

Then, the Eq. (2.10) takes the following form

$$\mathcal{M}(z) = M_0 + \frac{15}{4} \log \mu_G(z) + 5 \log_{10} \left[\frac{c/H_0}{Mpc} \right] + 25 , \quad (2.72)$$

and the apparent magnitude Eq. (2.11) can be written as

$$m(z, H_0, \Omega_{0m})_{th} = \mathcal{M}(z, H_0) + 5 \log_{10} [D_L(z, \Omega_{0m})] . \quad (2.73)$$

A mild tension at 2σ level in the best fit value of \mathcal{M} was found in between the low-redshfit ($z \lesssim 0.2$) data and the full Pantheon dataset in the context of a Λ CDM model. This tension can be interpreted as [12]

²⁶Adopting a semi-analytical model which takes into account the stretch of SnIa light curves but assumes fixed mass of Ni, obtaining SnIa light curves in the context of modified gravity Ref. [915] has claimed that L will increase as G increases.

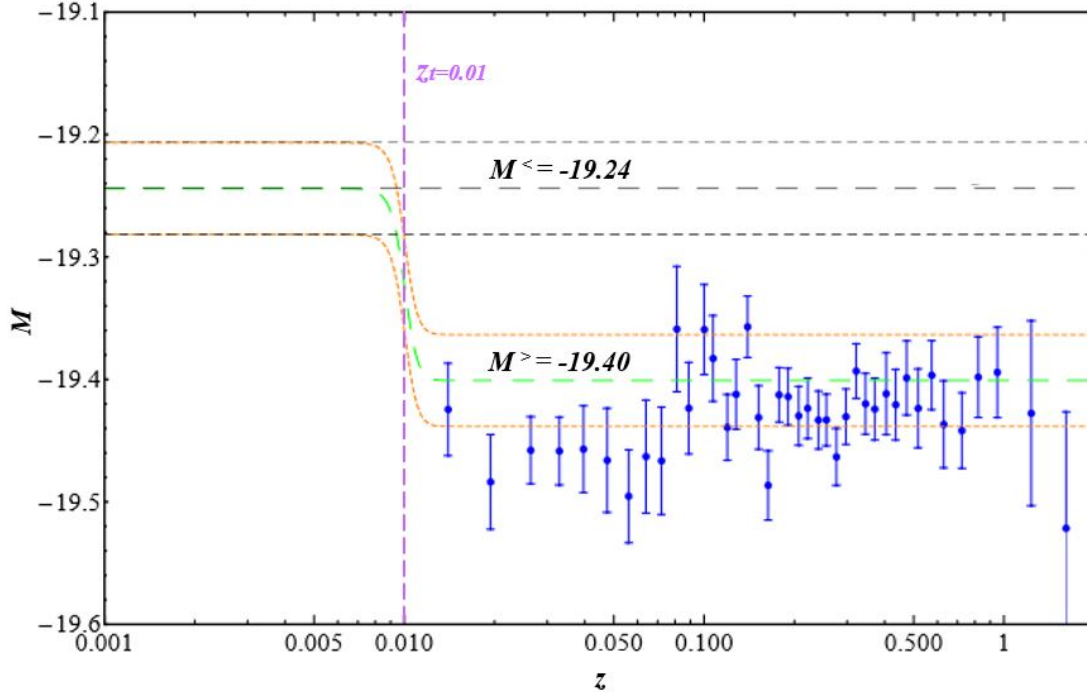


Figure 2.14: The Pantheon binned SNIa absolute magnitudes Eq. (2.76) M_i (blue points) [51] for a Planck/ Λ CDM luminosity distance. The data are inconsistent with the SNIa absolute magnitude $M^< = -19.24$ calibrated by Cepheids but the inconsistency disappears if there is a transition in the absolute magnitude with amplitude $\Delta M \simeq -0.2$ at redshift $z_t \simeq 0.01$ (from Ref. [52]).

- a locally higher value of H_0 by about 2%, corresponding to a local matter underdensity.
- a time variation of Newton's constant which implies an evolving Chandrasekhar mass and thus an evolving absolute luminosity L and absolute magnitude M of low z SNIa.

In addition, the oscillating features shown in Fig. 2.2 hint also to the possibility of evolutionary effects of M . As discussed below such evolutionary effects if they exist in the form of a transition may provide a solution to the Hubble and growth tensions.

Transition of the SNIa absolute magnitude M at a redshift $z \simeq 0.01$

Recently, Ref. [52] has proposed that a rapid transition (abrupt deformation) at a transition redshift $z_t \simeq 0.01$ in the value of the SNIa absolute magnitude M of the form

$$M^>(z) = M^< + \Delta M \Theta(z - z_t) , \quad (2.74)$$

(where Θ is the Heaviside step function) due to a rapid transition of the gravitational constant can address the Hubble tension.

In particular the analysis by Ref. [52] has shown that a 10% rapid transition in the value of the relative effective gravitational constant μ_G at $z_t \simeq 0.01$ is sufficient to induce the required reduction of M

$$\Delta M \equiv M^> - M^< \simeq -0.2 , \quad (2.75)$$

where $M^<$ is the SNIa absolute magnitude of Eq. (2.13) calibrated by Cepheids at $z < 0.01$ [269, 289] and $M^>$ is the SNIa absolute magnitude of Eq. (2.14) using the parametric-free inverse distance ladder of

[290]. Fig. 2.14 shows the Pantheon SnIa absolute magnitudes for a Planck/ Λ CDM luminosity distance [51] obtained from

$$M_i = m_i - 5 \log_{10} \left[\frac{d_L(z_i)}{Mpc} \right] - 25 , \quad (2.76)$$

where m_i are the apparent magnitude datapoints.

The data are in disagreement with the SnIa absolute magnitude $M^<$ calibrated by Cepheids but they become consistent if there is a transition in the absolute magnitude with amplitude $\Delta M \simeq -0.2$ [52]. Thus, this class of M -transition models avoids the M -problem of late time $H(z)$ deformation models.

Assuming the power law dependence Eq. (2.70) and using RSD and WL data [4, 50, 916] reported a best fit value $\Delta\mu_G \equiv \mu_G^> - \mu_G^< = -0.19 \pm 0.09$ ($\mu_G^>$ corresponds to $z > 0.01$ and $\mu_G^<$ corresponds to $z < 0.01$) in the context of a Λ CDM background $H(z)$. The analysis by Ref. [52] showed that a rapid $\sim 10\%$ increase of the effective gravitational constant roughly 150 million years ago can also solve Ω_m - σ_8 growth tension.

Recently, Ref. [606] has demonstrated that this model has an advantage over both early time and late time deformations of $H(z)$ to fully resolve the Hubble tension while at the same time improving the level of the Ω_m - σ_8 growth tension. In addition it has the potential to provide equally good fit to low z distance probes such as BAO and SnIa as the Planck18/ Λ CDM model.

More recently, Ref. [9] generalized the symmetron screening mechanism²⁷ [940, 941] by allowing for an explicit symmetry Z_2 breaking of the symmetron ϕ^4 potential (see in Chapter 11 for details). The explicit symmetry breaking can create an asymmeron wall network pinned on matter overdensities separating regions with distinct gravitational properties which could constitute a physical mechanism for the realization of gravitational transitions in redshift space that could help in the resolution of the Hubble and growth tensions. Another theoretical model leading to a gravitational transition could include a pressure non-crushing cosmological singularity in the recent past [942].

Late (low-redshift) $w - M$ phantom transition

The late (low-redshift) $w - M$ phantom transition [593] is a late time approach involving a combination of the previous two classes: the transition of the SnIa absolute luminosity and the deformation of the Hubble expansion rate $H(z)$. A rapid phantom transition of the dark energy equation of state parameter w at a transition redshift $z_t < 0.1$ of the form

$$w(z) = -1 + \Delta w \Theta(z_t - z) , \quad (2.77)$$

with $\Delta w < 0$ and a similar transition in the value of the SnIa absolute magnitude M of the form

$$M(z) = M_C + \Delta M \Theta(z - z_t) , \quad (2.78)$$

with $\Delta M < 0$ due to evolving fundamental constants can address the Hubble tension [593]. Where Θ is the Heaviside step function, M_C is the SnIa absolute magnitude Eq. (2.13) calibrated by Cepheids [269, 289] at $z < 0.01$ and ΔM , Δw are parameters to be fit by the data. Ref. [593] finds $\Delta M \simeq -0.1$, $\Delta w \simeq -4$ for $z_t = 0.02$ which imply a lower value of μ_G at $z > 0.02$ (about 6%) compared to the pure M -transition model.

The late (low-redshift) $w - M$ phantom transition (LwMPT) can lead to a resolution of the Hubble tension in a more consistent manner than smooth deformations of the Hubble tension and other types of late time transitions such as the Hubble expansion rate transition [609, 720]. Its main advantages include the consistency in the predicted value of the SnIa absolute magnitude M and the potential for simultaneous resolution of the growth tension.

Refs. [8, 56, 943] have analyzed the color-luminosity relation of Cepheids in anchor galaxies and SnIa host galaxies by identifying the color-luminosity relation for each individual galaxy instead of enforcing a

²⁷For reviews of modified gravity theories with screening mechanisms, such as the Vainshtein [917–919] and the chameleon [887, 888, 892, 920–926] models see Refs. [927–938] and for screening effects see Ref. [939].

universal color-luminosity relation to correct the NIR Cepheid magnitudes. A systematic brightening of Cepheids at distances larger than about 20 Mpc which could be enough to resolve the Hubble tension was found. In addition, Ref. [8] investigating the effects of variation of the Cepheid calibration empirical parameters (the color-luminosity parameter or the Cepheid absolute magnitude) finds hints for the presence of a fundamental physics transition taking place at a time more recent than 100 Myrs ago. The magnitude of the transition lead to value of H_0 that is consistent with the CMB inferred value thus eliminating the Hubble tension. The distance range/timescale corresponding to this transition is consistent with solar system history data [944] indicating an increase of the rate of impactors on the Moon and Earth surfaces by about a factor of 2-3 during the past 100 Myrs which correspond to $z < 0.008$ [945–951] and low redshift galaxy surveys data [952]. Such a transition is also consistent with a recent analysis by Ref. [477] indicating a transition in the context of the Tully-Fisher data.

In particular, using a robust dataset of 118 Tully-Fisher datapoints Ref. [477] has demonstrated that evidence for a transition in the evolution of BTFR appears at a level of more than 3σ . Such effect could be interpreted as a transition of the effective Newton's constant. The amplitude and sign of the gravitational transition are consistent with the mechanisms for the resolution of the Hubble and growth tension discussed above [52, 593] (see in [953], for a talk of the tensions of the Λ CDM and a gravitational transition).

2.3.5 Early time modifications of sound horizon

Modifying the scale of sound horizon r_s (i.e. the scale of the standard ruler) by introducing new physics before recombination that deform $H(z)$ at prerecombination redshifts $z \gtrsim 1100$ can increase the CMB inferred value of H_0 [954–957] and thus resolve the Hubble tension. Such deformation may be achieved by introducing various types of additional to the standard model components (see Ref. [958], for a review). These models have the problem of predicting stronger growth of perturbations than implied by dynamical probes like redshift space distortion (RSD) and weak lensing (WL) data and thus may worsen the Ω_m - σ_8 growth tension [331, 606].

A wide range of mechanisms has been proposed for the decrease of the the sound horizon scale at recombination. These mechanisms include the introduction of early dark energy, extra neutrinos or some other dark sector at recombination, features in the primordial power spectrum, modified scenarios of recombination etc. The following models and theories may be classified in this class of mechanisms: early dark energy e.g. [182], dark radiation e.g. [959], neutrino self-interactions e.g [960], large primordial non-Gaussianities [961], Heisenberg's uncertainty principle [962], early modified gravity [963], cosmological inflation physics [964–976], dark matter - photon coupling [977, 978], dark matter-neutrino interactions [979], interacting dark radiation [980], ultralight dark photon [981], primordial black holes [982, 983], primordial magnetic fields [984–986], non-standard recombination [987], unparticles dark energy [988], varying fundamental constants [989–993], early-time thermalization of cosmic components [994], CMB monopole temperature shift [995], open and hotter universe [996, 997], Axi-Higgs cosmology [998, 999], string Cosmology [1000, 1001] and dark massive vector fields [1002]. In this list of proposed cosmological models the tension on H_0 is alleviated with a significance ranging from the 1σ to the 3σ level.

Early dark energy

In the early dark energy (EDE) model [54, 181–183, 1003–1023] an additional dynamical scalar field behaves like a cosmological constant at early times (near matter-radiation equality but before recombination). This field decays rapidly after recombination thus leaving the rest of the expansion history practically unaffected up to a rescaling which modifies H_0 . This rescaling allows for the resolution of the Hubble constant tension. Using the Eq. (2.17) in a EDE model the radius of sound horizon at last scattering can be calculated by

$$r_s = \int_0^{t_d} \frac{c_s(a)}{a(t)} dt = \int_{z_d}^{\infty} \frac{c_s(z)}{H(z; \rho_b, \rho_\gamma, \rho_c, \rho_{DE})} dz = \int_0^{a_d} \frac{c_s(a)}{a^2 H(a; \rho_b, \rho_\gamma, \rho_c, \rho_{DE})} da, \quad (2.79)$$

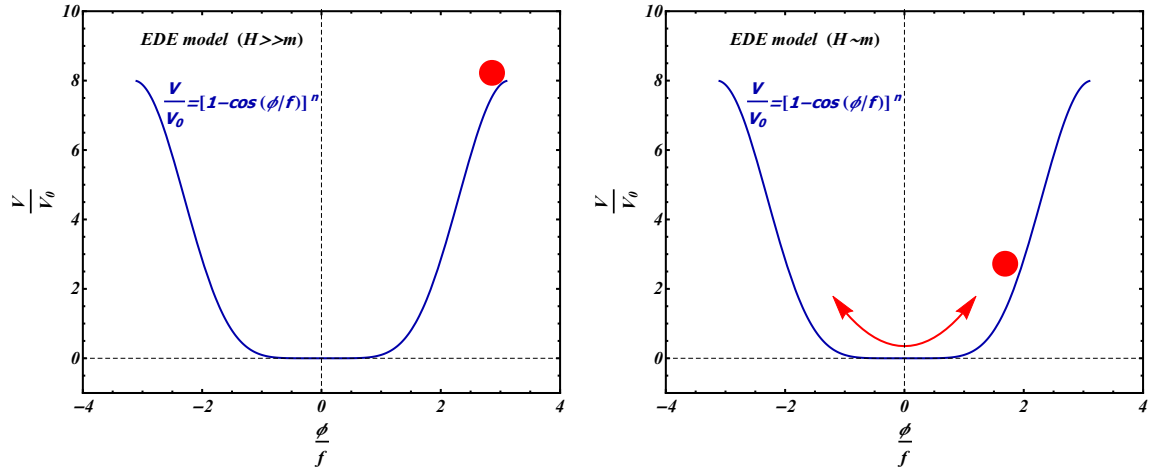


Figure 2.15: The potential V/V_0 (with $V_0 = m^2 f^2$, $n = 3$ in Eq. (2.80)) as a function of ϕ/f at early times ($H \gg m$) (left panel) when the field ϕ is initially frozen in its potential due to Hubble friction and acts as a cosmological constant with equation of state $w_\phi = -1$, and at a critical redshift z_c when the Hubble parameter drops below some value ($H \sim m$) (right panel) and the field becomes dynamical and begins to oscillate around its minimum which is locally $V \sim \phi^{2n}$.

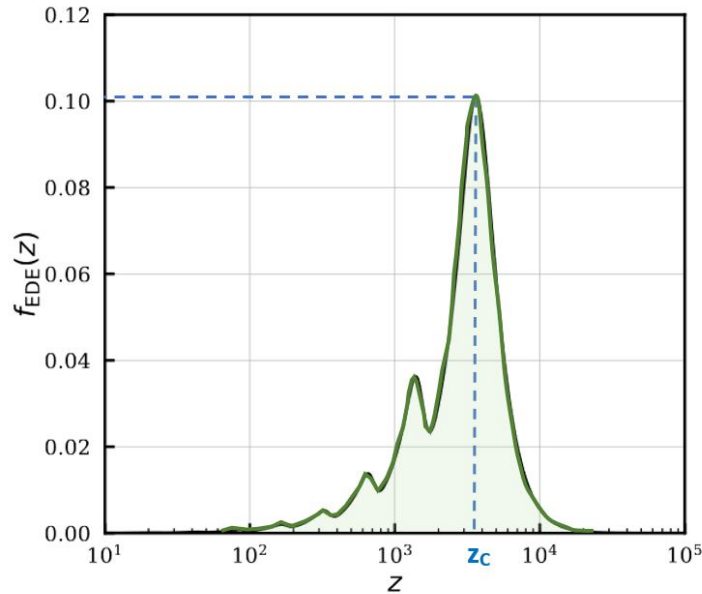


Figure 2.16: Fractional contribution of EDE to the cosmic energy budget as a function of redshift (adapted from Ref. [53]).

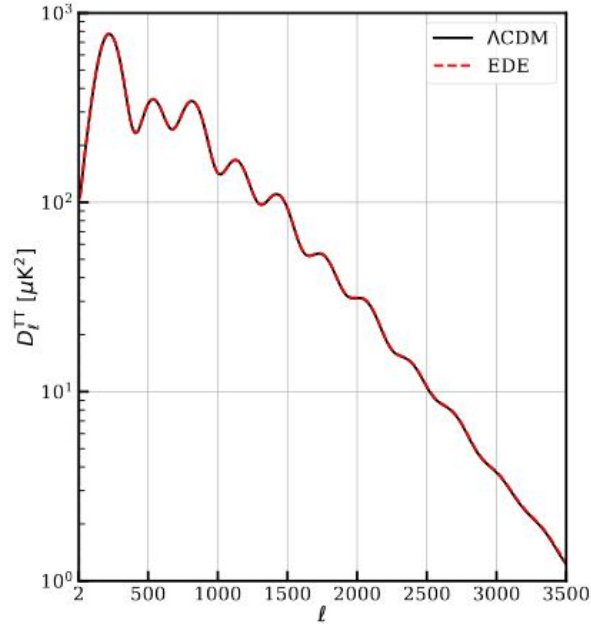


Figure 2.17: CMB TT power spectrum. The black solid and the red dashed lines correspond to Λ CDM model with $H_0 = 68.07 \text{ km s}^{-1} \text{ Mpc}^{-1}$ and EDE model with $H_0 = 71.15 \text{ km s}^{-1} \text{ Mpc}^{-1}$ respectively (from Ref. [53]).

The baryon-to-photon ratio, and thus c_s in Eq. (2.18), is tightly constrained by CMB fluctuations and BBN [862]. As a consequence a EDE phase before and around the recombination epoch would increase $H(z)$ and thus decrease the scale of the sound horizon r_s in Eq. (2.79). In the context of the degeneracy $H_0 r_s$ shown in Eq. (2.19) this decrease of r_s leads to an increased value of H_0 for a fixed measured value of θ_s .

An EDE model can be implemented by several functional forms of scalar field which contribute to the cosmic energy shortly before matter-radiation equality. Possible functional forms of scalar field are the axion-like potential (higher-order periodic potential) inspired by string axiverse scenarios for dark energy [181, 1024–1027], the single axion-like particle potential consisting of two cosine functions which unifies the inflaton and DM while reheating the universe [1028, 1029], the power-law potential [183], the acoustic dark energy [1014, 1030, 1031], the α -attractor-like potential [1032] and others.

Ref. [182] considers two physical models. One that involves an oscillating scalar field and another with a slowly-rolling scalar field. In the case of the first model of the proposal of Ref. [182], the potential of the scalar field ϕ is a generalization of the axion potential of the form

$$V(\phi) = m^2 f^2 (1 - \cos(\phi/f))^n, \quad (2.80)$$

where m is the field mass (for ultralight scalar field $m \sim 10^{-28} \text{ eV}$) and f is a decay constant.

Consider the time evolution of the EDE scalar field which may be written as

$$\ddot{\phi} + 3H\dot{\phi} + V'(\phi) = 0, \quad (2.81)$$

where the dot and the prime denote the derivatives with respect to cosmic time t and field ϕ respectively.

At early times, deep in the radiation era the field ϕ is initially frozen in its potential due to Hubble friction ($H \gg m$) and acts as a cosmological constant with equation of state $w_\phi = -1$ (hence the name Early Dark Energy), but when the Hubble parameter drops below some value ($H \sim m$) at a critical redshift z_c (for EDE this happens when $z_c \sim z_d$ for $m \sim 10^{-27} \text{ eV}$) the field becomes dynamical and

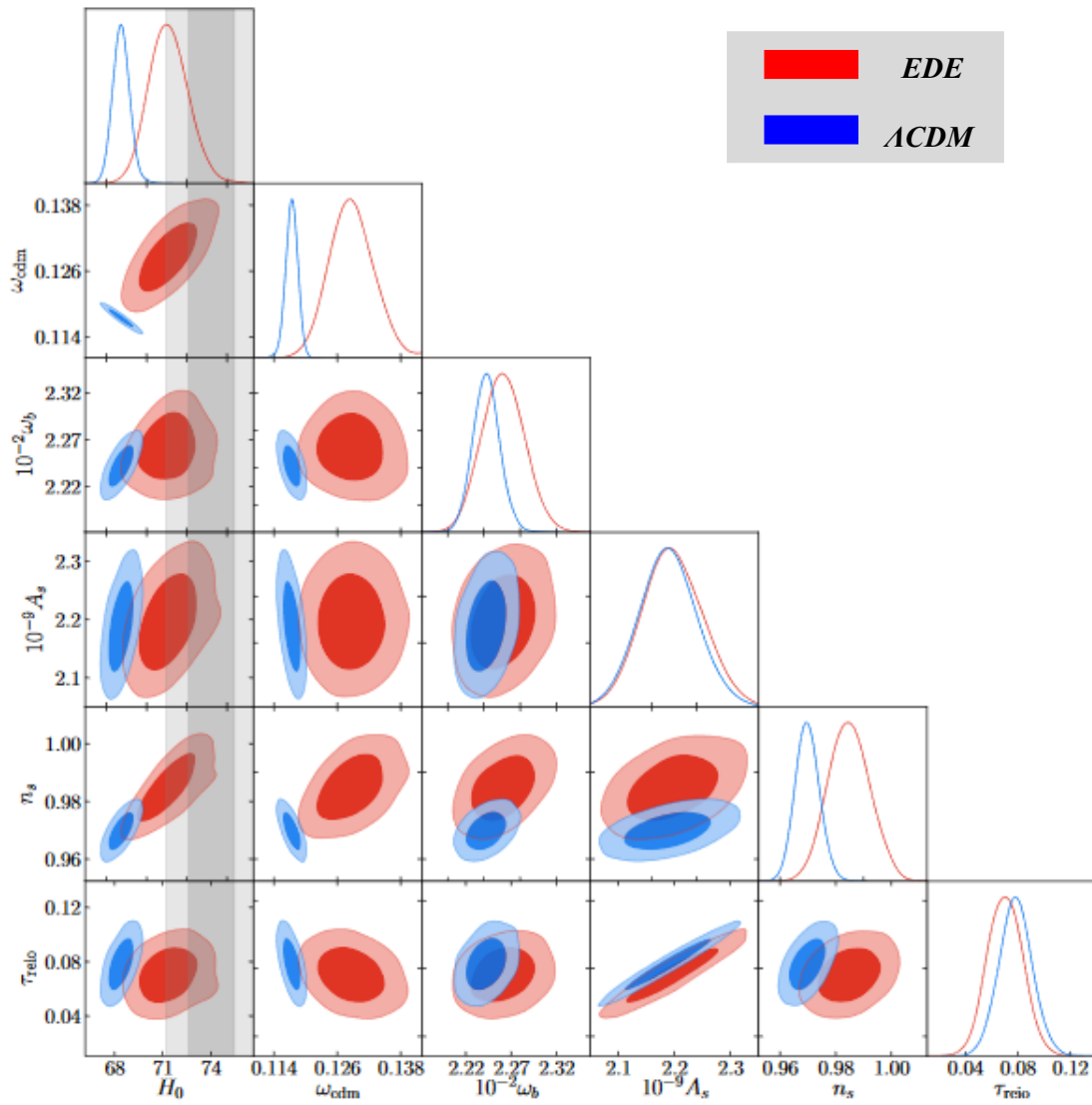


Figure 2.18: Posterior 1D and 2D distributions of the cosmological Λ CDM parameters reconstructed from a run to all data (including Planck high l polarization) in EDE (red) and the Λ CDM (blue) scenario. The grey bands correspond to the SH0ES determination of H_0 (adapted from Ref. [54]).

begins to oscillate around its minimum which is locally $V \sim \phi^{2n}$ (Fig. 2.15). It thus begins to behave like a fluid with an equation of state [1033]

$$w_\phi = \frac{n-1}{n+1}. \quad (2.82)$$

The energy density of the field dilutes as $a^{-3(1+w_\phi)}$ and thus when $n = 1$, $n = 2$ and $n \geq 3$ dilutes as cold dark matter (a^{-3} , $w_\phi = 0$), as radiation (a^{-4} , $w_\phi = 1/3$) and faster than radiation (a^{-x} with $x > 4$, $w_\phi > 1/3$) respectively. Also when $n \rightarrow \infty$ the energy density dilutes as free scalar field (stiff matter [1034]) (a^{-6} , $w_\phi = 1$) i.e. the scalar field is fully dominated by its kinetic energy.

The EDE models are parameterized by the critical redshift z_c , the dimensionless quantity $\theta_i = \phi_i/f$ (with ϕ_i the initial value of the scalar field and $0 < \theta_i < \pi$) and the peak EDE energy density fraction of the Universe $f_{EDE}(z_c)$ which is given by

$$f_{EDE}(z_c) \equiv \frac{\Omega_\phi(z_c)}{\Omega_{tot}(z_c)} = \frac{\rho_{EDE}(z_c)}{3M_{pl}^2 H(z_c)^2}, \quad (2.83)$$

where Ω_ϕ is the EDE energy density which evolves as [182, 1027]

$$\Omega_\phi(z) = \frac{2\Omega_\phi(z_c)}{[(1+z_c)/(1+z)]^{3(w_n+1)} + 1}. \quad (2.84)$$

The fractional contribution of EDE to the cosmic energy budget as a function of redshift, i.e. $f_{EDE}(z)$, is shown in Fig. 2.16 (from the analysis by Ref. [53]). Clearly, for $z \simeq z_c$ the EDE contributes the most to the total energy density ($\sim 10\%$), for $z > z_c$ the EDE is not dynamically important while for $z < z_c$ decays away as radiation or faster than radiation leaving the later evolution of the Universe relatively unchanged. By construction, the EDE models can nicely match the CMB TT power spectrum of Λ CDM and therefore of Planck as illustrated in Fig. 2.17. The black solid and the red dashed lines (almost identical) correspond to Λ CDM model with $H_0 = 68.07 \text{ km s}^{-1} \text{ Mpc}^{-1}$ and EDE model with $H_0 = 71.15 \text{ km s}^{-1} \text{ Mpc}^{-1}$ respectively [53].

EDE models face the fine-tuning issues [1013] and suffer from a coincidence problem [1012]. Refs. [1013, 1035] proposed a natural explanation for this coincidence using the idea of neutrino-assisted early dark energy.

EDE modifies growth and $H(z)$ at early times (around recombination) and higher matter density is required to compensate for this effect in the CMB. Higher matter density contradicts the required low value of matter density at late times from weak lensing and growth data as shown in Fig. 2.18. In particular the analysis by Refs. [1036, 1037] has shown that an EDE model can not practically resolve the Hubble tension because it results in higher value of the late-time density fluctuation amplitude σ_8 and thus the tension with LSS dynamical probes WL, RSD and CC data can get worse. In addition Ref. [331] argued that any model which attempts to reconcile the CMB inferred value of H_0 by solely reducing the sound horizon results into tension with either the BAO or the galaxy weak lensing data. Thus, a compelling and full resolution of the Hubble tension may require multiple modifications (more than just the size of the sound horizon) of the Λ CDM cosmology.

Recent studies by Refs. [332, 333] reexamining the above issue and using combined data method show that the EDE scenario remains a potential candidate solution to the Hubble tension. Future observations will provide data with improved quality and thus will enable more detailed tests of the EDE model.

Many alternative models have been proposed to implement the basic EDE scenario such as Chain EDE [1038], Axion EDE [1039, 1040], Anti-de Sitter EDE [1040–1045], assisted quintessence EDE [1046], EDE with extra radiation [1047], EDE in the framework of the ultralight scalar decay to massless fields [1048] and New EDE (NEDE) [1049–1053] which can potentially address the Hubble tension. In NEDE a vacuum first-order phase transition of the NEDE scalar field is assumed to have taken place before recombination in the early Universe. The NEDE sudden transition can be described by a scalar field

whose potential at some critical point develops two non-degenerate minima (true and false vacuum)²⁸. Ref. [1054] develop a phenomenological dark sector with decaying dark energy and ultra-light axions which addresses the Hubble tension similarly to the EDE and NEDE scenarios and simultaneously can resolve the S_8 tension. Refs. [1055–1057] argue that a EDE model may require a more complicated dynamics in order to soften both the H_0 and S_8 tensions. In particular, Ref. [1057] introduced the Early Dark Sector (EDS) model considering an EDE-dependence of the mass of dark matter. The considering form of the potential is given by Eq. (2.80) (with $n = 3$) and the form of the field-dependent mass given by

$$m(\phi) = m_0 \exp\left(\frac{c\phi}{M_{pl}}\right), \quad (2.85)$$

as motivated by the the Swampland Distance Conjecture (SDC) [1058] and its extension to axions [1059–1062].

Dark radiation

Modifications in the light relic sector can relieve the tension by changing the early-time dynamics of the Universe [1063, 1064]. The dark radiation model assumes an increased number of light relics [655, 954, 1065–1078] which are weakly interacting components of radiation (i.e. relativistic species). For example the addition of hidden photons, sterile neutrinos [1079–1082], Goldstone bosons, Majoron [1083], axions [1084–1086] which are predicted in many extensions of the Standard Model (SM) increases the value in the effective number of relativistic particles N_{eff} beyond its canonical expectation value $N_{\text{eff}}^{\text{SM}} \simeq 3.044$ [1087–1092]. These extra particles modify the time of matter-radiation equality and would lead to a lower r_s sound horizon. As a consequence a lower expansion rate of the Universe and a higher value of H_0 emerges from early-time physics [959] (see Eq. (2.19)).

Another interesting approach was presented by Refs. [860, 1064, 1093–1105], in which dark matter (DM) interacts with a new form of dark radiation (DR) aimed at solving H_0 tension. Assuming the Effective Theory of Structure Formation (ETHOS) paradigm [1106, 1107] the interaction between the dark matter and dark radiation components is a 2-to-2 scattering $\text{DM} + \text{DR} \leftrightarrow \text{DM} + \text{DR}$.

Neutrino self-interactions

The strong (massive) neutrino self-interactions cosmological model can provide a larger value of H_0 and smaller σ_8 , hence can resolve the tensions between cosmological datasets [960]. The strong neutrino self-interactions were proposed in Ref. [1108] and further studied in Refs. [1063, 1109]. The introduction of strong self-interacting neutrinos increases the value in the effective number of relativistic particles $N_{\text{eff}} = 4.02 \pm 0.29$ without extra neutrino species. This model modifies the standard neutrino free-streaming in the early Universe. The onset of neutrino free-streaming is delayed until close to the matter radiation equality epoch. This late-decoupling of the neutrinos shifts the CMB power spectra peaks towards smaller scales as compared to Λ CDM model. This shift modifies the scale of sound horizon r_s that can resolve the Hubble constant H_0 tension [960].

Furthermore self-interactions between the neutrinos or between other additional light relics was studied by Refs. [1110–1126]. The strong neutrino self-interactions models are basically excluded by various existing data or experimental tests [1116, 1120, 1127–1129]. The analysis by Ref. [1122] leads to conclusion that these models can not ease the Hubble tension more effectively than the Λ CDM+ N_{eff} approach alone.

Models with nonstandard neutrinos - dark matter interactions were studied by Refs. [1130–1140]. These models increase the value in the effective number of relativistic particle N_{eff} and thus can provide a solution to the Hubble problem. However, in this class of models it is not possible to solve simultaneously the Hubble and growth tensions [1138].

²⁸It has recently been pointed out [8, 9, 52, 477, 593, 944, 952] that a similar mechanism in the context of the ultra late transition taking place at a redshift $z \lesssim 0.01$ can lead to a resolution of the Hubble tension.

Large primordial non-Gaussianities

The presence of large primordial non-Gaussianity in the CMB can affect the higher-order n -point correlation functions statistics. A non-vanishing primordial trispectrum ($n = 4$) which is the Fourier transform of the connected four-point correlation function leads to the non-Gaussian covariance of the angular power spectrum estimators [1141–1143]. The trispectrum is nonzero when there is a strong coupling between long-wavelength (super-CMB) modes and short-wavelength modes. The non-Gaussian covariance scenario (Super- Λ CDM model) has two extra free parameters relative to those in Λ CDM and provides a larger value of H_0 reducing tension with late Universe measurements of the Hubble constant [961].

Heisenberg’s uncertainty principle

The Heisenberg’s uncertainty principle [1144, 1145] and the generalized uncertainty Principle [1146–1170] (see Ref. [1171], for a review) can provide constraints to the values for certain pairs of physical quantities of a particle and raise the possibility of the existence of observational signatures in cosmological data e.g. [3, 55]. Ref. [962] has argued that the Heisenberg’s uncertainty principle can provide an explanation for the Hubble constant H_0 tension. In particular the authors equate the luminosity distance (expanded for low z as in Eqs. (2.3) and (2.7)) with the photon (assumed massive) Compton wavelength

$$\lambda_C = \frac{\hbar}{m c} , \quad (2.86)$$

and express the corresponding effective “rest mass” of the photon as a function of the cosmological redshift

$$m = \frac{\hbar H_0}{z c^2 \left[1 + \frac{z}{2}(1 - q_0)\right]} , \quad (2.87)$$

Thus, choosing $z = 1$, fixing $q_0 = -1/2$ and setting $H_0 = 74 \text{ km s}^{-1} \text{ Mpc}^{-1}$ and $H_0 = 67 \text{ km s}^{-1} \text{ Mpc}^{-1}$ in Eq. (2.87) find $m = 1.61 \times 10^{-69} \text{ kg}$ and $m = 1.46 \times 10^{-69} \text{ kg}$ respectively²⁹. Thus using these results infer that the tension on the H_0 measurements can be the effect of the uncertainty on the photon mass i.e.

$$\frac{\Delta m}{m} = \frac{\Delta H_0}{H_0} \simeq 0.1 . \quad (2.88)$$

Note that the non-zero photon mass could emerge through the Heisenberg’s uncertainty principle and through the recent analysis of the Standard-Model Extension³⁰ [1175, 1176].

Early modified gravity

A ST modified gravity model can be described by the following action

$$S = \int d^4x \sqrt{-g} \left[\frac{F(\sigma)}{2} R - \frac{g^{\mu\nu}}{2} \partial_\mu \sigma \partial_\nu \sigma - \Lambda - V(\sigma) \right] + S_m , \quad (2.89)$$

where R is the Ricci scalar, Λ is the cosmological constant, S_m is the action for matter fields, σ is a scalar field non-minimally coupled to the Ricci scalar, $F(\sigma)$ is the coupling to the Ricci scalar and $V(\sigma)$ is the potential for the scalar field. A variety of possible types of the non-minimal coupling of the scalar field to the Ricci $F(\sigma)$ and of the potential for the scalar field which can alleviate the H_0 tension by reducing the sound horizon scale through modified early cosmic expansion, has been considered in the literature [1177–1181].

In particular Ref. [963] introduces a model of early modified gravity³¹. This model has a non-minimal coupling of the form [963]

$$F(\sigma) = M_{pl}^2 + \xi \sigma^2 , \quad (2.90)$$

²⁹The current upper limit on the photon mass is $m = 10^{-54} \text{ kg}$ [1172].

³⁰For studies of the massive photons in the Standard-Model Extension, see Refs. [1173, 1174].

³¹It should not be confused with the previously introduced differed model with the same name ‘Early Modified Gravity’ [1182–1184]. In this model gravity is allowed to be modified after BBN, before and during recombination.

and a quartic potential

$$V(\sigma) = \frac{\lambda\sigma^4}{4}, \quad (2.91)$$

where λ and ξ are dimensionless parameters. For $\xi = 0$ this model reduces to the EDE model of Ref. [183]. In the early modified gravity model, gravity changes with redshift in such a way that the H_0 estimate from CMB can have larger values. Ref. [963] has shown that this model can resolve the Hubble tension and at the same time, in contrast to an EDE model, results in lower value of the late-time density fluctuation amplitude σ_8 and thus the tension with LSS dynamical probes WL, RSD and CC data can be at least partially resolved. In general early modified gravity model compared to the EDE can provide a better fit to LSS data and can imply better predictions on LSS observables.

Chapter 3

Challenges for Λ CDM: Other Tensions

In this Chapter we provide a list of the non-standard signals in cosmological data and the tensions of the Λ CDM cosmology beyond the Hubble tension which is currently the most widely studied and among the most statistically significant tensions. In many cases the signals are controversial and there is currently debate in the literature on the possible physical or systematic origin of these signals. For completeness we refer to all signals we could identify in the literature referring also to references that dispute the physical origin of these signals.

3.1 Growth tension

The Planck/ Λ CDM parameter values in the context of GR indicate stronger growth of cosmological perturbations than the one implied by observational data of dynamical probes. In this section we review the observational evidence for this tension also known as the $\Omega_{0m} - \sigma_8$ tension or simply ‘growth tension’.

3.1.1 Methods and data

The value of the growth parameter combination $S_8 \equiv \sigma_8(\Omega_{0m}/0.3)^{0.5}$ (where σ_8 is discussed in more detail in what follows) is found by weak lensing (WL) [144, 145, 1185–1189], cluster counts (CC) [1190–1195] and redshift space distortion (RSD) data [4, 67, 146–148, 278, 1196–1198] to be lower compared to the Planck CMB (TT,TE,EE+lowE) value $S_8 = 0.834 \pm 0.016$ [14] at a level of about $2 - 3\sigma$ as shown¹ in Table 3.1 and in Fig. 3.1 (see Refs. [10, 141], for a recent review of this tension). The tension is also confirmed by the latest ACT+WMAP CMB analysis [554] which finds $S_8 = 0.840 \pm 0.030$.

This is also expressed by the fact that dynamical cosmological probes (WL, RSD, CC) favor lower value of the matter density parameter $\Omega_{0m} \approx 0.26 \pm 0.04$ [344] than geometric probes (CMB, BAO, SnIa). This could be a signal of weaker gravity than the predictions of General Relativity in the context of a Λ CDM background [4, 67, 147, 148, 1199] (for a recent study on a weak gravity in the context of a Λ CDM background, see Ref. [6]).

The observational evidence for weaker growth indicated by the dynamical probes of the cosmic expansion and the gravitational law on cosmological scales may be reviewed as follows:

¹The definition $S_8 = \sigma_8(\Omega_{0m}/0.3)^\alpha$ with $\alpha = 1/2$ has been uniformly used for all points. In those cases where $\alpha \neq 1/2$ has been used in some references, the value of S_8 with $\alpha = 1/2$ was recalculated (along with the uncertainties) using the constraints on σ_8 and Ω_{0m} shown in those references, assuming their errors σ_{σ_8} and $\sigma_{\Omega_{0m}}$ are Gaussian. The errors of the S_8 constraints are propagated according to $\sigma_{S_8}^2 = (\Omega_{0m}/0.3)^{2\alpha}\sigma_{\sigma_8}^2 + \sigma_8^2\alpha^2(\Omega_{0m}/0.3)^{2\alpha-2}\sigma_{\Omega_{0m}}^2$, with $\alpha = 1/2$.

Table 3.1: The value of the structure growth parameter combination $S_8 \equiv \sigma_8(\Omega_{0m}/0.3)^{0.5}$, the matter density parameter Ω_{0m} and the the power spectrum amplitude σ_8 at 68% CL through direct and indirect measurements by different methods.

Dataset	S_8	Ω_{0m}	σ_8	Refs.
CMB Planck TT,TE,EE+lowE	0.834 ± 0.016	0.3166 ± 0.0084	0.812 ± 0.007	[14]
CMB Planck TT,TE,EE+lowE+lens.	0.832 ± 0.013	0.3153 ± 0.0073	0.811 ± 0.006	[14]
CMB ACT+WMAP	0.832 ± 0.013	0.3153 ± 0.0073	0.840 ± 0.030	[554]
WL KiDS-1000	$0.759^{+0.024}_{-0.021}$	-	-	[1200]
WL KiDS + VIKING + DES-Y1	$0.755^{+0.019}_{-0.021}$	-	-	[1186]
WL KiDS + VIKING + DES-Y1	$0.762^{+0.025}_{-0.024}$	-	-	[1201]
WL KiDS+VIKING-450	$0.716^{+0.043}_{-0.038}$	-	-	[1202]
WL KiDS+VIKING-450	$0.737^{+0.040}_{-0.036}$	-	-	[1203]
WL KiDS-450	0.651 ± 0.058	-	-	[1187]
WL KiDS-450	0.745 ± 0.039	-	-	[1188]
WL DES-Y3	$0.759^{+0.025}_{-0.023}$	$0.290^{+0.039}_{-0.063}$	$0.783^{+0.073}_{-0.092}$	[1204, 1205]
WL DES-Y1	$0.782^{+0.027}_{-0.027}$	-	-	[550]
WL HSC-TPCF	$0.804^{+0.032}_{-0.029}$	$0.346^{+0.052}_{-0.100}$	$0.766^{+0.110}_{-0.098}$	[1206]
WL KiDS-1000 pseudo- C_l	$0.754^{+0.027}_{-0.029}$	-	-	[1207]
WL HSC-pseudo- C_l	$0.780^{+0.030}_{-0.033}$	-	-	[1208]
WL CFHTLenS	$0.740^{+0.033}_{-0.038}$	-	-	[1209]
WL+CMB lens. DES-Y3+SPT+Planck	$0.73^{+0.04}_{-0.03}$	$0.25^{+0.03}_{-0.04}$	$0.82^{+0.08}_{-0.07}$	[1210]
WL+GC ²	$0.795^{+0.049}_{-0.042}$	$0.383^{+0.028}_{-0.053}$	$0.718^{+0.044}_{-0.031}$	[1211]
WL+GC+CMB lensing ³	0.7781 ± 0.0094	$0.305^{+0.021}_{-0.025}$	0.774 ± 0.033	[1212]
WL+GC KiDS-1000 3×2 pt	$0.766^{+0.020}_{-0.014}$	$0.305^{+0.010}_{-0.015}$	$0.76^{+0.025}_{-0.020}$	[1213]
WL+GC KiDS-450 3×2 pt	0.742 ± 0.035	$0.243^{+0.026}_{-0.045}$	$0.832^{+0.080}_{-0.079}$	[144]
WL+GC KiDS+GAMA 3×2 pt	$0.800^{+0.029}_{-0.027}$	$0.33^{+0.05}_{-0.06}$	$0.78^{+0.06}_{-0.08}$	[1214]
WL+GC DES-Y3 3×2 pt	$0.776^{+0.017}_{-0.017}$	$0.339^{+0.032}_{-0.031}$	$0.733^{+0.039}_{-0.049}$	[1215]
WL+GC DES-Y1 3×2 pt	$0.773^{+0.026}_{-0.020}$	$0.267^{+0.030}_{-0.017}$	$0.817^{+0.045}_{-0.056}$	[145]
WL+GC KiDS+VIKING-450+BOSS	0.728 ± 0.026	$0.323^{+0.014}_{-0.017}$	0.702 ± 0.029	[1216]
GC BOSS DR12 bispectrum	0.751 ± 0.039	$0.32^{+0.01}_{-0.01}$	$0.722^{+0.032}_{-0.036}$	[375]
GC BOSS+eBOSS	0.72 ± 0.042	-	-	[1217]
GC BOSS galaxy power spectrum	0.703 ± 0.045	0.293 ± 0.012	0.713 ± 0.045	[376]
GC BOSS power spectra	0.736 ± 0.051	0.303 ± 0.0082	0.733 ± 0.047	[374]
GC BOSS DR12	0.729 ± 0.048	$0.317^{+0.015}_{-0.019}$	0.710 ± 0.049	[1216]
GC+CMB lensing DESI+Plank	0.73 ± 0.03	-	-	[1218]
GC+CMB lensing unWISE+Plank	0.784 ± 0.015	0.307 ± 0.018	0.775 ± 0.029	[1219]
CC AMICO KiDS-DR3	0.78 ± 0.04	$0.24^{+0.03}_{-0.04}$	0.86 ± 0.07	[1220]
CC SDSS-DR8	$0.79^{+0.05}_{-0.04}$	$0.22^{+0.05}_{-0.04}$	$0.91^{+0.11}_{-0.10}$	[1194]
CC ROSAT (WtG)	0.77 ± 0.05	0.26 ± 0.03	0.83 ± 0.04	[1221]
CC DES-Y1	$0.65^{+0.04}_{-0.04}$	$0.179^{+0.031}_{-0.038}$	$0.85^{+0.04}_{-0.06}$	[1189]
CC XMM-XXL	0.83 ± 0.11	0.40 ± 0.09	0.72 ± 0.07	[1222]
CC SPT-tSZ	0.749 ± 0.055	0.276 ± 0.047	0.781 ± 0.037	[1223]
CC Planck tSZ	0.785 ± 0.038	0.32 ± 0.02	0.76 ± 0.03	[1224]
CC Planck tSZ	0.792 ± 0.056	0.31 ± 0.04	0.78 ± 0.04	[1193]
RSD+BAO+Pantheon+CC	$0.777^{+0.026}_{-0.027}$	0.288 ± 0.008	$0.793^{+0.018}_{-0.020}$	[1225]
RSD+BAO+Pantheon	$0.762^{+0.030}_{-0.025}$	0.286 ± 0.008	$0.7808^{+0.021}_{-0.019}$	[1225]
RSD	$0.739^{+0.036}_{-0.040}$	$0.254^{+0.038}_{-0.058}$	$0.804^{+0.048}_{-0.071}$	[1225]
RSD	$0.700^{+0.038}_{-0.037}$	$0.201^{+0.036}_{-0.033}$	$0.857^{+0.044}_{-0.042}$	[510]
RSD	0.747 ± 0.029	0.279 ± 0.028	0.775 ± 0.018	[67]

Weak lensing

The weak gravitational lensing from matter fluctuations along the line of sight slightly distorts the shapes (shear) and size (magnification) of distant galaxies (see Ref. [1226–1228], for a review). This distortion is a powerful and principal cosmological probe of the mass distribution which can be predicted theoretically [1229–1232]. Using various statistical methods shape distortions can be measured by analyzing the angular shear correlation function, or its Fourier transform, the shear power spectrum [1200, 1208]. A special type of WL is the galaxy-galaxy lensing (GGL) [1233, 1234] which is the slight distortion of shapes of source galaxies in the background of a lens galaxy arising from the gravitational deflection of light due to the gravitational potential of the lens galaxy along the line of sight.

The WL surveys, the Kilo Degree Survey (KiDS) [1235–1238], the Subaru Hyper Suprime-Cam lensing survey (HSC) [1239, 1240] and the Dark Energy Survey (DES) [1241, 1242] provide data useful for cosmic shear studies. In particular WL measurements of S_8 obtained from the shear catalogues by the lensing analysis of the Canada-France-Hawaii Telescope Lensing (CFHTLenS) [1209, 1243–1247] and the KiDS [1187, 1188] appear to be lower compared to the Planck value at a level of about 3σ . The analysis by Ref. [1188] adopting a spatially flat Λ CDM model and using the KiDS-450 data reports $S_8 = 0.745 \pm 0.039$ which results in 2.3σ tension with the value estimated by Planck15. This KiDS-Planck discordance has also been investigated in Ref. [1187] where applying the quadratic estimator to KiDS-450 shear data reports $S_8 = 0.651 \pm 0.058$ which is in tension with the Planck2015 results at the 3.2σ level. Using a combination of the measurements of KiDS-450 and VISTA Kilo-Degree infrared Galaxy Survey (VIKING) [1248], Ref. [1203] finds $S_8 = 0.737^{+0.040}_{-0.036}$ which is discrepant with measurements from the Planck analysis at the 2.3σ level. For the KiDS+VIKING-450 (or KV450) Ref. [1202] reports an updated constraint of $S_8 = 0.716^{+0.043}_{-0.038}$. Meanwhile, using the DES first year (DES-Y1) data assuming a Λ CDM model Ref. [550] reports $S_8 = 0.782^{+0.027}_{-0.027}$ which is in $\sim 2.3\sigma$ tension⁴ with the Planck18 result. The constraint on S_8 from the combined tomographic weak lensing analysis of KiDS + VIKING + DES-Y1 adopting a flat Λ CDM model by Ref. [1201] is $S_8 = 0.762^{+0.025}_{-0.024}$ which is in 2.5σ tension with Planck18 result and by Ref. [1186] is $S_8 = 0.755^{+0.019}_{-0.021}$ which is in 3.2σ tension with Planck18 result. Analysing the most recent KiDS cosmic shear data release (KiDS-1000 [1250]) alone and assuming a spatially flat Λ CDM model the value $S_8 = 0.759^{+0.024}_{-0.021}$ was estimated by Ref. [1200]. Analysing the first-year data of HSC in the context of the flat Λ CDM model and using the pseudo-spectrum (pseudo- C_l) method⁵, Ref. [1208] finds $S_8 = 0.780^{+0.030}_{-0.033}$ and adopting the standard two-point correlation functions (TPCF) estimators, ξ_{\pm} , Ref. [1206] finds $S_8 = 0.804^{+0.032}_{-0.029}$. Recently, a analysis of the KiDS-1000 data using pseudo- C_l method by Ref. [1207] has lead to $S_8 = 0.754^{+0.027}_{-0.029}$. The latest cosmic shear analysis of the DES third Year (DES-Y3) [1204, 1205] in the context of the Λ CDM model constrains the clustering amplitude as $S_8 = 0.759^{+0.025}_{-0.023}$. Also, recently Ref. [1210] found $S_8 = 0.73^{+0.04}_{-0.03}$ using the cross-correlations of galaxy positions and shears from DES-Y3 with CMB lensing maps from SPT and Planck.

The analysis of galaxy clustering and weak gravitational lensing of the DES-Y1 data combining three two-point functions (the so-called 3×2 pt analysis) of gravitational lensing and galaxy positions (the cosmic shear correlation function, the galaxy clustering angular autocorrelation function, the galaxy-galaxy lensing cross-correlation function) by Ref. [145] gives $S_8 = 0.773^{+0.026}_{-0.020}$ and $\Omega_{0m} = 0.267^{+0.030}_{-0.017}$ in flat Λ CDM model. This value is in $\sim 2.3\sigma$ tension with Planck18 result. In the latest analysis by Ref. [1215] the constraints $S_8 = 0.776^{+0.017}_{-0.017}$ and $\Omega_{0m} = 0.339^{+0.032}_{-0.031}$ in flat Λ CDM model are obtained using an improvement in signal-to-noise of the DES-Y3 3×2 pt data relative to DES-Y1 by a factor of 2.1. Also, Ref. [1213] using 3×2 pt analysis of KiDS-1000+BOSS+ 2-degree Field Lensing Survey⁶ (2dFLenS) [1255] data finds $S_8 = 0.766^{+0.020}_{-0.014}$. While previous analyses 3×2 pt of KiDS+GAMA data and KiDS-450+BOSS+2dFLenS data by Ref. [1214] and Ref. [144] obtained $S_8 = 0.800^{+0.029}_{-0.027}$ and

⁴This tension was calculated by Ref. [1249]. The authors have explored a number of different methods to quantify the tension relative to the best-fit Planck2018 cosmology.

⁵For a realistic experiment the pseudo- C_l statistics from cut-sky maps which provide incomplete data are applied in order to obtain unbiased estimates of the angular power and cross-power spectra by correcting for the convolution with the survey window (see Refs. [1251–1254], for details of this method).

⁶<https://2dflens.swin.edu.au>

$S_8 = 0.742 \pm 0.035$ respectively. A combined analysis of KiDS+VIKING-450+BOSS data by Ref. [1216] resulted in $S_8 = 0.728 \pm 0.026$. Performing a Joint analysis of galaxy-galaxy weak lensing and galaxy clustering from first-year data of HSC and SDSS-III/BOSS DR11 Ref. [1211] found $S_8 = 0.795^{+0.049}_{-0.042}$. Also, from a combined analysis of KiDS-1000 and DES-Y1 cosmic shear and galaxy clustering, eBOSS quasars, DESI, Planck CMB lensing data Ref. [1212] obtains a constraint $S_8 = 0.7781 \pm 0.0094$.

Clearly, the tension between WL and CMB measurements is a level more than 2σ as seen in Table 3.1 and in Fig. 3.1. In addition, the tension with more recent measurements persists at the level of $\sim 2\sigma$. Finally, combined analyses of WL with galaxy clustering does not change the tension level.

Cluster counts

Galaxy clusters which are related to peaks in the matter density field on large scales constitute a probe of the growth history of structures [1256, 1257] (see Refs. [1258, 1259], for a review). Current analyses from the number counts of galaxy clusters use catalogs from surveys at different wavelengths of the electromagnetic spectrum. Such surveys include Planck⁷, South Pole Telescope (SPT) and Atacama Cosmology Telescope (ACT) in the microwave (millimeter) via the thermal Sunyaev-Zel’dovich (tSZ) effect⁸ [1263–1265], extended Roentgen survey with an imaging telescope array (eROSITA⁹) [1266–1269] in the X-ray that finds extended sources and measures the X-ray luminosity and temperature, Sloan Digital Sky Survey¹⁰ (SDSS) and Dark Energy Survey¹¹ (DES) in the optical/NIR. These surveys find peaks in the galaxy distribution and measure the richness of the corresponding clusters. The microwave/tSZ and X-ray surveys detection techniques are based on the hot ICM [1270, 1271] and in some cases require auxiliary data to obtain useful constraints e.g. redshift estimates (see Refs. [1272, 1273], for recent methods).

The CC method is based on the predicted halo abundance (number density) $n(M, z)$ of halos with mass less than M at redshift z which is also known as the halo mass function (HMF). This formalism was originally introduced by Press and Schechter [1274]. A general mathematical form for the comoving number density expression of haloes is e.g. [1275–1279]

$$\frac{dn}{dM} = f(\sigma) \frac{\bar{\rho}_m}{M} \frac{d \ln \sigma^{-1}}{dM}, \quad (3.1)$$

where $\bar{\rho}_m = \rho_{crit} \Omega_m$ is the mean matter density of the Universe, σ is the rms variance of the linear density field smoothed on a spherical volume containing a mass M , and $f(\sigma)$ is a model-dependent ‘universal’ halo multiplicity function¹². There are numerous parametrizations of the multiplicity function $f(\sigma)$ based on numerical N-body simulations or theoretical models. A popular parametrization provided by Ref. [1279] is

$$f(\sigma) = A \left[\left(\frac{\sigma}{b} \right)^{-\chi} + 1 \right] e^{-c/\sigma^2}, \quad (3.2)$$

where A, χ, b, c are four free parameters that depend on the halo definition and need to be calibrated.

Measurements of the abundance of galaxy clusters $n(M, z)$ provide consistent constraints on the density of matter Ω_{0m} , the root mean square density fluctuation σ_8 , the parameter combination $S_8(\alpha) = \sigma_8(\Omega_{0m}/0.3)^\alpha$ e.g. [1200, 1208, 1280] (where $\alpha \sim 0.2 - 0.6$ and $S_8 \equiv S_8(\alpha = 0.5)$), the dark energy equation-of-state w and the sum of the neutrino masses $\sum m_\nu$ (massive neutrinos can suppress the matter power spectrum on small scales and this directly affect the growth of cosmic structure) [186]. More recently, Ref. [1281, 1282] used a method of clustering measurements at higher redshift ($z = 4 - 10$)

⁷<https://www.cosmos.esa.int>

⁸The inverse Compton scattering between CMB photons and hot electrons in the intracluster medium (ICM) (see Refs. [1260–1262], for a review).

⁹<https://www.mpe.mpg.de/eROSITA>

¹⁰<https://www.sdss.org/>

¹¹<https://www.darkenergysurvey.org>

¹²For a publicly available cluster toolkit Python package, see in <https://cluster-toolkit.readthedocs.io/en/latest/source/massfunction.html>.

based on UV galaxy luminosity function data from the Hubble Space Telescope e.g. [1283, 1284]. They derive the large-scale matter clustering amplitude to be $\sigma_8 = 0.76_{-0.14}^{+0.12}$.

Using cluster abundance analysis in the SDSS DR8 for a flat Λ CDM cosmological model with massive neutrinos Ref. [1194] finds $S_8 = 0.79_{-0.04}^{+0.05}$. Ref. [1221] using Weighting the Giant (WtG) [1285, 1286] lensing analysis of the X-ray ROentgen SATellite (ROSAT) cluster catalogs [1287] finds $S_8 = 0.77 \pm 0.05$. The analysis of the counts and weak lensing signal of of the DES-Y1 dataset by Ref. [1189] gives $S_8 = 0.65 \pm 0.04$ and $\Omega_{0m} = 0.267_{-0.017}^{+0.030}$ in flat Λ CDM. Also, assuming a flat Λ CDM model and performing a galaxy cluster abundance analysis in the AMICO KiDS-DR3 catalogue Ref. [1220] obtains $S_8 = 0.78 \pm 0.04$.

Using galaxy clusters observed in millimeter wavelengths through the tSZ effect Ref. [1224] reports $S_8 = 0.785 \pm 0.038$ assuming Λ CDM model. The analysis of the Planck 2015 cluster counts via the tSZ signal by Ref. [1193] finds $S_8 = 0.792 \pm 0.056$. Recently, assuming a flat Λ CDM model, in which the total neutrino mass is a free parameter, the analysis of SPT tSZ cluster counts by Ref. [1223] results in $S_8 = 0.749 \pm 0.055$. Using X-ray clusters detected from the XMM-XXL survey [1288] for a flat Λ CDM cosmological model Ref. [1222] reports $S_8 = 0.83 \pm 0.10$. Also, constraints on structure growth parameter combination S_8 from cluster abundance data have been obtained by Ref. [1289–1294]. For example using GalWCat19 [1295], a catalog of 1800 galaxy clusters was derived from the SDSS-DR13 [1296] and assuming a flat Λ CDM cosmology Ref. [1290] measured the matter density and the amplitude of fluctuations to be $\Omega_m = 0.310_{-0.027}^{+0.023} \pm 0.041$ (systematic) and $\sigma_8 = 0.810_{-0.036}^{+0.031} \pm 0.035$ (systematic) respectively.

The results of S_8 from all cluster count experiments as seen in Table 3.1 and in Fig. 3.1 are in agreement with WL measurements and similarly prefer a lower value compared to the CMB measurements.

Redshift space distortion-Galaxy clustering

Peculiar motions of galaxies falling towards overdense region generate large scale galaxy clustering, anisotropic in redshift space. Measuring this illusory anisotropy that distorts the distribution of galaxies in redshift space (i.e. RSD) we can quantify the galaxy velocity field. This important probe of LSS can be used to constrain the growth rate of cosmic structures [1297–1299].

In particular the RSD is sensitive to the cosmological growth rate of matter density perturbations f which depends on the theory of gravity and is defined as [1300–1302]

$$f(a) \equiv \frac{d \ln \delta(a)}{d \ln a} \simeq [\Omega_m(a)]^{\gamma(a)}, \quad (3.3)$$

where $a = \frac{1}{1+z}$ is the scale factor, $\delta \equiv \frac{\delta \rho}{\rho}$ is the matter overdensity field (with ρ the matter density of the background and $\delta \rho$ its first order perturbation) and γ is the growth index e.g. [1303]. The nearly constant and scale-independent value $\gamma \simeq \frac{6}{11} \simeq 0.545$ corresponds to General Relativity (GR) prediction in the context of Λ CDM e.g. [1301].

The observable combination $f\sigma_8(a) \equiv f(a) \cdot \sigma(a)$ is measured at various redshifts by different surveys as a probe of the growth of matter density perturbations. On subhorizon scales (i.e. $k^2 \gg a^2 H^2$) the theoretically predicted value of this product can be obtained from the solution $\delta(a)$ of the equation [112, 1304–1308]

$$\delta''(a) + \left(\frac{3}{a} + \frac{H'(a)}{H(a)} \right) \delta'(a) - \frac{3}{2} \frac{\Omega_{0m} G_{\text{eff}}(a)/G}{a^5 H(a)^2 / H_0^2} \delta(a) = 0, \quad (3.4)$$

using the definition

$$\sigma(a) \equiv \sigma_8 \frac{\delta(a)}{\delta(a=1)}, \quad (3.5)$$

where G is Newton's constant as measured by local experiments, G_{eff} is the effective gravitational coupling which is related to the growth of matter perturbation, $\sigma(a)$ is the redshift dependent rms fluctuations of the linear density field within spheres of radius $R = 8h^{-1} \text{Mpc}$ and σ_8 is its value today.

Hence, the more robust bias free quantity $f\sigma_8$ is given by [1309]

$$f\sigma_8(a) = \frac{\sigma_8}{\delta(a=1)} a \delta'(a), \quad (3.6)$$

RSD growth data in the form of $f\sigma_8$ ¹³ have been provided by wide variety of surveys including the 2-degree Field Galaxy Redshift Survey (2dFGRS) [1312, 1313], VIMOS-VLT Deep Survey (VVDS) [1314], SDSS [340, 1315–1319], WiggleZ [1320], 6dFGS [355, 1321], Galaxy and Mass Assembly (GAMA) [1322], BOSS [48, 1323–1325], Subaru Fiber Multi-Object Spectrograph (FMOS) galaxy redshift survey (FastSound) [1326], VIMOS Public Extra-galactic Redshift Survey (VIPERS) [1327–1329], eBOSS [344, 1330–1335], DESI [451, 452]. Using such data the Ω_{0m} and σ_8 parameters in the context of a Λ CDM background can be constrained. Thus, Ref. [67] using a compilation of 63 RSD datapoints finds the Λ CDM best fit value $\Omega_{0m} = 0.279 \pm 0.028$ and $\sigma_8 = 0.775 \pm 0.018$. Ref. [510] using RSD selected data and assuming Λ CDM model reports $S_8 = 0.700^{+0.038}_{-0.037}$, $\Omega_{0m} = 0.201^{+0.036}_{-0.033}$ and $\sigma_8 = 0.857^{+0.044}_{-0.042}$ which are in 3σ tension with the Planck 2018 results. Recently, using RSD data and the RSD+BAO+Pantheon and RSD+BAO+Pantheon+CC dataset combinations Ref. [1225] finds $S_8 = 0.739^{+0.036}_{-0.040}$, $S_8 = 0.762^{+0.030}_{-0.025}$ and $S_8 = 0.777^{+0.026}_{-0.027}$ respectively.

Galaxy clustering methods, such as the galaxy power spectrum and bispectrum have also been used to constrain S_8 . Constraints from the BOSS galaxy power spectrum [376] gave $S_8 = 0.703 \pm 0.045$ and from BOSS DR12 bispectrum [375] gave $S_8 = 0.751 \pm 0.039$. Previous analysis of the BOSS DR12 data by Ref. [1216] gave $S_8 = 0.729 \pm 0.048$. A analysis of the power spectrum of eBOSS by Ref. [1217] resulted in $S_8 = 0.720 \pm 0.042$. Recently, using the BOSS power spectra Ref. [374] found $S_8 = 0.736 \pm 0.051$. Also, the combination of the auto- and cross-correlation signal of unWISE¹⁴ galaxies [1337] and Planck CMB lensing maps [1338] by Ref. [1219] gave $S_8 = 0.784 \pm 0.015$. Finally, using the luminous red galaxies of the DESI in combination with Planck CMB lensing maps Ref. [1218] found $S_8 = 0.73 \pm 0.03$.

Clearly, as seen in Table 3.1 and in Fig. 3.1 the analyses of RSD data gives S_8 values in tension with CMB measurements at level more than 2σ , in agreement with other dynamical cosmological probes (WL and CC).

3.1.2 Theoretical models

Non-gravitational mechanisms can address the S_8 tension (see Ref. [1339], for a review). Such mechanisms include the following:

- Dynamical dark energy models [366, 632, 633, 1340–1361] and running vacuum models [685–688, 690, 1362–1364], which modify the cosmological background $H(z)$ to a form different from Λ CDM (see Subsection 2.3.1). This modification may involve the presence of dynamical dark energy dominant at late cosmological times or at times before recombination.
- Interacting dark energy models, which modify the equation for the evolution of linear matter fluctuations as well as the $H(z)$ cosmological background [837–840] as discussed in Subsection 2.3.2. This class of models can address the structure growth σ_8 tension between the values inferred from the CMB and the WL measurements.
- Effects of massive neutrinos [955, 1354, 1365–1370] which are relativistic at early times and contribute to radiation while at late times they become non-relativistic but with significant velocities (hot dark matter) (see Ref. [1371–1374], for a review). The change of radiation to hot dark matter affects the Hubble expansion. Simultaneously the residual streaming velocities are still large enough at late times to slow down the growth of structure [1375]. This effect of massive neutrinos slows down the growth as required by the RSD data and relieves the S_8 tension coming from WL data [1369].

¹³For an extensive compilation of RSD data points $f\sigma_8$, see in Ref. [4] and for other compilations, see in Refs. [1, 67, 148, 1196, 1310]. Also for a publicly available RSD likelihood for MontePython see in Refs. [1198, 1311].

¹⁴Wide-field Infrared Survey Explorer (WISE) [1336] is a NASA infrared astronomy space telescope and is mapping the whole sky.

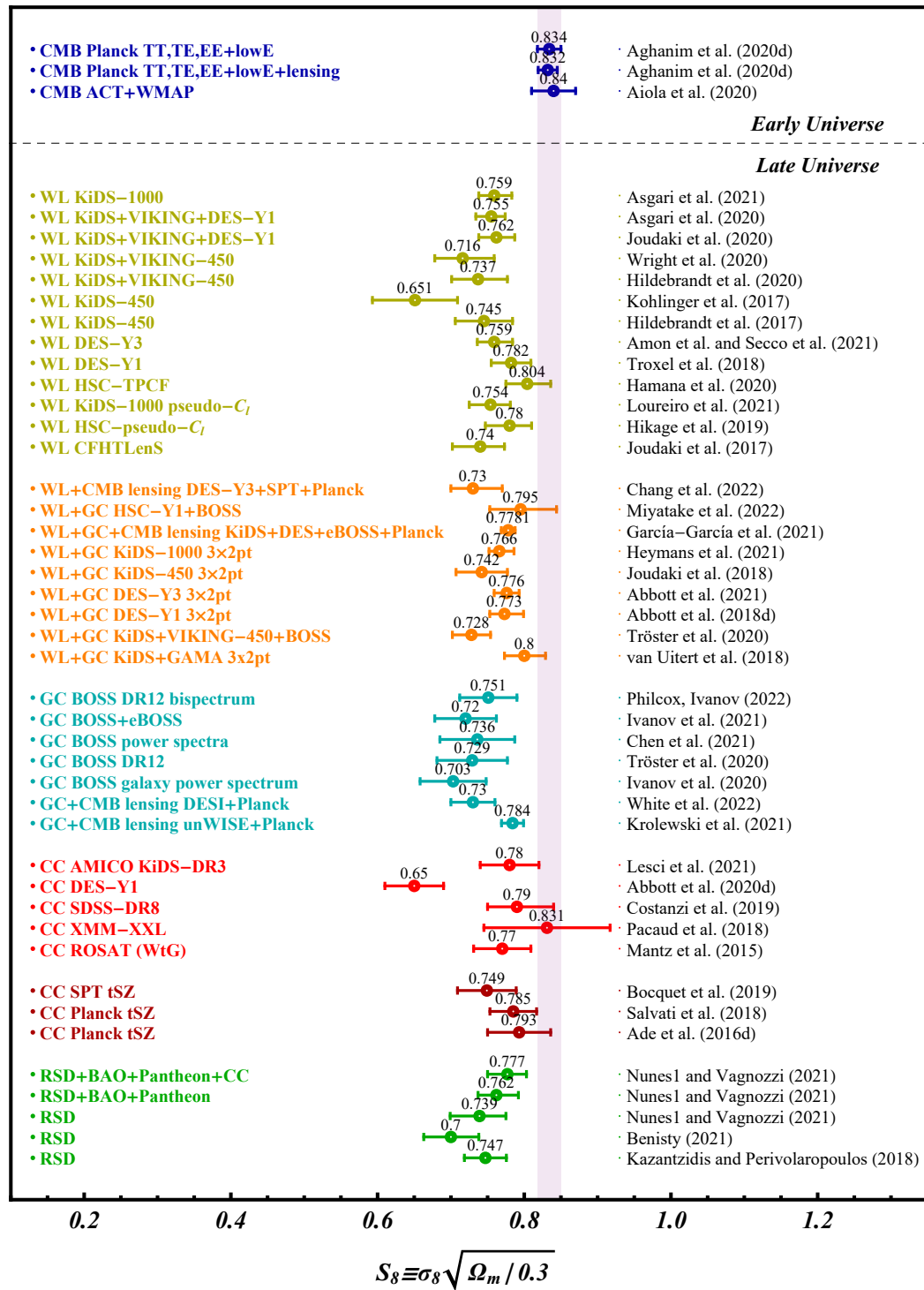


Figure 3.1: The value of S_8 with the 68% CL constraints derived by recent measurements.

- Primordial magnetic fields [984, 1376] (see Ref. [1377–1379], for a review) induce additional mildly non-linear, small-scale baryon inhomogeneities present in the plasma before recombination. The required field results in a reduction of the sound horizon scale at recombination and has the potential to resolve both the H_0 and S_8 tension [985, 986, 1380].
- Non-thermal dark radiation [1381] seems to help alleviate the S_8 tension to a great extent. However, the inclusion of BAO data reduces significantly the quality of fit of this model.

In addition to these non-gravitational mechanisms discussed above that can slow down growth at low redshifts a possible interesting new fundamental physics approach can also reduce the S_8 tension. Such an approach is most likely to affect three basic observable parameters: the Hubble parameter $H(z, w)$ (with w the dark energy equation of state parameter), as well as the effective Newton constants for growth of perturbations

$$\mu_G(z, k) \equiv \frac{G_{\text{eff}}(z, k)}{G}, \quad (3.7)$$

and lensing

$$\Sigma_G(z, k) \equiv \frac{G_L(z, k)}{G}, \quad (3.8)$$

where G is the locally measured value of the Newton's constant. According to Λ CDM $H(z) = H(z, w = -1)$, $\mu_G = 1$, $\Sigma_G = 1$.

The Bardeen potentials [1382] (the Newtonian potential Ψ and the spatial curvature potential Φ) appear in the scalar perturbed FLRW metric in the conformal Newtonian gauge [582, 1383, 1384]

$$ds^2 = -(1 + 2\Psi)dt^2 + a^2(1 - 2\Phi)d\vec{x}^2, \quad (3.9)$$

The LSS probes are sensitive to the Bardeen potentials Ψ and Φ . In particular the WL probe is sensitive to $\nabla^2(\Psi + \Phi)$. The galaxy clustering arises from the gravitational attraction of matter and is sensitive only to the potential Ψ . The RSD probe is sensitive to the rate of growth of matter density perturbations f (see Eq. (3.3)) and provides measurements of $f\sigma_8$ (see Eq. (3.6)) that depends on the potential Ψ .

At linear level, in modified gravity models, using the perturbed metric Eq. (3.9) and the gravitational field equations the following phenomenological equations in Fourier space emerge for the scalar perturbation potentials defining the functions $\mu_G(a, k)$ and $\Sigma_G(a, k)$ on subhorizon scales (i.e. $k^2 \gg a^2 H^2$)

$$k^2(\Psi + \Phi) = -8\pi G \Sigma_G(a, k) a^2 \rho \Delta, \quad (3.10)$$

$$k^2 \Psi = -4\pi G \mu_G(a, k) a^2 \rho \Delta, \quad (3.11)$$

where ρ is the matter density of the background, Δ the comoving matter density contrast defined as $\Delta \equiv \delta + 3Ha(1+w)v/k$ which is gauge-invariant [330], $w = p/\rho$ is the equation-of-state parameter and $v^i = -\nabla^i u$ is the irrotational component of the peculiar velocity u [587].

Using the gravitational slip parameter η (or anisotropic stress parameter) which describes the possible inequality [931, 1385] of the two Bardeen potentials that may occur in modified gravity theories

$$\eta(a, k) = \frac{\Phi(a, k)}{\Psi(a, k)}, \quad (3.12)$$

the two LSS parameters μ_G and Σ_G are related via

$$\Sigma_G(a, k) = \frac{1}{2} \mu_G(a, k) [1 + \eta(a, k)]. \quad (3.13)$$

The the Hubble parameter $H(z)$ is usually parametrized as wCDM

$$H(z) = H_0 \left[\Omega_{0m}(1+z)^3 + (1 - \Omega_{0m})(1+z)^{3(1+w)} \right]^{1/2}, \quad (3.14)$$

while the two LSS parameters μ_G and Σ_G do not have a commonly accepted parametrization. A model and scale independent parametrization for μ_G and Σ_G which reduce to the GR value at early times and at the present time as indicated by solar system (ignoring possible screening effects) and BBN constraints ($\mu_G = 1$ and $\mu'_G = 0$ for $a = 1$ and $\mu_G = 1$ for $a \ll 1$) [1386–1388] is of the form [4, 67, 148, 1389]

$$\mu_G = 1 + g_a(1-a)^n - g_a(1-a)^{2n} = 1 + g_a\left(\frac{z}{1+z}\right)^n - g_a\left(\frac{z}{1+z}\right)^{2n}, \quad (3.15)$$

$$\Sigma_G = 1 + g_b(1-a)^m - g_b(1-a)^{2m} = 1 + g_b\left(\frac{z}{1+z}\right)^m - g_b\left(\frac{z}{1+z}\right)^{2m}, \quad (3.16)$$

where g_a and g_b are parameters to be fit and n and m are integer parameters with $n \geq 2$ and $m \geq 2$. Alternatively, a rapid transition parametrization is of the form [52, 593]

$$\mu_G^>(z) = \mu_G^< + \Delta\mu_G \Theta(z - z_t), \quad (3.17)$$

$$\Sigma_G^>(z) = \Sigma_G^< + \Delta\Sigma_G \Theta(z - z_t), \quad (3.18)$$

where Θ is the Heaviside step function, z_t is a transition redshift, $\mu_G^>$ and $\Sigma_G^>$ correspond to $z > z_t$ and $\mu_G^<$ and $\Sigma_G^<$ correspond to $z < z_t$.

Various studies utilize modified gravity theories including Teleparallel theories of gravity¹⁵ [1402, 1403] (see Ref. [1404], for a review), Horndeski theories [1405, 1406] or theories beyond Horndeski [1407] to reduce the effective Newton's constant G_{eff} at low redshifts and slow down growth at low redshifts. The above parametrizations can be realized in the context of physical models based on the above theories.

3.2 CMB anisotropy anomalies

There is a wide range of other less discussed no-standard signals and statistical anomalies of the large angle fluctuations in the CMB [1408] with a typical 2 to 3 σ significance. As mentioned a main assumption of the Λ CDM model is that the fluctuations are Gaussian and statistically homogeneous and isotropic. Diverse anomalies have been noticed in the CMB at large angular scales by the space missions Cosmic Background Explorer (COBE) [1409], Wilkinson Microwave Anisotropy Probe (WMAP) [1410] and Planck satellite [1411], which appear to violate this assumption (see Refs. [149, 150], for a review). Ref. [1412] presents possible explanations of the observed CMB anomalies and Ref. [1413] explores the kinetic and the polarized Sunyaev-Zel'dovich effects as potential probes of physical models of these anomalies.

In what follows we discuss some of these signals. Note that some of these may not be independent¹⁶. Some of these signals have been attributed to the look-elsewhere effect. Based on this effect any large dataset will have a small number of peculiar features when there is a careful search for such features. However, this argument may not be applicable when the considered statistics are simple and generic as are most of the signals discussed below (see Refs. [1415–1417], for a detailed discussion).

3.2.1 Hints for a closed Universe (CMB vs BAO)

The Universe under the assumption of the cosmological principle is described by the Friedmann-Lemaître-Roberson-Walker (FLRW) metric

$$ds^2 = -dt^2 + a(t)^2 \left[\frac{dr^2}{1 - Kr^2} + r^2(d\theta^2 + \sin^2\theta d\phi^2) \right], \quad (3.19)$$

where K characterizes the constant spatial curvature of the spatial slices with $K = -1, 0, +1$ corresponding to open hyperbolic space (negative spatial curvature), flat Euclidean space (zero spatial curvature),

¹⁵Many authors have studied the extensions of the Teleparallel gravity such as the scalar-torsion theories of gravity [1390–1396] and the Teleparallel Horndeski theories [1397–1401].

¹⁶The covariance of CMB anomalies in the standard Λ CDM model has been studied by Ref. [1414]. This study focusing on the correlation of observed anomalies (i.e. the relationship or connection between all of them) examines the independence of large-angle CMB feature quantities.

and closed hyperspherical space (positive spatial curvature) respectively. The curvature density parameter is defined as $\Omega_K \equiv -K/(Ha)^2$ so that a closed Universe corresponds to $\Omega_K < 0$ and an open Universe to $\Omega_K > 0$. This parameter plays a crucial role in determining the evolution of the Universe, and is closely related with the early Universe physics.

The Planck18 temperature and polarization data [14] show a preference ($\sim 3.4\sigma$) for a closed Universe ($\Omega_K < 0$) in the context of Λ CDM. In particular using these data from Planck18 the curvature density parameter was constrained to be $-0.095 < \Omega_K < -0.007$ at 99% C.L [14, 1418]. This anomaly may be connected with other asymmetries of the CMB anisotropy spectrum discussed below. The preference for closed universe however disappears when the CMB data are combined with the BAO data. Refs. [1419–1421] pointed out that Planck+BAO can give a biased result because Planck and BAO are in disagreement at more than 3σ . Combining Planck18 data with recent BAO measurements the curvature density parameter was estimated to be $\Omega_K = 0.0008 \pm 0.0019$ [1419–1421] in agreement with a spatially flat Universe. Using the full-shape galaxy power spectrum measurements $P(k)$, Ref. [1422] has also confirmed that the Planck data are in tension with both the full-shape power spectrum and BAO with respect to Ω_K . The recent study by Ref. [1423] confirms the tension between Planck and BAO data in the context of cosmic curvature. Ref. [1423] used a new statistical analysis (the alternative Planck CamSpec likelihood TTTEEE instead of Plik as discussed in Ref. [1424]) to show that Planck favors a closed Universe at more than 99% CL. However, Planck+BAO was again found to be in agreement with a spatially flat Universe with $\Omega_K = 0.0004 \pm 0.0018$ thus confirming previous studies by Refs. [1420, 1421].

In an effort to further investigate this tension between Planck and BAO data, the analysis of Ref. [1425] combined Planck18 CMB temperature and polarization data with cosmic chronometer measurements and was lead to confirm that the Universe is consistent with spatial flatness to $\mathcal{O}(10^{-2})$ level.

A positive curvature (closed Universe) may be a plausible source of the anomalous lensing amplitude [1419–1421] (see Subsection 3.2.8).

3.2.2 Anomalously strong ISW effect

The decay of cosmological large-scale gravitational potential Ψ causes the integrated Sachs-Wolfe (ISW) effect [1426] which imprints tiny secondary anisotropies to the primary fluctuations of the CMB and is a complementary probe of dark energy e.g. [1427]. Using a stacking technique in the CMB data (see Refs. [1428, 1429], for a detailed discussion) anomalously strong integrated Sachs-Wolfe (ISW) signal ($> 3\sigma$) has been detected for supervoids and superclusters on scales larger than $100h^{-1}Mpc$ [1430, 1431]. This stronger than expected within standard Λ CDM signal of the ISW effect first emphasised in Ref. [1432] has been studied by Refs. [1433–1439].

In particular the analysis by Ref. [1438] for DES data alone found an excess ISW imprinted profile with $A_{ISW} \equiv \Delta T^{data}/\Delta T^{theory} \approx 4.1 \pm 2.0$ amplitude (where $A_{ISW} = 1$ corresponds to the Λ CDM prediction). Also a combination with independent BOSS data leads to $A_{ISW} = 5.2 \pm 1.6$. This is in 2.6σ tension with Λ CDM cosmology.

The average expansion rate approximation (AvERA) inhomogeneous cosmological simulation [1440] uses the separate Universe conjecture to calculates the spatial average of the expansion rate of local mini-Universes predicts. It indicates under the inhomogeneity assumption, about $\sim 2 - 5$ times higher ISW effect than Λ CDM depending on the l index of the spherical power spectrum [1441]. Thus large scale spatial inhomogeneities could provide an explanation to this ISW excess signal. Ref. [1442] uses angular cross-correlation techniques and combines several tracer catalogues to report $A_{ISW} \approx 1.38 \pm 0.32$.

Ref. [1443] investigated the early Integrated Sachs-Wolfe (eISW) effect (see e.g. [1444, 1445]) which is assumed to occur soon after recombination ($30 < z < 1100$), due to the presence of a non-negligible radiation. Constraints were thus imposed on the parameter A_{eISW} introduced by Ref. [1446]. Using Planck CMB data, this parameter was constrained to $A_{eISW} = 0.988 \pm 0.027$, in perfect agreement with Λ CDM. Note that in previous studies the parameter A_{eISW} was constrained to $A_{eISW} = 0.979 \pm 0.055$ using data from WMAP7+SPT [1446], to $A_{eISW} = 1.06 \pm 0.04$ from the Planck 2015 data release [1447], and to $A_{eISW} = 1.064 \pm 0.042$ from the Planck 2018 temperature data alone [1448].

In general the reported A_{ISW} amplitude varies in the literature depending on the dataset and the assumptions of the analysis. Further investigation of this issue is needed.

3.2.3 CMB cold spot

The cold (blue) spot was first found in WMAP 1-year temperature data by Ref. [1449] and was confirmed in Planck data [150, 1429, 1450] in the southern hemisphere at the galactic longitude and latitude $(l, b) = (209^\circ, -57^\circ)$. It is a statistical anomaly of the large-angle fluctuations in the CMB indicating non-Gaussian features. This inconsistency with Gaussian simulations has a p-value of $\sim 1\%$.

The cold spot is an unusually large region of low temperature with the mean temperature decrement $\Delta T \approx -100 \mu\text{K}$ and is not consistent with the prediction of gaussianity of the standard Λ CDM model [1451–1453].

Refs. [1437, 1454, 1455] pointed out that the anomalous nature of the cold spot corresponds to a rather cold area with an angular radius in the sky of about $5^\circ - 10^\circ$ from the centre surrounded by a hot ring.

Possible approaches for the explanation of the Cold Spot include: non-Gaussian feature due to a large statistical fluctuation [1449], an artifact of inflation [1451], the foreground [1452, 1456], multiple voids [1457], the imprint of a supervoid (about 140 – 200 Mpc radius completely empty void at $z \leq 1$) through the ISW effect [1430, 1458–1460], the axis of rotation of the Universe [1461], cosmic texture [1451, 1462], adiabatic perturbation on the last scattering surface [1463] (see Refs. [1464, 1465], for a review).

3.2.4 Cosmic hemispherical power asymmetry

The cosmic hemispherical power asymmetry (or dipolar asymmetry) is a directional dependency of the CMB angular power spectrum [1466–1469]. The continuous dipolar modulation of hemispherical power asymmetry corresponds to a hemispherical temperature variance asymmetry (signal in the CMB temperature field) [150, 1429, 1466, 1467, 1470–1474].

The dipolar modulated/observed CMB temperature fluctuation $\frac{\Delta T}{T}|_{mod}$ in the direction \hat{n} which appears to extend to $l_{max} \simeq 64$ can be expressed as [1472, 1475, 1476]¹⁷

$$\frac{\Delta T}{T}|_{mod}(\hat{n}) = [1 + A_{dm}\hat{n} \cdot \hat{p}] \frac{\Delta T}{T}|_{iso}(\hat{n}), \quad (3.20)$$

where $\frac{\Delta T}{T}|_{iso}$ is a statistically unmodulated/isotropic temperature fluctuation, A_{dm} denotes the amplitude of dipolar modulation and $\hat{n} \cdot \hat{p}$ corresponds to the dipolar modulation between the line-of-sight (LOS) of the observer (with unit vector \hat{n}) and the preferred dipolar direction (with unit vector \hat{p}). The amplitude of dipolar modulation A_{dm} is large at large angular scales $2 < l \lesssim 64$ ($k \lesssim 0.035 \text{ Mpc}^{-1}$), small at small angular scales $l \gtrsim 64$ and vanishes by a multipole moment of $\sim 500 - 600$ [150, 1429, 1450]. The scale dependence of the hemispherical power asymmetry was suggested by Refs. [1477–1487] and was investigated by Refs. [1488, 1489].

According to the hemispherical asymmetry nearly aligned with the Ecliptic, the temperature fluctuations are larger on one side of the CMB sky than on the other, resulting in an unexpected dipole configuration in the CMB power spectrum with an anomalously lower value of the variance in the northern sky compared to the southern sky [1450]. The preferred direction for the asymmetry from the Planck18 data is $(l, b) = (221^\circ, -20^\circ)$ in galactic coordinates and the amplitude is $A_{dm} \sim 0.07$ with statistically significant at the $\sim 3\sigma$ level [150]. This amplitude is ~ 2 times higher than expected asymmetry due to cosmic variance ($A_{dm} \sim 0.03$) and it is inconsistent with isotropy ($A_{dm} = 0$) at the $\sim 3\sigma$ level. The hemispherical power asymmetry in CMB can be explained by assuming a superhorizon perturbation [1475, 1490] or asymmetric initial states of the quantum perturbations [1486].

¹⁷Note that the hemispherical dipole is distinct from the usual CMB dipole. In the former case the *power spectrum* is assumed modulated discontinuously across a circle on the sky and in the second the actual temperature map has a component modulated by a smooth cosine function across the sky [1476].

3.2.5 Quadrupole-octopole alignment

The fluctuations in the standard Λ CDM model are Gaussian and statistically isotropic. Thus in harmonic space the quadrupole ($l = 2$) and octopole ($l = 3$) harmonics are expected to have independent and random orientations and shapes. The quadrupole and octopole have been observed to be planar and unexpectedly aligned with each other [1491–1496]. This implies a violation of statistical isotropy.

In particular in this low multipole moment anomaly the quadrupole and octopole planes are found to be mutually aligned with the direction of the cosmic dipole or CMB dipole (see Subsection 3.3 and Table 3.2) and perpendicular to the Ecliptic [149].

In order to study this large-angle anomaly one can use the maximum angular momentum dispersion [1491]

$$\langle \psi | (\hat{\mathbf{n}}_l \cdot \mathbf{L})^2 | \psi \rangle = \sum_{m=-l}^l m^2 |a_{lm}(\hat{\mathbf{n}}_l)|^2, \quad (3.21)$$

where the CMB map is represented by a wave function

$$\frac{\Delta T}{T}(\hat{\mathbf{n}}_l) \equiv \psi(\hat{\mathbf{n}}_l). \quad (3.22)$$

Here $a_{lm}(\hat{\mathbf{n}}_l)$ correspond to the spherical harmonic coefficients of the CMB map in a coordinate system with its z -axis in the the $\hat{\mathbf{n}}_l$ -direction.

The preferred axis $\hat{\mathbf{n}}_l$ is the axis around which the angular momentum dispersion is maximized. The directions of the quadrupole $\hat{\mathbf{n}}_2$ and the octopole $\hat{\mathbf{n}}_3$ are [1491]

$$\hat{\mathbf{n}}_2 = (-0.1145, -0.5265, 0.8424), \quad (3.23)$$

$$\hat{\mathbf{n}}_3 = (-0.2578, -0.4207, 0.8698), \quad (3.24)$$

with

$$|\hat{\mathbf{n}}_2 \cdot \hat{\mathbf{n}}_3| \simeq 0.9838. \quad (3.25)$$

This unexpected alignment of the $\hat{\mathbf{n}}_2$ and $\hat{\mathbf{n}}_3$ directions has only a $1/62$ probability of happening.

An approach in the analysis of this large-angle anomaly may also involve the use the multipole vectors [1497] (an alternative to the spherical harmonics) where each multipole order l is represented by l unit vectors i.e a dipole $l = 1$ can be constructed by a vector, a quadrupole by the product of two vectors/dipoles, an octopole from three vectors/dipoles etc.

The alignment of low multipoles indicates the existence of a preferred direction in the CMB temperature anisotropy. Furthermore possible relation between the quadrupole-octopole alignment and the dipolar asymmetry has been investigated by Refs. [1471, 1475]. A negligible relation between these anomalies was reported. However the analysis by Ref. [1498] has shown that a particular dipolar modulation including the scale dependence may be connected with the quadrupole-octopole alignment.

3.2.6 Lack of large-angle CMB temperature correlations

There is a lack of large-angle CMB temperature correlations as first was observed by COBE satellite [1499] and was confirmed by the WMAP [42, 1500] and Planck [150, 1429] temperature maps in the range $l = 2$ to 32. This is in tension with the Λ CDM prediction.

This anomaly is directly connected to the temperature T two-point angular correlation function $C^{TT}(\theta)$ of the CMB at large angular scale ($\theta \gtrsim 60^\circ$) which is unexpectedly close to zero [1495, 1501, 1502]. In angular space the two-point angular correlation function is defined as

$$C^{TT}(\theta) \equiv \langle T(\hat{\mathbf{n}}_1)T(\hat{\mathbf{n}}_2) \rangle = \frac{1}{4\pi} \sum_l (2l+1) C_l P_l(\cos \theta), \quad (3.26)$$

where the average is over all pairs of directions \hat{n} with $\hat{n}_1 \cdot \hat{n}_2 = \cos\theta$, $P_l(\cos\theta)$ are the Legendre polynomials and C_l is the angular power spectrum

$$C_l \equiv \frac{1}{2l+1} \sum_{m=-l}^l |a_{lm}|^2, \quad (3.27)$$

with a_{lm} the spherical harmonic coefficients of the temperature fluctuations.

The simplest and most useful statistic is $S_{1/2}$ first introduced in the WMAP first-year release [42] in order to measure the deviation of the angular correlation function from zero at angular scales $60^\circ < \theta < 180^\circ$. It is defined as

$$S_{1/2} = \int_{\mu_2}^{\mu_1} [C^{TT}(\theta)]^2 d(\cos\theta), \quad (3.28)$$

with $\mu_1 \equiv \cos\theta_1 = \cos 60^\circ = 1/2$ and $\mu_2 \equiv \cos\theta_2 = \cos 180^\circ = -1$.

A number of alternative statistics have been proposed in the literature [150, 1503–1505]. For example a generalization of the $S_{1/2}$ statistic suggested by Ref. [1506]. This statistic known as S^{TQ} uses the two-point angular correlation function between fluctuations in the temperature T and the Stokes parameter¹⁸ Q , $C^{TQ}(\theta)$, which can be expressed in terms of the two-point angular power spectrum, C_l^{TE} (with E the gradient mode of polarization). The significance of a test statistic can be quantified by using the p-value¹⁹, suggested by Ref. [1450].

No sufficient explanation has yet been suggested for this large-angle anomaly. Ref. [1512] studies the ISW effect, Ref. [1513] explores a non-trivial spatial topology of the Universe and Ref. [1514] studies the topology of the Planck CMB temperature fluctuations in order to find a possible explanation to the suppression of large-angle CMB temperature correlations. Also the low observed power in the quadrupole is a potential explanation for the lack of correlation in the temperature maps. Ref. [1501] argues that there is a cancellation between the combined contributions of C_l with multipoles $l \leq 5$ and the contributions of C_l with multipoles $l \geq 6$.

3.2.7 Anomaly on super-horizon scales

Ref. [1515] analysed the topological characteristics of the CMB temperature fluctuation. Using mathematical investigations on persistent homology to describe the cosmic mass distribution and performing experiments on Planck 2020 data release 4 (DR4) (based on the NPIPE data processing pipeline [1516]), Ref. [1515] claimed a detection of an anomalous topological signature in the Planck CMB maps indicating non-Gaussian fluctuations. In particular Ref. [1515] reports an anomaly in the behavior of the loops (a 4σ deviation in the number of loops) in the observed sky compared to the analysis of the redshift evolution of structure on simulations when the Λ CDM model is considered.

3.2.8 The lensing anomaly

The recent Planck18 release by Ref. [14] has confirmed the higher compared to that expected in the standard Λ CDM model, anomalous, lensing contribution in the CMB power spectra which is quantified by the phenomenological parameter, A_L [1517, 1518]. This weak lensing parameter A_L rescales the lensing potential power spectrum as²⁰

$$C_l^\Psi \rightarrow A_L C_l^\Psi, \quad (3.29)$$

¹⁸The Stokes parameters Q and U (for the Stokes parameters formalism see Ref. [1507]) are used to describe the state of CMB polarization e.g. [77, 1508]. These parameters are directly related to the E and B modes [1509–1511]. The polarization amplitude is given by $P = \sqrt{Q^2 + U^2}$.

¹⁹The probability value or p-value is the probability of measuring a test statistic equal to or more extreme as the observed one, considering that the null hypothesis is correct [1450]. It provides the lower value of significance at which the model would be ruled out. A low p-value means that there is strong indication of new physics beyond the null hypothesis.

²⁰Note that this is not the usual C_l but it is the additional contribution due to lensing.

where $A_L = 0$ corresponds to unlensed while $A_L = 1$ is the expected lensed result [1517] measuring the lensing effect in the CMB temperature power spectrum.

Since the main impacts of lensing on the CMB temperature power spectrum are to add power at small scales and to smooth the structure of the acoustic peaks and troughs (the peaks are reduced slightly, and the troughs between them filled in) [1519, 1520] the adding of parameter A_L changes the amount of smoothing of the CMB primary spectra peaks and troughs. A higher lensing amplitude ($A_L > 1$) than predicted in the flat Λ CDM cosmology ($A_L = 1$) by roughly 10% (at the level of 2.8σ) has been found in the temperature power spectra by the Planck team [14].

It should be noted that the oscillatory residuals between the Planck temperature power spectra and the best-fit Λ CDM model in the multipole range $l \in [900, 1700]$ are in opposite phase compared to the CMB and thus phenomenologically similar to the effects of gravitational lensing [1521, 1522].

A plausible explanation of the anomalous lensing amplitude is a positive curvature (closed Universe) which was investigated by Refs. [1419–1421]. Other possible sources which explain the lensing anomaly by mimicking a lensing effect are: a component of cold dark matter isocurvature (CDI) perturbation with a blue tilt (see Ref. [1523], for a detailed discussion) and oscillations in the primordial power spectrum which have the same frequency but opposite phase with the acoustic peaks [14]. All these effects are degenerate with the smoothing effect of lensing.

Furthermore, the modified gravity models could be candidates for a solution of the lensing anomaly [716, 862, 1524, 1525]. In particular the hints for $\Sigma_0 > 1$ (where Σ_0 the current value of parameter Σ which modifies the equation for the lensing potential i.e. Eq. (3.10)) are directly connected to the lensing anomaly as characterized by $A_L > 1$ [1524, 1525].

3.2.9 High-low l consistency

Ref. [1526] pointed out that there are internal inconsistencies in the Planck TT power spectrum. The Λ CDM parameter values derived by the high l part of the CMB anisotropy spectrum ($l > 1000$) are in $2 - 3\sigma$ tension with the corresponding values of these parameters derived from the low l part of the spectrum ($1 < 1000$). For example the low l multipoles predict a lower value of the cold dark matter density parameter ω_c than the high l multipoles, with discrepancy at 2.5σ [1526]. In addition it has been shown that the value of H_0 predicted by Planck from $l > 1000$, $H_0 = 64.1 \pm 1.7 \text{ km s}^{-1} \text{ Mpc}^{-1}$, disagrees with the value predicted by Planck from $l < 1000$, $H_0 = 69.7 \pm 1.7 \text{ km s}^{-1} \text{ Mpc}^{-1}$ at the 2.3σ level. Thus it is found that the value of H_0 depends on the CMB l -range examined.

This anomaly is probably related to the lensing anomaly i.e. the fact that Λ CDM is more consistent with the low l part of the spectrum that this not affected by the lensing anomaly (see Refs. [17, 1521, 1527], for a discussion).

3.2.10 The preference for odd parity correlations

There is an anomalous power excess (deficit) of odd (even) l multipoles in the CMB anisotropy spectrum on the largest angular scales ($2 < l < 30$), [150, 1528–1533]. A map consisting of odd (even) multipoles possesses odd (even) parity thus this effect may be considered as power (spectrum) asymmetry between even and odd parity map which is known as parity asymmetry.

In order to compare even and odd multipoles Ref. [1530] considers the parity asymmetry statistic defined as the ratio $P \equiv P^+/P^-$ of quantities P^+ and P^- which represent the mean power in even and odd only multipoles respectively for the range $2 \leq l \leq l_{max}$

$$P^\pm = \sum_2^{l_{max}} \frac{[1 \pm (-1)^l] l(l+1)C_l}{4\pi} . \quad (3.30)$$

A different statistic to quantify the parity asymmetry has been proposed by Ref. [1534].

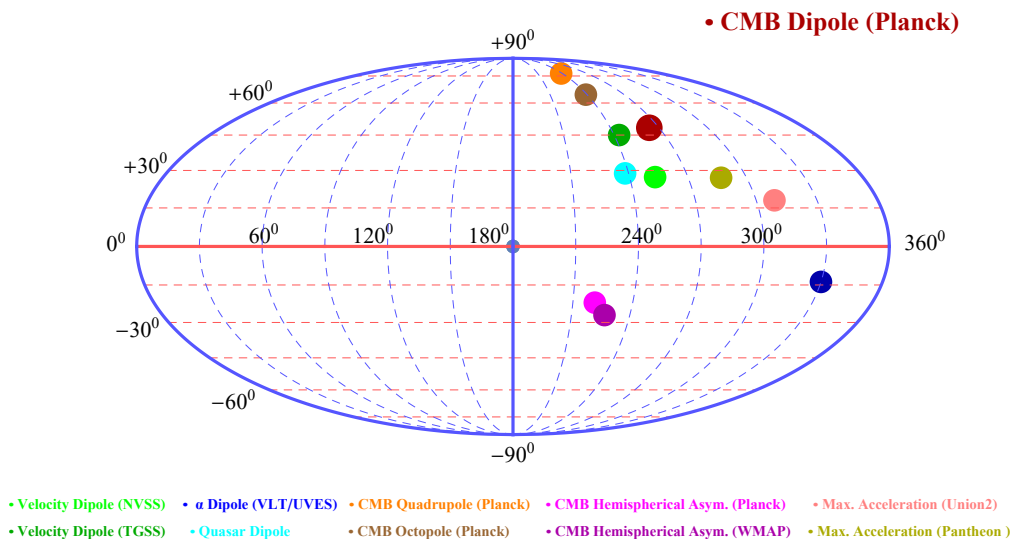


Figure 3.2: Mollweide-projection view of preferred directions in galactic coordinates for different cosmological observations (see Table 3.2).

3.3 Cosmic dipoles

There have been studies pointing out the presence of signals which indicate the violation of the cosmological principle. A physical mechanism producing such violation on Hubble scales is studied by Ref. [1535]. Various other possible mechanisms have been suggested to explain the observed violations of statistical isotropy e.g. superhorizon perturbations which introduce a preferred direction in our Universe [1490, 1536] (see also Ref. [1412], for a review). The dipole amplitudes and the directions (l, b) (galactic coordinates) from the different cosmological observations described below are shown in Fig. 3.2 and along with the corresponding references in Table 3.2.

The physical origin of these dipoles is described in the following subsections.

3.3.1 Velocity radio dipole

A large scale velocity flow dipole²² was pointed out in Refs. [151, 152]. The dipole moment of the peculiar velocity field (dipole bulk flow) which is a sensitive probe of the amplitude and growth rate of fluctuations on large scales [1544] was investigated by Refs. [151, 152, 1545–1551]. In many cases the results are controversial and there is a debate in the literature on the consistency with the Λ CDM model.

A recent detailed analysis has indicated that ‘tilted observers’ within the bulk flow can be misled into inferring acceleration [1552, 1553].

Ref. [1554] uses SnIa JLA data to demonstrate that the indications for cosmic acceleration found in the SnIa data disappears if a bulk flow induced anisotropy is allowed in the SnIa data. Thus, a bulk flow

²²For peculiar velocities as variation of the Hubble expansion produced by nearby nonlinear structures see in Ref. [153] and for dipole anisotropy in radio source count, see in Ref. [154].

Table 3.2: The amplitudes and the directions (l, b) (galactic coordinates) from different cosmological observations (Fig. 3.2) along with the corresponding references. The amplitude of CMB dipole has derived using the Eq. (3.33) (see e.g. Ref. [58]).

Observations	l [deg]	b [deg]	Amplitude	Refs.
CMB Dipole (Planck)	264.021 ± 0.011	48.253 ± 0.005	~ 0.007	[908, 1537]
Velocity Radio Dipole (TGSS)	243.00 ± 12.00	45.00 ± 3.00	0.070 ± 0.004	[154]
Velocity Radio Dipole (NVSS)	253.12 ± 11.00	27.28 ± 3.00	0.023 ± 0.004	[154]
Velocity Radio Dipole (NVSS)	253.00 ± 2.00	28.71 ± 12.00	0.019 ± 0.002	[1538]
Velocity Radio Dipole (NVSS)	253.00	32.00 ± 12.00	0.012 ± 0.005	[1539]
Quasar Dipole	238.20	28.80	0.01554	[58]
α Dipole (VLT/UVES)	330 ± 15	-13 ± 10	$0.97_{-0.20}^{+0.22} \times 10^{-5}$	[155]
CMB Quadrupole (Planck SMICA ²¹)	238.5	76.6		[1450]
CMB Octopole (Planck SMICA)	239.0	64.3		[1450]
CMB Hemispher. Asym. (Planck)	221	-22	0.07	[150]
CMB Hemispher. Asym. (WMAP)	227	-27	0.07	[1542]
Maximum Acceleration (Pantheon)	286.93 ± 18.52	27.02 ± 6.50	0.0018 ± 0.0002	[12]
Maximum Acceleration (Union2)	309_{-3}^{+23}	18_{-10}^{+11}		[1543]

dipole (at 3.9σ) aligned with the local bulk flow is identified while any monopole (which can be attributed to Λ) is consistent with zero (at 1.4σ).²³

It is usually assumed that our local (solar system) peculiar motion with respect to the CMB rest frame produces the CMB dipole anisotropy ($l = 1$) [1556, 1557] (also known as solar dipole [1537, 1558]). In the standard model, this implies that the LSS distribution should have a similar kinematic dipole known as the velocity dipole or radio dipole which arises from the Doppler boosting of the CMB monopole and from special relativistic aberration effects [1559].

In order to describe the origin of this dipole, a population of sources with power-law spectra depending on frequency ν is usually assumed

$$S_\nu \propto \nu^{-\alpha}, \quad (3.31)$$

where S_ν is the flux density and α ²⁴ is an individual spectral index with typically assumed value $\alpha \sim 0.75$ [1560]. The integral source counts per unit solid angle above some limiting flux density S_ν can be approximated by a power law

$$\frac{dN}{d\Omega}(> S) \propto S_\nu^{-x}, \quad (3.32)$$

where $x \sim 1$ and can be different for each survey. An observer moving with velocity $v \ll c$ with respect to the frame in which these sources are isotropically distributed sees a dipole anisotropy $1 + D \cos \theta$ over the sky with amplitude [1561]

$$D = [2 + x(1 + \alpha)] \frac{v}{c}. \quad (3.33)$$

According to the most recent measurements the inferred velocity of the Sun relative to the CMB rest frame is [908, 1537]

$$\beta \equiv \frac{v}{c} = (1.23357 \pm 0.00036) \times 10^{-3}, \quad (3.34)$$

²³A recent model independent analysis of SnIa data (Pantheon) data Ref. [1555] implementing machine learning has confirmed a $\sim 4.5\sigma$ detection of the accelerated expansion even though that analysis did not allow for anisotropic dipole effects.

²⁴The individual spectral index α should not be confused with the fine-structure constant α .

$$\text{or } v = 369.82 \pm 0.11 \text{ km s}^{-1}, \quad (3.35)$$

along the direction with galactic longitude and latitude $(l, b) = (264.021^0 \pm 0.011^0, 48.253^0 \pm 0.005^0)$ or $RA \sim 168^0$, $Dec \sim -7^0$ [908, 1537].

The CMB rest frame is conventionally taken to correspond to the standard of cosmic rest frame and is assumed to be statistically homogeneous and isotropic in the context of the FLRW model. In this rest frame the Hubble flow should be most uniform (minimum Hubble variation frame) and the comoving observers should not see a kinematic dipole. However it has been observed [153, 1562] that the dipole structure of the velocity field is less in the reference frame of the Local Group of galaxies than in the CMB frame. This persistence of the dipole structure of the velocity flow in the CMB frame at large distances is not unexpected if we are located in an underdensity [1563].

According to the standard model if the Universe is isotropic our velocity with respect to the CMB rest frame and our velocity relative to the LSS should be identical. However, as was first noted by Ref. [1564], while the direction of the radio dipole is consistent with that of the CMB, the velocity of our local motion obtained from the radio dipole exceeds that obtained from the CMB dipole. Radio continuum surveys which sample the Universe at intermediate redshifts ($z \sim 1$) have been used as an excellent probe to large scale isotropy and a discrepancy between the predicted and measured amplitudes of the velocity have been revealed [154, 1538, 1539, 1565–1567]. In particular the analysis by Ref. [154] has shown that the radio dipole using the sky distribution of radio sources from the NRAO VLA Sky Survey (NVSS) dataset [1568] and TIFR GMRT Sky Survey (TGSS) dataset [154, 1569, 1570] is ~ 2 and ~ 5 times larger than predicted by the mock realisations within the context of Λ CDM cosmology respectively. The above observed discrepancy between the radio and CMB dipoles has been confirmed by independent groups and could imply the existence of an anisotropic Universe.

Possible explanations of the violation of statistical isotropy are: systematics due to the incomplete sky coverage of the radio continuum surveys [1539, 1565, 1571], intrinsic dipole in the local LSS [1572], nearby nonlinear structures of voids and walls and filaments [153], remnant of the pre-inflationary Universe [1573] and superhorizon perturbation [1574, 1575].

3.3.2 Quasar dipole

The distribution of quasars across the sky may provide independent probe of the cosmological principle [1576]. As previously discussed there is an expected anisotropy related to the CMB dipole anisotropy (about 1 part in 1000) due to our motion with respect to the CMB rest frame.

Ref. [58] used mid-infrared data from the Wide-field Infrared Survey Explorer (WISE) [1336] to create reliable AGN/quasar catalogs and a custom quasar sample from the new CatWISE2020 data release [1577]. It was shown that there is a statistically significant dipole in the density of distant quasars with direction $(l, b) = (238.2^0, 28.8^0)$ which is 27.8^0 away from the direction of the CMB dipole. Its amplitude was found to be 0.01554, ~ 2 times larger than predicted, with statistical significance at the 4.9σ level (or with a p-value of 5×10^{-7}) for a normal distribution. This result is in conflict with the cosmological principle.

3.3.3 Fine structure constant α dipole

In the past 20 years there has been interest in the possibility of the variation of the fine structure constant $\alpha \equiv e^2/(4\pi\epsilon_0\hbar c)$ (where e , ϵ_0 , \hbar , and c are the electron charge, the vacuum permittivity, the reduced Planck’s constant, and the speed of light) [156, 1578–1586] (see Ref. [109], for review of varying fine structure constant).

The analysis by Refs. [155, 156] uses the “many multiplet” (MM) method [1587–1590] to analyze quasar absorption line spectra obtained using the Ultraviolet and Visual Echelle Spectrograph (UVES) [1591] on the Very Large Telescope (VLT). It indicates both the violation of the cosmological principle and the spatial variation of the fine structure constant α which is approximated as a spatial dipole with direction $(l, b) = (330^0 \pm 15^0, -13^0 \pm 10^0)$ and amplitude $0.97_{-0.20}^{+0.22} \times 10^{-5}$, preferred over a simple

monopole model with significance at the 4.2σ (see Refs. [1592–1594], for possible systematics in this analysis).

The variation of α across the sky was shown to be well fit by an angular dipole model of the form [155]

$$\frac{\Delta\alpha}{\alpha} \equiv \frac{\alpha - \alpha_0}{\alpha} = C_A \cos \theta + C_B , \quad (3.36)$$

where α_0 is the present local value, θ is the angle with respect to the dipole direction, C_A is the angular amplitude of the dipole term and C_B is a monopole term.

It is worth to note that the analysis by Ref. [1595] suggests that there are no robust indications of time or space variations of α . However recent measurements of quasar absorption-line spectra indicate a spatially dependent value of fine structure constant α at a $\sim 4\sigma$ significance level over a simple monopole (no-variation) model [1596, 1597]. In addition, it is found that the fine structure constant α dipole is anomalously aligned with other dipoles and the preferred direction in $\Delta\alpha/\alpha$ is correlated with the one in the distribution of SnIa [1598, 1599].

3.4 BAO curiosities

As mentioned above (see Subsection 2.2.2) the BAO measurements can be classified in two classes: galaxy BAO and $\text{Ly}\alpha$ BAO (with $\text{Ly}\alpha$ auto-correlation function and $\text{Ly}\alpha$ -quasar cross-correlation function). A $2.5 - 3\sigma$ discrepancy between the BAO peak position in the $\text{Ly}\alpha$ at an effective redshift of $z \sim 2.34$ and the CMB predictions from Planck/ Λ CDM cosmological model has been found [322, 359, 1600].

For example, Ref. [322] uses the $\text{Ly}\alpha$ auto-correlation function and the $\text{Ly}\alpha$ -quasar cross-correlation function to report the measurements of the BAO scale in the line-of-sight direction

$$D_H(z = 2.40)/r_s = 8.94 \pm 0.22 , \quad (3.37)$$

and in the transverse direction

$$D_M(z = 2.40)/r_s = 36.6 \pm 1.2 , \quad (3.38)$$

where $D_H(z) \equiv \frac{c}{H(z)}$ is the Hubble distance and $D_M(z) \equiv (1+z)D_A(z) = d_A(z)$ is the comoving angular diameter distance. These values are in $\sim 2.3\sigma$ tension with CMB predictions $D_H(z = 2.40)/r_s = 8.586 \pm 0.021$ and $D_M(z = 2.40)/r_s = 39.77 \pm 0.09$ by Planck 2015 flat Λ CDM cosmology [16].

The galaxy BAO peak position in the matter correlation function $\xi(s)$ (see Eq. (2.15) and Fig. 2.5) and the measurements $D_H(z = 2.40)/r_s$ and $D_M(z = 2.40)/r_s$ were found to be consistent with CMB predictions. This discrepancy between galaxy and $\text{Ly}\alpha$ BAO constitutes the BAO anomaly which has been investigated in Refs. [22, 157, 158].

Using new $\text{Ly}\alpha$ BAO measurements from the BOSS survey and from its extended version eBOSS in the SDSS DR14 the tension with CMB predictions was reduced to $\sim 1.7\sigma$ [357, 360] and from eBOSS in the SDSS DR16 to only $\sim 1.5\sigma$ [361].

Ref. [158] argues that this anomaly arises by cosmological effects at $z < 2.34$ and the tension is caused by evolution of dark energy equation of state $w(z)$ for redshift range $0.57 < z < 2.34$.

3.5 Parity violating rotation of CMB linear polarization (Cosmic Birefringence)

In the standard model of elementary particles and fields, parity violation is observed only in the weak interaction sector [1601, 1602]. A certain class of quintessence models should generically generate such parity asymmetric physics [1603, 1604]. In particular a parity violating (nearly) massless axionlike scalar field ϕ (dark matter or dark energy) would rotate CMB polarisation angles of CMB photons as they travel from the last scattering surface ($z \approx 1000$) to the present by a non-zero angle β_a (cosmic birefringence).

A Chern–Simons coupling between a time-dependent axionlike field $\phi(t)$ and the electromagnetic tensor and its dual in the Lagrangian density (e.g. [1603, 1605])

$$\mathcal{L} = \frac{1}{4} g_{\phi\gamma} \phi F_{\mu\nu} \tilde{F}^{\mu\nu} , \quad (3.39)$$

induces a cosmic isotropic birefringence angle (e.g. [1606, 1607])

$$\beta_a = \frac{1}{2} g_{\phi\gamma} \int_{t_s}^{t_0} \dot{\phi} dt , \quad (3.40)$$

and produces a non-zero observed EB spectrum [1608]

$$C_l^{EB} = \frac{1}{2} \sin(4\beta_a) (C_l^{EE} - C_l^{BB}) , \quad (3.41)$$

where $g_{\phi\gamma}$ is a Chern-Simons coupling constant which has mass-dimension -1 , $\tilde{F}^{\mu\nu}$ is the dual of the electromagnetic tensor of $F_{\mu\nu}$, and t_0 and t_s are the times at present and last scattering surface, respectively.

Using a novel method developed in Refs. [159–161], a non-zero value of the isotropic cosmic birefringence $\beta_a = 0.35 \pm 0.14$ deg (68% C.L) was recently detected in the Planck18 polarization data at a 2.4σ statistical significance level by Ref. [162]. This recent evidence of the non zero value of birefringence poses a problem for standard Λ CDM cosmology and indicates a hint of a new ingredient beyond this model.

An axion or an axion-like particle with a weak coupling to photon as a possible source of the cosmic birefringence was investigated by Ref. [1609]. Ref. [1610] showed that if an ultralight axion coupled to photons forms domain walls due to inflationary fluctuations, the domain-wall network can explain the hint for isotropic cosmic birefringence found by Ref. [162]. This model predicts a testable peculiar anisotropic cosmic birefringence as well. In contrast to the approach of Ref. [1609], this scenario explains the birefringence with the photon anomalous coefficient of the axion-like particle $\sim O(1)$. Furthermore, birefringence inducing axion-like particles could be candidates for an early dark energy resolution to the Hubble tension [1609]. Refs. [1611, 1612] study the anisotropic birefringence and constraints are derived. The axion field fluctuations over space and time generate anisotropic birefringence.

3.6 Small-scale curiosities

On small scales (on scales of hundreds of kpc and below) the predictions of Λ CDM model are in many cases inconsistent with observations [1613–1615]. In particular observations on galaxy scales indicate that the Λ CDM model faces several problems in describing structures at small scales ($\lesssim 1$ Mpc) (see Refs. [163, 164, 1616–1618], for a review). Alternative models that modify the nature of dark matter have been used to solve these problems e.g. warm [1619–1623], fuzzy [1624–1627], self-interacting [1628–1631] and meta-cold dark matter [1632] (see also Ref. [1633], for a review). Other models which have the potential to provide a solution to these problems have been proposed by Refs. [1094, 1101, 1107, 1634–1636]. In particular Refs. [1634, 1635] argued that the existence of a dissipative hidden dark matter sector (dark matter coupled to a massless dark photon) can solve some of these problems (core-cusp, missing satellites, and plane of satellites problem).

These small scale signals include the following:

3.6.1 The core-cusp curiosity

The core-cusp curiosity [1637, 1638] refers to a discrepancy between the density of a dark matter halo profile of low-mass galaxies $\rho(r) \propto r^{-x}$ in N-body simulations (an important tool for evaluating the

predictions of the Λ CDM model) with $1 \lesssim x \lesssim 1.5$ (cusp profile)²⁵ [1640–1643] and the astronomical observed profile with $x \sim 0$ (core profile) [1637, 1638, 1640, 1641, 1644–1648]. Ref. [1649] probes this problem in low surface brightness galaxies.

3.6.2 The missing satellites problem (or dwarf galaxy problem)

The missing satellites problem (or dwarf galaxy problem) [1650–1653] refers to an over-abundance of the predicted number of halo substructures in detailed collisionless N-body simulations compared to the observed number of satellite galaxies in the Local Group. In particular the Λ CDM model predicts orders of magnitude larger number of satellites (~ 1000) than the observed number of dwarf galaxies (~ 50) [1652, 1654].

3.6.3 The Too Big To Fail (TBTf) problem

The Too Big To Fail (TBTf) problem [1655–1660] refers to an inconsistency between the predicted mass of dark matter subhaloes in Λ CDM theory and the observed central mass of brightest satellite galaxies in the Local Group [1657, 1658] (also in the Milky Way [1655, 1656] or in the Andromeda (M31) [1659]).

In particular the Λ CDM predicted central densities of the most massive dark matter subhalos are systematically larger than the inferred from kinematics of the brightest Local Group satellites [1656, 1657, 1661]. An observed bright satellite is more likely to reside in subhalos with lower mass than is expected in a Λ CDM model. The simulated massive dark matter subhalos ‘*failed*’ to form a comparatively bright satellite galaxy.

This problem is possibly related to the missing satellites problem but it is a distinct problem which depends on the internal structure of subhalos or the central shapes of density profiles of satellite halos [1657].

Alternative models that modify the nature of dark matter have been investigated to solve this problem: non-trivial dark matter physics [1662, 1663], interaction between the dark matter and dark radiation components [1094, 1107], self-interacting dark matter [1664, 1665] and fuzzy dark matter [1626]

3.6.4 The problem of satellite planes

In the problem of satellite planes [1666–1670] several satellite galaxies of the Milky Way, of neighboring Andromeda galaxy (M31), and of Centaurus A (CenA) are part of thin plane that is approximately perpendicular to the Galactic disk. Moreover measurement of the motions of satellite galaxies has shown that their orbits appear to be correlated [1671–1673]. This flattened structure and coherent motions of satellite galaxy systems is in inconsistency with the prediction of the Λ CDM model as inferred from simulations [1670]. The simulations based on Λ CDM cosmology indicate uncorrelated and close to isotropic satellite structures [1674, 1675]. In these simulations the observed structure formations with spatial and kinematic coherence distribution are very rare with a probability $\sim 10^{-3}$ [1669, 1670].

3.6.5 The angular momentum catastrophe

The angular momentum catastrophe [1676] concerns a catastrophic angular momentum loss of gas during disk galaxies formation in Smooth Particle Hydrodynamics (SPH) [1677] simulations. The formed disks in simulations according to the predictions of Λ CDM have smaller scale lengths by a factor of 2 – 3 compared with observed ones [1678]. An axion dark matter model may resolve this discrepancy between the observed and predicted angular momentum distributions of baryons (ordinary cold dark matter) in the dwarf galaxies [1679].

²⁵The well know Navarro–Frenk–White profile [1639, 1640] is cusped with $\rho(r \rightarrow 0) \sim r^{-1}$.

3.6.6 Baryonic Tully-Fisher Relation (BTFR)

Baryonic Tully-Fisher Relation (BTFR) [470, 1680]. As mentioned above, the well known Tully-Fisher (TF) [464] empirical relation connects the velocity of rotation of a spiral galaxy with its intrinsic luminosity while the Baryonic Tully-Fisher Relation (BTFR) [466–468] Eq. (2.37) is a scaling relation between the observed total baryonic mass M_b (stars plus gas) of a spiral galaxy and its rotation velocity V_c (see Subsection 2.2.6). The problem for Λ CDM model as inferred from simulations (see e.g. Ref. [1681]) is that the BTFR leads to existence of a higher intrinsic scatter (~ 0.15 dex) and a lower slope ($s = 3$) compared to the observed (~ 0.10 dex and $s \sim 4$) [470]. Ref. [471] suggests the Modified Newtonian Dynamics (MOND) [901] as a possible solution to this problem. However some simulations or semi-analytic approaches of galaxy formation within a Λ CDM cosmological context can reproduce a realistic BTFR slope but not its small scatter e.g. [1682–1685].

3.6.7 The void phenomenon

The void phenomenon [1686] refers to the emptiness of voids (the number of small galaxies in the void). Cosmological N-body simulations in the context of Λ CDM have established a clear prediction [1687] that many small dark matter haloes should reside in voids [1688, 1689]. This is consistent with observations on large scales but is inconsistent with observations on small scales. In particular the local void contains much fewer galaxies than expected from Λ CDM theory [1690].

3.7 Age of the Universe

A lower limit can be set on the age of the Universe by the ages of the oldest stars (or oldest astrophysical objects) because on cosmological timescales they form shortly after the Big Bang. In the context of Λ CDM cosmology, the standard theory [1691–1695] and cosmological numerical simulations [1696–1698] predict that the first stars, the so-called population III (Pop III), formed in dark matter minihaloes of typical mass $M \sim 10^5 - 10^6 M_\odot$ at redshifts $z \sim 20 - 30$ (about 100 million years after the Big Bang i.e. about around the end of the cosmic dark ages) (see Refs. [1699, 1700], for models indicating late, $z \sim 2 - 7$, Pop III star formation).

The age of the Universe t_* as obtained from local measurements using the ages of oldest observed stars (the so-called population II (Pop II)) in the Milky way appears to be larger and in some tension with the corresponding age of the Universe t_U obtained using the CMB Planck data in the context of Λ CDM [165].

The age of the Universe in the flat Λ CDM model is an observable determined by the integral

$$t(z) = \int_0^{z_t} \frac{dz'}{(1+z')H(z')} = \frac{1}{H_0} \int_0^{z_t} \frac{dz'}{(1+z')[\Omega_{0m}(1+z')^3 + \Omega_{0r}(1+z')^4 + (1-\Omega_{0m})]^{1/2}}, \quad (3.42)$$

where t is the cosmic time corresponding to redshift z_t . Thus the age of the Universe is $t_U = t(z_t = \infty)$.

For example the age of the Milky Way Population II halo, metal deficient, high velocity subgiant HD-140283 (also known as Methuselah star) is estimated to be $t_* = 14.46 \pm 0.31$ Gyr by Ref. [1701] and using new sets of stellar models is estimated to be $t_* = 14.27 \pm 0.80$ Gyr by Ref. [1702]. These estimates of the age of this star are slightly higher ($\sim 2\sigma$) than the age of Universe $t_U = 13.800 \pm 0.024$ Gyr inferred by CMB Planck18 data [14] but within the errors it does not conflict with this age.

Despite of the above indications the analysis by Ref. [1703] using new parallaxes from the Gaia space mission [1704, 1705] in place of the older HST, reports a revision of the age of HD-140283 to $t_* = 13.5 \pm 0.7$ Gyr which is more compatible with the age t_U inferred by Planck data. Also the analysis by Ref. [1706] using populations of stars in globular clusters (very-low-metallicity stars) reports age of the Universe constrained to be larger than $t_* = 13.5_{-0.14}^{+0.16}$ Gyr.

Clearly, Eq. (3.42) indicates that in a Λ CDM Universe the quantities H_0 , t_U and Ω_{0m} are related. Therefore the determination of the age of older objects based on local Universe observations provides a test of the current cosmological model and plays an important role in the studies of Hubble and spatial curvature tensions [1419, 1420, 1703].

3.8 The Lithium problem

It has long been known (since the early 80's) that absorption lines in the photospheres of old, metal-poor (Population II) halo stars in the Milky Way's halo indicate ~ 3.5 times less primordial abundance of lithium isotope ${}^7\text{Li}$ compared to the prediction of the standard BBN theory [1707–1709]. The observed value of the lithium abundance²⁶ ${}^7\text{Li}/H = (1.6 \pm 0.3) \times 10^{-10}$ [1710] is smaller than the theoretically expected value ${}^7\text{Li}/H = (5.62 \pm 0.25) \times 10^{-10}$ [1711] at a level $\sim 5\sigma$. This constitutes the lithium problem [166]. No such problem exists for the observed abundances of other light elements ${}^2\text{H}$ (or D), ${}^3\text{He}$, and ${}^4\text{He}$ that are in broad quantitative agreement with BBN predictions + WMAP/Planck cosmic baryon density Ω_b which is deduced by the CMB [125, 1172].

A number of theoretical or experimental studies in the literature have attempted to address the lithium problem e.g. [1712–1725]. For example the analysis by Ref. [1726] shows that the variations in Nature's fundamental constants on primordial nucleosynthesis provide a possible solution to the lithium problem. Specifically, they determined that if the value of the fine-structure constant α at the primordial nucleosynthesis epoch was larger than the present one by ten parts per million of relative variation, the lithium problem could be resolved.

It was also proposed by Ref. [1727] that decaying dark matter into dark radiation in the early Universe can solve the long-standing lithium problem, leaving completely unaffected the abundance of other light elements. This mechanism was also proposed to alleviate the H_0 tension (see Subsection 2.3.1) but is severely constrained by the Planck data [863].

Measurements of lithium (e.g. [1728, 1729]) may not be representative of the cosmological production mechanism [1730, 1731]. It is thus possible that the solution to the lithium problem lies in the effects of stars in the lithium abundance. Therefore a precise knowledge of the stellar formation process and physics of stellar atmosphere is necessary to provide a fully satisfactory solution. Thus, possible solutions to this persistent problem can be classified into four categories (see Refs. [125, 166, 1732], for a review):

- Cosmological solutions (e.g. new theory beyond the standard BBN including variations of fundamental constants) [1720, 1726, 1733–1739]
- Nuclear Physics solutions (e.g. reactions destroy lithium during or after BBN) [1722–1724, 1740–1744]
- Astrophysical solutions (e.g. stars destroy lithium after BBN) [1745–1748]
- Extensions of the standard model (e.g. simultaneous imposition of photon cooling after BBN, X-particle decay and a primordial magnetic field [1714, 1749], destruction of ${}^7\text{Be}$ due to the decay of a sterile neutrino [1719] and including new particles or interactions [1718]).

3.9 Quasars Hubble diagram

The quasar distances can be estimated from their X-ray (coronal) emission generated by a plasma of hot relativistic electrons around the accretion disk. The emission is induced through inverse-Compton scattering processes and ultraviolet (UV) emission generated by the accretion disk where the gravitational energy of the infalling material is partially converted to radiation [167, 169].

²⁶Usually in the literature the abundance of lithium is expressed by $A({}^7\text{Li}) = 12 + \log_{10}[n({}^7\text{Li})/n(H)]$ where n is the number density of atoms and 12 is the solar hydrogen abundance.

In recent years model independent derivation²⁷ of the distance modulus–redshift relation using high- z quasars ($z \lesssim 7$) as distance indicators (quasars Hubble diagram) provides a new bright standard candle in the higher redshifts and earlier times beyond SNIa. The method used is based on a non-linear relation between the X-ray and the UV emissions at low redshift which is of the form [167]

$$\log_{10} L_X = \gamma_q \log_{10} L_{UV} + \beta_q , \quad (3.43)$$

where L_X and L_{UV} are the rest-frame monochromatic luminosities at 2 keV and at 2500 Å, respectively [1751]. Also $\gamma_q \sim 0.6$ [167] and β_q are fitting parameters of the luminosities.

Extending a Hubble diagram up to redshift $z = 5.5$ shows hints for phantom dark energy [167–169]. In particular the distance modulus-redshift relation for a sample of 1598 quasars at higher redshift ($0.5 < z < 5.5$) is in disagreement with the concordance model at a $\sim 4\sigma$ significance level²⁸ [167]. Moreover, the analysis by Ref. [169] building a Hubble diagram by combining three samples of Pantheon, quasars, and gamma-ray bursts (GRBs) reported tension at more than the $\sim 4\sigma$ statistical level with the flat Λ CDM model. Recently Ref. [1756] using an updated, larger QSO dataset [1757] containing 2421 QSO measurements with redshifts up to $z \sim 7.5$ has demonstrated that the L_X - L_{UV} relation parameter values depend on the cosmological model thus cannot be used to constrain cosmological parameters.

3.10 Oscillating signals in short range gravity experiments

The most constraining test of gravity at very short distance (sub-millimeter) scales looking for departures from Newtonian gravity is implemented via torsion balance experiments. A reanalysis of short range gravity experiments has indicated the presence of an oscillating force signal with sub-millimeter wavelength [170, 171]. In particular Ref. [170] has indicated the presence of a signal at 2σ level of spatially oscillating new force residuals in the torsion balance data of the Washington experiment [73]. As an extension of the previous analysis the study by Ref. [171] using Monte Carlo simulation and analysing the data of the Stanford Optically Levitated Microsphere Experiment (SOLME) which involves force measurements an optically levitated microsphere as a function of its distance z from a gold coated silicon cantilever [1758] reports a oscillating signal at about 2σ level.

The sub-millimeter scale of the quantum nature of dark energy may be written as

$$\lambda_{de} \equiv \sqrt[4]{\frac{\hbar c}{\rho_{de}}} \approx 0.085 \text{ mm} , \quad (3.44)$$

where it is assumed that $\Omega_{0m} = 0.3$ and $H_0 = 70 \text{ km s}^{-1} \text{ Mpc}^{-1}$.

Thus, if the accelerating expansion of the Universe is connected with effects of modified gravity due to quantum gravity it would be natural to expect some modification of Newton’s law at the submillimeter scale.

The deviations from Newton’s law of gravitation is usually described in the context of scalar-tensor [582, 1388] and flat extra dimension theories [1759–1765] by a short range Yukawa type potential of the form

$$V_{\text{eff}} = -G \frac{M}{r} (1 + \alpha_Y e^{-mr}) , \quad (3.45)$$

where α_Y and m are parameters to be constrained by the data.

Alternatively, a power law ansatz may also generalize the gravitational potential to the form

$$V_{\text{eff}} = -G \frac{M}{r} \left[1 + \bar{\beta}^k \left(\frac{1}{mr} \right)^{k-1} \right] . \quad (3.46)$$

²⁷Ref. [1750] argued that even though the data used in this approach are valid, their analysis involves significant uncertainties as it may lead to spurious artificial tensions.

²⁸The analyses of the high- z quasar data has lead to a wide range of conclusions [1750, 1752–1755]. For example Ref. [1750] concludes that the log polynomial expansion generically fails to recover flat Λ CDM beyond $z \sim 2$, thus implying that the previously derived $\sim 4\sigma$ tension may be artificial.

This power law parametrization is motivated by some brane world models [1766–1769].

For $m^2 < 0$ the Yukawa gravitational potential becomes oscillating and takes the form

$$V_{\text{eff}} = -G \frac{M}{r} [1 + \alpha_Y \cos(mr + \theta)] , \quad (3.47)$$

where θ is a parameter.

Recently a reanalysis of the data of the Washington experiment searching for modifications of Newton’s Law on sub-millimeter scales by Ref. [1197] has indicated that a spatially oscillating signal is hidden in this dataset. In addition it is shown that even though this signal cannot be explained in the context of standard modified gravity theories²⁹ (viable ST and $f(R)$ theories), it occurs naturally in nonlocal (infinite derivative) gravity theories [1770–1772] that predict such spatial oscillations without the presence of ghosts (instabilities) and has a well-defined Newtonian limit.

The origin of oscillating signals could be due to three possible effects:

- A statistical fluctuation of the data.
- A periodic distance-dependent systematic feature in the data.
- A signal for a short distance modification of GR (e.g. non-local modified theory of gravity).

In the later case, it is important to identify modified theories that are consistent with such an oscillating signal and are not associated with instabilities e.g. [1773, 1774].

3.11 Anomalously low baryon temperature

The Experiment to Detect the Global Epoch of Reionization Signature (EDGES) collaboration [172] report anomalously low baryon temperature $T_b \approx 4\text{K}$ at $z \approx 17$ (half of its expected value). This temperature was inferred from the detection of global (sky-averaged) 21-cm absorption signal which is centred at a frequency of $\sim 78\text{MHz}$. The absorption depth of cosmic CMB photons at redshifts range $15 \lesssim z \lesssim 20$ estimated by EDGES is more than twice the maximal value expected in the ΛCDM model, at $\sim 3.8\sigma$ significance.

Possible explanations of this discrepancy were investigated and various models were proposed (e.g. [1775–1778]). For example Ref. [1775] argue that EDE can explain this anomaly.

The EDGES observation has been used to constrain various cosmological models of dark matter and dark energy [767, 1775, 1779, 1780].

3.12 Colliding clusters with high velocity

Observed galaxy clusters like the massive ($\sim 10^{15}M_\odot$) high-redshift ($z = 0.87$) interacting pair known as El Gordo (ACT-CL J0102-4915) [1781] have a very high relative velocity. This implies that formation of large structures may have taken place earlier than expected in ΛCDM cosmology. Ref. [173] based on light cone tomography estimated that the too-early formation of El Gordo rules out ΛCDM cosmology at 6.16σ confidence. The early and rapid formation of clusters which consist of two colliding massive galaxy clusters at a high redshift may constitute a problem of the ΛCDM model. Ref. [173] argues that MOND with light sterile neutrinos model as suggested by Ref. [900] can resolve this issue.

²⁹For a free massive scalar Ref. [5] investigates the physical conditions that can eliminate the tachyonic instabilities or at least drastically change their lifetime.

Chapter 4

Constraining Power of Cosmological Observables on Cosmological Parameters as a Function of Redshift

The analysis presented in this chapter is based on the work which was done in collaboration with PhD student Lavrentios Kazantzidis and Prof. Leandros Perivolaropoulos and has been published in Physical Review D [1].

In this chapter, we determine the optimum and the blind redshift ranges of basic cosmological observables with respect to the cosmological parameters. In an optimum range of redshifts, the observable can constrain the parameter in the most effective manner while in the blind redshift ranges the observable values may be degenerate with respect to the cosmological parameter values and thus inefficient in constraining the given parameter.

As we discussed in Chapters 2 and 3 the validity of the Λ CDM cosmological model is currently under intense investigation using a wide range of cosmological observational probes including CMB experiments, galaxy photometric and spectroscopic surveys, attempts to BAO, WL, RSD, cluster counts, as well as the use of SNIa as standard candles. This investigation has revealed the presence of tensions within the Λ CDM model, i.e. inconsistencies among the parameter values determined using different observational probes. The following question therefore emerge: *Are these tensions an early indication of the need for a modified theory of gravity beyond the standard model or are they a result of systematic/statistical fluctuations in the data?* The analysis presented in this chapter aims to address this question.

4.1 Introduction

The main goal of completed, existing and upcoming CMB experiment and large scale structure surveys (see Subsection 12.2) is to provide explanation of the curiosities of Λ CDM cosmology. These surveys are classified in four stages. Stages I and II correspond to completed surveys and CMB experiments, while stages III and IV correspond to existing and upcoming projects respectively. For example stage II CMB experiments include WMAP [1782], Planck [14, 1783], Atacama Cosmology Telescope Polarimeter (ACTPol) [1784] and SPT-Pol [1785], while stage III CMB experiments include AdvACT [1786] and SPT-3G [1787]. Future stage IV CMB probes on the ground [1788] and in space such as Lite (Light) satellite for the studies of B-mode polarization and Inflation from cosmic background Radiation Detection (LiteBIRD) [1789, 1790] mainly aim to measure CMB lensing and the CMB-B modes in detail.

Improvement in the quality and quantity of data is expected in the coming two decades from large

scale structure surveys (see Table 4.1). Stage III large scale structure surveys include the Canada-France-Hawaii Telescope Lensing Survey (CFHTLenS) [1791], the Kilo Degree Survey (KiDS) [1792, 1793], the extended Baryon Oscillation Spectroscopic Survey (eBOSS) [1794], the Dark Energy Survey (DES) [1795–1797] and the Hobby Eberly Telescope Dark Energy Experiment (HETDEX) [1798]. Finally, stage IV large scale structure surveys include ground-based telescopes such as the Dark Energy Spectroscopic Instrument (DESI), the Large Synoptic Survey Telescope (LSST) [1799, 1800] and the Square Kilometer Array (SKA) [1801–1804] as well as space based telescopes such as Euclid [1805, 1806] and the Wide Field Infrared Survey Telescope (WFIRST) [1807, 1808]. The redshift ranges of some surveys with their type and duration are presented in Table 4.1.

Table 4.1: Some recent and future large-scale structure surveys. Photometric surveys focus mainly on WL, while spectroscopic surveys measure mainly RSD. The redshift range shifts to higher redshifts for stage III and stage IV surveys.

Survey	Redshift	Type	Duration	Refs.
SDSS	$0.1 < z < 0.6$	Spectroscopic	2006-2010	[1809]
WIGGLEZ	$0.4 < z < 0.8$	Spectroscopic	2006-2010	[1810]
BOSS	0.35, 0.6, 2.5	Spectroscopic	2009-2014	[1810]
KIDS	$0 < z < 0.8$	Photometric	2011-	[1792, 1793]
DES	$0.3 < z < 1.0$	Photometric	2012-2018	[1795–1797]
HETDEX	$1.9 < z < 3.5$	Spectroscopic	2015-2017	[1798]
eBOSS	$0.6 < z < 2.2$	Spectroscopic	2015-2018	[1794]
DESI	$0.6 < z < 1.7$	Spectroscopic	> 2019	[1811–1813]
DESI-Bright Galaxies	$0.0 < z < 0.4$	Spectroscopic	> 2019	[1811–1813]
Euclid	$0.8 < z < 2.0$	Spectroscopic	2022-2027	[1805, 1806, 1814]
LSST	$0.5 < z < 3$	Photometric	> 2019	[1799, 1800]
WFIRST	$1 < z < 3$	Spectroscopic	> 2020	[1807, 1808]

Clearly, the redshift ranges of more recent surveys tend to increase in comparison with earlier surveys. The assumption of increasing constraining power of observables on cosmological parameters with redshift therefore emerge. As demonstrated in our analysis however, this assumption is not always true.

Thus, we address the following questions:

- What is the redshift dependence of the constraining power of a given observable with respect to a given cosmological parameter?
- Is there an optimal redshift range where the constraining power of a given observable is maximal with respect to a given cosmological parameter?
- Are there blind redshift spots where a given observable is degenerate with respect to specific cosmological parameters?

A previous analysis [1307] has found the existence of degeneracies for the case of growth of fluctuations observable $f\sigma_8$ with respect to the equation of state parameter w in specific redshift ranges. In our study we extend these results to a wider range of observables and cosmological parameters.

In particular the goals of our analysis are the following:

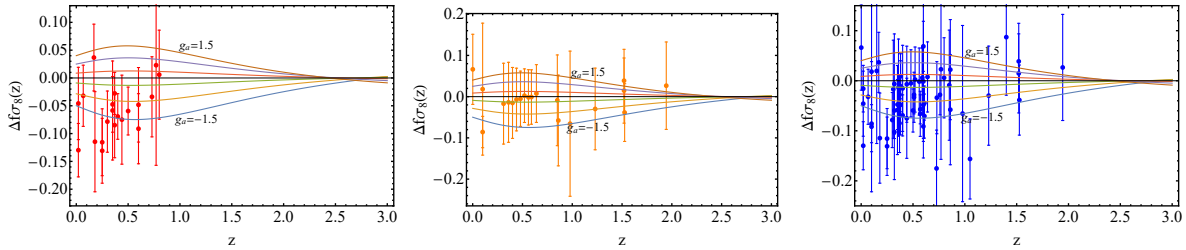


Figure 4.1: $\Delta f\sigma_8$ as a function of redshift for g_a in the range $g_a \in [-1.5, 1.5]$ superimposed with the early growth data (left panel), late data (middle panel) and full growth data (right panel).

- Extensive up-to-date compilations of recent measurements of cosmological observables including growth of perturbations, BAO, and luminosity distance observables.
- Identify the sensitivity of these observables as a function of redshift for three cosmological parameters: the present matter density parameter Ω_m , the dark energy equation of state parameter w (assumed constant), and a parameter g_a describing the evolution of the effective Newton's constant in the context of a well motivated parametrization [67, 148].
- Identify possible trends for deviations of the above parameters from their standard Planck/ Λ CDM values in the context of the above data compilations.

The Chapter is organised as follows. In the next Section 4.2 we review the basic equations determining the growth of cosmological density perturbations (see also Subsection 3.1.1). These equations can lead to the predicted evolution of the observable combination $f\sigma_8(a) \equiv f(a) \cdot \sigma(a)$, where a is the scale factor $a = \frac{1}{1+z}$, $f(a) \equiv d \ln \delta(a) / d \ln a$ is the growth rate of cosmological perturbations, $\delta(a) \equiv \delta\rho/\rho$ is the linear matter overdensity (with ρ the matter density of the background and $\delta\rho$ its first order perturbation), and σ_8 is the rms matter density fluctuations within spheres of radius $8h^{-1}Mpc$. We investigate the sensitivity of the observables $f\sigma_8(z)$ and $f(z)$ on the matter density parameter Ω_m , the equation of state parameter w and a modified gravity parameter g_a as a function of redshift. For these growth observables blind redshift spots and optimal redshift ranges are identified. The selection of these particular parameters (Ω_m , w and g_a) is important as their combination can lead to direct test of GR by simultaneously constraining the background expansion rate through $H(z)$ and the possible evolution of the effective Newton's constant $G_{\text{eff}}(z)$. It is important to notice that the evolution of the effective Newton's obtained through the parameter g_a is degenerate with $H(z)$ constant and can only be probed once $H(z)$ is also efficiently constrained through the parameters Ω_m and w . In Sec. 4.3 we consider cosmological observables obtained from BAO data, construct an updated extensive compilation of such data, and identify the sensitivity of the BAO observables on the parameters Ω_m , w and g_a as a function of redshift. As in the case of the growth observables, blind redshift spots and optimal redshift ranges are identified. The effects of the data redshift range on the shape and size of the uncertainty contours in the above cosmological parameter space are also identified. In Sec. 4.4 we use the luminosity distance moduli as obtained from SNIa and gravitational waves and identify the sensitivity of these observables to the parameters Ω_m , w and g_a as a function of redshift. Binned JLA data are superimposed on the plots to demonstrate the sensitivity of the distance moduli to the cosmological parameters. Finally in Sec. 4.5 we conclude and discuss the results of the analysis of this Chapter.

4.2 Growth of Density Perturbations: The Observables $f\sigma_8$ and $f(z)$

The evolution of the linear matter overdensity δ (see also Subsection 3.1.1) in the context of both GR and most modified gravity theories is given by

$$\ddot{\delta} + 2H\dot{\delta} - 4\pi G_{\text{eff}} \rho \delta \approx 0, \quad (4.1)$$

where dots denote differentiation with respect to time t , H is the Hubble parameter, ρ is the background matter density and G_{eff} is the effective Newton's constant which in general depends on redshift z and cosmological scale k . In terms of the scale factor Eq. (4.1) on subhorizon scales ($k^2 \gg a^2 H^2$) takes the form of Eq. (3.4), while in terms of the redshift z can be written as [112, 1304–1308]

$$\delta'' + \left(\frac{(H(z)^2)'}{2H(z)^2} - \frac{1}{1+z} \right) \delta' - \frac{3(1+z)}{2} \frac{\Omega_m G_{\text{eff}}(z, k)/G}{H(z)^2/H_0^2} \delta = 0, \quad (4.2)$$

where primes denote differentiation with respect to the redshift. The effective Newton's constant G_{eff} emerges from a generalized Poisson equation

$$\nabla^2 \Psi \approx 4\pi G_{\text{eff}} \rho \delta, \quad (4.3)$$

where Ψ is the perturbed metric potential in the Newtonian gauge where the perturbed FLRW metric takes the form of Eq. (3.9). Note that GR predicts a constant homogeneous $G_{\text{eff}}(z, k) = G$ (with G the Newton's constant as measured by local experiments).

Solar System [1389] and BBN [1815] constraints imply that G_{eff} is close to the GR predicted form in both low and high redshifts. In particular at low z we have [1389]

$$\left| \frac{G'_{\text{eff}}(z)}{G} \right|_{z=0} < 10^{-3} h^{-1} \ll 1, \quad (4.4)$$

while the second derivative is effectively unconstrained since

$$\left| \frac{G''_{\text{eff}}(z)}{G} \right|_{z=0} < 10^5 h^{-2}. \quad (4.5)$$

Furthermore, at high z and at 1σ , BBN [1815] impose the following constraint [1389]

$$|G_{\text{eff}}/G - 1| \leq 0.2. \quad (4.6)$$

A parametrization of $G_{\text{eff}}(z)$ respecting these constraints is off the following form [148]

$$\frac{G_{\text{eff}}(a, g_a, n)}{G} = 1 + g_a(1-a)^n - g_a(1-a)^{n+m} = 1 + g_a \left(\frac{z}{1+z} \right)^n - g_a \left(\frac{z}{1+z} \right)^{n+m}, \quad (4.7)$$

where n and m are integer parameters with $n \geq 2$ and $m > 0$ which we set equal to 2 in our analysis.

The observable $f\sigma_8(a)$ of Eq. (3.6) can be obtained from the solution $\delta(a)$ of Eq. (3.4) using the definitions $f(a)$ of Eq. (3.3) and $\sigma(a)$ of Eq. (3.5) (see Subsection 3.1.1).

Therefore, both the observable $f\sigma_8(a)$ and the growth rate $f(a)$ (or equivalently $f\sigma_8(z)$ and $f(z)$) can be obtained by numerically solving Eq. (3.4) (or Eq. (4.2)). The solution of these equations requires the specification of proper parametrizations for both the background expansion $H(z)$ and the effective Newton's constant $G_{\text{eff}}(z)$. In the context of our analysis we assume a flat universe and a w CDM model background expansion of the form

$$\begin{aligned} H^2(z) &= H_0^2 \left[\Omega_m(1+z)^3 + (1-\Omega_m)(1+z)^{3(1+w)} \right] \Rightarrow \\ E^2(z) &= \frac{H^2(z)}{H_0^2} = \Omega_m(1+z)^3 + (1-\Omega_m)(1+z)^{3(1+w)}, \end{aligned} \quad (4.8)$$

and G_{eff} parametrized by Eq. (4.7) with $n = m = 2$. Using these parametrizations and initial conditions corresponding to GR in the matter domination era ($\delta(a) \sim a$) we can obtain the predicted evolution of the observables $f\sigma_8$ and $f(z)$ for various parameter values around the standard Planck/ Λ CDM model parameters ($\Omega_m^P = 0.31$, $w = -1$, $g_a = 0$).

For each observable $O(\Omega_m, w, g_a)$ (e.g. $O = f\sigma_8(z)$) we consider the deviation¹ with respect to each cosmological parameter $P = (\Omega_m, w, g_a)$. Thus for parameter $P = \Omega_m$ the deviation of $O(\Omega_m, w, g_a)$ is defined as

$$\Delta O_{\Omega_m} \equiv O(\Omega_m, -1, 0) - O(\Omega_m^P, -1, 0) . \quad (4.9)$$

Similar deviations ΔO_w and ΔO_{g_a} are defined for the other two parameters in the context of a given observable O

$$\Delta O_w \equiv O(\Omega_m^P, w, 0) - O(\Omega_m^P, -1, 0) , \quad (4.10)$$

$$\Delta O_{g_a} \equiv O(\Omega_m^P, -1, g_a) - O(\Omega_m^P, -1, 0) . \quad (4.11)$$

In Fig. 4.1 we show the deviation $\Delta f\sigma_{8g_a}$ for g_a in the range $g_a \in [-1.5, 1.5]$ superposed with a recent compilation of the $f\sigma_8$ data [67] shown in Table B.1 in the Appendix B (with early data published before 2015 in the left panel, recent data published after 2016 in the middle panel and full dataset in the right panel). No fiducial model correction has been implemented for the datapoints shown, but the effects of this correction are less than about 3% [67, 147].

The following three comments can be made on the results shown in Fig. 4.1.

- Early data favor weaker gravity ($g_a < 0$) for redshifts around $z \simeq 0.5$ assuming a fixed Planck/ Λ CDM background. This trend is well known [147] and has been demonstrated and discussed extensively, e.g. in Refs. [146, 148, 507, 687, 688, 1196, 1310, 1816, 1817].
- The observable $f\sigma_8$ has a blind spot with respect to the parameter g_a at redshift $z \simeq 2.7$. Such a blind spot was also pointed out in Ref. [1307] with respect to a similar gravitational strength parameter (where it was called ‘‘sweet spot’’ in that Ref. [1307] even though the term ‘‘blind spot’’ should have been used).
- There is a redshift range around $z \simeq 0.5$ of optimal sensitivity of the observable $f\sigma_8$ with respect to the parameter g_a . Despite of the existence of this optimal redshift range much of the recent $f\sigma_8$ data appear at larger redshifts approaching the blind spot region. These datapoints have reduced sensitivity in identifying deviations of G_{eff} from its GR value G .

We may also quantify the existence of blind spots and optimal redshifts of an observable O with respect to a cosmological parameter P using the definition of the ‘sensitivity’ measure including the effects of the survey volume $V_{\text{eff}}(k, z)$. The effective survey volume probed for a particular k mode with the power spectrum $p(k, z)$ in a survey of sky area surveyed $\Delta\Omega$ is given by [1818, 1819]

$$V_{\text{eff}}(k, z) = \Delta\Omega \int_0^z \left[\frac{n(z')p(k, z')}{1 + n(z')p(k, z')} \right]^2 \frac{dV}{dz' d\Omega} dz' , \quad (4.12)$$

where z is the maximum redshift corresponding to the survey volume V_{eff} and $n(z)$ is the number density of galaxies that are detected, which is given as

$$n(z) = \int_{M_{\text{lim}}(z)}^{\infty} \frac{dN}{dV dM} dM . \quad (4.13)$$

The function $M_{\text{lim}}(z)$ is the limiting mass threshold which is detected for the given survey and dV is the infinitesimal comoving volume element

$$dV = \frac{r^2(z)}{H(z)} d\Omega dz , \quad (4.14)$$

¹In certain cases we consider the deviation around $\Omega_m = 0.3$ instead of $\Omega_m = \Omega_m^P$.

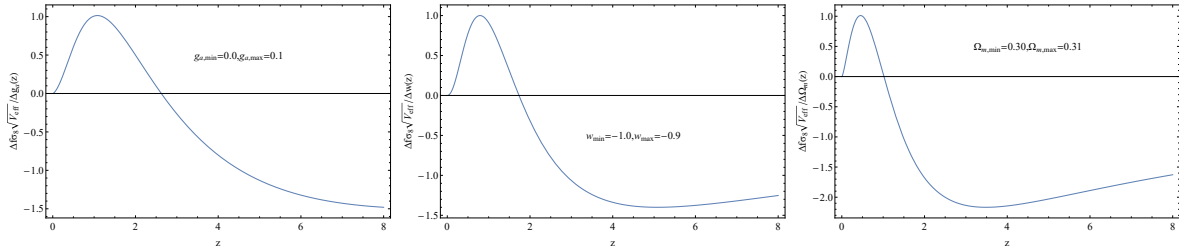


Figure 4.2: The sensitivity measure S for the observable $f\sigma_8$ (i.e. $\frac{\Delta f\sigma_8}{\Delta P} V_{\text{eff}}^{1/2}$) for $P = g_\alpha$ (left panel), $P = w$ (middle panel), and $P = \Omega_m$ (right panel)

where

$$r(z) = \frac{c}{H_0} \int_0^z \frac{dz'}{E(z')}, \quad (4.15)$$

and $E(z')$ is given by Eq. (4.8)

The constraining power of the observable O depends on the survey volume $V_{\text{eff}}(k, z)$, since the mean square fluctuation σ_p on the measurement of the power spectrum $p(k, z)$ increases as the effective survey volume $V_{\text{eff}}(k, z)$ decreases (i.e. as less k modes are measured by the survey) as [1818, 1820–1822]

$$\left(\frac{\sigma_p}{p(k, z)} \right)^2 = \frac{2}{4\pi k^3 \Delta(\log k)} \frac{(2\pi)^3}{V_{\text{eff}}(k, z)} \left[\frac{1 + n(z)p(k, z)}{n(z)p(k, z)} \right]^2. \quad (4.16)$$

Thus, since the the mean square fluctuation σ_p on the measurement of the power spectrum $p(k, z)$ is inversely proportional to the square root of the survey volume $V_{\text{eff}}(k, z)$, the 'sensitivity' measure is defined as

$$S_P^O \equiv \frac{\Delta O(P)}{\Delta P} \cdot V_{\text{eff}}(k, z)^{1/2}, \quad (4.17)$$

where ΔO is the deviation of the observable O when a given parameter varies in a fixed small range $\Delta P = P_{\text{max}} - P_{\text{min}}$ around a fiducial model value (e.g. Planck15/ Λ CDM). Plots of the sensitivity measure S for the observable $f\sigma_8$ for the three parameters g_α (left panel), w (middle panel) and Ω_m (right panel) are shown in Fig. 4.2. The presence of blind spots is manifest as roots of the sensitivity measure, while optimal redshifts appear as maxima of the magnitude of S . We have fixed k such as that $np = 3$ assuming sufficient signal to noise per pixel [1821]. We have also rescaled sensitivity measure statistic so that it is unity at its maximum absolute value. The nonlinear modes may be excluded by setting a minimum redshift which is of $O(10^{-2})$ and are much smaller than the derived optimal redshifts and blind spots identified in our analysis. Notice that the sensitivity measure indicates the existence of blind spots for all three parameters. For w the blind spot is close to $z \simeq 2$ while for Ω_m is close to $z \simeq 1$. The corresponding optimal redshifts are at $z \simeq 1.2$ for g_α , at $z \simeq 0.8$ for w and at $z \simeq 0.5$ for Ω_m . (Although the region $z > 2$ for w and Ω_m provides better sensitivity, there are currently almost no data available in this redshift range). Notice also in Figs. 4.1 and 4.2 that when including the effects of the survey volume the optimal redshifts shift to somewhat higher redshifts, while the blind spots remain unaffected.

As shown in Figs. 4.3 and 4.4 for both cases, recent data approach the blind spot regions in contrast to early published data that efficiently probed the optimal redshift regions for both parameters w and Ω_m . Also, early data seem to favor weaker growth of perturbations which occurs for lower, g_α , and Ω_m and higher w [67, 147, 148]. If this trend is partly attributed to a lower value of G_{eff} in the recent past, then it is difficult to reconcile with the most generic modified gravity theories like $f(R)$ and ST theories [148]. In particular $f(R)$ gravity theory generically predict stronger gravity at small z compared to its present time [1823].

We perform a similar analysis for the growth rate observable $f(z)$ which will be probed by the Euclid mission [1806]. Mock Euclid data assuming a Planck/ Λ CDM fiducial model are shown in Fig. 4.5 with proper redshifts and error bars [1806] along with the deviation of the observable $f(z)$ with respect to Ω_m

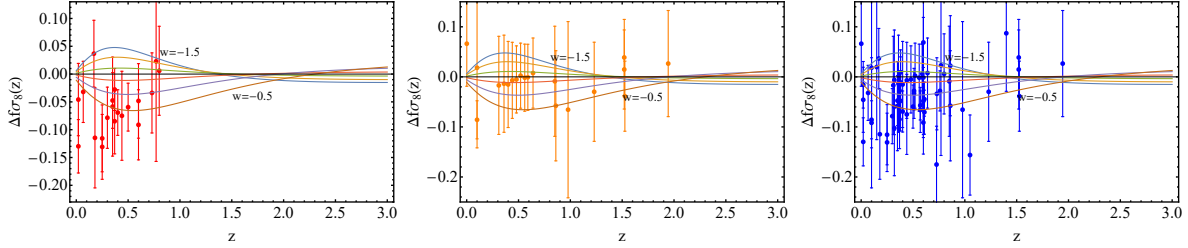


Figure 4.3: $\Delta f\sigma_8$ as a function of redshift for w in the range $w \in [-1.5, -0.5]$ superimposed with the early growth data (left panel), late data (middle panel) and full growth data (right panel).

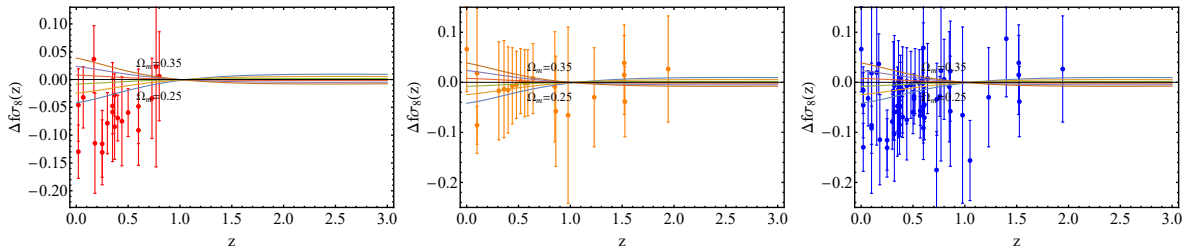


Figure 4.4: $\Delta f\sigma_8$ as a function of redshift for Ω_m in the range $\Omega_m \in [0.25, 0.35]$ superimposed with the early growth data (left panel), late data (middle panel) and full growth data (right panel).

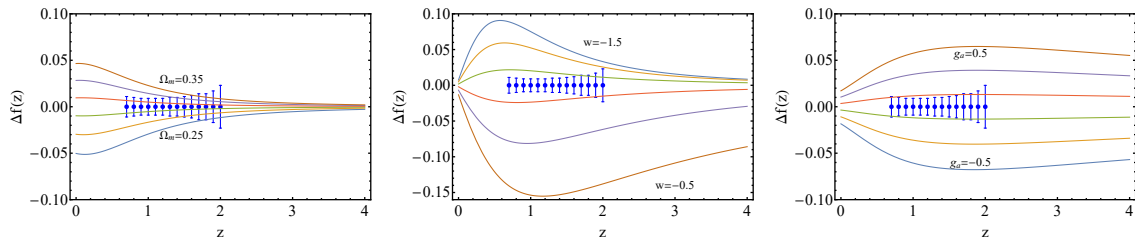


Figure 4.5: $\Delta f(z)$ as a function of redshift superimposed with the Euclid mock data for different values of Ω_m (left panel), w (middle panel), and g_α (right panel).

(left panel), w (middle panel) and g_a (right panel). Clearly, the predicted redshift range of the Euclid data is optimal for the identification of new gravitational physics (right panel), but it is not optimized for constraining the matter density parameter (left panel of Fig. 4.5) or the equation of state parameter if $w < -1$ (middle panel).

The observable $f(z)$ is considered due to the approach of Ref. [1806], where the Euclid team indicated that the large number of galaxies of the Euclid survey combined with the depth of the survey will allow a reliable estimate of the bias simultaneously with the growth rate $f(z)$ obtained through the redshift distortion factor β . The redshift distortion factor β is defined as

$$\beta(z) = \frac{\Omega_m(z)^\gamma}{b(z)} = \frac{f(z)}{b(z)}, \quad (4.18)$$

where $b(z)$ is the linear bias factor between galaxy and matter density distributions defined as $b \equiv \frac{\delta_g}{\delta}$ (with δ_g the galaxy overdensity).

Thus, the survey will not only probe the bias-free combination $f\sigma_8$, but also directly probe the growth observable $f(z)$ which is modeled in Ref. [1806] with errorbars and is also considered separately in our analysis. Of course, what is actually observable is the redshift distortion β factor which is obtained through the ratio between the monopoles of the correlation functions in real and in redshift space. Thus, the derived blind spot and optimal redshift for the growth rate $f(z)$ are accurate under the assumption that the bias $b(z)$ has a very weak dependence on the redshift.

4.3 Baryon Acoustic Oscillations: the Observables $D_V(z) \times \frac{r_s^{fid}}{r_s}$, $H \times \frac{r_s}{r_s^{fid}}$ and $D_A \times \frac{r_s^{fid}}{r_s}$

4.3.1 BAO Observables and their Variation with Cosmological Parameters.

In this section, we use a variety of isotropic and anisotropic BAO observables given in the literature.

Waves induced by radiation pressure in the pre-recombination plasma inflict a characteristic BAO scale on the late-time matter clustering at the radius of the sound horizon r_s defined by Eq. (2.17). This BAO scale appears as a peak in the correlation function or equivalently as damped oscillations in the large scale structure power spectrum (see Subsection 2.2.2). In the context of standard matter and radiation epochs, the Planck 2015 measurements of the matter and baryon densities Ω_m and Ω_b specify the BAO scale to great accuracy (uncertainty less than 1%). An anisotropic BAO analysis measuring the sound horizon scale along the line of sight and along the transverse direction can measure both $H(z)$ and the comoving angular diameter distance $D_M(z)$ related to the physical angular diameter distance D_A defined by Eq. (1.57) in Subsection 1.2.8 in a flat universe as [358]

$$D_M(z) = (1+z)D_A(z) = c \int_0^z \frac{dz'}{H(z')}. \quad (4.19)$$

Deviation of cosmological parameters can change r_s , so BAO measurements actually constrain the combinations $D_M(z) \times \frac{r_s^{fid}}{r_s}$ or equivalently $D_A(z) \times \frac{r_s^{fid}}{r_s}$, $H(z) \times \frac{r_s}{r_s^{fid}}$ where r_s^{fid} is the sound horizon (BAO scale) in the context of the fiducial cosmology assumed in the construction of the large-scale structure correlation function.

An angle-averaged galaxy BAO measurement constrains the combination

$$D_V(z) = \left[cz \frac{D_M^2(z)}{H(z)} \right]^{1/3}. \quad (4.20)$$

Taking into account the variation of cosmological parameters the constrained combination becomes $D_V(z) \times \frac{r_s^{fid}}{r_s}$. Statistical isotropy can be used to constrain the observable combination $H(z)D_M(z)$ using an anisotropic BAO analysis in the context of the Alcock-Paczynski test [1824].

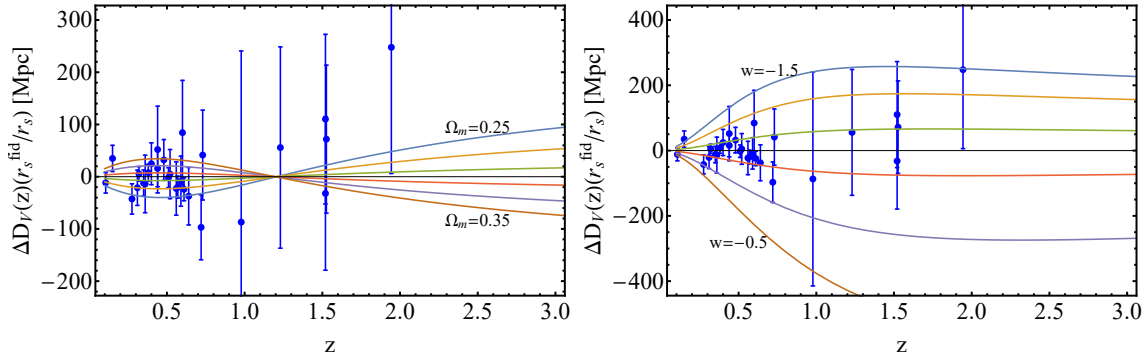


Figure 4.6: The deviation $\Delta D_V(z) \times \frac{r_s^{fid}}{r_s}$ as a function of the redshift z for different values of Ω_m (left panel) and w (right panel).

The sound horizon $r_s(z_d)$ at the drag epoch z_d that enters the BAO observables may be calculated in the context of a given cosmological model, either numerically (e.g. with CAMB [1825]) or using a fitting formula for z_d [317] of the form

$$z_d = \frac{1291(\Omega_m h^2)^{0.251}}{1 + 0.659(\Omega_m h^2)^{0.828}} [1 + b_1(\Omega_b h^2)^{b_2}] , \quad (4.21)$$

where

$$b_1 = 0.313(\Omega_m h^2)^{-0.419} [1 + 0.607(\Omega_m h^2)^{0.674}] , \quad (4.22)$$

$$b_2 = 0.238(\Omega_m h^2)^{0.223} , \quad (4.23)$$

and from Eq. (2.17)

$$r_s(z) = \frac{c}{\sqrt{3}} \int_{z_d}^{\infty} \frac{dz}{H(z) \sqrt{1 + \frac{3\Omega_b}{4\Omega_\gamma} \frac{1}{1+z}}} , \quad (4.24)$$

where $\Omega_\gamma = 2.469 \times 10^{-5} h^{-2}$ for $T_{\text{cmb}} = 2.725$ K, and

$$H(z) = H_0 \left[\Omega_m (1+z)^3 + \Omega_r (1+z)^4 + \Omega_\Lambda (1+z)^{3(1+w)} \right]^{1/2} , \quad (4.25)$$

with $\Omega_r = \Omega_\gamma (1 + 0.2271 N_{\text{eff}})$ ($N_{\text{eff}} \simeq 3$ is the number of neutrino species) and

$$\Omega_m + \Omega_r + \Omega_\Lambda = 1 , \quad (4.26)$$

in the context of a flat universe ($K = 0$). It has been shown [1826] that when the fitting formula is used to obtain z_d close to the Planck/ Λ CDM parameter values, a correction factor of 154.66/150.82 should be used on r_s obtained from Eq. (4.24) to obtain agreement with the more accurate numerical estimate of r_s .

Using Eqs. (1.57), (4.20), (4.24) and a Planck/ Λ CDM fiducial cosmology ($h = 0.676$, $\Omega_b h^2 = 0.0223$, $\Omega_m = 0.31$ and $r_s^{fid} = 147.49$ Mpc), it is straightforward to construct the theoretically predicted redshift dependence of the BAO observables $D_V(z) \times \frac{r_s^{fid}}{r_s}$, $H \times \frac{r_s}{r_s^{fid}}$ and $D_A \times \frac{r_s^{fid}}{r_s}$ for various values of the parameters Ω_m and w and superpose this dependence with corresponding currently available data shown in Table B.2 in the Appendix B.

The predicted evolution of the deviation of the observable $D_V(z) \times \frac{r_s^{fid}}{r_s}$ for various values of Ω_m (left panel) and of w (right panel) is shown in Fig. 4.6. The deviation of the parameter Ω_m (left panel) was performed around the value $\Omega_m = 0.3$ while the deviation of the parameter w was performed around the

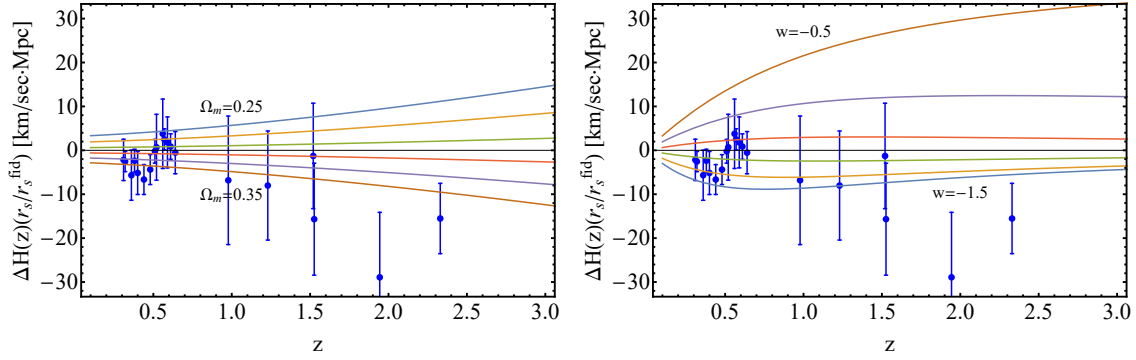


Figure 4.7: The deviation $\Delta H \times \frac{r_s}{r_s^{\text{fid}}}$ as a function of the redshift z for different values of Ω_m (left panel) and w (right panel)

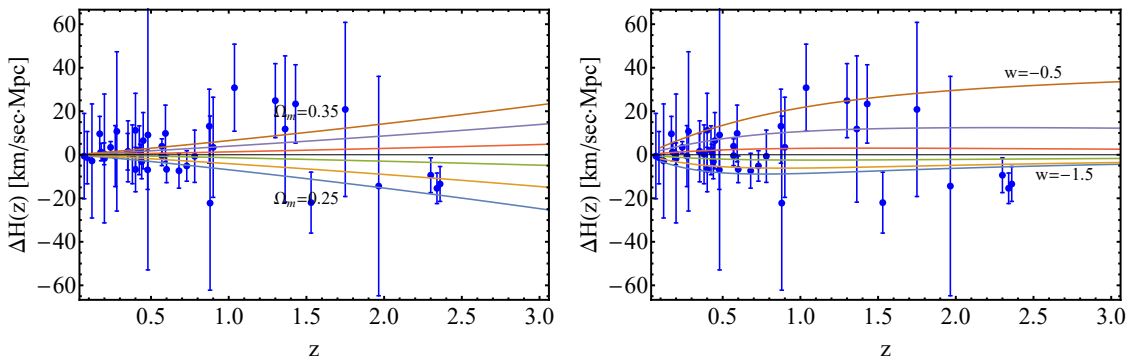


Figure 4.8: The deviation $\Delta H(z)$ as a function of redshift using the full compilation of Table B.4 in the Appendix B, for various values of Ω_m (left panel) and w (right panel).

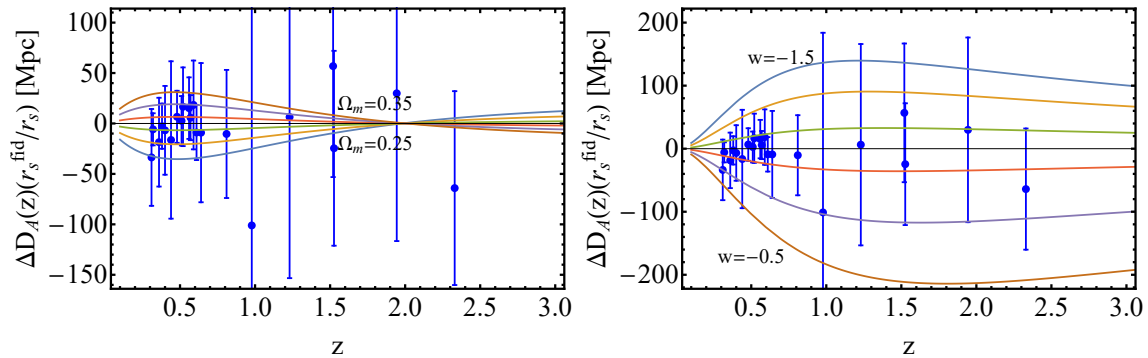


Figure 4.9: The deviation $\Delta D_A \times \frac{r_s^{fid}}{r_s}$ as a function of the redshift z for different values of Ω_m (left panel) and w (right panel)

Λ CDM value $w = -1$ (see Eq. (4.9)). Notice the existence of a blind spot at $z \simeq 1.2$ for the observable $D_V(z) \times \frac{r_s^{fid}}{r_s}$ with respect to the parameter Ω_m , while the optimal redshift in the same plot is $z \simeq 0.6$. Even though the region $z > 2$ also seems to be optimal, there are currently almost no data available in this redshift range. In contrast, for the same observable with respect to the parameter w there is no blind spot, while the optimal redshift range is at $z > 1.2$.

In Fig. 4.7 we show the predicted evolution of the deviation of the observable $H \times \frac{r_s^{fid}}{r_s}$ for various values of Ω_m (left panel) and of w (right panel). For this observable there is no blind redshift spot, while the sensitivity appears to increase monotonically with redshift for both observables. Notice the asymmetry obtained for the equation of state parameter which is due to the fact that for $w < -1$ at early times the effects of dark energy are negligible for all values of w , leading to a degeneracy for this range of parameters at high z . For comparison, in Fig. 4.8, we show the deviation of the observable Hubble expansion rate for various values of Ω_m (left panel) and of w (right panel) along with corresponding data obtained from the spectroscopic evolution of galaxies used as cosmic chronometers, shown in Table B.4 in the Appendix B along with the corresponding citations (for previous compilations see also Refs. [485, 1827, 1828]). Even though Figs. 4.7 and 4.8 are qualitatively similar, it is clear that the BAO data are significantly more constraining compared to the cosmic chronometer data with respect to both parameters Ω_m and w , especially at low redshifts.

In Fig. 4.9 we show the predicted evolution of the deviation of the observable $D_A \times \frac{r_s^{fid}}{r_s}$ for various values of Ω_m (left panel) and w (right panel). The behavior of this observable is similar to that of $D_V(z) \times \frac{r_s^{fid}}{r_s}$ even though the blind spot with respect to the parameter Ω_m appears at a higher redshift ($z \simeq 2$), while at higher redshifts the sensitivity of this observable with respect to the parameter Ω_m is significantly reduced compared to the sensitivity of $D_V(z) \times \frac{r_s^{fid}}{r_s}$.

A comparison of the three BAO observable distances $\frac{D_M(z)}{r_s \sqrt{z}}$, $\frac{D_V(z)}{r_s \sqrt{z}}$ and $\frac{z D_H(z)}{r_s \sqrt{z}}$ [as $D_H(z) = \frac{c}{H(z)}$] for the Planck/ Λ CDM best fit parameter values along with the corresponding data from Table B.2 of the Appendix B is shown in Fig. 4.10. This plot is in excellent agreement with the corresponding plot of Ref. [48] (Fig. 14) even though here we superpose the Planck/ Λ CDM prediction with a significantly larger compilation of datapoints. As demonstrated in the next subsection the BAO data are in good agreement with the Planck/ Λ CDM parameter values.

4.3.2 Contour Shapes and Redshift Ranges

The presence of optimal and blind redshift ranges for the BAO observables with respect to cosmological parameters has an effect on the form of maximum likelihood contours obtained from data at various redshift ranges. In particular, the Figure of Merit (reciprocal of the area of confidence contours in

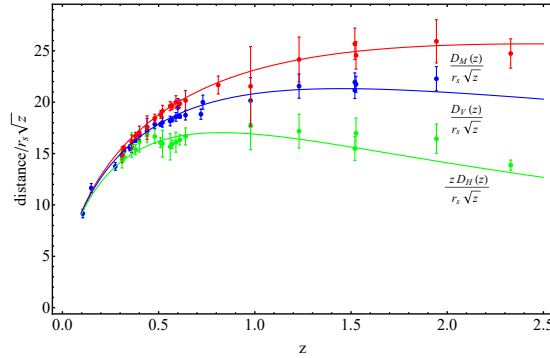


Figure 4.10: The BAO observable distances for the Planck/ Λ CDM best-fit parameter values along with the corresponding data from Table B.2 in the Appendix B. The data appear to be in good agreement with the Planck/ Λ CDM predictions.

parameter space) tends to decrease for datasets with redshifts close to blind redshift spots and increase for datasets with redshifts close to optimal redshift regions. In order to demonstrate this effect, we construct the confidence contours for the parameters Ω_m and w using the BAO observables in different redshift regions.

In order to construct χ^2 we first consider the vector

$$V_{BAO}^i(z_i, \Omega_m, w) \equiv BAO_i^m - BAO_{theoretical}^m, \quad (4.27)$$

where m runs from 1 to 3 indicating the different types of BAO data of Table B.2 in the Appendix B and the theoretical expressions for $D_A \times \frac{r_s^{fid}}{r_s}$, $D_V(z) \times \frac{r_s^{fid}}{r_s}$ and $H \times \frac{r_s}{r_s^{fid}}$ are given in Eqs. (1.57), (4.20) and (4.25) respectively. χ^2 is obtained as

$$\chi^2 = V^i F_{ij} V^j, \quad (4.28)$$

where F_{ij} is the Fisher matrix (inverse of the covariance matrix C_{ij}).

The covariance matrix for the $D_V(z) \times \frac{r_s^{fid}}{r_s}$ data takes the form

$$C_{ij, D_V \times (r_s^{fid}/r_s)}^{BAO, total} = \begin{pmatrix} \sigma_1^2 & 0 & 0 & \dots \\ 0 & C_{ij}^{WiggleZ} & 0 & \dots \\ 0 & 0 & \dots & \sigma_N^2 \end{pmatrix}, \quad (4.29)$$

where $N = 28$ and [1829]

$$C_{ij}^{WiggleZ} = F_{ij, WiggleZ}^{-1} = 10^4 \begin{pmatrix} 2.18 & -1.12 & 0.47 \\ -1.12 & 1.71 & -0.72 \\ 0.47 & -0.72 & 1.65 \end{pmatrix}^{-1}, \quad (4.30)$$

whereas for both $D_A \times \frac{r_s^{fid}}{r_s}$ and $H \times \frac{r_s}{r_s^{fid}}$ we have assumed a diagonal covariance matrix

$$C_{ij}^{BAO, total} = \begin{pmatrix} \sigma_1^2 & 0 & 0 & \dots \\ 0 & \sigma_2^2 & 0 & \dots \\ 0 & 0 & \dots & \sigma_N^2 \end{pmatrix}, \quad (4.31)$$

where N is equal to the considered number of datapoints.

The forms of Eqs. (4.29) and (4.31) are clearly oversimplifications of the actual covariance matrices, since these forms ignore possible correlations between the considered BAO data. However, to the best of

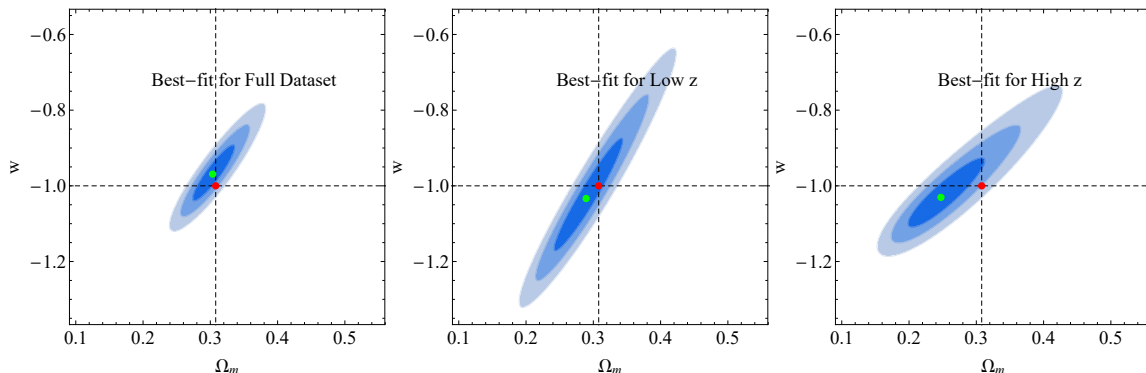


Figure 4.11: The $1\sigma - 3\sigma$ contours in the $\Omega_m - w$ parametric space. The contours describe the corresponding confidence regions using the full compilation of $D_V(z) \times \frac{r_s^{fid}}{r_s}$ data (left panel), low redshift ($z < 0.55$) data (middle panel) and high redshift ($z > 0.55$) data (right panel) from Table B.2 in the Appendix B. The red and green dots describe the Planck/ Λ CDM best fit and the best-fit values from the compilation of $D_V(z) \times \frac{r_s^{fid}}{r_s}$ data. Notice that at high z close to the blind spot for Ω_m and the optimum redshift for w , the thickness of the contours (uncertainty) increases along the Ω_m axis and decreases along the w axis (the contours are rotated clockwise) as expected from Fig. 4.6.

our knowledge the non-diagonal terms of the D_A and H covariance matrices are not publicly available. In order to estimate the magnitude of the effects of these terms we have performed Monte Carlo simulations including random nondiagonal terms to the covariance matrices for D_A and H of relative magnitude similar to the nondiagonal terms of the nondiagonal terms corresponding to D_V setting the magnitude of the matrix [67]

$$C_{ij} = \frac{1}{2} \sigma_i \cdot \sigma_j, \quad (4.32)$$

where σ_i and σ_j are the errors of the published datapoints i and j respectively. These simulations indicated that the likelihood contours and the best fit parameter values do not change more than 10% when we include the nondiagonal terms in the covariance matrix. Thus, possible reasonable correlations among datapoints are not expected to significantly affect our results [1830].

In the left panel of Fig. 4.11 we show the $1\sigma - 3\sigma$ $\Omega_m - w$ contour plots for the full $D_V(z) \times \frac{r_s^{fid}}{r_s}$ data of Table B.2 in the Appendix B using Eqs. (4.27)-(4.29) and ignoring the possible correlations among the datapoints. The best fit parameter values are within 1σ from the corresponding best fit Planck/ Λ CDM values (red dot).

Furthermore we construct the same contour plots for low-redshift $D_V(z) \times \frac{r_s^{fid}}{r_s}$ data (middle panel of Fig. 4.11), where $z < 0.55$ (14 datapoints), and for high-redshift $D_V(z) \times \frac{r_s^{fid}}{r_s}$ data (right panel of Fig. 4.11), where $z > 0.55$ (14 datapoints). The low-redshift data correspond to optimal redshift for the parameter Ω_m (see Fig. 4.6) and thus the confidence contours are thinner in the direction of the Ω_m axis while the contours are elongated in the w direction. In contrast the high-redshift data are close to the Ω_m blind spot and thus the confidence contours are thicker in the Ω_m direction (left panel), while the contours are suppressed in the w direction (as expected from Fig. 4.6) which indicates an optimal high-redshift range for the parameter w .

4.4 Distance Moduli from SNIa and from Gravitational Waves

The luminosity distance defined by Eq. (1.55) is an important cosmological observable that is measured using standard candles like SNIa or standard gravitational wave sirens, like merging binary neutron star

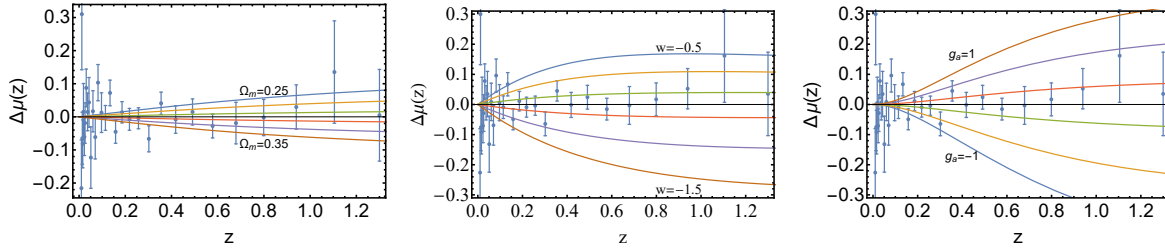


Figure 4.12: The deviation of the distance modulus observable $\Delta\mu$ as a function of redshift for Ω_m (left panel), w (middle panel) and g_α (right panel) superimposed with the JLA data of Table B.3 in the Appendix B.

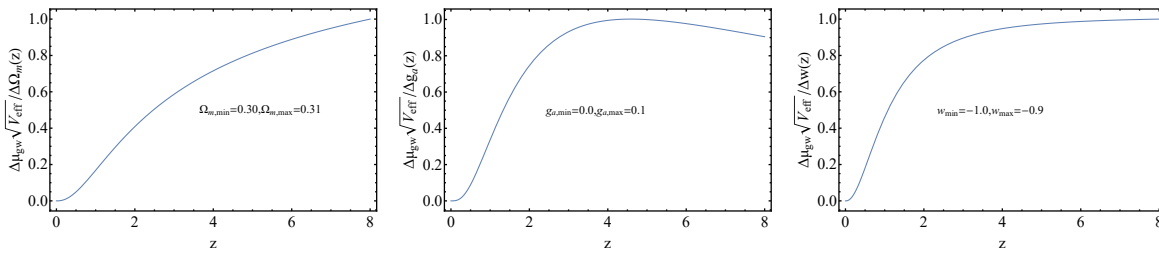


Figure 4.13: The sensitivity measure as a function of redshift z for Ω_m (left panel), g_α (middle panel) and w (right panel).

systems observed via multi-messenger observations (see Subsections 2.2.1 and 2.2.4).

The distance modulus $\mu = m - M$ is the difference between the apparent magnitude m and the absolute magnitude M of standard candle. Thus using Eq. (2.2) it is related to the luminosity distance d_L in Mpc as

$$\mu(z; \Omega_m, w) = 5 \log_{10} \left[\frac{d_L(z)}{\text{Mpc}} \right] + 25. \quad (4.33)$$

In the context of a varying effective Newton's constant $G_{\text{eff}}(z)$ the absolute magnitude of SnIa is expected to vary with redshift as [913, 914, 1831]

$$M - M_0 = \frac{15}{4} \log_{10} \left(\frac{G_{\text{eff}}}{G} \right), \quad (4.34)$$

where the subscript 0 refers to local value of M . Thus, for SnIa μ also depends on the evolution of $G_{\text{eff}}(z)$ (or equivalently on the parameter g_α) as

$$\mu(z; \Omega_m, w, g_\alpha) = 5 \log_{10}(d_L) + \frac{15}{4} \log_{10} \left(\frac{G_{\text{eff}}(z; g_\alpha)}{G} \right) + 25. \quad (4.35)$$

In the case of gravitational wave luminosity distance, the corresponding gravitational wave distance modulus obtained from standard sirens is of the form [1832]

$$\mu_{gw}(z; \Omega_m, w, g_\alpha) = 5 \log_{10} \left(d_L \sqrt{\frac{G_{\text{eff}}}{G}} \right) + 25. \quad (4.36)$$

In Fig. 4.12 we show the deviation $\Delta\mu$ as a function of redshift for Ω_m (left panel), w (middle panel) and g_α (right panel) superimposed with the JLA SnIa binned data of Table B.3 in the Appendix B. The corresponding sensitivity measure is shown in Fig. 4.13. Notice that even though the deviation

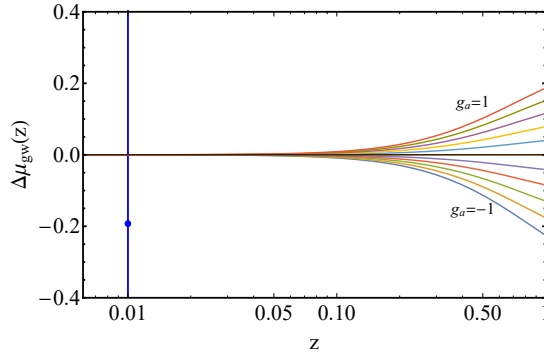


Figure 4.14: The deviation of the gravitational wave distance modulus with the parameter g_a . The only existing datapoint does not lead to any useful constraints.

$\Delta\mu_{gw}$ appears to be increasing with redshift for all the parameters considered, the absolute value of the sensitivity measure with respect to the parameter g_a has a maximum for redshifts in the range $z \in [4, 5]$, indicating the presence of an optimal redshift range.

The deviations $\Delta\mu_{gw}(z)$ with respect to the parameters Ω_m and w is identical to the corresponding deviations $\Delta\mu(z)$, since for $g_a = 0$ we have $\Delta\mu(z) = \Delta\mu_{gw}(z)$. The deviation $\Delta\mu_{gw}(z)$ with respect to the parameter g_a is shown in Fig. 4.14 along with the single available datapoint from the standard siren GW170817 [18, 1833]. Clearly even though standard siren data can in principle be used to constrain the evolution of G_{eff} , a dramatic improvement is required before such probes become competitive with growth and SnIa data.

4.5 Conclusions

In this Chapter we have demonstrated that the constraining power (sensitivity) of a wide range of cosmological observables on cosmological parameters is a rapidly varying function of the redshift where the observable is measured. In fact, this sensitivity in many cases does not vary monotonically with redshift but has degeneracy points (redshift blind spots) and maxima (optimal redshift ranges) which are relatively close in redshift space. The identification of such regions can contribute to the optimal design and redshift range selection of cosmological probes aimed at constraining specific cosmological parameters through measurement of cosmological observables.

In addition, we have shown that many of the recent $f\sigma_8$ RSD data, which tend to be at higher redshifts ($z > 0.8$) are close to blind spots of the observable $f\sigma_8$ with respect to all three cosmological parameters considered (Ω_m , w and g_a). A similar trend for probing higher redshifts also exists for upcoming surveys as demonstrated in Table 4.1. A more efficient strategy for this observable would be an improvement of the measurements at lower redshifts instead of focusing on higher redshifts. Such a strategy would lead to improved constraints on all three parameters considered.

Even though our analysis has revealed the generic existence of optimal redshifts and blind spots of observables with respect to specific cosmological parameters, it still has not taken into account all relevant effects that play a role in determining the exact location of these points in redshift space. For example, we have not explicitly taken into account the number of linear modes available to a survey in redshift space as well as the dependence of the effective volume V_{eff} on the number of tracers and their selection. We anticipate that these effects could mildly shift the location of the derived blind spots and optimal redshifts determined by our analysis.

The results of our analysis may be helpful in the proper design of upcoming missions aimed at measuring cosmological observables in specific redshift ranges.

Chapter 5

Modified Model for Gravity through Dimensional Reduction

The analysis presented in this chapter is based on the work which was done in collaboration with Prof. Leandros Perivolaropoulos and has been published in Physical Review D [2].

In this chapter using a dark matter density profile we reconstruct an effective field theory model for gravity at large distances from a central object by demanding that the vacuum solution has the same gravitational properties as the density profile has in the context of GR.

Modified theories of gravity include more degrees of freedom and parameters which are strongly constrained by a wide range of experiments and astrophysical/cosmological observations to be very close to the values predicted by GR (see e.g. [73–76]). Despite of its successes and simplicity, GR requires additional undetected matter/energy components to explain observations on galactic scales or larger. In particular, the existence of dark matter [87–90, 476, 1834, 1835] is required for the description of observed dynamics and structure formation on galactic scales or larger while dark energy with negative pressure or a fine tuned cosmological constant (see Ref. [81] for a review) is required for the consistency of GR with the observed accelerating cosmic expansion [118, 119, 1836]. Even on solar system scales or sub-mm scales there have been hints of possible inconsistency of the theory with particular observations (e.g. Pioneer anomaly [1837–1841]) or short range gravity experiments (peculiar oscillating signals in some datasets [1842]). In addition, the theory predicts the existence of unphysical singularities in a wide range of its solutions which should describe physical phenomena.

Any observed inconsistency between the geometric left hand side (LHS) of the Einstein equation and the matter-energy right hand side (RHS) is thus usually addressed by modifying the RHS through the conservative assumption of some yet undetected form of matter-energy chosen in such a way as to restore the equality of the geometric and matter parts of the Einstein equation. A more fundamental approach is to modify the geometric LHS of the Einstein which is equivalent to modifying the fundamental action of the gravitational theory. There is a wide range of modified gravity models aiming at the explanation of the accelerating expansion of the universe [135, 1843, 1844]. Such theories include scalar tensor theories [587, 1845–1847] including the most general class of Horndeski models [100, 1848], $f(R)$ theories [96, 111, 112, 584, 1849, 1850] which generalize the Ricci scalar R of the action to a general function $f(R)$, generalized teleparallel gravity $f(T)$ theories [114, 115, 1851, 1852] which generalize the torsion scalar T of the action to a general function of it, non-local gravity theories [1853–1855] which introduce nonlocal operators in the gravitational action which involve effectively an infinite sum of derivatives etc. On the other hand, modified gravity models (see Ref. [1856] for a review) aiming at the explanation of the dynamics of matter at galactic and cluster scales without dark matter are much more limited [1857, 1858]. This is due to the very diverse nature of matter dynamical behaviors that need to be

explained which appears to require a large number of parameters for the fundamental theory that would attempt to explain it without dark matter. The main representative of this class of theories is the modified Newtonian Dynamics (MOND) theory [1859–1861] based on the existence of a fundamental acceleration scale which has been recently shown however to be highly unlikely to exist [1862].

5.1 Introduction

An alternative approach towards a geometric fundamental description of the dynamics of matter on galactic and cluster scales without dark matter has been proposed by Grumiller [1863, 1864]. Assuming spherical symmetry of the metric and implementing dimensional reduction of the Einstein Hilbert action to two space-time dimensions ($t-r$) it was shown that the emerging 2-dimensional ST effective field theory action with a constant potential can be generalized to include a non-trivial potential. The simplest form of this potential with no infrared curvature singularities, leads to a generic Rindler constant acceleration term in the vacuum spherically symmetric metric of the new theory [1863]. It has been shown recently [1865] that such a term in the background metric can give rise to a new type of metastable topological defects (spherical domain walls). It was also argued that such a term can give rise to the observed velocity rotation curves of galaxies without incorporating dark matter [1866]. It was later shown [1867, 1868] however that the Rindler term is only able to provide acceptable fits to a relatively small number of observed velocity rotation curves which is limited to those rotation curves where the velocity continues to increase with distance through the halo. Such a behavior is not typical for most rotation curves which are either flat [87–89] or in fact tend to decrease with distance at large distances from the galactic core [1869]. Thus, the Rindler acceleration even though it is appealing due to its possible fundamental geometric origin, does not provide enough degrees of freedom to describe the data in contrast to the commonly used dark matter density profiles (Navarro-Frenk-White [1639, 1640] and Burkert [1870]) which provide excellent fits to the rotation curve data. Thus, the following questions arise:

- *Is it possible to generalize the fundamental 2-dimensional geometric effective action (and its scalar field potential emerging from dimensional reduction) such that the corresponding vacuum spherically symmetric metric reproduces the observed velocity rotation curves equally well as the standard dark matter density profiles?*
- *If yes, what is the form of the required geometric scalar field potential and how is it related to the simple Rindler potential of Refs. [1863, 1864]*
- *Can an arbitrary vacuum spherically symmetric metric be reproduced by a properly selected geometric scalar field potential?*

The goal of our analysis is to address these questions using both theoretical reconstruction of the fundamental action and direct comparison with specific velocity rotation data.

The structure of this Chapter is the following: In the next Section 5.2 we consider a class of simple spherically symmetric metrics in $3+1$ dimensions and identify the profiles and properties of the perfect fluids that can give rise to such metrics. In Section 5.3 we assume spherical symmetry and use it to dimensionally reduce the $3+1$ dimensional Einstein-Hilbert action to an effective two dimensional scalar-tensor action with a constant potential. We generalize this geometric potential thus modifying the gravitational action to an arbitrary form and derive the corresponding generalized vacuum spherically symmetric metric in terms of the geometric potential. In Section 5.4 we consider special forms of the geometric potential and of the background fluid and derive the corresponding metric. Thus the case of a constant potential (GR) we derive the Schwarzschild vacuum metric while for a simple quadratic potential we obtain the Rindler acceleration and cosmological constant terms in agreement with Ref. [1863]. We also reconstruct the geometric potential that leads to a vacuum metric that is identical with the metric derived assuming a given dark matter fluid density profile in the context of GR. In the context of a particular example we assume a Navarro-Frenk-White (NFW) [1639, 1640] density profile and derive the corresponding geometric potential and vacuum metric. We show that this metric generalizes the Rindler

term of the Grumiller metric and show fits of the velocity profiles it generates on typical galactic velocity rotation data. Finally in Section 5.5 we conclude and discuss the implications and possible extensions of our analysis. In what follows we assume a metric signature $+ - - -$.

5.2 Spherically Symmetric Metrics in GR and Perfect Fluids

Consider the spherically symmetric metric in 4-dimensions of the form

$$ds^2 = f(r)dt^2 - f(r)^{-1}dr^2 - r^2(d\theta^2 + \sin^2\theta d\phi^2) . \quad (5.1)$$

What is the most general form of perfect fluid energy momentum tensor that is consistent with this metric in the context of GR?

In order to address this question we set

$$f(r) = 1 - g(r) , \quad (5.2)$$

and obtain the Einstein tensor corresponding to this metric as

$$G_{\mu}^{\nu} = \begin{bmatrix} e_1(r) & 0 & 0 & 0 \\ 0 & e_1(r) & 0 & 0 \\ 0 & 0 & e_2(r) & 0 \\ 0 & 0 & 0 & e_2(r) \end{bmatrix} , \quad (5.3)$$

with

$$e_1(r) = \frac{g(r)}{r^2} + \frac{g'(r)}{r} , \quad (5.4)$$

$$e_2(r) = \frac{g'(r)}{r} + \frac{g''(r)}{2} . \quad (5.5)$$

Using Eqs. (5.4), (5.5) and the Einstein equations $G_{\nu}^{\mu} = \kappa T_{\nu}^{\mu}$ we find

$$\rho(r) = -p_r(r) = \frac{1}{\kappa r} \left[\frac{g(r)}{r} + g'(r) \right] , \quad (5.6)$$

$$p_{\theta}(r) = p_{\phi}(r) = -\frac{1}{2\kappa r} [2g'(r) + rg''(r)] , \quad (5.7)$$

where $\kappa = 8\pi G$ and the energy momentum tensor of the perfect fluid is

$$T_{\mu}^{\nu} = \text{diag} [\rho(r), -p_r(r), -p_{\theta}(r), -p_{\phi}(r)] . \quad (5.8)$$

Expanding $g(r)$ as a power series

$$f(r) = 1 - \sum_{n=-N}^N a_n r^n , \quad (5.9)$$

the Einstein tensor may be expressed as [1865]

$$G_{\nu}^{\mu} = \sum_{n=-N}^N \begin{bmatrix} a_n(n+1)r^{n-2} & 0 & 0 & 0 \\ 0 & a_n(n+1)r^{n-2} & 0 & 0 \\ 0 & 0 & \frac{1}{2}a_n n(n+1)r^{n-2} & 0 \\ 0 & 0 & 0 & \frac{1}{2}a_n n(n+1)r^{n-2} \end{bmatrix} . \quad (5.10)$$

Therefore, the energy - momentum tensor supporting the metric function Eq. (5.9) is

$$T_0^0 = \frac{1}{\kappa} \sum_{n=-N}^N a_n (1+n) r^{n-2} = \rho , \quad (5.11)$$

$$T_r^r = T_0^0 = -p_r , \quad (5.12)$$

$$T_\theta^\theta = \frac{1}{2\kappa} \sum_{n=-N}^N a_n n (1+n) r^{n-2} = -p_\theta , \quad (5.13)$$

$$T_\phi^\phi = T_\theta^\theta = -p_\phi . \quad (5.14)$$

As expected the term $n = -1$ (Schwarzschild metric) corresponds to the vacuum solution ($\rho = p = 0$) while for $n = 2$ we have the cosmological constant term (constant energy density-pressure). The Rindler constant acceleration term $n = 1$ is generated by a perfect fluid with

$$\rho = \frac{2a_1}{\kappa r} = -p_r = -2p_\theta = -2p_\phi . \quad (5.15)$$

For $n = 0$ (constant term in the metric function) we have the case of a global monopole (zero angular pressure components and energy density $\sim r^{-2}$ [1871–1875]). Thus any power law term of the spherically symmetric metric function $g(r)$ can be generated by a corresponding power law term of the energy momentum tensor of a perfect fluid provided that its radial pressure equation of state parameter w_r is -1 and there is equality between the angular pressure components.

The question we address in the next section is the following: *Can the spherically symmetric metric Eq. (5.1) also emerge as a vacuum solution in a modified gravity theory?* In other words, given a spherically symmetric fluid and its corresponding metric in the context of GR, what is the spherically symmetric modified gravity theory that leads to the same metric as its vacuum solution?

5.3 Modifying Spherically Symmetric GR through Dimensional Reduction

Consider the generalization of the spherically symmetric metric Eq. (5.1) to a d -dimensional form

$$ds^2 = f(r)dt^2 - f(r)^{-1}dr^2 - \Phi(r)^2 d\Omega , \quad (5.16)$$

where $\Phi(r)$ denotes the the surface radius and $d\Omega$ is the solid angle in $d - 2$ dimensions. The Einstein-Hilbert gravitational action describing the dynamics of the metric Eq. (5.16) in the context of GR is of the form

$$S = \frac{1}{2\kappa_d} \int d^d x \sqrt{-g^{(d)}} R^{(d)} + \int d^d x \sqrt{-g^{(d)}} \mathcal{L}_M^{(d)} , \quad (5.17)$$

where $R^{(d)}$ is the Ricci scalar in d dimensions and $\mathcal{L}_M^{(d)}$ is the matter Lagrangian density assumed to describe a spherically symmetric perfect fluid. It is straightforward to show using the metric Eq. (5.16) that the d -dimensional Ricci scalar can be expressed in terms of the corresponding 2-dimensional ($t - r$) scalar as [1876]

$$R^{(d)} = R^{(2)} - \frac{(d-2)(d-3)}{\Phi^2} [1 + (\partial\Phi)^2] - \frac{2(d-2)}{\Phi} \nabla^b \partial_b \Phi , \quad (5.18)$$

while for the d -dimensional spherically symmetric metric determinant we have

$$\sqrt{-g^{(d)}} = \Phi^{d-2} \sqrt{-g^{(2)}} . \quad (5.19)$$

Using Eqs. (5.18) and (5.19) in (5.17) we may integrate trivially over the angular coordinates and dimensionally reduce this action to a 2-dimensional ($t-r$) scalar-tensor action of the form

$$S = \frac{V_{d-2}}{2\kappa_d} \int d^2x \sqrt{-g^{(2)}} \left[\Phi^{d-2} R^{(2)} + (d-2)(d-3)\Phi^{d-4}(\partial\Phi)^2 - (d-2)(d-3)\Phi^{d-4} \right] + V_{d-2} \int d^2x \sqrt{-g^{(2)}} \mathcal{L}_M^{(2)}, \quad (5.20)$$

where V_{d-2} is the $d-2$ dimensional angular volume which is equal to 4π for $d=4$. For $d=4$ the 2-dimensional action takes the form

$$S = \frac{1}{4G} \int d^2x \sqrt{-g^{(2)}} \left[\Phi^2 R^{(2)} + 2(\partial\Phi)^2 - 2 \right] + S_M^{(2)}. \quad (5.21)$$

A modification of spherically symmetric GR can be implemented at this stage by generalizing the effective dimensionally reduced GR action Eq. (5.21) to a general ST action [1877, 1878] of the form

$$S = \frac{1}{4G} \int d^2x \sqrt{-g^{(2)}} \left[F(\Phi) R^{(2)} - Z(\Phi) (\partial\Phi)^2 - 2V(\Phi) \right] + S_M^{(2)}, \quad (5.22)$$

where $F(\Phi)$, $Z(\Phi)$, $V(\Phi)$ are arbitrary functions of the field Φ ¹

The origin of this generalized ST action Eq. (5.22) could either come from physics at the effective 2-dimensional ($t-r$) level or could emerge through dimensional reduction of a spherically symmetric ST theory.

In particular consider the d -dimensional scalar-tensor action

$$S = \frac{1}{2\kappa_d} \int d^d x \sqrt{-g^{(d)}} \left[\chi(\Phi) R^{(d)} - \zeta(\Phi) (\partial\Phi)^2 - U(\Phi) \right] + S_M^{(d)}, \quad (5.23)$$

which for $\chi(\Phi) = 1$, $\zeta(\Phi) = 0$ and $U(\Phi) = 0$ reduces to the Einstein - Hilbert action Eq. (5.17). It is straightforward to show that the action Eq. (5.23) can be dimensionally reduced using spherical symmetry and the metric Eq. (5.16) to the 2-dimensional action

$$S = \frac{V_{d-2}}{2\kappa_d} \int d^2x \sqrt{-g^{(2)}} \left\{ \chi(\Phi) \Phi^{d-2} R^{(2)} + [(d-2)(d-3)\chi(\Phi)\Phi^{d-4} + 2(d-2)\chi'(\Phi)\Phi^{d-3} - \zeta(\Phi)\Phi^{d-2}] (\partial\Phi)^2 - (d-2)(d-3)\chi(\Phi)\Phi^{d-4} - \Phi^{d-2} U(\Phi) \right\} + S_M^{(2)}, \quad (5.24)$$

where the prime ($'$) denotes derivative with respect to the surface radius field Φ . Clearly for $d=4$ the action Eq. (5.24) reduces to Eq. (5.22) by setting

$$F(\Phi) = \chi(\Phi)\Phi^2, \quad (5.25)$$

$$Z(\Phi) = -2\chi(\Phi) - 4\chi'(\Phi)\Phi + \zeta(\Phi)\Phi^2, \quad (5.26)$$

$$V(\Phi) = \chi(\Phi) + \frac{\Phi^2}{2} U(\Phi). \quad (5.27)$$

In what follows we set $d=4$. Variation of the action Eq. (5.22) with respect to Φ leads to the equation of motion (EOM)

$$F'(\Phi)R^{(2)} + Z'(\Phi)(\partial\Phi)^2 + 2Z(\Phi)\nabla^b\partial_b\Phi - 2V'(\Phi) = -2G \frac{\delta\mathcal{L}_M^{(2)}}{\delta\Phi}, \quad (5.28)$$

¹Note that for the dimensionally reduced metric $\Phi(r)$ can be considered as a scalar field (up to a dimensionful parameter) in correspondence with e.g. the radion field which is an effective scalar field in 4-dimensions describing the dynamics of extra dimensions in a cosmological setup [1762] in the context of an effective ST theory in 4-dimensions.

and variation with respect to $g^{\mu\nu}$ leads to the EOM

$$[\nabla_\mu \partial_\nu - g_{\mu\nu} \nabla^a \partial_a] F(\Phi) + Z(\Phi) \left[\partial_\mu \Phi \partial_\nu \Phi - \frac{1}{2} g_{\mu\nu} (\partial\Phi)^2 \right] = g_{\mu\nu} V(\Phi) - 2GT_{\mu\nu}^{(2)}. \quad (5.29)$$

Using the 2-dimensional metric

$$ds^2 = f(r)dt^2 - f(r)^{-1}dr^2, \quad (5.30)$$

it is straightforward to show that the 2-dimensional Ricci scalar is of the form

$$R^{(2)} = \frac{d^2 f}{dr^2}. \quad (5.31)$$

Using $\mathcal{L}_M^{(2)} = T = \rho^{(2)} - p_r^{(2)}$ [1879], Eq. (5.31) and the ansatz $\Phi = r$ in Eq. (5.28) we obtain the EOM

$$f''F' - 2Zf' - Z'f - 2V' = -2G(\rho'^{(2)} - p_r'^{(2)}), \quad (5.32)$$

where $\rho^{(2)}$ and $p_r^{(2)}$ are the 2-dimensional density and pressure respectively and the prime ($'$) denotes derivative with respect to r .

Also for $\mu = \nu = 0$ in Eq. (5.29) we obtain (with the same ansatz for Φ)

$$f'F' + 2fF'' + Zf - 2V = -4G\rho^{(2)}. \quad (5.33)$$

Similarly for $\mu = \nu = 1$ Eq. (5.29) gives

$$f'F' - Zf - 2V = 4Gp_r^{(2)}. \quad (5.34)$$

The system Eqs. (5.32)-(5.34) is overdetermined since there is only one unknown function $f(r)$. Thus for a solution to exist Eqs. (5.32)-(5.34) must be equivalent to each other (up to a constant of integration). It may be shown that this consistency requires that

$$Z = -F'' \quad , \quad \rho^{(2)} = -p_r^{(2)}. \quad (5.35)$$

Indeed using Eqs. (5.35), the system Eqs. (5.32)-(5.34) is equivalent to a single equation

$$f'F' + fF'' - 2V = -4G\rho^{(2)} = 4Gp_r^{(2)}. \quad (5.36)$$

The general equation Eq. (5.36) connects the metric function f with the geometric potential V emerging from dimensional reduction and the nonminimal coupling F in the presence of a static spherically symmetric perfect fluid whose equation of state parameter is -1 . Thus, any spherically symmetric metric of the form Eq. (5.1) can emerge either due to an appropriate perfect fluid or as a vacuum solution of dimensionally reduced modified gravity with properly selected nonminimal coupling F and/or potential V .

In what follows we focus on modifications of GR due to the geometric potential V and fix F to the GR form $F = \Phi^2$ implying $Z = -2$ (from Eq. (5.35)). Then Eq. (5.36) becomes

$$rf' + f - V = -2G\rho^{(2)} = 2Gp_r^{(2)}. \quad (5.37)$$

In order to quantify deviations from GR we set

$$f(r) = 1 - g(r), \quad (5.38)$$

$$V(\Phi) = 1 + V_1(\Phi), \quad (5.39)$$

and expressing the dimensionally reduced density $\rho^{(2)}$ in terms of its 4-dimensional counterpart ρ as

$$\rho^{(2)}(r) = 4\pi\Phi^2\rho(r), \quad (5.40)$$

in Eq. (5.37), we obtain

$$\rho_{tot}(r) = \rho_m(r) + \rho_V(r) = \frac{1}{\kappa r} \left[\frac{g(r)}{r} + g'(r) \right], \quad (5.41)$$

where the geometric effective energy density is defined as

$$\rho_V(r) \equiv -\frac{V_1(\Phi)}{\kappa r^2}. \quad (5.42)$$

Therefore the generalization of the scalar-tensor potential leads to an effective energy density of geometric origin which generates the same spherically symmetric metric as a corresponding spherically symmetric perfect fluid with equation of state parameter $w = -1$ and energy density $\rho_m(r) = \rho_V(r)$. This derived equivalence between geometric and matter energy density allows the reconstruction of the geometric potential by demanding that its gravitational effects in the vacuum should be identical with the gravitational effects of a given matter fluid in the context of GR. This reconstruction from a realistic dark matter profile will be the main focus of the next section.

5.4 Special Cases - Reconstruction of Gravitational Action

5.4.1 Vacuum GR and Grumiller's gravity model

A special case of the geometric potential introduced in the previous section has been considered by Grumiller [1863, 1864]. In particular, the following dimensionally reduced action was investigated

$$S = \frac{1}{4G} \int d^2x \sqrt{-g^{(2)}} [\Phi^2 R^{(2)} + 2(\partial\Phi)^2 + 6\Lambda\Phi^2 - 8\alpha\Phi - 2]. \quad (5.43)$$

This is a special case of the general action Eq. (5.22) with the GR coupling $F = \Phi^2$, $Z = -2$ and a geometric potential of the form

$$V(\Phi) = 1 + 4\alpha\Phi - 3\Lambda\Phi^2. \quad (5.44)$$

The ansatz $\Phi = r$ and our general reconstruction equation Eq. (5.41) leads to the Schwarzschild-Rindler-deSitter metric function as a vacuum solution ($\rho_m = 0$)

$$f(r) = 1 - 2GM/r + 2\alpha r - \Lambda r^2, \quad (5.45)$$

in agreement with Grumiller's metric [1863].

The main advantages of the Grumiller potential Eq. (5.44) include its simplicity and its generic nature as it involves terms that dominate at large distances while at the same time it does not lead to any curvature singularities at infinity where the Ricci scalar Eq. (5.31) remains finite. On the other hand the metric function Eq. (5.45) has been used to reconstruct the velocity profiles of galaxies without dark matter with mixed results [1866–1868]. Even though it was found that the constant acceleration Rindler term can provide satisfactory fits to the observed velocity rotation curves of some galaxies in regions where these curves are rising with distance it became clear that for universal fits more parameters are needed in the potential. Such parameters however should be introduced in a way that is most efficient phenomenologically i.e. inspired from observed dark matter density profiles while at the same time they preserve the advantages of the Grumiller potential (simplicity and lack of large scale singularities). Using these principles in the next subsection we generalize the Grumiller geometric potential by demanding that the new potential reproduces in the vacuum the gravitational effects of a well known dark matter density profile parametrization: the Navarro-Frenk-White density profile [1639, 1640].

5.4.2 Reconstruction of Geometric Potential

The Navarro-Frenk-White (NFW) profile [1639, 1640] can give good fits to a wide range of observed rotation curves of galaxies in the context of general relativity (GR). It is of the form

$$\rho_{NFW}(r) = \frac{\rho_o}{\frac{r}{R_s} \left(1 + \frac{r}{R_s}\right)^2}, \quad (5.46)$$

where the scale radius R_s and ρ_o are parameters which vary from halo to halo.

The GR gravitational effects of this profile can be reproduced in the vacuum of a modified gravity model with a geometric potential reconstructed using Eq. (5.42) as

$$\rho_V(r) \equiv -\frac{V_1(\Phi)}{\kappa r^2} = \rho_{NFW}(r), \quad (5.47)$$

which leads to a potential of the form

$$V(\Phi) = 1 + \frac{4\alpha\Phi}{(1 + \beta\Phi)^2}, \quad (5.48)$$

with $\beta = \frac{1}{R_s}$ and $\alpha = 2\pi G\rho_o R_s$. This potential reduces to the Rindler-Grumiller potential [1863] for $\beta = 0$. The new parameter β introduces no large scale curvature singularities while it is designed to maximize the efficiency of fits to the observed rotation curves to the extent that such fit is obtained by the NFW density profile in the context of GR. Also the above potential reconstruction method can be easily generalized for any other density profile.

Solving Eq. (5.41) in the vacuum ($\rho_m = 0$) with the geometric density ρ_V obtained from the reconstructed potential Eq. (5.48) we obtain the term $g(r)$ of the metric function

$$g(r) = \frac{C}{r} - \frac{4\alpha \left[\frac{1}{1+\beta r} + \ln(1 + \beta r) \right]}{\beta^2 r}, \quad (5.49)$$

where C is a constant of integration. Expansion of $g(r)$ of Eq. (5.49) as a power series demonstrates that this metric function is a generalization of the Rindler-Grumiller metric function Eq. (5.45) for $\Lambda = 0$

$$g(r) = \frac{C - \frac{4\alpha}{\beta^2}}{r} - 2\alpha r + \frac{8}{3}\alpha\beta r^2 + O(r)^3, \quad (5.50)$$

which after a redefinition of the integration constant C clearly reduces to the Rindler-Grumiller metric function for $\beta r \ll 1$. Setting $C = 2GM + \frac{4\alpha}{\beta^2}$ and using Eq. (5.38), the metric function $f(r)$ becomes

$$f(r) = 1 - \frac{2GM}{r} - 4\alpha \frac{1 - \frac{1}{1+\beta r} - \ln(1 + \beta r)}{\beta^2 r}, \quad (5.51)$$

which generalizes the Grumiller metric Eq. (5.45) with one additional parameter (β) and is based on the geometric potential reconstructed from the NFW density profile. In the next subsection we check the efficiency of this metric in fitting two representative observed velocity rotation curves. The quality of fit will also be compared with the corresponding fit of of the Rindler-Grumiller metric [1863].

5.4.3 Fitting Velocity Rotation Curves

It is straightforward to show that the radial timelike geodesics in a background metric of the form Eq. (5.1) may be written as

$$\frac{1}{2} \left(\frac{dr}{d\tau} \right)^2 + V^{\text{eff}} = \frac{k^2}{2}, \quad (5.52)$$

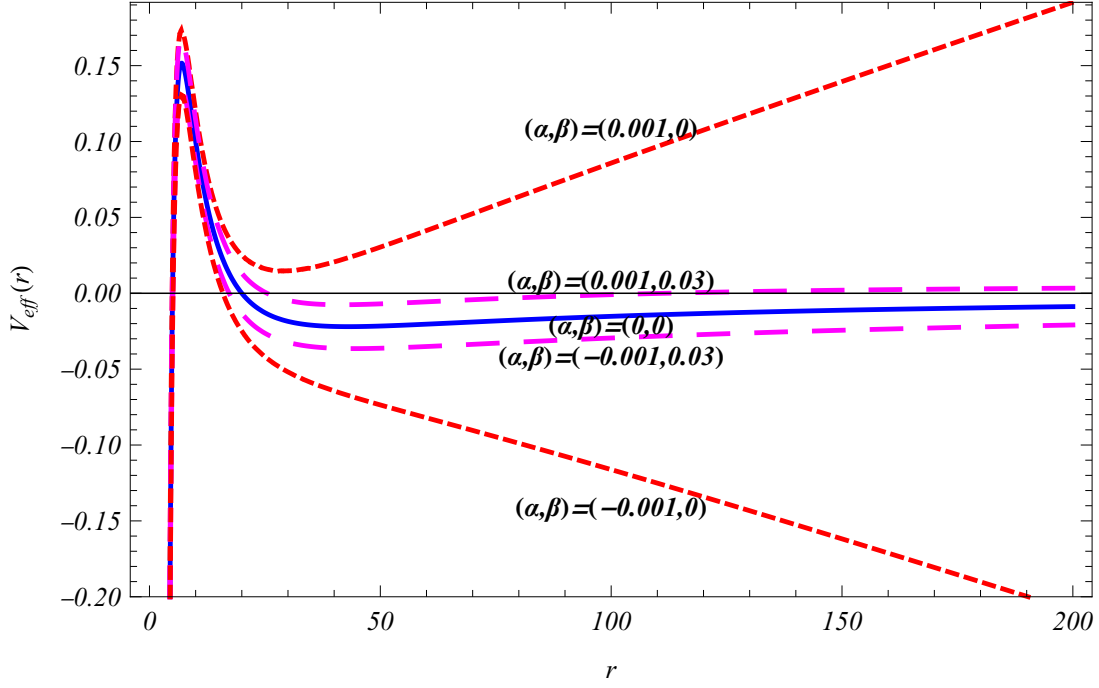


Figure 5.1: The effective potential Eq. (5.55) that determines the velocity rotation curves for parameter values $l = 10$, $M = 2$. The GR prediction (continuous blue line) is obtained for $\alpha = 0$ while the upper and lower red short-dashed lines correspond to the Rindler metric ($\beta = 0$) with $\alpha > 0$ and $\alpha < 0$ respectively. The upper and lower pink long-dashed lines correspond to the metric of the reconstructed potential ($\beta > 0$) for $\alpha > 0$ and $\alpha < 0$ respectively. In the later cases the GR prediction is obtained for large enough values of r .

where k is a constant,

$$V^{\text{eff}} = \frac{f(r)}{2} \left(1 + \frac{l^2}{r^2} \right), \quad (5.53)$$

is the effective potential and l is the constant angular momentum per unit mass.

In the special case of the vacuum Schwarzschild-Rindler-deSitter metric function Eq. (5.45) the effective potential reads

$$V^{\text{eff}} = -\frac{GM}{r} + \frac{l^2}{2r^2} - \frac{GMl^2}{r^3} - \frac{\Lambda r^2}{2} + \alpha r \left(1 + \frac{l^2}{r^2} \right). \quad (5.54)$$

In what follows we set $\Lambda = 0$ since the effects of the cosmological constant can be ignored on galactic scales. For the metric function Eq. (5.51) emerging from the NFW reconstructed potential Eq. (5.48) we have

$$V^{\text{eff}} = -\frac{GM}{r} + \frac{l^2}{2r^2} - \frac{GMl^2}{r^3} - \frac{2\alpha}{\beta^2 r} \left[1 - \frac{1}{1 + \beta r} - \ln(1 + \beta r) \right] \left(1 + \frac{l^2}{r^2} \right), \quad (5.55)$$

where we have dropped the constant terms on the RHS of Eqs. (5.54) and (5.55). A plot of this effective potential for various values of parameters is shown in Fig. 5.1. The predicted rotation velocities of test particles may be approximated as

$$v^2(r) \simeq r \left. \frac{\partial V^{\text{eff}}}{\partial r} \right|_{l=0}, \quad (5.56)$$

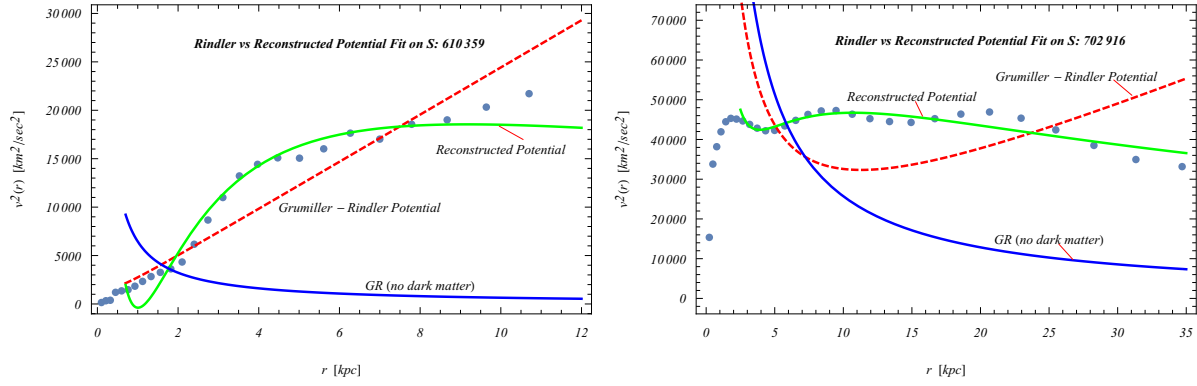


Figure 5.2: The best fit forms of the velocity profiles Eq. (5.57) (red dashed curve) and Eq. (5.58) (green continuous curve) on the observed halo profiles (thick dots) of two typical galaxies (S:610359 left panel and S:702916 right panel). The blue continuous shows the fit of GR without dark matter which is clearly poor.

where we have set $l = 0$ to avoid double counting of the angular momentum [1868]. Thus for the Schwarzschild-Rindler metric in the dark matter halo we have [1863, 1880]²

$$v^2(r) = \frac{GM}{r} + \alpha r, \quad (5.57)$$

where M is the luminous mass in the galactic core. For the velocity profile corresponding to the NFW reconstructed potential Eq. (5.55) we have

$$v^2(r) = \frac{GM}{r} + \frac{2\alpha}{\beta^2 r} \left[1 + \frac{\beta r - 1}{1 + \beta r} - \frac{\beta r}{(1 + \beta r)^2} - \ln(1 + \beta r) \right]. \quad (5.58)$$

The predicted rotation velocities Eqs. (5.57) and (5.58) can also be derived from the effective potentials Eqs. (5.54) and (5.55) assuming circular motion. Setting

$$\frac{dV^{\text{eff}}}{dr} = 0, \quad (5.59)$$

solving Eq. (5.59) for the angular momentum $l = vr$ and ignoring higher order terms. For example for the Grumiller effective potential Eq. (5.54) we obtain

$$v^2(r) \simeq \frac{GM}{r} + \alpha r + 2GM\alpha + \frac{3G^2M^2}{r^2} - \alpha^2 r^2, \quad (5.60)$$

which reduces to Eq. (5.57) if we ignore higher order terms in M and α .

The rotation curve is the sum of the following three terms expressed by

$$v^2(r) = v_G^2(r) + v_S^2(r) + v_{GM}^2(r), \quad (5.61)$$

where $v_G^2(r)$, $v_S^2(r)$ and $v_{GM}^2(r)$ are the different contributions in velocity of gas, stars and gravitational model (Rindler-Grumiller or reconstructed potential) respectively. The term $v_{GM}^2(r)$ gives rise to the velocity rotation curves of galaxies without incorporating dark matter halo. We assume that the density (of gas and stars) drops to zero at r_{min} . Thus, in our analysis, we use data in the range $r_{min} < r < r_{max}$ and for a total mass M we obtain the best fit forms of the velocity profiles corresponding the Rindler-Grumiller and reconstructed geometric potential.

²For further developments of this velocity profile see Refs. [1881, 1882]

Table 5.1: The best fit values of parameters and the corresponding value of the adjusted R^2 of the velocity profiles Eqs. (5.57) and (5.58) on the observed halo profiles of two typical galaxies S:610359 and S:702916 (rotation curve data obtained from Ref. [59]).

Galaxy	Grumiller-Rindler Potential			Reconstructed Potential			
	α [$\times 10^{-11} \frac{m}{s^2}$]	M [$\times 10^{10} M_\odot$]	R^2	α [$\times 10^{-9} \frac{m}{s^2}$]	β [$\times 10^{-20} m^{-1}$]	M [$\times 10^{10} M_\odot$]	R^2
S : 610359	7.90 ± 0.36	0.01 ± 0.02	0.959	-4.10 ± 0.16	3.17 ± 0.13	0.32 ± 0.02	0.983
S : 702916	4.64 ± 0.55	4.11 ± 0.47	0.923	-4.78 ± 0.38	1.79 ± 0.12	3.72 ± 0.27	0.998

In Fig. 5.2 we show the best fit forms of the velocity profiles Eqs. (5.57) (red dashed curve) and (5.58) (green continuous curve) on the observed halo profiles (thick dots) of two typical galaxies (S:610359 left panel and S:702916 right panel). Velocity rotation data were obtained from the 'S-sample' of Ref. [59]. The S:610359 [1883] (also known as UGC 10359) has a typical rising velocity profile and is a SB(s)cdpec³ galaxy from Gassendi H α survey of SPirals (GHASP) [1885]. The spiral galaxy S:702916 [1883] (also known as UGS 2916) has a flat and slowly dropping velocity profile and is a Sab⁴ galaxy from early type galaxies survey [1886].

Clearly the velocity profile corresponding to the reconstructed geometric potential provides a much better fit to the data for both observed velocity profiles and especially for the flat velocity profile. This is demonstrated quantitatively by the adjusted R^2 statistic [1887–1889] which measures the quality of fit of a parametrization to a given set of data penalizing also for increased number of parameters. As shown in Table 5.1, the value of the adjusted R^2 is much closer to its optimal value 1 in the case of the velocity profile corresponding the reconstructed geometric potential than the Grumiller Rindler potential or the simple Newtonian potential without dark matter. In Table 5.1 we also show the best fit values of parameters for each fitted velocity profile which in the case of Rindler potential agrees with previous studies [1864, 1868, 1890, 1891]. Notice that the best fit value of α for the reconstructed potential is $\alpha < 0$ with is consistent with Eq. (5.47) and the fact that $\rho_{NFW} > 0$.

5.5 Conclusions

In this Chapter we have used dimensional reduction of spherically symmetric gravity to construct a modified gravity model whose vacuum spherically symmetric metric has the same gravitational effects as the NFW dark matter density profile in GR. The model is a generalization of the Grumiller model whose vacuum spherically symmetric metric includes a Rindler term in addition to the standard Schwarzschild and cosmological constant terms. We have also shown that for any spherically symmetric perfect fluid with proper equation of state ($w = -1$) there is a modified gravity model, defined by a geometric potential,

³A late-type barred peculiar spiral galaxy. It have well-developed, open, and knotty spiral arms with little or no bulge and without rings structures (see Ref. [1884] for morphology types of galaxies)

⁴An intermediate-type unbarred spiral galaxy with tightly-wrapped spiral arms and a significant bulge (see Ref. [1884])

whose spherically symmetric vacuum metric is the same as the GR metric in the presence of the given fluid.

In particular we have shown that in order to reproduce the GR gravitational effects of the NFW density profile in the vacuum, the reconstructed dimensionally reduced geometric potential is of the form $V(\Phi) = 1 + 4\alpha\Phi/(1 + \beta\Phi)^2 - 3\Lambda\Phi^2$ where α, β are parameters and $\Phi(r)$ is a field emerging from dimensional reduction. In the limit $\beta \rightarrow 0$ this geometric potential reduces to the Grumiller potential Eq. (5.44) [1863, 1864].

The reconstructed potential has the following interesting features:

- It leads to a vacuum metric that provides significantly better fits to the velocity rotation profiles than the Grumiller linear potential term that leads to Rindler term in the vacuum metric.
- It leads to a vacuum metric that reduces to the GR vacuum on scales much larger than the β^{-1} or the galactic scales. Thus on cosmological scales it is consistent with Λ CDM. In contrast, the Grumiller-Rindler term is comparable to the cosmological constant on cosmological scales thus spoiling homogeneity and diverging from the standard Λ CDM cosmic accelerating expansion.
- Due to its non-polynomial form, it involves no IR curvature singularities while being distinct from the Grumiller potential thus demonstrating that this potential is not the only potential free from IR singularities.

The cosmological effects of the model considered could be examined under the assumption of the existence of a large number of homogeneously distributed isotropic centers leading to large scale homogeneity in addition to isotropy around a single center (spherical symmetry). In such a physical setup, the geometric fluid density ρ_V defined in Eq. (5.47) could be extended on cosmological scales as a homogeneous and isotropic fluid by replacing r with the scale factor a over the Hubble parameter H_0 . Thus, on dimensional grounds the corresponding homogeneous geometric fluid would have an energy density scaling as

$$\rho_V(a) = -\frac{4\alpha H_0}{\kappa a(1 + \beta a/H_0)^2}, \quad (5.62)$$

where the Hubble parameter H_0 has been introduced on dimensional grounds. The derivation of Eq. (5.62) has been heuristic and based mainly on dimensional analysis. A proper derivation would involve the detailed superposition of homogeneously distributed centers of isotropy and is beyond the goals of our analysis. Nevertheless, the following comments can be made on this predicted geometric homogeneous dark matter

- For $\beta = 0$ the geometric fluid energy density reduces to the Rindler fluid whose energy density scales like $1/r$ or $1/a$ in a cosmological setup. This scaling is distinct from the matter density ($\sim 1/a^3$), the effects of spatial curvature ($\sim 1/a^2$) and the cosmological constant (constant effective density). Such a physically motivated and simple term can be efficiently constrained using cosmological data probing the evolution of the Hubble parameter $H(a)$ even though a homogeneous component of ordinary dark matter would be required for a proper fit in addition to the cosmological constant.
- For $\beta \gg H_0$ which is expected for a value of β reconstructed from galactic rotation curves, the geometric fluid density Eq. (5.62) scales as $1/a^3$ ie as ordinary homogeneous dark matter. Thus such a geometric fluid would not only provide better fits of galactic rotation curves but could also provide the homogeneous dark matter on cosmological scales. Such a geometric dark matter would have a predicted scaling signature of the form Eq. (5.62) leading to constraints on β from both galactic rotation curve data and cosmological data probing the cosmic expansion rate. The consistency of these constraints could provide an efficient test for this class of models.

Other interesting extensions of our analysis include the following

- The reconstruction of the geometric potential obtained from other special cases of spherically symmetric vacua. Such metrics could have oscillating components leading to oscillating terms in Newton's law at sub-mm scales which appear to be mildly favored by some short range gravity experiment data [170, 171].
- The use of solar system data, short range gravity experiments data or other velocity profile data to impose constraints on the parameters α and β of the reconstructed potential Eq. (5.48).
- The generalization of the dimensionally reduced modified gravity model Eq. (5.22) in different directions including a more general form of the nonminimal coupling (beyond $F(\Phi) = \Phi^2$), the consideration of $f(R^{(2)})$ extensions of the dimensionally reduced model or the generalization of the ansatz $\Phi = r$ used for the derivation of the spherically symmetric vacuum metric.

In conclusion, dimensional reduction in the context of spherical symmetry offers an interesting point of view for the modification of GR and can lead to a wide range of testable physically motivated models for gravity.

Chapter 6

Observational Constraints on the GUP Parameter with Maximum Length Quantum Mechanics

The analysis presented in this chapter is based on the work which was done in collaboration with Prof. Leandros Perivolaropoulos and has been published in Physical Review D [3].

In this chapter, we derive the generalized form of the primordial power spectrum of cosmological perturbations generated during inflation due to the quantum fluctuations of scalar and tensor degrees of freedom in the context of a generalization of quantum mechanics involving a maximum measurable length scale.

A central issue of fundamental research is the unification of Quantum Theory (QT) and general relativity (GR) in the framework of Quantum Gravity (QG). A critical scale in the context of this unification is the Planck scale defined as $l_{pl} = \sqrt{\frac{\hbar G}{c^3}} = 10^{-35}$ m (see Ref. [1892], for a review) which has been shown to be the minimum measurable scale if both QT and GR are applicable. Indeed it may be shown [1893] that the high energies required to probe scales smaller than the Planck scale would lead to the formation of a black hole through the gravitational disturbances of spacetime structure which would prohibit any measurement on smaller scales. The existence of such a minimum measurable length would lead to a modification of the Heisenberg Uncertainty Principle [1144, 1145] (HUP) to the so-called Generalized (Gravitational) Uncertainty Principle (GUP) (see Ref. [1171], for a review)

$$\Delta x \Delta p \geq \frac{\hbar}{2} (1 + \beta \Delta p^2), \quad (6.1)$$

where β is the GUP parameter defined as $\beta = \beta_0 / M_{pl} c^2 = \beta_0 l_{pl}^2 / \hbar^2$, $M_{pl} c^2 = 10^{19}$ GeV, l_{pl} is the 4-dimensional fundamental Planck scale and β_0 is a dimensionless parameter expected to be of order unity. Such a GUP is closely related to the concept of noncommutative geometry [1894] and has been extensively investigated in Refs. [1146–1156, 1158–1161, 1163–1166, 1168]. In particular interest in a minimum measurable length or equivalently in a ultraviolet cutoff has been motivated by studies of string theory [1895–1901], loop quantum gravity [1902–1908], quantum geometry [1909], Doubly Special Relativity (DSR) [1910–1915] and by black hole physics [1148, 1157, 1162, 1169] or even Gedanken experiments [1916] and thermodynamic properties of gravity [1917].

Several phenomenological implications of minimal length theories and quantum gravity phenomenology were investigated and a number of researchers have studied phenomenological aspects of GUP effects in several contexts (e.g. in Refs. [1918, 1919] atomic physics experiments such as Lamb's shift and Landau levels have been considered and constraints on the minimum length scale parameter β have been

estimated). In Refs. [1920–1924] a model that is consistent with string theory, black hole physics and DSR is presented and discussed. This model of GUP predicts both a minimal observable length and a maximal momentum simultaneously [1921, 1925].

6.1 Introduction

The existence of a minimum measurable length is closely related to the existence of the black hole horizon which tends to form if length scales below the Planck scale are probed. Correspondingly, there is a maximum measurable length associated with the cosmological particle horizon [1926, 1927] which provides due to causality a maximum measurable length scale in the Universe. The particle horizon corresponds to the length scale of the boundary between the observable and the unobservable regions of the universe. This scale at any time defines the size of the observable universe. The physical distance to this maximum observable scale at the cosmic time t is given by e.g. [79, 1928]

$$l_{max}(t) = a(t) \int_0^t \frac{c dt}{a(t)}, \quad (6.2)$$

where $a(t)$ is the cosmic scale factor. For the best fit Λ CDM cosmic background at the present time t_0 we have

$$l_{max}(t_0) \simeq 14 \text{ Gpc} \simeq 10^{26} \text{ m}. \quad (6.3)$$

This existence of such a maximum measurable length would lead to modified version of the GUP of the form ¹ [55]

$$\Delta x \Delta p \geq \frac{\hbar}{2} \frac{1}{1 - \alpha \Delta x^2}. \quad (6.4)$$

As shown in Fig. 6.1, this GUP indicates the existence of maximum position uncertainty [55]

$$l_{max} \equiv \Delta x_{max} = \alpha^{-1/2}, \quad (6.5)$$

due to the divergence of the RHS of Eq. (6.4). As shown in Fig. 6.1 the existence of a maximum length scale is associated with the presence of a minimum momentum scale Δp_{min} .

The GUP (6.4) originates from a commutation relation of the form

$$[x, p] = i\hbar \frac{1}{1 - \alpha x^2}. \quad (6.6)$$

It is straightforward to show (see in Appendix C) that this commutation relation leads to the GUP (6.4) using the general uncertainty principle for the pair of non-commuting observables x, p

$$\Delta x \Delta p \geq \frac{\hbar}{2} | \langle [\hat{x}, \hat{p}] \rangle |, \quad (6.7)$$

with

$$\Delta x \equiv \sqrt{\langle (\hat{x} - \langle \hat{x} \rangle)^2 \rangle}, \quad (6.8)$$

$$\Delta p \equiv \sqrt{\langle (\hat{p} - \langle \hat{p} \rangle)^2 \rangle}, \quad (6.9)$$

where \hat{x}, \hat{p} are the operator representations of the observables x, p .

¹A perturbative version of this GUP was introduced in Ref. [1929] as $\Delta x \Delta p \geq 1 + \alpha \frac{\Delta x^2}{L_*^2}$ (where α is a constant of order unity and L_* is the characteristic, large length scale) and called extended uncertainty principle (EUP) by many authors [1917, 1929–1936]. Here we keep the notation 'GUP' instead of 'EUP' for consistency with Ref. [55].

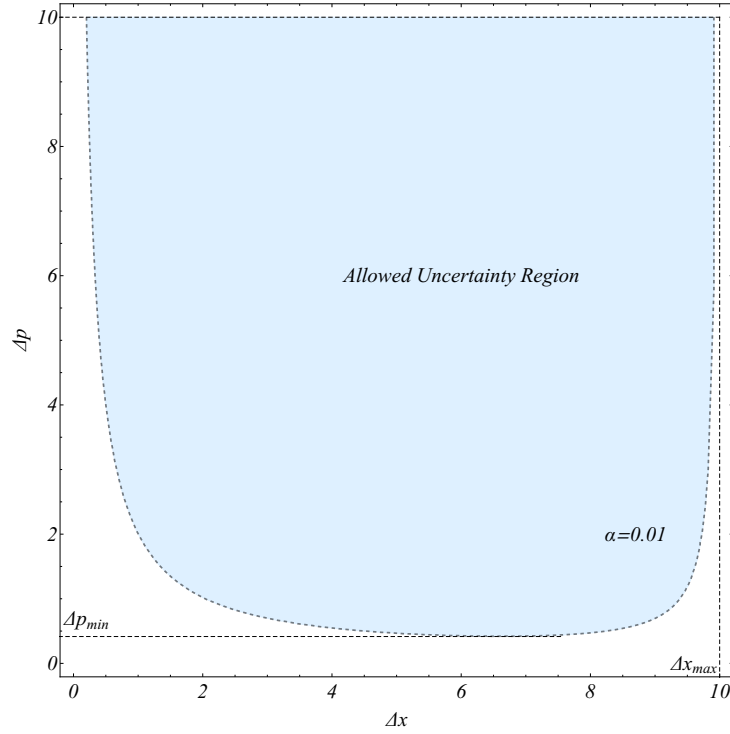


Figure 6.1: The deformation of the HUP in accordance with Eq. (6.4) after rescaling to dimensionless form using a characteristic length scale of the quantum system (from Ref. [55]).

The commutation relation (6.6) may be represented as shown in Appendix C by position and momentum operators of the form

$$p = \frac{1}{1 - \alpha x_0^2} p_0 = (1 + \alpha x_0^2 + \alpha^2 x_0^4 + \dots) p_0 , \quad (6.10)$$

$$x = x_0 , \quad (6.11)$$

where x_0 and p_0 are the usual position and momentum operators satisfying the Heisenberg commutation relation $[x_0, p_0] = i\hbar$.

The representation Eqs. (6.10), (6.11) may be used to solve the Schrodinger equation for simple quantum systems to find the dependence of the energy spectrum on the maximum measurable scale l_{max} . Such an analysis has indicated [55] that the current cosmic particle horizon is too large to lead to any observable effects in present day quantum systems. This however is not necessarily the case in the Early Universe when the particle horizon scale is much smaller and could leave an observable signature in the quantum generation of the primordial fluctuations during inflation. Thus, in our analysis we wish to address the following questions

- What is the deformation of the scale invariant spectrum of perturbations produced during inflation due to the Heisenberg algebra deformation Eq. (6.6) corresponding to the existence of a maximum measurable scale?
- What constraints can be imposed on the fundamental parameter $\alpha = l_{max}^{-2}$ from the observed power spectrum of primordial fluctuations?

The structure of this Chapter is the following: In the next Section 6.2 we consider a simple harmonic oscillator in the presence of a large maximum measurable scale and find the variance of the position as

a function of the parameter α and the corresponding variance in the context of the HUP ($\alpha = 0$). In Section 6.3 we generalize this analysis to the case of systems with infinite degrees of freedom (fields) and derive the spectrum and the spectral index of tensor and scalar perturbations generated during inflation as a function of the parameter α and of the corresponding spectrum obtained in the context of the HUP. In Section 6.4 we use the derived theoretical expression for the (running) spectral index along with the corresponding observationally allowed range of the index as a function of the scale k to derive constraints on the fundamental parameter α of the GUP. Finally in Section 6.5 we conclude and discuss the implications and possible extensions of our analysis.

6.2 Toy Model: The position variance of the Harmonic Oscillator under GUP

In order to quantize the simple harmonic oscillator under the assumption of the GUP (6.4) we need to generalize the expressions of the creation and annihilation operators \hat{a}^\dagger and \hat{a} in terms of x, p so that the commutation relation [1937]

$$[\hat{a}, \hat{a}^\dagger] = 1, \quad (6.12)$$

is retained while at the same time the GUP commutation relation (6.6) is also respected. Thus, in order to satisfy these conditions, we generalize the analysis of Refs. [1938, 1939] which applies to the GUP (6.1) and define

$$\hat{a} = \frac{1}{\sqrt{2\hbar\omega}} (\omega [x + f(\alpha, x)] + ip), \quad (6.13)$$

$$\hat{a}^\dagger = \frac{1}{\sqrt{2\hbar\omega}} (\omega [x + f(\alpha, x)] - ip), \quad (6.14)$$

where $f(\alpha, x)$ is a function chosen so that the commutation relations (6.12) and (6.6) are respected.

It is straightforward to show that the following function satisfies the aforementioned conditions simultaneously

$$f(\alpha, x) = \sum_{n=1}^{\infty} \frac{(-\alpha)^n}{2n+1} x^{2n+1}, \quad (6.15)$$

while it reduces to 0 in the limit $\alpha \rightarrow 0$ as it should.

Thus, we can rewrite Eqs.(6.13) and (6.14) as

$$\hat{a} = \frac{1}{\sqrt{2\hbar\omega}} \left(\omega \frac{1}{\sqrt{\alpha}} \arctan(\sqrt{\alpha}x) + ip \right), \quad (6.16)$$

$$\hat{a}^\dagger = \frac{1}{\sqrt{2\hbar\omega}} \left(\omega \frac{1}{\sqrt{\alpha}} \arctan(\sqrt{\alpha}x) - ip \right), \quad (6.17)$$

and the p and x operators are

$$p = -i\sqrt{\frac{\hbar\omega}{2}} (\hat{a} - \hat{a}^\dagger), \quad (6.18)$$

$$x = \frac{1}{\sqrt{\alpha}} \tan \left(\sqrt{\frac{\hbar\alpha}{2\omega}} (\hat{a} + \hat{a}^\dagger) \right). \quad (6.19)$$

Using $\tan x = x + \frac{x^3}{3} + \frac{2x^5}{15} + \dots$, we have

$$x = x_0 + \frac{\alpha x_0^3}{3} + \frac{2\alpha^2 x_0^5}{15} + \dots, \quad (6.20)$$

where

$$x_0 = \sqrt{\frac{\hbar}{2\omega}}(\hat{a} + \hat{a}^\dagger) , \quad (6.21)$$

is the position operator in the case of the HUP ($\alpha = 0$). Keeping the lower order terms in α (assuming $\frac{\alpha\hbar}{6\omega} \ll 1$) we obtain

$$x = x_0 + \frac{\alpha x_0^3}{3} \Rightarrow x = \sqrt{\frac{\hbar}{2\omega}}(\hat{a} + \hat{a}^\dagger) \left[1 + \frac{\alpha\hbar}{6\omega}(\hat{a} + \hat{a}^\dagger)^2 \right] . \quad (6.22)$$

For $\alpha = 0$ we have

$$x_0 = v(\omega, t)\tilde{a} + v^*(\omega, t)\tilde{a}^\dagger , \quad (6.23)$$

where

$$v(\omega, t) = \sqrt{\frac{\hbar}{2\omega}}e^{-i\omega t} , \quad (6.24)$$

is the properly normalized solution of the classical evolution equation of the harmonic oscillator $\frac{d^2v}{dt^2} + \omega^2v = 0$. Therefore the position operator may be expressed as

$$x = (v\tilde{a} + v^*\tilde{a}^\dagger) \left[1 + \frac{\alpha}{3}(v\tilde{a} + v^*\tilde{a}^\dagger)^2 \right] . \quad (6.25)$$

Thus the variance of the position in the ground state takes the form

$$\langle |x|^2 \rangle \equiv \langle 0|x^\dagger x|0 \rangle \Rightarrow \langle |x|^2 \rangle = |v(\omega, t)|^2 [1 + 2\alpha|v(\omega, t)|^2] , \quad (6.26)$$

which reduces to the familiar result for $\alpha = 0$ (see e.g. Refs. [77, 1940]).

In the next section we generalize the above analysis to the case of quantum field fluctuations involving infinite degrees of freedom aiming to derive the perturbation power spectrum generated during inflation in the context of the GUP.

6.3 Primordial spectra of cosmological fluctuations with GUP

According to the decomposition theorem [1941] the perturbations of each type evolve independently (at the linear level) and we can treat tensor (T) and scalar (S) perturbations of the metric separately. Therefore for spatially flat Friedmann-Robertson-Walker (FRW) background plus the perturbations we can write

$$ds_T^2 = a^2 [-d\tau^2 + (\delta_{ij} + H_{ij})dx^i dx^j] , \quad (6.27)$$

and in conformal Newtonian gauge [1383]

$$ds_S^2 = a^2 [-(1 + 2\Psi)d\tau^2 + \delta_{ij}(1 + 2\Phi)dx^i dx^j] , \quad (6.28)$$

where a is the scale factor, τ is the conformal time, Ψ corresponds to the gravitational potential of the perturbations, Φ is the perturbation of the spatial curvature² and H_{ij} is the tensor perturbation which has the form³

$$[H_{ij}] = \begin{bmatrix} h_+ & h_\times & 0 \\ h_\times & -h_+ & 0 \\ 0 & 0 & 0 \end{bmatrix} . \quad (6.29)$$

The classical evolution equations for the tensor mode perturbations h_T (where $T = +, \times$ for two polarization states [1943]) of the FRW metric during inflation in conformal time are obtained from the linearized Einstein equations and may be written as [1944]

$$h_T'' + 2\frac{a'}{a}h_T' + k^2h_T = 0 , \quad (6.30)$$

²In the absence of anisotropic stress ($\Pi = 0$) we have $\Psi = -\Phi$ [1942].

³It has this form in a coordinate system where wavevector \mathbf{k} points along the z -axis.

where primes denote derivatives with respect to τ . This becomes a simple harmonic oscillator equation by defining

$$\tilde{h}_T \equiv \frac{ah_T}{\sqrt{16\pi G}}, \quad (6.31)$$

and Eq. (6.30) takes the form

$$\tilde{h}_T'' + \omega^2 \tilde{h}_T = 0, \quad (6.32)$$

where

$$\omega^2 = k^2 - \frac{a''}{a}. \quad (6.33)$$

During slow roll inflation when the Hubble rate H is nearly constant [1945], the conformal time is [1940, 1946]

$$\tau \simeq \frac{-1}{aH}. \quad (6.34)$$

Thus we obtain

$$\omega^2 = k^2 - \frac{2}{\tau^2}. \quad (6.35)$$

We now quantize the tensor field fluctuations by promoting them to operators and imposing a generalized field commutation (GFC) relation [1947, 1948] corresponding to Eq. (6.6). This GFC takes the form ($\hbar = 1$)

$$[\tilde{h}_T(\mathbf{k}), \pi_{\tilde{h}_T}(\mathbf{k}')] = i\delta(\mathbf{k} - \mathbf{k}') \frac{1}{1 - \mu \tilde{h}_T^2(\mathbf{k})}, \quad (6.36)$$

where $\pi_{\tilde{h}_T}$ is the conjugate momentum to \tilde{h}_T which is given by

$$\pi_{\tilde{h}_T} = \tilde{h}_T' - \frac{a'}{a} \tilde{h}_T, \quad (6.37)$$

and μ is a GFC parameter

$$\mu \simeq \alpha^2 = l_{max}^{-4}, \quad (6.38)$$

where α is the parameter of the GUP (6.4). Thus we have an infinite number of decoupled harmonic oscillators corresponding to Eq. (6.32) which may be quantized in accordance with the GFC (6.36). Using the results of the previous section we connect the field normal modes with the creation and annihilation operators which satisfy the commutation relation $[\hat{a}_{\mathbf{k}}, \hat{a}_{\mathbf{k}'}^\dagger] = \delta^3(\mathbf{k} - \mathbf{k}')$, as

$$\tilde{h}_T(\mathbf{k}) = \frac{1}{\sqrt{\mu}} \tan\left(\sqrt{\frac{\mu}{2\omega}}(\hat{a}_{\mathbf{k}} + \hat{a}_{\mathbf{k}}^\dagger)\right), \quad (6.39)$$

$$\pi_{\tilde{h}_T}(\mathbf{k}) = -i\sqrt{\frac{\omega}{2}}(\hat{a}_{\mathbf{k}} - \hat{a}_{\mathbf{k}}^\dagger), \quad (6.40)$$

and obtain the variance of the perturbations as

$$\langle h_T^\dagger(\mathbf{k}, \tau) h_T(\mathbf{k}', \tau) \rangle = \frac{16\pi G}{a^2} |v(\mathbf{k}, \tau)|^2 [1 + 2\bar{\mu}|v(\mathbf{k}, \tau)|^2] (2\pi)^3 \delta^3(\mathbf{k} - \mathbf{k}') \equiv (2\pi)^3 P_h(k) \delta^3(\mathbf{k} - \mathbf{k}'), \quad (6.41)$$

where P_h is the power spectrum of the primordial tensor perturbations of the metric, the Dirac delta function enforces the independence of the different modes ($h(\mathbf{k}, \tau)$ is uncorrelated with $h(\mathbf{k}', \tau)$ if $\mathbf{k} \neq \mathbf{k}'$) and

$$\bar{\mu} = \mu V_*. \quad (6.42)$$

Here the volume scale $V_* = \delta^3(0) \simeq l_{max}^3$ is an infrared regulator [1949] while v satisfies the Mukhanov-Sasaki equation [1950–1952]

$$v''(k, \tau) + \left(k^2 - \frac{a''}{a}\right)v(k, \tau) = 0. \quad (6.43)$$

During slow-roll inflation with initial condition $v(k, \tau) = \frac{1}{\sqrt{2k}}e^{-ik\tau}$ and by virtue of Eq. (6.34) (as in spatially flat de Sitter background) we obtain the Bunch-Davies solution of Eq. (6.43) [1940, 1953–1955]

$$v(k, \tau) = \frac{e^{-ik\tau}}{\sqrt{2k}} \left(1 - \frac{i}{k\tau} \right) . \quad (6.44)$$

Using Eq. (6.41) we can write the primordial power spectrum for tensor modes as

$$P_h(k) = P_h^{(0)}(k) \left[1 + \frac{\bar{\mu}a^2}{8\pi G} P_h^{(0)}(k) \right] , \quad (6.45)$$

where

$$P_h^{(0)}(k) = \frac{16\pi G}{a^2} |v(k, \tau)|^2 . \quad (6.46)$$

Once $k|\tau| < 1$, the mode leaves the horizon, after which h remains constant. Thus, using Eqs. (6.44) and (6.46) we obtain

$$P_h^{(0)}(k) = \frac{16\pi G}{a^2} \frac{1}{2k^3\tau^2} = \frac{8\pi GH^2}{k^3} , \quad (6.47)$$

where the equality on the second line holds because we have assumed that H is constant and $\tau = -\frac{1}{aH}$ ⁴.

In a similar manner we may investigate scalar perturbations induced by quantum fluctuations of the inflaton scalar field ϕ [1940, 1956, 1957] of the form

$$\phi(\mathbf{x}, t) = \phi^{(0)}(t) + \delta\phi(\mathbf{x}, t) , \quad (6.48)$$

where $\phi^{(0)}$ is the zero-order part and $\delta\phi$ is the first-order perturbation.

The fluctuations $\delta\phi$ of the scalar field driving inflation evolve in conformal time τ according to the equation e.g. [1928]

$$\delta\phi'' + 2\frac{a'}{a}\delta\phi' + k^2\delta\phi = 0 . \quad (6.49)$$

Using the definition

$$\varphi = a\delta\phi , \quad (6.50)$$

Eq. (6.49) becomes

$$\varphi'' + \omega^2\varphi = 0 , \quad (6.51)$$

with $\omega^2 = k^2 - \frac{a''}{a}$.

In the context of the maximal measurable length GUP as applied to the case of the inflaton fluctuations, the field commutation relation gets generalized as

$$[\varphi(\mathbf{k}), \pi_\varphi(\mathbf{k}')] = i\delta(\mathbf{k} - \mathbf{k}') \frac{1}{1 - \mu\varphi^2(\mathbf{k})} , \quad (6.52)$$

where π_φ is the conjugate momentum to φ which is given by

$$\pi_\varphi = \varphi' - \frac{a'}{a}\varphi . \quad (6.53)$$

Since Eq. (6.49) is identical to Eq. (6.30) we can use the result of Eq. (6.45) without the factor $16\pi G$ in order to turn the dimensionless h into a field $\delta\phi$ with dimensions of mass

$$P_{\delta\phi}(k) = P_{\delta\phi}^{(0)}(k) \left[1 + 2\bar{\mu}a^2 P_{\delta\phi}^{(0)}(k) \right] , \quad (6.54)$$

where

$$P_{\delta\phi}^{(0)}(k) = \frac{H^2}{2k^3} . \quad (6.55)$$

⁴We evaluate H at the time when the mode leaves the horizon.

In the case $\bar{\mu} = 0$ Eqs. (6.45) and (6.54) reduce to the familiar results of HUP [1383].

The perturbation from the scalar field driving inflation $\delta\phi$ gets transferred to the gravitational potential Φ . The post inflation power spectrum of Φ is related to the horizon-crossing power spectrum of $\delta\phi$ via [77]

$$P_{\Phi} = \frac{16\pi G}{9\epsilon} P_{\delta\phi} , \quad (6.56)$$

where ϵ is the Hubble slow-roll parameter, defined as

$$\epsilon \equiv \frac{d}{dt} \left(\frac{1}{H} \right) . \quad (6.57)$$

We note that the Hubble slow-roll parameter ϵ is equal to the first potential slow-roll parameter ϵ_V , to leading order in the slow-roll approximation [1940, 1946, 1958–1960]

$$\epsilon \simeq \epsilon_V \equiv \frac{1}{16\pi G} \left(\frac{V'}{V} \right)^2 , \quad (6.58)$$

where V' is defined as the derivative of the potential V with respect to the field $\phi^{(0)}$.

In the case of single-field slow-roll models of inflation for modes which are outside the horizon ($k|\tau| \ll 1$) at the end of inflation, the primordial spectra of scalar and tensor perturbations do not depend on time⁵ and it is conventional to write [1946]

$$P_S(k) \equiv k^3 P_{\Phi}(k) \equiv A_S k^{n_s-1} , \quad (6.59)$$

$$P_T(k) \equiv k^3 P_h(k) \equiv A_T k^{n_T} , \quad (6.60)$$

where $A_S(A_T)$ is the scalar (tensor) amplitude and $n_s(n_T)$ is the scalar (tensor) spectral index. The special case with $n_s = 1$ ($n_T = 0$) results in the scale-invariant spectrum.

From Eqs. (6.45) and (6.60) we obtain

$$P_T(k) = P_T^{(0)}(k) \left[1 + \frac{\bar{\mu} a^2}{8\pi G k^3} P_T^{(0)}(k) \right] , \quad (6.61)$$

where (for $k|\tau| \ll 1$)

$$P_T^{(0)}(k) = \frac{8\pi G}{a^2 \tau^2} = 8\pi G H^2 . \quad (6.62)$$

It is straightforward to show at the horizon crossing time ($k = aH$)

$$P_T(k) = P_T^{(0)}(k) \left(1 + \frac{\bar{\mu}}{k} \right) . \quad (6.63)$$

In Eq. (6.60) the tensor spectral index is defined as

$$n_T \equiv \frac{d \ln P_T}{d \ln k} . \quad (6.64)$$

Also by virtue of Eq. (6.57) we have that the logarithmic derivative of Hubble rate at horizon crossing is

$$\frac{d \ln H}{d \ln k} = -\epsilon . \quad (6.65)$$

Therefore using Eqs. (6.62), (6.63) and (6.64) we obtain that the tensor spectral index runs as

$$n_T = -2\epsilon - \frac{\bar{\mu}}{k} . \quad (6.66)$$

⁵We assume that non-adiabatic pressure terms are negligible.

Similarly, from Eq. (6.54) and using $P_S = k^3 \frac{16\pi G}{9\epsilon} P_{\delta\phi}$ we obtain at horizon crossing time ($k = aH$)

$$P_S(k) = P_S^{(0)}(k) \left[1 + \frac{9\bar{\mu}\epsilon}{8\pi GH^2 k} P_S^{(0)}(k) \right], \quad (6.67)$$

where

$$P_S^{(0)}(k) = \frac{8\pi GH^2}{9\epsilon}. \quad (6.68)$$

It is straightforward to show that the

$$P_S(k) = P_S^{(0)}(k) \left(1 + \frac{\bar{\mu}}{k} \right). \quad (6.69)$$

Notice that Eqs. (6.67) and (6.68) have a generic form which could have been guessed even on the basis of dimensional analysis. However, here we have demonstrated in detail that these equations are not simply well motivated parametrizations based on dimensional analysis. Instead they constitute the unique and generic prediction of the inflationary power spectrum of fluctuations generated in the context of the GUP Eq. (6.52) as derived in the context of our analysis. Thus there is no room to modify Eq. (6.67) without violating the physical principle corresponding to the GUP (6.52).

In Eq. (6.59) the scalar spectral index is defined as

$$n_s - 1 \equiv \frac{d \ln P_\Phi}{d \ln k}. \quad (6.70)$$

Now using the Eq. (6.58) and the Hubble slow-roll parameter [1960]

$$\delta \equiv \frac{1}{H} \frac{d^2 \phi^{(0)}/dt^2}{d\phi^{(0)}/dt}, \quad (6.71)$$

we have that the logarithmic derivative of the slow-roll parameter ϵ is

$$\frac{d \ln \epsilon}{d \ln k} = 2(\epsilon + \delta). \quad (6.72)$$

Therefore using Eqs. (6.68), (6.69) and (6.70) we obtain that the scalar spectral index runs as

$$n_s = 1 - 4\epsilon - 2\delta - \frac{\bar{\mu}}{k}. \quad (6.73)$$

Alternatively using the the second potential slow-roll parameter $\eta \equiv \frac{1}{8\pi G} \frac{V''}{V}$ and the relation $\delta = \epsilon - \eta$ ⁶ [1946], we obtain

$$n_s = 1 - 6\epsilon + 2\eta - \frac{\bar{\mu}}{k}. \quad (6.74)$$

In the next subsection we use observational scalar spectral index data to obtain bounds on $\bar{\mu}$.

6.4 Observational Constraints

The predicted form of the running spectral index Eq. (6.74) reduces to the standard form [1945, 1946] for the HUP ($\bar{\mu} = 0$) and may be used along with observational constraints of the spectral index to impose constraints on the GFC parameter $\bar{\mu}$.

The parameters that can lead to deviations from scale invariance of the spectral index are the GFC parameter μ and the slow-roll parameter λ defined as

⁶The second slow-roll parameter δ and the second potential slow-roll parameter η are sometimes defined as η and η_V respectively, so that the relation has the form $\eta = \epsilon_V - \eta_V$.

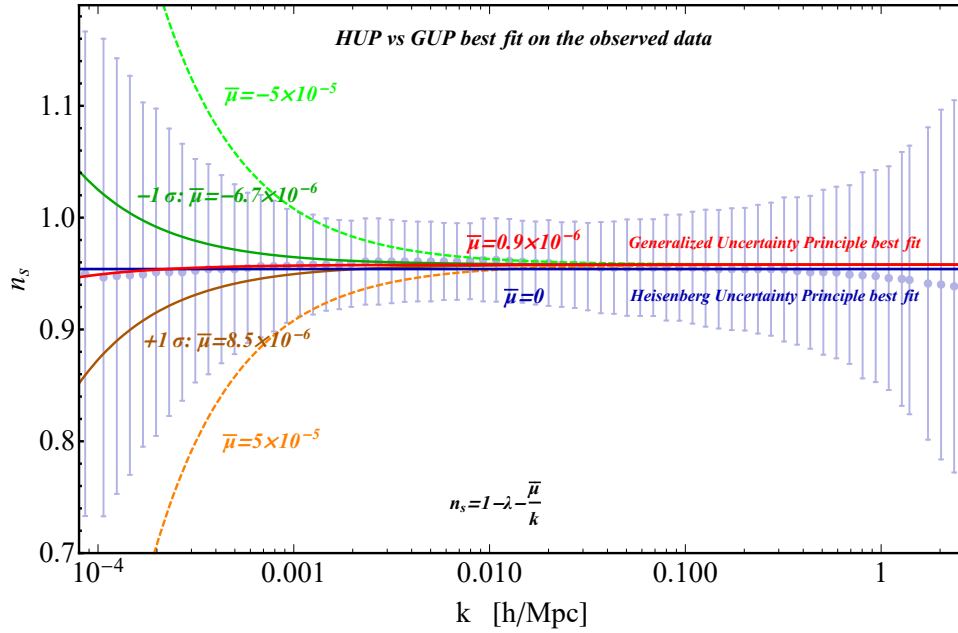


Figure 6.2: The best fit forms of the scalar spectral index Eq. (6.76) (blue curve for HUP and red curve for GFC Eq. (6.52)) on the observed data (thick dots). The green and brown continuous curves correspond to -1σ and $+1\sigma$ deviation of the parameter $\bar{\mu}$ respectively. The light green and the orange dashed curves correspond to observationally allowed range for the spectral index n_s at approximately 2σ level.

$$\lambda = 6\epsilon - 2\eta . \quad (6.75)$$

Thus using Eq. (6.74), the scalar spectral index takes the form

$$n_s = 1 - \lambda - \frac{\bar{\mu}}{k} . \quad (6.76)$$

In order to impose constraints on the parameters $\lambda, \bar{\mu}$ we use constraints on the scalar spectral index of Ref. [60] which are based on the angular power spectrum data of the 5 year Wilkinson Microwave Anisotropy Probe (WMAP5) Cosmic Microwave Background (CMB) temperature and polarization, the Large Scale Structure (LSS) data of the Sloan Digital Sky Survey (SDSS) data release 7 (DR7) Luminous Red Galaxy (LRG) power spectrum, and the Lyman-alpha forest (Lya) power spectrum constraints. The allowed range on n_s is shown in Fig. 6.2.

Expressing this range as a set of $N = 60$ datapoints leads to constraints on the parameters $\lambda, \bar{\mu}$ through the maximum likelihood method [1961]. As a first step for the construction of χ^2 , we consider the vector [1962]

$$V^i(k_i, \lambda, \bar{\mu}) \equiv n_{s,i}^{obs}(k_i) - n_{s,i}^{th}(k_i, \lambda, \bar{\mu}) , \quad (6.77)$$

where $n_{s,i}^{obs}(k_i)$ and $n_{s,i}^{th}(k_i, \lambda, \bar{\mu})$ are the observational and the theoretical spectral index at wavenumber k_i respectively ($i = 1, \dots, N$ with N corresponds to the number of datapoints). Then we obtain χ^2 as

$$\chi^2 = V^i F_{ij} V^j , \quad (6.78)$$

where F_{ij} is the Fisher matrix [1963] (the inverse of the covariance matrix C_{ij} of the data).

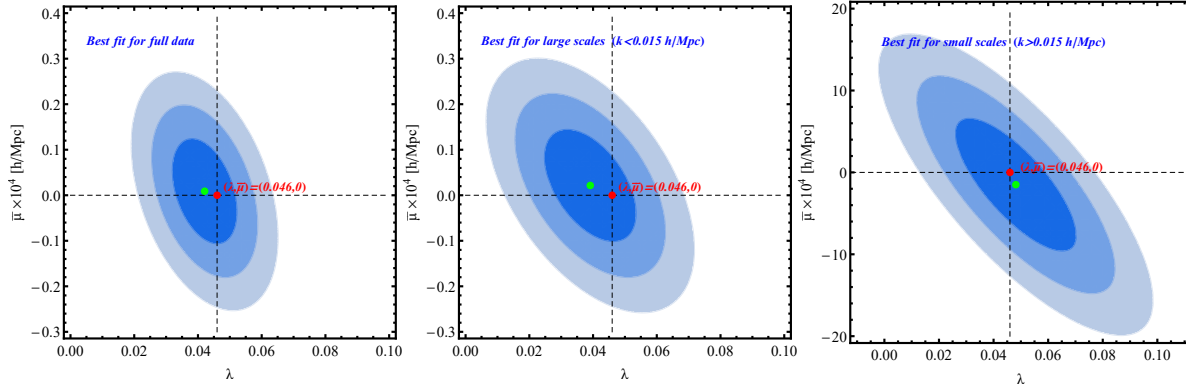


Figure 6.3: The $1\sigma - 3\sigma$ contours in the $(\lambda, \bar{\mu})$ parametric space. The contours describe the corresponding confidence regions obtained from the full data set (left panel), large scales ($k < 0.015 h/\text{Mpc}$) data (middle panel), and small scales ($k > 0.015 h/\text{Mpc}$) data (right panel). The red and green points correspond to the HUP and GUP best fits respectively.

The $N \times N$ covariance matrix is assumed to be of the form

$$[C_{ij}] = \begin{bmatrix} \sigma_1^2 & 0 & 0 & \cdots \\ 0 & \sigma_2^2 & 0 & \cdots \\ 0 & 0 & \cdots & \sigma_N^2 \end{bmatrix}, \quad (6.79)$$

where σ_i denotes the 1σ error of data point i .

The 68.3% (1σ), 95.4% (2σ) and 99.7% (3σ) confidence contours in the λ and $\bar{\mu}$ parametric space are shown in Fig. 6.3. The contours correspond to confidence regions obtained from the full data set (left panel), the large scales ($k < 0.015 h/\text{Mpc}$) data (middle panel), and the small scales ($k > 0.015 h/\text{Mpc}$) data (right panel). The 1σ - 3σ contours for parameters λ and $\bar{\mu}$ correspond to the curves $\chi^2(\lambda, \bar{\mu}) = \chi_{min}^2 + 2.3$, $\chi^2(\lambda, \bar{\mu}) = \chi_{min}^2 + 6.17$ and $\chi^2(\lambda, \bar{\mu}) = \chi_{min}^2 + 9.21$ respectively. Notice (in Fig. 6.3) that the large scales are most efficient in constraining the GFC parameter $\bar{\mu}$. The largest scales that correspond to small k give the largest value for the correction $\bar{\mu}/k$ of the power spectrum and the spectral index Eq. (6.76). Thus it is these scales that are more sensitive to the correction and lead to the strongest constraints as shown in Fig. 6.3.

In Table 6.1 we show the best fit values of parameters λ and $\bar{\mu}$ with the corresponding 1σ standard deviations. In the case of HUP ($\bar{\mu} = 0$) the result agrees with the current best fit values of the scalar spectral index from Planck which indicate that $\lambda \simeq 0.04$ [14].

Using Eq. (6.38) and the 1σ constraint on the GFC parameter $\bar{\mu} \lesssim 10^{-5} h/\text{Mpc}$ we can obtain the single GUP free parameter as

$$\alpha = \bar{\mu}^2 \lesssim 10^{-54} \text{ m}^{-2}, \quad (6.80)$$

and the corresponding maximum measurable scale as

$$l_{max} = \bar{\mu}^{-1} \gtrsim 10^{27} \text{ m}. \quad (6.81)$$

This result is one order of magnitude larger than the present day particle horizon ($l_{max}(t_0) \simeq 10^{26} \text{ m}$) given in Eq. (6.3). However, at about 2σ level the physically anticipated maximum measurable scale (the particle horizon scale) is included in the observationally allowed range of the maximum measurable scales. Thus, the emergence of the parameter μ in Eqs. (6.36) and (6.52) as a consequence of a maximum measurable length associated with the cosmological particle horizon remains an observationally viable

Table 6.1: The best fit values of parameters λ and $\bar{\mu}$ with the corresponding 1σ standard deviations for the fitted spectral index on the observed data [60].

GFC			
Parameter	Full Data (1σ)	Large Scales Data (1σ)	Small Scales Data (1σ)
$\bar{\mu}$	0.9 ± 7.6 [$\times 10^{-6}h/\text{Mpc}$]	2.1 ± 8.1 [$\times 10^{-6}h/\text{Mpc}$]	-149 ± 535 [$\times 10^{-6}h/\text{Mpc}$]
λ	0.042 ± 0.0067	0.039 ± 0.0095	0.048 ± 0.0146

hypothesis. The parameter $\bar{\mu}$ is a fundamental parameter connected to the GUP (6.52) and it is not necessarily connected with the detailed physics of inflation. Thus our analysis can not directly impose constraints on models of inflation even though there may be an indirect connection of the present day value of l_{max} with the scale of inflation. Such a connection would require a time dependent form to l_{max} and is beyond the scope of the present analysis.

6.5 Conclusions

In this Chapter we have derived the generalized form of the primordial power spectrum of cosmological perturbations generated during inflation due to the quantum fluctuations of scalar and tensor degrees of freedom in the context of a generalization of quantum mechanics involving a maximum measurable length scale. The existence of such a scale is motivated by the existence of the particle horizon in cosmology and would lead to a generalization of the uncertainty principle (GUP) to the form $\Delta x \Delta p \geq \frac{\hbar}{2} \frac{1}{1 - \alpha \Delta x^2}$, which implies the existence of a maximum position and a minimum momentum uncertainty (infrared cutoff) [55]. The GUP implies a generalization of the commutation relation between conjugate operators including fields and their conjugate momenta. For example we showed that the generalized field commutation (GFC) relation between a scalar field and its conjugate momentum $[\varphi(\mathbf{k}), \pi_\varphi(\mathbf{k}')] = i\delta(\mathbf{k} - \mathbf{k}') \frac{1}{1 - \mu \varphi^2(\mathbf{k})}$ which is implied by the GUP leads to a modified primordial spectrum of scalar perturbation are $P_S(k) = P_S^{(0)}(k) \left(1 + \frac{\bar{\mu}}{k}\right)$ with a running spectral index of the form $n_s = 1 - \lambda - \frac{\bar{\mu}}{k}$ with $\lambda = 6\epsilon - 2\eta$.

Using cosmological constraints of the scalar perturbations spectral index as a function of the scale k [1962] we imposed constraints on the parameter of the GFC $\bar{\mu} \simeq l_{max}^{-1}$. We found that $\bar{\mu} = (0.9 \pm 7.6) \cdot 10^{-6}h/\text{Mpc}$ at the 1σ level which corresponds to an upper bound scale l_{max} larger than the present horizon scale. At 2σ level we find that the observationally allowed range of l_{max} includes the current cosmological horizon scale $l_{max} \simeq 10^{26}$ m. Thus at 2σ level, the derived observational constraints on l_{max} are consistent with the physically anticipated maximum measurable scale which is the current cosmological particle horizon and are much more powerful than the corresponding constraints obtained using laboratory data measuring the energy spectrum of simple quantum systems obtained in Ref. [55].

Chapter 7

Tensions and Constraints on Modified Gravity Parameters from the E_G statistic and RSD data and Implications for Weakening Gravity

The analysis presented in this chapter is based on the work which was done in collaboration with Prof. Leandros Perivolaropoulos and has been published in Physical Review D [4].

In this chapter, we present phenomenologically motivated parametrizations for the effective Newton’s constant parameter and the light deflection parameter and describe how we use them in order to probe possible deviations from GR on cosmological scales using compilations of $f\sigma_8$ and E_G data.

A observational puzzle for Λ CDM involves persisting indications from observational probes measuring the growth of matter perturbations that the observed growth is weaker than the growth predicted by the standard Planck/ Λ CDM parameter values (see Section 3.1). Modified gravity (MG) models constitute a prime theoretical candidate to explain this tension. The combination of cosmological observational probes is a powerful tool for the identification of signatures of MG [144, 1964–1969]. Such observational probes may be divided in two classes: geometric and dynamical (or structure formation) probes [1850, 1970–1972]. Geometric observations measure cosmological distances using standard candles (e.g. Type Ia supernovae) and standard rulers (e.g. the horizon at the time of recombination probed through Baryon Acoustic Oscillations) and thus probe directly the cosmic metric, independent of the underlying theory of gravity (see Section 2.2). Dynamical observations probe the growth rate of cosmological perturbations and thus the gravitational laws and the consistency of GR with data provided the background geometry is known.

Dynamical probes include cluster counts (CC) [1190, 1191, 1972, 1973], weak lensing (WL) [144, 550, 1791–1793, 1797, 1974, 1975] and redshift-space distortions (RSD) [67, 147, 148, 1976, 1977] (see Subsection 3.1.1). These probes are consistent with each other pointing either to a lower value of the matter density parameter Ω_{0m} in the context of GR or to weaker gravitational growth power than the growth indicated by GR in the context of a Planck18/ Λ CDM background geometry at about $2 - 3\sigma$ level [67, 147, 148]. Such weak growth may be quantified by the parameter σ_8 which is the matter density rms fluctuations within spheres of radius $8h^{-1}Mpc$ and is determined by the amplitude of the primordial fluctuations power spectrum and by the growth rate of cosmological fluctuation.

Various possible mechanisms have been proposed to slow down growth at low redshifts and thus reduce the above tension (see e.g. Ref. [1978] and Subsection 3.1.2). Such mechanisms may be divided in two categories: non-gravitational and gravitational. The former includes the effects of interacting dark energy models [792, 837, 839, 1979], dynamical dark energy models [1358, 1360], running vacuum models [687, 688] and the effects of massive neutrinos [1369]. The latter includes the effects of MG theories with

Table 7.1: Planck18/ Λ CDM parameters values [14] based on TT,TE,EE+lowE+lensing likelihoods.

Parameter	Planck18/ Λ CDM
$\Omega_b h^2$	0.02237 ± 0.00015
$\Omega_c h^2$	0.1200 ± 0.0012
n_S	0.9649 ± 0.0042
$H_0 [km s^{-1} Mpc^{-1}]$	67.36 ± 0.54
Ω_{0m}	0.3153 ± 0.0073
w	-1
σ_8	0.8111 ± 0.0060

a reduced (compared to GR) evolving effective Newton’s constant G_{eff} at low redshifts [67, 148].

The effects of MG [65, 111, 1305, 1849, 1856, 1980–1984] models are indistinguishable from GR at the geometric cosmological background level [926, 1970, 1985]. Signatures of MG can only be obtained by investigating the dynamics of cosmological perturbations [1339, 1986] using specific statistics obtained through dynamical probe observables such as the two-point correlation and power spectrum of the galaxy distribution, the RSD and WL.

7.1 Introduction

A useful bias free statistic is the $f\sigma_8$ product of the rate of growth of matter density perturbations f times σ_8 discussed in more detail in what follows. An alternative observable statistic is the E_G which was constructed to be independent of both the clustering bias factor b and the parameter σ_8 on linear scales. This statistic was proposed in 2007 [1987] and thereafter has been used several times to test MG theories [1988, 1989]. The expectation value of E_G is equal to the ratio of the Laplacian of the sum of the Bardeen potentials [1382] Ψ (the Newtonian potential) and Φ (the spatial curvature potential) $\nabla^2(\Psi + \Phi)$ over the peculiar velocity divergence $\theta \equiv \nabla \cdot \frac{\vec{v}}{H(z)}$ (where \vec{v} is the peculiar velocity and $H(z)$ is the Hubble parameter in terms of the redshift z).

The E_G statistic has been proposed as a model independent test of any MG theory [1990] and is constructed from three different probes of large scale structure (LSS): the galaxy-galaxy lensing (GGL), the galaxy clustering and the galaxy velocity field which leads to galaxy redshift distortions. Alternatively, E_G may be constructed from galaxy-CMB lensing [1520] instead of galaxy-galaxy lensing as a more robust tracer of the lensing field at higher redshifts [1991, 1992].

The first probe, the GGL (a special type of WL), is the slight distortion of shapes of source galaxies in the background of a lens galaxy, which arises from the gravitational deflection of light due to the gravitational potential of the lens galaxy along the line of sight (see for example [1226, 1227, 1993, 1994]). This WL probe is sensitive to $\nabla^2(\Psi + \Phi)$, since relativistic particles collect equal contributions from the two Bardeen potentials which appear in the scalar perturbed FLRW metric in the Newtonian gauge Eq. (3.9) [582, 1383, 1384].

The second probe, the galaxy clustering arises from the gravitational attraction of matter and is sensitive only to the potential Ψ . Similarly, the third probe, the galaxy velocity field, is quantified by measuring RSD [355, 1297, 1299, 1810] (an illusory anisotropy that distorts the distribution of galaxies in redshift space generated by their peculiar motions falling towards overdense regions). This important probe of LSS is sensitive to the rate of growth of matter density perturbations f which depends on the theory of gravity and provides measurements of $f\sigma_8$ that depends on the potential Ψ .

In most MG theories the potentials Φ and Ψ obey generalized Poisson equations like the GR Newto-

nian potential where the MG effects are encoded in generalized space-time dependent effective Newton constants. These generalized Newton constants for the potential Ψ and for the lensing combination $\Psi + \Phi$ are usually described by two parameters: the effective Newton's constant parameter μ_G and the light deflection parameter Σ_G . In the modified Poisson equations [1995] the μ_G and Σ_G are connected with the potentials Ψ and $\Psi + \Phi$ respectively. In GR the value of μ_G and Σ_G coincides with unity while in a MG model μ_G and Σ_G can be in general functions of both time and scale [1964, 1996]. Using $f\sigma_8$ and E_G datasets constraints can be imposed on the parameters μ_G and Σ_G [76, 1968, 1997–2001]). Such analyses have revealed various levels of tension of the best fit forms of μ_G and Σ_G with the GR prediction of unity showing hints that these parameters may be less than unity implying weaker growth of perturbations than that predicted in GR. The goal of our analysis is to extend these studies and use an updated data compilation for both the $f\sigma_8$ and E_G statistics to identify the current level of tension with GR implied by these data compilations.

In particular, we address the following questions:

- What are efficient phenomenological redshift dependent parametrizations of the generalized normalized Newton constants $\mu_G(z)$ and $\Sigma_G(z)$ that are consistent with solar system and nucleosynthesis constraints that indicate that GR is restored at high z and at the present time in the solar system?
- What are the constraints imposed by the E_G and $f\sigma_8$ updated data compilations on the parameters of the above parametrizations and do these constraints amplify the hints for weakening gravity at low z implied by the $f\sigma_8$ data alone as indicated by previous studies?

The plan of this Chapter is the following: In the next Section 7.2 we present a brief review of the theoretical expression for E_G . We also present phenomenologically motivated parametrizations for μ_G and Σ_G and describe how we use them in order to probe possible deviations from GR on cosmological scales. In Section 7.3 we use compilations of $f\sigma_8$ and E_G data along with the theoretical expressions for $f\sigma_8$ and E_G which involve μ_G and Σ_G to derive constraints on these parameters and to identify the tension level between the Planck/ Λ CDM parameter values favoured by Planck 2018 [14] shown in Table 7.1 and the corresponding parameter values favored by the two datasets. Finally in Section 7.4 we conclude and discuss the implications and possible extensions of our analysis.

7.2 Theoretical background

7.2.1 E_G statistic

The E_G statistic [1987, 1990] is designed as a probe of the ratio of the Bardeen potentials of the perturbed FLRW metric in such a way as to be independent of the effects of galaxy bias at linear order. It is defined as the ratio of the cross correlation power spectrum $P_{g\nabla^2(\Phi+\Psi)}$ between lensing maps (cosmic shear or CMB) and galaxy positions, over the the cross-correlation power spectrum $P_{g\theta}$ between galaxies and velocity divergence field θ

$$E_G \equiv \frac{P_{g\nabla^2(\Phi+\Psi)}}{P_{g\theta}} . \quad (7.1)$$

In Fourier space the E_G statistic may also be expressed as [1987]

$$E_G(l, \Delta l) = \frac{C_{\kappa g}(l, \Delta l)}{3H_0^2 a^{-1} \sum_{\alpha} q_{\alpha}(l, \Delta l) P_{vg}^{\alpha}} , \quad (7.2)$$

where H_0 is the Hubble parameter today, l is the magnitude of two-dimensional wavenumber of the on-sky Fourier space, $C_{\kappa g}(l, \Delta l)$ is the galaxy-galaxy lensing cross correlation power spectrum in bins of Δl , P_{vg}^{α} is the galaxy-velocity cross correlations power spectrum between k_{α} and $k_{\alpha+1}$ (where k three-dimensional wavenumber of the on-sky Fourier transform with $k_1 < k_2 < \dots < k_{\alpha} < \dots$) and $q_{\alpha}(l, \Delta l)$ is the weighting function defined accordingly.

The corresponding expectation value of E_G , averaged over l is the the ratio of the Laplacian of the gravitational scalar potentials Ψ and Φ which appear in the scalar perturbed FLRW metric Eq. (3.9) over the peculiar velocity divergence [1988]

$$\langle E_G \rangle = \left[\frac{\nabla^2(\Psi + \Phi)}{3H_0^2 a^{-1} \theta} \right]_{k=l/\bar{\chi}, \bar{z}}, \quad (7.3)$$

where $\bar{\chi}$ is the comoving mean distance corresponding to the mean redshift \bar{z} .

In Λ CDM cosmology and assuming that the velocity field is generated under linear perturbation theory, the peculiar velocity divergence is connected to the growth rate f as $\theta = f\delta$ [121] where $\delta \equiv \frac{\delta\rho}{\rho}$ is the matter overdensity field (with ρ the matter density of the background and $\delta\rho$ its first order perturbation), $f(a) \equiv \frac{d \ln D(a)}{d \ln a}$ is the linear growth rate of structure and $D(a) \equiv \frac{\delta(a)}{\delta(a=1)}$ the growth factor (see also Subsection 3.1.1).

In the case of GR and in the absence of any anisotropic stress the Bardeen potentials are equal ($\Psi = \Phi$) and the gravitational field equations reduce to Poisson equations of the form

$$\nabla^2 \Phi = \nabla^2 \Psi = 4\pi G a^2 \rho \delta = \frac{3}{2} H_0^2 \Omega_{0m} a^{-1} \delta, \quad (7.4)$$

where $\Omega_{0m} = \Omega_m(z=0)$ is the matter density parameter today and the second equality is straightforwardly derived assuming non-relativistic matter species and using the equations $H_0^2 = \frac{8\pi G \rho_{c,0}}{3}$, $\rho = \rho_0 a^{-3}$ and $\Omega_{0m} = \frac{\rho_0}{\rho_{c,0}}$ (with ρ_0 the matter density today and $\rho_{c,0}$ the critical density today).

Therefore within GR Eq. (7.4), the Eq. (7.3) reduce to

$$E_G = \frac{\Omega_{0m}}{f(z)}, \quad (7.5)$$

where f is well approximated as $f(z) \simeq \Omega_m^\gamma(z)$ with the growth index γ in a narrow range near 0.55, for a wide variety of dark-energy models in GR [320, 1300–1303, 1308, 2002–2004]. Note that E_G in GR is scale independent (see Eq. (7.5)). This is not necessarily the case in the context of MG theories where the growth rate f may be strongly scale dependent even on subhorizon scales.

7.2.2 The effective Newton's constant parameter μ_G and the light deflection parameter Σ_G

The gravitational slip parameter η which is defined by Eq. (3.12) describes the possible inequality [931, 1385] of the two Bardeen potentials that may occur in MG theories. Clearly an observation of $\eta \neq 1$ would indicate physics beyond GR. In this case the gravitational field equations at linear level take the form of Poisson equations that generalize Eqs. (7.4). At linear level, in MG models, using the perturbed metric Eq. (3.9) and the gravitational field equations the phenomenological equations (3.10) and (3.11) emerge [330, 1977, 1996, 2005–2009] for the scalar perturbation potentials Ψ and Φ .

They are in general functions of time and scale encoding the possible modifications of General Relativity defined as¹ (see also Subsection 3.1.2)

$$\mu_G(a, k) \equiv \frac{G_{\text{eff}}(a, k)}{G}, \quad (7.6)$$

and

$$\Sigma_G(a, k) \equiv \frac{G_L(a, k)}{G}, \quad (7.7)$$

with G is the Newton's constant as measured by local experiments, G_{eff} is the effective Newton's constant which is related to the growth of matter perturbation and G_L is related to the lensing of light (the

¹Note that, in the literature μ_G and Σ_G are also referred to as G_M and G_L (e.g. in Refs. [148, 2008]) or as G_{matter} and G_{light} (e.g. in Refs. [1977, 2006]).

propagation of relativistic particles, such as photons when they traverse equal regions of space and time along null geodesics experiencing gravitational lensing collecting equal contributions from two gravitational potentials Ψ and Φ). Using the gravitational slip Eq. (3.12) and the ratios of the Poisson equations (3.10) and (3.11) defined above the two LSS functions μ_G and Σ_G are related via

$$\Sigma_G(a, k) = \frac{1}{2} \mu_G(a, k) [1 + \eta(a, k)] . \quad (7.8)$$

In GR which predicts a constant homogeneous $G_{\text{eff}} = G$, we obtain $\mu_G = 1$, $\eta = 1$ and $\Sigma_G = 1$.

Notice that Eqs. (3.10) and (3.11) indicate that a possible observation of reduced gravitational growth of the Bardeen potentials may be interpreted either as reduced strength of gravitational interaction (reduced μ_G and/or Σ_G) or due to reduced matter density ρ (or Ω_{0m}). In the context of a fixed value of matter density determined by geometric probes of the cosmological background, the reduced gravitational growth could be either interpreted as a tension within the Λ CDM parameter value for the matter density or as a hint for weakening gravity. Indeed, such hints of weaker than expected gravitational growth of the Bardeen potentials has been observed at low redshifts by a wide range of dynamical probes including RSD observations [67, 147, 148, 1977], WL [144, 550, 1792, 1793, 1797, 1975] and CC data [1190, 1191, 1972, 1973]. In most cases this weak growth has been interpreted as a tension for the parameters σ_8 and Ω_{0m} which are found by dynamical probes to be smaller than the values indicated by geometric probes in the context of Λ CDM .

The observables $f\sigma_8(a, k)$ and $E_G(a, k)$ can probe directly the gravitational strength functions $\mu_G(a, k)$ and $\Sigma_G(a, k)$. In particular $f\sigma_8$ is easily expressed in terms of the amplitude σ_8 and the matter overdensity δ using the matter overdensity evolution equation (4.1) (see e.g. Ref. [582]). In terms of redshift Eq. (4.1) takes the form [148, 582]

$$\delta''(z) + \left(\frac{(H(z)^2)'}{2 H(z)^2} - \frac{1}{1+z} \right) \delta'(z) - \frac{3(1+z) \Omega_{0m} \mu_G(z, k)}{2 H(z)^2 / H_0^2} \delta(z) = 0 , \quad (7.9)$$

where primes denote differentiation with respect to the redshift.

While in terms of the scale factor we have [1305, 1308, 1817]

$$\delta''(a) + \left(\frac{3}{a} + \frac{H'(a)}{H(a)} \right) \delta'(a) - \frac{3 \Omega_{0m} \mu_G(a, k)}{2 a^5 H(a)^2 / H_0^2} \delta(a) = 0 , \quad (7.10)$$

here primes denote differentiation with respect to the scale factor.

In Eqs. (7.9) and (7.10) possible deviations from GR are expressed by allowing for a scale and redshift-dependent $\mu_G = \mu_G(z, k)$. In the present Section and in Section 7.3.1 we ignore scale dependence due to the lack of good quality scale dependent $f\sigma_8$ and E_G data. However, in Section 7.3.2 we discuss the scale dependence of E_G data.

For a given parametrization of $\mu_G(a)$ and initial conditions deep in the matter era where GR is assumed to be valid leading to $\delta \sim a$ equations (7.9) and (7.10) may be easily solved numerically leading to a predicted form of $\delta(a)$ for a given Ω_{0m} and background expansion $H(z)$. In the context of the present analysis we assume a Λ CDM background $H(z)$

$$H^2(z) = H_0^2 [\Omega_{0m}(1+z)^3 + (1 - \Omega_{0m})] . \quad (7.11)$$

Once the evolution of δ is known, the observable product $f\sigma_8(a) \equiv f(a) \cdot \sigma(a)$ can be obtained using the definitions $f(a)$ of Eq. (3.3) and $\sigma(a)$ of Eq. (3.5) (see also Subsection 3.1.1). Thus, we have

$$f\sigma_8(a, \sigma_8, \Omega_{0m}, \mu_G) = \frac{\sigma_8}{\delta(a=1)} a \delta'(a, \Omega_{0m}, \mu_G) . \quad (7.12)$$

This theoretical prediction may now be used to compare with the observed $f\sigma_8$ data and obtain fits for the parameters Ω_{0m} , σ_8 and $\mu_G(z)$ (assuming a specific parametrization of $\mu_G(z)$).

The lensing gravity parameter $\Sigma_G(z)$ can be fit in the context of specific parametrizations using its connection with the $E_G(a)$ observable as [524, 2010, 2011]

$$E_G(a, \Omega_{0m}, \mu_G, \Sigma_G) = \frac{\Omega_{0m} \Sigma_G(a)}{f(a, \Omega_{0m}, \mu_G)}. \quad (7.13)$$

This equation assumes that the redshift of the lens galaxies can be approximated by a single value while E_G corresponds to average value along the line of sight [524]. In the context of Eq. (7.13) and assuming a specific parametrization for μ_G and Σ_G , the theoretical prediction for E_G may be used to compare with the observed E_G datapoints and lead to constraints on $\Omega_{0m}, \mu_G, \Sigma_G$. These constraints may be considered either separately from those of the $f\sigma_8$ data or jointly by combining the E_G and $f\sigma_8$ datasets. The allowed range of these parameters may then be compared with the standard Planck/ Λ CDM parameter values $\mu_G = 1, \Sigma_G = 1, \Omega_{0m} = 0.315 \pm 0.0073, \sigma_8 = 0.811 \pm 0.006$ to identify the likelihood of Planck/ Λ CDM in the context of the dynamical probe data E_G and $f\sigma_8$. This plan is implemented in what follows in the context of specific parametrizations describing the possible evolution of μ_G and Σ_G .

On scales much smaller than the Hubble scale for most modified gravity models the scale dependence of μ_G and Σ_G is weak. For example in ST model (for $k \gg aH$) μ_G is independent of the scale [2012]. Thus, we start by considering scale independent parametrizations for μ_G and Σ_G which reduce to the GR value at early times and at the present time as indicated by solar system (ignoring possible screening effects) and BBN constraints ($\mu_G = 1$ and $\mu'_G = 0$ for $a = 1$ and $\mu_G = 1$ for $a \ll 1$) [1386, 1388, 2013]. Such parametrizations are the Eqs. (3.15) and (3.16) with $n \geq 2$ and $m \geq 2$ which we set equal to 2 in our analysis [67, 148, 1389]

$$\mu_G = 1 + g_a(1-a)^2 - g_a(1-a)^4 = 1 + g_a\left(\frac{z}{1+z}\right)^2 - g_a\left(\frac{z}{1+z}\right)^4, \quad (7.14)$$

$$\Sigma_G = 1 + g_b(1-a)^2 - g_b(1-a)^4 = 1 + g_b\left(\frac{z}{1+z}\right)^2 - g_b\left(\frac{z}{1+z}\right)^4, \quad (7.15)$$

where g_a and g_b are parameters to be fit.

7.3 Observational Constraints

7.3.1 Scale Independent Analysis

The $f\sigma_8(z)$ and $E_G(z)$ updated data compilations used in our analysis are shown in Tables D.3 and D.4 of the Appendix D along with the references where each datapoint was originally published. The datapoints are also shown in Figs. 7.1 and 7.2 along with curves corresponding to the Planck/ Λ CDM prediction and the best fit parameter values. As it can be seen the datapoints from the various surveys are consistent with each other at any given redshift and at 1σ level. Clearly, in both cases the data appear to favor lower values of $f\sigma_8$ and E_G than the values corresponding to the Planck/ Λ CDM parameters. This trend combined with the indications for a Planck/ Λ CDM background from geometric probes may be interpreted as a need for a new degree of freedom which in our approach is coming from MG. In addition, we see that there is no tension between different $f\sigma_8$ datapoints. Instead, there is a combined trend of the datapoints to be in tension with the Planck/ Λ CDM prediction. This tension disappears when we keep the same Λ CDM background but allow for a MG evolution of the effective Newton's constant. In fact, this trend may be shown to be translated into a trend for lower values for the gravitational parameters μ_G and Σ_G and is quantified through a detailed maximum likelihood analysis.

Each $f\sigma_8(z)$ and $E_G(z)$ datapoint of the compilations of Tables D.3 and D.4 has been published separately in the context of independent analyses of distinct galaxy samples and lensing data. However, the correlations among the datapoints considered due to overlap of the analyzed galaxy samples may lead to an amplification of the existing trends indicated by the data and an amplification of the existing tension of the best fit parameters with Planck/ Λ CDM. Despite of this fact we have chosen to keep the relatively large number of distinct published datapoints in order to maximize the information encoded in the compilations considered keeping in mind that this may lead to an artificial amplification of the trends that already exist in the data.

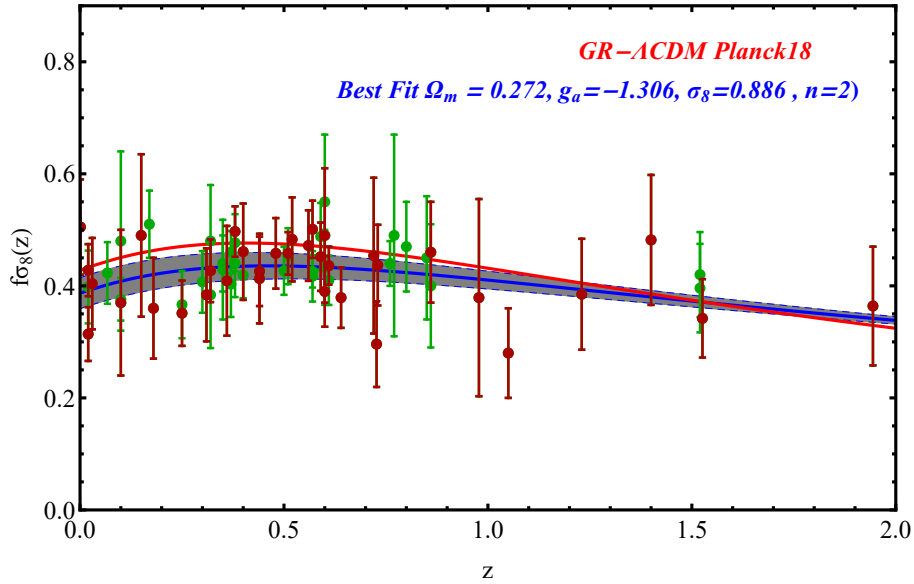


Figure 7.1: The $f\sigma_8(z)$ data compilation from Table D.3 used in the present analysis. The subset of the data with less correlation is indicated with dark red. The red curve shows the Planck18/ Λ CDM prediction (parameter values $\Omega_{0m} = 0.315$, $g_a = 0$, $\sigma_8 = 0.811$), the blue curve shows the best fit of the $f\sigma_8(z)$ in the context of parametrizations Eq. (7.14) with a Λ CDM background (parameter values $\Omega_{0m} = 0.272$, $g_a = -1.306$, $\sigma_8 = 0.886$) and the shaded regions correspond to 1σ confidence level around the best fit (see also Table 7.2).

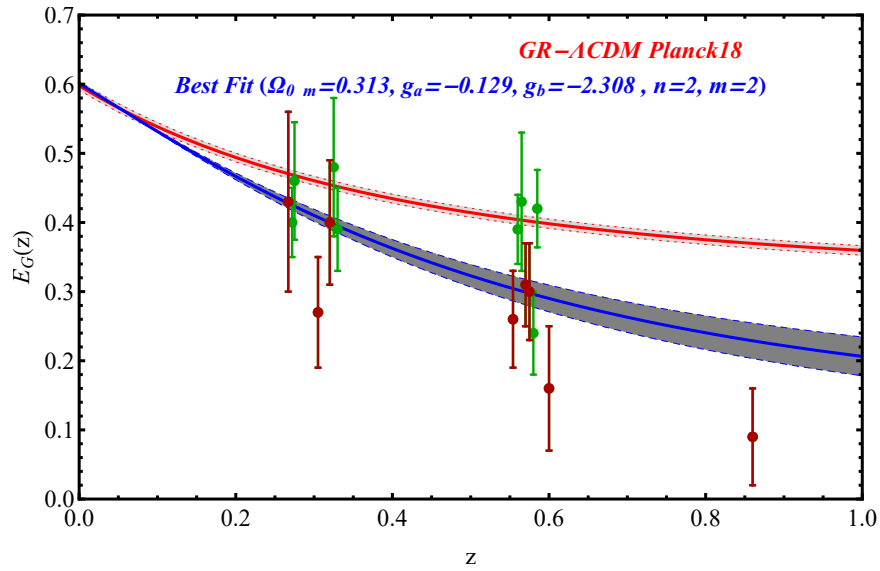


Figure 7.2: The $E_G(z)$ data compilation from Table D.4 (scales $3 < R < 150h^{-1}Mpc$) used in the present analysis. The subset of the data with less correlation is indicated with dark red. The red curve shows the theoretical prediction based on the Planck18/ Λ CDM parameter values ($\Omega_{0m} = 0.315$, $\sigma_8 = 0.811$, $\mu_G = 1$, $\Sigma_G = 1$), the blue curve shows the best fit theoretical prediction based on the parametrizations (7.14) and (7.15) with parameter values ($\Omega_{0m} = 0.313$, $g_a = -0.129$, $g_b = -2.308$). Notice that the best fit is significantly below the Planck/ Λ CDM theoretical prediction and implies weaker gravity ($\mu_G < 1$ and $\Sigma_G < 1$) at the 4.6σ level (see also Table 7.2).

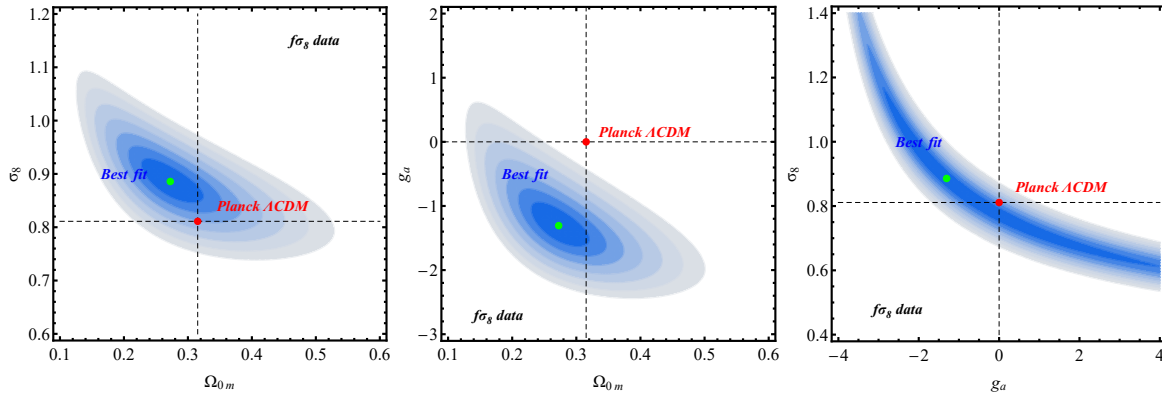


Figure 7.3: The three $1\sigma - 7\sigma$ confidence contours in 2D projected parameter spaces of the parameter space $(\Omega_{0m}, \sigma_8, g_a)$ in the context of parametrization Eq. (7.14) with $n = 2$ including the fiducial correction factor Eq. (7.17). The RSD data $f\sigma_8(z)$ from Table D.3 of the Appendix D was used. The third parameter in each contour was fixed to the best fit value. The red and green dots describe the Planck18/ Λ CDM best fit and the best-fit values from data.

An additional motivation for keeping the full set of published datapoints is that it is not always clear which one of the correlated points is more suitable to keep. Ignoring one of the correlated points arbitrarily or simply based on time of publication criteria could lead to loss of useful information or selection bias.

Keeping the full set of points does not significantly change the results and the level of tension between the growth data best fit parameter values corresponding to MG and Planck/ Λ CDM best fit in the context of GR. In order to demonstrate the validity of the above reasons we have repeated our analysis for a subset of the $f\sigma_8$ and E_G data where we have removed most earlier data that were subject to correlations with more recent data as indicated with bold font in the index of the Tables D.3 and D.4 and as shown in Figs. 7.1 and 7.2 with dark red. The result was a data compilation of about half the $f\sigma_8$ and E_G datapoints with significantly less correlation. The results of the statistical analysis of this dataset are presented in Appendix D and indicate a minor reduction of the overall tension.

For the construction of the likelihood contours of the model parameters in the context of the $f\sigma_8$ and E_G datasets we construct $\chi_{f\sigma_8}^2$ and $\chi_{E_G}^2$. For the construction of $\chi_{f\sigma_8}^2$ we use the vector [67]

$$V_{f\sigma_8}^i(z_i, p) \equiv f\sigma_{8,i}^{obs} - \frac{f\sigma_8^{th}(z_i, p)}{q(z_i, \Omega_{0m}, \Omega_{0m}^{fid})}, \quad (7.16)$$

where $f\sigma_{8,i}^{obs}$ is the value of the i th datapoint, with $i = 1, \dots, N_{f\sigma_8}$ (where $N_{f\sigma_8} = 66$ corresponds to the total number of datapoints of Table D.3) and $f\sigma_8^{th}(z_i, p)$ is the theoretical prediction, both at redshift z_i . The parameter vector p corresponds to the parameters $\sigma_8, \Omega_{0m}, g_a$ of Eq. (7.12) with the parametrization (7.14). The fiducial Alcock-Paczynski correction factor q [67, 147, 148] is defined as

$$q(z_i, \Omega_{0m}, \Omega_{0m}^{fid}) = \frac{H(z_i)d_A(z_i)}{H^{fid}(z_i)d_A^{fid}(z_i)}, \quad (7.17)$$

where $H(z)$, $d_A(z)$ correspond to the Hubble parameter and the angular diameter distance of the true cosmology and the superscript "fid" indicates the fiducial cosmology used in each survey to convert angles and redshift to distances for evaluating the correlation function. As shown in Table 7.2, the effects of this correction factor are less than about 10% in the derived best fit parameter values. Thus we obtain $\chi_{f\sigma_8}^2$ as

$$\chi_{f\sigma_8}^2(\Omega_{0m}, \sigma_8, g_a) = V_{f\sigma_8}^i F_{f\sigma_8, ij} V_{f\sigma_8}^j, \quad (7.18)$$

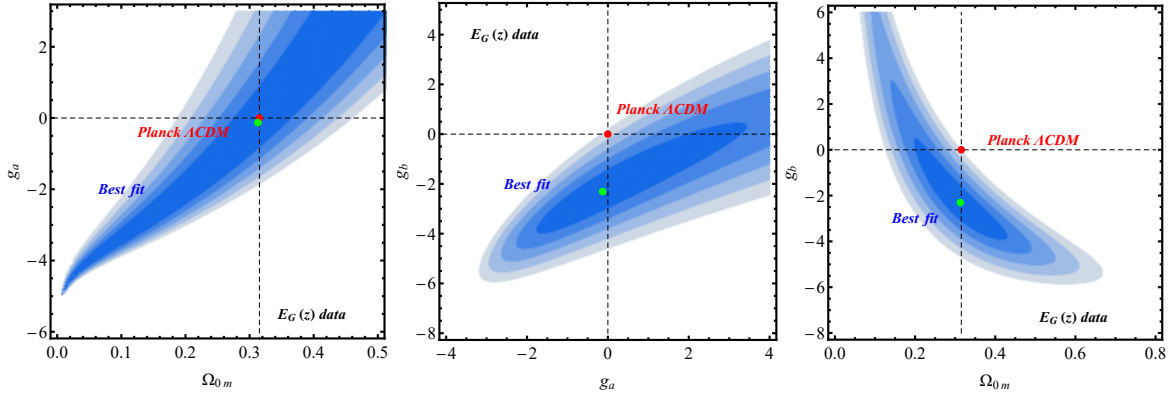


Figure 7.4: The three 1σ - 5σ confidence contours in 2D projected parameter spaces of the parameter space (Ω_{0m}, g_a, g_b) in the context of parametrizations Eqs. (7.14) and (7.15) with $n = 2, m = 2$. The data $E_G(z)$ from Table D.4 of the Appendix D were used. The third parameter in each contour was fixed to the best fit value. The red and green dots describe the Planck18/ Λ CDM best fit and the best-fit values from data.

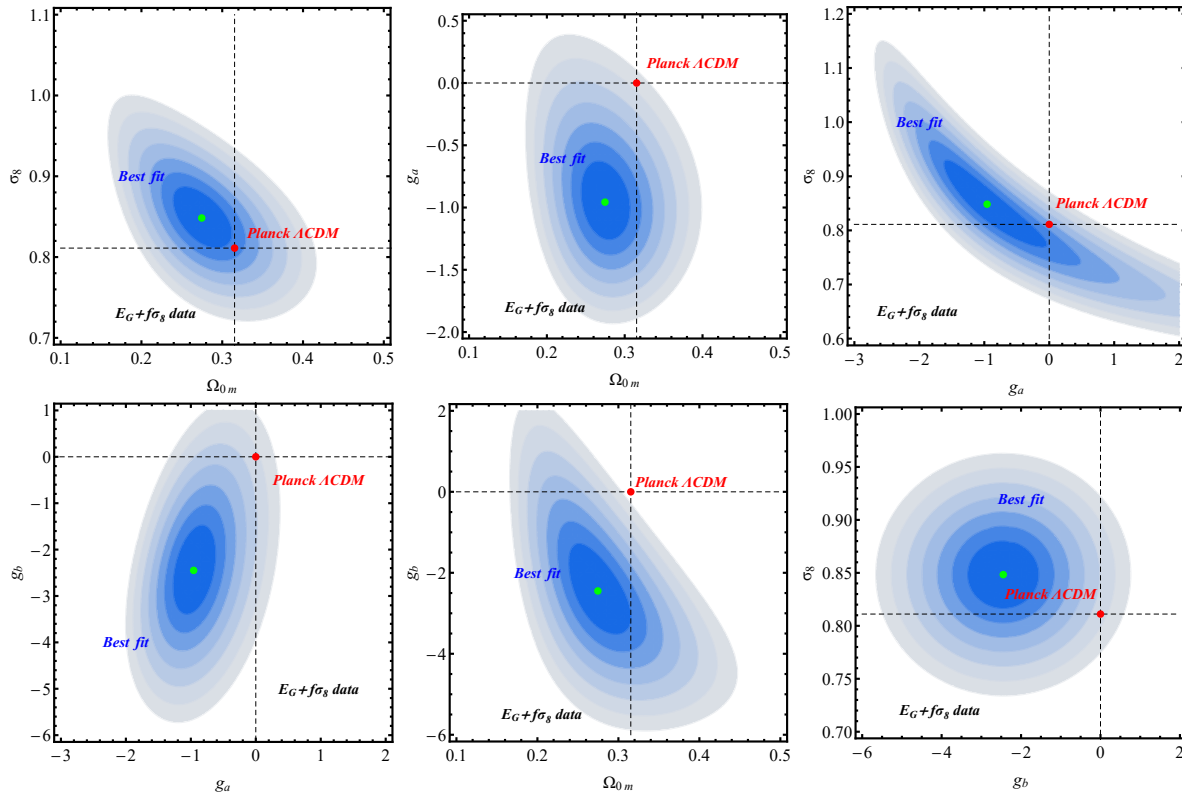


Figure 7.5: The six 1σ - 7σ confidence contours in 2D projected parameter spaces of the parameter space $(\Omega_{0m}, \sigma_8, g_a, g_b)$ in the context of parametrizations Eqs. (7.14) and (7.15) with $n = 2$ and $m = 2$ including the fiducial correction factor Eq. (7.17). The data $E_G(z)$ and $f\sigma_8(z)$ from Tables D.4 and D.3 of the Appendix D were used. The third and the fourth parameter in each contour were fixed to the best fit values. The red and green dots describe the Planck18/ Λ CDM best fit and the best-fit values from data.

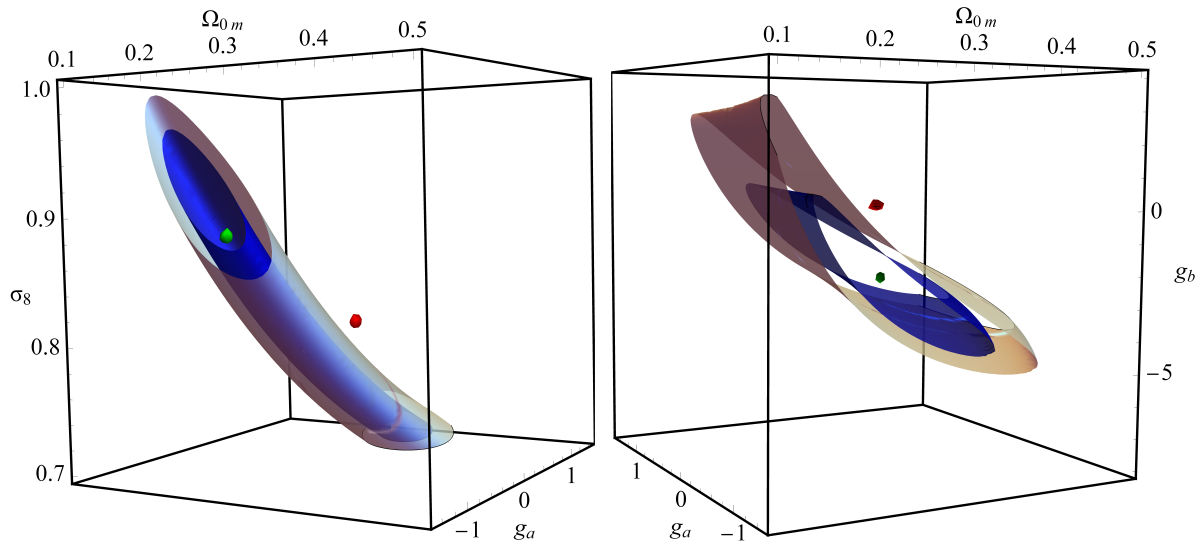


Figure 7.6: Left: The 1σ - 2σ confidence contour of the parameter space $(\Omega_{0m}, \sigma_8, g_a)$ in the context of parametrization Eq.(7.14) with $n = 2$ including the fiducial correction factor Eq. (7.17). The RSD data $f\sigma_8(z)$ from Table D.3 of the Appendix D was used. The red and green dots describe the Planck18/ Λ CDM best fit and the best-fit values from data. Right: The 1σ - 2σ confidence contour of the parameter space (Ω_{0m}, g_a, g_b) in the context of parametrizations Eqs. (7.14) and (7.15) with $n = 2$. The data $E_G(z)$ from Table D.4 of the Appendix D was used. The red and green dots describe the Planck18/ Λ CDM best fit and the best-fit values from data. The 3D contours include only the surfaces in 3D while the intermediate space is not filled. Thus, the white gaps that appear in the right figure between the surfaces, simply correspond to the white background seen from behind.

Table 7.2: Planck18/ Λ CDM based on TT,TE,EE+lowE+ lensing likelihoods best fit [14] and the best-fit values from data.

Param.	Planck18/ Λ CDM	Dataset $f\sigma_8(z)$. corr.	Dataset $f\sigma_8(z)$ no corr.	Dataset $E_G(z)$	Datasets $f\sigma_8(z) + E_G(z)$ corr.	Datasets $f\sigma_8(z) + E_G(z)$ no corr.
Ω_{0m}	0.3153 ± 0.0073	0.272 ± 0.019	0.263 ± 0.015	0.313 ± 0.024	0.275 ± 0.015	0.264 ± 0.012
σ_8	0.8111 ± 0.0060	0.886 ± 0.015	0.90 ± 0.016		0.848 ± 0.015	0.879 ± 0.015
g_a	0	-1.306 ± 0.140	-1.331 ± 0.138	-0.129 ± 0.490	-0.957 ± 0.144	-1.115 ± 0.137
g_b	0			-2.308 ± 0.423	-2.448 ± 0.414	-2.422 ± 0.416

where $F_{f\sigma_8,ij}$ is the Fisher matrix (the inverse of the covariance matrix $C_{f\sigma_8,ij}$ of the data) which is assumed to be diagonal with the exception of the 3×3 WiggleZ subspace (see Ref. [67] for more details on this compilation).

Similarly, for the construction of $\chi_{E_G}^2$, we consider the vector

$$V_{E_G}^i(z_i, p) \equiv E_{G,i}^{obs} - E_G^{th}(z_i, p), \quad (7.19)$$

where $E_{G,i}^{obs}$ is the value of the i th datapoint, with $i = 1, \dots, N_{E_G}$ (where $N_{E_G} = 16$ corresponds to the total number of datapoints of Table D.4), while $E_G^{th}(z_i, p)$ is the theoretical prediction (Eq. (7.13)), both at redshift z_i . The parameter vector p corresponds to the parameters of Eq. (7.13) with the parametrization (7.14) namely Ω_{0m}, g_a, g_b .

Thus we obtain $\chi_{E_G}^2$ as

$$\chi_{E_G}^2(\Omega_{0m}, g_a, g_b) = V_{E_G}^i F_{E_G,ij} V_{E_G}^j, \quad (7.20)$$

where $F_{E_G,ij}$ is the Fisher matrix also assumed to be diagonal.

By minimizing $\chi_{f\sigma_8}^2$, $\chi_{E_G}^2$ separately and combined as $\chi_{tot}^2 \equiv \chi_{f\sigma_8}^2 + \chi_{E_G}^2$ we obtain the constraints on the parameters $\Omega_{0m}, \sigma_8, g_a, g_b$ shown in Figs. 7.3, 7.4 and 7.5 respectively. Each one of these Figures corresponds to a 2D projection that goes through the best fit parameter point in parameter space of the full three or four dimensional contour plot in each case. The full number of parameters (three or four) was assumed when constructing the contour 2D projections. Previous studies [67, 148] have considered similar 2D projections that go through the Planck/ Λ CDM best fit parameter point in the higher dimensional parameter space. This later choice tends to change somewhat (in most projections it is increased) the apparent tension between the best fit MG parameter values and the best fit Planck/ Λ CDM parameters in the 2D projection parameter subspaces. This 2D tension may be in some cases misleading due to projection effects and thus in Table 7.3 we stress the tension in the full 3D or 4D parameter space.

The tension level between the best fit MG parameter values and the Planck/ Λ CDM best fit parameter values is significant in both the 2D projection parameter spaces shown in Figs. 7.3, 7.4 and 7.5 and in the higher 3D parameter space likelihood surfaces shown in Fig. 7.6. The best fit parameter values obtained in the context of the datasets considered and the tension levels in both the 2D projections and in the full 3D-4D parameter spaces are shown in Tables 7.2 and 7.3 respectively. In these Tables we also show the cases corresponding to fits without including the correction factor Eq. (7.17) in the $f\sigma_8$ data demonstrating that there is a small change in the best fit parameter values.

Table 7.3: Sigma differences of the best fit contours from Planck18/ Λ CDM.

Dataset	Space			2D Projected Space					
	$(\Omega_{0m}, \sigma_8, g_a)$	(Ω_{0m}, g_a, g_b)	$(\Omega_{0m}, \sigma_8, g_a, g_b)$	(Ω_{0m}, σ_8)	(Ω_{0m}, g_a)	(σ_8, g_a)	(g_a, g_b)	(Ω_{0m}, g_b)	(σ_8, g_b)
$f\sigma_8(z)$ corr.	3.70 σ			3.00 σ	$\sim 8\sigma$	2.08 σ			
$f\sigma_8(z)$ no corr.	4.15 σ			2.75 σ	$\sim 8\sigma$	1.13 σ			
$E_G(z)$		4.57			0.002 σ		4.45 σ	4.94 σ	
$E_G(z)+f\sigma_8(z)$ corr.			6.03	1.47 σ	6.39 σ	2.59 σ	5.74 σ	7.74 σ	5.58 σ
$E_G(z)+f\sigma_8(z)$ no corr.			6.33	2.17 σ	$\sim 8\sigma$	2.16 σ	7.53 σ	$\sim 8\sigma$	6.74 σ

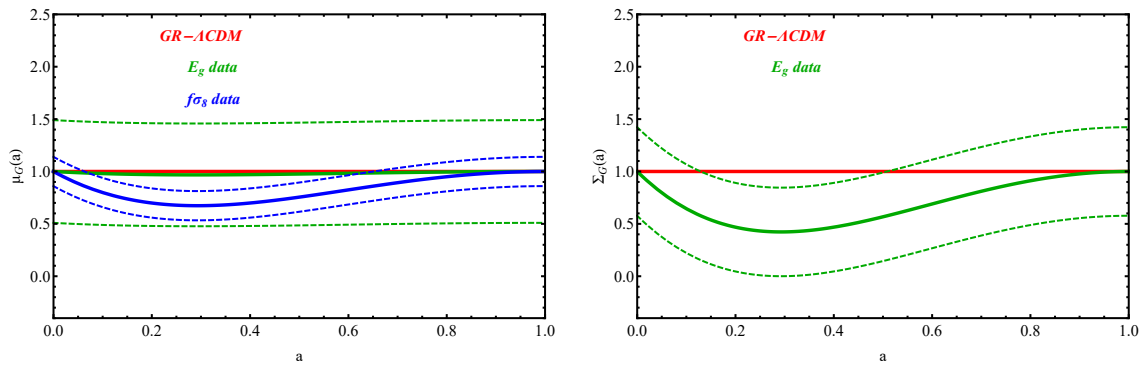


Figure 7.7: Evolution of μ_G and Σ_G as functions of the scale factor a considering the best fit values for g_a and g_b in the context of parametrizations Eqs. (7.14) and (7.15) with $n = 2, m = 2$. The data $E_G(z)$ and $f\sigma_8(z)$ from Tables D.4 and D.3 of the Appendix D was used. The dashed curves correspond to 1σ deviations of the parameters μ_G and Σ_G . The red lines correspond to the GR- Λ CDM model.

The following comments can be made on the results shown in Figs. 7.3, 7.4 and 7.5 and Tables 7.2 and 7.3:

- The left part of Table 7.3 shows the tension level in the full 3D or 4D parameter space. The tension level between Planck/ Λ CDM and best fit MG model parametrizations (7.14) and (7.15) in the context of the $f\sigma_8$ data is significant (about 3.5σ) but is less than the corresponding tension obtained using the E_G statistic data (more than 4σ). In fact for the combined $f\sigma_8 + E_g$ dataset the tension level increases to close to 6σ ! This significant tension level comes independently from both the $f\sigma_8$ and E_G data and hints towards weaker gravity (μ_G and Σ_G lower than 1) compared to the predictions of GR at low z . We stress however that this extreme level of tension is partly due to correlations among the considered datapoints which necessarily exist in our compilations.
- The weaker than expected gravitational growth indicated by the data is expressed as both a lower best fit Ω_{0m} than expected from Λ CDM and as negative best fit values for the gravitational strength evolution parameters g_a and g_b (see e.g. Fig. 7.5).
- Ignoring the fiducial model correction factor of Eq. (7.17) in most cases tends to slightly increase the tension level (compare e.g. the last two lines of Table 7.3). Thus the consideration of this correction in our analysis is a conservative approach.

The trend for weaker gravity at low redshifts is also evident in Fig. 7.7 which shows the best fit form of $\mu_G(a)$ and $\Sigma_G(a)$ in the context of each dataset.

Also, the likelihood contours in the σ_8 - Ω_m parameter space obtained using the growth data in the presence of the MG parameter g_a and in the context of GR ($g_a = 0$) are shown in Fig. 7.8. We have

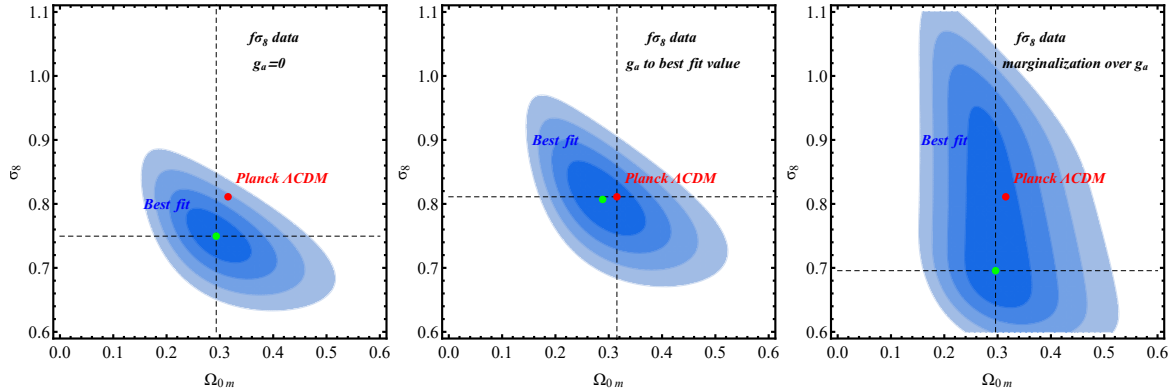


Figure 7.8: The confidence contours of the parameter space (σ_8 - Ω_m) in the context of GR (left panel) and in the presence of the MG parameter g_a (fixing $w = -1$) in the context of parametrization Eq. (7.14) with $n = 2$. We have considered both the case of a marginalized MG parameter value (right panel) and the case of setting g_a to its best fit value (middle panel). The red and green dots describe the Planck18/ Λ CDM best fit and the best-fit values from data. The $f\sigma_8(z)$ data compilations of datapoints with less correlation from Table D.3 of the Appendix D was used. Notice the reduction of tension between the growth data best fit and the Planck/ Λ CDM parameter values when the MG degree of freedom is introduced.

considered both the case of a marginalized MG parameter value and the case of setting g_a to its best fit value. Clearly the tension level between the best fit parameter values and Planck/ Λ CDM decreases significantly in the presence of the MG parameter g_a .

The introduction of additional parameters of any type would in general widen the likelihood contours and thus reduce the tension between growth data and geometric/CMB data. In general a faster expansion rate ($w < -1$) would tend to reduce the growth rate of perturbations in agreement with dynamical observables. However, geometric observables (SnIa, BAO etc.) do not allow significant deviations of the expansion rate from Λ CDM. Thus the most efficient way to produce a weaker growth of perturbations is the introduction of evolution of the MG parameters μ_G and Σ_G . In Fig. 7.9 we have demonstrated this effect by fixing $g_a = 0$, $g_b = 0$ and constructing the σ_8 - Ω_m contours with $w = -1$ and w free to vary in a range ($[-1.5, -0.5]$) consistent with geometric probes. The reduction of the tension in this case is significantly smaller compared to the introduction of MG degrees of freedom.

7.3.2 Scale Dependent Data Compilations

Scale dependent parametrizations for μ_G and η can describe a large class of MG models [330, 1996]. For example a scale dependent class of parametrizations predicted by scalar-tensor theories for μ_G and η is of the form [862, 1524]

$$\mu_G(a, k) = 1 + f_1(a) \frac{1 + c_1(\lambda H/k)^2}{1 + (\lambda H/k)^2}, \quad (7.21)$$

$$\eta(a, k) = 1 + f_2(a) \frac{1 + c_2(\lambda H/k)^2}{1 + (\lambda H/k)^2}, \quad (7.22)$$

where f_1 and f_2 are properly chosen functions that depend on the scale factor. Thus a physically motivated scale dependent generalization of the parametrizations (7.14) and (7.15) for μ_G and Σ_G may be written as

$$\mu_G(R, z) = 1 + \left[g_a \left(\frac{z}{1+z} \right)^n - g_a \left(\frac{z}{1+z} \right)^{2n} \right] \frac{1 + s_a(\lambda HR)^2}{1 + (\lambda HR)^2}, \quad (7.23)$$

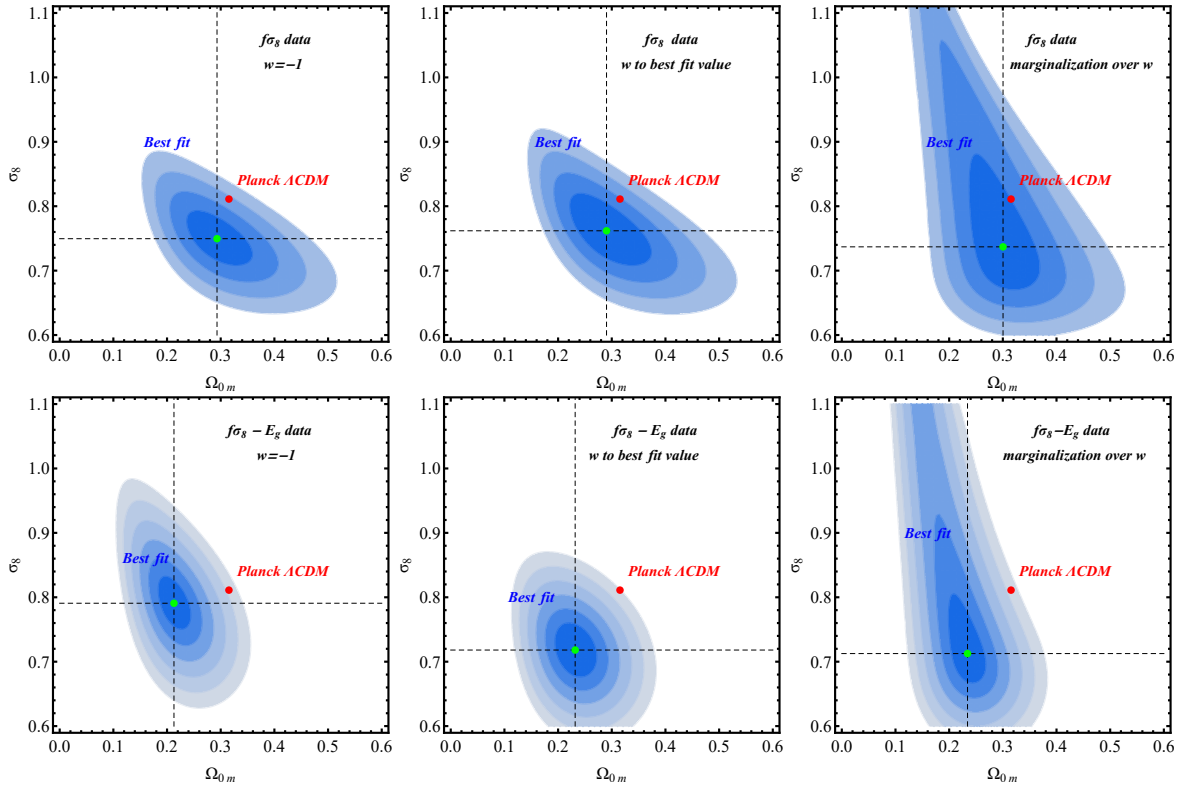


Figure 7.9: The confidence contours of the parameter space $(\sigma_8 - \Omega_m)$ in the context of GR (left panels) and in the presence of the w parameter (fixing $g_a = 0$ and $g_b = 0$). We have considered both the case of a marginalized w $([-1.5, -0.5])$ parameter value (right panels) and the case of setting w to its best fit value $(-0.94$ and -1.29 from $f\sigma_8(z)$ and $f\sigma_8(z) + E_G(z)$ data respectively) (middle panels). The red and green dots describe the Planck18/ Λ CDM best fit and the best-fit values from data. The $E_G(z)$ and $f\sigma_8(z)$ data compilations of datapoints with less correlation from Tables D.4 and D.3 of the Appendix D was used. Notice that the reduction of tension between the best fit parameter values and Planck/ Λ CDM is less efficient when the w degree of freedom (modified background expansion rate) is introduced compared to the MG degree of freedom g_a shown in Fig. 7.8.

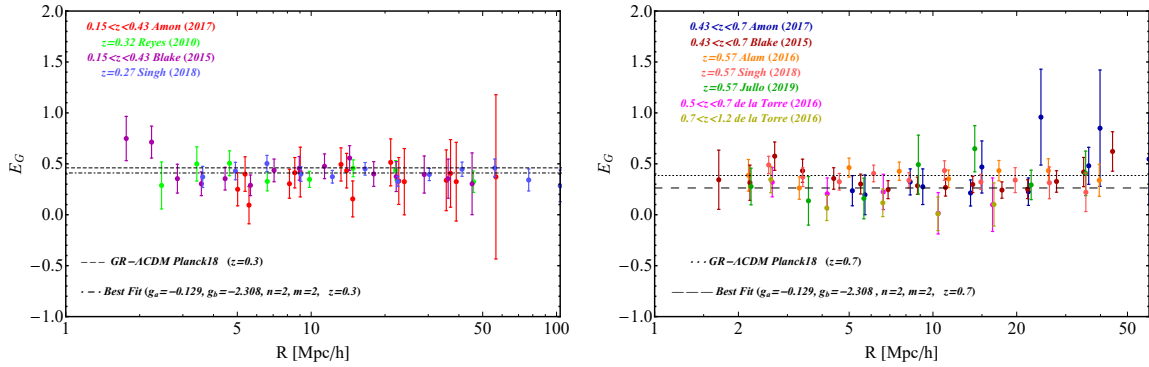


Figure 7.10: Measurements of E_G as a function of scale R in the range $0.15 < z < 0.43$ (left panel) and $0.43 < z < 1.2$ (right panel). The data $E_G(R)$ from Tables D.5 and D.6 of the Appendix D was used. The dashed black line shows the Planck18/ Λ CDM prediction at $z = 0.3$, the dotted black line shows the Planck18/ Λ CDM prediction at $z = 0.7$, while the dotdashed black line and the large dashed black line shows the best fit of the E_G in the context of parametrizations Eqs. (7.14) and (7.15) at $z = 0.3$ and at $z = 0.7$ respectively.

$$\Sigma_G(R, z) = 1 + \left[g_b \left(\frac{z}{1+z} \right)^m - g_b \left(\frac{z}{1+z} \right)^{2m} \right] \frac{1 + s_b (\lambda H R)^2}{1 + (\lambda H R)^2}, \quad (7.24)$$

where s_a , s_b and λ are parameters to be determined from a proper scale dependent dataset. Such a scale dependent data compilation for the statistic E_G in two redshift ranges is shown in Fig. 7.10 and in Tables D.5 and D.6 for low and high z respectively in the Appendix D. The analysis of this compilation may be performed in the context of the scale dependent parametrizations (7.23) and (7.24). Clearly as shown in Fig. 7.10, for both low and high z the scale independent MG parametrizations of Eqs. (7.14) and (7.15) at $z = 0.3$ and at $z = 0.7$, lead to a best fit value of E_G that is lower compared to the Planck/ Λ CDM prediction. The full scale dependent analysis leads to similar levels of tension as those indicated in Table 7.3 for the scale independent case and will be presented in detail elsewhere.

7.4 Conclusions

In this Chapter we have used up to date compilations of E_G and $f\sigma_8$ data (Tables D.3 and D.4) based on WL and RSD observations to obtain updated estimates of the tension between the Planck/ Λ CDM best fit parameter values and the best fit parameter values obtained in the context of an effective MG gravity model allowing for properly parametrized evolution of the growth and lensing gravitational constants μ_G and Σ_G . The scale independent parametrizations (Eqs.(7.14) and (7.15)) of μ_G and Σ_G depend on the parameters g_a and g_b respectively and are by construction consistent with GR at early times and at present as indicated by nucleosynthesis and solar system constraints assuming no screening is present. We have assumed a flat Λ CDM expansion background and we thus fit the parameters $(\Omega_{0m}, \sigma_8, g_a, g_b)$.

We find that the E_G data amplify the previously well known indications for low Ω_{0m} and/or weaker gravity ($\mu_G < 1$) at low z and favor weaker gravity for both the growth and the lensing gravitational constants ($\mu_G < 1$ and $\Sigma_G < 1$). The tension level between the Planck/ Λ CDM parameter values $(\Omega_{0m}, \sigma_8, g_a, g_b) = (0.31, 0.81, 0, 0)$ and the best fit parameter values obtained using the combined $E_G + f\sigma_8$ dataset $(\Omega_{0m}, \sigma_8, g_a, g_b) = (0.28, 0.85, -0.96, -2.45)$ is 6σ which is significantly larger compared to the tension obtained when only the $f\sigma_8$ dataset is used (3.7σ as shown in Table 7.3). Even though the absolute magnitude of the derived tension is overestimated due to the correlations among the datapoints the amplified trend for weaker gravity at low z is clearly indicated by both the $f\sigma_8$ and E_G data compilations and appears to be stronger for the case of the E_G data.

If this trend has some physical origin and is not due only to data systematics or physical effects in the context of GR, there are significant implications for theoretical models. In particular $f(R)$ theories generically predict stronger gravity at low z compared to its present time [1823] (thus the prediction is $\mu_G(z) > 1$, $g_a > 0$) and therefore if the identified tension has physical origin this can not be attributed to an $f(R)$ MG gravity theory for any expansion background. Similarly minimal ST theories [1197, 1823], Horndeski theories [1406, 2014] and beyond Horndeski Gleyzes-Langlois-Piazza-Vernizzi (GLPV) theories [1199] can only produce weaker gravity at low z under very specific and in some cases unnatural conditions [1305]. For example minimal scalar-tensor theories would require the existence of a phantom cosmological background expansion (equation of state parameter $w < -1$) [1197, 1823]. In fact, a very large class of MG models, the scalar-tensor Horndeski models, are not consistent with the observational indications of weakening gravity. In fact as stated in Ref. [2015] (p. 12), μ_G for stable Horndeski models is always larger than, or equal to, 1 so that matter perturbations in viable Horndeski models always grow faster than the corresponding GR models with the same backgrounds. Thus these MG models (which include $f(R)$ gravity theories) are unable to account for the weakening and would provide a worse fit than GR to the $f\sigma_8/E_G$ data. The search for MG models that can account for the observed indications for weakening gravity is thus an interesting extension of our analysis.

A partial cause of the E_G data tension with Planck/ Λ CDM is lensing magnification. As shown in Refs. [2016, 2017] the effects of lensing magnification modify the galaxy-galaxy lensing correlations as well as galaxy-galaxy correlations and as a consequence introduce systematic errors in the estimate of E_G while making it bias dependent. The effect is small for redshifts smaller than 1 (about 5 – 10%) but it can become as large as 20 – 40% for redshifts $z \simeq 1.5$. Thus, this systematic contribution can be relevant already for DES [1796, 1797, 2018–2020] and certainly for higher redshift surveys. However, the magnitude of lensing contribution at the redshifts of the data compilation we are using ($z < 1$) is not large enough to significantly reduce the identified tension which exists even at the level of the RSD data alone. The systematic effect discussed in Refs. [2016, 2017] is important especially for upcoming surveys like Euclid [1806] which probe higher redshifts even though even in that case it may not be large enough to be the only source the observed tension. An interesting feature of our compilation is the scale dependence the $E_G(R, z)$ data. This may be used to probe the parameters of scale dependent MG μ_G and Σ_G parametrizations which are well motivated physically. A key question to address is whether the addition of scale dependence in the parametrizations can improve significantly the overall fit. No such indications are currently known [862] but this may well change using more extensive and accurate scale dependent E_G and $f\sigma_8$ data.

Chapter 8

Scalar Tachyonic Instabilities in Gravitational Backgrounds: Existence and Growth Rate

The analysis presented in this chapter is based on the work which was done in collaboration with Prof. Leandros Perivolaropoulos and has been published in Physical Review D [5].

In this chapter, we study the tachyonic instabilities in the dynamic evolution of a free massive scalar field Φ with potential equation of the form $V(\phi) = m^2\phi^2$. We focus on the existence of instabilities and their growth rate in the following non flat (curved) gravitational backgrounds: Reissner-Nordstrom-deSitter (RN-dS) background, Schwarzschild-deSitter (SdS) background, pure deSitter background, pure Schwarzschild background.

Scalar fields are used to describe a wide range of degrees of freedom in a diverse set of physical systems in particle physics (e.g. the Higgs field and other symmetry breaking scalar fields [2021]), cosmology (e.g. the inflaton [2022] and the quintessence field [577]), gravitational theories (e.g. scalar field hair on black holes [2023]) or modified gravity scalar degrees of freedom like $f(R)$ theories [110–113, 584, 1849, 1850, 2024–2028] or Scalar Tensor (ST) theories [587]), condensed matter (e.g. the Bose-Einstein scalar field condensate [2029]) etc. A stabilizing effect of multiple horizons on tachyonic instabilities can provide various interesting implications. For example tachyonic instabilities of $f(R)$ and ST theories can get significantly delayed in backgrounds involving cosmological horizons with possible implications for the development of preheating after inflation [2030–2033].

8.1 Introduction

The dynamical evolution of a scalar field in a classical system is determined by three main factors

- The form of its Lagrangian density and especially the scalar field potential $V(\phi)$ which may be e.g. of the form $V(\phi) = m^2\phi^2$ for a simple massive scalar field or of a symmetry breaking form $V(\phi) = \frac{\lambda}{4}(\phi^2 - \eta^2)^2$ where η is the scale of symmetry breaking.
- The form of the background spacetime which may be for example flat Minkowski, cosmological Friedmann-Robertson-Walker (FRW), Schwarzschild etc.
- The boundary/initial conditions used for the solution of the resulting dynamical scalar field equation emerging from the above two factors.

The simplest Lagrangian density describing the evolution of a scalar field is that corresponding to a free massive scalar which is of the form

$$\mathcal{L} = \frac{1}{2} \partial_\mu \Phi \partial^\mu \Phi - m^2 \Phi^2 , \quad (8.1)$$

leading to the Klein-Gordon equation [2034]

$$\square \Phi + m^2 \Phi = 0 . \quad (8.2)$$

In flat Minkowski space this equation may be written as

$$\ddot{\Phi} - \nabla^2 \Phi = -m^2 \Phi . \quad (8.3)$$

Its solutions are propagating waves of the form

$$\Phi(\vec{r}, t) = A(\vec{k}) e^{i(\omega t - \vec{k}\vec{r})} + B(\vec{k}) e^{-i(\omega t - \vec{k}\vec{r})} , \quad (8.4)$$

with dispersion relation

$$\omega^2 = k^2 + m^2 . \quad (8.5)$$

For $m^2 > 0$ we have well behaved propagating waves. However, for $m^2 < 0$ we have

$$\omega = \pm \sqrt{k^2 - |m|^2} , \quad (8.6)$$

and exponentially growing tachyonic instabilities develop on large scales ($k < |m|$) where $Im(\omega) \neq 0$ [2031]. In the context of a spontaneous symmetry breaking potential, these instabilities usually imply the presence of a broken symmetry and the transition of the scalar field to a new stable (or metastable) vacuum. However, in the context of a potential that is unbounded from below they may also imply that the theory is unphysical and should be ruled out. This argument has lead to disfavor of a wide range of theories which involve scalar fields with negative m^2 including a wide range of massive Brans-Dicke (BD) theories and $f(R)$ theories where such tachyonic instabilities are also known as Dolgov-Kawasaki-Faraoni (DKF) instabilities [2035, 2036] (see also Refs. [2037–2042]). For example a massive BD scalar field has an action of the form¹ [1845, 2043–2046]

$$S = \frac{1}{16\pi G} \int d^4x \sqrt{-g} \left[\Phi R - \frac{\omega}{\Phi} g^{\mu\nu} \partial_\mu \Phi \partial_\nu \Phi - m^2 (\Phi - \Phi_0)^2 \right] . \quad (8.7)$$

In this theory (using finite boundary conditions at infinity) a small point mass M located at the origin creates a scalar field and metric configurations of the form

$$\Phi = \Phi_0 + \varphi , \quad (8.8)$$

$$g_{\mu\nu} = \eta_{\mu\nu} + h_{\mu\nu} , \quad (8.9)$$

where

$$\varphi = \frac{2GM}{(2\omega + 3)r} e^{-\bar{m}(\omega)r} , \quad (8.10)$$

$$h_{00} = \frac{2GM}{\Phi_0 r} \left(1 + \frac{1}{2\omega + 3} e^{-\bar{m}(\omega)r} \right) , \quad (8.11)$$

$$h_{ij} = \frac{2GM}{\Phi_0 r} \delta_{ij} \left(1 - \frac{1}{2\omega + 3} e^{-\bar{m}(\omega)r} \right) , \quad (8.12)$$

with $\bar{m}(\omega) = \sqrt{\frac{2\Phi_0 m^2}{2\omega + 3}}$ (Φ_0 is dimensionless) [2044].

¹The BD parameter ω should not be confused with angular frequency ω used above.

This h_{00} metric perturbation corresponds to an effective Newton's constant that has a Yukawa correction of the form

$$G_{\text{eff}} = \frac{G}{\Phi_0} \left(1 + \frac{1}{2\omega + 3} e^{-\bar{m}(\omega)r} \right). \quad (8.13)$$

This Yukawa correction is decaying exponentially for $m^2 > 0$ and is observationally/experimentally viable either for large values of $\omega > 40000$ [2047] (so that the amplitude of the Newtonian correction is small) or for large values of the scalar field mass m (so that the Newtonian correction decays fast) [2044].

For $m^2 < 0$ it is easy to show that the corresponding G_{eff} is spatially oscillating with wavelength $\lambda \simeq \frac{2\pi}{\bar{m}}$

$$G_{\text{eff}} = \frac{G}{\Phi_0} \left(1 + \frac{1}{2\omega + 3} \cos(\bar{m}(\omega)r + \theta) \right), \quad (8.14)$$

where θ is an arbitrary constant. For spatial oscillations of G_{eff} with wavelength less than sub-mm scales ($m \gtrsim 10^{-3}$ eV ($\lambda \lesssim 1$ mm) [73, 170]) these spatial oscillations of G_{eff} would have hardly any observational/experimental effects with current experiments/observations despite of the fact that there is no Newtonian limit as $m^2 \rightarrow 0^-$ [170, 2048]. This is due to the local spatial cancellation of the spatially oscillating force correction. However, the main problem with $m^2 < 0$ are tachyonic instabilities [2049–2052].

It is easy to show that perturbations of the BD scalar Eq. (8.10) obey in flat space a KG equation of the form

$$\ddot{\delta\varphi} - \nabla^2 \delta\varphi + m^2 \delta\varphi = 0, \quad (8.15)$$

which for $m^2 < 0$ implies the presence of exponentially growing with time tachyonic instabilities for large scales [170]. Thus, this theory with $m^2 < 0$ is only viable if the unstable scales are pushed beyond the cosmological horizon $\sim H_0^{-1}$ which corresponds to scalar field mass $|m| < 10^{-33}$ eV similar to a quintessence scalar field mass. Such spatially oscillating modes have a cosmological horizon scale wavelength and have no observable effects on small scale gravity experiments.

In the case of $f(R)$ theories which may be shown to be equivalent to BD theories with no kinetic term ($\omega = 0$) [2053–2057] a similar instability occurs. For example the $f(R)$ theory of the form (Starobinsky model [2058])

$$f(R) = R + \frac{1}{6m^2} R^2, \quad (8.16)$$

is easily shown to be equivalent to the BD theory with action [170, 2056, 2059–2063]

$$S_{BD} = \frac{1}{16\pi G} \int d^4x \sqrt{-g} \left[\Phi R - \frac{3}{2} m^2 (\Phi - 1)^2 \right] + S_{\text{matter}}, \quad (8.17)$$

and therefore has the same tachyonic instabilities as the above mentioned massive BD theory (DKF instability).

The parameter value $|m| \simeq 10^{-3}$ eV with $m^2 < 0$ leads to an oscillating Newton's constant with wavelength about 1 mm. In this case the lifetime of the unstable tachyonic modes in Minkowski spacetime would be about 10^{-11} sec. Thus, even though the mass range $|m| > 10^{-3}$ eV with $m^2 < 0$ leads to oscillating modifications of Newton's constant that are consistent with observations/experiments, in the context of $f(R)$ and BD theories and in a flat space background, this mass range is ruled out due to the predicted tachyonic instabilities. This inconsistency is undesirable in view of recent studies² [170, 171, 1197] that pointed out the existence of oscillating force signals in short range gravity experiments. It is therefore interesting to investigate if there are physical conditions that can eliminate these tachyonic instabilities or at least drastically change their lifetime.

A crucial assumption used in the derivation of the above tachyonic instability is the existence of a Minkowski background. The following questions therefore emerge:

- Do scalar tachyonic instabilities for $m^2 < 0$ persist in the presence of a non-flat background?

²For viable theoretical models with spatially oscillating G_{eff} see Refs. [1770, 2064, 2065].

- How do the instability lifetime and growth rate change in a curved background?
- What are the parameter values of a background metric required to significantly increase the instability lifetime compared to its value in a Minkowski spacetime?

The main goal of our analysis is to address these questions. In particular we solve the KG equation in a Reissner-Nordström-deSitter (RN-dS) background metric [2066, 2067] with charge Q , mass M and cosmological constant Λ , in the region between the event horizon and the cosmological horizon with boundary conditions corresponding to a finite scalar field Φ with exponential tachyonic instabilities. Using tortoise coordinates that shift these horizons to $\pm\infty$, the KG equation is reduced to a Schrodinger-like Regge-Wheeler equation whose bound states correspond to instability modes. We find the critical value of m^2 (m_{cr}^2) such that for $m^2 < m_{cr}^2$ bound states (instability modes) exist. For the tachyonic unstable modes ($m^2 < m_{cr}^2$) we also find the growth rate of the instabilities (ground state eigenvalues of Regge-Wheeler equation) and compare with the corresponding growth rate in a flat Minkowski background. We also consider special cases of the RN-dS metric including the Schwarzschild metric [2068], the deSitter (dS) metric [2069–2073], the Schwarzschild-deSitter (SdS) metric [2074, 2075] and the Reissner-Nordström (RN) metric [2076–2078].

In our analysis we focus on the existence of tachyonic exponentially growing solutions and do not consider propagating waves on the boundary horizons which would lead to calculation of Quasinormal Modes³ (QNMs) [2092, 2093] (see Refs. [2094–2098], for reviews on QNMs of black holes). Such investigation of QNMs has been performed in previous studies in Schwarzschild black hole [2099–2101], in SdS background for $m = 0$ [2102–2105], for $m^2 > 0$ in RN-dS background [2106–2109] and in Kerr-deSitter background [2110–2115] where a different type of instability was observed in the context of scalar field wave scattering. This instability is connected with the phenomenon of superradiance [2116–2125] in which a reflected wave has larger amplitude than the corresponding incident wave. Superradiant instabilities occur in rotating and in charged black holes embedded in a deSitter space and are based on the extraction of mass and/or rotational or electromagnetic energy from the black hole. This energy is then carried away from the black hole during a scattering process through the propagation of a reflected scalar field wave with amplitude increased compared to the incident scalar field wave. Superradiance would lead to a decrease in black hole energy and increase of the energy of the scalar field causing further enhancement of the instability. Thus, the endpoints of such instability could be the evacuation of matter from the black hole and/or the formation of a novel scalar field configuration around the black hole leading to a phenomenon called 'scalarization' and violation of the no-hair theorem, which states that black holes are fully characterized by their mass, charge and angular momentum. A crucial property of spacetimes with superradiant instabilities is the combination of an event horizon with a cosmological deSitter horizon in four or higher dimensions [2126, 2127]. In this context one of the goals of our analysis is the identification of the role of this combination of horizons on tachyonic instabilities and the discussion of their possible connection with superradiant instabilities which involve boundary conditions of propagating wave modes.

The structure of this Chapter is the following: In the next Section 8.2 we use spherical tortoise coordinates r_* in the context of an instability ansatz, to transform the KG equation to a Schrodinger-like Regge-Wheeler equation for the radial function $u_l(r_*)$ with potential that depends on the angular scale l , the dimensionless parameters $\xi \equiv 9M^2\Lambda$ and $q \equiv Q/M$ defined above as well as the scalar field mass m^2 . The existence of unstable modes that are finite at the two horizons, is equivalent with the existence of bound states of this Regge-Wheeler equation. In Section 8.3, we solve the Regge-Wheeler equation numerically and identify the range $m^2(q, \xi)$ for which bound states (unstable modes) exist. In the parameter range that remains unstable ($m^2 < m_{cr}^2(q, \xi)$) we find the growth rate Ω of the instabilities. In Section 8.4 we discuss the scalar tachyonic instabilities in the limiting cases of pure deSitter and pure Schwarzschild backgrounds. Finally, in Section 8.5 we conclude and discuss the physical implications of our results. We also discuss possible extensions of this analysis.

In what follows we use Planck units ($G = c = \hbar = 1$) and a metric signature $(+ - - -)$.

³A semi-analytical method for calculations of QNMs based on the Wentzel-Kramers-Brillouin (WKB) approximation [2079, 2080]. This method was used in a wide range of spacetimes and in a lot of studies (see e.g. Refs. [2081–2091]).

8.2 KG equation in SdS/RN-dS spacetimes

8.2.1 Schwarzschild-deSitter background

Consider a SdS background spacetime defined by the metric [2074]

$$ds^2 = f(r)dt^2 - \frac{1}{f(r)}dr^2 - r^2(d\theta^2 + \sin^2\theta d\phi^2) , \quad (8.18)$$

where

$$f(r) = 1 - \frac{2M}{r} - \frac{\Lambda}{3}r^2 . \quad (8.19)$$

In such a background the KG equation (8.2) takes the form

$$\frac{1}{f(r)} \frac{\partial^2 \Phi}{\partial t^2} - \frac{\partial}{\partial r} f(r) \frac{\partial \Phi}{\partial r} - \frac{2f(r)}{r} \frac{\partial \Phi}{\partial r} - \frac{\Delta_{\theta\phi} \Phi}{r^2} + m^2 \Phi = 0 , \quad (8.20)$$

with

$$\Delta_{\theta\phi} = \frac{1}{\sin\theta} \frac{\partial}{\partial\theta} \sin\theta \frac{\partial}{\partial\theta} + \frac{1}{\sin^2\theta} \frac{\partial^2}{\partial\phi^2} . \quad (8.21)$$

Using now the ansatz

$$\Phi(t, r, \theta, \phi) = \sum_{lm} \frac{\Psi_l(t, r)}{r} \Upsilon_{lm}(\theta, \phi) , \quad (8.22)$$

the eigenvalue equation

$$\Delta_{\theta\phi} \Upsilon_{lm}(\theta, \phi) = -l(l+1) \Upsilon_{lm}(\theta, \phi) , \quad (8.23)$$

and transforming to tortoise coordinates defined as e.g. [2128–2130]

$$dr_* \equiv \frac{dr}{f(r)} , \quad (8.24)$$

the KG equation reduces to

$$\left(\frac{\partial^2}{\partial t^2} - \frac{\partial^2}{\partial r_*^2} + V_l(r) \right) \Psi_l(t, r_*) = 0 , \quad (8.25)$$

where $V_l(r)$ is a Regge-Wheeler type potential which when expressed in the original radial coordinate is of the form

$$V_l(r) = f(r) \left(\frac{l(l+1)}{r^2} + \frac{f'(r)}{r} (1-s) + m^2 \right) , \quad (8.26)$$

with $s = 0$ (spin of the considered field) for the case of a scalar field. This type of effective potential was first derived for “axial” (vector type) perturbations in the Schwarzschild background by Regge-Wheeler [2131]. For “polar” (scalar type) gravitational perturbations the effective potential was first derived by Zerilli [2132, 2133]. As discussed in Ref. [2134], the Regge-Wheeler-Zerilli formalism is based on the assumption of spherical symmetry.

For the solution of Eq. (8.25) we need to express the Regge-Wheeler potential $V_l(r)$ in tortoise coordinates $V_{*l}(r_*) \equiv V_l(r(r_*))$. Thus we need to evaluate the integral

$$r_* \equiv \int \frac{dr}{f(r)} = \int \frac{dr}{\sqrt{1 - \frac{2M}{r} - \frac{\Lambda}{3}r^2}} , \quad (8.27)$$

To evaluate the integral (8.27) we follow Ref. [2135] (see also Ref. [2136]) and factorize $f(r)$. Let

$$\xi = 9M^2\Lambda . \quad (8.28)$$

For $\xi < 1$ there are three real solutions of $f(r) = 0$. Two of them correspond to the event and cosmological horizons (r_H and r_C) while the third is negative (r_N) and does not correspond to a physical horizon. The three horizon radii are [2129, 2130, 2135–2140]

$$r_H = \frac{2}{\sqrt{\Lambda}} \cos \left[\frac{1}{3} \cos^{-1}(3M\sqrt{\Lambda}) + \frac{\pi}{3} \right] , \quad (8.29)$$

$$r_C = \frac{2}{\sqrt{\Lambda}} \cos \left[\frac{1}{3} \cos^{-1}(3M\sqrt{\Lambda}) - \frac{\pi}{3} \right] , \quad (8.30)$$

$$r_N = -(r_H + r_C) . \quad (8.31)$$

For $\xi = 1$ which corresponds to the Nariai solution [2141, 2142]) we have an extremal SdS spacetime [2128, 2137, 2143, 2144]

$$r_H = r_C = \frac{2}{\sqrt{\Lambda}} \cos \frac{\pi}{3} = \frac{1}{\sqrt{\Lambda}} \simeq 10^{26} \text{ m} , \quad (8.32)$$

where in the last equality we have assumed the observed value of $\Lambda = 3H_0^2\Omega_\Lambda$. The surface gravity of the SdS metric at a coordinate radius r_0 is defined as [2104, 2128, 2129, 2145]

$$\kappa_0 \equiv \frac{1}{2} \frac{df}{dr} \Big|_{r=r_0} = \frac{M}{r_0^2} - \frac{1}{3} \Lambda r_0 , \quad (8.33)$$

and describes the gravitational acceleration of a test particle at position r_0 . Using Eqs. (8.29), (8.30) and (8.31) to factorize $f(r)$ in Eq. (8.27) and the definition (8.33) we may obtain $r_*(r)$ as [2104, 2135]

$$r_* = \int \frac{dr}{\sqrt{1 - \frac{2M}{r} - \frac{\Lambda}{3}r^2}} = \frac{1}{2\kappa_H} \ln \left(\frac{r}{r_H} - 1 \right) + \frac{1}{2\kappa_C} \ln \left(1 - \frac{r}{r_C} \right) + \frac{1}{2\kappa_N} \ln \left(1 - \frac{r}{r_N} \right) , \quad (8.34)$$

where we note that κ_C is negative.

Using now Eqs. (8.26) and (8.34) it is easy to make a parametric plot of $V_{*l}(r_*)$ by plotting pairs of $(r_*(r), V_l(r))$ for $r \in [r_H, r_C]$.

From Eq. (8.34) it is clear that the tortoise coordinates map the event and cosmological horizons to $\pm\infty$

$$\begin{aligned} r \rightarrow r_H &\implies r_* \rightarrow -\infty , \\ r \rightarrow r_C &\implies r_* \rightarrow +\infty . \end{aligned} \quad (8.35)$$

The Regge-Wheeler potential $V_{*l}(r_*)$ of Eq. (8.26) has the important property that it vanishes at both infinities ($\pm\infty$). This is easy to see since

$$\begin{aligned} V(r_H) = V(r_C) = 0 &\implies \\ V_*(r_* \rightarrow -\infty) = V_*(r_* \rightarrow +\infty) &= 0 . \end{aligned} \quad (8.36)$$

As shown below, this property leads to a simple asymptotic solution of Eq. (8.25).

At this point we introduce a rescaling of the radial and time coordinates by M ($r/M \rightarrow \bar{r}$, $t/M \rightarrow \bar{t}$) and use the dimensionless parameters ξ (defined in Eq. (8.28)) and

$$m M \equiv \frac{GMm}{\hbar c} . \quad (8.37)$$

In order to search for scalar field instabilities we also use the following ansatz in Eq. (8.25)

$$\Psi_l(t, r_*) = (C_1 e^{\Omega t} + C_2 e^{-\Omega t}) u_l(r_*) . \quad (8.38)$$

This ansatz along with the above rescaling transforms Eq. (8.25) to a Schrodinger-like Regge-Wheeler equation of the form

$$\frac{du_l^2}{dr_*^2} - M^2 (\Omega^2 + V_{*l}(r_*)) u_l(r_*) = 0 , \quad (8.39)$$

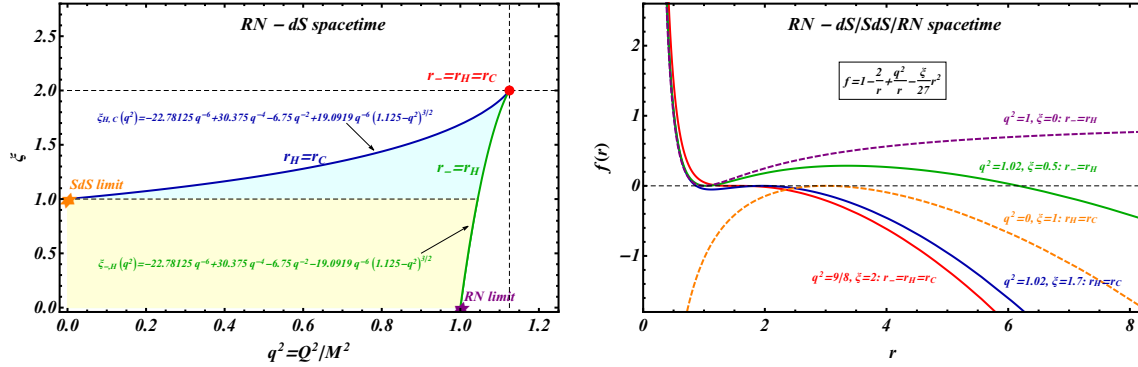


Figure 8.1: The critical values $\xi_{H,C}(q^2)$ (with $0 < q^2 < 9/8$) and $\xi_{-,H}(q^2)$ (with $1 < q^2 < 9/8$) as a function of q^2 at which $r_H = r_C$ and $r_- = r_H$ respectively (left panel). The colored shaded regions correspond to the physical corresponding regions of Fig. 8.6 discussed below. The metric function $f(r)$ as a function of r in the case of the RN-dS/SdS/RN spacetimes for critical value $\xi_{H,C}$ (when event and cosmological horizons coincide) and $\xi_{-,H}$ (when inner Cauchy and outer event horizons coincide) (right panel). The blue, green and red solid curves correspond to RN-dS spacetime while the purple and orange dashed curves correspond to RN and SdS spacetime respectively.

where $r_* \in (-\infty, +\infty)$ and

$$M^2 V_{*0}(r(r_*)) = \left(1 - \frac{2}{r(r_*)} - \frac{1}{27}\xi r(r_*)^2\right) \left(\frac{2}{r(r_*)^3} - \frac{2}{27}\xi + m^2 M^2\right). \quad (8.40)$$

In Eqs. (8.39) and (8.40) we have omitted the bar of the rescaled coordinates and in Eq. (8.40) we have fixed $l = 0$. Since $V_{*l}(r) > V_{*l=0}$, the most unstable scales are the large angular scales $l = 0$. This behavior is similar to the case of the Minkowski spacetime discussed in the introduction where the scale corresponding to $k = 0$ was the most unstable scale (largest growth rate, smallest lifetime). Thus in what follows we focus on the $l = 0$ modes. If these modes are stable then all scales ($l > 0$) are also stable.

8.2.2 Reissner-Nordström-deSitter background

We now generalize the metric of the previous section by including charge in the black hole metric. The RN-dS spacetime is defined by the metric function [2144, 2146]

$$f(r) = 1 - \frac{2M}{r} + \frac{Q^2}{r^2} - \frac{\Lambda}{3}r^2 = 1 - \frac{2}{r} + \frac{q^2}{r^2} - \frac{\xi}{27}r^2, \quad (8.41)$$

where ξ is defined in Eq. (8.28), $q \equiv \frac{Q}{M}$ (where Q is the black hole electric charge) and in the second equality we have used the rescaling $r/M \rightarrow r$.

The horizons are obtained by solving the equation $f(r) = 0$. For $\xi < 2$ and $q^2 < 9/8$ there are four real solutions [2144]. Two of them correspond to the inner (Cauchy) and outer (event) horizons of a RN black hole r_- and $r_+ = r_H$ (with $0 < r_- < r_H$) respectively. The third corresponds to the cosmological horizon r_C (with $r_C > r_H$) while the fourth r_N (with $r_N = -(r_- + r_H + r_C)$) is negative and does not correspond to a physical horizon.

The three horizons coincide at [2144]

$$r_- = r_H = r_C = \frac{3}{\sqrt{2\xi}}, \quad (8.42)$$

when $\xi = 2$ and $q^2 = 9/8$.

By demanding that two of the physical horizons coincide we set the discriminant of the quartic equation $f(r) = 0$ to zero and obtain the equation [2144, 2147])

$$1 - q^2 - \xi + \frac{4}{3}\xi q^2 - \frac{8}{27}\xi q^4 - \frac{16}{729}\xi^2 q^6 = 0, \quad (8.43)$$

which has real solutions for ξ when $0 < q^2 < \frac{9}{8}$. The critical value $\xi_{H,C}$ at which $r_H = r_C$ and the corresponding value $\xi_{-,H}$ at which $r_- = r_H$ may be obtained in terms of q^2 by solving Eq. (8.43) as

$$\xi_{H,C} = -22.7813q^{-6} + 30.375q^{-4} - 6.75q^{-2} + 19.0919q^{-6}(1.125 - q^2)^{\frac{3}{2}}, \quad (8.44)$$

$$\xi_{-,H} = -22.7813q^{-6} + 30.375q^{-4} - 6.75q^{-2} - 19.0919q^{-6}(1.125 - q^2)^{\frac{3}{2}}. \quad (8.45)$$

The first case corresponds to the charged Nariai solution [2147]. The critical values $\xi_{H,C}(q^2)$ and $\xi_{-,H}(q^2)$ as a function of q^2 are shown in Fig. 8.1 (left panel). The critical value $\xi_{H,C}(q^2)$ that leads to a coincidence between the event and cosmological horizons (blue line) varies between 1 (SdS limit, $q = 0$) and 2 (triple horizon coincidence limit, $q^2 = 9/8$). The corresponding form of the function $f(r)$ in these (and in other) limits is shown in Fig. 8.1 (right panel). The orange line corresponds to the coincidence of the event with the cosmological horizon $r_H = r_C$ in the SdS limit while the blue line shows the coincidence of the same roots of $f(r)$ ($r_H = r_C$) in the general RN-dS case with $q^2 = 1.02$. In both cases the local maximum of $f(r)$ occurs at $f(r) = 0$.

In the case of RN-dS, we study tachyonic instabilities of the neutral massive scalar field perturbations in the event-cosmological horizon region, defined as $r_+ = r_H < r < r_C$ using tortoise coordinates $r_*(r)$ defined as

$$\begin{aligned} r_* &= \int \frac{dr}{\sqrt{1 - \frac{2M}{r} + \frac{Q^2}{r^2} - \frac{\Lambda}{3}r^2}} = \\ &= \frac{1}{2\kappa_-} \ln \left(\frac{r}{r_-} - 1 \right) + \frac{1}{2\kappa_H} \ln \left(\frac{r}{r_H} - 1 \right) + \frac{1}{2\kappa_C} \ln \left(1 - \frac{r}{r_C} \right) + \frac{1}{2\kappa_N} \ln \left(1 - \frac{r}{r_N} \right), \end{aligned} \quad (8.46)$$

with κ_i ($i = -, H, C$) the surface gravity for the horizon $r = r_i$

$$\kappa_i \equiv \frac{1}{2} \frac{df}{dr} \Big|_{r=r_i} = \frac{M}{r_i^2} - \frac{Q^2}{r_i^3} - \frac{1}{3} \Lambda r_i, \quad (8.47)$$

where we note that $\kappa_- < 0$ and $\kappa_C < 0$. It is easy to see that the tortoise coordinates $r_*(r)$ shift the horizons r_H and r_C to $\pm\infty$.

The values of the inner (Cauchy) and outer (event) horizon in the case of RN background ($\Lambda = 0$) for $Q < M$ are e.g. [1943]

$$r_{\pm} = M \pm \sqrt{M^2 - Q^2}. \quad (8.48)$$

In the case of RN-dS spacetime a rescaling of the radial and time coordinates by M ($r/M \rightarrow r$, $t/M \rightarrow t$) and the introduction of the dimensionless parameters ξ (defined in Eq. (8.28)), $q = Q/M$ and mM (defined in Eq. (8.37)) lead to the Schrodinger-like equation (8.39) with maximum scale ($l = 0$) generalized Regge-Wheeler potential of the form

$$M^2 V_{*0}(r(r_*)) = \left(1 - \frac{2}{r(r_*)} + \frac{q^2}{r(r_*)^2} - \frac{1}{27}\xi r(r_*)^2 \right) \left(\frac{2}{r(r_*)^3} - \frac{2q^2}{r(r_*)^4} - \frac{2}{27}\xi + m^2 M^2 \right), \quad (8.49)$$

with $r_* \in (-\infty, +\infty)$.

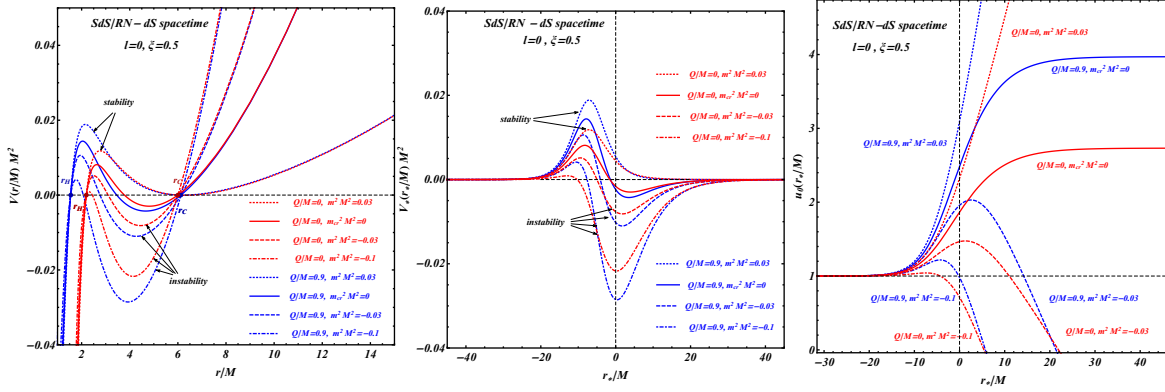


Figure 8.2: The $m^2 M^2$ dependent Regge-Wheeler dimensionless potentials $V M^2$ (left panel) and $V_* M^2$ (middle panel) as a function of r/M and r_*/M respectively in the cases of the SdS ($Q = 0$) (red curves) and RN-dS ($Q/M = 0.9$) (blue curves) spacetimes for angular scale $l = 0$ and dimensionless parameter fixed to $\xi = 0.5$. The solid curves correspond to the critical value of the scalar field mass $m_{cr}^2 M^2 = 0$. The right panel demonstrates the process for identifying the zero eigenvalue eigenstate i.e. setting $\Omega = 0$ in Eq. (8.39) and increasing the dimensionless parameter $m^2 M^2$ until the solution $u_0(r_*/M)$ satisfies both end boundary conditions (8.56)-(8.59) for $\Omega = 0$. This value of $m^2 M^2$ is the critical value for the considered value of ξ . The potential gets deeper and more accepting to bound states (instabilities) as the $m^2 M^2$ gets lower.

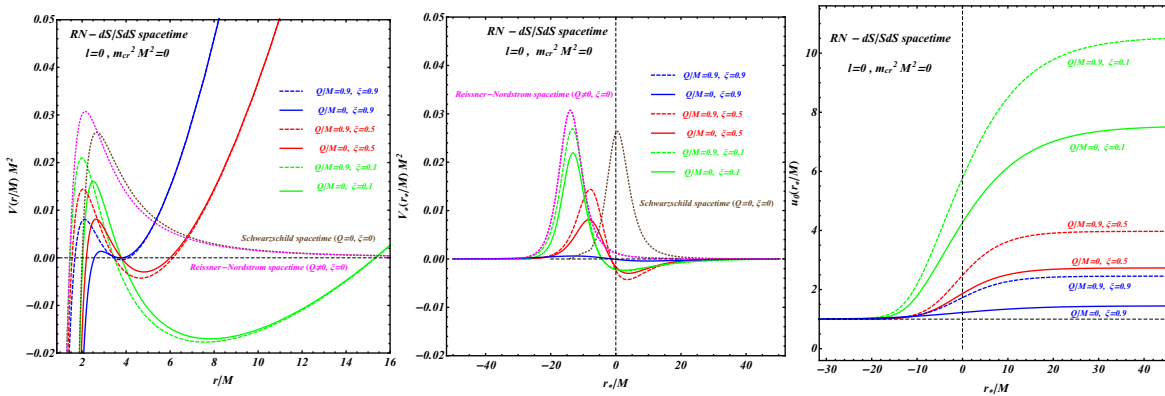


Figure 8.3: The ξ dependent Regge-Wheeler dimensionless potentials $V M^2$ (left panel) and $V_* M^2$ (middle panel) as a function of r/M and r_*/M respectively in the case of the SdS (solid curves) and RN-dS (dashed curves) spacetimes for angular scale $l = 0$ and critical value for $m^2 = m_{cr}^2 = 0$. The radial function $u_0(r_*/M)$ (right panel) which is the radial zero mode solution of Schrodinger like equation (8.39) with $\Omega = 0$ and boundary conditions (8.56) and (8.57) at large negative r_* . For critical value of the scalar field mass $m_{cr}^2 M^2 = 0$ the boundary conditions (8.58) and (8.59) at large positive r_* are satisfied. The brown and purple dotted curves correspond to the pure Schwarzschild ($Q = 0$, $\xi = 0$) and RN ($Q \neq 0$, $\xi = 0$) backgrounds respectively. The potential gets deeper as ξ decreases and Q/M increases. However, since the local maximum of the potential also increases as the potential gets deeper, the critical value $m_{cr} M$ for the existence of bound states remains the same and equal to zero in all cases.

8.3 Numerical solution: Parameter region for instability, Growth rate.

The questions we want to address in this section are the following:

- What is the critical value $m_{cr}(q, \xi)^2$ such that for $m^2 > m_{cr}^2$ Eq. (8.39) with a real Ω^2 has no bound state solutions (no instabilities) respecting the physically acceptable boundary conditions that correspond to finite field values at the two horizons ($r_* \rightarrow \pm\infty$)?
- What is the growth rate $\Omega(q, \xi, m^2 M^2)$ of tachyonic instabilities ($m^2 < m_{cr}^2$) and how does this growth rate compare with the corresponding growth rate in a flat Minkowski spacetime?

We thus solve the Schrodinger-like Regge-Wheeler equation (8.39) and for fixed values of q and ξ we start from a low negative m^2 and identify the ground state solution. Then we increase the value of m^2 until there are no bound states (instability modes) with physically acceptable boundary conditions. At the critical value $m^2 = m_{cr}^2$ there will only be a zero mode solution with eigenvalue $\Omega = 0$ (infinite lifetime mode). Such a mode may be interpreted as a scalar hair zero mode. As discussed in the 'Introduction', in Minkowski space ($M = \Lambda = Q = 0$), we have $m_{cr} = 0$. Does this value of m_{cr} change in RN-dS or in SdS spacetimes?

To address this question we must first find the required 'physical boundary conditions'. We demand that the physically acceptable solution should be finite on the two horizons i.e.

$$\begin{aligned} u_0(r_* \rightarrow \infty) &< +\infty, \\ u_0(r_* \rightarrow -\infty) &< +\infty. \end{aligned} \quad (8.50)$$

Since $V_{*0}(r_*)$ goes exponentially fast to 0 for $r_* \rightarrow \pm\infty$, we conclude that the general asymptotic solution of Eq. (8.39) is

$$u_0(r_* \rightarrow \pm\infty) = Ae^{\Omega r_*} + Be^{-\Omega r_*}. \quad (8.51)$$

For finiteness we demand

$$u_0(r_* \rightarrow +\infty) = Be^{-\Omega r_*}, \quad (8.52)$$

$$u_0(r_* \rightarrow -\infty) = Ae^{\Omega r_*}. \quad (8.53)$$

These imply

$$u'_0(r_* \rightarrow +\infty) = -\Omega Be^{-\Omega r_*}, \quad (8.54)$$

$$u'_0(r_* \rightarrow -\infty) = \Omega Ae^{\Omega r_*}, \quad (8.55)$$

where we can rescale $u_0(r_*)$ such that $A = 1$. These boundary conditions leading to instability may be associated with bound states ($\Omega^2 > 0$, $\Omega \in \mathbb{R}$) of the Schrodinger-like equation (8.39) with effective Regge-Wheeler potential $V_{*0}(r_*)$ (see Eq. (8.40) for SdS spacetime and Eq. (8.49) for RN-dS spacetime). Our search for scalar instabilities ($\Omega^2 > 0$) should be contrasted with the search for the values of QNMs which involves propagating boundary conditions at the horizons. These studies have also indicated the presence of scalar instabilities in a different physical setup (charged massive scalar field in Kerr-Newman black holes with positive m^2 [2148]).

The Regge-Wheeler potential $V_{*0}(r_*)$ is mostly accepting bound states for lower values of $m^2 M^2$ and for higher values of Q/M . This is demonstrated in Fig. 8.2 where we show the form of $V_{*0}(r_*)$ for various values of the dimensionless parameter $m^2 M^2$ in the cases of the SdS ($Q = 0$) and RN-dS ($Q/M = 0.9$) spacetimes for angular scale $l = 0$ and $\xi = 0.5$ indicating that as $m^2 M^2$ gets lower and as Q/M gets higher, the minimum of the Regge-Wheeler potential gets deeper and thus it becomes more accepting to the existence of bound states (instabilities). The critical value $m_{cr}(q, \xi)^2$ is such that for $m^2 > m_{cr}^2$ there are no bound states (instabilities) respecting the boundary conditions (8.52), (8.53), (8.54) and (8.55).

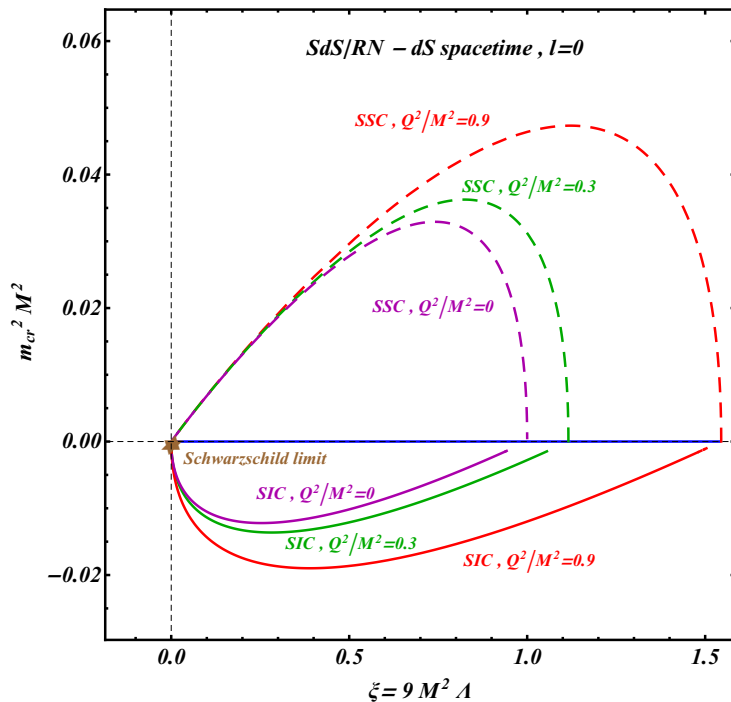


Figure 8.4: The critical value of the scalar field mass $m_{cr}^2 M^2$ is zero and independent of the dimensionless parameter ξ (with $\xi \in [0, \xi_{H,C}(q)]$) in the case of the SdS and RN-dS spacetime (blue straight line) for $l = 0$. The solid curves show the form of $m_{cr}(q, \xi)^2 M^2$ that saturates the Sufficient for Instability Criterion (SIC) Eq. (8.60) while the corresponding dashed curves show the forms of $m_{cr}(q, \xi)^2 M^2$ that saturate the Sufficient for Stability Criterion (SSC) Eq. (8.61) for three values of Q/M . As expected, the exact value of $m_{cr} M = 0$ is between the SIC lines (lower lines) and SSC lines (upper lines) so that none of the criteria is violated (SSC or SIC).

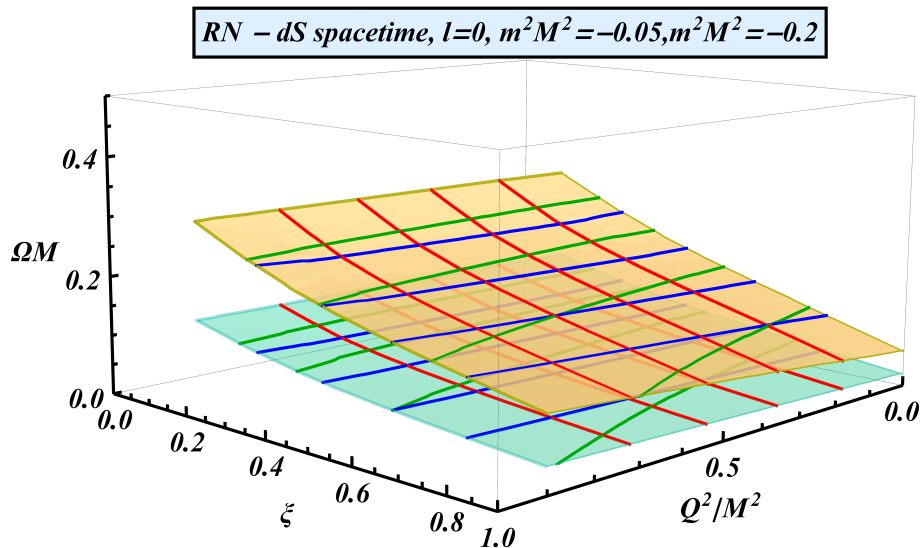


Figure 8.5: The dimensionless growth rate of the instability ΩM as a function of the dimensionless parameters ξ and $q^2 = Q^2/M^2$ for scalar field mass $m^2 M^2 = -0.05$ (cyan surface) and $m^2 M^2 = -0.2$ (yellow surface).

The critical value $m_{cr}(q, \xi)^2$ is obtained by solving Eq. (8.39) with boundary conditions (8.52), (8.53), (8.54) and (8.55) for a zero eigenvalue $\Omega = 0$ corresponding to a borderline unstable mode (zero mode) with infinite lifetime and zero growth rate. For such a zero mode, the boundary conditions (8.52), (8.53), (8.54) and (8.55) become

$$u_0(r_* \rightarrow -\infty) = 1, \quad (8.56)$$

$$u'_0(r_* \rightarrow -\infty) = 0, \quad (8.57)$$

$$u_0(r_* \rightarrow +\infty) = B, \quad (8.58)$$

$$u'_0(r_* \rightarrow +\infty) = 0, \quad (8.59)$$

where we have set $A = 1$.

In practice we use the shooting method in solving Eq. (8.39) with $\Omega = 0$, fixed ξ , q , boundary conditions (8.56), (8.57) at large negative r_* and adjust $m^2 M^2$ until the boundary conditions (8.58) and (8.59) are satisfied (see Fig. 8.2 right panel). By repeating this process for several values of $q^2 \in [0, \frac{9}{8}]$ and $\xi \in [0, \xi_{H,C}(q)]$ we have found $m_{cr}(\xi, q)^2 = 0$ i.e. the zero mode appears at $m^2 = 0$ for all parameter values ξ, q where there is a finite distance between the event and the cosmological horizons.

In Fig. 8.3 we show the form of the Regge-Wheeler potentials $V_0(r/M)$ and $V_{*0}(r_*/M)$ as well as the radial zero mode solution $u_0(r_*/M)$ for the critical value $m_{cr}(q, \xi) = 0$ for $\xi = 0.1, 0.5, 0.9$ in the case of the SdS spacetime ($q = 0$) and in the case of RN-dS spacetime ($q = 0.9$). Notice that in the absence of a cosmological horizon ($\xi = 0$, pure Schwarzschild and Reissner-Nordström spacetimes) the Regge-Wheeler potential V_* is positive everywhere for $m = 0$ and the absence of bound states is obvious. However, this is not the case for $\xi > 0$ which requires numerical solution of the Schrodinger-like equation for the determination of m_{cr} .

There is a simple semi-analytical way to derive sufficient conditions for instability and for stability and thus test the validity of the numerically obtained form of $m_{cr}^2 = 0$ for various values of the parameters ξ and q . It is well known that a sufficient condition for the existence of bound states in a Schrodinger equation potential $V_{*0}(r_*)$ is the following Sufficient for Instability Criterion (SIC) [2149–2151]

$$\begin{aligned} I_{SIC} &= \int_{-\infty}^{+\infty} V_{*0}(r_*) dr_* < 0 \implies \\ &\int_{r_H}^{r_C} \frac{V_0(r)}{f(r)} dr = \int_{r_H}^{r_C} \left(\frac{l(l+1)}{r^2} + \frac{f'(r)}{r} + m^2 \right)_{l=0} dr = \\ &\int_{r_H}^{r_C} \left(\frac{l(l+1)}{r^2} + \frac{2}{r^3} - \frac{2q^2}{r^4} - \frac{2}{27}\xi + m^2 M^2 \right)_{l=0} dr < 0, \end{aligned} \quad (8.60)$$

where we have used Eqs. (8.26) and (8.49) for the form of $V_0(r)$ and the dimensionless parameters ξ and q . In addition, a positive definite potential can not have bound states (negative eigenvalues corresponding to $\Omega^2 > 0$) and thus in such a potential we would only have stable oscillating modes ($\Omega^2 < 0$). Thus a Sufficient for Stability Criterion (SSC) is that the minimum of the Schrodinger potential should be positive i.e.

$$V_{0min}(r_{min}) > 0. \quad (8.61)$$

Using the SIC and the SSC we have constructed the upper and lower curves in Fig. 8.4 which correspond to the values of $m(\xi)^2 M^2$ that saturate the SSC (upper curves) and SIC (lower curves). Also, using the SSC we find an analytical expression $m^2(\xi) M^2$ for $Q = 0$ (upper curve in Fig. 8.4 see Appendix E). Thus, by construction all parameter values below the lower curves satisfy the SIC Eq. (8.60) and must correspond to tachyonic instabilities while all parameter values above the upper curves of Fig. 8.4 satisfy the SSC Eq. (8.61) and have no instabilities. As expected the precise numerically obtained values of $m_{cr}(\xi)^2 = 0$ are between the SIC and SSC curves so that none of the two sufficient (but not necessary) conditions is violated. Even though the value $m_{cr}(q, \xi) = 0$ for the emergence of tachyonic instabilities is independent of the metric parameters and remains the same in the RN-dS spacetime as in the flat Minkowski spacetime, the growth rate $\Omega(q, \xi, m)$ of tachyonic instabilities ($m^2 < 0$) does have

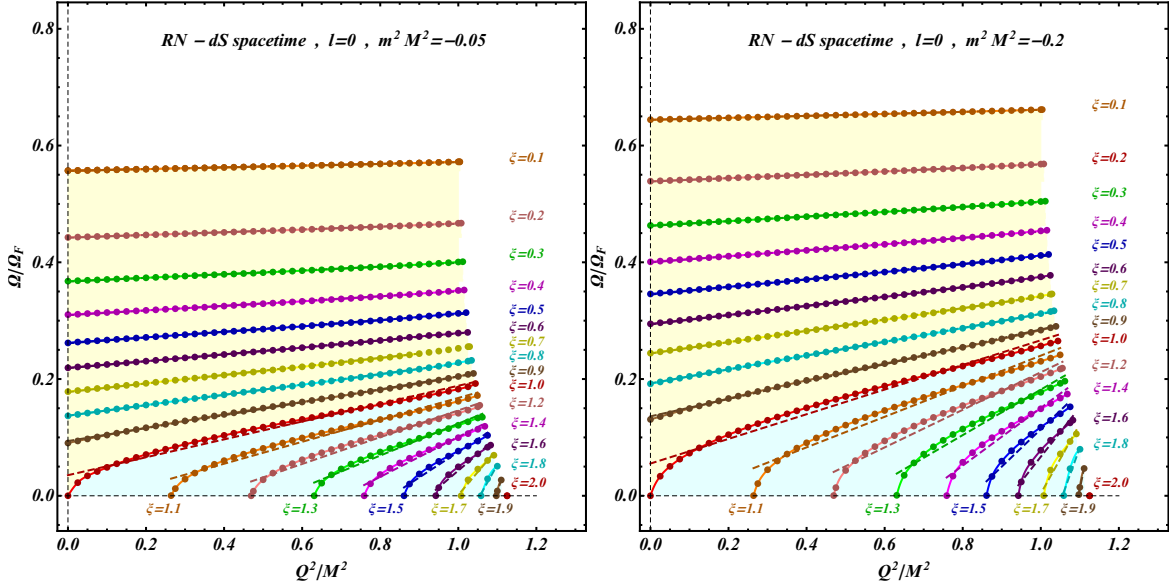


Figure 8.6: The ξ dependent relative growth rate of the instability Ω/Ω_F (with Ω_F the growth rate of the instability in flat spacetime) as a function of the dimensionless parameter $q^2 = Q^2/M^2$ for the scalar field mass $m^2 M^2 = -0.05$ (left panel) and $m^2 M^2 = -0.2$ (right panel). The curves for a given parameter value ξ (with $\xi < 1$) turn out to be straight lines. The range of values of ξ and q is determined by the physically interesting parameter region between the green and blue lines of Fig. 8.1. The parameter region corresponding to linear behavior of $\Omega(q^2)$ (yellow region) is also shown in Fig. 8.1.

a dependence on the metric parameters. In order to identify this dependence we consider an unstable mode with fixed $m^2 < m_{cr}(q, \xi)^2 = 0$ and given ξ and q , we find the growth rate Ω of the instability by finding the ground state eigenvalue⁴ Ω^2 and eigenfunction $u_0(r_*)$ of the Schrodinger-like equation (8.39) which has no nodes and obeys the boundary conditions (8.53)-(8.55), (8.52) and (8.54). We thus construct Fig. 8.5 which shows the dimensionless growth rate of the instability ΩM as a function of the dimensionless parameters ξ and $q^2 = Q^2/M^2$ for scalar field mass $m^2 M^2 = -0.05$ and $m^2 M^2 = -0.2$. Clearly, when ξ increases and/or q decreases towards 0, the growth rate of the instability ΩM decreases and as $m^2 M^2 \rightarrow 0$ we have $\Omega M \rightarrow 0$ (the zero mode is reached). In addition to this interesting monotonic behavior of the instability growth rate Ω with respect to the metric parameters, Ω also remains smaller than its flat space value $\Omega_F = |m|$. This is demonstrated in Fig. 8.6 where we show the dependence of $\frac{\Omega}{\Omega_F}$ on q^2 for various values of ξ for $m^2 M^2 = -0.05$ (left panel) and $m^2 M^2 = -0.2$ (right panel). We have considered parameter values between the green and blue lines of Fig. 8.1 where three distinct horizon exist in the RN-dS metric. The following observations can be made based on Figs. 8.5 and 8.6

- The relative growth rate of the tachyonic instabilities $\frac{\Omega}{\Omega_F}$ is a monotonically increasing function of q^2 and a monotonically decreasing function of ξ .
- $\frac{\Omega}{\Omega_F}$ is significantly smaller than unity. This reduction implies that background curvature and especially the combination of an event horizon with a cosmological horizon tend to delay the evolution of instabilities.
- There is a linear relation between $\frac{\Omega}{\Omega_F}$ and q^2 for fixed $\xi < 1$. This is evident in both Fig. 8.6 and in Fig. 8.5. For example the straight blue lines of Fig. 8.5 correspond to the dependence of ΩM on

⁴Possible excited states would correspond to lower values of Ω and thus lower growth rate. We thus find the maximum possible growth rate of instabilities for a given set of parameters.

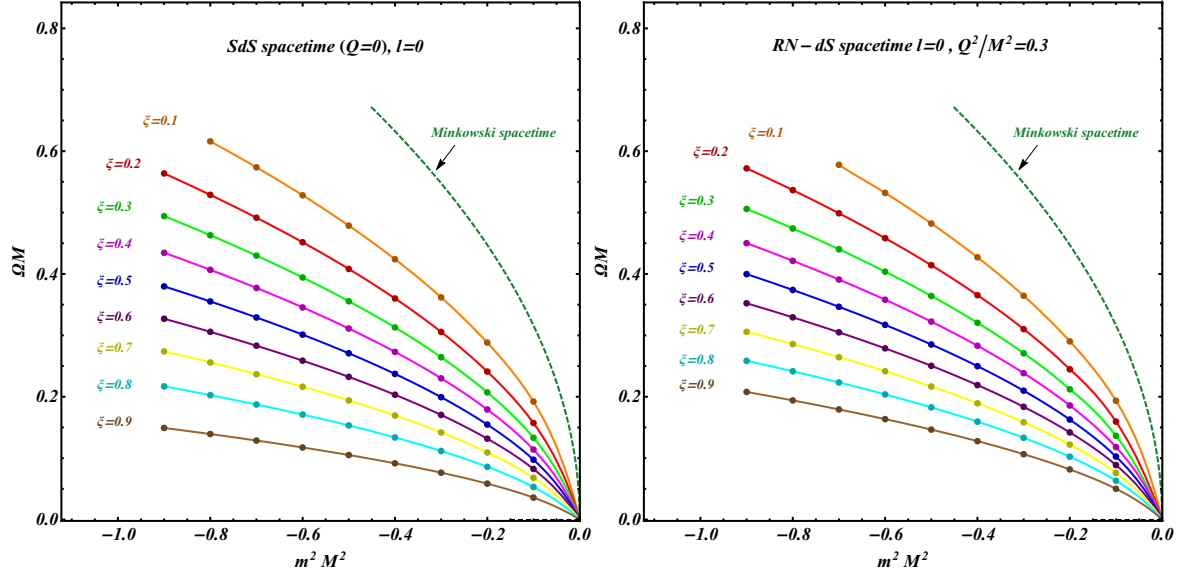


Figure 8.7: The ξ dependent dimensionless growth rate of the instability ΩM as a function of the scalar field mass $m^2 M^2$ (with $m(\xi)^2 < m_{cr}(\xi)^2 = 0$) for dimensionless parameters $Q^2/M^2 = 0$ (SdS spacetime) (left panel) and $Q^2/M^2 = 0.3$ (RN-dS spacetime) (right panel). The green dashed curves correspond to $\Omega M(m^2 M^2)$ in the case of the Minkowski spacetime. Clearly, for a given field mass, the growth rate is more suppressed in the absence of charge and for higher values of ξ .

q^2 for fixed ξ which are equivalent to the straight lines of Fig. 8.6. Notice that this linear relation is violated for $\xi > 1$ (see shaded regions in Figs. 8.1 and 8.6).

- The growth rate Ω is a decreasing function of $|m|^2$ which goes to zero as $m^2 \rightarrow m_{cr}^2 = 0$ where the zero mode develops. This is illustrated in more detail in Fig. 8.7.

The crucial feature of the RN-dS metric that has led to the above described trend for delay of instability growth of the tachyonic modes is the combination of the cosmological horizon with an event horizon. This combination, limits the range of negative values of the Regge-Wheeler potential in tortoise coordinates for $m^2 < 0$ and thus makes it less accepting to bound states and instabilities. In the absence of a cosmological horizon the Regge-Wheeler potential in tortoise coordinates would remain negative out to $r_* \rightarrow \infty$. This is illustrated in the next section.

8.4 Limiting cases with a single horizon: pure deSitter and pure Schwarzschild spacetimes

We now consider separately the two single horizon limiting cases: pure deSitter and pure Schwarzschild spacetimes in order to isolate the effects of the cosmological and event horizons.

8.4.1 Pure deSitter background

In the pure deSitter case ($M = 0, Q = 0$), the potential $V_{*0}(r_*)$ is shown in Fig. 8.8 for various values of m^2/Λ and may be obtained analytically as [2152]

$$V_{*0}(r_*) = \frac{m^2 - \frac{2}{3}\Lambda}{\cosh^2 \frac{r_*}{\sqrt{\frac{3}{\Lambda}}}} \simeq^{0 < r_* \ll \sqrt{\frac{3}{\Lambda}}} \left(m^2 - \frac{2}{3}\Lambda \right) + \frac{\Lambda}{9} (2\Lambda - 3m^2) r_*^2 + \mathcal{O}(r_*^4). \quad (8.62)$$

After a rescaling $r_*\sqrt{\Lambda} \rightarrow r_*$, $m^2/\Lambda \rightarrow m^2$ which practically amounts to setting $\Lambda = 1$ it is obvious that the SSC is satisfied for $m^2 > \frac{2}{3}$ which guarantees no instabilities for this range of m^2 . Since there is only cosmological horizon in this case, the range of the tortoise coordinate is $r_* \in [0, +\infty]$. For $\Omega = 0$ the Schrodinger-like equation to solve in this case takes the form

$$\frac{du_0^2}{dr_*^2} - \frac{1}{\Lambda} V_*(r_*) u_0(r_*) = 0 . \quad (8.63)$$

Since the potential vanishes at $+\infty$ due to the cosmological horizon, the physically interesting (finite) boundary condition at $r_* \rightarrow +\infty$ is

$$u_0(r_* \rightarrow +\infty) = C , \quad (8.64)$$

$$u_0'(r_* \rightarrow +\infty) = 0 . \quad (8.65)$$

At the other boundary $r_* \rightarrow 0$ we have

$$\frac{dr_*}{dr} = 1 \implies r_* = r , \quad (8.66)$$

and due to Eqs. (8.22) and (8.38) for a finite scalar field at $r = 0$ we must have

$$\Psi_0(r \rightarrow 0) = 0 \implies u_0(r \rightarrow 0) = u_0(r_* \rightarrow 0) = 0 . \quad (8.67)$$

Thus using Eqs. (8.62) and (8.63) it is straightforward to show that

$$u_0(r_* \rightarrow 0) = r_* , \quad (8.68)$$

where we have used the normalization freedom to set the slope of the linear function to unity. Thus in this case, the physical boundary conditions are

$$u_0'(r_* \rightarrow 0) = 1 , \quad (8.69)$$

$$u_0(r_* \rightarrow 0) = 0 , \quad (8.70)$$

$$u_0(r_* \rightarrow +\infty) = C , \quad (8.71)$$

$$u_0'(r_* \rightarrow +\infty) = 0 . \quad (8.72)$$

Solving Eq. (8.63) corresponding to $\Omega = 0$ from $r_* = 0$ with the boundary conditions (8.69) and (8.70), we obtain (8.71) and (8.72) only for $m_{cr} = 0$. Thus, despite of the negative effective Regge-Wheeler potential in the deSitter background, the tachyonic instabilities develop for the same range of m^2 as in the Minkowski space ($m^2 < 0$). It is straightforward to find the ground state eigenvalue and show that $\Omega(m^2/\Lambda) < |m|$ as in the case of other spacetimes where a cosmological horizon is present (see Fig. 8.9).

8.4.2 Pure Schwarzschild background

In the pure Schwarzschild background ($\Lambda = 0$) we have [2153, 2154]

$$f(r) = 1 - \frac{2M}{r} , \quad (8.73)$$

$$V(r) = \left(1 - \frac{2M}{r}\right) \left(\frac{l(l+1)}{r^2} + \frac{2M}{r^3} + m^2\right) , \quad (8.74)$$

$$r_*(r) = r + 2M \ln\left(\frac{r}{2M} - 1\right) . \quad (8.75)$$

It is easy to see that in both the tortoise and the Schwarzschild coordinates the Regge-Wheeler potential V_{*0} does not vanish asymptotically at $+\infty$. Instead we have (see also Fig. 8.10)

$$\lim_{r_* \rightarrow +\infty} V_{*0} = m^2 . \quad (8.76)$$

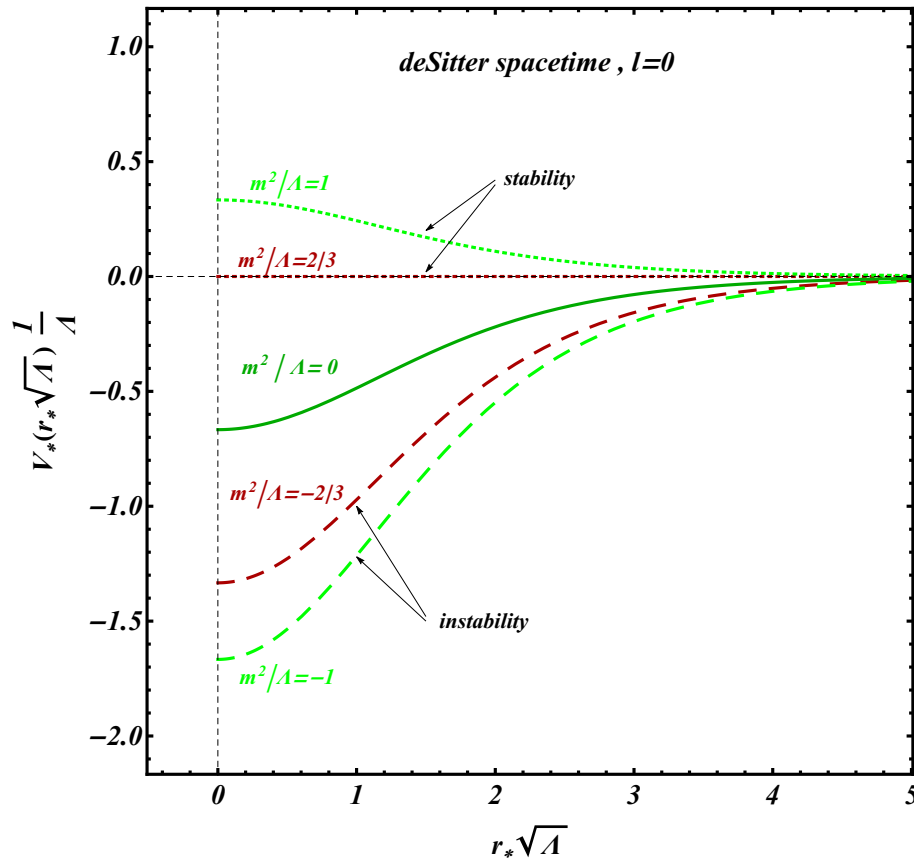


Figure 8.8: The m^2/Λ dependent Regge-Wheeler dimensionless potential V_*/Λ as a function of $r_*\sqrt{\Lambda}$ in the case of the deSitter spacetime ($M = 0$, $\xi = 0$) for angular scale $l = 0$. The green solid curve corresponds to the critical value of the scalar field mass $m_{cr}^2/\Lambda = 0$. The dotted ($m^2/\Lambda > 0$) and dashed ($m^2/\Lambda < 0$) curves correspond to non-existence of bound states (stabilities) and existence of bound states (instabilities) respectively.

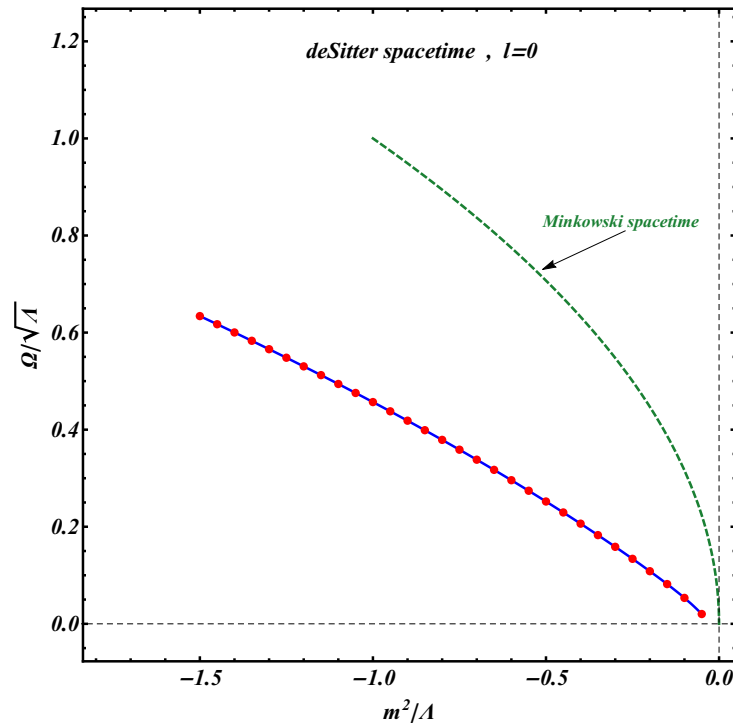


Figure 8.9: The dimensionless growth rate of the instability $\Omega/\sqrt{\Lambda}$ as a function of the scalar field mass m^2/Λ (with $m < m_{cr} = 0$) in the case of deSitter spacetime. Clearly $\Omega(m^2/\Lambda) < |m|$ as in the other cases where a cosmological horizon is present.

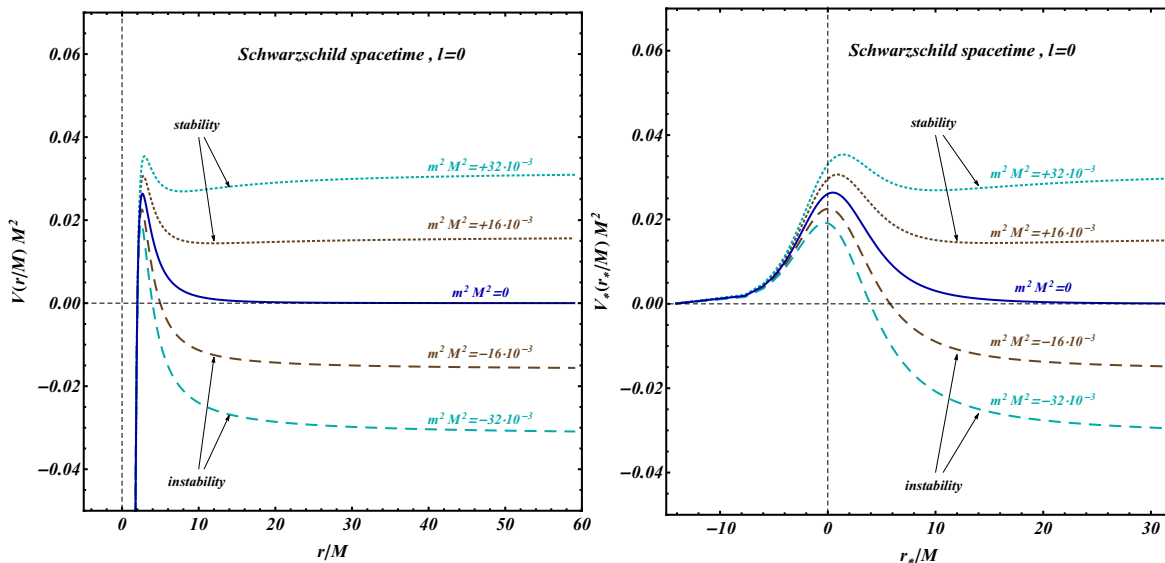


Figure 8.10: The $m^2 M^2$ dependent Regge-Wheeler dimensionless potentials $V M^2$ (left panel) and $V_* M^2$ (right panel) as a function of r/M and r_*/M respectively in the case of the Schwarzschild spacetime ($\Lambda = 0$, $\xi = 0$) for angular scale $l = 0$. The blue solid curves correspond to the critical value of the scalar field mass $m_{cr}^2 M^2 = 0$. The dotted ($m^2 M^2 > 0$) and dashed ($m^2 M^2 < 0$) curves correspond to non-existence of bound states (stabilities) and existence of bound states (instabilities) respectively.

This implies that for $m^2 < 0$ the SIC implies instability since

$$\int_{-\infty}^{\infty} V(r_*) dr_* = \int_{r_H}^{\infty} V(r) dr = \int_{r_H}^{\infty} \left(1 - \frac{2M}{r}\right) \left(\frac{l(l+1)}{r^2} + \frac{2M}{r^3} + m^2\right) dr = -\infty < 0. \quad (8.77)$$

Therefore for $m^2 < 0$ we have tachyonic instability just as in the Minkowski space. Similarly for $m^2 > 0$ we have $V(r) > 0$ and $V_{*0}(r_*) > 0$ which is the SSC (see also Fig. 8.10) which secures that we have stability. Thus in the Schwarzschild background, tachyonic instabilities develop for the same mass parameter range as for the Minkowski background.

In this case, for $m^2 < 0$, the boundary conditions (8.52)-(8.53) become

$$u_0(r_* \rightarrow +\infty) = B e^{-i\sqrt{|m|^2 - \Omega^2} r_*}, \quad (8.78)$$

$$u_0(r_* \rightarrow -\infty) = A e^{\Omega r_*}, \quad (8.79)$$

i.e. there are propagating waves towards $+\infty$ even for $m^2 < 0$. There are non-zero solutions satisfying these boundary conditions only for $\Omega \leq |m|$. This implies that the maximum growth rate of tachyonic instabilities in this case is the same as in flat space $\Omega = |m|$. This is due to the absence of a cosmological horizon.

8.5 Conclusions

In this Chapter we have shown that tachyonic scalar instabilities of the KG equation have a slower growth rate in RN-dS/ SdS metric background compared to flat Minkowski space for all values of metric parameters where a cosmological horizons exists. We have also identified the critical value of scalar field mass m_{cr}^2 that for $m^2 < m_{cr}^2$ tachyonic instabilities develop and confirmed that $m_{cr} = 0$ as in flat Minkowski spacetime.

The crucial property of the SdS spacetime that allows for this delayed growth of instabilities appears to be the presence of a cosmological horizon that forces the effective Regge-Wheeler potential to vanish at $+\infty$ in tortoise coordinates even for negative scalar field mass m^2 . Thus the r_* range where the Regge-Wheeler potential is negative is limited favoring increased eigenvalues and lower growth rate of instabilities.

This stabilizing effect of multiple horizons on tachyonic instabilities may have various interesting implications which include the following

- Symmetry breaking phase transitions in field theory is based on the existence of tachyonic instabilities in a scalar field potential which lead the system towards a new vacuum state with less symmetry. In the context of a RN-dS background the delay of such tachyonic instabilities could have interesting effects in the evolution of phase transitions in the Early Universe with possible interesting observable effects related e.g. to the efficiency of the formation of topological defects [2155, 2156].
- The backreaction effects of the tachyonic instabilities on the gravitational background may lead to superradiance and scalarization effects [2123, 2157] in RN-dS spacetime in the same way that scattering processes lead to similar effects in these spacetimes.
- The consideration of scalar field potentials supporting topological or semilocal defects (e.g. electroweak strings [2158]) may lead to interesting new stabilization mechanisms induced by a multi-horizon gravitational background.

These implications open up a wide range of extensions of our analysis. For example interesting extensions include the following:

- Consideration of more general background metrics to investigate the existence and growth rate of tachyonic instability modes. Such backgrounds may include Kerr-Newman-deSitter spacetime [2157, 2159–2166] or corresponding higher dimension spacetimes Gödel-like spacetime [2167, 2168] etc.
- Investigate the effects of such delay of instabilities in the Early Universe and in particular during inflation and cosmological phase transitions [2169–2172] in the context of more general scalar field potentials beyond the KG equation.
- Investigate different types of perturbations (Dirac and gravitational) in multihorizon backgrounds and in the presence of tachyonic modes.
- Consider different types of boundary conditions corresponding to scattering processes (propagating waves at infinity) leading to evaluation of QNMs and scattering amplitudes (superradiance).
- Investigate the stability of semilocal and electroweak strings in strongly curved backgrounds including multihorizon metrics.

In conclusion, the interesting non-trivial effects of the gravitational background on the tachyonic scalar instabilities pointed out in our analysis open up a wide range of new directions in the understanding of the dynamics of scalar fields in curved spacetimes.

Chapter 9

Constraints on Horndeski Modified Gravity - Weak Gravity on a Λ CDM Background

The analysis presented in this chapter is based on the work which was done in collaboration with Prof. Radouane Gannouji, Prof. Leandros Perivolaropoulos and Prof. David Polarski and has been published in Physical Review D [6].

In this chapter we study Horndeski modified gravity models obeying stability, velocity of gravitational waves c_T equals c and Quasi-Static Approximation (QSA) on subhorizon scales. We assume further a Λ CDM background expansion and a monotonic evolution on the cosmic background of the α functions. We take into account compilations of the $f\sigma_8$ and E_G data in order to derive constraints on μ_G and Σ_G parameters.

As mentioned in Chapter 3 the growth tension, if not due to statistical or systematic errors, may indicate the need for additional degrees of freedom extending Λ CDM. A generic physically motivated origin of such degrees of freedom is the extension of GR to Modified Gravity (MG) models. A great variety of MG models have been proposed so far to account for the growth tension. A wide class of such MG theories is provided by Horndeski gravity. Horndeski gravity models [100, 101] (see Refs. [102, 103], for a comprehensive review) is the most general ST theory involving a scalar degree of freedom in four dimensions with second order equations of motion therefore avoiding the Ostrogradsky instability [2173, 2174]. It provides a general framework to construct models of dark energy as well as inflation. It includes dark energy models inside GR such as quintessence as well as a wide variety of MG models, such as $f(R)$ gravity [112], BD theories [1845, 2175], galileons etc.

9.1 Introduction

The recent detection of gravitational waves emitted by binary systems has imposed stringent constraints on their speed c_T constraining the latter to be extremely close to the speed of light c ($c_T/c = 1 \pm 10^{-15}$) [2176, 2177]. We know that $c_T = c$ is a fundamental prediction of GR. This constraint has significantly restricted the observationally allowed subclasses of Horndeski models. Notice that a way to get around this constraint is to assume ab initio that c_T depends on its wavelength [2178]. The gravitational properties of Horndeski theories can be elegantly expressed by means of four free independent functions of time namely the α -basis $\alpha_i(t)$ ($i = M, K, B, T$) [2179], describing the linear perturbations, while the background expansion is given by the Hubble parameter $H(a)$ where a is the scale factor. These four time dependent phenomenological functions describe any departure from GR and also characterize

specific physical properties of the Horndeski models. GR is recovered when all α_i are set to zero.

For specific choices of the α_i the resulting theory may be unstable on a given background $H(a)$. Thus two types of instabilities may occur:

- Ghost instabilities [2180] which arise when the kinetic term of the background perturbations has the wrong sign giving negative energy modes. In this case the high energy vacuum is unstable with respect to the spontaneous production of particles.
- Gradient instabilities which arise when the background $H(a)$ evolves in a region where the sound speed of the perturbations becomes imaginary ($c_s^2 < 0$). This leads to the appearance of exponentially growing modes of the form $e^{c_s k t}$ at small scales.

The functions α_i of a physically acceptable Horndeski model should avoid such instabilities. As discussed below, this requirement restricts further the allowed Horndeski models [2181].

As we have mentioned above, the gravitational properties of Horndeski theories and the corresponding observable quantities are uniquely specified by the four independent $\alpha_i(a)$ functions [2179, 2182, 2183] and the background expansion rate $H(a)$. These quantities in turn are determined by the form of the Horndeski Lagrangian density as discussed in the next section and may be used to reconstruct them. The α_i functions are connected not only with the fundamental Horndeski Lagrangian density but also with gravitational observables like the (dimensionless, reduced) gravitational coupling entering the growth of perturbations $\mu_G(a) \equiv G_{\text{growth}}(a)/G$ (by G we mean here the usual numerical value of Newton's constant) and lensing properties $\Sigma_G(a) \equiv G_{\text{lensing}}(a)/G$ where G_{growth} , resp. G_{lensing} , is the effective gravitational coupling for the growth of cosmological perturbations, resp. for lensing ($8\pi G \equiv 1/M_p^2$ where M_p is the (reduced) Planck mass). The numerical value of G is obtained from local experiments (solar system, Eotvos type). Of course, depending on the models, these gravitational couplings can have a broader physical meaning. For example, in massless scalar-tensor models G_{growth} was called G_{eff} , the effective coupling for Newton's gravitational attraction law in a laboratory experiment [582, 587]. An efficient way to explore the physical content of Horndeski models as well as observational constraints on these theories is to parametrize the α_i functions [2184, 2185]. Such parametrizations usually assume the validity of GR at early times ($\alpha_i(a \simeq 0) = 0$) while they allow for a deviation from GR at late times in accordance with the observed accelerating expansion. Using such parametrizations, the gravitational strength observables μ_G and Σ_G may be derived and compared with cosmological observations leading to constraints on the parameters involved in the evolution of the α_i functions. However in view of what was mentioned above, a physically interesting parameter region should satisfy additional requirements beyond consistency with cosmological observations as it should correspond to viable Horndeski models. In this work we investigate stable Horndeski models and we assume an early time behavior consistent with GR, $c_T = c$, scale independence of the α functions on subhorizon scales in the QSA, and finally a background expansion $H(a)$ mimicking Λ CDM. We assume further a specific dependence of the α functions on a , viz. $\alpha_i = \alpha_{i0} a^s$, $i = M, B$, where α_{i0} are arbitrary parameters and s is some positive exponent.

With these assumptions, the goal of our analysis is to address the following questions:

- What is the allowed parameter space for our parametrization of the α functions?
- Which behavior for $\mu_G(a)$ and $\Sigma_G(a)$ is obtained especially at recent times $a \simeq 1$ and is it consistent with observational constraints?
- How does the growth index γ behave in the parameter space defining the functions α_i ?

The structure of this Chapter is the following: In the next Section 9.2 we present a brief review of the Horndeski models. In the context of the α parametrization and the above assumptions, we derive the allowed parameter regions for various values of the exponent s . We also obtain the allowed forms of μ_G and Σ_G , comparing our results with previous studies. In Section 9.3 we use compilations of $f\sigma_8$ and E_G data along with the theoretical expressions for $f\sigma_8$ and E_G statistics data in order to derive constraints on μ and Σ_G and to obtain the allowed range of the functions $\alpha_M(a)$ and $\alpha_B(a)$. In Section 9.4 we consider

the growth index $\gamma(z)$ and identify the $(\alpha_{M0}, \alpha_{B0}, s)$ parameter region that corresponds to specific signs of $\gamma_0 - \gamma_0^{\Lambda CDM}$, and $\gamma_1 - \gamma_1^{\Lambda CDM}$. Finally in Section 9.5 we conclude and discuss the implications of our analysis.

9.2 Stability and generic forms of μ_G and Σ_G for viable Horndeski theories

The Horndeski action, first written down in Ref. [100] and then rediscovered as a generalisation of galileons in Refs. [101, 2186], is given by

$$S = \int d^4x \sqrt{-g} \left[\sum_{i=2}^5 \mathcal{L}_i [g_{\mu\nu}, \phi] + \mathcal{L}_m [g_{\mu\nu}, \psi_m] \right], \quad (9.1)$$

where the Lagrangian density, \mathcal{L}_m , for all matter fields ψ_m is universally coupled to the metric $g_{\mu\nu}$ and does not have direct coupling with the scalar field, ϕ . The \mathcal{L}_i are the scalar-tensor Lagrangians which depend on the new degree of freedom ϕ , viz.

$$\begin{aligned} \mathcal{L}_2 &= K(\phi, X), \\ \mathcal{L}_3 &= -G_3(\phi, X) \square \phi, \\ \mathcal{L}_4 &= G_4(\phi, X) R + G_{4X}(\phi, X) \left[(\square \phi)^2 - \nabla_\mu \nabla_\nu \phi \nabla^\mu \nabla^\nu \phi \right], \\ \mathcal{L}_5 &= G_5(\phi, X) G_{\mu\nu} \nabla^\mu \nabla^\nu \phi - \frac{1}{6} G_{5X}(\phi, X) \left[(\square \phi)^3 \right. \\ &\quad \left. - 3 (\nabla_\mu \nabla_\nu \phi) (\nabla^\mu \nabla^\nu \phi) \square \phi \right. \\ &\quad \left. + 2 (\nabla_\mu \nabla^\nu \phi) (\nabla_\nu \nabla^\beta \phi) (\nabla_\beta \nabla^\mu \phi) \right], \end{aligned} \quad (9.2)$$

where $K(\phi, X) \equiv G_2(\phi, X)$ is the K-essence term, $G_i(\phi, X)$ ($i = 3, 4, 5$) are three coupling functions of the scalar field ϕ and its canonical kinetic energy $X \equiv -\frac{1}{2} \nabla^\mu \phi \nabla_\mu \phi$, R is the Ricci scalar, $G_{\mu\nu}$ is the Einstein tensor, $G_{iX} \equiv \partial G_i / \partial X$ and $G_{i\phi} \equiv \partial G_i / \partial \phi$. In principle the functions $G_i(\phi, X)$ can be chosen freely and determine a particular Horndeski model.

As mentioned above Horndeski models are characterized by means of four functions of time, $\alpha_i(t)$ ($i = M, K, B, T$) [2179] in addition to the background evolution encoded in the Hubble parameter $H(a)$. Thus using these functions which fully specify the linear evolution of perturbations allows us to disentangle the background expansion from the evolution of the perturbations. The functions $\alpha_K, \alpha_B, \alpha_T$ are connected to the Lagrangian terms as follows [2179]

$$\begin{aligned} H^2 M_*^2 \alpha_K &= 2X(K_X + 2XK_{XX} - 2G_{3\phi} - 2XG_{3\phi X}) + \\ &\quad + 12\dot{\phi}XH(G_{3X} + XG_{3XX} - 3G_{4\phi X} - 2XG_{4\phi XX}) + \\ &\quad + 12XH^2(G_{4X} + 8XG_{4XX} + 4X^2G_{4XXX}) - \\ &\quad - 12XH^2(G_{5\phi} + 5XG_{5\phi X} + 2X^2G_{5\phi XX}) + \\ &\quad + 4\dot{\phi}XH^3(3G_{5X} + 7XG_{5XX} + 2X^2G_{5XXX}), \end{aligned} \quad (9.3)$$

$$\begin{aligned} HM_*^2 \alpha_B &= 2\dot{\phi}(XG_{3X} - G_{4\phi} - 2XG_{4\phi X}) + \\ &\quad + 8XH(G_{4X} + 2XG_{4XX} - G_{5\phi} - XG_{5\phi X}) + \\ &\quad + 2\dot{\phi}XH^2(3G_{5X} + 2XG_{5XX}), \end{aligned} \quad (9.4)$$

$$M_*^2 \alpha_T = 2X(2G_{4X} - 2G_{5\phi} - (\ddot{\phi} - \dot{\phi}H)XG_{5X}). \quad (9.5)$$

Note that we use the definition α_B of Refs. [2179, 2187]. The quantities ϕ , X and H are evaluated on their background solution to give the particular time-dependence of the α_i functions for that solution. Also M_*^{-2} is proportional to the gravitational coupling entering the cosmological background evolution. Like in many MG models, it can depend on time and is given by [2179]

$$M_*^2 \equiv 2(G_4 - 2XG_{4X} + XG_{5\phi} - \dot{\phi}HXG_{5X}) , \quad (9.6)$$

where ϕ is the homogeneous value of the scalar field on the cosmic background and a dot denotes differentiation with respect to cosmic time t .

Each function $\alpha_i(t)$ is linked with a specific physical property and describes particular classes of models. In particular, the braiding function α_B describes the mixing of the kinetic terms of the scalar and metric, the kineticity α_K parametrizes the kinetic energy of the scalar perturbations, the tensor speed excess α_T quantifies how much the gravitational waves (tensor perturbations) speed c_T deviates from that of light, finally α_M describes the evolution of M_*^2 as follows [2179, 2188]

$$\alpha_M \equiv H^{-1} \frac{d \ln M_*^2}{dt} . \quad (9.7)$$

The Λ CDM model, and more generally GR, corresponds to the particular case $M_*^2 = M_p^2$ and $\alpha_M = \alpha_B = \alpha_K = \alpha_T = 0$.

In Horndeski theories, we obtain the Friedmann equations replacing M_p with the effective Planck mass M_* , so the Friedmann equations take the form [2179, 2187]

$$3H^2 = \frac{1}{M_*^2} (\rho_m + \mathcal{E}_{DE}) , \quad (9.8)$$

$$2\dot{H} + 3H^2 = -\frac{1}{M_*^2} (p_m + \mathcal{P}_{DE}) , \quad (9.9)$$

where \mathcal{E}_{DE} and \mathcal{P}_{DE} are the energy density and pressure associated to the additional degree of freedom (the full expressions are provided in the Appendix F). They are related to the energy density ρ_{DE} and pressure P_{DE} of the effective dark energy component as,

$$\rho_{DE} = \mathcal{E}_{DE} - 3(M_*^2 - M_p^2)H^2 , \quad (9.10)$$

$$P_{DE} = \frac{M_p^2}{M_*^2} \mathcal{P}_{DE} , \quad (9.11)$$

where in the last expression we have put $p_m = 0$ as we consider here dust-like matter. With these definitions the modified Friedmann equations are recast into an Einsteinian form, viz.

$$3H^2 = \frac{1}{M_p^2} (\rho_m + \rho_{DE}) , \quad (9.12)$$

$$2\dot{H} + 3H^2 = -\frac{1}{M_p^2} P_{DE} . \quad (9.13)$$

The stability conditions to be imposed on the functions $\alpha_i(a)$ are the following [2179, 2181]

$$\alpha_K + \frac{3}{2} \alpha_B^2 \geq 0 , \quad (9.14)$$

$$c_s^2 > 0 , \quad (9.15)$$

where c_s is the speed of sound which is connected to the α_i 's as follows [2179, 2188]

$$\left(\alpha_K + \frac{3}{2} \alpha_B^2 \right) c_s^2 = \frac{\dot{\alpha}_B}{H} - \frac{\rho_m}{H^2 M_*^2} - (2 - \alpha_B) \left[\frac{\dot{H}}{H^2} + \alpha_T - \alpha_M - \frac{\alpha_B}{2(1 + \alpha_T)} \right] . \quad (9.16)$$

The gravitational waves travel at the speed (with $c = 1$)

$$c_T^2 = 1 + \alpha_T . \quad (9.17)$$

Recent multimessenger constraints on gravitational waves using the neutron star inspiral GW170817 detected through both the emitted gravitational waves and γ -rays GRB 170817A [2176, 2177, 2189, 2190], imply that c_T is extremely close to the speed of light i.e. $c_T = 1 \pm 10^{-15}$. This constraint effectively eliminates all Horndeski theories with $\alpha_{T,0} \equiv \alpha_T(a=1) \neq 0$ (we take $a_0 = 1$). We consider in this analysis only those models satisfying $\alpha_T = 0$.

The α_i functions are independent of each other, i.e. they can be parametrized independently. However, for simplicity and in accordance with previous studies [1405, 2181], we assume that all the functions α_i have the same power law dependence on the scale factor a , viz.

$$\alpha_i = \alpha_{i0} a^s \quad \text{with } s > 0 , \quad (9.18)$$

where the constants α_{i0} are their current values. The exponent s determines the time evolution for the considered modified gravity model. One of the main goals of this analysis is to impose constraints on these parameters using cosmological observations and the assumptions mentioned earlier. From Eq. (9.7) we have for the quantity M_*

$$M_* = M_p e^{\int_0^a \alpha_M \frac{da'}{2a'}} = M_p e^{\alpha_{M0} \frac{a^s}{2s}} , \quad (9.19)$$

in accordance with our assumption $M_*(a=0) = M_p$. We obtain also

$$M_*(a=1) = M_p e^{\frac{\alpha_{M0}}{2s}} . \quad (9.20)$$

We have therefore $M_*(a=1) \approx M_p$ for $\alpha_{M0} \ll 2s$. Otherwise, the local value of the scalar field ϕ must differ from its value on cosmic scales. We recover $\frac{\dot{M}_*}{M_*} = \frac{\alpha_M}{2} H$ in accordance with Eq. (9.7), and in particular

$$\frac{\dot{M}_*}{M_*}(a=1) = \frac{\alpha_{M0}}{2} H_0 . \quad (9.21)$$

On subhorizon scales, the QSA applies to scales below the sound horizon of the scalar field ($k \gg aH/c_s$ or $\lambda \ll \lambda_J$ where λ_J is the Jeans length) [587, 1305, 2182] and the time-derivatives of the metric and of the scalar field perturbations are neglected compared to their spatial gradients. In the conformal Newtonian gauge, the perturbed FLRW metric takes the form of Eq. (3.9). This leads to the Eqs. (3.10) and (3.11) for the Bardeen potentials Ψ and Φ in Fourier space defining our functions $\Sigma_G(a, k)$ and $\mu_G(a, k)$. The functions $\Sigma_G(a, k)$ and $\mu_G(a, k)$ are generically time and scale dependent encoding the possible modifications of GR defined as¹

$$\mu_G(a, k) \equiv \frac{G_{\text{growth}}(a, k)}{G} , \quad (9.22)$$

$$\Sigma_G(a, k) \equiv \frac{G_{\text{lensing}}(a, k)}{G} , \quad (9.23)$$

where G is Newton's constant as measured by local experiments, G_{growth} is the effective gravitational coupling which is related to the growth of matter perturbation and G_{lensing} is the effective gravitational coupling associated with lensing. Anisotropic stress between the gravitational potentials Ψ and Φ is produced from the Planck mass run rate α_M and the tensor speed excess α_T [2191].

Using the gravitational slip parameter η (or anisotropic parameter) defined by Eq. (3.12) and the ratio of the Poisson equations (3.10) and (3.11), the two functions μ_G and Σ_G are related by Eq. (3.13). In GR we have $\mu_G = 1$, $\eta = 1$ and $\Sigma_G = 1$. The deviations from GR are expressed by allowing for a scale and time dependent μ_G and Σ_G but in the present analysis we ignore scale dependence in the context of the QSA and also due to the lack of good quality scale dependent data.

¹Note that the precise definitions of Σ_G and μ_G may vary in the literature (e.g. see in Ref. [2187]).

In the case of Horndeski modified gravity, in the quasistatic limit and fixing $\alpha_T = 0$ at all times, the functions $\mu_G(a)$ and $\Sigma_G(a)$ take the form [2187]

$$\mu_G(a) = \frac{M_p^2}{M_*^2} \left[1 + \frac{2(\alpha_M + \frac{1}{2}\alpha_B)^2}{c_s^2(\alpha_K + \frac{3}{2}\alpha_B^2)} \right], \quad (9.24)$$

$$\Sigma_G(a) = \frac{M_p^2}{M_*^2} \left[1 + \frac{(\alpha_M + \frac{1}{2}\alpha_B)(\alpha_M + \alpha_B)}{c_s^2(\alpha_K + \frac{3}{2}\alpha_B^2)} \right]. \quad (9.25)$$

Thus for theories with $\alpha_M = 0$ or $\alpha_B = -2\alpha_M$, μ_G is equivalent to Σ_G . Notice also that for $\alpha_M = 0$, we obtain $\mu_G > 1$ and $\Sigma_G > 1$. The case $\alpha_B = -2\alpha_M$ is a special case also known as No slip Gravity [1406] for which $\eta = 1$ and we have then

$$\mu_G(a) = \Sigma_G(a) = \frac{M_p^2}{M_*^2}. \quad (9.26)$$

Notice also that all expressions depend on the coefficient $c_s^2(\alpha_K + \frac{3}{2}\alpha_B^2)$ which from Eq. (9.16) shows that μ_G and Σ_G are actually independent of α_K . This parameter has minimal effect on subhorizon scales (i.e. $k/aH \gg 1$) [2179, 2181], while being uncorrelated with all other functions α_i [2192]. It is only independently constrained by stability considerations through Eq. (9.14). In addition, as we set $\alpha_T = 0$ at all times, the only functions that can be constrained with observations by the quantities μ_G and Σ_G are the functions $\alpha_M(a)$ and $\alpha_B(a)$. Finally, assuming the stability conditions (9.14) and (9.15), we have $\mu_G > M_p^2/M_*^2$ as noticed in Ref. [2015] but Σ_G remains unconstrained.

For any $w_{DE}(a = \infty) = w_\infty$ finite, we can consider two cases, depending on the sign of α_{M0} . In the asymptotic future, the Hubble function evolves as $H \propto a^{-3(1+w_\infty)/2}$ and therefore $\dot{H}/H^2 \rightarrow -3(1+w_\infty)/2$. Also $\dot{\alpha}_B/H = s \alpha_B$ where we have assumed Eq. (9.18). It is therefore easy to show that for large scale factor, we have

$$(\alpha_K + \frac{3}{2}\alpha_B^2)c_s^2 \rightarrow s\alpha_B - \frac{3}{2}(1+w_\infty)\alpha_B - \frac{\rho_m}{H^2 M_*^2} - \alpha_B(\alpha_M + \frac{\alpha_B}{2}). \quad (9.27)$$

The first two terms are always negligible compared to the last term, except for No Slip Gravity for which the last term is absent.

If $\alpha_{M0} < 0$, the coefficient $-\rho_m/H^2 M_*^2 = -\rho_m e^{-\alpha_{M0} a^s/s}/H^2 M_p^2$ is dominant because of the exponential behavior and hence c_s^2 is always negative for $a \rightarrow \infty$,

$$(\alpha_K + \frac{3}{2}\alpha_B^2)c_s^2 \propto -\rho_m/H^2 M_*^2 < 0, \quad (9.28)$$

and these models are excluded. On the other hand if $\alpha_{M0} > 0$, the matter component $-\rho_m/H^2 M_*^2 = -\rho_m e^{-\alpha_{M0} a^s/s}/H^2 M_p^2$ is negligible, we have for $a \rightarrow \infty$

$$(\alpha_K + \frac{3}{2}\alpha_B^2)c_s^2 \simeq -\frac{a^{2s}}{2}\alpha_{B0}(\alpha_{B0} + 2\alpha_{M0}), \quad (9.29)$$

from which we obtain the condition

$$\alpha_{B0}(\alpha_{B0} + 2\alpha_{M0}) \leq 0. \quad (9.30)$$

Therefore, we conclude that the only possible viable sector satisfies

$$\alpha_{B0} \leq 0 \quad \text{and} \quad \alpha_{M0} \geq -\alpha_{B0}/2. \quad (9.31)$$

Considering these restrictions we have at any time

$$\mu_G(a) \geq \Sigma_G(a). \quad (9.32)$$

In the case of No Slip Gravity, we have in the asymptotic future

$$(\alpha_K + \frac{3}{2}\alpha_B^2)c_s^2 \rightarrow \left[s - \frac{3}{2}(1 + w_\infty) \right] \alpha_B - \frac{\rho_m}{H^2 M_*^2} . \quad (9.33)$$

As previously, $\alpha_{M0} < 0$ is excluded because of the matter sector which produces a negative contribution. If $\alpha_{M0} > 0$, we need to impose the condition $s - \frac{3}{2}(1 + w_\infty) \geq 0$, which is irrelevant only if the asymptotic future is phantom $w_\infty < -1$, or if $w_\infty = -1$ which reduces to $s \geq 0$. Notice also that if $\alpha_{B0} < 0$ and assuming $c_T = 1$, we have from Eq. (9.4) $2\dot{\phi}(XG_{3X} - G_{4\phi}) < 0$. This condition reduces to $dF/dt > 0$ for scalar-tensor theories for which $G_4 = F(\phi)$ and $G_3 = 0$.

9.3 Reconstruction of the α_M , α_B functions from observational constraints on μ_G , Σ_G

In the spirit of this formalism disentangling the background from the perturbations, our background will be fixed. We assume the most conservative and realistic background, Λ CDM. Therefore, observational constraints come only from perturbations. We focus on the linear growth of matter perturbations

$$\ddot{\delta}_m + 2H\dot{\delta}_m - 4\pi G \mu_G(a) \rho_m \delta_m = 0 . \quad (9.34)$$

In terms of redshift, Eq. (9.34) takes the following form [148, 587, 1388]

$$\delta_m'' + \left[\frac{(H^2)'}{2H^2} - \frac{1}{1+z} \right] \delta_m' - \frac{3(1+z)}{2} \frac{\Omega_{m,0} \mu_G(z)}{H^2/H_0^2} \delta_m = 0 , \quad (9.35)$$

where a prime denotes differentiation with respect to the redshift.

Note that we have defined $\Omega_m = \frac{\rho_m}{3M_p^2 H^2}$. This definition assumes that general relativity is recovered at small scales. Therefore we presume a sufficient viable screening mechanism. It is important to notice that even if we have defined a power law dependence of the parameters (see Eq. 9.18), the Lagrangian is not totally fixed, principally because of an unconstrained α_k . The reconstruction of the Lagrangian from (α_B, α_M) is incomplete and therefore, the Lagrangian is left partially undefined. This freedom can be used to have additional non-linear operators in order to have a viable Vainshtein mechanism. Notice that in the static and spherically symmetric case, non-linear operators can be sufficient to eliminate the fifth force and recover general relativity at small scales as shown in [2193] but in a generic shift-symmetric k-mouflage model, the authors of [2194] (see also [2195], for explicit models) have shown that even if the fifth force is suppressed, a time dependence of the scalar field inside the Vainshtein radius remains and therefore at small scales $G_{\text{growth}} = 1/8\pi M_*^2(\phi(t))$ where $\phi(t)$ is the cosmological time evolution of the scalar field². Nevertheless, considering a non spherical problem, general relativity is recovered at small scales [2197]. In conclusion, the screening mechanism could be sufficient to recover general relativity at smaller scales. But it remains a delicate point and should be studied more extensively in the future.

It is usually convenient to introduce the growth function (3.3) from which it is straightforward to construct the growth index γ defined by

$$f = \Omega_m^\gamma . \quad (9.36)$$

We will constrain the parameters through the growth data $f\sigma_8$ obtained from Redshift Space distortions (RSD) [4, 67, 146–148, 681, 820, 1199, 1977, 1978] and the combination of the growth rate - weak lensing data expressed through the quantity E_G statistics [4, 144, 1988, 2198]. For a parametrization of μ_G and initial conditions deep in the matter era where GR is assumed to hold with $\delta_m \sim a$, equation (9.35)

²In this case, we would have a very strong constraint on the model. Because $|\dot{G}_{\text{growth}}/G_{\text{growth}}| = |\alpha_M|H$ and considering the Lunar Laser Ranging experiments constrain [2196] $|\dot{G}/G| < 0.02 H_0$, we would have $|\alpha_{M0}| < 0.02$ because at small scales G_{growth} should be identified with the gravitational constant G . But this result does not apply when the shift symmetry is broken like e.g. in the presence of a mass term.

may be easily solved numerically leading to a predicted form of $\delta_m(z)$ for a given $\Omega_{m,0}$ and background expansion $H(z)$. Once this evolution of δ_m is known, the observable product

$$f\sigma_8(z) \equiv f(z) \cdot \sigma_8(z) = f(z) \cdot \sigma_8 \frac{\delta_m(z)}{\delta_{m,0}} , \quad (9.37)$$

can be obtained, where $\sigma_8(z)$ is the redshift dependent rms fluctuations of the linear density field within spheres of (comoving) radius $R = 8h^{-1}Mpc$ while σ_8 is its value today. We obtain finally

$$f\sigma_8 = -(1+z)\sigma_8 \frac{\delta'_m(z)}{\delta_{m,0}} . \quad (9.38)$$

This theoretical prediction may now be used to compare with the observed $f\sigma_8$ data.

For given parametrizations of our models, we can constrain the function Σ_G (associated to lensing) using $E_G(a)$ data where the observable $E_G(a)$ is defined as [524, 2010, 2011]

$$E_G = \frac{\Omega_{m,0} \Sigma_G}{f(z)} . \quad (9.39)$$

This equation assumes that the redshift of the lens galaxies can be approximated by a single value while E_G corresponds to the average value along the line of sight [524]. Using Eq. (9.39) and assuming a specific parametrization for α_B and α_M , and a given background expansion, we can compare the theoretical prediction for E_G with the observed E_G datapoints in order to constrain our parameters $(\alpha_{B0}, \alpha_{M0})$. The $f\sigma_8(z)$ and $E_G(z)$ updated data compilations used in our analysis are shown in Tables F.1 and F.2 of the Appendix F along with the references where each datapoint was originally published.

We construct $\chi_{f\sigma_8}^2$ and $\chi_{E_G}^2$ as usual [2199] for the $f\sigma_8$ and E_G datasets. For the construction of $\chi_{f\sigma_8}^2$ we use the vector [67]

$$V_{f\sigma_8}^i(z_i, p) \equiv f\sigma_{8,i}^{obs} - \frac{f\sigma_8^{th}(z_i, p)}{q(z_i, \Omega_{m,0}, \Omega_{m,0}^{fid})} , \quad (9.40)$$

where $f\sigma_{8,i}^{obs}$ is the value of the i th datapoint, with $i = 1, \dots, N_{f\sigma_8}$ ($N_{f\sigma_8} = 35$ corresponds to the total number of datapoints of Table D.3) and $f\sigma_8^{th}(z_i, p)$ is the theoretical prediction, both at redshift z_i . The parameter vector p corresponds to the free parameters $\sigma_8, \Omega_{m,0}, \alpha_{B0}, \alpha_{M0}, s$ that we want to determine from the data.

The fiducial Alcock-Paczynski correction factor q [67, 147, 148] is defined as

$$q(z_i, \Omega_{m,0}, \Omega_{m,0}^{fid}) = \frac{H(z_i)d_A(z_i)}{H^{fid}(z_i)d_A^{fid}(z_i)} , \quad (9.41)$$

where $H(z)$, $d_A(z)$ correspond to the Hubble parameter and the angular diameter distance of the true cosmology and the superscript fid indicates the fiducial cosmology used in each survey to convert angles and redshifts to distances when evaluating the correlation function. Thus we obtain $\chi_{f\sigma_8}^2$ as

$$\chi_{f\sigma_8}^2(\Omega_{m,0}, \alpha_{B0}, \alpha_{M0}, s, \sigma_8) = V_{f\sigma_8}^i F_{f\sigma_8,ij} V_{f\sigma_8}^j , \quad (9.42)$$

where $F_{f\sigma_8,ij}$ is the Fisher matrix (the inverse of the covariance matrix $C_{f\sigma_8,ij}$ of the data) which is assumed to be diagonal with the exception of the 3×3 WiggleZ subspace (see Ref. [67] for more details on this compilation).

Similarly, for the construction of $\chi_{E_G}^2$, we consider the vector

$$V_{E_G}^i(z_i, p) \equiv E_{G,i}^{obs} - E_G^{th}(z_i, p) , \quad (9.43)$$

where $E_{G,i}^{obs}$ is the value of the i th datapoint, with $i = 1, \dots, N_{E_G}$ ($N_{E_G} = 8$ corresponds to the total number of datapoints of Table D.4), while $E_G^{th}(z_i, p)$ is the theoretical prediction (Eq. (9.39)), both at redshift z_i . Thus we obtain $\chi_{E_G}^2$ as

$$\chi_{E_G}^2(\Omega_{m,0}, \alpha_{B0}, \alpha_{M0}, s) = V_{E_G}^i F_{E_G,ij} V_{E_G}^j , \quad (9.44)$$

where $F_{E_G,ij}$ is the Fisher matrix also assumed to be diagonal.

By minimizing $\chi_{f\sigma_8}^2$ and $\chi_{E_G}^2$ separately and combined as $\chi_{tot}^2 = \chi_{f\sigma_8}^2 + \chi_{E_G}^2$ we obtain the constraints on the parameters α_{B0} and α_{M0} . In this work, we fix $\Omega_{m,0} = 0.315$ and $\sigma_8 = 0.811$ to the Planck/ Λ CDM parameter values favoured by Planck 2018 [14] and other geometric probes [48, 51]. These values are mainly determined by geometric probes which are independent of the underlying gravitational theory. Specifically, we explore our parameter space (p) for $s = 0.5, 1, 1.5, 2, 2.5, 3$.

9.4 Flat Λ CDM background

In what follows, in agreement with the constraints of most geometric probes [14, 48, 51], we assume a background Hubble expansion corresponding to a flat Λ CDM cosmology with $H(z)$ given by

$$H^2(z) = H_0^2 [\Omega_{m,0}(1+z)^3 + (1 - \Omega_{m,0})] , \quad (9.45)$$

where $\Omega_{m,0}$ is the fractional energy density of dust-like matter today.

Using the stability equation (9.15) (assumed valid for all values of the scale factor a) along with the parametrization (9.18) for various values of s , we show in Fig. 9.1 the stability region (defined by the positivity at all times of the quantity μ_G and of the sound speed c_s^2) in the $\alpha_{M0} - \alpha_{B0}$ parameter space. A Λ CDM background is assumed with a value of $\Omega_{m,0} = 0.315$ in accordance with the best fit values of CMB/Planck18 [14], BAO [48] and SNe Ia Pantheon [51] data.

For each region, we show in Fig. 9.1 the strong gravity regime today

$$\mu_G(z=0) > 1 , \quad (9.46)$$

and weak gravity regime today

$$\mu_G(z=0) < 1 . \quad (9.47)$$

We can see that for small values of $(\alpha_{B0}, \alpha_{M0})$ and for small s , we have $\mu_G < 1$ while for larger s gravity is stronger. Gravity is weak today for $s < 2$ and strong if $s > 2$ for most of the parameters in the range $-3 \leq \alpha_{B0} \leq 0$ and $0 \leq \alpha_{M0} \leq 3$.

The growth rate of perturbations evolves according to the equation

$$\frac{df}{dx} + f^2 + \frac{1}{2} \left(1 - \frac{d \ln \Omega_m}{dx} \right) f = \frac{3}{2} \frac{G_{growth}}{G} \Omega_m , \quad (9.48)$$

where $x \equiv \ln a$. From Eq. (3.3) we have that the density perturbation δ_m is connected to the growth rate f as

$$\delta_m(a) = \delta_i \exp \left[\int_{x_i}^x f(x') dx' \right] . \quad (9.49)$$

In the special case where the growing mode satisfies $\delta_m \propto a^p$, we have $f = p$ and thus $f \rightarrow 1$ in Λ CDM for large z as long as the decaying mode is negligible [2200]. In a Λ CDM universe we have

$$f = \Omega_m^{\gamma(z)} , \quad (9.50)$$

with $\gamma_0 \equiv \gamma(z=0) \approx \frac{6}{11}$, the latter corresponds to the exact value deep in the matter era and γ_0 is only slightly higher. In Λ CDM, γ is monotonically increasing with the expansion [2200]. In general, the growth index is thus redshift dependent, a strictly constant γ being excluded inside GR though it is often quasi-constant on redshifts between today till deep in the matter era [2004]. Using the above definitions, we have represented in the same figure, the values of the growth index today γ_0 and its derivative $\gamma_1 \equiv \gamma'(z=0)$, where γ_0, γ_1 are parameters to be fit to data.

The γ_0, γ_1 values are complementary to the μ_G values and add information about the perturbations dynamics in the past. On Fig. 9.1, $s = 2$, it is seen that the curve $\mu_G = 1$ crosses the curve $\gamma_0 = \gamma_0^{\Lambda CDM}$. As we have a fixed Λ CDM background, it follows from the evolution equation for γ that we must have

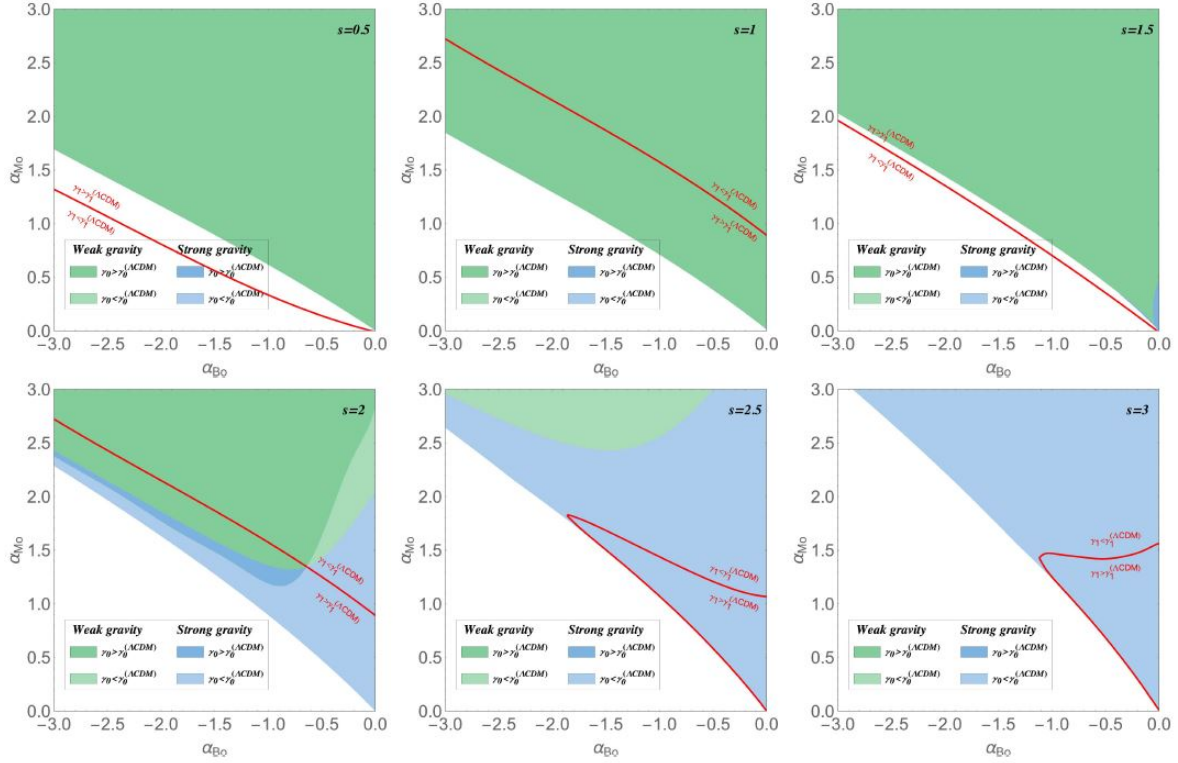


Figure 9.1: The stability (no ghost) region in the α_{M0} - α_{B0} parameter space is shown and divided into a weak gravity regime today, $\mu_{G,0} \equiv \mu_G(z=0) < 1$ (green area), and a strong gravity regime today, $\mu_{G,0} > 1$ (blue area). This is obtained by demanding $c_s^2(z) > 0$ at all times and assuming a flat Λ CDM background together with the parametrization Eq. (9.18) used here for the values $s = 0.5, 1, 1.5, 2, 2.5, 3$. The dark blue and dark green regions indicate $\gamma_0 > \gamma_0^{\Lambda CDM}$, while the light blue and light green regions correspond to $\gamma_0 < \gamma_0^{\Lambda CDM}$. Finally, the red curve determines the regions where either $\gamma_1 > \gamma_1^{\Lambda CDM}$ or $\gamma_1 < \gamma_1^{\Lambda CDM}$. We see in particular that for $s \leq 2$, essentially the weak gravity regime today is selected. In the light green region, μ_G crosses 1 downwards with expansion, while it crosses upwards in the dark blue region.

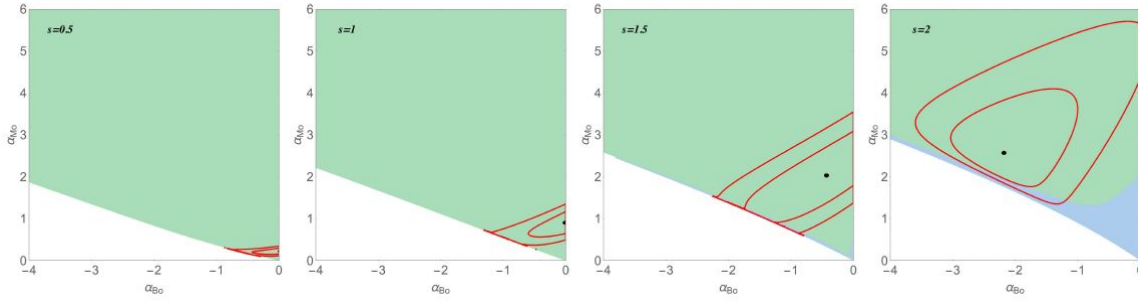


Figure 9.2: The best fit values of α_{B0} and α_{M0} are shown for $s = 0.5, 1, 1.5, 2$ using the combined constraints from the $f\sigma_8$ and E_G data, 1σ and 2σ confidence regions are drawn (red curves). As in Fig. 9.1, the green area corresponds to weak gravity today while the blue area represents strong gravity today. Observations give the constraint $\gamma_0 > \gamma_0^{\Lambda CDM}$ for $s < 2$, marginally allowing $\gamma_0 < \gamma_0^{\Lambda CDM}$ for $s = 2$. Note that for higher values of s , the best fit moves outside the colored region and is therefore ruled out.

there $\gamma_1 = \gamma_1^{\Lambda CDM}$ which is nicely exhibited on our Figure. Furthermore, for that specific point, the value of μ_G in the recent past satisfies $\mu_G \approx 1$ on those redshifts for which $\gamma \approx \gamma_0^{\Lambda CDM} + \gamma_1^{\Lambda CDM}(1 - a)$.

Notice that when $\gamma_0 = \gamma_0^{\Lambda CDM}$, we are in the weak gravity regime for $\gamma_1 < \gamma_1^{\Lambda CDM}$ and in the strong gravity regime for $\gamma_1 > \gamma_1^{\Lambda CDM}$. Also if we consider $\gamma_1 = \gamma_1^{\Lambda CDM}$, we have $\gamma_0 < \gamma_0^{\Lambda CDM}$ for strong gravity and $\gamma_0 > \gamma_0^{\Lambda CDM}$ for weak gravity today. These results obtained for our parametrized Horndeski models are in accordance with the results obtained earlier (see Fig. 7 in Ref. [2201]) in a gravity model independent way.

Using the observational constraints from $f\sigma_8$ and E_G data, we find that for larger values of s ($s \gtrsim 2$) the best fit selects an area violating the stability conditions, and therefore these values of s should be ignored. Therefore, assuming a Λ CDM background and these data, we find that $s \leq 2$ is allowed. This implies that our data select essentially a weak gravity regime today as we have noted earlier, see Fig. 9.1. Also, because we have $\Sigma_G \leq \mu_G$ from Eq. (9.32), we obtain $\Sigma_{G,0} \leq 1$, a result which we have confirmed numerically. Even for $s = 2$ where a small regime of strong gravity remains, we still have always $\Sigma_{G,0} \leq 1$. Fig. 9.2 exhibits these results with the 1σ and 2σ contour plots for the combined data.

9.5 Conclusions

Weak gravity is a difficult regime to be reached within viable modified gravity theories. We have shown that assuming a perfectly viable background solution, Λ CDM, we were able to constrain Horndeski models by using $f\sigma_8$ and E_G data. Assuming only a power law parametrization for the parameters (α_B, α_M) , we found that viable models should verify the condition

$$\alpha_{B,0} < 0 \quad \text{and} \quad \alpha_{M,0} > -\alpha_{B,0}/2, \quad (9.51)$$

which constrain G_{lensing} to be always smaller than G_{growth} .

Considering the Λ CDM background, we found that for $s < 2$, most of the parameters $(\alpha_{B0}, \alpha_{M0})$ produce weak gravity today while for $s > 2$, we found $\mu_{G,0} > 1$ for most of the parameters. The consideration of cosmological growth data favors $s \leq 2$, namely a mild evolution of the α_i parameters in the late universe, which in turn implies a weak gravity regime today and $\Sigma_{G,0} \leq 1$. We also found that for $s < 2$, $\gamma_0 > \gamma_0^{\Lambda CDM}$, while for $s > 2$ we obtain $\gamma_0 < \gamma_0^{\Lambda CDM}$. Therefore, data also select essentially $\gamma_0 > \gamma_0^{\Lambda CDM}$ except for $s = 2$ for which $\gamma_0 < \gamma_0^{\Lambda CDM}$ is marginally allowed. Note that for $s = 2$, in the region with $\mu_{G,0} < 1$ and $\gamma_0 < \gamma_0^{\Lambda CDM}$ (light green on Fig. 9.1), gravity was strong in the near past ($z \lesssim 1$), while in the region $\mu_{G,0} > 1$ and $\gamma_0 > \gamma_0^{\Lambda CDM}$ (dark blue on Fig. 9.1), gravity was weak in the recent past. In some sense, the value of γ_0 indicates that gravity was either weak ($\gamma_0 > \gamma_0^{\Lambda CDM}$

and $\mu_{G,0} > 1$) or strong ($\gamma_0 < \gamma_0^{\Lambda CDM}$ and $\mu_{G,0} < 1$) when we average over the recent past, while $\mu_{G,0}$ determines the strength of gravity today. For example, in the light green region where $\mu_{G,0} < 1$, the average of $\mu_G(z)$ over redshift (0, 1) is larger than 1. We encountered the same behavior in the dark blue region where gravity is strong today and weak on average for most part of the region. Therefore, the pairs (γ_0, γ_1) add information on the past dynamics of μ_G .

For models with $\gamma_1 = \gamma_1^{\Lambda CDM}$, we have $\gamma_0 < \gamma_0^{\Lambda CDM}$ when gravity is strong today and $\gamma_0 > \gamma_0^{\Lambda CDM}$ when gravity is weak today. Also when $\gamma_0 = \gamma_0^{\Lambda CDM}$, we have weak gravity when $\gamma_1 > \gamma_1^{\Lambda CDM}$ while we have strong gravity when $\gamma_1 < \gamma_1^{\Lambda CDM}$.

In summary, we have proved that under mild assumptions, we could have a consistent and viable weak gravity regime today. It is thus interesting to know how generic this result is. It is interesting that the model we have assumed is observationally incompatible at more than 2σ with $M_* = M_p$ today (at least for $s \gtrsim 0.5$). Hence the local value of M_* must be necessarily different from its assumed value on cosmic scales today, Eq. (9.20), and some screening mechanism must be at work in order to make the model viable. As we have mentioned earlier, this is a delicate issue. Even in the absence of screening, our results leave open the possibility to have viable models with $s < 0.5$ satisfying $\alpha_{M0} \ll 2s$. Of course, in that case, M_* would be (very) weakly varying at all times.

We can investigate in a future work the relevance, regarding the obtained results, of the two main assumptions made in this work, namely the power-law parametrization of the free functions α_i and the Λ CDM background expansion (for an alternative approach see e.g. Ref. [2202]). For example, in the case of minimal scalar-tensor theories, it has been shown that values of $w < -1$ can indeed lead to $\mu_G < 1$ [1823, 1978], while it is otherwise impossible to realize. Despite strong restrictions on Horndeski models coming from the gravitational waves speed, viable models could still provide interesting cosmological scenarios with varying gravitational couplings.

Chapter 10

Transition Model in light of Cepheid SnIa Calibrator data: Alleviating the Hubble Tension

The analysis presented in this chapter is based on the work which was done in collaboration with Prof. Leandros Perivolaropoulos and has been published in Physical Review D [8].

In this Chapter 10 we use Cepheid SnIa calibrator data to investigate the effects of variation of the Cepheid calibration empirical parameters R_W (Cepheid Wesenheit color-luminosity parameter) and M_H^W (Cepheid Wesenheit H-band absolute magnitude). We consider various cases (models) allowing for different types of empirical parameter variation and use criteria which penalize models with large numbers of parameters for model selection and model comparison. We investigate the impact of the allowed types of parameter variation on the SnIa absolute magnitude M_B and on the corresponding derived value of Hubble constant H_0 .

The most intriguing large scale tension is the Hubble crisis as we discussed in Chapter 2. Using a distance ladder approach (see Subsection 2.2.1), the local (late or low redshift) measurements of the Hubble constant H_0 lead to values that are significantly higher than those inferred using the angular scale of fluctuations of the CMB in the context of the Λ CDM model. Local direct measurements of H_0 are in more than 5σ tension with CMB indirect measurements of H_0 (see Refs. [7, 127, 185], for a review).

The local (late or low redshift) determination of the Hubble constant H_0 using a distance ladder method depends on a chain of distance measurements. In the cosmic distance ladder method each rung of the distance ladder uses the known intrinsic luminosity of a standard candle source to determine the absolute luminosity of a more luminous standard candle residing in the same galaxy. Thus highly luminous standard candles are calibrated for the next rung in order to reach out to greater distances. If one of these distance measures is subject to systematics or new physics all the subsequent steps of the cosmic distance ladder are off.

The distance ladder approach is based on a method pioneered by Henrietta Swan Leavitt. She realized that a type of pulsating stars known as Cepheid variable has a period of pulsation that depends on its luminosity. This period–luminosity (PL) relation is called the Leavitt law [217, 218]. Knowing the luminosity of a Cepheid means that its luminosity distance can be determined just by observing its brightness which has been dimmed by that distance. Therefore the Cepheids whose luminosities are correlated with their periods of variability can be the first standard candles in the cosmic distance ladder [2203–2210]. Trigonometric parallax methods (geometric anchors) may be used to calibrate the Cepheid variable star standard candles at the local Universe (primary distance indicators). Then using the measured luminosity distances of the calibrated Cepheid stars, the intrinsic luminosity of nearby

($D \approx 20\text{--}40 \text{ Mpc}$) incredibly bright type Ia supernova (SnIa) residing in the same galaxies as the Cepheids is obtained. This calibration of the new type of standard candle SnIa fixes its absolute magnitude M_B and is then used for SnIa at more distant galaxies (in the Hubble flow) to measure H_0 ($z \in [0.01, 0.1]$) and $H(z)$ ($z \in [0.01, 2.3]$) via the measurement of their luminosity distances. The angular diameter distance of standard rulers can also be used for the estimation of $H(z)$ (see Subsection 2.2.2). The values of H_0 determined in the late Universe with a calibration based on the Cepheid distance scale and the derived values of H_0 from analysis of the CMB anisotropy spectrum data are shown in Fig. 2.10. The uncertainties in these values have been decreasing for both methods and the recent measurements disagree beyond 5σ . The Hubble constant H_0 values at 68% CL through direct and indirect measurements obtained by the different methods are illustrated in Fig. 2.8, from which is evident that the SnIa distance scale calibrated by Cepheid variables is in tension with the CMB sound horizon scale.

If the Hubble tension is not due to systematic errors [185, 292, 299, 438, 880, 2211, 2212], it could be an indication of incorrect estimate of the sound horizon scale due e.g. to early dark energy [293] or to late phantom dark energy [50]. Theoretical models (see Subsection 2.3) addressing this discrepancy utilize either a recalibration of the Λ CDM standard ruler (the sound horizon) assuming new physics before the time of recombination [181–183, 1042] or a deformation of the Hubble expansion rate $H(z)$ at late times [50, 184, 712] or an abrupt transition of the SnIa absolute luminosity due to late time new physics [52] (see Refs. [7, 127, 185], for a review).

10.1 Introduction

As discussed in Subsection 2.3.4 the H_0 crisis may be viewed as a mismatch between the SnIa absolute magnitude $M_B^< = -19.244 \pm 0.037 \text{ mag}$ calibrated by Cepheids at $z < 0.01$ [269, 289] and the SnIa absolute magnitude $M_B^> = -19.401 \pm 0.027 \text{ mag}$ [290] obtained using the parametric free inverse distance ladder calibrating SnIa absolute magnitude using the sound horizon scale.. Since the two measurements are obtained at different redshifts they may indicate a transition in the absolute magnitude with amplitude $\Delta M_B = M_B^> - M_B^< \simeq -0.2 \text{ mag}$ at a transition redshift $z_t \lesssim 0.01$ (roughly 100-150 million years ago) [52, 593]. Note that hints of a possible weak evolution of the absolute magnitude M_B have been recently pointed out in Refs. [12, 281]. Such a transition may occur due to a transition of the strength of the gravitational interactions G_{eff} which modifies the SnIa intrinsic luminosity L by changing the value of the Chandrasekhar mass M_{Ch} as $L \sim M_{Ch} \sim G_{\text{eff}}^{-3/2}$ [914, 2213] even though corrections may be required to the above simplistic approach [915]. Using the normalized effective Newton constant $\mu_G \equiv G_{\text{eff}}/G$ (where G is the locally measured Newton's constant and $\mu_G = 1$ for $z < z_t \lesssim 0.01$) the absolute magnitude of SnIa M_B is expected to change as [1, 914, 1831, 2214]

$$\Delta M_B = \frac{15}{4} \log_{10}(\Delta \mu_G - 1) . \quad (10.1)$$

Thus for $\Delta M_B \simeq -0.2 \text{ mag}$ it is straightforward to show that the change of μ_G [52]

$$\Delta \mu_G \equiv \mu_G^> - \mu_G^< \simeq -0.12 , \quad (10.2)$$

where $\mu_G^>$ corresponds to $z > z_t$ and $\mu_G^<$ corresponds to $z < z_t$ in the context of a Λ CDM background $H(z)$.

This connection indicates that a 10% smaller G_{eff} for $z > z_t$ could potentially provide the required decrease of the absolute magnitude (increase of luminosity) at early times for the resolution of the Hubble tension. In fact such a decrease would also lower the growth rate of cosmological perturbations thus helping in the resolution of the growth tension [52, 1213]. Thus, the smaller G_{eff} ($G_{\text{eff}} < 1$) for $z > z_t$ hints towards weaker gravity as indicated by studies discussing the growth tension [4, 6, 67, 148, 1197, 1823, 2215].

A recent analysis [56], has analyzed the color-luminosity relation of Cepheids in anchor galaxies and SnIa host galaxies by identifying the color-luminosity relation for each individual galaxy instead of

enforcing a universal color-luminosity relation to correct the NIR Cepheid magnitudes. This analysis finds a systematic brightening of Cepheids at distances larger than about 20 Mpc (see Fig. 4 in Ref. [56]). As pointed out in Ref. [56] this brightening could be enough to resolve the Hubble tension. The authors attribute it to variation of dust properties but there is currently a debate on the actual cause of this brightening.

In our study we reproduce and extend the analysis of Ref. [56] by considering a varying among individual galaxies color-luminosity relation and (in a separate analysis) allowing the Cepheid absolute magnitude M_H^W to vary among individual galaxies instead of enforcing a universal absolute magnitude. We also explore the possibility that there are two universal absolute magnitudes: one applicable for low distance D Cepheids ($M_H^{W,<}$ for $D < D_c$) and a second, applicable for high distance D Cepheids ($M_H^{W,>}$ for $D > D_c$). We then test the consistency among the two absolute magnitudes searching for hints of a physics transition at some critical distance (time) D_c (D_c/c).

We thus address the following questions:

- Are there indications for variation of the color-luminosity relation and of the Cepheid absolute magnitude among individual galaxies?
- Is the color-luminosity relation and/or absolute magnitude of nearby Cepheids consistent with the corresponding properties of Cepheids in more distant galaxies?
- Are there indications for a Cepheid luminosity transition similar to the one required for the resolution of the Hubble tension?

In order to address these questions we use the same data and similar method as those used in Ref. [56] but in addition we extend the types of parameter variations allowed while implementing model selection criteria in order to compare the different allowed types of parameter variations (models) with the Base model which assumes universal Cepheid empirical parameter values. The data are obtained from Refs. [17, 39, 40] and displayed in the Appendix G. Our generalized approach is based on two extensions

- We break the assumption of universality not only on the color-luminosity relation but also on the absolute magnitude of Cepheids.
- In addition to fitting the Cepheid color-luminosity relation (or the absolute magnitude) for each galaxy separately, we also consider the case of two universality classes one for nearby and one for more distant galaxies thus introducing only one new parameter in each case compared to the standard universal approach.

The structure of this Chapter is the following: In the next Section 10.2 we present a brief review of the theoretical background and we describe the method used in our analysis as well as the data considered. In Section 10.3 we present our results focusing on the consistency of nearby and more distant samples with each other. We also compare with a Monte Carlo uniformized dataset in order to verify that any observed peculiar signal disappears in a Monte Carlo constructed homogeneous dataset. In Section 10.4 we consider various cases (models) allowing for different types of empirical parameter variation and use criteria for model selection and model comparison. In Section 10.5 we investigate the impact of the allowed types of parameter variation on the SnIa absolute magnitude M_B and on the corresponding derived value of H_0 . Finally in Section 10.6 we conclude and discuss possible extensions of our analysis. We also compare our results with previous analyses searching for similar transition effects in different datasets.

10.2 Theoretical background - Method - Data

In this section, we present a brief review of the theoretical expressions and describe the method and the dataset used.

10.2.1 Standard candles

In an expanding flat Universe, where the energy is not conserved due to the increase of the photon wavelength and period with time, the luminosity distance can be expressed by Eq. (1.55) [77, 78]. The luminosity distance is an important cosmological observable that is measured using standardizable candles like SnIa ($z < 2.3$) [51, 68, 118, 119] and gamma-ray bursts (GRBs) ($0.1 < z \lesssim 9$) [187–210].

As mentioned in Subsection 2.2.1 surveys can indicate the distance-redshift relation of SnIa by measuring their peak luminosity that is tightly correlated with the shape of their characteristic light curves (luminosity as a function of time after the explosion) [211] and the redshifts of host galaxies.

The use of SnIa in the measurement of H_0 and $H(z)$ relies on a basic assumption that they are standardizable and after proper calibration they have a fixed absolute magnitude independent of redshift in the redshift range $z \in [0.01, 2.3]$ [211]. This assumption has been tested in Refs. [12, 277, 279–285, 1978]. The possibility for intrinsic luminosity evolution of SnIa with redshift was first highlighted by Ref. [271]. Also, the assumption that the luminosity of SnIa is independent of host galaxy properties (e.g. host age, host morphology, host mass) and local star formation rate has been discussed in Refs. [272–276].

The apparent magnitude m_B of SnIa at redshift z in the context of a specified form of $H(z)$ is given by

$$m_B(z) = M_B + 5 \log_{10} \left[\frac{d_L(z)}{Mpc} \right] + 25 , \quad (10.3)$$

where M_B is the absolute magnitude, $d_L(z)$ is the luminosity distance in Mpc .

Using now the dimensionless Hubble free luminosity distance $D_L(z)$ (see Eq. (2.3) in Subsection 2.2.1) the apparent magnitude can be written as

$$m_B(z) = M_B + 5 \log_{10} [D_L(z)] + 5 \log_{10} \left[\frac{c/H_0}{Mpc} \right] + 25 . \quad (10.4)$$

Using the degenerate combination

$$\mathcal{M} = M_B + 5 \log_{10} \left[\frac{c/H_0}{Mpc} \right] + 25 , \quad (10.5)$$

into Eq. (10.4) we obtain

$$m_B(z) = \mathcal{M} + 5 \log_{10} [D_L(z)] . \quad (10.6)$$

The use of Eq. (10.4) to measure H_0 using the measured apparent magnitudes of SnIa requires knowledge of the value of the SnIa absolute magnitude M_B . This can be obtained using calibrators of local SnIa at $z < 0.01$ in the context of a distance ladder method (see e.g. Ref. [216]). Calibrators like Cepheid stars which are bright, variable supergiants are used in this context.

10.2.2 Cepheid calibration

As discussed in Subsection 2.2.1 for Cepheids in the distance anchor galaxies (MW, LMC and NGC 4258) there are three different approaches of geometric distance calibration of their luminosities: parallaxes in the MW [38, 40, 219–224], detached eclipsing binary stars (DEBs) in the LMC [225] and water masers¹ in NGC 4258 [227]. The DEBs method relies on surface-brightness relations and is one-step distance determination to nearby galaxies independent from Cepheids [228]. The Andromeda galaxy (M31) could serve as an anchor in the cosmic distance ladder but the uncertainty in its distance measurements is difficult to reduce [2216].

¹Very long baseline interferometric (VLBI) observations of water megamasers which are found in the accretion disks around supermassive black holes (SMBHs) in active galactic nuclei (AGN) have been demonstrated to be powerful one-step geometric probes for measuring extragalactic distances [455, 456].

The empirically-determined period-magnitude relationship of a Cepheid can be expressed as (see e.g. Ref. [292])

$$m_H - R_H E(V - I) = \mu + M_H + b_H[P] + Z_H[M/H] , \quad (10.7)$$

where m_H is the observed apparent magnitude in the near-infrared H (F160W) band which is centered at $\lambda_H \sim 1.63 \mu\text{m}$, V (F555W) and I (F814W) are the optical mean apparent magnitudes which are centered at $\lambda_V \sim 0.555 \mu\text{m}$ and $\lambda_I \sim 0.79 \mu\text{m}$ respectively, in the HST system², $E(V - I)$ is the color excess, R_H is the total to selective extinction parameter at H band³, $\mu \equiv 5 \log_{10} [d_L(z)/\text{Mpc}] + 25$ is the inferred distance modulus to the Cepheid, M_H is the absolute magnitude of a period $P = 10$ d Cepheid (d for days), b_H and Z_H are the slope parameters that represent the dependence of magnitude on both period and metallicity.

The $[M/H]$ is a measure of the metallicity of the Cepheid. The usual bracket shorthand notation for the metallicity $[M/H]$ represents the Cepheid metal abundance compared to that of the Sun

$$[M/H] \equiv \log(M/H) - \log(M/H)_\odot = \Delta \log(M/H) , \quad (10.8)$$

where M and H is the number of metal (any element other than hydrogen or helium) and hydrogen atoms per unit of volume respectively. The unit often used for metallicity is the dex (decimal exponent) defined as $n \text{ dex} = 10^n$.

Also, the bracket shorthand notation for the period $[P]$ is used as (P in units of days)

$$[P] \equiv \log P - 1 . \quad (10.9)$$

The color excess characterizes the amount of reddening associated with interstellar extinction, a combined effect of absorption and scattering of blue more than red light by dust and other matter [2217, 2218]. The color excess depends on the properties of dust and is defined as

$$E(V - I) \equiv A_V - A_I = (V - I) - (V - I)_0 , \quad (10.10)$$

where $V - I$ and $(V - I)_0$ are the observed and the intrinsic (normal) Cepheid color respectively. The latter is the hypothetical true Cepheid color which would be observed if there was no extinction.

Following the same formulation used by the SH0ES team [17, 39] in order to minimize the impact of extinction correction uncertainties for distance measurements and determination of the Hubble constant H_0 , we use the replacement $E(V - I) \rightarrow V - I$ in Eq. (10.7), the Hubble Space Telescope (HST) NIR H-band and the reddening-free "Wesenheit" magnitudes [2219]

$$m_H^W \equiv m_H - R_W(V - I) = \mu + M_H^W + b_W[P] + Z_W[M/H] , \quad (10.11)$$

where the empirical parameter R_W is the reddening-free "Wesenheit" color ratio and is different from R_H which can be derived from a dust law (e.g. the Fitzpatrick law [2220]). The parameter R_W corrects for both dust and intrinsic variations applied to observed blackbody colors $V - I$. Eq. (10.11) can be derived from Eq. (10.7) using Eq. (10.10) with a constant fixed parameter R_W under the important assumption that the intrinsic Cepheid color $(V - I)_0$ can be assumed to have the same distribution for all galaxies. This allows the absorption of the term $R_H(V - I)_0$ by the Cepheid absolute magnitude M_H thus defining the Cepheid Wesenheit H-band absolute magnitude M_H^W in Eq. (10.11). An additional logarithmic dependence of the intrinsic color on the Cepheid period is also allowed and would be absorbed by the parameter b_H leading to the parameter b_W . Thus, if there was a transition in the intrinsic Cepheid color $(V - I)_0$ at a given galactic distance, this transition would manifest itself as a shift of any or all of the parameters M_H^W , b_W and/or R_W at the same distance.

For distances based on NIR ($1 < \lambda < 2.5 \mu\text{m}$) measurements, both the impact of extinction by dust (gauged using the observed color $V - I$) and the impact of metallicity on the luminosities and colors

²HST uses the same three-band photometric system with the Wide Field Camera 3 (WFC3) with two optical filters (F555W and F814W) and one near-infrared filter (F160W).

³The total to selective extinction parameter at H band R_H is defined as $R_H \equiv A_H/(A_V - A_I) = A_H/E(V - I)$ (where A_H is the extinction due to dust along the line of sight).

of Cepheids, are less significant compared to the corresponding optical measurements [2203, 2221–2223] (for the metallicity effects which are still largely debated, see Refs. [2224–2228]). However the NIR measurements of Cepheids still suffer from crowding and blending (photometric contamination) from redder Red Giant Branch (RGB) and Asymptotic Giant Branch (AGB) disk stars, particularly as the distance increases [302, 2229, 2230].

Wesenheit magnitudes have the advantage of smaller dispersion in the PL relation caused by differential extinction and the nonzero temperature width of the Cepheid instability strip⁴ (see e.g. Ref. [2234]).

Following Ref. [17] and breaking the slope of the Leavitt law at a period of 10 days ($P = 10$ d) we include two different slopes b_W^s and b_W^l parameters in Eq. (10.11) for short and long period Cepheids with $P < 10$ d and $P > 10$ d respectively (for a discussion about the presence of a broken PL slope at $P = 10$ d, see Refs. [2235–2240]).

Ref. [17] considers a universal reddening law in all galaxies and thus assume a global fixed value $R_W = 0.386$. This value is derived from the reddening law of Ref. [2220] using a ratio of total to selective extinction at the B and V bands⁵ of the Johnson-Morgan or UBV (Ultraviolet, Blue, Visual) photometric system [2241] $R_V = 3.3$ to parameterize the shape of the extinction curve. In the literature the parameter R_W ranges from 0.3 to 0.5 at H band (e.g. $R_W = 0.41$ in Ref. [37]) and the universal parameter R_V ranges from 1 to 6 (the average value for the MW is $R_V = 3.1$) [2242–2252] depending on the reddening law [2253–2255].

As noted recently by Ref. [56] a global fixed value for parameter R_W could result in a systematic error in distance measurements and the determination of the Hubble constant H_0 . Refs. [56, 943] motivated by the observed variation in dust properties allowing for the parameter R_W to vary between galaxies. However these studies make no attempt to search for possible transitions within the low z galaxy data. In the present analysis we search for transition effects in Cepheid data at $z \lesssim 0.01$ ($\lesssim 40$ Mpc).

10.2.3 Datasets

We use a sample of 1630 Cepheids in the anchor galaxies and in the SnIa host galaxies. For 74 MW Cepheids including GAIA parallax measurements we use the dataset from Table 1 in Ref. [40] and for 70 LMC Cepheids we use the dataset from Table 2 in Ref. [39]. These data are shown in Tables G.1 and G.2 of the Appendix G. Fitting the distance ladder with the system of equations for the 70 LMC Cepheids an intrinsic scatter of 0.08 mag is added to the error estimates given in Table 2 of Ref. [39] (note that Ref. [39] include a intrinsic LMC dispersion of 0.07 mag) which is necessary in order to obtain a reduced chi-square of unity $\chi_{red}^2 = \chi_{min}^2/dof = 1$ [2256].

We obtain data for 1486 Cepheids in the anchor galaxy NGC 4258, in the M31 galaxy and in the 19 SnIa host galaxies from Table 4 in Ref [17] (for details, see Ref. [2257]). This data are shown in Table G.3 of the Appendix G.

We consider the revised distance modulus to NGC 4258 of $\mu_{N4258} = 29.397 \pm 0.032$ mag (7.576 ± 0.112 Mpc) reported by Ref. [227] using water masers data. Also we consider the distance modulus to the LMC of $\mu_{LMC} = 18.477 \pm 0.0263$ mag derived by Ref. [225] with 1% precision based on enhanced samples of late-type DEBs. This distance modulus is increased from that in Ref. [17] by 0.5%.

Finally for SnIa B-band magnitudes we adopt the data from Table 5 in Ref. [17], derived from the version 2.4 of SALT2⁶ modeling of SnIa light curves by Ref. [68]. These data are shown in Table G.4 of the Appendix G.

Following Ref. [39] for all LMC Cepheids we adopt the mean metallicity of -0.33 dex from Ref. [2263] and -0.27 dex from Ref. [2264], $[Fe/H] = -0.30$ dex which is slightly different than the value of

⁴The instability strip refers to a narrow, almost vertical temperature (spectral type) region on the Hertzsprung–Russell (H-R) diagram which contains several types of pulsating variable stars including Cepheid variables (see e.g. Refs. [2231–2233]). The Classical Cepheids (Population I Cepheids) are F6-K2 type supergiants ($\sim 4 - 20 M_\odot$) with a period of 1 to 70 days with an amplitude variation of 0.1 to 2.0 magnitudes.

⁵The total to selective extinction at B and V bands R_V is defined as $R_V \equiv A_V/E(B - V)$

⁶Spectral Adaptive Light Curve Template (SALT) is an empirical spectro-photometric model that is used in SnIa light curve fitting [2258–2260] (for SALT tests with simulations, see [2261]). SALT is publicly available at [2262].

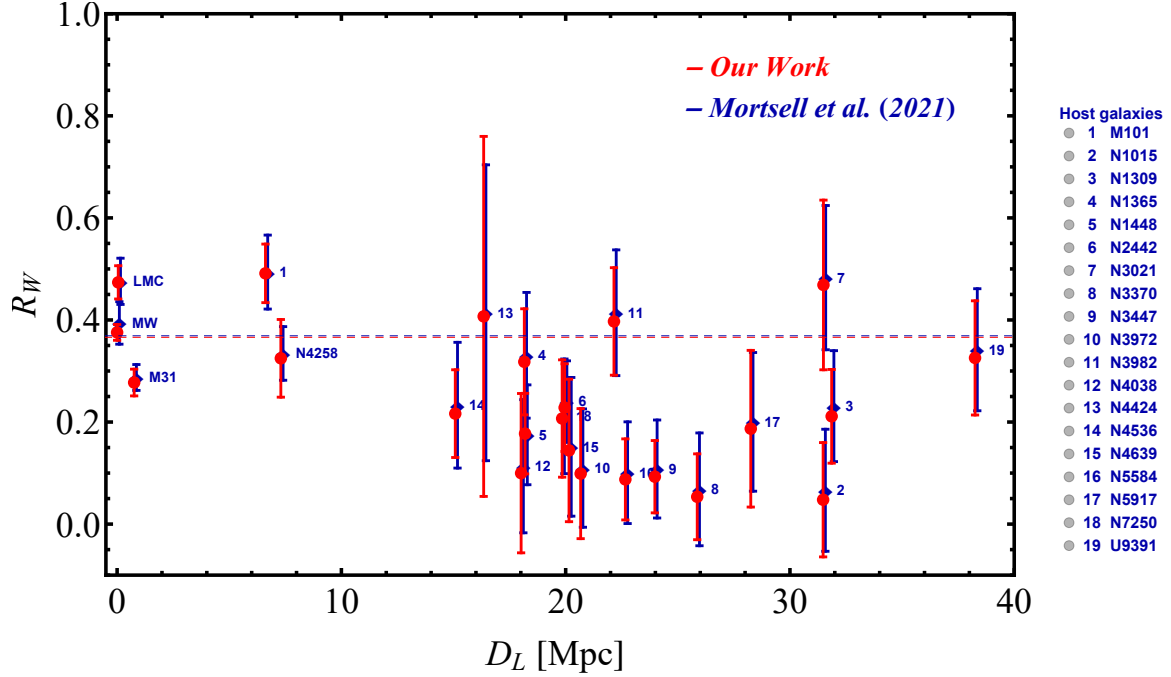


Figure 10.1: Fitting individual R_W to Cepheid data as derived from our work (red points) and from Ref. [56] (blue points). For illustration purposes, the D_L axis has been shifted slightly for our values so that the error bars do not overlap. The red and blue dotted lines correspond to $R_W = 0.366$ and $R_W = 0.369$ respectively. These R_W values are taken using the derived individual parameters of anchor galaxies and M31 (due to its proximity) $R_{W,k}$.

-0.25 dex adopted by Ref. [17]. Also following Ref. [39] we adopt $[O/H] = [Fe/H]$ (where O and Fe is the number of oxygen and iron atoms per unit of volume respectively) and we measure the metallicity in units of $Z = 12 + \log(O/H)$ (with Solar metallicity in these units $Z_\odot = 12 + \log(O/H)_\odot = 8.824$ [943]).

Note that since we use the datasets from Refs. [17, 39, 40] with the same filters we do not need to apply further corrections. The full datasets are available in [70].

10.3 Search for transition

Our analysis is closely related to the results of study by Ref. [56]. Using the same datasets that were used by Ref. [56] we first reproduce their results and then we search for a transition signal of the best fit parameter values R_W and M_H^W between data subsamples at low and high distances.

From Eq. (10.11) using the Wesenheit magnitude of the j th Cepheid in the i th galaxy, including the host and the anchor galaxies, here MW, NGC 4258 and the LMC, separating PL relations for short and long period Cepheids we have

$$m_{H,i,j}^W \equiv m_{H,i,j} - R_{W,i}(V - I)_{i,j} = \mu_i + M_{H,i}^W + b_W^s [P]_{i,j}^s + b_W^l [P]_{i,j}^l + Z_W [M/H]_{i,j}, \quad (10.12)$$

where $[P]_{i,j}^s = 0$ for Cepheids with $P > 10$ d and $[P]_{i,j}^l = 0$ for Cepheids with $P < 10$ d.

In the case where i th galaxy is the MW the distance modulus for the j th Cepheid is estimated using parallaxes in units of mas (mas for milliarcsec)

$$\pi_j + zp = 10^{-0.2(\mu_j - 10)}, \quad (10.13)$$

where zp is a residual parallax calibration offset.

Thus

$$\mu_j = 10 - \frac{5}{\ln 10} \left[\ln \pi_j + \ln \left(1 + \frac{zp}{\pi_j} \right) \right] \simeq 10 - \frac{5}{\ln 10} \left[\ln \pi_j + \frac{zp}{\pi_j} \right], \quad (10.14)$$

where higher order terms $\mathcal{O}(zp/\pi_j)^2$ are negligible. Using Eq. (10.14) into Eq. (10.12) in the case of MW Cepheids we obtain

$$m_{\pi,j}^W = m_{\pi,j} - R_W(V - I)_j = M_H^W + b_W^s [P]_j^s + b_W^l [P]_j^l + Z_W [M/H]_j + \frac{5}{\ln 10} \frac{zp}{\pi_j}, \quad (10.15)$$

where we use

$$m_{\pi,j}^W = m_{H,j}^W - 10 + \frac{5}{\ln 10} \ln \pi_j, \quad (10.16)$$

and

$$m_{\pi,j} = m_{H,j} - 10 + \frac{5}{\ln 10} \ln \pi_j, \quad (10.17)$$

Also in order to combine the measurements of SnIa and Cepheids we use the calibrated SnIa B-band peak magnitude in the *ith* host

$$m_{B,i} = \mu_i + M_B. \quad (10.18)$$

Using the data (see Section 10.2.3) for observed Cepheid magnitudes m_H , colors $V - I$, periods $[P]$, metallicities $[M/H]$, MW Cepheid parallaxes π , anchor distances μ_k together with the SnIa magnitudes m_B , we can fit simultaneously for R_W , b_W^s , b_W^l , Z_W , the host and the anchor galaxy distances μ_i , the parallax offset zp , the Cepheid absolute magnitude M_H^W and the SnIa absolute magnitude M_B .

Combining the equations for apparent magnitudes for Cepheids, Eqs. (10.12), (10.15), and for SnIa, Eq. (10.18), we relate data and parameters through the matrix equation

$$\mathbf{Y} = \mathbf{A}\mathbf{X}, \quad (10.19)$$

with \mathbf{Y} the matrix of measurements, \mathbf{X} the matrix of parameters and \mathbf{A} the equation (or design) matrix. Using these matrices with the measurement error matrix \mathbf{C} we fit the data by minimizing the chi squared χ^2 statistic expressed as

$$\chi^2 = (\mathbf{Y} - \mathbf{A}\mathbf{X})^T \mathbf{C}^{-1} (\mathbf{Y} - \mathbf{A}\mathbf{X}). \quad (10.20)$$

Note that we can solve the following expression for the maximum likelihood parameters \mathbf{X} analytically:

$$\mathbf{X}_{\text{best}} = (\mathbf{A}^T \mathbf{C}^{-1} \mathbf{A})^{-1} \mathbf{A}^T \mathbf{C}^{-1} \mathbf{Y}. \quad (10.21)$$

The standard errors for the parameters in \mathbf{X}_{best} are given by the covariance matrix

$$\mathbf{\Sigma} = (\mathbf{A}^T \mathbf{C}^{-1} \mathbf{A})^{-1}. \quad (10.22)$$

In the Appendix G we present the schematic form of the \mathbf{C} , \mathbf{Y} , \mathbf{X} and \mathbf{A} matrices. We adopt 2D fit including errors in the error matrix \mathbf{C} in both \mathbf{Y} and \mathbf{X} "axes". In particular we do not neglect to include in the error matrix \mathbf{C} the errors in the colors V and I. These errors for MW and LMC Cepheids as provided by the SH0ES team (see in Table 1 of Ref. [40] and in Table 2 of Ref. [39]) are shown in Table G.1 and in Table G.2 of the Appendix G respectively. For Cepheids in galaxies (other than MW and LMC) where the SH0ES team does not provide separate color errors we use total statistical uncertainties where the color errors are included. These total statistical uncertainties derived by the SH0ES team (see in column 8 of the Table 4 of Ref. [17]) are shown in Table G.3 of the Appendix G.

In the following subsections we study three cases where the questions mentioned in Introduction 10.1 will be addressed.

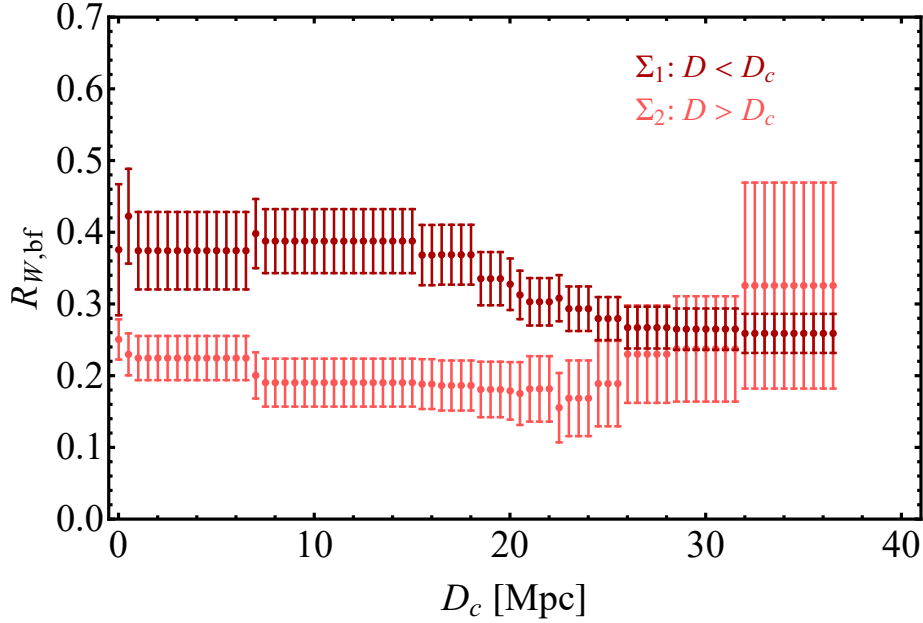


Figure 10.2: The best fit $R_{W,bf}$ for various Σ_1 and Σ_2 datasets as a function of the critical dividing distance $D_c \in [0.01, 37]$ Mpc as derived using the individual R_W (red points in Fig. 10.1). The dark red points correspond to the dataset with galaxies that have distance below D_c , whereas the red points regard galaxies with distances above D_c .

10.3.1 Case I: Fitting individual R_W and global M_H^W

We first allow, as done in Ref. [56], the parameter R_W to vary between galaxies and we consider a global value of the Cepheid absolute magnitude M_H^W . Despite slight differences in the analysis method, the results are in very good agreement with the results in Ref. [56] as illustrated in Fig. 10.1. Fitting individual parameters of galaxies $R_{W,i}$ to Cepheid data as derived from our work and from Ref. [56] correspond to red and blue points respectively. The inferred best fit value of the Cepheid absolute magnitude is $M_H^W = -5.958 \pm 0.028$ mag. The red and blue dotted lines correspond to $R_W = 0.365$ and $R_W = 0.369$. These R_W values are taken using the derived individual parameters of anchor galaxies (here MW, NGC 4258, and LMC) and M31 (due to its proximity) $R_{W,k}$ and minimizing the $\chi^2(R_W)$ with respect to the R_W

$$\chi^2(R_W) = \sum_{k=1}^N \frac{(R_{W,k} - R_W)^2}{\sigma_{R_{W,k}}^2 + \sigma_s^2}, \quad (10.23)$$

where $N = 4$. We fix the scatter to $\sigma_s = 0.08$ obtained by demanding that $\chi_{min}^2/N = 1$ (where χ_{min}^2 is the minimized value of χ^2).

Using the obtained best fit individual values for all galaxies $R_{W,i}$ (see red points in Fig. 10.1) we focus on a particular type of evolution, sharp transition of these best fit values at low and high distances. We thus use the Distance Split Sample (DSS) method which consists of the following steps:

- We consider a critical dividing distance $D_c \in [0.01, 37]$ Mpc and split the sample of galaxies in two subsamples Σ_1 and Σ_2 with distances $D < D_c$ and $D > D_c$ respectively.
- For each subsample we use the maximum likelihood method to find the best fit parameters $R_{W,bf}$ ($R_W^<$ and $R_W^>$) by minimizing $\chi_1^2(R_W^<)$ and $\chi_2^2(R_W^>)$ using a similar equation as Eq. (10.23). The best fit values $R_{W,bf}$ for various Σ_1 and Σ_2 datasets as a function of the critical distances D_c are shown in Fig. 10.2.

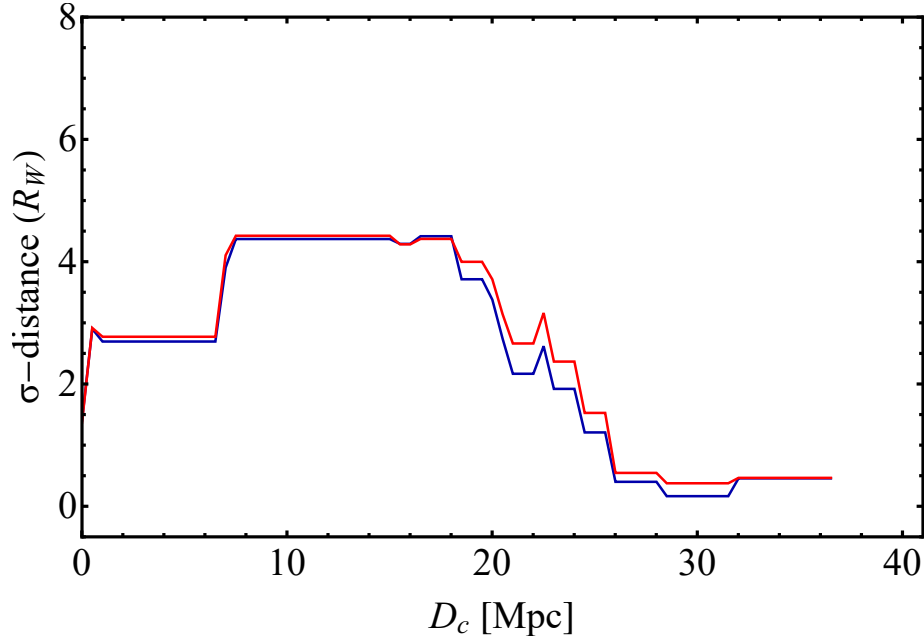


Figure 10.3: The σ -distances between the various Σ_1 and Σ_2 datasets as a function of the critical dividing distance D_c as derived using the individual values of R_W . The red and blue lines correspond to the red (our results) and blue (the results in Ref. [56]) points of Fig. 10.2 respectively. A transition of the σ -distance at $D_c \simeq 22$ Mpc is apparent.

- We evaluate the $\Delta\chi_{12}^2(D_c)$ of the best fit of each subsample Σ_1 with respect to the likelihood of the other subsample Σ_2 and vice versa

$$\Delta\chi_{12}^2(D_c) \equiv \chi_2^2(R_W^<)(D_c) - \chi_{2,min}^2(R_W^>)(D_c) , \quad (10.24)$$

$$\Delta\chi_{21}^2(D_c) \equiv \chi_1^2(R_W^>)(D_c) - \chi_{1,min}^2(R_W^<)(D_c) . \quad (10.25)$$

- Using these values we evaluate the distances $d_{\sigma,12}(D_c)$ and $d_{\sigma,21}(D_c)$ as a solution of the equation

$$\Delta\chi_{ij}^2 = 2Q^{-1} \left[\frac{M}{2}, 1 - \text{Erf} \left(\frac{d_{\sigma,ij}}{\sqrt{2}} \right) \right] , \quad (10.26)$$

where $ij = 12, 21$, M is the number of parameters to fit i.e $M = 1$, Q^{-1} is the inverse regularized incomplete Gamma function and Erf is the error function.

- We then define the σ -distance $d_\sigma(D_c)$ as the minimum of the distances $d_{\sigma,12}(D_c)$ and $d_{\sigma,21}(D_c)$ i.e.

$$d_\sigma(D_c) \equiv \text{Min} [d_{\sigma,12}(D_c), d_{\sigma,21}(D_c)] . \quad (10.27)$$

The anticipated value of d_σ is in the range of 1 – 2 in the context of a homogeneous sample as verified below using Monte Carlo simulations. We thus address the question: *'Does the real Cepheid sample have this property?'*

Fig. 10.3 shows the σ -distance $d_\sigma(D_c)$ between the various Σ_1 and Σ_2 datasets as a function of the critical distances D_c as derived using the individual values of R_W . The red and blue lines correspond to the red (our results) and blue (the results in Ref. [56]) points of Fig. 10.2 respectively.

Clearly, the Cepheid best fit $R_{W,bf}$ parameter indicates the presence of a transition at a critical distance D_c in the range between 8Mpc and 18Mpc or at a time between 25 Myrs and 55 Myrs ago. For this range of D_c the best fit value of $R_W^< = 0.388 \pm 0.042$ differs from the best fit value of $R_W^> = 0.206 \pm 0.033$ at a level more than 4σ with $\Delta R_W \equiv R_W^> - R_W^< = -0.182 \pm 0.056$.

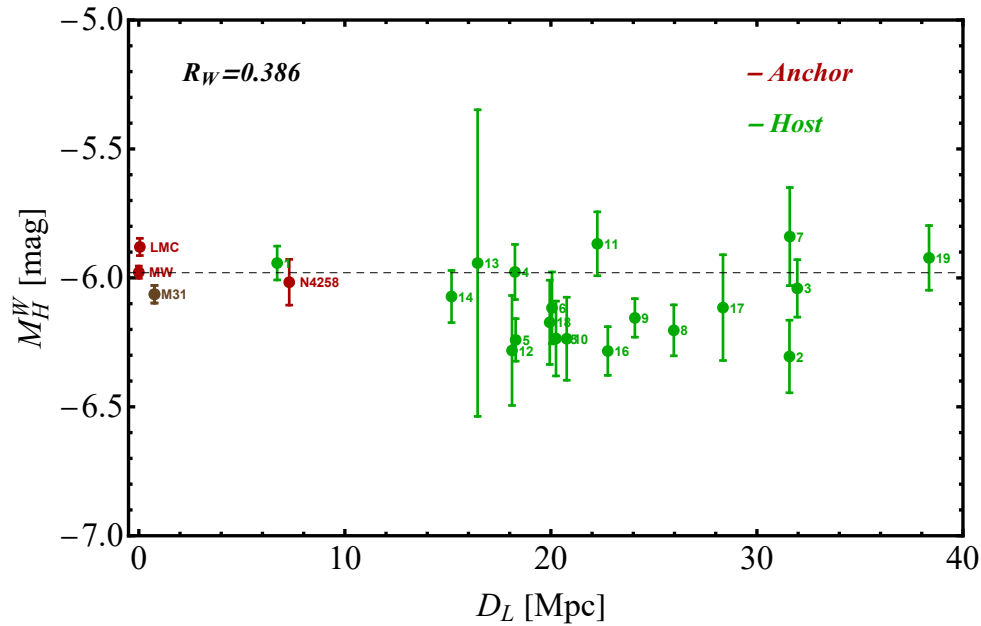


Figure 10.4: Fitting individual M_H^W to Cepheid data for global R_W with a fixed value 0.386. Anchor galaxies are denoted with dark red points and SnIa host galaxies with green points. The dotted line corresponds to $M_H^W = -5.98$ mag as derived using the individual values of anchor galaxies and M31 (due to its proximity) $M_{H,k}^W$.

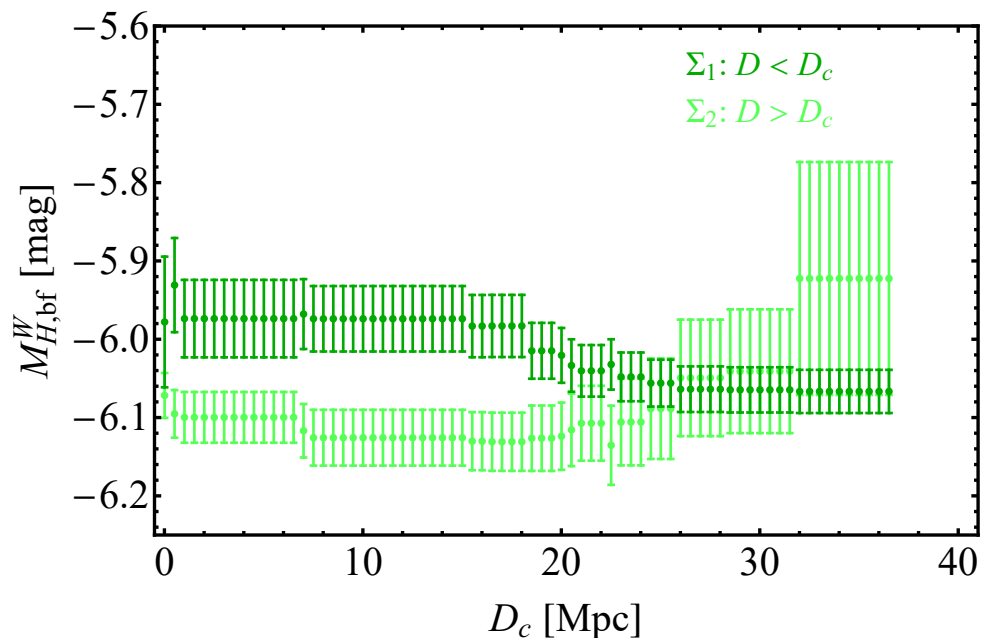


Figure 10.5: The best fit $M_{H,bf}^W$ for various Σ_1 and Σ_2 datasets as a function of the critical distances D_c as derived using the individual values of M_H^W (points in Fig. 10.4). The dark green points correspond to the dataset with galaxies that have distance below D_c , whereas the green points regard galaxies with distances above D_c .

10.3.2 Case II: Fitting individual M_H^W with fixed global R_W

In this case we allow the value of the Cepheid absolute magnitude M_H^W to vary between galaxies and we consider a global fixed parameter $R_W = 0.386$ in agreement with Refs. [17, 39, 40].

The results of fitting individual M_H^W to Cepheid data are illustrated in Fig. 10.4. Anchor galaxies are denoted with dark red points and SnIa host galaxies with green points. We see that Cepheids in nearby galaxies are fainter. The dotted line corresponds to $M_H^W = -5.98$ mag as derived using the individual parameters of anchor galaxies (here MW, NGC 4258, and LMC) and M31 (due to its proximity) $M_{H,k}^W$ and minimizing $\chi^2(M_H^W)$ with respect to the M_H^W

$$\chi^2(M_H^W) = \sum_{k=1}^N \frac{(M_{H,k}^W - M_H^W)^2}{\sigma_{M_{H,k}^W}^2 + \sigma_s^2}, \quad (10.28)$$

where $N = 4$. We fix the scatter to $\sigma_s = 0.08$ obtained by demanding that $\chi_{min}^2/N = 1$.

Using the obtained best fit individual values for all galaxies $M_{H,i}^W$ (see Fig. 10.4) we focus on a particular type of evolution, sharp transition of these best fit values at low and high distances. We follow the same DSS method as in the previous subsection. Thus

- First we consider a critical dividing distance $D_c \in [0.01, 37]$ Mpc and split the sample of galaxies in two subsamples Σ_1 and Σ_2 with distances $D < D_c$ and $D > D_c$ respectively.
- For each subsample we use the maximum likelihood method to find the best fit parameters $M_{H,bf}^W$ ($M_H^{W,<}$ and $M_H^{W,>}$) by minimizing $\chi_1^2(M_H^{W,<})$ and $\chi_2^2(M_H^{W,>})$. The best fit values of the $M_{H,bf}^W$ for various Σ_1 and Σ_2 datasets as a function of the critical distances D_c are shown in Fig. 10.5.
- We consider the $\Delta\chi_{12}^2(D_c)$ of the best fit of each subsample Σ_1 with respect to the likelihood of the other subsample Σ_2 and vice versa

$$\Delta\chi_{12}^2(D_c) \equiv \chi_2^2(M_H^{W,<})(D_c) - \chi_{2,min}^2(M_H^{W,>})(D_c), \quad (10.29)$$

$$\Delta\chi_{21}^2(D_c) \equiv \chi_1^2(M_H^{W,>})(D_c) - \chi_{1,min}^2(M_H^{W,<})(D_c). \quad (10.30)$$

- We evaluate the distances $d_{\sigma,12}(D_c)$ and $d_{\sigma,21}(D_c)$ as a solution of the corresponding Eq. (10.26).
- We then find the σ -distances $d_\sigma(D_c)$ as the minimum of the distances $d_{\sigma,12}(D_c)$ and $d_{\sigma,21}(D_c)$.

In Fig. 10.6 with the green line we show the σ -distances $d_\sigma(D_c)$ between the various Σ_1 and Σ_2 datasets as a function of the critical distances D_c as derived using the individual values of M_H^W . As in the previous case we see that the Cepheid best fit $M_{H,bf}^W$ parameter indicates the presence of a transition at a critical distance D_c in the range between 8 Mpc and 18 Mpc. For this range of D_c the best fit value of $M_H^{W,<} = -5.974 \pm 0.042$ mag differs from the best fit value of $M_H^{W,>} = -6.126 \pm 0.036$ mag at a level more than 3σ with $\Delta M_H^W \equiv M_H^{W,>} - M_H^{W,<} = -0.152 \pm 0.055$ mag.

In order to secure the robustness of our approach we use a Monte Carlo simulation allowing the galactic distances to vary randomly using their error bars. In particular, the simulations have been performed for randomly varying galaxy distance values with a Gaussian probability distribution (normal distribution) with mean equal to the measured distance and standard deviation equal to the corresponding 1σ error. In Fig. 10.7 we show the σ -distances as a function of the critical distances D_c for 100 sample datasets with random distance values, normally distributed inside their individual 1σ range as derived using the individual values of M_H^W . Clearly, the random variation of the galactic distances does not change the transition effect. The 68% (one standard deviation) range of the σ -distances as a function of the critical distances D_c produced by the Monte Carlo simulation of 100 sample datasets is shown in Fig. 10.8 with the green lines. Evidently, the Monte Carlo simulation demonstrates the robustness of the identified transition with respect to variation of galactic distances.

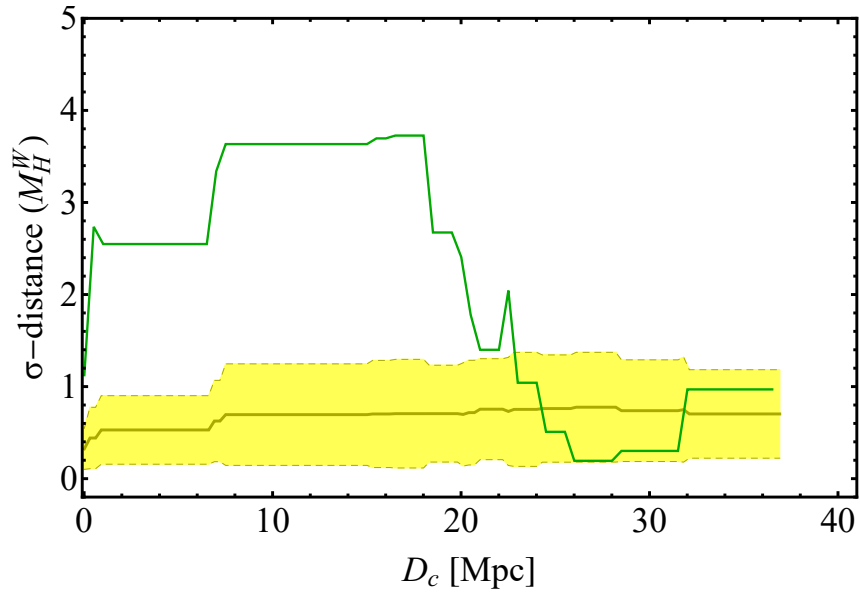


Figure 10.6: The green line represents the σ -distances between the various Σ_1 and Σ_2 datasets as a function of the critical distances D_c as derived using the individual values of M_H^W . In contrast the yellow lines correspond to 68% (one standard deviation) range of the σ -distances as a function of the critical distances D_c produced by a Monte Carlo simulation of 100 sample datasets assuming artificial homogeneity of the M_H^W data. The simulations have been performed for randomly varying M_H^W values with a Gaussian probability distribution with mean $M_H^W = -6$ mag provided by the full M_H^W datapoints and standard deviation equal to the corresponding 1σ error.

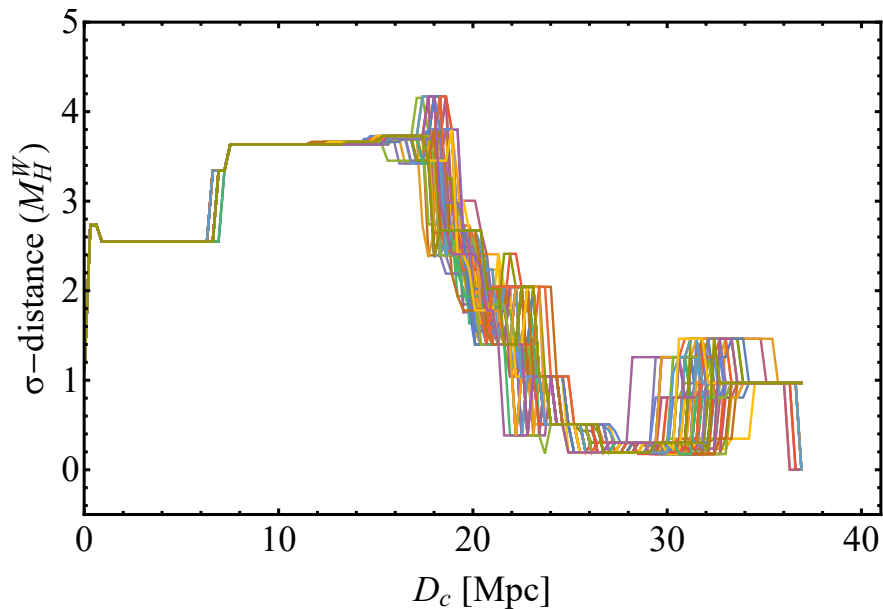


Figure 10.7: The σ -distances as a function of the critical distances D_c for 100 sample datasets with random distance values, normally distributed inside their individual $1\text{-}\sigma$ range as derived using the individual values of M_H^W . A transition of the σ -distance at $D_c \simeq 22$ Mpc remains present for practically all of the Monte Carlo samples.

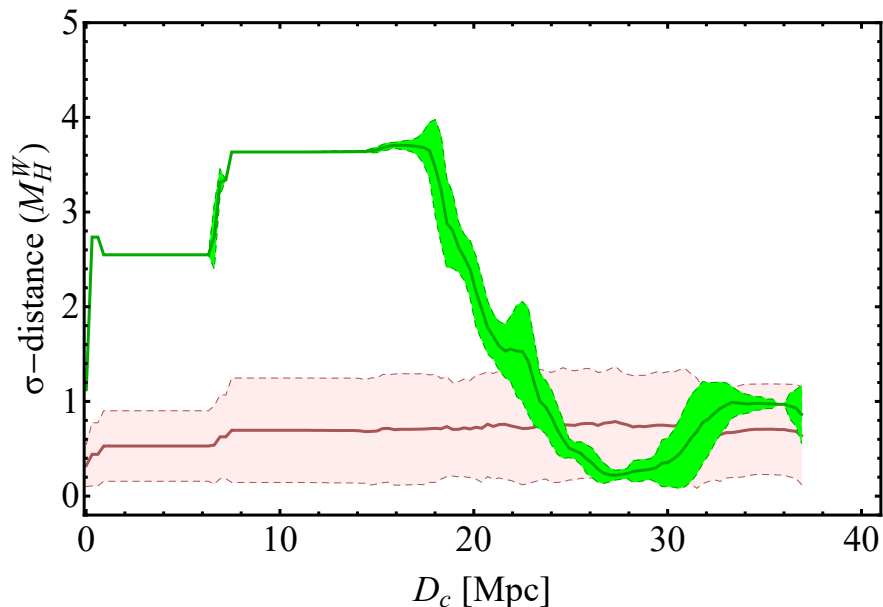


Figure 10.8: The green lines represent the 68% range of the σ -distances as a function of the critical distances D_c produced by a Monte Carlo simulation of 100 sample datasets. The simulations have been performed for randomly varying galaxy distance values with a Gaussian probability distribution with mean equal to the measured distance and standard deviation equal to the corresponding 1σ error. In contrast the pink region correspond to a Monte Carlo simulation of 100 sample datasets assuming artificial homogeneity of the M_H^W data. In addition to this homogeneity the simulations have been performed for randomly varying galaxy distance values with a Gaussian probability distribution.

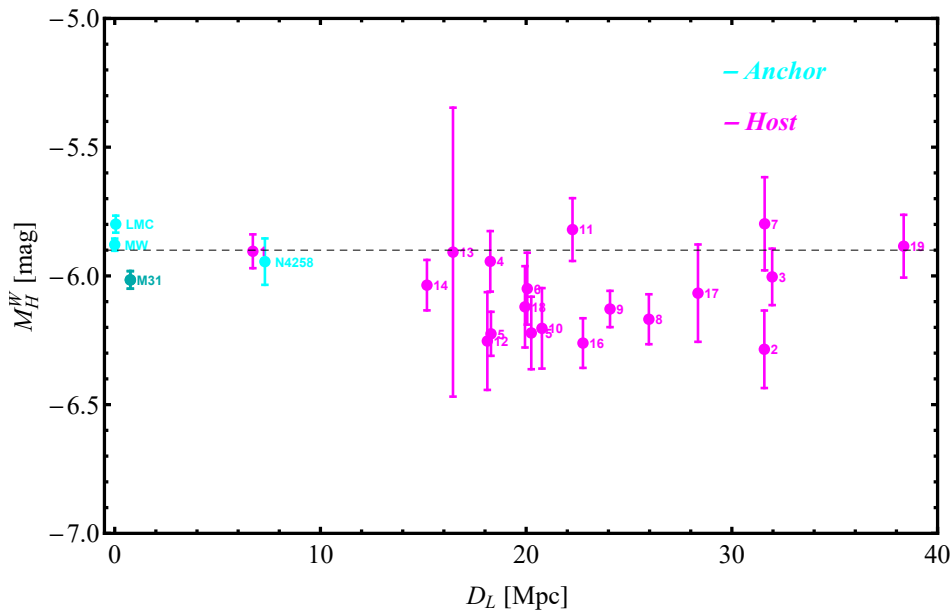


Figure 10.9: Fitting individual M_H^W to Cepheid data with a free global R_W . Anchor galaxies are denoted with cyan points and SnIa host galaxies with magenta points. The dotted line corresponds to $M_H^W = -5.90$ mag as derived using the individual values of anchor galaxies and M31 (due to its proximity) $M_{H,k}^W$.

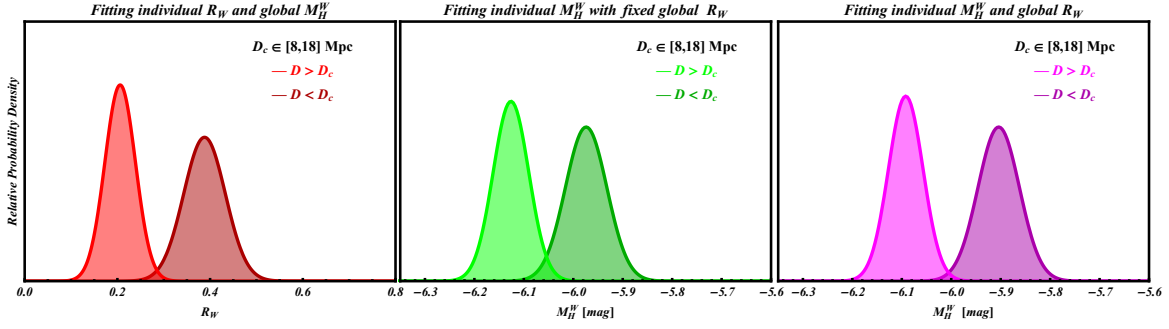


Figure 10.10: The one dimensional relative probability density values of the color luminosity parameter and the Cepheid absolute magnitude as derived using the DSS method for the cases I, II, and III. All measurements are shown as normalized Gaussian distributions. Notice that the best fit values one for galaxies at distances $D < D_c$ and one for galaxies at $D > D_c$ are inconsistent with each other at a level larger than 3σ .

We now test if the effect would disappear in the context of homogenized Monte-Carlo Cepheid datasets. In Fig. 10.6, we examine if this obvious transition of this case could be due to a systematic uncertainty of the Cepheid absolute magnitude value. Thus, the yellow region corresponds to the 68% range of the σ -distances as a function of the critical distances D_c produced by a Monte Carlo simulation of 100 sample datasets assuming artificial homogeneity of the M_H^W data. The simulations have been performed by randomly varying the M_H^W values with a Gaussian probability distribution with mean $M_H^W = -6$ mag as obtained by the full dataset with a universal M_H^W and standard deviation of each global universal fit which is equal to the corresponding 1σ error. For this Monte Carlo uniformized data there is no transition. This demonstrates that the observed transition is due to the actual Cepheid data and not to the method we used. As expected the same result persists if in addition to homogenizing the sample with respect to M_H^W we also randomly vary the galactic distances as described above assuming a Gaussian distribution (pink region in Fig. 10.8). Thus the observed transition effect as illustrated in Figs. 10.6 and 10.8 is robust with respect to random variation of the galactic distances and disappears only if we artificially homogenize the data in the context of Monte Carlo simulations.

10.3.3 Case III: Fitted individual M_H^W and a global R_W

In this case we assume a free to fit global parameter R_W and allow the value of the Cepheid absolute magnitude M_H^W to vary between galaxies. The results of fitting individual M_H^W to Cepheid data are illustrated in Fig. 10.9. The dotted line corresponds to $M_H^W = -5.90$ mag as derived using the individual parameters of anchor galaxies and M31 (due to its proximity) $M_{H,k}^W$ and minimizing $\chi^2(M_H^W)$ in Eq. (10.28) with respect to the M_H^W .

In this case we obtain the best fit value of the parameter $R_W = 0.310 \pm 0.021$ which is smaller than the global fixed value $R_W = 0.386$ used by Refs. [17, 39, 40]. We attribute this difference to the fact that we have used the full Cepheid sample for its determination and not just the anchor galaxies and we have not used a global value of the absolute magnitude M_H^W common for all Cepheids.

Using the same DSS method as in the two previous cases we find the best fit values of the $M_{H,bf}^W$ ($M_H^{W,<}$ and $M_H^{W,>}$) for various Σ_1 and Σ_2 datasets as a function of the critical distances D_c . As the previous cases the presence of a transition at a critical distance D_c in the range between 8 Mpc and 18 Mpc is obvious. For this range of D_c the best fit value of $M_H^{W,<} = -5.904 \pm 0.042$ mag differs from the best fit value of $M_H^{W,>} = -6.092 \pm 0.035$ mag at a level more than 4σ with $\Delta M_H^W \equiv M_H^{W,>} - M_H^{W,<} = -0.188 \pm 0.055$ mag.

In this case, we do not plot here the result since it is very similar to that plotted in the figures of previous cases but are available in our publicly available numerical analysis files [70].

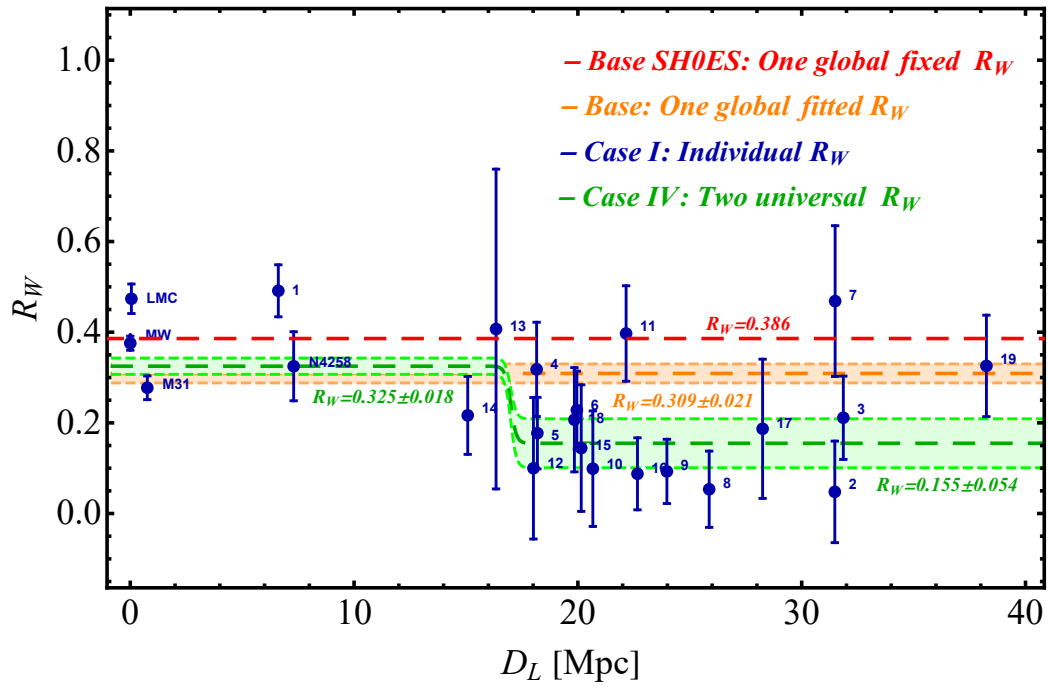


Figure 10.11: The best fit values of the parameter R_W for base/base-SH0ES, I and IV models as derived using Cepheid data. Note that in terms of the AIC and BIC, fitting for two universal values of R_W with global M_H^W is the preferred model (case IV, green region).

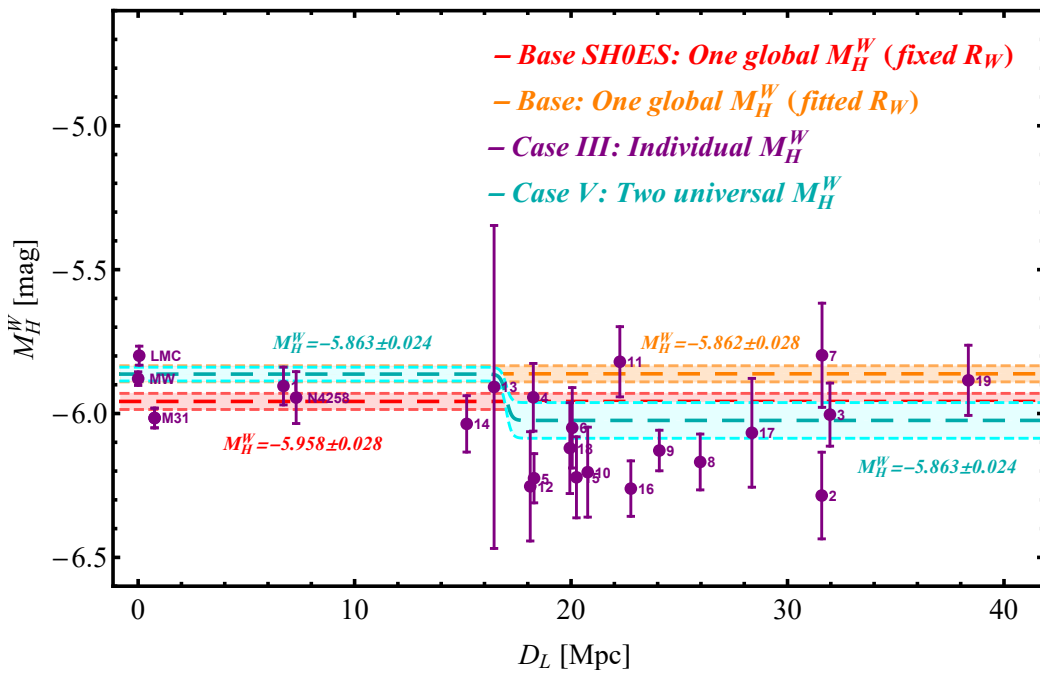


Figure 10.12: The best fit values of the parameter M_H^W for base/base-SH0ES, III and V models as derived using the Cepheid data. Note that in terms of the AIC and BIC, fitting for two universal values of M_H^W with global R_W is the preferred model among the models shown (case V, cyan region).

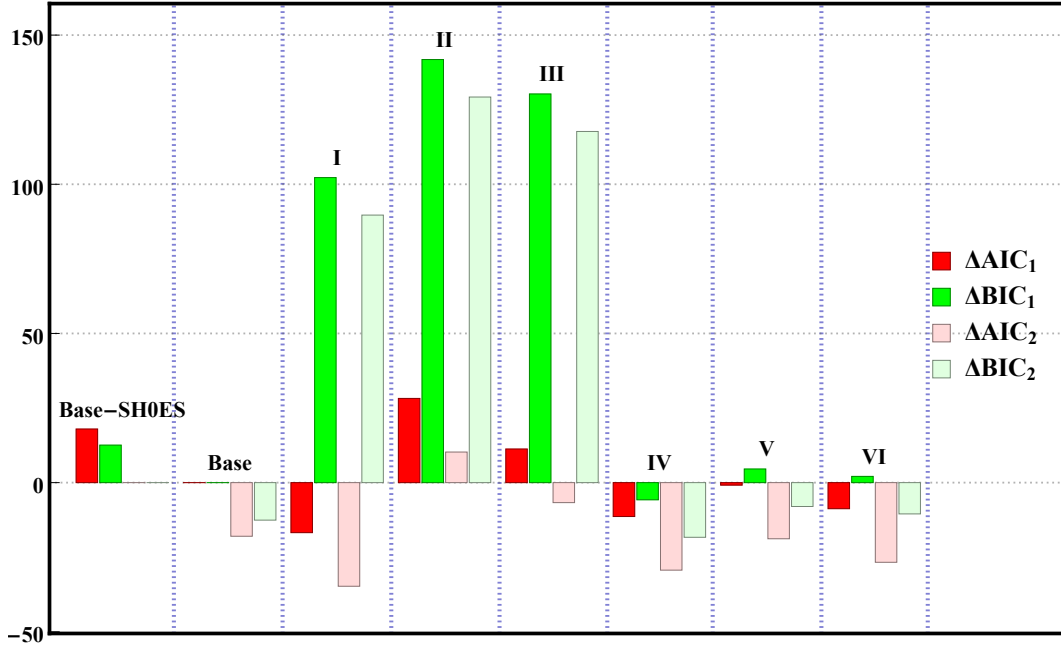


Figure 10.13: The ΔAIC and ΔBIC of models with different free parameter set compared to base (subindex 1) and base-SHOES (subindex 2) models. Clearly, the case IV (two universal R_W and a global M_H^W) is the best model and on the other hand, the case II (a global R_W and individual M_H^W) is the worst one.

Table 10.1: Fitting results and model comparison tests for different models. For the ΔAIC and ΔBIC the comparisons are made respect to base (base-SHOES) models. The value of H_0 derived using the Eq. (10.37) (black font) and the Eq. (10.39) (green font). The best fit parameters of SnIa absolute magnitude M_B and the value of H_0 in the parentheses correspond to intrinsic scatter of LMC Cepheids $\sigma_{LMC} = 0$.

Model	Best Fit Parameters (with 1σ ranges) $\sigma_{LMC} = 0.08$ ($\sigma_{LMC} = 0$)	Model Selection Criteria	Intrinsic scatter of LMC Cepheids	
			$\sigma_{LMC} = 0$	$\sigma_{LMC} = 0.08$
Base-SHOES	$R_W = 0.386$ (fixed) $M_H^W = -5.958 \pm 0.028$ $M_B = -19.251 \pm 0.057$ ($M_B = -19.261 \pm 0.057$) $H_0 = 72.86 \pm 1.95$, $H_0 = 73.50 \pm 1.96$ ($H_0 = 72.53 \pm 1.93$, $H_0 = 73.17 \pm 1.94$)	χ_{min}^2 χ_{red}^2 AIC ΔAIC BIC ΔBIC	1767.48 1.089 1823.48 7.65 (0) 1974.92 2.25 (0)	1644.79 1.014 1700.79 17.97 (0) 1852.23 12.57 (0)
Base	$R_W = 0.309 \pm 0.021$ $M_H^W = -5.862 \pm 0.028$ $M_B = -19.225 \pm 0.057$ ($M_B = -19.246 \pm 0.054$) $H_0 = 73.73 \pm 1.96$, $H_0 = 74.38 \pm 1.97$ ($H_0 = 73.03 \pm 1.86$, $H_0 = 73.67 \pm 1.86$)	χ_{min}^2 χ_{red}^2 AIC ΔAIC BIC ΔBIC	1759.47 1.084 1815.83 0 (-7.65) 1972.67 0 (-2.25)	1624.82 1.002 1682.82 0 (-17.97) 1839.66 0 (-12.57)
I Individual R_W Global M_H^W	$R_{W,i}$ red points in Fig. 10.1 $R_W^< = 0.388 \pm 0.045$ (using DSS) $R_W^> = 0.206 \pm 0.033$ (using DSS) $M_H^W = -5.958 \pm 0.028$	χ_{min}^2 χ_{red}^2 AIC	1676.76 1.049 1778.76	1564.06 0.978 1666.06

$N = 1650$ $M = 51$ $dof = 1599$	$\mathbf{M}_B = -19.43 \pm 0.056$ ($M_B = -19.491 \pm 0.056$) $\mathbf{H}_0 = 67.11 \pm 1.76, \mathbf{H}_0 = 67.69 \pm 1.77$ ($H_0 = 65.24 \pm 1.71, H_0 = 65.81 \pm 1.72$)	ΔAIC BIC ΔBIC	-37.07 (-44.72) 2054.59 81.92 (79.67)	-16.76 (-34.73) 1941.9 102.24 (89.74)
II Global R_W Individual M_H^W $N = 1650$ $M = 50$ $dof = 1600$	$R_W = 0.386$ (fixed) $M_{H,i}^W$ points in Fig. 10.4 $M_{H,<}^{W,<} = -5.974 \pm 0.042$ (using DSS) $M_{H,>}^{W,>} = -6.126 \pm 0.036$ (using DSS) $\mathbf{M}_B = -19.394 \pm 0.057$ ($M_B = -19.404 \pm 0.055$) $\mathbf{H}_0 = 68.22 \pm 1.82, \mathbf{H}_0 = 68.82 \pm 1.83$ ($H_0 = 67.90 \pm 1.75, H_0 = 68.50 \pm 1.76$)	χ_{min}^2 χ_{red}^2 AIC ΔAIC BIC ΔBIC	1732.05 1.083 1832.05 16.22 (8.57) 2102.48 129.81 (127.56)	1611.04 1.007 1711.04 28.22 (10.25) 1981.47 141.81 (129.24)
III Global R_W Individual M_H^W $N = 1650$ $M = 51$ $dof = 1599$	$R_W = 0.310 \pm 0.021$ $M_{H,i}^W$ points in Fig. 10.9 $M_{H,<}^{W,<} = -5.904 \pm 0.042$ (using DSS) $M_{H,<}^{W,<} = -6.092 \pm 0.035$ (using DSS) $\mathbf{M}_B = -19.428 \pm 0.057$ ($M_B = -19.424 \pm 0.056$) $\mathbf{H}_0 = 67.17 \pm 1.79, \mathbf{H}_0 = 67.76 \pm 1.80$ ($H_0 = 67.28 \pm 1.75, H_0 = 67.87 \pm 1.76$)	χ_{min}^2 χ_{red}^2 AIC ΔAIC BIC ΔBIC	1726.7 1.079 1828.7 12.87 (5.22) 2104.53 131.86 (129.61)	1592.09 0.996 1694.09 11.27 (-6.7) 1969.93 130.27 (117.7)
IV Two universal R_W Global M_H^W $N = 1650$ $M = 30$ $dof = 1620$	$R_W^{<} = 0.325 \pm 0.018$ $R_W^{>} = 0.155 \pm 0.054$ $M_H^W = -5.885 \pm 0.028$ $\mathbf{M}_B = -19.399 \pm 0.057$ ($M_B = -19.447 \pm 0.054$) $\mathbf{H}_0 = 68.06 \pm 1.80, \mathbf{H}_0 = 68.66 \pm 1.81$ ($H_0 = 66.59 \pm 1.66, H_0 = 67.17 \pm 1.67$)	χ_{min}^2 χ_{red}^2 AIC ΔAIC BIC ΔBIC	1744.19 1.077 1804.19 -13.34 (-18.99) 1966.44 -6.23 (-8.48)	1611.65 0.995 1671.46 -11.36 (-29.33) 1833.91 -5.75 (-18.32)
V Global R_W Two universal M_H^W $N = 1650$ $M = 30$ $dof = 1620$	$R_W = 0.308 \pm 0.021$ $M_{H,<}^{W,<} = -5.863 \pm 0.024$ $M_{H,<}^{W,<} = -6.024 \pm 0.062$ $\mathbf{M}_B = -19.361 \pm 0.057$ ($M_B = -19.399 \pm 0.057$) $\mathbf{H}_0 = 69.27 \pm 1.82, \mathbf{H}_0 = 69.88 \pm 1.83$ ($H_0 = 68.06 \pm 1.81, H_0 = 68.65 \pm 1.82$)	χ_{min}^2 χ_{red}^2 AIC ΔAIC BIC ΔBIC	1757.15 1.085 1817.15 1.32 (-6.33) 1979.41 6.74 (4.49)	1621.98 1.001 1681.98 -0.84 (-18.81) 1844.23 4.57 (-8.0)
VI Two universal R_W Two universal M_H^W $N = 1650$ $M = 31$ $dof = 1619$	$R_W^{<} = 0.329 \pm 0.018$ $R_W^{>} = 0.151 \pm 0.053$ $M_{H,<}^{W,<} = -5.891 \pm 0.024$ $M_{H,>}^{W,>} = -5.900 \pm 0.063$ $\mathbf{M}_B = -19.413 \pm 0.052$ ($M_B = -19.379 \pm 0.056$) $\mathbf{H}_0 = 67.62 \pm 1.64, \mathbf{H}_0 = 68.22 \pm 1.65$ ($H_0 = 68.70 \pm 1.81, H_0 = 69.30 \pm 1.81$)	χ_{min}^2 χ_{red}^2 AIC ΔAIC BIC ΔBIC	1743.26 1.077 1805.26 -10.57 (-18.22) 1972.93 0.26 (-1.99)	1612.09 0.996 1674.09 -8.73 (-26.7) 1841.75 2.09 (-10.48)

10.4 Model Selection

As pointed out in the previous subsections where we study three cases (I, II, and III) both the Cepheid best fit absolute magnitude and color luminosity parameters indicate the presence of a transition effect

Table 10.2: The interpretation of differences ΔAIC and ΔBIC according to the calibrated Jeffreys' scale [61] (see also Refs. [62–66]). However, it should be noted that the Jeffreys' scale has to be interpreted with care [63] because has been shown to lead to different qualitative conclusions.

ΔAIC			ΔBIC			
Level of empirical support for the model with the smaller AIC			Evidence against the model with the larger BIC			
0-2 Substantial	4-7 Strong	> 10 Very strong	0-2 Weak	2-6 Positive	6-10 Strong	> 10 Very strong

 Table 10.3: Ranking of models according to AIC and BIC criteria. We see that in terms of the AIC and BIC fitting for two universal values of R_W with global M_H^W is the preferred model (case IV).

Ranking	AIC		BIC	
	$\sigma_{LMC} = 0$	$\sigma_{LMC} = 0.08$	$\sigma_{LMC} = 0$	$\sigma_{LMC} = 0.08$
1	I	I	IV	IV
2	IV	IV	Base	Base
3	VI	VI	VI	VI
4	Base	V	Base-SH0ES	V
5	V	Base	V	Base-SH0ES
6	Base-SH0ES	III	I	I
7	III	Base-SH0ES	II	III
8	II	II	III	II

at a critical distance D_c in the range between 8 Mpc and 18 Mpc (see Fig. 10.10). This transition however becomes apparent when additional parameters are introduced (the individual R_W or M_H^W for each galaxy). Thus the questions we address in this section is the following:

- Is the introduction of additional parameters favored by model selection criteria like the Akaike Information Criterion (AIC) [2265] and the Bayesian Information Criterion (BIC) [595]?
- Could the introduction of a smaller number of parameters lead to more favored phenomenological models?

In order to address these questions we use model selection tests for eight cases with different number of free parameters. The additional five considered cases are the following⁷:

- **Base-SH0ES:** Like previous studies of SH0ES team we consider universality on the color-luminosity relation with a global fixed parameter $R_W = 0.386$ [17, 39, 40] and universality on the absolute magnitude of Cepheids SnIa calibrators with a global M_H^W to be fit by the Cepheid data. Thus in this case we use the base, commonly used parameter set in the field.

⁷Note that for all cases we fit other 27 additional parameters (see the schematic form of the matrix of parameters \mathbf{X} in Appendix G)

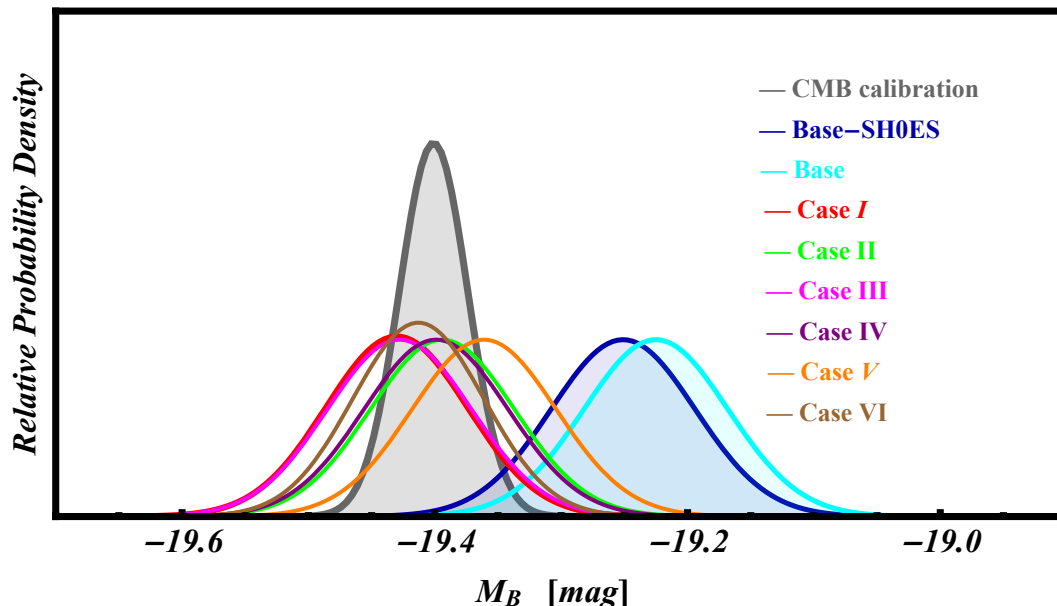


Figure 10.14: The one dimensional relative probability density value of SnIa absolute magnitude M_B for all cases studied in this analysis compared to that obtained using CMB calibration. All measurements are shown as normalized Gaussian distributions. Clearly, for all cases where we do not consider the universality of parameters R_W and M_H^W (i.e. I, II, III, IV, V, VI) the M_B is consistent with the CMB determination value.

- **Base:** We consider universality on the color-luminosity relation with a global parameter R_W to be fit by data and universality on the absolute magnitude of Cepheids SnIa calibrators with global M_H^W .
- **IV:** We consider a global M_H^W and two universal R_W ($R_W^<$ for galaxies at distances $D < 16$ Mpc and $R_W^>$ for galaxies at distances $D > 16$ Mpc).
- **V:** We consider a global R_W and two universal M_H^W ($M_H^{W,<}$ for galaxies at distances $D < 16$ Mpc and $M_H^{W,>}$ for galaxies at distances $D > 16$ Mpc).
- **VI:** We consider two universal R_W ($R_W^<$ for galaxies at distances $D < 16$ Mpc and $R_W^>$ for galaxies at distances $D > 16$ Mpc) and two universal M_H^W ($M_H^{W,<}$ for galaxies at distances $D < 16$ Mpc and $M_H^{W,>}$ for galaxies at distances $D > 16$ Mpc).

In order to compare the models we construct Table 10.1 with the fitting parameters for all cases. The best fit values of the parameter R_W for base/base-SHOES, I and IV models are shown in Fig. 10.11 and the best fit values of the parameter M_H^W for base/base-SHOES, III and V models are shown in Fig. 10.12. Various methods for model selection have been developed and model comparison techniques used [62, 601–603]. In table 10.1 we show the value of the minimum χ^2 (χ_{min}^2) for all cases and the reduced chi-squared which is a very popular method for model comparison. This is defined by

$$\chi_{red}^2 = \frac{\chi_{min}^2}{dof}, \quad (10.31)$$

where $dof = N - M$ is typically the number of degrees of freedom (with N is the number of datapoints used in the fit and M is the number of free parameters) for each model.

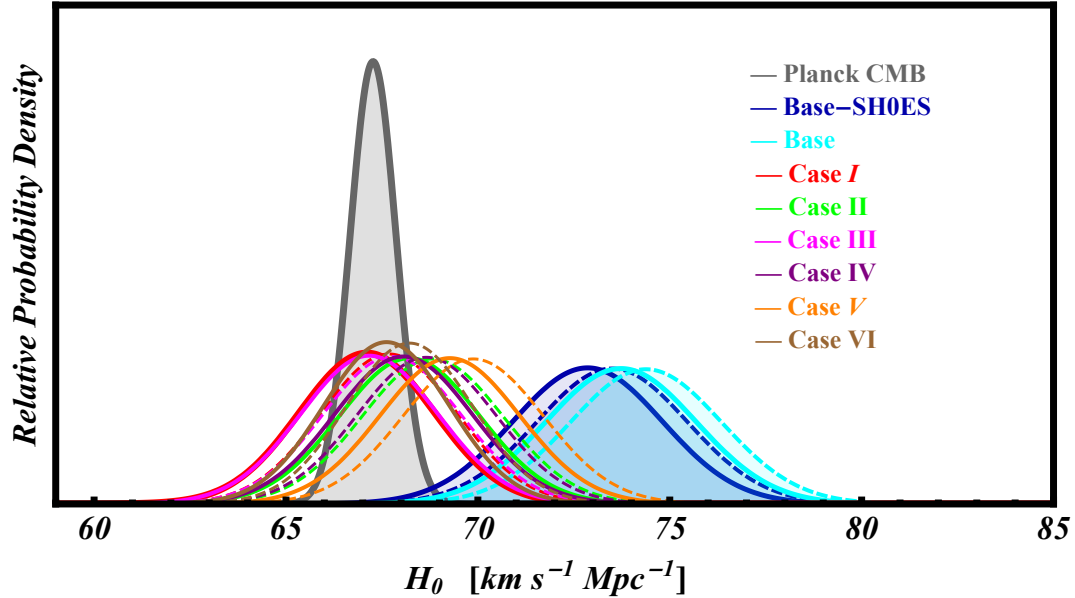


Figure 10.15: The one dimensional relative probability density value of H_0 as derived using the Eq. (10.37) (solid lines) and the Eq. (10.39) (dashed lines) for all cases studied in this analysis compared to that from the Planck CMB measurement (grey line). All measurements are shown as normalized Gaussian distributions. It is evident that for all cases where we break the assumption of universality of the parameters R_W and M_H^W (i.e. I, II, III, IV, V, VI) the derived values of H_0 are consistent with the corresponding predicted Planck CMB best fit value.

We also use the model selection methods like Akaike Information Criterion (AIC) [2265] and the Bayesian Information Criterion (BIC) [595] that penalize models with additional parameters. For a model with M parameters and a dataset with N total observations these are defined through the relations [62, 601, 602]

$$AIC = -2\ln\mathcal{L}_{max} + 2M = \chi_{min}^2 + 2M, \quad (10.32)$$

$$BIC = -2\ln\mathcal{L}_{max} + M\ln N = \chi_{min}^2 + M\ln N, \quad (10.33)$$

where $\mathcal{L}_{max} \equiv e^{-\chi_{min}^2/2}$ (e.g. [63, 2266]) is the maximum likelihood of the model under consideration. Note that a version of the AIC corrected for small sample sizes is important [2267, 2268]. This version is given by [2269] (see also Refs. [601, 1817])

$$AIC_{cor} = AIC + \frac{2M(M+1)}{N-M-1}. \quad (10.34)$$

For large samples as in our case ($N \gg M$) the correction term disappears but for small samples gives a more accurate answer.

The results for each candidate model are shown in Table 10.1 and the "preferred model" is the one which minimizes AIC and BIC. The absolute values of the AIC and BIC are not informative. Only the relative values between different competing models are relevant. Hence when comparing one model versus the base/base-SHOES we can use the model differences ΔAIC and ΔBIC .

The differences ΔAIC and ΔBIC with respect to the base/base-SHOES model defined as

$$\Delta AIC = AIC_i - AIC_s = \Delta\chi_{min}^2 + 2\Delta M, \quad (10.35)$$

$$\Delta BIC = BIC_i - BIC_s = \Delta\chi_{min}^2 + \Delta M(\ln N), \quad (10.36)$$

where the subindex i refers to value of AIC (BIC) for the model i and AIC_s (BIC_s) is the value of AIC (BIC) for the base/base-SHOES model. The resulting ΔAIC and ΔBIC are shown in Table 10.1 and in Fig. 10.13. Note that a positive value of ΔAIC or ΔBIC means a preference for base/base-SHOES model.

According to the calibrated Jeffreys' scales [61] showed in the Table 10.2 (see also Refs. [62–66]) a range $0 < |\Delta AIC| < 2$ means that the two comparable models have about the same support from the data, a range $4 < |\Delta AIC| < 7$ means this support is considerably less for the model with the larger AIC while for $|\Delta AIC| > 10$ the model with the larger AIC have no support i.e. the model is practically irrelevant. Similarly, for two competing models a range $0 < |\Delta BIC| < 2$ is regarded as weak evidence, a range $2 < |\Delta BIC| < 6$ is regarded as positive evidence, while for $|\Delta BIC| > 6$ the evidence is strong against the model with the larger value.

Ranking of the models considered according to AIC and BIC criteria are presented in Table 10.3. Clearly, in terms of the AIC and BIC, fitting for two universal values of R_W with global M_H^W is the preferred model (case IV). Base/base-SHOES model is considerable less supported by data with respect to the IV model (ΔAIC) and there is a positive/very strong evidence against it (ΔBIC). We attribute the difference between ΔAIC and ΔBIC for the models considered to the fact that the BIC penalizes additional parameters more strongly than the AIC as inferred by the Eqs. (10.32) and (10.33) for the used dataset with $\ln N > 2$ (see Refs. [62, 602, 2270]).

10.5 Transition as a possible solution of Hubble tension

In this section, we investigate whether the existence of transition of the Cepheid parameters can impact on the inferred value of Hubble constant H_0 and its corresponding uncertainties. Using the best fit values of SnIa absolute magnitude M_B the Hubble constant is given by

$$H_0 = 10^{0.2M_B + \alpha_B + 5}, \quad (10.37)$$

where the term α_B is the intercept of the SnIa magnitude-redshift relation defined as [17]

$$\alpha_B = \log \left[cz \left(1 + \frac{1}{2}(1 - q_0)z - \frac{1}{6}(1 - q_0 - 3q_0^2 + j_0)z^2 + \mathcal{O}(z^3) \right) \right] - 0.2m_B, \quad (10.38)$$

where $q_0 \equiv -\frac{1}{H_0^2} \frac{d^2 a(t)}{dt^2} \Big|_{t=t_0}$ and $j_0 \equiv \frac{1}{H_0^3} \frac{d^3 a(t)}{dt^3} \Big|_{t=t_0}$ are the deceleration and jerk parameters respectively.

The intercept α_B using 217 observed SnIa at redshifts $0.023 < z < 0.15$ with the deceleration and jerk parameters set to $q_0 = -0.55$ and $j_0 = 1$ is determined to be $\alpha_B = 0.71273 \pm 0.00176$ by Ref. [17].

Alternatively, using the the best fit value of degenerate combination $\mathcal{M} = 23.803 \pm 0.007$ as derived by Ref. [12] for full Pantheon dataset in Eq. (10.5) the Hubble constant can be estimated

$$H_0 = c 10^{0.2(M_B - \mathcal{M}) + 5}. \quad (10.39)$$

In Table 10.1 we show the best fit value of SnIa absolute magnitude M_B and the corresponding Hubble constant H_0 as derived using the Eq. (10.37) and the Eq. (10.39) (the values in the parentheses) for all cases studied in this analysis. Also the one dimensional relative probability density values of M_B and H_0 as derived using the Eq. (10.37) and the Eq. (10.39) (the values in the parentheses of table 10.1) compared to that from the Planck CMB measurement assuming flat Λ CDM are shown in Fig. 10.14 and Fig. 10.15 respectively.

Clearly, for all cases which break the assumption of universality of the parameters R_W and M_H^W (i.e. I, II, III, IV, V, VI) the best fit value of SnIa absolute magnitude M_B and the derived values of H_0 decrease and become consistent with the corresponding predicted CMB best fit values. For the preferred model (case IV) we obtain $H_0 = 68.06 \pm 1.80 \text{ km s}^{-1} \text{ Mpc}^{-1}$ with Planck tension $< 1\sigma$. Therefore the transition in the Cepheid calibrator parameters at $D_c \simeq 16 \text{ Mpc}$ can provide a resolution of the Hubble tension.

10.6 Conclusions

In this Chapter we have used Cepheid SnIa calibrator data to investigate the effects of variation of the Cepheid calibration empirical parameters. We have shown that models where such a variation is allowed are favored on the basis of model selection criteria AIC and BIC. The models that are consistently favored by both AIC and BIC involve a transition in either the color-luminosity parameter R_W or the Cepheid absolute magnitude M_H^W , at a distance in the range between 10 and 20 Mpc. In the context of a homogeneous Universe where the cosmological principle is respected this would be a transition in time between about 25 Myrs and 70 Myrs ago. Models involving a transition in R_W are slightly favored over models where there is a transition in M_H^W . Both classes of models, lead to values of H_0 that are consistent with the CMB inferred values thus eliminating the Hubble tension.

Such a transition of Cepheid parameters could be induced by a fundamental physics transition. The magnitude of the transition is consistent with the magnitude required for the resolution of the Hubble tension in the context of a fundamental gravitational transition occurring by a sudden increase of the strength of the gravitational interactions G_{eff} by about 10% [52] at a redshift $z_t \lesssim 0.01$ ($\lesssim 150$ million years). Such a transition would abruptly increase the SnIa absolute magnitude by $\Delta M_B \simeq 0.2$ [52, 593] (from $M_B = -19.401 \pm 0.027$ mag for $z > z_t$ [290] to $M_B = -19.244 \pm 0.037$ mag for $z < z_t$ [269, 289]) (see Subsection 2.3.4 for details). The distance range/timescale corresponding to this transition is consistent with a recent analysis indicating a similar transition in the context of the Tully-Fisher data [477] and with low redshift galaxy surveys data [952]. Such a transition is also consistent with the solar system history data [944] which indicate an increase of the rate of impactors on the Moon and Earth surfaces by about a factor of 2-3 during the past 100 Myrs which correspond to $z < 0.008$ [946, 949, 951].

An alternative origin of the observed effect is based on a scenario where the parameter R_W could vary across different sightlines and different galaxy distances, morphologies, environments and properties. Dust extinction differences between galaxies could be the origin for a systematic "mass step" (at $\sim 10^{10} M_\odot$) in the data [2271, 2272]: after standardization, SnIa in a high-mass galaxy appear brighter than those in a low-mass galaxy [51, 2273–2277]. Such an alternative scenario is testable using the methods presented here and it could also lead to a resolution of the Hubble tension. Such an extension is beyond the goals of our analysis.

Other interesting extensions of our analysis include the following:

- The search for transition in other parameters that can be constrained using the Cepheid data (for example the SnIa absolute magnitude M_B and its effect on the estimation of H_0).
- It would be interesting to search for a similar transition in the other SnIa calibrator such as the Tip (a sharp discontinuity) of the Red Giant Branch (TRGB) in the Hertzsprung-Russell diagram [229]. The Red Giant stars have nearly exhausted the hydrogen in their cores and have just began helium burning by the triple- α process (helium flash phase). The brightness of TRGB stars can be standardized using DEBs combined with parallax calibration. They can serve as excellent alternative standard candles [2278] visible in the local Universe for the subsequent calibration of SnIa [2279–2282] and thereby provide an independent determination of the Hubble constant H_0 [230, 301].

The indicated transition at a distance of about 10 – 20 Mpc could be interpreted as violating the cosmological principle according to which the distance of any galaxy from us should not impact its properties. The cosmological principle however is not necessarily violated in the transition models because a spatial transition can not be observationally distinguished from a temporal transition. If the transition is temporal and occurred at a specific time then there is no violation of the cosmological principle.

Even if the transition is spatial it could be interpreted as a result of a first order phase transition occurring very recently due to a decay of the false vacuum [2283]. Then we could live in 20 Mpc true vacuum bubble where a first order scalar-tensor physics transition has occurred. If the bubble was created at recent cosmological times (e.g. last 100 Myrs) in the context of a decay of a false vacuum (see e.g. Ref. [2283]) then we would not have been able to see the other true vacuum bubbles since light from them

may not have reached us yet. Thus even in that case there would be no apparent large-scale violation of the cosmological principle. The phenomenology of such recent false vacuum decay in the context of scalar-tensor theories is another interesting extension of our analysis. In this context it may be shown that for a transition energy scale similar to the present Hubble constant the typical scale of the true vacuum bubbles produced would be 15 – 20 Mpc. Fine tuning questions also arise in the context of the indicated transition: ‘What is special about the scale of 15 – 20 Mpc where the transition signal appears to exist?’. In the context of a false vacuum decay bubble there is no more fine tuning than in the Λ CDM . If we accept the scale of the cosmological constant and the fact that there is a first order phase transition to another vacuum of a similar energy scale (~ 0.002 eV) then the predicted spatial scale of the produced bubbles is theoretically predicted to be about 15 Mpc. If we allow for some true vacuum bubble growth (they expand with the speed of light) it could increase to the scale of 20 Mpc. This generic result may be demonstrated as follows [2283–2286]: For a very recent false vacuum decay with vacuum energy comparable to the cosmological constant the scale of the produced bubbles is

$$R_b = \delta/H_0 , \tag{10.40}$$

where δ depends logarithmically on the ratio of the Planck mass M_{pl} to the transition temperature energy scale $T_c = 2.7^\circ K \simeq 2 \times 10^{-4}$ eV as [2284]

$$\delta \simeq [4B_1 \ln (M_{pl}/T_c)]^{-1} , \tag{10.41}$$

where B_1 is a constant of $O(1)$. Using Eqs. (10.40) and (10.41) with $H_0 = 70 \text{ km s}^{-1} \text{ Mpc}^{-1}$ we obtain $R_b \simeq 15 \text{ Mpc}$ which is clearly within the range of transition scales favored by the Cepheid data by the present analysis and by the Tully-Fisher data as indicated by Ref. [2283, 2285, 2286].

In conclusion the revolutionary improvement in the quality and quantity of data from existing and upcoming missions/experiments raises the expectation of determining the origin of the existing transition effect shown in our analysis. One possible origin would be the presence of systematic errors affecting the adopted calibration method. Alternatively, if the source of the demonstrated transition is physical it could lead to new cosmological physics beyond the standard model which may include a very recent false vacuum decay.

Chapter 11

Gravitational Transitions via the Explicitly Broken Symmetron Screening Mechanism

The analysis presented in this chapter is based on the work which was done in collaboration with Prof. Leandros Perivolaropoulos and it is currently under review in Physical Review D [9].

In this Chapter we present the asymmetron model which offers an interesting novel approach for the modification of GR in distinct spatial sectors. We generalize the symmetron screening mechanism by allowing for an explicit symmetry breaking of the symmetron ϕ^4 potential by the inclusion of a cubic term $\varepsilon\phi^3$. Due to the explicit symmetry breaking induced by the cubic term we call this field the 'asymmetron'. In such a screening scalar field (asymmetron) the two local potentials in low density areas are not symmetric ($\phi_+ \neq -\phi_-$). Therefore there is a false vacuum and a single true vacuum. This is expected to result in an unstable asymmetron domain wall network that includes a transition to the value of the effective gravitational constant G_{eff} as the asymmetron wall is crossed.

As mentioned in Subsection 2.3.4 and previous Chapter 10 a fundamental physics phase transition taking place at a redshift $z_t \lesssim 0.01$ and leading to a sudden increase of the type Ia supernovae (SnIa) absolute magnitude M by about $\Delta M \simeq 0.2$ for $z < z_t$ [52, 593] can lead to a resolution of the Hubble tension [140] between the Planck estimate [14] and the SH0ES collaboration measurements [23] which is currently at the 5σ level (see Refs. [7, 10, 127, 185] for recent reviews). Under simple assumptions about the connection of the SnIa absolute magnitude with the effective gravitational constant G_{eff} [914, 915, 2213], this transition could be induced by a gravitational transition increasing the value of the gravitational constant up to about 10% for $z < z_t$. If such a transition were to imply weaker gravity [914, 2213] in the past it could also play an important role in the resolution of another tension of the standard Λ CDM model known as the σ_8 or 'growth' tension [4, 67, 141, 144, 147, 148, 278, 281, 1188, 1197].

In view of the effectiveness of such a transition in the resolution of the Hubble and growth tensions, the following questions emerge

- Is such a transition consistent with current observational and experimental constraints on the evolution of G_{eff} ?
- Are there any hints in observational data for such a transition?
- Are there theoretical models [6, 1199, 1823] that can generically predict such a transition at the spatial or temporal level at $z_t \lesssim 0.01$?

The answer to the first question is positive. In fact current constraints on the evolution of G_{eff} strongly constrain its time derivative at present and at specific times and distances in the past. However a abrupt

shift of G_{eff} is weakly constrained and the current bounds allow an abrupt change of G_{eff} by up to about 5 – 10% at some cosmological time in the past between the present time and the time of nucleosynthesis.

The answer to the second question is also positive. Hints for such a transition in the values of dynamical parameters connected to the gravitational constant have recently been pointed out in Cepheid SnIa calibrator data [8, 56], in Tully-Fisher data [477] and in solar system history data [944] which indicate an increase of the rate of impactors on the Moon and Earth surfaces by about a factor of 2-3 during the past 100Myrs which correspond to $z < 0.008$ [946, 949, 951]. Such a transition is also consistent with low redshift galaxy surveys data [952].

The answer to the third question may be approached at both the temporal and the spatial level. In the context of a temporal transition a nonminimal scalar field could be initially trapped either due to cosmic friction or due to a local minimum of a time-dependent potential and globally shift to a new minimum of the effective potential at z_t via a classical evolution of the potential which may be coupled to the matter density or via the reduction of the cosmic friction. An alternative scenario leading to a gravitational transition could include a pressure non-crushing cosmological singularity in the recent past [942].

In the context of a tunneling first order phase transition of spatial character we, as observers, may be located in a true or false vacuum bubble with scale of about 20 – 40 Mpc corresponding to $z < 0.01$ where the value of G_{eff} is up to about 10% higher than the value of G_{eff} of the other vacuum of a non-minimally coupled scalar field.

11.1 Introduction

A mechanism involving a transition with spatial character by a purely classical evolution may be realized in the context of a symmetron field used as a screening mechanism of modified gravity theories. Based in part on earlier work [2287, 2288] the authors of Ref. [940] proposed the symmetron screening mechanism with a specific form of the scalar-gravity coupling where the coupling strength is the density-dependent quantity. The scalar field is decoupled from matter and screened when the matter density is sufficiently high, while in regions of low density the scalar field is coupled to matter with a long-range mediated force of gravitational strength [940, 941] (see also Refs. [2289–2295] and the Section 11.2 for details).

At early times when the mean density of the universe is $\rho > \rho_*$ (where ρ_* is a critical density), the minimum of the effective potential everywhere is at $\phi = 0$ and GR is applicable. As the mean density drops below ρ_* the symmetry is spontaneously broken and the symmetron field relaxes at one of the minima, the potential develops in low density regions while in regions where density perturbations have grown to densities above ρ_* the field remains at the symmetric vacuum $\phi = 0$. Low density regions where the field has relaxed in different vacua are separated by symmetron domain walls¹ where the field by continuity goes through the local maximum of the potential $\phi = 0$. Due to the \mathbb{Z}_2 symmetry of the potential ϕ^2 is the same at the two vacua and the corresponding effective gravitational constant G_{eff} in the Jordan frame, is the same on the two sides of the symmetron wall. Thus in the context of the symmetron domain wall no transition of G_{eff} is expected as the symmetron domain wall is crossed.

This is not the case if the bare potential includes an explicit \mathbb{Z}_2 symmetry breaking term $\varepsilon\phi^3$. In this case the two local minima of the potential in low density regions are not symmetric ($\phi_+ \neq -\phi_-$) and this implies a transition in the value of the Jordan frame gravitational constant as the wall is crossed. In addition the coexistence of a true with a false vacuum implies that the wall network dynamics will involve instabilities and will thus be different from the wall network appearing in the context of symmetric equivalent vacua.

This work focuses on a symmetron mechanism that involves explicit symmetry breaking. For definiteness we call this type of generalized symmetron field the *asymmetron*.

¹A domain wall is a type of two dimensional (sheet-like) topological defect (solitonic configurations of field) in three spatial dimensions that occurs whenever a discrete symmetry of the potential is spontaneously broken [1865, 2169, 2296–2304]. It separates neighboring spatially domains where the field is in different vacua.

There are at least three main mechanisms that can lead to a gravitational transition observed in the recent cosmological lookback time:

- Evolving scalar field (extended quintessence) in a scalar tensor sharply varying scalar-tensor potential.
- False vacuum decay (first order phase transition) in the context of a scalar-tensor theory.
- A network of symmetron domain walls with explicitly broken Z_2 symmetry of the effective potential (asymmetron wall network).

Our analysis focuses on the third mechanism and aims to provide a better understanding of the scalar field dynamics involved in such a mechanism. The main questions addressed in this context are the following:

- How can a gravitational transition be realized in the context of an asymmetron wall network?
- What are the properties and evolution of an asymmetron field domain wall in the presence of a spherical matter shell overdensity?
- Are there cosmological observations that could be interpreted as results on an existing asymmetron domain wall network?

The Chapter is structured as follows. Section 11.2 introduces the necessary background and notation of symmetron screening. In Section 11.3 we introduce the asymmetron field and the explicit Z_2 symmetry breaking associated with it. We also present the energetics and dynamics of spherical symmetron and asymmetron domain walls. Static stable wall solutions in the presence of matter are derived in Section 11.4. We also point out that recent cluster profile data may be interpreted as revealing spatial cosmological sectors where distinct properties of gravity are present. We discuss the possible connection of such an effect with the existence of asymmetron domain walls. Finally in Section 11.5 we conclude, summarise and discuss possible extensions of our analysis.

In what follows we assume a metric signature $(-, +, +, +)$.

11.2 Review of the symmetron screening

In the context of the symmetron mechanism², screening is achieved via Z_2 symmetry restoration in regions with matter density larger than a critical density.

The symmetron model is a special case of a general scalar-tensor theory, thus its action in the Einstein frame (where the scalar field couples non-minimally to matter components and minimally to gravity) is described by the general scalar-tensor action [940, 941, 2289–2292]

$$S = \int d^4x \sqrt{-g} \left[\frac{R}{16\pi G} - \frac{1}{2} \nabla_\mu \phi \nabla^\mu \phi - V(\phi) \right] + S_m[\psi_i, \tilde{g}_{\mu\nu}] , \quad (11.1)$$

where G is Newton's constant as measured locally e.g. in Eotvos-type experiments, g is the determinant of the Einstein frame metric $g_{\mu\nu}$, R is the Ricci scalar, ϕ is a scalar field with self-interactions given by the potential $V(\phi)$, S_m is the action for the various matter fields and ψ_i represent these matter fields which are minimally coupled in the Jordan frame metric $\tilde{g}_{\mu\nu}$ ³. This is connected to the Einstein frame metric $g_{\mu\nu}$ via a conformal rescaling [940, 941, 2289–2292]

$$\tilde{g}_{\mu\nu} = A^2(\phi) g_{\mu\nu} \quad (11.2)$$

²For reviews of modified gravity theories with screening mechanisms, such as the Vainshtein [917–919] and the chameleon [887, 888, 892, 920–926] models see in Refs. [927–938].

³In the rest of this analysis, quantities associated to the Jordan frame metric $\tilde{g}_{\mu\nu}$ will be distinguished by a tilde.

The non-minimal coupling to matter is described by the coupling function $A(\phi)$ and leads to deviations from GR. The scalar field couples to the trace of the energy-momentum tensor and its equation of motion, obtained using standard variational methods, is [940, 941]

$$\square\phi = \frac{dV(\phi)}{d\phi} - \frac{dA(\phi)}{d\phi}A(\phi)^3\tilde{T}, \quad (11.3)$$

where \tilde{T} is the trace $\tilde{T} = \tilde{g}_{\mu\nu}\tilde{T}^{\mu\nu}$ of the Jordan frame energy-momentum tensor

$$\tilde{T}^{\mu\nu} \equiv \frac{-2}{\sqrt{-\tilde{g}}} \frac{\delta S_m}{\delta \tilde{g}_{\mu\nu}} = A(\phi)^{-6}T^{\mu\nu}, \quad (11.4)$$

which is covariantly conserved $\tilde{\nabla}_\mu\tilde{T}^{\mu\nu} = 0$.

For non-relativistic matter the trace of the Einstein energy-momentum tensor⁴ is $T = -\rho \approx -A(\phi)^3\tilde{\rho} = -A(\phi)^3\tilde{T}$, and the scalar field equation of motion (11.3) takes the form

$$\square\phi = \frac{dV(\phi)}{d\phi} + \frac{\beta(\phi)\rho}{M_{pl}} = \frac{dV_{\text{eff}}}{d\phi}, \quad (11.5)$$

where $M_{pl} = (8\pi G)^{-1/2}$ is the reduced Planck mass, V_{eff} is the effective potential⁵ [940, 941]

$$V_{\text{eff}}(\phi) = V(\phi) + \rho A(\phi), \quad (11.6)$$

and the β is the coupling between the scalar field and matter

$$\beta(\phi) = M_{pl} \frac{dA(\phi)}{d\phi}. \quad (11.7)$$

This coupling characterises the strength of the scalar fifth force which, in the nonrelativistic limit, is given by [2289, 2305, 2307]

$$\vec{F}_\phi = \frac{\beta(\phi)}{M_{pl}} \vec{\nabla}\phi. \quad (11.8)$$

This scalar fifth force is an additional contribution to the (Newtonian) gravitational force F_N .

The interaction potential and the coupling function are chosen to be of the spontaneous symmetry breaking form [940, 941, 2289]

$$V(\phi) = \frac{\lambda}{4}(\phi^2 - \eta^2)^2, \quad (11.9)$$

$$A(\phi) = 1 + \frac{\phi^2}{2M^2} + \mathcal{O}\left(\frac{\phi^4}{M^4}\right), \quad (11.10)$$

where M is the mass scale of symmetron field coupling to the matter density. It gives the strength of the interaction with the matter fields. The parameter λ is a positive dimensionless coupling securing that the energy of the ϕ^4 model [2308, 2309] is bounded from below [2303]. Also $\eta = \phi_0 = \phi(\rho = 0)$ is the expectation value of the scalar field at zero matter density. For the field range $(\frac{\phi}{M})^2 \ll 1$ the higher order correction terms of the coupling function can be consistently neglected [941, 2289].

The effective potential is

$$V_{\text{eff}}(\phi) = -\frac{1}{2}\mu^2 \left(1 - \frac{\rho}{\mu^2 M^2}\right) \phi^2 + \frac{\lambda}{4}\phi^4 + \frac{\lambda\eta^4}{4}, \quad (11.11)$$

⁴Note that in the Einstein frame the density ρ is not conserved but the 'density' $A(\phi)^3\tilde{\rho}$ is conserved [940, 2305] and ϕ -independent [941]. However the coupling function is assumed to be a weak function of ϕ ($A(\phi) \approx 1$), so that the two densities do not differ from each other significantly ($\rho \approx A(\phi)^3\tilde{\rho}$).

⁵Note that in the literature the effective potential is often defined as $V_{\text{eff}}(\phi) = V(\phi) + \rho[A(\phi) - 1]$ [930, 2290, 2291, 2306] or $V_{\text{eff}}(\phi) = V(\phi) + \rho \ln A(\phi)$ [928].

where $\mu^2 \equiv \lambda\eta^2$.

The effective potential is invariant with respect to the \mathbb{Z}_2 symmetry (reflection symmetry) transformation $\phi \rightarrow -\phi$ (as are $V(\phi)$ and $A(\phi)$ individually). The coefficient of the quadratic term (effective mass) changes sign at a critical density

$$\rho_* \equiv \mu^2 M^2 . \quad (11.12)$$

For density smaller than the critical density ($\rho < \rho_*$) the effective mass is negative, the \mathbb{Z}_2 symmetry is spontaneously broken and the effective potential has two nonzero degenerate minima located at

$$\phi_{\pm} = \pm\eta\sqrt{1 - \frac{\rho}{\rho_*}} , \quad (11.13)$$

leading to two degenerate vacua. Note that if $\rho \ll \rho_*$ then the vacua correspond to $\phi_{\pm} \approx \pm\eta = \pm\frac{\mu}{\sqrt{\lambda}}$.

For background density larger than the critical density ($\rho > \rho_*$) the symmetry gets restored (symmetric phase) and the effective potential has a unique global minimum at the origin ($\phi = 0$) about which it is symmetric.

From Eqs. (11.7) and (11.10) the coupling to matter at the minima of the effective potential is given by

$$\beta(\phi_{\pm}) = \frac{M_{pl}\phi_{\pm}}{M^2} = \begin{cases} 0 & \rho > \rho_* , \\ \pm\beta_0\sqrt{1 - \frac{\rho}{\rho_*}} & \rho < \rho_* , \end{cases} \quad (11.14)$$

where $\beta_0 \equiv \frac{M_{pl}\eta}{M^2}$ is the coupling at zero matter density (vacuum). Clearly, the strength of the coupling to matter depends on the background density. Thus in high density regions the field does not couple to matter and the fifth force in Eq. (11.8) is suppressed while in regions of low density the field couples to matter and mediates a force.

Using Eq. (11.11) we have for the effective mass of the symmetron field

$$\begin{aligned} m_{\text{eff}}^2 &\equiv \left. \frac{d^2 V_{\text{eff}}}{d\phi^2} \right|_{\text{min}} = \left(\frac{\rho}{\rho_*} - 1 \right) \mu^2 + 3\lambda\phi_{\pm}^2 \Rightarrow \\ m_{\text{eff}}^2 &= 2\mu^2 \left(1 - \frac{\rho}{\rho_*} \right) , \end{aligned} \quad (11.15)$$

and the range (Compton wavelength) of the field in density regions with $\rho < \rho_*$ is

$$l_{\phi} = \frac{1}{m_{\text{eff}}} = \frac{1}{\sqrt{2}\mu} \left(1 - \frac{\rho}{\rho_*} \right)^{-1/2} . \quad (11.16)$$

The spontaneous symmetry breaking phase can lead to the formation of a domain wall network via the Kibble mechanism. These walls are attracted to high density regions (see in Refs. [2292, 2310, 2311] for numerical studies of properties and dynamics of domain walls in the symmetron model). The physical origin of this interaction is described in the next section. The profile of such a static domain wall with boundary conditions $\phi(x \rightarrow \pm\infty) = \phi_{\pm}$, is obtained by solving Eq. (11.5) and is of the form

$$\phi(x) = \eta\sqrt{1 - \frac{\rho}{\rho_*}} \tanh \left[\sqrt{\frac{\lambda}{2}} \eta \sqrt{1 - \frac{\rho}{\rho_*}} x \right] . \quad (11.17)$$

Its width is

$$\delta = \frac{1}{\mu} \left(1 - \frac{\rho}{\rho_*} \right)^{-1/2} = \sqrt{2}l_{\phi} . \quad (11.18)$$

A slowly evolving wall network may be interpreted as a fluid with equation of state parameter [2302]

$$w_w = \frac{p_w}{\rho_w} = -\frac{2}{3} , \quad (11.19)$$

and density parameter [2292]

$$\Omega_w \equiv \frac{\rho_w}{\rho_c} = \frac{\sigma}{3H^2 M_{pl}^2 a d}, \quad (11.20)$$

where a is the scale factor and d is the comoving distance between the walls⁶, $\sigma \equiv \rho_w a d$ is the surface energy density (energy per unit area or tension) of the wall (with $\sigma = \frac{4}{3} \sqrt{\frac{\lambda}{2}} \eta^3$ for $\rho = 0$ [2302]), ρ_c is the critical density of the universe and $H = \dot{a}/a$ is the Hubble parameter.

In theories where the phase transition takes place in the recent past (around the onset of cosmic acceleration) the scale factor at the time of the symmetry breaking is given by [2289]

$$a_*^3 = \frac{\rho_0}{\rho_*} = \frac{3\Omega_{0m} H_0^2 M_{pl}^2}{\mu^2 M^2}, \quad (11.21)$$

where $\rho_0 = \rho(a = 1)$ and $\Omega_{0m} = \Omega_m(a = 1)$ are the matter density and the corresponding density parameter in the universe today respectively while H_0 is the Hubble constant. This equation fixes μ in terms of M and hence combining with the Eq. (11.16) we obtain for redshifts $z < z_*$ (with $z_* = \frac{1}{a_*} - 1$) in low density regions ($\rho \ll \rho_*$)

$$l_\phi^2 \simeq \frac{M^2}{6\Omega_{0m} M_{pl}^2 H_0^2} \frac{1}{(1+z_*)^3}. \quad (11.22)$$

As shown in Eq. (11.16), in density regions with $\rho < \rho_*$ there is a dependence of the symmetron range on the background matter density and hence the redshift. The range decreases as the redshift at the time of symmetry breaking increases. For a range $M \lesssim 10^{-3} M_{pl}$, the range of the scalar field force becomes $l_\phi \lesssim 1 Mpc$ [927, 2289, 2312]. The value $1 Mpc$ corresponds intergalactic distance in clusters and therefore dynamical observational cosmological effects are anticipated for this range.

The background cosmology, the evolution of perturbations and large-scale structure in the context of the symmetron model have been investigated in [941, 2289, 2313–2316]. Before the time of the symmetry breaking ($t < t_*$) we have $\phi \approx 0$ and the effective gravitational constant $G_{\text{eff}} = G$. While after the symmetry breaking ($t > t_*$) the field approaches the minima $\phi_\pm = \pm \eta$ in low density regions and the effective gravitational constant is (see in Ref. [2289] for details)

$$G_{\text{eff}} = \begin{cases} G & a/k \gg l_\phi, \\ G(1 + 2\beta_0^2) & a/k \ll l_\phi. \end{cases} \quad (11.23)$$

The implementation of N-body simulations constitutes a useful tool for cosmological studies and for observational predictions of the symmetron screening mechanism [2289, 2290, 2307, 2317–2321].

11.3 Asymmetron Domain Walls

In this Section we generalize the symmetron mechanism by allowing for an explicit symmetry Z_2 breaking of the symmetron potential (11.9). The explicit symmetry breaking is induced by the inclusion of a cubic term $\varepsilon\phi^3$ in the potential. In this case the two local minima of the effective potential in low density regions are not symmetric ($\phi_+ \neq -\phi_-$). We call this generalized symmetron field the *asymmetron*.

The explicit symmetry breaking can create domain walls which interpolate between spatial regions with the vacuum values ϕ_+ and ϕ_- . Also the coexistence of a true with a false vacuum implies that the wall network dynamics will involve instabilities in contrast to the wall network appearing in the case of symmetron model equivalent vacua $\phi_+ = |\phi_-|$. In addition it can lead to a transition in the value of gravitational constant G as the wall is crossed. Before the time of the symmetry breaking ($t < t_*$) we have $\phi \approx 0$ and the effective gravitational constant is $G_{\text{eff}} = G$ as in the case of symmetron field. After

⁶Assuming parallel domain walls separated by physical distance $a d$ which grows in proportion with the scale factor.

the symmetry breaking ($t > t_*$) the field approaches different minima $\phi_+ = \eta_1$ and $\phi_- = \eta_2$ in different domains. The effective gravitational constant is

$$G_{\text{eff}} = \begin{cases} G & a/k \gg l_\phi , \\ G(1 + 2\beta_{0i}^2) & a/k \ll l_\phi , \end{cases} \quad (11.24)$$

where $\beta_{0i} \equiv \frac{M_{pl}\eta_i}{M^2}$ (with $i = 1, 2$) are the coupling at the true and false vacua. Thus, low density regions in different domains would have different values of gravitational constant and thus different expansion rates since $H^2 \sim G_{\text{eff}}$.

11.3.1 Dynamical equations and energetics of spherical asymmetron configurations

The action describing the dynamics of the symmetron scalar field may be written as⁷

$$S = \int d^4x \sqrt{-g} [g^{\mu\nu} \partial_\mu \phi \partial_\nu \phi - V(\phi)] . \quad (11.25)$$

The dynamical equation for a spherically symmetric field configuration in flat space is

$$r^2 \ddot{\phi} - \frac{\partial}{\partial r} r^2 \frac{\partial \phi}{\partial r} = -\frac{1}{2} \frac{dV}{d\phi} r^2 , \quad (11.26)$$

where the dot denotes differentiation with respect to cosmic time t .

The corresponding energy is

$$E = 4\pi \int_0^\infty r^2 \left[\left(\frac{d\phi}{dr} \right)^2 + V(\phi) \right] dr . \quad (11.27)$$

We now assume a ϕ^4 potential which includes an explicit \mathbb{Z}_2 symmetry breaking term $\varepsilon\phi^3$

$$V(\phi) = \frac{\lambda}{2} (\phi^2 - \eta^2)^2 + 2\varepsilon\phi^3 , \quad (11.28)$$

with a coupling to matter

$$A(\phi) = 1 + \frac{\phi^2}{M^2} , \quad (11.29)$$

such that the effective potential is

$$V_{\text{eff}}(\phi) = -\mu^2 \left(1 - \frac{\rho}{\mu^2 M^2}\right) \phi^2 + \frac{\lambda}{2} \phi^4 + 2\varepsilon\phi^3 + \frac{\lambda}{2} \eta^4 , \quad (11.30)$$

where ε is a parameter.

By defining the effective rescaled potential $\bar{V}_{\text{eff}}(\bar{\phi}) \equiv V_{\text{eff}}(\phi)/\lambda\eta^4$ we obtain

$$\bar{V}_{\text{eff}}(\bar{\phi}) = -(1 - \bar{\rho}) \bar{\phi}^2 + \frac{1}{2} \bar{\phi}^4 + \frac{1}{2} + 2\bar{\varepsilon} \bar{\phi}^3 , \quad (11.31)$$

where the rescaled dimensionless quantities are

$$\bar{\phi} \equiv \frac{\phi}{\eta} , \quad \bar{\rho} \equiv \frac{\rho}{\lambda\eta^2 M^2} \equiv \frac{\rho}{m^2 M^2} , \quad \bar{\varepsilon} \equiv \frac{\varepsilon}{\lambda\eta} . \quad (11.32)$$

We set also

$$\bar{r} \equiv r\sqrt{\lambda\eta} , \quad \bar{E} \equiv \frac{E\sqrt{\lambda}}{4\pi\eta} , \quad (11.33)$$

⁷We have multiplied by a factor of 2 the usual form of the action to avoid the factor of $\frac{1}{2}$ in the kinetic term.

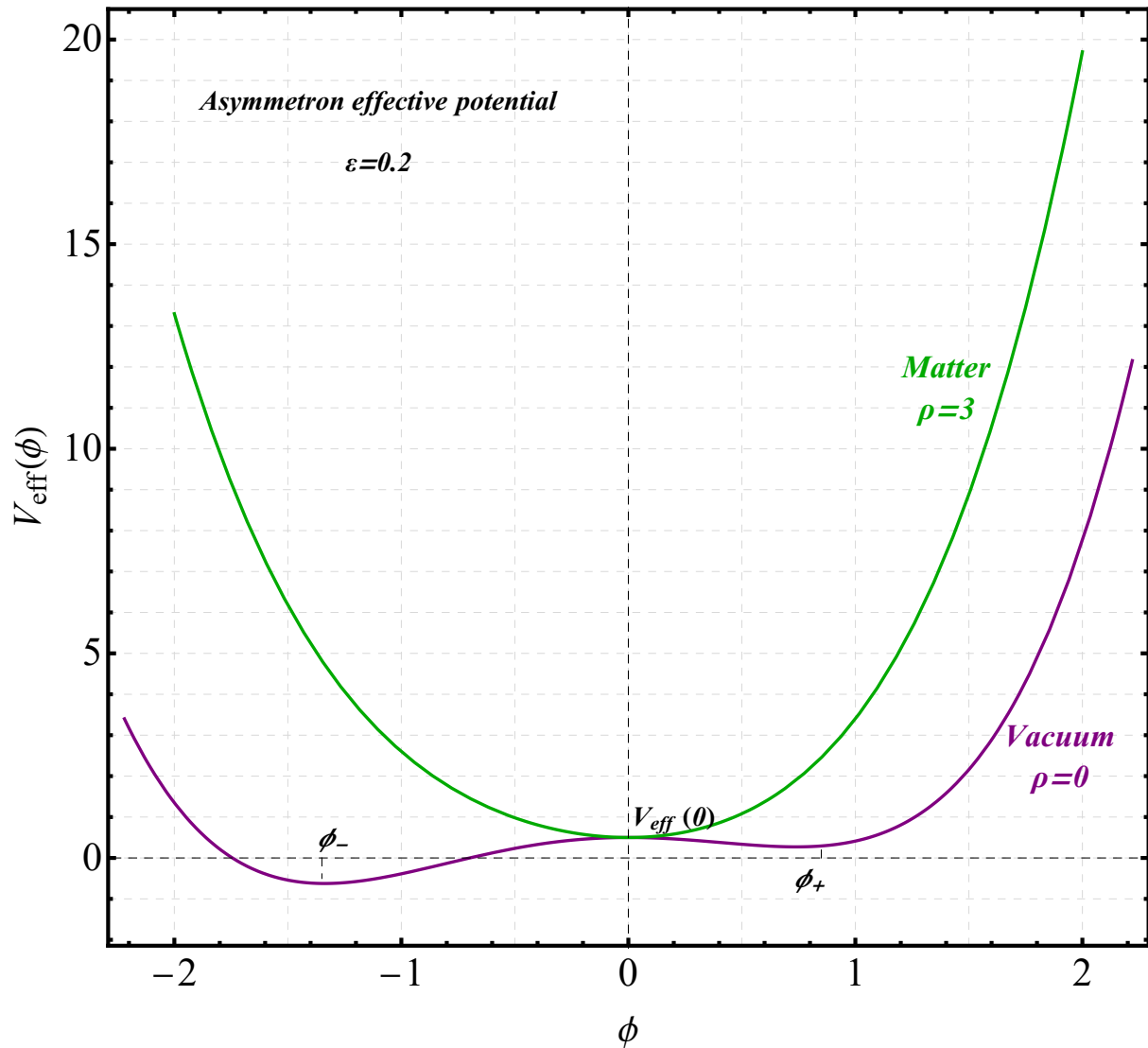


Figure 11.1: Schematic plots of the asymmetron effective potential Eq. (11.31) in vacuum (purple) and in high density (green) cosmological regions. Notice the asymmetric form of the effective potential in which the degeneracy of the vacua is slightly broken. However in the presence of sufficiently high density, a single minimum at $\phi = 0$ restores GR as in the symmetron case.

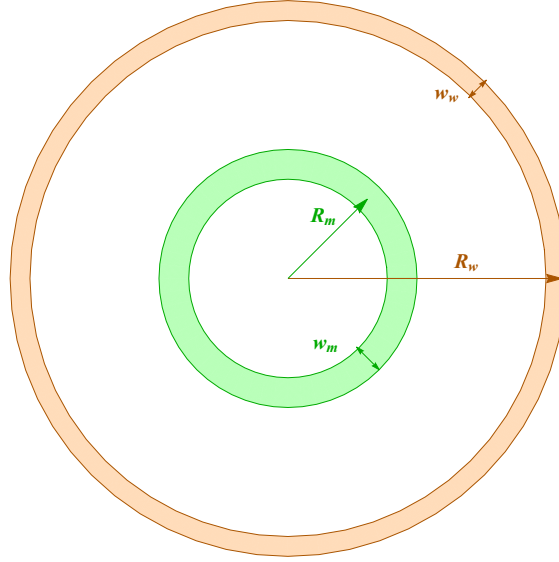


Figure 11.2: The geometry of the spherical domain wall in the presence of spherical matter shell.

and by taking into account the above redefinitions, we can rewrite the dynamical equation (11.26) as

$$\bar{r}^2 \bar{\phi}'' - \frac{\partial}{\partial \bar{r}} \bar{r}^2 \frac{\partial \bar{\phi}}{\partial \bar{r}} = -\frac{1}{2} \frac{d\bar{V}_{\text{eff}}}{d\bar{\phi}}(\bar{\phi}) \bar{r}^2, \quad (11.34)$$

and the corresponding energy Eq. (11.27) as

$$\bar{E} = \int_0^\infty \bar{r}^2 \left[\left(\frac{d\bar{\phi}}{d\bar{r}} \right)^2 + \bar{V}_{\text{eff}}(\bar{\phi}) \right] d\bar{r}. \quad (11.35)$$

We omit bar from now on and work with dimensionless quantities.

The two vacuum values (true and false) of ϕ , given by the equation

$$\left. \frac{dV_{\text{eff}}}{d\phi} \right|_{\phi_\pm} = 0, \quad (11.36)$$

read ϕ_\pm

$$\phi_\pm = \frac{1}{2} \left(-3\varepsilon \pm \sqrt{\Delta} \right), \quad (11.37)$$

where

$$\Delta = 4 + 9\varepsilon^2 - 4\rho. \quad (11.38)$$

In the case of explicit symmetry breaking (asymmetron wall formation) the symmetry gets restored, for a background density larger than the critical density corresponding to the symmetron field. For the asymmetron case we have $\rho > \rho_{*,as} = 1 + \frac{9}{4}\varepsilon^2$ which is larger than the critical density ($\rho_* = 1$) in the symmetron case.

The form of the asymmetron effective potential in vacuum and in high density cosmological regions is shown in Fig. 11.1. Clearly, in the case of asymmetron model the two local minima of the potential depend on the matter density as in the symmetron case. In the presence of sufficiently high density, the symmetry is restored along with GR since the coupling $A(\phi) \approx 1$. Thus a screened fifth force is associated with the *asymmetron* field. However, as indicated in Eqs. (11.37), (11.38) and in Fig. 11.1 in the case of asymmetron model the two local minima of the potential in low density regions are not symmetric $\phi_+ \neq |\phi_-|$ and non-degenerate. Thus, since the degeneracy of the vacua is broken, this double-well potential has a false vacuum and a true vacuum due to the explicit symmetry breaking induced by the cubic term. The difference between the false and true vacuum energies increases with ε as

$$V_{\text{eff}}(\phi_+) - V_{\text{eff}}(\phi_-) = \left[2\varepsilon(1 - \rho) + \frac{9}{2}\varepsilon^3 \right] \sqrt{\Delta}. \quad (11.39)$$

Clearly, the energy difference between the vacua increases linearly with ε for small ε .

11.3.2 Spherical wall interaction with a matter shell: A toy model

We consider a finite thickness spherical domain wall in the presence of spherical matter shell as a simple toy model (see Fig. 11.2). Although this model is too simple it enables us to draw useful conclusions.

The scalar field energy of the system if the wall and the matter shells are separate is approximated as⁸

$$E_s = V(0)w_m R_m^2 + V(0)w_w R_w^2, \quad (11.40)$$

where w_w (R_w) and w_m (R_m) are the widths (radii) of the domain wall and the matter shells respectively. In the matter shell region the field is at the minimum of the effective potential ($\phi = 0$) with energy density $\rho_\phi \simeq V(0)$ while at the domain wall radius the field is trapped at the local maximum of the effective potential ($\phi = 0$) with the same energy density $\rho_\phi \simeq V(0)$.

The energy of the system if the wall and the matter shells overlap is

$$E_o = V(0)w_w R_w^2, \quad (11.41)$$

where we assumed without loss of generality that $w_w > w_m$. Therefore, the energy difference of the two configurations is

$$\Delta E = E_o - E_s = -V(0)w_m R_m^2 < 0. \quad (11.42)$$

Thus $E_o < E_s$ and it is energetically favored for the wall to overlap with the matter shell. In contrast to the conventional domain walls, the symmetron and asymmetron walls tend to stay in regions where the matter density is high. This is confirmed numerically in what follows.

11.4 Static stable spherical wall configurations in the presence of matter

11.4.1 Analytic considerations

A spherical domain wall is a field configuration that interpolates between the two minima ϕ_\pm of the effective potential as the surface of the wall sphere in physical space is crossed. The wall is characterized by the surface energy density σ [2302] which depends not only on the configuration of ϕ but also on the matter density ρ . The corresponding to tension force per unit area is $p_\sigma \sim \sigma/R(t)$ (with $R(t)$ the curvature scale). In addition a pressure difference p (with $p \sim \varepsilon\eta^3$ for $\rho \ll \rho_*$ [2302]) pushes the wall toward the vacuum with the lowest energy (true vacuum). The dynamics of the spherical asymmetron wall surrounding a true vacuum region is determined by three factors:

⁸For simplicity, here we ignore the gradient energy which if included further enhances the attraction of the wall by the matter shell.

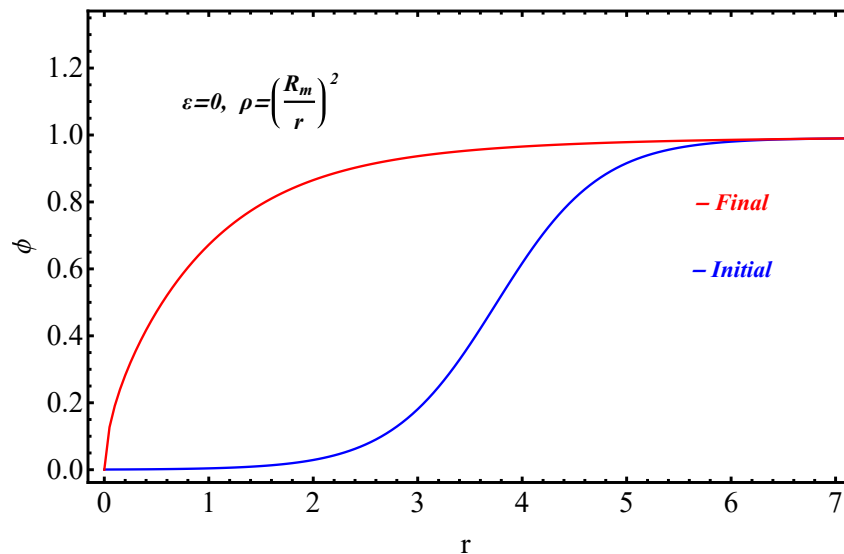


Figure 11.3: The scalar field ϕ as a function of the distance r corresponds to the solution in the case of monotonic matter density increasing towards the center (with $R_m = 1$). In this resulting minimum energy field configuration we see a collapse of the wall due to tension. The energy minimization was performed numerically using $N = 150$ lattice points.

- The tension term that favors contraction of the spherical wall with contribution to the energy $E_\sigma \sim \eta^3 R(t)^2$. This energy term increases with the wall radius.
- The vacuum energy difference term that favors expansion of the true vacuum domain with contribution to the energy (relative to the exterior false vacuum domain) $E_{vac} \sim -\varepsilon \eta^3 R(t)^3$ for small ε . This negative energy term decreases with wall radius $R(t)$ and favors expansion. If the wall surrounds a false instead of a true vacuum region, then the sign of E_{vac} will be positive and the fate of the wall radius in the absence of the coupling to matter is contraction and collapse due to both tension and false vacuum energy.
- The term due to the coupling to matter $E_{mat} \sim -w_m R_m^2 \eta^4 \delta(R(t) - R_m)$ which dominates over the effect of tension as shown in Eq. (11.42) when the wall overlaps with the matter density shell. The δ function should be replaced by a smooth function leading to an attractive force, in thick-smooth realistic density profiles as those discussed in the next section.

The first two terms can at best lead to an unstable spherical domain wall as it can easily be verified that they lead to a static configuration at an energy maximum (instability) with respect to R . These configurations would tend to contract if the initial spherical wall radius is less than a critical value and would tend to expand if the initial radius is larger than this value. This could have been anticipated also due to Derrick's theorem [2322]. Stability can only be achieved due to the last term which is due to the external coupling to the matter density shell which violates the assumptions of Derrick's theorem and allows for a stable static spherical wall configuration as demonstrated numerically in what follows. A similar stabilization mechanism has been recently considered using external gravitational fields instead of a coupling to matter density [1865].

11.4.2 Numerical energy minimization

The evolution of the spherical domain wall is described by the action (11.25) and the corresponding dynamical equation (11.34). The energy of the spherical wall, assumed initially static is given by Eq. (11.35).

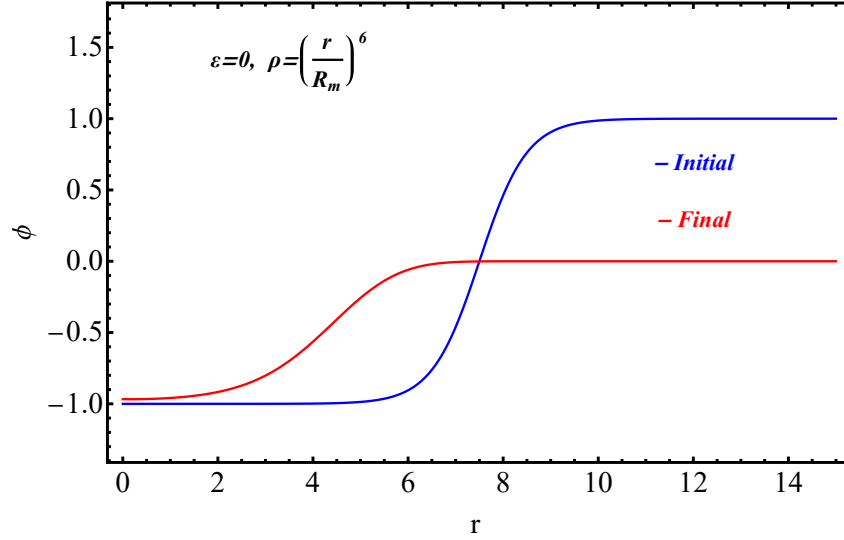


Figure 11.4: The scalar field ϕ as a function of the distance r corresponds to the solution obtained from the energy minimization method in the case of increasing matter density. This field configuration appears to be stabilized by the combined effects of the wall tension and the attraction of the increased matter density as r increases.

We search for a stable static wall configuration by minimizing the discretized integral of the field energy Eq. (11.35) starting from an initial guess that interpolates between the two vacua ϕ_+ , ϕ_- at a radius R_w

$$\phi(r) = \frac{\phi_+ - \phi_-}{2} \tanh\left(\frac{r - R_w}{w_w}\right) + \frac{\phi_+ + \phi_-}{2} . \quad (11.43)$$

We have verified that the precise form of the initial guess does not affect the final field configuration that minimizes the energy.

The boundary conditions may be set such that the spatial r derivative of the scalar field is 0 at the two boundaries of r ($r = 0$ and $r = r_{max}$). Alternatively the boundary condition can fix the field at the corresponding vacua at the two boundaries. Both types of boundary conditions lead to the same minimum energy static field configuration in the cases studied.

Therefore, a simple way to derive numerically the basic features of the evolution of the wall initial configuration Eq. (11.43) is to explicitly minimise the energy functional Eq. (11.35) with fixed boundary conditions. We thus use the Energy Minimization (EM) method which consists of the following steps:

1. We discretize the energy functional Eq. (11.35) as a sum over N lattice points as

$$E = dx \sum_{i=1}^N \left[r_i^2 \left(\frac{\phi_i - \phi_{i-1}}{dx} \right)^2 + r_i^2 V(\phi_i) \right] , \quad (11.44)$$

where $r_i = idx$, $dx = r_{max}/N$ and $\phi_i \equiv \phi(r_i)$.

2. We numerically minimize the sum (11.44) with respect to the N lattice values of the field ϕ_i (one value at each lattice point) keeping fixed the boundary conditions.

In particular, we consider the following cases:

I. Spherical Symmetron Walls

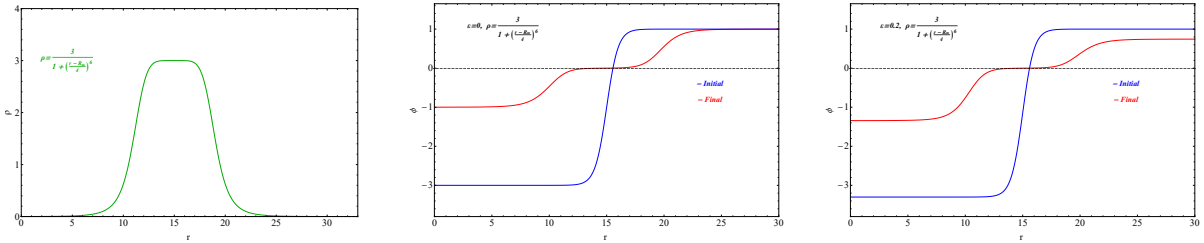


Figure 11.5: Left panel: The matter density of the spherical matter shell of the form (11.49) with radius $R_m = 15$. Middle panel: The scalar field ϕ in symmetron case ($\epsilon = 0$) as a function of the distance r corresponds to the solution obtained from the energy minimization method in the case of matter density of the spherical matter shell of the form (11.49) with radius $R_m = 15$. The final minimum energy configuration is independent of the initial guess shown here in blue. Right panel: The scalar field ϕ in asymmetron case ($\epsilon = 0.2$) as a function of the distance r corresponds to the solution obtained from the energy minimization method in the case of matter density of the spherical matter shell of the form (11.49) with radius $R_m = 15$.

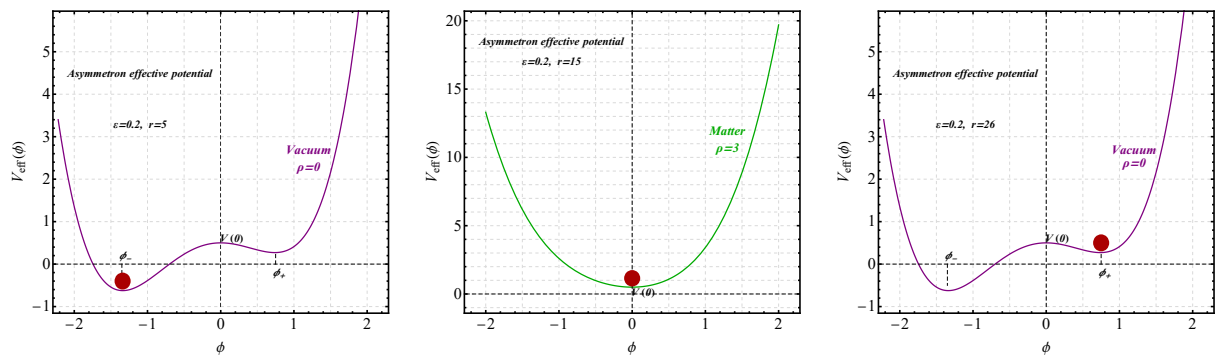


Figure 11.6: The form of the asymmetron (with $\epsilon = 0.2$) effective potential for the case $\rho = 0$ (vacuum) and $\rho = 3$ (high density) (see Figs. 11.1 and 11.5). The red points represent the value of the field and show how the asymmetron field changes as the wall is crossed by increasing r .

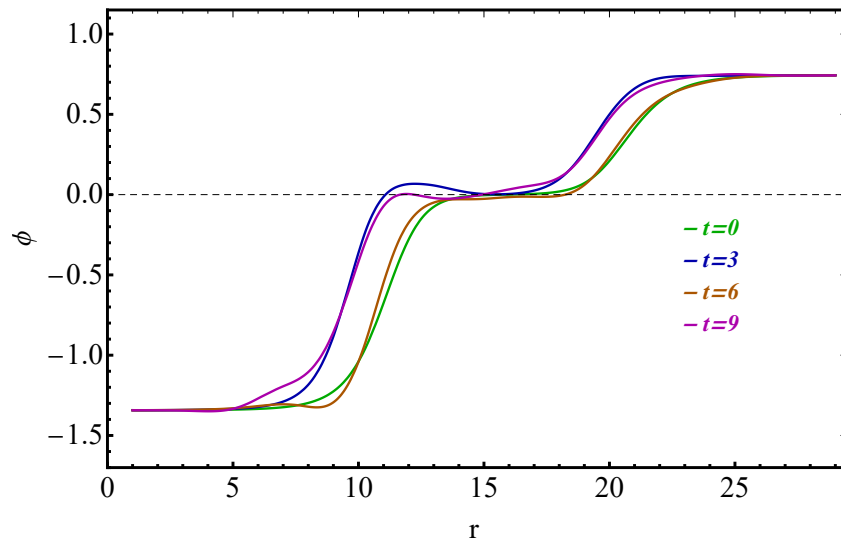


Figure 11.7: Simulation of time evolution of the perturbed scalar field corresponding to a perturbed spherical asymmetron domain wall. The wall gets trapped at the matter shell as expected (collapse is avoided).

We first allow only spontaneous symmetry breaking and set $\varepsilon = 0$. We consider the following matter density profiles:

- **Monotonic matter density increasing towards the center** of the form:

$$\rho(r) = \left(\frac{r}{R_m} \right)^{-2}, \quad (11.45)$$

with $R_m = 1$.

We fix the boundary conditions such that the field remains at the corresponding vacuum on each boundary (we choose ϕ_+ at the outer boundary where the matter density is low).

$$\phi(r = 0) = 0, \quad \phi(r = r_{max}) = \phi_+. \quad (11.46)$$

According to the above analytic arguments we anticipate an attractive force of the wall towards the center where the matter density is maximum in addition to the tension force which further amplifies this trend for collapse. In Fig. 11.3 we show the initial guess wall configuration and the final configuration emerging after the EM method. The minimization of the energy leads to a collapse of the wall due to tension as expected.

- **Increasing outward matter density** of the form:

$$\rho(r) = \left(\frac{r}{R_m} \right)^6, \quad (11.47)$$

with $R_m = 5$ and the following two boundary conditions

$$\phi'(r = 0) = 0, \quad \phi'(r = r_{max}) = 0. \quad (11.48)$$

Unlike the result of the previous case, here we anticipate an outward force driving the wall radius to larger values where the density is larger. This trend is expected to compete with the wall tension. Indeed, here the field configuration emerging after EM method appears to be stabilized by the combined effects of the wall tension and the attraction of the increased matter density as r increases. This resulting field configuration is shown in Fig. 11.4.

- **Shell-like matter density** of the form (see in left panel of Fig. 11.5)

$$\rho(r) = \frac{3}{1 + \left(\frac{r-R_m}{4}\right)^6}, \quad (11.49)$$

with $R_m = 15$ and boundary conditions:

$$\phi'(r=0) = 0, \quad \phi'(r=r_{max}) = 0. \quad (11.50)$$

As expected from the analytic arguments of Eq. (11.42) in this case the minimum energy field configuration corresponds to a wall radius overlapping with the matter shell radius (see in middle panel of Fig. 11.5).

II. Stable Spherical Asymmetron Walls

In the presence of an explicit symmetry breaking leading to the asymmetron field, the above results remain qualitatively unaffected. In this case we set $\varepsilon = 0.2$ and assume a shell-like spherical matter density of the form (11.49) (see in left panel of Fig. 11.5) and boundary conditions (11.50).

The resulting asymmetron field configuration after energy minimization is shown in right panel of Fig. 11.5. The form of the corresponding asymmetron effective potential and the field values as the distance from the center of the spherical matter overdensity increases is shown in Fig. 11.6. Snapshots of the potential and the corresponding field values are shown for matter density $\rho = 0$ (vacuum inside and outside the matter shell) and $\rho = 3$ (on the matter shell). The red points represent the position of the field and show how the field changes as the distance r from the center increases.

In order to further confirm the stability of the derived minimum energy configurations $\phi_s(r)$ we have perturbed them and implemented numerical dynamical evolution using an explicit Runge–Kutta algorithm [2323]. In particular, we solve numerically Eq. (11.34) with initial conditions

$$\phi(0, r) = \phi_s(r - \delta r), \quad \dot{\phi}(0, r) = 0, \quad (11.51)$$

with boundary conditions

$$\phi(t, 0) = \phi_s(0), \quad \dot{\phi}(t, 0) = 0, \quad (11.52)$$

$$\phi'(t, r_{max}) = 0, \quad \dot{\phi}(t, r_{max}) = 0, \quad (11.53)$$

where the dot denotes differentiation with respect to the cosmic time t and prime denotes differentiation with respect to the distance r .

The imposed perturbations on the minimum energy configuration of the right panel of Fig. 11.5 correspond to an initial shift by $\delta r < 1$ of the wall radius r .

The evolved scalar field configuration corresponds to a spherical wall with a radius that appears to be oscillating around the radius of the matter shell, effectively being trapped by it as shown in Fig. 11.7. This behavior is consistent with the stability of the spherical wall implied by both the analytic arguments of Subsection 11.4.1 and by the energy minimization procedure discussed above.

11.4.3 Observational considerations

If asymmetron walls exist in Nature there could be cosmological regions bounded by surface-like matter overdensities where the strength of gravity would be different from other regions. Thus, the expansion rate within these regions would be different as would be the growth rate of cosmological perturbations and formation of structure. This inhomogeneity of the expansion rate could be detectable as anisotropies of the SNIa luminosity distances at a given redshift and could also be related with some of the observed cosmic dipoles (alpha dipole, quasar dipole etc). These observations could be used to impose bounds on the explicit symmetry breaking parameter ε .

The variation of the growth rate of cosmological perturbations among different domains could manifest itself as variation of the cluster properties including the cluster pressure and density profiles [1256, 1257]

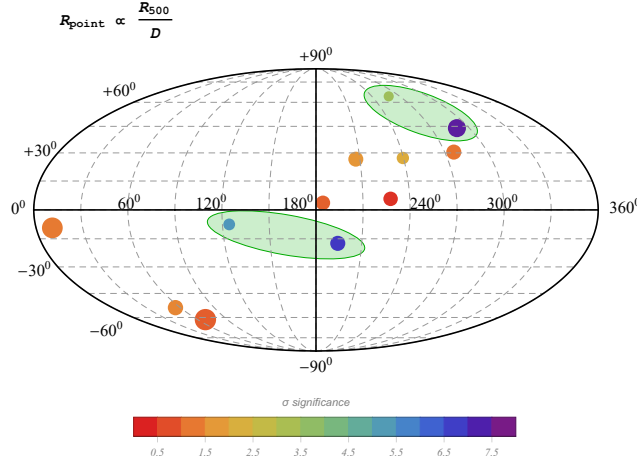


Figure 11.8: Mollweide projection view of 12 cluster locations of Ref. [57] in galactic coordinates (see Table H.1). The colour of the points on the plot corresponds to their σ significance for a deviation from the GR, which is indicated in the horizontal colour bar. Four clusters (in shaded green regions-bubbles) have large negative value for Ξ_1 parameter, significantly ($> 3\sigma$) different from the GR ($\Xi_1 = 0$) expectation. The size of the points R_{point} was designed according to the size of the clusters R_{500} and their distance D .

(see for a review in Refs. [1258, 1259]). Such variation in cluster properties which could be associated with properties of gravity has recently been identified in Ref. [57]. In what follows we explore the possible relevance of the results of Ref. [57] with the existence of asymmetron walls and their corresponding prediction for the existence of spatial cosmological domains with distinct properties of gravity.

Galaxy clusters are the largest gravitationally bound structures of the Cosmic Web. Thanks to the various surveys using dynamical, kinematic and weak lensing tracers, galaxy clusters can be used as a powerful cosmological probe of gravitational theories [57, 2324–2326] and screening mechanisms [2327–2329].

The cluster pressure and density profiles can be inferred using the Sunyaev-Zeldovich effect, the intergalactic gas, the so called Intra Cluster medium (ICM), the temperature from their X-ray emission and the velocities of the individual cluster members. These profiles can be used to search for possible changes of properties of gravity in different domains of cosmological space.

Recently the authors of Ref. [57] have used cluster profile properties to test and constrain the parameters of the Degenerate Higher-Order Scalar-Tensor (DHOST) theory [2330] (see also Refs. [2331–2337] for recent related studies and Refs. [103, 2338] for relevant reviews).

The modified gravitational potential for the DHOST theory in the galaxy cluster as a static spherically symmetric object is [2339–2343]

$$\frac{d\Phi(r)}{dr} = \frac{G_{\text{eff}} M(< r)}{r^2} + \Xi_1 G_{\text{eff}} \frac{d^2 M(< r)}{dr^2}, \quad (11.54)$$

where $M(< r) = \int_0^r 4\pi r'^2 \rho(r') dr'$ is the total mass (dark matter, gas, and galaxies) within the radial distance r , $G_{\text{eff}} = \tilde{\gamma} G$ is the effective Newton's constant and Ξ_1 is a dimensionless parameter which depends on the nonminimal coupling of the DHOST theory. The modified gravity parameters $\tilde{\gamma}$ and Ξ_1 can be recognized as quantifying the deviation of the DHOST theory from GR, which is recovered for $\tilde{\gamma} = 1$ and $\Xi_1 = 0$.

Ref. [57] uses cluster data profiles of the XMM-Cluster Outskirts Project (X-COP) [2344] to place constraints on the DHOST parameters defining the deviation from GR. This very large programme uses a joint analysis of XMM-Newton and Planck data and targets the outer regions ($R > R_{500}$ ⁹) of a sample of 13 massive ($10^{14}M \lesssim M_{500} \lesssim 10^{15}M$) local galaxy clusters in the redshift range $0.04 < z < 0.1$ at uniform depth.

The constraints on the DHOST parameter $\bar{\gamma} = \tilde{\gamma} \times M_{500}/M_{500}^{GR}$ and Ξ_1 as obtained for each of the clusters by Ref. [57] and the corresponding σ significance for deviation from GR expectation are shown in Table H.1 of the Appendix H. As illustrated in Fig. 11.8 4 clusters (A644, A1644, A2319 and A2255) have large negative value for Ξ_1 parameter, significantly ($> 3\sigma$) different from the GR. Also for these 4 clusters we have $\bar{\gamma} < 1$ ($G_{\text{eff}} < G$) with $\sim 2\sigma$ significance for a deviation from GR. These cluster constraints may be either interpreted as upper bounds on deviations of the DHOST parameters from their GR values or in a less conservative approach as possible hints for modification of gravity. On the contrary, the constraints on $\bar{\gamma}$ and Ξ_1 for the other 8 clusters are fully consistent with GR.

In Fig. 11.8 we show the green ellipses that surround observed regions-bubbles in space (~ 50 Mpc) where clusters with hints of weaker effective gravitational constant were found in Ref. [57]. These spatial sectors where the properties of gravity may be distinct from other regions may be consistent with the existence of asymmetron walls separating these sectors from other spatial sectors with slightly different properties of gravity.

11.5 Conclusions

In this Chapter we have generalized the symmetron screening mechanism by allowing for an explicit symmetry breaking of the symmetron ϕ^4 potential by the cubic term $\varepsilon\phi^3$. In such a screening scalar field (the *asymmetron*) the two local minima of the potential in low density regions are neither degenerate nor symmetric ($\phi_+ \neq -\phi_-$). Thus the asymmetron domain wall network that may form includes a transition in the value of the Jordan frame effective gravitational constant as the asymmetron wall is crossed.

We have implemented numerical energy minimization and simulation of evolution of spherical symmetron and asymmetron domain walls in the presence of a matter shell. We have thus demonstrated that the walls get trapped by matter overdensity shells as expected preventing the collapse of spherical symmetron and asymmetron walls and leading to stable spherical wall configurations. We have used a simple analytical energetic argument to describe this stabilization mechanism. The relevance of these asymmetron wall configurations with recent cluster profile data which may be interpreted as hinting towards distinct gravitational properties of certain clusters has also been discussed.

The possible existence of an asymmetron wall network pinned on matter overdensities separating regions with distinct gravitational properties could constitute a physical mechanism for the realization of gravitational transitions in redshift space that could help in the resolution of the Hubble and growth tensions as described in the Introduction. In this context, a wide range of possible extensions of the present analysis could be considered. Such extensions include the following:

- The search for anisotropies of the Hubble expansion rate in certain cosmological regions surrounded by matter overdensities which can not be explained by the observed sign and level of matter underdensities. If such local modifications of the Hubble expansion rate can not be explained by matter underdensities, they could be attributed to local modifications of the Friedmann equation due to local modifications of the properties of gravity.
- The comparison of the growth rate of cosmological perturbations in different cosmological spatial sectors using for example weak lensing, cluster count and/or redshift space distortion data.

⁹For a given overdensity Δ , the radius R_Δ is determined as the distance from the halo centre within which the mean density is Δ times the critical density, $\rho_c(z) = 3H^2(z)/(8\pi G)$, at the halo redshift. Thus $\Delta\rho_c(z) = M_\Delta/(4/3\pi R_\Delta^3)$, where M_Δ is the halo mass i.e. the mass enclosed in R_Δ .

- The implementation of N-body simulations is order to identify signatures of asymmetron walls on the large scale structure power spectrum and on the ISW effect.
- The construction of other physically motivated mechanisms that could lead to spatial gravitational transitions at low redshifts e.g. in the context of scalar tensor theories false vacuum decay.

In conclusion, the asymmetron model offers an interesting alternative modification of GR in distinct spatial sectors. The predicted gravitational transition in redshift space could lead to the resolution of the important cosmological tensions of the standard Λ CDM cosmology [7, 10, 127, 185]. Observable new effects and new physics beyond the standard model could also be realized in the context of the asymmetron domain wall network and corresponding constraints on the explicit symmetry breaking parameter can be imposed.

Chapter 12

Summary-Conclusions-Outlook

In this last chapter, we present the summary and the conclusions of this dissertation and the possible extensions. Existing and upcoming missions/experiments are presented which are expected to improve the quality and quantity of data. The analysis of these data may provide answers to the interesting open cosmological questions examined in this dissertation.

12.1 Summary and Conclusions

In Chapter 1, we reviewed the basic principles of the GR, the Cosmology and the Λ CDM cosmological model. In the Chapters 2 and 3, we discussed in a unified manner many existing curiosities in cosmological and astrophysical data that appear to be in some tension (2σ or larger) with the standard Λ CDM model as specified by the Planck18 parameter values. The Hubble tension is the most significant observational indication that the current standard model Λ CDM may need to be modified after more than 20 years since its establishment. In addition to the well known tensions (H_0 tension, S_8 tension and A_L anomaly), we provided a list of the non-standard cosmological signals in cosmological data. We presented the current status of these signals and their level of significance and also referred to recent resources where more details can be found for each signal. These signals have a lower statistical significance level than the H_0 tension but may also constitute hints towards new physics. We also briefly discussed possible theoretical approaches that have been considered in order to explain the non-standard nature of these signals. We also discussed the possible generic extensions of Λ CDM model. Generic extensions of Λ CDM may allow for a redshift dependence of the parameters w , μ_G , Σ_G and α as well as a possible large scale spatial dependence of these parameters which could violate the cosmological principle. *Varying fundamental constants* can potentially address the Hubble tension, the fine structure constant α dipole, the lithium problem, the growth tension, the curious SnIa M signals (variation of the SnIa absolute magnitude \mathcal{M}), quasar signals and the ISW CMB signal. In view of the above discussion of Chapters 2 and 3, the strategic approach required for the identification of new physics may include the following three steps:

- Tune current missions towards verification or rejection of non-standard signals.
- Identify favored parametrizations of $H(z, w(z), r)$, $\mu_G(z, r)$, $\Sigma_G(z, r)$, $\alpha(z, r)$ assuming that at least some of the non-standard signals are physical.
- Identify theoretical models (field Lagrangians) that are consistent with these parametrizations that can address simultaneously more than one of these tensions. Interestingly, for example only a small subset of modified gravity models is consistent with the weak gravity + Λ CDM background [6, 1823, 2345, 2346] suggested in the context of the S_8 tension.

In Chapter 4, we determined the optimum and the blind redshift ranges of basic cosmological observables with respect to three cosmological parameters: the matter density parameter Ω_m , the equation

of state parameter w (assumed constant), and a modified gravity parameter g_a which parametrizes a possible evolution of the effective Newton's constant as $G_{\text{eff}}(z) = G(1 + g_a(1 - a)^2 - g_a(1 - a)^4)$. We considered the following observables: the growth rate of matter density perturbations expressed through $f(z)$ and $f\sigma_8(z)$, the distance modulus $\mu(z)$, baryon acoustic oscillation observables, $H(z)$ measurements and the gravitational wave luminosity distance. We introduced a new statistic $S_P^O(z) \equiv \frac{\Delta O}{\Delta P}(z) \cdot V_{\text{eff}}^{1/2}$ including the effective survey volume V_{eff} , as a measure of the constraining power of a given observable O with respect to a cosmological parameter P as a function of redshift z . We found blind redshift spots z_b ($S_P^O(z_b) \simeq 0$) and optimal redshift spots z_s ($S_P^O(z_s) \simeq \text{max}$) for the above observables with respect to the parameters Ω_m , w and g_a . We found that probing high redshifts may in some cases be less effective than probing lower redshifts with higher accuracy. An interesting extension of our analysis could involve the consideration of other observables and additional cosmological parameters (e.g. an equation of state parameter that evolves with redshift). The existence of blind spots could be avoided by considering various functions and/or combinations of cosmic observables designed in such a way as to optimize sensitivity for given cosmological parameters in a given redshift range. The investigation of the efficiency of such combinations is also an interesting extension of our analysis.

In Chapter 5, we considered a class of simple spherically symmetric metrics in $3 + 1$ dimensions and identified the profiles and properties of the perfect fluids that can give rise to such metrics. We assumed spherical symmetry and used it to dimensionally reduce the $3+1$ dimensional Einstein-Hilbert action to an effective two dimensional scalar-tensor action with a constant potential. We generalized this geometric potential thus modifying the gravitational action to an arbitrary form and derived the corresponding generalized vacuum spherically symmetric metric in terms of the geometric potential. The generalization of the scalar-tensor potential leads to an effective energy density of geometric origin which generates the same spherically symmetric metric as a corresponding spherically symmetric perfect fluid with equation of state parameter $w = -1$ and energy density $\rho_m(r) = \rho_V(r)$. This derived equivalence between geometric and matter energy density allows the reconstruction of the geometric potential by demanding that its gravitational effects in the vacuum should be identical with the gravitational effects of a given matter fluid in the context of GR. We considered special forms of the geometric potential and of the background fluid and derived the corresponding metric. Thus the case of a constant potential (GR) we derived the Schwarzschild vacuum metric while for a simple quadratic potential we obtained the Rindler acceleration and cosmological constant terms. We also reconstructed the geometric potential that leads to a vacuum metric that is identical with the metric derived assuming a given dark matter fluid density profile in the context of GR. In the context of a particular example we assumed a NFW density profile and derived the corresponding geometric potential and vacuum metric. We showed that this metric generalizes the Rindler term of the Grumiller metric and showed fits of the velocity profiles it generates on typical galactic velocity rotation data. Generally, the dimensional reduction in the context of spherical symmetry can provide an interesting point of view for the modification of GR and can lead to a wide range of modified gravity models.

The existence of the cosmological particle horizon as the maximum measurable length l_{max} in the universe leads to a generalization of the quantum uncertainty principle (GUP) to the form $\Delta x \Delta p \geq \frac{\hbar}{2} \frac{1}{1 - \alpha \Delta x^2}$, where $\alpha \equiv l_{\text{max}}^{-2}$. The implication of this GUP and the corresponding generalized commutation relation $[x, p] = i\hbar \frac{1}{1 - \alpha x^2}$ on simple quantum mechanical systems has been discussed recently [55] and shown to have extremely small (beyond current measurements) effects of the energy spectra of these systems due to the extremely large scale of the current particle horizon. This may not be the case in the Early Universe during the quantum generation of the inflationary primordial fluctuation spectrum. In Chapter 6, we estimated the effects of such GUP on the primordial fluctuation spectrum and on the corresponding spectral index. In particular motivated by the above GUP we generalized the field commutation (GFC) relation to $[\varphi(\mathbf{k}), \pi_\varphi(\mathbf{k}')] = i\delta(\mathbf{k} - \mathbf{k}') \frac{1}{1 - \mu \varphi^2(\mathbf{k})}$, where $\mu \simeq \alpha^2 \equiv l_{\text{max}}^{-4}$ is a GFC parameter, φ denotes a scalar field and π_φ denotes its canonical conjugate momentum. In the context of this GFC we used standard methods to obtain the primordial scalar perturbations spectrum and showed that it is of the form $P_S(k) = P_S^{(0)}(k) \left(1 + \frac{\bar{\mu}}{k}\right)$ where $\bar{\mu} \equiv \mu V_* \simeq \sqrt{\alpha} = l_{\text{max}}^{-1}$ (here $V_* \simeq l_{\text{max}}^3$ is the volume corresponding to the maximum measurable scale l_{max}) and $P_S^{(0)}(k)$ is the standard primordial spectrum

obtained in the context of the Heisenberg uncertainty principle (HUP $\mu = 0$). We showed that the scalar spectral index predicted by the model, defined from $P_S(k) = A_S k^{n_s - 1}$ is running and may be written as $n_s = 1 - \lambda - \frac{\epsilon}{k}$ with $\lambda = 6\epsilon - 2\eta$ (where ϵ and η are the slow-roll parameters). Using observational constraints on the scale dependence of the spectral index n_s a cosmological constraint may be imposed on $\bar{\mu}$ as $\bar{\mu} = (0.9 \pm 7.6) \cdot 10^{-6} h/\text{Mpc}$. Using this result we estimated the GUP parameter $\alpha \lesssim 10^{-54} \text{ m}^{-2}$ at 1σ and $\alpha \lesssim 10^{-52} \text{ m}^{-2}$ at 2σ . The 2σ range of α corresponds to $l_{max} \gtrsim 10^{26} \text{ m}$ which is of the same order as the current particle horizon. Thus the assumption that a maximum measurable length could emerge as a result of presence of the cosmological particle horizon remains a viable assumption at the 2σ level. An interesting extension of this analysis would be the consideration of other types of GUP (e.g. the UV cutoff GUP of Eq. (6.1)) and the derivation of constraints on the corresponding fundamental parameters using cosmological data and constraints on the power spectrum index.

An alternative approach in deriving the effects of a GUP on the primordial perturbation spectrum involves the generalization of the position and momentum operators as described in the Section 6.1, but with an ultraviolet rather than infrared cutoff, while keeping the field theoretical commutation relations unchanged [2347, 2348]. According to [2347, 2348], this approach would also lead to a modification of the evolution of the field perturbation modes Eq. (6.49) even though this equation is derived before quantization at the classical level. This approach is questionable as it is implemented at the classical level. Nevertheless, it would be of interest to extend our analysis to include such effects of modification of the classical evolution of field perturbations due to a generalization of position and momentum operators.

In Chapter 7, we constructed an up to date compilation of E_G statistic data including both redshift and scale dependence. The E_G statistic c has been proposed as a model independent test of any MG theory. It is a powerful probe for detecting deviations from GR by combining weak lensing (WL), real-space clustering and redshift space distortion (RSD) measurements thus probing both the lensing and the growth effective Newton constants (G_L and G_{eff}). We combined the E_G data compilation with an up to date compilation of $f\sigma_8$ data from RSD observations to identify the current level of tension between the Planck/ Λ CDM standard model based on general relativity and a general model independent redshift evolution parametrization of G_L and G_{eff} . Each $f\sigma_8$ datapoint considered has been published separately in the context of independent analyses of distinct galaxy samples. However, there are correlations among the datapoints considered due to overlap of the analyzed galaxy samples. Due to these correlations the derived levels of tension of the best fit parameters with Planck/ Λ CDM are somewhat overestimated but this is the price to pay for maximizing the information encoded in the compilation considered. We find that the level of tension increases from about 3.5σ for the $f\sigma_8$ data compilation alone to about 6σ when the E_G data are also included in the analysis. The direction of the tension is the same as implied by the $f\sigma_8$ RSD growth data alone (lower Ω_m and/or weaker effective Newton constant at low redshifts for both the lensing and the growth effective Newton constants (G_L and G_{eff})). These results further amplify the hints for weakening modified gravity discussed in other recent analyses [67, 148, 1197, 1978].

The introduction of the MG parameters $\mu_G(a, k) \equiv \frac{G_{\text{eff}}(a, k)}{G}$ and $\Sigma_G(a, k) \equiv \frac{G_L(a, k)}{G}$ along with the variation of the matter density parameter Ω_m and the rms matter density fluctuations within spheres of radius $8h^{-1} \text{ Mpc}$ σ_8 leads to a model (MG- Λ CDM) that is a much better fit to the growth $f\sigma_8$ and E_G data than the Planck/ Λ CDM model in the context of GR. We have called this effect a 'tension' between the new best fit parameter values (MG- Λ CDM) and the GR-Planck/ Λ CDM parameter values (from Planck18 fit) which are $5-6\sigma$ away from the new best fit parameter values. On the other hand, the MG parameters do not seem to change significantly the fit of the Planck data as indicated in Ref. [1978] and in Planck18 [14] which indicate that pure CMB data appear to favor GR. Thus, the particular parametrization we have used does not seem to significantly reduce the tension between CMB and growth/weak lensing data since MG gravity appears to be favored by growth/weak lensing but not by the CMB. This is an issue we plan to investigate in more detail in the future by considering e.g. different MG parametrizations for the evolution of the μ_G and Σ_G parameters that will not only improve the fit to the $f\sigma_8 / E_G$ data but also improve the fit to the CMB data where some tensions are already evident (e.g. the lensing anomaly discussed in Planck18 [14]).

It is well known that the Klein Gordon (KG) equation $\square\Phi + m^2\Phi = 0$ has tachyonic unstable modes on large scales ($k^2 < |m|^2$) for $m^2 < m_{cr}^2 = 0$ in a flat Minkowski spacetime with maximum growth

rate $\Omega_F(m) = |m|$ achieved at $k = 0$. In Chapter 8 we investigated these instabilities in a Reissner-Nordström-deSitter (RN-dS) background spacetime with mass M , charge Q , cosmological constant $\Lambda > 0$ and multiple horizons. By solving the KG equation in the range between the event and cosmological horizons, using tortoise coordinates r_* , we identified the bound states of the emerging Schrodinger-like Regge-Wheeler equation corresponding to instabilities. We found that the critical value m_{cr} such that for $m^2 < m_{cr}^2$ bound states and instabilities appear, remains equal to the flat space value $m_{cr} = 0$ for all values of background metric parameters despite the locally negative nature of the Regge-Wheeler potential for $m = 0$. However, the growth rate Ω of tachyonic instabilities for $m^2 < 0$ gets significantly reduced compared to the flat case for all parameter values of the background metric ($\Omega(Q/M, M^2\Lambda, mM) < |m|$). This increased lifetime of tachyonic instabilities is maximal in the case of a near extreme Schwarzschild-deSitter (SdS) black hole where $Q = 0$ and the cosmological horizon is nearly equal to the event horizon ($\xi \equiv 9M^2\Lambda \simeq 1$). The physical reason for this delay of instability growth appears to be the existence of a cosmological horizon that tends to narrow the negative range of the Regge-Wheeler potential in tortoise coordinates.

In Chapter 9 we considered Horndeski modified gravity models obeying stability, velocity of gravitational waves c_T equals c and quasistatic approximation (QSA) on subhorizon scales. We assume further a Λ CDM background expansion and a monotonic evolution on the cosmic background of the α functions as $\alpha_i = \alpha_{i0} a^s$ where $i = M, B$, a is the scale factor and α_{i0} (α_{M0}, α_{B0}), s are arbitrary parameters. We showed that the growth and lensing reduced (dimensionless) gravitational couplings $\mu_G \equiv G_{\text{growth}}/G$, $\Sigma_G \equiv G_{\text{lensing}}/G$ exhibit the following generic properties today: $\Sigma_{G,0} < 1$ for all viable parameters, $\mu_{G,0} < 1$ (weak gravity today) is favored for small s while $\mu_{G,0} > 1$ is favored for large s . We established also the relation $\mu_G \geq \Sigma_G$ at all times. Taking into account the $f\sigma_8$ and E_G data constrained the parameter s to satisfy $s \lesssim 2$. Hence these data selected essentially the weak gravity regime today ($\mu_{G,0} < 1$) when $s < 2$, while $\mu_{G,0} > 1$ subsists only marginally for $s \approx 2$. At least the interval $0.5 \lesssim s \lesssim 2$ would be ruled out in the absence of screening. We considered further the growth index $\gamma(z)$ and identified the $(\alpha_{M0}, \alpha_{B0}, s)$ parameter region that corresponds to specific signs of the differences $\gamma_0 - \gamma_0^{\Lambda CDM}$, and $\gamma_1 - \gamma_1^{\Lambda CDM}$, where $\gamma_0 \equiv \gamma|_{z=0}$ and $\gamma_1 \equiv \frac{d\gamma}{dz}|_{z=0}$. In this way important information is gained on the past evolution of μ_G . We obtained in particular the signature $\gamma_0 > \gamma_0^{\Lambda CDM}$ for $s < 2$ in the selected weak gravity region.

In Chapter 10 we re-analyzed the Cepheid data used to infer the value of the Hubble constant H_0 by calibrating Type Ia supernovae. We did not enforce a universal value of the empirical Cepheid calibration parameters R_W (Cepheid Wesenheit color-luminosity parameter) and M_H^W (Cepheid Wesenheit H-band absolute magnitude). Instead we allowed for variation of either of these parameters for each individual galaxy. We also considered the case where these parameters have two universal values: one for low galactic distances $D < D_c$ and one for high galactic distances $D > D_c$ where D_c is a critical transition distance. We found hints for a 3σ level mismatch between the low and high galactic distance parameter values. We then used model selection criteria (AIC and BIC) which penalize models with large numbers of parameters, to compare and rank the following types of R_W and M_H^W parameter variations: Base models: Universal values for R_W and M_H^W (no parameter variation), I: Individual fitted galactic R_W with one universal fitted M_H^W , II: One universal fixed R_W with individual fitted galactic M_H^W , III: One universal fitted R_W with individual fitted galactic M_H^W , IV: Two universal fitted R_W (near and far) with one universal fitted M_H^W , V: One universal fitted R_W with two universal fitted M_H^W (near and far), VI: Two universal fitted R_W (near and far) with two universal fitted M_H^W (near and far). We found that the AIC and BIC model selection criteria consistently favor model IV instead of the commonly used Base model where no variation is allowed for the Cepheid empirical parameters. The best fit value of the SnIa absolute magnitude M_B and of H_0 implied by the favored model IV is consistent with the inverse distance ladder calibration based on the CMB sound horizon $H_0 = 67.4 \pm 0.5 \text{ km s}^{-1} \text{ Mpc}^{-1}$. Thus in the context of the favored model IV the Hubble crisis is not present. This model may imply the presence of a fundamental physics transition taking place at a time more recent than 100 Myrs ago.

In Chapter 11, we generalized the symmetron screening mechanism by allowing for an explicit symmetry breaking of the symmetron ϕ^4 potential. A coupling to matter of the form $A(\phi) = 1 + \frac{\phi^2}{M^2}$ leads to

Table 12.1: Some existing and upcoming large-scale structure missions/experiments.

Experiments	Type	Probes	Redshift	Wavelengths	Operator	Duration	Refs.
Euclid	Space	WL, BAO	$z \lesssim 6$	550 nm – 2 μ m	ESA	> 2023	[2349]
Vera C. Rubin	Ground	WL, BAO	$z \lesssim 7.5$	320 – 1060 nm	LSST	> 2022	[2350]
Gaia	Space	Astrometry	$z \simeq 0$	320 – 1000 nm	ESA	> 2013	[1705]
JWST	Space	WL	$z \lesssim 15$	0.6 – 28.3 μ m	NASA-ESA-CSA	> 2021	[2351]
GAUSS	Space	WL 3×2 pt	$z \lesssim 5$	0.5 – 5 nm		> 2035	[2352]

Table 12.2: Some existing and upcoming CMB missions/experiments.

Experim.	Type	Detectors	Frequencies ¹ (GHz)	Resolution ² (arcmin)	Sensitivity ³ (μ K arcmin)	Sky Cover	Duration	Refs.
Planck	Space	74	25 – 1000	5 – 33	~ 30	All	2009-2013	[908]
CMB S4	Ground	$500 \cdot 10^3$	30 – 270	0.8 – 11	~ 1	70%	> 2027	[2353]
SO LAT	Ground	$30 \cdot 10^3$	27 – 280	0.1	~ 6	40%	> 2021	[2354]
SO SATs	Ground	$30 \cdot 10^3$	90 – 280	0.5	~ 2	10%	> 2021	[2354]
SPT-3G	Ground	$16 \cdot 10^3$	90 – 280	1	$\sim 3.5, 6$	10%	> 2017	[2355]

an explicitly broken symmetry with effective potential $V_{\text{eff}}(\phi) = -\mu^2(1 - \frac{\rho}{\mu^2 M^2})\phi^2 + \frac{\lambda}{2}\phi^4 + 2\varepsilon\phi^3 + \frac{\lambda}{2}\eta^4$. Due to the explicit symmetry breaking induced by the cubic term we called this field the ‘asymmetron’. For large matter density $\rho > \rho_* \equiv \mu^2 M^2 + \frac{9}{4}\varepsilon\eta M^2$ the effective potential has a single minimum at $\phi = 0$ leading to restoration of GR as in the usual symmetron screening mechanism. For low matter density however, there is a false vacuum and a single true vacuum due to the explicit symmetry breaking. We presented the energetics and dynamics of spherical symmetron and asymmetron domain walls. We implemented numerical energy minimization and simulation of evolution of spherical symmetron and asymmetron domain walls in the presence of a matter shell. Thus we demonstrated that the walls get trapped by matter overdensity shells as expected preventing the collapse of spherical symmetron and asymmetron walls and leading to stable spherical wall configurations. We also pointed out that recent cluster profile data may be interpreted as revealing spatial cosmological sectors where distinct properties of gravity are present. This may be an interesting observational gravitational and expansion rate transition in redshift space. Such a transition has been recently proposed for the resolution of the Hubble and growth tensions.

Table 12.3: Some existing and upcoming GW experiments/observatories

Experiments.	Type/Detectors	Arms	Frequencies ⁴ (Hz)	Location	Duration	Refs.
Adv. LIGO	Ground/Laser interf.	2×4 km	$10 - 10^3$	Hanford, USA	> 2015	[439]
Adv. LIGO	Ground/Laser interf.	2×4 km	$10 - 10^3$	Livingston, USA	> 2015	[439]
Adv. Virgo	Ground/Laser interf.	2×3 km	$10 - 10^3$	Pisa, Italy	> 2016	[440]
KAGRA	Undergr./Laser interf.	2×3 km	$10 - 10^3$	Kamioka, Japan	> 2020	[2365]
CE	Ground/Laser interf.	2×40 km	$5 - 4 \cdot 10^3$	USA	> 2030	[2366]
LISA	Space/Laser interf.	3×2.5 Gm	$10^{-4} - 10^{-1}$	Heliocentric orbit	> 2034	[2367]
Taiji	Space/Laser interf.	3×2 Gm	$10^{-4} - 10^{-1}$	Heliocentric orbit	> 2033	[2368]
TianQin	Space/Laser interf.	3×0.1 Gm	$10^{-4} - 1$	Geocentric orbit	> 2035	[2369]
DECIGO	Space/Laser interf.	$4 \times 3 \times 1$ Mm	$1 - 10$	Heliocentric orbit	> 2027	[2370]
ET	Undergr./Laser interf.	$3 \times 2 \times 10$ km	$1 - 10^4$		> 2035	[2371]

12.2 Existing and Upcoming missions/experiments

In the next decades new observational data from existing and upcoming missions/experiments (see Tables 12.1, 12.2 and 12.3) will improve measurements and open up a wide range of new directions in the explanation of the curiosities of Λ CDM cosmology and understanding of cosmological physics. Here we provide an incomplete list of these missions:

- Euclid:** The European Space Agency (ESA) Euclid mission [2349] is planned for launch in 2023. The goals of Euclid are to investigate the nature of dark matter, dark energy and gravity and thus to provide a better knowledge of the origin of the accelerated expansion of the Universe [2349, 2372–2375]. The optical and near-infrared (NIR) Euclid survey using the cosmological WL and BAO probes will detect a high number of galaxy clusters up to redshift $z \sim 2$ (and possibly higher) in a redshift range that is sensitive to dark energy [2376] and will provide consistent growth rate data in both the low- z and high- z regimes. Therefore, Euclid will improve significantly the constraints on cosmological parameters such as σ_8 and the mass density parameter Ω_{0m} with a precision of $\sim 10^{-3}$ for Λ CDM [2374]. The Euclid survey will also measure the equation of state parameter of dark energy w_{DE} with higher precision ($\sim 1\%$) than precursor surveys. Stochastic inhomogeneities are expected to lead to an intrinsic uncertainty in the values of cosmological parameters obtained with such high redshift surveys. The corresponding cosmic variance in the context of Euclid for the measurement of H_0 has been shown to be limited to about 0.1% [2377]. Thus Euclid and other deep surveys ($z \gtrsim 0.15$) will provide an estimation of the H_0 which will be more precise than the low redshift surveys ($z \lesssim 0.15$). Such improved constraints from Euclid in combination with contemporary surveys will allow the verification or rejection of many of the non-standard signals discussed in this review and will also help distinguish among the favored theoretical models that have been proposed for the explanation of these signals.
- Vera C. Rubin Observatory Legacy Survey of Space and Time:** The Large Synoptic Survey Telescope (LSST), recently renamed the Vera C. Rubin Observatory LSST [2350, 2378] is a future survey of the southern sky planned for the beginning in 2022. The Vera C. Rubin Observatory based in Chile with an 8.4 m (6.5 m effective) telescope in six bands, targeting at least 18,000 deg^2 of high galactic latitude sky, will provide databases including 25 billion galaxies with $\gtrsim 0.2$ arcsecond pixel

sampling [2379]. The main cosmological goals of the Vera C. Rubin Observatory ground-based project are to investigate the nature of dark matter and the dynamical behavior of dark energy by measuring WL and BAO [2379]. Vera C. Rubin observatory will detect enormous number of galaxies and in combination with the Euclid BAO survey will probe an unprecedented range of redshifts. These surveys can determine $w_{DE}(z)$ in bins of redshift and their dark energy constraining power could be orders of magnitude greater than that of precursor surveys [2380]. The provided improved constraints on cosmological parameters allow to address potential systematics and to ensure that any measured tension is robust. In addition, the Vera C. Rubin project would be a useful tool in testing the models which have been used to explain these tensions.

- **CMB-S4:** The fourth generation⁵ (Stage-4) ground-based CMB experiment (CMB-S4) [2353, 2381, 2382], is planned to start observations in 2027. It is anticipated to be the definitive CMB polarization experiment. The goals of CMB-S4 are to detect the signature of primordial gravitational waves in order to shed light on models of inflation, to search for previously undiscovered light relic particles in order to study the dark Universe, to map normal and dark matter in the cosmos separately and to explore the time-variable millimeter-wave sky [2353]. The CMB-S4 survey in combination with external cluster surveys which are sensitive to different redshift ranges such as the Vera C. Rubin will provide detailed cluster data [2353]. These data will be used to study the growth of cluster scale perturbations, to improve constraints on cosmological parameters and to test the alternative models or extensions of Λ CDM which can be used to clarify the origin of many of the tensions and non-standard signals referred in the present review. The CMB-S4 will also contribute to neutrino cosmology providing compelling sensitivity in the constraint of the effective number of relativistic species, N_{eff} and of the sum of the neutrino masses $\sum m_\nu$. This project has also the potential to constrain $\Delta N_{\text{eff}} \equiv N_{\text{eff}} - N_{\text{eff}}^{\text{SM}} \simeq 0.060$ at 95% confidence level [2381]. Planck has provided a constraint $\Delta N_{\text{eff}} \simeq 0.126$ at 95% confidence level using temperature and polarization TT, TE, EE + lowE data [14]. The improved constraints on N_{eff} will enable us to test the scenarios with modifications of Λ CDM model in the light relic sector.
- **Gaia:** The Gaia satellite was launched at the end of 2013 [1704, 1705]. This European Space Agency (ESA) mission Gaia provides data that allow us to determine with high accuracy positions, parallaxes and proper motions for more than 1 billion sources. There have been two data releases GDR1 [2383] and GDR2 [296] of Gaia results. Using quasars Ref. [2384] finds that the GDR2 suffer from the parallax zero point (ZP) error. Ref. [40] refers to this additional error as parallax offset because it is not a single value but depends on the color or/and magnitude of the source and its position on the sky. Ref. [224] finds that the parallax offset can be measured directly from the Cepheids, but with a reduced precision of the distance scale from GDR2. This reduction leads to a increased uncertainty of the determination of H_0 value by a factor of 2.5.

Recently the Gaia team presented the Gaia Early Data Release 3 (EDR3) (the full Gaia DR3 release is expected in 2022) [180] with improved parallaxes since GDR2. Using the EDR3 parallaxes and Cepheid PL relation the latest analysis of the SH0ES Team [40] achieved a precision of 1.0% in the geometric calibration of Cepheid luminosities. The precision of the geometric calibration of Cepheids will approach 0.5% by Gaia DR4 [40]. This higher precision will be sufficient to confirm the present H_0 tension.

- **James Webb Space Telescope:** The James Webb Space Telescope (JWST or 'Webb') [2351, 2385] is a joint NASA-ESA-CSA (National Aeronautics and Space Administration -European Space Agency-Canadian Space Agency) large, cold (under 50 K), infrared optimized ($0.6 < \lambda < 28.3.0 \mu\text{m}$), space telescope and its launch is currently planned for 31 October 2021. JWST is a scientific successor to HST and will extend its discoveries to higher redshifts. It is nearly twice as big as HST with 6.6 m gold-plated primary mirror much larger than 2.4 m of HST.

⁵Planck was the third generation space mission which mapped the anisotropies of CMB.

The two main goals of this upcoming, next-generation telescope are to look much closer to the Big Bang and to investigate the light from the first stars and galaxies that formed in the Universe (see Ref. [2351], for other goals). The observational data of this mission will essentially enhance our understanding of the formation and evolution of galaxies, stars, and planetary systems. The JWST will detect galaxies out to a redshift of $z \geq 15$. It will probably be able to detect Pop III stars (see Subsection 3.7) in the high-redshift galaxies [2386, 2387] in a mass range $140 - 260 M_{\odot}$ as pair-instability supernovae [2388, 2389]. Various projects using the JWST observations will provide stronger nucleosynthesis constraints inside the first supernova [1695] and constraints on the nature of dark matter [2390, 2391]. These constraints and other unprecedented information from JWST could potentially help address the lithium problem, explain small-scale curiosities and improve constraints on the age of Universe.

- **Simons Observatory:** The Simons Observatory (SO) [2354, 2392, 2393] is a next generation CMB ground-based experiment. SO consists of one 6 m Large Aperture Telescope (LAT) and three 0.42 m Small Aperture Telescopes (SATs) at the Atacama Desert, Chile. It will provide more accurate measurements of the primary CMB temperature and polarization signals. The main targets of SO as described by [2354] are: primordial perturbations, effective number of relativistic species, neutrino mass, deviations from Λ CDM, galaxy evolution (feedback efficiency and non-thermal pressure in massive halos) and reionization (measurement of duration). Also a goal of SO survey is to provide a catalog of 16,000 galaxy clusters and more than 20,000 extragalactic sources. The sky region from SO survey overlaps with many surveys such as LSST, DES, DESI and Euclid at different wavelengths [2354]. This overlap is extremely beneficial as it will allow data cross correlation tests (see Ref. [2394], for a detailed discussion). Like CMB-S4, SO will provide improved constraints on the effective number of relativistic species N_{eff} , the sum of the neutrino masses $\sum m_{\nu}$ and the dark energy equation of state w_{DE} (see Ref. [2354], for the forecast constraints on cosmological parameters). Also the SO and CMB-S4 experiments will measure the primordial tensor-to-scalar ratio r to a target sensitivity of $\sigma_r \sim 0.002$ (for an $r = 0$ model). This will be an improvement by a factor of approximately 5 compared to Planck sensitivity. In addition the uncertainty of the determinations of H_0 from SO will be two and five times better than that inferred from Planck and local direct measurement respectively. Therefore, the SO data will enable us to improve constraints on extensions of Λ CDM which alleviate its tensions and curiosities. In addition the improved quality of lensing data from SO as well as CMB-S4 will improve our understanding of the CMB anisotropy anomalies.
- **SPT-3G:** This is a third generation CMB experiment [337, 2355]. It uses the third survey camera SPT-3G which was installed on the South Pole Telescope (SPT) in 2017. The SPT-3G with the 10-meter diameter telescope targets at least $1,500 \text{ deg}^2$ region of low-foreground sky in three spectral bands centered at 95, 150, and 220 GHz with $\sim 16,000$ detectors (10 times more than its predecessor SPTpol [1785, 2395]).

Its scientific goals aim to constrain the physics of the cosmic inflation, to explore the neutrino sector, and to constrain the relativistic energy density of the Universe [337, 2355]. The SPT-3G survey in combination with the deep and wide optical survey DES, will provide detailed data on $\sim 200 \text{ Mpc}$ scales which may be used to test General Relativity. The SPT-3G will also provide stringent and improved constraints on the effective number of relativistic species, N_{eff} and on the sum of the neutrino masses $\sum m_{\nu}$ by synergy with Planck.

- **GAUSS:** This space mission concept combines the WL and galaxy clustering probes using three two-point correlation functions ($3 \times 2\text{pt}$ analysis) of gravitational lensing and galaxy positions: the cosmic shear, the galaxy clustering and galaxy-galaxy lensing. GAUSS aims to fully map the cosmic web up to redshift $z \sim 5$ and to provide a catalog with the spectroscopic redshifts and the shapes of 10 billions of galaxies [2352] increased by a factor of approximately 10^3 compared to DESI which measures the spectra of 35 million galaxies and quasars [451]. The very large sky coverage and the high galaxy density provided by the GAUSS will facilitate the construction of the 3D matter power

spectrum of all scales (large and small) in detail. The 3×2 pt correlation functions in combination with 3D matter power spectrum will provide stronger constraints and break parameter degeneracies [2352]. The constraining power of the GAUSS will be an order of magnitude larger than that of any currently planned projects such as Euclid and Vera C. Rubin Observatory.

- **Laser Interferometer Gravitational-Wave Observatory:** The Laser Interferometer Gravitational-Wave Observatory (LIGO) proposed by Ref. [2396] is a large-scale experiment that uses ground-based laser interferometers with $L = L_x = L_y = 4$ km long orthogonal arms to detect GWs⁶.

There are two identical LIGO instruments, one in Hanford (LHO) and one in Livingston (LLO) separated by roughly 3000 km. The principle of operation of laser interferometers [2412, 2413] is similar to that of a simple interferometer, such as that used by Michelson and Morley. Detection of GWs with strain amplitude $h \sim 10^{-21}$ by a ground detector with arms of length $L = 4$ km requires length change measurement [2412]

$$\Delta L = \delta L_x - \delta L_y \sim hL \sim 4 \cdot 10^{-18} \text{ m} . \quad (12.1)$$

For the period between 2002 and 2010, the two LIGO observatories were unable to detect GWs. The detectors were later replaced by much improved Advanced LIGO versions [439, 2414]. The improved detectors that officially went into operation in 2015 have about ten times the sensitivity to detect GWs in the frequency range around ~ 100 Hz compared to the initial LIGO interferometers [439]. In addition Advanced LIGO extends the low frequency end from 40 Hz down to 10 Hz. Much of the research and development work for LIGO/Advanced LIGO projects was based on the groundbreaking work of the GEO 600 detector [2415, 2416] which is a 600 m interferometer in Hanover, Germany.

On February 11, 2016 the LIGO Scientific Collaboration [2417] and the Virgo Collaboration [2418, 2419] announced the first directly observed GWs from a signal detected on September 14, 2015 by the Advanced LIGO devices (the Virgo was not working at the time due to an upgrade). The detected signal was named GW150914 and its source was the merger of two stellar-mass BHs [2420].

The Advanced Virgo [440] with 3 km arm length interferometer contributes to the reliability of Advanced LIGO experimental device detections allowing for greater accuracy in locating the source in the sky (triangulation i.e 3-detector localization) [2421] and more accurate reconstruction of the signal waveform (see Refs. [2422–2426], for the relevant method). For example, in the case of the event GW170814 the three detectors improved the sky localization of the source, reducing the area of the 90% credible region from 1160 deg² using only the two LIGO detectors to 60 deg² using all three LIGO/Virgo detectors and reduced the luminosity distance uncertainty from 570_{-230}^{+300} Mpc to 540_{-210}^{+130} Mpc [2427].

In 2019 the Advanced LIGO [439], the Advanced Virgo [440] and the Japanese successor of the Tama300 [2428, 2429], Kamioka Gravitational (KAGRA) wave detector [2365, 2430, 2431] (previously called LCGT [2432]) signed collaboration agreement to begin joint observation. The LIGO, Virgo and KAGRA collaboration will be probably complemented by other interferometers like the planned Indian LIGO by the Indian Initiative in Gravitational Wave Observations (IndIGO) consortium [2433]. In addition a future third-generation ground-based detector the Cosmic Explorer (CE) [2366, 2434, 2435] is envisioned to begin operation in the 2030s in the USA. It will contribute to the GW Astronomy beyond LIGO. CE with ten times longer arms (40 km) than Advanced LIGO's will amplify the amplitude of the observed signals [2436, 2437] and will significantly increase the sensitivity of the observations [2434, 2435].

⁶Another class of GW detectors are the resonant mass antennas [2397–2400] in the frequency range from 15 Hz to few kHz. The principle of operation of mass resonance detectors is related to the periodic dimensional changes caused by the ripple effect of GWs on solid bodies. The Weber bar [2401] is a first generation resonant mass detector, the ALLEGRO [2402], NAUTILUS [2403–2405], EXPLORER [2406], AURIGA [2407], NIOBE [2408, 2409] are the second generation and Mario Schenberg [2410], MiniGRAIL [2411] are the third generation.

Many events (~ 50 compact binary coalescences) were observed by the Advanced LIGO/Virgo interferometers during three observing run periods (O1, O2 and O3)⁷. The full three-detector network provided data which enabled the standard siren measurement of the Hubble constant H_0 (see Subsections 2.2.4). These data are not yet sufficiently constraining the Hubble constant but in the future they are expected to improve significantly.

- **Laser Interferometer Space Antenna:** The Laser Interferometer Space Antenna (LISA) [2367, 2440] is a large-scale space mission proposed by ESA, planned for launch in 2034. It will consist of three spacecrafts placed in an equilateral triangle with arms 2.5 million kilometers long which will be placed near the Earth in a heliocentric orbit. In order to pave the way for the LISA mission ESA launched LISA Pathfinder in 2015 and it was operational from 2016 to 2017 [2441, 2442]. The results from scientific research show that LISA Pathfinder works exactly five times better than required, with a successful demonstration of the basic technologies for a large gravitational wave observatory.

LISA is designed to detect GWs in the frequency range from 0.1 mHz to 10^{-1} Hz [2443, 2444] targeting very different source populations from ground-based detectors such as LIGO, Virgo and KAGRA which operate in the frequency range⁸ from 10 Hz to 10^3 Hz [2445].

There are many different sources of GWs (see Refs. [2446–2448], for a review of GW physics). LIGO and Virgo can detect the merger events of binaries with masses $\lesssim 100M_\odot$ while LISA will be able to detect the merger of massive BHs ($10^5 - 10^7 M_\odot$) with higher signal-to-noise ratio (SNR) and thus to perform precision tests in the strong gravity regime of Λ CDM model. LISA will detect events lasting weeks, months or years allowing us to observe a much larger volume of the Universe. It may improve our understanding of the early Universe. In addition the LISA mission will be able to detect sources like primordial BHs ($\sim 10^{-12} M_\odot$) which correspond to the mHz frequency [2449–2451]. This possibility can help to test primordial BH dark matter scenario. Finally, LISA and the Big Bang Observer (BBO) [2452, 2453], which is a proposed LISA’s successor will detect many other known or currently unknown exotic sources. Thus it will enable us to explore alternative gravity theories and to address the problems of the Λ CDM cosmology.

- **Taiji:** Taiji [2368, 2454] meaning ‘supreme ultimate’ is a Chinese large-scale space mission, planned for launch in 2033. Like LISA, Taiji is a laser interferometric GW detector which will consist of three spacecraft placed in an equilateral triangle with arms 2 million kilometers long in orbit around the Sun. Taiji will detect GWs in the frequency range from 0.1 mHz to 10^{-1} Hz. Like LISA, Taiji can detect many possible GW sources such as a stochastic GW background generated in the early Universe and the merger of two super massive BHs.

A potential LISA-Taiji network was explored by [2455, 2456]. This network with a separation distance of about 0.7 AU can accurately localize the sky position of a GW source and may completely identify the host galaxy.

- **TianQin :** TianQin [2369, 2457] is a Chinese large-scale space mission. It aims to launch a laser interferometric GW detector around 2035. Like other space-base observatories, TianQin observatory consist of three spacecrafts placed in an equilateral triangle with arms ~ 0.1 Gm long but in geocentric orbit with an orbital radius of about 10^5 km [2369, 2457]. TianQin aims to detect GWs in the frequency range from 10^{-4} Hz to 1 Hz (overlapping with that of LISA near 10^{-4} Hz and with that of DECIGO near 1 Hz). It will search for GW signals from various cosmological sources such as the inspiral of supermassive BBH [2458], stellar-mass BBH [2459], the merger of massive BBHs [2460] and stochastic GW background originating from primordial BHs [2461] and/or cosmic strings [2462]. As a precursor mission of TianQin, TianQin-1 experimental satellite has been launched on

⁷For the first Gravitational Wave Transient Catalog (GWTC-1) during O1 and O2, see in [2438] and for second Gravitational Wave Transient Catalog (GWTC-2) from the first part of the third observing run (O3a), see in [2439].

⁸The frequency range from 0.1 mHz to 10^{-1} Hz is unobservable by any proposed ground based detectors, due to seismic noise.

20 December 2019. The results from scientific research shows that TianQin-1 satellite has exceeded all of its mission requirements.

- **Deci-hertz Interferometer Gravitational wave Observatory:** The DECi-hertz Interferometer Gravitational wave Observatory (DECIGO) is a Japanese large-scale space mission [2370, 2463–2465] which was proposed by Ref. [2466] and is planned for launch in 2027. DECIGO consists of four clusters (with two of them at the same position) and each cluster consists of three spacecrafts placed in an equilateral triangle with 1000 km arm lengths in heliocentric orbit [2467]. As a precursor mission of DECIGO, B-DECIGO (smaller version of DECIGO) will be launched before 2030 with 100 km arm lengths orbiting around the earth at 2000 km altitude above the surface of the earth [2467–2469].

DECIGO is designed to detect GWs in the frequency range from 0.1 Hz to 10 Hz which is located in a gap between the frequency band of the LISA/Taiji and ground-based detectors such as advanced LIGO, advanced Virgo, and KAGRA. It aims to observe the primordial gravitational waves i.e. the beginning of the universe ($10^{-36} - 10^{-34}$ sec right after the birth of the Universe), the formation of giant black holes in the center of galaxies and the compact binaries, such as white dwarf binaries [2470].

- **Einstein Telescope:** Einstein Telescope (ET) or Einstein Observatory is a European proposed underground laser interferometric GW detector [2371]. It will be located underground at a depth of about 100 – 300 m in order to reduce the seismic noises. ET will consist of three nested detectors placed in an equilateral triangle, each in turn composed of two interferometers with arms 10 km long. Using two arms in each side of the triangle will enable the determination of the polarisation of GWs. As a third-generation observatory is targeting a sensitivity 10 times better than of current second-generation laser-interferometric detectors such as advanced LIGO, advanced Virgo, and KAGRA [2471]. ET will reduce thermal noise compared to the first and second generations of GW detectors by operating the mirrors at cryogenic temperatures as low as 10 K [2472]. It is planned to start observations in 2035 with two candidate sites: north of Lula in Sardinia (Italy) and in Meuse-Rhine Euroregion (the border area of Belgium, Germany, and the Netherlands) [2473]. ET will detect GWs in the frequency range from ~ 1 Hz to ~ 10 kHz. This will allow the detection of BNS up to a redshift of $z \sim 2$, stellar-mass BBH at $z \sim 15$, and intermediate-mass BBH ($10^2 - 10^4 M_{\odot}$) at $z \sim 5$. The observations of these standard sirens will be useful to calibrate the cosmic distance ladder and will improve the estimation of the Hubble constant.

Cosmology is entering an even more exciting era! The combination of the existing puzzling observational signals discussed in this study, along with the upcoming revolutionary improvement in the quality and quantity of data creates anticipation for exciting new effects and new physics discoveries in the coming two decades.

Appendices

Appendix A

List of Used Acronyms

In this appendix we present the list of used acronyms.

Table A.1: List of used acronyms.

Acronym	Meaning	Acronym	Meaning
ACS	Advanced Camera for Surveys	LAT	Large Aperture Telescope
ACT	Atacama Cosmology Telescope	LDE	Late Dark Energy
ACTPol	Atacama Cosmology Telescope Polarimeter	LHS	Left Hand Side
AEDGE	Atomic Experiments for Dark Matter and Gravity Exploration	LIGO	Laser Interferometer Gravitational-Wave Observatory
AGB	Asymptotic Giant Branch	LISA	Laser Interferometer Space Antenna
AGN	Active Galactic Nucleus	LiteBIRD	Lite (Light) satellite for the studies of B-mode polarization and Inflation from cosmic background Radiation Detection
AIC	Akaike Information Criterion	LMC	Large Magellanic Cloud
AO	Adaptive Optics		
AvERA	Average Expansion Rate Approximation	LOS	Line-Of-Sight
BAO	Baryon Acoustic Oscillations	LSS	Large Scale Structure
BBH	Binary Black Holes	LSST	Large Synoptic Survey Telescope
BBN	Big Bang Nucleosynthesis	LwMPT	Late $w - M$ Phantom Transition
BBO	Big Bang Observer	MCP	Megamaser Cosmology Project
BD	Brans-Dicke	MCT	Multi-Cycle Treasury
BH	Black Hole	MEDE	Modified Emergent Dark Energy
BIC	Bayesian Information Criterion	MG	Modified Gravity
BNS	Binary Neutron Stars	MGS	Main Galaxy Sample
BOSS	Baryon Oscillation Spectroscopic Survey	MM	Many Multiplet
BTFR	Baryonic Tully Fisher Relation	MOND	Modified Newtonian Dynamics
CC	Cluster Counts	MST	Mass Sheet Transformation

Continued on next page

Table A.1 – continued from previous page

Acronym	Meaning	Acronym	Meaning
CCH	Cosmic CHronometric	MW	Milky Way
CCHP	Carnegie–Chicago Hubble Program	NANOGrav	North American Nanohertz Observatory for Gravitational-waves
CDI	Cold Dark matter Isocurvature	NASA	National Aeronautics and Space Administration
CDM	Cold Dark Matter	NEDE	New Early Dark Energy
CE	Cosmic Explorer	NFW	Navarro-Frenk-White
CFHTLenS	Canada-France-Hawaii Telescope Lensing	NIR	Near InfraRed
CHP	Carnegie Hubble Program	NRAO	National Radio Astronomy Observatory
CL	Confidence Level	NS	Neutron Star
CMB	Cosmic Microwave Background	NVSS	NRAO VLA Sky Survey
COBE	Cosmic Background Explorer	PEDE	Phenomenologically Emergent Dark Energy
COSMOGRAIL	COSmological MONitoring of GRAvitational Lenses	PL	Period–Luminosity
CP	Cosmological Principle	PTAs	Pulsar Timing Arrays
CPL	Chevallier - Polarski - Linder	QFT	Quantum Field Theory
CSA	Canadian Space Agency	QNMs	QuasiNormal Modes
CSP	Carnegie Supernova Project	QG	Quantum Gravity
DE	Dark Energy	QSA	Quasi-Static Approximation
DEBs	Detached Eclipsing Binary stars	QSO	Quasi-Stellar Object (quasar)
DECIGO	DECI-hertz Interferometer Gravitational wave Observatory	RHS	Right Hand Side
DES	Dark Energy Survey	RN-dS	Reissner-Nordstrom-deSitter
DESI	Dark Energy Spectroscopic Instrument	ROSAT	ROentgen SATellite
DHOST	Degenerate Higher-Order Scalar-Tensor	RSD	Redshift Space Distortions
DIC	Deviance Information Criterion	RVM	Running Vacuum Model
DKF	Dolgov-Kawasaki-Faraoni	SALT	Spectral Adaptive Light curve Template
DM	Dark Matter	SATs	Small Aperture Telescopes
DSR	Doubly Special Relativity	SBF	Surface Brightness Fluctuations
EBL	Extragalactic Background Light	SdS	Shwarzschild-deSitter
eBOSS	Extended Baryon Oscillation Spectroscopic Survey	SDSS	Sloan Digital Sky Survey
EDE	Early Dark Energy	SH0ES	Supernovae H_0 for the Equation of State
EDGES	Experiment to Detect the Global Epoch of Reionization Signature	SIC	Sufficient for Instability Criterion
EDR	Early Data Release	SKA	Square Kilometre Array
EDS	Early Dark Sector	SLACS	Sloan Lens ACS Survey
EFTofLSS	Effective Field Theory of Large-Scale Structure	SM	Standard Model
EM	ElectroMagnetic	SMBH	SuperMassive Black Hole
EPTA	European Pulsar Timing Array	SnIa	Supernova Type Ia
eROSITA	extended ROentgen Survey with an Imaging Telescope Array	SneII	Supernovae Type II

Continued on next page

Table A.1 – continued from previous page

Acronym	Meaning	Acronym	Meaning
ESA	European Space Agency	SNR	Signal-to-Noise Ratio
ET	Einstein Telescope	SO	Simons Observatory
ETHOS	Effective THEORY Of Structure formation	SOLME	Stanford Optically Levitated Microsphere Experiment
FJ	Faber–Jackson	SPH	Smooth Particle Hydrodynamics
FLRW	Friedmann-Lemaître-Roberson-Walker	SPT	South Pole Telescope
FMOS	Fiber Multi-Object Spectrograph	SSC	Sufficient for Stability Criterion
FP	Fundamental Plane	ST	Scalar Tensor
GAMA	Galaxy and Mass Assembly	STRIDES	STRong-lensing Insights into Dark Energy Survey
GAUSS	Gravitation And the Universe from large Scale-Structures	TBTF	Too Big To Fail
GDR	Gaia Data Release	TD	Time-Delay
GEDE	Generalised Emergent Dark Energy	TDCOSMO	Time-Delay COSMOgraphy
GEHR	Giant Extragalactic HII Region	TDE	Transitional Dark Energy
GFC	Generalized Field Commutation	TFR	Tully-Fisher Relation
GGL	Galaxy-Galaxy Lensing	TGSS	TIFR GMRT Sky Survey
GLPV	Gleyzes-Langlois-Piazza-Vernizzi	TIFR	Tata Institute of Fundamental Research
GMRT	Giant Metrewave Radio Telescope	TPCF	Two-Point Correlation Functions
GP	Gaussian Process	TRGB	Tip of the Red Giant Branch
GR	General Relativity	tSZ	thermal Sunyaev-Zel’dovich
GRB	Gamma-Ray Burst	UV	Ultraviolet
GUP	Generalization of the Uncertainty Principle	UVES	Ultraviolet and Visual Echelle Spectrograph
GW	Gravitational Waves	VCDM	Vacuum Cold Dark Matter
GWTC	Gravitational Wave Transient Catalog	VHE	Very High Energy
HETDEX	Hobby Eberly Telescope Dark Energy Experiment	VIKING	VISTA Kilo-Degree Infrared Galaxy
HMF	Halo Mass Function	VIMOS	ViSible MultiObject Spectrograph
HSC	Subaru Hyper Suprime-Cam lensing survey	VIPERS	VIMOS Public Extra-galactic Redshift Survey
HST	Hubble Space Telescope	VISTA	Visible and Infrared Survey Telescope for Astronomy
HUP	Heisenberg Uncertainty Principle	VLT	Very Large Telescope
H0LiCOW	H_0 Lenses in COSMOGRAIL’s Well-spring	VM	Vacuum Metamorphosis
ICM	IntraCluster Medium	VSF	Violent Star Formation
IDE	Interacting Dark Energy	VVDS	VIMOS-VLT Deep Survey
IGM	InterGalactic Medium	WFIRST	Wide Field Infrared Survey Telescope
ISW	Integrated Sachs–Wolfe	WISE	Wide-field Infrared Survey Explorer
JWST	James Webb Space Telescope	WKB	Wentzel-Kramers-Brillouin
IndIGO	Indian Initiative in Gravitational wave Observations consortium	WL	Weak Lensing
IPTA	International Pulsar Timing Array	WMAP	Wilkinson Microwave Anisotropy Probe
JLA	Joint Light-curve Analysis	WtG	Weighting the Giant

Continued on next page

Table A.1 – continued from previous page

Acronym	Meaning	Acronym	Meaning
KAGRA	Kamioka Gravitational	ZTF	Zwicky Transient Facility
KG	Klein Gordon	2dFGRS	2-degree Field Galaxy Redshift Survey
KiDS	Kilo Degree Survey	2dFlenS	2-degree Field Lensing Survey
		6dFGS	6-degree Field Galaxy Survey

Appendix B

Constraining Power of Cosmological Observables on Cosmological Parameters as a Function of Redshift

B.1 Data Used in the Analysis

In this appendix we present the data used in our analysis.

Table B.1: The compilation of RSD data used in our analysis (from Ref. [67]).

Index	Dataset	z	$f\sigma_8(z)$	Refs.	Year	Fiducial Cosmology
1	SDSS-LRG	0.35	0.440 ± 0.050	[2474]	2006	$(\Omega_m, \Omega_K, \sigma_8) = (0.25, 0, 0.756)$ [340]
2	VVDS	0.77	0.490 ± 0.18	[2474]	2009	$(\Omega_m, \Omega_K, \sigma_8) = (0.25, 0, 0.78)$
3	2dFGRS	0.17	0.510 ± 0.060	[2474]	2009	$(\Omega_m, \Omega_K) = (0.3, 0, 0.9)$
4	2MRS	0.02	0.314 ± 0.048	[2475], [2476]	2010	$(\Omega_m, \Omega_K, \sigma_8) = (0.266, 0, 0.65)$
5	SnIa+IRAS	0.02	0.398 ± 0.065	[1549], [2476]	2011	$(\Omega_m, \Omega_K, \sigma_8) = (0.3, 0, 0.814)$
6	SDSS-LRG-200	0.25	0.3512 ± 0.0583	[1315]	2011	$(\Omega_m, \Omega_K, \sigma_8) = (0.276, 0, 0.8)$
7	SDSS-LRG-200	0.37	0.4602 ± 0.0378	[1315]	2011	
8	SDSS-LRG-60	0.25	0.3665 ± 0.0601	[1315]	2011	$(\Omega_m, \Omega_K, \sigma_8) = (0.276, 0, 0.8)$
9	SDSS-LRG-60	0.37	0.4031 ± 0.0586	[1315]	2011	
10	WiggleZ	0.44	0.413 ± 0.080	[351]	2012	$(\Omega_m, h, \sigma_8) = (0.27, 0.71, 0.8)$
11	WiggleZ	0.60	0.390 ± 0.063	[351]	2012	
12	WiggleZ	0.73	0.437 ± 0.072	[351]	2012	
13	6dFGS	0.067	0.423 ± 0.055	[355]	2012	$(\Omega_m, \Omega_K, \sigma_8) = (0.27, 0, 0.76)$
14	SDSS-BOSS	0.30	0.407 ± 0.055	[1317]	2012	$(\Omega_m, \Omega_K, \sigma_8) = (0.25, 0, 0.804)$
15	SDSS-BOSS	0.40	0.419 ± 0.041	[1317]	2012	
16	SDSS-BOSS	0.50	0.427 ± 0.043	[1317]	2012	
17	SDSS-BOSS	0.60	0.433 ± 0.067	[1317]	2012	
18	Vipers	0.80	0.470 ± 0.080	[1327]	2013	$(\Omega_m, \Omega_K, \sigma_8) = (0.25, 0, 0.82)$
19	SDSS-DR7-LRG	0.35	0.429 ± 0.089	[2477]	2013	$(\Omega_m, \Omega_K, \sigma_8) = (0.25, 0, 0.809)$ [45]
20	GAMA	0.18	0.360 ± 0.090	[2478]	2013	$(\Omega_m, \Omega_K, \sigma_8) = (0.27, 0, 0.8)$
21	GAMA	0.38	0.440 ± 0.060	[2478]	2013	
22	BOSS-LOWZ	0.32	0.384 ± 0.095	[2479]	2013	$(\Omega_m, \Omega_K, \sigma_8) = (0.274, 0, 0.8)$
23	SDSS DR10+DR11	0.32	0.48 ± 0.10	[2479]	2013	$(\Omega_m, \Omega_K, \sigma_8) = (0.274, 0, 0.8)$ [2480]
24	SDSS DR10+DR11	0.57	0.417 ± 0.045	[2479]	2013	

25	SDSS-MGS	0.15	0.490 ± 0.145	[1319]	2015	$(\Omega_m, h, \sigma_8) = (0.31, 0.67, 0.83)$
26	SDSS-veloc	0.10	0.370 ± 0.130	[2481]	2015	$(\Omega_m, \Omega_K, \sigma_8) = (0.3, 0, 0.89)$ [2482]
27	FastSound	1.40	0.482 ± 0.116	[1326]	2015	$(\Omega_m, \Omega_K, \sigma_8) = (0.27, 0, 0.82)$ [2483]
28	SDSS-CMASS	0.59	0.488 ± 0.060	[2484]	2016	$(\Omega_m, h, \sigma_8) = (0.307115, 0.6777, 0.8288)$
29	BOSS DR12	0.38	0.497 ± 0.045	[48]	2016	$(\Omega_m, \Omega_K, \sigma_8) = (0.31, 0, 0.8)$
30	BOSS DR12	0.51	0.458 ± 0.038	[48]	2016	
31	BOSS DR12	0.61	0.436 ± 0.034	[48]	2016	
32	BOSS DR12	0.38	0.477 ± 0.051	[2485]	2016	$(\Omega_m, h, \sigma_8) = (0.31, 0.676, 0.8)$
33	BOSS DR12	0.51	0.453 ± 0.050	[2485]	2016	
34	BOSS DR12	0.61	0.410 ± 0.044	[2485]	2016	
35	Vipers v7	0.76	0.440 ± 0.040	[2486]	2016	$(\Omega_m, \sigma_8) = (0.308, 0.8149)$
36	Vipers v7	1.05	0.280 ± 0.080	[2486]	2016	
37	BOSS LOWZ	0.32	0.427 ± 0.056	[1325]	2016	$(\Omega_m, \Omega_K, \sigma_8) = (0.31, 0, 0.8475)$
38	BOSS CMASS	0.57	0.426 ± 0.029	[1325]	2016	
39	Vipers	0.727	0.296 ± 0.0765	[2487]	2016	$(\Omega_m, \Omega_K, \sigma_8) = (0.31, 0, 0.7)$
40	6dFGS+SnIa	0.02	0.428 ± 0.0465	[2488]	2016	$(\Omega_m, h, \sigma_8) = (0.3, 0.683, 0.8)$
41	Vipers	0.6	0.48 ± 0.12	[1989]	2016	$(\Omega_m, \Omega_b, n_s, \sigma_8) = (0.3, 0.045, 0.96, 0.831)$ [16]
42	Vipers	0.86	0.48 ± 0.10	[1989]	2016	
43	Vipers PDR-2	0.60	0.550 ± 0.120	[1328]	2016	$(\Omega_m, \Omega_b, \sigma_8) = (0.3, 0.045, 0.823)$
44	Vipers PDR-2	0.86	0.400 ± 0.110	[1328]	2016	
45	SDSS DR13	0.1	0.48 ± 0.16	[2489]	2016	$(\Omega_m, \sigma_8) = (0.25, 0.89)$ [2482]
46	2MTF	0.001	0.505 ± 0.085	[2490]	2017	$(\Omega_m, \sigma_8) = (0.3121, 0.815)$
47	Vipers PDR-2	0.85	0.45 ± 0.11	[2491]	2017	$(\Omega_b, \Omega_m, h) = (0.045, 0.30, 0.8)$
48	BOSS DR12	0.31	0.469 ± 0.098	[2492]	2017	$(\Omega_m, h, \sigma_8) = (0.307, 0.6777, 0.8288)$
49	BOSS DR12	0.36	0.474 ± 0.097	[2492]	2017	
50	BOSS DR12	0.40	0.473 ± 0.086	[2492]	2017	
51	BOSS DR12	0.44	0.481 ± 0.076	[2492]	2017	
52	BOSS DR12	0.48	0.482 ± 0.067	[2492]	2017	
53	BOSS DR12	0.52	0.488 ± 0.065	[2492]	2017	
54	BOSS DR12	0.56	0.482 ± 0.067	[2492]	2017	
55	BOSS DR12	0.59	0.481 ± 0.066	[2492]	2017	
56	BOSS DR12	0.64	0.486 ± 0.070	[2492]	2017	
57	SDSS DR7	0.1	0.376 ± 0.038	[2493]	2017	$(\Omega_m, \Omega_b, \sigma_8) = (0.282, 0.046, 0.817)$
58	SDSS-IV	1.52	0.420 ± 0.076	[2494]	2018	$(\Omega_m, \Omega_b h^2, \sigma_8) = (0.26479, 0.02258, 0.8)$
59	SDSS-IV	1.52	0.396 ± 0.079	[2495]	2018	$(\Omega_m, \Omega_b h^2, \sigma_8) = (0.31, 0.022, 0.8225)$
60	SDSS-IV	0.978	0.379 ± 0.176	[2496]	2018	$(\Omega_m, \sigma_8) = (0.31, 0.8)$
61	SDSS-IV	1.23	0.385 ± 0.099	[2496]	2018	
62	SDSS-IV	1.526	0.342 ± 0.070	[2496]	2018	
63	SDSS-IV	1.944	0.364 ± 0.106	[2496]	2018	

Table B.2: A compilation of BAO data that have been published from 2006 until 2018 in chronological order

Index	z_{eff}	$D_A \times (r_s^{fid.}/r_s)$ (Mpc)	$H(z) \times (r_s/r_s^{fid.})$ (km/sec Mpc)	$D_V \times (r_s^{fid.}/r_s)$ (Mpc)	Year	Ref.
1	0.275	-	-	1061.87 ± 29	2009	[2497]
2	0.106	-	-	439.3 ± 19.6	2011	[354]
3	0.35	-	-	1356 ± 25	2012	[2498]
4	0.44	-	-	1716 ± 83	2014	[1829]
5	0.60	-	-	2221 ± 100	2014	[1829]
6	0.73	-	-	2516 ± 86	2014	[1829]

7	0.15	-	-	664 ± 25	2015	[363]
8	0.38	1100 ± 22	81.5 ± 2.6	1477 ± 16	2016	[48]
9	0.51	1309.3 ± 24.5	90.5 ± 2.7	1877 ± 19	2016	[48]
10	0.61	1418 ± 27.3	97.3 ± 2.9	2140 ± 22	2016	[48]
11	0.32	980.3 ± 15.9	78.4 ± 2.3	1270 ± 14	2016	[48]
12	0.57	1387.9 ± 22.3	96.6 ± 2.4	2033 ± 21	2016	[48]
13	0.31	931.42 ± 48	78.3 ± 4.7	1208.36 ± 33.81	2016	[2499]
14	0.36	1047.04 ± 44	77.2 ± 5.7	1388.36 ± 55	2016	[2499]
15	0.40	1131.34 ± 44	79.72 ± 4.9	1560.06 ± 40	2016	[2499]
16	0.44	1188.78 ± 32	80.29 ± 3.4	1679.88 ± 35	2016	[2499]
17	0.48	1271.43 ± 25.8	84.69 ± 3.4	1820.44 ± 39	2016	[2499]
18	0.52	1336.53 ± 39	91.97 ± 7.5	1913.54 ± 47	2016	[2499]
19	0.56	1385.47 ± 30.5	97.3 ± 7.9	2001.91 ± 51	2016	[2499]
20	0.59	1423.43 ± 44	97.07 ± 5.8	2100.43 ± 48	2016	[2499]
21	0.64	1448.81 ± 69	97.70 ± 4.8	2207.51 ± 55	2016	[2499]
22	2.33	1669.7 ± 96.1	224 ± 8	-	2017	[358]
23	1.52	-	-	3843 ± 147	2017	[2500]
24	0.81	1586.7 ± 63.5	-	-	2017	[916]
25	0.72	-	-	2353 ± 63	2017	[2501]
26	1.52	1850 ± 110	162 ± 12	3985.2 ± 162.4	2018	[2494]
27	0.978	1586.18 ± 284.93	113.72 ± 14.63	2933.59 ± 327.71	2018	[2496]
28	1.230	1769.08 ± 159.67	131.44 ± 12.42	3522.04 ± 192.74	2018	[2496]
29	1.526	1768.77 ± 96.59	148.11 ± 12.75	3954.31 ± 141.71	2018	[2496]
30	1.944	1807.98 ± 146.46	172.63 ± 14.79	4575.17 ± 241.61	2018	[2496]

Table B.3: The JLA binned data used in our analysis (from Ref. [68]).

Index	z	μ	σ_μ
1	0.01	32.9539	0.145886
2	0.012	33.879	0.167796
3	0.014	33.8421	0.0784989
4	0.016	34.1186	0.0723539
5	0.019	34.5934	0.0854606
6	0.023	34.939	0.0561251
7	0.026	35.2521	0.0610683
8	0.031	35.7485	0.0567639
9	0.037	36.0698	0.0567956
10	0.043	36.4346	0.0751431
11	0.051	36.6511	0.0929013
12	0.06	37.158	0.0620892
13	0.07	37.4302	0.0658793
14	0.082	37.9566	0.0546505
15	0.097	38.2533	0.0599337
16	0.114	38.6129	0.0374341
17	0.134	39.0679	0.0386141
18	0.158	39.3414	0.0346886
19	0.186	39.7921	0.0321403
20	0.218	40.1565	0.0329616
21	0.257	40.565	0.0317198
22	0.302	40.9053	0.0392622
23	0.355	41.4214	0.0335758

24	0.418	41.7909	0.0415207
25	0.491	42.2315	0.0393713
26	0.578	42.617	0.0359453
27	0.679	43.0527	0.0627778
28	0.799	43.5042	0.0545914
29	0.94	43.9726	0.0668276
30	1.105	44.5141	0.154604
31	1.3	44.8219	0.138452

Table B.4: The $H(z)$ data compilation used in our analysis (from Ref. [69]).

Index	z	$H(z)$ (km/sec Mpc)	σ_H	Reference
1	0.070	69	19.6	[2502]
2	0.090	69	12	[2503]
3	0.120	68.6	26.2	[2502]
4	0.170	83	8	[2503]
5	0.179	75	4	[484]
6	0.199	75	5	[484]
7	0.200	72.9	29.6	[2502]
8	0.240	79.69	6.65	[2504]
9	0.270	77	14	[2503]
10	0.280	88.8	36.6	[2502]
11	0.300	81.7	6.22	[2505]
12	0.350	82.7	8.4	[2477]
13	0.352	83	14	[484]
14	0.3802	83	13.5	[485]
15	0.400	95	17	[2503]
16	0.4004	77	10.02	[485]
17	0.4247	87.1	11.2	[485]
18	0.430	86.45	3.68	[2504]
19	0.440	82.6	7.8	[351]
20	0.4497	92.8	12.9	[485]
21	0.4783	80.9	9	[485]
22	0.480	97	62	[2506]
23	0.570	92.900	7.855	[2507]
24	0.593	104	13	[484]
25	0.6	87.9	6.1	[351]
26	0.68	92	8	[484]
27	0.73	97.3	7.0	[351]
28	0.781	105	12	[484]
29	0.875	125	17	[484]
30	0.88	90	40	[2506]
31	0.9	117	23	[2503]
32	1.037	154	20	[484]
33	1.300	168	17	[2503]
34	1.363	160	22.6	[2508]
35	1.43	177	18	[2503]
36	1.53	140	14	[2503]
37	1.75	202	40	[2503]
38	1.965	186.5	50.4	[2508]
39	2.300	224	8	[2509]

40	2.34	222	7	[356]
41	2.36	226	8	[359]

Appendix C

Observational Constraints on the GUP Parameter with Maximum Length Quantum Mechanics

C.1 From generalized commutator to generalized uncertainty

We assume the commutation relation of the form

$$[x, p] = i\hbar \frac{1}{1 - \alpha x^2} \simeq i\hbar(1 + \alpha x^2) \quad (\text{C.1})$$

where the last approximate equality is applicable under the condition $\alpha x^2 \ll 1$. The commutation relation (C.1) may be represented by position and momentum operators of the form

$$p = \frac{1}{1 - \alpha x_0^2} p_0 = (1 + \alpha x_0^2 + \alpha^2 x_0^4 + \dots) p_0 \quad (\text{C.2})$$

$$x = x_0 \quad (\text{C.3})$$

where x_0 and p_0 are the usual position and momentum operators satisfying the Heisenberg commutation relation $[x_0, p_0] = i\hbar$.

The proof that the commutation relation (C.1) may be represented by position and momentum operators of the form (C.2) and (C.3) is

$$[x, p] = [x_0, (1 + \alpha x_0^2 + \alpha^2 x_0^4 + \dots) p_0] = [x_0, p_0] + \alpha x_0^2 [x_0, p_0] + \alpha^2 x_0^4 [x_0, p_0] + \dots = [x_0, p_0] \frac{1}{1 - \alpha x_0^2} = i\hbar \frac{1}{1 - \alpha x^2} \quad (\text{C.4})$$

Also, the proof that the commutation relation (C.1) leads to a GUP of the form (6.4) is

$$\begin{aligned} \Delta x \Delta p &\geq \frac{\hbar}{2} \langle \frac{1}{1 - \alpha x^2} \rangle = \frac{\hbar}{2} (1 + \alpha \langle x^2 \rangle + \alpha^2 \langle x^4 \rangle + \dots) \geq \frac{\hbar}{2} (1 + \alpha \langle x^2 \rangle + \alpha^2 \langle x^2 \rangle^2 + \dots) = \\ &\frac{\hbar}{2} (1 + \alpha (\Delta x^2 + \langle x \rangle^2) + \alpha^2 (\Delta x^2 + \langle x \rangle^2)^2 + \dots) = \frac{\hbar}{2} \frac{1}{1 - \alpha (\Delta x^2 + \langle x \rangle^2)} \geq \frac{\hbar}{2} \frac{1}{1 - \alpha \Delta x^2} \Rightarrow \\ \Delta x \Delta p &\geq \frac{\hbar}{2} \frac{1}{1 - \alpha \Delta x^2} \end{aligned} \quad (\text{C.5})$$

Appendix D

Tensions and Constraints on Modified Gravity Parameters from the E_G statistic and RSD data and Implications for Weakening Gravity

D.1 Analysis of subsets of datapoints with less correlation

In this Appendix we present the results of the statistical analysis of the $f\sigma_8(z)$ and $E_G(z)$ data compilations of datapoints with less correlation. These subsets of the data are indicated with bold font in the index of the Tables D.3 and D.4. Using these subsets of the data and repeating our analysis we obtain the best fit parameter values and the tension levels in both the 2D projections and in the full 3D-4D parameter spaces as shown in Tables D.1 and D.2 respectively.

Table D.1: Planck18/ Λ CDM based on TT,TE,EE+lowE+ lensing likelihoods best fit [14] and the best-fit values from data compilation of datapoints with less correlation.

Param.	Planck18/ Λ CDM	Dataset $f\sigma_8(z)$. corr.	Dataset $f\sigma_8(z)$ no corr.	Dataset $E_G(z)$	Datasets $f\sigma_8(z) + E_G(z)$ corr.	Datasets $f\sigma_8(z) + E_G(z)$ no corr.
Ω_{0m}	0.3153 ± 0.0073	0.289 ± 0.032	0.283 ± 0.028	0.285 ± 0.044	0.288 ± 0.026	0.282 ± 0.023
σ_8	0.8111 ± 0.0060	0.807 ± 0.024	0.819 ± 0.025		0.795 ± 0.024	0.810 ± 0.024
g_a	0	-0.767 ± 0.299	-0.826 ± 0.293	-0.621 ± 0.914	-0.627 ± 0.291	-0.723 ± 0.281
g_b	0			-3.510 ± 0.605	-3.562 ± 0.601	-3.563 ± 0.601

These results indicate that even though the tension level for the combined ($E_G + f\sigma_8$) reduces somewhat (from 6σ to about 5.5σ) it remains high enough to cause concerns for the self consistency of the Planck/ Λ CDM model and indications for the presence of weakening gravity.

Table D.2: Sigma differences of the best fit contours from Planck18/ Λ CDM. The $E_G(z)$ and $f\sigma_8(z)$ data compilations of datapoints with less correlation from Tables D.4 and D.3 was used.

Dataset	Space			2D Projected Space					
	$(\Omega_{0m}, \sigma_8, g_a)$	(Ω_{0m}, g_a, g_b)	$(\Omega_{0m}, \sigma_8, g_a, g_b)$	(Ω_{0m}, σ_8)	(Ω_{0m}, g_a)	(σ_8, g_a)	(g_a, g_b)	(Ω_{0m}, g_b)	(σ_8, g_b)
$f\sigma_8(z)$ corr.	2.39 σ			0.22 σ	2.19 σ	1.79 σ			
$f\sigma_8(z)$ no corr.	2.55 σ			0.19 σ	2.19 σ	1.48 σ			
$E_G(z)$		5.06			0.01 σ		4.04 σ	6.28 σ	
$E_G(z)+f\sigma_8(z)$ corr.			5.69	0.36 σ	1.35 σ	1.59 σ	4.31 σ	6.12 σ	5.12 σ
$E_G(z)+f\sigma_8(z)$ no corr.			5.78	0.31 σ	2.21 σ	1.33 σ	4.54 σ	6.38 σ	5.29 σ

D.2 Data used in the analysis

In this appendix we present the data used in our analysis.

Table D.3: The $f\sigma_8$ updated data compilation of Ref. [67] used in our analysis. The subset of the datapoints with less correlation is indicated with bold font in the index.

Index	Dataset	z	$f\sigma_8(z)$	Refs.	Year	Fiducial Cosmology
1	SDSS-LRG	0.35	0.440 ± 0.050	[2474]	2006	$(\Omega_m, \Omega_K, \sigma_8) = (0.25, 0, 0.756)$ [340]
2	VVDS	0.77	0.490 ± 0.18	[2474]	2009	$(\Omega_m, \Omega_K, \sigma_8) = (0.25, 0, 0.78)$
3	2dFGRS	0.17	0.510 ± 0.060	[2474]	2009	$(\Omega_m, \Omega_K) = (0.3, 0, 0.9)$
4	2MRS	0.02	0.314 ± 0.048	[2475], [2476]	2010	$(\Omega_m, \Omega_K, \sigma_8) = (0.266, 0, 0.65)$
5	SnIa+IRAS	0.02	0.398 ± 0.065	[1549], [2476]	2011	$(\Omega_m, \Omega_K, \sigma_8) = (0.3, 0, 0.814)$
6	SDSS-LRG-200	0.25	0.3512 ± 0.0583	[1315]	2011	$(\Omega_m, \Omega_K, \sigma_8) = (0.276, 0, 0.8)$
7	SDSS-LRG-200	0.37	0.4602 ± 0.0378	[1315]	2011	
8	SDSS-LRG-60	0.25	0.3665 ± 0.0601	[1315]	2011	$(\Omega_m, \Omega_K, \sigma_8) = (0.276, 0, 0.8)$
9	SDSS-LRG-60	0.37	0.4031 ± 0.0586	[1315]	2011	
10	WiggleZ	0.44	0.413 ± 0.080	[351]	2012	$(\Omega_m, h, \sigma_8) = (0.27, 0.71, 0.8)$
11	WiggleZ	0.60	0.390 ± 0.063	[351]	2012	
12	WiggleZ	0.73	0.437 ± 0.072	[351]	2012	
13	6dFGS	0.067	0.423 ± 0.055	[355]	2012	$(\Omega_m, \Omega_K, \sigma_8) = (0.27, 0, 0.76)$
14	SDSS-BOSS	0.30	0.407 ± 0.055	[1317]	2012	$(\Omega_m, \Omega_K, \sigma_8) = (0.25, 0, 0.804)$
15	SDSS-BOSS	0.40	0.419 ± 0.041	[1317]	2012	
16	SDSS-BOSS	0.50	0.427 ± 0.043	[1317]	2012	
17	SDSS-BOSS	0.60	0.433 ± 0.067	[1317]	2012	
18	VIPERS	0.80	0.470 ± 0.080	[1327]	2013	$(\Omega_m, \Omega_K, \sigma_8) = (0.25, 0, 0.82)$
19	SDSS-DR7-LRG	0.35	0.429 ± 0.089	[2477]	2013	$(\Omega_m, \Omega_K, \sigma_8) = (0.25, 0, 0.809)$ [?]
20	GAMA	0.18	0.360 ± 0.090	[2478]	2013	$(\Omega_m, \Omega_K, \sigma_8) = (0.27, 0, 0.8)$
21	GAMA	0.38	0.440 ± 0.060	[2478]	2013	
22	BOSS-LOWZ	0.32	0.384 ± 0.095	[2479]	2013	$(\Omega_m, \Omega_K, \sigma_8) = (0.274, 0, 0.8)$
23	SDSS DR10+DR11	0.32	0.48 ± 0.10	[2479]	2013	$(\Omega_m, \Omega_K, \sigma_8) = (0.274, 0, 0.8)$ [2480]
24	SDSS DR10+DR11	0.57	0.417 ± 0.045	[2479]	2013	
25	SDSS-MGS	0.15	0.490 ± 0.145	[1319]	2015	$(\Omega_m, h, \sigma_8) = (0.31, 0.67, 0.83)$
26	SDSS-veloc	0.10	0.370 ± 0.130	[2481]	2015	$(\Omega_m, \Omega_K, \sigma_8) = (0.3, 0, 0.89)$ [2482]
27	FastSound	1.40	0.482 ± 0.116	[1326]	2015	$(\Omega_m, \Omega_K, \sigma_8) = (0.27, 0, 0.82)$ [2483]
28	SDSS-CMASS	0.59	0.488 ± 0.060	[2484]	2016	$(\Omega_m, h, \sigma_8) = (0.307115, 0.6777, 0.8288)$
29	BOSS DR12	0.38	0.497 ± 0.045	[48]	2016	$(\Omega_m, \Omega_K, \sigma_8) = (0.31, 0, 0.8)$

30	BOSS DR12	0.51	0.458 ± 0.038	[48]	2016	
31	BOSS DR12	0.61	0.436 ± 0.034	[48]	2016	
32	BOSS DR12	0.38	0.477 ± 0.051	[2485]	2016	$(\Omega_m, h, \sigma_8) = (0.31, 0.676, 0.8)$
33	BOSS DR12	0.51	0.453 ± 0.050	[2485]	2016	
34	BOSS DR12	0.61	0.410 ± 0.044	[2485]	2016	
35	VIPERS v7	0.76	0.440 ± 0.040	[2486]	2016	$(\Omega_m, \sigma_8) = (0.308, 0.8149)$
36	VIPERS v7	1.05	0.280 ± 0.080	[2486]	2016	
37	BOSS LOWZ	0.32	0.427 ± 0.056	[1325]	2016	$(\Omega_m, \Omega_K, \sigma_8) = (0.31, 0, 0.8475)$
38	BOSS CMASS	0.57	0.426 ± 0.029	[1325]	2016	
39	VIPERS	0.727	0.296 ± 0.0765	[2487]	2016	$(\Omega_m, \Omega_K, \sigma_8) = (0.31, 0, 0.7)$
40	6dFGS+SnIa	0.02	0.428 ± 0.0465	[2488]	2016	$(\Omega_m, h, \sigma_8) = (0.3, 0.683, 0.8)$
41	VIPERS PDR2	0.60	0.550 ± 0.120	[1328]	2016	$(\Omega_m, \Omega_b, \sigma_8) = (0.3, 0.045, 0.823)$
42	VIPERS PDR2	0.86	0.400 ± 0.110	[1328]	2016	
43	SDSS DR13	0.1	0.48 ± 0.16	[2489]	2016	$(\Omega_m, \sigma_8) = (0.25, 0.89)$ [2482]
44	2MTF	0.001	0.505 ± 0.085	[2490]	2017	$(\Omega_m, \sigma_8) = (0.3121, 0.815)$
45	VIPERS PDR2	0.85	0.45 ± 0.11	[2491]	2017	$(\Omega_b, \Omega_m, h) = (0.045, 0.30, 0.8)$
46	BOSS DR12	0.31	0.384 ± 0.083	[2492]	2017	$(\Omega_m, h, \sigma_8) = (0.307, 0.6777, 0.8288)$
47	BOSS DR12	0.36	0.409 ± 0.098	[2492]	2017	
48	BOSS DR12	0.40	0.461 ± 0.086	[2492]	2017	
49	BOSS DR12	0.44	0.426 ± 0.062	[2492]	2017	
50	BOSS DR12	0.48	0.458 ± 0.063	[2492]	2017	
51	BOSS DR12	0.52	0.483 ± 0.075	[2492]	2017	
52	BOSS DR12	0.56	0.472 ± 0.063	[2492]	2017	
53	BOSS DR12	0.59	0.452 ± 0.061	[2492]	2017	
54	BOSS DR12	0.64	0.379 ± 0.054	[2492]	2017	
55	SDSS DR7	0.1	0.376 ± 0.038	[2493]	2017	$(\Omega_m, \Omega_b, \sigma_8) = (0.282, 0.046, 0.817)$
56	SDSS-IV	1.52	0.420 ± 0.076	[2494]	2018	$(\Omega_m, \Omega_b h^2, \sigma_8) = (0.26479, 0.02258, 0.8)$
57	SDSS-IV	1.52	0.396 ± 0.079	[2495]	2018	$(\Omega_m, \Omega_b h^2, \sigma_8) = (0.31, 0.022, 0.8225)$
58	SDSS-IV	0.978	0.379 ± 0.176	[2496]	2018	$(\Omega_m, \sigma_8) = (0.31, 0.8)$
59	SDSS-IV	1.23	0.385 ± 0.099	[2496]	2018	
60	SDSS-IV	1.526	0.342 ± 0.070	[2496]	2018	
61	SDSS-IV	1.944	0.364 ± 0.106	[2496]	2018	
62	VIPERS PDR2	0.60	0.49 ± 0.12	[1329]	2018	$(\Omega_b, \Omega_m, h, \sigma_8) = (0.045, 0.31, 0.7, 0.8)$
63	VIPERS PDR2	0.86	0.46 ± 0.09	[1329]	2018	
64	BOSS DR12 voids	0.57	0.501 ± 0.051	[2510]	2019	$(\Omega_b, \Omega_m, h, \sigma_8) = (0.0482, 0.307, 0.6777, 0.8228)$
65	2MTF 6dFGSv	0.03	0.404 ± 0.0815	[2511]	2019	$(\Omega_b, \Omega_m, h, \sigma_8) = (0.0491, 0.3121, 0.6571, 0.815)$
66	SDSS-IV	0.72	0.454 ± 0.139	[2512]	2019	$(\Omega_m, \Omega_b h^2, \sigma_8) = (0.31, 0.022, 0.8)$

Table D.4: The $E_G(z)$ data compilation used in our analysis. The subset of the datapoints with less correlation is indicated with bold font in the index.

Index	Dataset	z	$E_G(z)$	σ_{E_G}	Scale [Mpc/h]	Reference
1	KiDS GAMA	0.267	0.43	0.13	$5 < R < 40$	[2198]
2	SDSS BOSS LOWZ	0.27	0.40	0.05	$25 < R < 150$	[2513]
3	CMB lens BOSS LOWZ	0.27	0.46	0.085	$25 < R < 150$	[2513]
4	KiDS 2dFLenS BOSS LOWZ 2dFLOZ	0.305	0.27	0.08	$5 < R < 60$	[2198]
5	RCSLenS CFHTLenS WiggleZ BOSS WGZLoZ LOWZ	0.32	0.40	0.09	$R > 3$	[2514]
6	RCSLenS CFHTLenS WiggleZ BOSS WGZLoZ LOWZ	0.32	0.48	0.10	$R > 10$	[2514]
7	SDSS	0.32	0.39	0.06	$10 < Rp < 50$	[1990]
8	KiDS 2dFLenS BOSS CMASS 2dFHIZ	0.554	0.26	0.07	$5 < R < 60$	[2198]
9	RCSLenS CFHTLenS WiggleZ BOSS WGZHiZ CMASS	0.57	0.31	0.06	$R > 3$	[2514]

10	RCSLenS CFHTLenS WiggleZ BOSS WGZHiZ CMASS	0.57	0.30	0.07	$R > 10$	[2514]
11	SDSS-III BOSS CMB lens CMASS	0.57	0.24	0.06	$R > 150$	[1992]
12	CFHTLenS SDSS-III BOSS CMASS	0.57	0.42	0.056	$5 < R < 26$	[2515]
13	CMB lens BOSS CMASS	0.57	0.39	0.05	$25 < R < 150$	[2513]
14	CFHTLenS BOSS CMASS	0.57	0.43	0.10	$10 < R < 60$	[2516]
15	CFHTLenS VIPERS	0.60	0.16	0.09	$3 < R < 20$	[1989]
16	CFHTLenS VIPERS	0.86	0.09	0.07	$3 < R < 20$	[1989]

Table D.5: The $E_G(R)$ data compilation in the range $0.15 < z < 0.43$ used in our analysis.

Index	R [Mpc/h]	$E_G(R)$	σ_{E_G}	z	Reference
1	3.61	0.37	0.10	0.27	[2513]
2	4.91	0.42	0.08	0.27	[2513]
3	6.60	0.50	0.07	0.27	[2513]
4	9.07	0.39	0.07	0.27	[2513]
5	12.20	0.37	0.06	0.27	[2513]
6	16.58	0.45	0.06	0.27	[2513]
7	22.54	0.32	0.04	0.27	[2513]
8	30.30	0.39	0.05	0.27	[2513]
9	41.19	0.44	0.06	0.27	[2513]
10	55.99	0.45	0.08	0.27	[2513]
11	76.98	0.34	0.10	0.27	[2513]
12	103.47	0.28	0.15	0.27	[2513]
13	2.45	0.28	0.23	0.32	[1990]
14	3.41	0.49	0.16	0.32	[1990]
15	4.64	0.50	0.12	0.32	[1990]
16	6.62	0.32	0.09	0.32	[1990]
17	9.85	0.34	0.07	0.32	[1990]
18	14.83	0.45	0.08	0.32	[1990]
19	22.10	0.43	0.09	0.32	[1990]
20	45.87	0.32	0.10	0.32	[1990]
21	1.76	0.74	0.21	0.15-0.43	[2514]
22	2.23	0.71	0.15	0.15-0.43	[2514]
23	2.85	0.35	0.14	0.15-0.43	[2514]
24	3.56	0.30	0.11	0.15-0.43	[2514]
25	4.45	0.35	0.11	0.15-0.43	[2514]
26	5.65	0.28	0.10	0.15-0.43	[2514]
27	7.059	0.43	0.11	0.15-0.43	[2514]
28	8.94	0.45	0.11	0.15-0.43	[2514]
29	11.33	0.47	0.12	0.15-0.43	[2514]
30	14.34	0.55	0.12	0.15-0.43	[2514]
31	17.98	0.40	0.12	0.15-0.43	[2514]
32	22.21	0.37	0.14	0.15-0.43	[2514]
33	28.88	0.39	0.18	0.15-0.43	[2514]
34	36.15	0.35	0.19	0.15-0.43	[2514]
35	45.26	0.30	0.30	0.15-0.43	[2514]
36	5.01	0.25	0.16	0.15-0.43	[2198]
37	5.37	0.39	0.16	0.15-0.43	[2198]
38	5.58	0.094	0.18	0.15-0.43	[2198]
39	8.15	0.30	0.14	0.15-0.43	[2198]
40	8.57	0.41	0.14	0.15-0.43	[2198]

41	9.02	0.41	0.24	0.15-0.43	[2198]
42	13.23	0.49	0.16	0.15-0.43	[2198]
43	13.95	0.43	0.16	0.15-0.43	[2198]
44	14.76	0.15	0.17	0.15-0.43	[2198]
45	21.08	0.51	0.23	0.15-0.43	[2198]
46	22.75	0.33	0.23	0.15-0.43	[2198]
47	23.96	0.32	0.32	0.15-0.43	[2198]
48	35.52	0.33	0.29	0.15-0.43	[2198]
49	36.98	0.40	0.33	0.15-0.43	[2198]
50	39.00	0.32	0.38	0.15-0.43	[2198]
51	56.60	0.37	0.80	0.15-0.43	[2198]

Table D.6: The $E_G(R)$ data compilation in the range $0.43 < z < 1.2$ used in our analysis.

Index	R [Mpc/h]	$E_G(R)$	σ_{E_G}	z	Reference
1	5.13	0.23	0.14	0.43-0.7	[2198]
2	5.69	0.19	0.19	0.43-0.7	[2198]
3	8.28	0.32	0.12	0.43-0.7	[2198]
4	9.19	0.27	0.17	0.43-0.7	[2198]
5	13.69	0.21	0.12	0.43-0.7	[2198]
6	14.98	0.46	0.25	0.43-0.7	[2198]
7	24.43	0.95	0.47	0.43-0.7	[2198]
8	22.02	0.22	0.13	0.43-0.7	[2198]
9	36.28	0.48	0.18	0.43-0.7	[2198]
10	39.84	0.84	0.57	0.43-0.7	[2198]
11	59.78	0.54	0.45	0.43-0.7	[2198]
12	1.74	0.34	0.29	0.43-0.7	[2514]
13	2.25	0.31	0.17	0.43-0.7	[2514]
14	2.74	0.57	0.14	0.43-0.7	[2514]
15	3.46	0.43	0.11	0.43-0.7	[2514]
16	4.45	0.35	0.10	0.43-0.7	[2514]
17	5.56	0.30	0.09	0.43-0.7	[2514]
18	6.92	0.24	0.09	0.43-0.7	[2514]
19	8.84	0.28	0.08	0.43-0.7	[2514]
20	11.15	0.26	0.08	0.43-0.7	[2514]
21	13.90	0.29	0.07	0.43-0.7	[2514]
22	17.74	0.24	0.08	0.43-0.7	[2514]
23	21.96	0.25	0.09	0.43-0.7	[2514]
24	27.80	0.32	0.10	0.43-0.7	[2514]
25	34.81	0.41	0.14	0.43-0.7	[2514]
26	44.26	0.62	0.19	0.43-0.7	[2514]
27	2.17	0.38	0.15	0.57	[2515]
28	3.30	0.26	0.11	0.57	[2515]
29	4.99	0.46	0.09	0.57	[2515]
30	7.56	0.42	0.08	0.57	[2515]
31	11.38	0.35	0.08	0.57	[2515]
32	17.26	0.43	0.09	0.57	[2515]
33	25.99	0.43	0.11	0.57	[2515]
34	39.60	0.33	0.15	0.57	[2515]
35	2.56	0.48	0.08	0.57	[2513]
36	3.40	0.36	0.09	0.57	[2513]

37	4.60	0.32	0.08	0.57	[2513]
38	6.12	0.40	0.08	0.57	[2513]
39	8.20	0.33	0.07	0.57	[2513]
40	11.00	0.43	0.09	0.57	[2513]
41	14.87	0.32	0.07	0.57	[2513]
42	19.75	0.34	0.12	0.57	[2513]
43	26.21	0.31	0.15	0.57	[2513]
44	35.44	0.22	0.18	0.57	[2513]
45	2.22	0.27	0.17	0.57	[2516]
46	3.56	0.13	0.23	0.57	[2516]
47	5.64	0.16	0.19	0.57	[2516]
48	8.86	0.49	0.28	0.57	[2516]
49	14.13	0.64	0.22	0.57	[2516]
50	22.54	0.29	0.14	0.57	[2516]
51	35.37	0.40	0.21	0.57	[2516]
52	2.64	0.31	0.14	0.5-0.7	[1989]
53	4.17	0.20	0.15	0.5-0.7	[1989]
54	6.63	0.22	0.17	0.5-0.7	[1989]
55	10.44	0.01	0.20	0.5-0.7	[1989]
56	16.37	0.09	0.26	0.5-0.7	[1989]
57	2.61	0.34	0.12	0.7-1.2	[1989]
58	4.15	0.06	0.12	0.7-1.2	[1989]
59	6.60	0.11	0.13	0.7-1.2	[1989]
60	10.42	0.01	0.16	0.7-1.2	[1989]
61	16.56	0.10	0.21	0.7-1.2	[1989]

Appendix E

Scalar Tachyonic Instabilities in Gravitational Backgrounds

E.1 Analytical form of SSC curves

The Sufficient for Stability Criterion (SSC) is that the minimum of the Schrodinger potential should be larger than 0 (see Eq. (8.61)). Thus by demanding that the minimum of the Schrodinger potential

$$V_{0min}(r_{min}) = 0 \tag{E.1}$$

we can obtain the analytical form of SSC curves for various values of Q (see Fig. 8.4). The SSC curve for $Q = 0$ as function of ξ takes the following analytical form

$$m^2(\xi)M^2 = \frac{2(g(\xi) - 1)}{9g(\xi)^3} \tag{E.2}$$

where

$$g(\xi) = \frac{1}{\left(\sqrt{\xi^4 - \xi^3} - \xi^2\right)^{\frac{1}{3}}} + \frac{\left(\sqrt{\xi^4 - \xi^3} - \xi^2\right)^{\frac{1}{3}}}{\xi} \tag{E.3}$$

Appendix F

Constraints on Horndeski Modified Gravity - Weak Gravity on a Λ CDM Background

F.1 Definitions

The background quantities \mathcal{E}_{DE} and \mathcal{P}_{DE} are defined as [2179]

$$\begin{aligned} \mathcal{E}_{DE} \equiv & -K + 2X(K_X - G_{3\phi}) + 6\dot{\phi}H(XG_{3X} - G_{4\phi} - 2XG_{4\phi X}) + \\ & + 12H^2X(G_{4X} + 2XG_{4XX} - G_{5\phi} - XG_{5\phi X}) + 4\dot{\phi}H^3X(G_{5X} + XG_{5XX}) \end{aligned} \quad (\text{F.1})$$

$$\begin{aligned} \mathcal{P}_{DE} \equiv & K - 2X(G_{3\phi} - 2G_{4\phi\phi}) + 4\dot{\phi}H(G_{4\phi} - 2XG_{4\phi X} + XG_{5\phi\phi}) - \\ & - M_*^2\alpha_B H \frac{\ddot{\phi}}{\dot{\phi}} - 4H^2X^2G_{5\phi X} + 2\dot{\phi}H^3XG_{5X} \end{aligned} \quad (\text{F.2})$$

Note that in the literature there appear various definitions of the energy density associated to the dark energy (see [2015]). However we use here the effective DE energy density ρ_{DE} and pressure P_{DE} based on an Einsteinian representation of modified gravity [587, 1388].

F.2 Data used in the analysis

In this appendix we present the data used in our analysis.

Table F.1: The $f\sigma_8$ updated data compilation of Ref. [4] used in our analysis.

Index	Dataset	z	$f\sigma_8(z)$	Refs.	Year	Fiducial Cosmology
1	2MRS	0.02	0.314 ± 0.048	[2475], [2476]	2010	$(\Omega_m, \Omega_K, \sigma_8) = (0.266, 0, 0.65)$
2	SDSS-LRG-200	0.25	0.3512 ± 0.0583	[1315]	2011	$(\Omega_m, \Omega_K, \sigma_8) = (0.276, 0, 0.8)$
3	WiggleZ	0.44	0.413 ± 0.080	[351]	2012	$(\Omega_m, h, \sigma_8) = (0.27, 0.71, 0.8)$
4	WiggleZ	0.60	0.390 ± 0.063	[351]	2012	
5	WiggleZ	0.73	0.437 ± 0.072	[351]	2012	
6	GAMA	0.18	0.360 ± 0.090	[2478]	2013	$(\Omega_m, \Omega_K, \sigma_8) = (0.27, 0, 0.8)$
7	SDSS-MGS	0.15	0.490 ± 0.145	[1319]	2015	$(\Omega_m, h, \sigma_8) = (0.31, 0.67, 0.83)$
8	SDSS-veloc	0.10	0.370 ± 0.130	[2481]	2015	$(\Omega_m, \Omega_K, \sigma_8) = (0.3, 0, 0.89)$ [2482]
9	FastSound	1.40	0.482 ± 0.116	[1326]	2015	$(\Omega_m, \Omega_K, \sigma_8) = (0.27, 0, 0.82)$ [2483]

10	BOSS DR12	0.38	0.497 ± 0.045	[48]	2016	$(\Omega_m, \Omega_K, \sigma_8) = (0.31, 0, 0.8)$
11	BOSS DR12	0.51	0.458 ± 0.038	[48]	2016	
12	BOSS DR12	0.61	0.436 ± 0.034	[48]	2016	
13	VIPERS v7	1.05	0.280 ± 0.080	[2486]	2016	
14	BOSS LOWZ	0.32	0.427 ± 0.056	[1325]	2016	$(\Omega_m, \Omega_K, \sigma_8) = (0.31, 0, 0.8475)$
15	VIPERS	0.727	0.296 ± 0.0765	[2487]	2016	$(\Omega_m, \Omega_K, \sigma_8) = (0.31, 0, 0.7)$
16	6dFGS+SnIa	0.02	0.428 ± 0.0465	[2488]	2016	$(\Omega_m, h, \sigma_8) = (0.3, 0.683, 0.8)$
17	2MTF	0.001	0.505 ± 0.085	[2490]	2017	$(\Omega_m, \sigma_8) = (0.3121, 0.815)$
18	BOSS DR12	0.31	0.384 ± 0.083	[2492]	2017	$(\Omega_m, h, \sigma_8) = (0.307, 0.6777, 0.8288)$
19	BOSS DR12	0.36	0.409 ± 0.098	[2492]	2017	
20	BOSS DR12	0.40	0.461 ± 0.086	[2492]	2017	
21	BOSS DR12	0.44	0.426 ± 0.062	[2492]	2017	
22	BOSS DR12	0.48	0.458 ± 0.063	[2492]	2017	
23	BOSS DR12	0.52	0.483 ± 0.075	[2492]	2017	
24	BOSS DR12	0.56	0.472 ± 0.063	[2492]	2017	
25	BOSS DR12	0.59	0.452 ± 0.061	[2492]	2017	
26	BOSS DR12	0.64	0.379 ± 0.054	[2492]	2017	
27	SDSS-IV	0.978	0.379 ± 0.176	[2496]	2018	$(\Omega_m, \sigma_8) = (0.31, 0.8)$
28	SDSS-IV	1.23	0.385 ± 0.099	[2496]	2018	
29	SDSS-IV	1.526	0.342 ± 0.070	[2496]	2018	
30	SDSS-IV	1.944	0.364 ± 0.106	[2496]	2018	
31	VIPERS PDR2	0.60	0.49 ± 0.12	[1329]	2018	$(\Omega_b, \Omega_m, h, \sigma_8) = (0.045, 0.31, 0.7, 0.8)$
32	VIPERS PDR2	0.86	0.46 ± 0.09	[1329]	2018	
33	BOSS DR12 voids	0.57	0.501 ± 0.051	[2510]	2019	$(\Omega_b, \Omega_m, h, \sigma_8) = (0.0482, 0.307, 0.6777, 0.8228)$
34	2MTF 6dFGSv	0.03	0.404 ± 0.0815	[2511]	2019	$(\Omega_b, \Omega_m, h, \sigma_8) = (0.0491, 0.3121, 0.6571, 0.815)$
35	SDSS-IV	0.72	0.454 ± 0.139	[2512]	2019	$(\Omega_m, \Omega_b h^2, \sigma_8) = (0.31, 0.022, 0.8)$

Table F.2: The $E_G(z)$ data compilation of Ref. [4] used in our analysis.

Index	Dataset	z	$E_G(z)$	σ_{E_G}	Scale [Mpc/h]	Reference
1	KiDS GAMA	0.267	0.43	0.13	$5 < R < 40$	[2198]
2	KiDS 2dFLenS BOSS LOWZ 2dFLOZ	0.305	0.27	0.08	$5 < R < 60$	[2198]
3	RCSLenS CFHTLenS WiggleZ BOSS WGZLoZ LOWZ	0.32	0.40	0.09	$R > 3$	[2514]
4	KiDS 2dFLenS BOSS CMASS 2dFHIZ	0.554	0.26	0.07	$5 < R < 60$	[2198]
5	RCSLenS CFHTLenS WiggleZ BOSS WGZHIZ CMASS	0.57	0.31	0.06	$R > 3$	[2514]
6	RCSLenS CFHTLenS WiggleZ BOSS WGZHIZ CMASS	0.57	0.30	0.07	$R > 10$	[2514]
7	CFHTLenS VIPERS	0.60	0.16	0.09	$3 < R < 20$	[1989]
8	CFHTLenS VIPERS	0.86	0.09	0.07	$3 < R < 20$	[1989]

Appendix G

Transition Model in light of Cepheid SnIa Calibrator data: Alleviating the Hubble Tension

G.1 Matrices of system of equations

In this Appendix we present the schematic form of the error matrix \mathbf{C} , the matrix of measurements \mathbf{Y} , the matrix of parameters \mathbf{X} and the equation (or design) matrix \mathbf{A} used in the system of equations of our analysis (see Eqs. (10.19), (10.20), (10.21) and (10.22) in Section 10.3).

The schematic form of the error matrix \mathbf{C} is

$$\mathbf{C} = \begin{pmatrix} \sigma_{MW,j}^2 & 0 & \dots & & & & 0 \\ 0 & \sigma_{tot,j}^2 & 0 & \dots & & & \vdots \\ 0 & 0 & \sigma_{LMC,j}^2 & 0 & \dots & & \vdots \\ \vdots & & & \ddots & & & \\ & & & & \sigma^2(\mu_{N4258}) & & \\ & & & & & \sigma^2(\mu_{LMC}) & \\ & & & & & & \sigma^2(m_{B,1}) \\ & & & & & & \ddots \\ 0 & & & & & & \sigma^2(m_{B,19}) \end{pmatrix} \quad (\text{G.1})$$

where $\sigma(\mu_{LMC}) = 0.0263$ is the error of the distance modulus to the LMC reported by Ref. [225], $\sigma(\mu_{N4258}) = 0.032$ is the error of the distance modulus to the NGC 4258 reported by Ref. [227] and $\sigma(m_{B,k})$ ($k = 1, \dots, 19$) are the errors of SnIa B-band magnitudes obtained from Table 5 in Ref. [17] (see our Table G.4 of the Appendix G.2).

For MW j th Cepheid we use a total statistical uncertainty arising from the quadrature sum of four terms (higher order terms $\mathcal{O}(zp/\pi_j)^2$ are negligible)

$$\sigma_{MW,j}^2 = \sigma^2(m_{H,j}) + \left(\frac{5}{\ln 10} \frac{1}{\pi_j} \right)^2 \sigma^2(\pi_j) + R_W^2 \sigma^2(V_j) + R_W^2 \sigma^2(I_j) \quad (\text{G.2})$$

and for LMC Cepheids we use a total statistical uncertainty arising from the quadrature sum of four terms:

$$\sigma_{LMC,j}^2 = \sigma^2(m_{H,j}) + \sigma^2(\mu) + R_W^2 \sigma^2(V_j) + R_W^2 \sigma^2(I_j) \quad (\text{G.3})$$

We see that for the MW and LMC Cepheids where the color errors are provided by SH0ES team (see in Table 1 of Ref. [40] and in Table 2 of Ref. [39] or our Table G.1 and our Table G.2 of the Appendix G.2 respectively) we have included them in the error matrix \mathbf{C} in the proper 2D manner (i.e. 2D fit including errors in both \mathbf{Y} and \mathbf{X} "axes").

For the j th Cepheid in the i th galaxy (other than MW and LMC) where SH0ES does not provide separate color errors we use a total statistical uncertainty σ_{tot} arising from the quadrature sum of four terms: NIR photometric error, color error, intrinsic width and random-phase as derived by SH0ES team and shown in column 8 of Table 4 of Ref. [17]

$$\sigma_{tot,j}^2 = \sigma_{sky}^2 + \sigma_{col}^2 + \sigma_{int}^2 + (f_{pf}\sigma_{ph})^2 \quad (\text{G.4})$$

These total statistical uncertainties σ_{tot} are shown in our Table G.3 of the Appendix G.2. Note that even though the color errors are included implicitly in our fit, in order to make a full 2D fit we will need the separate color errors which are not publicly available for these Cepheids by SH0ES team.

The schematic form of the matrix of measurements \mathbf{Y} and the matrix of parameters \mathbf{X} are

$$\mathbf{Y} = \begin{pmatrix} m_{\pi,j} \\ m_{H,1,j} \\ \vdots \\ m_{H,19,j} \\ m_{H,N4258,j} \\ m_{H,M31,j} \\ m_{H,LMC,j} \\ \mu_{N4258} \\ \mu_{LMC} \\ m_{B,1} \\ \vdots \\ m_{B,19} \end{pmatrix}, \quad \mathbf{X} = \begin{pmatrix} R_{W,LMC} \\ R_{W,MW} \\ R_{W,1} \\ \vdots \\ R_{W,19} \\ R_{W,N4258} \\ R_{W,M31} \\ \mu_1 \\ \vdots \\ \mu_{19} \\ \mu_{N4258} \\ \mu_{M31} \\ \mu_{LMC} \\ M_{H,MW}^W \\ M_{H,1}^W \\ \vdots \\ M_{H,19}^W \\ M_{H,N4258}^W \\ M_{H,M31}^W \\ M_{H,LMC}^W \\ b_W^s \\ b_W^l \\ Z_W \\ z_p \\ M_B \end{pmatrix} \quad (\text{G.5})$$

G.2 Data used in the analysis

In this appendix we present the data used in our analysis.

Table G.1: Photometric data for MW Cepheids from Table 1 in Ref. [40].

Cepheid	log P	F 555W [mag]	σ [mag]	F 814W [mag]	σ [mag]	F 160W [mag]	σ [mag]	m_H^W [mag]	σ [mag]	[Fe/H]	π [mas]	σ [mas]	π_{EDR3} [mas]	σ [mas]
AA-GEM	1.053	9.9130	0.029	8.542	0.025	7.348	0.017	6.860	0.023	-0.080	0.259	0.008	0.311	0.019
AD-PUP	1.133	10.015	0.028	8.675	0.023	7.488	0.020	7.011	0.024	-0.060	0.214	0.006	0.254	0.018
AQ-CAR	0.990	8.9836	0.020	7.854	0.009	6.766	0.007	6.373	0.011	0.013	0.354	0.010	0.361	0.017
AQ-PUP	1.479	8.8671	0.018	7.120	0.014	5.487	0.013	4.859	0.016	0.060	0.340	0.010	0.294	0.025
BK-AUR	0.903	9.5609	0.036	8.220	0.038	7.015	0.021	6.539	0.029	0.070	0.371	0.011	0.426	0.016
BN-PUP	1.136	10.051	0.033	8.505	0.017	7.198	0.015	6.642	0.021	0.030	0.251	0.007	0.301	0.016
CD-CYG	1.232	9.1207	0.011	7.468	0.012	5.900	0.012	5.307	0.014	0.120	0.398	0.011	0.394	0.018
CP-CEP	1.252	10.757	0.015	8.638	0.052	6.871	0.022	6.095	0.030	0.050	0.270	0.008	0.279	0.022
CR-CAR	0.989	11.750	0.019	9.973	0.018	8.384	0.014	7.736	0.017	-0.080	0.190	0.005	0.194	0.016
CY-AUR	1.141	12.052	0.012	9.953	0.020	8.106	0.025	7.334	0.027	-0.150	0.183	0.006
DD-CAS	0.992	10.036	0.007	8.523	0.011	7.108	0.012	6.566	0.013	0.160	0.319	0.009	0.346	0.014
DL-CAS	0.903	9.1059	0.019	7.569	0.022	6.238	0.018	5.689	0.021	0.050	0.550	0.016
DR-VEL	1.049	9.7083	0.034	7.770	0.020	6.183	0.021	5.479	0.026	0.024	0.488	0.015	0.520	0.015
GQ-ORI	0.935	8.7199	0.020	7.632	0.024	6.523	0.032	6.146	0.034	0.250	0.418	0.013	0.408	0.023
HW-CAR	0.964	9.2782	0.016	8.007	0.013	6.798	0.005	6.350	0.009	0.060	0.370	0.010	0.397	0.013
KK-CEN	1.086	11.598	0.017	9.862	0.021	8.292	0.015	7.660	0.018	0.210	0.167	0.005	0.152	0.017
KN-CEN	1.532	10.062	0.023	7.924	0.017	5.856	0.006	5.076	0.013	0.550	0.273	0.008	0.251	0.020
RW-CAM	1.215	8.8673	0.015	7.044	0.014	5.451	0.021	4.794	0.022	0.080	0.519	0.015
RW-CAS	1.170	9.3719	0.021	7.863	0.016	6.483	0.022	5.944	0.024	0.280	0.322	0.010	0.334	0.021
RY-CAS	1.084	10.075	0.019	8.333	0.040	6.715	0.010	6.085	0.020	0.320	0.342	0.010	0.359	0.016
RY-SCO	1.308	8.2067	0.012	6.206	0.010	4.408	0.010	3.685	0.012	0.010	0.757	0.021	0.764	0.035
RY-VEL	1.449	8.5234	0.036	6.757	0.016	5.211	0.017	4.576	0.023	0.090	0.403	0.012	0.376	0.023
S-NOR	0.989	6.5779	0.011	5.410	0.012	4.391	0.012	3.990	0.014	0.100	1.054	0.030	1.099	0.024
S-VUL	1.839	9.1668	0.008	6.862	0.012	4.885	0.010	4.043	0.011	0.090	0.287	0.008	0.237	0.022
SS-CMA	1.092	10.121	0.012	8.444	0.008	6.894	0.011	6.289	0.012	0.012	0.315	0.009	0.308	0.014
SV-PER	1.046	9.2186	0.016	7.760	0.014	6.435	0.027	5.916	0.028	0.030	0.400	0.012
SV-VEL	1.149	8.7316	0.026	7.302	0.009	6.024	0.010	5.517	0.015	0.090	0.411	0.012	0.434	0.019
SV-VUL	1.653	7.2675	0.047	5.648	0.033	4.214	0.027	3.639	0.035	0.110	0.457	0.015	0.402	0.023
SY-NOR	1.102	9.8284	0.023	7.925	0.038	6.214	0.013	5.523	0.022	0.230	0.435	0.013
SZ-CYG	1.179	9.6209	0.013	7.756	0.017	6.004	0.008	5.329	0.012	0.150	0.426	0.012	0.445	0.014
T-MON	1.432	6.0680	0.023	4.828	0.016	3.725	0.021	3.298	0.024	0.040	0.749	0.022	0.745	0.057
U-CAR	1.589	6.3852	0.038	4.967	0.023	3.768	0.019	3.272	0.026	0.250	0.589	0.018	0.561	0.025
UU-MUS	1.066	9.9212	0.024	8.457	0.025	7.108	0.010	6.584	0.017	0.190	0.282	0.008	0.306	0.013
V-339-CEN	0.976	8.8402	0.024	7.321	0.016	5.990	0.024	5.448	0.026	-0.080	0.557	0.017	0.568	0.023
V-340-ARA	1.318	10.460	0.024	8.554	0.014	6.808	0.012	6.115	0.016	-0.080	0.245	0.007	0.239	0.022
VW-CEN	1.177	10.379	0.031	8.718	0.023	7.158	0.010	6.558	0.018	0.410	0.238	0.007	0.260	0.017
VX-PER	1.037	9.4589	0.008	7.906	0.006	6.470	0.009	5.914	0.010	0.030	0.407	0.011	0.392	0.019
VY-CAR	1.276	7.6162	0.014	6.253	0.007	4.991	0.004	4.513	0.007	0.080	0.539	0.015	0.565	0.018
VZ-PUP	1.365	9.7715	0.033	8.262	0.022	6.931	0.017	6.390	0.023	-0.010	0.200	0.006	0.220	0.016
WX-PUP	0.951	9.1909	0.030	7.944	0.012	6.807	0.010	6.368	0.016	-0.010	0.376	0.011	0.387	0.017

WZ-SGR	1.339	8.2021	0.012	6.481	0.013	4.858	0.009	4.242	0.011	0.280	0.547	0.015	0.612	0.031
X-CYG	1.214	6.5295	0.020	5.230	0.049	4.080	0.033	3.629	0.039	0.160	0.883	0.029	0.910	0.022
X-PUP	1.414	8.6949	0.019	7.128	0.010	5.628	0.008	5.069	0.012	0.020	0.341	0.010	0.397	0.022
XX-CAR	1.196	9.4627	0.027	8.067	0.015	6.833	0.022	6.337	0.025	0.010	0.264	0.008	0.305	0.016
XY-CAR	1.095	9.4660	0.011	7.927	0.009	6.455	0.006	5.904	0.008	0.012	0.375	0.010	0.390	0.015
XZ-CAR	1.221	8.7725	0.017	7.217	0.006	5.770	0.007	5.215	0.010	0.026	0.425	0.012	0.473	0.020
YZ-CAR	1.259	8.8644	0.016	7.401	0.007	5.991	0.013	5.471	0.015	-0.030	0.359	0.010	0.358	0.020
YZ-SGR	0.980	7.4662	0.021	6.176	0.014	5.103	0.020	4.653	0.022	0.120	0.786	0.023	0.860	0.027
Z-LAC	1.037	8.5686	0.022	7.157	0.015	5.917	0.018	5.417	0.021	0.070	0.509	0.015	0.510	0.023
AG-CRU	0.584	8.3175	0.013	7.307	0.011	6.414	0.027	6.068	0.028	0.020	0.748	0.023	0.758	0.022
AP-PUP	0.706	7.4560	0.016	6.412	0.014	5.534	0.027	5.177	0.028	-0.020	0.941	0.029	0.924	0.022
AP-SGR	0.704	7.1056	0.028	6.036	0.013	5.094	0.027	4.729	0.030	0.160	1.145	0.035	1.217	0.026
BF-OPH	0.609	7.5091	0.018	6.347	0.010	5.374	0.027	4.972	0.028	0.110	1.184	0.036	1.189	0.026
BG-VEL	0.840	7.7827	0.010	6.299	0.009	5.054	0.019	4.529	0.020	0.040	1.033	0.030	1.045	0.019
ER-CAR	0.888	6.9095	0.011	5.916	0.012	5.078	0.027	4.742	0.028	0.120	0.867	0.026	0.869	0.016
R-CRU	0.765	6.8479	0.017	5.856	0.016	4.984	0.027	4.649	0.028	0.100	1.088	0.033	1.078	0.031
R-MUS	0.876	6.4568	0.009	5.447	0.008	4.609	0.019	4.268	0.020	-0.110	1.117	0.033	1.076	0.019
R-TRA	0.530	6.7236	0.013	5.794	0.014	5.025	0.019	4.714	0.020	0.160	1.497	0.044	1.560	0.018
RV-SCO	0.783	7.1616	0.010	5.871	0.007	4.773	0.019	4.323	0.020	0.080	1.234	0.036	1.257	0.023
RX-CAM	0.898	7.8310	0.016	6.215	0.013	4.791	0.028	4.216	0.029	0.080	1.090	0.034
RY-CMA	0.670	8.2358	0.015	7.111	0.013	6.045	0.027	5.656	0.028	0.140	0.787	0.024	0.825	0.032
S-CRUe	0.671	6.6700	0.050	5.698	0.011	4.843	0.027	4.516	0.033	0.080	1.335	0.042	1.342	0.026
S-TRA	0.801	6.5171	0.013	5.553	0.012	4.752	0.027	4.429	0.028	0.010	1.150	0.035	1.120	0.024
SS-SCT	0.565	8.3122	0.010	7.073	0.005	6.034	0.019	5.600	0.019	0.110	0.948	0.028	0.934	0.025
T-VEL	0.667	8.1205	0.009	6.915	0.007	5.839	0.019	5.419	0.020	-0.160	0.904	0.026	0.940	0.018
TX-CYG	1.168	9.6108	0.024	7.083	0.015	4.789	0.027	3.862	0.029	0.260	0.844	0.026	0.829	0.020
U-AQL	0.847	6.5396	0.019	5.168	0.029	4.115	0.027	3.636	0.030	0.140	1.531	0.047
U-SGR	0.829	6.8864	0.018	5.388	0.011	4.143	0.027	3.615	0.028	0.140	1.588	0.049	1.605	0.025
V-CAR	0.826	7.4753	0.009	6.403	0.008	5.463	0.019	5.096	0.020	0.080	0.810	0.024	0.797	0.015
V-VEL	0.641	7.5198	0.013	6.555	0.010	5.693	0.027	5.366	0.028	0.000	0.951	0.029	0.953	0.019
V0386-CYG	0.721	9.8126	0.015	7.748	0.014	5.944	0.027	5.192	0.028	0.170	0.901	0.028	0.894	0.014
V0482-SCO	0.656	8.0697	0.013	6.773	0.013	5.697	0.027	5.242	0.028	0.019	0.982	0.030	0.993	0.028
V0636-SCO	0.832	6.8167	0.009	5.618	0.008	4.568	0.020	4.154	0.021	0.070	1.239	0.036	1.180	0.037
W-GEM	0.898	7.0841	0.057	5.899	0.018	4.863	0.027	4.454	0.036	-0.010	0.984	0.032	1.006	0.031

Table G.2: Photometric data for LMC Cepheids from Table 2 in Ref. [39].

Cepheid	RA	DEC	Geo	log Period	F 555W [mag]	σ [mag]	F 814W [mag]	σ [mag]	F 160W [mag]	σ [mag]	m_H^W [mag]	σ [mag]
OGL0434	74.114583	-69.379611	0.028	1.482	13.131	0.028	12.208	0.011	11.321	0.018	10.966	0.021
OGL0501	74.462625	-69.958250	0.034	1.367	13.623	0.022	12.693	0.012	11.770	0.021	11.406	0.023
OGL0510	74.523208	-69.454333	0.027	1.566	13.457	0.037	12.299	0.021	11.232	0.042	10.787	0.045
OGL0512	74.545000	-69.949694	0.033	1.595	13.134	0.025	12.005	0.017	11.038	0.017	10.598	0.020
OGL0528	74.636583	-70.346028	0.038	1.553	13.175	0.052	12.156	0.021	11.226	0.020	10.824	0.029
OGL0545	74.696292	-70.061583	0.034	1.199	14.414	0.045	13.349	0.010	12.311	0.018	11.895	0.025
OGL0590	74.921417	-69.456111	0.025	1.502	13.470	0.025	12.382	0.014	11.311	0.038	10.895	0.039
OGL0594	74.937833	-69.493194	0.025	0.828	15.279	0.012	14.352	0.011	13.525	0.030	13.171	0.030
OGL0648	75.201500	-69.531861	0.025	1.134	14.740	0.012	13.675	0.009	12.714	0.028	12.308	0.029

OGL0683	75.353917	-70.071750	0.031	1.166	14.446	0.009	13.350	0.009	12.481	0.020	12.056	0.021
OGL0712	75.477375	-68.904028	0.016	1.316	13.771	0.033	12.862	0.009	11.889	0.038	11.552	0.040
OGL0716	75.503958	-68.922833	0.016	1.085	14.958	0.012	13.895	0.011	12.938	0.023	12.541	0.024
OGL0727	75.542667	-69.539917	0.023	1.161	14.208	0.010	13.231	0.010	12.375	0.033	12.004	0.034
OGL0757	75.629333	-69.397056	0.021	0.924	15.153	0.012	14.214	0.012	13.364	0.023	13.010	0.024
OGL0770	75.714750	-68.784806	0.013	1.035	14.698	0.012	13.757	0.010	12.913	0.029	12.566	0.030
OGL0787	75.787750	-69.223333	0.018	1.243	14.243	0.009	13.186	0.009	12.281	0.042	11.884	0.042
OGL0798	75.848542	-69.000889	0.015	1.029	14.891	0.011	13.860	0.009	12.934	0.020	12.550	0.021
OGL0800	75.854417	-68.772500	0.012	1.101	14.541	0.018	13.584	0.011	12.712	0.043	12.359	0.044
OGL0812	75.908167	-69.063083	0.015	1.086	14.670	0.011	13.691	0.010	12.733	0.024	12.369	0.025
OGL0819	75.942333	-68.876778	0.013	1.348	14.162	0.014	13.013	0.010	11.987	0.029	11.560	0.030
OGL0821	75.956250	-68.934083	0.014	1.411	13.770	0.009	12.714	0.010	11.706	0.024	11.314	0.025
OGL0831	75.988583	-68.840056	0.012	0.987	14.761	0.012	13.827	0.010	12.969	0.023	12.625	0.024
OGL0844	76.064458	-69.026778	0.014	1.235	13.967	0.019	13.010	0.011	12.146	0.034	11.791	0.035
OGL0847	76.081833	-68.930306	0.013	1.314	14.437	0.009	13.317	0.011	12.320	0.030	11.904	0.031
OGL0848	76.087833	-68.728556	0.010	1.203	14.262	0.013	13.341	0.011	12.444	0.027	12.107	0.028
OGL0888	76.316875	-68.723472	0.009	0.971	14.889	0.010	13.960	0.010	13.135	0.022	12.796	0.022
OGL0915	76.424875	-68.851472	0.010	0.868	15.125	0.013	14.216	0.011	13.359	0.021	13.027	0.022
OGL0936	76.504708	-68.627361	0.007	0.920	15.046	0.015	14.101	0.012	13.260	0.023	12.917	0.024
OGL0949	76.570375	-68.676028	0.007	1.111	14.519	0.016	13.549	0.011	12.670	0.018	12.317	0.019
OGL0966	76.699875	-70.037056	0.024	1.676	12.944	0.026	11.861	0.014	10.896	0.023	10.483	0.025
OGL0969	76.720250	-68.723639	0.007	1.104	14.727	0.013	13.691	0.012	12.725	0.028	12.347	0.029
OGL0970	76.720708	-68.659889	0.006	1.242	14.369	0.014	13.249	0.011	12.260	0.031	11.850	0.032
OGL0975	76.742833	-68.611417	0.006	1.101	14.628	0.015	13.617	0.011	12.749	0.023	12.382	0.024
OGL0978	76.748792	-68.723972	0.007	1.022	14.855	0.011	13.817	0.010	12.908	0.021	12.529	0.022
OGL0986	76.782542	-68.888750	0.009	1.492	13.471	0.018	12.403	0.008	11.445	0.045	11.053	0.045
OGL0992	76.816583	-68.883500	0.009	1.723	12.305	0.016	11.297	0.011	10.436	0.073	10.067	0.073
OGL1001	76.840375	-68.338417	0.002	1.160	14.464	0.009	13.447	0.009	12.485	0.023	12.119	0.024
OGL1031	76.925542	-69.246694	0.013	1.266	14.455	0.011	13.348	0.009	12.284	0.021	11.873	0.022
OGL1058	77.076125	-68.779750	0.006	1.482	13.564	0.016	12.452	0.008	11.467	0.021	11.060	0.022
OGL1080	77.183292	-68.757778	0.005	1.270	14.135	0.014	13.061	0.011	12.097	0.025	11.706	0.026
OGL1109	77.316417	-68.741556	0.005	1.074	14.520	0.008	13.592	0.009	12.744	0.053	12.410	0.053
OGL1112	77.326458	-68.299556	-0.000	0.899	14.713	0.010	13.907	0.011	13.134	0.053	12.853	0.054
OGL1313	78.580750	-69.490056	0.008	0.834	15.128	0.012	14.278	0.012	13.529	0.026	13.222	0.027
OGL1374	78.857208	-69.340917	0.005	0.838	15.386	0.011	14.438	0.012	13.582	0.031	13.240	0.031
OGL1389	78.909875	-69.255500	0.004	0.862	14.965	0.011	14.139	0.012	13.382	0.019	13.088	0.020
OGL1411	78.991833	-69.712083	0.009	0.897	15.324	0.010	14.324	0.011	13.468	0.026	13.102	0.026
OGL1417	79.000917	-69.538167	0.007	0.938	14.879	0.009	13.954	0.010	13.138	0.031	12.803	0.031
OGL1424	79.016000	-69.247889	0.003	0.830	15.663	0.013	14.622	0.015	13.686	0.030	13.310	0.031
OGL1431	79.041083	-69.544306	0.007	1.010	14.829	0.010	13.841	0.009	13.028	0.027	12.669	0.027
OGL1463	79.228708	-69.330667	0.003	0.876	15.098	0.011	14.171	0.011	13.339	0.024	13.007	0.025
OGL1466	79.244417	-69.393889	0.004	0.789	15.581	0.012	14.607	0.013	13.719	0.031	13.368	0.032
OGL1490	79.353083	-69.349333	0.003	0.912	14.690	0.014	13.876	0.010	13.160	0.023	12.872	0.024
OGL1526	79.515792	-69.426639	0.003	0.828	15.147	0.012	14.287	0.011	13.475	0.025	13.169	0.026
OGL1539	79.592125	-69.363139	0.002	1.130	14.636	0.016	13.620	0.011	12.671	0.019	12.306	0.021
OGL1578	79.811667	-69.605028	0.005	1.123	14.329	0.017	13.379	0.010	12.590	0.023	12.248	0.024
OGL1587	79.865750	-69.508389	0.003	1.334	14.151	0.008	12.959	0.009	11.925	0.034	11.491	0.034
OGL1616	79.999708	-69.173722	-0.001	1.191	14.894	0.017	13.693	0.012	12.631	0.033	12.198	0.034
OGL1637	80.095833	-69.038194	-0.003	1.504	13.337	0.025	12.251	0.014	11.314	0.035	10.928	0.036
OGL1641	80.119292	-69.025500	-0.003	1.144	14.180	0.010	13.272	0.010	12.428	0.026	12.111	0.027
OGL1647	80.155792	-69.515722	0.002	0.939	14.833	0.019	13.957	0.015	13.157	0.028	12.846	0.030
OGL1677	80.301958	-69.052111	-0.004	1.372	13.717	0.013	12.716	0.017	11.816	0.020	11.463	0.022

OGL1862	81.056042	-69.500444	-0.001	1.118	14.868	0.013	13.763	0.010	12.753	0.028	12.357	0.028
OGL1939	81.370042	-69.912361	0.002	0.782	15.498	0.021	14.583	0.015	13.683	0.029	13.356	0.031
OGL1940	81.370625	-69.834194	0.001	0.972	16.659	0.022	15.055	0.017	13.509	0.026	12.917	0.028
OGL1941	81.372000	-69.920167	0.003	0.832	15.642	0.015	14.538	0.013	13.593	0.029	13.193	0.030
OGL1945	81.381000	-69.834361	0.001	0.885	16.166	0.020	14.832	0.016	13.610	0.023	13.123	0.025
OGL1994	81.594042	-69.602056	-0.002	0.889	14.779	0.022	13.946	0.011	13.229	0.019	12.939	0.022
OGL2012	81.708292	-69.764667	-0.000	0.872	15.061	0.011	14.136	0.010	13.327	0.025	13.000	0.025
OGL2019	81.732917	-69.980222	0.002	1.448	13.615	0.018	12.581	0.014	11.697	0.025	11.325	0.027
OGL2043	81.845667	-69.849444	0.000	0.867	15.246	0.011	14.320	0.012	13.495	0.038	13.167	0.039

Table G.3: WFC3-IR data for 1486 Cepheids in the anchor galaxy NGC 4258 and in the host galaxies from Table 4 in Ref. [17]. An electronic version of the complete table is available at [70].

Galaxy Name	α	δ	ID [mag]	P [days]	$V - I$ [mag]	H [mag]	σ_{tot} [mag]	Z^1 [dex]
N1309	50.513050	-15.412250	154632	38.10	1.08	25.46	0.22	8.582
N1309	50.514080	-15.405860	149317	39.31	1.34	25.31	0.42	8.722
N1309	50.537010	-15.412090	42756	39.42	1.14	25.28	0.24	8.793
N1309	50.536140	-15.385790	40303	39.50	1.00	25.19	0.24	8.758
N1309	50.534050	-15.388290	50270	39.83	1.22	25.56	0.26	8.866
N1309	50.520380	-15.397210	119907	40.84	1.40	24.57	0.55	8.974
N1309	50.516100	-15.386090	136479	41.02	1.15	25.07	0.18	8.646
N1309	50.531470	-15.406890	67093	41.77	1.23	24.45	0.45	9.037
N1309	50.528230	-15.408650	82654	41.94	1.05	24.24	0.50	8.987
N1309	50.540170	-15.394110	27150	42.11	1.03	24.49	0.28	8.860
N1309	50.533920	-15.386930	50545	44.14	1.11	25.34	0.57	8.825
N1309	50.534590	-15.392310	48826	44.32	1.65	24.54	0.34	8.975
N1309	50.522460	-15.384870	103930	44.60	0.89	24.95	0.22	8.739
N1309	50.520140	-15.408020	2099043	44.30	1.39	24.12	0.45	8.866
N1309	50.535980	-15.411540	47351	45.45	1.02	24.64	0.24	8.828
N1309	50.516850	-15.403490	2108877	47.59	1.34	24.78	0.53	8.841
N1309	50.513220	-15.403900	152242	47.82	0.95	24.76	0.33	8.715
N1309	50.514140	-15.404030	2117990	48.18	1.23	24.88	0.43	8.745
N1309	50.517600	-15.403870	134187	47.87	1.31	23.84	0.62	8.862
N1309	50.513500	-15.398810	150120	48.45	1.52	24.85	0.30	8.743
N1309	50.541640	-15.396450	22773	49.57	1.35	25.16	0.23	8.840
N1309	50.523070	-15.400960	105535	50.82	1.25	24.92	0.49	9.074
N1309	50.530380	-15.386750	66971	51.38	1.14	24.75	0.24	8.849
N1309	50.519300	-15.403510	126515	51.43	0.80	24.60	0.60	8.922
N1309	50.532360	-15.415870	65208	52.02	1.41	24.34	0.18	8.734
N1309	50.526790	-15.409480	89446	52.50	1.11	24.57	0.40	8.950
N1309	50.523400	-15.407320	105633	54.07	0.89	24.65	0.65	8.963
N1309	50.531490	-15.389480	62523	56.82	1.13	24.77	0.25	8.934
N1309	50.530220	-15.390540	68651	58.92	1.31	25.03	0.33	8.978
N1309	50.520230	-15.406500	122991	58.97	1.66	24.83	0.43	8.902
N1309	50.515030	-15.407650	145875	64.63	1.54	24.58	0.33	8.726

¹ $Z = 12 + \log(O/H)$

N1309	50.520350	-15.400180	120871	64.84	1.32	23.75	0.54	8.983
N1309	50.528410	-15.417520	83989	64.20	1.32	24.32	0.19	8.688
N1309	50.540600	-15.394620	25808	67.70	1.18	24.61	0.19	8.854
N1309	50.528080	-15.409230	83493	57.92	1.40	24.53	0.35	8.967
N1309	50.536050	-15.412330	47225	69.33	1.11	24.57	0.22	8.804
N1309	50.537880	-15.406430	37762	69.30	1.09	24.31	0.21	8.914
N1309	50.535540	-15.414100	49918	71.48	1.08	24.12	0.23	8.758
N1309	50.527070	-15.408140	87828	73.62	0.97	24.31	0.30	8.996
N1309	50.519710	-15.404750	124934	75.76	1.50	24.21	0.40	8.918
N1309	50.518570	-15.394630	127649	84.54	1.07	24.27	0.50	8.885
N1309	50.526840	-15.407730	88762	84.89	1.27	23.90	0.40	9.007
N1309	50.540840	-15.390800	24251	90.59	1.31	24.01	0.18	8.781
N1309	50.526100	-15.405700	91743	90.91	1.06	24.08	0.36	9.061
N1365	53.428340	-36.168310	111818	15.90	0.71	25.07	0.63	8.814
N1365	53.468230	-36.154760	140975	16.45	1.27	25.25	0.32	8.420
N1365	53.435410	-36.169560	123989	16.72	0.88	24.53	0.40	8.715
N1365	53.448980	-36.163290	132389	17.00	1.07	25.29	0.33	8.613
N1365	53.444760	-36.149450	103384	17.01	0.91	25.82	0.44	8.796
N1365	53.440820	-36.157210	111940	19.69	0.67	24.86	0.40	8.784
N1365	53.465100	-36.152740	136735	25.70	0.89	24.48	0.18	8.480
N1365	53.426190	-36.165250	101154	26.08	0.99	23.98	0.70	8.878
N1365	53.445370	-36.136230	63449	26.96	1.36	24.16	0.36	8.858
N1365	53.462490	-36.157290	138773	26.98	1.01	24.40	0.19	8.481
N1365	53.443040	-36.160620	120972	27.45	1.04	24.41	0.24	8.720
N1365	53.446770	-36.135500	65336	27.94	0.87	24.82	0.32	8.839
N1365	53.438940	-36.166810	124631	29.33	1.02	24.11	0.24	8.705
N1365	53.458140	-36.153810	130859	29.37	0.98	24.48	0.23	8.571
N1365	53.460390	-36.153990	133465	29.45	1.35	24.29	0.23	8.538
N1365	53.431590	-36.162200	105797	30.34	1.29	24.07	0.48	8.851
N1365	53.427620	-36.166050	106470	30.39	0.91	23.83	0.42	8.851
N1365	53.438980	-36.153370	100027	31.37	0.67	24.33	0.30	8.845
N1365	53.431200	-36.158650	94995	32.42	1.02	24.35	0.45	8.897
N1365	53.449180	-36.155960	122163	34.10	1.21	24.19	0.19	8.680
N1365	53.449310	-36.140060	87703	35.11	1.21	23.54	0.26	8.786
N1365	53.427540	-36.151730	61628	37.01	1.61	24.27	0.38	9.018
N1365	53.433170	-36.155410	90510	39.06	1.06	24.04	0.41	8.905
N1365	53.437550	-36.170950	128912	40.73	1.14	23.47	0.20	8.673
N1365	53.440360	-36.153510	103704	40.85	1.43	24.26	0.23	8.825
N1365	53.432210	-36.161310	104907	42.90	1.10	23.44	0.36	8.854
N1365	53.431420	-36.172780	123489	43.00	0.97	23.96	0.32	8.720
N1365	53.437390	-36.155420	101731	47.24	0.91	23.03	0.22	8.848
N1365	53.435220	-36.154740	94055	51.45	1.33	23.91	0.25	8.884
N1365	53.438630	-36.170270	129336	57.13	0.95	23.42	0.16	8.668
N1365	53.432110	-36.155840	88821	63.17	1.32	23.35	0.26	8.915
N1365	53.427080	-36.156250	75575	68.46	1.25	22.90	0.32	8.976

Table G.4: Approximations for distance parameters from Table 5 in Ref. [17].

Host Galaxy	SnIa	$m_{B,i}^0 + 5\alpha_B$ [mag]	σ [mag]	μ_{ceph} [mag]	σ [mag]	$M_{B,i}^0$ [mag]	σ [mag]
-------------	------	----------------------------------	-------------------	-----------------------	-------------------	----------------------	-------------------

M101	2011fe	13.310	0.117	29.135	0.045	-19.389	0.125
N1015	2009ig	17.015	0.123	32.497	0.081	-19.047	0.147
N1309	2002fk	16.756	0.116	32.523	0.055	-19.331	0.128
N1365	2012fr	15.482	0.125	31.307	0.057	-19.390	0.137
N1448	2001el	15.765	0.116	31.311	0.045	-19.111	0.125
N2442	2015F	15.840	0.142	31.511	0.053	-19.236	0.152
N3021	1995al	16.527	0.117	32.498	0.090	-19.535	0.147
N3370	1994ae	16.476	0.115	32.072	0.049	-19.161	0.125
N3447	2012ht	16.265	0.124	31.908	0.043	-19.207	0.131
N3972	2011by	16.048	0.116	31.587	0.070	-19.103	0.136
N3982	1998aq	15.795	0.115	31.737	0.069	-19.507	0.134
N4038	2007sr	15.797	0.114	31.290	0.112	-19.058	0.160
N4424	2012cg	15.110	0.109	31.080	0.292	-19.534	0.311
N4536	1981B	15.177	0.124	30.906	0.053	-19.293	0.135
N4639	1990N	15.983	0.115	31.532	0.071	-19.113	0.135
N5584	2007af	16.265	0.115	31.786	0.046	-19.085	0.124
N5917	2005cf	16.572	0.115	32.263	0.102	-19.255	0.154
N7250	2013dy	15.867	0.115	31.499	0.078	-19.196	0.139
U9391	2003du	17.034	0.114	32.919	0.063	-19.449	0.130

Appendix H

Gravitational Transitions via the Explicitly Broken Symmetron Screening Mechanism

H.1 Cluster collection

In this appendix we present the collection of 12 clusters.

Table H.1: The collection of 12 clusters. From left to right the columns correspond to: Abell names, galactic coordinates (from NED), redshifts (from NED), luminosity distances (from NED), the halo radii for overdensity of $\Delta = 500$ with respect to the critical density of the universe at the cluster's redshift, the modified gravity parameters Ξ_1 and $\bar{\gamma}$ which track the departure of DHOST theory from GR as derived by Ref. [57] and the corresponding σ significances.

Cluster	RA [Deg]	DEC [Deg]	z	D [Mpc]	GR R_{500} [Mpc]	DHOST R_{500} [Mpc]	Ξ_1	Sign. σ_{Ξ_1}	$\bar{\gamma}$	Sign. $\sigma_{\bar{\gamma}}$
A85	10.458750	-9.301944	0.05506	248	$1.270^{+0.010}_{-0.015}$	$1.292^{+0.017}_{-0.030}$	$0.30^{+0.11}_{-0.27}$	1.100	1.05 ± 0.28	0.179
A644	124.352083	-7.512778	0.07040	332	$1.175^{+0.020}_{-0.015}$	$0.980^{+0.028}_{-0.030}$	$-1.04^{+0.18}_{-0.19}$	5.470	0.58 ± 0.22	1.910
A1644	194.290417	-17.400278	0.04740	222	$1.003^{+0.019}_{-0.017}$	$0.844^{+0.020}_{-0.027}$	$-0.837^{+0.119}_{-0.090}$	7.034	0.59 ± 0.16	2.562
A1795	207.220833	26.595556	0.06248	293	$1.150^{+0.015}_{-0.010}$	$1.101^{+0.032}_{-0.035}$	$-0.169^{+0.111}_{-0.090}$	1.523	0.88 ± 0.25	0.480
A2029	227.729167	5.720000	0.07872	372	$1.369^{+0.019}_{-0.015}$	$1.352^{+0.089}_{-0.016}$	$-0.04^{+0.19}_{-0.12}$	0.211	1.03 ± 0.48	0.063
A2142	239.585833	27.226944	0.09090	430	$1.389^{+0.017}_{-0.017}$	$1.326^{+0.040}_{-0.024}$	$-0.203^{+0.101}_{-0.079}$	2.010	0.87 ± 0.38	0.342
A2255	258.129364	64.092572	0.08029	376	$1.180^{+0.023}_{-0.021}$	$0.953^{+0.046}_{-0.043}$	$-1.1^{+0.26}_{-0.32}$	3.438	0.53 ± 0.28	1.679
A2319	290.286667	43.958333	0.05570	254	$1.336^{+0.016}_{-0.006}$	$1.151^{+0.020}_{-0.016}$	$-0.827^{+0.108}_{-0.076}$	7.657	0.64 ± 0.15	2.400
A3158	55.724583	-53.635278	0.05917	273	$1.119^{+0.016}_{-0.012}$	$1.054^{+0.057}_{-0.029}$	$-0.23^{+0.15}_{-0.18}$	1.278	0.83 ± 0.33	0.515
A3266	67.850417	-61.443889	0.05906	273	$1.489^{+0.027}_{-0.030}$	$1.455^{+0.045}_{-0.055}$	$0.100^{+0.137}_{-0.079}$	0.730	0.93 ± 0.65	0.108

RXC1825	276.352917	30.441944	0.06500	299	$1.108^{+0.013}_{-0.012}$	$1.130^{+0.016}_{-0.018}$	$0.17^{+0.17}_{-0.13}$	1.000	1.06 ± 0.19	0.316
ZW1215	184.419167	3.662500	0.07708	366	$1.368^{+0.029}_{-0.029}$	$1.331^{+0.041}_{-0.076}$	$-0.21^{+0.27}_{-0.18}$	0.778	0.91 ± 0.64	0.141

Appendix I

Numerical Algorithms

In this appendix we provide the links of the github repositories which include the algorithms used for the numerical analysis and for construction of the figures of this dissertation.

1. The algorithms used for the numerical analysis and for construction of the figures of Chapter 5 can be found in the "Reconstructing a Model for Gravity at Large Distances from Dark Matter Density Profiles" repository [2517], [🔗](#).
2. The algorithms used for the numerical analysis and for construction of the figures of Chapter 6 can be found in the "Primordial Power Spectra of Cosmological Fluctuations with GUP" repository [2518], [🔗](#).
3. The algorithms used for the numerical analysis and for construction of the figures of Chapter 7 can be found in the "Tension of the E_G statistic and RSD data with the Λ CDM" repository [2519], [🔗](#).
4. The algorithms used for the numerical analysis and for construction of the figures of Chapter 8 can be found in the "Scalar tachyonic instabilities in gravitational background" repository [2520], [🔗](#).
5. The algorithms used for the numerical analysis and for construction of the figures of Chapter 10 can be found in the "Cepheid SnIa Calibrator Data Transition" repository [2521], [🔗](#).
6. The algorithms used for the numerical analysis and for construction of the figures of Chapter 11 can be found in the "Gravitational transitions via the explicitly broken symmetron screening mechanism" repository [2522], [🔗](#).

Bibliography

- [1] L. Kazantzidis, L. Perivolaropoulos, and F. Skara, *Constraining power of cosmological observables: blind redshift spots and optimal ranges*, *Phys. Rev. D* **99** (2019), no. 6 063537, [[arXiv:1812.05356](#)].
- [2] L. Perivolaropoulos and F. Skara, *Reconstructing a Model for Gravity at Large Distances from Dark Matter Density Profiles*, *Phys. Rev. D* **99** (2019), no. 12 124006, [[arXiv:1903.06554](#)].
- [3] F. Skara and L. Perivolaropoulos, *Primordial Power Spectra of Cosmological Fluctuations with Generalized Uncertainty Principle and Maximum Length Quantum Mechanics*, *Phys. Rev. D* **100** (2019), no. 12 123527, [[arXiv:1907.12594](#)].
- [4] F. Skara and L. Perivolaropoulos, *Tension of the E_G statistic and redshift space distortion data with the Planck - Λ CDM model and implications for weakening gravity*, *Phys. Rev. D* **101** (2020), no. 6 063521, [[arXiv:1911.10609](#)].
- [5] L. Perivolaropoulos and F. Skara, *Scalar tachyonic instabilities in gravitational backgrounds: Existence and growth rate*, *Phys. Rev. D* **102** (2020), no. 10 104034, [[arXiv:2009.05640](#)].
- [6] R. Gannouji, L. Perivolaropoulos, D. Polarski, and F. Skara, *Weak gravity on a Λ CDM background*, *Phys. Rev. D* **103** (2021), no. 6 063509, [[arXiv:2011.01517](#)].
- [7] L. Perivolaropoulos and F. Skara, *Challenges for Λ CDM: An update*, [arXiv:2105.05208](#).
- [8] L. Perivolaropoulos and F. Skara, *Hubble tension or a transition of the Cepheid S_nIa calibrator parameters?*, *Phys. Rev. D* **104** (2021), no. 12 123511, [[arXiv:2109.04406](#)].
- [9] L. Perivolaropoulos and F. Skara, *Gravitational transitions via the explicitly broken symmetron screening mechanism*, [arXiv:2203.10374](#).
- [10] E. Abdalla et al., *Cosmology Intertwined: A Review of the Particle Physics, Astrophysics, and Cosmology Associated with the Cosmological Tensions and Anomalies*, in *2022 Snowmass Summer Study*, 3, 2022. [arXiv:2203.06142](#).
- [11] E. Hubble, *A relation between distance and radial velocity among extra-galactic nebulae*, *Proc. Nat. Acad. Sci.* **15** (1929) 168–173.
- [12] L. Kazantzidis and L. Perivolaropoulos, *Hints of a Local Matter Underdensity or Modified Gravity in the Low z Pantheon data*, [arXiv:2004.02155](#).
- [13] D. J. Eisenstein, H.-j. Seo, and M. J. White, *On the Robustness of the Acoustic Scale in the Low-Redshift Clustering of Matter*, *Astrophys. J.* **664** (2007) 660–674, [[astro-ph/0604361](#)].
- [14] **Planck** Collaboration, N. Aghanim et al., *Planck 2018 results. VI. Cosmological parameters*, *Astron. Astrophys.* **641** (2020) A6, [[arXiv:1807.06209](#)]. [Erratum: *Astron. Astrophys.* 652, C4 (2021)].

- [15] **SDSS Collaboration**, D. J. Eisenstein et al., *Detection of the Baryon Acoustic Peak in the Large-Scale Correlation Function of SDSS Luminous Red Galaxies*, *Astrophys. J.* **633** (2005) 560–574, [[astro-ph/0501171](#)].
- [16] **Planck Collaboration**, P. A. R. Ade et al., *Planck 2015 results. XIII. Cosmological parameters*, *Astron. Astrophys.* **594** (2016) A13, [[arXiv:1502.01589](#)].
- [17] A. G. Riess et al., *A 2.4% Determination of the Local Value of the Hubble Constant*, *Astrophys. J.* **826** (2016), no. 1 56, [[arXiv:1604.01424](#)].
- [18] **LIGO Scientific, VINROUGE, Las Cumbres Observatory, DES, DLT40, Virgo, 1M2H, Dark Energy Camera GW-E, MASTER Collaboration**, B. P. Abbott et al., *A gravitational-wave standard siren measurement of the Hubble constant*, *Nature* **551** (2017), no. 7678 85–88, [[arXiv:1710.05835](#)].
- [19] **ACT Collaboration**, S. Aiola et al., *The Atacama Cosmology Telescope: DR4 Maps and Cosmological Parameters*, *JCAP* **12** (2020) 047, [[arXiv:2007.07288](#)].
- [20] Y. Wang, L. Xu, and G.-B. Zhao, *A measurement of the Hubble constant using galaxy redshift surveys*, *Astrophys. J.* **849** (2017), no. 2 84, [[arXiv:1706.09149](#)].
- [21] X. Zhang and Q.-G. Huang, *Constraints on H_0 from WMAP and BAO Measurements*, *Commun. Theor. Phys.* **71** (2019), no. 7 826–830, [[arXiv:1812.01877](#)].
- [22] G. Addison, D. Watts, C. Bennett, M. Halpern, G. Hinshaw, and J. Weiland, *Elucidating Λ CDM: Impact of Baryon Acoustic Oscillation Measurements on the Hubble Constant Discrepancy*, *Astrophys. J.* **853** (2018), no. 2 119, [[arXiv:1707.06547](#)].
- [23] A. G. Riess et al., *A Comprehensive Measurement of the Local Value of the Hubble Constant with 1 km/s/Mpc Uncertainty from the Hubble Space Telescope and the SH0ES Team*, [arXiv:2112.04510](#).
- [24] D. O. Jones et al., *Cosmological Results from the RAISIN Survey: Using Type Ia Supernovae in the Near Infrared as a Novel Path to Measure the Dark Energy Equation of State*, [arXiv:2201.07801](#).
- [25] C. D. Huang, A. G. Riess, W. Yuan, L. M. Macri, N. L. Zakamska, S. Casertano, P. A. Whitelock, S. L. Hoffmann, A. V. Filippenko, and D. Scolnic, *Hubble Space Telescope Observations of Mira Variables in the Type Ia Supernova Host NGC 1559: An Alternative Candle to Measure the Hubble Constant*, [arXiv:1908.10883](#).
- [26] J. P. Blakeslee, J. B. Jensen, C.-P. Ma, P. A. Milne, and J. E. Greene, *The Hubble Constant from Infrared Surface Brightness Fluctuation Distances*, *Astrophys. J.* **911** (2021), no. 1 65, [[arXiv:2101.02221](#)].
- [27] T. de Jaeger, L. Galbany, A. G. Riess, B. E. Stahl, B. J. Shappee, A. V. Filippenko, and W. Zheng, *A 5% measurement of the Hubble constant from Type II supernovae*, [arXiv:2203.08974](#).
- [28] K. C. Wong et al., *H0LiCOW – XIII. A 2.4 per cent measurement of H_0 from lensed quasars: 5.3 σ tension between early- and late-Universe probes*, *Mon. Not. Roy. Astron. Soc.* **498** (2020), no. 1 1420–1439, [[arXiv:1907.04869](#)].
- [29] **LIGO Scientific, Virgo Collaboration**, R. Abbott et al., *GW190814: Gravitational Waves from the Coalescence of a 23 Solar Mass Black Hole with a 2.6 Solar Mass Compact Object*, *Astrophys. J. Lett.* **896** (2020), no. 2 L44, [[arXiv:2006.12611](#)].

- [30] D. Pesce et al., *The Megamaser Cosmology Project. XIII. Combined Hubble constant constraints*, *Astrophys. J. Lett.* **891** (2020), no. 1 L1, [[arXiv:2001.09213](#)].
- [31] E. Kourkchi, R. B. Tully, G. S. Anand, H. M. Courtois, A. Dupuy, J. D. Neill, L. Rizzi, and M. Seibert, *Cosmicflows-4: The Calibration of Optical and Infrared Tully–Fisher Relations*, *Astrophys. J.* **896** (2020), no. 1 3, [[arXiv:2004.14499](#)].
- [32] H. Zeng and D. Yan, *Using the Extragalactic Gamma-Ray Background to Constrain the Hubble Constant and Matter Density of the Universe*, [arXiv:1907.10965](#).
- [33] H. Yu, B. Ratra, and F.-Y. Wang, *Hubble Parameter and Baryon Acoustic Oscillation Measurement Constraints on the Hubble Constant, the Deviation from the Spatially Flat Λ CDM Model, the Deceleration–Acceleration Transition Redshift, and Spatial Curvature*, *Astrophys. J.* **856** (2018), no. 1 3, [[arXiv:1711.03437](#)].
- [34] D. Fernández Arenas, E. Terlevich, R. Terlevich, J. Melnick, R. Chávez, F. Bresolin, E. Telles, M. Plionis, and S. Basilakos, *An independent determination of the local Hubble constant*, *Mon. Not. Roy. Astron. Soc.* **474** (2018), no. 1 1250–1276, [[arXiv:1710.05951](#)].
- [35] **HST** Collaboration, W. L. Freedman et al., *Final results from the Hubble Space Telescope key project to measure the Hubble constant*, *Astrophys. J.* **553** (2001) 47–72, [[astro-ph/0012376](#)].
- [36] A. G. Riess et al., *A Redetermination of the Hubble Constant with the Hubble Space Telescope from a Differential Distance Ladder*, *Astrophys. J.* **699** (2009) 539–563, [[arXiv:0905.0695](#)].
- [37] A. G. Riess, L. Macri, S. Casertano, H. Lampeitl, H. C. Ferguson, A. V. Filippenko, S. W. Jha, W. Li, and R. Chornock, *A 3% Solution: Determination of the Hubble Constant with the Hubble Space Telescope and Wide Field Camera 3*, *Astrophys. J.* **730** (2011) 119, [[arXiv:1103.2976](#)]. [Erratum: *Astrophys. J.* 732, 129 (2011)].
- [38] A. G. Riess et al., *New Parallaxes of Galactic Cepheids from Spatially Scanning the Hubble Space Telescope: Implications for the Hubble Constant*, *Astrophys. J.* **855** (2018), no. 2 136, [[arXiv:1801.01120](#)].
- [39] A. G. Riess, S. Casertano, W. Yuan, L. M. Macri, and D. Scolnic, *Large Magellanic Cloud Cepheid Standards Provide a 1% Foundation for the Determination of the Hubble Constant and Stronger Evidence for Physics beyond Λ CDM*, *Astrophys. J.* **876** (2019), no. 1 85, [[arXiv:1903.07603](#)].
- [40] A. G. Riess, S. Casertano, W. Yuan, J. B. Bowers, L. Macri, J. C. Zinn, and D. Scolnic, *Cosmic Distances Calibrated to 1% Precision with Gaia EDR3 Parallaxes and Hubble Space Telescope Photometry of 75 Milky Way Cepheids Confirm Tension with Λ CDM*, *Astrophys. J. Lett.* **908** (2021), no. 1 L6, [[arXiv:2012.08534](#)].
- [41] W. L. Freedman, B. F. Madore, V. Scowcroft, C. Burns, A. Monson, S. E. Persson, M. Seibert, and J. Rigby, *Carnegie Hubble Program: A Mid-Infrared Calibration of the Hubble Constant*, *Astrophys. J.* **758** (2012) 24, [[arXiv:1208.3281](#)].
- [42] **WMAP** Collaboration, D. N. Spergel et al., *First year Wilkinson Microwave Anisotropy Probe (WMAP) observations: Determination of cosmological parameters*, *Astrophys. J. Suppl.* **148** (2003) 175–194, [[astro-ph/0302209](#)].
- [43] **WMAP** Collaboration, D. N. Spergel et al., *Wilkinson Microwave Anisotropy Probe (WMAP) three year results: implications for cosmology*, *Astrophys. J. Suppl.* **170** (2007) 377, [[astro-ph/0603449](#)].

- [44] **WMAP** Collaboration, J. Dunkley et al., *Five-Year Wilkinson Microwave Anisotropy Probe (WMAP) Observations: Likelihoods and Parameters from the WMAP data*, *Astrophys. J. Suppl.* **180** (2009) 306–329, [[arXiv:0803.0586](#)].
- [45] **WMAP** Collaboration, E. Komatsu et al., *Seven-Year Wilkinson Microwave Anisotropy Probe (WMAP) Observations: Cosmological Interpretation*, *Astrophys. J. Suppl.* **192** (2011) 18, [[arXiv:1001.4538](#)].
- [46] **WMAP** Collaboration, C. L. Bennett et al., *Nine-Year Wilkinson Microwave Anisotropy Probe (WMAP) Observations: Final Maps and Results*, *Astrophys. J. Suppl.* **208** (2013) 20, [[arXiv:1212.5225](#)].
- [47] **Planck** Collaboration, P. A. R. Ade et al., *Planck 2013 results. XVI. Cosmological parameters*, *Astron. Astrophys.* **571** (2014) A16, [[arXiv:1303.5076](#)].
- [48] **BOSS** Collaboration, S. Alam et al., *The clustering of galaxies in the completed SDSS-III Baryon Oscillation Spectroscopic Survey: cosmological analysis of the DR12 galaxy sample*, *Mon. Not. Roy. Astron. Soc.* **470** (2017), no. 3 2617–2652, [[arXiv:1607.03155](#)].
- [49] P. Zarrouk et al., *The clustering of the SDSS-IV extended Baryon Oscillation Spectroscopic Survey DR14 quasar sample: measurement of the growth rate of structure from the anisotropic correlation function between redshift 0.8 and 2.2*, *Mon. Not. Roy. Astron. Soc.* **477** (2018), no. 2 1639–1663, [[arXiv:1801.03062](#)].
- [50] G. Alestas, L. Kazantzidis, and L. Perivolaropoulos, *H_0 Tension, Phantom Dark Energy and Cosmological Parameter Degeneracies*, [arXiv:2004.08363](#).
- [51] D. M. Scolnic et al., *The Complete Light-curve Sample of Spectroscopically Confirmed SNe Ia from Pan-STARRS1 and Cosmological Constraints from the Combined Pantheon Sample*, *Astrophys. J.* **859** (2018), no. 2 101, [[arXiv:1710.00845](#)].
- [52] V. Marra and L. Perivolaropoulos, *Rapid transition of G_{eff} at $z \simeq 0.01$ as a possible solution of the Hubble and growth tensions*, *Phys. Rev. D* **104** (2021), no. 2 L021303, [[arXiv:2102.06012](#)].
- [53] M. M. Ivanov, E. McDonough, J. C. Hill, M. Simonović, M. W. Toomey, S. Alexander, and M. Zaldarriaga, *Constraining Early Dark Energy with Large-Scale Structure*, *Phys. Rev. D* **102** (2020), no. 10 103502, [[arXiv:2006.11235](#)].
- [54] T. L. Smith, V. Poulin, and M. A. Amin, *Oscillating scalar fields and the Hubble tension: a resolution with novel signatures*, *Phys. Rev. D* **101** (2020), no. 6 063523, [[arXiv:1908.06995](#)].
- [55] L. Perivolaropoulos, *Cosmological Horizons, Uncertainty Principle and Maximum Length Quantum Mechanics*, *Phys. Rev. D* **95** (2017), no. 10 103523, [[arXiv:1704.05681](#)].
- [56] E. Mortsell, A. Goobar, J. Johansson, and S. Dhawan, *The Hubble Tension Bites the Dust: Sensitivity of the Hubble Constant Determination to Cepheid Color Calibration*, [arXiv:2105.11461](#).
- [57] B. S. Haridasu, P. Karmakar, M. De Petris, V. F. Cardone, and R. Maoli, *Testing generalized scalar-tensor theories of gravity with clusters of galaxies*, [arXiv:2111.01101](#).
- [58] N. J. Secrest, S. von Hausegger, M. Rameez, R. Mohayaee, S. Sarkar, and J. Colin, *A Test of the Cosmological Principle with Quasars*, *Astrophys. J. Lett.* **908** (2021), no. 2 L51, [[arXiv:2009.14826](#)].
- [59] <https://www.ioa.s.u-tokyo.ac.jp/~sofue/smd2018/>.

- [60] H. V. Peiris and L. Verde, *The Shape of the Primordial Power Spectrum: A Last Stand Before Planck*, *Phys. Rev.* **D81** (2010) 021302, [[arXiv:0912.0268](#)].
- [61] H. Jeffreys, *Theory of probability*. Oxford University Press, 3 ed., 1961.
- [62] A. R. Liddle, *How many cosmological parameters?*, *Mon. Not. Roy. Astron. Soc.* **351** (2004) L49–L53, [[astro-ph/0401198](#)].
- [63] S. Nesseris and J. Garcia-Bellido, *Is the Jeffreys’ scale a reliable tool for Bayesian model comparison in cosmology?*, *JCAP* **08** (2013) 036, [[arXiv:1210.7652](#)].
- [64] A. Bonilla Rivera and J. E. García-Farieta, *Exploring the Dark Universe: constraints on dynamical Dark Energy models from CMB, BAO and growth rate measurements*, *Int. J. Mod. Phys. D* **28** (2019), no. 09 1950118, [[arXiv:1605.01984](#)].
- [65] J. Pérez-Romero and S. Nesseris, *Cosmological constraints and comparison of viable $f(R)$ models*, *Phys. Rev.* **D97** (2018), no. 2 023525, [[arXiv:1710.05634](#)].
- [66] D. Camarena and V. Marra, *Impact of the cosmic variance on H_0 on cosmological analyses*, *Phys. Rev. D* **98** (2018), no. 2 023537, [[arXiv:1805.09900](#)].
- [67] L. Kazantzidis and L. Perivolaropoulos, *Evolution of the $f\sigma_8$ tension with the Planck15/ Λ CDM determination and implications for modified gravity theories*, *Phys. Rev.* **D97** (2018), no. 10 103503, [[arXiv:1803.01337](#)].
- [68] SDSS Collaboration, M. Betoule et al., *Improved cosmological constraints from a joint analysis of the SDSS-II and SNLS supernova samples*, *Astron. Astrophys.* **568** (2014) A22, [[arXiv:1401.4064](#)].
- [69] J. F. Jesus, T. M. Gregório, F. Andrade-Oliveira, R. Valentim, and C. A. O. Matos, *Bayesian correction of $H(z)$ data uncertainties*, *Mon. Not. Roy. Astron. Soc.* **477** (2018), no. 3 2867–2873, [[arXiv:1709.00646](#)].
- [70] https://github.com/FOTEINISKARA/Cepheid_SnIa_Calibrator_Data_Transition.
- [71] E. Fischbach and C. L. Talmadge, *The search for nonNewtonian gravity*. 1999.
- [72] C. M. Will, *The Confrontation between general relativity and experiment*, *Living Rev. Rel.* **9** (2006) 3, [[gr-qc/0510072](#)].
- [73] D. J. Kapner, T. S. Cook, E. G. Adelberger, J. H. Gundlach, B. R. Heckel, C. D. Hoyle, and H. E. Swanson, *Tests of the gravitational inverse-square law below the dark-energy length scale*, *Phys. Rev. Lett.* **98** (2007) 021101, [[hep-ph/0611184](#)].
- [74] C. Di Porto and L. Amendola, *Observational constraints on the linear fluctuation growth rate*, *Phys. Rev.* **D77** (2008) 083508, [[arXiv:0707.2686](#)].
- [75] S. Nesseris and L. Perivolaropoulos, *Testing Lambda CDM with the Growth Function $\delta(a)$: Current Constraints*, *Phys. Rev. D* **77** (2008) 023504, [[arXiv:0710.1092](#)].
- [76] S. F. Daniel, E. V. Linder, T. L. Smith, R. R. Caldwell, A. Cooray, A. Leauthaud, and L. Lombriser, *Testing General Relativity with Current Cosmological Data*, *Phys. Rev.* **D81** (2010) 123508, [[arXiv:1002.1962](#)].
- [77] S. Dodelson, *Modern Cosmology*. Academic Press, Amsterdam, 2003.
- [78] L. Perivolaropoulos, *Accelerating universe: observational status and theoretical implications*, *AIP Conf. Proc.* **848** (2006), no. 1 698–712, [[astro-ph/0601014](#)].

- [79] M. P. Hobson, G. P. Efstathiou, and A. N. Lasenby, *General relativity: An introduction for physicists*. 2006.
- [80] P. J. E. Peebles, *Tests of Cosmological Models Constrained by Inflation*, *Astrophys. J.* **284** (1984) 439–444.
- [81] P. J. E. Peebles and B. Ratra, *The Cosmological Constant and Dark Energy*, *Rev. Mod. Phys.* **75** (2003) 559–606, [[astro-ph/0207347](#)].
- [82] S. M. Carroll, *The Cosmological constant*, *Living Rev. Rel.* **4** (2001) 1, [[astro-ph/0004075](#)].
- [83] P. Bull et al., *Beyond Λ CDM: Problems, solutions, and the road ahead*, *Phys. Dark Univ.* **12** (2016) 56–99, [[arXiv:1512.05356](#)].
- [84] F. Zwicky, *Die Rotverschiebung von extragalaktischen Nebeln*, *Helv. Phys. Acta* **6** (1933) 110–127.
- [85] F. Zwicky, *On the Masses of Nebulae and of Clusters of Nebulae*, *Astrophys. J.* **86** (1937) 217–246.
- [86] K. Freeman, *On the disks of spiral and SO Galaxies*, *Astrophys. J.* **160** (1970) 811.
- [87] V. C. Rubin and W. K. Ford, Jr., *Rotation of the Andromeda Nebula from a Spectroscopic Survey of Emission Regions*, *Astrophys. J.* **159** (1970) 379–403.
- [88] V. C. Rubin, N. Thonnard, and W. K. Ford, Jr., *Rotational properties of 21 SC galaxies with a large range of luminosities and radii, from NGC 4605 / $R = 4kpc$ / to UGC 2885 / $R = 122 kpc$ /*, *Astrophys. J.* **238** (1980) 471.
- [89] A. Bosma, *21-cm line studies of spiral galaxies. 2. The distribution and kinematics of neutral hydrogen in spiral galaxies of various morphological types.*, *Astron. J.* **86** (1981) 1825.
- [90] G. Bertone, D. Hooper, and J. Silk, *Particle dark matter: Evidence, candidates and constraints*, *Phys. Rept.* **405** (2005) 279–390, [[hep-ph/0404175](#)].
- [91] S. M. Carroll, W. H. Press, and E. L. Turner, *The Cosmological constant*, *Ann. Rev. Astron. Astrophys.* **30** (1992) 499–542.
- [92] T. Padmanabhan, *Cosmological constant: The Weight of the vacuum*, *Phys. Rept.* **380** (2003) 235–320, [[hep-th/0212290](#)].
- [93] T. Padmanabhan, *Dark energy: The Cosmological challenge of the millennium*, *Curr. Sci.* **88** (2005) 1057, [[astro-ph/0411044](#)].
- [94] S. Weinberg, *The Cosmological Constant Problem*, *Rev. Mod. Phys.* **61** (1989) 1–23.
- [95] A. Einstein, *Cosmological Considerations in the General Theory of Relativity*, *Sitzungsber. Preuss. Akad. Wiss. Berlin (Math. Phys.)* **1917** (1917) 142–152.
- [96] A. A. Starobinsky, *A New Type of Isotropic Cosmological Models Without Singularity*, *Phys. Lett.* **B91** (1980) 99–102. [[771\(1980\)](#)].
- [97] A. H. Guth, *The Inflationary Universe: A Possible Solution to the Horizon and Flatness Problems*, *Phys. Rev.* **D23** (1981) 347–356. [Adv. Ser. Astrophys. Cosmol.3,139(1987)].
- [98] A. D. Linde, *A New Inflationary Universe Scenario: A Possible Solution of the Horizon, Flatness, Homogeneity, Isotropy and Primordial Monopole Problems*, *Phys. Lett.* **108B** (1982) 389–393. [Adv. Ser. Astrophys. Cosmol.3,149(1987)].

- [99] A. Albrecht and P. J. Steinhardt, *Cosmology for Grand Unified Theories with Radiatively Induced Symmetry Breaking*, *Phys. Rev. Lett.* **48** (1982) 1220–1223. [Adv. Ser. Astrophys. Cosmol.3,158(1987)].
- [100] G. W. Horndeski, *Second-order scalar-tensor field equations in a four-dimensional space*, *Int. J. Theor. Phys.* **10** (1974) 363–384.
- [101] C. Deffayet, X. Gao, D. A. Steer, and G. Zahariade, *From k-essence to generalised Galileons*, *Phys. Rev.* **D84** (2011) 064039, [[arXiv:1103.3260](#)].
- [102] R. Kase and S. Tsujikawa, *Dark energy in Horndeski theories after GW170817: A review*, *Int. J. Mod. Phys. D* **28** (2019), no. 05 1942005, [[arXiv:1809.08735](#)].
- [103] T. Kobayashi, *Horndeski theory and beyond: a review*, *Rept. Prog. Phys.* **82** (2019), no. 8 086901, [[arXiv:1901.07183](#)].
- [104] J. D. Bekenstein, *Fine Structure Constant: Is It Really a Constant?*, *Phys. Rev. D* **25** (1982) 1527–1539.
- [105] H. B. Sandvik, J. D. Barrow, and J. Magueijo, *A simple cosmology with a varying fine structure constant*, *Phys. Rev. Lett.* **88** (2002) 031302, [[astro-ph/0107512](#)].
- [106] J. D. Barrow, H. B. Sandvik, and J. Magueijo, *The behavior of varying alpha cosmologies*, *Phys. Rev. D* **65** (2002) 063504, [[astro-ph/0109414](#)].
- [107] J. D. Barrow and S. Z. W. Lip, *A Generalized Theory of Varying Alpha*, *Phys. Rev. D* **85** (2012) 023514, [[arXiv:1110.3120](#)].
- [108] J. D. Barrow and A. A. H. Graham, *General Dynamics of Varying-Alpha Universes*, *Phys. Rev. D* **88** (2013) 103513, [[arXiv:1307.6816](#)].
- [109] C. J. A. P. Martins, *The status of varying constants: a review of the physics, searches and implications*, [arXiv:1709.02923](#).
- [110] S. Nojiri and S. D. Odintsov, *Introduction to modified gravity and gravitational alternative for dark energy*, *eConf* **C0602061** (2006) 06, [[hep-th/0601213](#)].
- [111] S. Nojiri and S. D. Odintsov, *Unified cosmic history in modified gravity: from $F(R)$ theory to Lorentz non-invariant models*, *Phys. Rept.* **505** (2011) 59–144, [[arXiv:1011.0544](#)].
- [112] A. De Felice and S. Tsujikawa, *$f(R)$ theories*, *Living Rev. Rel.* **13** (2010) 3, [[arXiv:1002.4928](#)].
- [113] T. P. Sotiriou and V. Faraoni, *$f(R)$ Theories Of Gravity*, *Rev. Mod. Phys.* **82** (2010) 451–497, [[arXiv:0805.1726](#)].
- [114] R. Ferraro and F. Fiorini, *Modified teleparallel gravity: Inflation without inflaton*, *Phys. Rev.* **D75** (2007) 084031, [[gr-qc/0610067](#)].
- [115] S. Nesseris, S. Basilakos, E. N. Saridakis, and L. Perivolaropoulos, *Viable $f(T)$ models are practically indistinguishable from Λ CDM*, *Phys. Rev.* **D88** (2013) 103010, [[arXiv:1308.6142](#)].
- [116] Y.-F. Cai, S. Capozziello, M. De Laurentis, and E. N. Saridakis, *$f(T)$ teleparallel gravity and cosmology*, *Rept. Prog. Phys.* **79** (2016), no. 10 106901, [[arXiv:1511.07586](#)].
- [117] S. Capozziello, *Curvature quintessence*, *Int. J. Mod. Phys. D* **11** (2002) 483–492, [[gr-qc/0201033](#)].

- [118] **Supernova Search Team** Collaboration, A. G. Riess et al., *Observational evidence from supernovae for an accelerating universe and a cosmological constant*, *Astron. J.* **116** (1998) 1009–1038, [[astro-ph/9805201](#)].
- [119] **Supernova Cosmology Project** Collaboration, S. Perlmutter et al., *Measurements of Ω and Λ from 42 high redshift supernovae*, *Astrophys. J.* **517** (1999) 565–586, [[astro-ph/9812133](#)].
- [120] **WMAP** Collaboration, L. Page et al., *First year Wilkinson Microwave Anisotropy Probe (WMAP) observations: Interpretation of the TT and TE angular power spectrum peaks*, *Astrophys. J. Suppl.* **148** (2003) 233, [[astro-ph/0302220](#)].
- [121] F. Bernardeau, S. Colombi, E. Gaztanaga, and R. Scoccimarro, *Large scale structure of the universe and cosmological perturbation theory*, *Phys. Rept.* **367** (2002) 1–248, [[astro-ph/0112551](#)].
- [122] D. N. Schramm and M. S. Turner, *Big Bang Nucleosynthesis Enters the Precision Era*, *Rev. Mod. Phys.* **70** (1998) 303–318, [[astro-ph/9706069](#)].
- [123] G. Steigman, *Primordial Nucleosynthesis in the Precision Cosmology Era*, *Ann. Rev. Nucl. Part. Sci.* **57** (2007) 463–491, [[arXiv:0712.1100](#)].
- [124] F. Iocco, G. Mangano, G. Miele, O. Pisanti, and P. D. Serpico, *Primordial Nucleosynthesis: from precision cosmology to fundamental physics*, *Phys. Rept.* **472** (2009) 1–76, [[arXiv:0809.0631](#)].
- [125] R. H. Cyburt, B. D. Fields, K. A. Olive, and T.-H. Yeh, *Big Bang Nucleosynthesis: 2015*, *Rev. Mod. Phys.* **88** (2016) 015004, [[arXiv:1505.01076](#)].
- [126] T. Buchert, A. A. Coley, H. Kleinert, B. F. Roukema, and D. L. Wiltshire, *Observational Challenges for the Standard FLRW Model*, *Int. J. Mod. Phys. D* **25** (2016), no. 03 1630007, [[arXiv:1512.03313](#)].
- [127] E. Di Valentino, O. Mena, S. Pan, L. Visinelli, W. Yang, A. Melchiorri, D. F. Mota, A. G. Riess, and J. Silk, *In the realm of the Hubble tension—a review of solutions*, *Class. Quant. Grav.* **38** (2021), no. 15 153001, [[arXiv:2103.01183](#)].
- [128] N. Schöneberg, G. Franco Abellán, A. Pérez Sánchez, S. J. Witte, V. Poulin, and J. Lesgourgues, *The H_0 Olympics: A fair ranking of proposed models*, [[arXiv:2107.10291](#)].
- [129] L. A. Anchordoqui, E. Di Valentino, S. Pan, and W. Yang, *Dissecting the H_0 and S_8 tensions with Planck + BAO + supernova type Ia in multi-parameter cosmologies*, *JHEAp* **32** (2021) 121, [[arXiv:2107.13932](#)].
- [130] K. Schmitz, *Modern Cosmology, an Amuse-Gueule*, [[arXiv:2203.04757](#)].
- [131] J. Martin, *Everything You Always Wanted To Know About The Cosmological Constant Problem (But Were Afraid To Ask)*, *Comptes Rendus Physique* **13** (2012) 566–665, [[arXiv:1205.3365](#)].
- [132] C. P. Burgess, *The Cosmological Constant Problem: Why it’s hard to get Dark Energy from Micro-physics*, in *Proceedings, 100th Les Houches Summer School: Post-Planck Cosmology: Les Houches, France, July 8 - August 2, 2013*, pp. 149–197, 2015. [[arXiv:1309.4133](#)].
- [133] P. J. Steinhardt, *Cosmological Challenges for the 21st Century*, in *Critical Problems in Physics* (V. L. Fitch, D. R. Marlow, and M. A. E. Dementi, eds.), p. 123, 1997.
- [134] H. E. S. Velten, R. F. vom Marttens, and W. Zimdahl, *Aspects of the cosmological “coincidence problem”*, *Eur. Phys. J.* **C74** (2014), no. 11 3160, [[arXiv:1410.2509](#)].

- [135] E. J. Copeland, M. Sami, and S. Tsujikawa, *Dynamics of dark energy*, *Int. J. Mod. Phys. D* **15** (2006) 1753–1936, [[hep-th/0603057](#)].
- [136] J. Sola, *Cosmological constant and vacuum energy: old and new ideas*, *J. Phys. Conf. Ser.* **453** (2013) 012015, [[arXiv:1306.1527](#)].
- [137] L. Susskind, *The Anthropic landscape of string theory*, [hep-th/0302219](#).
- [138] S. Weinberg, *Anthropic Bound on the Cosmological Constant*, *Phys. Rev. Lett.* **59** (1987) 2607.
- [139] **Planck** Collaboration, N. Aghanim et al., *Planck 2018 results. I. Overview and the cosmological legacy of Planck*, *Astron. Astrophys.* **641** (2020) A1, [[arXiv:1807.06205](#)].
- [140] E. Di Valentino et al., *Cosmology Intertwined II: The Hubble Constant Tension*, [arXiv:2008.11284](#).
- [141] E. Di Valentino et al., *Cosmology Intertwined III: $f\sigma_8$ and S_8* , [arXiv:2008.11285](#).
- [142] E. Di Valentino, *A combined analysis of the H_0 late time direct measurements and the impact on the Dark Energy sector*, *Mon. Not. Roy. Astron. Soc.* **502** (2021), no. 2 2065–2073, [[arXiv:2011.00246](#)].
- [143] A. G. Riess, *The Expansion of the Universe is Faster than Expected*, *Nature Rev. Phys.* **2** (2019), no. 1 10–12, [[arXiv:2001.03624](#)].
- [144] S. Joudaki et al., *KiDS-450 + 2dFLenS: Cosmological parameter constraints from weak gravitational lensing tomography and overlapping redshift-space galaxy clustering*, *Mon. Not. Roy. Astron. Soc.* **474** (2018), no. 4 4894–4924, [[arXiv:1707.06627](#)].
- [145] **DES** Collaboration, T. M. C. Abbott et al., *Dark Energy Survey year 1 results: Cosmological constraints from galaxy clustering and weak lensing*, *Phys. Rev.* **D98** (2018), no. 4 043526, [[arXiv:1708.01530](#)].
- [146] S. Basilakos and S. Nesseris, *Conjoined constraints on modified gravity from the expansion history and cosmic growth*, *Phys. Rev.* **D96** (2017), no. 6 063517, [[arXiv:1705.08797](#)].
- [147] E. Macaulay, I. K. Wehus, and H. K. Eriksen, *Lower Growth Rate from Recent Redshift Space Distortion Measurements than Expected from Planck*, *Phys. Rev. Lett.* **111** (2013), no. 16 161301, [[arXiv:1303.6583](#)].
- [148] S. Nesseris, G. Pantazis, and L. Perivolaropoulos, *Tension and constraints on modified gravity parametrizations of $G_{\text{eff}}(z)$ from growth rate and Planck data*, *Phys. Rev.* **D96** (2017), no. 2 023542, [[arXiv:1703.10538](#)].
- [149] D. J. Schwarz, C. J. Copi, D. Huterer, and G. D. Starkman, *CMB Anomalies after Planck*, *Class. Quant. Grav.* **33** (2016), no. 18 184001, [[arXiv:1510.07929](#)].
- [150] **Planck** Collaboration, Y. Akrami et al., *Planck 2018 results. VII. Isotropy and Statistics of the CMB*, *Astron. Astrophys.* **641** (2020) A7, [[arXiv:1906.02552](#)].
- [151] R. Watkins, H. A. Feldman, and M. J. Hudson, *Consistently Large Cosmic Flows on Scales of 100 Mpc/h: a Challenge for the Standard Λ CDM Cosmology*, *Mon. Not. Roy. Astron. Soc.* **392** (2009) 743–756, [[arXiv:0809.4041](#)].
- [152] A. Kashlinsky, F. Atrio-Barandela, D. Kocevski, and H. Ebeling, *A measurement of large-scale peculiar velocities of clusters of galaxies: results and cosmological implications*, *Astrophys. J. Lett.* **686** (2009) L49–L52, [[arXiv:0809.3734](#)].

- [153] D. L. Wiltshire, P. R. Smale, T. Mattsson, and R. Watkins, *Hubble flow variance and the cosmic rest frame*, *Phys. Rev. D* **88** (2013) 083529, [[arXiv:1201.5371](#)].
- [154] C. Bengaly, R. Maartens, and M. Santos, *Probing the Cosmological Principle in the counts of radio galaxies at different frequencies*, *JCAP* **04** (2018) 031, [[arXiv:1710.08804](#)].
- [155] J. A. King, J. K. Webb, M. T. Murphy, V. V. Flambaum, R. F. Carswell, M. B. Bainbridge, M. R. Wilczynska, and F. E. Koch, *Spatial variation in the fine-structure constant – new results from VLT/UVES*, *Mon. Not. Roy. Astron. Soc.* **422** (2012) 3370–3413, [[arXiv:1202.4758](#)].
- [156] J. K. Webb, J. A. King, M. T. Murphy, V. V. Flambaum, R. F. Carswell, and M. B. Bainbridge, *Indications of a spatial variation of the fine structure constant*, *Phys. Rev. Lett.* **107** (2011) 191101, [[arXiv:1008.3907](#)].
- [157] A. Cuceu, J. Farr, P. Lemos, and A. Font-Ribera, *Baryon Acoustic Oscillations and the Hubble Constant: Past, Present and Future*, *JCAP* **10** (2019), no. 10 044, [[arXiv:1906.11628](#)].
- [158] J. Evslin, *Isolating the Lyman Alpha Forest BAO Anomaly*, *JCAP* **04** (2017) 024, [[arXiv:1604.02809](#)].
- [159] Y. Minami, H. Ochi, K. Ichiki, N. Katayama, E. Komatsu, and T. Matsumura, *Simultaneous determination of the cosmic birefringence and miscalibrated polarization angles from CMB experiments*, *PTEP* **2019** (2019), no. 8 083E02, [[arXiv:1904.12440](#)].
- [160] Y. Minami, *Determination of miscalibrated polarization angles from observed cosmic microwave background and foreground EB power spectra: Application to partial-sky observation*, *PTEP* **2020** (2020), no. 6 063E01, [[arXiv:2002.03572](#)].
- [161] Y. Minami and E. Komatsu, *Simultaneous determination of the cosmic birefringence and miscalibrated polarization angles II: Including cross frequency spectra*, *PTEP* **2020** (2020), no. 10 103E02, [[arXiv:2006.15982](#)].
- [162] Y. Minami and E. Komatsu, *New Extraction of the Cosmic Birefringence from the Planck 2018 Polarization Data*, *Phys. Rev. Lett.* **125** (2020), no. 22 221301, [[arXiv:2011.11254](#)].
- [163] A. Del Popolo and M. Le Delliou, *Small scale problems of the Λ CDM model: a short review*, *Galaxies* **5** (2017), no. 1 17, [[arXiv:1606.07790](#)].
- [164] J. S. Bullock and M. Boylan-Kolchin, *Small-Scale Challenges to the Λ CDM Paradigm*, *Ann. Rev. Astron. Astrophys.* **55** (2017) 343–387, [[arXiv:1707.04256](#)].
- [165] L. Verde, P. Protopapas, and R. Jimenez, *Planck and the local Universe: Quantifying the tension*, *Phys. Dark Univ.* **2** (2013) 166–175, [[arXiv:1306.6766](#)].
- [166] B. D. Fields, *The primordial lithium problem*, *Ann. Rev. Nucl. Part. Sci.* **61** (2011) 47–68, [[arXiv:1203.3551](#)].
- [167] G. Risaliti and E. Lusso, *Cosmological constraints from the Hubble diagram of quasars at high redshifts*, *Nature Astron.* **3** (2019), no. 3 272–277, [[arXiv:1811.02590](#)].
- [168] A. Banerjee, E. O. Colgáin, M. Sasaki, M. M. Sheikh-Jabbari, and T. Yang, *On cosmography in the cosmic dark ages: are we still in the dark?*, [[arXiv:2009.04109](#)].
- [169] E. Lusso, E. Piedipalumbo, G. Risaliti, M. Paolillo, S. Bisogni, E. Nardini, and L. Amati, *Tension with the flat Λ CDM model from a high-redshift Hubble diagram of supernovae, quasars, and gamma-ray bursts*, *Astron. Astrophys.* **628** (2019) L4, [[arXiv:1907.07692](#)].

- [170] L. Perivolaropoulos, *Submillimeter spatial oscillations of Newton’s constant: Theoretical models and laboratory tests*, *Phys. Rev. D* **95** (2017), no. 8 084050, [[arXiv:1611.07293](#)].
- [171] I. Antoniou and L. Perivolaropoulos, *Constraints on spatially oscillating sub-mm forces from the Stanford Optically Levitated Microsphere Experiment data*, *Phys. Rev. D* **96** (2017), no. 10 104002, [[arXiv:1708.02117](#)].
- [172] J. D. Bowman, A. E. E. Rogers, R. A. Monsalve, T. J. Mozdzen, and N. Mahesh, *An absorption profile centred at 78 megahertz in the sky-averaged spectrum*, *Nature* **555** (2018), no. 7694 67–70, [[arXiv:1810.05912](#)].
- [173] E. Asencio, I. Banik, and P. Kroupa, *A massive blow for Λ CDM – the high redshift, mass, and collision velocity of the interacting galaxy cluster El Gordo contradicts concordance cosmology*, *Mon. Not. Roy. Astron. Soc.* **500** (2020), no. 4 5249–5267, [[arXiv:2012.03950](#)].
- [174] D. Kraljic and S. Sarkar, *How rare is the Bullet Cluster (in a Λ CDM universe)?*, *JCAP* **04** (2015) 050, [[arXiv:1412.7719](#)].
- [175] D. Huterer and D. L. Shafer, *Dark energy two decades after: Observables, probes, consistency tests*, *Rept. Prog. Phys.* **81** (2018), no. 1 016901, [[arXiv:1709.01091](#)].
- [176] L. Perivolaropoulos, *Six Puzzles for Λ CDM Cosmology*, [arXiv:0811.4684](#).
- [177] L. Perivolaropoulos, *Λ CDM: Triumphs, Puzzles and Remedies*, *J. Cosmol.* **15** (2011) 6054, [[arXiv:1104.0539](#)].
- [178] P. Shah, P. Lemos, and O. Lahav, *A buyer’s guide to the Hubble constant*, *Astron. Astrophys. Rev.* **29** (2021), no. 1 9, [[arXiv:2109.01161](#)].
- [179] **CANTATA** Collaboration, E. N. Saridakis et al., *Modified Gravity and Cosmology: An Update by the CANTATA Network*, [arXiv:2105.12582](#).
- [180] G. Collaboration, A. G. A. Brown, A. Vallenari, T. Prusti, J. H. J. de Bruijne, C. Babusiaux, and M. Biermann, *Gaia early data release 3: Summary of the contents and survey properties*, 2020.
- [181] T. Karwal and M. Kamionkowski, *Dark energy at early times, the Hubble parameter, and the string axiverse*, *Phys. Rev. D* **94** (2016), no. 10 103523, [[arXiv:1608.01309](#)].
- [182] V. Poulin, T. L. Smith, T. Karwal, and M. Kamionkowski, *Early Dark Energy Can Resolve The Hubble Tension*, *Phys. Rev. Lett.* **122** (2019), no. 22 221301, [[arXiv:1811.04083](#)].
- [183] P. Agrawal, F.-Y. Cyr-Racine, D. Pinner, and L. Randall, *Rock ‘n’ Roll Solutions to the Hubble Tension*, [arXiv:1904.01016](#).
- [184] E. Di Valentino, A. Melchiorri, and J. Silk, *Reconciling Planck with the local value of H_0 in extended parameter space*, *Phys. Lett.* **B761** (2016) 242–246, [[arXiv:1606.00634](#)].
- [185] L. Verde, T. Treu, and A. G. Riess, *Tensions between the Early and the Late Universe*, *Nature Astron.* **3** (7, 2019) 891, [[arXiv:1907.10625](#)].
- [186] D. H. Weinberg, M. J. Mortonson, D. J. Eisenstein, C. Hirata, A. G. Riess, and E. Rozo, *Observational Probes of Cosmic Acceleration*, *Phys. Rept.* **530** (2013) 87–255, [[arXiv:1201.2434](#)].
- [187] L. Amati, C. Guidorzi, F. Frontera, M. Della Valle, F. Finelli, R. Landi, and E. Montanari, *Measuring the cosmological parameters with the E_p - i -Eiso correlation of Gamma-Ray Bursts*, *Mon. Not. Roy. Astron. Soc.* **391** (2008) 577–584, [[arXiv:0805.0377](#)].

- [188] L. Amati, R. D’Agostino, O. Luongo, M. Muccino, and M. Tantalò, *Addressing the circularity problem in the $E_p - E_{\text{iso}}$ correlation of gamma-ray bursts*, *Mon. Not. Roy. Astron. Soc.* **486** (2019), no. 1 L46–L51, [[arXiv:1811.08934](#)].
- [189] R. Salvaterra et al., *GRB 090423 reveals an exploding star at the epoch of re-ionization*, *Nature* **461** (2009) 1258, [[arXiv:0906.1578](#)].
- [190] N. R. Tanvir et al., *A gamma-ray burst at a redshift of $z \sim 8.2$* , *Nature* **461** (2009) 1254–1257.
- [191] L. Samushia and B. Ratra, *Constraining dark energy with gamma-ray bursts*, *Astrophys. J.* **714** (2010) 1347–1354, [[arXiv:0905.3836](#)].
- [192] B. E. Schaefer, *The Hubble Diagram to Redshift > 6 from 69 Gamma-Ray Bursts*, *Astrophys. J.* **660** (2007) 16–46, [[astro-ph/0612285](#)].
- [193] A. Cucchiara, A. J. Levan, D. B. Fox, N. R. Tanvir, T. N. Ukwatta, E. Berger, T. Krühler, A. Küpcü Yoldaş, X. F. Wu, K. Toma, J. Greiner, F. E. Olivares, A. Rowlinson, L. Amati, T. Sakamoto, K. Roth, A. Stephens, A. Fritz, J. P. U. Fynbo, J. Hjorth, D. Malesani, P. Jakobsson, K. Wiersema, P. T. O’Brien, A. M. Soderberg, R. J. Foley, A. S. Fruchter, J. Rhoads, R. E. Rutledge, B. P. Schmidt, M. A. Dopita, P. Podsiadlowski, R. Willingale, C. Wolf, S. R. Kulkarni, and P. D’Avanzo, *A Photometric Redshift of $z \sim 9.4$ for GRB 090429B*, *Astroph. J.* **736** (July, 2011) 7, [[arXiv:1105.4915](#)].
- [194] J. S. Wang, F. Y. Wang, K. S. Cheng, and Z. G. Dai, *Measuring dark energy with the $E_{\text{iso}} - E_p$ correlation of gamma-ray bursts using model-independent methods*, *Astron. Astrophys.* **585** (2016) A68, [[arXiv:1509.08558](#)].
- [195] M. Demianski, E. Piedipalumbo, D. Sawant, and L. Amati, *Cosmology with gamma-ray bursts: I. The Hubble diagram through the calibrated $E_{p,i} - E_{\text{iso}}$ correlation*, *Astron. Astrophys.* **598** (2017) A112, [[arXiv:1610.00854](#)].
- [196] C.-H. Tang, Y.-F. Huang, J.-J. Geng, and Z.-B. Zhang, *Statistical Study of Gamma-Ray Bursts with a Plateau Phase in the X-ray Afterglow*, *Astrophys. J. Suppl.* **245** (2019), no. 1 1, [[arXiv:1905.07929](#)].
- [197] V. F. Cardone, M. G. Dainotti, S. Capozziello, and R. Willingale, *Constraining cosmological parameters by Gamma Ray Burst X - ray afterglow lightcurves*, *Mon. Not. Roy. Astron. Soc.* **408** (2010) 1181, [[arXiv:1005.0122](#)].
- [198] N. Khadka and B. Ratra, *Constraints on cosmological parameters from gamma-ray burst peak photon energy and bolometric fluence measurements and other data*, *Mon. Not. Roy. Astron. Soc.* **499** (2020), no. 1 391–403, [[arXiv:2007.13907](#)].
- [199] N. Khadka, O. Luongo, M. Muccino, and B. Ratra, *Do gamma-ray burst measurements provide a useful test of cosmological models?*, *JCAP* **09** (2021) 042, [[arXiv:2105.12692](#)].
- [200] M. G. Dainotti, V. F. Cardone, E. Piedipalumbo, and S. Capozziello, *Slope evolution of GRB correlations and cosmology*, *Mon. Not. Roy. Astron. Soc.* **436** (2013) 82, [[arXiv:1308.1918](#)].
- [201] M. Dainotti and R. Del Vecchio, *Gamma Ray Burst afterglow and prompt-afterglow relations: an overview*, *New Astron. Rev.* **77** (2017) 23–61, [[arXiv:1703.06876](#)].
- [202] F. F. Dirirsa, S. Razzaque, F. Piron, M. Arimoto, M. Axelsson, D. Kocevski, F. Longo, M. Ohno, and S. Zhu, *Spectral analysis of Fermi-LAT gamma-ray bursts with known redshift and their potential use as cosmological standard candles*, *Astrophys. J.* **887** (2019) 13, [[arXiv:1910.07009](#)].

- [203] M. Demianski, E. Piedipalumbo, D. Sawant, and L. Amati, *Prospects of high redshift constraints on dark energy models with the E_p , $i - E_{iso}$ correlation in long gamma ray bursts*, *Mon. Not. Roy. Astron. Soc.* **506** (2021), no. 1 903–918, [[arXiv:1911.08228](#)].
- [204] S. Cao, N. Khadka, and B. Ratra, *Standardizing Dainotti-correlated gamma-ray bursts, and using them with standardized Amati-correlated gamma-ray bursts to constrain cosmological model parameters*, *Mon. Not. Roy. Astron. Soc.* **510** (2022), no. 2 2928–2947, [[arXiv:2110.14840](#)].
- [205] O. Luongo, M. Muccino, E. O. Colgáin, M. M. Sheikh-Jabbari, and L. Yin, *On Larger H_0 Values in the CMB Dipole Direction*, [[arXiv:2108.13228](#)].
- [206] S. Cao, M. Dainotti, and B. Ratra, *Standardizing Platinum Dainotti-correlated gamma-ray bursts, and using them with standardized Amati-correlated gamma-ray bursts to constrain cosmological model parameters*, *Mon. Not. Roy. Astron. Soc.* **512** (2022) 439–454, [[arXiv:2201.05245](#)].
- [207] Y. Liu, F. Chen, N. Liang, Z. Yuan, H. Yu, and P. Wu¹, *The improved Amati correlations from Gaussian copula*, [[arXiv:2203.03178](#)].
- [208] J. P. Hu, F. Y. Wang, and Z. G. Dai, *Measuring cosmological parameters with a luminosity–time correlation of gamma-ray bursts*, *Mon. Not. Roy. Astron. Soc.* **507** (2021), no. 1 730–742, [[arXiv:2107.12718](#)].
- [209] Y. Dai, X.-G. Zheng, Z.-X. Li, H. Gao, and Z.-H. Zhu, *Redshift evolution of the Amati relation: calibrated results from the Hubble diagram of quasars at high redshifts*, [[arXiv:2111.05544](#)].
- [210] O. Luongo and M. Muccino, *A Roadmap to Gamma-Ray Bursts: New Developments and Applications to Cosmology, Galaxies* **9** (2021), no. 4 77, [[arXiv:2110.14408](#)].
- [211] M. M. Phillips, *The absolute magnitudes of Type IA supernovae*, *Astrophys. J. Lett.* **413** (1993) L105–L108.
- [212] D. Brout et al., *The Pantheon+ Analysis: Cosmological Constraints*, [[arXiv:2202.04077](#)].
- [213] D. Scolnic et al., *The Pantheon+ Analysis: The Full Dataset and Light-Curve Release*, [[arXiv:2112.03863](#)].
- [214] E. R. Peterson et al., *The Pantheon+ Analysis: Evaluating Peculiar Velocity Corrections in Cosmological Analyses with Nearby Type Ia Supernovae*, [[arXiv:2110.03487](#)].
- [215] S. Brownsberger, D. Brout, D. Scolnic, C. W. Stubbs, and A. G. Riess, *The Pantheon+ Analysis: Dependence of Cosmological Constraints on Photometric-Zeropoint Uncertainties of Supernova Surveys*, [[arXiv:2110.03486](#)].
- [216] A. Sandage, G. Tammann, A. Saha, B. Reindl, F. Macchetto, and N. Panagia, *The Hubble Constant: A Summary of the HST Program for the Luminosity Calibration of Type Ia Supernovae by Means of Cepheids*, *Astrophys. J.* **653** (2006) 843–860, [[astro-ph/0603647](#)].
- [217] H. S. Leavitt, *1777 variables in the Magellanic Clouds*, *Harvard Obs. Annals* **60** (1908) 87–108.
- [218] H. S. Leavitt and E. C. Pickering, *Periods of 25 Variable Stars in the Small Magellanic Cloud*, *Harvard Obs. Circ.* **173** (1912) 1–3.
- [219] G. F. Benedict, B. E. McArthur, M. W. Feast, T. G. Barnes, T. E. Harrison, R. J. Patterson, J. W. Menzies, J. L. Bean, and W. L. Freedman, *Hubble Space Telescope Fine Guidance Sensor Parallaxes of Galactic Cepheid Variable Stars: Period-Luminosity Relations*, *Astron. J.* **133** (2007) 1810–1827, [[astro-ph/0612465](#)]. [Erratum: *Astron. J.* 133, 2980 (2007)].

- [220] F. van Leeuwen, M. W. Feast, P. A. Whitelock, and C. D. Laney, *Cepheid Parallaxes and the Hubble Constant*, *Mon. Not. Roy. Astron. Soc.* **379** (2007) 723–737, [[arXiv:0705.1592](#)].
- [221] S. Casertano et al., *Parallax of Galactic Cepheids from Spatially Scanning the Wide Field Camera 3 on the Hubble Space Telescope: The Case of SS Canis Majoris*, *Astrophys. J.* **825** (2016), no. 1 11, [[arXiv:1512.09371](#)].
- [222] A. G. Riess, S. Casertano, J. Anderson, J. Mackenty, and A. V. Filippenko, *Parallax Beyond a Kiloparsec from Spatially Scanning the Wide Field Camera 3 on the Hubble Space Telescope*, *Astrophys. J.* **785** (2014) 161, [[arXiv:1401.0484](#)].
- [223] L. Lindegren, U. Lammers, U. Bastian, and et al., *Gaia Data Release 1. Astrometry: one billion positions, two million proper motions and parallaxes*, *Astron. Astrophys.* **595** (Nov., 2016) A4, [[arXiv:1609.04303](#)].
- [224] A. G. Riess et al., *Milky Way Cepheid Standards for Measuring Cosmic Distances and Application to Gaia DR2: Implications for the Hubble Constant*, *Astrophys. J.* **861** (2018), no. 2 126, [[arXiv:1804.10655](#)].
- [225] G. Pietrzyński, D. Graczyk, A. Gellenne, W. Gieren, I. B. Thompson, B. Pilecki, P. Karczmarek, M. Górski, K. Suchomska, M. Taormina, B. Zgirski, P. Wielgórski, Z. Kołaczowski, P. Konorski, S. Villanova, N. Nardetto, P. Kervella, F. Bresolin, R. P. Kudritzki, J. Storm, R. Smolec, and W. Narloch, *A distance to the Large Magellanic Cloud that is precise to one per cent*, *Nature* **567** (Mar., 2019) 200–203, [[arXiv:1903.08096](#)].
- [226] W. Yuan, L. M. Macri, A. G. Riess, T. G. Brink, S. Casertano, A. V. Filippenko, S. L. Hoffmann, C. D. Huang, and D. Scolnic, *Absolute Calibration of Cepheid Period-Luminosity Relations in NGC 4258*, [[arXiv:2203.06681](#)].
- [227] M. Reid, D. Pesce, and A. Riess, *An Improved Distance to NGC 4258 and its Implications for the Hubble Constant*, *Astrophys. J. Lett.* **886** (2019), no. 2 L27, [[arXiv:1908.05625](#)].
- [228] G. Pietrzyński et al., *An eclipsing binary distance to the Large Magellanic Cloud accurate to 2 per cent*, *Nature* **495** (2013) 76–79, [[arXiv:1303.2063](#)].
- [229] R. L. Beaton et al., *The Carnegie-Chicago Hubble Program. I. An Independent Approach to the Extragalactic Distance Scale Using only Population II Distance Indicators*, *Astrophys. J.* **832** (2016), no. 2 210, [[arXiv:1604.01788](#)].
- [230] W. L. Freedman, B. F. Madore, T. Hoyt, I. S. Jang, R. Beaton, M. G. Lee, A. Monson, J. Neeley, and J. Rich, *Calibration of the Tip of the Red Giant Branch (TRGB)*, [[arXiv:2002.01550](#)].
- [231] C. D. Huang et al., *A Near-infrared Period–Luminosity Relation for Miras in NGC 4258, an Anchor for a New Distance Ladder*, *Astrophys. J.* **857** (2018), no. 1 67, [[arXiv:1801.02711](#)].
- [232] B. Czerny et al., *Astronomical Distance Determination in the Space Age. Secondary distance indicators*, *Space Sci. Rev.* **214** (2018), no. 1 32, [[arXiv:1801.00598](#)].
- [233] I. Iben and A. Renzini, *Asymptotic giant branch evolution and beyond*, *Ann. Rev. Astron. Astrophys.* **21** (1983) 271–342.
- [234] J. B. Jensen, J. L. Tonry, R. I. Thompson, E. A. Ajhar, T. R. Lauer, M. J. Rieke, M. Postman, and M. C. Liu, *The infrared surface brightness fluctuation hubble constant*, *Astrophys. J.* **550** (2001) 503, [[astro-ph/0011288](#)].
- [235] M. Cantiello et al., *A Precise Distance to the Host Galaxy of the Binary Neutron Star Merger GW170817 Using Surface Brightness Fluctuations*, *Astrophys. J. Lett.* **854** (2018), no. 2 L31, [[arXiv:1801.06080](#)].

- [236] N. Khetan et al., *A new measurement of the Hubble constant using Type Ia supernovae calibrated with surface brightness fluctuations*, *Astron. Astrophys.* **647** (2021) A72, [[arXiv:2008.07754](#)].
- [237] J. Tonry and D. P. Schneider, *A New Technique for Measuring Extragalactic Distances*, *Astron. J.* **96** (Sept., 1988) 807.
- [238] J. L. Tonry, J. P. Blakeslee, E. A. Ajhar, and A. Dressler, *The sbf survey of galaxy distances. I. sample selection, photometric calibration, and the hubble constant*, *Astrophys. J.* **475** (1997) 399–413, [[astro-ph/9609113](#)].
- [239] J. P. Blakeslee, E. A. Ajhar, and J. L. Tonry, *Distances from surface brightness fluctuations*, *Astrophys. Space Sci. Libr.* **237** (1999) 181, [[astro-ph/9807124](#)].
- [240] S. Mei, J. P. Blakeslee, J. L. Tonry, A. Jordan, E. W. Peng, P. Cote, L. Ferrarese, D. Merritt, M. Milosavljevic, and M. J. West, *The ACS Virgo Cluster Survey. 4. Data reduction procedures for surface brightness fluctuation measurements with the Advanced Camera for Surveys*, *Astrophys. J. Suppl.* **156** (2005) 113, [[astro-ph/0501325](#)].
- [241] I. Biscardi, G. Raimondo, M. Cantiello, and E. Brocato, *Optical Surface Brightness Fluctuations of shell galaxies towards 100 Mpc*, *Astrophys. J.* **678** (2008) 168, [[arXiv:0802.2509](#)].
- [242] J. P. Blakeslee, A. Jordan, S. Mei, P. Cote, L. Ferrarese, L. Infante, E. W. Peng, J. L. Tonry, and M. J. West, *The ACS Fornax Cluster Survey. V. Measurement and Recalibration of Surface Brightness Fluctuations and a Precise Value of the Fornax–Virgo Relative Distance*, *Astrophys. J.* **694** (2009) 556–572, [[arXiv:0901.1138](#)].
- [243] J. Blakeslee, *Surface Brightness Fluctuations as Primary and Secondary Distance Indicators*, *Astrophys. Space Sci.* **341** (2012) 179–186, [[arXiv:1202.0581](#)].
- [244] T. de Jaeger, B. Stahl, W. Zheng, A. Filippenko, A. Riess, and L. Galbany, *A measurement of the Hubble constant from Type II supernovae*, [arXiv:2006.03412](#).
- [245] A. V. Filippenko, *Optical spectra of supernovae*, *Ann. Rev. Astron. Astrophys.* **35** (1997) 309–355.
- [246] A. V. Filippenko, *Optical observations of type II supernovae*, *AIP Conf. Proc.* **522** (2000), no. 1 123, [[astro-ph/0002264](#)].
- [247] W. Li et al., *Nearby Supernova Rates from the Lick Observatory Supernova Search. II. The Observed Luminosity Functions and Fractions of Supernovae in a Complete Sample*, *Mon. Not. Roy. Astron. Soc.* **412** (2011) 1441, [[arXiv:1006.4612](#)].
- [248] O. Graur, F. B. Bianco, M. Modjaz, I. Shivvers, A. V. Filippenko, W. Li, and N. Smith, *LOSS Revisited - II: The relative rates of different types of supernovae vary between low- and high-mass galaxies*, *Astrophys. J.* **837** (2017), no. 2 121, [[arXiv:1609.02923](#)].
- [249] D. Richardson, R. L. Jenkins, J. Wright, and L. Maddox, *Absolute-Magnitude Distributions of Supernovae*, *Astron. J.* **147** (2014) 118, [[arXiv:1403.5755](#)].
- [250] R. P. Kirshner and J. Kwan, *Distances to extragalactic supernovae.*, *Astroph. J.* **193** (Oct., 1974) 27–36.
- [251] R. G. Eastman, B. P. Schmidt, and R. Kirshner, *The Atmospheres of Type II Supernovae and the Expanding Photosphere Method*, *Astroph. J.* **466** (Aug., 1996) 911.
- [252] L. Dessart and D. J. Hillier, *Distance determinations using Type II supernovae and the expanding photosphere method*, *Astron. Astrophys.* **439** (2005) 671, [[astro-ph/0505465](#)].

- [253] E. A. Baron, P. E. Nugent, D. Branch, and P. H. Hauschildt, *Type IIP supernovae as cosmological probes: A SEAM distance to SN 1999em*, *Astrophys. J. Lett.* **616** (2004) L91–L94, [[astro-ph/0410153](#)].
- [254] L. Dessart et al., *Using Quantitative Spectroscopic Analysis to Determine the Properties and Distances of Type II-Plateau Supernovae: SNe 2005cs and 2006bp*, *Astrophys. J.* **675** (2008) 644, [[arXiv:0711.1815](#)].
- [255] M. Hamuy and P. A. Pinto, *Type II supernovae as standardized candles*, *Astrophys. J. Lett.* **566** (2002) L63–L65, [[astro-ph/0201279](#)].
- [256] O. Rodríguez, A. Clocchiatti, and M. Hamuy, *Photospheric Magnitude Diagrams for Type II Supernovae: A Promising Tool to Compute Distances*, *Astron. J.* **148** (2014) 107, [[arXiv:1409.3198](#)].
- [257] d. J. T. et al., *A Hubble diagram from Type II Supernovae based solely on photometry: the Photometric-Colour Method*, *Astrophys. J.* **815** (2015) 121, [[arXiv:1511.05145](#)].
- [258] F. Olivares E. et al., *The Standardized Candle Method for Type II Plateau Supernovae*, *Astrophys. J.* **715** (2010) 833–853, [[arXiv:1004.2534](#)].
- [259] T. de Jaeger et al., *SN 2016jhj at redshift 0.34: extending the Type II supernova Hubble diagram using the standard candle method*, *Mon. Not. Roy. Astron. Soc.* **472** (2017), no. 4 4233–4243, [[arXiv:1709.01513](#)].
- [260] **DES** Collaboration, T. de Jaeger et al., *Studying Type II supernovae as cosmological standard candles using the Dark Energy Survey*, [arXiv:2005.09757](#).
- [261] D. Q. Lamb and D. E. Reichart, *Gamma-ray bursts as a probe of the very high redshift universe*, *Astrophys. J.* **536** (2000) 1–18, [[astro-ph/9909002](#)].
- [262] S. Basilakos and L. Perivolaropoulos, *Testing GRBs as Standard Candles*, *Mon. Not. Roy. Astron. Soc.* **391** (2008) 411–419, [[arXiv:0805.0875](#)].
- [263] F. Y. Wang, Z. G. Dai, and E. W. Liang, *Gamma-ray Burst Cosmology*, *New Astron. Rev.* **67** (2015) 1–17, [[arXiv:1504.00735](#)].
- [264] J. Liu and H. Wei, *Cosmological models and gamma-ray bursts calibrated by using Padé method*, *Gen. Rel. Grav.* **47** (2015), no. 11 141, [[arXiv:1410.3960](#)].
- [265] L. Amati et al., *Intrinsic spectra and energetics of BeppoSAX gamma-ray bursts with known redshifts*, *Astron. Astrophys.* **390** (2002) 81, [[astro-ph/0205230](#)].
- [266] G. Ghirlanda, G. Ghisellini, and D. Lazzati, *The Collimation-corrected GRB energies correlate with the peak energy of their νf_{ν} spectrum*, *Astrophys. J.* **616** (2004) 331–338, [[astro-ph/0405602](#)].
- [267] M. G. Dainotti, B. De Simone, T. Schiavone, G. Montani, E. Rinaldi, G. Lambiase, M. Bogdan, and S. Ugale, *On the Evolution of the Hubble Constant with the SNe Ia Pantheon Sample and Baryon Acoustic Oscillations: A Feasibility Study for GRB-Cosmology in 2030*, *Galaxies* **10** (2022), no. 1 24, [[arXiv:2201.09848](#)].
- [268] M. Moresco et al., *Unveiling the Universe with Emerging Cosmological Probes*, [arXiv:2201.07241](#).
- [269] D. Camarena and V. Marra, *Local determination of the Hubble constant and the deceleration parameter*, *Phys. Rev. Res.* **2** (2020), no. 1 013028, [[arXiv:1906.11814](#)].

- [270] S. Weinberg, *Cosmology*. 9, 2008.
- [271] B. M. Tinsley, *Evolution of the Stars and Gas in Galaxies*, *Astroph.J.* **151** (Feb., 1968) 547.
- [272] Y. Kang, Y.-W. Lee, Y.-L. Kim, C. Chung, and C. H. Ree, *Early-type Host Galaxies of Type Ia Supernovae. II. Evidence for Luminosity Evolution in Supernova Cosmology*, *Astrophys. J.* **889** (2020), no. 1 8, [[arXiv:1912.04903](#)].
- [273] B. M. Rose, P. M. Garnavich, and M. A. Berg, *Think Global, Act Local: The Influence of Environment Age and Host Mass on Type Ia Supernova Light Curves*, *Astrophys. J.* **874** (2019), no. 1 32, [[arXiv:1902.01433](#)].
- [274] D. O. Jones et al., *Should Type Ia Supernova Distances be Corrected for their Local Environments?*, *Astrophys. J.* **867** (2018), no. 2 108, [[arXiv:1805.05911](#)].
- [275] **Nearby Supernova Factory** Collaboration, M. Rigault et al., *Strong Dependence of Type Ia Supernova Standardization on the Local Specific Star Formation Rate*, *Astron. Astrophys.* **644** (2020) A176, [[arXiv:1806.03849](#)].
- [276] Y.-L. Kim, M. Smith, M. Sullivan, and Y.-W. Lee, *Environmental Dependence of Type Ia Supernova Luminosities from a Sample without a Local-Global Difference in Host Star Formation*, *Astroph.J.* **854** (Feb., 2018) 24, [[arXiv:1801.01192](#)].
- [277] E. O. Colgáin, *A hint of matter underdensity at low z ?*, *JCAP* **09** (2019) 006, [[arXiv:1903.11743](#)].
- [278] L. Kazantzidis and L. Perivolaropoulos, *σ_8 Tension. Is Gravity Getting Weaker at Low z ? Observational Evidence and Theoretical Implications*, [[arXiv:1907.03176](#)].
- [279] D. Sapone, S. Nesseris, and C. A. P. Bengaly, *Is there any measurable redshift dependence on the SN Ia absolute magnitude?*, *Phys. Dark Univ.* **32** (2021) 100814, [[arXiv:2006.05461](#)].
- [280] H. Koo, A. Shafieloo, R. E. Keeley, and B. L’Huillier, *Model-independent Constraints on Type Ia Supernova Light-curve Hyperparameters and Reconstructions of the Expansion History of the Universe*, *Astrophys. J.* **899** (2020), no. 1 9, [[arXiv:2001.10887](#)].
- [281] L. Kazantzidis, H. Koo, S. Nesseris, L. Perivolaropoulos, and A. Shafieloo, *Hints for possible low redshift oscillation around the best-fitting Λ CDM model in the expansion history of the Universe*, *Mon. Not. Roy. Astron. Soc.* **501** (2021), no. 3 3421–3426, [[arXiv:2010.03491](#)].
- [282] V. V. Luković, B. S. Haridasu, and N. Vittorio, *Exploring the evidence for a large local void with supernovae Ia data*, *Mon. Not. Roy. Astron. Soc.* **491** (2020), no. 2 2075–2087, [[arXiv:1907.11219](#)].
- [283] I. Tutusaus, B. Lamine, and A. Blanchard, *Model-independent cosmic acceleration and redshift-dependent intrinsic luminosity in type-Ia supernovae*, *Astron. Astrophys.* **625** (2019) A15, [[arXiv:1803.06197](#)].
- [284] I. Tutusaus, B. Lamine, A. Dupays, and A. Blanchard, *Is cosmic acceleration proven by local cosmological probes?*, *Astron. Astrophys.* **602** (2017) A73, [[arXiv:1706.05036](#)].
- [285] P. S. Drell, T. J. Loredo, and I. Wasserman, *Type Ia supernovae, evolution, and the cosmological constant*, *Astrophys. J.* **530** (2000) 593, [[astro-ph/9905027](#)].
- [286] J. Grande and L. Perivolaropoulos, *Generalized LTB model with Inhomogeneous Isotropic Dark Energy: Observational Constraints*, *Phys. Rev. D* **84** (2011) 023514, [[arXiv:1103.4143](#)].

- [287] M. Gasperini, G. Marozzi, F. Nugier, and G. Veneziano, *Light-cone averaging in cosmology: Formalism and applications*, *JCAP* **07** (2011) 008, [[arXiv:1104.1167](#)].
- [288] G. Fanizza, M. Gasperini, G. Marozzi, and G. Veneziano, *Generalized covariant prescriptions for averaging cosmological observables*, *JCAP* **02** (2020) 017, [[arXiv:1911.09469](#)].
- [289] D. Camarena and V. Marra, *On the use of the local prior on the absolute magnitude of Type Ia supernovae in cosmological inference*, *Mon. Not. Roy. Astron. Soc.* **504** (2021) 5164–5171, [[arXiv:2101.08641](#)].
- [290] D. Camarena and V. Marra, *A new method to build the (inverse) distance ladder*, *Mon. Not. Roy. Astron. Soc.* **495** (2020), no. 3 2630–2644, [[arXiv:1910.14125](#)].
- [291] L. Perivolaropoulos, “ H_0 Crisis: Systematics of distance calibrators or The End of Λ CDM?” <https://www.youtube.com/watch?v=RQODU88A2ik&t=15s>.
- [292] B. Follin and L. Knox, *Insensitivity of the distance ladder Hubble constant determination to Cepheid calibration modelling choices*, *Mon. Not. Roy. Astron. Soc.* **477** (2018), no. 4 4534–4542, [[arXiv:1707.01175](#)].
- [293] A. Chudaykin, D. Gorbunov, and N. Nedelko, *Combined analysis of Planck and SPTPol data favors the early dark energy models*, *JCAP* **08** (2020) 013, [[arXiv:2004.13046](#)].
- [294] M. Rameez and S. Sarkar, *Is there really a Hubble tension?*, *Class. Quant. Grav.* **38** (2021), no. 15 154005, [[arXiv:1911.06456](#)].
- [295] L. Breuval et al., *The Milky Way Cepheid Leavitt law based on Gaia DR2 parallaxes of companion stars and host open cluster populations*, *Astron. Astrophys.* **643** (2020) A115, [[arXiv:2006.08763](#)].
- [296] **Gaia** Collaboration, A. Brown et al., *Gaia Data Release 2: Summary of the contents and survey properties*, *Astron. Astrophys.* **616** (2018) A1, [[arXiv:1804.09365](#)].
- [297] S. Dhawan, S. W. Jha, and B. Leibundgut, *Measuring the Hubble constant with Type Ia supernovae as near-infrared standard candles*, *Astron. Astrophys.* **609** (2018) A72, [[arXiv:1707.00715](#)].
- [298] **CSP** Collaboration, C. R. Burns et al., *The Carnegie Supernova Project: Absolute Calibration and the Hubble Constant*, *Astrophys. J.* **869** (2018), no. 1 56, [[arXiv:1809.06381](#)].
- [299] S. M. Feeney, D. J. Mortlock, and N. Dalmasso, *Clarifying the Hubble constant tension with a Bayesian hierarchical model of the local distance ladder*, *Mon. Not. Roy. Astron. Soc.* **476** (2018), no. 3 3861–3882, [[arXiv:1707.00007](#)].
- [300] K. Krisciunas et al., *The Carnegie Supernova Project I: Third Photometry Data Release of Low-Redshift Type Ia Supernovae and Other White Dwarf Explosions*, *Astron. J.* **154** (2017), no. 5 211, [[arXiv:1709.05146](#)].
- [301] W. L. Freedman et al., *The Carnegie-Chicago Hubble Program. VIII. An Independent Determination of the Hubble Constant Based on the Tip of the Red Giant Branch*, [[arXiv:1907.05922](#)].
- [302] W. L. Freedman, *Measurements of the Hubble Constant: Tensions in Perspective*, [[arXiv:2106.15656](#)].
- [303] W. Yuan, A. G. Riess, L. M. Macri, S. Casertano, and D. Scolnic, *Consistent Calibration of the Tip of the Red Giant Branch in the Large Magellanic Cloud on the Hubble Space Telescope Photometric System and a Re-determination of the Hubble Constant*, *Astrophys. J.* **886** (2019) 61, [[arXiv:1908.00993](#)].

- [304] T. J. Hoyt, *On Zero Point Calibration of the Red Giant Branch Tip in the Magellanic Clouds*, [arXiv:2106.13337](#).
- [305] Y. J. Kim, J. Kang, M. G. Lee, and I. S. Jang, *Determination of the Local Hubble Constant from Virgo Infall Using TRGB Distances*, [arXiv:2010.01364](#).
- [306] I. D. Karachentsev, L. N. Makarova, R. B. Tully, L. Rizzi, and E. J. Shaya, *TRGB Distances to Galaxies in Front of the Virgo Cluster*, *Astrophys. J.* **858** (May, 2018) 62, [[arXiv:1804.00469](#)].
- [307] J. Soltis, S. Casertano, and A. G. Riess, *The Parallax of ω Centauri Measured from Gaia EDR3 and a Direct, Geometric Calibration of the Tip of the Red Giant Branch and the Hubble Constant*, *Astrophys. J. Lett.* **908** (2021), no. 1 L5, [[arXiv:2012.09196](#)].
- [308] G. S. Anand, R. B. Tully, L. Rizzi, A. G. Riess, and W. Yuan, *Comparing Tip of the Red Giant Branch Distance Scales: An Independent Reduction of the Carnegie-Chicago Hubble Program and the Value of the Hubble Constant*, [arXiv:2108.00007](#).
- [309] D. O. Jones et al., *Measuring the Properties of Dark Energy with Photometrically Classified Pan-STARRS Supernovae. I. Systematic Uncertainty from Core-Collapse Supernova Contamination*, *Astrophys. J.* **843** (2017), no. 1 6, [[arXiv:1611.07042](#)].
- [310] **DES** Collaboration, D. Brout et al., *First Cosmology Results Using Type Ia Supernovae From the Dark Energy Survey: Photometric Pipeline and Light Curve Data Release*, *Astrophys. J.* **874** (2019), no. 1 106, [[arXiv:1811.02378](#)].
- [311] S. Dhawan et al., *A Uniform Type Ia Supernova Distance Ladder with the Zwicky Transient Facility: Absolute Calibration Based on the Tip of the Red Giant Branch (TRGB) Method*, [arXiv:2203.04241](#).
- [312] E. C. Bellm et al., *The Zwicky transient facility: System overview, performance, and first results*, *Publications of the Astronomical Society of the Pacific* **131** (dec, 2018) 018002.
- [313] M. J. Graham et al., *The Zwicky Transient Facility: Science Objectives*, *Publ. Astron. Soc. Pac.* **131** (2019), no. 1001 078001, [[arXiv:1902.01945](#)].
- [314] P. Peebles, *Recombination of the Primeval Plasma*, *Astrophys. J.* **153** (1968) 1.
- [315] **2dFGRS** Collaboration, S. Cole et al., *The 2dF Galaxy Redshift Survey: Power-spectrum analysis of the final dataset and cosmological implications*, *Mon. Not. Roy. Astron. Soc.* **362** (2005) 505–534, [[astro-ph/0501174](#)].
- [316] S. D. Landy and A. S. Szalay, *Bias and variance of angular correlation functions*, *Astrophys. J.* **412** (1993) 64.
- [317] D. J. Eisenstein and W. Hu, *Baryonic features in the matter transfer function*, *Astrophys. J.* **496** (1998) 605, [[astro-ph/9709112](#)].
- [318] A. Meiksin, M. J. White, and J. A. Peacock, *Baryonic signatures in large scale structure*, *Mon. Not. Roy. Astron. Soc.* **304** (1999) 851–864, [[astro-ph/9812214](#)].
- [319] T. Matsubara, *Correlation function in deep redshift space as a cosmological probe*, *Astrophys. J.* **615** (2004) 573–585, [[astro-ph/0408349](#)].
- [320] P. J. E. Peebles, *The large-scale structure of the universe*. 1980.
- [321] L. Amendola and S. Tsujikawa, *Dark Energy: Theory and Observations*. Cambridge University Press, 1, 2015.

- [322] [U+FFFD] Aubourg et al., *Cosmological implications of baryon acoustic oscillation measurements*, *Phys. Rev. D* **92** (2015), no. 12 123516, [[arXiv:1411.1074](#)].
- [323] G. Efstathiou and J. R. Bond, *Cosmic confusion: Degeneracies among cosmological parameters derived from measurements of microwave background anisotropies*, *Mon. Not. Roy. Astron. Soc.* **304** (1999) 75–97, [[astro-ph/9807103](#)].
- [324] **WMAP** Collaboration, E. Komatsu et al., *Five-Year Wilkinson Microwave Anisotropy Probe (WMAP) Observations: Cosmological Interpretation*, *Astrophys. J. Suppl.* **180** (2009) 330–376, [[arXiv:0803.0547](#)].
- [325] W. Hu and S. Dodelson, *Cosmic Microwave Background Anisotropies*, *Ann. Rev. Astron. Astrophys.* **40** (2002) 171–216, [[astro-ph/0110414](#)].
- [326] G. E. Addison, G. Hinshaw, and M. Halpern, *Cosmological constraints from baryon acoustic oscillations and clustering of large-scale structure*, *Mon. Not. Roy. Astron. Soc.* **436** (2013) 1674–1683, [[arXiv:1304.6984](#)].
- [327] A. J. Cuesta, L. Verde, A. Riess, and R. Jimenez, *Calibrating the cosmic distance scale ladder: the role of the sound horizon scale and the local expansion rate as distance anchors*, *Mon. Not. Roy. Astron. Soc.* **448** (2015), no. 4 3463–3471, [[arXiv:1411.1094](#)].
- [328] R.-G. Cai, Z.-K. Guo, S.-J. Wang, W.-W. Yu, and Y. Zhou, *No-go guide for the Hubble tension : matter perturbations*, [arXiv:2202.12214](#).
- [329] N. Schöneberg, J. Lesgourgues, and D. C. Hooper, *The BAO+BBN take on the Hubble tension*, *JCAP* **1910** (2019), no. 10 029, [[arXiv:1907.11594](#)].
- [330] L. Pogosian, A. Silvestri, K. Koyama, and G.-B. Zhao, *How to optimally parametrize deviations from General Relativity in the evolution of cosmological perturbations?*, *Phys. Rev. D* **81** (2010) 104023, [[arXiv:1002.2382](#)].
- [331] K. Jedamzik, L. Pogosian, and G.-B. Zhao, *Why reducing the cosmic sound horizon can not fully resolve the Hubble tension*, [arXiv:2010.04158](#).
- [332] T. L. Smith, V. Poulin, J. L. Bernal, K. K. Boddy, M. Kamionkowski, and R. Murgia, *Early dark energy is not excluded by current large-scale structure data*, [arXiv:2009.10740](#).
- [333] A. Chudaykin, D. Gorbunov, and N. Nedelko, *Exploring an early dark energy solution to the Hubble tension with Planck and SPTPol data*, *Phys. Rev. D* **103** (2021), no. 4 043529, [[arXiv:2011.04682](#)].
- [334] C. L. Chang et al., *Snowmass2021 Cosmic Frontier: Cosmic Microwave Background Measurements White Paper*, in *2022 Snowmass Summer Study*, **3**, 2022. [arXiv:2203.07638](#).
- [335] G. Hinshaw, D. Larson, E. Komatsu, D. N. Spergel, C. L. Bennett, J. Dunkley, M. R. Nolte, M. Halpern, R. S. Hill, N. Odegard, L. Page, K. M. Smith, J. L. Weiland, B. Gold, N. Jarosik, A. Kogut, M. Limon, S. S. Meyer, G. S. Tucker, E. Wollack, and E. L. Wright, *Nine-year Wilkinson Microwave Anisotropy Probe (WMAP) Observations: Cosmological Parameter Results*, *The Astrophysical Journal Supplement* **208** (Oct., 2013) 19, [[arXiv:1212.5226](#)].
- [336] **SPT-3G** Collaboration, L. Balkenhol et al., *Constraints on Λ CDM extensions from the SPT-3G 2018 EE and TE power spectra*, *Phys. Rev. D* **104** (2021), no. 8 083509, [[arXiv:2103.13618](#)].
- [337] **SPT-3G** Collaboration, D. Dutcher et al., *Measurements of the E-mode polarization and temperature-E-mode correlation of the CMB from SPT-3G 2018 data*, *Phys. Rev. D* **104** (2021), no. 2 022003, [[arXiv:2101.01684](#)].

- [338] **SPT** Collaboration, J. W. Henning et al., *Measurements of the Temperature and E-Mode Polarization of the CMB from 500 Square Degrees of SPTpol Data*, *Astrophys. J.* **852** (2018), no. 2 97, [[arXiv:1707.09353](#)].
- [339] **SDSS** Collaboration, D. G. York et al., *The Sloan Digital Sky Survey: Technical Summary*, *Astron. J.* **120** (2000) 1579–1587, [[astro-ph/0006396](#)].
- [340] **SDSS** Collaboration, M. Tegmark et al., *Cosmological Constraints from the SDSS Luminous Red Galaxies*, *Phys. Rev.* **D74** (2006) 123507, [[astro-ph/0608632](#)].
- [341] **BOSS** Collaboration, K. S. Dawson et al., *The Baryon Oscillation Spectroscopic Survey of SDSS-III*, *Astron. J.* **145** (2013) 10, [[arXiv:1208.0022](#)].
- [342] **SDSS** Collaboration, M. R. Blanton et al., *Sloan Digital Sky Survey IV: Mapping the Milky Way, Nearby Galaxies and the Distant Universe*, *Astron. J.* **154** (2017), no. 1 28, [[arXiv:1703.00052](#)].
- [343] K. S. Dawson et al., *The SDSS-IV extended Baryon Oscillation Spectroscopic Survey: Overview and Early Data*, *Astron. J.* **151** (2016) 44, [[arXiv:1508.04473](#)].
- [344] **eBOSS** Collaboration, S. Alam et al., *Completed SDSS-IV extended Baryon Oscillation Spectroscopic Survey: Cosmological implications from two decades of spectroscopic surveys at the Apache Point Observatory*, *Phys. Rev. D* **103** (2021), no. 8 083533, [[arXiv:2007.08991](#)].
- [345] H. Gil-Marín et al., *The Completed SDSS-IV extended Baryon Oscillation Spectroscopic Survey: measurement of the BAO and growth rate of structure of the luminous red galaxy sample from the anisotropic power spectrum between redshifts 0.6 and 1.0*, *Mon. Not. Roy. Astron. Soc.* **498** (2020), no. 2 2492–2531, [[arXiv:2007.08994](#)].
- [346] R. Neveux et al., *The completed SDSS-IV extended Baryon Oscillation Spectroscopic Survey: BAO and RSD measurements from the anisotropic power spectrum of the quasar sample between redshift 0.8 and 2.2*, *Mon. Not. Roy. Astron. Soc.* **499** (2020), no. 1 210–229, [[arXiv:2007.08999](#)].
- [347] A. Raichoor et al., *The completed SDSS-IV extended Baryon Oscillation Spectroscopic Survey: Large-scale Structure Catalogues and Measurement of the isotropic BAO between redshift 0.6 and 1.1 for the Emission Line Galaxy Sample*, *Mon. Not. Roy. Astron. Soc.* **500** (2020), no. 3 3254–3274, [[arXiv:2007.09007](#)].
- [348] J. Hou et al., *The Completed SDSS-IV extended Baryon Oscillation Spectroscopic Survey: BAO and RSD measurements from anisotropic clustering analysis of the Quasar Sample in configuration space between redshift 0.8 and 2.2*, *Mon. Not. Roy. Astron. Soc.* **500** (2020), no. 1 1201–1221, [[arXiv:2007.08998](#)].
- [349] M. J. Drinkwater et al., *The WiggleZ Dark Energy Survey: Survey Design and First Data Release*, *Mon. Not. Roy. Astron. Soc.* **401** (2010) 1429–1452, [[arXiv:0911.4246](#)].
- [350] C. Blake et al., *The WiggleZ Dark Energy Survey: mapping the distance-redshift relation with baryon acoustic oscillations*, *Mon. Not. Roy. Astron. Soc.* **418** (2011) 1707–1724, [[arXiv:1108.2635](#)].
- [351] C. Blake, S. Brough, M. Colless, C. Contreras, W. Couch, S. Croom, D. Croton, T. M. Davis, M. J. Drinkwater, K. Forster, D. Gilbank, M. Gladders, K. Glazebrook, B. Jelliffe, R. J. Jurek, I.-h. Li, B. Madore, D. C. Martin, K. Pimblet, G. B. Poole, M. Pracy, R. Sharp, E. Wisnioski, D. Woods, T. K. Wyder, and H. K. C. Yee, *The WiggleZ Dark Energy Survey: joint measurements of the expansion and growth history at $z \sim 1$* , *mnras* **425** (Sept., 2012) 405–414, [[arXiv:1204.3674](#)].

- [352] **2DFGRS** Collaboration, M. Colless et al., *The 2dF Galaxy Redshift Survey: Spectra and redshifts*, *Mon. Not. Roy. Astron. Soc.* **328** (2001) 1039, [[astro-ph/0106498](#)].
- [353] D. H. Jones et al., *The 6dF Galaxy Survey: Final Redshift Release (DR3) and Southern Large-Scale Structures*, *Mon. Not. Roy. Astron. Soc.* **399** (2009) 683, [[arXiv:0903.5451](#)].
- [354] F. Beutler, C. Blake, M. Colless, D. H. Jones, L. Staveley-Smith, L. Campbell, Q. Parker, W. Saunders, and F. Watson, *The 6dF Galaxy Survey: Baryon Acoustic Oscillations and the Local Hubble Constant*, *Mon. Not. Roy. Astron. Soc.* **416** (2011) 3017–3032, [[arXiv:1106.3366](#)].
- [355] F. Beutler, C. Blake, M. Colless, D. H. Jones, L. Staveley-Smith, G. B. Poole, L. Campbell, Q. Parker, W. Saunders, and F. Watson, *The 6dF Galaxy Survey: $z \approx 0$ measurement of the growth rate and σ_8* , *Mon. Not. Roy. Astron. Soc.* **423** (2012) 3430–3444, [[arXiv:1204.4725](#)].
- [356] **BOSS** Collaboration, T. Delubac et al., *Baryon acoustic oscillations in the Ly α forest of BOSS DR11 quasars*, *Astron. Astrophys.* **574** (2015) A59, [[arXiv:1404.1801](#)].
- [357] V. de Sainte Agathe et al., *Baryon acoustic oscillations at $z = 2.34$ from the correlations of Ly α absorption in eBOSS DR14*, *Astron. Astrophys.* **629** (2019) A85, [[arXiv:1904.03400](#)].
- [358] J. E. Bautista et al., *Measurement of baryon acoustic oscillation correlations at $z = 2.3$ with SDSS DR12 Ly α -Forests*, *Astron. Astrophys.* **603** (2017) A12, [[arXiv:1702.00176](#)].
- [359] **BOSS** Collaboration, A. Font-Ribera et al., *Quasar-Lyman α Forest Cross-Correlation from BOSS DR11 : Baryon Acoustic Oscillations*, *JCAP* **1405** (2014) 027, [[arXiv:1311.1767](#)].
- [360] M. Blomqvist et al., *Baryon acoustic oscillations from the cross-correlation of Ly α absorption and quasars in eBOSS DR14*, *Astron. Astrophys.* **629** (2019) A86, [[arXiv:1904.03430](#)].
- [361] H. du Mas des Bourboux et al., *The Completed SDSS-IV Extended Baryon Oscillation Spectroscopic Survey: Baryon Acoustic Oscillations with Ly α Forests*, *Astrophys. J.* **901** (2020), no. 2 153, [[arXiv:2007.08995](#)].
- [362] **SDSS-IV** Collaboration, R. Ahumada et al., *The 16th Data Release of the Sloan Digital Sky Surveys: First Release from the APOGEE-2 Southern Survey and Full Release of eBOSS Spectra*, *Astrophys. J. Suppl.* **249** (2020), no. 1 3, [[arXiv:1912.02905](#)].
- [363] A. J. Ross, L. Samushia, C. Howlett, W. J. Percival, A. Burden, and M. Manera, *The clustering of the SDSS DR7 main Galaxy sample – I. A 4 per cent distance measure at $z = 0.15$* , *Mon. Not. Roy. Astron. Soc.* **449** (2015), no. 1 835–847, [[arXiv:1409.3242](#)].
- [364] **eBOSS** Collaboration, S. Alam et al., *Completed SDSS-IV extended Baryon Oscillation Spectroscopic Survey: Cosmological implications from two decades of spectroscopic surveys at the Apache Point Observatory*, *Phys. Rev. D* **103** (2021), no. 8 083533, [[arXiv:2007.08991](#)].
- [365] G. D’Amico, J. Gleyzes, N. Kokron, D. Markovic, L. Senatore, P. Zhang, F. Beutler, and H. Gil-Marín, *The Cosmological Analysis of the SDSS/BOSS data from the Effective Field Theory of Large-Scale Structure*, *JCAP* **05** (2020) 005, [[arXiv:1909.05271](#)].
- [366] G. D’Amico, L. Senatore, and P. Zhang, *Limits on w CDM from the EFTofLSS with the PyBird code*, *JCAP* **01** (2021) 006, [[arXiv:2003.07956](#)].
- [367] D. Baumann, A. Nicolis, L. Senatore, and M. Zaldarriaga, *Cosmological Non-Linearities as an Effective Fluid*, *JCAP* **07** (2012) 051, [[arXiv:1004.2488](#)].
- [368] J. J. M. Carrasco, M. P. Hertzberg, and L. Senatore, *The Effective Field Theory of Cosmological Large Scale Structures*, *JHEP* **09** (2012) 082, [[arXiv:1206.2926](#)].

- [369] R. A. Porto, L. Senatore, and M. Zaldarriaga, *The Lagrangian-space Effective Field Theory of Large Scale Structures*, *JCAP* **05** (2014) 022, [[arXiv:1311.2168](#)].
- [370] A. Perko, L. Senatore, E. Jennings, and R. H. Wechsler, *Biased Tracers in Redshift Space in the EFT of Large-Scale Structure*, [arXiv:1610.09321](#).
- [371] T. Colas, G. D’amico, L. Senatore, P. Zhang, and F. Beutler, *Efficient Cosmological Analysis of the SDSS/BOSS data from the Effective Field Theory of Large-Scale Structure*, *JCAP* **06** (2020) 001, [[arXiv:1909.07951](#)].
- [372] L. Pogosian, G.-B. Zhao, and K. Jedamzik, *Recombination-independent determination of the sound horizon and the Hubble constant from BAO*, [arXiv:2009.08455](#).
- [373] P. Zhang, G. D’Amico, L. Senatore, C. Zhao, and Y. Cai, *BOSS Correlation Function analysis from the Effective Field Theory of Large-Scale Structure*, *JCAP* **02** (2022), no. 02 036, [[arXiv:2110.07539](#)].
- [374] S.-F. Chen, Z. Vlah, and M. White, *A new analysis of galaxy 2-point functions in the BOSS survey, including full-shape information and post-reconstruction BAO*, *JCAP* **02** (2022), no. 02 008, [[arXiv:2110.05530](#)].
- [375] O. H. E. Philcox and M. M. Ivanov, *BOSS DR12 full-shape cosmology: Λ CDM constraints from the large-scale galaxy power spectrum and bispectrum monopole*, *Phys. Rev. D* **105** (2022), no. 4 043517, [[arXiv:2112.04515](#)].
- [376] M. M. Ivanov, M. Simonović, and M. Zaldarriaga, *Cosmological Parameters from the BOSS Galaxy Power Spectrum*, *JCAP* **05** (2020) 042, [[arXiv:1909.05277](#)].
- [377] G. S. Farren, O. H. E. Philcox, and B. D. Sherwin, *Determining the Hubble constant without the sound horizon: Perspectives with future galaxy surveys*, [arXiv:2112.10749](#).
- [378] O. H. Philcox, B. D. Sherwin, G. S. Farren, and E. J. Baxter, *Determining the Hubble Constant without the Sound Horizon: Measurements from Galaxy Surveys*, [arXiv:2008.08084](#).
- [379] S. Refsdal, *On the possibility of determining Hubble’s parameter and the masses of galaxies from the gravitational lens effect*, *Mon. Not. Roy. Astron. Soc.* **128** (1964) 307.
- [380] **DES** Collaboration, A. Shajib et al., *STRIDES: a 3.9 per cent measurement of the Hubble constant from the strong lens system DES J0408-5354*, *Mon. Not. Roy. Astron. Soc.* **494** (2020), no. 4 6072–6102, [[arXiv:1910.06306](#)].
- [381] S. Birrer et al., *TDCOSMO - IV. Hierarchical time-delay cosmography – joint inference of the Hubble constant and galaxy density profiles*, *Astron. Astrophys.* **643** (2020) A165, [[arXiv:2007.02941](#)].
- [382] T. Treu and P. J. Marshall, *Time Delay Cosmography*, *Astron. Astrophys. Rev.* **24** (2016), no. 1 11, [[arXiv:1605.05333](#)].
- [383] S. H. Suyu, T.-C. Chang, F. Courbin, and T. Okumura, *Cosmological distance indicators*, *Space Sci. Rev.* **214** (2018), no. 5 91, [[arXiv:1801.07262](#)].
- [384] M. Oguri, *Strong gravitational lensing of explosive transients*, *Rept. Prog. Phys.* **82** (2019), no. 12 126901, [[arXiv:1907.06830](#)].
- [385] S. H. Suyu, P. J. Marshall, M. W. Auger, S. Hilbert, R. D. Blandford, L. V. E. Koopmans, C. D. Fassnacht, and T. Treu, *Dissecting the Gravitational Lens B1608+656. II. Precision Measurements of the Hubble Constant, Spatial Curvature, and the Dark Energy Equation of State*, *Astrophys. J.* **711** (2010) 201–221, [[arXiv:0910.2773](#)].

- [386] S. H. Suyu et al., *HOLiCOW – I. H₀ Lenses in COSMOGRAIL’s Wellspring: program overview*, *Mon. Not. Roy. Astron. Soc.* **468** (2017), no. 3 2590–2604, [[arXiv:1607.00017](#)].
- [387] C. R. Keeton and C. S. Kochanek, *Determining the Hubble constant from the gravitational lens PG-1115+080*, *Astrophys. J.* **487** (1997) 42, [[astro-ph/9611216](#)].
- [388] C. S. Kochanek, *Gravitational lens time delays in cdm*, *Astrophys. J.* **583** (2003) 49–57, [[astro-ph/0206006](#)].
- [389] M. Oguri, *Gravitational Lens Time Delays: A Statistical Assessment of Lens Model Dependences and Implications for the Global Hubble Constant*, *Astrophys. J.* **660** (2007) 1–15, [[astro-ph/0609694](#)].
- [390] V. Bonvin et al., *HOLiCOW – V. New COSMOGRAIL time delays of HE 0435–1223: H₀ to 3.8 per cent precision from strong lensing in a flat Λ CDM model*, *Mon. Not. Roy. Astron. Soc.* **465** (2017), no. 4 4914–4930, [[arXiv:1607.01790](#)].
- [391] C. S. Kochanek, N. D. Morgan, E. E. Falco, B. A. McLeod, J. N. Winn, J. Dembicky, and B. Ketzeback, *The Time delays of gravitational lens HE0435-1223: An Early-type galaxy with a rising rotation curve*, *Astrophys. J.* **640** (2006) 47–61, [[astro-ph/0508070](#)].
- [392] C. D. Fassnacht, T. J. Pearson, A. C. S. Readhead, I. W. A. Browne, L. V. E. Koopmans, S. T. Myers, and P. N. Wilkinson, *A determination of h₀ with the class gravitational lens b1608+656: I. time delay measurements with the vla*, *Astrophys. J.* **527** (1999) 498, [[astro-ph/9907257](#)].
- [393] A. Eigenbrod, F. Courbin, S. Dye, G. Meylan, D. Sluse, P. Saha, C. Vuissoz, and P. Magain, *Cosmograil: the cosmological monitoring of gravitational lenses. 2. sdss j0924+0219: the redshift of the lensing galaxy, the quasar spectral variability and the Einstein rings*, *Astron. Astrophys.* **451** (2006) 747, [[astro-ph/0510641](#)].
- [394] J.-Z. Qi, Y. Cui, W.-H. Hu, J.-F. Zhang, J.-L. Cui, and X. Zhang, *Strongly lensed type Ia supernovae as a precise late-universe probe of measuring the Hubble constant and cosmic curvature*, [arXiv:2202.01396](#).
- [395] E. E. Falco, M. V. Gorenstein, and I. I. Shapiro, *On model-dependent bounds on H₀ from gravitational images : application to Q 0957+561 A, B.*, *The Astrophysical Journal* **289** (Feb., 1985) L1–L4.
- [396] M. V. Gorenstein, E. E. Falco, and I. I. Shapiro, *Degeneracies in Parameter Estimates for Models of Gravitational Lens Systems*, *Astroph.J.* **327** (Apr., 1988) 693.
- [397] P. Saha and L. L. R. Williams, *Gravitational lensing model degeneracies: Is steepness all-important?*, *Astrophys. J.* **653** (2006) 936–941, [[astro-ph/0608496](#)].
- [398] P. Schneider and D. Sluse, *Source-position transformation – an approximate invariance in strong gravitational lensing*, *Astron. Astrophys.* **564** (2014) A103, [[arXiv:1306.4675](#)].
- [399] C. S. Kochanek, *What do gravitational lens time delays measure?*, *Astrophys. J.* **578** (2002) 25–32, [[astro-ph/0205319](#)].
- [400] C. S. Kochanek, *Overconstrained gravitational lens models and the Hubble constant*, *Mon. Not. Roy. Astron. Soc.* **493** (2020), no. 2 1725–1735, [[arXiv:1911.05083](#)].
- [401] C. S. Kochanek, *Overconstrained models of time delay lenses redux: how the angular tail wags the radial dog*, *Mon. Not. Roy. Astron. Soc.* **501** (2021), no. 4 5021–5028, [[arXiv:2003.08395](#)].

- [402] K. Liao, A. Shafieloo, R. E. Keeley, and E. V. Linder, *A model-independent determination of the Hubble constant from lensed quasars and supernovae using Gaussian process regression*, *Astrophys. J. Lett.* **886** (2019), no. 1 L23, [[arXiv:1908.04967](#)].
- [403] K. Liao, A. Shafieloo, R. E. Keeley, and E. V. Linder, *Determining Model-independent H_0 and Consistency Tests*, *Astrophys. J. Lett.* **895** (2020), no. 2 L29, [[arXiv:2002.10605](#)].
- [404] T. Yang, S. Birrer, and B. Hu, *The first simultaneous measurement of Hubble constant and post-Newtonian parameter from Time-Delay Strong Lensing*, *Mon. Not. Roy. Astron. Soc.* **497** (2020), no. 1 L56–L61, [[arXiv:2003.03277](#)].
- [405] M. Millon et al., *TDCOSMO. I. An exploration of systematic uncertainties in the inference of H_0 from time-delay cosmography*, *Astron. Astrophys.* **639** (2020) A101, [[arXiv:1912.08027](#)].
- [406] A. S. Bolton, S. Burles, L. V. E. Koopmans, T. Treu, and L. A. Moustakas, *The sloan lens acs survey. 1. a large spectroscopically selected sample of massive early-type lens galaxies*, *Astrophys. J.* **638** (2006) 703–724, [[astro-ph/0511453](#)].
- [407] G. C. F. Chen et al., *A SHARP view of H0LiCOW: H_0 from three time-delay gravitational lens systems with adaptive optics imaging*, *Mon. Not. Roy. Astron. Soc.* **490** (2019), no. 2 1743–1773, [[arXiv:1907.02533](#)].
- [408] P. Denzel, J. P. Coles, P. Saha, and L. L. R. Williams, *The Hubble constant from eight time-delay galaxy lenses*, *Mon. Not. Roy. Astron. Soc.* **501** (2021), no. 1 784–801, [[arXiv:2007.14398](#)].
- [409] J.-Z. Qi, J.-W. Zhao, S. Cao, M. Biesiada, and Y. Liu, *Measurements of the Hubble constant and cosmic curvature with quasars: ultracompact radio structure and strong gravitational lensing*, *Mon. Not. Roy. Astron. Soc.* **503** (2021), no. 2 2179–2186, [[arXiv:2011.00713](#)].
- [410] B. F. Schutz, *Determining the Hubble Constant from Gravitational Wave Observations*, *Nature* **323** (1986) 310–311.
- [411] D. E. Holz and S. A. Hughes, *Using gravitational-wave standard sirens*, *Astrophys. J.* **629** (2005) 15–22, [[astro-ph/0504616](#)].
- [412] N. Dalal, D. E. Holz, S. A. Hughes, and B. Jain, *Short grb and binary black hole standard sirens as a probe of dark energy*, *Phys. Rev. D* **74** (2006) 063006, [[astro-ph/0601275](#)].
- [413] S. Nissanke, D. E. Holz, S. A. Hughes, N. Dalal, and J. L. Sievers, *Exploring short gamma-ray bursts as gravitational-wave standard sirens*, *Astrophys. J.* **725** (2010) 496–514, [[arXiv:0904.1017](#)].
- [414] S. Nissanke, D. E. Holz, N. Dalal, S. A. Hughes, J. L. Sievers, and C. M. Hirata, *Determining the Hubble constant from gravitational wave observations of merging compact binaries*, [[arXiv:1307.2638](#)].
- [415] D. Eichler, M. Livio, T. Piran, and D. N. Schramm, *Nucleosynthesis, Neutrino Bursts and Gamma-Rays from Coalescing Neutron Stars*, *Nature* **340** (1989) 126–128.
- [416] D. Coulter et al., *Swope Supernova Survey 2017a (SSS17a), the Optical Counterpart to a Gravitational Wave Source*, *Science* **358** (2017) 1556, [[arXiv:1710.05452](#)].
- [417] **DES, Dark Energy Camera GW-EM Collaboration**, M. Soares-Santos et al., *The Electromagnetic Counterpart of the Binary Neutron Star Merger LIGO/Virgo GW170817. I. Discovery of the Optical Counterpart Using the Dark Energy Camera*, *Astrophys. J. Lett.* **848** (2017), no. 2 L16, [[arXiv:1710.05459](#)].

- [418] H.-Y. Chen, M. Fishbach, and D. E. Holz, *A two per cent Hubble constant measurement from standard sirens within five years*, *Nature* **562** (2018), no. 7728 545–547, [[arXiv:1712.06531](#)].
- [419] K. Kiuchi, M. Shibata, P. J. Montero, and J. A. Font, *Gravitational waves from the Papaloizou-Pringle instability in black hole-torus systems*, *Phys. Rev. Lett.* **106** (2011) 251102, [[arXiv:1105.5035](#)].
- [420] K. Belczynski et al., *The Effect of Pair-Instability Mass Loss on Black Hole Mergers*, *Astron. Astrophys.* **594** (2016) A97, [[arXiv:1607.03116](#)].
- [421] P. V. P. Cunha, C. A. R. Herdeiro, and E. Radu, *Fundamental photon orbits: black hole shadows and spacetime instabilities*, *Phys. Rev. D* **96** (2017), no. 2 024039, [[arXiv:1705.05461](#)].
- [422] S. Aretakis, *Stability and Instability of Extreme Reissner-Nordström Black Hole Spacetimes for Linear Scalar Perturbations I*, *Commun. Math. Phys.* **307** (2011) 17–63, [[arXiv:1110.2007](#)].
- [423] G. Alestas, G. V. Kraniotis, and L. Perivolaropoulos, *Existence and stability of static spherical fluid shells in a Schwarzschild-Rindler-anti-de Sitter metric*, *Phys. Rev. D* **102** (2020), no. 10 104015, [[arXiv:2005.11702](#)].
- [424] M. Graham et al., *Candidate Electromagnetic Counterpart to the Binary Black Hole Merger Gravitational Wave Event S190521g*, *Phys. Rev. Lett.* **124** (2020), no. 25 251102, [[arXiv:2006.14122](#)].
- [425] **LIGO Scientific, Virgo** Collaboration, R. Abbott et al., *Properties and Astrophysical Implications of the 150 M_{\odot} Binary Black Hole Merger GW190521*, *Astrophys. J. Lett.* **900** (2020), no. 1 L13, [[arXiv:2009.01190](#)].
- [426] B. McKernan, K. Ford, I. Bartos, M. Graham, W. Lyra, S. Marka, Z. Marka, N. Ross, D. Stern, and Y. Yang, *Ram-pressure stripping of a kicked Hill sphere: Prompt electromagnetic emission from the merger of stellar mass black holes in an AGN accretion disk*, *Astrophys. J. Lett.* **884** (2019), no. 2 L50, [[arXiv:1907.03746](#)].
- [427] C. Messenger and J. Read, *Measuring a cosmological distance-redshift relationship using only gravitational wave observations of binary neutron star coalescences*, *Phys. Rev. Lett.* **108** (2012) 091101, [[arXiv:1107.5725](#)].
- [428] S. R. Taylor and J. R. Gair, *Cosmology with the lights off: standard sirens in the Einstein Telescope era*, *Phys. Rev. D* **86** (2012) 023502, [[arXiv:1204.6739](#)].
- [429] W. M. Farr, M. Fishbach, J. Ye, and D. Holz, *A Future Percent-Level Measurement of the Hubble Expansion at Redshift 0.8 With Advanced LIGO*, *Astrophys. J. Lett.* **883** (2019), no. 2 L42, [[arXiv:1908.09084](#)].
- [430] H. Leandro, V. Marra, and R. Sturani, *Measuring the Hubble constant with black sirens*, *Phys. Rev. D* **105** (2022), no. 2 023523, [[arXiv:2109.07537](#)].
- [431] X. Ding, M. Biesiada, X. Zheng, K. Liao, Z. Li, and Z.-H. Zhu, *Cosmological inference from standard sirens without redshift measurements*, *JCAP* **04** (2019) 033, [[arXiv:1801.05073](#)].
- [432] E. Trott and D. Huterer, *Challenges for the statistical gravitational-wave method to measure the Hubble constant*, [[arXiv:2112.00241](#)].
- [433] **LIGO Scientific, Virgo** Collaboration, M. Fishbach et al., *A Standard Siren Measurement of the Hubble Constant from GW170817 without the Electromagnetic Counterpart*, *Astrophys. J. Lett.* **871** (2019), no. 1 L13, [[arXiv:1807.05667](#)].

- [434] N. Andersson and K. D. Kokkotas, *Gravitational waves and pulsating stars: What can we learn from future observations?*, *Phys. Rev. Lett.* **77** (1996) 4134–4137, [[gr-qc/9610035](#)].
- [435] P. Jaranowski, A. Krolak, K. D. Kokkotas, and G. Tsegas, *On the estimation of parameters of the gravitational-wave signal from a coalescing binary by a network of detectors*, *Class. Quant. Grav.* **13** (1996) 1279–1307.
- [436] K. D. Kokkotas and N. Stergioulas, *Gravitational waves from compact sources*, in *5th International Workshop on New Worlds in Astroparticle Physics*, 6, 2005. [[gr-qc/0506083](#)].
- [437] K. D. Kokkotas, *Gravitational Wave Astronomy*, *Rev. Mod. Astron.* **20** (2008) 140, [[arXiv:0809.1602](#)].
- [438] B. R. Zhang, M. J. Childress, T. M. Davis, N. V. Karpenka, C. Lidman, B. P. Schmidt, and M. Smith, *A blinded determination of H_0 from low-redshift Type Ia supernovae, calibrated by Cepheid variables*, *Mon. Not. Roy. Astron. Soc.* **471** (2017), no. 2 2254–2285, [[arXiv:1706.07573](#)].
- [439] **LIGO Scientific** Collaboration, J. Aasi et al., *Advanced LIGO*, *Class. Quant. Grav.* **32** (2015) 074001, [[arXiv:1411.4547](#)].
- [440] **VIRGO** Collaboration, F. Acernese et al., *Advanced Virgo: a second-generation interferometric gravitational wave detector*, *Class. Quant. Grav.* **32** (2015), no. 2 024001, [[arXiv:1408.3978](#)].
- [441] K. Hotokezaka, E. Nakar, O. Gottlieb, S. Nissanke, K. Masuda, G. Hallinan, K. P. Mooley, and A. T. Deller, *A Hubble constant measurement from superluminal motion of the jet in GW170817*, *Nature Astron.* **3** (2019), no. 10 940–944, [[arXiv:1806.10596](#)].
- [442] F. Gerardi, S. M. Feeney, and J. Alsing, *Unbiased likelihood-free inference of the Hubble constant from light standard sirens*, [arXiv:2104.02728](#).
- [443] **DES, NOAO Data Lab** Collaboration, T. Abbott et al., *The Dark Energy Survey Data Release 1*, *Astrophys. J. Suppl.* **239** (2018), no. 2 18, [[arXiv:1801.03181](#)].
- [444] **DES, LIGO Scientific, Virgo** Collaboration, M. Soares-Santos et al., *First Measurement of the Hubble Constant from a Dark Standard Siren using the Dark Energy Survey Galaxies and the LIGO/Virgo Binary–Black-hole Merger GW170814*, *Astrophys. J. Lett.* **876** (2019), no. 1 L7, [[arXiv:1901.01540](#)].
- [445] **LIGO Scientific, Virgo** Collaboration, B. P. Abbott et al., *A Gravitational-wave Measurement of the Hubble Constant Following the Second Observing Run of Advanced LIGO and Virgo*, *Astrophys. J.* **909** (2021), no. 2 218, [[arXiv:1908.06060](#)].
- [446] S. Mukherjee, A. Ghosh, M. J. Graham, C. Karathanasis, M. M. Kasliwal, I. Magaña Hernandez, S. M. Nissanke, A. Silvestri, and B. D. Wandelt, *First measurement of the Hubble parameter from bright binary black hole GW190521*, [arXiv:2009.14199](#).
- [447] V. Varma, S. E. Field, M. A. Scheel, J. Blackman, D. Gerosa, L. C. Stein, L. E. Kidder, and H. P. Pfeiffer, *Surrogate models for precessing binary black hole simulations with unequal masses*, *Phys. Rev. Research.* **1** (2019) 033015, [[arXiv:1905.09300](#)].
- [448] H.-Y. Chen, C.-J. Haster, S. Vitale, W. M. Farr, and M. Isi, *A Standard Siren Cosmological Measurement from the Potential GW190521 Electromagnetic Counterpart ZTF19abnrhr*, [arXiv:2009.14057](#).
- [449] **LIGO Scientific, VIRGO, KAGRA** Collaboration, R. Abbott et al., *Constraints on the cosmic expansion history from GWTC-3*, [arXiv:2111.03604](#).

- [450] A. Palmese, C. R. Bom, S. Mucesh, and W. G. Hartley, *A standard siren measurement of the Hubble constant using gravitational wave events from the first three LIGO/Virgo observing runs and the DESI Legacy Survey*, [arXiv:2111.06445](#).
- [451] DESI Collaboration, A. Aghamousa et al., *The DESI Experiment Part I: Science, Targeting, and Survey Design*, [arXiv:1611.00036](#).
- [452] DESI Collaboration, A. Aghamousa et al., *The DESI Experiment Part II: Instrument Design*, [arXiv:1611.00037](#).
- [453] V. Gayathri, J. Healy, J. Lange, B. O’Brien, M. Szczepanczyk, I. Bartos, M. Campanelli, S. Klimentko, C. O. Lousto, and R. O’Shaughnessy, *Measuring the Hubble Constant with GW190521 as an Eccentric black hole Merger and Its Potential Electromagnetic Counterpart*, *Astrophys. J. Lett.* **908** (2021), no. 2 L34, [[arXiv:2009.14247](#)].
- [454] S. Mukherjee, A. Krolewski, B. D. Wandelt, and J. Silk, *Cross-correlating dark sirens and galaxies: measurement of H_0 from GWTC-3 of LIGO-Virgo-KAGRA*, [arXiv:2203.03643](#).
- [455] J. R. Herrnstein, J. M. Moran, L. J. Greenhill, P. J. Diamond, M. Inoue, N. Nakai, M. Miyoshi, C. Henkel, and A. Riess, *A Geometric distance to the galaxy NGC 4258 from orbital motions in a nuclear gas disk*, *Nature* **400** (1999) 539–541, [[astro-ph/9907013](#)].
- [456] E. M. L. Humphreys, M. J. Reid, J. M. Moran, L. J. Greenhill, and A. L. Argon, *Toward a New Geometric Distance to the Active Galaxy NGC 4258. III. Final Results and the Hubble Constant*, *Astrophys. J.* **775** (2013) 13, [[arXiv:1307.6031](#)].
- [457] M. J. Reid, J. A. Braatz, J. J. Condon, K. Y. Lo, C. Y. Kuo, C. M. V. Impellizzeri, and C. Henkel, *The Megamaser Cosmology Project: IV. A Direct Measurement of the Hubble Constant from UGC 3789*, *Astrophys. J.* **767** (2013) 154, [[arXiv:1207.7292](#)].
- [458] M. J. Reid, J. A. Braatz, J. J. Condon, L. J. Greenhill, C. Henkel, and K. Y. Lo, *The Megamaser Cosmology Project: I. VLBI observations of UGC 3789*, *Astrophys. J.* **695** (2009) 287–291, [[arXiv:0811.4345](#)].
- [459] C. Kuo, J. A. Braatz, M. J. Reid, F. K. Y. Lo, J. J. Condon, C. M. V. Impellizzeri, and C. Henkel, *The Megamaser Cosmology Project. V. An Angular Diameter Distance to NGC 6264 at 140 Mpc*, *Astrophys. J.* **767** (2013) 155, [[arXiv:1207.7273](#)].
- [460] C. Y. Kuo, J. A. Braatz, K. Y. Lo, M. J. Reid, S. H. Suyu, D. W. Pesce, J. J. Condon, C. Henkel, and C. M. V. Impellizzeri, *The Megamaser Cosmology Project. VI. Observations of NGC 6323*, *Astrophys. J.* **800** (2015), no. 1 26, [[arXiv:1411.5106](#)].
- [461] F. Gao, J. A. Braatz, M. J. Reid, K. Y. Lo, J. J. Condon, C. Henkel, C. Y. Kuo, C. M. V. Impellizzeri, D. W. Pesce, and W. Zhao, *The Megamaser Cosmology Project VIII. A Geometric Distance to NGC 5765b*, *Astrophys. J.* **817** (2016), no. 2 128, [[arXiv:1511.08311](#)].
- [462] S. M. Faber and R. E. Jackson, *Velocity dispersions and mass to light ratios for elliptical galaxies*, *Astrophys. J.* **204** (1976) 668.
- [463] S. Djorgovski and M. Davis, *Fundamental properties of elliptical galaxies*, *Astrophys. J.* **313** (1987) 59.
- [464] R. B. Tully and J. R. Fisher, *A New method of determining distances to galaxies*, *Astron. Astrophys.* **54** (1977) 661–673.
- [465] S. Sakai et al., *The Hubble Space Telescope Key Project on the Extragalactic Distance Scale. 24. The Calibration of Tully-Fisher relations and the value of the Hubble Constant*, *Astrophys. J.* **529** (2000) 698, [[astro-ph/9909269](#)].

- [466] S. S. McGaugh, J. M. Schombert, G. D. Bothun, and W. J. G. de Blok, *The Baryonic Tully-Fisher relation*, *Astrophys. J. Lett.* **533** (2000) L99–L102, [[astro-ph/0003001](#)].
- [467] M. A. W. Verheijen, *The Ursa Major Cluster of Galaxies. 5. H I Rotation Curve Shapes and the Tully-Fisher Relations*, *Astrophys. J.* **563** (2001) 694–715, [[astro-ph/0108225](#)].
- [468] S. Gurovich, S. S. McGaugh, K. C. Freeman, H. Jerjen, L. Staveley-Smith, and W. J. G. De Blok, *The Baryonic Tully Fisher relation*, *Publ. Astron. Soc. Austral.* **21** (2004), no. 4 412, [[astro-ph/0411521](#)].
- [469] S. S. McGaugh, *The Baryonic Tully-Fisher relation of galaxies with extended rotation curves and the stellar mass of rotating galaxies*, *Astrophys. J.* **632** (2005) 859–871, [[astro-ph/0506750](#)].
- [470] F. Lelli, S. S. McGaugh, and J. M. Schombert, *The Small Scatter of the Baryonic Tully-fisher Relation*, *Astrophys. J. Lett.* **816** (2016), no. 1 L14, [[arXiv:1512.04543](#)].
- [471] S. McGaugh, *The Baryonic Tully-Fisher Relation of Gas Rich Galaxies as a Test of LCDM and MOND*, *Astron. J.* **143** (2012) 40, [[arXiv:1107.2934](#)].
- [472] G. Iorio, F. Fraternali, C. Nipoti, E. Di Teodoro, J. I. Read, and G. Battaglia, *Little things in 3d: robust determination of the circular velocity of dwarf irregular galaxies.*, *Monthly Notices of the Royal Astronomical Society* (Dec, 2016) stw3285.
- [473] F. Lelli, S. S. McGaugh, J. M. Schombert, H. Desmond, and H. Katz, *The baryonic Tully-Fisher relation for different velocity definitions and implications for galaxy angular momentum*, *Mon. Not. Roy. Astron. Soc.* **484** (2019), no. 3 3267–3278, [[arXiv:1901.05966](#)].
- [474] J. Schombert, S. McGaugh, and F. Lelli, *Using The Baryonic Tully-Fisher Relation to Measure H_0* , *Astron. J.* **160** (2020), no. 2 71, [[arXiv:2006.08615](#)].
- [475] M. Aaronson, J. Huchra, and J. Mould, *The infrared luminosity/H I velocity-width relation and its application to the distance scale.*, *Astroph.J.* **229** (Apr., 1979) 1–13.
- [476] K. C. Freeman, *On the Disks of Spiral and S0 Galaxies*, *Astroph.J.* **160** (June, 1970) 811.
- [477] G. Alestas, I. Antoniou, and L. Perivolaropoulos, *Hints for a gravitational constant transition in Tully-Fisher data*, [[arXiv:2104.14481](#)].
- [478] F. Lelli, S. S. McGaugh, and J. M. Schombert, *SPARC: Mass Models for 175 Disk Galaxies with Spitzer Photometry and Accurate Rotation Curves*, *Astron. J.* **152** (2016) 157, [[arXiv:1606.09251](#)].
- [479] M. G. Hauser and E. Dwek, *The cosmic infrared background: measurements and implications*, *Ann. Rev. Astron. Astrophys.* **39** (2001) 249–307, [[astro-ph/0105539](#)].
- [480] R. Gould and G. Schröder, *Opacity of the Universe to High-Energy Photons*, *Phys. Rev. Lett.* **16** (1966), no. 6 252–254.
- [481] A. Domínguez, R. Wojtak, J. Finke, M. Ajello, K. Helgason, F. Prada, A. Desai, V. Paliya, L. Marcotulli, and D. Hartmann, *A new measurement of the Hubble constant and matter content of the Universe using extragalactic background light γ -ray attenuation*, [[arXiv:1903.12097](#)].
- [482] A. Domínguez and F. Prada, *Measurement of the Expansion Rate of the Universe from γ -Ray Attenuation*, *Astrophys. J. Lett.* **771** (2013) L34, [[arXiv:1305.2163](#)].
- [483] R. Jimenez and A. Loeb, *Constraining cosmological parameters based on relative galaxy ages*, *Astrophys. J.* **573** (2002) 37–42, [[astro-ph/0106145](#)].

- [484] M. Moresco et al., *Improved constraints on the expansion rate of the Universe up to z 1.1 from the spectroscopic evolution of cosmic chronometers*, *JCAP* **1208** (2012) 006, [[arXiv:1201.3609](#)].
- [485] M. Moresco, L. Pozzetti, A. Cimatti, R. Jimenez, C. Maraston, L. Verde, D. Thomas, A. Citro, R. Tojeiro, and D. Wilkinson, *A 6% measurement of the Hubble parameter at $z \sim 0.45$: direct evidence of the epoch of cosmic re-acceleration*, *JCAP* **1605** (2016), no. 05 014, [[arXiv:1601.01701](#)].
- [486] Y. Chen, S. Kumar, and B. Ratra, *Determining the Hubble constant from Hubble parameter measurements*, *Astrophys. J.* **835** (2017), no. 1 86, [[arXiv:1606.07316](#)].
- [487] O. Farooq, F. R. Madiyar, S. Crandall, and B. Ratra, *Hubble Parameter Measurement Constraints on the Redshift of the Deceleration–acceleration Transition, Dynamical Dark Energy, and Space Curvature*, *Astrophys. J.* **835** (2017), no. 1 26, [[arXiv:1607.03537](#)].
- [488] A. Gómez-Valent and L. Amendola, *H_0 from cosmic chronometers and Type Ia supernovae, with Gaussian Processes and the novel Weighted Polynomial Regression method*, *JCAP* **04** (2018) 051, [[arXiv:1802.01505](#)].
- [489] M. Seikel, C. Clarkson, and M. Smith, *Reconstruction of dark energy and expansion dynamics using Gaussian processes*, *JCAP* **06** (2012) 036, [[arXiv:1204.2832](#)].
- [490] A. Shafieloo, A. G. Kim, and E. V. Linder, *Gaussian Process Cosmography*, *Phys. Rev. D* **85** (2012) 123530, [[arXiv:1204.2272](#)].
- [491] S. Yahya, M. Seikel, C. Clarkson, R. Maartens, and M. Smith, *Null tests of the cosmological constant using supernovae*, *Phys. Rev. D* **89** (2014), no. 2 023503, [[arXiv:1308.4099](#)].
- [492] S. Joudaki, M. Kaplinghat, R. Keeley, and D. Kirkby, *Model independent inference of the expansion history and implications for the growth of structure*, *Phys. Rev. D* **97** (2018), no. 12 123501, [[arXiv:1710.04236](#)].
- [493] C. E. Rasmussen and C. K. I. Williams, *Gaussian Processes for Machine Learning (Adaptive Computation and Machine Learning)*. The MIT Press, 2005.
- [494] E. Ó Colgáin and M. M. Sheikh-Jabbari, *Elucidating cosmological model dependence with H_0* , *Eur. Phys. J. C* **81** (2021), no. 10 892, [[arXiv:2101.08565](#)].
- [495] D. Benisty, J. Mifsud, J. L. Said, and D. Staicova, *On the Robustness of the Constancy of the Supernova Absolute Magnitude: Non-parametric Reconstruction & Bayesian approaches*, [[arXiv:2202.04677](#)].
- [496] C. Escamilla-Rivera, J. Levi Said, and J. Mifsud, *Performance of non-parametric reconstruction techniques in the late-time universe*, *JCAP* **10** (2021) 016, [[arXiv:2105.14332](#)].
- [497] X. Ren, S.-F. Yan, Y. Zhao, Y.-F. Cai, and E. N. Saridakis, *Gaussian processes and effective field theory of $f(T)$ gravity under the H_0 tension*, [[arXiv:2203.01926](#)].
- [498] T. Holsclaw, U. Alam, B. Sanso, H. Lee, K. Heitmann, S. Habib, and D. Higdon, *Nonparametric Reconstruction of the Dark Energy Equation of State*, *Phys. Rev. D* **82** (2010) 103502, [[arXiv:1009.5443](#)].
- [499] R. E. Keeley, A. Shafieloo, B. L’Huillier, and E. V. Linder, *Debiasing Cosmic Gravitational Wave Sirens*, *Mon. Not. Roy. Astron. Soc.* **491** (2020), no. 3 3983–3989, [[arXiv:1905.10216](#)].
- [500] T. Holsclaw, U. Alam, B. Sanso, H. Lee, K. Heitmann, S. Habib, and D. Higdon, *Nonparametric Dark Energy Reconstruction from Supernova Data*, *Phys. Rev. Lett.* **105** (2010) 241302, [[arXiv:1011.3079](#)].

- [501] C. Bengaly, *A null test of the Cosmological Principle with BAO measurements*, *Phys. Dark Univ.* **35** (2022) 100966, [[arXiv:2111.06869](#)].
- [502] M.-J. Zhang and J.-Q. Xia, *Test of the cosmic evolution using Gaussian processes*, *JCAP* **12** (2016) 005, [[arXiv:1606.04398](#)].
- [503] V. C. Busti, C. Clarkson, and M. Seikel, *Evidence for a Lower Value for H_0 from Cosmic Chronometers Data?*, *Mon. Not. Roy. Astron. Soc.* **441** (2014) 11, [[arXiv:1402.5429](#)].
- [504] M. Seikel and C. Clarkson, *Optimising Gaussian processes for reconstructing dark energy dynamics from supernovae*, [arXiv:1311.6678](#).
- [505] V. Sahni, A. Shafieloo, and A. A. Starobinsky, *Model independent evidence for dark energy evolution from Baryon Acoustic Oscillations*, *Astrophys. J.* **793** (2014), no. 2 L40, [[arXiv:1406.2209](#)].
- [506] B. L’Huillier and A. Shafieloo, *Model-independent test of the FLRW metric, the flatness of the Universe, and non-local measurement of H_{0rd}* , *JCAP* **01** (2017) 015, [[arXiv:1606.06832](#)].
- [507] B. L’Huillier, A. Shafieloo, and H. Kim, *Model-independent cosmological constraints from growth and expansion*, [arXiv:1712.04865](#).
- [508] G. A. Marques, J. Liu, J. M. Z. Matilla, Z. Haiman, A. Bernui, and C. P. Novaes, *Constraining neutrino mass with weak lensing Minkowski Functionals*, *JCAP* **06** (2019) 019, [[arXiv:1812.08206](#)].
- [509] F. Renzi and A. Silvestri, *A look at the Hubble speed from first principles*, [arXiv:2011.10559](#).
- [510] D. Benisty, *Quantifying the S_8 tension with the Redshift Space Distortion data set*, *Phys. Dark Univ.* **31** (2021) 100766, [[arXiv:2005.03751](#)].
- [511] A. Bonilla, S. Kumar, R. C. Nunes, and S. Pan, *Reconstruction of the dark sectors’ interaction: A model-independent inference and forecast from GW standard sirens*, [arXiv:2102.06149](#).
- [512] A. Bonilla, S. Kumar, and R. C. Nunes, *Measurements of H_0 and reconstruction of the dark energy properties from a model-independent joint analysis*, *Eur. Phys. J. C* **81** (2021), no. 2 127, [[arXiv:2011.07140](#)].
- [513] W. Sun, K. Jiao, and T.-J. Zhang, *Influence of the Bounds of the Hyperparameters on the Reconstruction of the Hubble Constant with the Gaussian Process*, *Astrophys. J.* **915** (2021), no. 2 123, [[arXiv:2105.12618](#)].
- [514] S. Dhawan, J. Alsing, and S. Vagnozzi, *Non-parametric spatial curvature inference using late-Universe cosmological probes*, *Mon. Not. Roy. Astron. Soc.* **506** (2021), no. 1 L1, [[arXiv:2104.02485](#)].
- [515] P. Mukherjee and N. Banerjee, *Nonparametric reconstruction of interaction in the cosmic dark sector*, *Phys. Rev. D* **103** (2021), no. 12 123530, [[arXiv:2105.09995](#)].
- [516] R. E. Keeley, A. Shafieloo, G.-B. Zhao, J. A. Vazquez, and H. Koo, *Reconstructing the Universe: Testing the Mutual Consistency of the Pantheon and SDSS/eBOSS BAO Data Sets with Gaussian Processes*, *Astron. J.* **161** (2021), no. 3 151, [[arXiv:2010.03234](#)].
- [517] F. Avila, A. Bernui, R. C. Nunes, E. de Carvalho, and C. P. Novaes, *The homogeneity scale and the growth rate of cosmic structures*, *Mon. Not. Roy. Astron. Soc.* **509** (2021), no. 2 2994–3003, [[arXiv:2111.08541](#)].

- [518] J. Ruiz-Zapatero, C. García-García, D. Alonso, P. G. Ferreira, and R. D. P. Grumitt, *Model-independent constraints on Ω_m and $H(z)$ from the link between geometry and growth*, [arXiv:2201.07025](#).
- [519] R. Sharma, A. Mukherjee, and H. K. Jassal, *Reconstruction of latetime cosmology using principal component analysis*, *Eur. Phys. J. Plus* **137** (2022), no. 2 219, [[arXiv:2004.01393](#)].
- [520] F. Renzi, N. B. Hogg, and W. Giarè, *The resilience of the Etherington–Hubble relation*, [arXiv:2112.05701](#).
- [521] R. C. Nunes, S. K. Yadav, J. F. Jesus, and A. Bernui, *Cosmological parameter analyses using transversal BAO data*, *Mon. Not. Roy. Astron. Soc.* **497** (2020), no. 2 2133–2141, [[arXiv:2002.09293](#)].
- [522] B. L’Huillier, A. Shafieloo, D. Polarski, and A. A. Starobinsky, *Defying the laws of Gravity I: Model-independent reconstruction of the Universe expansion from growth data*, *Mon. Not. Roy. Astron. Soc.* **494** (2020), no. 1 819–826, [[arXiv:1906.05991](#)].
- [523] E. Belgacem, S. Foffa, M. Maggiore, and T. Yang, *Gaussian processes reconstruction of modified gravitational wave propagation*, *Phys. Rev. D* **101** (2020), no. 6 063505, [[arXiv:1911.11497](#)].
- [524] A. M. Pinho, S. Casas, and L. Amendola, *Model-independent reconstruction of the linear anisotropic stress η* , *JCAP* **1811** (2018), no. 11 027, [[arXiv:1805.00027](#)].
- [525] R.-G. Cai, N. Tamanini, and T. Yang, *Reconstructing the dark sector interaction with LISA*, *JCAP* **05** (2017) 031, [[arXiv:1703.07323](#)].
- [526] B. S. Haridasu, V. V. Luković, M. Moresco, and N. Vittorio, *An improved model-independent assessment of the late-time cosmic expansion*, *JCAP* **10** (2018) 015, [[arXiv:1805.03595](#)].
- [527] M.-J. Zhang and H. Li, *Gaussian processes reconstruction of dark energy from observational data*, *Eur. Phys. J. C* **78** (2018), no. 6 460, [[arXiv:1806.02981](#)].
- [528] D. Wang and X.-H. Meng, *Improved constraints on the dark energy equation of state using Gaussian processes*, *Phys. Rev. D* **95** (2017), no. 2 023508, [[arXiv:1708.07750](#)].
- [529] A. Shafieloo, B. L’Huillier, and A. A. Starobinsky, *Falsifying Λ CDM: Model-independent tests of the concordance model with eBOSS DR14Q and Pantheon*, *Phys. Rev. D* **98** (2018), no. 8 083526, [[arXiv:1804.04320](#)].
- [530] C. A. P. Bengaly, C. Clarkson, and R. Maartens, *The Hubble constant tension with next-generation galaxy surveys*, *JCAP* **05** (2020) 053, [[arXiv:1908.04619](#)].
- [531] C. A. P. Bengaly, *Evidence for cosmic acceleration with next-generation surveys: A model-independent approach*, *Mon. Not. Roy. Astron. Soc.* **499** (2020), no. 1 L6–L10, [[arXiv:1912.05528](#)].
- [532] R. Briffa, S. Capozziello, J. Levi Said, J. Mifsud, and E. N. Saridakis, *Constraining teleparallel gravity through Gaussian processes*, *Class. Quant. Grav.* **38** (2020), no. 5 055007, [[arXiv:2009.14582](#)].
- [533] E.-K. Li, M. Du, Z.-H. Zhou, H. Zhang, and L. Xu, *Testing the effect of H_0 on $f\sigma_8$ tension using a Gaussian process method*, *Mon. Not. Roy. Astron. Soc.* **501** (2021), no. 3 4452–4463, [[arXiv:1911.12076](#)].
- [534] J. Melnick, R. Terlevich, and E. Terlevich, *Hii galaxies as deep cosmological probes*, *Mon. Not. Roy. Astron. Soc.* **311** (2000) 629, [[astro-ph/9908346](#)].

- [535] E. R. Siegel, R. Guzman, J. P. Gallego, M. Orduna Lopez, and P. Rodriguez Hidalgo, *Towards a precision cosmology from starburst galaxies at $z > 2$* , *Mon. Not. Roy. Astron. Soc.* **356** (2005) 1117–1122, [[astro-ph/0410612](#)].
- [536] M. Plionis, R. Terlevich, S. Basilakos, F. Bresolin, E. Terlevich, J. Melnick, and R. Chavez, *A Strategy to Measure the Dark Energy Equation of State using the HII galaxy Hubble Relation & X-ray AGN Clustering: Preliminary Results*, *Mon. Not. Roy. Astron. Soc.* **416** (2011) 2981, [[arXiv:1106.4558](#)].
- [537] R. Chávez, E. Terlevich, R. Terlevich, M. Plionis, F. Bresolin, S. Basilakos, and J. Melnick, *Determining the Hubble constant using Giant extragalactic HII regions and HII galaxies*, *Mon. Not. Roy. Astron. Soc.* **425** (2012) 56, [[arXiv:1203.6222](#)].
- [538] R. Chávez, R. Terlevich, E. Terlevich, F. Bresolin, J. Melnick, M. Plionis, and S. Basilakos, *The L - σ relation for massive bursts of star formation*, *Mon. Not. Roy. Astron. Soc.* **442** (2014), no. 4 3565–3597, [[arXiv:1405.4010](#)].
- [539] R. Terlevich, E. Terlevich, J. Melnick, R. Chávez, M. Plionis, F. Bresolin, and S. Basilakos, *On the road to precision cosmology with high-redshift H II galaxies*, *Mon. Not. Roy. Astron. Soc.* **451** (2015), no. 3 3001–3010, [[arXiv:1505.04376](#)].
- [540] J.-J. Wei, X.-F. Wu, and F. Melia, *The HII Galaxy Hubble Diagram Strongly Favors $R_h = ct$ over Λ CDM*, *Mon. Not. Roy. Astron. Soc.* **463** (2016), no. 2 1144–1152, [[arXiv:1608.02070](#)].
- [541] R. Chávez, M. Plionis, S. Basilakos, R. Terlevich, E. Terlevich, J. Melnick, F. Bresolin, and A. L. González-Morán, *Constraining the dark energy equation of state with HII galaxies*, *Mon. Not. Roy. Astron. Soc.* **462** (2016), no. 3 2431–2439, [[arXiv:1607.06458](#)].
- [542] M. K. Yennapureddy and F. Melia, *Reconstruction of the HII Galaxy Hubble Diagram using Gaussian Processes*, *JCAP* **11** (2017) 029, [[arXiv:1711.03454](#)].
- [543] A. L. González-Morán, R. Chávez, R. Terlevich, E. Terlevich, F. Bresolin, D. Fernández-Arenas, M. Plionis, S. Basilakos, J. Melnick, and E. Telles, *Independent cosmological constraints from high- z H II galaxies*, *Mon. Not. Roy. Astron. Soc.* **487** (2019), no. 4 4669–4694, [[arXiv:1906.02195](#)].
- [544] K. Leaf and F. Melia, *A two-point diagnostic for the H II galaxy Hubble diagram*, *Mon. Not. Roy. Astron. Soc.* **474** (2018), no. 4 4507–4513, [[arXiv:1711.10793](#)].
- [545] C.-Z. Ruan, F. Melia, Y. Chen, and T.-J. Zhang, *Using spatial curvature with HII galaxies and cosmic chronometers to explore the tension in H_0* , *Astrophys. J.* **881** (1, 2019) 137, [[arXiv:1901.06626](#)].
- [546] D. Wang and X.-H. Meng, *Determining H_0 with the latest HII galaxy measurements*, *Astrophys. J.* **843** (2017), no. 2 100, [[arXiv:1612.09023](#)].
- [547] S. H. Suyu et al., *The Hubble constant and new discoveries in cosmology*, [[arXiv:1202.4459](#)].
- [548] G. Chen and B. Ratra, *Median statistics and the Hubble constant*, *Publ. Astron. Soc. Pac.* **123** (2011) 1127–1132, [[arXiv:1105.5206](#)].
- [549] **DES** Collaboration, T. Abbott et al., *Dark Energy Survey Year 1 Results: A Precise H_0 Estimate from DES Y1, BAO, and D/H Data*, *Mon. Not. Roy. Astron. Soc.* **480** (2018), no. 3 3879–3888, [[arXiv:1711.00403](#)].
- [550] **DES** Collaboration, M. A. Troxel et al., *Dark Energy Survey Year 1 results: Cosmological constraints from cosmic shear*, *Phys. Rev.* **D98** (2018), no. 4 043528, [[arXiv:1708.01538](#)].

- [551] **DES** Collaboration, E. Krause et al., *Dark Energy Survey Year 1 Results: Multi-Probe Methodology and Simulated Likelihood Analyses*, [arXiv:1706.09359](#).
- [552] E. J. Baxter and B. D. Sherwin, *Determining the Hubble Constant without the Sound Horizon Scale: Measurements from CMB Lensing*, *Mon. Not. Roy. Astron. Soc.* **501** (2021), no. 2 1823–1835, [[arXiv:2007.04007](#)].
- [553] K. Dutta, A. Roy, Ruchika, A. A. Sen, and M. Sheikh-Jabbari, *Cosmology with low-redshift observations: No signal for new physics*, *Phys. Rev. D* **100** (2019), no. 10 103501, [[arXiv:1908.07267](#)].
- [554] **ACT** Collaboration, S. Aiola et al., *The Atacama Cosmology Telescope: DR4 Maps and Cosmological Parameters*, *JCAP* **12** (2020) 047, [[arXiv:2007.07288](#)].
- [555] S. Cao and B. Ratra, *Using lower-redshift, non-CMB, data to constrain the Hubble constant and other cosmological parameters*, [arXiv:2203.10825](#).
- [556] S. Cao, J. Ryan, and B. Ratra, *Using Pantheon and DES supernova, baryon acoustic oscillation, and Hubble parameter data to constrain the Hubble constant, dark energy dynamics, and spatial curvature*, *Mon. Not. Roy. Astron. Soc.* **504** (2021), no. 1 300–310, [[arXiv:2101.08817](#)].
- [557] S. Cao, J. Ryan, and B. Ratra, *Cosmological constraints from H ii starburst galaxy, quasar angular size, and other measurements*, *Mon. Not. Roy. Astron. Soc.* **509** (2022) 4745–4757, [[arXiv:2109.01987](#)].
- [558] S. Cao, J. Ryan, N. Khadka, and B. Ratra, *Cosmological constraints from higher redshift gamma-ray burst, H ii starburst galaxy, and quasar (and other) data*, *Mon. Not. Roy. Astron. Soc.* **501** (2021), no. 1 1520–1538, [[arXiv:2009.12953](#)].
- [559] S. Cao, J. Ryan, and B. Ratra, *Cosmological constraints from H ii starburst galaxy apparent magnitude and other cosmological measurements*, *Mon. Not. Roy. Astron. Soc.* **497** (2020), no. 3 3191–3203, [[arXiv:2005.12617](#)].
- [560] F. Okamoto, T. Sekiguchi, and T. Takahashi, *H_0 tension without CMB data: Beyond the Λ CDM*, *Phys. Rev. D* **104** (2021), no. 2 023523, [[arXiv:2105.12312](#)].
- [561] R. B. Tully, *Origin of the Hubble constant controversy*, *Nature* **334** (July, 1988) 209–212.
- [562] G. de Vaucouleurs and W. L. Peters, *A preliminary mapping of the extragalactic velocity field near the plane of the local supercluster*, *Astroph.J.* **297** (Oct., 1985) 27–36.
- [563] G. de Vaucouleurs, *New results on the distance scale and the Hubble constant.*, in *Galaxy Distances and Deviations from Universal Expansion* (B. F. Madore and R. B. Tully, eds.), vol. 180 of *NATO Advanced Study Institute (ASI) Series C*, pp. 1–6, Jan., 1986.
- [564] A. Sandage and G. A. Tammann, *Steps toward the Hubble constant. V. The Hubble constant from nearby galaxies and the regularity of the local velocity field.*, *Astroph.J.* **196** (Mar., 1975) 313–328.
- [565] A. Sandage and G. A. Tammann, *The Hubble constant as derived from 21 cm linewidths*, *Nature* **307** (Jan., 1984) 326–329.
- [566] M. S. Turner, *The Road to Precision Cosmology*, [arXiv:2201.04741](#).
- [567] Y. Fujii, *Origin of the Gravitational Constant and Particle Masses in Scale Invariant Scalar - Tensor Theory*, *Phys. Rev. D* **26** (1982) 2580.

- [568] L. Ford, *COSMOLOGICAL CONSTANT DAMPING BY UNSTABLE SCALAR FIELDS*, *Phys. Rev. D* **35** (1987) 2339.
- [569] C. Wetterich, *The Cosmon model for an asymptotically vanishing time dependent cosmological 'constant'*, *Astron. Astrophys.* **301** (1995) 321–328, [[hep-th/9408025](#)].
- [570] C. Wetterich, *Cosmology and the Fate of Dilatation Symmetry*, *Nucl. Phys.* **B302** (1988) 668–696, [[arXiv:1711.03844](#)].
- [571] B. Ratra and P. J. E. Peebles, *Cosmological Consequences of a Rolling Homogeneous Scalar Field*, *Phys. Rev.* **D37** (1988) 3406.
- [572] T. Chiba, N. Sugiyama, and T. Nakamura, *Cosmology with x matter*, *Mon. Not. Roy. Astron. Soc.* **289** (1997) L5–L9, [[astro-ph/9704199](#)].
- [573] P. G. Ferreira and M. Joyce, *Structure formation with a selftuning scalar field*, *Phys. Rev. Lett.* **79** (1997) 4740–4743, [[astro-ph/9707286](#)].
- [574] P. G. Ferreira and M. Joyce, *Cosmology with a primordial scaling field*, *Phys. Rev. D* **58** (1998) 023503, [[astro-ph/9711102](#)].
- [575] E. J. Copeland, A. R. Liddle, and D. Wands, *Exponential potentials and cosmological scaling solutions*, *Phys. Rev. D* **57** (1998) 4686–4690, [[gr-qc/9711068](#)].
- [576] R. R. Caldwell, R. Dave, and P. J. Steinhardt, *Cosmological imprint of an energy component with general equation of state*, *Phys. Rev. Lett.* **80** (1998) 1582–1585, [[astro-ph/9708069](#)].
- [577] I. Zlatev, L.-M. Wang, and P. J. Steinhardt, *Quintessence, cosmic coincidence, and the cosmological constant*, *Phys. Rev. Lett.* **82** (1999) 896–899, [[astro-ph/9807002](#)].
- [578] S. Tsujikawa, *Quintessence: A Review*, *Class. Quant. Grav.* **30** (2013) 214003, [[arXiv:1304.1961](#)].
- [579] R. J. Scherrer, *Exact general solutions for cosmological scalar field evolution in a background-dominated expansion*, [arXiv:2202.01132](#).
- [580] P. J. Steinhardt, L.-M. Wang, and I. Zlatev, *Cosmological tracking solutions*, *Phys. Rev. D* **59** (1999) 123504, [[astro-ph/9812313](#)].
- [581] A. R. Liddle and R. J. Scherrer, *A Classification of scalar field potentials with cosmological scaling solutions*, *Phys. Rev. D* **59** (1999) 023509, [[astro-ph/9809272](#)].
- [582] G. Esposito-Farese and D. Polarski, *Scalar tensor gravity in an accelerating universe*, *Phys. Rev.* **D63** (2001) 063504, [[gr-qc/0009034](#)].
- [583] L. Amendola, R. Gannouji, D. Polarski, and S. Tsujikawa, *Conditions for the cosmological viability of $f(R)$ dark energy models*, *Phys. Rev. D* **75** (2007) 083504, [[gr-qc/0612180](#)].
- [584] S. Fay, S. Nesseris, and L. Perivolaropoulos, *Can $f(R)$ Modified Gravity Theories Mimic a Λ CDM Cosmology?*, *Phys. Rev.* **D76** (2007) 063504, [[gr-qc/0703006](#)].
- [585] S. Nojiri and S. D. Odintsov, *Modified gravity as an alternative for Λ -CDM cosmology*, *J. Phys. A* **40** (2007) 6725–6732, [[hep-th/0610164](#)].
- [586] L. Perivolaropoulos, *Crossing the phantom divide barrier with scalar tensor theories*, *JCAP* **10** (2005) 001, [[astro-ph/0504582](#)].

- [587] B. Boisseau, G. Esposito-Farese, D. Polarski, and A. A. Starobinsky, *Reconstruction of a scalar tensor theory of gravity in an accelerating universe*, *Phys. Rev. Lett.* **85** (2000) 2236, [[gr-qc/0001066](#)].
- [588] K. Bamba, S. Capozziello, S. Nojiri, and S. D. Odintsov, *Dark energy cosmology: the equivalent description via different theoretical models and cosmography tests*, *Astrophys. Space Sci.* **342** (2012) 155–228, [[arXiv:1205.3421](#)].
- [589] E. Di Valentino, A. Melchiorri, and O. Mena, *Can interacting dark energy solve the H_0 tension?*, *Phys. Rev.* **D96** (2017), no. 4 043503, [[arXiv:1704.08342](#)].
- [590] W. Yang, S. Pan, R. C. Nunes, and D. F. Mota, *Dark calling Dark: Interaction in the dark sector in presence of neutrino properties after Planck CMB final release*, *JCAP* **04** (2020) 008, [[arXiv:1910.08821](#)].
- [591] Z. Berezhiani, A. Dolgov, and I. Tkachev, *Reconciling Planck results with low redshift astronomical measurements*, *Phys. Rev. D* **92** (2015), no. 6 061303, [[arXiv:1505.03644](#)].
- [592] P. Fosalba and E. Gaztañaga, *Explaining Cosmological Anisotropy: Evidence for Causal Horizons from CMB data*, [arXiv:2011.00910](#).
- [593] G. Alestas, L. Kazantzidis, and L. Perivolaropoulos, *$w - M$ phantom transition at $z_t < 0.1$ as a resolution of the Hubble tension*, *Phys. Rev. D* **103** (2021), no. 8 083517, [[arXiv:2012.13932](#)].
- [594] H. Akaike, *A new look at the statistical model identification*, *IEEE Transactions on Automatic Control* **19** (1974), no. 6 716–723.
- [595] G. Schwarz, *Estimating the Dimension of a Model*, *Annals Statist.* **6** (1978) 461–464.
- [596] D. J. Spiegelhalter, N. G. Best, B. P. Carlin, and A. van der Linde, *Bayesian measures of model complexity and fit*, *J. Roy. Statist. Soc. B* **64** (2002), no. 4 583–639.
- [597] T. D. Saini, J. Weller, and S. L. Bridle, *Revealing the nature of dark energy using Bayesian evidence*, *Mon. Not. Roy. Astron. Soc.* **348** (2004) 603, [[astro-ph/0305526](#)].
- [598] A. Mehrabi and J. L. Said, *Gaussian discriminators between Λ CDM and w CDM cosmologies using expansion data*, [arXiv:2203.01817](#).
- [599] R. E. Keeley and A. Shafieloo, *On The Distribution of Bayesian Evidences*, [arXiv:2111.04231](#).
- [600] H. Koo, R. E. Keeley, A. Shafieloo, and B. L’Huillier, *Bayesian vs frequentist: comparing Bayesian model selection with a frequentist approach using the iterative smoothing method*, *JCAP* **03** (2022), no. 03 047, [[arXiv:2110.10977](#)].
- [601] A. R. Liddle, *Information criteria for astrophysical model selection*, *Mon. Not. Roy. Astron. Soc.* **377** (2007) L74–L78, [[astro-ph/0701113](#)].
- [602] F. Arevalo, A. Cid, and J. Moya, *AIC and BIC for cosmological interacting scenarios*, *Eur. Phys. J.* **C77** (2017), no. 8 565, [[arXiv:1610.09330](#)].
- [603] M. Kerscher and J. Weller, *On Model Selection in Cosmology*, [arXiv:1901.07726](#).
- [604] A. Banerjee, H. Cai, L. Heisenberg, E. O. Colgáin, M. M. Sheikh-Jabbari, and T. Yang, *Hubble sinks in the low-redshift swampland*, *Phys. Rev. D* **103** (2021), no. 8 L081305, [[arXiv:2006.00244](#)].
- [605] B.-H. Lee, W. Lee, E. O. Colgáin, M. M. Sheikh-Jabbari, and S. Thakur, *Is Local H_0 At Odds With Dark Energy EFT?*, [arXiv:2202.03906](#).

- [606] G. Alestas and L. Perivolaropoulos, *Late time approaches to the Hubble tension deforming $H(z)$, worsen the growth tension*, *Mon. Not. Roy. Astron. Soc.* **504** (2021) 3956, [[arXiv:2103.04045](#)].
- [607] G. Alestas, D. Camarena, E. Di Valentino, L. Kazantzidis, V. Marra, S. Nesseris, and L. Perivolaropoulos, *Late-transition versus smooth $H(z)$ -deformation models for the resolution of the Hubble crisis*, *Phys. Rev. D* **105** (2022), no. 6 063538, [[arXiv:2110.04336](#)].
- [608] W. Yang, E. Di Valentino, S. Pan, Y. Wu, and J. Lu, *Dynamical dark energy after Planck CMB final release and H_0 tension*, *Mon. Not. Roy. Astron. Soc.* **501** (2021), no. 4 5845–5858, [[arXiv:2101.02168](#)].
- [609] G. Benevento, W. Hu, and M. Raveri, *Can Late Dark Energy Transitions Raise the Hubble constant?*, *Phys. Rev. D* **101** (2020), no. 10 103517, [[arXiv:2002.11707](#)].
- [610] G. Efstathiou, *To H_0 or not to H_0 ?*, [[arXiv:2103.08723](#)].
- [611] N. Arendse et al., *Cosmic dissonance: new physics or systematics behind a short sound horizon?*, *Astron. Astrophys.* **639** (2020) A57, [[arXiv:1909.07986](#)].
- [612] A. Theodoropoulos and L. Perivolaropoulos, *The Hubble Tension, the M Crisis of Late Time $H(z)$ Deformation Models and the Reconstruction of Quintessence Lagrangians*, *Universe* **7** (2021), no. 8 300, [[arXiv:2109.06256](#)].
- [613] C. Krishnan, R. Mohayaee, E. O. Colgáin, M. M. Sheikh-Jabbari, and L. Yin, *Does Hubble tension signal a breakdown in FLRW cosmology?*, *Class. Quant. Grav.* **38** (2021), no. 18 184001, [[arXiv:2105.09790](#)].
- [614] J. L. Bernal, L. Verde, R. Jimenez, M. Kamionkowski, D. Valcin, and B. D. Wandelt, *The trouble beyond H_0 and the new cosmic triangles*, *Phys. Rev. D* **103** (2021), no. 10 103533, [[arXiv:2102.05066](#)].
- [615] S. Vagnozzi, F. Pacucci, and A. Loeb, *Implications for the Hubble tension from the ages of the oldest astrophysical objects*, [[arXiv:2105.10421](#)].
- [616] R.-G. Cai, Z.-K. Guo, S.-J. Wang, W.-W. Yu, and Y. Zhou, *No-go guide for the Hubble tension: Late-time solutions*, *Phys. Rev. D* **105** (2022), no. 2 L021301, [[arXiv:2107.13286](#)].
- [617] J. Sola and H. Stefancic, *Dynamical dark energy or variable cosmological parameters?*, *Mod. Phys. Lett. A* **21** (2006) 479–494, [[astro-ph/0507110](#)].
- [618] X. Li and A. Shafieloo, *A Simple Phenomenological Emergent Dark Energy Model can Resolve the Hubble Tension*, *Astrophys. J. Lett.* **883** (2019), no. 1 L3, [[arXiv:1906.08275](#)].
- [619] E. Di Valentino, E. V. Linder, and A. Melchiorri, *Vacuum phase transition solves the H_0 tension*, *Phys. Rev.* **D97** (2018), no. 4 043528, [[arXiv:1710.02153](#)].
- [620] N. Khosravi, S. Baghran, N. Afshordi, and N. Altamirano, *H_0 tension as a hint for a transition in gravitational theory*, *Phys. Rev.* **D99** (2019), no. 10 103526, [[arXiv:1710.09366](#)].
- [621] M. Martinelli and I. Tutusaus, *CMB tensions with low-redshift H_0 and S_8 measurements: impact of a redshift-dependent type-Ia supernovae intrinsic luminosity*, *Symmetry* **11** (2019), no. 8 986, [[arXiv:1906.09189](#)].
- [622] L. Heisenberg, H. Villarrubia-Rojo, and J. Zosso, *Can late-time extensions solve the H_0 and σ_8 tensions?*, [[arXiv:2202.01202](#)].
- [623] L. Heisenberg, H. Villarrubia-Rojo, and J. Zosso, *Simultaneously solving the H_0 and σ_8 tensions with late dark energy*, [[arXiv:2201.11623](#)].

- [624] R.-Y. Guo, J.-F. Zhang, and X. Zhang, *Can the H_0 tension be resolved in extensions to Λ CDM cosmology?*, *JCAP* **1902** (2019) 054, [[arXiv:1809.02340](#)].
- [625] W.-M. Dai, Y.-Z. Ma, and H.-J. He, *Reconciling Hubble Constant Discrepancy from Holographic Dark Energy*, *Phys. Rev. D* **102** (2020) 121302, [[arXiv:2003.03602](#)].
- [626] E. O. Colgáin and M. M. Sheikh-Jabbari, *A Holographic Dark Energy Catch-22*, [arXiv:2102.09816](#).
- [627] M. H. P. M. van Putten, *Evidence for galaxy dynamics tracing background cosmology below the de Sitter scale of acceleration*, *Astrophys. J.* **848** (2017), no. 1 28, [[arXiv:1709.05944](#)].
- [628] M. H. P. M. van Putten, *Alleviating tension in Λ CDM and the local distance ladder from first principles with no free parameters*, *Monthly Notices of the Royal Astronomical Society: Letters* **491** (10, 2019) L6–L10.
- [629] W. J. C. da Silva and R. Silva, *Cosmological Perturbations in the Tsallis Holographic Dark Energy Scenarios*, [arXiv:2011.09520](#).
- [630] A. Hernández-Almada, G. Leon, J. Magaña, M. A. García-Aspeitia, V. Motta, E. N. Saridakis, and K. Yesmakhanova, *Kaniadakis holographic dark energy: observational constraints and global dynamics*, [arXiv:2111.00558](#).
- [631] P. Adhikary, S. Das, S. Basilakos, and E. N. Saridakis, *Barrow holographic dark energy in a nonflat universe*, *Phys. Rev. D* **104** (2021), no. 12 123519, [[arXiv:2104.13118](#)].
- [632] M. Chevallier and D. Polarski, *Accelerating universes with scaling dark matter*, *Int. J. Mod. Phys. D* **10** (2001) 213–224, [[gr-qc/0009008](#)].
- [633] E. V. Linder, *Exploring the expansion history of the universe*, *Phys. Rev. Lett.* **90** (2003) 091301, [[astro-ph/0208512](#)].
- [634] N. Kitazawa, *Polarizations of CMB and the Hubble tension*, [arXiv:2010.12164](#).
- [635] W. Yang, S. Pan, E. Di Valentino, and E. N. Saridakis, *Observational constraints on dynamical dark energy with pivoting redshift*, *Universe* **5** (2019), no. 11 219, [[arXiv:1811.06932](#)].
- [636] H. Miao and Z. Huang, *The H_0 Tension in Non-flat Q CDM Cosmology*, *Astrophys. J.* **868** (2018), no. 1 20, [[arXiv:1803.07320](#)].
- [637] U. Alam, S. Bag, and V. Sahni, *Constraining the Cosmology of the Phantom Brane using Distance Measures*, *Phys. Rev. D* **95** (2017), no. 2 023524, [[arXiv:1605.04707](#)].
- [638] S. Bag, V. Sahni, A. Shafieloo, and Y. Shtanov, *Phantom braneworld and the Hubble tension*, [arXiv:2107.03271](#).
- [639] L. Visinelli, S. Vagnozzi, and U. Danielsson, *Revisiting a negative cosmological constant from low-redshift data*, *Symmetry* **11** (2019), no. 8 1035, [[arXiv:1907.07953](#)].
- [640] R. Calderón, R. Gannouji, B. L’Huillier, and D. Polarski, *Negative cosmological constant in the dark sector?*, *Phys. Rev. D* **103** (2021), no. 2 023526, [[arXiv:2008.10237](#)].
- [641] A. A. Sen, S. A. Adil, and S. Sen, *Do cosmological observations allow a negative Λ ?*, [arXiv:2112.10641](#).
- [642] K. Dutta, Ruchika, A. Roy, A. A. Sen, and M. M. Sheikh-Jabbari, *Beyond Λ CDM with low and high redshift data: implications for dark energy*, *Gen. Rel. Grav.* **52** (2020), no. 2 15, [[arXiv:1808.06623](#)].

- [643] Ö. Akarsu, J. D. Barrow, L. A. Escamilla, and J. A. Vazquez, *Graduated dark energy: Observational hints of a spontaneous sign switch in the cosmological constant*, *Phys. Rev. D* **101** (2020), no. 6 063528, [[arXiv:1912.08751](#)].
- [644] G. Acquaviva, O. Akarsu, N. Katirci, and J. A. Vazquez, *Simple-graduated dark energy and spatial curvature*, *Phys. Rev. D* **104** (2021), no. 2 023505, [[arXiv:2104.02623](#)].
- [645] O. Akarsu, S. Kumar, E. Özlüker, and J. A. Vazquez, *Relaxing cosmological tensions with a sign switching cosmological constant*, *Phys. Rev. D* **104** (2021), no. 12 123512, [[arXiv:2108.09239](#)].
- [646] R. E. Keeley, S. Joudaki, M. Kaplinghat, and D. Kirkby, *Implications of a transition in the dark energy equation of state for the H_0 and σ_8 tensions*, *JCAP* **12** (2019) 035, [[arXiv:1905.10198](#)].
- [647] S. L. Adler, *Implications of a frame dependent dark energy for the spacetime metric, cosmography, and effective Hubble constant*, *Phys. Rev. D* **100** (2019), no. 12 123503, [[arXiv:1905.08228](#)].
- [648] M. G. Dainotti, B. De Simone, T. Schiavone, G. Montani, E. Rinaldi, and G. Lambiase, *On the Hubble constant tension in the SNe Ia Pantheon sample*, *Astrophys. J.* **912** (2021) 150, [[arXiv:2103.02117](#)].
- [649] C. Krishnan, E. O. Colgáin, M. M. Sheikh-Jabbari, and T. Yang, *Running Hubble Tension and a H_0 Diagnostic*, *Phys. Rev. D* **103** (2021), no. 10 103509, [[arXiv:2011.02858](#)].
- [650] Z. Sakr and D. Sapone, *Can varying the gravitational constant alleviate the tensions?*, *JCAP* **03** (2022), no. 03 034, [[arXiv:2112.14173](#)].
- [651] E. Elizalde, J. Gluza, and M. Khurshudyan, *An approach to cold dark matter deviation and the H_0 tension problem by using machine learning*, [arXiv:2104.01077](#).
- [652] E. Di Valentino, A. Mukherjee, and A. A. Sen, *Dark Energy with Phantom Crossing and the H_0 Tension*, *Entropy* **23** (2021), no. 4 404, [[arXiv:2005.12587](#)].
- [653] E. Di Valentino, A. Melchiorri, E. V. Linder, and J. Silk, *Constraining Dark Energy Dynamics in Extended Parameter Space*, *Phys. Rev.* **D96** (2017), no. 2 023523, [[arXiv:1704.00762](#)].
- [654] E. Di Valentino, A. Melchiorri, and J. Silk, *Cosmological constraints in extended parameter space from the Planck 2018 Legacy release*, *JCAP* **01** (2020) 013, [[arXiv:1908.01391](#)].
- [655] S. Vagnozzi, *New physics in light of the H_0 tension: an alternative view*, *Phys. Rev. D* **102** (2020), no. 2 023518, [[arXiv:1907.07569](#)].
- [656] Q.-G. Huang and K. Wang, *How the dark energy can reconcile Planck with local determination of the Hubble constant*, *Eur. Phys. J. C* **76** (2016), no. 9 506, [[arXiv:1606.05965](#)].
- [657] J. Sola and H. Stefancic, *Effective equation of state for dark energy: Mimicking quintessence and phantom energy through a variable lambda*, *Phys. Lett. B* **624** (2005) 147–157, [[astro-ph/0505133](#)].
- [658] I. L. Shapiro, J. Sola, and H. Stefancic, *Running G and Λ at low energies from physics at $M(X)$: Possible cosmological and astrophysical implications*, *JCAP* **01** (2005) 012, [[hep-ph/0410095](#)].
- [659] I. L. Shapiro and J. Sola, *Can the cosmological 'constant' run? - It may run*, [arXiv:0808.0315](#).
- [660] I. L. Shapiro and J. Sola, *On the possible running of the cosmological 'constant'*, *Phys. Lett. B* **682** (2009) 105–113, [[arXiv:0910.4925](#)].

- [661] S. Basilakos, D. Polarski, and J. Sola, *Generalizing the running vacuum energy model and comparing with the entropic-force models*, *Phys. Rev. D* **86** (2012) 043010, [[arXiv:1204.4806](#)].
- [662] E. L. D. Perico, J. A. S. Lima, S. Basilakos, and J. Sola, *Complete Cosmic History with a dynamical $\Lambda = \Lambda(H)$ term*, *Phys. Rev. D* **88** (2013) 063531, [[arXiv:1306.0591](#)].
- [663] S. Basilakos, N. E. Mavromatos, and J. Solà, *Starobinsky-like inflation and running vacuum in the context of Supergravity*, *Universe* **2** (2016), no. 3 14, [[arXiv:1505.04434](#)].
- [664] P. Tsiapi and S. Basilakos, *Testing dynamical vacuum models with CMB power spectrum from Planck*, *Mon. Not. Roy. Astron. Soc.* **485** (2019), no. 2 2505–2510, [[arXiv:1810.12902](#)].
- [665] S. Banerjee, D. Benisty, and E. I. Guendelman, *Running Dark Energy and Dark Matter from Dynamical Spacetime*, *Bulg. J. Phys.* **48** (2021), no. 2 117–137, [[arXiv:1910.03933](#)].
- [666] C. R. Farrugia, J. Sultana, and J. Mifsud, *Endowing Λ with a dynamic nature: Constraints in a spatially curved universe*, *Phys. Rev. D* **102** (2020), no. 2 024013, [[arXiv:1812.02790](#)].
- [667] S. Basilakos, N. E. Mavromatos, and J. Solà Peracaula, *Gravitational and Chiral Anomalies in the Running Vacuum Universe and Matter-Antimatter Asymmetry*, *Phys. Rev. D* **101** (2020), no. 4 045001, [[arXiv:1907.04890](#)].
- [668] J. A. S. Lima, S. Basilakos, and J. Sola, *Expansion History with Decaying Vacuum: A Complete Cosmological Scenario*, *Mon. Not. Roy. Astron. Soc.* **431** (2013) 923–929, [[arXiv:1209.2802](#)].
- [669] C. Moreno-Pulido and J. Solà, *Running vacuum in quantum field theory in curved spacetime: renormalizing ρ_{vac} without $\sim m^4$ terms*, *Eur. Phys. J. C* **80** (2020), no. 8 692, [[arXiv:2005.03164](#)].
- [670] S. Basilakos, N. E. Mavromatos, and J. Solà Peracaula, *Quantum Anomalies, Running Vacuum and Leptogenesis: an Interplay*, *PoS CORFU2018* (2019) 044, [[arXiv:1905.05685](#)].
- [671] N. E. Mavromatos, *Gravitational anomalies, axions and a string-inspired running vacuum model in Cosmology*, in *16th Marcel Grossmann Meeting on Recent Developments in Theoretical and Experimental General Relativity, Astrophysics and Relativistic Field Theories*, 8, 2021. [[arXiv:2108.03998](#)].
- [672] M. Rezaei, J. Solà Peracaula, and M. Malekjani, *Cosmographic approach to Running Vacuum dark energy models: new constraints using BAOs and Hubble diagrams at higher redshifts*, *Mon. Not. Roy. Astron. Soc.* **509** (2021), no. 2 2593–2608, [[arXiv:2108.06255](#)].
- [673] N. E. Mavromatos and J. Solà Peracaula, *Inflationary physics and trans-Planckian conjecture in the stringy running vacuum model: from the phantom vacuum to the true vacuum*, *Eur. Phys. J. Plus* **136** (2021), no. 11 1152, [[arXiv:2105.02659](#)].
- [674] N. E. Mavromatos and J. Solà Peracaula, *Stringy-running-vacuum-model inflation: from primordial gravitational waves and stiff axion matter to dynamical dark energy*, *Eur. Phys. J. ST* **230** (2021), no. 9 9, [[arXiv:2012.07971](#)].
- [675] I. L. Shapiro and J. Sola, *Cosmological constant, renormalization group and Planck scale physics*, *Nucl. Phys. B Proc. Suppl.* **127** (2004) 71–76, [[hep-ph/0305279](#)].
- [676] S. Basilakos, N. E. Mavromatos, and J. Solà Peracaula, *Quantum Anomalies in String-Inspired Running Vacuum Universe: Inflation and Axion Dark Matter*, *Phys. Lett. B* **803** (2020) 135342, [[arXiv:2001.03465](#)].
- [677] J. S. Peracaula, *The Cosmological Constant Problem and Running Vacuum in the Expanding Universe*, [[arXiv:2203.13757](#)].

- [678] J. Sola, *Cosmologies with a time dependent vacuum*, *J. Phys. Conf. Ser.* **283** (2011) 012033, [[arXiv:1102.1815](#)].
- [679] J. Solà and A. Gómez-Valent, *The $\bar{\Lambda}$ CDM cosmology: From inflation to dark energy through running Λ* , *Int. J. Mod. Phys. D* **24** (2015) 1541003, [[arXiv:1501.03832](#)].
- [680] J. Sola, *Vacuum energy and cosmological evolution*, *AIP Conf. Proc.* **1606** (2015), no. 1 19–37, [[arXiv:1402.7049](#)].
- [681] J. Solà, *Cosmological constant vis-a-vis dynamical vacuum: bold challenging the Λ CDM*, *Int. J. Mod. Phys.* **A31** (2016), no. 23 1630035, [[arXiv:1612.02449](#)].
- [682] N. E. Mavromatos, *Geometrical origins of the Universe dark sector: string-inspired torsion and anomalies as seeds for inflation and dark matter*, *Phil. Trans. Roy. Soc. Lond. A* **380** (2022) 20210188, [[arXiv:2108.02152](#)].
- [683] N. E. Mavromatos, *Torsion in String-Inspired Cosmologies and the Universe Dark Sector*, *Universe* **7** (2021), no. 12 480, [[arXiv:2111.05675](#)].
- [684] J. Solà, A. Gómez-Valent, and J. de Cruz Pérez, *The H_0 tension in light of vacuum dynamics in the Universe*, *Phys. Lett.* **B774** (2017) 317–324, [[arXiv:1705.06723](#)].
- [685] J. Solà, A. Gómez-Valent, and J. de Cruz Pérez, *Hints of dynamical vacuum energy in the expanding Universe*, *Astrophys. J. Lett.* **811** (2015) L14, [[arXiv:1506.05793](#)].
- [686] J. Solà, A. Gómez-Valent, and J. de Cruz Pérez, *First evidence of running cosmic vacuum: challenging the concordance model*, *Astrophys. J.* **836** (2017), no. 1 43, [[arXiv:1602.02103](#)].
- [687] A. Gomez-Valent and J. Sola, *Relaxing the σ_8 -tension through running vacuum in the Universe*, *EPL* **120** (2017), no. 3 39001, [[arXiv:1711.00692](#)].
- [688] A. Gómez-Valent and J. Solà, *Density perturbations for running vacuum: a successful approach to structure formation and to the σ_8 -tension*, [[arXiv:1801.08501](#)].
- [689] J. Solà Peracaula, *Running vacuum interacting with dark matter or with running gravitational coupling. Phenomenological implications*, [[arXiv:2109.12086](#)].
- [690] J. Solà Peracaula, A. Gómez-Valent, J. de Cruz Perez, and C. Moreno-Pulido, *Running vacuum against the H_0 and σ_8 tensions*, *EPL* **134** (2021), no. 1 19001, [[arXiv:2102.12758](#)].
- [691] J. Sola, *Dark energy: A Quantum fossil from the inflationary Universe?*, *J. Phys. A* **41** (2008) 164066, [[arXiv:0710.4151](#)].
- [692] I. L. Shapiro and J. Sola, *On the scaling behavior of the cosmological constant and the possible existence of new forces and new light degrees of freedom*, *Phys. Lett. B* **475** (2000) 236–246, [[hep-ph/9910462](#)].
- [693] I. L. Shapiro and J. Sola, *Scaling behavior of the cosmological constant: Interface between quantum field theory and cosmology*, *JHEP* **02** (2002) 006, [[hep-th/0012227](#)].
- [694] C. Moreno-Pulido and J. S. Peracaula, *Renormalizing the vacuum energy in cosmological spacetime: implications for the cosmological constant problem*, [[arXiv:2201.05827](#)].
- [695] A. Gómez-Valent, J. Solà, and S. Basilakos, *Dynamical vacuum energy in the expanding Universe confronted with observations: a dedicated study*, *JCAP* **01** (2015) 004, [[arXiv:1409.7048](#)].
- [696] J. Solà Peracaula, J. de Cruz Pérez, and A. Gómez-Valent, *Possible signals of vacuum dynamics in the Universe*, *Mon. Not. Roy. Astron. Soc.* **478** (2018), no. 4 4357–4373, [[arXiv:1703.08218](#)].

- [697] S. Pan, W. Yang, E. Di Valentino, A. Shafieloo, and S. Chakraborty, *Reconciling H_0 tension in a six parameter space?*, *JCAP* **06** (2020), no. 06 062, [[arXiv:1907.12551](#)].
- [698] W. Yang, E. Di Valentino, S. Pan, and O. Mena, *Emergent Dark Energy, neutrinos and cosmological tensions*, *Phys. Dark Univ.* **31** (2021) 100762, [[arXiv:2007.02927](#)].
- [699] Z. Liu and H. Miao, *Update constraints on neutrino mass and mass hierarchy in light of dark energy models*, *Int. J. Mod. Phys. D* **29** (2020), no. 13 2050088, [[arXiv:2002.05563](#)].
- [700] M. Rezaei, T. Naderi, M. Malekjani, and A. Mehrabi, *A Bayesian comparison between Λ CDM and phenomenologically emergent dark energy models*, *Eur. Phys. J. C* **80** (2020), no. 5 374, [[arXiv:2004.08168](#)].
- [701] W. Yang, E. Di Valentino, S. Pan, and O. Mena, *Emergent Dark Energy, neutrinos and cosmological tensions*, *Phys. Dark Univ.* **31** (2021) 100762, [[arXiv:2007.02927](#)].
- [702] E. Di Valentino, S. Gariazzo, C. Giunti, O. Mena, S. Pan, and W. Yang, *Minimal dark energy: key to sterile neutrino and Hubble constant tensions?*, [[arXiv:2110.03990](#)].
- [703] X. Li and A. Shafieloo, *Evidence for Emergent Dark Energy*, *Astrophys. J.* **902** (2020), no. 1 58, [[arXiv:2001.05103](#)].
- [704] W. Yang, E. Di Valentino, S. Pan, A. Shafieloo, and X. Li, *Generalized Emergent Dark Energy Model and the Hubble Constant Tension*, [[arXiv:2103.03815](#)].
- [705] A. Hernández-Almada, G. Leon, J. Magaña, M. A. García-Aspeitia, and V. Motta, *Generalized Emergent Dark Energy: observational Hubble data constraints and stability analysis*, [[arXiv:2002.12881](#)].
- [706] H. B. Benaoum, W. Yang, S. Pan, and E. Di Valentino, *Modified Emergent Dark Energy and its Astronomical Constraints*, [[arXiv:2008.09098](#)].
- [707] Z. Zhou, G. Liu, and L. Xu, *Can late dark energy restore the Cosmic concordance?*, [[arXiv:2105.04258](#)].
- [708] E. Di Valentino, E. V. Linder, and A. Melchiorri, *H_0 ex machina: Vacuum metamorphosis and beyond H_0* , *Phys. Dark Univ.* **30** (2020) 100733, [[arXiv:2006.16291](#)].
- [709] E. Di Valentino, S. Pan, W. Yang, and L. A. Anchordoqui, *The touch of Neutrinos on the Vacuum Metamorphosis: is the H_0 Solution Back?*, [[arXiv:2102.05641](#)].
- [710] L. Parker and A. Raval, *New quantum aspects of a vacuum dominated universe*, *Phys. Rev. D* **62** (2000) 083503, [[gr-qc/0003103](#)]. [Erratum: *Phys.Rev.D* 67, 029903 (2003)].
- [711] L. Parker and D. A. T. Vanzella, *Acceleration of the universe, vacuum metamorphosis, and the large time asymptotic form of the heat kernel*, *Phys. Rev. D* **69** (2004) 104009, [[gr-qc/0312108](#)].
- [712] R. R. Caldwell, W. Komp, L. Parker, and D. A. T. Vanzella, *A Sudden gravitational transition*, *Phys. Rev. D* **73** (2006) 023513, [[astro-ph/0507622](#)].
- [713] A. D. Sakharov, *Vacuum quantum fluctuations in curved space and the theory of gravitation*, *Usp. Fiz. Nauk* **161** (1991), no. 5 64–66.
- [714] A. Banihashemi, N. Khosravi, and A. H. Shirazi, *Ginzburg-Landau Theory of Dark Energy: A Framework to Study Both Temporal and Spatial Cosmological Tensions Simultaneously*, *Phys. Rev. D* **99** (2019), no. 8 083509, [[arXiv:1810.11007](#)].
- [715] A. Banihashemi, N. Khosravi, and A. H. Shirazi, *Phase transition in the dark sector as a proposal to lessen cosmological tensions*, *Phys. Rev. D* **101** (2020), no. 12 123521, [[arXiv:1808.02472](#)].

- [716] H. Moshafi, S. Baghran, and N. Khosravi, *CMB lensing in a modified Λ CDM model in light of the H_0 tension*, *Phys. Rev. D* **104** (2021), no. 6 063506, [[arXiv:2012.14377](#)].
- [717] A. Banihashemi, N. Khosravi, and A. Shafieloo, *Dark Energy as a Critical Phenomenon: a Resolution for Hubble Tension*, [arXiv:2012.01407](#).
- [718] M. Farhang and N. Khosravi, *Phenomenological Gravitational Phase Transition: Reconciliation between the Late and Early Universe*, *Phys. Rev. D* **103** (2021), no. 8 083523, [[arXiv:2011.08050](#)].
- [719] M. J. Mortonson, W. Hu, and D. Huterer, *Hiding dark energy transitions at low redshift*, *Phys. Rev. D* **80** (2009) 067301, [[arXiv:0908.1408](#)].
- [720] S. Dhawan, D. Brout, D. Scolnic, A. Goobar, A. G. Riess, and V. Miranda, *Cosmological Model Insensitivity of Local H_0 from the Cepheid Distance Ladder*, *Astrophys. J.* **894** (2020), no. 1 54, [[arXiv:2001.09260](#)].
- [721] M. Lucca, *Multi-interacting dark energy and its cosmological implications*, *Phys. Rev. D* **104** (2021), no. 8 083510, [[arXiv:2106.15196](#)].
- [722] L.-Y. Gao, S.-S. Xue, and X. Zhang, *Relieving the H_0 tension with a new interacting dark energy model*, [arXiv:2101.10714](#).
- [723] S. Kumar, *Remedy of some cosmological tensions via effective phantom-like behavior of interacting vacuum energy*, *Phys. Dark Univ.* **33** (2021) 100862, [[arXiv:2102.12902](#)].
- [724] X. Li, A. Shafieloo, V. Sahni, and A. A. Starobinsky, *Revisiting Metastable Dark Energy and Tensions in the Estimation of Cosmological Parameters*, *Astrophys. J.* **887** (4, 2019) 153, [[arXiv:1904.03790](#)].
- [725] W. Yang, E. Di Valentino, S. Pan, S. Basilakos, and A. Paliathanasis, *Metastable dark energy models in light of Planck 2018 data: Alleviating the H_0 tension*, *Phys. Rev. D* **102** (2020), no. 6 063503, [[arXiv:2001.04307](#)].
- [726] S. Panpanich, P. Burikham, S. Ponglertsakul, and L. Tannukij, *Resolving Hubble Tension with Quintom Dark Energy Model*, *Chin. Phys. C* **45** (2021), no. 1 015108, [[arXiv:1908.03324](#)].
- [727] M. A. Buen-Abad, R. Emami, and M. Schmaltz, *Cannibal Dark Matter and Large Scale Structure*, *Phys. Rev. D* **98** (2018), no. 8 083517, [[arXiv:1803.08062](#)].
- [728] J. B. Jiménez, D. Bettoni, D. Figueruelo, and F. A. Teppa Pannia, *On cosmological signatures of baryons-dark energy elastic couplings*, *JCAP* **08** (2020) 020, [[arXiv:2004.14661](#)].
- [729] S. Vagnozzi, L. Visinelli, O. Mena, and D. F. Mota, *Do we have any hope of detecting scattering between dark energy and baryons through cosmology?*, *Mon. Not. Roy. Astron. Soc.* **493** (2020), no. 1 1139–1152, [[arXiv:1911.12374](#)].
- [730] F. Ferlito, S. Vagnozzi, D. F. Mota, and M. Baldi, *Cosmological direct detection of dark energy: non-linear structure formation signatures of dark energy scattering with visible matter*, [arXiv:2201.04528](#).
- [731] E. Ó Colgáin, M. H. P. M. van Putten, and H. Yavartanoo, *de Sitter Swampland, H_0 tension & observation*, *Phys. Lett. B* **793** (2019) 126–129, [[arXiv:1807.07451](#)].
- [732] E. O. Colgáin and H. Yavartanoo, *Testing the Swampland: H_0 tension*, *Phys. Lett. B* **797** (2019) 134907, [[arXiv:1905.02555](#)].

- [733] P. Agrawal, G. Obied, and C. Vafa, *H_0 tension, swampland conjectures, and the epoch of fading dark matter*, *Phys. Rev. D* **103** (2021), no. 4 043523, [[arXiv:1906.08261](#)].
- [734] E. Belgacem, Y. Dirian, S. Foffa, and M. Maggiore, *Nonlocal gravity. Conceptual aspects and cosmological predictions*, *JCAP* **1803** (2018), no. 03 002, [[arXiv:1712.07066](#)].
- [735] E. Belgacem, Y. Dirian, A. Finke, S. Foffa, and M. Maggiore, *Gravity in the infrared and effective nonlocal models*, *JCAP* **04** (2020) 010, [[arXiv:2001.07619](#)].
- [736] E. Di Valentino, R. Z. Ferreira, L. Visinelli, and U. Danielsson, *Late time transitions in the quintessence field and the H_0 tension*, *Phys. Dark Univ.* **26** (2019) 100385, [[arXiv:1906.11255](#)].
- [737] J. Renk, M. Zumalacárregui, F. Montanari, and A. Barreira, *Galileon gravity in light of ISW, CMB, BAO and H_0 data*, *JCAP* **1710** (2017), no. 10 020, [[arXiv:1707.02263](#)].
- [738] M. Zumalacárregui, *Gravity in the Era of Equality: Towards solutions to the Hubble problem without fine-tuned initial conditions*, *Phys. Rev. D* **102** (2020), no. 2 023523, [[arXiv:2003.06396](#)].
- [739] S. Peirone, G. Benevento, N. Frusciante, and S. Tsujikawa, *Cosmological data favor Galileon ghost condensate over Λ CDM*, *Phys. Rev. D* **100** (2019), no. 6 063540, [[arXiv:1905.05166](#)].
- [740] N. Frusciante, S. Peirone, L. Atayde, and A. De Felice, *Phenomenology of the generalized cubic covariant Galileon model and cosmological bounds*, *Phys. Rev. D* **101** (2020), no. 6 064001, [[arXiv:1912.07586](#)].
- [741] L. Heisenberg and H. Villarrubia-Rojo, *Proca in the sky*, *JCAP* **03** (2021) 032, [[arXiv:2010.00513](#)].
- [742] S. D. Odintsov, D. Sáez-Chillón Gómez, and G. S. Sharov, *Analyzing the H_0 tension in $F(R)$ gravity models*, *Nucl. Phys. B* **966** (2021) 115377, [[arXiv:2011.03957](#)].
- [743] R. D'Agostino and R. C. Nunes, *Measurements of H_0 in modified gravity theories: The role of lensed quasars in the late-time Universe*, *Phys. Rev. D* **101** (2020), no. 10 103505, [[arXiv:2002.06381](#)].
- [744] D. Wang, *Can $f(R)$ gravity relieve H_0 and σ_8 tensions?*, [[arXiv:2008.03966](#)].
- [745] N. M. Jiménez Cruz and C. Escamilla-Rivera, *Late-time and Big Bang Nucleosynthesis constraints for generic modified gravity surveys*, *Eur. Phys. J. Plus* **136** (2021), no. 1 51, [[arXiv:2011.09623](#)].
- [746] R. C. Nunes, *Structure formation in $f(T)$ gravity and a solution for H_0 tension*, *JCAP* **05** (2018) 052, [[arXiv:1802.02281](#)].
- [747] D. Wang and D. Mota, *Can $f(T)$ gravity resolve the H_0 tension?*, *Phys. Rev. D* **102** (2020), no. 6 063530, [[arXiv:2003.10095](#)].
- [748] X. Ren, T. H. T. Wong, Y.-F. Cai, and E. N. Saridakis, *Data-driven Reconstruction of the Late-time Cosmic Acceleration with $f(T)$ Gravity*, *Phys. Dark Univ.* **32** (2021) 100812, [[arXiv:2103.01260](#)].
- [749] Y.-F. Cai, M. Khurshudyan, and E. N. Saridakis, *Model-independent reconstruction of $f(T)$ gravity from Gaussian Processes*, *Astrophys. J.* **888** (2020) 62, [[arXiv:1907.10813](#)].
- [750] M. Hashim, W. El Hanafy, A. Golovnev, and A. El-Zant, *Toward a concordance teleparallel Cosmology I: Background Dynamics*, [[arXiv:2010.14964](#)].

- [751] D. Benisty, E. I. Guendelman, A. van de Venn, D. Vasak, J. Struckmeier, and H. Stoecker, *The dark side of the torsion: dark energy from propagating torsion*, *Eur. Phys. J. C* **82** (2022), no. 3 264, [[arXiv:2109.01052](#)].
- [752] S. Bahamonde, K. F. Dialektopoulos, M. Hohmann, J. L. Said, C. Pfeifer, and E. N. Saridakis, *No Strong Coupling in Non-Flat FLRW $f(T)$ cosmology*, [arXiv:2203.00619](#).
- [753] C. Escamilla-Rivera and J. Levi Said, *Cosmological viable models in $f(T, B)$ theory as solutions to the H_0 tension*, *Class. Quant. Grav.* **37** (2020), no. 16 165002, [[arXiv:1909.10328](#)].
- [754] S. Mandal, D. Wang, and P. K. Sahoo, *Cosmography in $f(Q)$ gravity*, *Phys. Rev. D* **102** (2020) 124029, [[arXiv:2011.00420](#)].
- [755] J. Solà Peracaula, A. Gomez-Valent, J. de Cruz Pérez, and C. Moreno-Pulido, *Brans–Dicke Gravity with a Cosmological Constant Smooths Out Λ CDM Tensions*, *Astrophys. J. Lett.* **886** (2019), no. 1 L6, [[arXiv:1909.02554](#)].
- [756] J. Solà Peracaula, A. Gómez-Valent, J. de Cruz Pérez, and C. Moreno-Pulido, *Brans–Dicke cosmology with a Λ -term: a possible solution to Λ CDM tensions*, *Class. Quant. Grav.* **37** (2020), no. 24 245003, [[arXiv:2006.04273](#)].
- [757] J. C. N. de Araujo, A. De Felice, S. Kumar, and R. C. Nunes, *Minimal theory of massive gravity in the light of CMB data and the S8 tension*, *Phys. Rev. D* **104** (2021), no. 10 104057, [[arXiv:2106.09595](#)].
- [758] P. D. Alvarez, B. Koch, C. Laporte, and A. Rincon, *Can scale-dependent cosmology alleviate the H_0 tension?*, [arXiv:2009.02311](#).
- [759] A. Perez, D. Sudarsky, and E. Wilson-Ewing, *Resolving the H_0 tension with diffusion*, *Gen. Rel. Grav.* **53** (2021), no. 1 7, [[arXiv:2001.07536](#)].
- [760] F. X. Linares Cedeño and U. Nucamendi, *Revisiting cosmological diffusion models in Unimodular Gravity and the H_0 tension*, *Phys. Dark Univ.* **32** (2021) 100807, [[arXiv:2009.10268](#)].
- [761] H. Desmond, B. Jain, and J. Sakstein, *Local resolution of the Hubble tension: The impact of screened fifth forces on the cosmic distance ladder*, *Phys. Rev.* **D100** (2019), no. 4 043537, [[arXiv:1907.03778](#)].
- [762] H. Desmond and J. Sakstein, *Screened fifth forces lower the TRGB-calibrated Hubble constant too*, *Phys. Rev. D* **102** (2020), no. 2 023007, [[arXiv:2003.12876](#)].
- [763] A. De Felice, S. Mukohyama, and M. C. Pookkillath, *Addressing H_0 tension by means of VCDM*, *Phys. Lett. B* **816** (2021) 136201, [[arXiv:2009.08718](#)].
- [764] D. Berechya and U. Leonhardt, *Lifshitz cosmology: quantum vacuum and Hubble tension*, *Mon. Not. Roy. Astron. Soc.* **507** (2021), no. 3 3473, [[arXiv:2008.04789](#)].
- [765] R. G. Vishwakarma, *Resolving Hubble tension with the Milne model*, *Int. J. Mod. Phys. D* **29** (2020), no. 14 2043025, [[arXiv:2011.12146](#)].
- [766] D. Wang and D. Mota, *4D Gauss–Bonnet gravity: Cosmological constraints, H_0 tension and large scale structure*, *Phys. Dark Univ.* **32** (2021) 100813, [[arXiv:2103.12358](#)].
- [767] W. Yang, S. Pan, S. Vagnozzi, E. Di Valentino, D. F. Mota, and S. Capozziello, *Dawn of the dark: unified dark sectors and the EDGES Cosmic Dawn 21-cm signal*, *JCAP* **1911** (2019) 044, [[arXiv:1907.05344](#)].

- [768] W. Yang, S. Pan, A. Paliathanasis, S. Ghosh, and Y. Wu, *Observational constraints of a new unified dark fluid and the H_0 tension*, *Mon. Not. Roy. Astron. Soc.* **490** (2019), no. 2 2071–2085, [[arXiv:1904.10436](#)].
- [769] V. G. Gurzadyan and A. Stepanian, *H_0 tension: clue to common nature of dark sector?*, *Eur. Phys. J. C* **79** (2019), no. 7 568, [[arXiv:1905.03442](#)].
- [770] V. G. Gurzadyan and A. Stepanian, *Hubble tension vs two flows*, *Eur. Phys. J. Plus* **136** (2021), no. 2 235, [[arXiv:2102.10100](#)].
- [771] M. Benetti, W. Miranda, H. A. Borges, C. Pigozzo, S. Carneiro, and J. S. Alcaniz, *Looking for interactions in the cosmological dark sector*, *JCAP* **12** (2019) 023, [[arXiv:1908.07213](#)].
- [772] M. Benetti, H. Borges, C. Pigozzo, S. Carneiro, and J. Alcaniz, *Dark sector interactions and the curvature of the Universe in light of Planck’s 2018 data*, [[arXiv:2102.10123](#)].
- [773] E. Elizalde, M. Khurshudyan, S. D. Odintsov, and R. Myrzakulov, *Analysis of the H_0 tension problem in the Universe with viscous dark fluid*, *Phys. Rev. D* **102** (2020), no. 12 123501, [[arXiv:2006.01879](#)].
- [774] W. J. C. da Silva and R. Silva, *Growth of matter perturbations in the extended viscous dark energy models*, *Eur. Phys. J. C* **81** (2021), no. 5 403, [[arXiv:2011.09516](#)].
- [775] W. Yang, S. Pan, E. Di Valentino, A. Paliathanasis, and J. Lu, *Challenging bulk viscous unified scenarios with cosmological observations*, *Phys. Rev. D* **100** (2019), no. 10 103518, [[arXiv:1906.04162](#)].
- [776] B. D. Normann and I. H. Brevik, *Can the Hubble tension be resolved by bulk viscosity?*, *Mod. Phys. Lett. A* **36** (2021), no. 27 2150198, [[arXiv:2107.13533](#)].
- [777] C. Ortiz, *Surface Tension: Accelerated Expansion, Coincidence Problem & Hubble Tension*, *Int. J. Mod. Phys. D* **29** (2020), no. 16 2050115, [[arXiv:2011.02317](#)].
- [778] R. C. Nunes, S. Vagnozzi, S. Kumar, E. Di Valentino, and O. Mena, *New tests of dark sector interactions from the full-shape galaxy power spectrum*, [[arXiv:2203.08093](#)].
- [779] M. S. Linton, R. Crittenden, and A. Pourtsidou, *Momentum transfer models of interacting dark energy*, [[arXiv:2107.03235](#)].
- [780] N. B. Hogg and M. Bruni, *Shan–Chen interacting vacuum cosmology*, [[arXiv:2109.08676](#)].
- [781] A. S. Mancini and A. Pourtsidou, *KiDS-1000 Cosmology: machine learning – accelerated constraints on Interacting Dark Energy with COSMOPOWER*, [[arXiv:2110.07587](#)].
- [782] M. K. Sharma and S. Sur, *Imprints of interacting dark energy on cosmological perturbations*, *Int. J. Mod. Phys. D* **31** (2022), no. 03 2250017, [[arXiv:2112.08477](#)].
- [783] P. Carrilho, C. Moretti, B. Bose, K. Markovič, and A. Pourtsidou, *Interacting dark energy from redshift-space galaxy clustering*, *JCAP* **10** (2021) 004, [[arXiv:2106.13163](#)].
- [784] P. Carrilho, K. Carrion, B. Bose, A. Pourtsidou, J. C. Hidalgo, L. Lombriser, and M. Baldi, *On the road to percent accuracy VI: the nonlinear power spectrum for interacting dark energy with baryonic feedback and massive neutrinos*, [[arXiv:2111.13598](#)].
- [785] L. Amendola, *Coupled quintessence*, *Phys. Rev. D* **62** (2000) 043511, [[astro-ph/9908023](#)].
- [786] P. Wang and X.-H. Meng, *Can vacuum decay in our universe?*, *Class. Quant. Grav.* **22** (2005) 283–294, [[astro-ph/0408495](#)].

- [787] V. Salvatelli, A. Marchini, L. Lopez-Honorez, and O. Mena, *New constraints on Coupled Dark Energy from the Planck satellite experiment*, *Phys. Rev. D* **88** (2013), no. 2 023531, [[arXiv:1304.7119](#)].
- [788] A. A. Costa, X.-D. Xu, B. Wang, E. G. M. Ferreira, and E. Abdalla, *Testing the Interaction between Dark Energy and Dark Matter with Planck Data*, *Phys. Rev. D* **89** (2014), no. 10 103531, [[arXiv:1311.7380](#)].
- [789] A. Pourtsidou, C. Skordis, and E. Copeland, *Models of dark matter coupled to dark energy*, *Phys. Rev. D* **88** (2013), no. 8 083505, [[arXiv:1307.0458](#)].
- [790] V. Pettorino, *Testing modified gravity with Planck: the case of coupled dark energy*, *Phys. Rev. D* **88** (2013) 063519, [[arXiv:1305.7457](#)].
- [791] V. Salvatelli, N. Said, M. Bruni, A. Melchiorri, and D. Wands, *Indications of a late-time interaction in the dark sector*, *Phys. Rev. Lett.* **113** (2014), no. 18 181301, [[arXiv:1406.7297](#)].
- [792] S. Kumar and R. C. Nunes, *Probing the interaction between dark matter and dark energy in the presence of massive neutrinos*, *Phys. Rev.* **D94** (2016), no. 12 123511, [[arXiv:1608.02454](#)].
- [793] D.-M. Xia and S. Wang, *Constraining interacting dark energy models with latest cosmological observations*, *Mon. Not. Roy. Astron. Soc.* **463** (2016), no. 1 952–956, [[arXiv:1608.04545](#)].
- [794] S. Kumar and R. C. Nunes, *Echo of interactions in the dark sector*, *Phys. Rev.* **D96** (2017), no. 10 103511, [[arXiv:1702.02143](#)].
- [795] C. Van De Bruck and J. Mifsud, *Searching for dark matter - dark energy interactions: going beyond the conformal case*, *Phys. Rev. D* **97** (2018), no. 2 023506, [[arXiv:1709.04882](#)].
- [796] W. Yang, S. Pan, and D. F. Mota, *Novel approach toward the large-scale stable interacting dark-energy models and their astronomical bounds*, *Phys. Rev. D* **96** (2017), no. 12 123508, [[arXiv:1709.00006](#)].
- [797] W. Yang, S. Pan, L. Xu, and D. F. Mota, *Effects of anisotropic stress in interacting dark matter – dark energy scenarios*, *Mon. Not. Roy. Astron. Soc.* **482** (2019), no. 2 1858–1871, [[arXiv:1804.08455](#)].
- [798] W. Yang, S. Pan, R. Herrera, and S. Chakraborty, *Large-scale (in) stability analysis of an exactly solved coupled dark-energy model*, *Phys. Rev. D* **98** (2018), no. 4 043517, [[arXiv:1808.01669](#)].
- [799] W. Yang, A. Mukherjee, E. Di Valentino, and S. Pan, *Interacting dark energy with time varying equation of state and the H_0 tension*, *Phys. Rev.* **D98** (2018), no. 12 123527, [[arXiv:1809.06883](#)].
- [800] W. Yang, S. Pan, E. Di Valentino, R. C. Nunes, S. Vagnozzi, and D. F. Mota, *Tale of stable interacting dark energy, observational signatures, and the H_0 tension*, *JCAP* **1809** (2018), no. 09 019, [[arXiv:1805.08252](#)].
- [801] H.-L. Li, L. Feng, J.-F. Zhang, and X. Zhang, *Models of vacuum energy interacting with cold dark matter: Constraints and comparison*, *Sci. China Phys. Mech. Astron.* **62** (2019), no. 12 120411, [[arXiv:1812.00319](#)].
- [802] R. An, A. A. Costa, L. Xiao, J. Zhang, and B. Wang, *Testing a quintessence model with Yukawa interaction from cosmological observations and N -body simulations*, *Mon. Not. Roy. Astron. Soc.* **489** (2019), no. 1 297–309, [[arXiv:1809.03224](#)].
- [803] J. E. Gonzalez, H. H. B. Silva, R. Silva, and J. S. Alcaniz, *Physical constraints on interacting dark energy models*, *Eur. Phys. J. C* **78** (2018), no. 9 730, [[arXiv:1809.00439](#)].

- [804] S. Kumar, R. C. Nunes, and S. K. Yadav, *Dark sector interaction: a remedy of the tensions between CMB and LSS data*, *Eur. Phys. J.* **C79** (2019), no. 7 576, [[arXiv:1903.04865](#)].
- [805] S. Pan, W. Yang, C. Singha, and E. N. Saridakis, *Observational constraints on sign-changeable interaction models and alleviation of the H_0 tension*, *Phys. Rev.* **D100** (2019), no. 8 083539, [[arXiv:1903.10969](#)].
- [806] W. Yang, O. Mena, S. Pan, and E. Di Valentino, *Dark sectors with dynamical coupling*, *Phys. Rev.* **D100** (2019), no. 8 083509, [[arXiv:1906.11697](#)].
- [807] A. Gómez-Valent, V. Pettorino, and L. Amendola, *Update on coupled dark energy and the H_0 tension*, *Phys. Rev. D* **101** (2020), no. 12 123513, [[arXiv:2004.00610](#)].
- [808] M. Aljaf, D. Gregoris, and M. Khurshudyan, *Constraints on interacting dark energy models through cosmic chronometers and Gaussian process*, [arXiv:2005.01891](#).
- [809] E. Di Valentino, A. Melchiorri, O. Mena, and S. Vagnozzi, *Interacting dark energy in the early 2020s: A promising solution to the H_0 and cosmic shear tensions*, *Phys. Dark Univ.* **30** (2020) 100666, [[arXiv:1908.04281](#)].
- [810] M. Martinelli, N. B. Hogg, S. Peirone, M. Bruni, and D. Wands, *Constraints on the interacting vacuum-geodesic CDM scenario*, *Mon. Not. Roy. Astron. Soc.* **488** (2019), no. 3 3423–3438, [[arXiv:1902.10694](#)].
- [811] E. Di Valentino, A. Melchiorri, O. Mena, S. Pan, and W. Yang, *Interacting Dark Energy in a closed universe*, *Mon. Not. Roy. Astron. Soc.* **502** (2021), no. 1 L23–L28, [[arXiv:2011.00283](#)].
- [812] Y.-H. Yao and X.-H. Meng, *A new coupled three-form dark energy model and implications for the H_0 tension*, *Phys. Dark Univ.* **30** (2020) 100729.
- [813] Y. Yao and X. Meng, *Relieve the H_0 tension with a new coupled generalized three-form dark energy model*, [arXiv:2011.09160](#).
- [814] M. Lucca and D. C. Hooper, *Shedding light on dark matter-dark energy interactions*, *Phys. Rev. D* **102** (2020), no. 12 123502, [[arXiv:2002.06127](#)].
- [815] W. Yang, E. Di Valentino, O. Mena, S. Pan, and R. C. Nunes, *All-inclusive interacting dark sector cosmologies*, *Phys. Rev. D* **101** (2020), no. 8 083509, [[arXiv:2001.10852](#)].
- [816] W. Yang, E. Di Valentino, O. Mena, and S. Pan, *Dynamical Dark sectors and Neutrino masses and abundances*, *Phys. Rev. D* **102** (2020), no. 2 023535, [[arXiv:2003.12552](#)].
- [817] H. Amirhashchi and A. K. Yadav, *Interacting Dark Sectors in Anisotropic Universe: Observational Constraints and H_0 Tension*, [arXiv:2001.03775](#).
- [818] J. P. Johnson, A. Sangwan, and S. Shankaranarayanan, *Cosmological perturbations in the interacting dark sector: Observational constraints and predictions*, [arXiv:2102.12367](#).
- [819] S. Pan, W. Yang, E. Di Valentino, E. N. Saridakis, and S. Chakraborty, *Interacting scenarios with dynamical dark energy: Observational constraints and alleviation of the H_0 tension*, *Phys. Rev.* **D100** (2019), no. 10 103520, [[arXiv:1907.07540](#)].
- [820] B. Wang, E. Abdalla, F. Atrio-Barandela, and D. Pavon, *Dark Matter and Dark Energy Interactions: Theoretical Challenges, Cosmological Implications and Observational Signatures*, *Rept. Prog. Phys.* **79** (2016), no. 9 096901, [[arXiv:1603.08299](#)].
- [821] Y. L. Bolotin, A. Kostenko, O. A. Lemets, and D. A. Yerokhin, *Cosmological Evolution With Interaction Between Dark Energy And Dark Matter*, *Int. J. Mod. Phys. D* **24** (2014), no. 03 1530007, [[arXiv:1310.0085](#)].

- [822] D. Comelli, M. Pietroni, and A. Riotto, *Dark energy and dark matter*, *Phys. Lett. B* **571** (2003) 115–120, [[hep-ph/0302080](#)].
- [823] G. Huey and B. D. Wandelt, *Interacting quintessence. The Coincidence problem and cosmic acceleration*, *Phys. Rev. D* **74** (2006) 023519, [[astro-ph/0407196](#)].
- [824] R.-G. Cai and A. Wang, *Cosmology with interaction between phantom dark energy and dark matter and the coincidence problem*, *JCAP* **03** (2005) 002, [[hep-th/0411025](#)].
- [825] D. Pavon and W. Zimdahl, *Holographic dark energy and cosmic coincidence*, *Phys. Lett. B* **628** (2005) 206–210, [[gr-qc/0505020](#)].
- [826] X. Zhang, *Coupled quintessence in a power-law case and the cosmic coincidence problem*, *Mod. Phys. Lett. A* **20** (2005) 2575, [[astro-ph/0503072](#)].
- [827] S. del Campo, R. Herrera, G. Olivares, and D. Pavon, *Interacting models of soft coincidence*, *Phys. Rev. D* **74** (2006) 023501, [[astro-ph/0606520](#)].
- [828] M. S. Berger and H. Shojaei, *Interacting dark energy and the cosmic coincidence problem*, *Phys. Rev. D* **73** (2006) 083528, [[gr-qc/0601086](#)].
- [829] S. del Campo, R. Herrera, and D. Pavon, *Interacting models may be key to solve the cosmic coincidence problem*, *JCAP* **01** (2009) 020, [[arXiv:0812.2210](#)].
- [830] J.-H. He and B. Wang, *Effects of the interaction between dark energy and dark matter on cosmological parameters*, *JCAP* **06** (2008) 010, [[arXiv:0801.4233](#)].
- [831] E. Di Valentino, A. Melchiorri, O. Mena, and S. Vagnozzi, *Nonminimal dark sector physics and cosmological tensions*, *Phys. Rev. D* **101** (2020), no. 6 063502, [[arXiv:1910.09853](#)].
- [832] L.-F. Wang, D.-Z. He, J.-F. Zhang, and X. Zhang, *Constraints on interacting dark energy model from lensed quasars: Relieving the H_0 tension from 5.3σ to 1.7σ* , [[arXiv:2102.09331](#)].
- [833] S. Gariazzo, E. Di Valentino, O. Mena, and R. C. Nunes, *Robustness of non-standard cosmologies solving the Hubble constant tension*, [[arXiv:2111.03152](#)].
- [834] R. C. Nunes and E. Di Valentino, *Dark sector interaction and the supernova absolute magnitude tension*, *Phys. Rev. D* **104** (2021), no. 6 063529, [[arXiv:2107.09151](#)].
- [835] R.-Y. Guo, L. Feng, T.-Y. Yao, and X.-Y. Chen, *Exploration of interacting dynamical dark energy model with interaction term including the equation-of-state parameter: alleviation of the H_0 tension*, *JCAP* **12** (2021), no. 12 036, [[arXiv:2110.02536](#)].
- [836] S. Pan, W. Yang, and A. Paliathanasis, *Nonlinear interacting cosmological models after Planck 2018 legacy release and the H_0 tension*, [[arXiv:2002.03408](#)].
- [837] A. Pourtsidou and T. Tram, *Reconciling CMB and structure growth measurements with dark energy interactions*, *Phys. Rev.* **D94** (2016), no. 4 043518, [[arXiv:1604.04222](#)].
- [838] R. An, C. Feng, and B. Wang, *Relieving the Tension between Weak Lensing and Cosmic Microwave Background with Interacting Dark Matter and Dark Energy Models*, *JCAP* **02** (2018) 038, [[arXiv:1711.06799](#)].
- [839] B. J. Barros, L. Amendola, T. Barreiro, and N. J. Nunes, *Coupled quintessence with a Λ CDM background: removing the σ_8 tension*, *JCAP* **1901** (2019), no. 01 007, [[arXiv:1802.09216](#)].
- [840] S. Camera, M. Martinelli, and D. Bertacca, *Does quartessence ease cosmic tensions?*, *Phys. Dark Univ.* **23** (2019) 100247, [[arXiv:1704.06277](#)].

- [841] M. Gavela, D. Hernandez, L. Lopez Honorez, O. Mena, and S. Rigolin, *Dark coupling*, *JCAP* **07** (2009) 034, [[arXiv:0901.1611](#)]. [Erratum: *JCAP* 05, E01 (2010)].
- [842] S. Pan, G. S. Sharov, and W. Yang, *Field theoretic interpretations of interacting dark energy scenarios and recent observations*, *Phys. Rev. D* **101** (2020), no. 10 103533, [[arXiv:2001.03120](#)].
- [843] J.-H. He, B. Wang, and E. Abdalla, *Stability of the curvature perturbation in dark sectors' mutual interacting models*, *Phys. Lett. B* **671** (2009) 139–145, [[arXiv:0807.3471](#)].
- [844] K. Ichiki, M. Oguri, and K. Takahashi, *WMAP constraints on decaying cold dark matter*, *Phys. Rev. Lett.* **93** (2004) 071302, [[astro-ph/0403164](#)].
- [845] **DES** Collaboration, A. Chen et al., *Constraints on dark matter to dark radiation conversion in the late universe with DES-Y1 and external data*, [arXiv:2011.04606](#).
- [846] A. Chudaykin, D. Gorbunov, and I. Tkachev, *Dark matter component decaying after recombination: Sensitivity to baryon acoustic oscillation and redshift space distortion probes*, *Phys. Rev. D* **97** (2018), no. 8 083508, [[arXiv:1711.06738](#)].
- [847] O. E. Bjaelde, S. Das, and A. Moss, *Origin of ΔN_{eff} as a Result of an Interaction between Dark Radiation and Dark Matter*, *JCAP* **10** (2012) 017, [[arXiv:1205.0553](#)].
- [848] M.-Y. Wang, A. H. G. Peter, L. E. Strigari, A. R. Zentner, B. Arant, S. Garrison-Kimmel, and M. Rocha, *Cosmological simulations of decaying dark matter: implications for small-scale structure of dark matter haloes*, *Mon. Not. Roy. Astron. Soc.* **445** (2014), no. 1 614–629, [[arXiv:1406.0527](#)].
- [849] L. A. Anchordoqui, V. Barger, H. Goldberg, X. Huang, D. Marfatia, L. H. M. da Silva, and T. J. Weiler, *IceCube neutrinos, decaying dark matter, and the Hubble constant*, *Phys. Rev. D* **92** (2015), no. 6 061301, [[arXiv:1506.08788](#)]. [Erratum: *Phys.Rev.D* 94, 069901 (2016)].
- [850] L. Xiao, L. Zhang, R. An, C. Feng, and B. Wang, *Fractional Dark Matter decay: cosmological imprints and observational constraints*, *JCAP* **01** (2020) 045, [[arXiv:1908.02668](#)].
- [851] G. Choi, M. Suzuki, and T. T. Yanagida, *Quintessence Axion Dark Energy and a Solution to the Hubble Tension*, *Phys. Lett. B* **805** (2020) 135408, [[arXiv:1910.00459](#)].
- [852] G. Choi, M. Suzuki, and T. T. Yanagida, *Degenerate Sub-keV Fermion Dark Matter from a Solution to the Hubble Tension*, *Phys. Rev. D* **101** (2020), no. 7 075031, [[arXiv:2002.00036](#)].
- [853] A. Nygaard, T. Tram, and S. Hannestad, *Updated constraints on decaying cold dark matter*, *JCAP* **05** (2021) 017, [[arXiv:2011.01632](#)].
- [854] K. Enqvist, S. Nadathur, T. Sekiguchi, and T. Takahashi, *Decaying dark matter and the tension in σ_8* , *JCAP* **1509** (2015) 067, [[arXiv:1505.05511](#)].
- [855] G. F. Abellan, R. Murgia, V. Poulin, and J. Laval, *Hints for decaying dark matter from S_8 measurements*, [arXiv:2008.09615](#).
- [856] K. L. Pandey, T. Karwal, and S. Das, *Alleviating the H_0 and σ_8 anomalies with a decaying dark matter model*, *JCAP* **07** (2020) 026, [[arXiv:1902.10636](#)].
- [857] V. Poulin, P. D. Serpico, and J. Lesgourgues, *A fresh look at linear cosmological constraints on a decaying dark matter component*, *JCAP* **1608** (2016) 036, [[arXiv:1606.02073](#)].
- [858] A. Chudaykin, D. Gorbunov, and I. Tkachev, *Dark matter component decaying after recombination: Lensing constraints with Planck data*, *Phys. Rev. D* **94** (2016) 023528, [[arXiv:1602.08121](#)].

- [859] T. Bringmann, F. Kahlhoefer, K. Schmidt-Hoberg, and P. Walia, *Converting nonrelativistic dark matter to radiation*, *Phys. Rev. D* **98** (2018), no. 2 023543, [[arXiv:1803.03644](#)].
- [860] J. Lesgourgues, G. Marques-Tavares, and M. Schmaltz, *Evidence for dark matter interactions in cosmological precision data?*, *JCAP* **02** (2016) 037, [[arXiv:1507.04351](#)].
- [861] S. Ando and K. Ishiwata, *Constraints on decaying dark matter from the extragalactic gamma-ray background*, *JCAP* **05** (2015) 024, [[arXiv:1502.02007](#)].
- [862] **Planck** Collaboration, P. A. R. Ade et al., *Planck 2015 results. XIV. Dark energy and modified gravity*, *Astron. Astrophys.* **594** (2016) A14, [[arXiv:1502.01590](#)].
- [863] L. A. Anchordoqui, *Decaying dark matter, the H_0 tension, and the lithium problem*, *Phys. Rev. D* **103** (2021), no. 3 035025, [[arXiv:2010.09715](#)].
- [864] L. A. Anchordoqui, V. Barger, D. Marfatia, and J. F. Soriano, *Decay of multiple dark matter particles to dark radiation in different epochs does not alleviate the Hubble tension*, [arXiv:2203.04818](#).
- [865] J. Alcaniz, N. Bernal, A. Masiero, and F. S. Queiroz, *Light dark matter: A common solution to the lithium and H_0 problems*, *Phys. Lett. B* **812** (2021) 136008, [[arXiv:1912.05563](#)].
- [866] A. Desai, K. R. Dienes, and B. Thomas, *Constraining Dark-Matter Ensembles with Supernova Data*, *Phys. Rev. D* **101** (2020), no. 3 035031, [[arXiv:1909.07981](#)].
- [867] G. Blackadder and S. M. Koushiappas, *Dark matter with two- and many-body decays and supernovae type Ia*, *Phys. Rev.* **D90** (2014), no. 10 103527, [[arXiv:1410.0683](#)].
- [868] N. Blinov, C. Keith, and D. Hooper, *Warm Decaying Dark Matter and the Hubble Tension*, *JCAP* **06** (2020) 005, [[arXiv:2004.06114](#)].
- [869] K. Vattis, S. M. Koushiappas, and A. Loeb, *Dark matter decaying in the late Universe can relieve the H_0 tension*, *Phys. Rev.* **D99** (2019), no. 12 121302, [[arXiv:1903.06220](#)].
- [870] S. J. Clark, K. Vattis, and S. M. Koushiappas, *CMB constraints on late-universe decaying dark matter as a solution to the H_0 tension*, [arXiv:2006.03678](#).
- [871] B. S. Haridasu and M. Viel, *Late-time decaying dark matter: constraints and implications for the H_0 -tension*, *Mon. Not. Roy. Astron. Soc.* **497** (2020), no. 2 1757–1764, [[arXiv:2004.07709](#)].
- [872] G. F. Abellán, R. Murgia, and V. Poulin, *Linear cosmological constraints on 2-body decaying dark matter scenarios and robustness of the resolution to the S_8 tension*, [arXiv:2102.12498](#).
- [873] T. Binder, M. Gustafsson, A. Kamada, S. M. R. Sandner, and M. Wiesner, *Reannihilation of self-interacting dark matter*, *Phys. Rev.* **D97** (2018), no. 12 123004, [[arXiv:1712.01246](#)].
- [874] A. Hryczuk and K. Jodłowski, *Self-interacting dark matter from late decays and the H_0 tension*, *Phys. Rev. D* **102** (2020), no. 4 043024, [[arXiv:2006.16139](#)].
- [875] J. Jaeckel and W. Yin, *Boosted Neutrinos and Relativistic Dark Particles as Messengers from Reheating*, *JCAP* **02** (2021) 044, [[arXiv:2007.15006](#)].
- [876] J. Jaeckel and W. Yin, *Using the spectrum of dark radiation as a probe of reheating*, *Phys. Rev. D* **103** (2021), no. 11 115019, [[arXiv:2102.00006](#)].
- [877] K. R. Dienes, F. Huang, J. Kost, B. Thomas, and H.-B. Yu, *Evaluating Lyman- α Constraints for General Dark-Matter Velocity Distributions: Multiple Scales and Cautionary Tales*, [arXiv:2112.09105](#).

- [878] M. Kasai and T. Futamase, *A possible solution to the Hubble constant discrepancy – Cosmology where the local volume expansion is driven by the domain average density*, *PTEP* **2019** (2019), no. 7 073E01, [[arXiv:1904.09689](#)].
- [879] R.-G. Cai, Z.-K. Guo, L. Li, S.-J. Wang, and W.-W. Yu, *Chameleon dark energy can resolve the Hubble tension*, [arXiv:2102.02020](#).
- [880] H.-Y. Wu and D. Huterer, *Sample variance in the local measurements of the Hubble constant*, *Mon. Not. Roy. Astron. Soc.* **471** (2017), no. 4 4946–4955, [[arXiv:1706.09723](#)].
- [881] J. B. Jiménez, D. Bettoni, and P. Brax, *Charged dark matter and the H_0 tension*, *Phys. Rev. D* **103** (2021), no. 10 103505, [[arXiv:2004.13677](#)].
- [882] J. Beltran Jimenez, D. Bettoni, and P. Brax, *Screening away the H_0 tension*, *Int. J. Mod. Phys. D* **29** (2020), no. 14 2043010, [[arXiv:2007.11029](#)].
- [883] J. Beltran Jimenez, D. Bettoni, and P. Brax, *Inhomogeneous Hubble diagram from vector K -mouflage*, *Class. Quant. Grav.* **38** (2021), no. 13 134001, [[arXiv:2103.03627](#)].
- [884] Ö. Akarsu, S. Kumar, S. Sharma, and L. Tedesco, *Constraints on a Bianchi type I spacetime extension of the standard Λ CDM model*, *Phys. Rev. D* **100** (2019), no. 2 023532, [[arXiv:1905.06949](#)].
- [885] A. Heinesen and T. Buchert, *Solving the curvature and Hubble parameter inconsistencies through structure formation-induced curvature*, *Class. Quant. Grav.* **37** (2020), no. 16 164001, [[arXiv:2002.10831](#)]. [Erratum: *Class.Quant.Grav.* 37, 229601 (2020)].
- [886] K. Bolejko, *Emerging spatial curvature can resolve the tension between high-redshift CMB and low-redshift distance ladder measurements of the Hubble constant*, *Phys. Rev. D* **97** (2018), no. 10 103529, [[arXiv:1712.02967](#)].
- [887] J. Khoury and A. Weltman, *Chameleon fields: Awaiting surprises for tests of gravity in space*, *Phys. Rev. Lett.* **93** (2004) 171104, [[astro-ph/0309300](#)].
- [888] J. Khoury and A. Weltman, *Chameleon cosmology*, *Phys. Rev. D* **69** (2004) 044026, [[astro-ph/0309411](#)].
- [889] P. Brax, C. van de Bruck, A.-C. Davis, D. F. Mota, and D. J. Shaw, *Detecting chameleons through Casimir force measurements*, *Phys. Rev. D* **76** (2007) 124034, [[arXiv:0709.2075](#)].
- [890] N. Banerjee, S. Das, and K. Ganguly, *Chameleon field and the late time acceleration of the universe*, *Pramana* **74** (2010) L481–L489, [[arXiv:0801.1204](#)].
- [891] S. Das and N. Banerjee, *Brans-Dicke Scalar Field as a Chameleon*, *Phys. Rev. D* **78** (2008) 043512, [[arXiv:0803.3936](#)].
- [892] P. Brax, C. van de Bruck, D. F. Mota, N. J. Nunes, and H. A. Winther, *Chameleons with Field Dependent Couplings*, *Phys. Rev. D* **82** (2010) 083503, [[arXiv:1006.2796](#)].
- [893] J. Wang, L. Hui, and J. Khoury, *No-Go Theorems for Generalized Chameleon Field Theories*, *Phys. Rev. Lett.* **109** (2012) 241301, [[arXiv:1208.4612](#)].
- [894] A. Upadhye, W. Hu, and J. Khoury, *Quantum Stability of Chameleon Field Theories*, *Phys. Rev. Lett.* **109** (2012) 041301, [[arXiv:1204.3906](#)].
- [895] J. Khoury, *Chameleon Field Theories*, *Class. Quant. Grav.* **30** (2013) 214004, [[arXiv:1306.4326](#)].

- [896] S. Vagnozzi, L. Visinelli, P. Brax, A.-C. Davis, and J. Sakstein, *Direct detection of dark energy: The XENON1T excess and future prospects*, *Phys. Rev. D* **104** (2021), no. 6 063023, [[arXiv:2103.15834](#)].
- [897] D. Benisty and A.-C. Davis, *Dark energy interactions near the Galactic Center*, *Phys. Rev. D* **105** (2022), no. 2 024052, [[arXiv:2108.06286](#)].
- [898] L. Lombriser, *Consistency of the local Hubble constant with the cosmic microwave background*, *Phys. Lett. B* **803** (2020) 135303, [[arXiv:1906.12347](#)].
- [899] W. D. Kenworthy, D. Scolnic, and A. Riess, *The Local Perspective on the Hubble Tension: Local Structure Does Not Impact Measurement of the Hubble Constant*, *Astrophys. J.* **875** (2019), no. 2 145, [[arXiv:1901.08681](#)].
- [900] M. Haslbauer, I. Banik, and P. Kroupa, *The KBC void and Hubble tension contradict Λ CDM on a Gpc scale – Milgromian dynamics as a possible solution*, *Mon. Not. Roy. Astron. Soc.* **499** (2020), no. 2 2845–2883, [[arXiv:2009.11292](#)].
- [901] M. Milgrom, *A Modification of the Newtonian dynamics: Implications for galaxies*, *Astrophys. J.* **270** (1983) 371–383.
- [902] S. Dodelson and L. M. Widrow, *Sterile-neutrinos as dark matter*, *Phys. Rev. Lett.* **72** (1994) 17–20, [[hep-ph/9303287](#)].
- [903] A. Boyarsky, O. Ruchayskiy, and M. Shaposhnikov, *The Role of sterile neutrinos in cosmology and astrophysics*, *Ann. Rev. Nucl. Part. Sci.* **59** (2009) 191–214, [[arXiv:0901.0011](#)].
- [904] A. Kusenko, *Sterile neutrinos: The Dark side of the light fermions*, *Phys. Rept.* **481** (2009) 1–28, [[arXiv:0906.2968](#)].
- [905] K. N. Abazajian et al., *Light Sterile Neutrinos: A White Paper*, [arXiv:1204.5379](#).
- [906] M. Drewes, *The Phenomenology of Right Handed Neutrinos*, *Int. J. Mod. Phys. E* **22** (2013) 1330019, [[arXiv:1303.6912](#)].
- [907] R. C. Keenan, A. J. Barger, and L. L. Cowie, *Evidence for a ~ 300 Megaparsec Scale Under-density in the Local Galaxy Distribution*, *Astrophys. J.* **775** (2013) 62, [[arXiv:1304.2884](#)].
- [908] **Planck** Collaboration, N. Aghanim et al., *Planck 2018 results. I. Overview and the cosmological legacy of Planck*, *Astron. Astrophys.* **641** (2020) A1, [[arXiv:1807.06205](#)].
- [909] E. Gaztanaga, *The size of our causal Universe*, *Mon. Not. Roy. Astron. Soc.* **494** (2020), no. 2 2766–2772, [[arXiv:2003.11544](#)].
- [910] E. Gaztanaga, *The Cosmological Constant as a Zero Action Boundary*, *Mon. Not. Roy. Astron. Soc.* **502** (2021), no. 1 436–444, [[arXiv:2101.07368](#)].
- [911] E. d. Gaztanaga, “The Black Hole Universe (BHU) from a FLRW cloud.” submitted to MNRAS, see darkcosmos.com, Dec., 2021.
- [912] E. Gaztanaga, *The Cosmological Constant as Event Horizon*, *Symmetry* **14** (2022), no. 2 300, [[arXiv:2202.00641](#)].
- [913] E. Garcia-Berro, E. Gaztanaga, J. Isern, O. Benvenuto, and L. Althaus, *On the evolution of cosmological type Ia supernovae and the gravitational constant*, [astro-ph/9907440](#).
- [914] E. Gaztanaga, E. Garcia-Berro, J. Isern, E. Bravo, and I. Dominguez, *Bounds on the possible evolution of the gravitational constant from cosmological type Ia supernovae*, *Phys. Rev.* **D65** (2002) 023506, [[astro-ph/0109299](#)].

- [915] B. S. Wright and B. Li, *Type Ia supernovae, standardizable candles, and gravity*, *Phys. Rev. D* **97** (2018), no. 8 083505, [[arXiv:1710.07018](#)].
- [916] **DES** Collaboration, T. M. C. Abbott et al., *Dark Energy Survey Year 1 Results: Measurement of the Baryon Acoustic Oscillation scale in the distribution of galaxies to redshift 1*, Submitted to: *Mon. Not. Roy. Astron. Soc.* (2017) [[arXiv:1712.06209](#)].
- [917] A. I. Vainshtein, *To the problem of nonvanishing gravitation mass*, *Phys. Lett. B* **39** (1972) 393–394.
- [918] N. Arkani-Hamed, H. Georgi, and M. D. Schwartz, *Effective field theory for massive gravitons and gravity in theory space*, *Annals Phys.* **305** (2003) 96–118, [[hep-th/0210184](#)].
- [919] C. Deffayet, G. R. Dvali, G. Gabadadze, and A. I. Vainshtein, *Nonperturbative continuity in graviton mass versus perturbative discontinuity*, *Phys. Rev. D* **65** (2002) 044026, [[hep-th/0106001](#)].
- [920] S. S. Gubser and J. Khoury, *Scalar self-interactions loosen constraints from fifth force searches*, *Phys. Rev. D* **70** (2004) 104001, [[hep-ph/0405231](#)].
- [921] P. Brax, C. van de Bruck, A.-C. Davis, J. Khoury, and A. Weltman, *Detecting dark energy in orbit: The cosmological chameleon*, *Phys. Rev. D* **70** (2004) 123518, [[astro-ph/0408415](#)].
- [922] P. Brax, C. van de Bruck, A. C. Davis, J. Khoury, and A. Weltman, *Chameleon dark energy*, *AIP Conf. Proc.* **736** (2004), no. 1 105–110, [[astro-ph/0410103](#)].
- [923] A. Upadhye, S. S. Gubser, and J. Khoury, *Unveiling chameleons in tests of gravitational inverse-square law*, *Phys. Rev. D* **74** (2006) 104024, [[hep-ph/0608186](#)].
- [924] D. F. Mota and D. J. Shaw, *Strongly coupled chameleon fields: New horizons in scalar field theory*, *Phys. Rev. Lett.* **97** (2006) 151102, [[hep-ph/0606204](#)].
- [925] D. F. Mota and D. J. Shaw, *Evading Equivalence Principle Violations, Cosmological and other Experimental Constraints in Scalar Field Theories with a Strong Coupling to Matter*, *Phys. Rev. D* **75** (2007) 063501, [[hep-ph/0608078](#)].
- [926] P. Brax, C. van de Bruck, A.-C. Davis, and D. J. Shaw, *$f(R)$ Gravity and Chameleon Theories*, *Phys. Rev. D* **78** (2008) 104021, [[arXiv:0806.3415](#)].
- [927] J. Khoury, *Theories of Dark Energy with Screening Mechanisms*, [[arXiv:1011.5909](#)].
- [928] C. Burrage and J. Sakstein, *Tests of Chameleon Gravity*, *Living Rev. Rel.* **21** (2018), no. 1 1, [[arXiv:1709.09071](#)].
- [929] J. Sakstein, *Stellar Oscillations in Modified Gravity*, *Phys. Rev. D* **88** (2013), no. 12 124013, [[arXiv:1309.0495](#)].
- [930] P. Brax, A.-C. Davis, B. Li, and H. A. Winther, *A Unified Description of Screened Modified Gravity*, *Phys. Rev. D* **86** (2012) 044015, [[arXiv:1203.4812](#)].
- [931] B. Jain and J. Khoury, *Cosmological Tests of Gravity*, *Annals Phys.* **325** (2010) 1479–1516, [[arXiv:1004.3294](#)].
- [932] A.-C. Davis, E. A. Lim, J. Sakstein, and D. Shaw, *Modified Gravity Makes Galaxies Brighter*, *Phys. Rev. D* **85** (2012) 123006, [[arXiv:1102.5278](#)].
- [933] L. Hui, A. Nicolis, and C. Stubbs, *Equivalence Principle Implications of Modified Gravity Models*, *Phys. Rev. D* **80** (2009) 104002, [[arXiv:0905.2966](#)].

- [934] C. Burrage and J. Sakstein, *A Compendium of Chameleon Constraints*, *JCAP* **11** (2016) 045, [[arXiv:1609.01192](#)].
- [935] A. Joyce, B. Jain, J. Khoury, and M. Trodden, *Beyond the Cosmological Standard Model*, *Phys. Rept.* **568** (2015) 1–98, [[arXiv:1407.0059](#)].
- [936] P. Brax, S. Casas, H. Desmond, and B. Elder, *Testing Screened Modified Gravity*, *Universe* **8** (2021), no. 1 11, [[arXiv:2201.10817](#)].
- [937] T. Baker et al., *Novel Probes Project: Tests of gravity on astrophysical scales*, *Rev. Mod. Phys.* **93** (2021), no. 1 015003, [[arXiv:1908.03430](#)].
- [938] J. Sakstein, *Astrophysical tests of screened modified gravity*, *Int. J. Mod. Phys. D* **27** (2018), no. 15 1848008, [[arXiv:2002.04194](#)].
- [939] C. Renevey, R. McManus, C. Dalang, and L. Lombriser, *The effect of screening mechanisms on black hole binary inspiral waveforms*, [arXiv:2106.05678](#).
- [940] K. Hinterbichler and J. Khoury, *Symmetron Fields: Screening Long-Range Forces Through Local Symmetry Restoration*, *Phys. Rev. Lett.* **104** (2010) 231301, [[arXiv:1001.4525](#)].
- [941] K. Hinterbichler, J. Khoury, A. Levy, and A. Matas, *Symmetron Cosmology*, *Phys. Rev. D* **84** (2011) 103521, [[arXiv:1107.2112](#)].
- [942] S. D. Odintsov and V. K. Oikonomou, *Did the Universe Experienced a Pressure non-Crushing Type Cosmological Singularity in the Recent Past?*, [arXiv:2201.07647](#).
- [943] E. Mortsell, A. Goobar, J. Johansson, and S. Dhawan, *The Hubble Tension Revisited: Additional Local Distance Ladder Uncertainties*, [arXiv:2106.09400](#).
- [944] L. Perivolaropoulos, *Is the Hubble crisis connected with the extinction of dinosaurs?*, [arXiv:2201.08997](#).
- [945] E. M. Shoemaker, *Impact Cratering Through Geologic Time*, *J. R. Astron. Soc. Can.* **92** (Dec., 1998) 297.
- [946] T. Gehrels, *Hazards Due to Comets and Asteroids*. 1995.
- [947] A. S. McEwen, J. M. Moore, and E. M. Shoemaker, *The Phanerozoic impact cratering rate: Evidence from the farside of the Moon*, *Journal of Geophysical Research: planets* **102** (Jan., 1997) 9231–9242.
- [948] J. A. Grier, A. S. McEwen, P. G. Lucey, M. Milazzo, and R. G. Strom, *Optical maturity of ejecta from large rayed lunar craters*, *Journal of Geophysical Research: planets* **106** (Dec., 2001) 32847–32862.
- [949] S. N. Ward and S. Day, *Terrestrial crater counts : Evidence of a two to four-fold increase in bolide flux at 125 ma*, 2007.
- [950] S. Mazrouei, R. R. Ghent, W. F. Bottke, A. H. Parker, and T. M. Gernon, *Response to Comment on “Earth and Moon impact flux increased at the end of the Paleozoic”*, *Science* **365** (July, 2019) aaw9895.
- [951] W. F. Bottke, D. Vokrouhlický, and D. Nesvorný, *An asteroid breakup 160Myr ago as the probable source of the K/T impactor*, *Nature* **449** (2007) 48–53.
- [952] G. Alestas, L. Perivolaropoulos, and K. Tanidis, *Constraining a late time transition of G_{eff} using low- z galaxy survey data*, [arXiv:2201.05846](#).

- [953] L. Perivolaropoulos, “The tensions of the Λ CDM and a gravitational transition.”
<https://www.youtube.com/watch?v=GKubKmPXDM8>.
- [954] J. L. Bernal, L. Verde, and A. G. Riess, *The trouble with H_0* , *JCAP* **1610** (2016), no. 10 019, [[arXiv:1607.05617](https://arxiv.org/abs/1607.05617)].
- [955] V. Poulin, K. K. Boddy, S. Bird, and M. Kamionkowski, *Implications of an extended dark energy cosmology with massive neutrinos for cosmological tensions*, *Phys. Rev. D* **97** (2018), no. 12 123504, [[arXiv:1803.02474](https://arxiv.org/abs/1803.02474)].
- [956] K. Aylor, M. Joy, L. Knox, M. Millea, S. Raghunathan, and W. L. K. Wu, *Sounds Discordant: Classical Distance Ladder & Λ CDM -based Determinations of the Cosmological Sound Horizon*, *Astrophys. J.* **874** (2019), no. 1 4, [[arXiv:1811.00537](https://arxiv.org/abs/1811.00537)].
- [957] L. Knox and M. Millea, *The Hubble Hunter’s Guide*, [arXiv:1908.03663](https://arxiv.org/abs/1908.03663).
- [958] P. Asadi et al., *Early-Universe Model Building*, [arXiv:2203.06680](https://arxiv.org/abs/2203.06680).
- [959] D. Green et al., *Messengers from the Early Universe: Cosmic Neutrinos and Other Light Relics*, *Bull. Am. Astron. Soc.* **51** (2019), no. 7 159, [[arXiv:1903.04763](https://arxiv.org/abs/1903.04763)].
- [960] C. D. Kreisch, F.-Y. Cyr-Racine, and O. Doré, *Neutrino puzzle: Anomalies, interactions, and cosmological tensions*, *Phys. Rev. D* **101** (2020), no. 12 123505, [[arXiv:1902.00534](https://arxiv.org/abs/1902.00534)].
- [961] S. Adhikari and D. Huterer, *Super-CMB fluctuations and the Hubble tension*, *Phys. Dark Univ.* **28** (2020) 100539, [[arXiv:1905.02278](https://arxiv.org/abs/1905.02278)].
- [962] S. Capozziello, M. Benetti, and A. D. A. M. Spallicci, *Addressing the cosmological H_0 tension by the Heisenberg uncertainty*, *Found. Phys.* **50** (2020), no. 9 893–899, [[arXiv:2007.00462](https://arxiv.org/abs/2007.00462)].
- [963] M. Braglia, M. Ballardini, F. Finelli, and K. Koyama, *Early modified gravity in light of the H_0 tension and LSS data*, *Phys. Rev. D* **103** (2021), no. 4 043528, [[arXiv:2011.12934](https://arxiv.org/abs/2011.12934)].
- [964] E. H. Tanin and T. Tenkanen, *Gravitational wave constraints on the observable inflation*, *JCAP* **01** (2021) 053, [[arXiv:2004.10702](https://arxiv.org/abs/2004.10702)].
- [965] L. Aresté Saló, D. Benisty, E. I. Guendelman, and J. d. Haro, *Quintessential Inflation and Cosmological See-Saw Mechanism: Reheating and Observational Constraints*, [arXiv:2102.09514](https://arxiv.org/abs/2102.09514).
- [966] D. K. Hazra, A. Shafieloo, and T. Souradeep, *Parameter discordance in Planck CMB and low-redshift measurements: projection in the primordial power spectrum*, *JCAP* **04** (2019) 036, [[arXiv:1810.08101](https://arxiv.org/abs/1810.08101)].
- [967] T. Tram, R. Vallance, and V. Vennin, *Inflation Model Selection meets Dark Radiation*, *JCAP* **01** (2017) 046, [[arXiv:1606.09199](https://arxiv.org/abs/1606.09199)].
- [968] E. Di Valentino and F. R. Bouchet, *A comment on power-law inflation with a dark radiation component*, *JCAP* **10** (2016) 011, [[arXiv:1609.00328](https://arxiv.org/abs/1609.00328)].
- [969] E. Di Valentino and L. Mersini-Houghton, *Testing Predictions of the Quantum Landscape Multiverse 2: The Exponential Inflationary Potential*, *JCAP* **03** (2017) 020, [[arXiv:1612.08334](https://arxiv.org/abs/1612.08334)].
- [970] R.-Y. Guo and X. Zhang, *Constraints on inflation revisited: An analysis including the latest local measurement of the Hubble constant*, *Eur. Phys. J. C* **77** (2017), no. 12 882, [[arXiv:1704.04784](https://arxiv.org/abs/1704.04784)].
- [971] C.-T. Chiang and A. Slosar, *Inferences of H_0 in presence of a non-standard recombination*, [arXiv:1811.03624](https://arxiv.org/abs/1811.03624).

- [972] E. Di Valentino, A. Melchiorri, Y. Fantaye, and A. Heavens, *Bayesian evidence against the Harrison-Zel'dovich spectrum in tensions with cosmological data sets*, *Phys. Rev. D* **98** (2018), no. 6 063508, [[arXiv:1808.09201](#)].
- [973] M. Liu and Z. Huang, *Band-limited Features in the Primordial Power Spectrum Do Not Resolve the Hubble Tension*, *Astrophys. J.* **897** (2020) 166, [[arXiv:1910.05670](#)].
- [974] R. E. Keeley, A. Shafieloo, D. K. Hazra, and T. Souradeep, *Inflation Wars: A New Hope*, *JCAP* **09** (2020) 055, [[arXiv:2006.12710](#)].
- [975] G. Ye, B. Hu, and Y.-S. Piao, *Implication of the Hubble tension for primordial Universe in light of recent cosmological data*, [arXiv:2103.09729](#).
- [976] F. Takahashi and W. Yin, *Cosmological implications of $n_s \approx 1$ in light of the Hubble tension*, [arXiv:2112.06710](#).
- [977] S. Kumar, R. C. Nunes, and S. K. Yadav, *Cosmological bounds on dark matter-photon coupling*, *Phys. Rev. D* **98** (2018), no. 4 043521, [[arXiv:1803.10229](#)].
- [978] S. K. Yadav, *Constraints on Dark Matter-Photon Coupling in the Presence of Time-Varying Dark Energy*, *Mod. Phys. Lett.* **A33** (2019) 1950358, [[arXiv:1907.05886](#)].
- [979] A. Paul, A. Chatterjee, A. Ghoshal, and S. Pal, *Shedding light on dark matter and neutrino interactions from cosmology*, *JCAP* **10** (2021) 017, [[arXiv:2104.04760](#)].
- [980] N. Blinov and G. Marques-Tavares, *Interacting radiation after Planck and its implications for the Hubble Tension*, *JCAP* **09** (2020) 029, [[arXiv:2003.08387](#)].
- [981] V. V. Flambaum and I. B. Samsonov, *Ultralight dark photon as a model for early universe dark matter*, *Phys. Rev. D* **100** (2019), no. 6 063541, [[arXiv:1908.09432](#)].
- [982] S. Nesseris, D. Sapone, and S. Sypsas, *Evaporating primordial black holes as varying dark energy*, *Phys. Dark Univ.* **27** (2020) 100413, [[arXiv:1907.05608](#)].
- [983] M. M. Flores and A. Kusenko, *Primordial Black Holes from Long-Range Scalar Forces and Scalar Radiative Cooling*, *Phys. Rev. Lett.* **126** (2021), no. 4 041101, [[arXiv:2008.12456](#)].
- [984] K. Jedamzik and A. Saveliev, *Stringent Limit on Primordial Magnetic Fields from the Cosmic Microwave Background Radiation*, *Phys. Rev. Lett.* **123** (2019), no. 2 021301, [[arXiv:1804.06115](#)].
- [985] K. Jedamzik and L. Pogosian, *Relieving the Hubble tension with primordial magnetic fields*, *Phys. Rev. Lett.* **125** (2020), no. 18 181302, [[arXiv:2004.09487](#)].
- [986] L. Thiele, Y. Guan, J. C. Hill, A. Kosowsky, and D. N. Spergel, *Can small-scale baryon inhomogeneities resolve the Hubble tension? An investigation with ACT DR4*, *Phys. Rev. D* **104** (2021), no. 6 063535, [[arXiv:2105.03003](#)].
- [987] M. Liu, Z. Huang, X. Luo, H. Miao, N. K. Singh, and L. Huang, *Can Non-standard Recombination Resolve the Hubble Tension?*, *Sci. China Phys. Mech. Astron.* **63** (2020), no. 9 290405, [[arXiv:1912.00190](#)].
- [988] M. Artymowski, I. Ben-Dayan, and U. Kumar, *Emergent dark energy from unparticles*, [arXiv:2010.02998](#).
- [989] S. A. Franchino-Viñas and M. E. Mosquera, *The cosmological lithium problem, varying constants and the H_0 tension*, [arXiv:2107.02243](#).

- [990] L. Hart and J. Chluba, *New constraints on time-dependent variations of fundamental constants using Planck data*, *Mon. Not. Roy. Astron. Soc.* **474** (2018), no. 2 1850–1861, [[arXiv:1705.03925](#)].
- [991] T. Sekiguchi and T. Takahashi, *Early recombination as a solution to the H_0 tension*, *Phys. Rev. D* **103** (2021), no. 8 083507, [[arXiv:2007.03381](#)].
- [992] L. Hart and J. Chluba, *Updated fundamental constant constraints from Planck 2018 data and possible relations to the Hubble tension*, *Mon. Not. Roy. Astron. Soc.* **493** (2020), no. 3 3255–3263, [[arXiv:1912.03986](#)].
- [993] L. Hart and J. Chluba, *Varying fundamental constants principal component analysis: additional hints about the Hubble tension*, *Mon. Not. Roy. Astron. Soc.* **510** (2022), no. 2 2206–2227, [[arXiv:2107.12465](#)].
- [994] H. Velten, I. Costa, and W. Zimdahl, *Early-time thermalization of cosmic components? A hint for solving cosmic tensions*, [arXiv:2104.05352](#).
- [995] M. M. Ivanov, Y. Ali-Haïmoud, and J. Lesgourgues, *H_0 tension or T_0 tension?*, *Phys. Rev. D* **102** (2020), no. 6 063515, [[arXiv:2005.10656](#)].
- [996] B. Bose and L. Lombriser, *Easing cosmic tensions with an open and hotter universe*, *Phys. Rev. D* **103** (2021), no. 8 L081304, [[arXiv:2006.16149](#)].
- [997] C. A. P. Bengaly, J. E. Gonzalez, and J. S. Alcaniz, *Is there evidence for a hotter Universe?*, *Eur. Phys. J. C* **80** (2020), no. 10 936, [[arXiv:2007.13789](#)].
- [998] L. W. Fung, L. Li, T. Liu, H. N. Luu, Y.-C. Qiu, and S. H. H. Tye, *Axi-Higgs Cosmology*, [arXiv:2102.11257](#).
- [999] L. W. Fung, L. Li, T. Liu, H. N. Luu, Y.-C. Qiu, and S. H. H. Tye, *The Hubble Constant in the Axi-Higgs Universe*, [arXiv:2105.01631](#).
- [1000] L. A. Anchordoqui, *Hubble Hullabaloo and String Cosmology*, 5, 2020. [arXiv:2005.01217](#).
- [1001] L. A. Anchordoqui, I. Antoniadis, D. Lüst, J. F. Soriano, and T. R. Taylor, *H_0 tension and the String Swampland*, *Phys. Rev. D* **101** (2020) 083532, [[arXiv:1912.00242](#)].
- [1002] L. A. Anchordoqui and S. E. Perez Bergliffa, *Hot thermal universe endowed with massive dark vector fields and the Hubble tension*, *Phys. Rev. D* **100** (2019), no. 12 123525, [[arXiv:1910.05860](#)].
- [1003] A. Klypin, V. Poulin, F. Prada, J. Primack, M. Kamionkowski, V. Avila-Reese, A. Rodriguez-Puebla, P. Behroozi, D. Hellinger, and T. L. Smith, *Clustering and Halo Abundances in Early Dark Energy Cosmological Models*, [arXiv:2006.14910](#).
- [1004] L. Herold, E. G. M. Ferreira, and E. Komatsu, *New constraint on Early Dark Energy from Planck and BOSS data using the profile likelihood*, [arXiv:2112.12140](#).
- [1005] A. La Posta, T. Louis, X. Garrido, and J. C. Hill, *Constraints on Pre-Recombination Early Dark Energy from SPT-3G Public Data*, [arXiv:2112.10754](#).
- [1006] A. Gómez-Valent, Z. Zheng, L. Amendola, V. Pettorino, and C. Wetterich, *Early dark energy in the pre- and postrecombination epochs*, *Phys. Rev. D* **104** (2021), no. 8 083536, [[arXiv:2107.11065](#)].
- [1007] E. Fondi, A. Melchiorri, and L. Pagano, *No evidence for EDE from Planck data in extended scenarios*, [arXiv:2203.12930](#).

- [1008] J. C. Hill et al., *The Atacama Cosmology Telescope: Constraints on Pre-Recombination Early Dark Energy*, [arXiv:2109.04451](#).
- [1009] V. Poulin, T. L. Smith, and A. Bartlett, *Dark energy at early times and ACT data: A larger Hubble constant without late-time priors*, *Phys. Rev. D* **104** (2021), no. 12 123550, [[arXiv:2109.06229](#)].
- [1010] S. Nojiri, S. D. Odintsov, D. Saez-Chillon Gomez, and G. S. Sharov, *Modeling and testing the equation of state for (Early) dark energy*, *Phys. Dark Univ.* **32** (2021) 100837, [[arXiv:2103.05304](#)].
- [1011] A. Moss, E. Copeland, S. Bamford, and T. Clarke, *A model-independent reconstruction of dark energy to very high redshift*, [arXiv:2109.14848](#).
- [1012] V. Pettorino, L. Amendola, and C. Wetterich, *How early is early dark energy?*, *Phys. Rev. D* **87** (2013) 083009, [[arXiv:1301.5279](#)].
- [1013] J. Sakstein and M. Trodden, *Early dark energy from massive neutrinos – a natural resolution of the Hubble tension*, [arXiv:1911.11760](#).
- [1014] M.-X. Lin, G. Benevento, W. Hu, and M. Raveri, *Acoustic Dark Energy: Potential Conversion of the Hubble Tension*, *Phys. Rev. D* **100** (2019), no. 6 063542, [[arXiv:1905.12618](#)].
- [1015] K. V. Berghaus and T. Karwal, *Thermal Friction as a Solution to the Hubble Tension*, *Phys. Rev. D* **101** (2020), no. 8 083537, [[arXiv:1911.06281](#)].
- [1016] M. Lucca, *The role of CMB spectral distortions in the Hubble tension: a proof of principle*, *Phys. Lett. B* **810** (2020) 135791, [[arXiv:2008.01115](#)].
- [1017] S. Alexander and E. McDonough, *Axion-Dilaton Destabilization and the Hubble Tension*, *Phys. Lett. B* **797** (2019) 134830, [[arXiv:1904.08912](#)].
- [1018] E. Mörtzell and S. Dhawan, *Does the Hubble constant tension call for new physics?*, *JCAP* **1809** (2018), no. 09 025, [[arXiv:1801.07260](#)].
- [1019] N. Kaloper, *Dark energy, H_0 and weak gravity conjecture*, *Int. J. Mod. Phys. D* **28** (2019), no. 14 1944017, [[arXiv:1903.11676](#)].
- [1020] R. Murgia, G. F. Abellán, and V. Poulin, *Early dark energy resolution to the Hubble tension in light of weak lensing surveys and lensing anomalies*, *Phys. Rev. D* **103** (2021), no. 6 063502, [[arXiv:2009.10733](#)].
- [1021] A. Gogoi, R. K. Sharma, P. Chanda, and S. Das, *Early Mass-varying Neutrino Dark Energy: Nugget Formation and Hubble Anomaly*, *Astrophys. J.* **915** (2021), no. 2 132, [[arXiv:2005.11889](#)].
- [1022] B. S. Haridasu, M. Viel, and N. Vittorio, *Sources of H_0 -tension in dark energy scenarios*, *Phys. Rev. D* **103** (2021), no. 6 063539, [[arXiv:2012.10324](#)].
- [1023] T. L. Smith, M. Lucca, V. Poulin, G. F. Abellan, L. Balkenhol, K. Benabed, S. Galli, and R. Murgia, *Hints of Early Dark Energy in Planck, SPT, and ACT data: new physics or systematics?*, [arXiv:2202.09379](#).
- [1024] D. J. E. Marsh, *The Axiverse Extended: Vacuum Destabilisation, Early Dark Energy and Cosmological Collapse*, *Phys. Rev. D* **83** (2011) 123526, [[arXiv:1102.4851](#)].
- [1025] D. J. E. Marsh, *Axion Cosmology*, *Phys. Rept.* **643** (2016) 1–79, [[arXiv:1510.07633](#)].

- [1026] M. Kamionkowski, J. Pradler, and D. G. E. Walker, *Dark energy from the string axiverse*, *Phys. Rev. Lett.* **113** (2014), no. 25 251302, [[arXiv:1409.0549](#)].
- [1027] V. Poulin, T. L. Smith, D. Grin, T. Karwal, and M. Kamionkowski, *Cosmological implications of ultralight axionlike fields*, *Phys. Rev. D* **98** (2018), no. 8 083525, [[arXiv:1806.10608](#)].
- [1028] R. Daido, F. Takahashi, and W. Yin, *The ALP miracle: unified inflaton and dark matter*, *JCAP* **05** (2017) 044, [[arXiv:1702.03284](#)].
- [1029] R. Daido, F. Takahashi, and W. Yin, *The ALP miracle revisited*, *JHEP* **02** (2018) 104, [[arXiv:1710.11107](#)].
- [1030] M.-X. Lin, W. Hu, and M. Raveri, *Testing H_0 in Acoustic Dark Energy with Planck and ACT Polarization*, *Phys. Rev. D* **102** (2020) 123523, [[arXiv:2009.08974](#)].
- [1031] L. Yin, *Reducing the H_0 Tension with Exponential Acoustic Dark Energy*, [arXiv:2012.13917](#).
- [1032] M. Braglia, W. T. Emond, F. Finelli, A. E. Gumrukcuoglu, and K. Koyama, *Unified framework for early dark energy from α -attractors*, *Phys. Rev. D* **102** (2020), no. 8 083513, [[arXiv:2005.14053](#)].
- [1033] M. S. Turner, *Coherent Scalar Field Oscillations in an Expanding Universe*, *Phys. Rev. D* **28** (1983) 1243.
- [1034] P.-H. Chavanis, *Cosmology with a stiff matter era*, *Phys. Rev. D* **92** (2015), no. 10 103004, [[arXiv:1412.0743](#)].
- [1035] M. Carrillo González, Q. Liang, J. Sakstein, and M. Trodden, *Neutrino-Assisted Early Dark Energy: Theory and Cosmology*, [arXiv:2011.09895](#).
- [1036] J. C. Hill, E. McDonough, M. W. Toomey, and S. Alexander, *Early Dark Energy Does Not Restore Cosmological Concordance*, [arXiv:2003.07355](#).
- [1037] S. J. Clark, K. Vattis, J. Fan, and S. M. Koushiappas, *The H_0 and S_8 tensions necessitate early and late time changes to Λ CDM*, [arXiv:2110.09562](#).
- [1038] K. Freese and M. W. Winkler, *Chain Early Dark Energy: Solving the Hubble Tension and Explaining Today's Dark Energy*, [arXiv:2102.13655](#).
- [1039] G. D'Amico, L. Senatore, P. Zhang, and H. Zheng, *The Hubble Tension in Light of the Full-Shape Analysis of Large-Scale Structure Data*, [arXiv:2006.12420](#).
- [1040] J.-Q. Jiang and Y.-S. Piao, *Towards early dark energy and $n_s=1$ with Planck, ACT and SPT*, [arXiv:2202.13379](#).
- [1041] H. Wang and Y.-S. Piao, *Testing dark energy after pre-recombination early dark energy*, [arXiv:2201.07079](#).
- [1042] G. Ye and Y.-S. Piao, *Is the Hubble tension a hint of AdS phase around recombination?*, *Phys. Rev. D* **101** (2020), no. 8 083507, [[arXiv:2001.02451](#)].
- [1043] G. Ye, J. Zhang, and Y.-S. Piao, *Resolving both H_0 and S_8 tensions with AdS early dark energy and ultralight axion*, [arXiv:2107.13391](#).
- [1044] G. Ye and Y.-S. Piao, *T_0 censorship of early dark energy and AdS vacua*, *Phys. Rev. D* **102** (2020), no. 8 083523, [[arXiv:2008.10832](#)].
- [1045] J.-Q. Jiang and Y.-S. Piao, *Testing AdS early dark energy with Planck, SPTpol, and LSS data*, *Phys. Rev. D* **104** (2021), no. 10 103524, [[arXiv:2107.07128](#)].

- [1046] V. I. Sabla and R. R. Caldwell, *No H_0 assistance from assisted quintessence*, *Phys. Rev. D* **103** (2021), no. 10 103506, [[arXiv:2103.04999](#)].
- [1047] O. Seto and Y. Toda, *Comparing early dark energy and extra radiation solutions to the Hubble tension with BBN*, [arXiv:2101.03740](#).
- [1048] M. Gonzalez, M. P. Hertzberg, and F. Rompineve, *Ultralight Scalar Decay and the Hubble Tension*, *JCAP* **10** (2020) 028, [[arXiv:2006.13959](#)].
- [1049] F. Niedermann and M. S. Sloth, *Hot new early dark energy*, *Phys. Rev. D* **105** (2022), no. 6 063509, [[arXiv:2112.00770](#)].
- [1050] F. Niedermann and M. S. Sloth, *Hot New Early Dark Energy: Towards a Unified Dark Sector of Neutrinos, Dark Energy and Dark Matter*, [arXiv:2112.00759](#).
- [1051] F. Niedermann and M. S. Sloth, *New early dark energy*, *Phys. Rev. D* **103** (2021), no. 4 L041303, [[arXiv:1910.10739](#)].
- [1052] F. Niedermann and M. S. Sloth, *Resolving the Hubble tension with new early dark energy*, *Phys. Rev. D* **102** (2020), no. 6 063527, [[arXiv:2006.06686](#)].
- [1053] F. Niedermann and M. S. Sloth, *New Early Dark Energy is compatible with current LSS data*, [arXiv:2009.00006](#).
- [1054] I. J. Allali, M. P. Hertzberg, and F. Rompineve, *A Dark Sector to Restore Cosmological Concordance*, [arXiv:2104.12798](#).
- [1055] T. Karwal, M. Raveri, B. Jain, J. Khoury, and M. Trodden, *Chameleon early dark energy and the Hubble tension*, *Phys. Rev. D* **105** (2022), no. 6 063535, [[arXiv:2106.13290](#)].
- [1056] V. I. Sabla and R. R. Caldwell, *The Microphysics of Early Dark Energy*, [arXiv:2202.08291](#).
- [1057] E. McDonough, M.-X. Lin, J. C. Hill, W. Hu, and S. Zhou, *The Early Dark Sector, the Hubble Tension, and the Swampland*, [arXiv:2112.09128](#).
- [1058] H. Ooguri and C. Vafa, *On the Geometry of the String Landscape and the Swampland*, *Nucl. Phys. B* **766** (2007) 21–33, [[hep-th/0605264](#)].
- [1059] D. Klaeuer and E. Palti, *Super-Planckian Spatial Field Variations and Quantum Gravity*, *JHEP* **01** (2017) 088, [[arXiv:1610.00010](#)].
- [1060] M. Scalisi and I. Valenzuela, *Swampland distance conjecture, inflation and α -attractors*, *JHEP* **08** (2019) 160, [[arXiv:1812.07558](#)].
- [1061] R. Blumenhagen, I. Valenzuela, and F. Wolf, *The Swampland Conjecture and F-term Axion Monodromy Inflation*, *JHEP* **07** (2017) 145, [[arXiv:1703.05776](#)].
- [1062] F. Baume and E. Palti, *Backreacted Axion Field Ranges in String Theory*, *JHEP* **08** (2016) 043, [[arXiv:1602.06517](#)].
- [1063] L. Lancaster, F.-Y. Cyr-Racine, L. Knox, and Z. Pan, *A tale of two modes: Neutrino free-streaming in the early universe*, *JCAP* **1707** (2017), no. 07 033, [[arXiv:1704.06657](#)].
- [1064] M. A. Buen-Abad, M. Schmaltz, J. Lesgourgues, and T. Brinckmann, *Interacting Dark Sector and Precision Cosmology*, *JCAP* **01** (2018) 008, [[arXiv:1708.09406](#)].
- [1065] S. Ghosh, S. Kumar, and Y. Tsai, *Free-streaming and Coupled Dark Radiation Isocurvature Perturbations: Constraints and Application to the Hubble Tension*, [arXiv:2107.09076](#).

- [1066] M. Wyman, D. H. Rudd, R. Vanderveld, and W. Hu, *Neutrinos Help Reconcile Planck Measurements with the Local Universe*, *Phys. Rev. Lett.* **112** (2014), no. 5 051302, [[arXiv:1307.7715](#)].
- [1067] M. Archidiacono, E. Giusarma, S. Hannestad, and O. Mena, *Cosmic dark radiation and neutrinos*, *Adv. High Energy Phys.* **2013** (2013) 191047, [[arXiv:1307.0637](#)].
- [1068] L. Ackerman, M. R. Buckley, S. M. Carroll, and M. Kamionkowski, *Dark Matter and Dark Radiation*, *Phys. Rev. D* **79** (2009) 023519, [[arXiv:0810.5126](#)].
- [1069] M. Blennow, E. Fernandez-Martinez, O. Mena, J. Redondo, and P. Serra, *Asymmetric Dark Matter and Dark Radiation*, *JCAP* **07** (2012) 022, [[arXiv:1203.5803](#)].
- [1070] J. P. Conlon and M. C. D. Marsh, *The Cosmophenomenology of Axionic Dark Radiation*, *JHEP* **10** (2013) 214, [[arXiv:1304.1804](#)].
- [1071] H. Vogel and J. Redondo, *Dark Radiation constraints on minicharged particles in models with a hidden photon*, *JCAP* **02** (2014) 029, [[arXiv:1311.2600](#)].
- [1072] C. Dvorkin, M. Wyman, D. H. Rudd, and W. Hu, *Neutrinos help reconcile Planck measurements with both the early and local Universe*, *Phys. Rev. D* **90** (2014), no. 8 083503, [[arXiv:1403.8049](#)].
- [1073] B. Leistedt, H. V. Peiris, and L. Verde, *No new cosmological concordance with massive sterile neutrinos*, *Phys. Rev. Lett.* **113** (2014) 041301, [[arXiv:1404.5950](#)].
- [1074] D. Aloni, A. Berlin, M. Joseph, M. Schmaltz, and N. Weiner, *A Step in Understanding the Hubble Tension*, [arXiv:2111.00014](#).
- [1075] L. Feng, J.-F. Zhang, and X. Zhang, *A search for sterile neutrinos with the latest cosmological observations*, *Eur. Phys. J. C* **77** (2017), no. 6 418, [[arXiv:1703.04884](#)].
- [1076] O. Seto and Y. Toda, *Hubble tension in lepton asymmetric cosmology with an extra radiation*, [arXiv:2104.04381](#).
- [1077] W. Giarè, E. Di Valentino, A. Melchiorri, and O. Mena, *New cosmological bounds on hot relics: axions and neutrinos*, *Mon. Not. Roy. Astron. Soc.* **505** (2021), no. 2 2703–2711, [[arXiv:2011.14704](#)].
- [1078] A. Aboubrahim, M. Klasen, and P. Nath, *Resolving the Hubble tension through hidden sector dynamics in the early universe*, [arXiv:2202.04453](#).
- [1079] L. Feng, R.-Y. Guo, J.-F. Zhang, and X. Zhang, *Cosmological search for sterile neutrinos after Planck 2018*, *Phys. Lett. B* **827** (2022) 136940, [[arXiv:2109.06111](#)].
- [1080] S. Carneiro, P. C. de Holanda, C. Pigozzo, and F. Sobreira, *Is the H_0 tension suggesting a fourth neutrino generation?*, *Phys. Rev.* **D100** (2019), no. 2 023505, [[arXiv:1812.06064](#)].
- [1081] G. B. Gelmini, A. Kusenko, and V. Takhistov, *Hints of Sterile Neutrinos in Recent Measurements of the Hubble Parameter*, [arXiv:1906.10136](#).
- [1082] G. B. Gelmini, M. Kawasaki, A. Kusenko, K. Murai, and V. Takhistov, *Big Bang Nucleosynthesis constraints on sterile neutrino and lepton asymmetry of the Universe*, *JCAP* **09** (2020) 051, [[arXiv:2005.06721](#)].
- [1083] E. Fernandez-Martinez, M. Pierre, E. Pinsard, and S. Rosauero-Alcaraz, *Inverse Seesaw, dark matter and the Hubble tension*, *Eur. Phys. J. C* **81** (2021), no. 10 954, [[arXiv:2106.05298](#)].
- [1084] Y. Gu, L. Wu, and B. Zhu, *Axion Dark Radiation and Late Decaying Dark Matter in Neutrino Experiment*, [arXiv:2105.07232](#).

- [1085] F. D’Eramo, R. Z. Ferreira, A. Notari, and J. L. Bernal, *Hot Axions and the H_0 tension*, *JCAP* **1811** (2018), no. 11 014, [[arXiv:1808.07430](#)].
- [1086] A. J. Cuesta, M. E. Gómez, J. I. Illana, and M. Masip, *Cosmology of an Axion-Like Majoron*, [arXiv:2109.07336](#).
- [1087] G. Mangano, G. Miele, S. Pastor, T. Pinto, O. Pisanti, and P. D. Serpico, *Relic neutrino decoupling including flavor oscillations*, *Nucl. Phys.* **B729** (2005) 221–234, [[hep-ph/0506164](#)].
- [1088] P. F. de Salas and S. Pastor, *Relic neutrino decoupling with flavour oscillations revisited*, *JCAP* **1607** (2016), no. 07 051, [[arXiv:1606.06986](#)].
- [1089] K. Akita and M. Yamaguchi, *A precision calculation of relic neutrino decoupling*, *JCAP* **08** (2020) 012, [[arXiv:2005.07047](#)].
- [1090] M. Escudero Abenza, *Precision early universe thermodynamics made simple: N_{eff} and neutrino decoupling in the Standard Model and beyond*, *JCAP* **05** (2020) 048, [[arXiv:2001.04466](#)].
- [1091] J. J. Bennett, G. Buldgen, P. F. De Salas, M. Drewes, S. Gariazzo, S. Pastor, and Y. Y. Y. Wong, *Towards a precision calculation of N_{eff} in the Standard Model II: Neutrino decoupling in the presence of flavour oscillations and finite-temperature QED*, *JCAP* **04** (2021) 073, [[arXiv:2012.02726](#)].
- [1092] J. Froustey, C. Pitrou, and M. C. Volpe, *Neutrino decoupling including flavour oscillations and primordial nucleosynthesis*, *JCAP* **12** (2020) 015, [[arXiv:2008.01074](#)].
- [1093] F.-Y. Cyr-Racine, R. de Putter, A. Raccanelli, and K. Sigurdson, *Constraints on Large-Scale Dark Acoustic Oscillations from Cosmology*, *Phys. Rev. D* **89** (2014), no. 6 063517, [[arXiv:1310.3278](#)].
- [1094] J. A. Schewtschenko, C. M. Baugh, R. J. Wilkinson, C. Boehm, S. Pascoli, and T. Sawala, *Dark matter–radiation interactions: the structure of Milky Way satellite galaxies*, *Mon. Not. Roy. Astron. Soc.* **461** (2016), no. 3 2282–2287, [[arXiv:1512.06774](#)].
- [1095] M. A. Buen-Abad, G. Marques-Tavares, and M. Schmaltz, *Non-Abelian dark matter and dark radiation*, *Phys. Rev. D* **92** (2015), no. 2 023531, [[arXiv:1505.03542](#)].
- [1096] Z. Chacko, Y. Cui, S. Hong, T. Okui, and Y. Tsai, *Partially Acoustic Dark Matter, Interacting Dark Radiation, and Large Scale Structure*, *JHEP* **12** (2016) 108, [[arXiv:1609.03569](#)].
- [1097] P. Ko and Y. Tang, *Light dark photon and fermionic dark radiation for the Hubble constant and the structure formation*, *Phys. Lett. B* **762** (2016) 462–466, [[arXiv:1608.01083](#)].
- [1098] P. Ko and Y. Tang, *Residual Non-Abelian Dark Matter and Dark Radiation*, *Phys. Lett. B* **768** (2017) 12–17, [[arXiv:1609.02307](#)].
- [1099] Y. Tang, *Interacting Scalar Radiation and Dark Matter in Cosmology*, *Phys. Lett. B* **757** (2016) 387–392, [[arXiv:1603.00165](#)].
- [1100] R. Krall, F.-Y. Cyr-Racine, and C. Dvorkin, *Wandering in the Lyman-alpha Forest: A Study of Dark Matter-Dark Radiation Interactions*, *JCAP* **09** (2017) 003, [[arXiv:1705.08894](#)].
- [1101] M. Archidiacono, S. Bohr, S. Hannestad, J. H. Jørgensen, and J. Lesgourgues, *Linear scale bounds on dark matter–dark radiation interactions and connection with the small scale crisis of cold dark matter*, *JCAP* **11** (2017) 010, [[arXiv:1706.06870](#)].
- [1102] M. Archidiacono, D. C. Hooper, R. Murgia, S. Bohr, J. Lesgourgues, and M. Viel, *Constraining Dark Matter-Dark Radiation interactions with CMB, BAO, and Lyman- α* , *JCAP* **10** (2019) 055, [[arXiv:1907.01496](#)].

- [1103] P. Ko, N. Nagata, and Y. Tang, *Hidden Charged Dark Matter and Chiral Dark Radiation*, *Phys. Lett. B* **773** (2017) 513–520, [[arXiv:1706.05605](#)].
- [1104] N. Becker, D. C. Hooper, F. Kahlhoefer, J. Lesgourgues, and N. Schöneberg, *Cosmological constraints on multi-interacting dark matter*, *JCAP* **02** (2021) 019, [[arXiv:2010.04074](#)].
- [1105] G. Choi, T. T. Yanagida, and N. Yokozaki, *A model of interacting dark matter and dark radiation for H_0 and σ_8 tensions*, *JHEP* **01** (2021) 127, [[arXiv:2010.06892](#)].
- [1106] F.-Y. Cyr-Racine, K. Sigurdson, J. Zavala, T. Bringmann, M. Vogelsberger, and C. Pfrommer, *ETHOS—an effective theory of structure formation: From dark particle physics to the matter distribution of the Universe*, *Phys. Rev. D* **93** (2016), no. 12 123527, [[arXiv:1512.05344](#)].
- [1107] M. Vogelsberger, J. Zavala, F.-Y. Cyr-Racine, C. Pfrommer, T. Bringmann, and K. Sigurdson, *ETHOS – an effective theory of structure formation: dark matter physics as a possible explanation of the small-scale CDM problems*, *Mon. Not. Roy. Astron. Soc.* **460** (2016), no. 2 1399–1416, [[arXiv:1512.05349](#)].
- [1108] F.-Y. Cyr-Racine and K. Sigurdson, *Limits on Neutrino-Neutrino Scattering in the Early Universe*, *Phys. Rev. D* **90** (2014), no. 12 123533, [[arXiv:1306.1536](#)].
- [1109] I. M. Oldengott, T. Tram, C. Rampf, and Y. Y. Y. Wong, *Interacting neutrinos in cosmology: exact description and constraints*, *JCAP* **11** (2017) 027, [[arXiv:1706.02123](#)].
- [1110] A. Das and S. Ghosh, *Flavor-specific Interaction Favours Strong Neutrino Self-coupling*, [[arXiv:2011.12315](#)].
- [1111] S. Roy Choudhury, S. Hannestad, and T. Tram, *Updated constraints on massive neutrino self-interactions from cosmology in light of the H_0 tension*, *JCAP* **03** (2021) 084, [[arXiv:2012.07519](#)].
- [1112] A. Mazumdar, S. Mohanty, and P. Parashari, *Flavour specific neutrino self-interaction: H_0 tension and IceCube*, [[arXiv:2011.13685](#)].
- [1113] F. Forastieri, M. Lattanzi, and P. Natoli, *Cosmological constraints on neutrino self-interactions with a light mediator*, *Phys. Rev. D* **100** (2019), no. 10 103526, [[arXiv:1904.07810](#)].
- [1114] H.-J. He, Y.-Z. Ma, and J. Zheng, *Resolving Hubble Tension by Self-Interacting Neutrinos with Dirac Seesaw*, *JCAP* **11** (2020) 003, [[arXiv:2003.12057](#)].
- [1115] M. Berbig, S. Jana, and A. Trautner, *The Hubble tension and a renormalizable model of gauged neutrino self-interactions*, *Phys. Rev. D* **102** (2020), no. 11 115008, [[arXiv:2004.13039](#)].
- [1116] K.-F. Lyu, E. Stamou, and L.-T. Wang, *Self-interacting neutrinos: Solution to Hubble tension versus experimental constraints*, *Phys. Rev. D* **103** (2021), no. 1 015004, [[arXiv:2004.10868](#)].
- [1117] S. Hannestad, R. S. Hansen, and T. Tram, *How Self-Interactions can Reconcile Sterile Neutrinos with Cosmology*, *Phys. Rev. Lett.* **112** (2014), no. 3 031802, [[arXiv:1310.5926](#)].
- [1118] M. Archidiacono, S. Hannestad, R. S. Hansen, and T. Tram, *Cosmology with self-interacting sterile neutrinos and dark matter - A pseudoscalar model*, *Phys. Rev. D* **91** (2015), no. 6 065021, [[arXiv:1404.5915](#)].
- [1119] X. Chu, B. Dasgupta, and J. Kopp, *Sterile neutrinos with secret interactions—lasting friendship with cosmology*, *JCAP* **10** (2015) 011, [[arXiv:1505.02795](#)].
- [1120] N. Blinov, K. J. Kelly, G. Z. Krnjaic, and S. D. McDermott, *Constraining the Self-Interacting Neutrino Interpretation of the Hubble Tension*, *Phys. Rev. Lett.* **123** (2019), no. 19 191102, [[arXiv:1905.02727](#)].

- [1121] S. Ghosh, R. Khatri, and T. S. Roy, *Dark Neutrino interactions phase out the Hubble tension*, [arXiv:1908.09843](#).
- [1122] T. Brinckmann, J. H. Chang, and M. LoVerde, *Self-interacting neutrinos, the Hubble parameter tension, and the Cosmic Microwave Background*, [arXiv:2012.11830](#).
- [1123] M. Archidiacono, S. Gariazzo, C. Giunti, S. Hannestad, and T. Tram, *Sterile neutrino self-interactions: H_0 tension and short-baseline anomalies*, *JCAP* **12** (2020) 029, [[arXiv:2006.12885](#)].
- [1124] M. A. Corona, R. Murgia, M. Cadeddu, M. Archidiacono, S. Gariazzo, C. Giunti, and S. Hannestad, *Pseudoscalar sterile neutrino self-interactions in light of Planck, SPT and ACT data*, [arXiv:2112.00037](#).
- [1125] M. Archidiacono, S. Hannestad, R. S. Hansen, and T. Tram, *Sterile neutrinos with pseudoscalar self-interactions and cosmology*, *Phys. Rev. D* **93** (2016), no. 4 045004, [[arXiv:1508.02504](#)].
- [1126] M. Archidiacono, S. Gariazzo, C. Giunti, S. Hannestad, R. Hansen, M. Laveder, and T. Tram, *Pseudoscalar—sterile neutrino interactions: reconciling the cosmos with neutrino oscillations*, *JCAP* **08** (2016) 067, [[arXiv:1606.07673](#)].
- [1127] T. Brune and H. Päs, *Massive Majorons and constraints on the Majoron-neutrino coupling*, *Phys. Rev. D* **99** (2019), no. 9 096005, [[arXiv:1808.08158](#)].
- [1128] F. F. Deppisch, L. Graf, W. Rodejohann, and X.-J. Xu, *Neutrino Self-Interactions and Double Beta Decay*, *Phys. Rev. D* **102** (2020), no. 5 051701, [[arXiv:2004.11919](#)].
- [1129] V. Brdar, M. Lindner, S. Vogl, and X.-J. Xu, *Revisiting neutrino self-interaction constraints from Z and τ decays*, *Phys. Rev. D* **101** (2020), no. 11 115001, [[arXiv:2003.05339](#)].
- [1130] G.-y. Huang and W. Rodejohann, *Solving the Hubble tension without spoiling Big Bang Nucleosynthesis*, [arXiv:2102.04280](#).
- [1131] M. Escudero and S. J. Witte, *The Hubble Tension as a Hint of Leptogenesis and Neutrino Mass Generation*, [arXiv:2103.03249](#).
- [1132] A. Boyarsky, M. Ovchinnikov, N. Sabti, and V. Syvolap, *When FIMPs Decay into Neutrinos: The N_{eff} Story*, [arXiv:2103.09831](#).
- [1133] G. Mangano, A. Melchiorri, P. Serra, A. Cooray, and M. Kamionkowski, *Cosmological bounds on dark matter-neutrino interactions*, *Phys. Rev. D* **74** (2006) 043517, [[astro-ph/0606190](#)].
- [1134] R. J. Wilkinson, C. Boehm, and J. Lesgourgues, *Constraining Dark Matter-Neutrino Interactions using the CMB and Large-Scale Structure*, *JCAP* **05** (2014) 011, [[arXiv:1401.7597](#)].
- [1135] M. R. Mosbech, C. Boehm, S. Hannestad, O. Mena, J. Stadler, and Y. Y. Y. Wong, *The full Boltzmann hierarchy for dark matter-massive neutrino interactions*, *JCAP* **03** (2021) 066, [[arXiv:2011.04206](#)].
- [1136] J. Stadler, C. Boehm, and O. Mena, *Comprehensive Study of Neutrino-Dark Matter Mixed Damping*, *JCAP* **08** (2019) 014, [[arXiv:1903.00540](#)].
- [1137] K.-Y. Choi, J. Kim, and C. Rott, *Constraining dark matter-neutrino interactions with IceCube-170922A*, *Phys. Rev. D* **99** (2019), no. 8 083018, [[arXiv:1903.03302](#)].
- [1138] E. Di Valentino, C. Bøehm, E. Hivon, and F. R. Bouchet, *Reducing the H_0 and σ_8 tensions with Dark Matter-neutrino interactions*, *Phys. Rev. D* **97** (2018), no. 4 043513, [[arXiv:1710.02559](#)].

- [1139] F. Arias-Aragon, E. Fernandez-Martinez, M. Gonzalez-Lopez, and L. Merlo, *Neutrino Masses and Hubble Tension via a Majoron in MFV*, *Eur. Phys. J. C* **81** (2021), no. 1 28, [[arXiv:2009.01848](#)].
- [1140] M. Escudero and S. J. Witte, *A CMB search for the neutrino mass mechanism and its relation to the Hubble tension*, *Eur. Phys. J. C* **80** (2020), no. 4 294, [[arXiv:1909.04044](#)].
- [1141] W. Hu, *Angular trispectrum of the CMB*, *Phys. Rev. D* **64** (2001) 083005, [[astro-ph/0105117](#)].
- [1142] K. M. Smith, L. Senatore, and M. Zaldarriaga, *Optimal analysis of the CMB trispectrum*, [arXiv:1502.00635](#).
- [1143] S. Adhikari, A.-S. Deutsch, and S. Shandera, *Statistical anisotropies in temperature and polarization fluctuations from a scale-dependent trispectrum*, *Phys. Rev. D* **98** (2018), no. 2 023520, [[arXiv:1805.00037](#)].
- [1144] W. a Heisenberg, *Über den anschaulichen Inhalt der quantentheoretischen Kinematik und Mechanik*, *Z. Phys.* **43** (1927) 172–198.
- [1145] H. P. Robertson, *The Uncertainty Principle*, *Phys. Rev.* **34** (1929) 163–164.
- [1146] C. A. Mead, *Possible Connection Between Gravitation and Fundamental Length*, *Phys. Rev.* **135** (1964) B849–B862.
- [1147] M. Maggiore, *The Algebraic structure of the generalized uncertainty principle*, *Phys. Lett.* **B319** (1993) 83–86, [[hep-th/9309034](#)].
- [1148] M. Maggiore, *A Generalized uncertainty principle in quantum gravity*, *Phys. Lett.* **B304** (1993) 65–69, [[hep-th/9301067](#)].
- [1149] M. Maggiore, *Quantum groups, gravity and the generalized uncertainty principle*, *Phys. Rev.* **D49** (1994) 5182–5187, [[hep-th/9305163](#)].
- [1150] A. Kempf, G. Mangano, and R. B. Mann, *Hilbert space representation of the minimal length uncertainty relation*, *Phys. Rev.* **D52** (1995) 1108–1118, [[hep-th/9412167](#)].
- [1151] H. Hinrichsen and A. Kempf, *Maximal localization in the presence of minimal uncertainties in positions and momenta*, *J. Math. Phys.* **37** (1996) 2121–2137, [[hep-th/9510144](#)].
- [1152] A. Kempf, *On quantum field theory with nonzero minimal uncertainties in positions and momenta*, *J. Math. Phys.* **38** (1997) 1347–1372, [[hep-th/9602085](#)].
- [1153] A. Kempf, *String / quantum gravity motivated uncertainty relations and regularization in field theory*, in *Quantum group. Proceedings, Symposium at the 21st International Colloquium on Group Theoretical Methods in Physics, Group'21, ICGTMP'96, Goslar, Germany, July 15-20, 1996*, 1996. [hep-th/9612082](#).
- [1154] H. S. Snyder, *Quantized space-time*, *Phys. Rev.* **71** (1947) 38–41.
- [1155] C. N. Yang, *On quantized space-time*, *Phys. Rev.* **72** (1947) 874. [,7(1947)].
- [1156] F. Karolyhazy, *Gravitation and quantum mechanics of macroscopic objects*, *Nuovo Cim.* **A42** (1966) 390–402.
- [1157] R. J. Adler, P. Chen, and D. I. Santiago, *The Generalized uncertainty principle and black hole remnants*, *Gen. Rel. Grav.* **33** (2001) 2101–2108, [[gr-qc/0106080](#)].
- [1158] A. Ashoorioon, A. Kempf, and R. B. Mann, *Minimum length cutoff in inflation and uniqueness of the action*, *Phys. Rev.* **D71** (2005) 023503, [[astro-ph/0410139](#)].

- [1159] A. Ashoorioon and R. B. Mann, *Generation of cosmological seed magnetic fields from inflation with cutoff*, *Phys. Rev.* **D71** (2005) 103509, [[gr-qc/0410053](#)].
- [1160] A. Ashoorioon and R. B. Mann, *On the tensor/scalar ratio in inflation with UV cut off*, *Nucl. Phys.* **B716** (2005) 261–279, [[gr-qc/0411056](#)].
- [1161] A. Ashoorioon, J. L. Hovdebo, and R. B. Mann, *Running of the spectral index and violation of the consistency relation between tensor and scalar spectra from trans-Planckian physics*, *Nucl. Phys.* **B727** (2005) 63–76, [[gr-qc/0504135](#)].
- [1162] K. Nozari, P. Pedram, and M. Molkara, *Minimal length, maximal momentum and the entropic force law*, *Int. J. Theor. Phys.* **51** (2012) 1268–1275, [[arXiv:1111.2204](#)].
- [1163] M. Faizal, M. M. Khalil, and S. Das, *Time Crystals from Minimum Time Uncertainty*, *Eur. Phys. J.* **C76** (2016), no. 1 30, [[arXiv:1501.03111](#)].
- [1164] A. F. Ali, M. Faizal, and M. M. Khalil, *Short Distance Physics of the Inflationary de Sitter Universe*, *JCAP* **1509** (2015), no. 09 025, [[arXiv:1505.06963](#)].
- [1165] A. Mohammadi, A. F. Ali, T. Golanbari, A. Aghamohammadi, K. Saaidi, and M. Faizal, *Inflationary universe in the presence of a minimal measurable length*, *Annals Phys.* **385** (2017) 214–224, [[arXiv:1505.04392](#)].
- [1166] M. Faizal, *Supersymmetry breaking as a new source for the generalized uncertainty principle*, *Phys. Lett.* **B757** (2016) 244–246, [[arXiv:1605.00925](#)].
- [1167] M. J. Lake, *Minimum length uncertainty relations in the presence of dark energy*, *Galaxies* **7** (2019), no. 1 11, [[arXiv:1712.00271](#)].
- [1168] Q. Zhao, M. Faizal, and Z. Zaz, *Short distance modification of the quantum virial theorem*, *Phys. Lett.* **B770** (2017) 564–568, [[arXiv:1707.00636](#)].
- [1169] E. C. Vagenas, L. Alasfar, S. M. Alsaleh, and A. F. Ali, *The GUP and quantum Raychaudhuri equation*, *Nucl. Phys.* **B931** (2018) 72–78, [[arXiv:1706.06502](#)].
- [1170] M. J. Lake, *A New Approach to Generalised Uncertainty Relations*, [[arXiv:2008.13183](#)].
- [1171] A. N. Tawfik and A. M. Diab, *Review on Generalized Uncertainty Principle*, *Rept. Prog. Phys.* **78** (2015) 126001, [[arXiv:1509.02436](#)].
- [1172] **Particle Data Group** Collaboration, M. Tanabashi et al., *Review of Particle Physics*, *Phys. Rev. D* **98** (2018), no. 3 030001.
- [1173] J. A. Helayël-Neto and A. D. A. M. Spallicci, *Frequency variation for in vacuo photon propagation in the Standard-Model Extension*, *Eur. Phys. J. C* **79** (2019), no. 7 590, [[arXiv:1904.11035](#)].
- [1174] A. D. A. M. Spallicci, J. A. Helayël-Neto, M. López-Corredoira, and S. Capozziello, *Cosmology and the massive photon frequency shift in the Standard-Model Extension*, *Eur. Phys. J. C* **81** (2021), no. 1 4, [[arXiv:2011.12608](#)].
- [1175] L. Bonetti, L. R. dos Santos Filho, J. A. Helayël-Neto, and A. D. A. M. Spallicci, *Effective photon mass by Super and Lorentz symmetry breaking*, *Phys. Lett. B* **764** (2017) 203–206, [[arXiv:1607.08786](#)].
- [1176] L. Bonetti, L. R. dos Santos Filho, J. A. Helayël-Neto, and A. D. A. M. Spallicci, *Photon sector analysis of Super and Lorentz symmetry breaking: effective photon mass, bi-refringence and dissipation*, *Eur. Phys. J. C* **78** (2018), no. 10 811, [[arXiv:1709.04995](#)].

- [1177] M. Ballardini, M. Braglia, F. Finelli, D. Paoletti, A. A. Starobinsky, and C. Umiltà, *Scalar-tensor theories of gravity, neutrino physics, and the H_0 tension*, *JCAP* **10** (2020) 044, [[arXiv:2004.14349](#)].
- [1178] M. Braglia, M. Ballardini, W. T. Emond, F. Finelli, A. E. Gumrukcuoglu, K. Koyama, and D. Paoletti, *Larger value for H_0 by an evolving gravitational constant*, *Phys. Rev. D* **102** (2020), no. 2 023529, [[arXiv:2004.11161](#)].
- [1179] M. Rossi, M. Ballardini, M. Braglia, F. Finelli, D. Paoletti, A. A. Starobinsky, and C. Umiltà, *Cosmological constraints on post-Newtonian parameters in effectively massless scalar-tensor theories of gravity*, *Phys. Rev. D* **100** (2019), no. 10 103524, [[arXiv:1906.10218](#)].
- [1180] G. Ballesteros, A. Notari, and F. Rompineve, *The H_0 tension: ΔG_N vs. ΔN_{eff}* , *JCAP* **11** (2020) 024, [[arXiv:2004.05049](#)].
- [1181] T. Abadi and E. D. Kovetz, *Can conformally coupled modified gravity solve the Hubble tension?*, *Phys. Rev. D* **103** (2021), no. 2 023530, [[arXiv:2011.13853](#)].
- [1182] P. Brax, C. van de Bruck, S. Clesse, A.-C. Davis, and G. Sculthorpe, *Early Modified Gravity: Implications for Cosmology*, *Phys. Rev. D* **89** (2014), no. 12 123507, [[arXiv:1312.3361](#)].
- [1183] V. Pettorino and L. Amendola, *Friction in Gravitational Waves: a test for early-time modified gravity*, *Phys. Lett. B* **742** (2015) 353–357, [[arXiv:1408.2224](#)].
- [1184] N. A. Lima, V. Smer-Barreto, and L. Lombriser, *Constraints on decaying early modified gravity from cosmological observations*, *Phys. Rev. D* **94** (2016), no. 8 083507, [[arXiv:1603.05239](#)].
- [1185] A. Hall, *Cosmology from weak lensing alone and implications for the Hubble tension*, [arXiv:2104.12880](#).
- [1186] M. Asgari et al., *KiDS+VIKING-450 and DES-Y1 combined: Mitigating baryon feedback uncertainty with COSEBIs*, *Astron. Astrophys.* **634** (2020) A127, [[arXiv:1910.05336](#)].
- [1187] F. Köhlinger et al., *KiDS-450: The tomographic weak lensing power spectrum and constraints on cosmological parameters*, *Mon. Not. Roy. Astron. Soc.* **471** (2017), no. 4 4412–4435, [[arXiv:1706.02892](#)].
- [1188] H. Hildebrandt et al., *KiDS-450: Cosmological parameter constraints from tomographic weak gravitational lensing*, *Mon. Not. Roy. Astron. Soc.* **465** (2017) 1454, [[arXiv:1606.05338](#)].
- [1189] **DES** Collaboration, T. Abbott et al., *Dark Energy Survey Year 1 Results: Cosmological constraints from cluster abundances and weak lensing*, *Phys. Rev. D* **102** (2020), no. 2 023509, [[arXiv:2002.11124](#)].
- [1190] D. Rapetti, S. W. Allen, A. Mantz, and H. Ebeling, *Constraints on modified gravity from the observed X-ray luminosity function of galaxy clusters*, *Mon. Not. Roy. Astron. Soc.* **400** (2009) 699, [[arXiv:0812.2259](#)].
- [1191] **DSDD** Collaboration, E. Rozo et al., *Cosmological Constraints from the SDSS *maxBCG* Cluster Catalog*, *Astrophys. J.* **708** (2010) 645–660, [[arXiv:0902.3702](#)].
- [1192] A. Mantz, S. W. Allen, D. Rapetti, and H. Ebeling, *The Observed Growth of Massive Galaxy Clusters I: Statistical Methods and Cosmological Constraints*, *Mon. Not. Roy. Astron. Soc.* **406** (2010) 1759–1772, [[arXiv:0909.3098](#)].
- [1193] **Planck** Collaboration, P. Ade et al., *Planck 2015 results. XXIV. Cosmology from Sunyaev-Zeldovich cluster counts*, *Astron. Astrophys.* **594** (2016) A24, [[arXiv:1502.01597](#)].

- [1194] **DES** Collaboration, M. Costanzi et al., *Methods for cluster cosmology and application to the SDSS in preparation for DES Year 1 release*, *Mon. Not. Roy. Astron. Soc.* **488** (2019), no. 4 4779–4800, [[arXiv:1810.09456](#)].
- [1195] **DES, SPT** Collaboration, M. Costanzi et al., *Cosmological constraints from DES Y1 cluster abundances and SPT multiwavelength data*, *Phys. Rev. D* **103** (2021), no. 4 043522, [[arXiv:2010.13800](#)].
- [1196] B. Sagredo, S. Nesseris, and D. Sapone, *Internal Robustness of Growth Rate data*, *Phys. Rev. D* **98** (2018), no. 8 083543, [[arXiv:1806.10822](#)].
- [1197] L. Perivolaropoulos and L. Kazantzidis, *Hints of modified gravity in cosmos and in the lab?*, *Int. J. Mod. Phys. D* **28** (2019), no. 05 1942001, [[arXiv:1904.09462](#)].
- [1198] R. Arjona, J. García-Bellido, and S. Nesseris, *Cosmological constraints on nonadiabatic dark energy perturbations*, *Phys. Rev. D* **102** (2020), no. 10 103526, [[arXiv:2006.01762](#)].
- [1199] S. Tsujikawa, *Possibility of realizing weak gravity in redshift space distortion measurements*, *Phys. Rev. D* **92** (2015), no. 4 044029, [[arXiv:1505.02459](#)].
- [1200] **KiDS** Collaboration, M. Asgari et al., *KiDS-1000 Cosmology: Cosmic shear constraints and comparison between two point statistics*, *Astron. Astrophys.* **645** (2021) A104, [[arXiv:2007.15633](#)].
- [1201] S. Joudaki et al., *KiDS+VIKING-450 and DES-Y1 combined: Cosmology with cosmic shear*, *Astron. Astrophys.* **638** (2020) L1, [[arXiv:1906.09262](#)].
- [1202] A. H. Wright, H. Hildebrandt, J. L. van den Busch, C. Heymans, B. Joachimi, A. Kannawadi, and K. Kuijken, *KiDS+VIKING-450: Improved cosmological parameter constraints from redshift calibration with self-organising maps*, *Astron. Astrophys.* **640** (2020) L14, [[arXiv:2005.04207](#)].
- [1203] H. Hildebrandt et al., *KiDS+VIKING-450: Cosmic shear tomography with optical and infrared data*, *Astron. Astrophys.* **633** (2020) A69, [[arXiv:1812.06076](#)].
- [1204] **DES** Collaboration, A. Amon et al., *Dark Energy Survey Year 3 results: Cosmology from cosmic shear and robustness to data calibration*, *Phys. Rev. D* **105** (2022), no. 2 023514, [[arXiv:2105.13543](#)].
- [1205] **DES** Collaboration, L. F. Secco et al., *Dark Energy Survey Year 3 results: Cosmology from cosmic shear and robustness to modeling uncertainty*, *Phys. Rev. D* **105** (2022), no. 2 023515, [[arXiv:2105.13544](#)].
- [1206] T. Hamana et al., *Cosmological constraints from cosmic shear two-point correlation functions with HSC survey first-year data*, *Publ. Astron. Soc. Jap.* **72** no. 1 Publications of the Astronomical Society of Japan, Volume 72, Issue 1, February 2020, 16, [[arXiv:1906.06041](#)].
- [1207] **KiDS, Euclid** Collaboration, A. Loureiro et al., *KiDS & Euclid: Cosmological implications of a pseudo angular power spectrum analysis of KiDS-1000 cosmic shear tomography*, [[arXiv:2110.06947](#)].
- [1208] **HSC** Collaboration, C. Hikage et al., *Cosmology from cosmic shear power spectra with Subaru Hyper Suprime-Cam first-year data*, *Publ. Astron. Soc. Jap.* **71** no. 2 Publications of the Astronomical Society of Japan, Volume 71, Issue 2, April 2019, 43, [[arXiv:1809.09148](#)].
- [1209] S. Joudaki et al., *CFHTLenS revisited: assessing concordance with Planck including astrophysical systematics*, *Mon. Not. Roy. Astron. Soc.* **465** (2017), no. 2 2033–2052, [[arXiv:1601.05786](#)].

- [1210] **DES, SPT** Collaboration, C. Chang et al., *Joint analysis of DES Year 3 data and CMB lensing from SPT and Planck II: Cross-correlation measurements and cosmological constraints*, [arXiv:2203.12440](#).
- [1211] H. Miyatake et al., *Cosmological inference from the emulator based halo model II: Joint analysis of galaxy-galaxy weak lensing and galaxy clustering from HSC-Y1 and SDSS*, [arXiv:2111.02419](#).
- [1212] C. García-García, J. R. Zapatero, D. Alonso, E. Bellini, P. G. Ferreira, E.-M. Mueller, A. Nicola, and P. Ruiz-Lapuente, *The growth of density perturbations in the last ~ 10 billion years from tomographic large-scale structure data*, *JCAP* **10** (2021) 030, [[arXiv:2105.12108](#)].
- [1213] C. Heymans et al., *KiDS-1000 Cosmology: Multi-probe weak gravitational lensing and spectroscopic galaxy clustering constraints*, *Astron. Astrophys.* **646** (2021) A140, [[arXiv:2007.15632](#)].
- [1214] E. van Uitert et al., *KiDS+GAMA: cosmology constraints from a joint analysis of cosmic shear, galaxy-galaxy lensing, and angular clustering*, *Mon. Not. Roy. Astron. Soc.* **476** (2018), no. 4 4662–4689, [[arXiv:1706.05004](#)].
- [1215] **DES** Collaboration, T. M. C. Abbott et al., *Dark Energy Survey Year 3 Results: Cosmological Constraints from Galaxy Clustering and Weak Lensing*, [arXiv:2105.13549](#).
- [1216] T. Tröster et al., *Cosmology from large-scale structure: Constraining Λ CDM with BOSS*, *Astron. Astrophys.* **633** (2020) L10, [[arXiv:1909.11006](#)].
- [1217] M. M. Ivanov, *Cosmological constraints from the power spectrum of eBOSS emission line galaxies*, *Phys. Rev. D* **104** (2021), no. 10 103514, [[arXiv:2106.12580](#)].
- [1218] M. White et al., *Cosmological constraints from the tomographic cross-correlation of DESI Luminous Red Galaxies and Planck CMB lensing*, *JCAP* **02** (2022), no. 02 007, [[arXiv:2111.09898](#)].
- [1219] A. Krolewski, S. Ferraro, and M. White, *Cosmological constraints from unWISE and Planck CMB lensing tomography*, *JCAP* **12** (2021), no. 12 028, [[arXiv:2105.03421](#)].
- [1220] G. F. Lesci et al., *AMICO galaxy clusters in KiDS-DR3: cosmological constraints from counts and stacked weak-lensing*, *Astron. Astrophys.* **659** (2022) A88, [[arXiv:2012.12273](#)].
- [1221] A. B. Mantz et al., *Weighing the giants – IV. Cosmology and neutrino mass*, *Mon. Not. Roy. Astron. Soc.* **446** (2015) 2205–2225, [[arXiv:1407.4516](#)].
- [1222] **XXL** Collaboration, F. Pacaud et al., *The XXL Survey: XXV. Cosmological analysis of the C1 cluster number counts*, *Astron. Astrophys.* **620** (2018) A10, [[arXiv:1810.01624](#)].
- [1223] **SPT** Collaboration, S. Bocquet et al., *Cluster Cosmology Constraints from the 2500 deg² SPT-SZ Survey: Inclusion of Weak Gravitational Lensing Data from Magellan and the Hubble Space Telescope*, *Astrophys. J.* **878** (2019), no. 1 55, [[arXiv:1812.01679](#)].
- [1224] L. Salvati, M. Douspis, and N. Aghanim, *Constraints from thermal Sunyaev-Zel’dovich cluster counts and power spectrum combined with CMB*, *Astron. Astrophys.* **614** (2018) A13, [[arXiv:1708.00697](#)].
- [1225] R. C. Nunes and S. Vagnozzi, *Arbitrating the S8 discrepancy with growth rate measurements from redshift-space distortions*, *Mon. Not. Roy. Astron. Soc.* **505** (2021), no. 4 5427–5437, [[arXiv:2106.01208](#)].
- [1226] M. Bartelmann and P. Schneider, *Weak gravitational lensing*, *Phys. Rept.* **340** (2001) 291–472, [[astro-ph/9912508](#)].

- [1227] M. Kilbinger, *Cosmology with cosmic shear observations: a review*, *Rept. Prog. Phys.* **78** (2015) 086901, [[arXiv:1411.0115](#)].
- [1228] R. Mandelbaum, *Weak lensing for precision cosmology*, *Ann. Rev. Astron. Astrophys.* **56** (2018) 393–433, [[arXiv:1710.03235](#)].
- [1229] D. J. Bacon, A. R. Refregier, and R. S. Ellis, *Detection of weak gravitational lensing by large-scale structure*, *Mon. Not. Roy. Astron. Soc.* **318** (2000) 625, [[astro-ph/0003008](#)].
- [1230] N. Kaiser, G. Wilson, and G. A. Luppino, *Large scale cosmic shear measurements*, [astro-ph/0003338](#).
- [1231] D. M. Wittman, J. A. Tyson, D. Kirkman, I. Dell’Antonio, and G. Bernstein, *Detection of weak gravitational lensing distortions of distant galaxies by cosmic dark matter at large scales*, *Nature* **405** (2000) 143–149, [[astro-ph/0003014](#)].
- [1232] L. van Waerbeke et al., *Detection of correlated galaxy ellipticities on CFHT data: First evidence for gravitational lensing by large scale structures*, *Astron. Astrophys.* **358** (2000) 30–44, [[astro-ph/0002500](#)].
- [1233] T. G. Brainerd, R. D. Blandford, and I. Smail, *Measuring galaxy masses using galaxy - galaxy gravitational lensing*, *Astrophys. J.* **466** (1996) 623, [[astro-ph/9503073](#)].
- [1234] M. J. Hudson, S. D. J. Gwyn, H. Dahle, and N. Kaiser, *Galaxy-galaxy lensing in the Hubble Deep Field: The Halo Tully-Fisher relation at intermediate redshift*, *Astrophys. J.* **503** (1998) 531, [[astro-ph/9711341](#)].
- [1235] **Astro-WISE, KiDS** Collaboration, J. T. A. de Jong, G. A. Verdoes Kleijn, K. H. Kuijken, and E. A. Valentijn, *The Kilo-Degree Survey, Exper. Astron.* **35** (2013) 25–44, [[arXiv:1206.1254](#)].
- [1236] J. T. A. de Jong et al., *The first and second data releases of the Kilo-Degree Survey*, *Astron. Astrophys.* **582** (2015) A62, [[arXiv:1507.00742](#)].
- [1237] J. T. A. de Jong et al., *The third data release of the Kilo-Degree Survey and associated data products*, *Astron. Astrophys.* **604** (2017) A134, [[arXiv:1703.02991](#)].
- [1238] K. Kuijken et al., *Gravitational Lensing Analysis of the Kilo Degree Survey*, *Mon. Not. Roy. Astron. Soc.* **454** (2015), no. 4 3500–3532, [[arXiv:1507.00738](#)].
- [1239] S. Miyazaki et al., *Properties of Weak Lensing Clusters Detected on Hyper Suprime-Cam’s 2.3 deg² Field*, *Astrophys. J.* **807** (2015), no. 1 22, [[arXiv:1504.06974](#)].
- [1240] H. Aihara et al., *First Data Release of the Hyper Suprime-Cam Subaru Strategic Program*, *Publ. Astron. Soc. Jap.* **70** (2018) S8, [[arXiv:1702.08449](#)].
- [1241] **DES** Collaboration, T. Abbott et al., *The dark energy survey*, [astro-ph/0510346](#).
- [1242] **DES** Collaboration, M. Jarvis et al., *The DES Science Verification Weak Lensing Shear Catalogues*, *Mon. Not. Roy. Astron. Soc.* **460** (2016), no. 2 2245–2281, [[arXiv:1507.05603](#)].
- [1243] C. Heymans et al., *CFHTLenS: The Canada-France-Hawaii Telescope Lensing Survey*, *Mon. Not. Roy. Astron. Soc.* **427** (2012) 146, [[arXiv:1210.0032](#)].
- [1244] H. Hildebrandt et al., *CFHTLenS: Improving the quality of photometric redshifts with precision photometry*, *Mon. Not. Roy. Astron. Soc.* **421** (2012) 2355, [[arXiv:1111.4434](#)].
- [1245] T. Erben et al., *CFHTLenS: The Canada-France-Hawaii Telescope Lensing Survey - Imaging Data and Catalogue Products*, *Mon. Not. Roy. Astron. Soc.* **433** (2013) 2545, [[arXiv:1210.8156](#)].

- [1246] C. Heymans et al., *CFHTLenS tomographic weak lensing cosmological parameter constraints: Mitigating the impact of intrinsic galaxy alignments*, *Mon. Not. Roy. Astron. Soc.* **432** (2013) 2433, [[arXiv:1303.1808](#)].
- [1247] L. Miller et al., *Bayesian Galaxy Shape Measurement for Weak Lensing Surveys - III. Application to the Canada-France-Hawaii Telescope Lensing Survey*, *Mon. Not. Roy. Astron. Soc.* **429** (2013) 2858–2880, [[arXiv:1210.8201](#)].
- [1248] M. Arnaboldi, M. J. Neeser, L. C. Parker, P. Rosati, M. Lombardi, J. P. Dietrich, and W. Hummel, *ESO Public Surveys with the VST and VISTA*, *The Messenger* **127** (Mar., 2007) 28.
- [1249] **DES Collaboration**, P. Lemos et al., *Assessing tension metrics with Dark Energy Survey and Planck data*, [arXiv:2012.09554](#).
- [1250] K. Kuijken et al., *The fourth data release of the Kilo-Degree Survey: ugri imaging and nine-band optical-IR photometry over 1000 square degrees*, *Astron. Astrophys.* **625** (2019) A2, [[arXiv:1902.11265](#)].
- [1251] E. Hivon, K. M. Gorski, C. B. Netterfield, B. P. Crill, S. Prunet, and F. Hansen, *Master of the cosmic microwave background anisotropy power spectrum: a fast method for statistical analysis of large and complex cosmic microwave background data sets*, *Astrophys. J.* **567** (2002) 2, [[astro-ph/0105302](#)].
- [1252] M. L. Brown, P. G. Castro, and A. N. Taylor, *CMB temperature and polarisation pseudo- $C(l)$ estimators and covariances*, *Mon. Not. Roy. Astron. Soc.* **360** (2005) 1262–1280, [[astro-ph/0410394](#)].
- [1253] **LSST Dark Energy Science Collaboration**, D. Alonso, J. Sanchez, and A. Slosar, *A unified pseudo- C_ℓ framework*, *Mon. Not. Roy. Astron. Soc.* **484** (2019), no. 3 4127–4151, [[arXiv:1809.09603](#)].
- [1254] B. D. Wandelt, E. Hivon, and K. M. Gorski, *The pseudo- c_l method: cosmic microwave background anisotropy power spectrum statistics for high precision cosmology*, *Phys. Rev. D* **64** (2001) 083003, [[astro-ph/0008111](#)].
- [1255] C. Blake et al., *The 2-degree Field Lensing Survey: design and clustering measurements*, *Mon. Not. Roy. Astron. Soc.* **462** (2016), no. 4 4240–4265, [[arXiv:1608.02668](#)].
- [1256] A. E. Evrard, *Biased Cold Dark Matter Theory: Trouble from Rich Clusters?*, *The Astrophysical Journal* **341** (June, 1989) L71.
- [1257] P. J. E. Peebles, R. A. Daly, and R. Juszkiewicz, *The Masses of Rich Clusters of Galaxies as a Test of the Biased Cold Dark Matter Theory*, *Astroph. J.* **347** (Dec., 1989) 563.
- [1258] S. W. Allen, A. E. Evrard, and A. B. Mantz, *Cosmological Parameters from Observations of Galaxy Clusters*, *Ann. Rev. Astron. Astrophys.* **49** (2011) 409–470, [[arXiv:1103.4829](#)].
- [1259] A. Kravtsov and S. Borgani, *Formation of Galaxy Clusters*, *Ann. Rev. Astron. Astrophys.* **50** (2012) 353–409, [[arXiv:1205.5556](#)].
- [1260] M. Birkinshaw, *The Sunyaev-Zel’dovich effect*, *Phys. Rept.* **310** (1999) 97–195, [[astro-ph/9808050](#)].
- [1261] J. E. Carlstrom, G. P. Holder, and E. D. Reese, *Cosmology with the Sunyaev-Zel’dovich effect*, *Ann. Rev. Astron. Astrophys.* **40** (2002) 643–680, [[astro-ph/0208192](#)].

- [1262] T. Mroczkowski et al., *Astrophysics with the Spatially and Spectrally Resolved Sunyaev-Zeldovich Effects: A Millimetre/Submillimetre Probe of the Warm and Hot Universe*, *Space Sci. Rev.* **215** (2019), no. 1 17, [[arXiv:1811.02310](#)].
- [1263] R. Sunyaev and Y. Zeldovich, *The Interaction of matter and radiation in the hot model of the universe*, *Astrophys. Space Sci.* **7** (1970) 20–30.
- [1264] R. Sunyaev and Y. Zeldovich, *The Observations of relic radiation as a test of the nature of X-Ray radiation from the clusters of galaxies*, *Comments Astrophys. Space Phys.* **4** (1972) 173–178.
- [1265] R. A. Sunyaev and Y. B. Zeldovich, *Microwave background radiation as a probe of the contemporary structure and history of the universe*, *Ann. Rev. Astron. Astrophys.* **18** (1980) 537–560.
- [1266] P. Predehl et al., *eROSITA on SRG*, *Proc. SPIE Int. Soc. Opt. Eng.* **7732** (2010) 77320U, [[arXiv:1001.2502](#)].
- [1267] **eROSITA** Collaboration, A. Merloni et al., *eROSITA Science Book: Mapping the Structure of the Energetic Universe*, [arXiv:1209.3114](#).
- [1268] A. Pillepich, C. Porciani, and T. H. Reiprich, *The X-ray cluster survey with eROSITA: forecasts for cosmology, cluster physics, and primordial non-Gaussianity*, *Mon. Not. Roy. Astron. Soc.* **422** (2012) 44–69, [[arXiv:1111.6587](#)].
- [1269] F. Hofmann, J. S. Sanders, N. Clerc, K. Nandra, J. Ridl, K. Dennerl, M. Ramos-Ceja, A. Finoguenov, and T. H. Reiprich, *eROSITA cluster cosmology forecasts: cluster temperature substructure bias*, *Astron. Astrophys.* **606** (2017) A118, [[arXiv:1708.05205](#)].
- [1270] M. Hasselfield et al., *The Atacama Cosmology Telescope: Sunyaev-Zel’dovich selected galaxy clusters at 148 GHz from three seasons of data*, *JCAP* **07** (2013) 008, [[arXiv:1301.0816](#)].
- [1271] **SPT** Collaboration, L. E. Bleem et al., *Galaxy Clusters Discovered via the Sunyaev-Zel’dovich Effect in the 2500-square-degree SPT-SZ survey*, *Astrophys. J. Suppl.* **216** (2015), no. 2 27, [[arXiv:1409.0850](#)].
- [1272] **DES** Collaboration, M. Klein et al., *A multicomponent matched filter cluster confirmation tool for eROSITA: initial application to the RASS and DES-SV data sets*, *Mon. Not. Roy. Astron. Soc.* **474** (2018), no. 3 3324–3343, [[arXiv:1706.06577](#)].
- [1273] **SPT**, **DES** Collaboration, L. Bleem et al., *The SPTpol Extended Cluster Survey*, *Astrophys. J. Suppl.* **247** (2020), no. 1 25, [[arXiv:1910.04121](#)].
- [1274] W. H. Press and P. Schechter, *Formation of galaxies and clusters of galaxies by selfsimilar gravitational condensation*, *Astrophys. J.* **187** (1974) 425–438.
- [1275] A. Jenkins, C. Frenk, S. D. White, J. Colberg, S. Cole, A. E. Evrard, H. Couchman, and N. Yoshida, *The Mass function of dark matter halos*, *Mon. Not. Roy. Astron. Soc.* **321** (2001) 372, [[astro-ph/0005260](#)].
- [1276] R. K. Sheth and G. Tormen, *An Excursion Set Model of Hierarchical Clustering : Ellipsoidal Collapse and the Moving Barrier*, *Mon. Not. Roy. Astron. Soc.* **329** (2002) 61, [[astro-ph/0105113](#)].
- [1277] M. J. White, *The Mass function*, *Astrophys. J. Suppl.* **143** (2002) 241, [[astro-ph/0207185](#)].
- [1278] M. S. Warren, K. Abazajian, D. E. Holz, and L. Teodoro, *Precision determination of the mass function of dark matter halos*, *Astrophys. J.* **646** (2006) 881–885, [[astro-ph/0506395](#)].

- [1279] J. L. Tinker, A. V. Kravtsov, A. Klypin, K. Abazajian, M. S. Warren, G. Yepes, S. Gottlober, and D. E. Holz, *Toward a halo mass function for precision cosmology: The Limits of universality*, *Astrophys. J.* **688** (2008) 709–728, [[arXiv:0803.2706](#)].
- [1280] M. Kilbinger et al., *CFHTLenS: Combined probe cosmological model comparison using 2D weak gravitational lensing*, *Mon. Not. Roy. Astron. Soc.* **430** (2013) 2200–2220, [[arXiv:1212.3338](#)].
- [1281] N. Sabti, J. B. Muñoz, and D. Blas, *Galaxy luminosity function pipeline for cosmology and astrophysics*, *Phys. Rev. D* **105** (2022), no. 4 043518, [[arXiv:2110.13168](#)].
- [1282] N. Sabti, J. B. Muñoz, and D. Blas, *New Roads to the Small-Scale Universe: Measurements of the Clustering of Matter with the High-Redshift UV Galaxy Luminosity Function*, [[arXiv:2110.13161](#)].
- [1283] H. Atek, J. Richard, J.-P. Kneib, and D. Schaerer, *The Extreme Faint End of the UV Luminosity Function at $z \sim 6$ Through Gravitational Telescopes: a comprehensive assessment of strong lensing uncertainties*, *Mon. Not. Roy. Astron. Soc.* **479** (2018), no. 4 5184–5195, [[arXiv:1803.09747](#)].
- [1284] R. J. Bouwens et al., *UV Luminosity Functions at redshifts $z \sim 4$ to $z \sim 10$: 10000 Galaxies from HST Legacy Fields*, *Astrophys. J.* **803** (2015), no. 1 34, [[arXiv:1403.4295](#)].
- [1285] A. von der Linden et al., *Weighing the Giants – I. Weak-lensing masses for 51 massive galaxy clusters: project overview, data analysis methods and cluster images*, *Mon. Not. Roy. Astron. Soc.* **439** (2014), no. 1 2–27, [[arXiv:1208.0597](#)].
- [1286] D. E. Applegate, A. von der Linden, P. L. Kelly, M. T. Allen, S. W. Allen, P. R. Burchat, D. L. Burke, H. Ebeling, A. Mantz, and R. G. Morris, *Weighing the Giants – III. Methods and measurements of accurate galaxy cluster weak-lensing masses*, *Mon. Not. Roy. Astron. Soc.* **439** (2014), no. 1 48–72, [[arXiv:1208.0605](#)].
- [1287] J. Truemper, *ROSAT-A New Look at the X-ray Sky*, *Science* **260** (June, 1993) 1769–1771.
- [1288] M. Pierre et al., *The XXL Survey - I. Scientific motivations – XMM-Newton observing plan – Follow-up observations and simulation programme*, *Astron. Astrophys.* **592** (2016) A1, [[arXiv:1512.04317](#)].
- [1289] SPT Collaboration, T. de Haan et al., *Cosmological Constraints from Galaxy Clusters in the 2500 square-degree SPT-SZ Survey*, *Astrophys. J.* **832** (2016), no. 1 95, [[arXiv:1603.06522](#)].
- [1290] M. H. Abdullah, A. Klypin, and G. Wilson, *Cosmological Constraints on Ω_m and σ_8 from Cluster Abundances Using the GalWCat19 Optical-spectroscopic SDSS Catalog*, *Astrophys. J.* **901** (2020), no. 2 90, [[arXiv:2002.11907](#)].
- [1291] M. Kirby, E. Rozo, R. G. Morris, S. W. Allen, M. Costanzi, T. E. Jeltema, A. B. Mantz, A. K. Romer, E. S. Rykoff, and A. von der Linden, *Improved Cosmological Constraints from SDSS redMaPPer Clusters via X-ray Follow-up of a Complete Subsample of Systems*, [[arXiv:1910.13548](#)].
- [1292] G. Schellenberger and T. H. Reiprich, *HICOSMO: cosmology with a complete sample of galaxy clusters – II. Cosmological results*, *Mon. Not. Roy. Astron. Soc.* **471** (2017), no. 2 1370–1389, [[arXiv:1705.05843](#)].
- [1293] M. Ntampaka, K. Rines, and H. Trac, *Cluster Cosmology with the Velocity Distribution Function of the HeCS-SZ Sample*, *Astrophys. J.* **880** (2019) 154, [[arXiv:1906.07729](#)].

- [1294] I. n. Zubeldia and A. Challinor, *Cosmological constraints from Planck galaxy clusters with CMB lensing mass bias calibration*, *Mon. Not. Roy. Astron. Soc.* **489** (2019), no. 1 401–419, [[arXiv:1904.07887](#)].
- [1295] M. H. Abdullah, G. Wilson, A. Klypin, L. Old, E. Praton, and G. Ali, *GalWeight Application: A Publicly Available Catalog of Dynamical Parameters of 1800 Galaxy Clusters from SDSS-DR13, (GalWCat19)*, *Astrophys. J. Suppl.* **246** (2020), no. 1 2, [[arXiv:1907.05061](#)].
- [1296] **SDSS** Collaboration, F. D. Albareti et al., *The 13th Data Release of the Sloan Digital Sky Survey: First Spectroscopic Data from the SDSS-IV Survey Mapping Nearby Galaxies at Apache Point Observatory*, *Astrophys. J. Suppl.* **233** (2017), no. 2 25, [[arXiv:1608.02013](#)].
- [1297] N. Kaiser, *Clustering in real space and in redshift space*, *Mon. Not. Roy. Astron. Soc.* **227** (1987) 1–27.
- [1298] A. J. S. Hamilton, *Measuring Omega and the real correlation function from the redshift correlation function*, *Astrophys. J. Lett.* **385** (1992) L5–L8.
- [1299] A. J. S. Hamilton, *Linear redshift distortions: A Review*, in *Ringberg Workshop on Large Scale Structure Ringberg, Germany, September 23-28, 1996*, 1997. [astro-ph/9708102](#).
- [1300] L.-M. Wang and P. J. Steinhardt, *Cluster abundance constraints on quintessence models*, *Astrophys. J.* **508** (1998) 483–490, [[astro-ph/9804015](#)].
- [1301] E. V. Linder, *Cosmic growth history and expansion history*, *Phys. Rev.* **D72** (2005) 043529, [[astro-ph/0507263](#)].
- [1302] D. Polarski and R. Gannouji, *On the growth of linear perturbations*, *Phys. Lett.* **B660** (2008) 439–443, [[arXiv:0710.1510](#)].
- [1303] O. Lahav, P. B. Lilje, J. R. Primack, and M. J. Rees, *Dynamical effects of the cosmological constant*, *Mon. Not. Roy. Astron. Soc.* **251** (1991) 128–136.
- [1304] A. De Felice, S. Mukohyama, and S. Tsujikawa, *Density perturbations in general modified gravitational theories*, *Phys. Rev. D* **82** (2010) 023524, [[arXiv:1006.0281](#)].
- [1305] S. Tsujikawa, *Matter density perturbations and effective gravitational constant in modified gravity models of dark energy*, *Phys. Rev.* **D76** (2007) 023514, [[arXiv:0705.1032](#)].
- [1306] S. Nesseris and A. Mazumdar, *Newton’s constant in $f(R, R_{\mu\nu}R^{\mu\nu}, \square R)$ theories of gravity and constraints from BBN*, *Phys. Rev. D* **79** (2009) 104006, [[arXiv:0902.1185](#)].
- [1307] S. Nesseris, C. Blake, T. Davis, and D. Parkinson, *The WiggleZ Dark Energy Survey: constraining the evolution of Newton’s constant using the growth rate of structure*, *JCAP* **1107** (2011) 037, [[arXiv:1107.3659](#)].
- [1308] S. Nesseris and D. Sapone, *Accuracy of the growth index in the presence of dark energy perturbations*, *Phys. Rev.* **D92** (2015), no. 2 023013, [[arXiv:1505.06601](#)].
- [1309] W. J. Percival, *Cosmological structure formation in a homogeneous dark energy background*, *Astron. Astrophys.* **443** (2005) 819, [[astro-ph/0508156](#)].
- [1310] S. Basilakos and S. Nesseris, *Testing Einstein’s gravity and dark energy with growth of matter perturbations: Indications for new physics?*, *Phys. Rev.* **D94** (2016), no. 12 123525, [[arXiv:1610.00160](#)].
- [1311] W. Cardona, R. Arjona, A. Estrada, and S. Nesseris, *Cosmological constraints with the Effective Fluid approach for Modified Gravity*, [arXiv:2012.05282](#).

- [1312] J. A. Peacock et al., *A Measurement of the cosmological mass density from clustering in the 2dF Galaxy Redshift Survey*, *Nature* **410** (2001) 169–173, [[astro-ph/0103143](#)].
- [1313] E. Hawkins et al., *The 2dF Galaxy Redshift Survey: Correlation functions, peculiar velocities and the matter density of the universe*, *Mon. Not. Roy. Astron. Soc.* **346** (2003) 78, [[astro-ph/0212375](#)].
- [1314] L. Guzzo et al., *A test of the nature of cosmic acceleration using galaxy redshift distortions*, *Nature* **451** (2008) 541–545, [[arXiv:0802.1944](#)].
- [1315] L. Samushia, W. J. Percival, and A. Raccanelli, *Interpreting large-scale redshift-space distortion measurements*, *Monthly Notices of the Royal Astronomical Society* **420** (2012), no. 3 2102–2119.
- [1316] B. A. Reid et al., *The clustering of galaxies in the SDSS-III Baryon Oscillation Spectroscopic Survey: measurements of the growth of structure and expansion rate at $z=0.57$ from anisotropic clustering*, *Mon. Not. Roy. Astron. Soc.* **426** (2012) 2719, [[arXiv:1203.6641](#)].
- [1317] R. Tojeiro, W. J. Percival, J. Brinkmann, J. R. Brownstein, D. J. Eisenstein, M. Manera, C. Maraston, C. K. McBride, D. Muna, B. Reid, A. J. Ross, N. P. Ross, L. Samushia, N. Padmanabhan, D. P. Schneider, R. Skibba, A. G. Sánchez, M. E. C. Swanson, D. Thomas, J. L. Tinker, L. Verde, D. A. Wake, B. A. Weaver, and G.-B. Zhao, *The clustering of galaxies in the sdss-iii baryon oscillation spectroscopic survey: measuring structure growth using passive galaxies*, *Monthly Notices of the Royal Astronomical Society* **424** (2012), no. 3 2339–2344.
- [1318] C.-H. Chuang et al., *The clustering of galaxies in the SDSS-III Baryon Oscillation Spectroscopic Survey: single-probe measurements and the strong power of normalized growth rate on constraining dark energy*, *Mon. Not. Roy. Astron. Soc.* **433** (2013) 3559, [[arXiv:1303.4486](#)].
- [1319] C. Howlett, A. Ross, L. Samushia, W. Percival, and M. Manera, *The clustering of the SDSS main galaxy sample – II. Mock galaxy catalogues and a measurement of the growth of structure from redshift space distortions at $z = 0.15$* , *Mon. Not. Roy. Astron. Soc.* **449** (2015), no. 1 848–866, [[arXiv:1409.3238](#)].
- [1320] C. Blake et al., *The WiggleZ Dark Energy Survey: the growth rate of cosmic structure since redshift $z=0.9$* , *Mon. Not. Roy. Astron. Soc.* **415** (2011) 2876, [[arXiv:1104.2948](#)].
- [1321] A. Johnson et al., *The 6dF Galaxy Survey: cosmological constraints from the velocity power spectrum*, *Mon. Not. Roy. Astron. Soc.* **444** (2014), no. 4 3926–3947, [[arXiv:1404.3799](#)].
- [1322] F. Simpson, C. Blake, J. A. Peacock, I. Baldry, J. Bland-Hawthorn, A. Heavens, C. Heymans, J. Loveday, and P. Norberg, *Galaxy and mass assembly: Redshift space distortions from the clipped galaxy field*, *Phys. Rev. D* **93** (2016), no. 2 023525, [[arXiv:1505.03865](#)].
- [1323] M. White, B. Reid, C.-H. Chuang, J. L. Tinker, C. K. McBride, F. Prada, and L. Samushia, *Tests of redshift-space distortions models in configuration space for the analysis of the BOSS final data release*, *Mon. Not. Roy. Astron. Soc.* **447** (2015) 234–245, [[arXiv:1408.5435](#)].
- [1324] Z. Li, Y. Jing, P. Zhang, and D. Cheng, *Measurement of Redshift-Space Power Spectrum for BOSS galaxies and the Growth Rate at redshift 0.57*, *Astrophys. J.* **833** (2016), no. 2 287, [[arXiv:1609.03697](#)].
- [1325] H. Gil-Marín, W. J. Percival, L. Verde, J. R. Brownstein, C.-H. Chuang, F.-S. Kitaura, S. A. Rodríguez-Torres, and M. D. Olmstead, *The clustering of galaxies in the SDSS-III Baryon Oscillation Spectroscopic Survey: RSD measurement from the power spectrum and bispectrum of the DR12 BOSS galaxies*, *Mon. Not. Roy. Astron. Soc.* **465** (2017), no. 2 1757–1788, [[arXiv:1606.00439](#)].

- [1326] T. Okumura et al., *The Subaru FMOS galaxy redshift survey (FastSound). IV. New constraint on gravity theory from redshift space distortions at $z \sim 1.4$* , *Publ. Astron. Soc. Jap.* **68** (2016), no. 3, id. 38 24, [[arXiv:1511.08083](#)].
- [1327] S. de la Torre et al., *The VIMOS Public Extragalactic Redshift Survey (VIPERS). Galaxy clustering and redshift-space distortions at $z=0.8$ in the first data release*, *Astron. Astrophys.* **557** (2013) A54, [[arXiv:1303.2622](#)].
- [1328] A. Pezzotta et al., *The VIMOS Public Extragalactic Redshift Survey (VIPERS): The growth of structure at $0.5 < z < 1.2$ from redshift-space distortions in the clustering of the PDR-2 final sample*, *Astron. Astrophys.* **604** (2017) A33, [[arXiv:1612.05645](#)].
- [1329] F. G. Mohammad et al., *The VIMOS Public Extragalactic Redshift Survey (VIPERS): Unbiased clustering estimate with VIPERS slit assignment*, *Astron. Astrophys.* **619** (2018) A17, [[arXiv:1807.05999](#)].
- [1330] G.-B. Zhao et al., *The clustering of the SDSS-IV extended Baryon Oscillation Spectroscopic Survey DR14 quasar sample: a tomographic measurement of cosmic structure growth and expansion rate based on optimal redshift weights*, *Mon. Not. Roy. Astron. Soc.* **482** (2019), no. 3 3497–3513, [[arXiv:1801.03043](#)].
- [1331] A. Tamone et al., *The Completed SDSS-IV extended Baryon Oscillation Spectroscopic Survey: Growth rate of structure measurement from anisotropic clustering analysis in configuration space between redshift 0.6 and 1.1 for the Emission Line Galaxy sample*, *Mon. Not. Roy. Astron. Soc.* **499** (2020), no. 4 5527–5546, [[arXiv:2007.09009](#)].
- [1332] C. Zhao et al., *The Completed SDSS-IV extended Baryon Oscillation Spectroscopic Survey: one thousand multi-tracer mock catalogues with redshift evolution and systematics for galaxies and quasars of the final data release*, *Mon. Not. Roy. Astron. Soc.* **503** (2021), no. 1 1149–1173, [[arXiv:2007.08997](#)].
- [1333] J. E. Bautista et al., *The Completed SDSS-IV extended Baryon Oscillation Spectroscopic Survey: measurement of the BAO and growth rate of structure of the luminous red galaxy sample from the anisotropic correlation function between redshifts 0.6 and 1*, *Mon. Not. Roy. Astron. Soc.* **500** (2020), no. 1 736–762, [[arXiv:2007.08993](#)].
- [1334] G.-B. Zhao et al., *The Completed SDSS-IV extended Baryon Oscillation Spectroscopic Survey: a multi-tracer analysis in Fourier space for measuring the cosmic structure growth and expansion rate*, [arXiv:2007.09011](#).
- [1335] A. de Mattia et al., *The Completed SDSS-IV extended Baryon Oscillation Spectroscopic Survey: measurement of the BAO and growth rate of structure of the emission line galaxy sample from the anisotropic power spectrum between redshift 0.6 and 1.1*, *Mon. Not. Roy. Astron. Soc.* **501** (2021), no. 4 5616–5645, [[arXiv:2007.09008](#)].
- [1336] E. L. Wright et al., *The Wide-field Infrared Survey Explorer (WISE): Mission Description and Initial On-orbit Performance*, *Astron. J.* **140** (2010) 1868, [[arXiv:1008.0031](#)].
- [1337] E. F. Schlafly, A. M. Meisner, and G. M. Green, *The unWISE Catalog: Two Billion Infrared Sources from Five Years of WISE Imaging*, *The Astrophysical Journal Supplement* **240** (Feb., 2019) 30, [[arXiv:1901.03337](#)].
- [1338] **Planck** Collaboration, N. Aghanim et al., *Planck 2018 results. VIII. Gravitational lensing*, *Astron. Astrophys.* **641** (2020) A8, [[arXiv:1807.06210](#)].
- [1339] M. Ishak, *Testing General Relativity in Cosmology*, *Living Rev. Rel.* **22** (2019), no. 1 1, [[arXiv:1806.10122](#)].

- [1340] N. Roy, S. Goswami, and S. Das, *Quintessence or Phantom: Study of scalar field dark energy models through a general parametrization of the Hubble parameter*, [arXiv:2201.09306](#).
- [1341] A. R. Cooray and D. Huterer, *Gravitational lensing as a probe of quintessence*, *Astrophys. J. Lett.* **513** (1999) L95–L98, [[astro-ph/9901097](#)].
- [1342] G. Efstathiou, *Constraining the equation of state of the universe from distant type Ia supernovae and cosmic microwave background anisotropies*, *Mon. Not. Roy. Astron. Soc.* **310** (1999) 842–850, [[astro-ph/9904356](#)].
- [1343] P. Astier, *Can luminosity distance measurements probe the equation of state of dark energy*, *Phys. Lett. B* **500** (2001) 8–15, [[astro-ph/0008306](#)].
- [1344] J. Weller and A. Albrecht, *Future supernovae observations as a probe of dark energy*, *Phys. Rev. D* **65** (2002) 103512, [[astro-ph/0106079](#)].
- [1345] B. Feng, M. Li, Y.-S. Piao, and X. Zhang, *Oscillating quintom and the recurrent universe*, *Phys. Lett. B* **634** (2006) 101–105, [[astro-ph/0407432](#)].
- [1346] S. Nesseris and L. Perivolaropoulos, *Comparison of the legacy and gold snia dataset constraints on dark energy models*, *Phys. Rev. D* **72** (2005) 123519, [[astro-ph/0511040](#)].
- [1347] H. K. Jassal, J. S. Bagla, and T. Padmanabhan, *Observational constraints on low redshift evolution of dark energy: How consistent are different observations?*, *Phys. Rev. D* **72** (2005) 103503, [[astro-ph/0506748](#)].
- [1348] E. M. Barboza, Jr. and J. S. Alcaniz, *A parametric model for dark energy*, *Phys. Lett. B* **666** (2008) 415–419, [[arXiv:0805.1713](#)].
- [1349] W. Yang, R. C. Nunes, S. Pan, and D. F. Mota, *Effects of neutrino mass hierarchies on dynamical dark energy models*, *Phys. Rev. D* **95** (2017), no. 10 103522, [[arXiv:1703.02556](#)].
- [1350] F. Melia, *The Linear Growth of Structure in the $R_h=ct$ Universe*, *Mon. Not. Roy. Astron. Soc.* **464** (2017), no. 2 1966–1976, [[arXiv:1609.08576](#)].
- [1351] W. Yang, S. Pan, and A. Paliathanasis, *Latest astronomical constraints on some non-linear parametric dark energy models*, *Mon. Not. Roy. Astron. Soc.* **475** (2018), no. 2 2605–2613, [[arXiv:1708.01717](#)].
- [1352] S. Pan, E. N. Saridakis, and W. Yang, *Observational Constraints on Oscillating Dark-Energy Parametrizations*, *Phys. Rev. D* **98** (2018), no. 6 063510, [[arXiv:1712.05746](#)].
- [1353] M. Rezaei, M. Malekjani, S. Basilakos, A. Mehrabi, and D. F. Mota, *Constraints to Dark Energy Using PADE Parameterizations*, *Astrophys. J.* **843** (2017), no. 1 65, [[arXiv:1706.02537](#)].
- [1354] S. Joudaki et al., *KiDS-450: Testing extensions to the standard cosmological model*, *Mon. Not. Roy. Astron. Soc.* **471** (2017), no. 2 1259–1279, [[arXiv:1610.04606](#)].
- [1355] M. Du, W. Yang, L. Xu, S. Pan, and D. F. Mota, *Future constraints on dynamical dark-energy using gravitational-wave standard sirens*, *Phys. Rev. D* **100** (2019), no. 4 043535, [[arXiv:1812.01440](#)].
- [1356] S. Vagnozzi, S. Dhawan, M. Gerbino, K. Freese, A. Goobar, and O. Mena, *Constraints on the sum of the neutrino masses in dynamical dark energy models with $w(z) \geq -1$ are tighter than those obtained in Λ CDM*, *Phys. Rev. D* **98** (2018), no. 8 083501, [[arXiv:1801.08553](#)].
- [1357] G.-B. Zhao et al., *Dynamical dark energy in light of the latest observations*, *Nature Astron.* **1** (2017), no. 9 627–632, [[arXiv:1701.08165](#)].

- [1358] G. Lambiase, S. Mohanty, A. Narang, and P. Parashari, *Testing dark energy models in the light of σ_8 tension*, *Eur. Phys. J.* **C79** (2019), no. 2 141, [[arXiv:1804.07154](#)].
- [1359] J. Ooba, B. Ratra, and N. Sugiyama, *Planck 2015 constraints on spatially-flat dynamical dark energy models*, [arXiv:1802.05571](#).
- [1360] W. Yang, S. Pan, E. Di Valentino, E. N. Saridakis, and S. Chakraborty, *Observational constraints on one-parameter dynamical dark-energy parametrizations and the H_0 tension*, *Phys. Rev.* **D99** (2019), no. 4 043543, [[arXiv:1810.05141](#)].
- [1361] D. Benisty and D. Staicova, *Constraining the dark energy models using the BAO data: An approach independent of $H_0 \cdot r_d$* , [arXiv:2107.14129](#).
- [1362] Y. Wang, L. Pogosian, G.-B. Zhao, and A. Zucca, *Evolution of dark energy reconstructed from the latest observations*, *Astrophys. J. Lett.* **869** (2018) L8, [[arXiv:1807.03772](#)].
- [1363] E. Colgáin, M. M. Sheikh-Jabbari, and L. Yin, *Can dark energy be dynamical?*, [arXiv:2104.01930](#).
- [1364] J. Beltrán Jiménez, D. Bettoni, D. Figueruelo, F. A. Teppa Pannia, and S. Tsujikawa, *Probing elastic interactions in the dark sector and the role of $S8$* , *Phys. Rev. D* **104** (2021), no. 10 103503, [[arXiv:2106.11222](#)].
- [1365] F. Marulli, C. Carbone, M. Viel, L. Moscardini, and A. Cimatti, *Effects of Massive Neutrinos on the Large-Scale Structure of the Universe*, *Mon. Not. Roy. Astron. Soc.* **418** (2011) 346, [[arXiv:1103.0278](#)].
- [1366] R. A. Battye and A. Moss, *Evidence for Massive Neutrinos from Cosmic Microwave Background and Lensing Observations*, *Phys. Rev. Lett.* **112** (2014), no. 5 051303, [[arXiv:1308.5870](#)].
- [1367] M. Costanzi, B. Sartoris, M. Viel, and S. Borgani, *Neutrino constraints: what large-scale structure and CMB data are telling us?*, *JCAP* **10** (2014) 081, [[arXiv:1407.8338](#)].
- [1368] M. Zennaro, J. Bel, J. Dossett, C. Carbone, and L. Guzzo, *Cosmological constraints from galaxy clustering in the presence of massive neutrinos*, *Mon. Not. Roy. Astron. Soc.* **477** (2018), no. 1 491–506, [[arXiv:1712.02886](#)].
- [1369] A. Diaz Rivero, V. Miranda, and C. Dvorkin, *Observable Predictions for Massive-Neutrino Cosmologies with Model-Independent Dark Energy*, *Phys. Rev.* **D100** (2019), no. 6 063504, [[arXiv:1903.03125](#)].
- [1370] R. Biswas, K. Heitmann, S. Habib, A. Upadhye, A. Pope, and N. Frontiere, *Effects of Massive Neutrinos and Dynamical Dark Energy on the Cluster Mass Function*, [arXiv:1901.10690](#).
- [1371] J. Lesgourgues and S. Pastor, *Massive neutrinos and cosmology*, *Phys. Rept.* **429** (2006) 307–379, [[astro-ph/0603494](#)].
- [1372] Y. Y. Y. Wong, *Neutrino mass in cosmology: status and prospects*, *Ann. Rev. Nucl. Part. Sci.* **61** (2011) 69–98, [[arXiv:1111.1436](#)].
- [1373] J. Lesgourgues and S. Pastor, *Neutrino mass from Cosmology*, *Adv. High Energy Phys.* **2012** (2012) 608515, [[arXiv:1212.6154](#)].
- [1374] J. Lesgourgues and S. Pastor, *Neutrino cosmology and Planck*, *New J. Phys.* **16** (2014) 065002, [[arXiv:1404.1740](#)].
- [1375] J. R. Bond, G. Efstathiou, and J. Silk, *Massive Neutrinos and the Large Scale Structure of the Universe*, *Phys. Rev. Lett.* **45** (1980) 1980–1984.

- [1376] R. Banerjee and K. Jedamzik, *The Evolution of cosmic magnetic fields: From the very early universe, to recombination, to the present*, *Phys. Rev. D* **70** (2004) 123003, [[astro-ph/0410032](#)].
- [1377] R. Durrer and A. Neronov, *Cosmological Magnetic Fields: Their Generation, Evolution and Observation*, *Astron. Astrophys. Rev.* **21** (2013) 62, [[arXiv:1303.7121](#)].
- [1378] K. Subramanian, *The origin, evolution and signatures of primordial magnetic fields*, *Rept. Prog. Phys.* **79** (2016), no. 7 076901, [[arXiv:1504.02311](#)].
- [1379] T. Vachaspati, *Progress on cosmological magnetic fields*, *Rept. Prog. Phys.* **84** (2021), no. 7 074901, [[arXiv:2010.10525](#)].
- [1380] M. Rashkovetskyi, J. B. Muñoz, D. J. Eisenstein, and C. Dvorkin, *Small-scale clumping at recombination and the Hubble tension*, *Phys. Rev. D* **104** (2021), no. 10 103517, [[arXiv:2108.02747](#)].
- [1381] S. Das, A. Maharana, V. Poulin, and R. Kumar, *Non-thermal hot dark matter in light of the S_8 tension*, [arXiv:2104.03329](#).
- [1382] J. M. Bardeen, *Gauge Invariant Cosmological Perturbations*, *Phys. Rev.* **D22** (1980) 1882–1905.
- [1383] V. F. Mukhanov, H. A. Feldman, and R. H. Brandenberger, *Theory of cosmological perturbations. Part 1. Classical perturbations. Part 2. Quantum theory of perturbations. Part 3. Extensions*, *Phys. Rept.* **215** (1992) 203–333.
- [1384] C.-P. Ma and E. Bertschinger, *Cosmological perturbation theory in the synchronous and conformal Newtonian gauges*, *Astrophys. J.* **455** (1995) 7–25, [[astro-ph/9506072](#)].
- [1385] L. Pogosian and A. Silvestri, *The pattern of growth in viable $f(R)$ cosmologies*, *Phys. Rev.* **D77** (2008) 023503, [[arXiv:0709.0296](#)]. [Erratum: *Phys. Rev.*D81,049901(2010)].
- [1386] J. Muller, J. G. Williams, and S. G. Turyshev, *Lunar laser ranging contributions to relativity and geodesy*, *Astrophys. Space Sci. Libr.* **349** (2008) 457–472, [[gr-qc/0509114](#)].
- [1387] E. V. Pitjeva and N. P. Pitjev, *Relativistic effects and dark matter in the Solar system from observations of planets and spacecraft*, *Mon. Not. Roy. Astron. Soc.* **432** (2013) 3431, [[arXiv:1306.3043](#)].
- [1388] R. Gannouji, D. Polarski, A. Ranquet, and A. A. Starobinsky, *Scalar-Tensor Models of Normal and Phantom Dark Energy*, *JCAP* **0609** (2006) 016, [[astro-ph/0606287](#)].
- [1389] S. Nesseris and L. Perivolaropoulos, *The Limits of Extended Quintessence*, *Phys. Rev.* **D75** (2007) 023517, [[astro-ph/0611238](#)].
- [1390] C.-Q. Geng, C.-C. Lee, and E. N. Saridakis, *Observational Constraints on Teleparallel Dark Energy*, *JCAP* **1201** (2012) 002, [[arXiv:1110.0913](#)].
- [1391] C.-Q. Geng, C.-C. Lee, E. N. Saridakis, and Y.-P. Wu, *$\hat{a}^{[U+0080]} [U+009C]$ Teleparallel $\hat{a}^{[U+0080]} [U+009D]$ dark energy*, *Phys. Lett.* **B704** (2011) 384–387, [[arXiv:1109.1092](#)].
- [1392] M. Gonzalez-Espinoza, R. Herrera, G. Otalora, and J. Saavedra, *Reconstructing inflation in scalar-torsion $f(T, \phi)$ gravity*, *Eur. Phys. J. C* **81** (2021), no. 8 731, [[arXiv:2106.06145](#)].
- [1393] A. Paliathanasis, *Dynamics in Interacting Scalar-Torsion Cosmology*, *Universe* **7** (2021), no. 7 244, [[arXiv:2107.05880](#)].
- [1394] M. A. Skugoreva, E. N. Saridakis, and A. V. Toporensky, *Dynamical features of scalar-torsion theories*, *Phys. Rev.* **D91** (2015) 044023, [[arXiv:1412.1502](#)].

- [1395] G. Kofinas, E. Papantonopoulos, and E. N. Saridakis, *Self-Gravitating Spherically Symmetric Solutions in Scalar-Torsion Theories*, *Phys. Rev.* **D91** (2015), no. 10 104034, [[arXiv:1501.00365](#)].
- [1396] G. Leon, A. Paliathanasis, E. N. Saridakis, and S. Basilakos, *Unified dark sectors in scalar-torsion theories of gravity*, [arXiv:2203.14866](#).
- [1397] K. F. Dialektopoulos, J. L. Said, and Z. Oikonomopoulou, *Classification of Teleparallel Horndeski Cosmology via Noether Symmetries*, [arXiv:2112.15045](#).
- [1398] R. C. Bernardo, J. L. Said, M. Caruana, and S. Appleby, *Well-tempered teleparallel Horndeski cosmology: a teleparallel variation to the cosmological constant problem*, *JCAP* **10** (2021) 078, [[arXiv:2107.08762](#)].
- [1399] S. Bahamonde, M. Caruana, K. F. Dialektopoulos, V. Gakis, M. Hohmann, J. Levi Said, E. N. Saridakis, and J. Sultana, *Gravitational-wave propagation and polarizations in the teleparallel analog of Horndeski gravity*, *Phys. Rev. D* **104** (2021), no. 8 084082, [[arXiv:2105.13243](#)].
- [1400] S. Bahamonde, K. F. Dialektopoulos, M. Hohmann, and J. Levi Said, *Post-Newtonian limit of Teleparallel Horndeski gravity*, *Class. Quant. Grav.* **38** (2020), no. 2 025006, [[arXiv:2003.11554](#)].
- [1401] S. Bahamonde, K. F. Dialektopoulos, and J. Levi Said, *Can Horndeski Theory be recast using Teleparallel Gravity?*, *Phys. Rev.* **D100** (2019), no. 6 064018, [[arXiv:1904.10791](#)].
- [1402] R. D’Agostino and O. Luongo, *Growth of matter perturbations in nonminimal teleparallel dark energy*, *Phys. Rev. D* **98** (2018), no. 12 124013, [[arXiv:1807.10167](#)].
- [1403] M. Gonzalez-Espinoza, G. Otalora, J. Saavedra, and N. Videla, *Growth of matter overdensities in non-minimal torsion-matter coupling theories*, *Eur. Phys. J. C* **78** (2018), no. 10 799, [[arXiv:1808.01941](#)].
- [1404] S. Bahamonde, K. F. Dialektopoulos, C. Escamilla-Rivera, G. Farrugia, V. Gakis, M. Hendry, M. Hohmann, J. L. Said, J. Mifsud, and E. Di Valentino, *Teleparallel Gravity: From Theory to Cosmology*, [arXiv:2106.13793](#).
- [1405] J. Kennedy, L. Lombriser, and A. Taylor, *Reconstructing Horndeski theories from phenomenological modified gravity and dark energy models on cosmological scales*, *Phys. Rev.* **D98** (2018), no. 4 044051, [[arXiv:1804.04582](#)].
- [1406] E. V. Linder, *No Slip Gravity*, *JCAP* **1803** (2018), no. 03 005, [[arXiv:1801.01503](#)].
- [1407] G. D’Amico, Z. Huang, M. Mancarella, and F. Vernizzi, *Weakening Gravity on Redshift-Survey Scales with Kinetic Matter Mixing*, *JCAP* **02** (2017) 014, [[arXiv:1609.01272](#)].
- [1408] A. Rassat, J.-L. Starck, P. Paykari, F. Sureau, and J. Bobin, *Planck CMB Anomalies: Astrophysical and Cosmological Secondary Effects and the Curse of Masking*, *JCAP* **08** (2014) 006, [[arXiv:1405.1844](#)].
- [1409] J. C. Mather et al., *A Preliminary measurement of the Cosmic Microwave Background spectrum by the Cosmic Background Explorer (COBE) satellite*, *Astrophys. J. Lett.* **354** (1990) L37–L40.
- [1410] **WMAP** Collaboration, C. Bennett et al., *The Microwave Anisotropy Probe (MAP) mission*, *Astrophys. J.* **583** (2003) 1–23, [[astro-ph/0301158](#)].
- [1411] **Planck** Collaboration, R. Adam et al., *Planck 2015 results. I. Overview of products and scientific results*, *Astron. Astrophys.* **594** (2016) A1, [[arXiv:1502.01582](#)].

- [1412] L. Perivolaropoulos, *Large Scale Cosmological Anomalies and Inhomogeneous Dark Energy, Galaxies* **2** (2014) 22–61, [[arXiv:1401.5044](#)].
- [1413] J. I. Cayuso and M. C. Johnson, *Towards testing CMB anomalies using the kinetic and polarized Sunyaev-Zel'dovich effects, Phys. Rev. D* **101** (2020), no. 12 123508, [[arXiv:1904.10981](#)].
- [1414] J. Muir, S. Adhikari, and D. Huterer, *Covariance of CMB anomalies, Phys. Rev. D* **98** (2018), no. 2 023521, [[arXiv:1806.02354](#)].
- [1415] A. E. Bayer and U. Seljak, *The look-elsewhere effect from a unified Bayesian and frequentist perspective, JCAP* **10** (2020) 009, [[arXiv:2007.13821](#)].
- [1416] H. V. Peiris, *Considerations in the Interpretation of Cosmological Anomalies, IAU Symp.* **306** (2014) 124–130, [[arXiv:1410.3837](#)].
- [1417] E. Gross and O. Vitells, *Trial factors for the look elsewhere effect in high energy physics, Eur. Phys. J. C* **70** (2010) 525–530, [[arXiv:1005.1891](#)].
- [1418] **Planck** Collaboration, N. Aghanim et al., *Planck 2018 results. V. CMB power spectra and likelihoods, Astron. Astrophys.* **641** (2020) A5, [[arXiv:1907.12875](#)].
- [1419] E. Di Valentino et al., *Cosmology Intertwined IV: The Age of the Universe and its Curvature, arXiv:2008.11286*.
- [1420] E. Di Valentino, A. Melchiorri, and J. Silk, *Planck evidence for a closed Universe and a possible crisis for cosmology, Nature Astron.* **4** (2019), no. 2 196–203, [[arXiv:1911.02087](#)].
- [1421] W. Handley, *Curvature tension: evidence for a closed universe, arXiv:1908.09139*.
- [1422] S. Vagnozzi, E. Di Valentino, S. Gariazzo, A. Melchiorri, O. Mena, and J. Silk, *Listening to the BOSS: the galaxy power spectrum take on spatial curvature and cosmic concordance, arXiv:2010.02230*.
- [1423] G. Efstathiou and S. Gratton, *The evidence for a spatially flat Universe, arXiv:2002.06892*.
- [1424] G. Efstathiou and S. Gratton, *A Detailed Description of the CamSpec Likelihood Pipeline and a Reanalysis of the Planck High Frequency Maps, arXiv:1910.00483*.
- [1425] S. Vagnozzi, A. Loeb, and M. Moresco, *Eppur è piatto? The Cosmic Chronometers Take on Spatial Curvature and Cosmic Concordance, Astrophys. J.* **908** (2021), no. 1 84, [[arXiv:2011.11645](#)].
- [1426] R. K. Sachs and A. M. Wolfe, *Perturbations of a cosmological model and angular variations of the microwave background, Astrophys. J.* **147** (1967) 73–90.
- [1427] P. Fosalba and E. Gaztanaga, *Measurement of the gravitational potential evolution from the cross-correlation between wmap and the apm galaxy survey, Mon. Not. Roy. Astron. Soc.* **350** (2004) L37–L41, [[astro-ph/0305468](#)].
- [1428] A. Marcos-Caballero, R. Fernández-Cobos, E. Martínez-González, and P. Vielva, *The shape of CMB temperature and polarization peaks on the sphere, JCAP* **04** (2016) 058, [[arXiv:1512.07412](#)].
- [1429] **Planck** Collaboration, P. Ade et al., *Planck 2015 results. XVI. Isotropy and statistics of the CMB, Astron. Astrophys.* **594** (2016) A16, [[arXiv:1506.07135](#)].
- [1430] B. R. Granett, M. C. Neyrinck, and I. Szapudi, *An Imprint of Super-Structures on the Microwave Background due to the Integrated Sachs-Wolfe Effect, Astrophys. J. Lett.* **683** (2008) L99–L102, [[arXiv:0805.3695](#)].

- [1431] B. R. Granett, M. C. Neyrinck, and I. Szapudi, *Dark Energy Detected with Supervoids and Superclusters*, [arXiv:0805.2974](#).
- [1432] P. Hunt and S. Sarkar, *Constraints on large scale inhomogeneities from WMAP-5 and SDSS: confrontation with recent observations*, *Mon. Not. Roy. Astron. Soc.* **401** (2010) 547, [[arXiv:0807.4508](#)].
- [1433] S. Nadathur, S. Hotchkiss, and S. Sarkar, *The integrated Sachs-Wolfe imprints of cosmic superstructures: a problem for Λ CDM*, *JCAP* **06** (2012) 042, [[arXiv:1109.4126](#)].
- [1434] S. Flender, S. Hotchkiss, and S. Nadathur, *The stacked ISW signal of rare superstructures in Λ CDM*, *JCAP* **02** (2013) 013, [[arXiv:1212.0776](#)].
- [1435] S. Ilic, M. Langer, and M. Douspis, *On the detection of the integrated Sachs-Wolfe effect with stacked voids*, *Astron. Astrophys.* **556** (2013) A51, [[arXiv:1301.5849](#)].
- [1436] Y.-C. Cai, M. Neyrinck, Q. Mao, J. A. Peacock, I. Szapudi, and A. A. Berlind, *The lensing and temperature imprints of voids on the Cosmic Microwave Background*, *Mon. Not. Roy. Astron. Soc.* **466** (2017), no. 3 3364–3375, [[arXiv:1609.00301](#)].
- [1437] A. Kovács, *The part and the whole: voids, supervoids, and their ISW imprint*, *Mon. Not. Roy. Astron. Soc.* **475** (2018), no. 2 1777–1790, [[arXiv:1701.08583](#)].
- [1438] **DES** Collaboration, A. Kovács et al., *More out of less: an excess integrated Sachs-Wolfe signal from supervoids mapped out by the Dark Energy Survey*, *Mon. Not. Roy. Astron. Soc.* **484** (2019) 5267–5277, [[arXiv:1811.07812](#)].
- [1439] F. Dong, Y. Yu, J. Zhang, X. Yang, and P. Zhang, *Measuring the integrated Sachs–Wolfe effect from the low-density regions of the universe*, *Mon. Not. Roy. Astron. Soc.* **500** (2020), no. 3 3838–3853, [[arXiv:2006.14202](#)].
- [1440] G. Rácz, L. Dobos, R. Beck, I. Szapudi, and I. Csabai, *Concordance cosmology without dark energy*, *Mon. Not. Roy. Astron. Soc.* **469** (2017), no. 1 L1–L5, [[arXiv:1607.08797](#)].
- [1441] R. Beck, I. Csabai, G. Rácz, and I. Szapudi, *The integrated Sachs–Wolfe effect in the AvERA cosmology*, *Mon. Not. Roy. Astron. Soc.* **479** (2018), no. 3 3582–3591, [[arXiv:1801.08566](#)].
- [1442] T. Giannantonio, R. Crittenden, R. Nichol, and A. J. Ross, *The significance of the integrated Sachs-Wolfe effect revisited*, *Mon. Not. Roy. Astron. Soc.* **426** (2012) 2581–2599, [[arXiv:1209.2125](#)].
- [1443] S. Vagnozzi, *Consistency tests of Λ CDM from the early integrated Sachs-Wolfe effect: Implications for early-time new physics and the Hubble tension*, *Phys. Rev. D* **104** (2021), no. 6 063524, [[arXiv:2105.10425](#)].
- [1444] R. Bowen, S. H. Hansen, A. Melchiorri, J. Silk, and R. Trotta, *The Impact of an extra background of relativistic particles on the cosmological parameters derived from microwave background anisotropies*, *Mon. Not. Roy. Astron. Soc.* **334** (2002) 760, [[astro-ph/0110636](#)].
- [1445] S. Galli, M. Martinelli, A. Melchiorri, L. Pagano, B. D. Sherwin, and D. N. Spergel, *Constraining Fundamental Physics with Future CMB Experiments*, *Phys. Rev. D* **82** (2010) 123504, [[arXiv:1005.3808](#)].
- [1446] Z. Hou, R. Keisler, L. Knox, M. Millea, and C. Reichardt, *How Massless Neutrinos Affect the Cosmic Microwave Background Damping Tail*, *Phys. Rev. D* **87** (2013) 083008, [[arXiv:1104.2333](#)].

- [1447] G. Cabass, M. Gerbino, E. Giusarma, A. Melchiorri, L. Pagano, and L. Salvati, *Constraints on the early and late integrated Sachs-Wolfe effects from the Planck 2015 cosmic microwave background anisotropies in the angular power spectra*, *Phys. Rev. D* **92** (2015), no. 6 063534, [[arXiv:1507.07586](#)].
- [1448] J. A. Kable, G. E. Addison, and C. L. Bennett, *Deconstructing the Planck TT Power Spectrum to Constrain Deviations from Λ CDM*, *Astrophys. J.* **905** (2020), no. 2 164, [[arXiv:2008.01785](#)].
- [1449] P. Vielva, E. Martínez-González, R. Barreiro, J. Sanz, and L. Cayon, *Detection of non-Gaussianity in the WMAP 1 - year data using spherical wavelets*, *Astrophys. J.* **609** (2004) 22–34, [[astro-ph/0310273](#)].
- [1450] **Planck** Collaboration, P. A. R. Ade et al., *Planck 2013 results. XXIII. Isotropy and statistics of the CMB*, *Astron. Astrophys.* **571** (2014) A23, [[arXiv:1303.5083](#)].
- [1451] M. Cruz, E. Martínez-González, P. Vielva, and L. Cayon, *Detection of a non-gaussian spot in wmap*, *Mon. Not. Roy. Astron. Soc.* **356** (2005) 29–40, [[astro-ph/0405341](#)].
- [1452] M. Cruz, M. Tucci, E. Martínez-González, and P. Vielva, *The non-gaussian cold spot in wmap: significance, morphology and foreground contribution*, *Mon. Not. Roy. Astron. Soc.* **369** (2006) 57–67, [[astro-ph/0601427](#)].
- [1453] M. Cruz, L. Cayon, E. Martínez-González, P. Vielva, and J. Jin, *The non-gaussian cold spot in the 3-year wmap data*, *Astrophys. J.* **655** (2007) 11–20, [[astro-ph/0603859](#)].
- [1454] R. Zhang and D. Huterer, *Disks in the Sky: A Reassessment of the WMAP ‘Cold Spot’*, *Astropart. Phys.* **33** (2010) 69–74, [[arXiv:0908.3988](#)].
- [1455] S. Nadathur, M. Lavinto, S. Hotchkiss, and S. Räsänen, *Can a supervoid explain the Cold Spot?*, *Phys. Rev. D* **90** (2014), no. 10 103510, [[arXiv:1408.4720](#)].
- [1456] M. Hansen, W. Zhao, A. M. Frejse, P. D. Naselsky, J. Kim, and O. V. Verkhodanov, *Faraday Rotation as a diagnostic of Galactic foreground contamination of CMB maps*, *Mon. Not. Roy. Astron. Soc.* **426** (2012) 57–69, [[arXiv:1202.1711](#)].
- [1457] K. Naidoo, A. Benoit-Lévy, and O. Lahav, *Could multiple voids explain the Cosmic Microwave Background Cold Spot anomaly?*, *Mon. Not. Roy. Astron. Soc.* **459** (2016), no. 1 L71–L75, [[arXiv:1512.02694](#)].
- [1458] K. T. Inoue and J. Silk, *Local voids as the origin of large-angle cosmic microwave background anomalies I*, *Astrophys. J.* **648** (2006) 23–30, [[astro-ph/0602478](#)].
- [1459] K. T. Inoue and J. Silk, *Local Voids as the Origin of Large-angle Cosmic Microwave Background Anomalies: The Effect of a Cosmological Constant*, *Astrophys. J.* **664** (2007) 650–659, [[astro-ph/0612347](#)].
- [1460] L. Rudnick, S. Brown, and L. R. Williams, *Extragalactic Radio Sources and the WMAP Cold Spot*, *Astrophys. J.* **671** (2007) 40–44, [[arXiv:0704.0908](#)].
- [1461] T. R. Jaffe, A. J. Banday, H. K. Eriksen, K. M. Gorski, and F. K. Hansen, *Evidence of vorticity and shear at large angular scales in the WMAP data: A Violation of cosmological isotropy?*, *Astrophys. J. Lett.* **629** (2005) L1–L4, [[astro-ph/0503213](#)].
- [1462] W. Zhao, *Local properties of WMAP Cold Spot*, *Mon. Not. Roy. Astron. Soc.* **433** (2013) 3498–3505, [[arXiv:1209.1174](#)].
- [1463] W. Valkenburg, *Perceiving the equation of state of Dark Energy while living in a Cold Spot*, *JCAP* **01** (2012) 047, [[arXiv:1106.6042](#)].

- [1464] M. Cruz, E. Martinez-Gonzalez, and P. Vielva, *The WMAP cold spot*, [arXiv:0901.1986](#).
- [1465] P. Vielva, *A Comprehensive overview of the Cold Spot*, *Adv. Astron.* **2010** (2010) 592094, [[arXiv:1008.3051](#)].
- [1466] H. Eriksen, F. Hansen, A. Banday, K. Gorski, and P. Lilje, *Asymmetries in the Cosmic Microwave Background anisotropy field*, *Astrophys. J.* **605** (2004) 14–20, [[astro-ph/0307507](#)]. [Erratum: *Astrophys. J.* 609, 1198 (2004)].
- [1467] F. K. Hansen, A. J. Banday, and K. M. Gorski, *Testing the cosmological principle of isotropy: Local power spectrum estimates of the WMAP data*, *Mon. Not. Roy. Astron. Soc.* **354** (2004) 641–665, [[astro-ph/0404206](#)].
- [1468] H. K. Eriksen, A. J. Banday, K. M. Gorski, F. K. Hansen, and P. B. Lilje, *Hemispherical power asymmetry in the three-year Wilkinson Microwave Anisotropy Probe sky maps*, *Astrophys. J. Lett.* **660** (2007) L81–L84, [[astro-ph/0701089](#)].
- [1469] F. Paci, A. Gruppuso, F. Finelli, P. Cabella, A. De Rosa, N. Mandolesi, and P. Natoli, *Power Asymmetries in the Cosmic Microwave Background Temperature and Polarization patterns*, *Mon. Not. Roy. Astron. Soc.* **407** (2010) 399–404, [[arXiv:1002.4745](#)].
- [1470] C. Monteserin, R. Barreiro, P. Vielva, E. Martinez-Gonzalez, M. Hobson, and A. Lasenby, *A low CMB variance in the WMAP data*, *Mon. Not. Roy. Astron. Soc.* **387** (2008) 209–219, [[arXiv:0706.4289](#)].
- [1471] J. Hoftuft, H. Eriksen, A. Banday, K. Gorski, F. Hansen, and P. Lilje, *Increasing evidence for hemispherical power asymmetry in the five-year WMAP data*, *Astrophys. J.* **699** (2009) 985–989, [[arXiv:0903.1229](#)].
- [1472] Y. Akrami, Y. Fantaye, A. Shafieloo, H. K. Eriksen, F. K. Hansen, A. J. Banday, and K. M. Gorski, *Power asymmetry in WMAP and Planck temperature sky maps as measured by a local variance estimator*, *Astrophys. J. Lett.* **784** (2014) L42, [[arXiv:1402.0870](#)].
- [1473] A. Bernui, A. F. Oliveira, and T. S. Pereira, *North-South non-Gaussian asymmetry in PLANCK CMB maps*, *JCAP* **10** (2014) 041, [[arXiv:1404.2936](#)].
- [1474] M. O’Dwyer, C. J. Copi, J. M. Nagy, C. B. Netterfield, J. Ruhl, and G. D. Starkman, *Hemispherical Variance Anomaly and Reionization Optical Depth*, [arXiv:1912.02376](#).
- [1475] C. Gordon, *Broken Isotropy from a Linear Modulation of the Primordial Perturbations*, *Astrophys. J.* **656** (2007) 636–640, [[astro-ph/0607423](#)].
- [1476] C. L. Bennett et al., *Seven-Year Wilkinson Microwave Anisotropy Probe (WMAP) Observations: Are There Cosmic Microwave Background Anomalies?*, *Astrophys. J. Suppl.* **192** (2011) 17, [[arXiv:1001.4758](#)].
- [1477] A. L. Erickcek, M. Kamionkowski, and S. M. Carroll, *A Hemispherical Power Asymmetry from Inflation*, *Phys. Rev. D* **78** (2008) 123520, [[arXiv:0806.0377](#)].
- [1478] A. R. Liddle and M. Cortês, *Cosmic microwave background anomalies in an open universe*, *Phys. Rev. Lett.* **111** (2013), no. 11 111302, [[arXiv:1306.5698](#)].
- [1479] D. H. Lyth, *Generating f_{NL} at $\ell \lesssim 60$* , *JCAP* **04** (2015) 039, [[arXiv:1405.3562](#)].
- [1480] D.-G. Wang, W. Zhao, Y. Zhang, and Y.-F. Cai, *Scale-dependent CMB power asymmetry from primordial speed of sound and a generalized δN formalism*, *JCAP* **02** (2016) 019, [[arXiv:1509.02541](#)].

- [1481] S. Mukherjee and T. Souradeep, *Litmus Test for Cosmic Hemispherical Asymmetry in the Cosmic Microwave Background B-mode polarization*, *Phys. Rev. Lett.* **116** (2016), no. 22 221301, [[arXiv:1509.06736](#)].
- [1482] Q. Yang, Y. Liu, and H. Di, *Hemispherical Power Asymmetry of the Cosmic Microwave Background from a Remnant of a pre-Inflationary Topological Defect*, *Phys. Rev. D* **96** (2017), no. 8 083516, [[arXiv:1612.03708](#)].
- [1483] C. T. Byrnes, D. Regan, D. Seery, and E. R. M. Tarrant, *Implications of the cosmic microwave background power asymmetry for the early universe*, *Phys. Rev. D* **93** (2016), no. 12 123003, [[arXiv:1601.01970](#)].
- [1484] C. T. Byrnes, D. Regan, D. Seery, and E. R. M. Tarrant, *The hemispherical asymmetry from a scale-dependent inflationary bispectrum*, *JCAP* **06** (2016) 025, [[arXiv:1511.03129](#)].
- [1485] C. Byrnes, G. Domènech, M. Sasaki, and T. Takahashi, *Strongly scale-dependent CMB dipolar asymmetry from super-curvature fluctuations*, *JCAP* **12** (2016) 020, [[arXiv:1610.02650](#)].
- [1486] A. Ashoorioon and T. Koivisto, *Hemispherical Anomaly from Asymmetric Initial States*, *Phys. Rev. D* **94** (2016), no. 4 043009, [[arXiv:1507.03514](#)].
- [1487] S. Jazayeri, A. V. Sadr, and H. Firouzjahi, *Primordial anisotropies from cosmic strings during inflation*, *Phys. Rev. D* **96** (2017), no. 2 023512, [[arXiv:1703.05714](#)].
- [1488] M. Shiraishi, J. B. Muñoz, M. Kamionkowski, and A. Raccanelli, *Violation of statistical isotropy and homogeneity in the 21-cm power spectrum*, *Phys. Rev. D* **93** (2016), no. 10 103506, [[arXiv:1603.01206](#)].
- [1489] B. Li, Z. Chen, Y.-F. Cai, and Y. Mao, *Testing the scale-dependent hemispherical asymmetry with the 21-cm power spectrum from the epoch of reionization*, *Mon. Not. Roy. Astron. Soc.* **487** (2019), no. 4 5564–5571, [[arXiv:1904.04683](#)].
- [1490] C. Gordon, W. Hu, D. Huterer, and T. M. Crawford, *Spontaneous isotropy breaking: a mechanism for cmb multipole alignments*, *Phys. Rev. D* **72** (2005) 103002, [[astro-ph/0509301](#)].
- [1491] A. de Oliveira-Costa, M. Tegmark, M. Zaldarriaga, and A. Hamilton, *The Significance of the largest scale CMB fluctuations in WMAP*, *Phys. Rev. D* **69** (2004) 063516, [[astro-ph/0307282](#)].
- [1492] D. J. Schwarz, G. D. Starkman, D. Huterer, and C. J. Copi, *Is the low- l microwave background cosmic?*, *Phys. Rev. Lett.* **93** (2004) 221301, [[astro-ph/0403353](#)].
- [1493] C. J. Copi, D. Huterer, D. Schwarz, and G. Starkman, *On the large-angle anomalies of the microwave sky*, *Mon. Not. Roy. Astron. Soc.* **367** (2006) 79–102, [[astro-ph/0508047](#)].
- [1494] C. Copi, D. Huterer, D. Schwarz, and G. Starkman, *The Uncorrelated Universe: Statistical Anisotropy and the Vanishing Angular Correlation Function in WMAP Years 1-3*, *Phys. Rev. D* **75** (2007) 023507, [[astro-ph/0605135](#)].
- [1495] C. J. Copi, D. Huterer, D. J. Schwarz, and G. D. Starkman, *Large angle anomalies in the CMB*, *Adv. Astron.* **2010** (2010) 847541, [[arXiv:1004.5602](#)].
- [1496] C. J. Copi, D. Huterer, D. J. Schwarz, and G. D. Starkman, *Large-scale alignments from WMAP and Planck*, *Mon. Not. Roy. Astron. Soc.* **449** (2015), no. 4 3458–3470, [[arXiv:1311.4562](#)].
- [1497] C. J. Copi, D. Huterer, and G. D. Starkman, *Multipole vectors - A New representation of the CMB sky and evidence for statistical anisotropy or non-Gaussianity at $2 \leq l \leq 8$* , *Phys. Rev. D* **70** (2004) 043515, [[astro-ph/0310511](#)].

- [1498] A. Marcos-Caballero and E. Martínez-González, *Scale-dependent dipolar modulation and the quadrupole-octopole alignment in the CMB temperature*, *JCAP* **10** (2019) 053, [[arXiv:1909.06093](#)].
- [1499] G. Hinshaw, A. J. Banday, C. L. Bennett, K. M. Gorski, A. Kogut, C. H. Lineweaver, G. F. Smoot, and E. L. Wright, *2-point correlations in the COBE DMR 4-year anisotropy maps*, *Astrophys. J. Lett.* **464** (1996) L25–L28, [[astro-ph/9601061](#)].
- [1500] **WMAP** Collaboration, C. Bennett et al., *First year Wilkinson Microwave Anisotropy Probe (WMAP) observations: Preliminary maps and basic results*, *Astrophys. J. Suppl.* **148** (2003) 1–27, [[astro-ph/0302207](#)].
- [1501] C. J. Copi, D. Huterer, D. J. Schwarz, and G. D. Starkman, *No large-angle correlations on the non-Galactic microwave sky*, *Mon. Not. Roy. Astron. Soc.* **399** (2009) 295–303, [[arXiv:0808.3767](#)].
- [1502] C. J. Copi, D. Huterer, D. J. Schwarz, and G. D. Starkman, *Lack of large-angle TT correlations persists in WMAP and Planck*, *Mon. Not. Roy. Astron. Soc.* **451** (2015), no. 3 2978–2985, [[arXiv:1310.3831](#)].
- [1503] A. Hajian, *Analysis of the apparent lack of power in the cosmic microwave background anisotropy at large angular scales*, [astro-ph/0702723](#).
- [1504] G. Efstathiou, Y.-Z. Ma, and D. Hanson, *Large-Angle Correlations in the Cosmic Microwave Background*, *Mon. Not. Roy. Astron. Soc.* **407** (2010) 2530, [[arXiv:0911.5399](#)].
- [1505] A. Gruppuso, *Two-point correlation function of Wilkinson Microwave Anisotropy Probe 9-yr data*, *Mon. Not. Roy. Astron. Soc.* **437** (2014), no. 3 2076–2082, [[arXiv:1310.2822](#)].
- [1506] C. J. Copi, D. Huterer, D. J. Schwarz, and G. D. Starkman, *Large-Angle CMB Suppression and Polarization Predictions*, *Mon. Not. Roy. Astron. Soc.* **434** (2013) 3590–3596, [[arXiv:1303.4786](#)].
- [1507] J. D. Jackson, *Classical Electrodynamics*. Wiley, 1998.
- [1508] M. Zaldarriaga and U. Seljak, *An all sky analysis of polarization in the microwave background*, *Phys. Rev. D* **55** (1997) 1830–1840, [[astro-ph/9609170](#)].
- [1509] M. Kamionkowski, A. Kosowsky, and A. Stebbins, *Statistics of cosmic microwave background polarization*, *Phys. Rev. D* **55** (1997) 7368–7388, [[astro-ph/9611125](#)].
- [1510] A. Lewis, A. Challinor, and N. Turok, *Analysis of CMB polarization on an incomplete sky*, *Phys. Rev. D* **65** (2002) 023505, [[astro-ph/0106536](#)].
- [1511] E. F. Bunn, M. Zaldarriaga, M. Tegmark, and A. de Oliveira-Costa, *E/B decomposition of finite pixelized CMB maps*, *Phys. Rev. D* **67** (2003) 023501, [[astro-ph/0207338](#)].
- [1512] C. J. Copi, M. O’Dwyer, and G. D. Starkman, *The ISW effect and the lack of large-angle CMB temperature correlations*, *Mon. Not. Roy. Astron. Soc.* **463** (2016), no. 3 3305–3310, [[arXiv:1605.09732](#)].
- [1513] A. Bernui, C. P. Novaes, T. S. Pereira, and G. D. Starkman, *Topology and the suppression of CMB large-angle correlations*, [arXiv:1809.05924](#).
- [1514] P. Pranav, R. J. Adler, T. Buchert, H. Edelsbrunner, B. J. T. Jones, A. Schwartzman, H. Wagner, and R. van de Weygaert, *Unexpected Topology of the Temperature Fluctuations in the Cosmic Microwave Background*, *Astron. Astrophys.* **627** (2019) A163, [[arXiv:1812.07678](#)].

- [1515] P. Pranav, *Loops abound in the cosmic microwave background: A 4σ anomaly on super-horizon scales*, [arXiv:2101.02237](#).
- [1516] **Planck** Collaboration, Y. Akrami et al., *Planck intermediate results. LVII. Joint Planck LFI and HFI data processing*, *Astron. Astrophys.* **643** (2020) A42, [[arXiv:2007.04997](#)].
- [1517] E. Calabrese, A. Slosar, A. Melchiorri, G. F. Smoot, and O. Zahn, *Cosmic Microwave Weak lensing data as a test for the dark universe*, *Phys. Rev.* **D77** (2008) 123531, [[arXiv:0803.2309](#)].
- [1518] M. Zaldarriaga and U. Seljak, *Gravitational lensing effect on cosmic microwave background polarization*, *Phys. Rev. D* **58** (1998) 023003, [[astro-ph/9803150](#)].
- [1519] A. Lewis and A. Challinor, *Weak gravitational lensing of the CMB*, *Phys. Rept.* **429** (2006) 1–65, [[astro-ph/0601594](#)].
- [1520] **Planck** Collaboration, P. A. R. Ade et al., *Planck 2015 results. XV. Gravitational lensing*, *Astron. Astrophys.* **594** (2016) A15, [[arXiv:1502.01591](#)].
- [1521] **Planck** Collaboration, N. Aghanim et al., *Planck intermediate results. LI. Features in the cosmic microwave background temperature power spectrum and shifts in cosmological parameters*, *Astron. Astrophys.* **607** (2017) A95, [[arXiv:1608.02487](#)].
- [1522] P. Motloch and W. Hu, *Lensinglike tensions in the Planck legacy release*, *Phys. Rev. D* **101** (2020), no. 8 083515, [[arXiv:1912.06601](#)].
- [1523] **Planck** Collaboration, Y. Akrami et al., *Planck 2018 results. X. Constraints on inflation*, [arXiv:1807.06211](#).
- [1524] E. Di Valentino, A. Melchiorri, and J. Silk, *Cosmological hints of modified gravity?*, *Phys. Rev.* **D93** (2016), no. 2 023513, [[arXiv:1509.07501](#)].
- [1525] E. Di Valentino, S. Gariazzo, O. Mena, and S. Vagnozzi, *Soundness of Dark Energy properties*, *JCAP* **07** (2020), no. 07 045, [[arXiv:2005.02062](#)].
- [1526] G. Addison, Y. Huang, D. Watts, C. Bennett, M. Halpern, G. Hinshaw, and J. Weiland, *Quantifying discordance in the 2015 Planck CMB spectrum*, *Astrophys. J.* **818** (2016), no. 2 132, [[arXiv:1511.00055](#)].
- [1527] **Planck** Collaboration, N. Aghanim et al., *Planck 2018 results. V. CMB power spectra and likelihoods*, [arXiv:1907.12875](#).
- [1528] K. Land and J. Magueijo, *Is the Universe odd?*, *Phys. Rev. D* **72** (2005) 101302, [[astro-ph/0507289](#)].
- [1529] J. Kim and P. Naselsky, *Anomalous parity asymmetry of WMAP power spectrum data at low multipoles: is it cosmological or systematics?*, *Phys. Rev. D* **82** (2010) 063002, [[arXiv:1002.0148](#)].
- [1530] J. Kim and P. Naselsky, *Anomalous parity asymmetry of the Wilkinson Microwave Anisotropy Probe power spectrum data at low multipoles*, *Astrophys. J. Lett.* **714** (2010) L265–L267, [[arXiv:1001.4613](#)].
- [1531] J. Kim and P. Naselsky, *Lack of angular correlation and odd-parity preference in cosmic microwave background data*, *The Astrophysical Journal* **739** (Sep, 2011) 79.
- [1532] A. Gruppuso, F. Finelli, P. Natoli, F. Paci, P. Cabella, A. De Rosa, and N. Mandolesi, *New constraints on Parity Symmetry from a re-analysis of the WMAP-7 low resolution power spectra*, *Mon. Not. Roy. Astron. Soc.* **411** (2011) 1445–1452, [[arXiv:1006.1979](#)].

- [1533] A. Gruppuso, N. Kitazawa, M. Lattanzi, N. Mandolesi, P. Natoli, and A. Sagnotti, *The Evens and Odds of CMB Anomalies*, *Phys. Dark Univ.* **20** (2018) 49–64, [[arXiv:1712.03288](#)].
- [1534] P. K. Aluri and P. Jain, *Parity Asymmetry in the CMBR Temperature Power Spectrum*, *Mon. Not. Roy. Astron. Soc.* **419** (2012) 3378, [[arXiv:1108.5894](#)].
- [1535] J. C. Bueno Sanchez and L. Perivolaropoulos, *Topological Quintessence*, *Phys. Rev. D* **84** (2011) 123516, [[arXiv:1110.2587](#)].
- [1536] A. L. Erickcek, S. M. Carroll, and M. Kamionkowski, *Superhorizon Perturbations and the Cosmic Microwave Background*, *Phys. Rev. D* **78** (2008) 083012, [[arXiv:0808.1570](#)].
- [1537] **Planck** Collaboration, N. Aghanim et al., *Planck 2018 results. III. High Frequency Instrument data processing and frequency maps*, *Astron. Astrophys.* **641** (2020) A3, [[arXiv:1807.06207](#)].
- [1538] J. Colin, R. Mohayaee, M. Rameez, and S. Sarkar, *High redshift radio galaxies and divergence from the CMB dipole*, *Mon. Not. Roy. Astron. Soc.* **471** (2017), no. 1 1045–1055, [[arXiv:1703.09376](#)].
- [1539] P. Tiwari and A. Nusser, *Revisiting the NVSS number count dipole*, *JCAP* **03** (2016) 062, [[arXiv:1509.02532](#)].
- [1540] **Planck** Collaboration, Y. Akrami et al., *Planck 2018 results. IV. Diffuse component separation*, *Astron. Astrophys.* **641** (2020) A4, [[arXiv:1807.06208](#)].
- [1541] J. Cardoso, M. Le Jeune, J. Delabrouille, M. Betoule, and G. Patanchon, *Component separation with flexible models—application to multichannel astrophysical observations*, *IEEE Journal of Selected Topics in Signal Processing* **2** (2008), no. 5 735–746.
- [1542] M. Axelsson, Y. Fantaye, F. K. Hansen, A. J. Banday, H. K. Eriksen, and K. M. Gorski, *Directional dependence of Λ CDM cosmological parameters*, *Astrophys. J. Lett.* **773** (2013) L3, [[arXiv:1303.5371](#)].
- [1543] I. Antoniou and L. Perivolaropoulos, *Searching for a Cosmological Preferred Axis: Union2 Data Analysis and Comparison with Other Probes*, *JCAP* **12** (2010) 012, [[arXiv:1007.4347](#)].
- [1544] J. Koda, C. Blake, T. Davis, C. Magoulas, C. M. Springob, M. Scrimgeour, A. Johnson, G. B. Poole, and L. Staveley-Smith, *Are peculiar velocity surveys competitive as a cosmological probe?*, *Mon. Not. Roy. Astron. Soc.* **445** (2014), no. 4 4267–4286, [[arXiv:1312.1022](#)].
- [1545] H. A. Feldman, R. Watkins, and M. J. Hudson, *Cosmic Flows on 100 Mpc/h Scales: Standardized Minimum Variance Bulk Flow, Shear and Octupole Moments*, *Mon. Not. Roy. Astron. Soc.* **407** (2010) 2328–2338, [[arXiv:0911.5516](#)].
- [1546] A. Kashlinsky, F. Atrio-Barandela, H. Ebeling, A. Edge, and D. Kocevski, *A new measurement of the bulk flow of X-ray luminous clusters of galaxies*, *Astrophys. J. Lett.* **712** (2010) L81–L85, [[arXiv:0910.4958](#)].
- [1547] A. Nusser and M. Davis, *The cosmological bulk flow: consistency with Λ CDM and $z \approx 0$ constraints on σ_8 and γ* , *Astrophys. J.* **736** (2011) 93, [[arXiv:1101.1650](#)].
- [1548] Y.-Z. Ma and D. Scott, *Cosmic bulk flows on 50 h^{-1} Mpc scales: A Bayesian hyper-parameter method and multi-shells likelihood analysis*, *Mon. Not. Roy. Astron. Soc.* **428** (2013) 2017, [[arXiv:1208.2028](#)].
- [1549] S. J. Turnbull, M. J. Hudson, H. A. Feldman, M. Hicken, R. P. Kirshner, and R. Watkins, *Cosmic flows in the nearby universe from type ia supernovae*, *Monthly Notices of the Royal Astronomical Society* **420** (2012), no. 1 447–454.

- [1550] A. Kashlinsky, F. Atrio-Barandela, and H. Ebeling, *Measuring bulk motion of X-ray clusters via the kinematic Sunyaev-Zeldovich effect: summarizing the 'dark flow' evidence and its implications*, [arXiv:1202.0717](#).
- [1551] T. Hong, C. M. Springob, L. Staveley-Smith, M. I. Scrimgeour, K. L. Masters, L. M. Macri, B. S. Koribalski, D. H. Jones, and T. H. Jarrett, *2MTF – IV. A bulk flow measurement of the local Universe*, *Mon. Not. Roy. Astron. Soc.* **445** (2014), no. 1 402–413, [[arXiv:1409.0287](#)].
- [1552] C. G. Tsagas, *Peculiar motions, accelerated expansion and the cosmological axis*, *Phys. Rev. D* **84** (2011) 063503, [[arXiv:1107.4045](#)].
- [1553] C. G. Tsagas and M. I. Kadiltzoglou, *Deceleration parameter in tilted Friedmann universes*, *Phys. Rev. D* **92** (2015), no. 4 043515, [[arXiv:1507.04266](#)].
- [1554] J. Colin, R. Mohayaee, M. Rameez, and S. Sarkar, *Evidence for anisotropy of cosmic acceleration*, *Astron. Astrophys.* **631** (2019) L13, [[arXiv:1808.04597](#)].
- [1555] R. Arjona and S. Nesseris, *What can Machine Learning tell us about the background expansion of the Universe?*, *Phys. Rev. D* **101** (2020), no. 12 123525, [[arXiv:1910.01529](#)].
- [1556] A. Kogut et al., *Dipole anisotropy in the COBE DMR first year sky maps*, *Astrophys. J.* **419** (1993) 1, [[astro-ph/9312056](#)].
- [1557] D. J. Fixsen, E. S. Cheng, J. M. Gales, J. C. Mather, R. A. Shafer, and E. L. Wright, *The Cosmic Microwave Background spectrum from the full COBE FIRAS data set*, *Astrophys. J.* **473** (1996) 576, [[astro-ph/9605054](#)].
- [1558] **Planck** Collaboration, N. Aghanim et al., *Planck intermediate results. XLVI. Reduction of large-scale systematic effects in HFI polarization maps and estimation of the reionization optical depth*, *Astron. Astrophys.* **596** (2016) A107, [[arXiv:1605.02985](#)].
- [1559] Y. Itoh, K. Yahata, and M. Takada, *A dipole anisotropy of galaxy distribution: Does the CMB rest-frame exist in the local universe?*, *Phys. Rev. D* **82** (2010) 043530, [[arXiv:0912.1460](#)].
- [1560] **SKA** Collaboration, D. J. Bacon et al., *Cosmology with Phase 1 of the Square Kilometre Array: Red Book 2018: Technical specifications and performance forecasts*, *Publ. Astron. Soc. Austral.* **37** (2020) e007, [[arXiv:1811.02743](#)].
- [1561] G. F. R. Ellis and J. E. Baldwin, *On the expected anisotropy of radio source counts*, *Monthly Notices of the Royal Astronomical Society* **206** (01, 1984) 377–381, [<https://academic.oup.com/mnras/article-pdf/206/2/377/18187025/mnras206-0377.pdf>].
- [1562] J. H. McKay and D. L. Wiltshire, *Defining the frame of minimum non-linear Hubble expansion variation*, *Mon. Not. Roy. Astron. Soc.* **457** (2016), no. 3 3285–3305, [[arXiv:1503.04192](#)]. [Erratum: *Mon. Not. Roy. Astron. Soc.* 463, 3113 (2016)].
- [1563] D. Kraljic and S. Sarkar, *Frames of most uniform Hubble flow*, *JCAP* **10** (2016) 016, [[arXiv:1607.07377](#)].
- [1564] A. K. Singal, *Large peculiar motion of the solar system from the dipole anisotropy in sky brightness due to distant radio sources*, *Astrophys. J. Lett.* **742** (2011) L23, [[arXiv:1110.6260](#)].
- [1565] C. Gibelyou and D. Huterer, *Dipoles in the Sky*, *Mon. Not. Roy. Astron. Soc.* **427** (2012) 1994–2021, [[arXiv:1205.6476](#)].
- [1566] M. Rubart and D. J. Schwarz, *Cosmic radio dipole from NVSS and WENSS*, *Astron. Astrophys.* **555** (2013) A117, [[arXiv:1301.5559](#)].

- [1567] P. Tiwari, R. Kothari, A. Naskar, S. Nadkarni-Ghosh, and P. Jain, *Dipole anisotropy in sky brightness and source count distribution in radio NVSS data*, *Astropart. Phys.* **61** (2014) 1–11, [[arXiv:1307.1947](#)].
- [1568] J. J. Condon, W. D. Cotton, E. W. Greisen, Q. F. Yin, R. A. Perley, G. B. Taylor, and J. J. Broderick, *The NRAO VLA Sky survey*, *Astron. J.* **115** (1998) 1693–1716.
- [1569] H. T. Intema, P. Jagannathan, K. P. Mooley, and D. A. Frail, *The GMRT 150 MHz All-sky Radio Survey: First Alternative Data Release TGSS ADR1*, *Astron. Astrophys.* **598** (2017) A78, [[arXiv:1603.04368](#)].
- [1570] A. K. Singal, *Large disparity in cosmic reference frames determined from the sky distributions of radio sources and the microwave background radiation*, *Phys. Rev. D* **100** (2019), no. 6 063501, [[arXiv:1904.11362](#)].
- [1571] C. Blake and J. Wall, *Detection of the velocity dipole in the radio galaxies of the nrao vla sky survey*, *Nature* **416** (2002) 150–152, [[astro-ph/0203385](#)].
- [1572] R. Fernández-Cobos, P. Vielva, D. Pietrobon, A. Balbi, E. Martínez-González, and R. B. Barreiro, *Searching for a dipole modulation in the large-scale structure of the Universe*, *Mon. Not. Roy. Astron. Soc.* **441** (2014), no. 3 2392–2397, [[arXiv:1312.0275](#)].
- [1573] M. S. Turner, *A Tilted Universe (and Other Remnants of the Preinflationary Universe)*, *Phys. Rev. D* **44** (1991) 3737–3748.
- [1574] S. Ghosh, *Generating Intrinsic Dipole Anisotropy in the Large Scale Structures*, *Phys. Rev. D* **89** (2014) 063518, [[arXiv:1309.6547](#)].
- [1575] K. K. Das, K. Sankharva, and P. Jain, *Explaining Excess Dipole in NVSS Data Using Superhorizon Perturbation*, [[arXiv:2101.11016](#)].
- [1576] A. K. Singal, *Peculiar motion of the solar system derived from a dipole anisotropy in the redshift distribution of distant quasars*, *Mon. Not. Roy. Astron. Soc.* **488** (2019), no. 1 L104–L108, [[arXiv:1405.4796](#)].
- [1577] P. R. M. Eisenhardt, F. Marocco, J. W. Fowler, A. M. Meisner, J. D. Kirkpatrick, N. Garcia, T. H. Jarrett, R. Koontz, E. J. Marchese, S. A. Stanford, D. Caselden, M. C. Cushing, R. M. Cutri, J. K. Faherty, C. R. Gelino, A. H. Gonzalez, A. Mainzer, B. Mobasher, D. J. Schlegel, D. Stern, H. I. Teplitz, and E. L. Wright, *The CatWISE preliminary catalog: Motions from WISE and NEOWISE data*, *The Astrophysical Journal Supplement Series* **247** (apr, 2020) 69.
- [1578] M. T. Murphy, J. K. Webb, and V. V. Flambaum, *Further evidence for a variable fine-structure constant from Keck/HIRES QSO absorption spectra*, *Mon. Not. Roy. Astron. Soc.* **345** (2003) 609, [[astro-ph/0306483](#)].
- [1579] P. Molaro et al., *The UVES Large Program for Testing Fundamental Physics: I Bounds on a change in alpha towards quasar HE 2217-2818*, *Astron. Astrophys.* **555** (2013) A68, [[arXiv:1305.1884](#)].
- [1580] J. C. Berengut, V. V. Flambaum, A. Ong, J. K. Webb, J. D. Barrow, M. A. Barstow, S. P. Preval, and J. B. Holberg, *Limits on the dependence of the fine-structure constant on gravitational potential from white-dwarf spectra*, *Phys. Rev. Lett.* **111** (2013), no. 1 010801, [[arXiv:1305.1337](#)].
- [1581] J. K. Webb, A. Wright, F. E. Koch, and M. T. Murphy, *Enhanced heavy magnesium isotopes in quasar absorption systems and varying alpha*, *Mem. Soc. Ast. It.* **85** (2014), no. 1 57–62.

- [1582] T. M. Evans et al., *The UVES Large Program for testing fundamental physics – III. Constraints on the fine-structure constant from three telescopes*, *Mon. Not. Roy. Astron. Soc.* **445** (2014), no. 1 128–150, [[arXiv:1409.1923](#)].
- [1583] M. B. Bainbridge et al., *Probing the Gravitational Dependence of the Fine-Structure Constant from Observations of White Dwarf Stars*, *Universe* **3** (2017), no. 2 32, [[arXiv:1702.01757](#)].
- [1584] J. Hu et al., *Constraining the magnetic field on white dwarf surfaces; Zeeman effects and fine structure constant variation*, *Mon. Not. Roy. Astron. Soc.* **485** (2019), no. 4 5050–5058, [[arXiv:1812.11480](#)].
- [1585] D. Milaković, C.-C. Lee, R. F. Carswell, J. K. Webb, P. Molaro, and L. Pasquini, *A new era of fine structure constant measurements at high redshift*, *Mon. Not. Roy. Astron. Soc.* **500** (2020), no. 1 1–21, [[arXiv:2008.10619](#)].
- [1586] C.-C. Lee, J. K. Webb, D. Milaković, and R. F. Carswell, *Non-uniqueness in quasar absorption models and implications for measurements of the fine structure constant*, [arXiv:2102.11648](#).
- [1587] J. K. Webb, V. V. Flambaum, C. W. Churchill, M. J. Drinkwater, and J. D. Barrow, *Evidence for time variation of the fine structure constant*, *Phys. Rev. Lett.* **82** (1999) 884–887, [[astro-ph/9803165](#)].
- [1588] V. A. Dzuba, V. V. Flambaum, and J. K. Webb, *Space-Time Variation of Physical Constants and Relativistic Corrections in Atoms*, *Phys. Rev. Lett.* **82** (1999) 888–891, [[physics/9802029](#)].
- [1589] J. K. Webb, M. T. Murphy, V. V. Flambaum, V. A. Dzuba, J. D. Barrow, C. W. Churchill, J. X. Prochaska, and A. M. Wolfe, *Further evidence for cosmological evolution of the fine structure constant*, *Phys. Rev. Lett.* **87** (2001) 091301, [[astro-ph/0012539](#)].
- [1590] M. T. Murphy, J. K. Webb, V. V. Flambaum, V. A. Dzuba, C. W. Churchill, J. X. Prochaska, J. D. Barrow, and A. M. Wolfe, *Possible evidence for a variable fine structure constant from QSO absorption lines: Motivations, analysis and results*, *Mon. Not. Roy. Astron. Soc.* **327** (2001) 1208, [[astro-ph/0012419](#)].
- [1591] H. Dekker, S. D’Odorico, A. Kaufer, B. Delabre, and H. Kotzlowski, *Design, construction, and performance of UVES, the echelle spectrograph for the UT2 Kueyen Telescope at the ESO Paranal Observatory*, in *Optical and IR Telescope Instrumentation and Detectors* (M. Iye and A. F. M. Moorwood, eds.), vol. 4008, pp. 534 – 545, International Society for Optics and Photonics, SPIE, 2000.
- [1592] E. Cameron and T. Pettitt, *On the Evidence for Cosmic Variation of the Fine Structure Constant: A Bayesian Reanalysis of the Quasar Dataset*, [arXiv:1207.6223](#).
- [1593] N. Kanekar, G. I. Langston, J. T. Stocke, C. L. Carilli, and K. M. Menten, *Constraining fundamental constant evolution with HI and OH lines*, *Astrophys. J. Lett.* **746** (2012) L16, [[arXiv:1201.3372](#)].
- [1594] S. A. Levshakov, F. Combes, F. Boone, I. I. Agafonova, D. Reimers, and M. G. Kozlov, *An upper limit to the variation in the fundamental constants at redshift $z = 5.2$* , *Astron. Astrophys.* **540** (2012) L9, [[arXiv:1203.3649](#)].
- [1595] C. J. A. P. Martins and A. M. M. Pinho, *Stability of fundamental couplings: a global analysis*, *Phys. Rev. D* **95** (2017), no. 2 023008, [[arXiv:1701.08724](#)].
- [1596] V. Dumont and J. K. Webb, *Modelling long-range wavelength distortions in quasar absorption echelle spectra*, *Mon. Not. Roy. Astron. Soc.* **468** (2017), no. 2 1568–1574, [[arXiv:1701.03176](#)].

- [1597] M. R. Wilczynska et al., *Four direct measurements of the fine-structure constant 13 billion years ago*, *Sci. Adv.* **6** (2020), no. 17 eaay9672, [[arXiv:2003.07627](#)].
- [1598] A. Mariano and L. Perivolaropoulos, *Is there correlation between Fine Structure and Dark Energy Cosmic Dipoles?*, *Phys. Rev. D* **86** (2012) 083517, [[arXiv:1206.4055](#)].
- [1599] A. Mariano and L. Perivolaropoulos, *CMB Maximum temperature asymmetry Axis: Alignment with other cosmic asymmetries*, *Phys. Rev. D* **87** (2013), no. 4 043511, [[arXiv:1211.5915](#)].
- [1600] H. du Mas des Bourboux et al., *Baryon acoustic oscillations from the complete SDSS-III Ly α -quasar cross-correlation function at $z = 2.4$* , *Astron. Astrophys.* **608** (2017) A130, [[arXiv:1708.02225](#)].
- [1601] T. D. Lee and C.-N. Yang, *Question of Parity Conservation in Weak Interactions*, *Phys. Rev.* **104** (1956) 254–258.
- [1602] C. S. Wu, E. Ambler, R. W. Hayward, D. D. Hoppes, and R. P. Hudson, *Experimental Test of Parity Conservation in β Decay*, *Phys. Rev.* **105** (1957) 1413–1414.
- [1603] S. M. Carroll, G. B. Field, and R. Jackiw, *Limits on a Lorentz and Parity Violating Modification of Electrodynamics*, *Phys. Rev. D* **41** (1990) 1231.
- [1604] S. M. Carroll, *Quintessence and the rest of the world*, *Phys. Rev. Lett.* **81** (1998) 3067–3070, [[astro-ph/9806099](#)].
- [1605] M. S. Turner and L. M. Widrow, *Inflation Produced, Large Scale Magnetic Fields*, *Phys. Rev. D* **37** (1988) 2743.
- [1606] D. Harari and P. Sikivie, *Effects of a Nambu-Goldstone boson on the polarization of radio galaxies and the cosmic microwave background*, *Phys. Lett. B* **289** (1992) 67–72.
- [1607] T. Fujita, Y. Minami, K. Murai, and H. Nakatsuka, *Probing Axion-like Particles via CMB Polarization*, [[arXiv:2008.02473](#)].
- [1608] A. Lue, L.-M. Wang, and M. Kamionkowski, *Cosmological signature of new parity violating interactions*, *Phys. Rev. Lett.* **83** (1999) 1506–1509, [[astro-ph/9812088](#)].
- [1609] T. Fujita, K. Murai, H. Nakatsuka, and S. Tsujikawa, *Detection of isotropic cosmic birefringence and its implications for axion-like particles including dark energy*, *Phys. Rev. D* **103** (2021) 043509, [[arXiv:2011.11894](#)].
- [1610] F. Takahashi and W. Yin, *Kilobyte Cosmic Birefringence from ALP Domain Walls*, *JCAP* **04** (2021) 007, [[arXiv:2012.11576](#)].
- [1611] **SPT** Collaboration, F. Bianchini et al., *Searching for Anisotropic Cosmic Birefringence with Polarization Data from SPTpol*, *Phys. Rev. D* **102** (2020), no. 8 083504, [[arXiv:2006.08061](#)].
- [1612] T. Namikawa et al., *Atacama Cosmology Telescope: Constraints on cosmic birefringence*, *Phys. Rev. D* **101** (2020), no. 8 083527, [[arXiv:2001.10465](#)].
- [1613] P. Kroupa, B. Famaey, K. S. de Boer, J. Dabringhausen, M. S. Pawlowski, C. M. Boily, H. Jerjen, D. Forbes, G. Hensler, and M. Metz, *Local-Group tests of dark-matter Concordance Cosmology: Towards a new paradigm for structure formation?*, *Astron. Astrophys.* **523** (2010) A32, [[arXiv:1006.1647](#)].
- [1614] D. H. Weinberg, J. S. Bullock, F. Governato, R. Kuzio de Naray, and A. H. G. Peter, *Cold dark matter: controversies on small scales*, *Proc. Nat. Acad. Sci.* **112** (2015) 12249–12255, [[arXiv:1306.0913](#)].

- [1615] T. Nakama, J. Chluba, and M. Kamionkowski, *Shedding light on the small-scale crisis with CMB spectral distortions*, *Phys. Rev. D* **95** (2017), no. 12 121302, [[arXiv:1703.10559](#)].
- [1616] P. Kroupa, *The dark matter crisis: falsification of the current standard model of cosmology*, *Publ. Astron. Soc. Austral.* **29** (2012) 395–433, [[arXiv:1204.2546](#)].
- [1617] P. Kroupa, *Galaxies as simple dynamical systems: observational data disfavor dark matter and stochastic star formation*, *Can. J. Phys.* **93** (2015), no. 2 169–202, [[arXiv:1406.4860](#)].
- [1618] P. Salucci, *The distribution of dark matter in galaxies*, *Astron. Astrophys. Rev.* **27** (2019), no. 1 2, [[arXiv:1811.08843](#)].
- [1619] P. Bode, J. P. Ostriker, and N. Turok, *Halo formation in warm dark matter models*, *Astrophys. J.* **556** (2001) 93–107, [[astro-ph/0010389](#)].
- [1620] K. Abazajian, *Linear cosmological structure limits on warm dark matter*, *Phys. Rev. D* **73** (2006) 063513, [[astro-ph/0512631](#)].
- [1621] M. Viel, J. Lesgourgues, M. G. Haehnelt, S. Matarrese, and A. Riotto, *Constraining warm dark matter candidates including sterile neutrinos and light gravitinos with WMAP and the Lyman-alpha forest*, *Phys. Rev. D* **71** (2005) 063534, [[astro-ph/0501562](#)].
- [1622] A. Schneider, D. Anderhalden, A. Maccio, and J. Diemand, *Warm dark matter does not do better than cold dark matter in solving small-scale inconsistencies*, *Mon. Not. Roy. Astron. Soc.* **441** (2014) 6, [[arXiv:1309.5960](#)].
- [1623] M. Viel, G. D. Becker, J. S. Bolton, and M. G. Haehnelt, *Warm dark matter as a solution to the small scale crisis: New constraints from high redshift Lyman- α forest data*, *Phys. Rev. D* **88** (2013) 043502, [[arXiv:1306.2314](#)].
- [1624] W. Hu, R. Barkana, and A. Gruzinov, *Cold and fuzzy dark matter*, *Phys. Rev. Lett.* **85** (2000) 1158–1161, [[astro-ph/0003365](#)].
- [1625] L. Hui, J. P. Ostriker, S. Tremaine, and E. Witten, *Ultralight scalars as cosmological dark matter*, *Phys. Rev. D* **95** (2017), no. 4 043541, [[arXiv:1610.08297](#)].
- [1626] H.-Y. Schive, T. Chiueh, and T. Broadhurst, *Cosmic Structure as the Quantum Interference of a Coherent Dark Wave*, *Nature Phys.* **10** (2014) 496–499, [[arXiv:1406.6586](#)].
- [1627] V. Iršič, M. Viel, M. G. Haehnelt, J. S. Bolton, and G. D. Becker, *First constraints on fuzzy dark matter from Lyman- α forest data and hydrodynamical simulations*, *Phys. Rev. Lett.* **119** (2017), no. 3 031302, [[arXiv:1703.04683](#)].
- [1628] E. D. Carlson, M. E. Machacek, and L. J. Hall, *Self-interacting dark matter*, *Astrophys. J.* **398** (1992) 43–52.
- [1629] M. Blennow, S. Clementz, and J. Herrero-Garcia, *Self-interacting inelastic dark matter: A viable solution to the small scale structure problems*, *JCAP* **03** (2017) 048, [[arXiv:1612.06681](#)].
- [1630] C. Garcia-Cely and X. Chu, *Self-interacting dark matter as a solution to the problems in small-scale structures*, in *52nd Rencontres de Moriond on EW Interactions and Unified Theories*, pp. 307–314, 2017. [[arXiv:1705.06221](#)].
- [1631] S. Tulin and H.-B. Yu, *Dark Matter Self-interactions and Small Scale Structure*, *Phys. Rept.* **730** (2018) 1–57, [[arXiv:1705.02358](#)].
- [1632] L. E. Strigari, M. Kaplinghat, and J. S. Bullock, *Dark Matter Halos with Cores from Hierarchical Structure Formation*, *Phys. Rev. D* **75** (2007) 061303, [[astro-ph/0606281](#)].

- [1633] I. de Martino, S. S. Chakrabarty, V. Cesare, A. Gallo, L. Ostorero, and A. Diaferio, *Dark matters on the scale of galaxies*, *Universe* **6** (2020), no. 8 107, [[arXiv:2007.15539](#)].
- [1634] R. Foot and S. Vagnozzi, *Dissipative hidden sector dark matter*, *Phys. Rev. D* **91** (2015) 023512, [[arXiv:1409.7174](#)].
- [1635] R. Foot and S. Vagnozzi, *Solving the small-scale structure puzzles with dissipative dark matter*, *JCAP* **07** (2016) 013, [[arXiv:1602.02467](#)].
- [1636] T. Sawala et al., *The APOSTLE simulations: solutions to the Local Group’s cosmic puzzles*, *Mon. Not. Roy. Astron. Soc.* **457** (2016), no. 2 1931–1943, [[arXiv:1511.01098](#)].
- [1637] B. Moore, *Evidence against dissipationless dark matter from observations of galaxy haloes*, *Nature* **370** (1994) 629.
- [1638] R. A. Flores and J. R. Primack, *Observational and theoretical constraints on singular dark matter halos*, *Astrophys. J. Lett.* **427** (1994) L1–4, [[astro-ph/9402004](#)].
- [1639] J. F. Navarro, C. S. Frenk, and S. D. M. White, *The Structure of cold dark matter halos*, *Astrophys. J.* **462** (1996) 563–575, [[astro-ph/9508025](#)].
- [1640] J. F. Navarro, C. S. Frenk, and S. D. M. White, *A Universal density profile from hierarchical clustering*, *Astrophys. J.* **490** (1997) 493–508, [[astro-ph/9611107](#)].
- [1641] J. F. Navarro, V. R. Eke, and C. S. Frenk, *The cores of dwarf galaxy halos*, *Mon. Not. Roy. Astron. Soc.* **283** (1996) L72–L78, [[astro-ph/9610187](#)].
- [1642] B. Moore, T. R. Quinn, F. Governato, J. Stadel, and G. Lake, *Cold collapse and the core catastrophe*, *Mon. Not. Roy. Astron. Soc.* **310** (1999) 1147–1152, [[astro-ph/9903164](#)].
- [1643] I. Ferrero, M. G. Abadi, J. F. Navarro, L. V. Sales, and S. Gurovich, *The dark matter halos of dwarf galaxies: a challenge for the LCDM paradigm?*, *Mon. Not. Roy. Astron. Soc.* **425** (2012) 2817–2823, [[arXiv:1111.6609](#)].
- [1644] M. Davis, G. Efstathiou, C. S. Frenk, and S. D. M. White, *The Evolution of Large Scale Structure in a Universe Dominated by Cold Dark Matter*, *Astrophys. J.* **292** (1985) 371–394.
- [1645] G. Battaglia, A. Helmi, E. Tolstoy, M. Irwin, V. Hill, and P. Jablonka, *The kinematic status and mass content of the Sculptor dwarf spheroidal galaxy*, *Astrophys. J. Lett.* **681** (2008) L13, [[arXiv:0802.4220](#)].
- [1646] M. G. Walker and J. Penarrubia, *A Method for Measuring (Slopes of) the Mass Profiles of Dwarf Spheroidal Galaxies*, *Astrophys. J.* **742** (2011) 20, [[arXiv:1108.2404](#)].
- [1647] N. C. Amorisco and N. W. Evans, *Dark Matter Cores and Cusps: The Case of Multiple Stellar Populations in Dwarf Spheroidals*, *Mon. Not. Roy. Astron. Soc.* **419** (2012) 184–196, [[arXiv:1106.1062](#)].
- [1648] A. Genina, A. Benítez-Llambay, C. S. Frenk, S. Cole, A. Fattahi, J. F. Navarro, K. A. Oman, T. Sawala, and T. Theuns, *The core–cusp problem: a matter of perspective*, *Monthly Notices of the Royal Astronomical Society* **474** (Nov, 2017) 1398–1411.
- [1649] S. S. McGaugh and W. J. G. de Blok, *Testing the dark matter hypothesis with low surface brightness galaxies and other evidence*, *Astrophys. J.* **499** (1998) 41, [[astro-ph/9801123](#)].
- [1650] G. Kauffmann, S. D. M. White, and B. Guiderdoni, *The Formation and Evolution of Galaxies Within Merging Dark Matter Haloes*, *Mon. Not. Roy. Astron. Soc.* **264** (1993) 201.

- [1651] A. A. Klypin, A. V. Kravtsov, O. Valenzuela, and F. Prada, *Where are the missing Galactic satellites?*, *Astrophys. J.* **522** (1999) 82–92, [[astro-ph/9901240](#)].
- [1652] B. Moore, S. Ghigna, F. Governato, G. Lake, T. R. Quinn, J. Stadel, and P. Tozzi, *Dark matter substructure within galactic halos*, *Astrophys. J. Lett.* **524** (1999) L19–L22, [[astro-ph/9907411](#)].
- [1653] J. S. Bullock, *Notes on the Missing Satellites Problem*, [arXiv:1009.4505](#).
- [1654] M. Mateo, *Dwarf galaxies of the Local Group*, *Ann. Rev. Astron. Astrophys.* **36** (1998) 435–506, [[astro-ph/9810070](#)].
- [1655] M. Boylan-Kolchin, J. S. Bullock, and M. Kaplinghat, *Too big to fail? The puzzling darkness of massive Milky Way subhaloes*, *Mon. Not. Roy. Astron. Soc.* **415** (2011) L40, [[arXiv:1103.0007](#)].
- [1656] M. Boylan-Kolchin, J. S. Bullock, and M. Kaplinghat, *The Milky Way’s bright satellites as an apparent failure of LCDM*, *Mon. Not. Roy. Astron. Soc.* **422** (2012) 1203–1218, [[arXiv:1111.2048](#)].
- [1657] S. Garrison-Kimmel, M. Boylan-Kolchin, J. S. Bullock, and E. N. Kirby, *Too Big to Fail in the Local Group*, *Mon. Not. Roy. Astron. Soc.* **444** (2014), no. 1 222–236, [[arXiv:1404.5313](#)].
- [1658] E. Papastergis, R. Giovanelli, M. P. Haynes, and F. Shankar, *Is there a “too big to fail” problem in the field?*, *Astron. Astrophys.* **574** (2015) A113, [[arXiv:1407.4665](#)].
- [1659] E. J. Tollerud, M. Boylan-Kolchin, and J. S. Bullock, *M31 Satellite Masses Compared to LCDM Subhaloes*, *Mon. Not. Roy. Astron. Soc.* **440** (2014), no. 4 3511–3519, [[arXiv:1403.6469](#)].
- [1660] M. Kaplinghat, M. Valli, and H.-B. Yu, *Too Big To Fail in Light of Gaia*, *Mon. Not. Roy. Astron. Soc.* **490** (2019), no. 1 231–242, [[arXiv:1904.04939](#)].
- [1661] J. I. Read, M. I. Wilkinson, N. W. Evans, G. Gilmore, and J. T. Kleyna, *The importance of tides for the local group dwarf spheroidals*, *Mon. Not. Roy. Astron. Soc.* **367** (2006) 387–399, [[astro-ph/0511759](#)].
- [1662] M. R. Lovell, V. Gonzalez-Perez, S. Bose, A. Boyarsky, S. Cole, C. S. Frenk, and O. Ruchayskiy, *Addressing the too big to fail problem with baryon physics and sterile neutrino dark matter*, *Mon. Not. Roy. Astron. Soc.* **468** (2017), no. 3 2836–2849, [[arXiv:1611.00005](#)].
- [1663] B. Bozek et al., *Warm FIRE: Simulating Galaxy Formation with Resonant Sterile Neutrino Dark Matter*, *Mon. Not. Roy. Astron. Soc.* **483** (2019), no. 3 4086–4099, [[arXiv:1803.05424](#)].
- [1664] J. Zavala, M. Vogelsberger, and M. G. Walker, *Constraining Self-Interacting Dark Matter with the Milky Way’s dwarf spheroidals*, *Mon. Not. Roy. Astron. Soc.* **431** (2013) L20–L24, [[arXiv:1211.6426](#)].
- [1665] M. Vogelsberger, J. Zavala, and A. Loeb, *Subhaloes in Self-Interacting Galactic Dark Matter Haloes*, *Mon. Not. Roy. Astron. Soc.* **423** (2012) 3740, [[arXiv:1201.5892](#)].
- [1666] P. Kroupa, C. Theis, and C. M. Boily, *The Great disk of Milky Way satellites and cosmological sub-structures*, *Astron. Astrophys.* **431** (2005) 517–521, [[astro-ph/0410421](#)].
- [1667] N. G. Ibata, R. A. Ibata, B. Famaey, and G. F. Lewis, *Velocity anti-correlation of diametrically opposed galaxy satellites in the low redshift universe*, *Nature* **511** (2014) 563, [[arXiv:1407.8178](#)].
- [1668] A. R. Conn et al., *The Three-Dimensional Structure of the M31 Satellite System: Strong Evidence for an Inhomogeneous Distribution of Satellites*, *Astrophys. J.* **766** (2013) 120, [[arXiv:1301.7131](#)].

- [1669] M. S. Pawlowski et al., *Co-orbiting satellite galaxy structures are still in conflict with the distribution of primordial dwarf galaxies*, *Mon. Not. Roy. Astron. Soc.* **442** (2014), no. 3 2362–2380, [[arXiv:1406.1799](#)].
- [1670] M. S. Pawlowski, *The Planes of Satellite Galaxies Problem, Suggested Solutions, and Open Questions*, *Mod. Phys. Lett. A* **33** (2018), no. 06 1830004, [[arXiv:1802.02579](#)].
- [1671] M. S. Pawlowski, J. Pflamm-Altenburg, and P. Kroupa, *The VPOS: a vast polar structure of satellite galaxies, globular clusters and streams around the Milky Way*, *Mon. Not. Roy. Astron. Soc.* **423** (2012) 1109, [[arXiv:1204.5176](#)].
- [1672] R. A. Ibata et al., *A Vast Thin Plane of Co-rotating Dwarf Galaxies Orbiting the Andromeda Galaxy*, *Nature* **493** (2013) 62–65, [[arXiv:1301.0446](#)].
- [1673] S. T. Sohn, E. Patel, M. A. Fardal, G. Besla, R. P. van der Marel, M. Geha, and P. Guhathakurta, *Hst proper motions of ngc 147 and ngc 185: Orbital histories and tests of a dynamically coherent andromeda satellite plane*, *The Astrophysical Journal* **901** (Sep, 2020) 43.
- [1674] N. I. Libeskind, C. S. Frenk, S. Cole, J. C. Helly, A. Jenkins, J. F. Navarro, and C. Power, *The Distribution of satellite galaxies: The Great pancake*, *Mon. Not. Roy. Astron. Soc.* **363** (2005) 146–152, [[astro-ph/0503400](#)].
- [1675] A. R. Zentner, A. V. Kravtsov, O. Y. Gnedin, and A. A. Klypin, *The Anisotropic distribution of Galactic satellites*, *Astrophys. J.* **629** (2005) 219, [[astro-ph/0502496](#)].
- [1676] F. C. van den Bosch, A. Burkert, and R. A. Swaters, *The angular momentum content of dwarf galaxies: new challenges for the theory of galaxy formation*, *Mon. Not. Roy. Astron. Soc.* **326** (2001) 1205, [[astro-ph/0105082](#)].
- [1677] J. J. Monaghan, *Smoothed particle hydrodynamics*, *Ann. Rev. Astron. Astrophys.* **30** (1992) 543–574.
- [1678] J. S. Bullock, A. Dekel, T. S. Kolatt, A. V. Kravtsov, A. A. Klypin, C. Porciani, and J. R. Primack, *A Universal angular momentum profile for galactic halos*, *Astrophys. J.* **555** (2001) 240–257, [[astro-ph/0011001](#)].
- [1679] N. Banik and P. Sikivie, *Axions and the Galactic Angular Momentum Distribution*, *Phys. Rev. D* **88** (2013) 123517, [[arXiv:1307.3547](#)].
- [1680] S. S. McGaugh, *A Novel Test of the Modified Newtonian Dynamics with Gas Rich Galaxies*, *Phys. Rev. Lett.* **106** (2011) 121303, [[arXiv:1102.3913](#)]. [Erratum: *Phys.Rev.Lett.* 107, 229901 (2011)].
- [1681] A. A. Dutton, *The baryonic Tully-Fisher relation and galactic outflows*, *Mon. Not. Roy. Astron. Soc.* **424** (2012) 3123, [[arXiv:1206.1855](#)].
- [1682] L. V. Sales et al., *The low-mass end of the baryonic Tully-Fisher relation*, *Mon. Not. Roy. Astron. Soc.* **464** (2017), no. 2 2419–2428, [[arXiv:1602.02155](#)].
- [1683] A. Di Cintio and F. Lelli, *The mass discrepancy acceleration relation in a Λ CDM context*, *Mon. Not. Roy. Astron. Soc.* **456** (2016), no. 1 L127–L131, [[arXiv:1511.06616](#)].
- [1684] M. Geha, M. R. Blanton, M. Masjedi, and A. A. West, *The Baryon Content of Extremely Low Mass Dwarf Galaxies*, *Astrophys. J.* **653** (2006) 240–254, [[astro-ph/0608295](#)].
- [1685] I. M. Santos-Santos, C. B. Brook, G. Stinson, A. Di Cintio, J. Wadsley, R. Domínguez-Tenreiro, S. Gottlöber, and G. Yepes, *The distribution of mass components in simulated disc galaxies*, *Mon. Not. Roy. Astron. Soc.* **455** (2016), no. 1 476–483, [[arXiv:1510.02474](#)].

- [1686] P. J. E. Peebles, *The void phenomenon*, *Astrophys. J.* **557** (2001) 495–504, [[astro-ph/0101127](#)].
- [1687] S. Gottloeber, E. L. Lokas, A. Klypin, and Y. Hoffman, *The Structure of voids*, *Mon. Not. Roy. Astron. Soc.* **344** (2003) 715, [[astro-ph/0305393](#)].
- [1688] P. J. E. Peebles, *Open problems in cosmology*, *Nucl. Phys. B Proc. Suppl.* **138** (2005) 5–9, [[astro-ph/0311435](#)].
- [1689] P. Peebles, *Galaxies as a cosmological test*, *Nuovo Cim. B* **122** (2007) 1035–1042, [[arXiv:0712.2757](#)].
- [1690] A. Tikhonov and A. Klypin, *The emptiness of voids: yet another over-abundance problem for the Λ CDM model*, *Mon. Not. Roy. Astron. Soc.* **395** (2009) 1915, [[arXiv:0807.0924](#)].
- [1691] Z. Haiman, A. A. Thoul, and A. Loeb, *Cosmological formation of low mass objects*, *Astrophys. J.* **464** (1996) 523, [[astro-ph/9507111](#)].
- [1692] V. Bromm, P. S. Coppi, and R. B. Larson, *The formation of the first stars. I. The Primordial star forming cloud*, *Astrophys. J.* **564** (2002) 23–51, [[astro-ph/0102503](#)].
- [1693] T. Abel, G. L. Bryan, and M. L. Norman, *The formation of the first star in the Universe*, *Science* **295** (2002) 93, [[astro-ph/0112088](#)].
- [1694] V. Bromm and R. B. Larson, *The First stars*, *Ann. Rev. Astron. Astrophys.* **42** (2004) 79–118, [[astro-ph/0311019](#)].
- [1695] V. Bromm, *Formation of the First Stars*, *Rept. Prog. Phys.* **76** (2013) 112901, [[arXiv:1305.5178](#)].
- [1696] N. Yoshida, T. Abel, L. Hernquist, and N. Sugiyama, *Simulations of early structure formation: Primordial gas clouds*, *Astrophys. J.* **592** (2003) 645–663, [[astro-ph/0301645](#)].
- [1697] S. Hirano, T. Hosokawa, N. Yoshida, K. Omukai, and H. W. Yorke, *Primordial star formation under the influence of far ultraviolet radiation: 1540 cosmological haloes and the stellar mass distribution*, *Mon. Not. Roy. Astron. Soc.* **448** (2015), no. 1 568–587, [[arXiv:1501.01630](#)].
- [1698] H. Xu, K. Ahn, M. L. Norman, J. H. Wise, and B. W. O’Shea, *X-ray Background at High Redshifts from Pop III Remnants: Results from Pop III star formation rates in the Renaissance Simulations*, *Astrophys. J. Lett.* **832** (2016), no. 1 L5, [[arXiv:1607.02664](#)].
- [1699] L. Tornatore, A. Ferrara, and R. Schneider, *Population III stars: hidden or disappeared ?*, *Mon. Not. Roy. Astron. Soc.* **382** (2007) 945, [[arXiv:0707.1433](#)].
- [1700] J. L. Johnson, *Population III Star Clusters in the Reionized Universe*, *Mon. Not. Roy. Astron. Soc.* **404** (2010) 1425, [[arXiv:0911.1294](#)].
- [1701] H. E. Bond, E. P. Nelan, D. A. Vandenberg, G. H. Schaefer, and D. Harmer, *HD 140283: A Star in the Solar Neighborhood that Formed Shortly After the Big Bang*, *Astrophys. J. Lett.* **765** (2013) L12, [[arXiv:1302.3180](#)].
- [1702] D. A. Vandenberg, H. E. Bond, E. P. Nelan, P. E. Nissen, G. H. Schaefer, and D. Harmer, *THREE ANCIENT HALO SUBGIANTS: PRECISE PARALLAXES, COMPOSITIONS, AGES, AND IMPLICATIONS FOR GLOBULAR CLUSTERS*, *The Astrophysical Journal* **792** (aug, 2014) 110.
- [1703] R. Jimenez, A. Cimatti, L. Verde, M. Moresco, and B. Wandelt, *The local and distant Universe: stellar ages and H_0* , *JCAP* **03** (2019) 043, [[arXiv:1902.07081](#)].

- [1704] M. A. C. Perryman, K. S. de Boer, G. Gilmore, E. Hog, M. G. Lattanzi, L. Lindegren, X. Luri, F. Mignard, O. Pace, and P. T. de Zeeuw, *GAIA: Composition, formation and evolution of the Galaxy*, *Astron. Astrophys.* **369** (2001) 339–363, [[astro-ph/0101235](#)].
- [1705] **Gaia** Collaboration, T. Prusti et al., *The Gaia Mission*, *Astron. Astrophys.* **595** (2016), no. Gaia Data Release 1 A1, [[arXiv:1609.04153](#)].
- [1706] D. Valcin, J. L. Bernal, R. Jimenez, L. Verde, and B. D. Wandelt, *Inferring the Age of the Universe with Globular Clusters*, [arXiv:2007.06594](#).
- [1707] R. H. Cyburt, B. D. Fields, and K. A. Olive, *Primordial nucleosynthesis in light of WMAP*, *Phys. Lett. B* **567** (2003) 227–234, [[astro-ph/0302431](#)].
- [1708] M. Asplund, D. L. Lambert, P. E. Nissen, F. Primas, and V. V. Smith, *Lithium isotopic abundances in metal-poor halo stars*, *Astrophys. J.* **644** (2006) 229–259, [[astro-ph/0510636](#)].
- [1709] R. H. Cyburt, B. D. Fields, and K. A. Olive, *An Update on the big bang nucleosynthesis prediction for $Li-7$: The problem worsens*, *JCAP* **11** (2008) 012, [[arXiv:0808.2818](#)].
- [1710] **Particle Data Group** Collaboration, P. A. Zyla et al., *Review of Particle Physics*, *PTEP* **2020** (2020), no. 8 083C01.
- [1711] C. Pitrou, A. Coc, J.-P. Uzan, and E. Vangioni, *Precision big bang nucleosynthesis with improved Helium-4 predictions*, *Phys. Rept.* **754** (2018) 1–66, [[arXiv:1801.08023](#)].
- [1712] F. Hammache et al., *Search for new resonant states in $10C$ and $11C$ and their impact on the cosmological lithium problem*, *Phys. Rev. C* **88** (2013), no. 6 062802, [[arXiv:1312.0894](#)].
- [1713] R. G. Pizzone, R. Sparta, C. A. Bertulani, C. Spitaleri, M. La Cognata, J. Lalmansingh, L. Lamia, A. Mukhamedzhanov, and A. Tumino, *Big Bang nucleosynthesis revisited via Trojan Horse Method measurements*, *Astrophys. J.* **786** (2014) 112, [[arXiv:1403.4909](#)].
- [1714] D. G. Yamazaki, M. Kusakabe, T. Kajino, G. J. Mathews, and M.-K. Cheoun, *Cosmological solutions to the Lithium problem: Big-bang nucleosynthesis with photon cooling, X -particle decay and a primordial magnetic field*, *Phys. Rev. D* **90** (2014), no. 2 023001, [[arXiv:1407.0021](#)].
- [1715] M. Kusakabe, K. S. Kim, M.-K. Cheoun, T. Kajino, Y. Kino, and G. J. Mathews, *Revised Big Bang Nucleosynthesis with long-lived negatively charged massive particles: updated recombination rates, primordial 9Be nucleosynthesis, and impact of new 6Li limits*, *Astrophys. J. Suppl.* **214** (2014) 5, [[arXiv:1403.4156](#)].
- [1716] V. Poulin and P. D. Serpico, *Loophole to the Universal Photon Spectrum in Electromagnetic Cascades and Application to the Cosmological Lithium Problem*, *Phys. Rev. Lett.* **114** (2015), no. 9 091101, [[arXiv:1502.01250](#)].
- [1717] J. Sato, T. Shimomura, and M. Yamanaka, *A Solution to Lithium Problem by Long-Lived Stau*, *Int. J. Mod. Phys. E* **26** (2017), no. 08 1741005, [[arXiv:1604.04769](#)].
- [1718] A. Goudelis, M. Pospelov, and J. Pradler, *Light Particle Solution to the Cosmic Lithium Problem*, *Phys. Rev. Lett.* **116** (2016), no. 21 211303, [[arXiv:1510.08858](#)].
- [1719] L. Salvati, L. Pagano, M. Lattanzi, M. Gerbino, and A. Melchiorri, *Breaking Be: a sterile neutrino solution to the cosmological lithium problem*, *JCAP* **08** (2016) 022, [[arXiv:1606.06968](#)].
- [1720] S. Q. Hou, J. J. He, A. Parikh, D. Kahl, C. A. Bertulani, T. Kajino, G. J. Mathews, and G. Zhao, *Non-extensive Statistics to the Cosmological Lithium Problem*, *Astrophys. J.* **834** (2017), no. 2 165, [[arXiv:1701.04149](#)].

- [1721] A. Coc and E. Vangioni, *Primordial nucleosynthesis*, *Int. J. Mod. Phys. E* **26** (2017), no. 08 1741002, [[arXiv:1707.01004](#)].
- [1722] K. Mori and M. Kusakabe, *Roles of ${}^7\text{Be}(n,p){}^7\text{Li}$ resonances in big bang nucleosynthesis with time-dependent quark mass and Li reduction by a heavy quark mass*, *Phys. Rev. D* **99** (2019), no. 8 083013, [[arXiv:1901.03943](#)].
- [1723] S. Hayakawa et al., *Experimental Study on the ${}^7\text{Be}(n,p){}^7\text{Li}$ and the ${}^7\text{Be}(n,\alpha){}^4\text{He}$ Reactions for Cosmological Lithium Problem*, *JPS Conf. Proc.* **31** (2020) 011036.
- [1724] S. Ishikawa et al., *Experimental Study of the ${}^7\text{Be}(n,p_1){}^7\text{Li}^*$ Reaction for the Cosmological Lithium Problem*, *JPS Conf. Proc.* **31** (2020) 011037.
- [1725] C. Iliadis and A. Coc, *Thermonuclear reaction rates and primordial nucleosynthesis*, *Astrophys. J.* **901** (2020), no. 2 127, [[arXiv:2008.12200](#)].
- [1726] M. Clara and C. Martins, *Primordial nucleosynthesis with varying fundamental constants: Improved constraints and a possible solution to the Lithium problem*, *Astron. Astrophys.* **633** (2020) L11, [[arXiv:2001.01787](#)].
- [1727] P. Di Bari, S. F. King, and A. Merle, *Dark Radiation or Warm Dark Matter from long lived particle decays in the light of Planck*, *Phys. Lett. B* **724** (2013) 77–83, [[arXiv:1303.6267](#)].
- [1728] L. Sbordone et al., *The metal-poor end of the Spite plateau. 1: Stellar parameters, metallicities and lithium abundances*, *Astron. Astrophys.* **522** (2010) A26, [[arXiv:1003.4510](#)].
- [1729] J. Melendez, L. Casagrande, I. Ramirez, M. Asplund, and W. Schuster, *Observational evidence for a broken Li Spite plateau and mass-dependent Li depletion*, *Astron. Astrophys.* **515** (2010) L3, [[arXiv:1005.2944](#)].
- [1730] M. Spite, F. Spite, and P. Bonifacio, *The cosmic lithium problem: an observer’s perspective*, *Mem. Soc. Astron. Ital. Suppl.* **22** (2012) 9, [[arXiv:1208.1190](#)].
- [1731] F. Iocco, *The lithium problem, a phenomenologist’s perspective*, *Mem. Soc. Astron. Ital. Suppl.* **22** (2012) 19, [[arXiv:1206.2396](#)].
- [1732] G. J. Mathews, A. Kedia, N. Sasankan, M. Kusakabe, Y. Luo, T. Kajino, D. Yamazaki, T. Makki, and M. E. Eid, *Cosmological Solutions to the Lithium Problem*, *JPS Conf. Proc.* **31** (2020) 011033, [[arXiv:1909.01245](#)].
- [1733] J. Larena, J.-M. Alimi, and A. Serna, *Big Bang nucleosynthesis in scalar tensor gravity: The key problem of the primordial Li-7 abundance*, *Astrophys. J.* **658** (2007) 1–10, [[astro-ph/0511693](#)].
- [1734] K. Kohri and F. Takayama, *Big bang nucleosynthesis with long lived charged massive particles*, *Phys. Rev. D* **76** (2007) 063507, [[hep-ph/0605243](#)].
- [1735] J. C. Berengut, V. V. Flambaum, and V. F. Dmitriev, *Effect of quark-mass variation on big bang nucleosynthesis*, *Phys. Lett. B* **683** (2010) 114–118, [[arXiv:0907.2288](#)].
- [1736] M. Kawasaki and M. Kusakabe, *Destruction of ${}^7\text{Be}$ in big bang nucleosynthesis via long-lived sub-strongly interacting massive particles as a solution to the Li problem*, *Phys. Rev. D* **83** (2011) 055011, [[arXiv:1012.0435](#)].
- [1737] M.-K. Cheoun, T. Kajino, M. Kusakabe, and G. J. Mathews, *Time Dependent Quark Masses and Big Bang Nucleosynthesis Revisited*, *Phys. Rev. D* **84** (2011) 043001, [[arXiv:1104.5547](#)].
- [1738] A. Coc, N. J. Nunes, K. A. Olive, J.-P. Uzan, and E. Vangioni, *Coupled Variations of Fundamental Couplings and Primordial Nucleosynthesis*, *Phys. Rev. D* **76** (2007) 023511, [[astro-ph/0610733](#)].

- [1739] Y. Luo, T. Kajino, M. Kusakabe, and G. J. Mathews, *Big Bang Nucleosynthesis with an Inhomogeneous Primordial Magnetic Field Strength*, *Astrophys. J.* **872** (2019), no. 2 172, [[arXiv:1810.08803](#)].
- [1740] R. H. Cyburt, B. D. Fields, and K. A. Olive, *Solar neutrino constraints on the BBN production of Li*, *Phys. Rev. D* **69** (2004) 123519, [[astro-ph/0312629](#)].
- [1741] R. N. Boyd, C. R. Brune, G. M. Fuller, and C. J. Smith, *New Nuclear Physics for Big Bang Nucleosynthesis*, *Phys. Rev. D* **82** (2010) 105005, [[arXiv:1008.0848](#)].
- [1742] N. Chakraborty, B. D. Fields, and K. A. Olive, *Resonant Destruction as a Possible Solution to the Cosmological Lithium Problem*, *Phys. Rev. D* **83** (2011) 063006, [[arXiv:1011.0722](#)].
- [1743] A. Coc, S. Goriely, Y. Xu, M. Saimpert, and E. Vangioni, *Standard Big-Bang Nucleosynthesis up to CNO with an improved extended nuclear network*, *Astrophys. J.* **744** (2012) 158, [[arXiv:1107.1117](#)].
- [1744] C. Brogini, L. Canton, G. Fiorentini, and F. L. Villante, *The cosmological ${}^7\text{Li}$ problem from a nuclear physics perspective*, *JCAP* **06** (2012) 030, [[arXiv:1202.5232](#)].
- [1745] M. H. Pinsonneault, G. Steigman, T. P. Walker, and V. K. Narayanan, *Stellar mixing and the primordial lithium abundance*, *Astrophys. J.* **574** (2002) 398–411, [[astro-ph/0105439](#)].
- [1746] O. Richard, G. Michaud, and J. Richer, *Implications of WMAP observations on Li abundance and stellar evolution models*, *Astrophys. J.* **619** (2005) 538–548, [[astro-ph/0409672](#)].
- [1747] A. J. Korn, F. Grundahl, O. Richard, P. S. Barklem, L. Mashonkina, R. Collet, N. Piskunov, and B. Gustafsson, *A probable stellar solution to the cosmological lithium discrepancy*, *Nature* **442** (2006) 657–659, [[astro-ph/0608201](#)].
- [1748] X. Fu, A. Bressan, P. Molaro, and P. Marigo, *Lithium evolution in metal-poor stars: from pre-main sequence to the Spite plateau*, *Monthly Notices of the Royal Astronomical Society* **452** (07, 2015) 3256–3265, [<https://academic.oup.com/mnras/article-pdf/452/3/3256/4901646/stv1384.pdf>].
- [1749] D. G. Yamazaki, M. Kusakabe, T. Kajino, G. J. Mathews, and M.-K. Cheoun, *The new hybrid BBN model with the photon cooling, X particle, and the primordial magnetic field*, *Int. J. Mod. Phys. E* **26** (2017), no. 08 1741006.
- [1750] T. Yang, A. Banerjee, and E. O. Colgáin, *Cosmography and flat Λ CDM tensions at high redshift*, *Phys. Rev. D* **102** (2020), no. 12 123532, [[arXiv:1911.01681](#)].
- [1751] Y. Avni and H. Tananbaum, *X-Ray Properties of Optically Selected QSOs*, *Astroph. J.* **305** (June, 1986) 83.
- [1752] F. Melia, *Cosmological test using the Hubble diagram of high- z quasars*, *Mon. Not. Roy. Astron. Soc.* **489** (2019), no. 1 517–523, [[arXiv:1907.13127](#)].
- [1753] N. Khadka and B. Ratra, *Quasar X-ray and UV flux, baryon acoustic oscillation, and Hubble parameter measurement constraints on cosmological model parameters*, *Mon. Not. Roy. Astron. Soc.* **492** (2020), no. 3 4456–4468, [[arXiv:1909.01400](#)].
- [1754] X. Li, R. E. Keeley, A. Shafieloo, X. Zheng, S. Cao, M. Biesiada, and Z.-H. Zhu, *Hubble diagram at higher redshifts: Model independent calibration of quasars*, [arXiv:2103.16032](#).
- [1755] H. Velten and S. Gomes, *Is the Hubble diagram of quasars in tension with concordance cosmology?*, *Phys. Rev. D* **101** (2020), no. 4 043502, [[arXiv:1911.11848](#)].

- [1756] N. Khadka and B. Ratra, *Determining the range of validity of quasar X-ray and UV flux measurements for constraining cosmological model parameters*, [arXiv:2012.09291](#).
- [1757] E. Lusso et al., *Quasars as standard candles III. Validation of a new sample for cosmological studies*, *Astron. Astrophys.* **642** (2020) A150, [[arXiv:2008.08586](#)].
- [1758] A. D. Rider, D. C. Moore, C. P. Blakemore, M. Louis, M. Lu, and G. Gratta, *Search for Screened Interactions Associated with Dark Energy Below the 100 μm Length Scale*, *Phys. Rev. Lett.* **117** (2016), no. 10 101101, [[arXiv:1604.04908](#)].
- [1759] N. Arkani-Hamed, S. Dimopoulos, and G. R. Dvali, *The Hierarchy problem and new dimensions at a millimeter*, *Phys. Lett. B* **429** (1998) 263–272, [[hep-ph/9803315](#)].
- [1760] N. Arkani-Hamed, S. Dimopoulos, and G. R. Dvali, *Phenomenology, astrophysics and cosmology of theories with submillimeter dimensions and TeV scale quantum gravity*, *Phys. Rev. D* **59** (1999) 086004, [[hep-ph/9807344](#)].
- [1761] I. Antoniadis, N. Arkani-Hamed, S. Dimopoulos, and G. R. Dvali, *New dimensions at a millimeter to a Fermi and superstrings at a TeV*, *Phys. Lett. B* **436** (1998) 257–263, [[hep-ph/9804398](#)].
- [1762] L. Perivolaropoulos and C. Sourdis, *Cosmological effects of radion oscillations*, *Phys. Rev. D* **66** (2002) 084018, [[hep-ph/0204155](#)].
- [1763] L. Perivolaropoulos, *Equation of state of oscillating Brans-Dicke scalar and extra dimensions*, *Phys. Rev. D* **67** (2003) 123516, [[hep-ph/0301237](#)].
- [1764] E. G. Floratos and G. K. Leontaris, *Low scale unification, Newton’s law and extra dimensions*, *Phys. Lett. B* **465** (1999) 95–100, [[hep-ph/9906238](#)].
- [1765] A. Kehagias and K. Sfetsos, *Deviations from the $1/r^{**2}$ Newton law due to extra dimensions*, *Phys. Lett. B* **472** (2000) 39–44, [[hep-ph/9905417](#)].
- [1766] A. Donini and S. G. Marimón, *Micro-orbits in a many-brane model and deviations from Newton’s $1/r^2$ law*, *Eur. Phys. J. C* **76** (2016), no. 12 696, [[arXiv:1609.05654](#)].
- [1767] R. Benichou and J. Estes, *The Fate of Newton’s Law in Brane-World Scenarios*, *Phys. Lett. B* **712** (2012) 456–459, [[arXiv:1112.0565](#)].
- [1768] K. A. Bronnikov, S. A. Kononogov, and V. N. Melnikov, *Brane world corrections to Newton’s law*, *Gen. Rel. Grav.* **38** (2006) 1215–1232, [[gr-qc/0601114](#)].
- [1769] S. Nojiri and S. D. Odintsov, *Newton potential in deSitter brane world*, *Phys. Lett. B* **548** (2002) 215–223, [[hep-th/0209066](#)].
- [1770] J. Edholm, A. S. Koshelev, and A. Mazumdar, *Behavior of the Newtonian potential for ghost-free gravity and singularity-free gravity*, *Phys. Rev. D* **94** (2016), no. 10 104033, [[arXiv:1604.01989](#)].
- [1771] A. Kehagias and M. Maggiore, *Spherically symmetric static solutions in a nonlocal infrared modification of General Relativity*, *JHEP* **08** (2014) 029, [[arXiv:1401.8289](#)].
- [1772] V. P. Frolov and A. Zelnikov, *Head-on collision of ultrarelativistic particles in ghost-free theories of gravity*, *Phys. Rev. D* **93** (2016), no. 6 064048, [[arXiv:1509.03336](#)].
- [1773] E. T. Tomboulis, *Superrenormalizable gauge and gravitational theories*, [hep-th/9702146](#).
- [1774] T. Biswas, A. Conroy, A. S. Koshelev, and A. Mazumdar, *Generalized ghost-free quadratic curvature gravity*, *Class. Quant. Grav.* **31** (2014) 015022, [[arXiv:1308.2319](#)]. [Erratum: *Class.Quant.Grav.* **31**, 159501 (2014)].

- [1775] J. C. Hill and E. J. Baxter, *Can Early Dark Energy Explain EDGES?*, *JCAP* **08** (2018) 037, [[arXiv:1803.07555](#)].
- [1776] S. Fraser et al., *The EDGES 21 cm Anomaly and Properties of Dark Matter*, *Phys. Lett. B* **785** (2018) 159–164, [[arXiv:1803.03245](#)].
- [1777] J. B. Muñoz and A. Loeb, *A small amount of mini-charged dark matter could cool the baryons in the early Universe*, *Nature* **557** (2018), no. 7707 684, [[arXiv:1802.10094](#)].
- [1778] A. Boyarsky, D. Iakubovskiy, O. Ruchayskiy, A. Rudakovskiy, and W. Valkenburg, *21-cm observations and warm dark matter models*, *Phys. Rev. D* **100** (2019), no. 12 123005, [[arXiv:1904.03097](#)].
- [1779] R. Barkana, N. J. Outmeuguine, D. Redigolo, and T. Volansky, *Strong constraints on light dark matter interpretation of the EDGES signal*, *Phys. Rev. D* **98** (2018), no. 10 103005, [[arXiv:1803.03091](#)].
- [1780] E. D. Kovetz, V. Poulin, V. Gluscevic, K. K. Boddy, R. Barkana, and M. Kamionkowski, *Tighter limits on dark matter explanations of the anomalous EDGES 21 cm signal*, *Phys. Rev. D* **98** (2018), no. 10 103529, [[arXiv:1807.11482](#)].
- [1781] F. Menanteau et al., *The Atacama Cosmology Telescope: ACT-CL J0102-4215 ‘El Gordo,’ a Massive Merging Cluster at Redshift 0.87*, *Astrophys. J.* **748** (2012) 7, [[arXiv:1109.0953](#)].
- [1782] **WMAP** Collaboration, G. Hinshaw et al., *Nine-Year Wilkinson Microwave Anisotropy Probe (WMAP) Observations: Cosmological Parameter Results*, *Astrophys. J. Suppl.* **208** (2013) 19, [[arXiv:1212.5226](#)].
- [1783] **Planck** Collaboration, R. Adam et al., *Planck 2015 results. I. Overview of products and scientific results*, *Astron. Astrophys.* **594** (2016) A1, [[arXiv:1502.01582](#)].
- [1784] **ACTPol** Collaboration, S. Naess et al., *The Atacama Cosmology Telescope: CMB Polarization at $200 < \ell < 9000$* , *JCAP* **10** (2014) 007, [[arXiv:1405.5524](#)].
- [1785] **SPT** Collaboration, R. Keisler et al., *Measurements of Sub-degree B-mode Polarization in the Cosmic Microwave Background from 100 Square Degrees of SPTpol Data*, *Astrophys. J.* **807** (2015), no. 2 151, [[arXiv:1503.02315](#)].
- [1786] S. W. Henderson et al., *Advanced ACTPol Cryogenic Detector Arrays and Readout*, *J. Low. Temp. Phys.* **184** (2016), no. 3-4 772–779, [[arXiv:1510.02809](#)].
- [1787] **SPT** Collaboration, R. Keisler et al., *Measurements of Sub-degree B-mode Polarization in the Cosmic Microwave Background from 100 Square Degrees of SPTpol Data*, *Astrophys. J.* **807** (2015), no. 2 151, [[arXiv:1503.02315](#)].
- [1788] **CMB-S4** Collaboration, K. N. Abazajian et al., *CMB-S4 Science Book, First Edition*, [[arXiv:1610.02743](#)].
- [1789] A. Suzuki et al., *The LiteBIRD Satellite Mission - Sub-Kelvin Instrument*, in *17th International Workshop on Low Temperature Detectors (LTD 17) Kurume City, Japan, July 17-21, 2017*, 2018. [[arXiv:1801.06987](#)].
- [1790] T. Matsumura et al., *Mission design of LiteBIRD*, [[arXiv:1311.2847](#)]. [*J. Low. Temp. Phys.* 176,733(2014)].
- [1791] C. Heymans et al., *CFHTLenS: The Canada-France-Hawaii Telescope Lensing Survey*, *Mon. Not. Roy. Astron. Soc.* **427** (2012) 146, [[arXiv:1210.0032](#)].

- [1792] H. Hildebrandt et al., *KiDS-450: Cosmological parameter constraints from tomographic weak gravitational lensing*, *Mon. Not. Roy. Astron. Soc.* **465** (2017) 1454, [[arXiv:1606.05338](#)].
- [1793] F. Köhlinger et al., *KiDS-450: The tomographic weak lensing power spectrum and constraints on cosmological parameters*, *Mon. Not. Roy. Astron. Soc.* **471** (2017), no. 4 4412–4435, [[arXiv:1706.02892](#)].
- [1794] K. S. Dawson et al., *The SDSS-IV extended Baryon Oscillation Spectroscopic Survey: Overview and Early Data*, *Astron. J.* **151** (2016) 44, [[arXiv:1508.04473](#)].
- [1795] **DES** Collaboration, T. Abbott et al., *Cosmology from cosmic shear with Dark Energy Survey Science Verification data*, *Phys. Rev.* **D94** (2016), no. 2 022001, [[arXiv:1507.05552](#)].
- [1796] **DES** Collaboration, M. A. Troxel et al., *Dark Energy Survey Year 1 results: Cosmological constraints from cosmic shear*, *Phys. Rev.* **D98** (2018), no. 4 043528, [[arXiv:1708.01538](#)].
- [1797] **DES** Collaboration, T. M. C. Abbott et al., *Dark Energy Survey year 1 results: Cosmological constraints from galaxy clustering and weak lensing*, *Phys. Rev.* **D98** (2018), no. 4 043526, [[arXiv:1708.01530](#)].
- [1798] Y.-K. Chiang et al., *Surveying Galaxy Proto-clusters in Emission: A Large-scale Structure at $z = 2.44$ and the Outlook for HETDEX*, *Astrophys. J.* **808** (2015), no. 1 37, [[arXiv:1505.03877](#)].
- [1799] **LSST Science, LSST Project** Collaboration, P. A. Abell et al., *LSST Science Book, Version 2.0*, [arXiv:0912.0201](#).
- [1800] **LSST** Collaboration, P. Marshall et al., *Science-Driven Optimization of the LSST Observing Strategy*, [arXiv:1708.04058](#).
- [1801] P. Bull, P. G. Ferreira, P. Patel, and M. G. Santos, *Late-time cosmology with 21cm intensity mapping experiments*, *Astrophys. J.* **803** (2015), no. 1 21, [[arXiv:1405.1452](#)].
- [1802] M. J. Jarvis, D. Bacon, C. Blake, M. L. Brown, S. N. Lindsay, A. Raccañelli, M. Santos, and D. Schwarz, *Cosmology with SKA Radio Continuum Surveys*, [arXiv:1501.03825](#).
- [1803] D. Bacon et al., *Synergy between the Large Synoptic Survey Telescope and the Square Kilometre Array*, *PoS AASKA14* (2015) 145, [[arXiv:1501.03977](#)].
- [1804] S. Yahya, P. Bull, M. G. Santos, M. Silva, R. Maartens, P. Okouma, and B. Bassett, *Cosmological performance of SKA HI galaxy surveys*, *Mon. Not. Roy. Astron. Soc.* **450** (2015), no. 3 2251–2260, [[arXiv:1412.4700](#)].
- [1805] **EUCLID** Collaboration, R. Laureijs et al., *Euclid Definition Study Report*, [arXiv:1110.3193](#).
- [1806] L. Amendola et al., *Cosmology and fundamental physics with the Euclid satellite*, *Living Rev. Rel.* **21** (2018), no. 1 2, [[arXiv:1606.00180](#)].
- [1807] D. Spergel et al., *Wide-Field Infrared Survey Telescope-Astrophysics Focused Telescope Assets WFIRST-AFTA 2015 Report*, [arXiv:1503.03757](#).
- [1808] R. Hounsell et al., *Simulations of the WFIRST Supernova Survey and Forecasts of Cosmological Constraints*, [arXiv:1702.01747](#).
- [1809] **BOSS** Collaboration, L. Anderson et al., *The clustering of galaxies in the SDSS-III Baryon Oscillation Spectroscopic Survey: baryon acoustic oscillations in the Data Releases 10 and 11 Galaxy samples*, *Mon. Not. Roy. Astron. Soc.* **441** (2014), no. 1 24–62, [[arXiv:1312.4877](#)].

- [1810] L. Samushia et al., *The clustering of galaxies in the SDSS-III Baryon Oscillation Spectroscopic Survey: measuring growth rate and geometry with anisotropic clustering*, *Mon. Not. Roy. Astron. Soc.* **439** (2014), no. 4 3504–3519, [[arXiv:1312.4899](#)].
- [1811] DESI Collaboration, A. Aghamousa et al., *The DESI Experiment Part I: Science, Targeting, and Survey Design*, [arXiv:1611.00036](#).
- [1812] DESI Collaboration, A. Aghamousa et al., *The DESI Experiment Part II: Instrument Design*, [arXiv:1611.00037](#).
- [1813] <https://www.desi.lbl.gov/>.
- [1814] <http://sci.esa.int/euclid/>.
- [1815] C. J. Copi, A. N. Davis, and L. M. Krauss, *A New nucleosynthesis constraint on the variation of G* , *Phys. Rev. Lett.* **92** (2004) 171301, [[astro-ph/0311334](#)].
- [1816] S. Alam, S. Ho, and A. Silvestri, *Testing deviations from Λ CDM with growth rate measurements from six large-scale structure surveys at $z=0.06-1$* , *Mon. Not. Roy. Astron. Soc.* **456** (2016), no. 4 3743–3756, [[arXiv:1509.05034](#)].
- [1817] R. Arjona, W. Cardona, and S. Nesseris, *Unraveling the effective fluid approach for $f(R)$ models in the sub-horizon approximation*, [arXiv:1811.02469](#).
- [1818] H. A. Feldman, N. Kaiser, and J. A. Peacock, *Power spectrum analysis of three-dimensional redshift surveys*, *Astrophys. J.* **426** (1994) 23–37, [[astro-ph/9304022](#)].
- [1819] M. Tegmark, *Measuring cosmological parameters with galaxy surveys*, *Phys. Rev. Lett.* **79** (1997) 3806–3809, [[astro-ph/9706198](#)].
- [1820] S. F. Huelga, C. Macchiavello, T. Pellizzari, A. K. Ekert, M. B. Plenio, and J. I. Cirac, *On the improvement of frequency standards with quantum entanglement*, *Phys. Rev. Lett.* **79** (1997) 3865, [[quant-ph/9707014](#)].
- [1821] A. R. Duffy, *Probing the nature of dark energy through galaxy redshift surveys with radio telescopes*, *Annalen Phys.* **526** (2014) 283–293, [[arXiv:1405.7465](#)].
- [1822] F. B. Abdalla and S. Rawlings, *Probing dark energy with baryonic oscillations and future radio surveys of neutral hydrogen*, *Mon. Not. Roy. Astron. Soc.* **360** (2005) 27–40, [[astro-ph/0411342](#)].
- [1823] R. Gannouji, L. Kazantzidis, L. Perivolaropoulos, and D. Polarski, *Consistency of modified gravity with a decreasing $G_{\text{eff}}(z)$ in a Λ CDM background*, *Phys. Rev.* **D98** (2018), no. 10 104044, [[arXiv:1809.07034](#)].
- [1824] C. Alcock and B. Paczynski, *An evolution free test for non-zero cosmological constant*, *Nature* **281** (1979) 358–359.
- [1825] A. Lewis, A. Challinor, and A. Lasenby, *Efficient computation of CMB anisotropies in closed FRW models*, *Astrophys. J.* **538** (2000) 473–476, [[astro-ph/9911177](#)].
- [1826] J. Hamann, S. Hannestad, J. Lesgourgues, C. Rampf, and Y. Y. Y. Wong, *Cosmological parameters from large scale structure - geometric versus shape information*, *JCAP* **1007** (2010) 022, [[arXiv:1003.3999](#)].
- [1827] F. K. Anagnostopoulos and S. Basilakos, *Constraining the dark energy models with $H(z)$ data: An approach independent of H_0* , *Phys. Rev.* **D97** (2018), no. 6 063503, [[arXiv:1709.02356](#)].

- [1828] R.-Y. Guo and X. Zhang, *Constraining dark energy with Hubble parameter measurements: an analysis including future redshift-drift observations*, *Eur. Phys. J.* **C76** (2016), no. 3 163, [[arXiv:1512.07703](#)].
- [1829] E. A. Kazin et al., *The WiggleZ Dark Energy Survey: improved distance measurements to $z = 1$ with reconstruction of the baryonic acoustic feature*, *Mon. Not. Roy. Astron. Soc.* **441** (2014), no. 4 3524–3542, [[arXiv:1401.0358](#)].
- [1830] <http://leandros.physics.uoi.gr/dim-reduction/>.
- [1831] S. Nesseris and L. Perivolaropoulos, *Evolving newton’s constant, extended gravity theories and snia data analysis*, *Phys. Rev.* **D73** (2006) 103511, [[astro-ph/0602053](#)].
- [1832] E. Belgacem, Y. Dirian, S. Foffa, and M. Maggiore, *Gravitational-wave luminosity distance in modified gravity theories*, *Phys. Rev.* **D97** (2018), no. 10 104066, [[arXiv:1712.08108](#)].
- [1833] **LIGO Scientific Collaboration and Virgo Collaboration** Collaboration, B. P. e. a. Abbott, *Gw170817: Observation of gravitational waves from a binary neutron star inspiral*, *Phys. Rev. Lett.* **119** (Oct, 2017) 161101.
- [1834] F. Zwicky, *Die Rotverschiebung von extragalaktischen Nebeln*, *Helvetica Physica Acta* **6** (1933) 110–127.
- [1835] F. Zwicky, *On the Masses of Nebulae and of Clusters of Nebulae*, *Astroph.J.* **86** (Oct., 1937) 217.
- [1836] A. G. Riess et al., *BV RI light curves for 22 type Ia supernovae*, *Astron. J.* **117** (1999) 707–724, [[astro-ph/9810291](#)].
- [1837] J. D. Anderson, P. A. Laing, E. L. Lau, A. S. Liu, M. M. Nieto, and S. G. Turyshev, *Indication, from Pioneer 10 / 11, Galileo, and Ulysses data, of an apparent anomalous, weak, long range acceleration*, *Phys. Rev. Lett.* **81** (1998) 2858–2861, [[gr-qc/9808081](#)].
- [1838] J. D. Anderson, P. A. Laing, E. L. Lau, A. S. Liu, M. M. Nieto, and S. G. Turyshev, *Study of the anomalous acceleration of Pioneer 10 and 11*, *Phys. Rev.* **D65** (2002) 082004, [[gr-qc/0104064](#)].
- [1839] **PIONEER** Collaboration, H. Dittus et al., *A Mission to explore the Pioneer anomaly*, *ESA Spec. Publ.* **588** (2005) 3–10, [[gr-qc/0506139](#)].
- [1840] C. Lammerzahl, O. Preuss, and H. Dittus, *Is the physics within the Solar system really understood?*, *Astrophys. Space Sci. Libr.* **349** (2008) 75–101, [[gr-qc/0604052](#)].
- [1841] S. G. Turyshev, V. T. Toth, G. Kinsella, S.-C. Lee, S. M. Lok, and J. Ellis, *Support for the thermal origin of the Pioneer anomaly*, *Phys. Rev. Lett.* **108** (2012) 241101, [[arXiv:1204.2507](#)].
- [1842] J. Chiaverini, S. J. Smullin, A. A. Geraci, D. M. Weld, and A. Kapitulnik, *New experimental constraints on nonNewtonian forces below 100 microns*, *Phys. Rev. Lett.* **90** (2003) 151101, [[hep-ph/0209325](#)].
- [1843] J. Frieman, M. Turner, and D. Huterer, *Dark Energy and the Accelerating Universe*, *Ann. Rev. Astron. Astrophys.* **46** (2008) 385–432, [[arXiv:0803.0982](#)].
- [1844] R. R. Caldwell and M. Kamionkowski, *The Physics of Cosmic Acceleration*, *Ann. Rev. Nucl. Part. Sci.* **59** (2009) 397–429, [[arXiv:0903.0866](#)].
- [1845] C. Brans and R. H. Dicke, *Mach’s principle and a relativistic theory of gravitation*, *Phys. Rev.* **124** (1961) 925–935.
- [1846] J.-P. Uzan, *Cosmological scaling solutions of nonminimally coupled scalar fields*, *Phys. Rev.* **D59** (1999) 123510, [[gr-qc/9903004](#)].

- [1847] C. Schimd, J.-P. Uzan, and A. Riazuelo, *Weak lensing in scalar-tensor theories of gravity*, *Phys. Rev.* **D71** (2005) 083512, [[astro-ph/0412120](#)].
- [1848] C. Charmousis, E. J. Copeland, A. Padilla, and P. M. Saffin, *General second order scalar-tensor theory, self tuning, and the Fab Four*, *Phys. Rev. Lett.* **108** (2012) 051101, [[arXiv:1106.2000](#)].
- [1849] W. Hu and I. Sawicki, *Models of $f(R)$ Cosmic Acceleration that Evade Solar-System Tests*, *Phys. Rev.* **D76** (2007) 064004, [[arXiv:0705.1158](#)].
- [1850] S. Basilakos, S. Nesseris, and L. Perivolaropoulos, *Observational constraints on viable $f(R)$ parametrizations with geometrical and dynamical probes*, *Phys. Rev.* **D87** (2013), no. 12 123529, [[arXiv:1302.6051](#)].
- [1851] R. Ferraro and F. Fiorini, *On Born-Infeld Gravity in Weitzenbock spacetime*, *Phys. Rev.* **D78** (2008) 124019, [[arXiv:0812.1981](#)].
- [1852] E. V. Linder, *Einstein's Other Gravity and the Acceleration of the Universe*, *Phys. Rev.* **D81** (2010) 127301, [[arXiv:1005.3039](#)]. [Erratum: *Phys. Rev.* **D82**,109902(2010)].
- [1853] B. Mashhoon, *Nonlocal theory of accelerated observers*, *Phys. Rev.* **A47** (1993) 4498–4501.
- [1854] B. Mashhoon, *Nonlocal Special Relativity*, *Annalen Phys.* **17** (2008) 705–727, [[arXiv:0805.2926](#)].
- [1855] S. Deser and R. P. Woodard, *Nonlocal Cosmology*, *Phys. Rev. Lett.* **99** (2007) 111301, [[arXiv:0706.2151](#)].
- [1856] T. Clifton, P. G. Ferreira, A. Padilla, and C. Skordis, *Modified Gravity and Cosmology*, *Phys. Rept.* **513** (2012) 1–189, [[arXiv:1106.2476](#)].
- [1857] S. Capozziello, V. F. Cardone, S. Carloni, and A. Troisi, *Can higher order curvature theories explain rotation curves of galaxies?*, *Phys. Lett.* **A326** (2004) 292–296, [[gr-qc/0404114](#)].
- [1858] C. F. Martins and P. Salucci, *Analysis of Rotation Curves in the framework of R^{**n} gravity*, *Mon. Not. Roy. Astron. Soc.* **381** (2007) 1103–1108, [[astro-ph/0703243](#)].
- [1859] M. Milgrom, *A Modification of the Newtonian dynamics as a possible alternative to the hidden mass hypothesis*, *Astrophys. J.* **270** (1983) 365–370.
- [1860] R. H. Sanders and S. S. McGaugh, *Modified Newtonian dynamics as an alternative to dark matter*, *Ann. Rev. Astron. Astrophys.* **40** (2002) 263–317, [[astro-ph/0204521](#)].
- [1861] B. Famaey and S. McGaugh, *Modified Newtonian Dynamics (MOND): Observational Phenomenology and Relativistic Extensions*, *Living Rev. Rel.* **15** (2012) 10, [[arXiv:1112.3960](#)].
- [1862] D. C. Rodrigues, V. Marra, A. del Popolo, and Z. Davari, *Absence of a fundamental acceleration scale in galaxies*, *Nat. Astron.* **2** (2018), no. 8 668–672, [[arXiv:1806.06803](#)].
- [1863] D. Grumiller, *Model for gravity at large distances*, *Phys. Rev. Lett.* **105** (2010) 211303, [[arXiv:1011.3625](#)]. [Erratum: *Phys. Rev. Lett.* **106**,039901(2011)].
- [1864] D. Grumiller and F. Preis, *Rindler force at large distances*, *Int. J. Mod. Phys.* **D20** (2011) 2761–2766, [[arXiv:1107.2373](#)].
- [1865] G. Alestas and L. Perivolaropoulos, *Evading Derrick's theorem in curved space: Static metastable spherical domain wall*, [[arXiv:1901.06659](#)].
- [1866] H.-N. Lin, M.-H. Li, X. Li, and Z. Chang, *Galaxies Rotation Curves in the Grumiller's Modified Gravity*, *Mon. Not. Roy. Astron. Soc.* **430** (2013), no. 1 450–458, [[arXiv:1209.3532](#)].

- [1867] J. Mastache, J. L. Cervantes-Cota, and A. de la Macorra, *Testing modified gravity at large distances with the HI Nearby Galaxy Survey's rotation curves*, *Phys. Rev.* **D87** (2013), no. 6 063001, [[arXiv:1212.5167](#)].
- [1868] J. L. Cervantes-Cota and J. A. Gomez-Lopez, *Testing Grumiller's modified gravity at galactic scales*, *Phys. Lett.* **B728** (2014) 537–542, [[arXiv:1312.1321](#)].
- [1869] P. Salucci, A. Lapi, C. Tonini, G. Gentile, I. Yegorova, and U. Klein, *The Universal Rotation Curve of Spiral Galaxies. 2. The Dark Matter Distribution out to the Virial Radius*, *Mon. Not. Roy. Astron. Soc.* **378** (2007) 41–47, [[astro-ph/0703115](#)].
- [1870] A. Burkert, *The Structure of dark matter halos in dwarf galaxies*, *IAU Symp.* **171** (1996) 175, [[astro-ph/9504041](#)]. [*Astrophys. J.*447,L25(1995)].
- [1871] M. Barriola and A. Vilenkin, *Gravitational Field of a Global Monopole*, *Phys. Rev. Lett.* **63** (1989) 341.
- [1872] X. Shi and X.-z. Li, *The Gravitational field of a global monopole*, *Class. Quant. Grav.* **8** (1991) 761–767, [[arXiv:0903.3085](#)].
- [1873] D. P. Bennett and S. H. Rhie, *Cosmological evolution of global monopoles and the origin of large scale structure*, *Phys. Rev. Lett.* **65** (1990) 1709–1712.
- [1874] D. Harari and C. Lousto, *Repulsive gravitational effects of global monopoles*, *Phys. Rev.* **D42** (1990) 2626–2631.
- [1875] N. Dadhich, K. Narayan, and U. A. Yajnik, *Schwarzschild black hole with global monopole charge*, *Pramana* **50** (1998) 307–314, [[gr-qc/9703034](#)].
- [1876] D. Grumiller, W. Kummer, and D. V. Vassilevich, *Dilaton gravity in two-dimensions*, *Phys. Rept.* **369** (2002) 327–430, [[hep-th/0204253](#)].
- [1877] J. G. Russo and A. A. Tseytlin, *Scalar tensor quantum gravity in two-dimensions*, *Nucl. Phys.* **B382** (1992) 259–275, [[hep-th/9201021](#)].
- [1878] S. D. Odintsov and I. L. Shapiro, *One loop renormalization of two-dimensional induced quantum gravity*, *Phys. Lett.* **B263** (1991) 183–189.
- [1879] P. P. Avelino and R. P. L. Azevedo, *Perfect fluid Lagrangian and its cosmological implications in theories of gravity with nonminimally coupled matter fields*, *Phys. Rev.* **D97** (2018), no. 6 064018, [[arXiv:1802.04760](#)].
- [1880] M. Halilsoy, O. Gurtug, and S. Habib Mazharimousavi, *Rindler modified Schwarzschild geodesics*, *Gen. Rel. Grav.* **45** (2013) 2363–2381, [[arXiv:1312.5574](#)].
- [1881] P. D. Mannheim, *Alternatives to dark matter and dark energy*, *Prog. Part. Nucl. Phys.* **56** (2006) 340–445, [[astro-ph/0505266](#)].
- [1882] P. D. Mannheim and J. G. O'Brien, *Impact of a global quadratic potential on galactic rotation curves*, *Phys. Rev. Lett.* **106** (2011) 121101, [[arXiv:1007.0970](#)].
- [1883] Y. Sofue, *Rotation curve decomposition for size–mass relations of bulge, disk, and dark halo components in spiral galaxies*, *Publ. Astron. Soc. Jap.* **68** (2016), no. 1 2, [[arXiv:1510.05752](#)].
- [1884] R. J. Buta et al., *A Classical Morphological Analysis of Galaxies in the Spitzer Survey of Stellar Structure in Galaxies (S^4G)*, *Astrophys. J. Suppl.* **217** (2015), no. 2 32, [[arXiv:1501.00454](#)].

- [1885] O. Garrido, M. Marcelin, P. Amram, C. Balkowski, J. L. Gach, and J. Boulesteix, *GHASP: an Ha kinematic survey of spiral and irregular galaxies – IV. 44 new velocity fields. Extension, shape and asymmetry of Ha rotation curves*, *Monthly Notices of the Royal Astronomical Society* **362** (09, 2005) 127–166, [<http://oup.prod.sis.lan/mnras/article-pdf/362/1/127/6027059/362-1-127.pdf>].
- [1886] E. Noordermeer, J. M. van der Hulst, R. Sancisi, R. S. Swaters, and T. S. van Albada, *The mass distribution in early-type disk galaxies: Declining rotation curves and correlations with optical properties*, *Mon. Not. Roy. Astron. Soc.* **376** (2007) 1513–1546, [[astro-ph/0701731](https://arxiv.org/abs/astro-ph/0701731)].
- [1887] L. J. Edwards, K. E. Muller, R. D. Wolfinger, B. F. Qaqish, and O. Schabenberger, *An r^2 statistic for fixed effects in the linear mixed model*, *Statistics in Medicine* **27** (2008), no. 29 6137–6157, [<https://onlinelibrary.wiley.com/doi/pdf/10.1002/sim.3429>].
- [1888] D. Zhang, *A coefficient of determination for generalized linear models*, *The American Statistician* **71** (2017), no. 4 310–316, [<https://doi.org/10.1080/00031305.2016.1256839>].
- [1889] P. Yin and X. Fan, *Estimating r^2 shrinkage in multiple regression: A comparison of different analytical methods*, *The Journal of Experimental Education* **69** (2001), no. 2 203–224, [<https://doi.org/10.1080/00220970109600656>].
- [1890] S. Carloni, D. Grumiller, and F. Preis, *Solar system constraints on Rindler acceleration*, *Phys. Rev.* **D83** (2011) 124024, [[arXiv:1103.0274](https://arxiv.org/abs/1103.0274)].
- [1891] L. Iorio, *Solar system constraints on a Rindler-type extra-acceleration from modified gravity at large distances*, *JCAP* **1105** (2011) 019, [[arXiv:1012.0226](https://arxiv.org/abs/1012.0226)].
- [1892] L. J. Garay, *Quantum gravity and minimum length*, *Int. J. Mod. Phys.* **A10** (1995) 145–166, [[gr-qc/9403008](https://arxiv.org/abs/gr-qc/9403008)].
- [1893] A. D. K. Plato, C. N. Hughes, and M. S. Kim, *Gravitational Effects in Quantum Mechanics*, *Contemp. Phys.* **57** (2016), no. 4 477–495, [[arXiv:1602.03878](https://arxiv.org/abs/1602.03878)].
- [1894] A. Connes, *Noncommutative geometry*. 1994.
- [1895] G. Veneziano, *A Stringy Nature Needs Just Two Constants*, *Europhys. Lett.* **2** (1986) 199.
- [1896] D. J. Gross and P. F. Mende, *The High-Energy Behavior of String Scattering Amplitudes*, *Phys. Lett.* **B197** (1987) 129–134.
- [1897] D. J. Gross and P. F. Mende, *String Theory Beyond the Planck Scale*, *Nucl. Phys.* **B303** (1988) 407–454.
- [1898] D. Amati, M. Ciafaloni, and G. Veneziano, *Superstring Collisions at Planckian Energies*, *Phys. Lett.* **B197** (1987) 81.
- [1899] D. Amati, M. Ciafaloni, and G. Veneziano, *Can Space-Time Be Probed Below the String Size?*, *Phys. Lett.* **B216** (1989) 41–47.
- [1900] K. Konishi, G. Paffuti, and P. Provero, *Minimum Physical Length and the Generalized Uncertainty Principle in String Theory*, *Phys. Lett.* **B234** (1990) 276–284.
- [1901] M. Kato, *Particle Theories With Minimum Observable Length and Open String Theory*, *Phys. Lett.* **B245** (1990) 43–47.
- [1902] C. Rovelli and L. Smolin, *Loop Space Representation of Quantum General Relativity*, *Nucl. Phys.* **B331** (1990) 80–152.

- [1903] C. Rovelli and L. Smolin, *Discreteness of area and volume in quantum gravity*, *Nucl. Phys.* **B442** (1995) 593–622, [[gr-qc/9411005](#)]. [Erratum: *Nucl. Phys.*B456,753(1995)].
- [1904] B. Carr, L. Modesto, and I. Premont-Schwarz, *Generalized Uncertainty Principle and Self-dual Black Holes*, [arXiv:1107.0708](#).
- [1905] C. Rovelli, *Quantum Gravity*. Cambridge Monographs on Mathematical Physics. Cambridge University Press, 2004.
- [1906] A. Ashtekar and J. Lewandowski, *Background independent quantum gravity: A Status report*, *Class. Quant. Grav.* **21** (2004) R53, [[gr-qc/0404018](#)].
- [1907] T. Thiemann, *Loop Quantum Gravity: An Inside View*, *Lect. Notes Phys.* **721** (2007) 185–263, [[hep-th/0608210](#)].
- [1908] T. Thiemann, *Lectures on loop quantum gravity*, *Lect. Notes Phys.* **631** (2003) 41–135, [[gr-qc/0210094](#)]. [41(2002)].
- [1909] S. Capozziello, G. Lambiase, and G. Scarpetta, *Generalized uncertainty principle from quantum geometry*, *Int. J. Theor. Phys.* **39** (2000) 15–22, [[gr-qc/9910017](#)].
- [1910] G. Amelino-Camelia, *Relativity in space-times with short distance structure governed by an observer independent (Planckian) length scale*, *Int. J. Mod. Phys.* **D11** (2002) 35–60, [[gr-qc/0012051](#)].
- [1911] J. L. Cortes and J. Gamboa, *Quantum uncertainty in doubly special relativity*, *Phys. Rev.* **D71** (2005) 065015, [[hep-th/0405285](#)].
- [1912] J. Magueijo and L. Smolin, *Lorentz invariance with an invariant energy scale*, *Phys. Rev. Lett.* **88** (2002) 190403, [[hep-th/0112090](#)].
- [1913] J. Magueijo and L. Smolin, *Generalized Lorentz invariance with an invariant energy scale*, *Phys. Rev.* **D67** (2003) 044017, [[gr-qc/0207085](#)].
- [1914] G. Amelino-Camelia, *Doubly special relativity*, *Nature* **418** (2002) 34–35, [[gr-qc/0207049](#)].
- [1915] J. Magueijo and L. Smolin, *String theories with deformed energy momentum relations, and a possible nontachyonic bosonic string*, *Phys. Rev.* **D71** (2005) 026010, [[hep-th/0401087](#)].
- [1916] F. Scardigli, *Generalized uncertainty principle in quantum gravity from micro - black hole Gedanken experiment*, *Phys. Lett.* **B452** (1999) 39–44, [[hep-th/9904025](#)].
- [1917] T. Zhu, J.-R. Ren, and M.-F. Li, *Influence of Generalized and Extended Uncertainty Principle on Thermodynamics of FRW universe*, *Phys. Lett.* **B674** (2009) 204–209, [[arXiv:0811.0212](#)].
- [1918] S. Das and E. C. Vagenas, *Universality of Quantum Gravity Corrections*, *Phys. Rev. Lett.* **101** (2008) 221301, [[arXiv:0810.5333](#)].
- [1919] S. Das and E. C. Vagenas, *Phenomenological Implications of the Generalized Uncertainty Principle*, *Can. J. Phys.* **87** (2009) 233–240, [[arXiv:0901.1768](#)].
- [1920] A. F. Ali, S. Das, and E. C. Vagenas, *Discreteness of Space from the Generalized Uncertainty Principle*, *Phys. Lett.* **B678** (2009) 497–499, [[arXiv:0906.5396](#)].
- [1921] A. F. Ali, S. Das, and E. C. Vagenas, *A proposal for testing Quantum Gravity in the lab*, *Phys. Rev.* **D84** (2011) 044013, [[arXiv:1107.3164](#)].
- [1922] K. Nozari and A. Etemadi, *Minimal length, maximal momentum and Hilbert space representation of quantum mechanics*, *Phys. Rev.* **D85** (2012) 104029, [[arXiv:1205.0158](#)].

- [1923] S. Das, E. C. Vagenas, and A. F. Ali, *Discreteness of Space from GUP II: Relativistic Wave Equations*, *Phys. Lett.* **B690** (2010) 407–412, [[arXiv:1005.3368](#)]. [Erratum: *Phys. Lett.* **B692**,342(2010)].
- [1924] S. Basilakos, S. Das, and E. C. Vagenas, *Quantum Gravity Corrections and Entropy at the Planck time*, *JCAP* **1009** (2010) 027, [[arXiv:1009.0365](#)].
- [1925] S. Das and R. B. Mann, *Planck scale effects on some low energy quantum phenomena*, *Phys. Lett.* **B704** (2011) 596–599, [[arXiv:1109.3258](#)].
- [1926] V. Faraoni, *Cosmological apparent and trapping horizons*, *Phys. Rev.* **D84** (2011) 024003, [[arXiv:1106.4427](#)].
- [1927] T. M. Davis, *Fundamental aspects of the expansion of the universe and cosmic horizons*. PhD thesis, New South Wales U., 2003. [astro-ph/0402278](#).
- [1928] E. W. Kolb and M. S. Turner, *The Early Universe*, *Front. Phys.* **69** (1990) 1–547.
- [1929] M.-i. Park, *The Generalized Uncertainty Principle in (A)dS Space and the Modification of Hawking Temperature from the Minimal Length*, *Phys. Lett.* **B659** (2008) 698–702, [[arXiv:0709.2307](#)].
- [1930] C. Bambi and F. R. Urban, *Natural extension of the Generalised Uncertainty Principle*, *Class. Quant. Grav.* **25** (2008) 095006, [[arXiv:0709.1965](#)].
- [1931] S. Mignemi, *Extended uncertainty principle and the geometry of (anti)-de Sitter space*, *Mod. Phys. Lett.* **A25** (2010) 1697–1703, [[arXiv:0909.1202](#)].
- [1932] S. Ghosh and S. Mignemi, *Quantum mechanics in de Sitter space*, *Int. J. Theor. Phys.* **50** (2011) 1803–1808, [[arXiv:0911.5695](#)].
- [1933] R. N. C. Filho, J. P. Braga, J. H. Lira, and J. S. Andrade, *Extended uncertainty from first principles*, *Physics Letters B* **755** (2016) 367 – 370.
- [1934] T. Schürmann, *Uncertainty principle on 3-dimensional manifolds of constant curvature*, *Found. Phys.* **48** (2018) 716–725, [[arXiv:1804.02551](#)].
- [1935] J. R. Mureika, *Extended Uncertainty Principle Black Holes*, *Phys. Lett.* **B789** (2019) 88–92, [[arXiv:1812.01999](#)].
- [1936] M. P. Dabrowski and F. Wagner, *Extended Uncertainty Principle for Rindler and cosmological horizons*, *Eur. Phys. J.* **C79** (2019), no. 8 716, [[arXiv:1905.09713](#)].
- [1937] J. J. Sakurai, *Modern quantum mechanics; rev. ed.* Addison-Wesley, Reading, MA, 1994.
- [1938] A. Camacho, *Generalized uncertainty principle and quantum electrodynamics*, *Gen. Rel. Grav.* **35** (2003) 1153–1160, [[gr-qc/0303061](#)].
- [1939] K. Nozari and T. Azizi, *Coherent states of harmonic oscillator and generalized uncertainty principle*, *Int. J. Quant. Inf.* **3** (2005) 623–632, [[gr-qc/0504090](#)].
- [1940] D. Baumann, *Inflation*, in *Physics of the large and the small, TASI 09, proceedings of the Theoretical Advanced Study Institute in Elementary Particle Physics, Boulder, Colorado, USA, 1-26 June 2009*, pp. 523–686, 2011. [arXiv:0907.5424](#).
- [1941] E. Lifshitz, *Republication of: On the gravitational stability of the expanding universe*, *J. Phys.(USSR)* **10** (1946) 116. [*Gen. Rel. Grav.* **49**,no.2,18(2017)].

- [1942] E. Bertschinger, *Cosmological perturbation theory and structure formation*, in *Cosmology 2000: Proceedings, Conference, Lisbon, Portugal, 12-15 Jul 2000*, pp. 1–25, 2001. [astro-ph/0101009](#).
- [1943] C. W. Misner, K. S. Thorne, and J. A. Wheeler, *Gravitation*. W. H. Freeman, San Francisco, 1973.
- [1944] L. P. Grishchuk, *Amplification of gravitational waves in an isotropic universe*, *Sov. Phys. JETP* **40** (1975) 409–415. [*Zh. Eksp. Teor. Fiz.*67,825(1974)].
- [1945] D. H. Lyth and A. R. Liddle, *Interpreting large scale structure observations*, in *2nd Journee Cosmologique within the framework of the International School of Astrophysics, D. Chalonge Paris, France, June 2-4, 1994*, pp. 0255–299, 1994. [astro-ph/9408066](#).
- [1946] D. H. Lyth and A. Riotto, *Particle physics models of inflation and the cosmological density perturbation*, *Phys. Rept.* **314** (1999) 1–146, [[hep-ph/9807278](#)].
- [1947] T. Matsuo and Y. Shibusa, *Quantization of fields based on generalized uncertainty principle*, *Mod. Phys. Lett.* **A21** (2006) 1285–1296, [[hep-th/0511031](#)].
- [1948] M. Kober, *Generalized Quantization Principle in Canonical Quantum Gravity and Application to Quantum Cosmology*, *Int. J. Mod. Phys.* **A27** (2012) 1250106, [[arXiv:1109.4629](#)].
- [1949] B. Oblak, *BMS Particles in Three Dimensions*. PhD thesis, Brussels U., 2016. [arXiv:1610.08526](#).
- [1950] V. F. Mukhanov, *Quantum Theory of Gauge Invariant Cosmological Perturbations*, *Sov. Phys. JETP* **67** (1988) 1297–1302. [*Zh. Eksp. Teor. Fiz.*94N7,1(1988)].
- [1951] H. Kodama and M. Sasaki, *Cosmological Perturbation Theory*, *Prog. Theor. Phys. Suppl.* **78** (1984) 1–166.
- [1952] E. D. Stewart and D. H. Lyth, *A More accurate analytic calculation of the spectrum of cosmological perturbations produced during inflation*, *Phys. Lett.* **B302** (1993) 171–175, [[gr-qc/9302019](#)].
- [1953] N. D. Birrell and P. C. W. Davies, *Quantum Fields in Curved Space*. Cambridge Monographs on Mathematical Physics. Cambridge Univ. Press, Cambridge, UK, 1984.
- [1954] L. E. Parker and D. Toms, *Quantum Field Theory in Curved Spacetime*. Cambridge Monographs on Mathematical Physics. Cambridge University Press, 2009.
- [1955] W. H. Kinney, *TASI Lectures on Inflation*, [arXiv:0902.1529](#).
- [1956] A. R. Liddle and D. H. Lyth, *The Cold dark matter density perturbation*, *Phys. Rept.* **231** (1993) 1–105, [[astro-ph/9303019](#)].
- [1957] J. E. Lidsey, A. R. Liddle, E. W. Kolb, E. J. Copeland, T. Barreiro, and M. Abney, *Reconstructing the inflation potential : An overview*, *Rev. Mod. Phys.* **69** (1997) 373–410, [[astro-ph/9508078](#)].
- [1958] A. R. Liddle and D. H. Lyth, *Cosmological inflation and large scale structure*. 2000.
- [1959] A. R. Liddle, P. Parsons, and J. D. Barrow, *Formalizing the slow roll approximation in inflation*, *Phys. Rev.* **D50** (1994) 7222–7232, [[astro-ph/9408015](#)].
- [1960] A. R. Liddle and D. H. Lyth, *COBE, gravitational waves, inflation and extended inflation*, *Phys. Lett.* **B291** (1992) 391–398, [[astro-ph/9208007](#)].

- [1961] W. H. Press, S. A. Teukolsky, W. T. Vetterling, and B. P. Flannery, *Numerical Recipes in FORTRAN - The Art of Scientific Computing, 2nd Edition*. Cambridge University Press, 1992.
- [1962] L. Verde, *Statistical methods in cosmology, Lect. Notes Phys.* **800** (2010) 147–177, [[arXiv:0911.3105](#)].
- [1963] R. A. Fisher, *The logic of inductive inference, Journal of the Royal Statistical Society* **98** (1935), no. 1 39–82.
- [1964] G.-B. Zhao, L. Pogosian, A. Silvestri, and J. Zylberberg, *Searching for modified growth patterns with tomographic surveys, Phys. Rev.* **D79** (2009) 083513, [[arXiv:0809.3791](#)].
- [1965] Y.-C. Cai and G. Bernstein, *Combining weak lensing tomography and spectroscopic redshift surveys, Mon. Not. Roy. Astron. Soc.* **422** (2012) 1045–1056, [[arXiv:1112.4478](#)].
- [1966] S. Joudaki and M. Kaplinghat, *Dark Energy and Neutrino Masses from Future Measurements of the Expansion History and Growth of Structure, Phys. Rev.* **D86** (2012) 023526, [[arXiv:1106.0299](#)].
- [1967] I. Tereno, E. Semboloni, and T. Schrabback, *COSMOS weak-lensing constraints on modified gravity, Astron. Astrophys.* **530** (2011) A68, [[arXiv:1012.5854](#)].
- [1968] F. Simpson et al., *CFHTLenS: Testing the Laws of Gravity with Tomographic Weak Lensing and Redshift Space Distortions, Mon. Not. Roy. Astron. Soc.* **429** (2013) 2249, [[arXiv:1212.3339](#)].
- [1969] G. Zhao, D. Bacon, R. Maartens, M. Santos, and A. Raccanelli, *Model-independent constraints on dark energy and modified gravity with the SKA, PoS AASKA14* (2015) 165.
- [1970] E. Bertschinger, *On the Growth of Perturbations as a Test of Dark Energy, Astrophys. J.* **648** (2006) 797–806, [[astro-ph/0604485](#)].
- [1971] S. Nesseris and L. Perivolaropoulos, *Crossing the Phantom Divide: Theoretical Implications and Observational Status, JCAP* **0701** (2007) 018, [[astro-ph/0610092](#)].
- [1972] E. J. Ruiz and D. Huterer, *Testing the dark energy consistency with geometry and growth, Phys. Rev.* **D91** (2015) 063009, [[arXiv:1410.5832](#)].
- [1973] **SPT** Collaboration, S. Bocquet et al., *Mass Calibration and Cosmological Analysis of the SPT-SZ Galaxy Cluster Sample Using Velocity Dispersion σ_v and X-ray Y_X Measurements, Astrophys. J.* **799** (2015), no. 2 214, [[arXiv:1407.2942](#)].
- [1974] F. Schmidt, *Weak Lensing Probes of Modified Gravity, Phys. Rev.* **D78** (2008) 043002, [[arXiv:0805.4812](#)].
- [1975] **DES** Collaboration, T. M. C. Abbott et al., *Dark Energy Survey Year 1 Results: Constraints on Extended Cosmological Models from Galaxy Clustering and Weak Lensing, Phys. Rev.* **D99** (2019), no. 12 123505, [[arXiv:1810.02499](#)].
- [1976] L. Samushia et al., *The Clustering of Galaxies in the SDSS-III DR9 Baryon Oscillation Spectroscopic Survey: Testing Deviations from Λ and General Relativity using anisotropic clustering of galaxies, Mon. Not. Roy. Astron. Soc.* **429** (2013) 1514–1528, [[arXiv:1206.5309](#)].
- [1977] A. Johnson, C. Blake, J. Dossett, J. Koda, D. Parkinson, and S. Joudaki, *Searching for Modified Gravity: Scale and Redshift Dependent Constraints from Galaxy Peculiar Velocities, Mon. Not. Roy. Astron. Soc.* **458** (2016), no. 3 2725–2744, [[arXiv:1504.06885](#)].
- [1978] L. Kazantzidis and L. Perivolaropoulos, *Is gravity getting weaker at low z ? Observational evidence and theoretical implications, arXiv:1907.03176*.

- [1979] S. Camera, M. Martinelli, and D. Bertacca, *Does quartessence ease cosmic tensions?*, *Phys. Dark Univ.* **23** (2019) 100247, [[arXiv:1704.06277](#)].
- [1980] R. Gannouji, B. Moraes, and D. Polarski, *The growth of matter perturbations in $f(R)$ models*, *JCAP* **0902** (2009) 034, [[arXiv:0809.3374](#)].
- [1981] S. Capozziello and M. De Laurentis, *Extended Theories of Gravity*, *Phys. Rept.* **509** (2011) 167–321, [[arXiv:1108.6266](#)].
- [1982] L. Boubekur, E. Giusarma, O. Mena, and H. Ramírez, *Current status of modified gravity*, *Phys. Rev.* **D90** (2014), no. 10 103512, [[arXiv:1407.6837](#)].
- [1983] Y.-F. Cai, C. Li, E. N. Saridakis, and L. Xue, *$f(T)$ gravity after GW170817 and GRB170817A*, *Phys. Rev.* **D97** (2018), no. 10 103513, [[arXiv:1801.05827](#)].
- [1984] S. Nojiri, S. D. Odintsov, and V. K. Oikonomou, *Modified Gravity Theories on a Nutshell: Inflation, Bounce and Late-time Evolution*, *Phys. Rept.* **692** (2017) 1–104, [[arXiv:1705.11098](#)].
- [1985] Y.-S. Song, W. Hu, and I. Sawicki, *The Large Scale Structure of $f(R)$ Gravity*, *Phys. Rev.* **D75** (2007) 044004, [[astro-ph/0610532](#)].
- [1986] K. Koyama, *Cosmological Tests of Modified Gravity*, *Rept. Prog. Phys.* **79** (2016), no. 4 046902, [[arXiv:1504.04623](#)].
- [1987] P. Zhang, M. Liguori, R. Bean, and S. Dodelson, *Probing Gravity at Cosmological Scales by Measurements which Test the Relationship between Gravitational Lensing and Matter Overdensity*, *Phys. Rev. Lett.* **99** (2007) 141302, [[arXiv:0704.1932](#)].
- [1988] C. D. Leonard, P. G. Ferreira, and C. Heymans, *Testing gravity with E_G : mapping theory onto observations*, *JCAP* **1512** (2015), no. 12 051, [[arXiv:1510.04287](#)].
- [1989] S. de la Torre et al., *The VIMOS Public Extragalactic Redshift Survey (VIPERS). Gravity test from the combination of redshift-space distortions and galaxy-galaxy lensing at $0.5 < z < 1.2$* , *Astron. Astrophys.* **608** (2017) A44, [[arXiv:1612.05647](#)].
- [1990] R. Reyes, R. Mandelbaum, U. Seljak, T. Baldauf, J. E. Gunn, L. Lombriser, and R. E. Smith, *Confirmation of general relativity on large scales from weak lensing and galaxy velocities*, *Nature* **464** (2010) 256–258, [[arXiv:1003.2185](#)].
- [1991] A. R. Pullen, S. Alam, and S. Ho, *Probing gravity at large scales through CMB lensing*, *Mon. Not. Roy. Astron. Soc.* **449** (2015), no. 4 4326–4335, [[arXiv:1412.4454](#)].
- [1992] A. R. Pullen, S. Alam, S. He, and S. Ho, *Constraining Gravity at the Largest Scales through CMB Lensing and Galaxy Velocities*, *Mon. Not. Roy. Astron. Soc.* **460** (2016), no. 4 4098–4108, [[arXiv:1511.04457](#)].
- [1993] H. Hoekstra, H. K. C. Yee, and M. D. Gladders, *Properties of galaxy dark matter halos from weak lensing*, *Astrophys. J.* **606** (2004) 67–77, [[astro-ph/0306515](#)].
- [1994] R. Mandelbaum, C. M. Hirata, U. Seljak, J. Guzik, N. Padmanabhan, C. Blake, M. R. Blanton, R. Lupton, and J. Brinkmann, *Systematic errors in weak lensing: Application to SDSS galaxy-galaxy weak lensing*, *Mon. Not. Roy. Astron. Soc.* **361** (2005) 1287–1322, [[astro-ph/0501201](#)].
- [1995] E. Bertschinger, *One Gravitational Potential or Two? Forecasts and Tests*, *Phil. Trans. Roy. Soc. Lond.* **A369** (2011) 4947–4961, [[arXiv:1111.4659](#)].

- [1996] E. Bertschinger and P. Zukin, *Distinguishing Modified Gravity from Dark Energy*, *Phys. Rev. D* **78** (2008) 024015, [[arXiv:0801.2431](#)].
- [1997] G.-B. Zhao, T. Giannantonio, L. Pogosian, A. Silvestri, D. J. Bacon, K. Koyama, R. C. Nichol, and Y.-S. Song, *Probing modifications of General Relativity using current cosmological observations*, *Phys. Rev. D* **81** (2010) 103510, [[arXiv:1003.0001](#)].
- [1998] Y.-S. Song, G.-B. Zhao, D. Bacon, K. Koyama, R. C. Nichol, and L. Pogosian, *Complementarity of Weak Lensing and Peculiar Velocity Measurements in Testing General Relativity*, *Phys. Rev. D* **84** (2011) 083523, [[arXiv:1011.2106](#)].
- [1999] S. F. Daniel and E. V. Linder, *Confronting General Relativity with Further Cosmological Data*, *Phys. Rev. D* **82** (2010) 103523, [[arXiv:1008.0397](#)].
- [2000] B. Hu, M. Liguori, N. Bartolo, and S. Matarrese, *Parametrized modified gravity constraints after Planck*, *Phys. Rev. D* **88** (2013), no. 12 123514, [[arXiv:1307.5276](#)].
- [2001] A. Ferté, D. Kirk, A. R. Liddle, and J. Zuntz, *Testing gravity on cosmological scales with cosmic shear, cosmic microwave background anisotropies, and redshift-space distortions*, *Phys. Rev. D* **99** (2019), no. 8 083512, [[arXiv:1712.01846](#)].
- [2002] E. V. Linder and R. N. Cahn, *Parameterized Beyond-Einstein Growth*, *Astropart. Phys.* **28** (2007) 481–488, [[astro-ph/0701317](#)].
- [2003] R. Gannouji and D. Polarski, *The growth of matter perturbations in some scalar-tensor DE models*, *JCAP* **0805** (2008) 018, [[arXiv:0802.4196](#)].
- [2004] D. Polarski, A. A. Starobinsky, and H. Giacomini, *When is the growth index constant?*, *JCAP* **1612** (2016), no. 12 037, [[arXiv:1610.00363](#)].
- [2005] L. Amendola, M. Kunz, and D. Sapone, *Measuring the dark side (with weak lensing)*, *JCAP* **0804** (2008) 013, [[arXiv:0704.2421](#)].
- [2006] S. F. Daniel and E. V. Linder, *Constraining Cosmic Expansion and Gravity with Galaxy Redshift Surveys*, *JCAP* **1302** (2013) 007, [[arXiv:1212.0009](#)].
- [2007] D. Huterer et al., *Growth of Cosmic Structure: Probing Dark Energy Beyond Expansion*, *Astropart. Phys.* **63** (2015) 23–41, [[arXiv:1309.5385](#)].
- [2008] E.-M. Mueller, W. Percival, E. Linder, S. Alam, G.-B. Zhao, A. G. Sánchez, F. Beutler, and J. Brinkmann, *The clustering of galaxies in the completed SDSS-III Baryon Oscillation Spectroscopic Survey: constraining modified gravity*, *Mon. Not. Roy. Astron. Soc.* **475** (2018), no. 2 2122–2131, [[arXiv:1612.00812](#)].
- [2009] L. Perenon, J. Bel, R. Maartens, and A. de la Cruz-Dombriz, *Optimising growth of structure constraints on modified gravity*, *JCAP* **1906** (2019), no. 06 020, [[arXiv:1901.11063](#)].
- [2010] L. Amendola, M. Kunz, M. Motta, I. D. Saltas, and I. Sawicki, *Observables and unobservables in dark energy cosmologies*, *Phys. Rev. D* **87** (2013), no. 2 023501, [[arXiv:1210.0439](#)].
- [2011] M. Motta, I. Sawicki, I. D. Saltas, L. Amendola, and M. Kunz, *Probing Dark Energy through Scale Dependence*, *Phys. Rev. D* **88** (2013), no. 12 124035, [[arXiv:1305.0008](#)].
- [2012] J. C. B. Sanchez and L. Perivolaropoulos, *Evolution of Dark Energy Perturbations in Scalar-Tensor Cosmologies*, *Phys. Rev. D* **81** (2010) 103505, [[arXiv:1002.2042](#)].
- [2013] E. V. Pitjeva and N. P. Pitjev, *Relativistic effects and dark matter in the Solar system from observations of planets and spacecraft*, *Mon. Not. Roy. Astron. Soc.* **432** (2013) 3431, [[arXiv:1306.3043](#)].

- [2014] R. Arjona, W. Cardona, and S. Nesseris, *Designing Horndeski and the effective fluid approach*, *Phys. Rev. D* **100** (2019), no. 6 063526, [[arXiv:1904.06294](#)].
- [2015] L. Amendola, D. Bettoni, A. M. Pinho, and S. Casas, *Measuring gravity at cosmological scales*, *Universe* **6** (2020), no. 2 20, [[arXiv:1902.06978](#)].
- [2016] A. Moradinezhad Dizgah and R. Durrer, *Lensing corrections to the $E_g(z)$ statistics from large scale structure*, *JCAP* **1609** (2016) 035, [[arXiv:1604.08914](#)].
- [2017] B. Ghosh and R. Durrer, *The observable E_g statistics*, *JCAP* **1906** (2019), no. 06 010, [[arXiv:1812.09546](#)].
- [2018] **DES** Collaboration, A. Drlica-Wagner et al., *Dark Energy Survey Year 1 Results: Photometric Data Set for Cosmology*, *Astrophys. J. Suppl.* **235** (2018), no. 2 33, [[arXiv:1708.01531](#)].
- [2019] **DES** Collaboration, B. Hoyle et al., *Dark Energy Survey Year 1 Results: Redshift distributions of the weak lensing source galaxies*, *Mon. Not. Roy. Astron. Soc.* **478** (2018), no. 1 592–610, [[arXiv:1708.01532](#)].
- [2020] **DES** Collaboration, J. Elvin-Poole et al., *Dark Energy Survey year 1 results: Galaxy clustering for combined probes*, *Phys. Rev. D* **98** (2018), no. 4 042006, [[arXiv:1708.01536](#)].
- [2021] L. Susskind, *Dynamics of Spontaneous Symmetry Breaking in the Weinberg-Salam Theory*, *Phys. Rev. D* **20** (1979) 2619–2625.
- [2022] A. D. Linde, *Chaotic Inflation*, *Phys. Lett.* **129B** (1983) 177–181.
- [2023] C. A. Herdeiro and E. Radu, *Asymptotically flat black holes with scalar hair: a review*, *Int. J. Mod. Phys. D* **24** (2015), no. 09 1542014, [[arXiv:1504.08209](#)].
- [2024] S. M. Carroll, V. Duvvuri, M. Trodden, and M. S. Turner, *Is cosmic speed - up due to new gravitational physics?*, *Phys. Rev. D* **70** (2004) 043528, [[astro-ph/0306438](#)].
- [2025] S. Capozziello, V. F. Cardone, and A. Troisi, *Reconciling dark energy models with $f(R)$ theories*, *Phys. Rev. D* **71** (2005) 043503, [[astro-ph/0501426](#)].
- [2026] S. Nojiri and S. D. Odintsov, *Modified $f(R)$ gravity consistent with realistic cosmology: From matter dominated epoch to dark energy universe*, *Phys. Rev. D* **74** (2006) 086005, [[hep-th/0608008](#)].
- [2027] S. Nojiri and S. D. Odintsov, *Modified $f(R)$ gravity unifying R^m inflation with Lambda CDM epoch*, *Phys. Rev. D* **77** (2008) 026007, [[arXiv:0710.1738](#)].
- [2028] S. Capozziello and M. Francaviglia, *Extended Theories of Gravity and their Cosmological and Astrophysical Applications*, *Gen. Rel. Grav.* **40** (2008) 357–420, [[arXiv:0706.1146](#)].
- [2029] M. Anderson, J. Ensher, M. Matthews, C. Wieman, and E. Cornell, *Observation of Bose-Einstein condensation in a dilute atomic vapor*, *Science* **269** (1995) 198–201.
- [2030] R. Allahverdi, R. Brandenberger, F.-Y. Cyr-Racine, and A. Mazumdar, *Reheating in Inflationary Cosmology: Theory and Applications*, *Ann. Rev. Nucl. Part. Sci.* **60** (2010) 27–51, [[arXiv:1001.2600](#)].
- [2031] G. N. Felder, J. Garcia-Bellido, P. B. Greene, L. Kofman, A. D. Linde, and I. Tkachev, *Dynamics of symmetry breaking and tachyonic preheating*, *Phys. Rev. Lett.* **87** (2001) 011601, [[hep-ph/0012142](#)].
- [2032] M. He, R. Jinno, K. Kamada, A. A. Starobinsky, and J. Yokoyama, *Occurrence of Tachyonic Preheating in the Mixed Higgs- R^2 Model*, [arXiv:2007.10369](#).

- [2033] M. A. Amin, M. P. Hertzberg, D. I. Kaiser, and J. Karouby, *Nonperturbative Dynamics Of Reheating After Inflation: A Review*, *Int. J. Mod. Phys. D* **24** (2014) 1530003, [[arXiv:1410.3808](#)].
- [2034] L. Landau and E. Lifschits, *The Classical Theory of Fields*, vol. Volume 2 of *Course of Theoretical Physics*. Pergamon Press, Oxford, 1975.
- [2035] A. Dolgov and M. Kawasaki, *Can modified gravity explain accelerated cosmic expansion?*, *Phys. Lett. B* **573** (2003) 1–4, [[astro-ph/0307285](#)].
- [2036] V. Faraoni, *Matter instability in modified gravity*, *Phys. Rev. D* **74** (2006) 104017, [[astro-ph/0610734](#)].
- [2037] M. Soussa and R. Woodard, *The force of gravity from a Lagrangian containing inverse powers of the ricci scalar*, *Gen. Rel. Grav.* **36** (2004) 855–862, [[astro-ph/0308114](#)].
- [2038] T. Kobayashi and K.-i. Maeda, *Relativistic stars in $f(R)$ gravity, and absence thereof*, *Phys. Rev. D* **78** (2008) 064019, [[arXiv:0807.2503](#)].
- [2039] S. Nojiri and S. D. Odintsov, *Modified gravity with negative and positive powers of the curvature: Unification of the inflation and of the cosmic acceleration*, *Phys. Rev. D* **68** (2003) 123512, [[hep-th/0307288](#)].
- [2040] S. Nojiri and S. D. Odintsov, *Modified gravity with $\ln R$ terms and cosmic acceleration*, *Gen. Rel. Grav.* **36** (2004) 1765–1780, [[hep-th/0308176](#)].
- [2041] M. D. Seifert, *Stability of spherically symmetric solutions in modified theories of gravity*, *Phys. Rev. D* **76** (2007) 064002, [[gr-qc/0703060](#)].
- [2042] I. Sawicki and W. Hu, *Stability of Cosmological Solution in $f(R)$ Models of Gravity*, *Phys. Rev. D* **75** (2007) 127502, [[astro-ph/0702278](#)].
- [2043] J. Alsing, E. Berti, C. M. Will, and H. Zaglauer, *Gravitational radiation from compact binary systems in the massive Brans-Dicke theory of gravity*, *Phys. Rev. D* **85** (2012) 064041, [[arXiv:1112.4903](#)].
- [2044] L. Perivolaropoulos, *PPN Parameter gamma and Solar System Constraints of Massive Brans-Dicke Theories*, *Phys. Rev. D* **81** (2010) 047501, [[arXiv:0911.3401](#)].
- [2045] D. F. Torres, *Quintessence, superquintessence and observable quantities in Brans-Dicke and nonminimally coupled theories*, *Phys. Rev. D* **66** (2002) 043522, [[astro-ph/0204504](#)].
- [2046] S. Sen and T. Seshadri, *Selfinteracting Brans-Dicke cosmology and quintessence*, *Int. J. Mod. Phys. D* **12** (2003) 445–460, [[gr-qc/0007079](#)].
- [2047] C. M. Will, *The Confrontation between General Relativity and Experiment*, *Living Rev. Rel.* **17** (2014) 4, [[arXiv:1403.7377](#)].
- [2048] G. J. Olmo, *Post-Newtonian constraints on $f(R)$ cosmologies in metric and Palatini formalism*, *Phys. Rev. D* **72** (2005) 083505, [[gr-qc/0505135](#)].
- [2049] S. Capozziello, M. De Laurentis, and V. Faraoni, *A Bird's eye view of $f(R)$ -gravity*, *Open Astron. J.* **3** (2010) 49, [[arXiv:0909.4672](#)].
- [2050] V. Faraoni and N. Lanahan-Tremblay, *Comments on 'Solar System constraints to general $f(R)$ gravity'*, *Phys. Rev. D* **77** (2008) 108501, [[arXiv:0712.3252](#)].
- [2051] S. Nojiri and S. D. Odintsov, *Newton law corrections and instabilities in $f(R)$ gravity with the effective cosmological constant epoch*, *Phys. Lett. B* **652** (2007) 343–348, [[arXiv:0706.1378](#)].

- [2052] G. Cognola, E. Elizalde, S. Nojiri, S. Odintsov, L. Sebastiani, and S. Zerbini, *A Class of viable modified $f(R)$ gravities describing inflation and the onset of accelerated expansion*, *Phys. Rev. D* **77** (2008) 046009, [[arXiv:0712.4017](#)].
- [2053] T. Chiba, *1/R gravity and scalar - tensor gravity*, *Phys. Lett. B* **575** (2003) 1–3, [[astro-ph/0307338](#)].
- [2054] P. Teyssandier and P. Tourenç, *The Cauchy problem for the $R + R^2$ theories of gravity without torsion*, *J. Math. Phys.* **24** (1983) 2793.
- [2055] D. Wands, *Extended gravity theories and the Einstein-Hilbert action*, *Class. Quant. Grav.* **11** (1994) 269–280, [[gr-qc/9307034](#)].
- [2056] V. Faraoni, *Solar System experiments do not yet veto modified gravity models*, *Phys. Rev. D* **74** (2006) 023529, [[gr-qc/0607016](#)].
- [2057] S. Capozziello, A. Stabile, and A. Troisi, *Comparing scalar-tensor gravity and $f(R)$ -gravity in the Newtonian limit*, *Phys. Lett. B* **686** (2010) 79–83, [[arXiv:1002.1364](#)].
- [2058] A. A. Starobinsky, *A new type of isotropic cosmological models without singularity*, *Physics Letters B* **91** (Mar., 1980) 99–102.
- [2059] C. P. L. Berry and J. R. Gair, *Linearized $f(R)$ Gravity: Gravitational Radiation and Solar System Tests*, *Phys. Rev. D* **83** (2011) 104022, [[arXiv:1104.0819](#)]. [Erratum: *Phys.Rev.D* **85**, 089906 (2012)].
- [2060] S. Capozziello, A. Stabile, and A. Troisi, *A General solution in the Newtonian limit of $f(R)$ -gravity*, *Mod. Phys. Lett. A* **24** (2009) 659–665, [[arXiv:0901.0448](#)].
- [2061] S. Capozziello, A. Stabile, and A. Troisi, *The Newtonian Limit of $f(R)$ gravity*, *Phys. Rev. D* **76** (2007) 104019, [[arXiv:0708.0723](#)].
- [2062] T. Chiba, T. L. Smith, and A. L. Erickcek, *Solar System constraints to general $f(R)$ gravity*, *Phys. Rev. D* **75** (2007) 124014, [[astro-ph/0611867](#)].
- [2063] G. J. Olmo, *Limit to general relativity in $f(R)$ theories of gravity*, *Phys. Rev. D* **75** (2007) 023511, [[gr-qc/0612047](#)].
- [2064] J. Edholm and A. Conroy, *Newtonian Potential and Geodesic Completeness in Infinite Derivative Gravity*, *Phys. Rev. D* **96** (2017), no. 4 044012, [[arXiv:1705.02382](#)].
- [2065] A. Conroy, T. Koivisto, A. Mazumdar, and A. Teimouri, *Generalized quadratic curvature, non-local infrared modifications of gravity and Newtonian potentials*, *Class. Quant. Grav.* **32** (2015), no. 1 015024, [[arXiv:1406.4998](#)].
- [2066] K. Lake, *Reissner-Nordstrom-de Sitter metric, the third law, and cosmic censorship*, *Phys. Rev. D* **19** (1979) 421–429.
- [2067] H. Laue and M. Weiss, *Maximally extended Reissner-Nordstrom manifold with cosmological constant*, *Phys. Rev. D* **16** (1977) 3376–3379.
- [2068] K. Schwarzschild, *On the gravitational field of a mass point according to Einstein's theory*, *Sitzungsber. Preuss. Akad. Wiss. Berlin (Math. Phys.)* **1916** (1916) 189–196, [[physics/9905030](#)].
- [2069] W. de Sitter, *Einstein's theory of gravitation and its astronomical consequences, First Paper*, *Mon. Not. Roy. Astron. Soc.* **76** (1916) 699–728.

- [2070] W. de Sitter, *Einstein's theory of gravitation and its astronomical consequences, Second Paper*, *Mon. Not. Roy. Astron. Soc.* **77** (1916) 155–184.
- [2071] W. de Sitter, *Einstein's theory of gravitation and its astronomical consequences, Third Paper*, *Mon. Not. Roy. Astron. Soc.* **78** (1917) 3–28.
- [2072] S. Hawking and G. Ellis, *The Large Scale Structure of Space-Time*. Cambridge Monographs on Mathematical Physics. Cambridge University Press, 2, 2011.
- [2073] R. Bousso, *Adventures in de Sitter space*, in *Workshop on Conference on the Future of Theoretical Physics and Cosmology in Honor of Steven Hawking's 60th Birthday*, pp. 539–569, 5, 2002. [hep-th/0205177](#).
- [2074] R. C. Tolman, *Relativity, Thermodynamics, and Cosmology*. 1934.
- [2075] H. Stephani, D. Kramer, M. A. MacCallum, C. Hoenselaers, and E. Herlt, *Exact solutions of Einstein's field equations*. Cambridge Monographs on Mathematical Physics. Cambridge Univ. Press, Cambridge, 2003.
- [2076] H. Reissner, *Über die Eigengravitation des elektrischen Feldes nach der Einsteinschen Theorie*, *Annalen der Physik* **355** (Jan., 1916) 106–120.
- [2077] G. Nordström, *On the Energy of the Gravitation field in Einstein's Theory*, *Koninklijke Nederlandse Akademie van Wetenschappen Proceedings Series B Physical Sciences* **20** (Jan., 1918) 1238–1245.
- [2078] J. B. Griffiths and J. Podolsky, *Exact Space-Times in Einstein's General Relativity*. Cambridge Monographs on Mathematical Physics. Cambridge University Press, Cambridge, 2009.
- [2079] B. F. Schutz and C. M. Will, *BLACK HOLE NORMAL MODES: A SEMIANALYTIC APPROACH*, *Astrophys. J. Lett.* **291** (1985) L33–L36.
- [2080] S. Iyer and C. M. Will, *Black Hole Normal Modes: A WKB Approach. 1. Foundations and Application of a Higher Order WKB Analysis of Potential Barrier Scattering*, *Phys. Rev. D* **35** (1987) 3621.
- [2081] R. Konoplya, *Quasinormal behavior of the d -dimensional Schwarzschild black hole and higher order WKB approach*, *Phys. Rev. D* **68** (2003) 024018, [[gr-qc/0303052](#)].
- [2082] R. Konoplya, *Quasinormal modes of the electrically charged dilaton black hole*, *Gen. Rel. Grav.* **34** (2002) 329–335, [[gr-qc/0109096](#)].
- [2083] R. Konoplya, *Gravitational quasinormal radiation of higher dimensional black holes*, *Phys. Rev. D* **68** (2003) 124017, [[hep-th/0309030](#)].
- [2084] H. T. Cho, *Dirac quasinormal modes in Schwarzschild black hole space-times*, *Phys. Rev. D* **68** (2003) 024003, [[gr-qc/0303078](#)].
- [2085] H. Yang, D. A. Nichols, F. Zhang, A. Zimmerman, Z. Zhang, and Y. Chen, *Quasinormal-mode spectrum of Kerr black holes and its geometric interpretation*, *Phys. Rev. D* **86** (2012) 104006, [[arXiv:1207.4253](#)].
- [2086] J. Matyjasek and M. Opala, *Quasinormal modes of black holes. The improved semianalytic approach*, *Phys. Rev. D* **96** (2017), no. 2 024011, [[arXiv:1704.00361](#)].
- [2087] Y. Hatsuda, *Quasinormal modes of black holes and Borel summation*, *Phys. Rev. D* **101** (2020), no. 2 024008, [[arXiv:1906.07232](#)].

- [2088] S. Devi, R. Roy, and S. Chakrabarti, *Quasinormal modes and greybody factors of the novel four dimensional Gauss–Bonnet black holes in asymptotically de Sitter space time: scalar, electromagnetic and Dirac perturbations*, *Eur. Phys. J. C* **80** (2020), no. 8 760, [[arXiv:2004.14935](#)].
- [2089] M. Churilova, *Quasinormal modes of the Dirac field in the novel 4D Einstein-Gauss-Bonnet gravity*, [arXiv:2004.00513](#).
- [2090] M. Churilova, *Quasinormal modes of the test fields in the novel 4D Einstein-Gauss-Bonnet-de Sitter gravity*, [arXiv:2004.14172](#).
- [2091] M. Lagos, P. G. Ferreira, and O. J. Tattersall, *Anomalous decay rate of quasinormal modes*, *Phys. Rev. D* **101** (2020), no. 8 084018, [[arXiv:2002.01897](#)].
- [2092] C. Vishveshwara, *Stability of the schwarzschild metric*, *Phys. Rev. D* **1** (1970) 2870–2879.
- [2093] L. Edelstein and C. Vishveshwara, *Differential equations for perturbations on the schwarzschild metric*, *Phys. Rev. D* **1** (1970) 3514–3517.
- [2094] K. D. Kokkotas and B. G. Schmidt, *Quasinormal modes of stars and black holes*, *Living Rev. Rel.* **2** (1999) 2, [[gr-qc/9909058](#)].
- [2095] H.-P. Nollert, *TOPICAL REVIEW: Quasinormal modes: the characteristic ‘sound’ of black holes and neutron stars*, *Class. Quant. Grav.* **16** (1999) R159–R216.
- [2096] E. Berti, V. Cardoso, and A. O. Starinets, *Quasinormal modes of black holes and black branes*, *Class. Quant. Grav.* **26** (2009) 163001, [[arXiv:0905.2975](#)].
- [2097] V. Ferrari and L. Gualtieri, *Quasi-Normal Modes and Gravitational Wave Astronomy*, *Gen. Rel. Grav.* **40** (2008) 945–970, [[arXiv:0709.0657](#)].
- [2098] K. Destounis, *Dynamical behavior of black-hole spacetimes*. PhD thesis, Lisbon, IST, 2019. [arXiv:1909.08597](#).
- [2099] S. Hod, *Bohr’s correspondence principle and the area spectrum of quantum black holes*, *Phys. Rev. Lett.* **81** (1998) 4293, [[gr-qc/9812002](#)].
- [2100] L.-H. Xue, Z.-X. Shen, B. Wang, and R.-K. Su, *Numerical simulation of quasinormal modes in time dependent background*, *Mod. Phys. Lett. A* **19** (2004) 239, [[gr-qc/0304109](#)].
- [2101] V. Cardoso, J. P. Lemos, and S. Yoshida, *Quasinormal modes of Schwarzschild black holes in four-dimensions and higher dimensions*, *Phys. Rev. D* **69** (2004) 044004, [[gr-qc/0309112](#)].
- [2102] A. Zhidenko, *Quasinormal modes of Schwarzschild de Sitter black holes*, *Class. Quant. Grav.* **21** (2004) 273–280, [[gr-qc/0307012](#)].
- [2103] E. Abdalla, C. Molina, and A. Saa, *Field propagation in the Schwarzschild-de Sitter black hole*, [gr-qc/0309078](#).
- [2104] T. R. Choudhury and T. Padmanabhan, *Quasinormal modes in Schwarzschild-deSitter space-time: A Simple derivation of the level spacing of the frequencies*, *Phys. Rev. D* **69** (2004) 064033, [[gr-qc/0311064](#)].
- [2105] A. Maassen van den Brink, *Approach to the extremal limit of the Schwarzschild-de sitter black hole*, *Phys. Rev. D* **68** (2003) 047501, [[gr-qc/0304092](#)].
- [2106] S. Hod, *Stability of the extremal Reissner-Nordstroem black hole to charged scalar perturbations*, *Phys. Lett. B* **713** (2012) 505–508, [[arXiv:1304.6474](#)].

- [2107] Z. Zhu, S.-J. Zhang, C. Pellicer, B. Wang, and E. Abdalla, *Stability of Reissner-Nordström black hole in de Sitter background under charged scalar perturbation*, *Phys. Rev. D* **90** (2014), no. 4 044042, [[arXiv:1405.4931](#)]. [Addendum: *Phys.Rev.D* 90, 049904 (2014)].
- [2108] S. Hod, *The instability spectra of near-extremal Reissner-Nordström-de Sitter black holes*, *Phys. Lett. B* **786** (2018) 217, [[arXiv:1808.04077](#)]. [Erratum: *Phys.Lett.B* 796, 256 (2019)].
- [2109] R. Konoplya and A. Zhidenko, *Charged scalar field instability between the event and cosmological horizons*, *Phys. Rev. D* **90** (2014), no. 6 064048, [[arXiv:1406.0019](#)].
- [2110] S. L. Detweiler, *KLEIN-GORDON EQUATION AND ROTATING BLACK HOLES*, *Phys. Rev. D* **22** (1980) 2323–2326.
- [2111] R. Konoplya and A. Zhidenko, *Stability and quasinormal modes of the massive scalar field around Kerr black holes*, *Phys. Rev. D* **73** (2006) 124040, [[gr-qc/0605013](#)].
- [2112] S. R. Dolan, *Instability of the massive Klein-Gordon field on the Kerr spacetime*, *Phys. Rev. D* **76** (2007) 084001, [[arXiv:0705.2880](#)].
- [2113] V. Cardoso and S. Yoshida, *Superradiant instabilities of rotating black branes and strings*, *JHEP* **07** (2005) 009, [[hep-th/0502206](#)].
- [2114] H. Witek, V. Cardoso, A. Ishibashi, and U. Sperhake, *Superradiant instabilities in astrophysical systems*, *Phys. Rev. D* **87** (2013), no. 4 043513, [[arXiv:1212.0551](#)].
- [2115] H. Okawa, H. Witek, and V. Cardoso, *Black holes and fundamental fields in Numerical Relativity: initial data construction and evolution of bound states*, *Phys. Rev. D* **89** (2014), no. 10 104032, [[arXiv:1401.1548](#)].
- [2116] J. Bekenstein, *Extraction of energy and charge from a black hole*, *Phys. Rev. D* **7** (1973) 949–953.
- [2117] T. Damour, N. Deruelle, and R. Ruffini, *On Quantum Resonances in Stationary Geometries*, *Lett. Nuovo Cim.* **15** (1976) 257–262.
- [2118] R. Konoplya and A. Zhidenko, *Quasinormal modes of black holes: From astrophysics to string theory*, *Rev. Mod. Phys.* **83** (2011) 793–836, [[arXiv:1102.4014](#)].
- [2119] V. Cardoso, *Black hole bombs and explosions: from astrophysics to particle physics*, *Gen. Rel. Grav.* **45** (2013) 2079–2097, [[arXiv:1307.0038](#)].
- [2120] Y. Shlapentokh-Rothman, *Exponentially growing finite energy solutions for the Klein-Gordon equation on sub-extremal Kerr spacetimes*, *Commun. Math. Phys.* **329** (2014) 859–891, [[arXiv:1302.3448](#)].
- [2121] C. A. R. Herdeiro, J. C. Degollado, and H. F. Rúnarsson, *Rapid growth of superradiant instabilities for charged black holes in a cavity*, *Phys. Rev. D* **88** (2013) 063003, [[arXiv:1305.5513](#)].
- [2122] C.-Y. Zhang, S.-J. Zhang, and B. Wang, *Superradiant instability of Kerr-de Sitter black holes in scalar-tensor theory*, *JHEP* **08** (2014) 011, [[arXiv:1405.3811](#)].
- [2123] R. Brito, V. Cardoso, and P. Pani, *Superradiance: Energy Extraction, Black-Hole Bombs and Implications for Astrophysics and Particle Physics*, vol. 906. Springer, 2015.
- [2124] N. Sanchis-Gual, J. C. Degollado, P. J. Montero, J. A. Font, and C. Herdeiro, *Explosion and Final State of an Unstable Reissner-Nordström Black Hole*, *Phys. Rev. Lett.* **116** (2016), no. 14 141101, [[arXiv:1512.05358](#)].

- [2125] G. Moschidis, *Superradiant instabilities for short-range non-negative potentials on Kerr spacetimes and applications*, [arXiv:1608.02041](#).
- [2126] A. Zhidenko, *Linear perturbations of black holes: stability, quasi-normal modes and tails*. PhD thesis, Sao Paulo U., 2009. [arXiv:0903.3555](#).
- [2127] K. Destounis, *Superradiant instability of charged scalar fields in higher-dimensional Reissner-Nordström-de Sitter black holes*, *Phys. Rev. D* **100** (2019), no. 4 044054, [[arXiv:1908.06117](#)].
- [2128] V. Cardoso and J. P. Lemos, *Quasinormal modes of the near extremal Schwarzschild-de Sitter black hole*, *Phys. Rev. D* **67** (2003) 084020, [[gr-qc/0301078](#)].
- [2129] T. R. Choudhury and T. Padmanabhan, *Concept of temperature in multi-horizon spacetimes: Analysis of Schwarzschild-de Sitter metric*, *Gen. Rel. Grav.* **39** (2007) 1789–1811, [[gr-qc/0404091](#)].
- [2130] B. Toshmatov and Z. Stuchlík, *Slowly decaying resonances of massive scalar fields around Schwarzschild-de Sitter black holes*, *Eur. Phys. J. Plus* **132** (2017), no. 7 324, [[arXiv:1707.07419](#)].
- [2131] T. Regge and J. A. Wheeler, *Stability of a Schwarzschild singularity*, *Phys. Rev.* **108** (1957) 1063–1069.
- [2132] F. Zerilli, *Gravitational field of a particle falling in a schwarzschild geometry analyzed in tensor harmonics*, *Phys. Rev. D* **2** (1970) 2141–2160.
- [2133] F. J. Zerilli, *Effective potential for even parity Regge-Wheeler gravitational perturbation equations*, *Phys. Rev. Lett.* **24** (1970) 737–738.
- [2134] G. G. Nashed and S. Capozziello, *Charged spherically symmetric black holes in $f(R)$ gravity and their stability analysis*, *Phys. Rev. D* **99** (2019), no. 10 104018, [[arXiv:1902.06783](#)].
- [2135] S. Bhattacharya, *Particle creation by de Sitter black holes revisited*, *Phys. Rev. D* **98** (2018), no. 12 125013, [[arXiv:1810.13260](#)].
- [2136] Z. Stuchlík, P. Slany, and J. Kovar, *Pseudo-Newtonian and general relativistic barotropic tori in Schwarzschild-de Sitter spacetimes*, *Class. Quant. Grav.* **26** (2009) 215013, [[arXiv:0910.3184](#)].
- [2137] Z. Stuchlík, *The Motion of Test Particles in Black-Hole Backgrounds with Non-Zero Cosmological Constant*, *Bulletin of the Astronomical Institutes of Czechoslovakia* **34** (June, 1983) 129.
- [2138] G. Gibbons and S. Hawking, *Cosmological Event Horizons, Thermodynamics, and Particle Creation*, *Phys. Rev. D* **15** (1977) 2738–2751.
- [2139] J. Guven and D. Núñez, *Schwarzschild-de Sitter space and its perturbations*, *Phys. Rev. D* **42** (1990), no. 8 2577–2584.
- [2140] A. Ashtekar and B. Krishnan, *Dynamical horizons and their properties*, *Phys. Rev. D* **68** (2003) 104030, [[gr-qc/0308033](#)].
- [2141] H. Nariai, *On some static solutions of Einstein's gravitational field equations in a spherically symmetric case*, *Sci. Rep. Tohoku Univ. Eighth Ser.* **34** (Jan., 1950) 160.
- [2142] R. Bousso and S. W. Hawking, *(Anti)evaporation of Schwarzschild-de Sitter black holes*, *Phys. Rev. D* **57** (1998) 2436–2442, [[hep-th/9709224](#)].

- [2143] K. Lake and R. Roeder, *Effects of a Nonvanishing Cosmological Constant on the Spherically Symmetric Vacuum Manifold*, *Phys. Rev. D* **15** (1977) 3513–3519.
- [2144] L. Romans, *Supersymmetric, cold and lukewarm black holes in cosmological Einstein-Maxwell theory*, *Nucl. Phys. B* **383** (1992) 395–415, [[hep-th/9203018](#)].
- [2145] S. Hawking, *Particle Creation by Black Holes*, *Commun. Math. Phys.* **43** (1975) 199–220. [Erratum: *Commun.Math.Phys.* 46, 206 (1976)].
- [2146] P. R. Brady, C. M. Chambers, W. Krivan, and P. Laguna, *Telling tails in the presence of a cosmological constant*, *Phys. Rev. D* **55** (1997) 7538–7545, [[gr-qc/9611056](#)].
- [2147] M. Montero, T. Van Riet, and G. Venken, *Festina Lente: EFT Constraints from Charged Black Hole Evaporation in de Sitter*, *JHEP* **01** (2020) 039, [[arXiv:1910.01648](#)].
- [2148] R. Konoplya and A. Zhidenko, *Massive charged scalar field in the Kerr-Newman background I: quasinormal modes, late-time tails and stability*, *Phys. Rev. D* **88** (2013) 024054, [[arXiv:1307.1812](#)].
- [2149] W. F. Buell and B. A. Shadwick, *Potentials and bound states*, *American Journal of Physics* **63** (1995), no. 3 256–258, [<https://doi.org/10.1119/1.17935>].
- [2150] G. Dotti and R. J. Gleiser, *Gravitational instability of Einstein-Gauss-Bonnet black holes under tensor mode perturbations*, *Class. Quant. Grav.* **22** (2005) L1, [[gr-qc/0409005](#)].
- [2151] Y. S. Myung and D.-C. Zou, *Instability of Reissner–Nordström black hole in Einstein-Maxwell-scalar theory*, *Eur. Phys. J. C* **79** (2019), no. 3 273, [[arXiv:1808.02609](#)].
- [2152] D.-P. Du, B. Wang, and R.-K. Su, *Quasinormal modes in pure de Sitter space-times*, *Phys. Rev. D* **70** (2004) 064024, [[hep-th/0404047](#)].
- [2153] D. B. Sibandze, R. Goswami, S. D. Maharaj, A. M. Nzioki, and P. K. S. Dunsby, *Scattering of Ricci scalar perturbations from Schwarzschild black holes in modified gravity*, *Eur. Phys. J. C* **77** (2017), no. 6 364, [[arXiv:1611.06043](#)].
- [2154] W.-D. Li, Y.-Z. Chen, and W.-S. Dai, *Scattering state and bound state of scalar field in Schwarzschild spacetime: Exact solution*, *Annals Phys.* **409** (2019) 167919, [[arXiv:1612.02644](#)].
- [2155] J. Ye and R. H. Brandenberger, *The Formation and Evolution of $U(1)$ Gauged Vortices in an Expanding Universe*, *Nucl. Phys. B* **346** (1990) 149–159.
- [2156] A. Achúcarro, J. Borrill, and A. R. Liddle, *The Formation rate of semilocal strings*, *Phys. Rev. Lett.* **82** (1999) 3742–3745, [[hep-ph/9802306](#)].
- [2157] E. Winstanley, *On classical superradiance in Kerr-Newman - anti-de Sitter black holes*, *Phys. Rev. D* **64** (2001) 104010, [[gr-qc/0106032](#)].
- [2158] M. James, L. Perivolaropoulos, and T. Vachaspati, *Stability of electroweak strings*, *Phys. Rev. D* **46** (1992) R5232–R5235.
- [2159] B. Carter, *Global structure of the Kerr family of gravitational fields*, *Phys. Rev.* **174** (1968) 1559–1571.
- [2160] Z. Stuchlik, G. Bao, E. Ostgaard, and S. Hledik, *Kerr-Newman-de Sitter black holes with a restricted repulsive barrier of equatorial photon motion*, *Phys. Rev. D* **58** (1998) 084003.
- [2161] J. Podolsky and J. Griffiths, *Accelerating Kerr-Newman black holes in (anti-)de Sitter space-time*, *Phys. Rev. D* **73** (2006) 044018, [[gr-qc/0601130](#)].

- [2162] Z. Stuchlik and S. Hledik, *Equatorial photon motion in the Kerr-Newman spacetimes with a non-zero cosmological constant*, *Class. Quant. Grav.* **17** (2000) 4541–4576, [[arXiv:0803.2539](#)].
- [2163] G. Kraniotis, *Gravitational lensing and frame dragging of light in the Kerr-Newman and the Kerr-Newman-(anti) de Sitter black hole spacetimes*, *Gen. Rel. Grav.* **46** (2014), no. 11 1818, [[arXiv:1401.7118](#)].
- [2164] G. Kraniotis, *The Klein–Gordon–Fock equation in the curved spacetime of the Kerr–Newman (anti) de Sitter black hole*, *Class. Quant. Grav.* **33** (2016), no. 22 225011, [[arXiv:1602.04830](#)].
- [2165] G. Kraniotis, *The massive Dirac equation in the Kerr-Newman-de Sitter and Kerr-Newman black hole spacetimes*, *J. Phys. Comm.* **3** (2019) 035026, [[arXiv:1801.03157](#)].
- [2166] G. Kraniotis, *Gravitational redshift/blueshift of light emitted by geodesic test particles, frame-dragging and pericentre-shift effects, in the Kerr-Newman-de Sitter and Kerr-Newman black hole geometries*, [arXiv:1912.10320](#).
- [2167] R. A. Konoplya, *Superluminal neutrinos and the tachyon’s stability in the rotating Universe*, *Phys. Lett. B* **706** (2012) 451–455, [[arXiv:1109.6215](#)].
- [2168] R. A. Konoplya and A. Zhidenko, *Stability of tardyons and tachyons in the rotating and expanding Universe*, *Phys. Rev. D* **86** (2012) 023531, [[arXiv:1110.2015](#)].
- [2169] T. W. B. Kibble, *Topology of Cosmic Domains and Strings*, *J. Phys. A* **9** (1976) 1387–1398.
- [2170] W. Zurek, *Cosmological Experiments in Superfluid Helium?*, *Nature* **317** (1985) 505–508.
- [2171] A. Rajantie, ‘Phase transitions in the early universe’ and ‘Defect formation’, in *COSLAB Workshop on Cosmological Phase Transitions and Topological Defects*, 11, 2003. [hep-ph/0311262](#).
- [2172] T. Kibble, *Some Implications of a Cosmological Phase Transition*, *Phys. Rept.* **67** (1980) 183.
- [2173] M. Ostrogradsky, *Mémoires sur les équations différentielles, relatives au problème des isopérimètres*, *Mem. Acad. St. Petersburg* **6** (1850), no. 4 385–517.
- [2174] R. P. Woodard, *Ostrogradsky’s theorem on Hamiltonian instability*, *Scholarpedia* **10** (2015), no. 8 32243, [[arXiv:1506.02210](#)].
- [2175] A. De Felice and S. Tsujikawa, *Generalized Brans-Dicke theories*, *JCAP* **07** (2010) 024, [[arXiv:1005.0868](#)].
- [2176] **LIGO Scientific, Virgo** Collaboration, B. P. Abbott et al., *GW170817: Observation of Gravitational Waves from a Binary Neutron Star Inspiral*, *Phys. Rev. Lett.* **119** (2017), no. 16 161101, [[arXiv:1710.05832](#)].
- [2177] A. Goldstein et al., *An Ordinary Short Gamma-Ray Burst with Extraordinary Implications: Fermi-GBM Detection of GRB 170817A*, *Astrophys. J. Lett.* **848** (2017), no. 2 L14, [[arXiv:1710.05446](#)].
- [2178] C. de Rham and S. Melville, *Gravitational Rainbows: LIGO and Dark Energy at its Cutoff*, *Phys. Rev. Lett.* **121** (2018), no. 22 221101, [[arXiv:1806.09417](#)].
- [2179] E. Bellini and I. Sawicki, *Maximal freedom at minimum cost: linear large-scale structure in general modifications of gravity*, *JCAP* **1407** (2014) 050, [[arXiv:1404.3713](#)].
- [2180] F. Sbisà, *Classical and quantum ghosts*, *Eur. J. Phys.* **36** (2015) 015009, [[arXiv:1406.4550](#)].

- [2181] M. Denissenya and E. V. Linder, *Gravity’s Islands: Parametrizing Horndeski Stability*, *JCAP* **1811** (2018), no. 11 010, [[arXiv:1808.00013](#)].
- [2182] A. De Felice, T. Kobayashi, and S. Tsujikawa, *Effective gravitational couplings for cosmological perturbations in the most general scalar-tensor theories with second-order field equations*, *Phys. Lett.* **B706** (2011) 123–133, [[arXiv:1108.4242](#)].
- [2183] I. Sawicki and E. Bellini, *Limits of quasistatic approximation in modified-gravity cosmologies*, *Phys. Rev.* **D92** (2015), no. 8 084061, [[arXiv:1503.06831](#)].
- [2184] J. Espejo, S. Peirone, M. Raveri, K. Koyama, L. Pogosian, and A. Silvestri, *Phenomenology of Large Scale Structure in scalar-tensor theories: joint prior covariance of w_{DE} , Σ and μ in Horndeski*, *Phys. Rev. D* **99** (2019), no. 2 023512, [[arXiv:1809.01121](#)].
- [2185] F. Pace, R. A. Battye, B. Bolliet, and D. Trinh, *Dark sector evolution in Horndeski models*, *JCAP* **09** (2019) 018, [[arXiv:1905.06795](#)].
- [2186] T. Kobayashi, M. Yamaguchi, and J. Yokoyama, *Generalized G-inflation: Inflation with the most general second-order field equations*, *Prog. Theor. Phys.* **126** (2011) 511–529, [[arXiv:1105.5723](#)].
- [2187] M. Ishak et al., *Modified Gravity and Dark Energy models Beyond $w(z)$ CDM Testable by LSST*, [[arXiv:1905.09687](#)].
- [2188] J. Gleyzes, D. Langlois, and F. Vernizzi, *A unifying description of dark energy*, *Int. J. Mod. Phys.* **D23** (2015), no. 13 1443010, [[arXiv:1411.3712](#)].
- [2189] V. Savchenko et al., *INTEGRAL Detection of the First Prompt Gamma-Ray Signal Coincident with the Gravitational-wave Event GW170817*, *Astrophys. J.* **848** (2017), no. 2 L15, [[arXiv:1710.05449](#)].
- [2190] **LIGO Scientific, Virgo, Fermi-GBM, INTEGRAL** Collaboration, B. P. Abbott et al., *Gravitational Waves and Gamma-rays from a Binary Neutron Star Merger: GW170817 and GRB 170817A*, *Astrophys. J.* **848** (2017), no. 2 L13, [[arXiv:1710.05834](#)].
- [2191] I. D. Saltas, I. Sawicki, L. Amendola, and M. Kunz, *Anisotropic Stress as a Signature of Nonstandard Propagation of Gravitational Waves*, *Phys. Rev. Lett.* **113** (2014), no. 19 191101, [[arXiv:1406.7139](#)].
- [2192] R. Reischke, A. Spurio Mancini, B. M. Schäfer, and P. M. Merkel, *Investigating scalar–tensor gravity with statistics of the cosmic large-scale structure*, *Mon. Not. Roy. Astron. Soc.* **482** (2019), no. 3 3274–3287, [[arXiv:1804.02441](#)].
- [2193] A. De Felice, R. Kase, and S. Tsujikawa, *Vainshtein mechanism in second-order scalar-tensor theories*, *Phys. Rev. D* **85** (2012) 044059, [[arXiv:1111.5090](#)].
- [2194] E. Babichev, C. Deffayet, and G. Esposito-Farese, *Constraints on Shift-Symmetric Scalar-Tensor Theories with a Vainshtein Mechanism from Bounds on the Time Variation of G* , *Phys. Rev. Lett.* **107** (2011) 251102, [[arXiv:1107.1569](#)].
- [2195] R. Kimura, T. Kobayashi, and K. Yamamoto, *Vainshtein screening in a cosmological background in the most general second-order scalar-tensor theory*, *Phys. Rev. D* **85** (2012) 024023, [[arXiv:1111.6749](#)].
- [2196] J. G. Williams, S. G. Turyshev, and D. H. Boggs, *Progress in lunar laser ranging tests of relativistic gravity*, *Phys. Rev. Lett.* **93** (2004) 261101, [[gr-qc/0411113](#)].

- [2197] F. Dar, C. De Rham, J. T. Deskins, J. T. Giblin, and A. J. Tolley, *Scalar Gravitational Radiation from Binaries: Vainshtein Mechanism in Time-dependent Systems*, *Class. Quant. Grav.* **36** (2019), no. 2 025008, [[arXiv:1808.02165](https://arxiv.org/abs/1808.02165)].
- [2198] A. Amon et al., *KiDS+2dFLenS+GAMA: Testing the cosmological model with the E_G statistic*, *Mon. Not. Roy. Astron. Soc.* **479** (2018), no. 3 3422–3437, [[arXiv:1711.10999](https://arxiv.org/abs/1711.10999)].
- [2199] L. Verde, *Statistical methods in cosmology*, *Lecture Notes in Physics* (2010) 147–177.
- [2200] R. Calderon, D. Felbacq, R. Gannouji, D. Polarski, and A. A. Starobinsky, *Global properties of the growth index of matter inhomogeneities in the universe*, *Phys. Rev.* **D100** (2019), no. 8 083503, [[arXiv:1908.00117](https://arxiv.org/abs/1908.00117)].
- [2201] R. Gannouji and D. Polarski, *Consistency of the expansion of the Universe with density perturbations*, *Phys. Rev. D* **98** (2018), no. 8 083533, [[arXiv:1805.08230](https://arxiv.org/abs/1805.08230)].
- [2202] C. Garcia-Quintero, M. Ishak, and O. Ning, *Current constraints on deviations from General Relativity using binning in redshift and scale*, [arXiv:2010.12519](https://arxiv.org/abs/2010.12519).
- [2203] B. F. Madore and W. L. Freedman, *The Cepheid distance scale*, *Publ. Astron. Soc. Pac.* **103** (1991) 933–957.
- [2204] G. H. Jacoby, D. Branch, R. Ciardullo, R. L. Davies, W. E. Harris, M. J. Pierce, C. J. Pritchett, J. L. Tonry, and D. L. Welch, *A Critical Review of Selected Techniques for Measuring Extragalactic Distances*, *Publ. Astron. Soc. Pac.* **104** (Aug., 1992) 599.
- [2205] M. Feast, *Cepheids as Distance Indicators*, *Publ. Astron. Soc. Pac.* **111** (July, 1999) 775–793.
- [2206] G. Wallerstein, *The cepheids of population ii and related stars*, *Publ. Astron. Soc. Pac.* **114** (2002), no. 797 689–699.
- [2207] A. Sandage and G. A. Tammann, *Absolute magnitude calibrations of population i and ii cepheids and other pulsating variables in the instability strip of the hertzsprung-russell diagram*, *Annu. Rev. Astron. Astrophys.* **44** (2006), no. 1 93–140, [<https://doi.org/10.1146/annurev.astro.43.072103.150612>].
- [2208] P. Fouque, J. Storm, and W. Gieren, *Calibration of the distance scale from Cepheids*, *Lect. Notes Phys.* **635** (2003) 21–44, [[astro-ph/0301291](https://arxiv.org/abs/astro-ph/0301291)].
- [2209] P. Fouque et al., *A new calibration of Galactic Cepheid Period-Luminosity relations from B to K bands, and a comparison to LMC PL relations*, *Astron. Astrophys.* **476** (2007) 73–81, [[arXiv:0709.3255](https://arxiv.org/abs/0709.3255)].
- [2210] W. L. Freedman and B. F. Madore, *The Hubble Constant*, *Ann. Rev. Astron. Astrophys.* **48** (2010) 673–710, [[arXiv:1004.1856](https://arxiv.org/abs/1004.1856)].
- [2211] G. Efstathiou, *H_0 Revisited*, *Mon. Not. Roy. Astron. Soc.* **440** (2014), no. 2 1138–1152, [[arXiv:1311.3461](https://arxiv.org/abs/1311.3461)].
- [2212] W. Cardona, M. Kunz, and V. Pettorino, *Determining H_0 with Bayesian hyper-parameters*, *JCAP* **1703** (2017), no. 03 056, [[arXiv:1611.06088](https://arxiv.org/abs/1611.06088)].
- [2213] L. Amendola, P. S. Corasaniti, and F. Occhionero, *Time variability of the gravitational constant and type Ia supernovae*, [astro-ph/9907222](https://arxiv.org/abs/astro-ph/9907222).
- [2214] E. Garcia-Berro, E. Gaztanaga, J. Isern, O. Benvenuto, and L. Althaus, *On the evolution of cosmological type ia supernovae and the gravitational constant*, [astro-ph/9907440](https://arxiv.org/abs/astro-ph/9907440).

- [2215] L. Amendola, M. Kunz, I. D. Saltas, and I. Sawicki, *Fate of Large-Scale Structure in Modified Gravity After GW170817 and GRB170817A*, *Phys. Rev. Lett.* **120** (2018), no. 13 131101, [[arXiv:1711.04825](#)].
- [2216] S. Li, A. G. Riess, M. P. Busch, S. Casertano, L. M. Macri, and W. Yuan, *A sub-2% Distance to M31 from Photometrically Homogeneous Near-Infrared Cepheid Period-Luminosity Relations Measured with the Hubble Space Telescope*, [arXiv:2107.08029](#).
- [2217] B. T. Draine, *Interstellar dust grains*, *Ann. Rev. Astron. Astrophys.* **41** (2003) 241–289, [[astro-ph/0304489](#)].
- [2218] B. W. Carroll and D. A. Ostlie, *An Introduction to Modern Astrophysics*. Cambridge University Press, 2 ed., 2017.
- [2219] B. F. Madore, *The period-luminosity relation. IV. Intrinsic relations and reddenings for the Large Magellanic Cloud Cepheids.*, *Astroph.J.* **253** (Feb., 1982) 575–579.
- [2220] E. L. Fitzpatrick, *Correcting for the effects of interstellar extinction*, *Publ. Astron. Soc. Pac.* **111** (1999) 63–75, [[astro-ph/9809387](#)].
- [2221] R. McGonegal, C. W. McAlary, B. F. Madore, and R. A. McLaren, *The Cepheid distance scale - A new application for infrared photometry*, *Astroph.J.* **257** (June, 1982) L33–L36.
- [2222] W. L. Freedman, C. D. Wilson, and B. F. Madore, *New Cepheid Distances to Nearby Galaxies Based on BVRI CCD Photometry. II. The Local Group Galaxy M33*, *Astroph.J.* **372** (May, 1991) 455.
- [2223] L. M. Macri et al., *NICMOS observations of extragalactic Cepheids. 1. Photometry database and a test of the standard extinction law*, *Astrophys. J.* **549** (2001) 721, [[astro-ph/0102125](#)].
- [2224] P. Wielgórski, G. Pietrzyński, W. Gieren, M. Górski, R.-P. Kudritzki, B. Zgirski, F. Bresolin, J. Storm, N. Matsunaga, D. Graczyk, and I. Soszyński, *A Precision Determination of the Effect of Metallicity on Cepheid Absolute Magnitudes in VIJHK Bands from Magellanic Cloud Cepheids*, *Astroph.J.* **842** (June, 2017) 116, [[arXiv:1705.10855](#)].
- [2225] W. Gieren, J. Storm, P. Konorski, M. Górski, B. Pilecki, I. Thompson, G. Pietrzyński, D. Graczyk, T. G. Barnes, P. Fouqué, N. Nardetto, A. Gallenne, P. Karczmarek, K. Suchomska, P. Wielgórski, M. Taormina, and B. Zgirski, *The effect of metallicity on Cepheid period-luminosity relations from a Baade-Wesselink analysis of Cepheids in the Milky Way and Magellanic Clouds*, *Astron. Astrophys.* **620** (Dec., 2018) A99, [[arXiv:1809.04073](#)].
- [2226] M. A. T. Groenewegen, *The Cepheid period-luminosity-metallicity relation based on Gaia DR2 data*, *Astron. Astrophys.* **619** (Nov., 2018) A8, [[arXiv:1808.05796](#)].
- [2227] V. Ripepi, G. Catanzaro, R. Molinaro, M. Marconi, G. Clementini, F. Cusano, G. De Somma, S. Leccia, I. Musella, and V. Testa, *Period-luminosity-metallicity relation of classical Cepheids*, *Astron. Astrophys.* **642** (Oct., 2020) A230, [[arXiv:2008.04608](#)].
- [2228] L. Breuval, P. Kervella, P. Wielgórski, W. Gieren, D. Graczyk, B. Trahin, G. Pietrzyński, F. Arenou, B. Javanmardi, and B. Zgirski, *The Influence of Metallicity on the Leavitt Law from Geometrical Distances of Milky Way and Magellanic Cloud Cepheids*, *Astroph.J.* **913** (May, 2021) 38, [[arXiv:2103.10894](#)].
- [2229] W. L. Freedman, B. F. Madore, D. Hatt, T. J. Hoyt, I. S. Jang, R. L. Beaton, C. R. Burns, M. G. Lee, A. J. Monson, J. R. Neeley, M. M. Phillips, J. A. Rich, and M. Seibert, *The carnegie-chicago hubble program. VIII. an independent determination of the hubble constant based on the tip of the red giant branch*, *Astroph. J.* **882** (aug, 2019) 34.

- [2230] A. G. Riess, W. Yuan, S. Casertano, L. M. Macri, and D. Scolnic, *The Accuracy of the Hubble Constant Measurement Verified through Cepheid Amplitudes*, *Astrophys. J.* **896** (2020), no. 2 L43, [[arXiv:2005.02445](#)].
- [2231] J. D. Fernie, *The Structure of the Cepheid Instability Strip*, *Astroph.J.* **354** (May, 1990) 295.
- [2232] A. Sandage and G. A. Tammann, *Temperature Differences in the Cepheid Instability Strip Require Differences in the Period-Luminosity Relation in Slope and Zero Point*, *Astrophys. J.* **686** (2008) 779–784, [[arXiv:0803.3836](#)].
- [2233] B. F. Madore, W. L. Freedman, and S. Moak, *A Method for Improving Galactic Cepheid Reddenings and Distances*, *Astroph.J.* **842** (June, 2017) 42.
- [2234] O. Pejcha and C. S. Kochanek, *A Global Physical Model for Cepheids*, *Astrophys. J.* **748** (2012) 107, [[arXiv:1112.3038](#)].
- [2235] G. A. Tammann, B. Reindl, F. Thim, A. Saha, and A. Sandage, *Cepheids, Supernovae, H_0 , and the Age of the Universe*, in *A New Era in Cosmology* (N. Metcalfe and T. Shanks, eds.), vol. 283 of *Astronomical Society of the Pacific Conference Series*, p. 258, Jan., 2002. [astro-ph/0112489](#).
- [2236] G. A. Tammann, A. Sandage, and B. Reindl, *New period - luminosity and period - color relations of classical Cepheids: 1. Cepheids in the Galaxy*, *Astron. Astrophys.* **404** (2003) 423–448, [[astro-ph/0303378](#)].
- [2237] A. Sandage, G. A. Tammann, and B. Reindl, *New period - luminosity and period - color relations of classical Cepheids: 2. Cepheids in LMC*, *Astron. Astrophys.* **424** (2004) 43–71, [[astro-ph/0402424](#)].
- [2238] C.-C. Ngeow, S. M. Kanbur, S. Nikolaev, J. Buonaccorsi, K. H. Cook, and D. L. Welch, *Further empirical evidence for the non-linearity of the period-luminosity relations as seen in the Large Magellanic Cloud Cepheids*, *Mon. Not. Roy. Astron. Soc.* **363** (2005) 831–846, [[astro-ph/0507601](#)].
- [2239] A. Sandage, G. A. Tammann, and B. Reindl, *New period-luminosity and period-color relations of classical Cepheids: III. Cepheids in SMC*, *Astron. Astrophys.* **493** (2009) 471–479, [[arXiv:0810.1780](#)].
- [2240] A. Bhardwaj, S. M. Kanbur, L. M. Macri, H. P. Singh, C.-C. Ngeow, and E. E. O. Ishida, *Large Magellanic Cloud Near-Infrared Synoptic Survey - III. A statistical study of non-linearity in the Leavitt Laws*, *Mon. Not. Roy. Astron. Soc.* **457** (Apr., 2016) 1644–1665, [[arXiv:1601.00953](#)].
- [2241] H. L. Johnson and J. Borgman, *The law of interstellar extinction*, *BAN* **17** (Dec., 1963) 115.
- [2242] K. Krisciunas, J. L. Prieto, P. M. Garnavich, J.-L. G. Riley, A. Rest, C. Stubbs, and R. McMillan, *Photometry of the type ia supernovae 1999cc, 1999cl, and 2000cf*, *Astron. J.* **131** (2006) 1639–1647, [[astro-ph/0511162](#)].
- [2243] S. Nobili and A. Goobar, *The colour-lightcurve shape relation of Type Ia supernovae and the reddening law*, *Astron. Astrophys.* **487** (2008) 19, [[arXiv:0712.1155](#)].
- [2244] M. M. Fausnaugh, C. S. Kochanek, J. R. Gerke, L. M. Macri, A. G. Riess, and K. Z. Stanek, *The Cepheid distance to the maser-host galaxy NGC 4258: studying systematics with the Large Binocular Telescope*, *Mon. Not. Roy. Astron. Soc.* **450** (05, 2015) 3597–3619, [<https://academic.oup.com/mnras/article-pdf/450/4/3597/5831120/stv881.pdf>].
- [2245] A. Goobar, *Low R_v from circumstellar dust around supernovae*, *Astrophys. J. Lett.* **686** (2008) L103–L106, [[arXiv:0809.1094](#)].

- [2246] G. Folatelli et al., *The Carnegie Supernova Project: Analysis of the First Sample of Low-Redshift Type-Ia Supernovae*, *Astron. J.* **139** (2010) 120–144, [[arXiv:0910.3317](#)].
- [2247] SDSS Collaboration, H. Lampeitl et al., *The Effect of Host Galaxies on Type Ia Supernovae in the SDSS-II Supernova Survey*, *Astrophys. J.* **722** (2010) 566–576, [[arXiv:1005.4687](#)].
- [2248] A. Goobar et al., *The Rise of SN 2014J in the Nearby Galaxy M82*, *Astrophys. J. Lett.* **784** (2014) L12, [[arXiv:1402.0849](#)].
- [2249] R. Amanullah et al., *The peculiar extinction law of SN2014J measured with The Hubble Space Telescope*, *Astrophys. J. Lett.* **788** (2014), no. 2 L21, [[arXiv:1404.2595](#)].
- [2250] R. Amanullah et al., *Diversity in extinction laws of Type Ia supernovae measured between 0.2 and 2 μm* , *Mon. Not. Roy. Astron. Soc.* **453** (2015), no. 3 3300–3328, [[arXiv:1504.02101](#)].
- [2251] A. Cikota, S. Deustua, and F. Marleau, *Determining Type Ia Supernovae Host galaxy extinction probabilities and a statistical approach to estimating the absorption-to-reddening ratio R_V* , *Astrophys. J.* **819** (2016), no. 2 152, [[arXiv:1601.05659](#)].
- [2252] R. Biswas et al., *Two c 's in a pod: Cosmology independent measurement of the Type Ia supernova colour-luminosity relation with a sibling pair*, [arXiv:2103.16978](#).
- [2253] J. A. Cardelli, G. C. Clayton, and J. S. Mathis, *The relationship between infrared, optical, and ultraviolet extinction*, *Astrophys. J.* **345** (1989) 245–256.
- [2254] J. E. O'Donnell, *R_v -dependent Optical and Near-Ultraviolet Extinction*, *Astroph. J.* **422** (Feb., 1994) 158.
- [2255] D. M. Nataf et al., *Interstellar extinction curve variations towards the inner Milky Way: a challenge to observational cosmology*, *Mon. Not. Roy. Astron. Soc.* **456** (2016), no. 3 2692–2706, [[arXiv:1510.01321](#)].
- [2256] G. Efstathiou, *A Lockdown Perspective on the Hubble Tension (with comments from the SH0ES team)*, [arXiv:2007.10716](#).
- [2257] S. L. Hoffmann et al., *Optical Identification of Cepheids in 19 Host Galaxies of Type Ia Supernovae and NGC 4258 with the Hubble Space Telescope*, *Astrophys. J.* **830** (2016), no. 1 10, [[arXiv:1607.08658](#)].
- [2258] SNLS Collaboration, J. Guy, P. Astier, S. Nobili, N. Regnault, and R. Pain, *SALT: A Spectral adaptive Light curve Template for Type Ia supernovae*, *Astron. Astrophys.* **443** (2005) 781–791, [[astro-ph/0506583](#)].
- [2259] SNLS Collaboration, J. Guy et al., *SALT2: Using distant supernovae to improve the use of Type Ia supernovae as distance indicators*, *Astron. Astrophys.* **466** (2007) 11–21, [[astro-ph/0701828](#)].
- [2260] SNLS Collaboration, J. Guy et al., *The Supernova Legacy Survey 3-year sample: Type Ia Supernovae photometric distances and cosmological constraints*, *Astron. Astrophys.* **523** (2010) A7, [[arXiv:1010.4743](#)].
- [2261] J. Mosher et al., *Cosmological Parameter Uncertainties from SALT-II Type Ia Supernova Light Curve Models*, *Astrophys. J.* **793** (2014) 16, [[arXiv:1401.4065](#)].
- [2262] <http://supernovae.in2p3.fr/salt/doku.php>.
- [2263] M. Romaniello, F. Primas, M. Mottini, S. Pedicelli, B. Lemasle, G. Bono, P. Francois, M. A. T. Groenewegen, and C. D. Laney, *The influence of chemical composition on the properties of Cepheid stars. II-The iron content*, *Astron. Astrophys.* **488** (2008) 731, [[arXiv:0807.1196](#)].

- [2264] S. Choudhury, A. Subramaniam, and A. A. Cole, *Photometric metallicity map of the Large Magellanic Cloud*, *Mon. Not. Roy. Astron. Soc.* **455** (11, 2015) 1855–1880, [<https://academic.oup.com/mnras/article-pdf/455/2/1855/18513939/stv2414.pdf>].
- [2265] H. Akaike, *A new look at the statistical model identification*, *IEEE Transactions on Automatic Control* **19** no. 6 716–723.
- [2266] M. V. John and J. V. Narlikar, *Comparison of cosmological models using bayesian theory*, *Phys. Rev. D* **65** (2002) 043506, [[astro-ph/0111122](https://arxiv.org/abs/astro-ph/0111122)].
- [2267] K. P. Burnham and D. R. Anderson, *Model selection and multimodel inference*. Springer-Verlag, 2 ed., 2002.
- [2268] K. P. Burnham and D. R. Anderson, *Multimodel Inference: Understanding AIC and BIC in Model Selection*, *Sociol. Method.* **33** (2004) 261.
- [2269] N. Sugiura, *Further analysts of the data by akaike's information criterion and the finite corrections*, *Communications in Statistics - Theory and Methods* **7** (1978), no. 1 13–26, [<https://doi.org/10.1080/03610927808827599>].
- [2270] M. Rezaei, M. Malekjani, and J. Sola, *Can dark energy be expressed as a power series of the Hubble parameter?*, *Phys. Rev. D* **100** (2019), no. 2 023539, [[arXiv:1905.00100](https://arxiv.org/abs/1905.00100)].
- [2271] D. Brout and D. Scolnic, *It's Dust: Solving the Mysteries of the Intrinsic Scatter and Host-galaxy Dependence of Standardized Type Ia Supernova Brightnesses*, *Astrophys. J.* **909** (2021), no. 1 26, [[arXiv:2004.10206](https://arxiv.org/abs/2004.10206)].
- [2272] J. e. a. Johansson, *Near-IR Type Ia SN distances: host galaxy extinction and mass-step corrections revisited*, [[arXiv:2105.06236](https://arxiv.org/abs/2105.06236)].
- [2273] M. Hamuy, M. M. Phillips, J. Maza, N. B. Suntzeff, R. A. Schommer, and R. Aviles, *A Hubble Diagram of Distant Type Ia Supernovae*, *Astron.J.* **109** (Jan., 1995) 1.
- [2274] **Supernova Cosmology Project** Collaboration, M. Sullivan et al., *The Hubble diagram of Type Ia supernovae as a function of host galaxy morphology*, *Mon. Not. Roy. Astron. Soc.* **340** (2003) 1057, [[astro-ph/0211444](https://arxiv.org/abs/astro-ph/0211444)].
- [2275] M. J. Childress et al., *Host Galaxy Properties and Hubble Residuals of Type Ia Supernovae from the Nearby Supernova Factory*, *Astrophys. J.* **770** (2013) 108, [[arXiv:1304.4720](https://arxiv.org/abs/1304.4720)].
- [2276] **DES** Collaboration, P. Wiseman et al., *Supernova Host Galaxies in the Dark Energy Survey: I. Deep Coadds, Photometry, and Stellar Masses*, *Mon. Not. Roy. Astron. Soc.* **495** (2020), no. 4 4040–4060, [[arXiv:2001.02640](https://arxiv.org/abs/2001.02640)].
- [2277] **DES** Collaboration, L. Kelsey et al., *Skip Nav Destination The effect of environment on Type Ia supernovae in the Dark Energy Survey three-year cosmological sample*, *Mon. Not. Roy. Astron. Soc.* **501** (2021), no. 4 4861–4876, [[arXiv:2008.12101](https://arxiv.org/abs/2008.12101)].
- [2278] S. Cassisi and M. Salaris, *A critical investigation on the discrepancy between the observational and theoretical red giant luminosity function bump*, *Mon. Not. Roy. Astron. Soc.* **285** (1997) 593, [[astro-ph/9702029](https://arxiv.org/abs/astro-ph/9702029)].
- [2279] I. S. Jang and M. G. Lee, *The Tip of the Red Giant Branch Distances to Type Ia Supernova Host Galaxies. III. NGC 4038/39 and NGC 5584*, *Astroph.J.* **807** (July, 2015) 133, [[arXiv:1506.03089](https://arxiv.org/abs/1506.03089)].

- [2280] I. S. Jang and M. G. Lee, *The Tip of the Red Giant Branch Distances to Type Ia Supernova Host Galaxies. V. NGC 3021, NGC 3370, and NGC 1309 and the Value of the Hubble Constant*, *Astrophys. J.* **836** (2017), no. 1 74, [[arXiv:1702.01118](#)].
- [2281] D. Hatt et al., *The Carnegie-Chicago Hubble Program. IV. The Distance to NGC 4424, NGC 4526, and NGC 4356 via the Tip of the Red Giant Branch*, *Astrophys. J.* **861** (2018), no. 2 104, [[arXiv:1806.02900](#)].
- [2282] D. Hatt et al., *The Carnegie-Chicago Hubble Program. V. The Distances to NGC 1448 and NGC 1316 via the Tip of the Red Giant Branch*, *Astrophys. J.* **866** (2018), no. 2 145, [[arXiv:1809.01741](#)].
- [2283] S. R. Coleman, *The Fate of the False Vacuum. 1. Semiclassical Theory*, *Phys. Rev. D* **15** (1977) 2929–2936. [Erratum: *Phys.Rev.D* 16, 1248 (1977)].
- [2284] A. V. Patwardhan and G. M. Fuller, *Late-time vacuum phase transitions: Connecting sub-eV scale physics with cosmological structure formation*, *Phys. Rev. D* **90** (2014), no. 6 063009, [[arXiv:1401.1923](#)].
- [2285] C. G. Callan, Jr. and S. R. Coleman, *The Fate of the False Vacuum. 2. First Quantum Corrections*, *Phys. Rev. D* **16** (1977) 1762–1768.
- [2286] M. Doran and G. Robbers, *Early dark energy cosmologies*, *JCAP* **06** (2006) 026, [[astro-ph/0601544](#)].
- [2287] K. A. Olive and M. Pospelov, *Environmental dependence of masses and coupling constants*, *Phys. Rev. D* **77** (2008) 043524, [[arXiv:0709.3825](#)].
- [2288] M. Pietroni, *Dark energy condensation*, *Phys. Rev. D* **72** (2005) 043535, [[astro-ph/0505615](#)].
- [2289] A.-C. Davis, B. Li, D. F. Mota, and H. A. Winther, *Structure Formation in the Symmetron Model*, *Astrophys. J.* **748** (2012) 61, [[arXiv:1108.3081](#)].
- [2290] M. B. Gronke, C. Llinares, and D. F. Mota, *Gravitational redshift profiles in the $f(R)$ and symmetron models*, *Astron. Astrophys.* **562** (2014) A9, [[arXiv:1307.6994](#)].
- [2291] M. Gronke, C. Llinares, D. F. Mota, and H. A. Winther, *Halo velocity profiles in screened modified gravity theories*, *Mon. Not. Roy. Astron. Soc.* **449** (2015), no. 3 2837–2844, [[arXiv:1412.0066](#)].
- [2292] C. Llinares and L. Pogosian, *Domain walls coupled to matter: the symmetron example*, *Phys. Rev. D* **90** (2014), no. 12 124041, [[arXiv:1410.2857](#)].
- [2293] M. Gronke, D. F. Mota, and H. A. Winther, *Universal predictions of screened modified gravity on cluster scales*, *Astron. Astrophys.* **583** (2015) A123, [[arXiv:1505.07129](#)].
- [2294] R. Voivodic, M. Lima, C. Llinares, and D. F. Mota, *Modelling Void Abundance in Modified Gravity*, *Phys. Rev. D* **95** (2017), no. 2 024018, [[arXiv:1609.02544](#)].
- [2295] A. Hammami and D. F. Mota, *Cosmological simulations with hydrodynamics of screened scalar-tensor gravity with non-universal coupling*, *Astron. Astrophys.* **584** (2015) A57, [[arXiv:1505.06803](#)].
- [2296] Y. B. Zeldovich, I. Y. Kobzarev, and L. B. Okun, *Cosmological Consequences of the Spontaneous Breakdown of Discrete Symmetry*, *Zh. Eksp. Teor. Fiz.* **67** (1974) 3–11.
- [2297] T. W. B. Kibble, G. Lazarides, and Q. Shafi, *Walls Bounded by Strings*, *Phys. Rev. D* **26** (1982) 435.

- [2298] A. Vilenkin, *Cosmic Strings and Domain Walls*, *Phys. Rept.* **121** (1985) 263–315.
- [2299] T. Vachaspati and A. Vilenkin, *Formation and Evolution of Cosmic Strings*, *Phys. Rev. D* **30** (1984) 2036.
- [2300] M. B. Hindmarsh and T. W. B. Kibble, *Cosmic strings*, *Rept. Prog. Phys.* **58** (1995) 477–562, [[hep-ph/9411342](#)].
- [2301] A. Vilenkin and E. P. S. Shellard, *Cosmic Strings and Other Topological Defects*. Cambridge University Press, 7, 2000.
- [2302] T. Vachaspati, *Kinks and domain walls: An introduction to classical and quantum solitons*. Cambridge University Press, 4, 2010.
- [2303] N. S. Manton and P. Sutcliffe, *Topological solitons*. Cambridge Monographs on Mathematical Physics. Cambridge University Press, 2004.
- [2304] L. Perivolaropoulos, *Gravitational Interactions of Finite Thickness Global Topological Defects with Black Holes*, *Phys. Rev. D* **97** (2018), no. 12 124035, [[arXiv:1804.08098](#)].
- [2305] T. P. Waterhouse, *An Introduction to Chameleon Gravity*, [astro-ph/0611816](#).
- [2306] M. Sami and R. Gannouji, *Spontaneous symmetry breaking in the late Universe and glimpses of the early Universe phase transitions à la baryogenesis*, *Int. J. Mod. Phys. D* **30** (2021), no. 13 2130005, [[arXiv:2106.00843](#)].
- [2307] H. A. Winther, D. F. Mota, and B. Li, *Environment Dependence of Dark Matter Halos in Symmetron Modified Gravity*, *Astrophys. J.* **756** (2012) 166, [[arXiv:1110.6438](#)].
- [2308] R. F. Dashen, B. Hasslacher, and A. Neveu, *Nonperturbative Methods and Extended Hadron Models in Field Theory 2. Two-Dimensional Models and Extended Hadrons*, *Phys. Rev. D* **10** (1974) 4130–4138.
- [2309] A. M. Polyakov, *Particle Spectrum in Quantum Field Theory*, *JETP Lett.* **20** (1974) 194–195.
- [2310] J. A. Pearson, *Simulating the symmetron: domain walls and symmetry-restoring impurities*, *Phys. Rev. D* **90** (2014), no. 12 125011, [[arXiv:1409.6570](#)]. [Addendum: *Phys.Rev.D* 91, 049901 (2015)].
- [2311] M. Peyravi, N. Riazi, and F. S. N. Lobo, *Evolution of spherical domain walls in solitonic symmetron models*, *Phys. Rev. D* **95** (2017), no. 6 064047, [[arXiv:1606.05269](#)].
- [2312] J. Sakstein, *Astrophysical Tests of Modified Gravity*. PhD thesis, Cambridge U., DAMTP, 2014. [[arXiv:1502.04503](#)].
- [2313] P. Brax, C. van de Bruck, A.-C. Davis, B. Li, B. Schmauch, and D. J. Shaw, *Linear Growth of Structure in the Symmetron Model*, *Phys. Rev. D* **84** (2011) 123524, [[arXiv:1108.3082](#)].
- [2314] J. Clampitt, B. Jain, and J. Khoury, *Halo Scale Predictions of Symmetron Modified Gravity*, *JCAP* **01** (2012) 030, [[arXiv:1110.2177](#)].
- [2315] C. Llinares and D. F. Mota, *Shape of Clusters of Galaxies as a Probe of Screening Mechanisms in Modified Gravity*, *Phys. Rev. Lett.* **110** (2013), no. 15 151104, [[arXiv:1205.5775](#)].
- [2316] L. Taddei, R. Catena, and M. Pietroni, *Spherical collapse and halo mass function in the symmetron model*, *Phys. Rev. D* **89** (2014), no. 2 023523, [[arXiv:1310.6175](#)].
- [2317] P. Brax, A.-C. Davis, B. Li, H. A. Winther, and G.-B. Zhao, *Systematic Simulations of Modified Gravity: Symmetron and Dilaton Models*, *JCAP* **10** (2012) 002, [[arXiv:1206.3568](#)].

- [2318] C. Llinares and D. Mota, *Releasing scalar fields: cosmological simulations of scalar-tensor theories for gravity beyond the static approximation*, *Phys. Rev. Lett.* **110** (2013), no. 16 161101, [[arXiv:1302.1774](#)].
- [2319] C. Llinares and D. F. Mota, *Cosmological simulations of screened modified gravity out of the static approximation: effects on matter distribution*, *Phys. Rev. D* **89** (2014), no. 8 084023, [[arXiv:1312.6016](#)].
- [2320] C. Llinares, D. F. Mota, and H. A. Winther, *ISIS: a new N-body cosmological code with scalar fields based on RAMSES. Code presentation and application to the shapes of clusters*, *Astron. Astrophys.* **562** (2014) A78, [[arXiv:1307.6748](#)].
- [2321] R. Hagala, C. Llinares, and D. F. Mota, *Cosmological simulations with disformally coupled symmetron fields*, *Astron. Astrophys.* **585** (2016) A37, [[arXiv:1504.07142](#)].
- [2322] G. H. Derrick, *Comments on nonlinear wave equations as models for elementary particles*, *J. Math. Phys.* **5** (1964) 1252–1254.
- [2323] W. H. Press, S. A. Teukolsky, W. T. Vetterling, and B. P. Flannery, *Numerical Recipes 3rd Edition: The Art of Scientific Computing*. Cambridge University Press, USA, 3 ed., 2007.
- [2324] J. Sakstein, H. Wilcox, D. Bacon, K. Koyama, and R. C. Nichol, *Testing Gravity Using Galaxy Clusters: New Constraints on Beyond Horndeski Theories*, *JCAP* **07** (2016) 019, [[arXiv:1603.06368](#)].
- [2325] V. Salzano, D. F. Mota, S. Capozziello, and M. Donahue, *Breaking the Vainshtein screening in clusters of galaxies*, *Phys. Rev. D* **95** (2017), no. 4 044038, [[arXiv:1701.03517](#)].
- [2326] E. Laudato, V. Salzano, and K. Umetsu, *Multi-component DHOST analysis in galaxy clusters*, [arXiv:2110.11019](#).
- [2327] A. Terukina, L. Lombriser, K. Yamamoto, D. Bacon, K. Koyama, and R. C. Nichol, *Testing chameleon gravity with the Coma cluster*, *JCAP* **04** (2014) 013, [[arXiv:1312.5083](#)].
- [2328] H. Wilcox et al., *The XMM Cluster Survey: Testing chameleon gravity using the profiles of clusters*, *Mon. Not. Roy. Astron. Soc.* **452** (2015), no. 2 1171–1183, [[arXiv:1504.03937](#)].
- [2329] L. Pizzuti, I. D. Saltas, and L. Amendola, *mg-mamposst: a code to test modifications of gravity with internal kinematics and lensing analyses of galaxy clusters*, *Mon. Not. Roy. Astron. Soc.* **506** (2021), no. 1 595–612, [[arXiv:2011.15089](#)].
- [2330] D. Langlois and K. Noui, *Degenerate higher derivative theories beyond Horndeski: evading the Ostrogradski instability*, *JCAP* **02** (2016) 034, [[arXiv:1510.06930](#)].
- [2331] M. Zumalacárregui and J. García-Bellido, *Transforming gravity: from derivative couplings to matter to second-order scalar-tensor theories beyond the Horndeski Lagrangian*, *Phys. Rev. D* **89** (2014) 064046, [[arXiv:1308.4685](#)].
- [2332] D. Langlois and K. Noui, *Hamiltonian analysis of higher derivative scalar-tensor theories*, *JCAP* **07** (2016) 016, [[arXiv:1512.06820](#)].
- [2333] M. Crisostomi, K. Koyama, and G. Tasinato, *Extended Scalar-Tensor Theories of Gravity*, *JCAP* **04** (2016) 044, [[arXiv:1602.03119](#)].
- [2334] J. Ben Achour, D. Langlois, and K. Noui, *Degenerate higher order scalar-tensor theories beyond Horndeski and disformal transformations*, *Phys. Rev. D* **93** (2016), no. 12 124005, [[arXiv:1602.08398](#)].

- [2335] H. Motohashi, K. Noui, T. Suyama, M. Yamaguchi, and D. Langlois, *Healthy degenerate theories with higher derivatives*, *JCAP* **07** (2016) 033, [[arXiv:1603.09355](#)].
- [2336] J. Ben Achour, M. Crisostomi, K. Koyama, D. Langlois, K. Noui, and G. Tasinato, *Degenerate higher order scalar-tensor theories beyond Horndeski up to cubic order*, *JHEP* **12** (2016) 100, [[arXiv:1608.08135](#)].
- [2337] D. Langlois, M. Mancarella, K. Noui, and F. Vernizzi, *Effective Description of Higher-Order Scalar-Tensor Theories*, *JCAP* **05** (2017) 033, [[arXiv:1703.03797](#)].
- [2338] D. Langlois, *Dark energy and modified gravity in degenerate higher-order scalar–tensor (DHOST) theories: A review*, *Int. J. Mod. Phys. D* **28** (2019), no. 05 1942006, [[arXiv:1811.06271](#)].
- [2339] T. Kobayashi, Y. Watanabe, and D. Yamauchi, *Breaking of Vainshtein screening in scalar-tensor theories beyond Horndeski*, *Phys. Rev. D* **91** (2015), no. 6 064013, [[arXiv:1411.4130](#)].
- [2340] M. Crisostomi and K. Koyama, *Vainshtein mechanism after GW170817*, *Phys. Rev. D* **97** (2018), no. 2 021301, [[arXiv:1711.06661](#)].
- [2341] D. Langlois, R. Saito, D. Yamauchi, and K. Noui, *Scalar-tensor theories and modified gravity in the wake of GW170817*, *Phys. Rev. D* **97** (2018), no. 6 061501, [[arXiv:1711.07403](#)].
- [2342] N. Bartolo, P. Karmakar, S. Matarrese, and M. Scomparin, *Cosmic structures and gravitational waves in ghost-free scalar-tensor theories of gravity*, *JCAP* **05** (2018) 048, [[arXiv:1712.04002](#)].
- [2343] A. Dima and F. Vernizzi, *Vainshtein Screening in Scalar-Tensor Theories before and after GW170817: Constraints on Theories beyond Horndeski*, *Phys. Rev. D* **97** (2018), no. 10 101302, [[arXiv:1712.04731](#)].
- [2344] D. Eckert, S. Ettori, E. Pointecouteau, S. Molendi, S. Paltani, and C. Tchernin, *The XMM cluster outskirts project (X-COP)*, *Astron. Nachr.* **338** (2017), no. 2/3 293–298, [[arXiv:1611.05051](#)].
- [2345] M. Wittner, G. Laverda, O. F. Piattella, and L. Amendola, *Transient weak gravity in scalar-tensor theories*, [arXiv:2003.08950](#).
- [2346] L. Pizzuti, I. D. Saltas, S. Casas, L. Amendola, and A. Biviano, *Future constraints on the gravitational slip with the mass profiles of galaxy clusters*, *Mon. Not. Roy. Astron. Soc.* **486** (2019), no. 1 596–607, [[arXiv:1901.01961](#)].
- [2347] A. Kempf, *Mode generating mechanism in inflation with cutoff*, *Phys. Rev.* **D63** (2001) 083514, [[astro-ph/0009209](#)].
- [2348] G. A. Palma and S. P. Patil, *Inflation with a stringy minimal length, reworked*, *JHEP* **04** (2009) 005, [[arXiv:0810.5532](#)].
- [2349] **EUCLID** Collaboration, R. Laureijs et al., *Euclid Definition Study Report*, [arXiv:1110.3193](#).
- [2350] **LSST Science, LSST Project** Collaboration, P. A. Abell et al., *LSST Science Book, Version 2.0*, [arXiv:0912.0201](#).
- [2351] J. P. Gardner et al., *The James Webb Space Telescope*, *Space Sci. Rev.* **123** (2006) 485, [[astro-ph/0606175](#)].
- [2352] A. Blanchard et al., *Gravitation And the Universe from large Scale-Structures: The GAUSS mission concept*, [arXiv:2102.03931](#).
- [2353] **CMB-S4** Collaboration, K. N. Abazajian et al., *CMB-S4 Science Book, First Edition*, [arXiv:1610.02743](#).

- [2354] **Simons Observatory** Collaboration, P. Ade et al., *The Simons Observatory: Science goals and forecasts*, *JCAP* **02** (2019) 056, [[arXiv:1808.07445](#)].
- [2355] **SPT-3G** Collaboration, B. A. Benson et al., *SPT-3G: A Next-Generation Cosmic Microwave Background Polarization Experiment on the South Pole Telescope*, *Proc. SPIE Int. Soc. Opt. Eng.* **9153** (2014) 91531P, [[arXiv:1407.2973](#)].
- [2356] S. L. Detweiler, *Pulsar timing measurements and the search for gravitational waves*, *Astrophys. J.* **234** (1979) 1100–1104.
- [2357] R. S. Foster and D. C. Backer, *Constructing a Pulsar Timing Array*, *Astrophys. J.* **361** (Sept., 1990) 300.
- [2358] R. w. Hellings and G. s. Downs, *UPPER LIMITS ON THE ISOTROPIC GRAVITATIONAL RADIATION BACKGROUND FROM PULSAR TIMING ANALYSIS*, *Astrophys. J. Lett.* **265** (1983) L39–L42.
- [2359] G. Janssen et al., *Gravitational wave astronomy with the SKA*, *PoS AASKA14* (2015) 037, [[arXiv:1501.00127](#)].
- [2360] M. A. McLaughlin, *The North American Nanohertz Observatory for Gravitational Waves*, *Class. Quant. Grav.* **30** (2013) 224008, [[arXiv:1310.0758](#)].
- [2361] G. Desvignes et al., *High-precision timing of 42 millisecond pulsars with the European Pulsar Timing Array*, *Mon. Not. Roy. Astron. Soc.* **458** (2016), no. 3 3341–3380, [[arXiv:1602.08511](#)].
- [2362] G. Hobbs, *The Parkes Pulsar Timing Array*, *Class. Quant. Grav.* **30** (2013) 224007, [[arXiv:1307.2629](#)].
- [2363] J. P. W. Verbiest et al., *The International Pulsar Timing Array: First Data Release*, *Mon. Not. Roy. Astron. Soc.* **458** (2016), no. 2 1267–1288, [[arXiv:1602.03640](#)].
- [2364] **AEDGE** Collaboration, Y. A. El-Neaj et al., *AEDGE: Atomic Experiment for Dark Matter and Gravity Exploration in Space*, *EPJ Quant. Technol.* **7** (2020) 6, [[arXiv:1908.00802](#)].
- [2365] **KAGRA** Collaboration, K. Somiya, *Detector configuration of KAGRA: The Japanese cryogenic gravitational-wave detector*, *Class. Quant. Grav.* **29** (2012) 124007, [[arXiv:1111.7185](#)].
- [2366] **LIGO Scientific** Collaboration, B. P. Abbott et al., *Exploring the Sensitivity of Next Generation Gravitational Wave Detectors*, *Class. Quant. Grav.* **34** (2017), no. 4 044001, [[arXiv:1607.08697](#)].
- [2367] **LISA** Collaboration, P. Amaro-Seoane et al., *Laser Interferometer Space Antenna*, [[arXiv:1702.00786](#)].
- [2368] W.-R. Hu and Y.-L. Wu, *The Taiji Program in Space for gravitational wave physics and the nature of gravity*, *Natl. Sci. Rev.* **4** (2017), no. 5 685–686.
- [2369] **TianQin** Collaboration, J. Luo et al., *TianQin: a space-borne gravitational wave detector*, *Class. Quant. Grav.* **33** (2016), no. 3 035010, [[arXiv:1512.02076](#)].
- [2370] S. Kawamura et al., *The Japanese space gravitational wave antenna DECIGO*, *Class. Quant. Grav.* **23** (2006) S125–S132.
- [2371] M. Punturo et al., *The Einstein Telescope: A third-generation gravitational wave observatory*, *Class. Quant. Grav.* **27** (2010) 194002.
- [2372] **EUCLID** Collaboration, A. Refregier, *The Dark UNiverse Explorer (DUNE): Proposal to ESA’s Cosmic Vision*, *Exper. Astron.* **23** (2009) 17–37, [[arXiv:0802.2522](#)].

- [2373] A. Cimatti, R. Laureijs, B. Leibundgut, S. Lilly, R. Nichol, A. Refregier, P. Rosati, M. Steinmetz, N. Thatte, and E. Valentijn, *Euclid Assessment Study Report for the ESA Cosmic Visions*, [arXiv:0912.0914](#).
- [2374] B. Sartoris et al., *Next Generation Cosmology: Constraints from the Euclid Galaxy Cluster Survey*, *Mon. Not. Roy. Astron. Soc.* **459** (2016), no. 2 1764–1780, [[arXiv:1505.02165](#)].
- [2375] **Euclid Theory Working Group** Collaboration, L. Amendola et al., *Cosmology and fundamental physics with the Euclid satellite*, *Living Rev. Rel.* **16** (2013) 6, [[arXiv:1206.1225](#)].
- [2376] **Euclid** Collaboration, R. Adam et al., *Euclid preparation III. Galaxy cluster detection in the wide photometric survey, performance and algorithm selection*, *Astron. Astrophys.* **627** (2019), no. 627 A23, [[arXiv:1906.04707](#)].
- [2377] G. Fanizza, B. Fiorini, and G. Marozzi, *Cosmic variance of H_0 in light of forthcoming high-redshift surveys*, [arXiv:2102.12419](#).
- [2378] **LSST** Collaboration, v. Z. Ivezić et al., *LSST: from Science Drivers to Reference Design and Anticipated Data Products*, *Astrophys. J.* **873** (2019), no. 2 111, [[arXiv:0805.2366](#)].
- [2379] **LSST** Collaboration, P. Marshall et al., *Science-Driven Optimization of the LSST Observing Strategy*, [arXiv:1708.04058](#).
- [2380] **LSST Dark Energy Science** Collaboration, A. Abate et al., *Large Synoptic Survey Telescope: Dark Energy Science Collaboration*, [arXiv:1211.0310](#).
- [2381] K. Abazajian et al., *CMB-S4 Science Case, Reference Design, and Project Plan*, [arXiv:1907.04473](#).
- [2382] **CMB-S4** Collaboration, K. Abazajian et al., *CMB-S4: Forecasting Constraints on Primordial Gravitational Waves*, [arXiv:2008.12619](#).
- [2383] **Gaia** Collaboration, A. G. A. Brown et al., *Gaia Data Release 1: Summary of the astrometric, photometric, and survey properties*, *Astron. Astrophys.* **595** (2016), no. Gaia Data Release 1 A2, [[arXiv:1609.04172](#)].
- [2384] L. Lindegren et al., *Gaia Data Release 2: The astrometric solution*, *Astron. Astrophys.* **616** (2018) A2, [[arXiv:1804.09366](#)].
- [2385] P. A. Sabelhaus and J. E. Decker, *An overview of the James Webb Space Telescope (JWST) project*, in *Optical, Infrared, and Millimeter Space Telescopes* (J. C. Mather, ed.), vol. 5487 of *Society of Photo-Optical Instrumentation Engineers (SPIE) Conference Series*, pp. 550–563, Oct., 2004.
- [2386] E. Zackrisson, C. E. Rydberg, D. Schaerer, G. Ostlin, and M. Tuli, *The spectral evolution of the first galaxies. I. James Webb Space Telescope detection limits and color criteria for population III galaxies*, *Astrophys. J.* **740** (2011) 13, [[arXiv:1105.0921](#)].
- [2387] C.-E. Rydberg, E. Zackrisson, P. Lundqvist, and P. Scott, *Detection of isolated population III stars with the James Webb Space Telescope*, *Mon. Not. Roy. Astron. Soc.* **429** (2013) 3658–3664, [[arXiv:1206.0007](#)].
- [2388] D. J. Whalen, C. L. Fryer, D. E. Holz, A. Heger, S. E. Woosley, M. Stiavelli, W. Even, and L. L. Frey, *Seeing the First Supernovae at the Edge of the Universe with JWST*, *Astrophys. J. Lett.* **762** (2013) L6, [[arXiv:1209.3457](#)].
- [2389] T. Hartwig, V. Bromm, and A. Loeb, *Detection strategies for the first supernovae with JWST*, *Mon. Not. Roy. Astron. Soc.* **479** (2018), no. 2 2202–2213, [[arXiv:1711.05742](#)].

- [2390] C. Schultz, J. Oñorbe, K. N. Abazajian, and J. S. Bullock, *The High- z Universe Confronts Warm Dark Matter: Galaxy Counts, Reionization and the Nature of Dark Matter*, *Mon. Not. Roy. Astron. Soc.* **442** (2014), no. 2 1597–1609, [[arXiv:1401.3769](#)].
- [2391] U. Maio and M. Viel, *The First Billion Years of a Warm Dark Matter Universe*, *Mon. Not. Roy. Astron. Soc.* **446** (2015) 2760–2775, [[arXiv:1409.6718](#)].
- [2392] N. Galitzki et al., *The Simons Observatory: Instrument Overview*, *Proc. SPIE Int. Soc. Opt. Eng.* **10708** (2018) 1070804, [[arXiv:1808.04493](#)].
- [2393] **Simons Observatory** Collaboration, M. H. Abitbol et al., *The Simons Observatory: Astro2020 Decadal Project Whitepaper*, *Bull. Am. Astron. Soc.* **51** (2019) 147, [[arXiv:1907.08284](#)].
- [2394] S. Dodelson, K. Heitmann, C. Hirata, K. Honscheid, A. Roodman, U. Seljak, A. Slosar, and M. Trodden, *Cosmic Visions Dark Energy: Science*, [arXiv:1604.07626](#).
- [2395] J. E. Austermann et al., *SPTpol: an instrument for CMB polarization measurements with the South Pole Telescope*, in *Millimeter, Submillimeter, and Far-Infrared Detectors and Instrumentation for Astronomy VI* (W. S. Holland and J. Zmuidzinas, eds.), vol. 8452 of *Society of Photo-Optical Instrumentation Engineers (SPIE) Conference Series*, p. 84521E, Sept., 2012. [arXiv:1210.4970](#).
- [2396] A. Abramovici et al., *LIGO: The Laser interferometer gravitational wave observatory*, *Science* **256** (1992) 325–333.
- [2397] G. Pizzella, *Resonant detectors for the search for gravitational waves*, *Class. Quant. Grav.* **14** (1997) 1481–1485.
- [2398] M. Maggiore, *Gravitational wave experiments and early universe cosmology*, *Phys. Rept.* **331** (2000) 283–367, [[gr-qc/9909001](#)].
- [2399] O. D. Aguiar, *The Past, Present and Future of the Resonant-Mass Gravitational Wave Detectors*, *Res. Astron. Astrophys.* **11** (2011) 1–42, [[arXiv:1009.1138](#)].
- [2400] P. Astone et al., *IGEC2: A 17-month search for gravitational wave bursts in 2005-2007*, *Phys. Rev. D* **82** (2010) 022003, [[arXiv:1002.3515](#)].
- [2401] J. Weber, *Detection and Generation of Gravitational Waves*, *Phys. Rev.* **117** (1960) 306–313.
- [2402] E. Mauceli, Z. K. Geng, W. O. Hamilton, W. W. Johnson, S. Merkowitz, A. Morse, B. Price, and N. Solomonson, *The ALLEGRO gravitational wave detector: Data acquisition and analysis*, *Phys. Rev. D* **54** (1996) 1264–1275, [[gr-qc/9609058](#)].
- [2403] E. Amaldi et al., *Sensitivity of the Rome gravitational wave experiment with the Explorer cryogenic resonant antenna operating at 2-K*, *Europhys. Lett.* **12** (1990) 5–11.
- [2404] P. Astone et al., *Upper limit for a gravitational wave stochastic background with the EXPLORER and NAUTILUS resonant detectors*, *Phys. Lett. B* **385** (1996) 421–424.
- [2405] P. Astone et al., *The Gravitational wave detector NAUTILUS operating at $T = 0.1$ -K*, *Astropart. Phys.* **7** (1997) 231–243.
- [2406] I. Ciufolini and F. Fidecaro, *GRAVITATIONAL WAVES: Sources and Detectors*, *booktitle = Gravitational Waves*, pp. 1–382.
- [2407] M. Cerdonio et al., *The Ultracryogenic gravitational wave detector AURIGA*, *Class. Quant. Grav.* **14** (1997) 1491–1494.

- [2408] D. G. Blair, E. N. Ivanov, M. E. Tobar, P. J. Turner, F. van Kann, and I. S. Heng, *High sensitivity gravitational wave antenna with parametric transducer readout*, *Phys. Rev. Lett.* **74** (1995) 1908–1911.
- [2409] I. S. Heng, D. G. Blair, E. N. Ivanov, and M. E. Tobar, *Long term operation of a niobium resonant bar gravitational wave antenna*, *Phys. Lett. A* **218** (1996) 190–196.
- [2410] O. D. Aguiar et al., *The status of the Brazilian spherical detector*, *Class. Quant. Grav.* **19** (2002) 1949–1953.
- [2411] A. de Waard, L. Gottardi, J. van Houwelingen, A. Shumack, and G. Frossati, *MiniGRAIL, the first spherical detector*, *Class. Quant. Grav.* **20** (2003) S143–S151.
- [2412] M. E. Gertsenshtein and V. I. Pustovoit, *On the Detection of Low Frequency Gravitational Waves*, *Sov. Phys. JETP* **16** (1962) 433.
- [2413] G. E. Moss, L. R. Miller, and R. L. Forward, *Photon-noise-limited laser transducer for gravitational antenna*, *Appl. Opt.* **10** (1971) 2495–2498.
- [2414] **LIGO Scientific** Collaboration, G. M. Harry, *Advanced LIGO: The next generation of gravitational wave detectors*, *Class. Quant. Grav.* **27** (2010) 084006.
- [2415] B. Willke et al., *The GEO 600 gravitational wave detector*, *Class. Quant. Grav.* **19** (2002) 1377–1387.
- [2416] C. Affeldt et al., *Advanced techniques in GEO 600*, *Class. Quant. Grav.* **31** (2014), no. 22 224002.
- [2417] **LIGO Scientific** Collaboration, B. P. Abbott et al., *LIGO: The Laser interferometer gravitational-wave observatory*, *Rept. Prog. Phys.* **72** (2009) 076901, [[arXiv:0711.3041](#)].
- [2418] A. Giazotto, *The Virgo Project: A Wide Band Antenna for Gravitational Wave Detection*, *Nucl. Instrum. Meth. A* **289** (1990) 518–525.
- [2419] F. Acernese et al., *Status of Virgo*, *Class. Quant. Grav.* **25** (2008) 114045.
- [2420] **LIGO Scientific, Virgo** Collaboration, B. P. Abbott et al., *Observation of Gravitational Waves from a Binary Black Hole Merger*, *Phys. Rev. Lett.* **116** (2016), no. 6 061102, [[arXiv:1602.03837](#)].
- [2421] L. P. Singer and L. R. Price, *Rapid Bayesian position reconstruction for gravitational-wave transients*, *Phys. Rev. D* **93** (2016), no. 2 024013, [[arXiv:1508.03634](#)].
- [2422] N. J. Cornish and T. B. Littenberg, *BayesWave: Bayesian Inference for Gravitational Wave Bursts and Instrument Glitches*, *Class. Quant. Grav.* **32** (2015), no. 13 135012, [[arXiv:1410.3835](#)].
- [2423] T. B. Littenberg and N. J. Cornish, *Bayesian inference for spectral estimation of gravitational wave detector noise*, *Phys. Rev. D* **91** (2015), no. 8 084034, [[arXiv:1410.3852](#)].
- [2424] N. J. Cornish, T. B. Littenberg, B. Bécsy, K. Chatziioannou, J. A. Clark, S. Ghonge, and M. Millhouse, *BayesWave analysis pipeline in the era of gravitational wave observations*, *Phys. Rev. D* **103** (2021), no. 4 044006, [[arXiv:2011.09494](#)].
- [2425] G. Dálya, P. Raffai, and B. Bécsy, *Bayesian Reconstruction of Gravitational-wave Signals from Binary Black Holes with Nonzero Eccentricities*, *Class. Quant. Grav.* **38** (2021), no. 6 065002, [[arXiv:2006.06256](#)].

- [2426] S. Ghonge, K. Chatziioannou, J. A. Clark, T. Littenberg, M. Millhouse, L. Cadonati, and N. Cornish, *Reconstructing gravitational wave signals from binary black hole mergers with minimal assumptions*, *Phys. Rev. D* **102** (2020), no. 6 064056, [[arXiv:2003.09456](#)].
- [2427] **LIGO Scientific, Virgo** Collaboration, B. P. Abbott et al., *GW170814: A Three-Detector Observation of Gravitational Waves from a Binary Black Hole Coalescence*, *Phys. Rev. Lett.* **119** (2017), no. 14 141101, [[arXiv:1709.09660](#)].
- [2428] **TAMA** Collaboration, M. Ando et al., *Stable operation of a 300-m laser interferometer with sufficient sensitivity to detect gravitational wave events within our galaxy*, *Phys. Rev. Lett.* **86** (2001) 3950, [[astro-ph/0105473](#)].
- [2429] **TAMA** Collaboration, K. Arai, *Recent progress of TAMA300*, *J. Phys. Conf. Ser.* **120** (2008) 032010.
- [2430] **KAGRA** Collaboration, Y. Aso, Y. Michimura, K. Somiya, M. Ando, O. Miyakawa, T. Sekiguchi, D. Tatsumi, and H. Yamamoto, *Interferometer design of the KAGRA gravitational wave detector*, *Phys. Rev. D* **88** (2013), no. 4 043007, [[arXiv:1306.6747](#)].
- [2431] **KAGRA** Collaboration, T. Akutsu et al., *Overview of KAGRA : KAGRA science*, [arXiv:2008.02921](#).
- [2432] **LCGT** Collaboration, K. Kuroda, *Status of LCGT*, *Class. Quant. Grav.* **27** (2010) 084004.
- [2433] C. S. Unnikrishnan, *IndIGO and LIGO-India: Scope and plans for gravitational wave research and precision metrology in India*, *Int. J. Mod. Phys. D* **22** (2013) 1341010, [[arXiv:1510.06059](#)].
- [2434] D. Reitze et al., *The US Program in Ground-Based Gravitational Wave Science: Contribution from the LIGO Laboratory*, *Bull. Am. Astron. Soc.* **51** (3, 2019) 141, [[arXiv:1903.04615](#)].
- [2435] D. Reitze et al., *Cosmic Explorer: The U.S. Contribution to Gravitational-Wave Astronomy beyond LIGO*, *Bull. Am. Astron. Soc.* **51** (7, 2019) 035, [[arXiv:1907.04833](#)].
- [2436] R. Essick, S. Vitale, and M. Evans, *Frequency-dependent responses in third generation gravitational-wave detectors*, *Phys. Rev. D* **96** (2017), no. 8 084004, [[arXiv:1708.06843](#)].
- [2437] K. Chamberlain and N. Yunes, *Theoretical Physics Implications of Gravitational Wave Observation with Future Detectors*, *Phys. Rev. D* **96** (2017), no. 8 084039, [[arXiv:1704.08268](#)].
- [2438] **LIGO Scientific, Virgo** Collaboration, B. Abbott et al., *GWTC-1: A Gravitational-Wave Transient Catalog of Compact Binary Mergers Observed by LIGO and Virgo during the First and Second Observing Runs*, *Phys. Rev. X* **9** (2019), no. 3 031040, [[arXiv:1811.12907](#)].
- [2439] **LIGO Scientific, Virgo** Collaboration, R. Abbott et al., *GWTC-2: Compact Binary Coalescences Observed by LIGO and Virgo During the First Half of the Third Observing Run*, [arXiv:2010.14527](#).
- [2440] C. Caprini et al., *Science with the space-based interferometer eLISA. II: Gravitational waves from cosmological phase transitions*, *JCAP* **04** (2016) 001, [[arXiv:1512.06239](#)].
- [2441] M. Armano et al., *Sub-Femto- g Free Fall for Space-Based Gravitational Wave Observatories: LISA Pathfinder Results*, *Phys. Rev. Lett.* **116** (2016), no. 23 231101.
- [2442] M. Armano et al., *Measuring the Galactic Cosmic Ray Flux with the LISA Pathfinder Radiation Monitor*, *Astropart. Phys.* **98** (2018) 28–37, [[arXiv:1711.07427](#)].
- [2443] P. Amaro-Seoane et al., *eLISA/NGO: Astrophysics and cosmology in the gravitational-wave millihertz regime*, *GW Notes* **6** (2013) 4–110, [[arXiv:1201.3621](#)].

- [2444] P. Amaro-Seoane et al., *Low-frequency gravitational-wave science with eLISA/NGO*, *Class. Quant. Grav.* **29** (2012) 124016, [[arXiv:1202.0839](#)].
- [2445] **KAGRA, LIGO Scientific, VIRGO** Collaboration, B. P. Abbott et al., *Prospects for Observing and Localizing Gravitational-Wave Transients with Advanced LIGO, Advanced Virgo and KAGRA*, *Living Rev. Rel.* **21** (2018), no. 1 3, [[arXiv:1304.0670](#)].
- [2446] B. S. Sathyaprakash and B. F. Schutz, *Physics, Astrophysics and Cosmology with Gravitational Waves*, *Living Rev. Rel.* **12** (2009) 2, [[arXiv:0903.0338](#)].
- [2447] M. C. Guzzetti, N. Bartolo, M. Liguori, and S. Matarrese, *Gravitational waves from inflation*, *Riv. Nuovo Cim.* **39** (2016), no. 9 399–495, [[arXiv:1605.01615](#)].
- [2448] R.-G. Cai, Z. Cao, Z.-K. Guo, S.-J. Wang, and T. Yang, *The Gravitational-Wave Physics*, *Natl. Sci. Rev.* **4** (2017), no. 5 687–706, [[arXiv:1703.00187](#)].
- [2449] N. Bartolo, V. De Luca, G. Franciolini, A. Lewis, M. Peloso, and A. Riotto, *Primordial Black Hole Dark Matter: LISA Serendipity*, *Phys. Rev. Lett.* **122** (2019), no. 21 211301, [[arXiv:1810.12218](#)].
- [2450] N. Bartolo, V. De Luca, G. Franciolini, M. Peloso, D. Racco, and A. Riotto, *Testing primordial black holes as dark matter with LISA*, *Phys. Rev. D* **99** (2019), no. 10 103521, [[arXiv:1810.12224](#)].
- [2451] R.-g. Cai, S. Pi, and M. Sasaki, *Gravitational Waves Induced by non-Gaussian Scalar Perturbations*, *Phys. Rev. Lett.* **122** (2019), no. 20 201101, [[arXiv:1810.11000](#)].
- [2452] J. Crowder and N. J. Cornish, *Beyond LISA: Exploring future gravitational wave missions*, *Phys. Rev. D* **72** (2005) 083005, [[gr-qc/0506015](#)].
- [2453] G. M. Harry, P. Fritschel, D. A. Shaddock, W. Folkner, and E. S. Phinney, *Laser interferometry for the big bang observer*, *Class. Quant. Grav.* **23** (2006) 4887–4894. [Erratum: *Class.Quant.Grav.* **23**, 7361 (2006)].
- [2454] W.-H. Ruan, Z.-K. Guo, R.-G. Cai, and Y.-Z. Zhang, *Taiji program: Gravitational-wave sources*, *Int. J. Mod. Phys. A* **35** (2020), no. 17 2050075, [[arXiv:1807.09495](#)].
- [2455] W.-H. Ruan, C. Liu, Z.-K. Guo, Y.-L. Wu, and R.-G. Cai, *The LISA-Taiji network: precision localization of massive black hole binaries*, [[arXiv:1909.07104](#)].
- [2456] W.-H. Ruan, C. Liu, Z.-K. Guo, Y.-L. Wu, and R.-G. Cai, *The LISA-Taiji network*, *Nature Astron.* **4** (2020) 108–109, [[arXiv:2002.03603](#)].
- [2457] **TianQin** Collaboration, J. Mei et al., *The TianQin project: current progress on science and technology*, [[arXiv:2008.10332](#)].
- [2458] W.-F. Feng, H.-T. Wang, X.-C. Hu, Y.-M. Hu, and Y. Wang, *Preliminary study on parameter estimation accuracy of supermassive black hole binary inspirals for TianQin*, *Phys. Rev. D* **99** (2019), no. 12 123002, [[arXiv:1901.02159](#)].
- [2459] S. Liu, Y.-M. Hu, J.-d. Zhang, and J. Mei, *Science with the TianQin observatory: Preliminary results on stellar-mass binary black holes*, *Phys. Rev. D* **101** (2020), no. 10 103027, [[arXiv:2004.14242](#)].
- [2460] H.-T. Wang et al., *Science with the TianQin observatory: Preliminary results on massive black hole binaries*, *Phys. Rev. D* **100** (2019), no. 4 043003, [[arXiv:1902.04423](#)].

- [2461] H. Di and Y. Gong, *Primordial black holes and second order gravitational waves from ultra-slow-roll inflation*, *JCAP* **07** (2018) 007, [[arXiv:1707.09578](#)].
- [2462] S. Olmez, V. Mandic, and X. Siemens, *Gravitational-Wave Stochastic Background from Kinks and Cusps on Cosmic Strings*, *Phys. Rev. D* **81** (2010) 104028, [[arXiv:1004.0890](#)].
- [2463] S. Kawamura et al., *The Japanese space gravitational wave antenna: DECIGO*, *Class. Quant. Grav.* **28** (2011) 094011.
- [2464] S. Kawamura et al., *The Japanese space gravitational wave antenna - DECIGO*, *J. Phys. Conf. Ser.* **122** (2008) 012006.
- [2465] S. Kawamura et al., *The Japanese space gravitational wave antenna: DECIGO*, *J. Phys. Conf. Ser.* **120** (2008) 032004.
- [2466] N. Seto, S. Kawamura, and T. Nakamura, *Possibility of direct measurement of the acceleration of the universe using 0.1-Hz band laser interferometer gravitational wave antenna in space*, *Phys. Rev. Lett.* **87** (2001) 221103, [[astro-ph/0108011](#)].
- [2467] S. Kawamura et al., *Current status of space gravitational wave antenna DECIGO and B-DECIGO*, [arXiv:2006.13545](#).
- [2468] S. Sato et al., *The status of DECIGO*, *J. Phys. Conf. Ser.* **840** (2017), no. 1 012010.
- [2469] S. Kawamura et al., *Space gravitational-wave antennas DECIGO and B-DECIGO*, *Int. J. Mod. Phys. D* **28** (2019), no. 12 1845001.
- [2470] A. J. Farmer and E. S. Phinney, *The gravitational wave background from cosmological compact binaries*, *Mon. Not. Roy. Astron. Soc.* **346** (2003) 1197, [[astro-ph/0304393](#)].
- [2471] S. Hild, S. Chelkowski, A. Freise, J. Franc, N. Morgado, R. Flaminio, and R. DeSalvo, *A Xylophone Configuration for a third Generation Gravitational Wave Detector*, *Class. Quant. Grav.* **27** (2010) 015003, [[arXiv:0906.2655](#)].
- [2472] S. Hild et al., *Sensitivity Studies for Third-Generation Gravitational Wave Observatories*, *Class. Quant. Grav.* **28** (2011) 094013, [[arXiv:1012.0908](#)].
- [2473] F. Amann et al., *Site-selection criteria for the Einstein Telescope*, *Rev. Sci. Instrum.* **91** (2020), no. 9 9, [[arXiv:2003.03434](#)].
- [2474] Y.-S. Song and W. J. Percival, *Reconstructing the history of structure formation using Redshift Distortions*, *JCAP* **0910** (2009) 004, [[arXiv:0807.0810](#)].
- [2475] M. Davis, A. Nusser, K. Masters, C. Springob, J. P. Huchra, and G. Lemson, *Local Gravity versus Local Velocity: Solutions for β and nonlinear bias*, *Mon. Not. Roy. Astron. Soc.* **413** (2011) 2906, [[arXiv:1011.3114](#)].
- [2476] M. J. Hudson and S. J. Turnbull, *The growth rate of cosmic structure from peculiar velocities at low and high redshifts*, *The Astrophysical Journal Letters* **751** (2012), no. 2 L30.
- [2477] C.-H. Chuang and Y. Wang, *Modelling the anisotropic two-point galaxy correlation function on small scales and single-probe measurements of $h(z)$, $da(z)$ and $f(z)\sigma_8(z)$ from the sloan digital sky survey dr7 luminous red galaxies*, *Monthly Notices of the Royal Astronomical Society* **435** (2013), no. 1 255–262.
- [2478] C. Blake et al., *Galaxy And Mass Assembly (GAMA): improved cosmic growth measurements using multiple tracers of large-scale structure*, *Mon. Not. Roy. Astron. Soc.* **436** (2013) 3089, [[arXiv:1309.5556](#)].

- [2479] A. G. Sanchez et al., *The clustering of galaxies in the SDSS-III Baryon Oscillation Spectroscopic Survey: cosmological implications of the full shape of the clustering wedges in the data release 10 and 11 galaxy samples*, *Mon. Not. Roy. Astron. Soc.* **440** (2014), no. 3 2692–2713, [[arXiv:1312.4854](#)].
- [2480] **BOSS** Collaboration, L. Anderson et al., *The clustering of galaxies in the SDSS-III Baryon Oscillation Spectroscopic Survey: baryon acoustic oscillations in the Data Releases 10 and 11 Galaxy samples*, *Mon. Not. Roy. Astron. Soc.* **441** (2014), no. 1 24–62, [[arXiv:1312.4877](#)].
- [2481] M. Feix, A. Nusser, and E. Branchini, *Growth Rate of Cosmological Perturbations at $z \approx 0.1$ from a New Observational Test*, *Phys. Rev. Lett.* **115** (2015), no. 1 011301, [[arXiv:1503.05945](#)].
- [2482] **SDSS** Collaboration, M. Tegmark et al., *The 3-D power spectrum of galaxies from the SDSS*, *Astrophys. J.* **606** (2004) 702–740, [[astro-ph/0310725](#)].
- [2483] **WMAP** Collaboration, G. Hinshaw et al., *Nine-Year Wilkinson Microwave Anisotropy Probe (WMAP) Observations: Cosmological Parameter Results*, *Astrophys. J. Suppl.* **208** (2013) 19, [[arXiv:1212.5226](#)].
- [2484] C.-H. Chuang et al., *The clustering of galaxies in the SDSS-III Baryon Oscillation Spectroscopic Survey: single-probe measurements from CMASS anisotropic galaxy clustering*, *Mon. Not. Roy. Astron. Soc.* **461** (2016), no. 4 3781–3793, [[arXiv:1312.4889](#)].
- [2485] **BOSS** Collaboration, F. Beutler et al., *The clustering of galaxies in the completed SDSS-III Baryon Oscillation Spectroscopic Survey: Anisotropic galaxy clustering in Fourier-space*, *Mon. Not. Roy. Astron. Soc.* **466** (2017), no. 2 2242–2260, [[arXiv:1607.03150](#)].
- [2486] M. J. Wilson, *Geometric and growth rate tests of General Relativity with recovered linear cosmological perturbations*. PhD thesis, Edinburgh U., 2016. [[arXiv:1610.08362](#)].
- [2487] A. J. Hawken et al., *The VIMOS Public Extragalactic Redshift Survey: Measuring the growth rate of structure around cosmic voids*, *Astron. Astrophys.* **607** (2017) A54, [[arXiv:1611.07046](#)].
- [2488] D. Huterer, D. Shafer, D. Scolnic, and F. Schmidt, *Testing Λ CDM at the lowest redshifts with SN Ia and galaxy velocities*, *JCAP* **1705** (2017), no. 05 015, [[arXiv:1611.09862](#)].
- [2489] M. Feix, E. Branchini, and A. Nusser, *Speed from light: growth rate and bulk flow at $z \approx 0.1$ from improved SDSS DR13 photometry*, *Mon. Not. Roy. Astron. Soc.* **468** (2017), no. 2 1420–1425, [[arXiv:1612.07809](#)].
- [2490] C. Howlett, L. Staveley-Smith, P. J. Elahi, T. Hong, T. H. Jarrett, D. H. Jones, B. S. Koribalski, L. M. Macri, K. L. Masters, and C. M. Springob, *2MTF VI. Measuring the velocity power spectrum*, *Mon. Not. Roy. Astron. Soc.* **471** (2017) 3135, [[arXiv:1706.05130](#)].
- [2491] F. G. Mohammad et al., *The VIMOS Public Extragalactic Redshift Survey (VIPERS): An unbiased estimate of the growth rate of structure at $\langle z \rangle = 0.85$ using the clustering of luminous blue galaxies*, [[arXiv:1708.00026](#)].
- [2492] Y. Wang, G.-B. Zhao, C.-H. Chuang, M. Pellejero-Ibanez, C. Zhao, F.-S. Kitaura, and S. Rodriguez-Torres, *The clustering of galaxies in the completed SDSS-III Baryon Oscillation Spectroscopic Survey: a tomographic analysis of structure growth and expansion rate from anisotropic galaxy clustering*, [[arXiv:1709.05173](#)].
- [2493] F. Shi et al., *Mapping the Real Space Distributions of Galaxies in SDSS DR7: II. Measuring the growth rate, linear mass variance and biases of galaxies at redshift 0.1*, [[arXiv:1712.04163](#)].

- [2494] H. Gil-Marín et al., *The clustering of the SDSS-IV extended Baryon Oscillation Spectroscopic Survey DR14 quasar sample: structure growth rate measurement from the anisotropic quasar power spectrum in the redshift range $0.8 < z < 2.2$* , *Mon. Not. Roy. Astron. Soc.* **477** (2018), no. 2 1604–1638, [[arXiv:1801.02689](#)].
- [2495] J. Hou et al., *The clustering of the SDSS-IV extended Baryon Oscillation Spectroscopic Survey DR14 quasar sample: anisotropic clustering analysis in configuration-space*, [arXiv:1801.02656](#).
- [2496] G.-B. Zhao et al., *The clustering of the SDSS-IV extended Baryon Oscillation Spectroscopic Survey DR14 quasar sample: a tomographic measurement of cosmic structure growth and expansion rate based on optimal redshift weights*, [arXiv:1801.03043](#).
- [2497] SDSS Collaboration, W. J. Percival et al., *Baryon Acoustic Oscillations in the Sloan Digital Sky Survey Data Release 7 Galaxy Sample*, *Mon. Not. Roy. Astron. Soc.* **401** (2010) 2148–2168, [[arXiv:0907.1660](#)].
- [2498] K. T. Mehta, A. J. Cuesta, X. Xu, D. J. Eisenstein, and N. Padmanabhan, *A 2% Distance to $z = 0.35$ by Reconstructing Baryon Acoustic Oscillations - III : Cosmological Measurements and Interpretation*, *Mon. Not. Roy. Astron. Soc.* **427** (2012) 2168, [[arXiv:1202.0092](#)].
- [2499] BOSS Collaboration, G.-B. Zhao et al., *The clustering of galaxies in the completed SDSS-III Baryon Oscillation Spectroscopic Survey: tomographic BAO analysis of DR12 combined sample in Fourier space*, *Mon. Not. Roy. Astron. Soc.* **466** (2017), no. 1 762–779, [[arXiv:1607.03153](#)].
- [2500] M. Ata et al., *The clustering of the SDSS-IV extended Baryon Oscillation Spectroscopic Survey DR14 quasar sample: first measurement of baryon acoustic oscillations between redshift 0.8 and 2.2*, *Mon. Not. Roy. Astron. Soc.* **473** (2018), no. 4 4773–4794, [[arXiv:1705.06373](#)].
- [2501] J. E. Bautista et al., *The SDSS-IV extended Baryon Oscillation Spectroscopic Survey: Baryon Acoustic Oscillations at redshift of 0.72 with the DR14 Luminous Red Galaxy Sample*, [arXiv:1712.08064](#).
- [2502] C. Zhang, H. Zhang, S. Yuan, T.-J. Zhang, and Y.-C. Sun, *Four new observational $H(z)$ data from luminous red galaxies in the Sloan Digital Sky Survey data release seven*, *Res. Astron. Astrophys.* **14** (2014), no. 10 1221–1233, [[arXiv:1207.4541](#)].
- [2503] J. Simon, L. Verde, and R. Jimenez, *Constraints on the redshift dependence of the dark energy potential*, *Phys. Rev.* **D71** (2005) 123001, [[astro-ph/0412269](#)].
- [2504] E. Gaztanaga, A. Cabre, and L. Hui, *Clustering of Luminous Red Galaxies IV: Baryon Acoustic Peak in the Line-of-Sight Direction and a Direct Measurement of $H(z)$* , *Mon. Not. Roy. Astron. Soc.* **399** (2009) 1663–1680, [[arXiv:0807.3551](#)].
- [2505] A. Oka, S. Saito, T. Nishimichi, A. Taruya, and K. Yamamoto, *Simultaneous constraints on the growth of structure and cosmic expansion from the multipole power spectra of the SDSS DR7 LRG sample*, *Mon. Not. Roy. Astron. Soc.* **439** (2014) 2515–2530, [[arXiv:1310.2820](#)].
- [2506] D. Stern, R. Jimenez, L. Verde, M. Kamionkowski, and S. A. Stanford, *Cosmic Chronometers: Constraining the Equation of State of Dark Energy. I: $H(z)$ Measurements*, *JCAP* **1002** (2010) 008, [[arXiv:0907.3149](#)].
- [2507] L. Anderson et al., *The clustering of galaxies in the SDSS-III Baryon Oscillation Spectroscopic Survey: measuring D_A and H at $z = 0.57$ from the baryon acoustic peak in the Data Release 9 spectroscopic Galaxy sample*, *Mon. Not. Roy. Astron. Soc.* **439** (2014), no. 1 83–101, [[arXiv:1303.4666](#)].

- [2508] M. Moresco, *Raising the bar: new constraints on the Hubble parameter with cosmic chronometers at $z > 2$* , *Mon. Not. Roy. Astron. Soc.* **450** (2015), no. 1 L16–L20, [[arXiv:1503.01116](#)].
- [2509] N. G. Busca et al., *Baryon Acoustic Oscillations in the Ly- α forest of BOSS quasars*, *Astron. Astrophys.* **552** (2013) A96, [[arXiv:1211.2616](#)].
- [2510] S. Nadathur, P. M. Carter, W. J. Percival, H. A. Winther, and J. Bautista, *Beyond BAO: Improving cosmological constraints from BOSS data with measurement of the void-galaxy cross-correlation*, *Phys. Rev.* **D100** (2019), no. 2 023504, [[arXiv:1904.01030](#)].
- [2511] F. Qin, C. Howlett, and L. Staveley-Smith, *The redshift-space momentum power spectrum – II. Measuring the growth rate from the combined 2MTF and 6dFGSv surveys*, *Mon. Not. Roy. Astron. Soc.* **487** (2019), no. 4 5235–5247, [[arXiv:1906.02874](#)].
- [2512] M. Icaza-Lizaola et al., *The clustering of the SDSS-IV extended Baryon Oscillation Spectroscopic Survey DR14 LRG sample: structure growth rate measurement from the anisotropic LRG correlation function in the redshift range $0.6 < z < 1.0$* , [[arXiv:1909.07742](#)].
- [2513] S. Singh, S. Alam, R. Mandelbaum, U. Seljak, S. Rodriguez-Torres, and S. Ho, *Probing gravity with a joint analysis of galaxy and CMB lensing and SDSS spectroscopy*, *Mon. Not. Roy. Astron. Soc.* **482** (2019), no. 1 785–806, [[arXiv:1803.08915](#)].
- [2514] C. Blake et al., *RCSLenS: Testing gravitational physics through the cross-correlation of weak lensing and large-scale structure*, *Mon. Not. Roy. Astron. Soc.* **456** (2016), no. 3 2806–2828, [[arXiv:1507.03086](#)].
- [2515] S. Alam, H. Miyatake, S. More, S. Ho, and R. Mandelbaum, *Testing gravity on large scales by combining weak lensing with galaxy clustering using CFHTLenS and BOSS CMASS*, *Mon. Not. Roy. Astron. Soc.* **465** (2017), no. 4 4853–4865, [[arXiv:1610.09410](#)].
- [2516] E. Jullo et al., *Testing gravity with galaxy-galaxy lensing and redshift-space distortions using CFHT-Stripe 82, CFHTLenS and BOSS CMASS datasets*, *Astron. Astrophys.* **627** (2019) A137, [[arXiv:1903.07160](#)].
- [2517] <https://github.com/FOTEINISKARA/Reconstructing-a-Model-for-Gravity-at-Large-Distances-from-Dark-Matter-Density-Profiles>.
- [2518] <https://github.com/FOTEINISKARA/Primordial-Power-Spectra-of-Cosmological-Fluctuations-with-GUP>.
- [2519] <https://github.com/FOTEINISKARA/Tension-of-the-EG-statistic-and-RSD-data-with-the-LambdaCDM>.
- [2520] <https://github.com/FOTEINISKARA/Scalar-tachyonic-instabilities-in-gravitational-background>.
- [2521] https://github.com/FOTEINISKARA/Cepheid_SnIa_Calibrator_Data_Transition.
- [2522] https://github.com/FOTEINISKARA/Gravitational_transitions_via_the_explicitly_broken_symmetron_screening_mechanism.